

## REPORT DOCUMENTATION PAGE

AFRL-SR-AR-TR-04-

Public reporting burden for this collection of information is estimated to average 1 hour per response, including the time for reviewing instructions, searching existing data sources, gathering the necessary data, reviewing the collection of information, and completing and reviewing the collection of information. Send comments regarding this burden estimate or any other aspect of this collection of information, including suggestions for reducing the burden, to Washington Headquarters Services, Directorate for Information Operations and Reports, 1215 Jefferson Davis Highway, Suite 1204, Arlington, VA 22202-4302, and to the Office of Management and Budget, Paperwork Reduction Project (0102)

1. AGENCY USE ONLY (Leave blank)

2. REPORT DATE

3. REPORT TYPE AND DATES COVERED

01 Jan 2001 - 31 Dec 2001 FINAL

4. TITLE AND SUBTITLE

SYMPOSIUM G: GAN AND RELATED ALLOYS

5. FUNDING NUMBERS

61102F

2305/BX

6. AUTHOR(S)

DR. PACHAVIS

7. PERFORMING ORGANIZATION NAME(S) AND ADDRESS(ES)

MATERIALS RESEARCH SOCIETY

506 KEYSTONE DRIVE

WARRENDALE PA 15086-7573

8. PERFORMING ORGANIZATION  
REPORT NUMBER

9. SPONSORING/MONITORING AGENCY NAME(S) AND ADDRESS(ES)

AFOSR/NE

4015 WILSON BLVD

SUITE 713

ARLINGTON VA 22203

10. SPONSORING/MONITORING  
AGENCY REPORT NUMBER

F49620-01-1-0121

11. SUPPLEMENTARY NOTES

12a. DISTRIBUTION AVAILABILITY STATEMENT

DISTRIBUTION STATEMENT A. Distribution unlimited

12b. DISTRIBUTION CODE

13. ABSTRACT (Maximum 200 words)

A symposium entitled "GaN and Related Alloys - 2002" was held in connection with the Materials Research Society Fall Meeting, December 2002. The symposium organizers included Christian Wetzel (Tampa, FL), Edward Yu (La Jolla, CA), James Speck (Santa Barbara, CA), Angela Rizzi (Jülich, Germany) and Yasuhiko Arakawa (Tokyo, Japan). Symposium sessions were held over all five days of the general meeting. Session attendance was uniformly high. A selected and edited group of the total symposium papers are included in this volume.

20040303 208

14. SUBJECT TERMS

GAN and Related Alloys

15. NUMBER OF PAGES

16. PRICE CODE

17. SECURITY CLASSIFICATION  
OF REPORT

Unclassified

18. SECURITY CLASSIFICATION  
OF THIS PAGE

Unclassified

19. SECURITY CLASSIFICATION  
OF ABSTRACT

Unclassified

20. LIMITATION OF ABSTRACT

UL

Standard Form 298 (Rev. 2-89) (EG)  
Prescribed by ANSI Std. Z39.18  
Designed using Perform Pro, WHS/DIOR, Oct 94

## **GaN and Related Alloys—2002**

---

**MATERIALS RESEARCH SOCIETY  
SYMPOSIUM PROCEEDINGS VOLUME 743**

---

# **GaN and Related Alloys—2002**

Symposium held December 2–6, 2002, Boston, Massachusetts, U.S.A.

**EDITORS:**

**Christian Wetzel**

Uniroyal Optoelectronics  
Tampa, Florida, U.S.A.

**Edward T. Yu**

University of California-San Diego  
La Jolla, California, U.S.A.

**James S. Speck**

University of California-Santa Barbara  
Santa Barbara, California, U.S.A.

**Angela Rizzi**

Forschungszentrum Jülich  
Jülich, Germany  
and  
Georg-August-Universität  
Göttingen, Germany

**Yasuhiko Arakawa**

University of Tokyo  
Tokyo, Japan



**Materials Research Society**  
Warrendale, Pennsylvania

**DISTRIBUTION STATEMENT A**  
Approved for Public Release  
Distribution Unlimited

Effort sponsored by the Air Force Office of Scientific Research, Air Force Material Command, USAF, under F49620-02-1-0418. The U.S. Government is authorized to reproduce and distribute reprints for Governmental purposes notwithstanding any copyright notation thereon. The views and conclusions herein are those of the authors and should not be interpreted as necessarily representing the official policies or endorsements, either expressed or implied, of the Air Force Office of Scientific Research or the U.S. Government.

This work was supported in part by the Office of Naval Research under Grant Number N00014-02-1-0882. The United States Government has a royalty-free license throughout the world in all copyrightable material contained herein.

Single article reprints from this publication are available through  
University Microfilms Inc., 300 North Zeeb Road, Ann Arbor, Michigan 48106

CODEN: MRSPDH

Copyright 2003 by Materials Research Society.  
All rights reserved.

This book has been registered with Copyright Clearance Center, Inc. For further information, please contact the Copyright Clearance Center, Salem, Massachusetts.

Published by:

Materials Research Society  
506 Keystone Drive  
Warrendale, PA 15086  
Telephone (724) 779-3003  
Fax (724) 779-8313  
Web site: <http://www.mrs.org/>

Manufactured in the United States of America

---

## CONTENTS

Preface.....	xxi
Materials Research Society Symposium Proceedings.....	xxii

### *EPITAXY—DEVICES AND DEFECT REDUCTION*

Large-Area, Device Quality GaN on Si Using a Novel Transition Layer Scheme.....	3
Pradeep Rajagopal, Thomas Gehrke, John C. Roberts, J.D. Brown, T. Warren Weeks, Edwin L. Piner, and Kevin J. Linthicum	
III-Nitride Growth on Lithium Niobate: A New Substrate Material for Polarity Engineering in III-Nitride Heteroepitaxy.....	9
W. Alan Doolittle, Gon Namkoong, Alexander Carver, Walter Henderson, Dieter Jundt, and April S. Brown	
Cantilever Epitaxy of GaN on Sapphire: Further Reductions in Dislocation Density .....	15
D.M. Follstaedt, P.P. Provencio, D.D. Koleske, C.C. Mitchell, A.A. Allerman, N.A. Missert, and C.I.H. Ashby	
Lateral Growth of $\text{Al}_x\text{Ga}_{1-x}\text{N}$ and GaN on SiC Substrates Patterned by Photo-Electrochemical Etching.....	21
U. Rossow, N. Riedel, F. Hitzel, T. Riedl, and A. Hangleiter	
Distinct Magnesium Incorporation Behavior in Laterally Grown AlGaIn .....	27
R. Liu, A. Bell, F.A. Ponce, D. Cherns, H. Amano, and I. Akasaki	

### *DEFECTS AND CHARACTERIZATION*

Distinguishing Negatively-Charged and Highly Conductive Dislocations in Gallium Nitride Using Scanning Kelvin Probe and Conductive Atomic Force Microscopy .....	35
Blake S. Simpkins, Edward T. Yu, Patrick Waltereit, and James S. Speck	
The Effect of Growth Stoichiometry on the GaN Dislocation Core Structure.....	41
Marcus Q. Baines, David Cherns, Julia W.P. Hsu, and Michael J. Manfra	

<b>* Properties of Surface States on GaN and Related Compounds and Their Passivation by Dielectric Films.....</b>	<b>47</b>
Hideki Hasegawa and Tamotsu Hashizume	

### *POSTER SESSION*

<b>Searching for the Influence of the Sapphire Nitridation Conditions on GaN Films Grown by Cyclic PLD.....</b>	<b>61</b>
P. Sanguino, M. Niehus, S. Koynov, L. Melo, R. Schwarz, M.J. Soares, C. Boemare, and T. Monteiro	

<b>Study on Chemical Treatment and High Temperature Nitridation of Sapphire for III-Nitride Heteroepitaxial Growth .....</b>	<b>67</b>
F. Dwikusuma, D. Saulys, and T.F. Kuech	

<b>Ion Beam Study of Early Stages of Growth of GaN Films on Sapphire .....</b>	<b>73</b>
Eugen M. Trifan and David C. Ingram	

<b>Low-Temperature Laser-Assisted Gas Phase Reactivity of TMGa with NH<sub>3</sub> and Oxygen-Containing Compounds (H<sub>2</sub>O, CH<sub>3</sub>OH, O(CH<sub>3</sub>)<sub>2</sub>) in Constrained Pulsed Expansions.....</b>	<b>79</b>
Alexander Demchuk, Michael Lynch, Steven Simpson, and Brent Koplitz	

<b>High-Mobility Ga-Polarity GaN Achieved by NH<sub>3</sub>-MBE .....</b>	<b>85</b>
J.X. Wang, X.L. Wang, D.Z. Sun, J.M. Li, Y.P. Zeng, G.X. Hu, H.X. Liu, and L.Y. Lin	

<b>Phase Transitions on GaN Surfaces .....</b>	<b>91</b>
C. Adelmann, L. Lymperakis, J. Brault, G. Mula, J. Neugebauer, and B. Daudin	

<b>Nitrogen Gas-Cluster Ion Beam—A New Nitrogen Source for GaN Growth .....</b>	<b>97</b>
Y. Shao, T.C. Chen, D.B. Fenner, T.D. Moustakas, and George Chu	

<b>Growth of Oriented Gallium Nitride Films on Amorphous Substrates by Self Assembly.....</b>	<b>103</b>
Hongwei Li and Mahendra K. Sunkara	

\*Invited Paper

---

<b>Raman Mapping and Finite Element Analysis of Epitaxial Lateral Overgrown GaN on Sapphire Substrates .....</b>	<b>109</b>
M. Benyoucef, M. Kuball, B. Beaumont, V. Bousquet, and P. Gibart	
<b>Characterization of Dark-Block Defects in Cantilever Epitaxial GaN on Sapphire.....</b>	<b>115</b>
P.P. Provencio, D.M. Follstaedt, N.A. Missert, D.D. Koleske, C.C. Mitchell, A.A. Allerman, and C.I.H. Ashby	
<b>Study of the Origin of Misorientation in GaN Grown by Pendeo-Epitaxy .....</b>	<b>121</b>
D.N. Zakharov, Z. Liliental-Weber, A.M. Roskowski, S. Einfeldt, and R.F. Davis	
<b>Effect of Growth Temperature on the Microstructure of the Nucleation Layers of GaN Grown by MOCVD on (1120) Sapphire .....</b>	<b>127</b>
T. Wojtowicz, P. Ruterana, M.E. Twigg, R.L. Henry, D.D. Koleske, and A.E. Wickenden	
<b>Growth and Characterization of Non-Polar (11-20) GaN and AlGaIn/GaN MQWs on R-Plane (10-12) Sapphire.....</b>	<b>133</b>
Sandeep Iyer, David J. Smith, A. Bhattacharyya, K. Ludwig Jr., and T.D. Moustakas	
<b>Epitaxial Growth of AlN on 6H-SiC (1120) by Molecular-Beam Epitaxy and Effect of Low-Temperature Buffer Layer.....</b>	<b>139</b>
N. Onojima, J. Suda, and H. Matsunami	
<b>Electrical Properties of GaN/Si Grown by MOCVD .....</b>	<b>145</b>
Seikoh Yoshida, Jiang Li, Takahiro Wada, and Hironari Takehara	
<b>Studies on Epitaxial Relationship and Interface Structure of AlN/Si(111) and GaN/Si(111) Heterostructures .....</b>	<b>151</b>
T.A. Rawdanowicz, H. Wang, A. Kvit, and J. Narayan	
<b>Correlation Between the AlN Buffer Layer Thickness and the GaN Polarity in GaN/AlN/Si(111) Grown by MBE .....</b>	<b>157</b>
A.M. Sanchez, P. Ruterana, P. Vennegues, F. Semond, F.J. Pacheco, S.I. Molina, R. Garcia, M.A. Sanchez-Garcia, and E. Calleja	

<b>Single Crystalline InN Films Grown on Si Substrates by Using a Brief Substrate Nitridation Process .....</b>	<b>163</b>
Tomohiro Yamaguchi, Kazuhiro Mizuo, Yoshiki Saito, Takuma Noguchi, Tsutomu Araki, Yasushi Nanishi, Takao Miyajima, and Yoshihiro Kudo	
<b>Study on Cubic GaN Growth on (001) Rutile TiO<sub>2</sub> Substrates by ECR-MBE .....</b>	<b>169</b>
T. Araki, H. Mamiya, K. Kitamura, and Y. Nanishi	
<b>Characterization of Cubic GaN Films Using an AlN/GaN Ordered Alloy on GaAs (100) by RF-MBE .....</b>	<b>175</b>
Junichi Shike, Atsushi Shigemori, Koichi Ishida, Kiyoshi Takahashi, and Ryuhei Kimura	
<b>Aluminum Nitride Crystal Growth by Halide Vapor Transport Epitaxy .....</b>	<b>181</b>
V.L. Tassev, D.F. Bliss, D. Weyburne, J.S. Bailey, and S.-Q. Wang	
<b>Experimental and Theoretical Analysis of Heat and Mass Transport in the System for AlN Bulk Crystal Growth .....</b>	<b>187</b>
M.V. Bogdanov, S.Yu. Karpov, A.V. Kulik, M.S. Ramm, Yu.N. Makarov, R. Schlessner, R.F. Dalmau, and Z. Sitar	
<b>The Influence of Substrate Surface Polarity on Optical Properties of GaN Grown on Single Crystal Bulk AlN .....</b>	<b>193</b>
G. Tamulaitis, I. Yilmaz, M.S. Shur, R. Gaska, C. Chen, J. Yang, E. Kuokstis, A. Khan, J.C. Rojo, and L.J. Schowalter	
<b>Optical Characterization of Bulk GaN Grown From a Na/Ga Flux .....</b>	<b>201</b>
K. Palle, L. Chen, H.X. Liu, B.J. Skromme, H. Yamane, M. Aoki, C.B. Hoffman, and F.J. DiSalvo	
<b>Background Impurity Reduction and Iron Doping of Gallium Nitride Wafers.....</b>	<b>207</b>
Robert P. Vaudo, Xueping Xu, Allan D. Salant, Joseph A. Malcarne, Edward L. Hutchins, and George R. Brandes	
<b>Low-Electron-Energy Cathodoluminescence Study of Polishing and Etching Effects on the Optical Properties of Bulk Single-Crystal Gallium Nitride .....</b>	<b>213</b>
Lawrence H. Robins, Bruce Steiner, Norman A. Sanford, and Carmen Menoni	

<b>Production of Sapphire Blanks and Substrates for Blue LEDs and LDs .....</b>	<b>219</b>
Chandra P. Khattak, Frederick Schmid, Paul J. Guggenheim, Maynard B. Smith, Henry H. Rogers, and Kurt Schmid	
<b>Transport and Chemical Mechanisms in GaN Hydride Vapor Phase Epitaxy .....</b>	<b>225</b>
Sergey Yu. Karpov, Alexander S. Segal, Darya V. Zimina, Sergey A. Smirnov, Alexander P. Sid'ko, Alexey V. Kondratyev, Yuri N. Makarov, Denis Martin, Volker Wagner, and Marc Illegems	
<b>Lattice Constant Variation in GaN:Si Layers Grown by HVPE .....</b>	<b>231</b>
A. Usikov, O.V. Kovalenkov, M.M. Mastro, D.V. Tsvetkov, A.I. Pechnikov, V.A. Soukhoveev, Y.V. Shapovalova, and G.H. Gainer	
<b>Theoretical Analysis of &lt;0001&gt; Tilt Grain Boundaries in GaN at the Atomic Scale .....</b>	<b>237</b>
Jun Chen, Pierre Ruterana, and Gérard Nouet	
<b>Screw Dislocations in MBE GaN Layers Grown on Top of HVPE Layers: Are They Different?.....</b>	<b>243</b>
Z. Liliental-Weber, D. Zakharov, J. Jasinski, J. Washburn, M.A. O'Keefe, and H. Morkoç	
<b>Photoreflectance Probing of Below Gap States in GaN/AlGaIn High Electron Mobility Transistor Structures .....</b>	<b>249</b>
D.K. Gaskill, O.J. Glembocki, B. Peres, R. Henry, D. Koleske, and A. Wickenden	
<b>Compositional Fluctuations in Al<sub>x</sub>Ga<sub>1-x</sub>N Layers Grown on 6H-SiC (0001) by Metal Organic Vapor Phase Epitaxy.....</b>	<b>255</b>
R. Kröger, S. Einfeldt, Z.J. Reitmeier, R. Chierchia, P. Ryder, D. Hommel, and R.F. Davis	
<b>High-Spatial-Resolution Cathodoluminescence Measurement of InGaIn.....</b>	<b>261</b>
Hisashi Kanie, Hiroaki Okado, and Takaya Yoshimura	
<b>Comparisons of Gallium Nitride and Indium Nitride Properties After CF<sub>4</sub>/Argon Reactive Ion Etching.....</b>	<b>267</b>
Marie Wintrebert-Fouquet, K. Scott A. Butcher, and Simon K.H. Lam	

<b>Photoreflectance Characterization and Control of Defects in GaN by Etching With an Inductively Coupled Plasma .....</b>	<b>273</b>
O.J. Glembocki, D.K. Gaskill, S.M. Prokes, and S.W. Pearton	

<b>Electroreflectance and Photoreflectance Studies of Electric Fields in Pt/GaN Schottky Diodes and AlGaIn/GaN Heterostructures .....</b>	<b>279</b>
S. Shokhovets, R. Goldhahn, G. Gobsch, O. Ambacher, I.P. Smorchkova, J.S. Speck, U. Mishra, A. Link, M. Hermann, and M. Eickhoff	

<b>Effect of Oxygen Pressure on Magnesium Oxide Dielectrics Grown on GaN by Plasma Assisted Gas Source Molecular Beam Epitaxy .....</b>	<b>285</b>
A.H. Onstine, B.P. Gila, J. Kim, D. Stodilka, K. Allums, C.R. Abernathy, F. Ren, and S.J. Pearton	

### ***EPITAXY—NONPOLAR ORIENTATIONS AND ALLOYS***

<b>Morphology and Surface Reconstructions of m-Plane GaN.....</b>	<b>293</b>
C.D. Lee, R.M. Feenstra, J.E. Northrup, L. Lymperakis, and J. Neugebauer	

<b>GaN Epilayers and AlGaIn/GaN Multiple Quantum Wells Grown on Freestanding [1100] Oriented GaN Substrates .....</b>	<b>299</b>
C.Q. Chen, M.E. Gaevski, W.H. Sun, E. Kuokstis, J.W. Yang, G. Simin, M.A. Khan, H.P. Maruska, D.W. Hill, M.M.C. Chou, J.J. Gallagher, B.H. Chai, J.H. Song, M.Y. Ryu, and P.W. Yu	

<b>Growth of Quaternary AlInGaIn/GaN Heterostructures by Plasma Assisted MBE.....</b>	<b>305</b>
E. Monroy, N. Gogneau, D. Jalabert, F. Enjalbert, E. Bellet-Amalric, Y. Hori, Le Si Dang, and B. Daudin	

<b>Lattice Relaxation of AlN Buffer on Surface-Treated SiC in Molecular-Beam Epitaxy for Growth of High-Quality GaN.....</b>	<b>311</b>
Jun Suda, Kouhei Miura, Misako Honaga, Norio Onojima, Yusuke Nishi, and Hiroyuki Matsunami	

<b>Growth of Thick InN by Molecular Beam Epitaxy.....</b>	<b>317</b>
Hai Lu, William J. Schaff, Lester F. Eastman, J. Wu, Wladek Walukiewicz, David C. Look, and Richard J. Molnar	

<b>Optical Characterization of High Quality GaN Produced by High Rate Magnetron Sputter Epitaxy.....</b>	<b>323</b>
Minseo Park, E. Carlson, Y.C. Chang, J.F. Muth, J. Bumgarner, R.M. Kolbas, J.J. Cuomo, and R.J. Nemanich	

### ***OPTICAL PROPERTIES***

<b>Role of Polarization in the Photoluminescence of C- and M-Plane Oriented GaN/AlGaIn Multiple Quantum Wells.....</b>	<b>331</b>
E. Kuokstis, C.Q. Chen, M.E. Gaevski, W.H. Sun, J.W. Yang, G. Simin, M. Asif Khan, H.P. Maruska, D.W. Hill, M.M.C. Chou, J.J. Gallagher, and B.H. Chai	

<b>Cathodoluminescence of MBE-Grown Cubic AlGaIn/GaN Multi-Quantum Wells on GaAs (001) Substrates.....</b>	<b>337</b>
D.J. As, S. Potthast, U. Köhler, A. Khartchenko, and K. Lischka	

<b>Microscopic Description of Radiative Recombinations in InGaIn/GaN Quantum Systems.....</b>	<b>343</b>
Aurelien Morel, Pierre Lefebvre, Thierry Taliercio, Bernard Gil, Nicolas Grandjean, Benjamin Damilano, and Jean Massies	

<b>Subpicosecond Luminescence Studies of Carrier Dynamics in Nitride Semiconductors Grown Homoepitaxially by MBE on GaN Templates.....</b>	<b>349</b>
G.A. Garrett, A.V. Sampath, C.J. Collins, F. Semendy, K. Aliberti, H. Shen, M. Wraback, Y. Fedyunin, and T.D. Moustakas	

<b>Deep Donor-Acceptor Pair Luminescence in Codoped GaN.....</b>	<b>355</b>
Bing Han, Joel M. Gregie, Melville P. Ulmer, and Bruce W. Wessels	

<b>Dielectric Function of "Narrow" Band Gap InN .....</b>	<b>361</b>
R. Goldhahn, S. Shokhovets, V. Cimalla, L. Spiess, G. Ecke, O. Ambacher, J. Furthmüller, F. Bechstedt, H. Lu, and W.J. Schaff	

## **POSTER SESSION**

<b>In as a Surfactant for the Growth of AlGa<sub>N</sub>/Ga<sub>N</sub> Heterostructures by Plasma Assisted MBE .....</b>	<b>369</b>
E. Monroy, N. Gogneau, E. Bellet-Amalric, F. Enjalbert, J. Barjon, D. Jalabert, J. Brault, Le Si Dang, and B. Daudin	
<b>Molecular Beam Epitaxial Growth of AlN/GaN Multiple Quantum Wells .....</b>	<b>375</b>
Hong Wu, William J. Schaff, Goutam Koley, Madalina Furis, A.N. Cartwright, Karen A. Mkhoyan, John Silcox, Walter Henderson, W. Alan Doolittle, and A.V. Osinsky	
<b>Evolution of Subgrain Boundaries in Heteroepitaxial Ga<sub>N</sub>/AlN/6H-SiC Grown by Metalorganic Chemical Vapor Deposition .....</b>	<b>381</b>
H.X. Liu, G.N. Ali, K.C. Palle, M.K. Mikhov, B.J. Skromme, Z.J. Reitmeyer, and R.F. Davis	
<b>Segregation Effects and Bandgap Engineering in InGa<sub>N</sub> Quantum-Well Heterostructures.....</b>	<b>387</b>
Kirill A. Bulashevich, Sergey Yu. Karpov, Roman A. Talalaev, Igor Yu. Evstratov, and Yuri N. Makarov	
<b>Indium Distribution Inside Quantum Wells: The Effect of Growth Interruption in MBE .....</b>	<b>393</b>
A.M. Sanchez, P. Ruterana, S. Kret, P. Dluzewski, G. Maciejewski, N. Grandjean, and B. Damilano	
<b>Thermoelectric Properties of III-Nitrides and III-Oxynitrides Prepared by Reactive RF-Sputtering: Targetting a Thermopower Device .....</b>	<b>399</b>
S. Yamaguchi, Y. Iwamura, and A. Yamamoto	
<b>X-ray Diffraction Analysis of Ga<sub>N</sub> and AlGa<sub>N</sub>.....</b>	<b>405</b>
H. Kang, N. Spencer, D. Nicol, Z.C. Feng, I. Ferguson, S.P. Guo, M. Pophristic, and B. Peres	
<b>Electron Microprobe and Photoluminescence Analysis of Europium-Doped Gallium Nitride Light Emitters .....</b>	<b>411</b>
R.W. Martin, S. Dalmaso, K.P. O'Donnell, Y. Nakanishi, A. Wakahara, A. Yoshida, and the RENiBEI Network	

<b>Lattice Location and Cathodoluminescence Studies of Ytterbium/Thulium Implanted 2H-Aluminium Nitride.....</b>	<b>417</b>
U. Vetter, M.F. Reid, H. Hofsäss, C. Ronning, J. Zenneck, M. Dietrich, and ISOLDE Collaboration	
<b>The Properties of a P-Implanted GaN Light-Emitting Diode .....</b>	<b>423</b>
J. Kikawa, S. Yoshida, and Y. Itoh	
<b>Effect of Thickness Variation in High-Efficiency InGaN/GaN Light Emitting Diodes .....</b>	<b>427</b>
J. Narayan, H. Wang, Jinlin Ye, Schang-Jing Hon, Kenneth Fox, Jyh Chia Chen, H.K. Choi, and John C.C. Fan	
<b>Efficient GaN-Based Micro-LED Arrays .....</b>	<b>433</b>
H.W. Choi, C.W. Jeon, M.D. Dawson, P.R. Edwards, and R.W. Martin	
<b>Growth and Characterization of Deep UV Emitter Structures Grown on Single Crystal Bulk AlN Substrates.....</b>	<b>439</b>
X. Hu, R. Gaska, C. Chen, J. Yang, E. Kuokstis, A. Khan, G. Tamulaitis, I. Yilmaz, M.S. Shur, J.C. Rojo, and L.J. Schowalter	
<b>Deposition of GaN Films on Glass Substrate and Its Application to UV Electroluminescent Devices .....</b>	<b>445</b>
Tohru Honda, Kenichi Iga, Hideo Kawanishi, Takahiro Sakaguchi, and Fumio Koyama	
<b>Growth and Fabrication of High Reverse Breakdown Heterojunction n-GaN: p- 6H-SiC Diodes.....</b>	<b>449</b>
A.V. Sampath, A. Bhattacharyya, R. Singh, C.R. Eddy, P. Lamarre, W.F. Stacey, R.S. Morris, and T.D. Moustakas	
<b>Properties of Surface Acoustic Waves in AlN and GaN.....</b>	<b>455</b>
Jianyu Deng, Daumantas Ciplys, Gang Bu, Michael Shur, and Remis Gaska	
<b>Surface Acoustic Wave Resonator From Thick MOVPE-Grown Layers of GaN(0001) on Sapphire.....</b>	<b>461</b>
Sverre V. Pettersen, Thomas Tybell, Arne Rønnekleiv, Stig Rooth, Veit Schwegler, and Jostein K. Grepstad	

#### ***UV EMITTERS AND DETECTORS***

<b>A GaN-Free LED Structure for High UV-Light Extraction.....</b>	<b>469</b>
Toshio Nishida, Tomoyuki Ban, and Naoki Kobayashi	

<b>Room and Cryogenic Temperature Operation of 280 nm Deep Ultraviolet Light Emitting Diodes .....</b>	<b>475</b>
Maxim Shatalov, Vinod Adivarahan, Jian Ping Zhang, Ashay Chitnis, Shuai Wu, Radhika Pachipulusu, Vasavi Mandavilli, and M. Asif Khan	
<b>New UV Light Emitter Based on AlGaIn Heterostructures With Graded Electron and Hole Injectors .....</b>	<b>481</b>
M.A.L. Johnson, J.P. Long, and J.F. Schetzina	
<b>High Power 325 Light Emitting Diode Arrays by Flip-Chip Packaging.....</b>	<b>487</b>
Ashay Chitnis, Maxim Shatalov, Vinod Adivarahan, Jian Ping Zhang, Shuai Wu, Jie Sun, and M. Asif Khan	
<b>Micro-Raman Spectroscopy: Self-Heating Effects in Deep UV Light Emitting Diodes .....</b>	<b>493</b>
A. Sarua, M. Kuball, M.J. Uren, A. Chitnis, J.P. Zhang, V. Adivarahan, M. Shatalov, and M. Asif Khan	
<b>Epitaxial Growth for Solar-Blind AlGaIn Photodetector Imaging Arrays by Metalorganic Chemical Vapor Deposition.....</b>	<b>499</b>
Uttiya Chowdhury, Charles J. Collins, Michael M. Wong, Ting Gang Zhu, Jonathan C. Denyszyn, Jin Ho Choi, Bo Yang, Joe C. Campbell, and Russell D. Dupuis	
<b>Crack Nucleation in AlGaIn/GaN Heterostructures .....</b>	<b>505</b>
Peter J. Parbrook, Malcolm A. Whitehead, Richard J. Lynch, and Robert T. Murray	
<b>Solar-Blind AlGaIn-Based Schottky Photodiodes With High Detectivity and Low Noise .....</b>	<b>511</b>
Necmi Biyikli, Orhan Aytur, Ibrahim Kimukin, Turgut Tut, and Ekmel Ozbay	

### ***VISIBLE LIGHT EMITTERS***

<b>Formation of Quantum Dots by Self-Rearrangement of Metastable 2D GaN .....</b>	<b>519</b>
N. Gogneau, D. Jalabert, E. Monroy, C. Adelmann, and B. Daudin	

---

## ***ELECTRONIC DEVICES***

<b>* Material and Device Issues of AlGaIn/GaN HEMTs on Silicon Substrates.....</b>	<b>527</b>
P. Javorka, A. Alam, M. Marso, M. Wolter, A. Fox, M. Heuken, and P. Kordos	
<b>AlGaIn/GaN Heterostructure Field-Effect Transistors With Back-Doping Design for High-Power Applications: High Current Density With High Transconductance Characteristics.....</b>	<b>537</b>
Narihiko Maeda, Kotaro Tsubaki, Tadashi Saitoh, Takehiko Tawara, and Naoki Kobayashi	
<b>High-Quality AlGaIn/GaN HFET Structures Grown by MOCVD Using Intermediate High Temperature AlGaIn/GaN Superlattices .....</b>	<b>543</b>
Alexander Demchuk, Don Olson, Minseub Shin, Dan Olson, Peter Nussbaum, Andy Strom, Simon Bates, Frank Hofmann, and Gordon Munns	
<b>High Performance HFET Devices on Sapphire and SiC: Passivation With AlN .....</b>	<b>549</b>
Jennifer A. Bardwell, Ying Liu, James B. Webb, Haipeng Tang, Stephen J. Rolfe, and Jean Lapointe	
<b>Self-Heating Effects in Multi-Finger AlGaIn/GaN HFETs .....</b>	<b>555</b>
M. Kuball, S. Rajasingam, A. Sarua, M.J. Uren, T. Martin, R.S. Balmer, and K.P. Hilton	
<b>Gate Current Modeling for Insulating Gate III-N Heterostructure Field-Effect Transistors.....</b>	<b>561</b>
Frederick W. Clarke, Fat Duen Ho, M. Asif Khan, Grigory Simin, J. Yang, Remis Gaska, Michael S. Shur, Jianyu Deng, and S. Karmalkar	
<b>AlGaIn/GaN Metal-Oxide-Semiconductor Heterostructure Field-Effect Transistors (MOSHFETs) With the Delta-Doped Barrier Layer .....</b>	<b>567</b>
Z.Y. Fan, J. Li, J.Y. Lin, H.X. Jiang, Y. Liu, J.A. Bardwell, J.B. Webb, and H. Tang	

\*Invited Paper

**CHARACTERIZATION OF  
DEFECTS AND TRANSPORT**

<b>* Electrical, Optical, Structural, and Analytical Properties of Very Pure GaN.....</b>	<b>575</b>
D.C. Look, J.R. Sizelove, J. Jasinski, Z. Liliental-Weber, K. Saarinen, S.S. Park, and J.H. Han	
<b>Observations of Electron Velocity Overshoot During High-Field Transport in AlN.....</b>	<b>591</b>
Ramón Collazo, Raoul Schlessler, Amy Roskowski, Robert F. Davis, and Z. Sitar	
<b>Determination of AlGaIn/GaN HFET Electric Fields Using Electroreflectance .....</b>	<b>597</b>
S.R. Kurtz, A.A. Allerman, D.D. Koleske, A.G. Baca, and R.D. Briggs	
<b>Optical and Electrical Properties of Semi-Insulating GaN:C Grown by MBE .....</b>	<b>603</b>
R. Armitage, Qing Yang, H. Feick, S.Y. Tzeng, J. Lim, and E.R. Weber	
<b>Hollow Core Dislocations in Mg-Doped AlGaIn .....</b>	<b>609</b>
D. Cherns, Y.Q. Wang, R. Liu, F.A. Ponce, H. Amano, and I. Akasaki	
<b>Development of a High Lateral Resolution Electron Beam Induced Current Technique for Electrical Characterization of InGaIn-Based Quantum Well Light Emitting Diodes .....</b>	<b>615</b>
Kristin L. Bunker, Juan Carlos Gonzalez, Dale Batchelor, Terrence J. Stark, and Phillip E. Russell	
<b>X-ray Spectroscopic Studies of the Bulk Electronic Structure of InGaIn Alloys.....</b>	<b>621</b>
Cornac McGuinness, James E. Downes, Philip Ryan, Kevin E. Smith, Dharanipal Doppalapudi, and Theodore D. Moustakas	

**POSTER SESSION**

<b>Blue Luminescence in Undoped and Zn-Doped GaN .....</b>	<b>629</b>
M.A. Reshchikov, H. Morkoç, R.J. Molnar, D. Tsvetkov, and V. Dmitriev	

\*Invited Paper

---

<b>Surface-Related Photoluminescence Effects in GaN.....</b>	<b>635</b>
M.A. Reshchikov, M. Zafar Iqbal, D. Huang, L. He, and H. Morkoç	
<b>Excitons Bound to Surface Defects in GaN .....</b>	<b>641</b>
M.A. Reshchikov, D. Huang, and H. Morkoç	
<b>Tunnel Radiation in the Luminescence Spectra of GaN-Based Heterostructures .....</b>	<b>647</b>
A.E. Yunovich, V.E. Kudryashov, A.N. Turkin, M. Leroux, and S. Dalmaso	
<b>Self-Induced Photon Absorption by Screening of the Electric Fields in Nitride-Based Quantum Wells .....</b>	<b>653</b>
S. Kalliakos, P. Lefebvre, T. Taliercio, and B. Gil	
<b>Time Resolved Optical Studies of InGaN Layers Grown on LGO .....</b>	<b>659</b>
Maurice Cheung, Gon Namkoong, Madalina Furis, Fei Chen, Alexander N. Cartwright, W. Alan Doolittle, and April Brown	
<b>Femtosecond Pump and Probe Spectroscopy of Optical Nonlinearities in an InGaN/GaN Heterostructure .....</b>	<b>665</b>
Fei Chen and A.N. Cartwright	
<b>Excitons of the Structure in Zinc-Blende <math>\text{In}_x\text{Ga}_{1-x}\text{N}</math> and Their Properties .....</b>	<b>671</b>
Dimitre Alexandrov	
<b>Simultaneous TEM and Cathodoluminescence Imaging of Non-Uniformity in <math>\text{In}_{0.1}\text{Ga}_{0.9}\text{N}</math> Quantum Wells.....</b>	<b>677</b>
Nicholas M. Boyall, Ken Durose, and Ian M. Watson	
<b>An In Situ TEM-Cathodoluminescence Study of Electron Beam Degradation of Luminescence From GaN and <math>\text{In}_{0.1}\text{Ga}_{0.9}\text{N}</math> Quantum Wells .....</b>	<b>683</b>
Nicholas M. Boyall, Ken Durose, and Ian M. Watson	
<b>Room-Temperature Time-Resolved Photoluminescence Studies of UV Emission From GaN/AlN Quantum Wells.....</b>	<b>689</b>
Madalina Furis, Fei Chen, Alexander N. Cartwright, Hong Wu, and William J. Schaff	

<b>Measurements of the Refractive Indices of MOCVD and HVPE Grown AlGa<sub>N</sub> Films Using Prism-Coupling Techniques Correlated With Spectroscopic Reflection/Transmission Analysis .....</b>	<b>695</b>
Norman A. Sanford, Lawrence H. Robins, Albert V. Davydov, Alexander J. Shapiro, Denis V. Tsvetkov, Vladimir A. Dmitriev, Stacia Keller, Umesh K. Mishra, and Steven P. DenBaars	
<b>Optical Band Gap Measurements of InN Films in the Strong Degeneracy Limit.....</b>	<b>701</b>
D.B. Haddad, J.S. Thakur, V.M. Naik, G.W. Auner, R. Naik, and L.E. Wenger	
<b>A Study of Indium Nitride Films Grown Under Conditions Resulting in Apparent Band Gaps From 0.7 eV to 2.3 eV .....</b>	<b>707</b>
K.S.A. Butcher, M. Wintrebert-Fouquet, Motlan, S.K. Shrestha, H. Timmers, K.E. Prince, and T.L. Tansley	
<b>Effect of Pressure on the Energy Band Gaps of In<sub>x</sub>Ga<sub>1-x</sub>N and In<sub>x</sub>Al<sub>1-x</sub>N .....</b>	<b>713</b>
Z. Dridi, B. Bouhafs, and P. Ruterana	
<b>Electrical and Optical Properties of InN/Si Heterostructure .....</b>	<b>719</b>
K. Mizuo, T. Yamaguchi, Y. Saito, T. Araki, and Y. Nanishi	
<b>Optical Properties of Controllable Self-Assembled Lateral Nanostructures on InN, InAlN, and AlN Thin Films.....</b>	<b>725</b>
Yuri Danylyuk, Dmitri Romanov, Eric McCullen, Daad Haddad, Ratna Naik, and Gregory Auner	
<b>A Study of the Decomposition of GaN During Annealing Over a Wide Range of Temperatures .....</b>	<b>731</b>
M.A. Rana, H.W. Choi, M.B.H. Breese, T. Osipowicz, S.J. Chua, and F. Watt	
<b>Electron Stimulated Desorption of Deuterium from GaN (0001) Surface.....</b>	<b>737</b>
Y. Yang, J. Lee, and B.D. Thoms	
<b>Dislocation-Related Deep States Induced by Irradiation in HVPE n-GaN.....</b>	<b>743</b>
A. Castaldini, A. Cavallini, and L. Polenta	

<b>High-Temperature Illumination-Induced Metastability in Undoped Semi-Insulating GaN Grown by Metalorganic Vapor Phase Epitaxy .....</b>	<b>749</b>
Z.-Q. Fang, B.B. Claflin, D.C. Look, T.H. Myers, D.D. Koleske, A.E. Wickenden, and R.L. Henry	
<b>Spectroscopic Characterization of Ion-Implanted GaN .....</b>	<b>755</b>
L. Chen and B.J. Skromme	
<b>Plane-Wave Pseudopotential Study on Mechanical and Electronic Properties for Group III-V Binary Phases.....</b>	<b>761</b>
S.Q. Wang and H.Q. Ye	
<b>Surface Passivation of AlGaIn Terminated and GaN Terminated HEMT Structures Studied by XPS.....</b>	<b>767</b>
B.P. Gila, E. Lambers, B. Luo, A.H. Onstine, K.K. Allums, C.R. Abernathy, F. Ren, and S.J. Pearton	
<b>Properties of Delta Doped Al<sub>0.25</sub>Ga<sub>0.75</sub>N and GaN Epitaxial Layers .....</b>	<b>773</b>
Jeffrey S. Flynn, Leah G. Wallace, Joe A. Dion, Edward L. Hutchins, Helder Antunes, and George R. Brandes	
<b>AlGaIn/GaN HFETs for Automotive Applications.....</b>	<b>779</b>
Ronald Birkhahn, David Gotthold, Nathan Cauffman, Boris Peres, and Seikoh Yoshida	
<b>Transport Studies on Two-Subband-Populated AlGaIn/GaN Heterostructures .....</b>	<b>783</b>
D.R. Hang, C.F. Huang, Y.F. Chen, and B. Shen	
<b>A Structural Analysis of the Pd/GaN Ohmic Contact Annealing Behavior .....</b>	<b>789</b>
C.C. Kim, P. Ruterana, and J.H. Je	
<b>Ti/Al-GaN Reaction Mechanism Forming Low Contact Resistivity.....</b>	<b>795</b>
Yoshimichi Fukasawa, Tomonori Nakamura, and Tohru Nakamura	
<b>Comparative Morphology of AuTiAlTi, AuPdAlTi and AuAlTi Ohmic Contacts to AlGaIn/GaN.....</b>	<b>801</b>
M.W. Fay, G. Moldovan, I. Harrison, R.S. Balmer, K.P. Hilton, B.T. Hughes, M.J. Uren, T. Martin, and P.D. Brown	

<b>Stable Ohmic Contacts on GaAs and GaN Devices for High Temperatures .....</b>	<b>807</b>
A. Piotrowska, E. Kaminska, A. Barcz, K. Golaszewska, H. Wrzesinska, T.T. Piotrowski, E. Dynowska, and R. Jakiela	
<b>Ohmic and Rectifying Contacts to n- and p-Type GaN Films.....</b>	<b>813</b>
H.P. Hall, M.A. Awaah, A. Kumah, K. Das, and F. Semendy	
<b>Activation of Mg Acceptors in GaN:Mg Monitored by Electron Paramagnetic Resonance Spectroscopy.....</b>	<b>819</b>
D. Matlock, M.E. Zvanut, Jeffrey R. DiMaio, R.F. Davis, R.L. Henry, Daniel Koleske, and Alma Wickenden	
<b>Microstructural Defects in Mg-Doped AlGaIn Layers Grown by Metalorganic Chemical Vapor Deposition.....</b>	<b>825</b>
Hyung Koun Cho and Gye Mo Yang	

***CONTACTS, PROCESSING AND  
p-TYPE NITRIDES***

<b>Contacts to High Aluminum Fraction p-type Aluminum Gallium Nitride .....</b>	<b>833</b>
Brett A. Hull, Suzanne E. Mohny, Uttiya Chowdhury, Russell D. Dupuis, David Gotthold, Ronald Birkhahn, and Milan Pophristic	
<b>Structural Defects in Mg-Doped GaN and AlGaIn Grown by MOCVD .....</b>	<b>839</b>
S. Tomiya, S. Goto, M. Takeya, and M. Ikeda	
<b>The First Wafer-Fused AlGaAs-GaAs-GaN Heterojunction Bipolar Transistor .....</b>	<b>845</b>
Sarah Estrada, Andreas Stonas, Andrew Huntington, Huili Xing, Larry Coldren, Steven DenBaars, Umesh Mishra, and Evelyn Hu	
<b>Author Index .....</b>	<b>851</b>
<b>Subject Index.....</b>	<b>859</b>

---

## PREFACE

Symposium L, "GaN and Related Alloys—2002," was held December 2–6 at the 2002 MRS Fall Meeting in Boston, Massachusetts. During nine half-day oral sessions, nine invited talks and 85 contributed talks were given. In three poster sessions, 161 posters were presented.

This year's nitride symposium again was characterized by a wide scope of nitride related advances spanning from basic materials physics over process technology to high performance devices. Strong development was reported in bulk growth of GaN and AlN, growth on various substrates and substrate orientations, optical properties of InN, defect and doping analysis of p-doped GaN, and full consideration of polarization properties. These led to new performance records in visible light emitter technology, i.e., higher efficiency/higher brightness, UV emitters with shorter wavelength, and UV and photo detectors. A strong development is also seen in nitride-based electronic devices with new heterostructure FET designs for RF power applications including such on Si substrates and wafer fusion.

These symposium proceedings capture a crosscut of the exciting developments in this rapidly progressing and commercializing field. This volume will be useful for researchers working in the field of nitrides, and for students who seek entry into the subject.

Christian Wetzel  
Edward T. Yu  
James S. Speck  
Angela Rizzi  
Yasuhiko Arakawa

December 2002

## MATERIALS RESEARCH SOCIETY SYMPOSIUM PROCEEDINGS

- Volume 715— Amorphous and Heterogeneous Silicon-Based Films—2002, J.R. Abelson, J.B. Boyce, J.D. Cohen, H. Matsumura, J. Robertson, 2002, ISBN: 1-55899-651-6
- Volume 716— Silicon Materials—Processing, Characterization and Reliability, J. Veteran, D.L. O'Meara, V. Misra, P. Ho, 2002, ISBN: 1-55899-652-4
- Volume 717— Silicon Front-End Junction Formation Technologies, D.F. Downey, M.E. Law, A. Claverie, M.J. Rendon, 2002, ISBN: 1-55899-653-2
- Volume 718— Perovskite Materials, K. Poeppelmeier, A. Navrotsky, R. Wentzcovitch, 2002, ISBN: 1-55899-654-0
- Volume 719— Defect and Impurity Engineered Semiconductors and Devices III, S. Ashok, J. Chevallier, N.M. Johnson, B.L. Sopori, H. Okushi, 2002, ISBN: 1-55899-655-9
- Volume 720— Materials Issues for Tunable RF and Microwave Devices III, S.C. Tidrow, J.S. Horwitz, J. Levy, X. Xi, 2002, ISBN: 1-55899-656-7
- Volume 721— Magnetic and Electronic Films—Microstructure, Texture and Application to Data Storage, P.W. DeHaven, D.P. Field, S.D. Harkness IV, J.A. Sutliff, J.A. Szpunar, L. Tang, T. Thomson, M.D. Vaudin, 2002, ISBN: 1-55899-657-5
- Volume 722— Materials and Devices for Optoelectronics and Microphotonics, R.B. Wehrspohn, S. Noda, C. Soukoulis, R. März, 2002, ISBN: 1-55899-658-3
- Volume 723— Molecularly Imprinted Materials—Sensors and Other Devices, K.J. Shea, M.J. Roberts, M. Yan, 2002, ISBN: 1-55899-659-1
- Volume 724— Biological and Biomimetic Materials—Properties to Function, J. McKittrick, J. Aizenberg, C. Orme, P. Vekilov, 2002, ISBN: 1-55899-660-5
- Volume 725— Organic and Polymeric Materials and Devices—Optical, Electrical and Optoelectronic Properties, G.E. Jabbour, N.S. Sariciftci, S.T. Lee, S. Carter, J. Kido, 2002, ISBN: 1-55899-661-3
- Volume 726— Organic/Inorganic Hybrid Materials—2002, R.M. Laine, C. Sanchez, S. Yang, C.J. Brinker, 2002, ISBN: 1-55899-662-1
- Volume 727— Nanostructured Interfaces, G. Duscher, J.M. Plitzko, Y. Zhu, H. Ichinose, 2002, ISBN: 1-55899-663-X
- Volume 728— Functional Nanostructured Materials through Multiscale Assembly and Novel Patterning Techniques, Steven C. Moss, 2002, ISBN: 1-55899-664-8
- Volume 729— BioMEMS and Bionanotechnology, L.P. Lee, J.T. Borenstein, R.P. Manginell, M. Okandan, P.J. Hesketh, 2002, ISBN: 1-55899-665-6
- Volume 730— Materials for Energy Storage, Generation and Transport, G. Ceder, S.A. Ringel, R.B. Schwarz, 2002, ISBN: 1-55899-666-4
- Volume 731— Modeling and Numerical Simulation of Materials Behavior and Evolution, V. Tikare, E.A. Olevisky, A. Zavaliangos, 2002, ISBN: 1-55899-667-2
- Volume 732E—Chemical-Mechanical Planarization, S.V. Babu, R. Singh, N. Hayasaka, M. Oliver, 2002, ISBN: 1-55899-668-0
- Volume 733E—Polymer Nanocomposites, S. Nutt, R. Vaia, W. Rodgers, G.L. Hagnauer, G.W. Beall, 2002, ISBN: 1-55899-669-9
- Volume 734— Polymer/Metal Interfaces and Defect Mediated Phenomena in Ordered Polymers, E.D. Manias, G.G. Malliaras, 2003, ISBN: 1-55899-671-0
- Volume 735— Bioinspired Nanoscale Hybrid Systems, G. Schmid, U. Simon, S.J. Stranick, S.M. Arrivo, S. Hong, 2003, ISBN: 1-55899-672-9
- Volume 736— Electronics on Unconventional Substrates—Electrotextiles and Giant-Area Flexible Circuits, M.S. Shur, P. Wilson, D. Urban, 2003, ISBN: 1-55899-673-7
- Volume 737— Quantum Confined Semiconductor Nanostructures, J.M. Buriak, D.D.M. Wayner, F. Priolo, B. White, V. Klimov, L. Tsybeskov, 2003, ISBN: 1-55899-674-5
- Volume 738— Spatially Resolved Characterization of Local Phenomena in Materials and Nanostructures, D.A. Bonnell, J. Piqueras, A.P. Shreve, F. Zypman, 2003, ISBN: 1-55899-675-3
- Volume 739— Three-Dimensional Nanoengineered Assemblies, T.M. Orlando, L. Merhari, K. Ikuta, D.P. Taylor, 2003, ISBN: 1-55899-676-1
- Volume 740— Nanomaterials for Structural Applications, C. Berndt, T.E. Fischer, I. Ovid'ko, G. Skandan, T. Tsakalakos, 2003, ISBN: 1-55899-677-X

---

## MATERIALS RESEARCH SOCIETY SYMPOSIUM PROCEEDINGS

- Volume 741— Nano- and Microelectromechanical Systems (NEMS and MEMS) and Molecular Machines, A.A. Ayon, T. Buchheit, D.A. LaVan, M. Madou, 2003, ISBN: 1-55899-678-8
- Volume 742— Silicon Carbide 2002—Materials, Processing and Devices, S.E. Saddow, D.J. Larkin, N.S. Saks, A. Schoener, 2003, ISBN: 1-55899-679-6
- Volume 743— GaN and Related Alloys—2002, E.T. Yu, C.M. Wetzel, J.S. Speck, A. Rizzi, Y. Arakawa, 2003, ISBN: 1-55899-680-X
- Volume 744— Progress in Semiconductors II—Electronic and Optoelectronic Applications, B.D. Weaver, M.O. Manasreh, C.C. Jagadish, S. Zollner, 2003, ISBN: 1-55899-681-8
- Volume 745— Novel Materials and Processes for Advanced CMOS, M.I. Gardner, J-P. Maria, S. Stemmer, S. De Gendt, 2003, ISBN: 1-55899-682-6
- Volume 746— Magnetoelctronics and Magnetic Materials—Novel Phenomena and Advanced Characterization, S. Zhang, W. Kuch, G. Guentherodt, C. Broholm, A. Kent, M.R. Fitzsimmons, I. Schuller, J.B. Kortright, T. Shinjo, Y. Zhu, 2003, ISBN: 1-55899-683-4
- Volume 747— Crystalline Oxide-Silicon Heterostructures and Oxide Optoelectronics, D.S. Ginley, S. Guha, S. Carter, S.A. Chambers, R. Droopad, H. Hosono, D.C. Paine, D.G. Schlom, J. Tate, 2003, ISBN: 1-55899-684-2
- Volume 748— Ferroelectric Thin Films XI, D. Kaufman, S. Hoffmann-Eifert, S.R. Gilbert, S. Aggarwal, M. Shimizu, 2003, ISBN: 1-55899-685-0
- Volume 749— Morphological and Compositional Evolution of Thin Films, N. Bartelt, M.J. Aziz, I. Berbezier, J.B. Hannon, S. Heame, 2003, ISBN: 1-55899-686-9
- Volume 750— Surface Engineering 2002—Synthesis, Characterization and Applications, A. Kumar, W.J. Meng, Y-T. Cheng, J. Zabinski, G.L. Doll, S. Veprek, 2003, ISBN: 1-55899-687-7
- Volume 751— Structure-Property Relationships of Oxide Surfaces and Interfaces II, X. Pan, K.B. Alexander, C.B. Carter, R.W. Grimes, T. Wood, 2003, ISBN: 1-55899-688-5
- Volume 752— Membranes—Preparation, Properties and Applications, V.N. Burganos, R.D. Noble, M. Asaeda, A. Ayral, J.D. LeRoux, 2003, ISBN: 1-55899-689-3
- Volume 753— Defect Properties and Related Phenomena in Intermetallic Alloys, E.P. George, H. Inui, M.J. Mills, G. Eggeler, 2003, ISBN: 1-55899-690-7
- Volume 754— Supercooled Liquids, Glass Transition and Bulk Metallic Glasses, A.L. Greer, T. Egami, A. Inoue, S. Ranganathan, 2003, ISBN: 1-55899-691-5
- Volume 755— Solid-State Chemistry of Inorganic Materials IV, M. Greenblatt, M.A. Alario-Franco, M.S. Whittingham, G. Rohrer, 2003, ISBN: 1-55899-692-3
- Volume 756— Solid-State Ionics—2002, P. Knauth, J-M. Tarascon, E. Traversa, H.L. Tuller, 2003, ISBN: 1-55899-693-1
- Volume 757— Scientific Basis for Nuclear Waste Management XXVI, R.J. Finch, D.B. Bullen, 2003, ISBN: 1-55899-694-X
- Volume 758— Rapid Prototyping Technologies, A.S. Holmes, A. Piqué, D.B. Dimos, 2003, ISBN: 1-55899-695-8
- Volume 759— Granular Material-Based Technologies, S. Sen, M.L. Hunt, A.J. Hurd, 2003, ISBN: 1-55899-696-6
- Volume 760E—The Undergraduate Curriculum in Materials Science and Engineering, E.P. Douglas, O.D. Dubón Jr., J.A. Isaacs, W.B. Knowlton, M. Stanley Whittingham, 2003, ISBN: 1-55899-697-4
- Volume 761E—Molecular Electronics, M-I. Baraton, E.L. Garfunkel, D.C. Martin, S.S.P. Parkin, 2003, ISBN: 1-55899-698-2

---

## **Epitaxy—Devices and Defect Reduction**

### Large-Area, Device Quality GaN on Si Using a Novel Transition Layer Scheme

Pradeep Rajagopal, Thomas Gehrke, John C. Roberts, J. D. Brown, T. Warren Weeks,  
Edwin L. Piner, Kevin J. Linthicum  
Nitronex Corporation, 628 Hutton Street, Suite 106, Raleigh, NC 27606

#### ABSTRACT

The emergence of III-nitride technology and fabrication of high quality GaN based devices is possible due to the advances in the heteroepitaxial growth of III-N thin-films on lattice-mismatched substrates. Typically, the substrate of choice is either SiC or sapphire. We have adopted 100mm Si as our substrate of choice; uniform substrates of high quality are inexpensive and plentiful due to decades of use in the microelectronics industry. Growth of device quality GaN on Si is challenged by the ~17% lattice mismatch and an additional thermal expansion coefficient (TEC) mismatch of ~56%. In order to accommodate this strain and TEC mismatch between Si and GaN, a novel transition layer was designed, grown and successfully optimized, obviating the need for either a PENDEO® based overgrowth process or a SiC interlayer-based process. This growth technique (SIGANTIC®) does not require any wafer conditioning prior to growth and thus reduces the process complexity and maintains the cost effectiveness of the GaN on Si strategy. We will report on this manufacturable 100mm MOCVD heteroepitaxial process that consistently produces device quality AlGaIn/GaN heterostructures with two dimensional electron gas (2DEG) mobilities typically around 1400 cm<sup>2</sup>/Vs at room temperature. Structural and electrical properties as determined by optical reflectance, atomic force microscopy, capacitance-voltage and van der Pauw Hall measurements, which are measured across the 100mm wafer, will be presented. Device results will be mentioned to show continuous wave (CW) RF operation at 2 GHz with competitive power output, gain and power added efficiency (PAE).

#### INTRODUCTION

Growth of high quality GaN on Si (111) can be achieved only by addressing the significant levels of lattice misfit (~17%) and TEC (~56%) mismatch. A schematic of the lattice misfit is shown in Figure 1 (a). It is clear, that the lattice misfit effects will dominate the Si/III-N interface, where a high density of misfit dislocations are expected to form during growth. For example, the choice of using AlN as a nucleation layer on Si (111) results in the formation of an estimated maximum of  $\sim 3 \times 10^{12}$  cm<sup>-2</sup> misfit dislocations near the Si/AlN interface. It will be shown that despite the high density of defects that are expected to be present in the AlN layer, these do not appear to impact the 2DEG properties of subsequently deposited AlGaIn/GaN device layers.

The TEC mismatch between GaN and Si ( $\alpha_{\text{GaN}} = 5.59 \times 10^{-6}/\text{K}$ , for  $T \geq 300\text{K}$ ,  $\alpha_{\text{Si}} = 3.59 \times 10^{-6}/\text{K}$  @ 300K<sup>1)</sup>) poses a completely different challenge and is shown in figure 1 (b). The TEC mismatch results in stress ( $\sigma$ ) within the film, which can be calculated from equation 1 as,

$$\sigma = \Delta\alpha\Delta TE_f \quad (1)$$

Where  $\Delta\alpha$  is the TEC mismatch between GaN and Si,  $\Delta T$  is the difference between the growth temperature of the film and room temperature, and  $E_f$  is the Young's modulus of the film. The magnitude of this stress is fixed for a given combination of substrate, film and growth temperature. This stress manifests itself during cooldown, and must be adequately accommodated by the film-substrate combination to result in crack free GaN films.

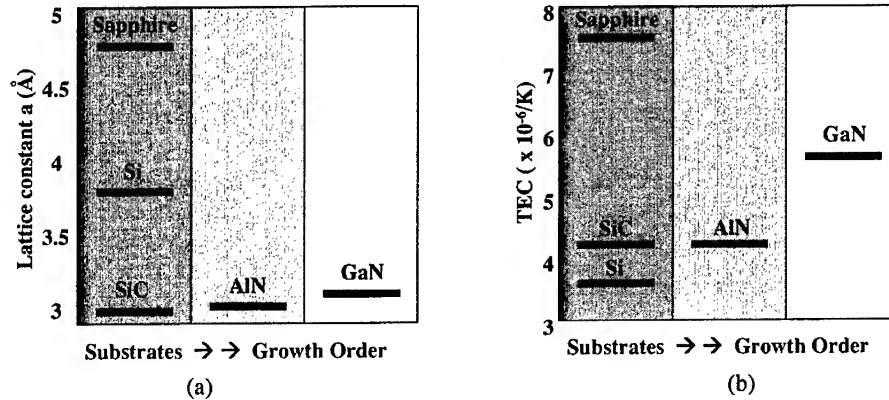


**Figure 1.** Schematic of the epitaxial challenges in growing crack free GaN on Si (111) including (a) the lattice misfit and (b) the TEC mismatch. In both figures, the typical substrates are grouped to the left, AlN in the middle and GaN to the right in order to preserve a typical growth sequence.

Several groups have made efforts to manage this high level of lattice and thermal mismatch<sup>2, 3, 4, 5, 6</sup>, with varying degrees of success. At Nitronex, a novel growth process, SIGANTIC<sup>®</sup>, has been developed that results in the growth of crack-free GaN, which has been used to fabricate GaN-based devices in both microelectronic and optoelectronic areas<sup>7, 8, 9, 10</sup>. Previously at Nitronex, this approach was successfully used to develop InGaN/GaN MQW LEDs emitting at a nominal wavelength of 450 nm<sup>11</sup>. This paper will focus on the growth and characterization of AlGaIn/GaN based high electron mobility transistor (HEMT) structures for high-power and high frequency applications. Material and electron transport characteristics will be reported along with a brief mention of the device characteristics.

## EXPERIMENTAL

The AlGaIn/GaN heterostructures were grown on 100 mm Si (111) wafers in a custom-built, cold wall, rotating disc MOCVD reactor at nominally 1000 °C. The device layers consisted of ~250 Å of 25% UID AlGaIn capped with 50 Å of UID GaN. The reactor design enables control of temperature and flow across multiple zones allowing for development of uniform processes. Trimethylgallium (TMG) and trimethylaluminum (TMA) precursors were carried by Pd-diffused hydrogen and ammonia (NH<sub>3</sub>) was used as the N precursor. The material and electron transport characteristics of the wafers were characterized using white light reflectance thickness mapping, atomic force microscopy (AFM), scanning transmission electron microscopy (STEM), Hg-probe capacitance-voltage (C-V) profiling, van der Pauw Hall measurements and four-point probe sheet resistance mapping. The two dimensional electron gas (2DEG) channel characterization by van der Pauw Hall effect measurements were made on 7mm x 7mm samples,

which were diced from as grown wafers. Channel sheet resistance was also measured on  $100\ \mu\text{m} \times 100\ \mu\text{m}$  van der Pauw mesa structures, which are fabricated adjacent to and concurrently with production die. A Ti/Al/Ni/Au annealed ohmic contact scheme was used for both measurements.

## RESULTS AND DISCUSSION

The highlights of the HEMT growth process are as follows: (a) heat up the wafers in an environment that prevents nitridation of the Si (111) wafers, (b) AlN is nucleated on Si (111) which also acts as a barrier against undesirable Ga-Si interaction, (c) the (Al, Ga) N transition layer is deposited using optimized process conditions (d) unintentionally doped (UID) GaN buffer is deposited and (e)  $\text{Al}_x\text{Ga}_{1-x}\text{N}$  device layers are deposited. Using this single step approach, crack free GaN with excellent material characteristics and uniformity are routinely deposited on 100 mm Si (111) substrates. Wafers also exhibit negligible bow as is evidenced by radii of curvature in excess of 30 m.

The growth conditions were optimized to result in a high level of thickness uniformity, as measured by white light reflectance shown in Figure 2. The total film thickness was 2020 nm with a total thickness variation of 5.1% (5 mm edge exclusion). AFM performed on  $5\ \mu\text{m} \times 5\ \mu\text{m}$  areas revealed a smooth surface with an RMS roughness in the 5-10 Å range. A similar scan of a  $1\ \mu\text{m} \times 1\ \mu\text{m}$  shows roughness in the 2.5-5 Å range as shown in Figure 3a. A defect density on the order of  $\sim 2 \times 10^9\ \text{cm}^{-2}$  was estimated from the AFM image. The sharpness of the AlGaIn/GaN heterointerface is also confirmed by scanning transmission electron microscopy (STEM) as shown in Figure 3b.

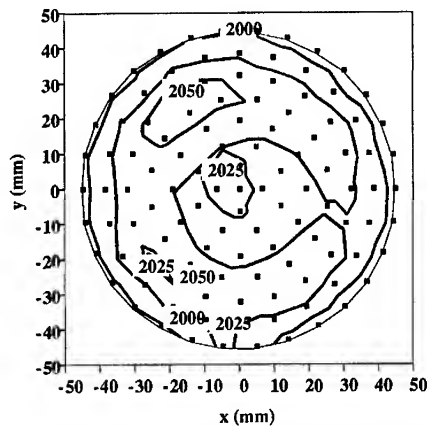


**Figure 2.** White light reflectance thickness map of an AlGaIn/GaN HEMT wafer grown on a 100 mm Si (111) substrate. The average epi thickness was 2020 nm with a total thickness variation of 5.1%.

Transport characteristics of the channel have been evaluated by several methods. Room temperature (RT) van der Pauw Hall measurements are periodically performed and routinely result in mobilities in the  $1300\text{--}1500\ \text{cm}^2/\text{V}\cdot\text{s}$  range and sheet charge densities in the  $7.5\text{--}8.5 \times 10^{12}\ \text{cm}^{-2}$  range. Non-destructive sheet resistance measurements are also performed on van der

Pauw test mesas that are distributed across fully fabricated wafers. Sheet resistances in the range of 450-550 ohms/square are typically observed and are in good agreement with the sheet resistances obtained from Hall measurements. Figure 4a shows a typical 100 mm wafer map of sheet resistance measured across a fully fabricated wafer; the range of values is distributed between 450-550 ohms/square, with the majority of the data in the 450-470 ohms/square range. Figure 4b tabulates RT mobility, sheet charge, and sheet resistance data obtained from destructive Hall measurement at five points from the center toward the edge of the 100 mm wafer. The high values of mobility validate the quality of the epitaxial film and the interface smoothness, resulting in a high quality channel obtained uniformly across the 100 mm wafer.

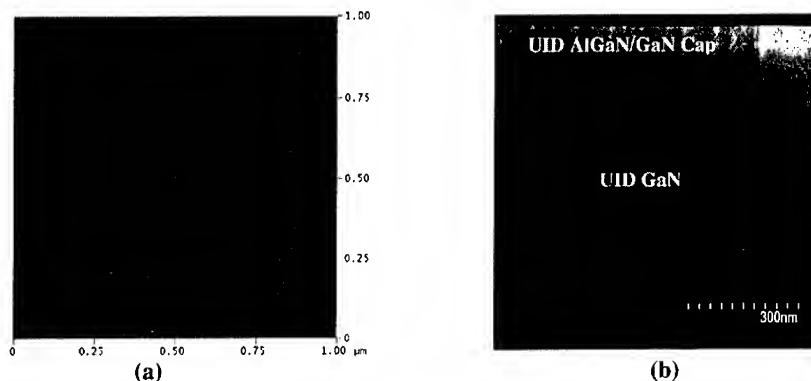
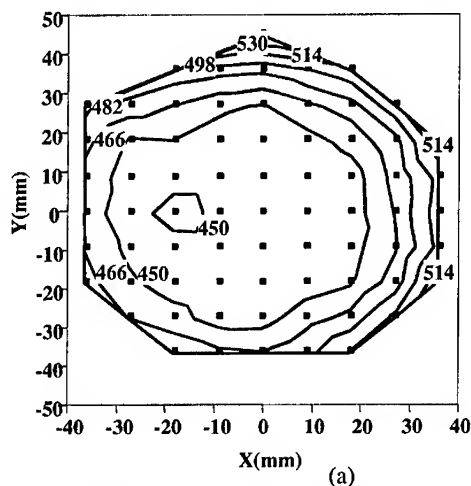


**Figure 3.** (a)  $1\ \mu\text{m} \times 1\ \mu\text{m}$  AFM image of the AlGaIn/GaN HEMT wafer with an RMS roughness of  $2.5\ \text{\AA}$  (b) STEM image of the AlGaIn/GaN heterostructure.



Position from center (mm)	Mobility ( $\text{cm}^2/\text{V s}$ )	Sheet Charge ( $\times 10^{12}\text{cm}^{-2}$ )	Sheet Resistance (ohms/square)	AlN% <sup>12, 13</sup>
8	1553	7.7	520	24.6
15	1581	8.1	487	25.7
22	1572	8.7	455	26.8
30	1541	8.4	481	27.3
38	1436	7.8	560	27.3

(b)

**Figure 4.** (a) Sheet resistance map (ohms/square) taken from van der Pauw mesas over a fully fabricated 100 mm wafer, (b) Mobility ( $\text{cm}^2/\text{V s}$ ), sheet charge ( $\text{cm}^{-2}$ ), and sheet resistance (ohms/square) derived from destructive Hall measurement at five points across an as-grown epi wafer.

Characteristics of the AlGaIn/GaN HEMT channel are also routinely assessed by Hg-probe C-V measurements. Doping vs. depth profiles were calculated from raw C-V data using commercial software. The C-V data for a typical AlGaIn/GaN HEMT is shown in Figure 5, which exhibits a pinch off voltage of  $\sim 4.4$  V. The plot of doping vs. depth exhibits a maximum electron concentration of  $\sim 1 \times 10^{20} \text{ cm}^{-3}$  at a depth of  $\sim 200 \text{ \AA}$  from the surface. The high concentration of electronic charge indicated by the steep doping profile is another indication of a high degree of channel confinement. The absence of a complete peak (i.e., no “roll over”) in the doping vs. depth profile is apparently a result of zero-volt surface depletion of the mercury contact.

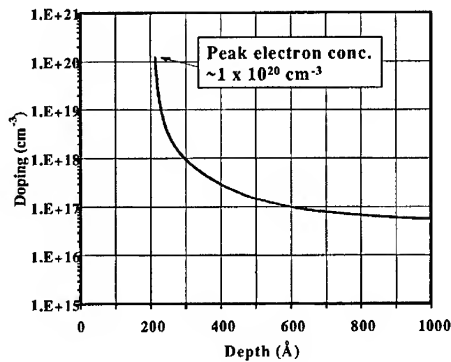


**Figure 5.** Doping vs. depth profile derived from C-V measurements.

The absence of cracks and excellent electrical and material characteristics imply that the lattice misfit and TEC mismatch have been adequately addressed by the transition layer scheme described above. The transition layer addresses the two challenges necessary for the successful growth of GaN on Si: It manages both the lattice and thermal mismatch between the two materials. A simplified explanation would be to speculate that the AlN/Si interface absorbs most of the lattice mismatch while the (Al,Ga)N transition layer is successful in absorbing the stresses that arise due to the TEC mismatch. Initial investigations have revealed that in order to prevent cracking of the AlGaIn/GaN HEMT wafer, it is important to optimize the thickness and the nature of the composition profile of the transition layer. The growth conditions of the transition layer have also been determined to be significant; this suggests a role played by the nature and density of defects and the resultant material properties of the transition layer. Studies are underway to gain further insight into the effectiveness of the transition layer; it is hoped that this will lead to a physical model to help explain the stress states in GaN on Si.

The AlGaIn/GaN HEMT wafers grown using the SIGANTIC® process were fabricated into power transistors. The transistor was fabricated with Ti/Al/Ni/Au source and drain ohmic contacts, a Ni/Au Schottky gate with  $1 \mu\text{m}$  gate length, and a  $\text{SiN}_x$  passivant deposited by plasma enhanced chemical vapor deposition. The median values for  $I_{\text{dss}}$ ,  $I_{\text{dmax}}$  and maximum  $g_m$  for the 25% UID AlGaIn/GaN HEMT over a recent batch of 19 wafers were 576 mA/mm, 862 mA/mm and 183 mS/mm respectively. (The term  $I_{\text{dmax}}$  refers to the maximum drain current and is measured at a fixed forward gate voltage of 3.5 V with the drain biased at 7 V). The continuous wave (CW) RF characteristics of 300  $\mu\text{m}$  devices at 2 GHz were measured where the test conditions were  $V_{\text{ds}} = 30$  V and the gate was biased for optimized class A operation. Under

these conditions, a power density of 3.3 W/mm of saturated RF power was achieved. The linear gain was 16 dBm with a maximum power added efficiency (PAE) of 30%. We also measured devices with 18 mm total gate width at 2.14 GHz, CW operation with the device in class AB mode and the drain at 28 V; the saturated power, linear gain and PAE were 27 W, 14 dB and 45% respectively<sup>9</sup> for this large device. These numbers are among the highest reported for AlGaIn/GaN power devices.

## CONCLUSIONS

High quality AlGaIn/GaN HEMT structures grown on 100 mm Si (111) substrates have been uniformly deposited using an (Al,Ga)N based transition layer scheme. The crack free wafers exhibit exceptional transport characteristics, which imply the presence of a high quality 2DEG with high channel mobilities (1300-1500 cm<sup>2</sup>/Vs) and channel sheet charge densities (7.5-8.5 x 10<sup>12</sup> cm<sup>-2</sup>). Fabrication of power transistors on these wafers produced excellent DC and RF characteristics (CW) that are among the highest reported for AlGaIn/GaN HEMTs.

## ACKNOWLEDGEMENTS

We would like to acknowledge the Office of Naval Research (ONR) for supporting this work under contracts N00014-00-M-0159 (Phase I, Colin Wood contract monitor) and N00014-01-C-0253 (Phase II, John Zolper and Harry Dietrich contract monitors).

## REFERENCES

- <sup>1</sup> P. R. Hageman, S. Haffouz, A. Grzegoreczk, V. Kirilyuk, and P. K. Larsen, *Mat. Res. Soc. Symp. Proc.* **693**, 105 (2002).
- <sup>2</sup> Min-Ho Kim, Young-Gu Do, Hyon Chol Kang, Do Young Noh and Seong-Ju Park, *Appl. Phys. Lett.* **79**, 2713 (2001).
- <sup>3</sup> Eric Feltin, B. Beaumont, M. Laugt, P. de Mierry, P. Vennéguès, H. Lahrechè, M. Leroux, and P. Gibart, *App. Phys. Lett.* **79**, 3230 (2001).
- <sup>4</sup> A. Dadgar, M. Poschenrieder, J. Bläsing, K. Fehse, A. Diez, and A. Krost, *Appl. Phys. Lett.* **80**, 3670 (2002)
- <sup>5</sup> Yankun Fu, and Daniel A. Gulino, *J. Vac. Sci. Technol. A* **18**(3), 965 (2000).
- <sup>6</sup> Eduardo M. Chumbes, A. T. Schremer, Joseph A. Smart, Y. Wang, Noel C. MacDonald, D. Hogue, James J. Komiak, Stephen J. Lichwalla, Robert E. Leoni, James R. Shealy, *IEEE Transactions of Electron Devices*, **48**, No. 3, March 2001, 420 (2001).
- <sup>7</sup> Walter Nagy, Jeff Brown, Ricardo Borges, and Sameer Singhal, to be published.
- <sup>8</sup> A. Vescan, J. D. Brown, J. W. Johnson, R. Therrien, T. Gehrke, P. Rajagopal, J. C. Roberts, S. Singhal, W. Nagy, R. Borges, E. Piner, and K. Linthicum, *Phys. Stat. Sol. (c)* (2002) to be published.
- <sup>9</sup> S. Singhal, J.D. Brown, R. Borges, E. Piner, W. Nagy, A. Vescan, *GAAS 2002 Conference Proceedings, Milan, Italy*, Sept. 23-27 (2002).
- <sup>10</sup> J. D. Brown, Ric Borges, Edwin Piner, Andrei Vescan, Sameer Singhal, Robert Therrien, *Solid State Electronics*, **46** 1535 (2002).
- <sup>11</sup> Warren Weeks, Ricardo Borges, *Compound Semiconductor*, **7**, 63 (2001).
- <sup>12</sup> L. S. Yu, D. Qiao, S. S. Lau, and J. M. Redwing, *App. Phys. Lett.*, **75**, 1419 (1999).
- <sup>13</sup> H. Jiang, G. Y. Zhao, H. Ishikawa, T. Egawa, T. Jimbo, M. Umeno, *J. App. Phys.*, **89**, 1046 (2001).

### III-Nitride Growth on Lithium Niobate: A New Substrate Material for Polarity Engineering in III-Nitride Heteroepitaxy

W. Alan Doolittle<sup>1</sup>, Gon Namkoong, Alexander Carver, Walter Henderson, Dieter Jundt<sup>2</sup> and April S. Brown<sup>3</sup>

<sup>1</sup>Georgia Institute of Technology, School of Electrical and Computer Engineering, 777 Atlantic Dr., Atlanta, GA 30332-0269, USA, alan.doolittle@ece.gatech.edu

<sup>2</sup>Crystal Technology, Inc., Palo Alto, CA, USA

<sup>3</sup>Duke University, Durham, NC, USA

#### ABSTRACT

Herein, we discuss the use of a novel new substrate for III-Nitride epitaxy, Lithium Niobate. It is shown that Lithium Niobate (LN) has a smaller lattice mismatch to III-Nitrides than sapphire and can be used to control the polarity of III-Nitride films grown by plasma assisted molecular beam epitaxy. Results from initial growth studies are reported including using various nitridation/buffer conditions along with structural and optical characterization. Comparisons of data obtained from GaN and AlN buffer layers are offered and details of the film adhesion dependence on buffer layer conditions is presented. Lateral polarization heterostructures grown on periodically poled LN are also demonstrated. While work is still required to establish the limits of the methods proposed herein, these initial studies offer the promise for mixing III-Nitride semiconductor materials with lithium niobate allowing wide bandgap semiconductors to utilize the acoustic, pyroelectric/ferroelectric, electro-optic, and non-linear optical properties of this new substrate material as well as the ability to engineer various polarization structures for future devices.

#### INTRODUCTION

Currently, no commercially available native substrate exists for III-Nitrides. Thus, sapphire and silicon carbide have become the dominant substrates for III-Nitride epitaxy. Each of these substrates has advantages for common devices developed over the last decade, but alternative substrates exist that offer more flexibility for novel device design. Lithium Niobate (LN) is one such alternative substrate offering unique characteristics not found in other substrates. LN is a CZ grown oxide that is cheaper than sapphire, available in 6 inch diameter wafers and is produced in quantities exceeding 60 tons per year [1] primarily for use in optoelectronic modulators and surface acoustic wave devices.

The most common substrate

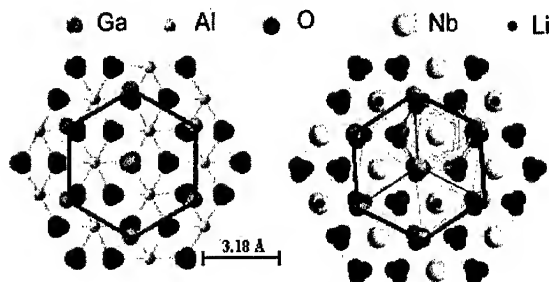


Figure 1.) Crystal structures of a) sapphire (left) and b) lithium niobate (right) along the c-axis showing the GaN unit cell alignment on the oxygen sublattice.

material for the growth of III-Nitride semiconductors is sapphire. While the unit cell lattice mismatch of GaN-Sapphire is ~33%, the commonly quoted lattice mismatch of GaN to sapphire of ~16% occurs by alignment of the GaN hexagonal base along the oxygen sub-lattice of sapphire [2] as shown in figure 1a. This requires a rotation of the GaN unit cell about the c-axis by 30 degrees and results in a slightly distorted GaN unit cell. While the bulk crystal structure of lithium niobate is more complex than that of sapphire due to the "staircase spiraling" nature of the oxygen octahedra resulting in a larger dispersion than in sapphire of the oxygen atomic positions around their central locations, the surface structure of the lithium niobate on the c-plane is similar to sapphire. The main difference between these surfaces is that the  $\text{LiNbO}_3$  surface structure has a larger oxygen sub-lattice spacing, resulting in a better average lattice mismatch to III-Nitrides and to SiC. When the average lattice match is determined via computer modeling [3], one finds a lattice mismatch to GaN (lattice constant of the unit cell being 3.185 angstroms) of 15.7% for sapphire and 6.8% for lithium niobate as shown in figure 1b. A similar analysis for the lithium niobate mismatch to AlN (3.1114 angstroms), 4H SiC ( $a=3.0730$ ) and 6H SiC ( $a=3.0806$  angstroms) results in lattice mismatches of 4.4%, 3.1% and 3.3% showing the versatility of mixing epitaxial wide bandgap semiconductors on ferroelectrics and vice versa. These lattice mismatches, while better than the sapphire most commonly used for wide bandgap epitaxy, are not very good. At best, only a minimal improvement in crystal structure can be expected, possibly reduced grain tilting. Indeed, evidence of this will be shown later. A more important advantage of these substrates, the ability to control polarization allowing new polarization engineered structures.

## EXPERIMENTAL DETAILS

### Structural and Optical Properties of GaN on Lithium Niobate

As a starting point, GaN was grown on LN using various nucleation conditions including, nitridation and GaN buffer growth at 500 °C, nitridation and GaN buffer growth at ~250 °C, and nitridation and AlN buffer growth at ~950 °C. Unless otherwise noted, all results presented here are from the 500 °C buffer

conditions. All bulk GaN films were grown at 680 °C, using 0.32 sccm nitrogen, a 0.5  $\mu\text{m/hr}$  growth rate using an Veeco Applied EPI nitrogen plasma source. Figure 2 shows the omega-two theta X-ray diffraction spectra of such a GaN film on Lithium Niobate. The dominant reflections present are the symmetric reflections (c-axis, (000n)) of GaN and lithium niobate, indicating alignment of the (0001) direction of GaN along the (0001) direction of lithium niobate. The GaN (0002) omega-2theta FWHM is 275 arc-sec,

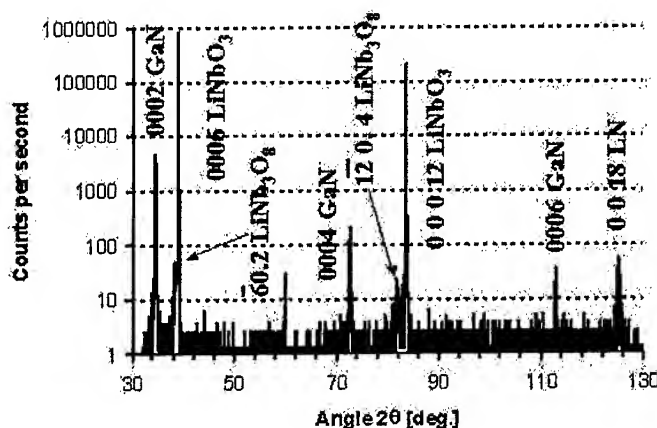


Figure 2.) The x-ray diffraction  $\omega$ -2 $\theta$  spectra of the GaN film on lithium niobate substrate.

comparable to that of GaN on sapphire. An additional diffraction peak is found at a two theta of 38.1 degrees. We suspect that this peak is related to lithium triniobate,  $\text{LiNb}_3\text{O}_8$  [4], a stable monoclinic phase in the lithium oxide/niobium oxide system resulting from preferential desorption of  $\text{Li}_2\text{O}$  near the sample surface [5]. This preferential desorption results in an imbalance in the lithium oxide/niobium oxide ratio which becomes 1:3  $\text{Li}_2\text{O}:\text{Nb}_2\text{O}_5$  in the near-surface regions. Hence, the preliminary work to eliminate this phase has involved lower temperature nitridation procedures to minimize the  $\text{Li}_2\text{O}$  desorption and an alternative approach, growth initiation above 925 °C where it is reported [5] that this lithium triniobate phase cannot form.

Figure 3 shows the reciprocal space map for the GaN on lithium niobate. Again, the (0002), (0006) and  $(\bar{6}0.2)$  reflections of GaN, lithium niobate and  $\text{LiNb}_3\text{O}_8$  are clearly visible. The GaN is aligned on the lithium niobate. Additionally, the magnitude of the lithium triniobate peak is ~100 times smaller than the lithium niobate and GaN peaks, supporting our conclusion that this phase results from a thin niobium oxide rich surface layer. No evidence was found for the existence of the lithium triniobate phase in as-received lithium niobate.

As shown in figure 4, the use of high temperature nitridation and AlN buffer conditions (950 °C) results in a reduction of the lithium triniobate phase at the expense of crystalline quality. The reduction of crystalline quality is likely due to the loss of indium used to mount the sample at these elevated temperatures and the subsequent cooling and inconsistent sample heating during subsequent bulk growth. When grown on (0001) oriented LN, initially, a reproducible, well defined 2x2 reconstruction was observed during the 950 °C AlN buffer layer growth. The AlN layer was graded to GaN as the substrate temperature was lowered to 680 °C resulting in broadened AlN and GaN peaks in figure 4. Attempts to

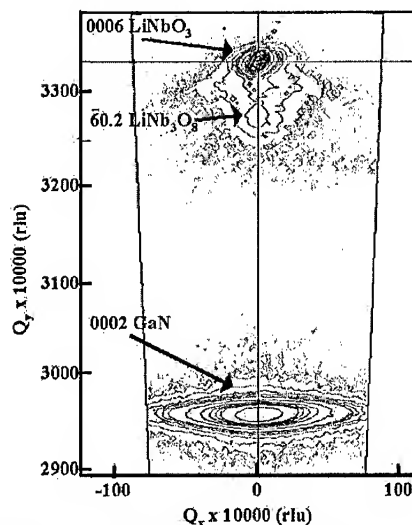


Figure 3.) The reciprocal space map for GaN on lithium niobate. The wave vectors  $Q_x$  and  $Q_y$  are expressed in units of  $1/2d$ , where  $l$  is the x-ray wavelength 1.54 angstroms,  $d$  is the plane separation in angstroms and rlu stands for reciprocal lattice units.

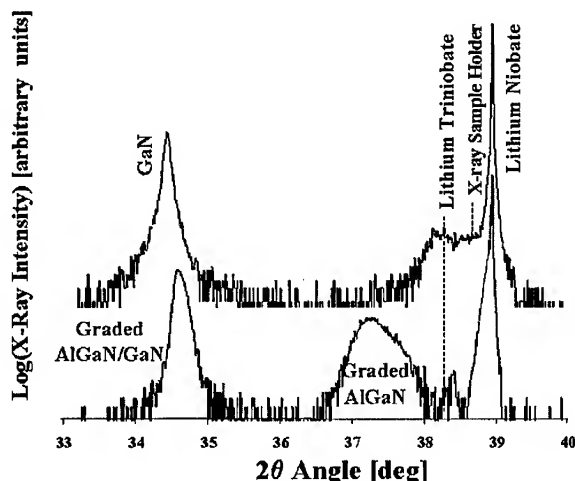


Figure 4.) Comparison of the X-ray diffraction spectra of GaN films grown on the 500 °C GaN buffers (top) versus those grown on the ~950 °C AlN graded buffers (bottom). Note the reduction of the lithium triniobate phase.

initiate growth at low substrate temperatures ( $\sim 250^\circ\text{C}$ ) resulted only in amorphous RHEED images and, thus, were deemed not practical.

Figure 5 shows the photoluminescence of a GaN sample doped to  $1 \times 10^{18} \text{ cm}^{-3}$  using silicon. Whereas X-ray diffraction is a measure of the structural quality of the films, photoluminescence is a measure of the point defect density. The sample shows strong excitonic emission, but does show a faint sub-bandgap emission indicative of point defects in the film. While these initial results are encouraging, further optimization will be required to eliminate the defects resulting in the yellow band luminescence. Additionally, further studies are needed to determine if the Al rich buffer layers can block the diffusion of lithium from the substrate as was shown for lithium gallate [6].

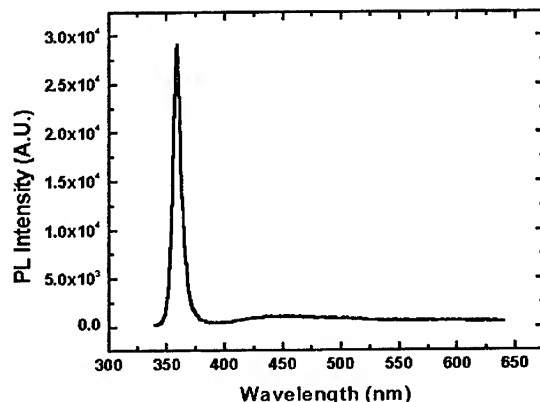


Figure 5.) The photoluminescence spectrum of the GaN on lithium niobate at the room temperature. GaN shows very strong excitonic emission at the band-edge transition.

#### Control over polarization using Poled Lithium Niobate

When exposed to a phosphoric acid solution [7] for 20 minutes at  $150^\circ\text{C}$ , GaN films grown on (0001) oriented and poled  $\text{LiNbO}_3$  were found to be Ga-polar, presumably due to the minimization of interface charge as described by Gauss's law. Specifically, the highly polar surface of LN resulting from the high spontaneous polarization (varying from  $\sim 71$  to  $\sim 30 \mu\text{C}/\text{cm}^2$  from room temperature to the highest growth temperature used herein) along with the anomalously high Curie temperature exceeding  $\sim 1142$ - $1210^\circ\text{C}$  [1,5] establish a surface charge that is minimized by the continuation of the polarity of the substrate into the GaN film.

Likewise, films grown on (000 $\bar{1}$ ) oriented and poled  $\text{LiNbO}_3$  were found to be N-polar by the same procedure. No ambiguity in the etch result was observed. Specifically, the Ga-polar films were weakly attacked by the acid solution, while the N-polar films were completely removed after 20 minutes.

#### Growth of GaN on Periodically Poled Lithium Niobate

Since lithium niobate is a ferroelectric material, its polarization can be controlled by the application of an external electric field. Furthermore, the Curie temperature (temperature where the material stops being ferroelectric, thus, losing its spontaneous polarization) is anomalously high compared to other ferroelectrics, ranging from  $\sim 1142$  to  $>1210^\circ\text{C}$  [1,5]. Using these features a pattern of polarized material can be written into the material by the application of an electric field in patterns on the wafer surface. Unlike more common perovskite ferroelectrics which have multiple degrees of atomic movement (oxygen octahedra and internal metal atom movement) lithium niobate only has one degree of freedom for atomic movement, the displacement of Li atoms along the three-fold symmetry axis (z-axis) [5]. Thus, the overall lattice is left unperturbed by the poling, with only the Li atomic position changing within the

interior of the unit cell. A key point to recognize about this process is the ferroelectric poling in lithium niobate does not change the surface chemistry, the lattice constant, nor the thermal properties (thermal expansion, etc...) of the lithium niobate. The poling only changes the polarization and thus, the induced charge on the surfaces.

A GaN film grown on periodically poled lithium niobate is shown in figure 6 using cross-polarized light to distinguish subtle changes in the N-polar

(000 $\bar{1}$ ) directions from the Ga-polar (0001) directions. Phosphoric acid etching [7] of such a film resulted in etching modulated by the period of the periodically poled LN domains as is expected. This approach allows polarization patterns to be "engineered" by first writing them into the substrate. Once grown, these "frozen polarization" structures can be used for advanced control of the device electrostatics. It also offers an option of studying the growth kinetics on +/- poled substrates simultaneously without any change in growth conditions.

#### Adhesion Control versus Polarity Control

As has been found for the oxygen-terminated face of lithium gallate previously [8], adhesion problems can result when growing III-Nitrides on lithium niobate using GaN buffer layers. Specifically, if films are grown to thicknesses greater than  $\sim 0.5 \mu\text{m}$  using a GaN buffer on poled LN, delamination can occur. The use of a thick  $\sim 60 \text{ nm}$  AlN buffer eliminates this delamination problem, but results in the film being converted to predominantly Ga-polarity. A thin  $\sim 1\text{-}5 \text{ nm}$  AlN buffer layer maintains control over polarity while eliminating the delamination.

## RESULTS AND DISCUSSION

Stutzmann et al [9] first suggested and demonstrated the idea of lateral polarity heterojunctions formed by lithographically patterned regions with varying polarity. They also suggested transistors structures and demonstrated enhanced light emission at polarity boundaries. The primary limitation of the approach of Stutzmann was the loss of surface planarity because of the need to etch the AlN buffer layers used in their approach. The current approach eliminates this weakness allowing the growth surface to be flat across polarization boundaries. Thus, quantum well structures can be grown using the current approach with well boundaries aligned within the growth plane. Using this procedure, 3D wells could potentially be formed using bandgap variations to confine carriers in the growth direction and polarization discontinuities to confine carriers in the lateral directions. The limitation of such an approach is the ability to pole LN substrates with narrow dimensions, currently limited to a few  $\mu\text{m}$ . However, the ability to grow quantum wells straddling polarization boundaries but aligned in the growth direction could lead to dramatic luminescence enhancement at the boundary beyond that already observed in bulk films by Stutzmann et al. This luminescence enhancement is due to the strong electron-hole

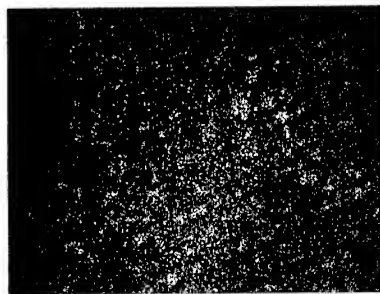


Figure 6.) Optical micrograph of a GaN sample grown on a periodically poled lithium niobate substrate as imaged using a cross-polarizer to highlight subtle index changes in the (0001) and (000 $\bar{1}$ ) stripes. Though the growth face of the sample is extremely smooth, it is transparent with a rough metalized back coating giving the sample an apparent rough texture in the image.

pair separation due to polarization-induced electric fields within quantum wells in III-Nitrides. Electrons and holes are separated in opposite directions in N-polar versus Ga-Polar quantum wells. Thus, at the polarity interface, a region exists where electron and hole wave functions overlap, leading to strong radiative recombination is expected. In this work, so far such structures have only been attempted on the thin GaN buffer films ( $<0.5\ \mu\text{m}$ ) and thus, are hampered by lower quality due to the adhesion limited thickness constraints described above. However, enhanced photoluminescence associated with polarization boundaries has been observed in GaN/InGaN quantum well structures grown on periodically poled LN. Due to the overall low intensity of the photoluminescence observed from these samples, at this time, it is unclear as to whether this enhanced photoluminescence intensity can offer promise for brighter emitters than can currently be obtained from conventional approaches. Quantum well structures using the improved buffer conditions detailed above will be investigated in the future.

## CONCLUSIONS

Lithium niobate has been theoretically and experimentally shown to be a promising substrate for III-Nitride epitaxy due to its slightly improved lattice mismatch and more importantly, its ability to control/define polarization in III-Nitride films. Initial results indicate structural quality comparable to III-Nitrides on sapphire but more effort is required to minimize thermally induced phase transformations in the lithium niobate. Methods of overcoming adhesion difficulties have been presented and periodically poled GaN has been demonstrated on periodically poled lithium niobate. A vast array of material properties found in lithium niobate but not in III-Nitrides such as electro-optic, nonlinear optical, various acoustic advantages, and strongly pyroelectric/ferroelectric properties can be integrated into III-Nitride device designs using heteroepitaxy.

## ACKNOWLEDGEMENTS

The authors would like to thank Colin Wood and the Office of Naval Research as well as the Georgia Tech Broadband Institute for the partial support of this work. Additionally, discussions with David Lederman regarding X-ray diffraction results were helpful.

## REFERENCES

- <sup>1</sup> Crystal Technologies Web Page, [www.crystaltechnology.com](http://www.crystaltechnology.com)
- <sup>2</sup> R. G. Powell, N.-E. Lee, Y.-W. Kim, and J. E. Greene, *J. Appl. Phys.* 73, 189 (1993)
- <sup>3</sup> Commercial crystal modeling program, Diamond™ version 2.1e, copyright 1996-2001 Crystal Impact GbR, Author Klaus Brandenburg
- <sup>4</sup> Lithium triniobate X-ray card 36-0307 from International Centre for Diffraction Data (ICDD) 1997 JCPDS
- <sup>5</sup> A. M. Prokhorov and Y. S. Kuz'minov, *Physics and Chemistry of crystalline lithium niobate*, Adam Hilger/IOP Publishing, New York, (1990)
- <sup>6</sup> W. A. Doolittle, A. S. Brown, S. Kang, S. W. Seo, S. Huang, N. M. Jokerst, *Phys. Stat. Sol. (a)*, vol.188, no.2 p.491-5, 23 Nov. (2001)
- <sup>7</sup> P. Visconti, D. Huang, M. A. Reshchikov, F. Yun, T. King, A. A. Baski, R. Cingolani, C. W. Litton, J. Jasinski, Z. Liliental-Weber, and H. Morkoc, *Phys. Stat. Sol.(b)* 228, 513. (2001)
- <sup>8</sup> W. A. Doolittle, T. Kroppenwicki, C. Carter-Coman, S. Stock, P. Kohl, N. M. Jokerst, R. A. Metzger, S. Kang, K. Lee, G. May, and A. S. Brown, *J. Vac. Sci. & Tech. B*, Vol. 16, No. 3, pp. 1300-1304, May/June, (1998)
- <sup>9</sup> M. Stutzmann, O. Ambacher, M. Eickhoff, U. Karrier, A. Lima Pimenta, R. Neuberger, J. Schalwig, R. Dimitrov, P. J. Schuck, and R. D. Grober, *Phys. stat. sol. (b)*, 228, No 2, p. 505-512, (2001).

### Cantilever Epitaxy of GaN on Sapphire: Further Reductions in Dislocation Density

D. M. Follstaedt, P. P. Provencio, D. D. Koleske, C. C. Mitchell, A. A. Allerman,  
N. A. Missert and C. I. H. Ashby  
Sandia National Laboratories, Albuquerque, NM 87185-1056

#### ABSTRACT

The density of vertical threading dislocations at the surface of GaN grown on sapphire by cantilever epitaxy has been reduced with two new approaches. First, narrow mesas ( $<1\ \mu\text{m}$  wide) were used and  $\{11\text{-}22\}$  facets formed over them early in growth to redirect dislocations from vertical to horizontal. Cross-sectional transmission electron microscopy was used to demonstrate this redirection and to identify optimum growth and processing conditions. Second, a GaN nucleation layer with delayed  $3\text{D} \rightarrow 2\text{D}$  growth transition and inherently lower threading dislocation density was adapted to cantilever epitaxy. Several techniques show that a dislocation density of only  $2\text{-}3 \times 10^7/\text{cm}^2$  was achieved by combining these two approaches. We also suggest other developments of cantilever epitaxy for reducing dislocations in heteroepitaxial systems.

#### INTRODUCTION

Gallium nitride is receiving much attention because of its favorable optical and electronic properties [1]. Because substrates lattice-matched to GaN are not readily available, it is often grown on sapphire or SiC. The hexagonal crystal structure of these substrates provides a template for oriented growth of GaN, but their large lattice mismatches (13.5% and 3.3%, respectively) lead to high densities of vertical threading dislocations (VTDs) that propagate to the surface during growth, as high as  $10^9\text{--}10^{10}$  VTDs/ $\text{cm}^2$ . Lateral growth methods have been developed to reduce VTDs, such as ELO [2], LEO [3], and FACELO [4]. These methods seed vertical growth through openings in a mask of  $\text{SiO}_2$  or  $\text{Si}_3\text{N}_4$  and then laterally overgrow the mask. The VTDs propagate through the opening but are blocked and not formed in material grown over the mask, leading to lower overall densities and areas that are nearly dislocation free. In pendeo-epitaxy [5], mesas and trenches are patterned into GaN already grown on a planar substrate and material is grown laterally from the mesas over the trenches to obtain low VTD density; thus the complete method requires two growth sequences. We have developed an alternative lateral method, cantilever epitaxy (CE), to remove VTDs. With CE, the substrate is first patterned with mesas and trenches, then GaN is nucleated on the mesa and laterally grown over the trenches. This method has the advantage of requiring only one growth sequence in the reactor since substrates are patterned before growth. We have focussed on CE growth on sapphire [6,7], while others have used similar methods with Si and SiC substrates as well [8-10].

In our initial CE growths [6], VTDs formed over the mesa were expected to propagate to the surface; the reduction in overall density is then ideally the fractional wafer area covered by mesas. Our recent work has implemented two new approaches for further reduction. First, mesa widths were decreased to  $<1\ \mu\text{m}$  with cantilever spans  $6\ \mu\text{m}$  wide; if additional VTDs did not form at cantilever coalescence fronts, this would reduce the overall density by an order of magnitude. However, we also lowered the growth temperature after nucleation to form  $\{11\text{-}22\}$  facets on GaN over the mesas; during subsequent lateral cantilever growth, these turn VTDs from vertical to horizontal and away from device areas above [4,11]. Here we use transmission electron

microscopy (TEM) to demonstrate this redirection of VTDs and identify processing and growth conditions for its optimization [7]. Second, a new nucleation procedure giving low VTD densities on planar sapphire [12] was adapted to CE with narrow mesas and faceting. Below we show that VTD densities in this material are only  $2\text{-}3 \times 10^7/\text{cm}^2$ . With these approaches, CE offers the possibility of low VTD density over entire wafers. With the new approaches, isolated defects several micrometers in size have formed that we label “dark-block” defects. To help discover their causes, their microstructures are described in an accompanying paper [13]. Finally, we discuss how CE may reduce dislocations further, and indicate other applications in heteroepitaxy.

### REDIRECTION OF VTDs TO HORIZONTAL DIRECTION

To evaluate redirection, two types of specimens were grown on narrow mesas extending in the [11-20] sapphire ([1-100] GaN) direction. The substrate was lithographically patterned for  $5\text{ }\mu\text{m}$  wide trenches and  $2\text{ }\mu\text{m}$  wide mesas, but final mesa widths were reduced to  $<1\text{ }\mu\text{m}$  by the sputtering-dominated etch with  $\text{BCl}_3$  in an inductively coupled plasma reactor. Trenches were etched  $2\text{ }\mu\text{m}$  deep to allow sufficient time to form the facets and to finish lateral growth and coalescence of adjoining cantilevers before GaN growing upward in the trenches contacted the cantilevers. Both specimens used an AlN nucleation layer deposited at  $480^\circ\text{C}$ . This nucleation layer and our metalorganic chemical vapor deposition (MOCVD) methods [14] produced a VTD density of  $\sim 2 \times 10^9/\text{cm}^2$  for planar growth of GaN on sapphire as determined by atomic force microscopy (AFM). The first specimen was grown at  $1050^\circ\text{C}$  to an initial thickness of  $0.6\text{ }\mu\text{m}$ ; this temperature is expected to form a flat (0001) surface and vertical sidewalls. Lateral growth was then done at  $1100^\circ\text{C}$  to coalesce cantilevers followed by growth at  $1050^\circ\text{C}$  to a thickness of  $4\text{ }\mu\text{m}$ . The second specimen was grown to  $0.1\text{ }\mu\text{m}$  thick at  $1050^\circ\text{C}$ ; the temperature was then reduce to  $950^\circ\text{C}$  to form {11-22} facets during  $0.5\text{ }\mu\text{m}$  vertical growth. Subsequent lateral and vertical growths were identical to those of the first specimen. To verify that the intended faceted structures had formed, growth was halted in identical specimens after  $0.6\text{ }\mu\text{m}$ . Scanning electron microscope images (SEM) in Fig.1 show the expected (0001) and {11-22} faceted surfaces.

In the specimen without facetting, cross-sectional TEM (XTEM) images over mesas as in Fig. 2(a) show many VTDs turned horizontal but a comparable number remain vertical, 30 - 70%. This redirection and some detected in our earlier work [6] suggest that VTDs within  $\sim 0.5\text{ }\mu\text{m}$  of mesa

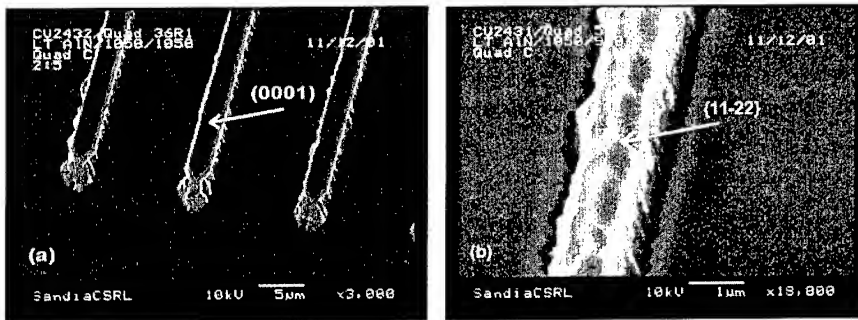


**Figure 1.** SEM images of GaN on sapphire mesas where growth was halted (a) after  $0.6\text{ }\mu\text{m}$  at  $1050^\circ\text{C}$ , and (b) after  $0.1\text{ }\mu\text{m}$  at  $1050^\circ\text{C}$  plus  $0.5\text{ }\mu\text{m}$  at  $950^\circ\text{C}$  to form {11-22} facets.

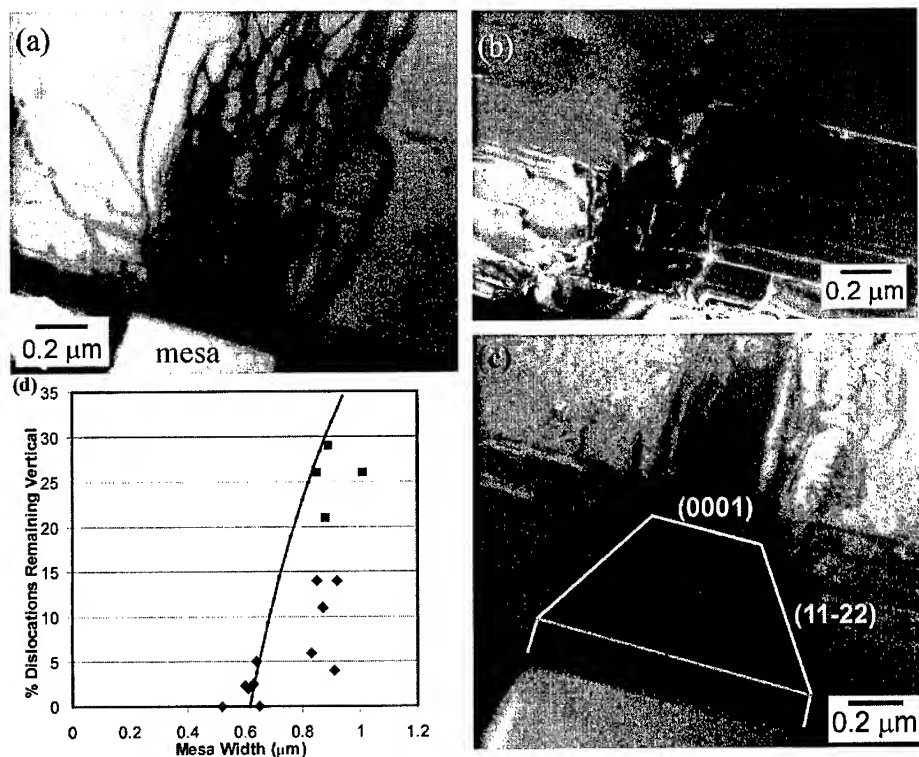


**Figure 2.** (a)-(c) Cross-sectional TEM images of dislocations over mesas imaged with (11-20) two-beam diffraction conditions in (a) specimen grown without initial faceting (bright field), (b) with faceting, mesa width 0.65 μm, all VTDs turned (dark field), and (c) with faceting, mesa width 1.0 μm, 26% of VTDs remain vertical (bright field). (d) Percentage of VTDs remaining vertical versus mesa width. Curve shows percentage of mesa not covered by facets.

edges are likely to be turned horizontal. This may be due to image forces on VTDs near the vertical sidewalls or to dislocation interactions. Images with both  $g = (11-20)$  and  $(0002)$  diffraction vectors, we find that comparable fractions of edge (Burgers vector  $\mathbf{b} = \mathbf{a}$ ) and mixed ( $\mathbf{b} = \mathbf{a} + \mathbf{c}$ ) VTDs were turned. Other microstructures in this specimen are discussed elsewhere [6,13].

The percentage of VTDs remaining vertical is much less with faceting and depends on mesa width; see Figs. 2(b-d). In Fig. 2(b), all VTDs are turned to horizontal. Vertical growth of 0.5 μm was used in the faceting step; since  $\{11-22\}$  facets are tilted 58° from horizontal, facets on each side of the mesa could completely cover widths up to 0.62 μm, about the width of the mesa in Fig. 2(b). However, the 1.0 μm-wide mesa in Fig. 2(c) has 26% VTDs remaining vertical. Drawn on this image is the expected facet structure. The  $\{11-22\}$  facets correspond well with where VTDs turn near the sides, and the (0001) facet over the center intercepts most VTDs remaining

vertical. In Fig. 2(d), the percentage of VTDs remaining vertical is plotted versus width for a number of mesas. The curve is the fraction of mesa width not covered by facets; it accounts well for the onset of unturned VTDs near  $0.6\ \mu\text{m}$  and for the upper limit on unturned VTDs. Lesser percentages found for mesa widths of  $0.8 - 1.0\ \mu\text{m}$  are believed due to the additional turning mechanism discussed above for growth without facetting.

This analysis indicates how to optimize the removal of VTDs over mesas: **A)** The growth height and time of the facetting step need to be sufficient to cover all mesas completely with slanted facets. This places requirements on substrate processing and growth methods: **B)** Mesa widths need to be uniform and trenches deep enough to allow the time needed for facet growth and lateral growth of cantilevers before GaN growing upward from the trenches intercepts the cantilevers. We have also found that turning VTDs with facets reduced tilting between GaN over mesas and cantilevers when compared to the specimen without facetting [7]. Overall, the specimen with facetting had VTD densities of  $3-8 \times 10^7/\text{cm}^2$ , an  $\sim 40$ -fold reduction compared to similar growth on planar sapphire, whereas a factor of  $\sim 7$  was expected based on mesa area.

#### Cantilever Epitaxy using Low VTD-Density Nucleation Layer

In the second new approach, we used a different nucleation layer that had been shown to give a low VTD density for GaN on planar sapphire,  $2-4 \times 10^8/\text{cm}^2$  [12]. Sapphire was patterned for narrow mesas as before, and a nucleation layer of GaN was grown at  $540^\circ\text{C}$ . This layer was ramped to  $1050^\circ\text{C}$  over 8.5 min. and then annealed at this temperature for 1 min. However, when growth is initiated at high temperatures with the introduction of trimethylgallium, a low  $\text{NH}_3$  flow of 2.25 slm was used for 15 minutes instead of the usual (and final) 6.0 slm flow. This delays the transition from the initially nucleated 3D islands to 2D planar growth as monitored by in situ reflectance. The islands develop a faceted structure before forming a continuous planar surface. This nucleation scheme was followed by growth of  $\{11-22\}$ -faceted GaN over mesas at  $950^\circ\text{C}$  as described above, with final growth to a thickness of  $3\ \mu\text{m}$ .

The VTD density at the surface was examined with AFM, TEM and cathodo-luminescence (CL) as seen in Figs. 3, 4 and 5. Plan-view TEM and CL both indicated a density of  $2-3 \times 10^7/\text{cm}^2$ . The AFM images gave about one half this value,  $1.3 \times 10^7/\text{cm}^2$ . Thus CE has further reduced the VTD density by a factor of  $\sim 10$  relative to planar low-VTD growth. We believe all dislocations are accounted for (within the uncertainty range) based on the following. First, there is good agreement between plan-view TEM and CL, which examines much broader areas. Moreover, the value for AFM is also in agreement since AFM is relatively insensitive to pure edge dislocations

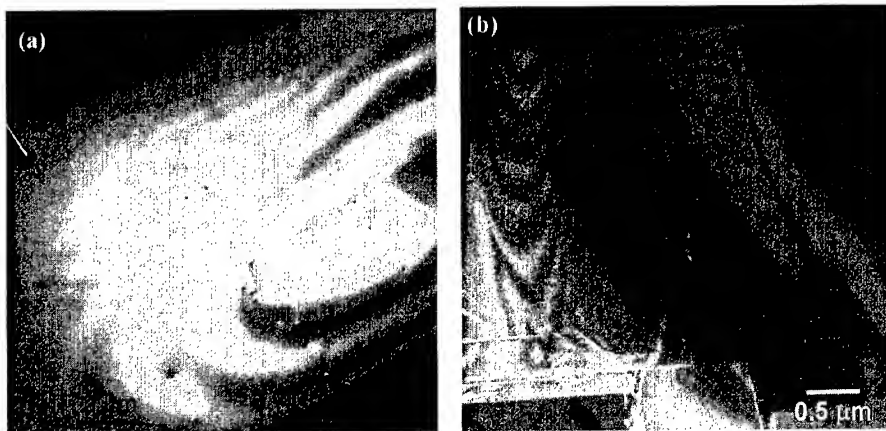


Figure 3. AFM image of the surface of CE GaN grown with delayed recovery GaN nucleation layer, narrow mesas and initial faceted growth. Note step-flow growth across more than two CE periods and the low density of dislocations, seen as terrace steps ending at a point.

( $\mathbf{b} = \mathbf{a}$ ), which are about one-half of all VTDs, whereas mixed ( $\mathbf{b} = \mathbf{a} + \mathbf{c}$ ) and pure screw ( $\mathbf{b} = \mathbf{c}$ ) dislocations leave steps at the surface that AFM detects. CL is expected to detect all types of dislocations since they are centers of non-radiative recombination [15]. Plan-view TEM might not detect pure screw ( $\mathbf{b} = \mathbf{c}$ ) dislocations since their Burgers vector is out of the plane and orthogonal to in-plane diffraction vectors  $\mathbf{g} = (hkl0)$ . However, we tilted a specimen  $32^\circ$  to obtain diffraction contrast from  $\mathbf{g} = (11\bar{2}2)$  with a component along the  $\mathbf{c}$  direction; moreover, the projected lengths of VTDs through the thin specimen are increased by the tilting, making them easier to detect. This orientation gave only a modest 3% increase in VTD density. Since the same density was obtained in several wafer dies spaced several centimeters apart with these three methods, the above density accurately represents the specimen as a whole.

#### FURTHER DEVELOPMENTS OF CANTILEVER EPITAXY

We envision several future developments of CE. The VTD densities in GaN on sapphire have been greatly reduced, but removal of VTDs over mesas is incomplete. With more uniform mesas



**Figure 4** (above). TEM images of GaN with low-VTD nucleation, obtained with (11-20) diffraction conditions: (a) (left) Bright-field, plan-view image showing rows of VTDs over mesas and at cantilever coalescences. A defect with lateral dislocations is seen at the far left. (b) (right) Weak-beam, cross-sectional image showing dislocations emerging from the mesa and turned to horizontal, and two remaining VTDs threading to the surface.

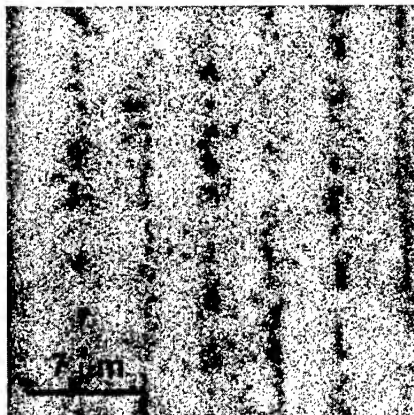


**Figure 5** (left). Scanning CL image of GaN with low VTD nucleation, obtained with 5 keV electrons and broad-band optical detection. VTDs over mesas and at coalescences are non-radiative and appear as dark spots. The area is about  $500 (\mu\text{m})^2$ .

or new growth schemes, it appears possible to turn all VTDs over mesas. Cantilever growth and coalescence need to be improved to remove dislocations and eliminate the “dark-block” defects [13]. Comparable numbers of VTDs are seen over mesas and at coalescences in Fig. 5, and thus both need attention. All told, we think our results indicate that CE can produce sufficiently low VTD densities in GaN to place devices continuously across wafers. A potentially important application of CE is AlGaIn growth for UV emitters. Since AlGaIn nucleates on SiO<sub>2</sub> as well as sapphire and SiC, the lateral growth methods using SiO<sub>2</sub> layers will not be useful, whereas CE will not be affected. It also appears likely that GaN substrates will one day be readily available. Then, CE appears important for AlGaIn growth on GaN to remove VTDs formed at GaN/AlGaIn interfaces. It is also possible to use 2D patterns parallelogram-shaped mesas for growth initiation; our initial attempts were successful. This scheme could further reduce VTD densities. More generally, CE can be used to reduce threading dislocations in other heteroepitaxial systems.

We thank M. P. Moran and A. K. Norman for developing TEM specimen preparation methods for the difficult CE-GaN/sapphire materials, and A. Kim for discussions about TEM imaging of dislocations. Sandia is a multiprogram laboratory operated by Sandia Corporation, a Lockheed Martin Company, for the U. S. Department of Energy under contract DE-AC04-94AL85000.

## REFERENCES

1. J. S. Speck and S. J. Rosner, *Physica B* **273-274**, 24 (1999).
2. T. S. Zheleva, O.-H. Nam, M. D. Bremser and R. F. Davis, *Appl. Phys. Lett.* **71**, 2472 (1997).
3. D. Kapolnek, S. Keller, R. Vetry, R. D. Underwood, P. Kozodoy, S. P. DenBaars and U. K. Mishra, *Appl. Phys. Lett.* **71**, 1024 (1997).
4. K. Hiramatsu, K. Nishiyama, M. Onishi, H. Mizutani, M. Narukawa, A. Motogaito, H. Miyake, Y. Iyechika and T. Maeda, *J. Cryst. Gro.* **221**, 316 (2000).
5. K. Linthicum, T. Gehrke, D. Thomson, E. Carlson, P. Rajagopal, T. Smith, D. Batchelor and R. Davis, *Appl. Phys. Lett.* **75**, 196 (1999).
6. C. I. H. Ashby, C. C. Mitchell, J. Han, N. A. Missert, P. P. Provencio, D. M. Follstaedt, G. M. Peake and L. Griego, *Appl. Phys. Lett.* **77**, 3233 (2000).
7. D. M. Follstaedt, P. P. Provencio, N. A. Missert, C. C. Mitchell, D. D. Koleske, A. A. Allerman and C. I. H. Ashby, *Appl. Phys. Lett.* **81**, 2758 (2002).
8. T. M. Katona, M. D. Craven, P. T. Fini, J. S. Speck and S. P. DenBaars, *Appl. Phys. Lett.* **79**, 2907 (2001).
9. A. Strittmatter, S. Rodt, L. Reißmann, D. Bimberg, H. Schröder, E. Obermeier, T. Riemann, J. Christen and A. Krost, *Appl. Phys. Lett.* **76**, 727 (2001).
10. T. Detchprohm, M. Yano, S. Sano, R. Nakamura, S. Mochiduki, T. Nakamura, H. Amano and I. Akasaki, *Jpn. J. Appl. Phys.* **40**, L16 (2001).
11. A. Sakai, H. Sunakawa and A. Usui, *Appl. Phys. Lett.* **71**, 2259 (1997); *Appl. Phys. Lett.* **76**, 442 (2000).
12. D. D. Koleske, A. J. Fischer, A. A. Allerman, C. C. Mitchell, K. C. Cross, S. R. Kurtz, J. J. Figiel, K. W. Fullmer, and W. G. Breiland, *Appl. Phys. Lett.* **81**, 1940 (2002).
13. P. P. Provencio, D. M. Follstaedt, N. A. Missert, D. D. Koleske, C. C. Mitchell, A. A. Allerman and C. I. H. Ashby, paper L3.15, these proceedings.
14. M. E. Coultrin, C. C. Willan, M. E. Bartram, J. Han, N. Missert, M. H. Crawford and A. G. Baca, *MRS Internet J. Nitride Semicond. Res.* **4S1**, G6.9 (1999).
15. S. J. Rosner, E. C. Carr, M. J. Lodowise, G. Girolami and H. I. Erikson, *J. Appl. Phys.* **70**, 420 (1997).

## Lateral growth of $\text{Al}_x\text{Ga}_{1-x}\text{N}$ and GaN on SiC substrates patterned by photo-electrochemical etching

U. Rossow\*, N. Riedel, F. Hitzel, T. Riedl, and A. Hangleiter  
TU Braunschweig, Inst. f. Techn. Physik, D-38106 Braunschweig, Germany

PACS: 81.15.Gh, 81.05.Ea, 68.55.Ac, 81.65.Cf, 82.45.Vp, 61.72.Ff, 68.37.Hk

### Abstract

The large defect densities in heteroepitaxially grown group-III-nitride layers on sapphire or SiC cannot be tolerated in applications such as lasers. We report here on a defect reduction by overgrowth of patterned n-6H-SiC(0001) surfaces.

First, we formed mesa structures in the windows of metal masks and then after removal of the masks layers of  $\text{Al}_x\text{Ga}_{1-x}\text{N}$  and GaN were grown by low-pressure MOVPE under conditions of high lateral growth rates. We demonstrate that layers and layered structures can be grown with smooth surfaces and reduced defect densities.

## 1 Introduction

The defect densities of conventionally grown GaN layers are typically around  $10^9\text{cm}^{-2}$  or slightly below independent on whether sapphire or SiC is used as substrate material. Such a high defect density reduces the performance and lifetime of light emitting devices such as lasers or high brightness LEDs. Therefore, lateral overgrowth processes such as ELOG [1, 2, 3, 4], pendeo-epitaxy [5] or variations of it [6, 7] are mostly used to reduce the defect density.

In the conventional ELOG process first a GaN layer is grown and on top masks of  $\text{SiO}_2$  or  $\text{SiN}_x$  are produced which are laterally overgrown in a second growth process. The reported defect densities in the regions above the masks are reduced to levels in the  $10^6\text{cm}^{-2}$  range. The disadvantage of this process is that the GaN layers grown in the second step maybe contaminated by silicon or oxygen and therefore usually thick GaN layers are needed for devices. Furthermore, conventional GaN surface preparation such as KOH or HCl etching may damage the masks and thus GaN in the window regions cannot be well prepared.

While the classical ELOG process works well with sapphire substrates for SiC the total thickness of the layered structure is limited because of crack formation. Therefore, the pendeo-epitaxy process was developed in which GaN was grown on an Al-containing buffer

\*Email: u.rossow@tu-bs.de

layer and then the deposited layer were etched back in windows of prepared masks. In a second step GaN is grown such that it starts growing from the sidewalls of the structure with the advantage that GaN is not growing on SiC (under the chosen growth conditions). However, for laser structures GaN buffer layers are not well suited. Furthermore, reactive ion etching used to etch back creates lattice defects and may lead to surface contamination.

We used another approach namely to pattern the SiC substrate first and then to overgrow the structure. Hence, the structure formation and growth process are separated. In addition, we show in this paper that we can use GaN and  $\text{Al}_x\text{Ga}_{1-x}\text{N}$  as buffer layers.

## 2 Experimental

As substrate material we used in this study commercially available n-type doped ( $0.04\Omega\text{cm}$ ), Si-face, on-axis 6H-SiC(0001) (Cree Inc.).

We developed a patterning process for n-type doped SiC substrates based on photo-electrochemical (PEC) etching. In a first step platinum masks were produced by conventional photolithography. In a second step the substrate with ohmic reverse side contact was mounted in a PTFE cell equipped with a platinum grid as top electrode. Sulfuric acid (obtained by diluting conc. sulfuric acid with DI water 1:3 by volume) was used as electrolyte. The substrates were etched under mercury high pressure lamp (200W) illumination with forward bias of typically 1-3V for about 90minutes. Oxide layers are formed in the windows which are etched in a final step by HF. We obtain mesa structures of width 2-6  $\mu\text{m}$  and periodic lengths of 6-10  $\mu\text{m}$ . The stripe pattern is aligned along either  $[1\bar{1}00]$  or  $[11\bar{2}0]$  directions (see Fig. 1).

The silicon doped GaN and  $\text{Al}_x\text{Ga}_{1-x}\text{N}$  layers were grown by low pressure metal-organic vapor phase epitaxy (MOVPE) (Aixtron AIX 200RF) in an horizontal reactor with trimethyl-gallium (TMG), trimethylaluminum (TMAI), and ammonia ( $\text{NH}_3$ ) as precursors and hydrogen as carrier gas. In some cases  $\text{Al}_x\text{Ga}_{1-x}\text{N}$  layers were grown with trimethylindium (TMI) in the background to enhance the lateral to vertical growth rates. Growth started with a thin (10-50nm thick)  $\text{Al}_x\text{Ga}_{1-x}\text{N}$  nucleation layer grown at  $1190^\circ\text{C}$  with  $x \sim 0.3$ . GaN buffer layers were grown afterwards at  $1180^\circ\text{C}$  and pressure of 100mbar with hydrogen as carrier gas. The typical growth conditions were: Total flux 6slpm,  $\text{NH}_3$  2000sccm, V/III ratio approximately 1355.  $\text{Al}_x\text{Ga}_{1-x}\text{N}$  buffer layers were grown at  $1190^\circ\text{C}$ , 50mbar, V/III ratios of about 2500, and with compositions  $x = 0.1 \dots 0.2$  (same total flux or increased to 10slpm). PL data indicate that the compositions are the same as on plane substrates. In most cases a GaN layer was grown on top with an intermediate GaN layer grown with higher V/III ratio of 2560 and thickness 160nm.

All temperatures are readings of a thermocouple placed in the susceptor in which a disk with the sample rotates. Due to the limited thermal contact between disk and susceptor the temperatures at the growth front are estimated to be  $100^\circ\text{C}$  to  $150^\circ\text{C}$  lower than the

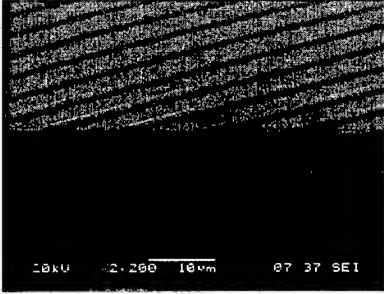


Figure 1: Mesa structure in 6H-SiC formed by photoelectrochemical etching using platinum masks after oxide removal. Mesa widths are typically  $2\text{-}6\mu\text{m}$  and periodic lengths are  $6\text{-}10\mu\text{m}$ .

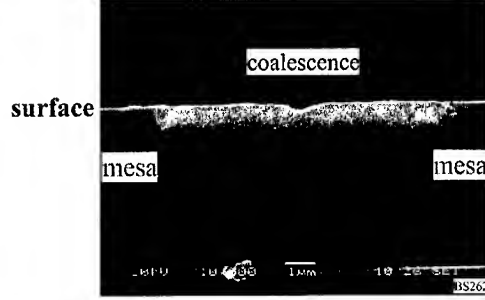


Figure 2: View from the side (SEM) of an overgrown structure (here thin  $\text{Al}_x\text{Ga}_{1-x}\text{N}$  nucleation followed by GaN). The surface is smooth, essentially no growth on top of mesa.

thermocouple readings.

Growth was monitored in-situ by reflectometry. After growth the samples were characterized by AFM, SEM, conventional photoluminescence (PL) at room and low temperatures (20K and lower) using an Ar-ion (334nm) or He-Cd laser (325nm) and PL taken under near-field optical microscope conditions (SNOM).

### 3 Results and Discussion

The patterned SiC substrates have been overgrown by GaN and  $\text{Al}_x\text{Ga}_{1-x}\text{N}$  layers. Growth started always with a thin  $\text{Al}_x\text{Ga}_{1-x}\text{N}$  nucleation layer followed by a GaN or  $\text{Al}_x\text{Ga}_{1-x}\text{N}$  buffer layer. Fig. 2 shows a SEM picture from the side of structure (mesa width  $3\mu\text{m}$ , periodicity about  $10\mu\text{m}$ ) grown with a thin  $\text{Al}_x\text{Ga}_{1-x}\text{N}$  nucleation and buffer layer and thin GaN buffer. For plane substrates the total  $\text{Al}_x\text{Ga}_{1-x}\text{N}$  thickness would be about  $150\text{nm}$  and that of the GaN layer  $220\text{nm}$ . The regions between the mesa are completely filled and not much material was grown on top of the mesa. This is a first indication that growth starts from the sidewalls and not from the top of the mesa structure as expected. Furthermore, the height of the mesa is above  $1\mu\text{m}$  and hence, the growth rate is much higher compared to plane substrates again in agreement with an assumed lateral growth mode.

A smoothening of the growth front was also observed when taking  $\text{Al}_x\text{Ga}_{1-x}\text{N}$  as thick buffer layer which is shown in Fig. 3. In this case the composition was about 13% Al and a plane thickness of about  $1.6\mu\text{m}$ . The GaN layer on top has a total thickness of  $900\text{nm}$ . While in the case of GaN buffer layers we observed an instability of the growth in some

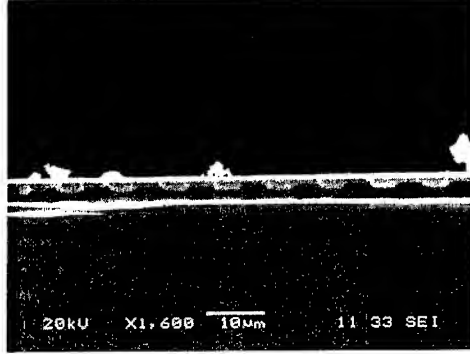


Figure 3: View from the side (SEM) of an overgrown structure (here thick  $\text{Al}_x\text{Ga}_{1-x}\text{N}$ , GaN cap layer). The layered structure is homogeneous, no voids visible.

parts of the sample indicated by large crystallite-like features, in the case of  $\text{Al}_x\text{Ga}_{1-x}\text{N}$  the growth was uniform.

In the case of the GaN buffer layer we performed an analysis of the defect structure by photoelectrochemical etching in KOH:water (0.025M) which indicates dislocation lines by whisker formation [8]. The resulting surface structure is shown in Fig. 4. We observe a

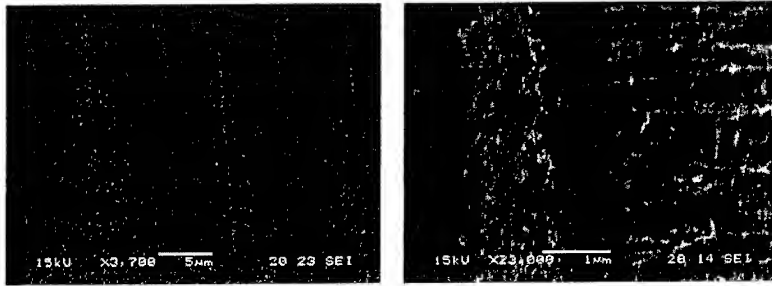


Figure 4: Defect structure revealed by photoelectrochemical etching by KOH:H<sub>2</sub>O of sample shown in Fig. 1 (left: low magnification, right: high magnification). High density of dislocation above mesa, between mesa dislocation lines parallel to surface visible.

high density of dislocations above the mesa and low density in between. Furthermore, some dislocation lines are apparent which are aligned parallel to surface again indicating lateral growth and in agreement with a defect reduction in the upper part of the layered structure. SNOM is also showing an increased near-bandedge emission intensity of a factor 3-4 above the inbetween regions relative to that above the mesa.

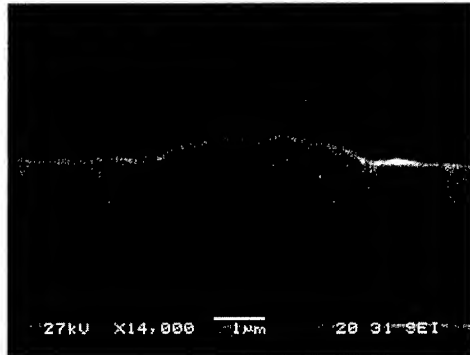


Figure 5: View from the side (SEM) of an overgrown structure (here thin  $\text{Al}_x\text{Ga}_{1-x}\text{N}$ , thin GaN). Two facets are visible. That with the higher inclination angle seems to be parallel to the sidewall of mesa.

We gained further inside into the growth mode from a growth experiment in which we stopped growth in an early stage (total  $\text{Al}_x\text{Ga}_{1-x}\text{N}$  thickness corresponding to 100nm on plane substrate, 75nm GaN). We observe material essentially grown only at the sidewalls of the mesa. This material shows three facets: Above the mesa oriented in c-direction, a facet with small angle and a facet which likely corresponds to one of the  $(1\bar{1}01)$ -planes. The latter one seems to be parallel to the (inclined) sidewalls of the mesa. This and other pictures indicate that the growth front propagates until one from the neighbor mesa is reached and material may or may not – for unknown reasons – fill up the coalescence region. The facet of lower inclination angle may tilt towards the horizontal possibly by establishing step bunches which may smooth out in a latter stage. Further experiments are needed to clarify this part of the growth process.

We note that until now we have no indication that there is a distinction in the properties of the layers with mesa orientation along  $[1\bar{1}00]$  or  $[11\bar{2}0]$  directions which is in contrast to observations of conventional ELOG.

## 4 Summary and conclusion

We patterned n-type doped 6H-SiC(0001) surfaces by photoelectrochemical etching (PEC). In this way prepared substrates were overgrown by GaN and  $\text{Al}_x\text{Ga}_{1-x}\text{N}$  layers under growth conditions which allow for high lateral growth rates.

The layers grown are continuous without voids and have smooth surfaces in most cases after approximately  $2\mu\text{m}$  material has been deposited. Defect etching shows an reduction of defect density in the layers in between the mesa. With GaN cap layers we find no evidence

of crack formation (though cracks are found in heterostructures without GaN cap layers). GaN layers show bright near bandedge luminescence.

Surprisingly, growth seems to be dominated by material nucleating on the sidewalls of the mesa with the growth front propagating in lateral direction.

The described lateral growth mode process seems to work and is very promising for defect reduction especially for laser structures.

### Acknowledgements

This work was funded by the German ministry for education and research (BMBF) Blue laser initiative.

### References

- [1] A. Usui, H. Sunakawa, A. Sakai, A. A. Yamaguchi: Jpn. J. Appl. Phys. Part 2, **36**, L899 (1997).
- [2] S. Nakamura, M. Senoh, S. Nagahama, N. Iwasa, T. Yamada, T. Matsushita, H. Kiyoku, Y. Sugimoto, T. Kozaki, H. Umemoto, M. Sano, K. Chocho: Appl. Phys. Lett. **72**, 211 (1998).
- [3] X. Li, S. G. Bishop, J. J. Coleman: MRS Internet J. Nitride Semicond. Res **4S1**, G4.8 (1999).
- [4] S. Tomiya, H. Nakajima, K. Funato, T. Miyajima, K. Kobayashi, T. Hino, S. Kijima, T. Asano, M. Ikeda: Phys. Stat. Sol. (a)**188**, 69 (2001).
- [5] R. F. Davis, T. Gehrke, K. J. Linthicum, P. Rajagopal, A. M. Roskowski, T. Zheleva, E. A. Preble, C. A. Zorman, M. Mehregany, U. Schwarz, J. Schuck, R. Grober: MRS Internet J. Nitride Semicond. Res. **6**, 14 (2001).
- [6] Y. Chen, R. Schneider, S. Y. Wang, R. S. Kern, C. H. Chen, C. P. Kuo: Appl. Phys. Lett. **75**, 2062 (1999).
- [7] C. I. H. Ashby, C. C. Mitchell, J. Han, N. A. Missert, P. P. Provencio, D. M. Follstaedt, G. M. Peake, L. Griego: Appl. Phys. Lett. **77**, 3233 (2000).
- [8] C. Youtsey, L. T. Romano, I. Adesida: Appl. Phys. Lett. **73**, 797 (1998).

### Distinct Magnesium Incorporation Behavior in Laterally Grown AlGa<sub>N</sub>

R. Liu, A. Bell, F.A. Ponce, D. Cherns\*, H. Amano\*\* and I. Akasaki\*\*

Dept. Physics and Astronomy, Arizona State University, Tempe, AZ, 85287-1504

\*H. H. Wills Physics Laboratory, Bristol, BS8 1TL, UK

\*\*Dept. of Materials Science and Engineering, Meijo University, Nagoya 468, Japan

#### ABSTRACT

Different magnesium incorporation behavior has been observed in heavily Mg-doped AlGa<sub>N</sub> epitaxial layers. The films were grown by metal-organic vapor phase epitaxy involving a lateral overgrowth technique on patterned sapphire substrates. TEM observations show that direct growth on sapphire exhibits pyramidal defects, while lateral overgrowth is homogeneous and free of structural defects. The orientation of the growth front significantly influences the microstructure, and the {0001} growth facet appears to be essential for the formation of the pyramidal defects. In addition, cylindrical and funnel-shaped nanopipes have been observed at dislocations with an edge component. The relationship between Mg segregation and these defects is discussed, and formation mechanisms are proposed taking into consideration the orientation of the growth front.

#### INTRODUCTION

The development of p-type doping of nitride semiconductors has made possible a number of technological advances including high-efficiency visible light emitting devices and blue laser diodes. Magnesium is currently the most commonly used p-type dopant. The activation of magnesium as an acceptor was first achieved by low-energy electron beam irradiation [1] and subsequently by thermal annealing [2]. In order to fabricate high-performance blue and ultraviolet laser diodes, it is necessary to improve p-type layer conductivity in Al<sub>x</sub>Ga<sub>1-x</sub>N films. The acceptor levels in these alloys are typically more than 230 meV from the valence band edge, with consequent low thermal activation ratios (<1%). High p-type conductivity then requires Mg doping levels of the order of 10<sup>19</sup> to 10<sup>20</sup> cm<sup>-3</sup>. At these levels, the solid solubility limit is sometimes exceeded giving rise to the formation of precipitates and other crystalline defects [3]. Polarity inversion due to Mg doping has been reported for molecular-beam epitaxy films [4,5]. Pyramidal defects have been observed under a variety of growth conditions [6,7]. Additionally, in bulk crystal and delta Mg-doping metal-organic vapor phase epitaxy (MOVPE) films, rectangular shape defects and highly-ordered polytypoids were also reported [6]. For the pyramidal defects, the Mg-rich chemical property has been proved by an energy dispersive x-ray spectrometry study [8]. From these observations it is clear that Mg doping plays a role in pyramidal defect formation and polarity inversion, but so far their precise crystalline nature is not completely understood. In this report, a TEM study is presented of highly Mg-doped AlGa<sub>N</sub> films grown by a process involving epitaxial lateral overgrowth (ELO) on patterned sapphire substrates. The formation mechanism of the pyramidal defects is discussed by examining their microstructure and distinct distribution in the epilayers. Additionally, the role of dislocations in Mg segregation is also reported.

## EXPERIMENTAL

The  $\text{Al}_{0.03}\text{Ga}_{0.97}\text{N}$  sample was grown by MOVPE on a patterned sapphire substrate with grooves along  $[1\bar{1}20]_{\text{sapphire}}$  or  $[1\bar{1}00]_{\text{nitride}}$  [9]. A  $5\mu\text{m}$ -thick epilayer was deposited on a  $\sim 20\text{ nm}$  thick low temperature AlN buffer layer at  $1100^\circ\text{C}$ . The doping concentration of  $9 \times 10^{19}\text{ cm}^{-3}$  was measured by secondary ion mass spectrometry. Transmission electron microscopy (TEM) observations were made using a JEOL 4000EX microscope for lattice imaging with an acceleration voltage of  $400\text{ kV}$  (resolution limit  $\sim 1.7\text{ \AA}$ ), and a Philips EM430 and a CM200 microscope for  $g\cdot b$  diffraction analysis with an acceleration voltage of  $250\text{ kV}$  and  $200\text{ kV}$  respectively. TEM cross-section specimens were thinned by ion milling with an ion energy of  $4.5\text{ keV}$  after mechanical polishing.

## RESULTS AND DISCUSSION

### Pyramidal defect distribution

Figure 1 shows a cross sectional TEM image along the groove direction (i.e.  $[1\bar{1}00]_{\text{AlGaN}}$ ). The progression of the growth fronts is schematically illustrated using three sets of parallel dashed lines. The seeding domain has a growth front parallel to the basal plane, while the ELO domain grows on a  $\{11\bar{2}2\}$  front. The boundary between these domains is marked with an inclined solid curve line. The slope of the boundary will decrease if lateral growth is enhanced. Figure 2 (a) shows the AlGaN sample in the vicinity of the ELO domain. A dashed line marks the boundary between the seeding and the ELO domain. In the seeding domain, a high density of pyramidal defects measuring  $\sim 20\text{ nm}$  across the basal facet is observed in addition to the dislocations. However, the neighboring ELO domain exhibits perfect microstructure. The differences that are observed in the two domains appear to be a result of the discrete growth fronts. This was also observed in an ELO GaN sample, which consists of a relatively flat domain boundary due to a faster lateral growth (Fig.2 (b)). These findings indicate that the formation of pyramidal defects depends on the growth front. The implication is that growth on fronts other than  $\{0001\}$  can have superior homogeneity properties even under a heavy doping condition. The growth front parallel to  $\{0001\}$  plane appears to be a key factor for creating these defects.

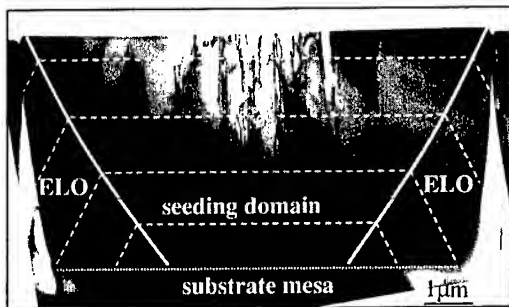


**Figure 1.** Schematic of growth front evolution shown in a cross section. Horizontal dashed lines correspond to  $\{0001\}$  growth fronts; while the inclined dashed lines are ELO  $\{11\bar{2}2\}$  growth fronts.

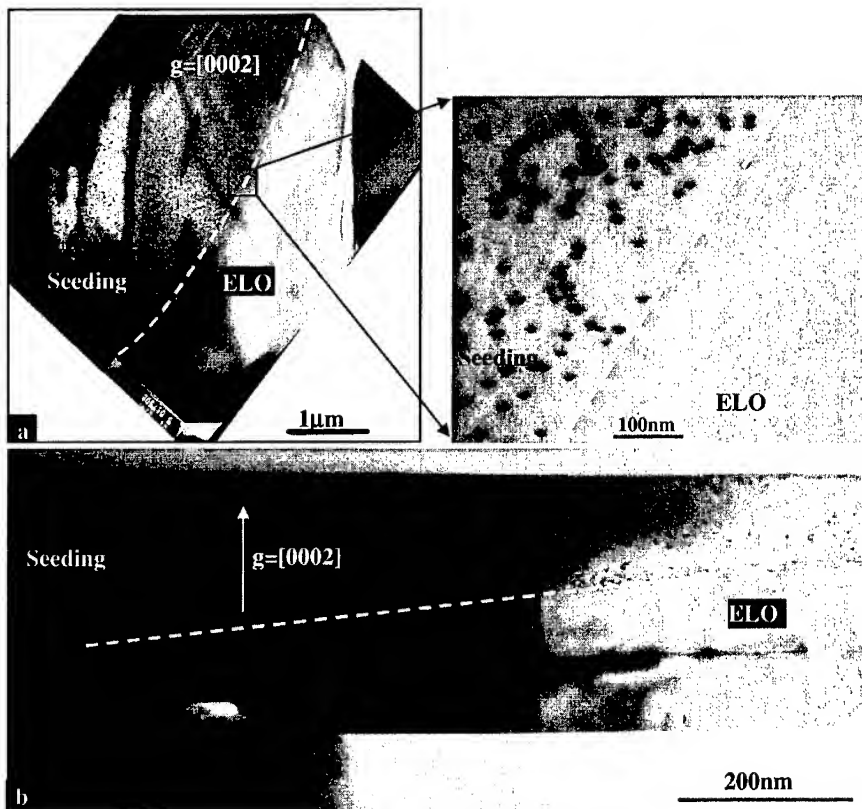


**Figure 2.** Bright-field cross-section images showing the distribution of pyramidal defects in highly Mg-doped AlGaIn (a) and GaN (b) layers. The sharp boundary between the regions with and without pyramidal defects (inset) arises from the  $\{0001\}$  and  $\{11\bar{2}2\}$  growth fronts shown in Fig. 1.

Optical properties were characterized using cathodoluminescence (CL) and they were found to be closely correlated with the microstructure [3]. Mg acceptor concentration was uniform across the whole film, according to monochromatic CL imaging. However, the near-band-edge emission was only observed in the ELO domain, indicating that the ELO domain has a much-reduced density of point defects. The superior optical properties in the ELO domain indicate that the ELO process has a distinct impurity incorporation mechanism, which is favorable compared with the typical  $\{0001\}$  growth front mode.

#### **Mg segregation in pyramidal defects**

In order to understand the distribution and formation mechanism of the pyramidal defects, the microstructure needs to be analyzed. Lattice images of the pyramidal defects

projected along  $[1\bar{1}20]$  and  $[\bar{1}\bar{1}00]$  zone axes are shown in figure 3 (a) and (b). The angle between the inclined facet and the basal plane is  $\sim 47^\circ$  and  $\sim 43^\circ$  in the  $[\bar{1}\bar{1}00]$  and  $[1\bar{1}\bar{2}2]_{\text{AlGaIn}}$  projection respectively. Similar angles were measured for pyramidal defects in GaN in which the structure of the pyramid was proposed to consist of a hexagonal basal-plane facet and six side facets of  $\{1\bar{1}\bar{2}3\}$ , and they were identified as inversion domains [7]. The lattice image in figure 3 (a) is in agreement with the result. The slight displacement in basal-plane lattice is indicated by a dashed line across the pyramidal defect, which results from the flipping of Ga and N atoms across inversion domain boundaries [10]. A schematic is shown in figure 4 to illustrate the formation of the inversion domain boundary due to Mg segregation.

The microstructure analysis indicates that the pyramidal defects have a six-fold symmetry along c-axis, which is present on the  $\{0001\}$  growth front, but is absent on the  $\{1\bar{1}\bar{2}2\}$  growth front. The incorporation of the pyramidal defects is sensitive to the symmetry of the growth front. This leads to the defects forming only in the  $[0001]$  growth direction, as shown in figure 2.

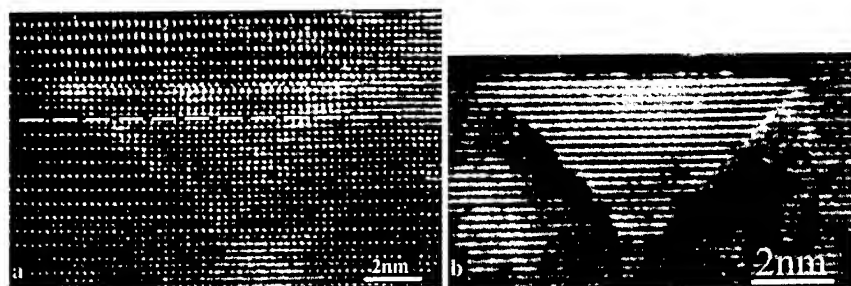


**Figure 3.** Lattice images of pyramidal defects, projected along (a)  $[1\bar{1}\bar{2}0]$  and (b)  $[\bar{1}\bar{1}00]$ . A broken white line drawn across the defect indicates shift in lattice point consistent with an inversion domain.

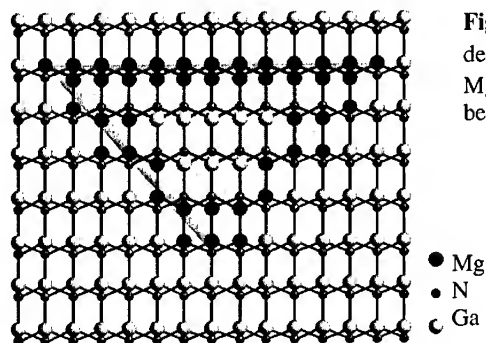


**Figure 4.** A schematic of a pyramidal defect viewed along  $[1\bar{1}00]$  projection. Mg segregation on the boundary is believed to induce the defect.

### **Mg interaction with dislocations**

In the vicinity of some dislocations, the density of the pyramidal defects is found to be substantially reduced. One of these regions is shown in figure 5. The images taken under different diffraction conditions indicate that this region is full of dislocations with an edge component. Instead of forming Mg-rich pyramidal defects, Mg impurities prefer to segregate to the dislocations. An enlarged image of this region is shown in figure 5 (c), and indicates that these dislocations with an edge component are decorated with funnel-shape defects. No specific facets are identified for these funnel-shape structures. In some other regions, the dislocations are also found to open up into a cylindrical shape. These defects show strong contrast under slightly defocus condition, suggesting that they are voids. Mg segregation to the dislocation core is believed to result in the nanopipe structure [11].

The various shapes of the nanopipes may result from the fluctuation of impurity level. However, the transformation from cylindrical to funnel-shape void was observed during focused electron beam irradiation, as shown in figure 6. The electron beam of 200 keV was focused at the top portion of the nanopipe. The cylindrical nanopipe transformed to a funnel-shape structure by rearranging the neighboring atoms. This transformation is not reversible, suggesting that the funnel-shape void structure is energetically more stable than the cylindrical one.

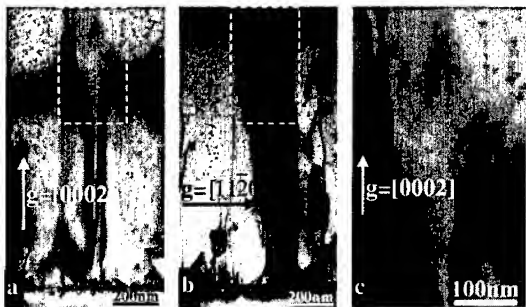


**Figure 5.** Cross-sectional images to show dislocations with (a) screw and (b) edge component. A region (marked in a box) denuded of pyramidal defects is evident in the vicinity of dislocations with an edge component. An enlarged view of this region is shown in figure (c).

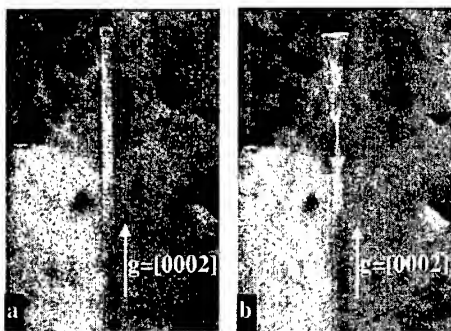


**Figure 6.** Cross-sectional images to show the irradiation effect of a 200 keV electron beam on the nanopipe structure; figure (b) was taken after several minutes of electron beam irradiation on figure (a).

## CONCLUSIONS

On  $\{11\bar{2}2\}$  growth fronts, lateral growth is free of pyramidal defects, even though a high density of pyramidal defects is present in the adjacent domain grown along the  $c$ -axis direction. Mg segregation on the  $\{0001\}$  growth front probably induces the pyramidal inversion domain defects. The six-fold symmetry of the  $\{0001\}$  growth front is critical for creating the pyramidal defects. Dislocations with an edge component are found to be more favorable Mg segregation sites than the pyramidal defects. Mg segregation results in dislocations decorated by nanopipes with various shapes. Focused electron beam irradiation is found to transform nanopipes from cylindrical to funnel-shape structure. So far, the possibility cannot be excluded that the funnel-shape voids were transformed from cylindrical nanopipes during TEM sample preparation and observation, rather than as-grown.

## ACKNOWLEDGEMENTS

This study was supported by a grant from the New Energy and Industrial Technology Development Organization (NEDO Project No. 01-MB10).

## REFERENCES

- [1] H. Amano, M. Kito, K. Hiramatsu, and I. Akasaki, *Jpn. J. Appl. Phys.* **28**, L2112 (1989).
- [2] S. Nakamura, T. Mukai, M. Senoh, and N. Iwasa, *Jpn. J. Appl. Phys.* **31**, L139 (1992).
- [3] A. Bell, R. Liu, F. A. Ponce, H. Amano, I. Akasaki, and D. Cherns, *Appl. Phys. Lett.* (accepted for publishing).
- [4] V. Ramachandran, R. M. Feenstra, W. L. Sarney, L. Salamanca-Riba, J. E. Northrup, L. T. Romano, and D. W. Greve, *Appl. Phys. Lett.* **75**, 808 (1999).
- [5] L. T. Romano, J. E. Northrup, A. J. Ptak and T. H. Myers, *Appl. Phys. Lett.* **77**, 2479 (2000).
- [6] Z. Lilliental-Weber, M. Benamara, W. Swider, J. Washburn, I. Grzegory, S. Porowski, D. J. H. Lambert, C. J. Eiting and R. D. Dupuis, *Appl. Phys. Lett.* **75**, 4159 (1999).
- [7] P. Venegues, M. Benaissa, B. Beaumont, E. Feltin, P. De Mierry, S. Dalmaso, M. Leroux, and P. Gibart, *Appl. Phys. Lett.* **77**, 880 (2000).
- [8] M. Leroux, P. Venegues, S. Dalmaso, M. Benaissa, E. Feltin, P. De Mierry, B. Beaumont, B. Damlano, N. Grandjean, and P. Gibart, *Phys. Stat. Sol. (a)* **192**, 394 (2002).
- [9] T. Detchprohm, M. Yano, S. Sano, R. Nakamura, S. Mochiduki, T. Nakamura, H. Amano and I. Akasaki, *Jpn. J. Appl. Phys.* **40** L16 (2001).
- [10] D. Cherns, W. T. Young, M. Saunders, J. W. Steeds, F. A. Ponce, and S. Nakamura, *Phil. Mag. A* **77**, 273 (1998).
- [11] D. Cherns, Y.Q. Wang, R. Liu, and F.A. Ponce, *Appl. Phys. Lett.* (accepted for publishing).

---

## **Defects and Characterization**

### **Distinguishing negatively-charged and highly conductive dislocations in gallium nitride using scanning Kelvin probe and conductive atomic force microscopy**

Blake S. Simpkins and Edward T. Yu  
Department of Electrical and Computer Engineering and Program in Materials Science  
University of California at San Diego  
La Jolla, CA 92093-0407

Patrick Waltereit and James S. Speck  
Materials Department, University of California, Santa Barbara, Santa Barbara, California

#### **ABSTRACT**

Scanning Kelvin probe microscopy (SKPM) and conductive atomic force microscopy (C-AFM) are used to image surfaces of GaN grown by molecular beam epitaxy (MBE). Numerical simulations are used to assist in the interpretation of SKPM images. Detailed analysis of the same area using both techniques allows imaging of surface potential variations arising from the presence of negatively charged dislocations and dislocation-related current leakage paths. Correlations between the charge state of dislocations, conductivity of leakage current paths, and possibly dislocation type can thereby be established. Approximately 25% of the leakage paths appear to be spatially correlated with negatively charged dislocation features. This is approximately the level of correlation expected due to spatial overlap of randomly distributed, distinct features of the size observed, suggesting that the negatively charged dislocations are distinct from those responsible for localized leakage paths found in GaN. The effects of charged dislocation networks on the local potential profile is modeled and discussed.

#### **INTRODUCTION**

Group III-nitride semiconductors have been the subject of intensive research in recent years for optoelectronic and high power, high-speed electronic devices [1,2]. Although progress has been made in improving material quality and device performance, substantial challenges remain. In particular, the lack of readily available homoepitaxial substrates necessitates growth on either sapphire or SiC, both of which lead to degradation in material quality predominantly through the presence of high dislocation densities. These dislocations in GaN are known to degrade device performance through carrier scattering [3], non-radiative recombination [4], and increased reverse-bias leakage current [5,6]; however, the correlation among dislocation type, electronic properties such as charge and conductivity, remain subjects of active investigation.

Negatively charged dislocation features have previously been imaged using scanning Kelvin probe microscopy (SKPM) on both AlGaIn/GaN heterostructures grown by MBE [7] and GaN grown by hydride vapor phase epitaxy (HVPE) [8]. These charged features have also been imaged using scanning capacitance microscopy (SCM) on MOCVD GaN [9] and MOCVD AlGaIn/GaN HFETs on SiC [10]; however, the precise crystallographic nature of these charged dislocations was not determined. Mobility degradation in GaN films has been analyzed by modeling coulombic carrier scattering events at negatively charged dislocations [3] while pure screw dislocations have been implicated as the source for localized reverse bias current leakage paths [5], but the correlation between these leakage paths and the negatively charged dislocations

has yet to be examined. Correlating device degradation mechanisms with specific dislocation types will help determine which dislocation types are most harmful to device performance and will contribute to a more complete characterization of dislocations in GaN.

## EXPERIMENT

In the present work, MBE GaN layers deposited on MOCVD GaN templates on sapphire were studied. The templates are produced with thin low-temperature GaN nucleation layers followed by  $\sim 2\mu\text{m}$  of high temperature GaN growth. A  $\sim 350\text{nm}$  GaN layer was then grown by MBE in the gallium droplet region [11]. Previous TEM studies indicate a total dislocation densities of  $\sim 0.5\text{--}1 \times 10^9\text{cm}^{-2}$  is typical for these templates [12]. The MBE films grown on these templates have been shown to retain the defect structure and density of the template [11].

Samples were stored in ambient conditions and cleaned with trichloroethylene, acetone, and methanol in an ultrasonic bath prior to examination. Ohmic contacts were fabricated by deposition of Al/Ti metallization and subsequent rapid thermal annealing in  $\text{H}_2/\text{N}_2$  at  $650^\circ\text{C}$  for 1min. Atomic force microscopy (AFM), SKPM, and conductive atomic force microscopy (C-AFM) data were obtained in a Digital Instruments Nanoscope® IIIa MultiMode™ microscope under ambient conditions ( $\sim 20^\circ\text{C}$  with 50% humidity). Co/Cr and conductive diamond coated tips were used for the SKPM and C-AFM experiments, respectively.

The basic principles of SKPM have been described in detail elsewhere [13,14]. In brief, SKPM is used to image variations in the surface contact potential difference,  $\Delta\phi$ , between a conducting probe tip and the sample under investigation;  $\Delta\phi$  is defined [15] as  $(\phi_{\text{tip}} - \phi_{\text{GaN}})/q$ , where  $\phi_{\text{tip}}$  and  $\phi_{\text{GaN}}$  are the workfunctions of the tip and sample surface, respectively and  $q$  is the magnitude of the electron charge. In this experiment, a bias voltage is applied directly to the tip, holding the sample at ground potential. A feedback loop continually adjusts the “nulling” bias to maintain a condition of minimum force, occurring when the tip bias equals the contact potential. This tip bias is recorded as a function of position, yielding a map of the contact potential.

The C-AFM procedures have been described previously [5]. Briefly, a conductive probe tip is scanned over the sample in contact mode and acts as a Schottky contact to the sample. A positive bias is applied to an ohmic back contact to the sample while the current through the tip is measured with a current amplifier. The current is measured simultaneously with topography, revealing nonuniformities in sample conductivity. The specific features of interest are localized, highly conductive current leakage paths associated with threading dislocations [5,6].

SKP response was first mapped over a large area of the sample ( $\sim 40 \times 40\mu\text{m}^2$ ). The probe tip was then disengaged and replaced, without disturbing the sample position. The instrument was then reengaged in C-AFM mode. Small shifts in the scan area position, guided by topographic feature comparison, aligned C-AFM scan areas with previously recorded surface potential maps.

## RESULTS

Figure 1 shows representative images of (a) topography, (b) surface potential, and (c) reverse-bias current for a  $5\mu\text{m} \times 5\mu\text{m}$  area. Sample topography exhibits atomic terraces with a measured height of  $\sim 0.3\text{nm}$ , in close agreement with the  $0.26\text{nm}$  bilayer spacing of GaN. Based on examination of this and several larger areas, a total density of screw and mixed dislocations of  $\sim 2.4 \times 10^8\text{cm}^{-2}$  is found from the density of growth hillocks, each of which forms about a screw or mixed dislocation at its center. Dark features,  $\sim 10\text{mV}$  in amplitude, are seen in the surface

potential map of figure 1(b), and correspond to regions where the surface Fermi level is closer to the valence band [16]. The contrast observed here is consistent, in sign, with previous studies associating such contrast with negatively charged dislocations in GaN [7,8,17]. Although references 8 associates bright contrast with negative charge it should be noted that, in that study, the nulling bias was applied to the sample rather than tip. Reference 17 also associates bright contrast with negative charge; however, surface potential image contrast was inverted in that work in order to reflect the “electronic” potential. The observed feature amplitude in the current work is somewhat smaller than in the previously cited studies; however, surface contamination [18] or an increased tip size [8] would result in a decreased feature magnitude. A detailed examination of surface potential images yields a density of negatively charged dislocations of  $\sim 3 \times 10^8 \text{ cm}^{-2}$ ; however, the true density may be higher due to surface potential feature overlap which will be discussed later. The dark features in figure 1(c) correspond to localized reverse-bias leakage paths, occurring at a density of  $\sim 3 \times 10^7 \text{ cm}^{-2}$ . Localized reverse-biased leakage paths in GaN have been postulated to be associated with pure screw dislocations [5] and are the primary sources for reverse-bias leakage current in MBE grown GaN [6].

By superimposing SKPM and C-AFM images, which reveal negatively charged dislocations and local current leakage paths, respectively, the correlation between these features may be examined. Figure 2 shows (a) topographic and (b) surface potential images with the location of leakage paths marked by squares. Note first that every leakage path coincides with a growth hillock. This was seen consistently over several larger scan areas. However, consistent with previous findings [5,6], not every growth hillock is associated with a leakage path. The negatively charged surface potential features, on the other hand, are often, but not universally, associated with growth hillocks. Finally, it can be seen in figure 2(b) that only  $\sim 25\%$  of the leakage paths are spatially correlated with regions of decreased surface potential. The surface potential and leakage path feature densities, as well as the correlation percentages, are consistent over several scanned areas.

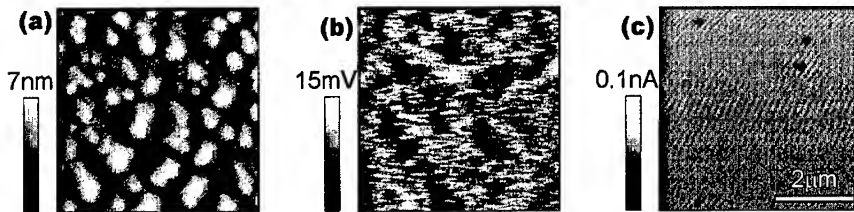


**Figure 1.** (a) AFM topography, (b) surface potential of a representative  $5\mu\text{m} \times 5\mu\text{m}$  area. (c) Typical current map of a  $5\mu\text{m} \times 5\mu\text{m}$  area. The gray scales correspond to a range of 7nm for topography, 15mV for surface potential, and  $10^{-10}\text{A}$  for the current map.

The lack of correlation between the negatively charged features and the leakage paths demonstrates that these features have different origins. TEM studies of similarly grown films show the dislocation structure consists primarily of edge and mixed dislocations [11]. This abundance of edge and mixed dislocations, relative to screws, is commonly observed in GaN films grown by MOCVD that exhibit a microstructure characterized by slightly misoriented domains where edge dislocations are formed at low-angle boundaries [12,19]. The majority of growth hillocks form around mixed dislocations while only a small subset ( $\sim 10\%$ ) form about pure screws. In our study,  $\sim 10\%$  of hillocks exhibit leakage. Our results suggest that dislocations having an edge component, i.e., both edge and mixed, behave as though negatively charged,

while only screw dislocations act as leakage paths. These conclusions are consistent with work implicating only pure screw dislocations as being responsible for localized leakage current [5] as well as theoretical studies predicting the presence of negative charge located at the core of edge dislocations [20]. Using the previously calculated total density of mixed and screw dislocations of  $\sim 2.4 \times 10^8 \text{ cm}^{-2}$ , based on hillock density, and a pure screw density of  $\sim 3 \times 10^7 \text{ cm}^{-2}$ , based on leakage path density, the density of mixed dislocations is  $\sim 2 \times 10^8 \text{ cm}^{-2}$ , consistent with previous studies of similar samples [19].

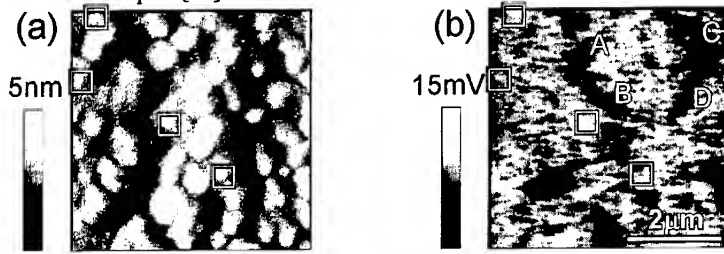


**Figure 2.** (a) AFM topography and (b) surface potential maps of a  $5\mu\text{m} \times 5\mu\text{m}$  area with boxes indicating the locations of leakage paths. Letters A-D indicate locations of section analysis of potential features. Scales correspond to 5nm for topography and 10mV for surface potential.

Regions of extended dark SKP contrast, such as the large arc encircling an area of the surface in the upper right of figure 2(b), are likely due to groups of pure edge dislocations forming at island coalescence boundaries. These dislocations have been found to occur with separations of 40-70nm [21] leading to dislocation-induced surface potential feature overlap. We have modeled this to understand the effects of dislocation bunching on the resulting potential profile. Each dislocation is defined as a cylindrical region with radius equal to the  $a$  lattice constant of GaN and containing an acceptor type defect at every  $c$  lattice spacing effectively pinning the Fermi level at the defect position, assumed to be 1eV above the valence band maximum (VBM) [22], and is shown in the simulation results of figure 3. The plan view conduction-band-energy profile, with threading dislocations going into the page, is depicted using constant-potential contours in figure 3(a). From left to right, there is a group of 5 dislocations, then a group of 2 followed by an individual dislocation at the far right. The groups have inter-dislocation spacing of 40nm. The conduction-band-energy profile along a section taken through the dislocation cores is plotted in figure 3(b). This energy is plotted relative to the bulk Fermi level. At the individual dislocation cores, the Fermi level is pinned at the acceptor defect level resulting in a peak potential feature magnitude of 2.4V. This is true for all dislocations whether they are part of a group or isolated. Although the peak potential value is not affected by the presence of neighboring dislocations, the spatial extent of the feature is. This effect will be examined by comparing a characteristic decay length, the distance at which the potential has fallen to  $1/e$  of its maximum value, for various dislocation configurations. The transverse extent of the potential feature, (in the  $y$ -direction in figure 3), is increased by a factor of 1.7 and 2.8 for the groupings of 2 and 5 dislocations, respectively, when compared to the potential associated with a single dislocation. The longitudinal increase can be seen in figure 3(b) by comparing the conduction band profile of a single dislocation with that of the ensemble (dotted and solid lines, respectively). Although the conduction band profile at the end of the grouping, for the far left dislocation in figure 3(b), coincides closely with the profile of the single

dislocation, the profile between neighboring dislocations is increased significantly. Dislocation bunching not only increases the measured feature size but also its magnitude. Although the peak potential value for the ensemble does not increase above that of the individual dislocation, a spatially larger feature results in an increase in the magnitude of the measured surface potential shift when the feature size is comparable to the size of the probe [8].

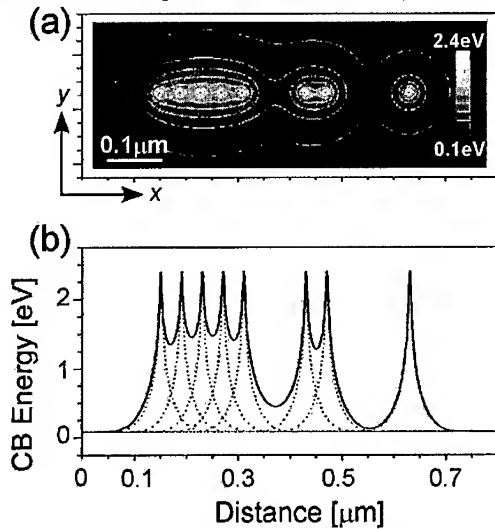


**Figure 3.** Numerical simulation results showing potential distribution of closely spaced charged dislocations. (a) Plan view (dislocations going into page) depicting potential distribution using constant-potential contours and (b) conduction band profile along section taken through the dislocation cores. Dotted and solid lines represent profiles of the individual and group, respectively. Conduction band energy is measured in reference to the bulk Fermi level.

The prominent extended features in figures 1(b) and 2(b) are likely due to groups of charged dislocations. Sections through the arc feature in figure 2(b) were taken at positions labeled A-D. The sections were taken perpendicular to the arc. Potential feature magnitudes were between 5.6mV and 10.1mV and feature radii of 200-250nm were measured. On the other hand, the single dark potential feature located near the center of this circular boundary has a magnitude of ~4.5mV and a radius of ~125nm. Applying the conclusions of the numerical simulation, it is likely that the large arc is composed of closely spaced negatively charged dislocations while the single feature located near the center of the circle is due to a single charged dislocation.

Although screw dislocations appear to be uncharged, a fraction of the leakage paths appear to be spatially correlated with surface potential features; however, it should be noted that surface potential features can be up to several hundred nanometers in size, making it plausible that an uncharged screw dislocation may be located within the range of the potential created by a nearby, dislocation. Assuming a potential feature radius of 200nm and a negatively charged dislocation density of  $3 \times 10^8 \text{ cm}^{-2}$ , ~35% of the surface area will show reduced surface potential. It is therefore reasonable to assume that approximately this percentage of screws will be located within these potential features. Since we observe that ~25% of the leakage paths are within an

area of reduced surface potential, our results are consistent with the postulate that screw dislocations are uncharged and conductive while mixed and edge dislocations are charged and nonconductive.

## CONCLUSIONS

In summary, we have studied the local surface potential and conductance of a GaN sample grown by MBE. Features associated with negatively charged dislocations and with dislocation-related leakage paths are observed. Through spatially resolved and correlated measurements of topography, surface potential, and leakage current, we have established that negatively charged features, associated with dislocations, are not responsible for localized leakage. Our results suggest that dislocations of pure screw type are the source of localized leakage while edge and mixed type dislocations are likely negatively charged.

## ACKNOWLEDGEMENTS

Part of this work was supported by ONR (POLARIS MURI) and by Raytheon Corporation.

## REFERENCES

- <sup>1</sup> S. Nakamura, M. Senoh, S. Nagahama, N. Iwasawa, T. Yamada, T. Matsushita, H. Kiyohu, and Y. Sguimoto, *Jpn. J. Appl. Phys.* **35**, L74 (1996).
- <sup>2</sup> Y. F. Wu, B. P. Keller, P. Fini, S. Keller, T. J. Jenkins, L. T. Kechias, S. P. Denbaars, and U. K. Mishra, *IEEE Electron Device Lett.* **19**, 50 (1998).
- <sup>3</sup> H.M. Ng, D. Doppalapudi, T.D. Moustakas, N.G. Weimann, and L.F. Eastman, *Appl. Phys. Lett.* **73**, 821 (1998).
- <sup>4</sup> T. Sugahara, H. Sato, M. Hao, Y. Naoi, S. Tottori, K. Yamashita, K. Nishino, L.T. Romano, and S. Sakai, *Jpn. J. Appl. Phys.* **37**, L398 (1998).
- <sup>5</sup> J. W. Hsu, M. J. Manfra, R. J. Molnar, B. Heying, and J. S. Speck, *Appl. Phys. Lett.* **81**, 79 (2002).
- <sup>6</sup> E.J. Miller, D.M. Schaadt, E.T. Yu, C. Poblenz, C. Elsass, and J. S. Speck, *J. Appl. Phys.*, **91**, 9821 (2002).
- <sup>7</sup> J. W. Hsu, M. J. Manfra, D. V. Lang, K. W. Baldwin, L. N. Pfeiffer, and R. J. Molnar, *J. Electronic Mater.*, **30**, 110 (2001).
- <sup>8</sup> B. S. Simpkins, D. M. Schaadt, E. T. Yu, and R. J. Molnar, *J. Appl. Phys.*, **91**, 9924 (2002).
- <sup>9</sup> P. J. Hansen, Y. E. Strausser, A. N. Erickson, E. J. Tarsa, P. Kozodoy, E. G. Brazel, J. P. Ibbetson, U. Mishra, V. Narayanamurti, S. P. Denbaars, and J. S. Speck, *Appl. Phys. Lett.*, **72**, 2247 (1998).
- <sup>10</sup> D. M. Schaadt, E. J. Miller, E. T. Yu, J. M. Redwing, *Appl. Phys. Lett.*, **78**, 88 (2001).
- <sup>11</sup> B. Heying, R. Averbek, L. F. Chen, E. Haus, H. Riechert, and J. S. Speck, *J. Appl. Phys.*, **88**, 1855 (2000).
- <sup>12</sup> X. H. Wu, L. M. Brown, D. Kapolnek, S. Keller, B. Keller, S. P. Denbaars, and J. S. Speck, *J. Appl. Phys.* **80**, 3228 (1996).
- <sup>13</sup> M. Nonnenmacher, M.P. O'Boyle, and H.K. Wickramasinghe, *Appl. Phys. Lett.* **58**, 2921 (1991).
- <sup>14</sup> H. O. Jacobs, H. F. Knapp, S. Müller, and A. Stemmer, *Ultramicroscopy*, **69**, 39 (1997).
- <sup>15</sup> S. M. Sze, *Physics of Semiconductor Devices*, 2<sup>nd</sup> ed., p.246, (1981).
- <sup>16</sup> F. Robin, H. Jacobs, O. Homan, A. Stemmer, and W. Bachtold, *Appl. Phys. Lett.*, **76**, 2907 (2000).
- <sup>17</sup> G. Koley and M. G. Spencer, *Appl. Phys. Lett.*, **78**, 2873 (2001).
- <sup>18</sup> J. W. P. Hsu, H. M. Ng, A. M. Sergeant, and S. N. G. Chu, *Appl. Phys. Lett.*, **81**, 3579 (2002).
- <sup>19</sup> X. H. Wu, P. Fini, E. J. Tarsa, B. Heying, S. Keller, U. K. Mishra, S. P. Denbaars, and J. S. Speck, *J. Crystal Growth*, **189/190**, 231 (1998).
- <sup>20</sup> A. F. Wright and U. Grossner, *Appl. Phys. Lett.*, **73**, 2751 (1998).
- <sup>21</sup> X. J. Ning, F. R. Chien, P. Pirouz, J. W. Yang, and M. Asif Khan, *J. Materials Res.*, **11**, 580 (1996).
- <sup>22</sup> J. Elsner, R. Jones, M. I. Heggie, P. K. Sitch, M. Haugk, Th. Frauenheim, S. Öberg, and P. R. Briddon, *Phys. Rev. B*, **58**, 12571 (1998).

### The Effect of Growth Stoichiometry on the GaN Dislocation Core Structure

Marcus Q. Baines<sup>1</sup>, David Cherns<sup>1</sup>, Julia W. P. Hsu<sup>2</sup> and Michael J. Manfra<sup>2</sup>

<sup>1</sup>H.H. Wills Physics Laboratory, University of Bristol, Tyndall Avenue, Bristol, BS8 1TL, UK

<sup>2</sup>Bell Laboratories, Lucent Technologies, 700 Mountain Avenue, Murray Hill, NJ 07974

#### ABSTRACT

Plan-view transmission electron microscopy was used to study the core structures of different dislocations in (0001) GaN layers grown under Ga-rich and Ga-lean conditions by molecular beam epitaxy. In Ga-rich samples at least one third of mixed type dislocations were open-core, and edge dislocations were observed to be closed-core. In contrast, under Ga-lean conditions, all dislocations were observed to be closed-core, and many were associated with pits at the sample surface. High resolution studies of the open core dislocations revealed that many were decorated with a disordered deposit, the origin of which is discussed.

#### INTRODUCTION

The growth of GaN devices on substrates such as (0001) sapphire and SiC leads to high densities of threading dislocations, often exceeding  $10^9 \text{ cm}^{-2}$ . These dislocations have attracted much attention because of their influence on device properties.

An important question which bears on the electronic properties is whether threading dislocations have open or closed core structure. This in part depends on the dislocation type, i.e. whether the dislocations are of a-type (edge dislocations with Burgers vectors  $\mathbf{b} = 1/3\langle 11\bar{2}0 \rangle$ ), a+c-type (mixed dislocations,  $\mathbf{b} = 1/3\langle 11\bar{2}3 \rangle$ ) or c-type (screw dislocations,  $\mathbf{b} = \langle 0001 \rangle$ ). In undoped material grown by metalorganic chemical vapour deposition (MOCVD), previous studies have shown that screw dislocations can be open-core, with diameters in the range 5-25nm [1]. Open-core screw dislocations have also been observed in n-doped GaN [2]. The work of Liliental-Weber *et al* indicates that the formation and density of open-core screw dislocations may depend on impurities (e.g. O) and dopants (e.g. Si) [3].

In p-doped GaN, the situation appears to be different. Recently, we reported the first observations of open cores on edge and mixed dislocations in a Mg-doped MOCVD sample. The segregation of Mg to dislocations seemed to be a factor in the creation of open-cores [4].

It has also been shown that core structure is affected by stoichiometry. Hsu *et al* have compared the structure and electrical properties of dislocations in GaN grown by molecular beam epitaxy (MBE) under Ga-rich and Ga-lean conditions [5]. Transmission electron microscope (TEM) studies, carried out on cross sectional samples, suggested that under Ga-rich conditions, dislocations with a screw component (i.e.  $\mathbf{b}=\mathbf{c}$  or  $\mathbf{c}+\mathbf{a}$ ) may have extended cores, with some evidence that the cores were decorated with excess Ga. Under Ga-lean conditions, the dislocations had conventional, closed cores. Using scanning current-voltage microscopy (SIVM) it was found that samples grown under Ga-rich conditions show three orders of magnitude higher reverse bias leakage than those grown under Ga-lean conditions, and that the reverse bias current was predominantly being carried by pure screw dislocations [6].

In this paper we investigate, in detail, the effect of growth stoichiometry on dislocation core structure, using plan-view TEM. It is shown that under Ga-rich conditions, many mixed-

type ( $b=c+a$ ) dislocations are open-core, i.e. nanopipes. Edge dislocations have been observed to be closed core.

## EXPERIMENTAL

GaN films were grown by plasma-assisted MBE on thick GaN templates prepared by hydride vapour phase epitaxy (HVPE) on a sapphire (0001) substrate. The growth rate was 250nm/hr and growth was carried out at a substrate temperature of 745°C. The MBE layers were not intentionally doped while the HVPE templates were partially Zn compensated. Ga-rich samples were grown with excess Ga coverage such that Ga droplets were observed on the film surface. We have previously reported that samples grown under lower Ga flux present no Ga droplets and display a roughened surface morphology. Such samples are grown under Ga-lean conditions. Detailed information on the MBE growth is reported elsewhere [7]. Following growth, samples were prepared in plan view using conventional techniques of mechanical polishing and ion-thinning, for the purpose of studying the MBE film. They were examined in a Philips EM430 microscope operating at 250 kV. High-resolution studies were undertaken using a Hitachi HF2000 field-emission TEM operating at 200 kV.

## RESULTS

In figure 1 we compare the general features of the Ga-rich and Ga-lean samples. In both cases, image contrast depends on thickness variations. Figure 1a) is a TEM micrograph of the Ga-rich material taken under standard bright field conditions with the sample oriented close to the [0001] zone axis. Many dislocations are visible as points of contrast, merging in places to produce a granular structure. It is worth noting that the foil is relatively smoothly varying in thickness. This contrasts with observations of the Ga-lean material illustrated in figure 1(b), which is taken at a  $\langle 10\bar{1}0 \rangle$  reflection. Deep pits in the sample surface (arrowed) are visible as changes in background contrast in the thicker regions of the foil, whereas those in the near edge region of the sample are holes. A closer examination showed that these pits were roughly conical

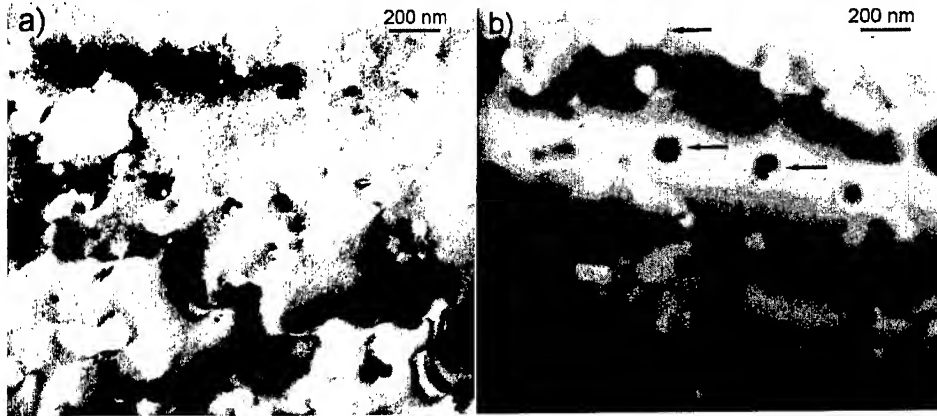


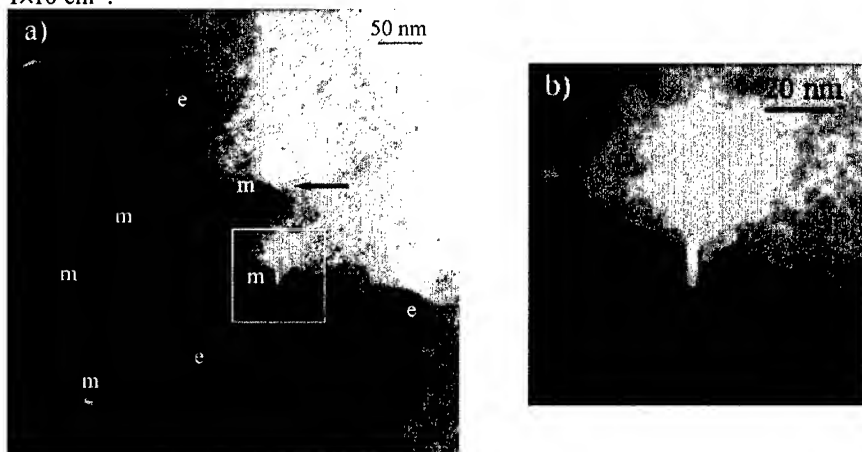
**Figure 1.** Plan view TEM micrographs of a) Ga-rich GaN oriented close to the [0001] zone axis, and b) Ga-lean GaN taken with operating vector  $g=[10\bar{1}0]$ .

with diameters in the range of 80-120nm. This is consistent with results from cross-sectional samples that have previously been reported [5]. Roughly one third of pits have a dislocation at their centre, and a minority of dislocations were found away from pits. Dislocations in this sample were found to be of primarily mixed-type, and, most importantly, all had closed cores.

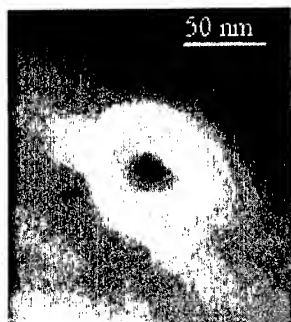
The total dislocation density in the Ga-rich material was roughly  $4 \pm 2 \times 10^9 \text{ cm}^{-2}$ , in the Ga-lean material it was a little lower at around  $2 \pm 2 \times 10^9 \text{ cm}^{-2}$ .

Figure 2 shows dislocations in the Ga-rich material at a higher magnification, and is taken with  $g=[10\bar{1}0]$ . Under this condition, a dislocation will only show long range diffraction contrast if it has an edge component. The two defects arrowed show light contrast close to the core, characteristic of nanopipes, while the longer range contrast is indicative of a dislocation. The defects are therefore hollow-core dislocations. In some cases the contrast from a hollow-core dislocation is less clear than that of a closed-core dislocation, indicative of free surface relaxation. Figure 2b is an enlargement of the region around a nanopipe, outlined in figure 2a. It clearly shows that the dislocation is both displaying contrast (in the  $g=[10\bar{1}0]$  condition) and open core.

Images taken with  $g=[10\bar{1}1]$  (tilted by  $28^\circ$  from the c-axis), showed the two nanopipes in contrast again. An edge component (with say  $b = 1/3[11\bar{2}0]$ ) will show contrast in two out of the three  $\langle 10\bar{1}1 \rangle$  reflections (i.e. when  $g = [10\bar{1}1]$  and  $[0\bar{1}11]$ , but not when  $g = [1\bar{1}01]$ ), whereas a screw component will show contrast in all three. A full analysis showed that the nanopipes were mixed type dislocations. Three other dislocations in the figure are mixed type (labelled m), and there are three edge types present (labelled e). In the sample, the ratio of edge to mixed dislocations was approximately 3:4, with a much lower proportion of screw dislocations. A small number of nanopipes were found to be pure screw type, but none appeared to be pure edge. All nanopipes were associated with dislocations. Direct confirmation that dislocations were open core became more difficult as the foil thickness increased. However, it was confirmed that at least one in five of all dislocations were open core, giving a nanopipe density in the region of  $1 \times 10^9 \text{ cm}^{-2}$ .



**Figure 2a).** Plan view TEM micrograph a Ga-rich sample taken under bright-field two-beam conditions  $g=[10\bar{1}0]$ , showing multiple dislocations. **b):** Magnified image of area outlined in figure 2a).



**Figure 3.** Plan view of Ga-lean sample showing a single dislocation and associated pit  $g=[1\bar{1}20]$ .

In comparison with figure 2b), a single dislocation of the *Ga-lean* material is displayed in figure 3. The dislocation shows simple black/white contrast and is circled by a white region because of its associated pit. It can be seen that at least at the diffraction contrast scale, the dislocation is closed core.

By tilting the Ga-rich sample away from the  $[0001]$  direction in a thicker region, the structure along the length of the nanopipes can be observed, as shown in figure 4, where a sample has been tilted by  $28^\circ$  to the  $g=[10\bar{1}1]$  condition. Four nanopipes are arrowed in this figure, but they appear to have differing structures. They all seem to be partially filled, and show periodic, void-like contrast along their length (creating nanopipes), but this varies from one pipe to another. The nanopipe in the bottom-left corner appears the longest because the foil is thickest in this region. It is unclear whether this difference in structure is caused by a difference in



**Figure 4.** Plan view TEM micrograph of a thicker area in a Ga-rich sample, taken under bright-field two-beam conditions with  $g=[10\bar{1}1]$ , i.e. tilted by  $28^\circ$  from the  $[0001]$  direction. Nanopipes are arrowed.

dislocation type or perhaps variations in the local availability of mobile Gallium to fill the cores.

High resolution TEM confirmed the nanopipe observations; lattice images are displayed in figure 5. Figure 5a) shows what appears to be a partially filled-core dislocation with a diameter of only about 2nm, it is difficult to tell whether the core is sufficiently open to call it a nanopipe. Drawing a Burgers circuit around this (and others) small nanopipe gave a resultant of one atomic spacing, i.e. an edge component. This is consistent with the **g.b** analysis showing **c+a** type. Figures 5b) and c) show nanopipes with diameters of around 5nm (the most common size), although interestingly, the nanopipe in figure 5c) is not circular, and measures about 15nm across at its widest point. If this dislocation was actually circular, but with an axis at an angle to the [0001] direction, then we would expect the contrast from the inside of the nanopipe to be much less uniform. All nanopipes were filled, at least partially, with amorphous material. Energy dispersive X-ray (EDX) measurements from nanopipes like these, using small probes (about 10nm diameter), showed a proportionately higher Ga signal (about 40%) compared with the surrounding matrix, suggesting segregation of Ga to the core regions. However, as we are unable to detect Nitrogen to use as a reference, this result is somewhat tentative.

We found that after a period of a minute or so under the electron beam, the smallest nanopipes lost their contrast. In the case of the larger nanopipes (i.e. diameter around 5nm) the transition could be observed; the material inside the nanopipe began to rapidly change contrast. The core then became darker and similar to the surrounding GaN. Since gallium melts at close to room temperature (303 K), the heating under the electron beam could cause changes in the materials inside the nanopipes if they are rich in Ga. Further studies are needed to determine whether the change in contrast is due to perhaps rearrangement of material inside the nanopipe, or simply radiation and/or contamination effects.

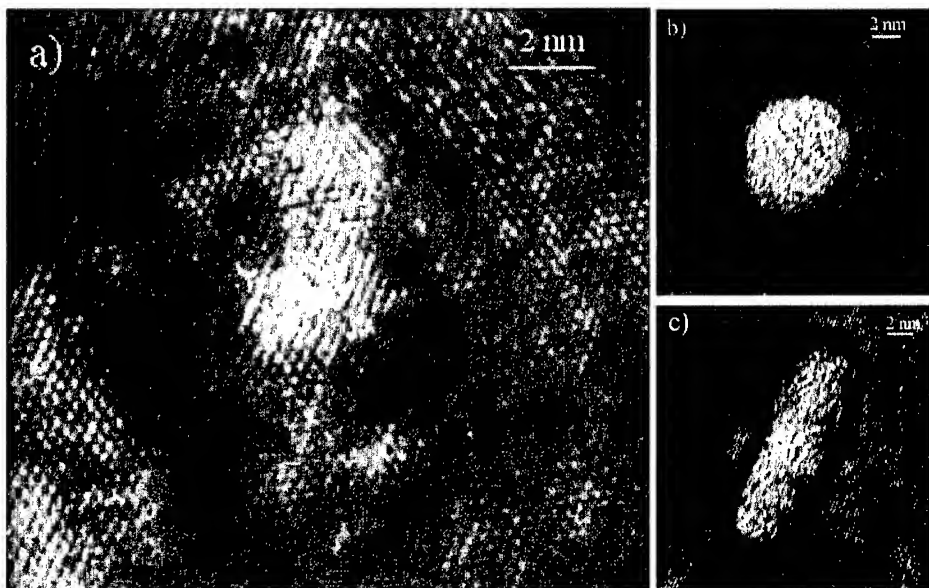


**Figure 5.** Lattice images of nanopipes in Ga-rich material. **a)** small nanopipe. **b)** circular nanopipe. **c)** oval nanopipe.

## DISCUSSION

Whereas open-cores in Mg-doped samples seem to be formed by triangular defects merging [4], the cores in this work appear to be of more constant diameter along the dislocation, i.e. nanopipes. Although the mechanism of formation for these hollow-core structures is unclear, the fact remains that they are only observed under Ga-rich conditions, and not under Ga-lean conditions.

It has been calculated that for screw dislocations it is energetically favourable to have open cores [8], essentially due to a trade-off between surface and strain energy. This line of reasoning would suggest that open cores are energetically favourable in mixed type dislocations as well, because the Burgers vector is of greater magnitude ( $\mathbf{b}=\mathbf{c}+\mathbf{a}$ , 6.1 Å, as opposed to  $\mathbf{b}=\mathbf{c}$ , 5.2 Å), leading to increased strain in the lattice. The energy required to create the surface of the open-cored nanopipe would be more than compensated for by the energy gained from reducing the strain, and one might expect to see larger core diameters.

First-principles total energy calculations by Northrup [9] indicate that for *pure screw* dislocations, a Ga-filled core is more stable than a hollow-core in Ga-rich conditions. This core is theoretically observable in high-resolution TEM as a 6° rotation relative to the rest of the lattice. In our observations of the core structure of *mixed* type dislocations no such crystalline structure was found. It is proposed that during Ga-rich growth, the highly-mobile excess Ga on the sample surface segregates to sinks on the growth surface caused by dislocations.

## CONCLUSIONS

TEM results show that mixed type dislocations in addition to screw dislocations in Ga-rich material can be open-core, and partially filled. Both edge and mixed dislocations have, in some cases, been observed to be closed core. In Ga-lean material, all dislocations were found to be closed-core.

## ACKNOWLEDGMENTS

We would like to thank R. Molnar for the HVPE templates. MB is funded by the Engineering and Physical Sciences Research Council (EPSRC) and is sponsored by Arima optoelectronics.

## REFERENCES

1. D. Cherns, W.T. Young, J.W. Steeds, F.A. Ponce and S. Nakamura, *J. Cryst Growth* **178** (1-2): 201-206 (1997).
2. D. Cherns, *J. Phys. Condens. Matter* **12**, 10205 (2000).
3. Z. Liliental-Weber, *J. Electron Microscopy* **49** (2): 339-348 (2000).
4. D. Cherns, M.Q. Baines, Y.Q. Wang, R. Liu, F.A. Ponce, H. Amano and I. Akasaki, Proceedings of IWN, Aachen, 22-25 July 2002, *Phys. Stat. Sol. B* (2002) (in press).
5. J.W.P. Hsu, M.J. Manfra, S.N.G. Chu, C.H. Chen, L.N. Pfeiffer and R.J. Molnar, *Appl. Phys. Lett.* **78**, 3980 (2001).
6. J.W.P. Hsu, M.J. Manfra, R.J. Molnar, B. Heying, J.S. Speck, *Appl. Phys. Lett.* **81**, 79 (2002).
7. M.J. Manfra, N.G. Weimann, J.W.P. Hsu, L.N. Pfeiffer et al, *J. Appl. Phys.* **92**, 338 (2002).
8. J. Elsner, R. Jones, P.K. Sitch, V.D. Porezag, M. Elstner, T. Frauenheim, M.I. Heggie, S. Oberg and P.R. Briddon, *Phys. Rev. Lett.* **79**, 3672 (1997).
9. J. E. Northrup, *Appl. Phys. Lett.* **78** (16), 2288-2290 (2001).

### Properties of Surface States on GaN and Related Compounds and Their Passivation by Dielectric Films

Hideki HASEGAWA and Tamotsu HASHIZUME

Research Center for Integrated Quantum Electronics (RCIQE) and  
Graduate School of Electronics and Information Engineering, Hokkaido University  
N-13, W-8, Kita-ku, Sapporo, 060-8628 Japan

#### ABSTRACT

This paper reviews the authors' recent efforts to clarify the properties of electronic states near surfaces of GaN and AlGa<sub>0.28</sub>Ga<sub>0.72</sub>N by using various *in-situ* and *ex-situ* characterization techniques, including UHV contactless C-V, photoluminescence surface state spectroscopy (PLS<sup>3</sup>), cathode luminescence in-depth spectroscopy (CLIS), and gateless FET techniques that have been developed by the authors' group.

As a result, a model including a U-shaped surface state continuum, having a particular charge neutrality level, combined with frequent appearance of near-surface N-vacancy related deep donor states having a discrete level at  $E_c - 0.37\text{eV}$  is proposed as a unified model that can explain large gate leakage currents and current collapse in AlGa<sub>0.28</sub>Ga<sub>0.72</sub>N HFETs. Hydrogen plasma treatment and SiO<sub>2</sub> deposition increase N-vacancy related deep donors. Reasonably good surface passivation can be achieved by ECR-plasma SiN<sub>x</sub> films and by ECR-plasma oxidized Al<sub>2</sub>O<sub>3</sub> films both combined with ECR N<sub>2</sub> plasma treatment.

#### INTRODUCTION

GaN and related compounds such as AlGa<sub>0.28</sub>Ga<sub>0.72</sub>N and InGa<sub>0.28</sub>Ga<sub>0.72</sub>N have recently established their position as the key materials for applications to high-power microwave/millimeter-wave electronic devices and blue/UV optoelectronic devices. Great progress has been made on metal-organic vapor phase epitaxy (MOVPE) growth of these materials on sapphire and SiC substrates. Molecular beam epitaxy (MBE)-growth method has also demonstrated unique features such as achievements of high electron mobility values [1], a lower growth temperature reducing thermally induced strain, availability of larger In fractions in InGa<sub>0.28</sub>Ga<sub>0.72</sub>N and reduced hydrogen passivation of dopants such as Mg, making it also a seemingly viable growth technique.

However, AlGa<sub>0.28</sub>Ga<sub>0.72</sub>N heterostructure field effect transistor (HFET) devices are known to exhibit various anomalous behavior including anomalously large gate leakage currents [2], I-V dispersion, drain current collapse [3,4], gate- and drain-lag [4], etc which are closely related to details of processing applied to the surface during device fabrication. Thus, understanding and control of surface are essentially important to produce viable devices with acceptable performance and reliability.

The purpose of the present paper is to review the results of our recent efforts to clarify and control the properties of near-surface electronic states of GaN and AlGa<sub>0.28</sub>Ga<sub>0.72</sub>N using various *in-situ* and *ex-situ* characterization techniques. The topics discussed here include characterization techniques, properties of free surfaces, current transport in Schottky barriers and processes for surface passivation.

#### EXPERIMENTAL

##### Sample structures and their preparation

GaN and AlGa<sub>0.28</sub>Ga<sub>0.72</sub>N epitaxial wafers grown on sapphire substrates by MOVPE were used mainly in our study. AlGa<sub>0.28</sub>Ga<sub>0.72</sub>N wafers had a structure of Al<sub>0.28</sub>Ga<sub>0.72</sub>N (5nm)/n<sup>+</sup>-Al<sub>0.28</sub>Ga<sub>0.72</sub>N (20nm)/Al<sub>0.28</sub>Ga<sub>0.72</sub>N (5nm)/

undoped-GaN(1  $\mu\text{m}$ ) with a Hall mobility of 900  $\text{cm}^2/\text{Vs}$  and a sheet carrier density of  $1.1 \times 10^{13} \text{cm}^{-2}$  at room temperature. They showed clear Shubnikov-de Haas (SdH) oscillations at 2K where electron concentrations from the Landau plot agreed well with those by Hall measurements at the same temperature, confirming the existence of 2DEG at the AlGaN/GaN heterointerface.

In order to partly study the properties of MBE-grown clean surfaces of GaN, undoped homoepitaxial layers were grown at 750  $^\circ\text{C}$  by RF-radical assisted MBE on a thermally cleaned surface of an air-exposed n-type MOVPE GaN/sapphire templates [5]. Nitrogen radicals excited at a microwave power of 300W were used. The MBE growth rate was 0.15  $\mu\text{m}/\text{h}$ . Air exposed MOVPE- grown GaN layers showed a clear (1x1) RHEED pattern after thermal cleaning at 750  $^\circ\text{C}$ . The pattern changed immediately to a streaky (2x2) reconstruction pattern on initiation of MBE growth and was maintained during and after growth. From the integrated intensity ratio of Ga3d to N1s peaks in the in-situ XPS spectra, an exactly stoichiometric composition of the MBE GaN layer was confirmed. The MOVPE template and the MBE layer showed clear band-edge emissions at 363 nm similar to those of MOVPE and MBE layers previously reported [6, 7].

For Schottky current transport study, circular Schottky contact structures were used [2]. Detailed I-V measurements were made for various temperatures.

#### **In-situ and ex-situ characterization of surfaces**

Various *in-situ* and *ex-situ* characterization techniques were used to characterize surfaces of GaN and AlGaN. *In-situ* characterization was made in a UHV multi-chamber system installed at our research center (RCIQE). It has a base pressure of  $2 \times 10^{-10}$  Torr and contains an MBE chamber, XPS chamber, UHV contactless C-V chamber, UHV-PL chamber, ECR deposition chamber etc. XPS study was performed with a Perkin Elmer PHI 1600C spectrometer having a monochromated Al K $\alpha$  x-ray source. Contactless C-V measurements were done in the UHV contactless C-V chamber. UHV-PL measurements were carried out using a He-Cd laser light with a wavelength of 325 nm. *Ex-situ* techniques included X-ray diffraction (XRD), Raman spectroscopy, atomic force microscopy (AFM), cathodoluminescence in-depth spectroscopy (CLIS), gateless FET technique for current transport study and standard Hall, I-V and MIS C-V measurements.

Among above techniques, UHV contactless C-V technique, photoluminescence surface state spectroscopy (PLS<sup>3</sup>) technique, CLIS technique and gateless FET technique for current transport study have been developed by the authors' group, and their brief descriptions are given below.

#### **UHV contactless C-V technique**

Using the basic set-up shown in **figure 1(a)**, MIS C-V measurements on free surfaces are carried out using a UHV gap as an insulator [8] whose thickness is measured optically, using a laser beam. Parallelism between the sample surface and the field plate is maintained by a piezoelectric mechanism with feedback of capacitance from the three parallelism electrodes surrounding the field plate. The original version of this method required conducting substrate. In order to allow lateral capacitance assessment on insulating substrates, a ring-shaped reference electrode was added wafer periphery, and procedures to correct for two dimensional RC distributed network nature of MIS structure underneath the field plate as well as for the position-dependent series resistance are established theoretically by a computer analysis [9].

Here, PL quantum efficiency ( $I_{PL}/\phi$ ) is plotted versus  $\phi$ , as shown in figure 1 (b), and the resulting plots are analyzed to determine the most likely surface state density distributions, using our one-dimensional vector-matrix computer program for PLS<sup>3</sup> [10, 11].

According to the PLS<sup>3</sup> theory, photo-excitation causes gradual saturation of surface states as SRH centers, leading to a transition region with gradual increase of  $I_{PL}/\phi$  vs  $\phi$ . It also causes splitting of quasi-Fermi levels for electrons ( $E_{Fn}$ ) and holes ( $E_{Fp}$ ), and changes the energy range of surface states contributing to surface recombination. Thus,  $I_{PL}/\phi$  vs.  $\phi$  plots show strong correlation with the distribution shape and density of surface states. For example, a discrete surface state peak gives a unity slope for the transition region, provided that the doping is not too high. A U-shaped continuum gives a slope less than unity. Larger surface state densities shift the transition region at higher photon flux densities.

In order to fit theoretical  $I_{PL}/\phi$  curves to experiments, various combinations of energy distributions of surface state density,  $N_{ss}$ , are assumed for trial. Two typical  $N_{ss}$  distribution shapes are shown in figure 1(b). They are a U-shaped continuous distribution and a peaked discrete distribution. In case of the U-shaped distribution, the following formula can be used in accordance with the disorder-gap state (DIGS) model [12].

$$N_{ss}(E) = N_{ss0} \exp(|E - E_{HO}|/E_{Oj})^{n_j} \quad (1)$$

where  $N_{ss0}$  is the minimum surface state density and  $E_{HO}$  is the energy position of the charge neutrality level.  $E_{Oj}$  and  $n_j$  determine the distribution shape with  $j = d$  for donor-like gap states located below  $E_{HO}$ , and  $j = a$  for acceptor-like gap states above  $E_{HO}$ . The position of  $E_{HO}$  is determined by the mean hybrid orbital energy of the semiconductor crystal in the tight-binding context [12]. Using the branch point data by Kampen and Mönch [13], its position for  $Al_xGa_{1-x}N$  may be deduced by the following formula

$$E_{HO}(\text{eV}) = E_V + 2.37 + 0.60x \quad (2).$$

For the discrete level, on the other hand, donor-type or acceptor-type Gaussian peaks at various peak energy positions with suitable FWHM values can be assumed.

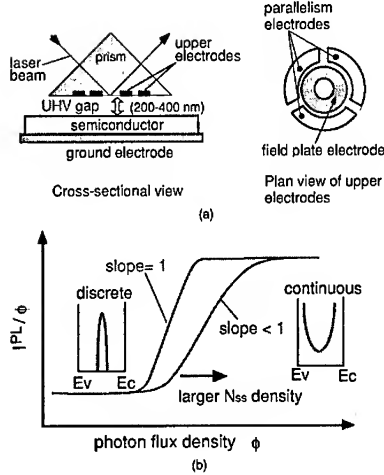


Figure 1 (a) A basic set-up of UHV contactless C-V technique. (b) Behavior of PL efficiency spectra.

### Cathodoluminescence in-depth spectroscopy (CLIS) technique

Noting that the penetration depth of electron beam in cathodoluminescence can be changed by changing acceleration voltage, we have recently proposed CLIS technique as contactless and non-destructive depth-resolved measurement technique including surface [14, 15]. Its principle is shown in figure 2 for a simple heterostructure. This gives two near-bandgap CL peaks, A and B, at an electron acceleration voltage,  $V_{acc}$ . Since the electron penetration depth is strongly dependent on  $V_{acc}$ , CL intensities changes with  $V_{acc}$ . Plots of CL intensities vs. the electron acceleration voltage,  $V_{acc}$  are defined here as the CLIS spectra. At low values of  $V_{acc}$ , CLIS spectra are extremely sensitive for near-surface processes including surface recombination. For a theoretical analysis of CLIS spectra, we have modified the above mentioned program for PLS<sup>3</sup> technique [16] so that electron-hole pair generation by electron beam is included by using Everhart-Hoff electron energy loss curves [17,18]. The program includes SRH surface recombination processes through the U-shaped DIGS continuum consisting of donor-type and acceptor-type states, as well as that through particular types of discrete donor or acceptor states with peaked densities of states.

CLIS spectra have been measured on GaAs, GaN, InGaP/GaAs heterostructures and quantum wells, and AlGaIn/GaN heterostructure wafers produced by MOVPE and MBE, and they have been successfully analyzed [14, 15, 19].

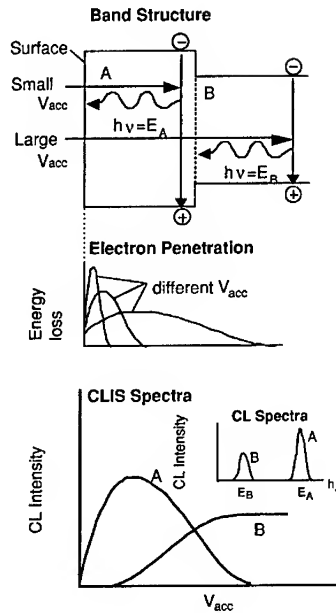


Figure 2 Principle of CLIS technique.

### Gateless FET technique

The structure of the gateless HFET used in this study is shown in figure 3. Use of such a gateless FET structure for current transport study was done first by our group on sulfur passivation of GaAs long time ago [20]. This technique is extremely powerful in correlating various surface processing with inner current transport. The transport measurements can be done under D.C., sinusoidal A.C. and pulsed conditions. In our study, the sample in figure 3 was fabricated by mesa isolation with UV light-assisted KOH wet etching and drain and source ohmic metallization by alloying Ti/Al/Ti/Au.

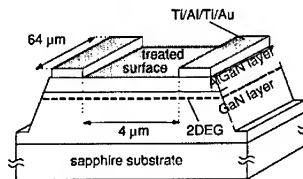


Figure 3 Structure of gateless HFET.

### SURFACE STATES ON FREE SURFACES OF GaN AND AlGaIn

#### XPS, PL and CLIS study of free surfaces of GaN

A convenient method to detect presence of Fermi level pinning due to surface states on free surfaces is the XPS band bending measurements. Using the reported value of the separation between the Ga 3d core level and the valence band maximum of 17.7 eV [21, 22],  $E_{F_s}$  was found to lie at  $E_v + 2.3$  eV on the air-exposed MOVPE GaN surface [5], indicating a relatively large upward band bending of 1.0 - 1.1 eV due to Fermi level pinning. On the MBE-grown clean surface, a clear peak shift toward a higher binding energy

took place, reducing band bending by 0.5 - 0.6 eV.

In order to get more detailed information on surface states, PLS<sup>3</sup> study was carried out on these surfaces[5]. Measured quantum efficiency ( $I_{PL}/\phi$ ) of the band-edge PL emission at room temperature is plotted vs. excitation photon flux density,  $\phi$ , in figure 4(a) for the air-exposed MOVPE and the MBE-grown clean surfaces. After many trials, excellent fits were obtained by assuming a U-shaped distribution together with presence of a discrete donor peak at  $E_C - 0.4$  eV. The fitting results are also shown in figure 4(a) by the solid curves, and the  $N_{ss}$  distributions obtained by such fitting are shown in figure 4(b). Calculations also gave the positions of the surface Fermi level in the dark. They were  $E_{Fs} = E_C - 0.89$  eV for the MOVPE surface and  $E_{Fs} = E_C - 0.36$  eV for the MBE surface, respectively. These values agree reasonably well with the XPS band bending results.

As seen in figure 4(b), the air exposed MOVPE surface is dominated by high-density surface states with a U-shaped distribution. Similar U-shaped distributions were also detected more directly by UHV contactless C-V measurements on air-exposed MOVPE GaN surface recently [9]. Presence of a U-shaped surface state continuum is a common feature of air-exposed surfaces of III-V materials as reported previously for GaAs, InP and their related materials [12]. Surface states are most probably due to surface disorder caused by presence of non-stoichiometric natural oxides with random strain [12]. The U-shaped continuous states drastically reduced after growth of a clean (2x2) MBE layer, indicating the partial recovery of the surface order with removal of natural oxide. Remaining states are most probably due to bond disorder in the reconstructed surface structures. However, the MBE layer has a high density of the discrete state at  $E_C - 0.4$  eV. By combining various previous reports [23-27], the observed 0.4 eV discrete level is most likely due to donors related to N-vacancies formed during MBE growth. It seems likely that high density of native N-vacancies are produced due to highly non-equilibrium growth conditions as well as an extremely low solubility of nitrogen into GaN at the growth temperature.

An example of measured CLIS spectra for a band edge emission from an air exposed MOVPE GaN sample is shown in figure 5(a) together with a calculated CLIS spectra assuming U-shaped  $N_{ss}$  distributions given in figure 5(b). It also confirms presence of a U-shaped surface state continuum on the surface.

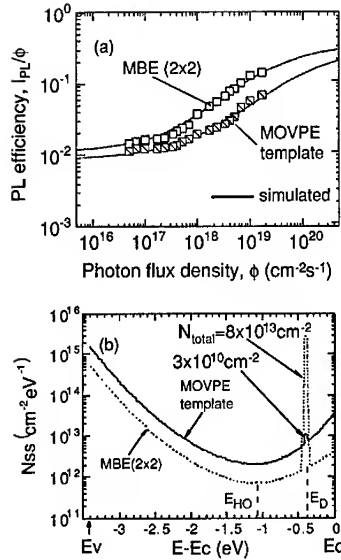


Figure 4 (a) PL efficiency of the band-edge emission. (b)  $N_{ss}$  distribution obtained from the PLS<sup>3</sup> simulation.

#### Gateless FET study of plasma-treated free surfaces of AlGaIn/GaN heterostructures

It is difficult to obtain information concerning surface states on free surfaces of the AlGaIn/GaN wafer by conventional MIS C-V method, or by our contactless C-V and PLS<sup>3</sup> methods, due to its complicated structure with a very thin and extremely wide-gap AlGaIn layer. Here, the gateless HFET technique shown in figure 3 has been applied to the air-exposed surface as well as plasma-treated free surfaces of the AlGaIn/GaN wafer [28]. Plasma surface treatments on the air-exposed portion of the gateless HFET included  $\text{H}_2$ -plasma treatment,  $\text{N}_2$ -plasma treatment and formation of a  $\text{SiO}_2$  passivation film. Both plasma treatments,

which may be used for native oxide removal, were applied for 1 min at 200 °C under ECR plasma excited at a microwave frequency of 2.75 GHz and a power of 50 - 100 W with gas flow rates of 5 - 10 sccm. On the other hand, since current collapse takes in a pronounced way in SiO<sub>2</sub> passivated devices, a SiO<sub>2</sub> film formed by the standard plasma CVD process using SiH<sub>4</sub> and N<sub>2</sub>O on the HF treated surface was chosen as the test passivation film.

DC  $I_{DS}$ - $V_{DS}$  curves of gateless HFETs before and after various treatments are summarized in figure 6(a). Since the electric field strength was too small to cause significant velocity saturation, the observed highly non-linear DC I-V curves similar to those of a gated device can only be explained in terms of presence of strong Fermi level pinning by surface states which behave like a "virtual gate". In fact, data could be reasonably well fitted to the theoretical  $I_{DS}$ - $V_{DS}$  curves based on the gradual channel approximation. This gave a surface Fermi level position of  $E_{FS} = E_C - 1.4$  eV for the air exposed sample after taking account of the polarization effect. In the H<sub>2</sub>-plasma and SiO<sub>2</sub> samples, the saturation current decreased, whereas it slightly increased in the N<sub>2</sub>-plasma sample, indicating treatment-induced changes of the pinning position. Except the N<sub>2</sub>-plasma sample, AC  $I_{DS}$ - $V_{DS}$  curves showed frequency dependences, indicating that the so-called I-V dispersion takes place also in gateless HFETs.

Results of current transient measurements are summarized in figure 6 (b). The quencient bias was kept at  $V_{DS} = 0.5$  V in the linear region. After applying a positive voltage with a variable peak value of  $V_{DSp}$  for 50 s, the current transients were measured. When the value of  $V_{DSp}$  was small, no change of  $I_{DS}$  was observed in all cases. When  $V_{DSp}$  went deep into saturation region, transients became visible especially in H<sub>2</sub>-plasma and SiO<sub>2</sub> samples. The current showed a "fast" and dominant exponential transient with a large amplitude followed by subsequent smaller, slow and highly non-exponential response. In the air-exposed sample, transient became visible at  $V_{DSp} \approx 15$  V whereas no transient was seen even up to  $V_{DSp} = 15$  V in the N<sub>2</sub>-plasma sample.

The time constant of the initial exponential transient is plotted in figure 7 vs. inverse temperature for the H<sub>2</sub>-plasma sample and SiO<sub>2</sub> sample. This indicated that a discrete trap level with an activation energy of 0.37 eV and a capture cross section of  $1.2 \times 10^{-16}$  cm<sup>2</sup> plays a dominant role in the transient in both samples. Subsequent small, slow and highly non-exponential response is a typical response of a surface state continuum including a wide range of time constant.

In order to get information on the origin of the discrete trap, *in situ* XPS measurements were made on the treated AlGaIn surfaces. The XPS Ga3d and N1s core-level spectra taken after the H<sub>2</sub> plasma

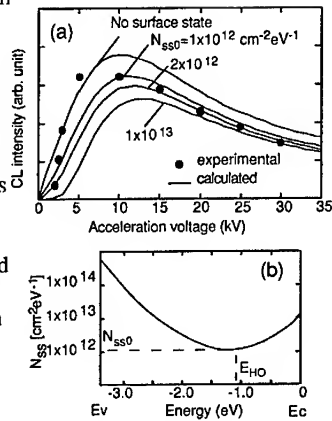


Figure 5 (a) Measured and calculated CLIS spectra of an air exposed MOVPE GaN sample. (b)  $N_{ss}$  distribution used for the simulation.

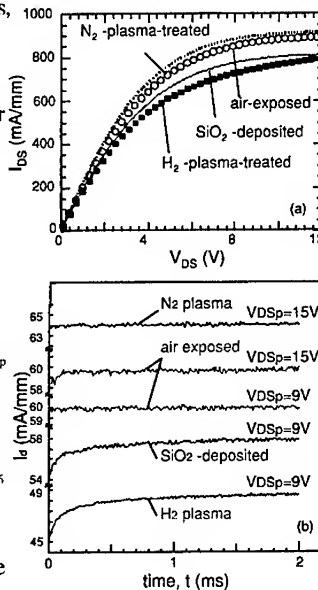


Figure 6 (a) DC I-V characteristics and (b) drain current transients of the gateless HFETs.

and  $N_2$  plasma treatments are shown in figure 8. Photoemission was detected at an electron escape angle of  $10^\circ$ . As shown in figure 8, systematic peak shifts of about 0.4 eV toward lower binding energies were observed for the  $H_2$ -plasma treated surface. This indicates that the magnitude of upward band-bending is larger for the  $H_2$ -plasma treated surface than the  $N_2$ -plasma treated surface, being consistent with the electrically detected difference of the surface barrier heights of 0.5 eV. In the  $N1s$  core-level spectrum of the  $H_2$ -plasma treated sample, a shoulder peak appeared at around 399 eV, which corresponds to the binding energy of the  $N-H_x$  bond [29]. Additionally, decrease of the peak intensity of the  $N1s$  core level was observed. The V/III ratio of the AlGaIn surface after the  $H_2$ -plasma treatment was far below unity, strongly indicating decrease of N atoms at the surface. Thus, during the  $H_2$  plasma treatment, highly active hydrogen plasma species such as hydrogen radicals react with the AlGaIn surface to form volatile  $NH_x$  products. This leads to decrease of N atoms and formation of Ga and Al clusters at the topmost AlGaIn surface. Such a surface reaction process is thus most likely to introduce N-vacancy related defects in AlGaIn surface region of.

As regards the energy position of the N-vacancy related traps, a theoretical calculation by Yamaguchi and Junnarkar [30] predicted that the N-vacancy defects form s-like deep donor levels at around Ec-0.4 eV in GaN and AlGaIn.

On the other hand, no such decrease of N atoms was observed after the  $N_2$ -plasma treatment, although it was equally effective in removing oxides from the surface.

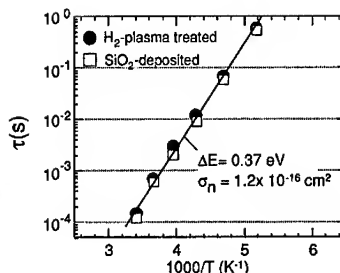


Figure 7 Arrhenius plots of the time constant of "fast" transient current.

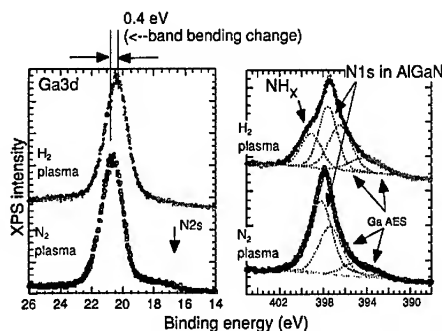


Figure 8 XPS core-level spectra of plasma-treated AlGaIn surfaces.

## CURRENT TRANSPORT MECHANISM IN GaN AND AlGaIn SCHOTTKY CONTACTS

### I-V-T characteristics

Accurate control of depletion width by Schottky gates with small reverse leakage currents is vitally important in MESFETs and HFETs. However, in GaN-based high-power HFETs, Schottky contacts show anomalously large reverse leakage whose mechanism has not been explained so far satisfactorily.

In order to clarify the current transport mechanism of GaN and AlGaIn Schottky contacts, detailed I-V measurements were made changing the measurement temperature. Measured room temperature I-V characteristics of various n-type GaN Schottky diodes (Pt, Ni, Au and Ag) formed by the standard vacuum deposition process showed thermionic emission (TE)-like behavior with ideality factors of  $n = 1.1-1.2$  and barrier heights of 0.5-1.1 eV under forward bias. However, the reverse currents were large, and they increased almost exponentially with bias. When the temperature was lowered, changes of I-V curves were found to be much smaller in both forward and reverse directions than those of the TE transport, deviating from the TE

behavior by many orders of magnitudes. Similar behavior was observed in AlGaIn Schottky diodes, as shown for a Ni/AlGaIn Schottky contact in **figure 9**. Temperature dependences of I-V curves are extremely small, and reverse currents are also anomalously large. At low temperatures, the I-V curves showed hysteresis. None of previous Schottky transport models can explain such behavior.

### TSB model

On the basis of a detailed analysis of the measured I-V-T curves [31], we have proposed a novel thin surface barrier (TSB) model shown in **figure 10(a)**. According to this model, the thickness of the Schottky barrier produced by the U-shaped surface state continuum

becomes extremely thin in the TSB region due to presence of high density defect donors in the near-surface region which are positively ionized. TSB regions are distributed near the metal/ semiconductor interface due to high non-uniformity of the GaN surface involving many dislocations. In each TSB region, Gaussian beams of electrons pass through the TSB region by the thermionic field emission (TFE) mechanism [32]. Based on this model, formulas for I-V-T behavior have been derived. For example, the ideality factor for forward currents,  $n_F$ , is given by the following formula.

$$n_F = \frac{E_{00}}{kT} \coth\left(\frac{E_{00}}{kT}\right) \quad (3a)$$

$$E_{00} = (qh/4\pi)(N_{DS}/m^* \epsilon_s \epsilon_0)^{1/2} \quad (3b)$$

where  $N_{DS}$  is the defect donor concentration. Comparison of measured values of  $n_F$  with theory is given for a Ni/AlGaIn Schottky contacts in **figure 10(b)**. The values of  $N_{DS}$  obtained by fitting were much larger than the doping concentrations of shallow donors in the epitaxial layers.

As for the origin of the defect donors, we believe that they are again N-vacancy related 0.37 eV donors discussed in the previous sections. In the case of Schottky contacts, deposition of high energy metal atoms leads to formation of nitrogen vacancies underneath the metal film. Presence of such deep donors can also explain the observed hysteresis effect of the I-V curves.

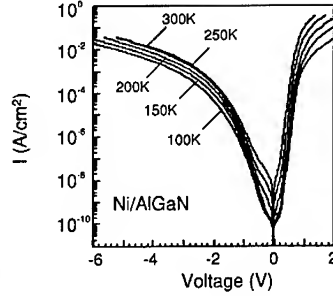


Figure 9 I-V-T characteristics of Ni/AlGaIn Schottky contact..

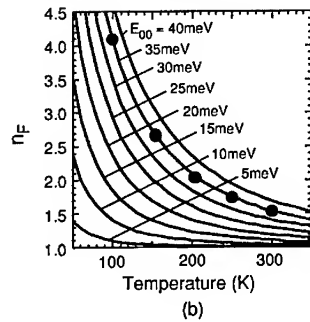
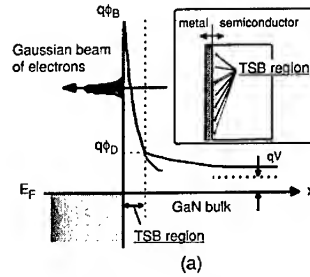


Figure 10 (a) Thin surface barrier (TSB) model. (b)  $n_F$  value of the Ni/AlGaIn contact as a function of temperature.

Our new model[33] for near-surface electronic states based on the various studies in the previous sections is shown in **figure 11**. Similarly to other III-V semiconductors [12], a U-shaped high density surface state continuum is formed due to bond disorder, and this DIGS continuum pins the surface Fermi level near the charge neutrality level (CNL). The position of CNL for AlGaIn is given by Eq.(2). Depending on details of processings such as plasma treatments, passivation and metal deposition, high density deep donors related to N-vacancies may be created near surface. Due to Fermi level pinning near CNL both at free surfaces and at Schottky interface, these deep donors are ionized, supplying electrons to 2DEG together with those due to shallow donors and intrinsic and piezoelectric polarization [34]. This produces a thin surface barrier (TSB) region shown in **figures 10(a) and 11**.

In the case of HFET transport, injection of high-energy electrons takes place from the 2DEG channel into the AlGaIn region near the drain edge under the application of a large  $V_{DS}$ . Due to electron injection, near-surface traps and surface states are filled near the drain edge, reducing 2DEG density and expanding the depletion width. This causes current collapse. Then, after switching back the drain voltage, electrons in these states are emitted, leading to recovery transients.

To confirm such a picture, a computer simulation of current transients was attempted using a combined state distribution consisting of a U-shaped surface state continuum and a discrete near-surface donor level. For the U-shaped distribution, the formula given in Eq. (1) was used in accordance with the disorder-induced gap state (DIGS) model. A value of  $E_{H0} = E_C - 1.7$  eV was used according to Eq.(2) for  $Al_{0.26}Ga_{0.72}N$ . For the discrete near-surface donor level, a donor-type Gaussian peak at the measured energy position of 0.37 eV was assumed, treating the near-surface deep donors as projected surface states for simplicity. The transients were calculated using the following equation.

$$N_{emit}(t) = \int N_{ss}(E) [1 - \exp(-\frac{t}{\tau(E)})] dE \quad (4).$$

After many trials, excellent fits were obtained as shown in **figures 12(a) and (b)** by assuming a U-shaped distribution combined with a discrete state density distribution as shown in **figure 12 (c)**. As shown in **figure 12(a)**, a dominant fast transient is due to the electron emission from the discrete level. The total density of the 0.37-eV level was determined to be  $5 \times 10^{11} \text{ cm}^{-2}$ . On the other hand, as shown in **figure 12 (b)**, slow increase of current at longer time regime is due to the emission from continuous surface states that have a wide range of time constant. It is noted that the combined distribution obtained in **figure 12 (c)** is very similar to that in **figure 4 (b)** obtained on the free surface of GaN by PLS<sup>3</sup> method.

On the other hand, in the case of the Schottky contact, the TSB region provides thermionic-field emission paths for current transport, giving rise to large leakage currents in HFETs. Based on this model, formulas for I-V-T behavior have been derived[31]. The new model has reproduced the experimental I-V-T curves not only qualitatively, but also quantitatively in both of forward and reverse directions. As an example, experimental and calculated reverse currents are compared in **figures 13(a) and (b)** for a Ni/n-GaN diode.

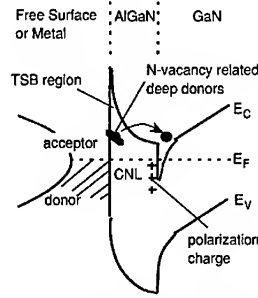


Figure 11 A model for near-surface electronic states.

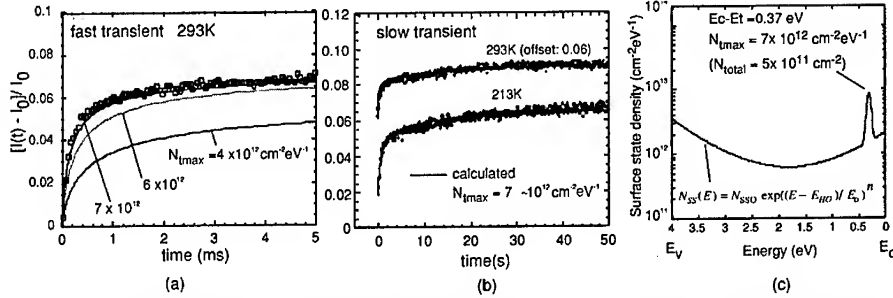


Figure 12 Fitting results for (a) fast transient at RT and (b) slow transient at RT and 213 K. (c) Surface state density distribution obtained from the fitting of the transient currents.

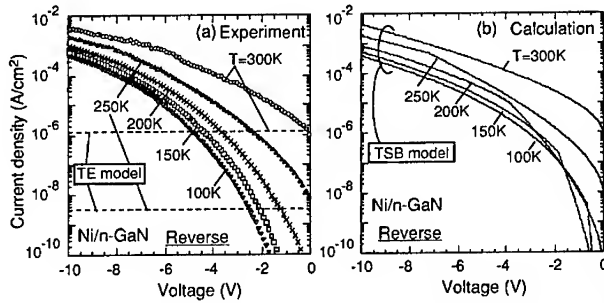


Figure 13 (a) Experimental and (b) calculated reverse currents of a Ni/n-GaN diode.

### Passivation and removal of near-surface electronic states

Practical AlGaIn/GaN HFET devices require suitable surface passivation in addition to gate metallization. For these processing steps, native oxides should be removed from the air-exposed surfaces of AlGaIn/GaN wafers by a suitable low energy oxide removal process, and then suitable metal or insulating films should be deposited by low energy deposition processes. The present study indicates that minimization of process-induced generation of N-vacancy is a key factor in all of these processing steps.

As a processing for removal of native oxide, surface treatment in a heated  $\text{NH}_4\text{OH}$  solution (typically at  $50^\circ\text{C}$  for 5–10 min) has been found considerably effective [35, 36]. But, it does not completely remove native oxide particularly in the case of the AlGaIn surface. According to the present study, the optimized ECR  $\text{N}_2$ -plasma treatment seems to provide the best solution to this problem.  $\text{H}_2$ -plasma treatment should be avoided for oxide removal. It should be also reminded here that  $\text{H}_2$ -plasma is frequently involved also in various dry etching processes where we have recently found inclusion of  $\text{N}_2$  is beneficial [37].

As for the insulating layers for passivation, it has been found that silicon nitride ( $\text{SiN}_x$ ) film produced by the ECR plasma deposition works much better than the silicon dioxide ( $\text{SiO}_2$ ) film [38, 39]. For example, surface state density distributions measured by standard high frequency MIS C-V measurements at 1 MHz are compared in figure 14 for silicon nitride and silicon dioxide MIS capacitors formed on n-type GaN after

the ECR  $N_2$ -plasma treatment and ECR  $H_2$ -plasma treatment. It is seen that  $SiN_x$  passivation after  $N_2$ -plasma treatment gave the best result.  $SiN_x$  passivation after  $H_2$ -plasma treatment produced a distribution peak at around  $E_c - 0.45$  eV. This can be interpreted as the density peak due to near surface N-vacancy related defects whose projected energy position is modified due to band bending. In the case of  $SiO_2$  passivation, state densities were high even with  $N_2$ -plasma treatment. Probably, subcutaneous oxidation selectively attacks Ga atoms of GaN, producing high densities of N-vacancies and related bond disorder in the surface region. This leads to pronounced current collapse in  $SiO_2$ -passivated HFETs.

For gate metalization, it seems difficult to completely suppress N-vacancy formation in the standard vacuum deposition process, since it involves bombardment and subsequent condensation of high energy metal atoms. From such a viewpoint, an attempt has been made to suppress formation of N-vacancies by a low temperature and low energy pulsed electro-deposition process where oxide removal and metal deposition are done in-situ in a suitable electrolyte at room temperature. This process reduced the reverse leakage currents by 4 orders of magnitude [40].

Another more promising approach that can achieve reduction of gate leakage and good surface passivation at the same time is to insert a suitable passivation film as the gate dielectric for HFETs. Silicon nitride does not seem to be the optimum choice, since its bandgap is about 5 eV, and not large enough to put on AlGaIn. From such a viewpoint, we have recently developed a novel formation of  $Al_2O_3$  films by the ECR-plasma oxidation of Al [41]. The processing steps are: (1)  $NH_4OH$  treatment at 50 °C for 15 min in air; (2) deposition of 3-nm-thick Al layer at RT in MBE chamber; (3) UHV annealing at 700 °C for 10 min; (4) oxidation of Al by ECR- $O_2$  plasma; (5) UHV annealing at 700 °C for 10 min. Steps from (2) to (5) were continuously carried out in UHV environments without exposing the sample to air. The resultant  $Al_2O_3$ /AlGaIn/GaN IG-HFETs allowed a much larger gate voltage swing up with a high linearity, and much reduced gate leakage currents as compared with the Schottky gate device as shown in figure 15.

## CONCLUSION

Properties of electronic states near surfaces of GaN and AlGaIn have been investigated by using various *in-situ* and *ex-situ* characterization techniques. As a result, a model including a U-shaped surface state continuum, having a particular charge neutrality level, combined with frequent appearance of near-surface N-vacancy related deep donor states having a discrete level at  $E_c - 0.37$  eV is proposed as a unified model that can explain large gate currents and current collapse in AlGaIn/GaN HFETs. Hydrogen plasma treatment and  $SiO_2$  deposition increases N-vacancy related deep donors. Reasonably good surface passivation can be achieved by ECR-plasma deposited  $SiN_x$  films and by ECR-plasma oxidized  $Al_2O_3$  films both being combined with the ECR  $N_2$  plasma treatment.

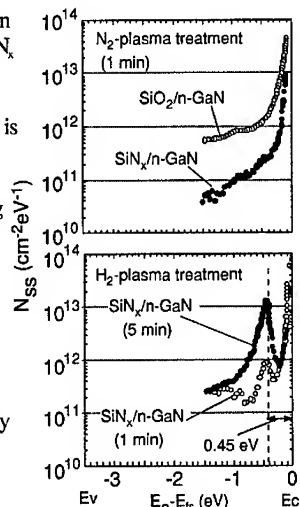


Figure 14 Interface state density distributions of the  $SiO_2$ /GaN and  $SiN_x$ /GaN interfaces.

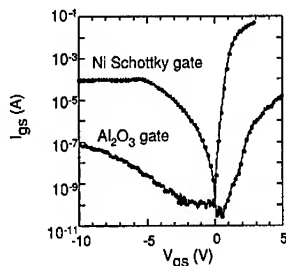


Figure 15 I-V characteristics of Ni Schottky gate and  $Al_2O_3$  insulated gate on AlGaIn/GaN HFET.

## ACKNOWLEDGEMENTS

The present work is supported in part by 21COE Project on "Meme-media technology approach to the R&D of next-generation information technologies" from Ministry of Education, Culture, Sports, Science and Technology.

## REFERENCES

- [1] M.J. Manfra et al., Appl. Phys. Lett., **77**, 2888(2000).
- [2] S. Oyama, T. Hashizume and H. Hasegawa, Appl. Sur. Sci. **190**, 322(2002).
- [3] R. Vetry, N.Q. Zhang, S. Keller and U.K. Mishra, IEEE Trans. Electron. Dev. **48**, 560(2001).
- [4] S. C. Binari et al., IEEE Trans. Ele. Dev. **48**, 465(2001).
- [5] M. Konishi, S. Anantathanasarn, T. Hashizume and H. Hasegawa, Inst. Phys. Conf. Ser., **170**, 837(2002).
- [6] E.J. Tarsa, B. Heying, X.H. Wu, P. Fini, S.P. DenBaars and J.S. Speck, J. Appl. Phys., **82**, 5472(1997).
- [7] L.C. Chao and A.J. Steckl, Appl. Phys. Lett., **74**, 2364(1999).
- [8] H. Hasegawa et al., Mat. Sci. Eng. B **80**, 147(2001).
- [9] M. Akazawa and H. Hasegawa, presented at 2002 EXMATEC, Budapest, May 26-29, 2002, to appear in Mat. Sci. Eng. B.
- [10] T. Saitoh, H. Iwade and H. Hasegawa, Jpn. J. Appl. Phys., **30**, 3750(1991).
- [11] T. Sawada, K. Numata, S. Tohdoh, T. Saitoh and H. Hasegawa, Jpn. J. Appl. Phys., **32**, 511(1993).
- [12] H. Hasegawa and H. Ohno, J. Vac. Sci. Technol. B **4**, 1130(1986).
- [13] T.U. Kampen and W. Mönch, Appl. Sur. Sci., **117/118**, 388(1977).
- [14] F. Ishikawa and H. Hasegawa, Inst. Phys. Conf. Ser. **170**, 461(2002).
- [15] F. Ishikawa and H. Hasegawa, Appl. Surf. Sci. **190**, 508(2002).
- [16] B. Adamowicz and H. Hasegawa, J. J. Appl. Phys. **37**, 1631(1998).
- [17] T. E. Everhart and P. H. Hoff, J. Appl. Phys. **42**, 5837(1971).
- [18] H. J. Leamy, J. Appl. Phys. **53**, 51(1982).
- [19] F. Ishikawa and H. Hasegawa, presented at ICSFS-11, Marseille, July 8-12, 2002, to appear in Appl. Surf. Sci.
- [20] H. Hasegawa et al, J. Vac. Sci. Technol. B **5**, 1097 (1987).
- [21] J.R. Waldrop and R.W. Grant, Appl. Phys. Lett. **68**, 2879(1996).
- [22] C.I. Wu and A. Kahn, J. Vac. Sci. Technol. B **16**, 2218(1998).
- [23] O. Ambacher et al, J. Vac. Sci. Technol. B, **14**, 3532(1996).
- [24] G.H. Hughes et al, J. Vac. Sci. Technol. B, **16**, 2237(1998).
- [25] T.L. Tansley and R.J. Egan, Phys. Rev. B **45**, 10942(1992).
- [26] J. Neugebauer and C.G. Van de Walle, Phys. Rev. B **50**, 8067(1994).
- [27] P. Boguslauski, E.L. Briggs and J. Bernholc, Phys. Rev. B **51**, 17255(1995).
- [28] T. Inagaki, T. Hashizume and H. Hasegawa, presented at ISCSI-4, Karuizawa, October 21-24, 2002, to appear in Appl. Sur. Sci.
- [29] X. Y. Zhu, M. Wolf and J. M. White, J. Vac. Sci. Technol. A **11**, 838(1993).
- [30] E. Yamaguchi, and M. R. Junnarkar, J. Crystal Growth **189/190**, 570(1998).
- [31] H. Hasegawa and S. Oyama, J. Vac. Sci. Technol. B **20**, 1467(2002)
- [32] F. A. Padovani and R. Stratton, Solid State Electron. **9**, 695(1966).
- [33] H. Hasegawa et al., presented at 2002 ISCS, Lausanne, October 7-10, 2002, to appear in Inst. Phys. Conf. Ser.
- [34] O. Ambacher et al, J. Appl. Phys., **85**, 3222(1999).
- [35] T. Hashizume et al, Appl. Phys. Lett., **76**, 2880(2000).
- [36] T. Hashizume, R. Nakasaki, S. Ootomo, S. Oyama, and H. Hasegawa, Mat. Sci. Eng. B **80**, 201(2001).
- [37] Z. Jin, T. Hashizume and H. Hasegawa, Appl. Sur. Sci. **190**, 361(2002).
- [38] R. Nakasaki, T. Hashizume and H. Hasegawa, Physica E **7**, 953(2000).
- [39] T. Hashizume, S. Ootomo, S. Oyama, M. Konishi and H. Hasegawa, J. Vac. Sci. Technol. B **19**, 1675 (2001).
- [40] T. Sato, Oyama and Hasegawa, presented at ICPS-26, Edinburgh, UK, July 29- August 2, 2002.
- [41] S. Ootomo, T. Hashizume and H. Hasegawa, presented at TWN-2002, Aachen, July 22-25, 2002, to appear in phys. stat. solidi (b).

---

## **Poster Session**

### Searching for the Influence of the Sapphire Nitridation Conditions on GaN Films Grown by Cyclic PLD

P. Sanguino<sup>1</sup>, M. Niehus<sup>1</sup>, S. Koynov<sup>2</sup>, L. Melo<sup>1</sup>, R. Schwarz<sup>1</sup>,  
M. J. Soares<sup>3</sup>, C. Boemare<sup>3</sup>, T. Monteiro<sup>3</sup>

<sup>1</sup> Physics Department, Instituto Superior Técnico, Lisbon, Portugal

<sup>2</sup> CL-SENES, Bulgarian Academy of Sciences, Sofia, Bulgaria

<sup>3</sup> Physics Department, Aveiro University, Aveiro, Portugal

#### Abstract

We have deposited highly c-axis oriented GaN films on sapphire by the Cyclic Pulsed Laser Deposition Technique. Nitridation of the sapphire substrates for these samples was performed at 200 °C, 400 °C and 600 °C. For that purposed, we used a radio frequency nitrogen plasma during four hours. The films were compared in terms of crystal structure, surface morphology and optical quality. Although small, the biggest differences were detected in the surface morphology of the films. Additionally, a typical GaN sample nitridated at 200 °C was analysed by photoluminescence and showed the typical donor bound excitonic luminescence ( $D^0X$ ) transition at 3.47 eV and a line near 3.42 eV. These lines show a FWHM of 20 meV and 30 meV at 13K, respectively.

#### Introduction

The preparation of high quality semiconductor films of group-III nitrides (GaN, AlN, InN and their alloys) is a forefront task of the present technological research because of the attractive applications of such films in "blue and UV" optoelectronic devices such as blue LEDs and Blue laser diodes [1,2]. The Pulsed Laser Deposition (PLD) is a promising alternative of the common MOCVD and MBE techniques for preparation of these materials [3-8].

The heteroepitaxial growth of GaN is usually done on sapphire substrates due to their wide availability. The most usual solution to circumvent the large lattice mismatch between sapphire and GaN is the nitridation treatment of the substrate prior to the low temperature buffer layer growth. It has been reported by various groups that this nitridation step is crucial to the structural and optical properties of the GaN epilayer [9-11]. Depending on the deposition method, the nitridation is usually done with ammonia ( $NH_3$ ) or nitrogen plasma. High temperature (850 °C to 1050 °C) is usually necessary to thermally dissociate the  $NH_3$  in active nitrogen species. This is not the case if nitrogen plasma is used. Here, the plasma generates the active species and a high temperature is not necessary. In fact it has been reported that oxygen diffusion from the  $Al_2O_3$  occurs over distances of about 1.5  $\mu m$  in samples nitridated at high temperatures [12]. Recent studies have pointed to the 200 °C as the best temperature for nitridation with nitrogen plasma [13]. In this work, we investigate the influence of the temperature of the sapphire nitridation process on the growth of GaN films grown by cyclic PLD. The GaN samples thus obtained are compared in terms of optical and structural quality. X-ray diffraction, UV-visible transmission

spectroscopy, atomic force microscopy (AFM) and photoluminescence are the techniques used to characterise and compare the deposited films.

## Experiment

The GaN thin films were deposited with Cyclic-PLD on sapphire substrates (0001). Details of the deposition system can be found elsewhere [14,15]. Briefly, the liquid Ga target is ablated with a Nd: YAG laser, operated at 1064 nm, 5 Hz, 10 mJ and 5 ns per pulse. The substrates were degreased in isopropanol alcohol for 5 minutes, then etched in a hot solution of sulphuric acid / phosphoric acid (solution ratio 3:1) for 1 hour and finally rinsed in DI water. After degassing the substrates at 800 °C during 1 hour under vacuum, nitridation of the sapphire substrates was done with the help of a nitrogen r.f. plasma set at 13,56 MHz, 1 mbar, 6 W, and for 4 hours. Three different nitridation temperatures were used: 200 °C, 400 °C and 600 °C. The Ga target was then pre-ablated for 15 minutes with the sample surface protected by a shutter. Then, a GaN buffer layer was grown at 400 °C during 15 minutes (approx. 20 nm thickness).

The film growth was done at 650 °C in a cycle composed of two steps. In the first step, the Ga is ablated for 15 seconds under a 10-Watt, 1 mbar nitrogen rf plasma. In the second step, the laser is stopped for 5 seconds in order to incorporate the possible missing nitrogen. The cycle was repeated during 5 hours and the deposition rate varied from 0,06 µm/hour to 0,08 µm/hour. A fourth GaN sample was deposited for 10 hours on sapphire nitridated at 200 °C.

The thickness of the films was determined with a profilometer. Crystal orientation of the as grown GaN films was analysed by a Siemens D 5000 diffractometer in a  $\theta$ -2 $\theta$  configuration equipped with a Molybdenum source. Surface morphology of the films was investigated by atomic force microscopy (AFM). Transmission measurements were done at room temperature. PL measurements were carried out with a 325 nm CW He-Cd laser and the excitation power density was typically less than 0.6 W.cm<sup>-2</sup>. A 325 nm band pass filter was used to attenuate lines other than the 325 nm laser line. PL was measured at temperatures between 13K and 300K using a closed cycle helium cryostat. The luminescence was dispersed by a Spex 1704 monochromator (1m, 1200/mm) and detected by a Hamamatsu R928 photomultiplier.

## Results and Discussion

All the samples deposited exhibit a yellow brown colour and a non-glossy surface. There was also some evidence of Ga droplets.

The X-ray diffraction scans obtained in the  $\theta$ -2 $\theta$  geometry for three GaN films deposited on substrates submitted to different nitridation temperature treatments are presented in figure 1. As we can see, the growth of the films is clearly c-axis oriented. The magnitude of the (0002) peak and the absence of the (10.0) and (10.1) peaks suggests a high degree of texture for both films. Only the (0002) family of planes is present in the X-ray pattern. Only the (0002) family of planes is presented in the X-ray pattern.

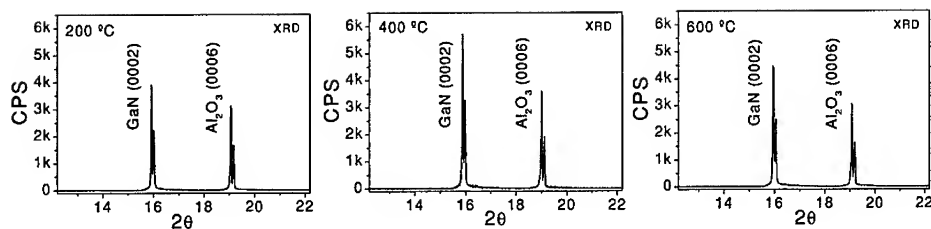


Figure 1. X-ray diffraction scans of three GaN films deposited on c-axis sapphire substrates that were nitridated at 3 different temperatures: 200 °C, 400 °C and 600 °C. The double lines correspond to the splitting of  $K_{\alpha 1}$  and  $K_{\alpha 2}$ . A Mo source was used.

If we take in consideration the thickness of the films, the intensity of the (0002) GaN remains approximately the same whatever the nitridation temperature used on the sapphire substrate. The FWHM of the  $K_{\alpha 1}$  (0002) peak is 0.05 ° for all the samples and comparing with the sapphire peak, this seems to be due to the resolution of the diffractometer.

Fig. 2 shows the surface morphology of the 3 deposited GaN thin films. All the samples have a grain like structure with the grains approaching an hexagonal shape. The average size of the grains is bigger for the sample whose sapphire was nitridated at 600 °C (250 nm). The smallest grain size was obtained for the 400 °C (150 nm). For the 200 °C the grain size was around 200 nm. The mean roughness was 19 nm for 200°C, 7 nm for 400° C and 16 nm for 600 °C of nitridation. For this deposited samples we found that the surface morphology did not varied much with the temperature of the nitridation treatment.

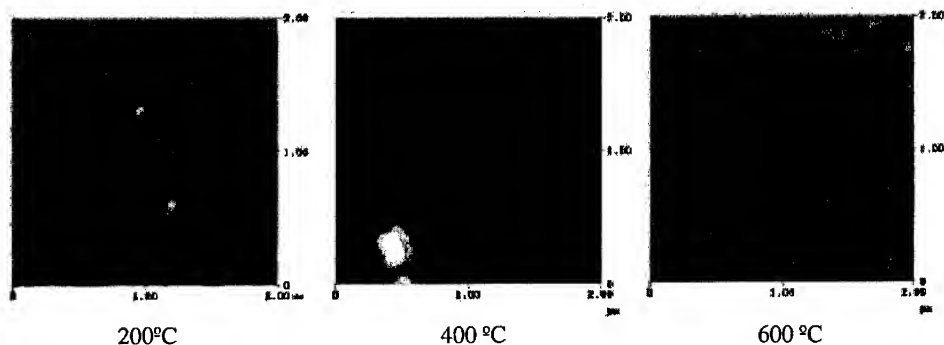


Figure 2. Surface morphology of the GaN films examined by atomic force microscopy (AFM) for 3 samples deposited on (0001) sapphire that was nitridated at different temperatures (200 °C, 400 °C and 600 °C).

In figure 3 we present the UV-Visible optical transmission measurements and the square absorption coefficient as a function of photon energy. All the transmission spectra (fig. 3a) show a relatively sharp step reflecting a strong light absorption near the 360 nm. Due to the rough surface of the films, no interference fringes are observed. From these spectra the optical band gap can be extracted by plotting the square of the absorption coefficient versus energy of light. The intersection of the linear fit with the origin gives a value around 3.3 eV for all the samples (fig. 3b). These values are in agreement with the ones reported by other group [3] for PLD GaN.

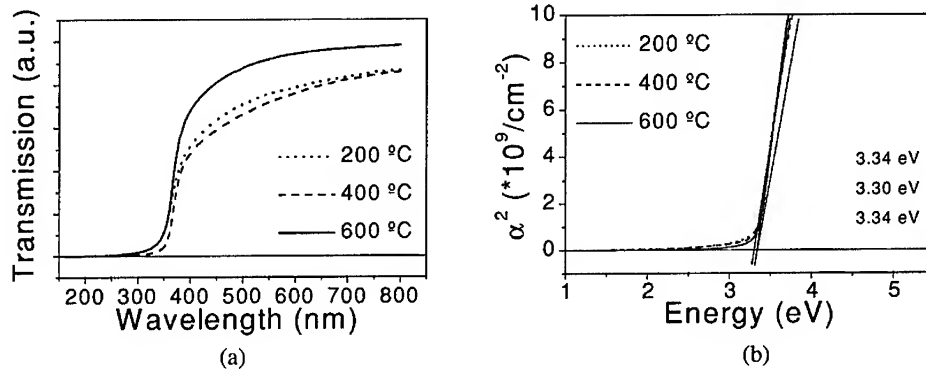


Figure 3. UV-Visible optical transmission (a) and the square absorption coefficient as a function of photon energy (b) for the 3 GaN films.

Photoluminescence (PL) measurements at 13 K were done in the fourth sample in order to evaluate the optical quality of the films - figure 4. The relative intensity of the yellow luminescence (YL) to the near band edge emission (NBE) was strongly dependent on the laser spot location (fig. 4a). We believe that this originates from the grain structure of the material. The high energy spectrum (fig. 4b) of this sample is characterised by the presence of the donor bound exciton transition ( $D^0X$ ) at 3.471 eV and a line near 3.42 eV. These lines show a FWHM of 20 meV and 30 meV at 13K, respectively. Moreover, even when different spot incidences are made on the samples the NBE lines could always be resolved even when the intensity ratio between the NBE and YB changes. The 3.41-3.42 eV line, commonly in samples grown by different methods [15-19], has been attributed to a free-to bound exciton related with O [16], an exciton bounded to stacking faults [15,17-19] and to crystal structural imperfection and rough surface morphology [20]. In low temperature PLD grown layers, few published results have been achieved by PL studies [21, 22]. In [18], only the  $I_3$  and  $I_4$  lines related with strong localised

excitons were reported. While in [21], a NBE peak near 3.41 eV with a FWHM  $\sim 80$  meV at 20K was observed, and in [22] the authors found the DX recombination at 3.47 eV, the 3.41 eV and the DAP recombination at 3.27 eV.

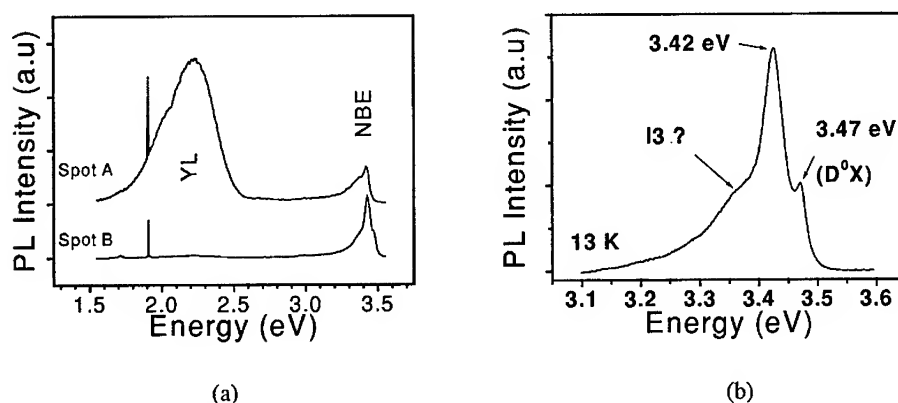


Figure 4. Photoluminescence of  $1\mu\text{m}$  GaN film deposited by cyclic PLD on sapphire nitridated at  $200^\circ\text{C}$

## Conclusions

We have deposited three GaN films thin films in (0001) sapphire nitridated at  $200^\circ\text{C}$ ,  $400^\circ\text{C}$  and  $600^\circ\text{C}$ . All the films exhibited a high degree of texture along the 0002 GaN orientation. The intensity of this X-ray peak per film thickness remained similar for all the samples. In the same way, the optical band gap extracted from the plot of the square of the absorption coefficient versus light energy was around 3.3 eV. In the surface morphology analysis, both the crystal grain size and surface roughness varied slightly. At  $400^\circ\text{C}$  nitridation the mean crystal grain size and surface roughness presented the smallest values of 150 nm and 7 nm respectively. The biggest average grain size was achieved at  $600^\circ\text{C}$  nitridation with a value of 250 nm. For this temperature the mean surface roughness increased to 16 nm and the shape of the grains was the nearest to the hexagonal. At  $200^\circ\text{C}$  nitridation, the 19 nm of mean surface roughness was similar to  $600^\circ\text{C}$  and the grain size reduced to 200 nm. A thicker sample ( $1\mu\text{m}$ ) deposited on a sapphire nitridated at  $200^\circ\text{C}$  showed the typical donor bound excitonic luminescence ( $\text{D}^0\text{X}$ ) transition at 3.47 eV and a line near 3.42 eV. These lines show a FWHM of 20 meV and 30 meV at 13K, respectively. Altogether, only small changes in the characteristics of the films with nitridation temperature were observed.

## Acknowledgments

The authors are thankful to Isabel Cabaço for support in X-ray measurements, to Virginia Chu for the help in profilometric measurements and to Paula Louro in transmission measurements. P.

Sanguino acknowledges support from grant given by Fundação para a Ciência e a Tecnologia (FCT). The work at IST is supported through project PRAXIS/P/FIS/10178/1998 and by the European Union through the COPERNICUS project IC15-CT98-0819

## References

1. S. Nakamura, M. Senoh, N. Iwasa, and S. I. Nagahama, *Appl. Phys. Lett.*, 1995 (13); 67: 1868-1870.
2. S. Nakamura, M. Senoh, S. Nagahama, N. Iwasa, T. Yamada, T. Matsushita, H. Kiyoku and Y. Sugimoto, *Appl. Phys. Lett.*, 1996; 68 (15): 2105-2107.
3. V. Talyansky, R. Vispute, R. Sharma, S. Choopun, M. Downes, T. Venkatesan, Y. X. Li, L. Salamanca-Riba, M. Wood, R. Lareau, K. Jones, *MRS Symp. Proc.* 468 (1997) 99
4. Vispute, H. Wu, J. Narayan, *Appl. Phys. Lett.* 67 (1995) 1549
5. A. Yoshida, K. Ouyang, B. S. Chang, A. Wakahara, *Thin Solid Films* 342-344 (1999) 127
6. M. Cazzanelli, D. Cole, J. Donegan, J. Lunney, P. Middleton, K. O'Donnell, C. Vinegoni, L. Pavesi, *Appl. Phys. Lett.* 73 (1998) 3390
7. P. R. Willmott and F. Antoni, *Appl. Phys. Lett.* 73 (1998) 1394
8. H. Opower, *phys. stat. sol. (a)* 166 (1998) 555.
9. K. Uchida, A. Watanabe, F. Yano, M. Kouguchi, T. Tanaka, and S. Minagawa, *J. Appl. Phys.*, 1995; 79(7): 3487-3491.
10. N. Grandjean, J. Massies, and M. Leroux, *Appl. Phys. Lett.*, 1996 (14); 69: 2071-2073.
11. N. Grandjean, J. Massies, P. Vennéguès, M. Laugt, and M. Leroux, *Appl. Phys. Lett.*, 1996 (5); 70: 643-645.
12. F. Widmann, G. Feuillet, B. Daudin, and J. L. Rouvière, *J. Appl. Phys.*, 1999; 85(3): 1550-1555.
13. G. Namkoong, W. A. Doolittle, A. S. Brown, M. Losurdo, P. Capezzuto, G. Bruno, *J. Appl. Phys.*, 2002; 91(4): 2499-2507.
14. P. Sanguino, S. Koynov, M. Niehus, L. Melo, R. Schwarz, H. Alves, B. K. Meyer, *Mat. Res. Soc. Symp. Proc.*, 2002; 693: 81-86.
15. P. Sanguino, M. Niehus, S. Koynov, R. Schwarz, H. Alves, B. K. Meyer, *Mat. Res. Soc. Symp. Proc.*, 2002; 722: 181-186.
16. A. V. Andrianov, D.E. Lacklison, J.W. Orton, D.J. Dewsnip, S.E. Hooper, C.T. Foxon, *Sem. Sci. Technol.*, 11 (1996) 366.
17. Z.Z. Bandic, T.C. McGill, Z. Ikonic, *Phys. Rev. B* 56 (1997) 3564.
18. C. Stampfl, C.G. Van de Walle, *Phys. Rev. B*, 57 (1998) R15052.
19. G. Salviati, M. Albrecht, C. Zanotti-Fregonara, N. Armani, M. Mayer, Y.G. Shreter, M. Guzzi, Yu. V. Melnik, K. Vassilevski, V. A. Dmitriev, H. P. Strunk, *Phys. Sta. Sol. (a)* 171 (1999) 325.
20. S.T. Kim, Y. J. Lee, S.H. Chung, D.C. Moon, *Sem. Sci. Technol.*, 14 (1999) 156.
21. M. Cazzanelli, D. Cole, J.F. Donegan, J.G. Lunney, P. G. Middleton, K.P. O'Donnell, C. Vinegoni, L. Pavesi, *Appl. Phys. Lett.*, 73 (1998) 3390.
22. X. W. Sun, R. F. Xiao, H. S. Know, *J. Appl. Phys.*, 84 (1998) 5776.

### Study on Chemical Treatment and High Temperature Nitridation of Sapphire for III-Nitride Heteroepitaxial Growth

F. Dwikusuma<sup>1</sup>, D. Saulys<sup>2</sup>, and T. F. Kuech<sup>1</sup>

<sup>1</sup>Department of Chemical Engineering, University of Wisconsin, Madison, WI 53706

<sup>2</sup>Materials Research Science and Engineering Center, University of Wisconsin, Madison, WI 53706

#### ABSTRACT

We have systematically studied the effects of wet chemical etching and high temperature nitridation on the resulting sapphire surface morphology and chemical transformation. The etching of *c*-plane sapphire substrates using H<sub>2</sub>SO<sub>4</sub>, H<sub>3</sub>PO<sub>4</sub>, and a 3:1 H<sub>2</sub>SO<sub>4</sub>:H<sub>3</sub>PO<sub>4</sub> mixture as a function of temperature and etching time was studied and compared with H<sub>2</sub> etching at 1100°C and air-annealing at 1400°C. The surface nitridation using NH<sub>3</sub> and N<sub>2</sub> at 1100°C was studied as a function of NH<sub>3</sub> concentration, nitridation time, and surface pretreatment. Atomic force microscopy and x-ray photoelectron spectroscopy were used to study the surface morphology and chemical composition. The detailed surface morphology after chemical etching was a function of the chemical composition and the specific time and temperatures. The smoothest, pit-free sapphire surface was obtained by etching in pure H<sub>2</sub>SO<sub>4</sub> at 300°C for 30 min. Sulfuric acid etching at higher temperatures or for longer periods generated an insoluble mixture of Al<sub>2</sub>(SO<sub>4</sub>)<sub>3</sub> and Al<sub>2</sub>(SO<sub>4</sub>)<sub>3</sub>·17H<sub>2</sub>O crystalline deposits on the surface. Phosphoric acid and the 3:1 H<sub>2</sub>SO<sub>4</sub>:H<sub>3</sub>PO<sub>4</sub> mixture etched the sapphire preferentially at defect sites and resulted in pits formation on the surface. The high temperature sapphire nitridation resulted in nitrogen incorporation into the surface. The nitrogen content of nitridation layer depends on NH<sub>3</sub> concentration, nitridation time, and surface pretreatment. The nitrogen contents of sapphire treated with H<sub>2</sub>SO<sub>4</sub> and 3:1 H<sub>2</sub>SO<sub>4</sub>:H<sub>3</sub>PO<sub>4</sub> are about the same as the as-received sapphire. While the nitrogen content of the air-annealed sapphire is ~1.6 times higher than the nitrogen content of the as-received sapphire.

#### INTRODUCTION

Sapphire ( $\alpha$ -Al<sub>2</sub>O<sub>3</sub>) has been the most widely used substrate for GaN growth despite of having ~16% lattice-mismatch and ~34% thermal expansion coefficient mismatch with GaN. Prior to GaN growth, the chemical treatment of sapphire has been used to remove residual polishing damages<sup>1</sup> and surface nitridation has been used to improve film nucleation.<sup>2</sup> A routinely employed chemical treatment is etching using a 3:1 H<sub>2</sub>SO<sub>4</sub>:H<sub>3</sub>PO<sub>4</sub> mixture and H<sub>2</sub> at ~1100°C. Another approach to sapphire surface preparation is to anneal the sapphire in air at high temperature ( $\geq 1000^\circ\text{C}$ ).<sup>3</sup> The chemical and physical states of sapphire surface after these chemical treatments have not been studied in detail despite their widespread use.

It is now well established that nitridation of sapphire surface prior to GaN growth can improve the material properties.<sup>2</sup> Although there has been a general consensus on all sapphire nitridation studies that nitrogen was incorporated into the sapphire surface layer, the compound containing nitrogen formed upon nitridation and the surface morphology of the nitridated

sapphire seems to largely depend on the nitrogen source and the nitridation conditions (*i.e.* temperature, pressure, flow rates, and carrier gas).<sup>4,5</sup>

In this study, the treatments of *c*-plane sapphire substrates using H<sub>2</sub>SO<sub>4</sub>, H<sub>3</sub>PO<sub>4</sub>, and a 3:1 H<sub>2</sub>SO<sub>4</sub>:H<sub>3</sub>PO<sub>4</sub> mixture as a function of temperature and etching time were investigated and compared with H<sub>2</sub> etching at 1100°C and air-annealing at 1400°C. The surface nitridation using NH<sub>3</sub> in N<sub>2</sub> carrier gas at 1100°C was studied as a function of NH<sub>3</sub> concentration, nitridation time, and surface pretreatment.

## EXPERIMENTAL PROCEDURE

The as-received sapphire substrates were initially solvent degreased in acetone, methanol, and rinsed in deionized (DI) water before any treatments. The substrates were then immersed in the hot etching solution. Three different etching solutions were studied: 98 wt% H<sub>2</sub>SO<sub>4</sub>, 85 wt% H<sub>3</sub>PO<sub>4</sub>, and a 3:1 by volume mixture of H<sub>2</sub>SO<sub>4</sub>:H<sub>3</sub>PO<sub>4</sub>. The solution was heated to a different temperature up to 400°C. Following the etching, the substrates were rinsed in DI water for 5 min. In H<sub>2</sub> etching study, the substrates were loaded into a vertical reactor heated by a resistance furnace to 1100°C. In the annealing study, the substrates were loaded into a room-temperature furnace, which then heated to 1400°C and held at this temperature for 1 hr.

The nitridation of sapphire was performed in a vertical reactor at 1100°C. Prior to nitridation, the sapphire was heated to 1100°C under N<sub>2</sub> atmosphere for 5 min. Nitridation was carried out by exposing the sapphire to a mixture of NH<sub>3</sub> and N<sub>2</sub> at a total flow rate of 2 slpm and a total pressure of 1 atm. Three NH<sub>3</sub> partial pressures (P<sub>NH<sub>3</sub></sub>) were studied: 0.2, 0.5, and 1 atm. At each P<sub>NH<sub>3</sub></sub> value, the nitridation time was varied from 5 to 30 min. Sapphire with different surface pretreatments were studied: air-annealed, H<sub>2</sub>SO<sub>4</sub> etched, and 3:1 H<sub>2</sub>SO<sub>4</sub>:H<sub>3</sub>PO<sub>4</sub> etched.

After chemical treatment and nitridation, the sapphire surface morphology was characterized using atomic force microscopy (AFM). Double crystal x-ray diffraction (DCXRD) was used to identify the insoluble reaction products after etching in H<sub>2</sub>SO<sub>4</sub> at 400°C. The chemical composition of sapphire surface was examined using an *ex situ* x-ray photoelectron spectroscopy (XPS) with a Mg K<sub>α</sub> line (1253.6 eV) as the x-ray source. The core-level photoemission binding energies were corrected for sample charging using the C 1s binding energy at 284.8 eV for adventitious surface carbon.

## RESULTS AND DISCUSSION

### Sapphire chemical treatments

AFM images of the sapphire surface after being etched in H<sub>3</sub>PO<sub>4</sub>, H<sub>2</sub>SO<sub>4</sub>, and 3:1 mixture of H<sub>2</sub>SO<sub>4</sub>:H<sub>3</sub>PO<sub>4</sub> are shown in Figure 1(a), (b), and (c), respectively. At 100°C, no noted changes in the surface morphology are visible. When the temperature is increased to 200°C, the initial scratches widen. In H<sub>3</sub>PO<sub>4</sub> and 3:1 H<sub>2</sub>SO<sub>4</sub>:H<sub>3</sub>PO<sub>4</sub> etching, small pits start forming along the scratches and the surface becomes slightly rougher. These surface pits become larger as the etching time and temperature increase. Phosphoric acid preferentially etches the *c*-plane sapphire at the high-energy defected regions, which results in formation of surface pits. These defects can originate from either the grown-in bulk dislocation or polishing damage. Most of the surface pits observed after etching at 200°C originate from the initial polishing damages due to the fact that the pits form along the scratches and the surface pit density is much higher than the dislocation

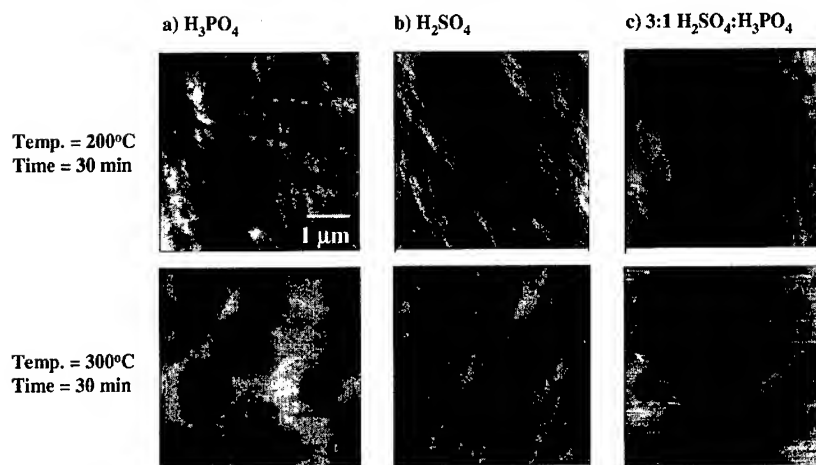


**Figure 1.** AFM images of sapphire surface after etching in a)  $\text{H}_3\text{PO}_4$ , b)  $\text{H}_2\text{SO}_4$ , and c) 3:1  $\text{H}_2\text{SO}_4\text{:H}_3\text{PO}_4$  mixture at different temperatures. The image size is  $5 \times 5 \mu\text{m}^2$  with a z scale of 5 nm.

density of the bulk Czochralski-grown sapphire, which is about  $0.8\text{-}2.0 \times 10^4 \text{ cm}^{-2}$ .<sup>6</sup> Increasing the temperature to  $300^\circ\text{C}$  causes the scratches to further widen until the initial shallow scratches are completely removed. The surface pits observed after etching at  $300^\circ\text{C}$  most likely originate from the grown-in bulk dislocation since most of the scratches are already removed. Over a  $50 \times 50 \mu\text{m}^2$  area scan, the number of surface pits formed by etching in 3:1  $\text{H}_2\text{SO}_4\text{:H}_3\text{PO}_4$  mixture is about 25 times higher than the number of pits formed by etching in  $\text{H}_3\text{PO}_4$  under the same conditions.

In contrast with  $\text{H}_3\text{PO}_4$ ,  $\text{H}_2\text{SO}_4$  does not preferentially etch at defect sites, therefore no pits are observed on the surface. Etching at  $300^\circ\text{C}$  for 30 min is sufficient to remove most of the scratches. At this point,  $\sim 1.16 \mu\text{m}$  thick of sapphire is removed and the surface becomes smoother with a root-mean-square (RMS) roughness of  $\sim 0.3 \text{ nm}$ . When the temperature is increased further to  $400^\circ\text{C}$ , the scratches are completely removed in 10 min. However, when the etching is continued to 30 min at  $400^\circ\text{C}$ , insoluble large crystals appear on the surface, as visible in Figure 2. These crystals are identified using DCXRD as a mixture of polycrystalline aluminum sulfates,  $\text{Al}_2(\text{SO}_4)_3$  and  $\text{Al}_2(\text{SO}_4)_3 \cdot 17\text{H}_2\text{O}$ . Past studies reported that sapphire was covered by insoluble deposits after etching in  $\text{H}_2\text{SO}_4$  at temperature range of  $180$  to  $450^\circ\text{C}$ ; however the etching time was not stated.<sup>1</sup> In our study, the insoluble deposits are not observed after 30 min etching up to  $300^\circ\text{C}$ , which emphasizes the importance of time as a critical process parameter.

AFM images of the sapphire surface after  $\text{H}_2$  etching and air-annealing are shown in Figure 3. After  $\text{H}_2$  etching, the scratches remain on the surface and no surface pits are observed. The surface becomes slightly rougher with a RMS roughness of  $\sim 0.5 \text{ nm}$ . During air-annealing, it is difficult to determine whether the sapphire was partially etched or only recrystallized. The

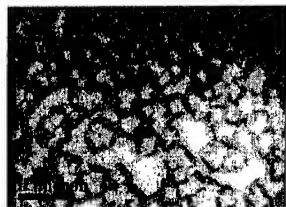


**Figure 2.** Nomarski optical image of sapphire surface after 30 min etching in  $\text{H}_2\text{SO}_4$  at  $400^\circ\text{C}$ .

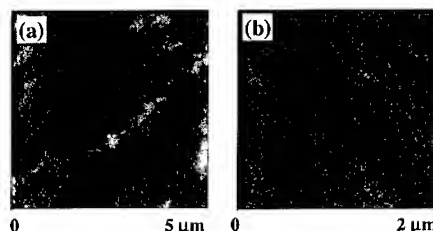


**Figure 3.** AFM images of sapphire surface after: a)  $\text{H}_2$  etching at  $1100^\circ\text{C}$  for 50 min (z scale = 5 nm) and b) air-annealing at  $1400^\circ\text{C}$  for 1 hr (z scale = 2 nm).

atomic steps are developed on the surface with random terrace widths and step heights. The steps originate from wafer cutting misorientation from the (0001) plane. The dimensions of terrace widths and step heights depend on the initial condition of the surface (*e.g.*, degree of misorientation, extent of polishing damage) and the annealing conditions.<sup>8</sup> The surface becomes very smooth with a RMS roughness of  $\sim 0.13$  nm.

The detailed surface morphology after etching depends on the extent and nature of the surface damage. More complete result on chemical etching has been published somewhere else.<sup>9</sup> It is important to realize that the each surface treatment will also change the surface energy of the substrate and hence affect the subsequent nucleation and growth of the epitaxial film.

### **High Temperature Nitridation**

The XPS spectra of sapphire substrates after nitridation contain a distinct N 1s core-level photoelectron peak, indicating that nitrogen was incorporated into the sapphire surface. A typical N 1s photoelectron spectrum from nitridated sapphire surface is seen in Figure 4 along with the N 1s peak from a standard AlN film. Comparison of N 1s peaks from the standard AlN film and the nitridated sapphire clearly shows that the N 1s peak from nitridated sapphire originates from at least two different nitrogen chemical bonding states. The first peak at  $\sim 396.7$  eV is attributed to N-Al bonds since it coincides with the N 1s binding energy from the standard AlN film. The second peak shifts to a higher energy at  $\sim 398.0$  eV indicating that nitrogen is in oxygen rich environment, since O is more electronegative than Al. This peak is due to incomplete substitution of O by N, so that some of the nearest neighboring Al atoms are still bonded to O. In this paper, this peak is labeled as 'N-O'. The exact bonding state of this peak is still not understood. Past XPS study of AlN powders did not attribute this peak to aluminum oxynitride compound since the N 1s binding energy in aluminum oxynitride was reported to occur at  $\sim 6.5$  eV higher than the N-Al peak binding energy.<sup>10</sup> For all surface pretreatments, the N 1s peak is not observed after exposure to only  $\text{N}_2$  at  $1100^\circ\text{C}$  for 30 min. Thus, the incorporated nitrogen in the sapphire surface is caused only by interactions between  $\text{NH}_3$  with sapphire. Also, a previous study reported that a reaction between sapphire and  $\text{N}_2$  only occurred at temperatures greater than  $1200^\circ\text{C}$ .<sup>11</sup>

The N 1s peak intensity as a function of surface pretreatments is shown in Figure 5. The intensity is normalized to Al 2p peak. The nitrogen content of sapphire etched with  $\text{H}_2\text{SO}_4$  and 3:1  $\text{H}_2\text{SO}_4$ : $\text{H}_3\text{PO}_4$  are about the same as the nitrogen content of the as-received sapphire. While

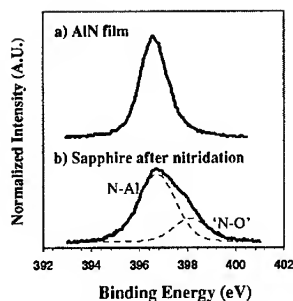


**Figure 4.** XPS spectra of N 1s peak from a) a standard AlN film and b) a sapphire after 30 min nitridation in  $P_{\text{NH}_3}=0.5$  atm.

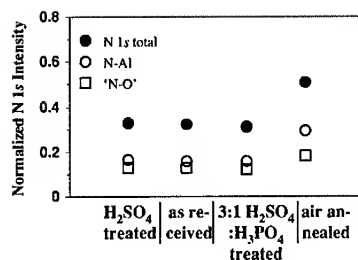


**Figure 5.** Normalized N 1s intensity as a function of substrate pretreatment after 10 min nitridation in  $P_{\text{NH}_3}=0.5$  atm.

the nitrogen content of the air-annealed sapphire is ~1.6 times higher compares to the nitrogen content of the as-received sapphire. The reason for a higher nitrogen content in the air-annealed sapphire is still not understood

Figure 6 shows the N 1s peak intensity as a function of nitridation time and  $P_{\text{NH}_3}$  value. The intensity is normalized to the area of the Al 2p peak. The total nitrogen content of sapphire surface increases with nitridation time, as well as with  $P_{\text{NH}_3}$  value. For each  $P_{\text{NH}_3}$  value, the N-Al content increases with nitridation time, while the 'N-O' content stays about the same. No protrusions are observed on the sapphire surface after up to 60 min nitridation. No significant changes in RMS roughness are observed for all nitridated samples when compare to the as-received sapphire.

## CONCLUSIONS

The effects of chemical treatments and high temperature nitridation of sapphire substrates on the resulting surface morphology and chemical transformation were systematically studied. For chemical etching, temperature and time are the important process parameters that determine the finished surface morphology. A smooth, pit-free surface resulted from wet chemical etching using pure H<sub>2</sub>SO<sub>4</sub> at 300°C for 30 min. Under these conditions, the initial surface scratches were removed without forming surface pits. Etching at higher temperatures or for longer periods generates insoluble Al<sub>2</sub>(SO<sub>4</sub>)<sub>3</sub> and Al<sub>2</sub>(SO<sub>4</sub>)<sub>3</sub>·17H<sub>2</sub>O crystalline deposits on the surface. Phosphoric acid and 3:1 H<sub>2</sub>SO<sub>4</sub>:H<sub>3</sub>PO<sub>4</sub> mixture preferentially etch defects on sapphire surface and results in formation of surface pits. H<sub>2</sub> treatment at 1100°C does not eliminate the surface damage. The air-annealing at 1400°C produces an atomically smooth surface with a terrace-and-step structure. The high temperature sapphire nitridation resulted in nitrogen incorporation into the surface. The total nitrogen content of sapphire surface increases with nitridation time as well as with  $P_{\text{NH}_3}$  value. There is no significant difference in the nitrogen content of sapphire treated with H<sub>2</sub>SO<sub>4</sub> and 3:1 H<sub>2</sub>SO<sub>4</sub>:H<sub>3</sub>PO<sub>4</sub> when compared to the as-received sapphire. The total nitrogen content of the air-annealed sapphire is ~1.6 times higher compares to the as-received sapphire. No protrusions were observed on the sapphire surface after nitridation for up to 60 min.

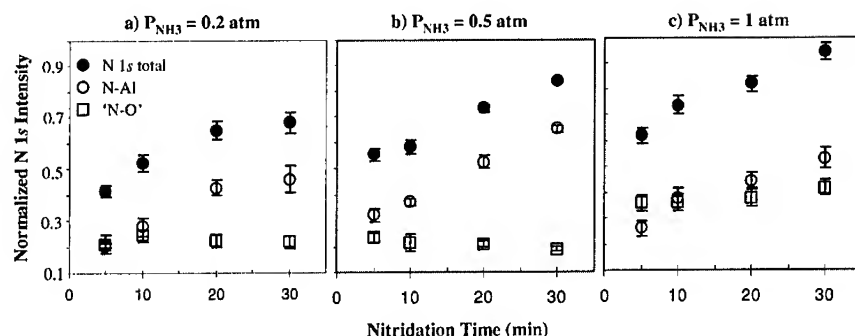


**Figure 6.** Normalized N 1s, N-Al, and N-O peak intensity as a function of nitridation time. The nitridation was carried out using  $P_{\text{NH}_3}$ : a) 0.2 atm, b) 0.5 atm, and c) 1.0 atm.

## ACKNOWLEDGMENTS

The financial support of DARPA is gratefully acknowledged. Additional facilities support was provided by the NSF-funded Materials Research Science and Engineering Center at University of Wisconsin-Madison.

## REFERENCES

1. A. Reisman, M. Berkenblit, J. Cuomo, and S. A. Chan, *J. Electrochem. Soc.* **118**, 1653 (1971).
2. S. Keller, B. P. Kemmer, Y. F. Wu, B. Heyring, D. Kapolnek, J. S. Speck, U. K. Mishra, and S. P. DenBaars, *Appl. Phys. Lett.* **68**, 1525 (1996).
3. J. Cui, A. Sun, M. Reshchikov, F. Yun, A. Baski, and H. Morkoç, *MRS Internet J. Nitride Semicond. Res.* **5**, 7 (2000).
4. T. Hashimoto, Y. Terakoshi, M. Ishida, M. Yuri, O. Imafuji, T. Sugino, A. Yoshikawa, and K. Itoh, *J. Cryst. Growth* **189/190**, 254 (1998).
5. N. Grandjean, J. Massies, Y. Martinez, P. Vennéguès, M. Leroux, and M. Laügt, *J. Cryst. Growth* **179**, 220 (1997).
6. K. Heikkinen, private communication, Saint-Gobain Crystal & Detectors, Washougal, WA (2001).
7. E. A. Soares, M. A. Van Hove, C. F. Walters, and K. F. McCarty, *Phys. Rev. B* **65**, 195405 (2002).
8. J. R. Heffelfinger, M. W. Bench, and C. B. Carter, *Surf. Sci.* **370**, L168 (1997).
9. F. Dwikusuma, D. Saulys, and T. F. Kuech, *J. Electrochem. Soc.* **149**, G603-G608 (2002).
10. C. K. Hwangbo, L. J. Lingg, J. P. Lehan, H. A. Macleod, and F. Suits, *Appl. Opt.* **28**, 2779 (1989).
11. P. M. Dryburgh, *J. Cryst. Growth* **94**, 23 (1989).

### **Ion Beam Study of Early Stages of Growth of GaN films on Sapphire**

Eugen M. Trifan and David C. Ingram

Ohio University, Department of Physics and Astronomy, Athens, OH 45701, U.S.A.

#### **ABSTRACT**

An innovative approach for in-situ characterization has been used in this work to investigate the composition, growth mode, morphology and crystalline ordering of the early stages of growth of GaN films grown on sapphire by MOCVD for substrate temperatures in the range of 450°C to 1050°C. We have performed in-situ characterization by Rutherford Backscattering Spectroscopy (RBS), Ion Channeling, X-ray Photoelectron Spectroscopy (XPS), and Low Energy Electron Diffraction. Ex-situ the films have been characterized by Scanning Electron Microscopy (SEM), X-ray Diffraction (XRD) and thickness profilometry. The films have been grown in an in-house designed and build MOCVD reactor that is attached by UHV lines to the analysis facilities. RBS analysis indicated that the films have the correct stoichiometry, have variable thickness and for low substrate temperature completely cover the substrate while for temperatures 850°C and higher islands are formed that may cover as few as 5 percent of the substrate. From Ion Channeling and LEED we have determined the crystallographic phase to be wurtzite. The crystalline quality increases with higher deposition temperature and with thickness. The films are epitaxially grown with the <0001> crystallographic axis and planes of the GaN films aligned with the sapphire within 0.2 degrees.

#### **INTRODUCTION**

GaN is a useful material in the field of optoelectronic applications [1] and in high frequency, high temperature electronic devices. In order to achieve the level of performance needed for such devices an improvement of the quality of the films is needed. At this time there is no inexpensive substrate with a matched lattice constant and sapphire is one of the most used materials. Lowest reported defect densities are in the mid  $10^7 \text{ cm}^{-2}$  requiring complicated patterning and substrate preparation [2]. MOCVD is the commercial growth method for GaN, but most of the in-situ studies have been concentrating on MBE. We have investigated in-situ the early stages of growth of GaN films by MOCVD using an in-house designed and assembled reactor that is attached via UHV transfer lines to the analysis facilities.

#### **EXPERIMENTAL SETUP**

The experiment has been designed in such a way to be able to do the analysis of the sample without exposing it to air and to maintain the samples in UHV conditions except when growth is occurring. The experimental setup ('W.M. Keck Thin Film Analysis Facility') consists of three chambers, connected together by UHV transfer lines. First chamber is dedicated to the pretreatment of the substrate and the actual growth of the film. The second chamber is connected to the Ohio University accelerator beam line and the third one is equipped for surface analysis

(UPS/XPS/AES) using a Kratos XSAM800 electron spectrometer. The second chamber is equipped with the LEED system and a six axis goniometer used for measurements combining RBS and ion channeling. For RBS analysis we have used 2.2 MeV  $4\text{He}^{++}$  particles from the Tandem Van der Graaf accelerator at Ohio University. The beam has been collimated to better than 0.06 degrees and the spot size is  $2 \times 1$  mm. Typical currents used are 5-20 nA and the integrated charge for RBS analysis was typically 1-50  $\mu\text{C}$ . The RBS measurements were simulated using the program 'RUMP'[3]. Modifications have been performed on the original goniometer sample holder (a ceramic heater has been incorporated.) in order to be able to transfer it in the other two chambers.

A diagram of the MOCVD reactor setup is presented in Figure 1 and consists of a spherical chamber with the sample holder assembly placed at the center, sample transfer system, gas admission and exhaust control system, vacuum pumping system, pressure monitors and ports for temperature measurements.

The control of the admission of the gases in the chamber is achieved by using mass flow controllers (MFCs). For each of the gases used a flow control line has been assembled. These lines are all mounted inside a thermally insulated box that can be heated up to  $150^\circ\text{C}$  for outgasing. Since reaction between gases during transport needs to be prevented, two separate gas lines are used to deliver the precursor gases into the chamber: TMGa carried by hydrogen enters the deposition chamber in a horizontal direction, while a mixture of ammonia and nitrogen enters the reactor chamber at an angle of 45 degrees with respect to the horizontal. Typical flows of the gases used in the experiment are as follows: ammonia 0.5 standard liters per minute (slm), Hydrogen 0.5 slm, TMGa 0.5 standard cubic centimeter (sccm), and Nitrogen 0.5 slm. The ratio of nitrogen to gallium (V/III ratio) delivered in the chamber is a critical deposition parameter and is usually determined empirically for each reactor chamber. The numbers reported in the literature varies widely (500-15000) and they depend on the method used to introduce the TMGa and the geometry of the deposition chamber [4,5]. We have found out that for our system a molar ratio of 1000 produces films with the correct stoichiometry.

We have used TMGa in this experiment with a boiling point of  $55^\circ\text{C}$  and the vapor pressure at  $0^\circ\text{C}$  of 65.4 torr.

The reactor is operating in a viscous flow regime and the total flow of gas through the chamber is of the order of 1.5 l/s, the pressure inside the chamber is kept at 50 torr throughout the entire process and the residence time of the gases is of the order of 2 seconds. The byproducts of the reaction are

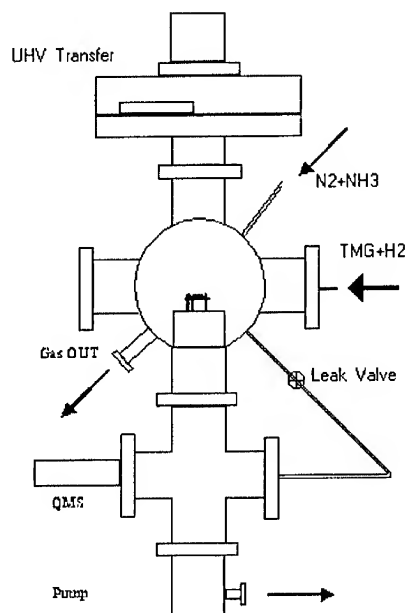


**Figure 1** In-house designed and built MOCVD deposition reactor and auxiliary systems (not to scale)

evacuated through an outlet situated on the lower side of the chamber opposite the input inlets.

The heating of the substrate is critical, in this experiment, to sustain the endothermic reaction that leads to the deposition of gallium and dissociation of ammonia. The temperature of the substrate is regulated by adjusting the power on the ceramic heater incorporated in the sample holder and is measured by optical pyrometry.

We have optimized the deposition parameters by looking at the ion channeling of the samples and their optical transmission. Different gas combinations, gas flow rates, and geometries of the input gases with respect to the sample position have been tried.

Sapphire substrates were degreased in acetone, annealed in air at 1400°C for 30 minutes and loaded into the deposition chamber. Before film growth they were flash heated at 850°C in vacuum and at 1050°C in H<sub>2</sub> and nitridated in ammonia at 850°C for 300 seconds. Films were grown for 100 seconds in similar conditions with the exception of the substrate temperature that was changed in the range 450°C -1050°C. After the sample was cooled down in flowing N<sub>2</sub>, the reactor chamber was pumped down to high vacuum and the sample transferred to the analysis chambers for XPS and LEED followed by RBS/Channeling. After the in-situ analysis the samples were taken-out of the UHV environment and characterized by scanning electron microscopy (SEM) X-Ray diffraction (XRD) and thickness profilometry.

## RESULTS AND DISCUSSION

From RBS we have determined that the films have the correct stoichiometry of GaN and have non-uniform thickness across the surface of the substrate with the maximum thickness in the direction where the gas is introduced in the chamber.

Figure 2 shows the maximum and minimum thickness of the film as a function of growing temperature. For the lowest temperature investigated (450°C) the growth rate is small (0.36 µm/hr), and it rapidly increases and saturates around the value of 20 µm/hr for intermediate temperatures and decreases again to 0.04µm/hr for the highest temperature (1050°C).

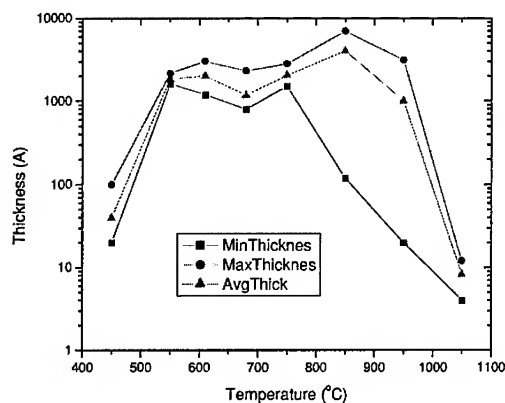


**Figure 2** Maximum, minimum and average thickness of the GaN films vs. temperature of the sapphire substrate

Depicted on the graph is the average thickness computed from 5 points across the samples: 4 at the corners of the substrate and one in the center. Ex-situ we have re-measured the thickness by profilometry and the results are within 10% of the values obtained by RBS assuming the bulk density of GaN.

The films grown in the interval 550°C-750°C have smooth surfaces and have completely covered the substrate. Their thickness varies by a factor of two from approx. 300 nm at the highest point oriented towards gas sources to the minimum situated towards the opposite edge.

At 850°C we have determined from the height of the Ga signal in the RBS spectra that the film is very non-uniform with a 3D structure of islands as high as 700 nm that covers only a fraction of the substrate. From the RUMP simulations of this sample (Figure 3), we have also inferred that the islands are sitting on a continuous layer of GaN with a thickness of about 8 nm  $\pm$  1 nm. This is indicative of a growth of the type layer-by-layer followed by islands growth on top of the initial layers. Optical microscopy shows macroscopic regions of less deposited material sharply delimited by higher deposits. The SEM micrograph (Figure 4) of the same region shows the different coverage density and the estimated average nuclei size is 1  $\mu$ m. The average nuclei separation is 3.5  $\mu$ m that corresponds to a nucleation density of  $8 \times 10^6$  cm<sup>-2</sup>.

At 950°C the film grows by islands and the growth rate is decreased, while at 1050°C we cannot determine the growth mode due to the small thickness of the film.

For all samples we have studied the surface structure using LEED and we have found that no patterns can be obtained for samples grown at 620°C and lower. Diffuse hexagonal patterns are obtained for the substrate temperature 680°C and higher. One complication for this analysis is the extreme charging of the sample which makes the measurement difficult.

Film composition obtained from XPS analysis showed that besides Ga and N we have a small percentage of carbon incorporation in the film and some oxygen contamination on the

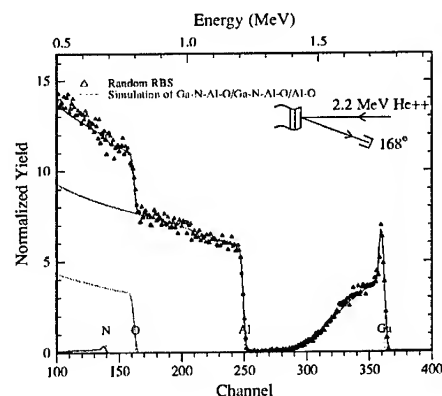


**Figure 3** RBS spectrum of the film grown at 850°C showing incomplete coverage of tall islands on a thin continuous layer



**Figure 4** SEM micrograph of the sample grown at 850°C showing regions with different coverage. Micron size nuclei are visible.

surface for all the samples independent of the growth temperature. Due to their small concentration and low atomic number we have not been able to observe these two elements (O, C) in RBS. The signals coming from the substrate (Al and O) are also visible in XPS for the very thin samples grown at 450°C and 1050°C.

The crystalline quality, symmetry and orientation of the films have been investigated by Ion Channeling. For each sample we have chosen two to three points with different thickness and we have determined the minimum yield from the random and aligned RBS spectra.

For films grown at temperatures 450°C to 620°C no channeling planes and axes have been detected and we measured only marginal decrease in yield when the samples are optically aligned with the ion beam. This is consistent with previous work that shows that at 600°C the films are either amorphous or polycrystalline [6,7].

For temperatures 680°C and higher, directions of crystallographic planes and axis can be determined and the symmetry of the crystal can be inferred. From the hexagonal patterns of the channeling yield we deduced that the wurtzite phase of GaN has been grown. By comparing the RBS signal coming from the substrate (Al) and from the film (Ga) we have also determined that the GaN film is epitaxially grown with the  $\langle 0001 \rangle$  crystallographic axis and planes aligned to the sapphire substrate within  $0.2^\circ$ , which is the step size used in the angular measurements.

The best crystalline quality has been found for the film grown at 950°C (Figure 5) with a minimum yield of approx. 3%, comparable to approx. 1.5% for commercial single crystal substrates. This value is good considering the small thickness of the film (300nm) and the trend that we have observed that the yield is decreasing as the film gets thicker.

The analysis across the samples at points with different thickness shows that the minimum yield decreases with the increased thickness of the film. This is consistent with the fact that defect density decreases with the thickness of the epilayer [7].

X-ray diffraction (XRD) analysis shows only the diffraction peaks specific to wurtzite phase for all samples, the FWHM decreasing with the increase in growth temperature. The wurtzite phase diffraction peaks are present even for samples that exhibit no channeling (450-620°C).

Since channeling planes and the  $\langle 0001 \rangle$  crystallographic axis are only detectable for samples grown at 680°C and higher but XRD shows wurtzite peaks for all samples we conclude that around the above temperature, the films become wurtzite single-crystalline rather than polycrystalline wurtzite with a preferred orientation along the  $\langle 0001 \rangle$  direction.

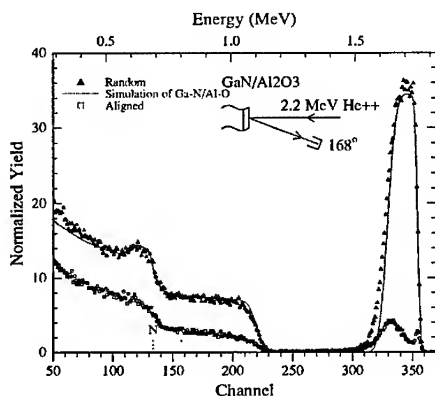


**Figure 5** Random and aligned RBS for the film grown at 950°C. The simulation is for a GaN 290 nm thick on sapphire. The minimum yield is approx. 3%.

## CONCLUSIONS

Thin GaN films were grown by MOCVD in an in-house design and build reactor that is connected by UHV transfer lines to the analysis facilities.

The results show that in the early stages of growth, the crystalline ordering, growth mode and morphology of GaN films are strongly influenced by the substrate temperature and deposition conditions. Similar to other studies [8-10] both two dimensional and two dimensional followed by island growth modes have been observed as a function of the substrate temperature.

RBS/Ion channeling has been used to determine the crystalline quality, symmetry, and orientation of the films. We have determined that at temperatures 680°C and higher the films become single-crystal and are epitaxially aligned with the sapphire substrate. LEED and XRD analysis confirms the wurtzite phase is deposited.

## ACKNOWLEDGEMENTS

Financial support of the W. M. Keck Foundation, the Condensed Matter and Surface Science Program at Ohio University, and the Office of Naval Research through grant #N00014-96-1-0782 is gratefully acknowledged (Contract Monitor Dr. Colin Wood).

## REFERENCES

1. S. Nakamura, T. Mukai M. Senoh, *Appl. Phys. Lett.* **64** 1687 (1994)
2. A. Usui, H. Sunakawa, A. Sakai, A.A. Yamaguchi, *Jap. J. of App. Phys. Part 2 – Lett.* **36**: (7B) L899-L902 1997
3. RUMP (program), Computer Graphic Service, 52 Genung Circle, Ithaca, NY 14850-2042, USA.
4. R. Paskiewicz, R. Korbutowicz, D. Radziewicz, M. Panek, B. Paszkiewicz, J. Kozlowski, B. Boratnyski, M. Tlaczala, S.V. Novikov, *Vacuum* **50** (1-2) pp. 211-214 (1998)
5. S. Fuke, H. Teshigawara, K. Kuwahara, Y. Takano, T. Ito, M. Yanagihara, K. Ohtsuka, *Journal of Applied Physics* **83** (2) 764-767 (1998)
6. O. Briot, J.P. Alexis, M. Tchounkeu, R.L. Aulombard, *Materials Science and Engineering* **B43** 147-153 (1997)
7. X. H. Wu, D. Kapolnek, E. J. Tarsa, B. Heying, S. Keller, B. P. Keller, U. K. Mishra, S. P. DenBaars, J. S. Speck, *Appl. Phys. Lett.*, **68**, 10, 1371-1373 (1996)
8. Z. Sitar, L.L. Smith, R.F. Davis *Journal of Crystal Growth* **141** 11-21 (1994)
9. V. Ramachandran, A. R. Smith, and R. M. Feenstra D. W. Greve *J. Vac. Sci. Technol. A* **17** 4 1289 (1999)
10. N. Grandjean, J. Massies, P. Vennegeues, and M. Leroux, F. Demangeot, M. Renucci, and J. Frandon, *J. Appl. Phys.* **83** (3) 1379 (1998)

**Low Temperature Laser-Assisted Gas Phase Reactivity of TMGa  
with NH<sub>3</sub> and Oxygen-Containing Compounds (H<sub>2</sub>O, CH<sub>3</sub>OH, O(CH<sub>3</sub>)<sub>2</sub>)  
in Constrained Pulsed Expansions**

Alexander Demchuk<sup>1</sup>, Michael Lynch, Steven Simpson and Brent Koplitz  
Department of Chemistry, Tulane University, New Orleans, LA 70118, U.S.A.  
<sup>1</sup>APA Optics, Inc., 2950 NE 84<sup>th</sup> Lane, Blaine, MN 55449, U.S.A.

**ABSTRACT**

The present work reports on the study of III-V gas phase reactivity in constrained gas pulse expansions of trimethylgallium (TMGa) and oxygen derivative compounds (H<sub>2</sub>O, CH<sub>3</sub>OH, O(CH<sub>3</sub>)<sub>2</sub>) with and without ammonia. The precursors are introduced separately into a high vacuum chamber via a multipulsed gas nozzle assembly. The gas mixtures are then exposed to a UV pulse from an ArF excimer laser ( $\lambda=193$  nm) and the products are mass analyzed with a quadrupole mass spectrometer. The efficient laser-assisted growth of Ga-O-containing clusters in the form of [(CH<sub>3</sub>)<sub>2</sub>GaOR]<sub>x</sub>, where R is H or CH<sub>3</sub>, has been revealed. Different behavior can be seen in the reaction of TMG and the oxygen species depending on the presence of H atoms bonded to the oxygen. Significant influence of NH<sub>3</sub> on cluster formation and oxygen incorporation is demonstrated.

**INTRODUCTION**

Previously, we have reported on our efforts to explore low temperature III-V material growth in a gaseous environment by combining UV laser photolysis and the metalorganic chemical vapor deposition (MOCVD) technique using trimethylgallium (or trimethylaluminum) and ammonia as precursors [1-3]. The main gas phase reaction at low temperature in this process is directed by a strong interaction between the metal alkyls and ammonia to form the Lewis acid-base adduct compound (CH<sub>3</sub>)<sub>3</sub>M:NH<sub>3</sub>, where M is Al or Ga [4-8]. Laser irradiation of such gas mixtures with 193-nm photons revealed extensive (CH<sub>3</sub>)<sub>k</sub>M<sub>l</sub>(NH<sub>2</sub>)<sub>m</sub>(NH)<sub>n</sub> cluster formation in the gas phase as a result of photolysis reactions of the precursor and adduct molecules [1-3].

In the current paper, we present recent research the gas phase reactivity of TMGa with the oxygen-containing compounds: H<sub>2</sub>O, CH<sub>3</sub>OH and O(CH<sub>3</sub>)<sub>2</sub>, as well as ammonia. The reaction of TMGa with these oxygen compounds, especially H<sub>2</sub>O, can be used to study MOCVD side reactions, as water is a main impurity in commercial ammonia and could thus be a primary source for the oxygen found in nitride films.

**EXPERIMENTAL**

The experimental apparatus consists of a high vacuum chamber equipped with a quadrupole mass spectrometer (QMS) and a specialized pulsed nozzle source that is described elsewhere [1,2]. The TMGa ((CH<sub>3</sub>)<sub>3</sub>Ga), ammonia (NH<sub>3</sub>), and oxygen compounds [water (H<sub>2</sub>O), methanol (CH<sub>3</sub>OH), and dimethylether (O(CH<sub>3</sub>)<sub>2</sub>)] are introduced into the high vacuum chamber via the nozzle assembly. TMGa is used with Ar as the carrier gas. The water and methanol (liquid in normal conditions) are heated to 100 °C and 60 °C, respectively, and introduced into the mixing

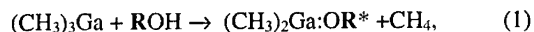
region under their own vapor pressures. Pulsed flows of each sample gas (TMGa, oxygen compound, and/or NH<sub>3</sub>) are simultaneously and independently injected into the mixing/reaction region of the nozzle assembly. The opening time of each pulsed valve was adjusted to be ~0.2-0.3 ms with repetition rates of 10 Hz. The 193 nm output from an ArF excimer laser (Lambda Physik LEXtra 200, 23 ns pulse duration) with 10 mJ pulse energy is focused into the mixing/reaction region of the nozzle. The delay time between the sample injections and the laser pulse was typically ~5 ms. The reaction products are mass analyzed by an Extrel MEXM2000 QMS with a crossbeam electron impact (EI) ionizer. The deuterated ammonia (ND<sub>3</sub>) was used in order to label the products and distinguish different reaction pathways.

## RESULTS AND DISCUSSION

### Reactivity of TMGa with O(CH<sub>3</sub>)<sub>2</sub>, CH<sub>3</sub>OH and H<sub>2</sub>O in the absence/presence of photons

Figure 1a represents the mass spectrum resulting from the reaction of TMGa with O(CH<sub>3</sub>)<sub>2</sub> in the absence of photons. This spectrum reveals a set of peaks at mass 145/147 that correspond to the (CH<sub>3</sub>)<sub>3</sub>Ga:O(CH<sub>3</sub>)<sub>2</sub><sup>+</sup> adduct parent signal. In contrast, the mass spectrum resulting from the reaction of TMGa with CH<sub>3</sub>OH shows the formation of not only monomer adduct species, but also [(CH<sub>3</sub>)<sub>2</sub>GaO(CH<sub>3</sub>)<sub>2</sub>]<sub>2</sub> dimer and [(CH<sub>3</sub>)<sub>2</sub>GaO(CH<sub>3</sub>)<sub>2</sub>]<sub>3</sub> trimer cluster products (see Fig. 2a). Note in order to show only those species that arrive at the detector as a result of this reactivity, the TMGa spectrum has been subtracted from the TMGa/CH<sub>3</sub>OH spectrum. The spectrum resulting from the reaction of TMGa with H<sub>2</sub>O shows the primary product to be the [(CH<sub>3</sub>)<sub>2</sub>Ga(OH)]<sub>3</sub> trimer (see Fig. 3a). The predominant ion signal in this spectrum is found at 333/335/337 amu. This corresponds to the (CH<sub>3</sub>)<sub>5</sub>Ga<sub>3</sub>(OH)<sub>3</sub><sup>+</sup> ion, which represents [(CH<sub>3</sub>)<sub>2</sub>Ga(OH)]<sub>3</sub> trimer products with the loss of CH<sub>3</sub> due to EI fragmentation. Also a strong signal at 315/317/319 amu indicates the loss of H<sub>2</sub>O from (CH<sub>3</sub>)<sub>5</sub>Ga<sub>3</sub>(OH)<sub>3</sub><sup>+</sup> as a daughter ion fragmentation route during EI ionization.

The fact that the reaction of TMGa with methanol and water results in dimer and trimer formation, as opposed to simple coordination compounds such as dimethylether does is not surprising. It is a similar type of Lewis acid-base relationship that is the basis for the bonding between many oxygen-containing species and metal alkyls. Coordination of oxygen-containing compounds to group III alkyls is facilitated through the donor properties of oxygen and the acceptor properties of the metal alkyl [4,9]. It has been shown that compounds such as methanol and water that contain hydrogen atom(s) bonded to a donor atom (oxygen in this case), when reacted with TMGa, can eliminate methane to form more stable cluster products [9,10]. In this case, the following reaction would take place:



where **R** is H or CH<sub>3</sub> and “\*” indicates a radical.

Laser irradiation of the expanding gas mixtures results in extensive cluster formation when dimethylether and methanol are used. Figure 1b represents the mass spectrum from the reaction of TMGa/O(CH<sub>3</sub>)<sub>2</sub> under UV laser influence. As shown above, the spectrum obtained without laser radiation shows only evidence of the 1:1 (CH<sub>3</sub>)<sub>3</sub>Ga:O(CH<sub>3</sub>)<sub>2</sub> adduct product. With the 193

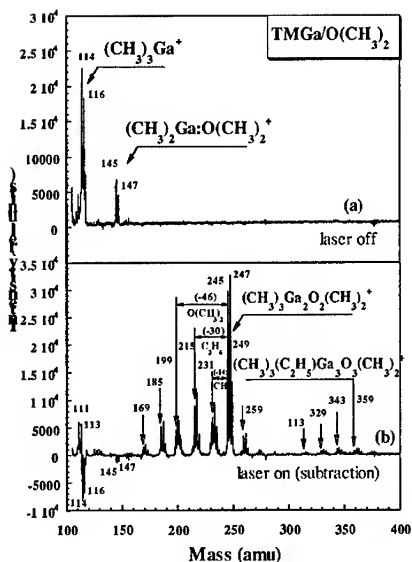


**Figure 1.** Mass spectra of TMGa/O(CH<sub>3</sub>)<sub>2</sub> expansions (a) without and (b) with laser excitation.

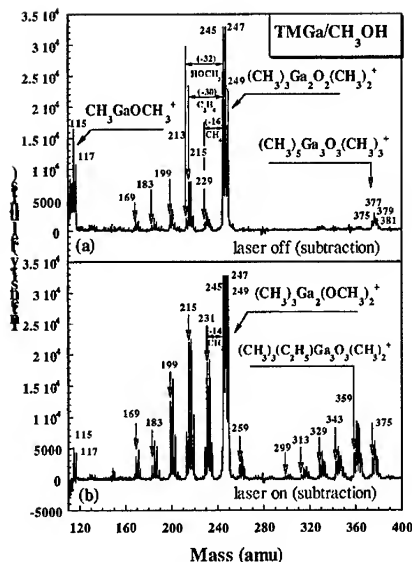


**Figure 2.** Mass spectra of TMGa/CH<sub>3</sub>OH expansions (a) without and (b) with laser excitation.

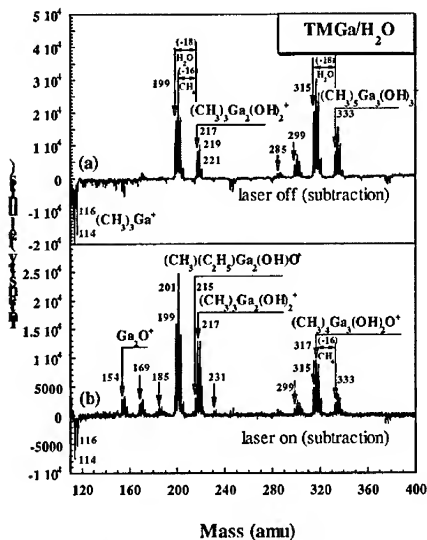


**Figure 3.** Mass spectra of TMGa/H<sub>2</sub>O expansions (a) without and (b) with laser excitation.

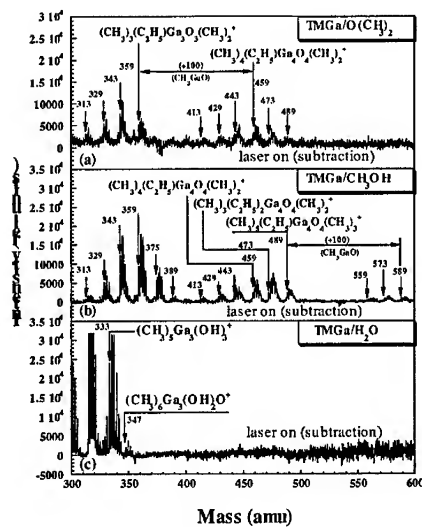


**Figure 4.** Mass spectra of (a) TMGa/O(CH<sub>3</sub>)<sub>2</sub> and (b) TMGa/CH<sub>3</sub>OH and (c) TMGa/H<sub>2</sub>O expansions with laser excitation.

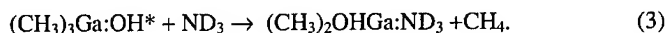
nm laser pulse, however, there is significant evidence of larger aggregations of atoms. In the observed spectrum one sees peaks that can be attributed to dimeric  $[(CH_3)_2GaO(CH_3)]_2$  and trimeric  $[(CH_3)_2GaO(CH_3)]_3$  species. The most intense peak in the spectrum corresponds to the dimeric product, the  $(CH_3)_3Ga_2O_2(CH_3)_2^+$  ion, which could result from the loss of  $CH_3$  from the parent dimer  $[(CH_3)_2GaO(CH_3)]_2$ , or it could be a fragment from a higher mass cluster.

Figure 2b shows the mass spectrum obtained when TMGa/ $CH_3OH$  is introduced into the reaction chamber with a laser pulse. Note the reported spectrum was obtained after subtraction of the spectrum taken in the absence of laser radiation accordingly. It is evident that the laser pulse enhances the cluster formation. Studies at higher mass also revealed the formation tetramer and pentamer clusters such as  $[(CH_3)_2GaO(CH_3)]_x$ , where  $x \leq 5$  for TMGa/ $O(CH_3)_2$  and TMGa/ $CH_3OH$  combinations, but not for the TMGa/ $H_2O$  (see Fig. 4). During laser enhanced TMGa/ $H_2O$  gas expansions, clusters of mass no higher than trimeric species have been found and reactions appear to shift to different Ga-O-containing species (see Fig. 3b).

#### **Reactivity of TMG with $NH_3$ and $O(CH_3)_2$ , $CH_3OH$ , $H_2O$ in the absence/presence of photons**

The mass spectra of the triple pulsed TMGa/ $NH_3/O(CH_3)_2$  gas expansions without laser excitation revealed the formation monomer adducts involving ammonia  $[(CH_3)_3Ga:NH_3]$  as well as with dimethylether  $[(CH_3)_3Ga:O(CH_3)_2]$  (see Fig. 5a). During laser irradiation of these gases, a mixture of Ga-O-N-containing clusters are created (see Fig. 5b). Comparison of the spectrum obtained only with the TMGa/ $O(CH_3)_2$  dual gas pulse expansion (see Fig. 1b) shows that the intensity of Ga-O-containing clusters, for example at mass 245/247/249 amu (Fig. 5b), is significantly reduced. With increasing ammonia pressure, the intensity of the  $(CH_3)_3Ga_2O(CH_3)_2^+$  ion at mass 245/247/249 amu sharply decreases to zero (see Fig. 6). At the same time, a significant increase in the intensity of  $(CH_3)_3Ga_2(NH_2)_2^+$  ion at mass 215/217/219 amu is observed (see Fig. 6) due to ammonia reactivity [2,11]. The mixture of Ga-O-N-containing clusters are noted at mass 230/232/234 amu and can be represented by the cluster ion  $(CH_3)_3Ga_2(NH_2)OCH_3^+$  (see Fig. 5b).

The triple pulsed TMGa/ $NH_3/H_2O$  gas expansion revealed cluster formation without any laser irradiation (see Fig. 7a). It is important to note that the presence of  $NH_3$  reduces the intensity of Ga-O-containing clusters, as is evidenced by the negative peaks in the Ga-O-cluster region of figure 7b. Note, figure 7b shows the mass spectrum in subtraction mode with the TMGa/ $H_2O$  gas expansion spectrum subtracted from the TMGa/ $NH_3/H_2O$  spectrum. Another feature of this spectrum is the emergence of the  $(CH_3)_2Ga:NH_3^+$  ion signal, indicating the interaction of the ammonia with the TMGa. Moreover, by using  $ND_3$ , the formation of cluster mixtures such as  $[(CH_3)_2GaND_2]_x[(CH_3)_2GaOH]_y$ , where  $x = 1, 2$  and  $y = 1, 2$ , have been noted (see Fig. 8). However, the most interesting signal in this spectrum can be seen at mass 117/119 amu. This particular signal can be represented by the  $(CH_3)_2GaND_2^+$  ion (Fig. 8). By comparing the different subtraction spectra (TMGa/ $NH_3/H_2O$  minus TMGa/ $ND_3$  vs. TMGa/ $NH_3/H_2O$  minus TMGa/ $H_2O$ ), one can see that this signal appears only when all three of the gas precursors have been mixed. The most reasonable explanation for such TMGa and  $H_2O$  reactivity in the presence of  $NH_3$  is that ammonia interrupts the pathway for formation of Ga-O-clusters, equation (2), by forming a new stable adduct as follows:



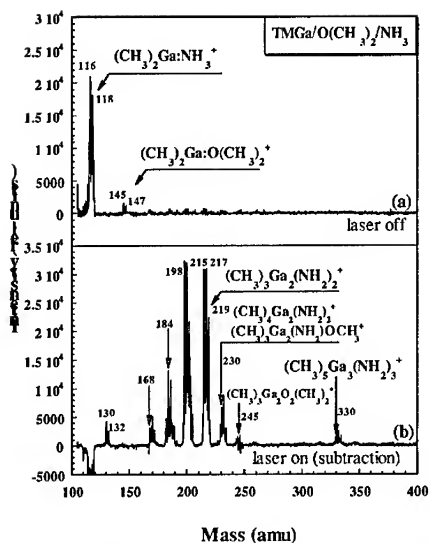


**Figure 5.** Mass spectra of  $\text{TMGa}/\text{O}(\text{CH}_3)_2/\text{NH}_3$  expansions (a) without and (b) with laser excitation.

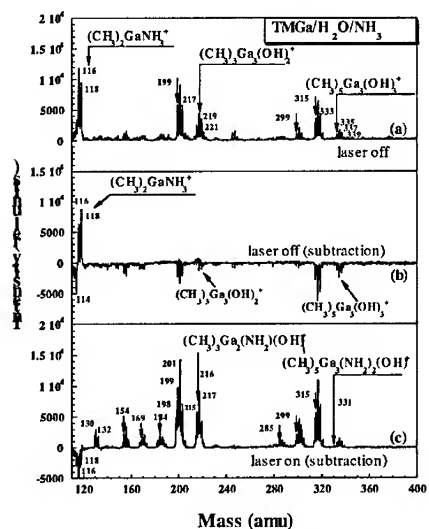


**Figure 7.** Mass spectra of  $\text{TMGa}/\text{H}_2\text{O}/\text{NH}_3$  expansions (a) and (b) without and (b) with laser excitation.

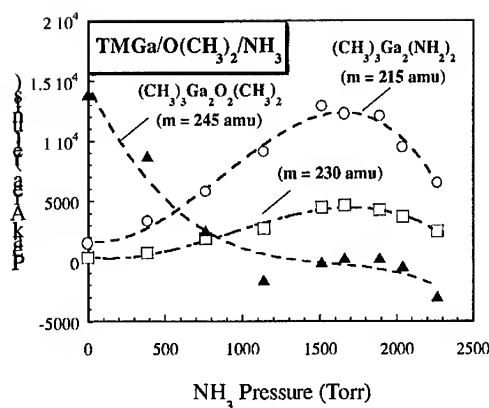


**Figure 6.** Peak area of ion mass 215 amu, ion mass 230 amu and ion mass 245 amu as a function of ammonia sample pressure ( $\text{TMGa}/\text{O}(\text{CH}_3)_2/\text{NH}_3$  expansions with laser excitation).

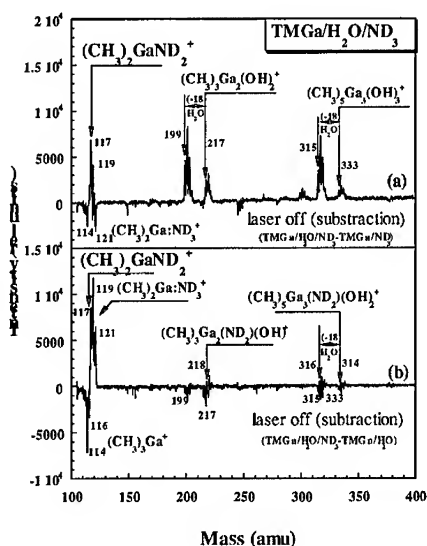


**Figure 8.** Mass spectra of  $\text{TMGa}/\text{H}_2\text{O}/\text{ND}_3$  expansions without laser excitation.

The EI ionization of this  $(\text{CH}_3)_2\text{OHGa}:\text{ND}_3$  adduct results in  $(\text{CH}_3)_2\text{GaND}_2^+$  ion formation with the loss of water (HOD). Note, similar fragmentation patterns (release of water) have been seen through all mass spectra from TMGa/H<sub>2</sub>O or TMGa/H<sub>2</sub>O/NH<sub>3</sub> expansions (see Fig. 3 and Fig. 8).

Laser irradiation of this gas mixture results in the formation of Ga-O-N-mixtures of clusters similar to those shown above, also with a reduction of Ga-O-clustering (see Fig. 7c). Such chemistry may play a role in reducing oxygen incorporation in the gas phase.

## CONCLUSIONS

Extensive cluster formation in the gas phase during the mixing of trimethylgallium and oxygen compounds (H<sub>2</sub>O, CH<sub>3</sub>OH, O(CH<sub>3</sub>)<sub>2</sub>) has been observed. Laser irradiation of these gas mixtures enhances cluster growth in the gas phase in the form of  $[(\text{CH}_3)_2\text{GaOR}]_x$ , where R is H or CH<sub>3</sub>. A significant influence of the presence of ammonia on cluster formation and oxygen incorporation has been identified. Further characterization is still needed in order to understand all reaction mechanisms involved in this photoinduced chemistry.

## ACKNOWLEDGMENTS

Financial support from the Department of Energy, NASA, the State of Louisiana via the Louisiana Education Quality Support Fund, and the National Science Foundation through Tulane University's Center for Photoinduced Processes is very much appreciated. An equipment denotation from AT&T/Lucent is also gratefully noted.

## REFERENCES

1. A. Demchuk, J. Porter, A. Beuscher, A. Dilkey, and B. Koplitz, *Chem. Phys. Lett.* 283, 231 (1998).
2. A. Demchuk, J. Porter, and B. Koplitz, *J. Phys. Chem. A* 102, 8841 (1998).
3. A. Demchuk, S. Simpson and B. Koplitz in *Fundamental Gas-Phase and Surface Chemistry of Vapor-Phase Deposition II*, edited by M.T. Swihart, M.D. Allendorf, and M. Meyyappan, (Electrochem. Soc. Proc. 2001-13, Pennington, NJ, 2001) pp. 389-396.
4. G. E. Coates, *J. Chem. Soc.* 2003, 1951.
5. A. Zaouk, E. Salvétat, J. Sakaya, F. Maury, and G. Constant, *J. Crystal Growth.* 55, 135 (1981).
6. R. H. Moss, *J. Crystal Growth* 68, 78 (1984).
7. M. J. Almond, M. G. B. Drew, C. E. Jenkins, and D. A. Rice *J. Chem. Soc. Dalton Trans.* 1, 5 (1992).
8. R. M. Watwe, J. A. Dumesic, T. F. Kuech, *J. Cryst. Growth.* 221, 751 (2000).
9. J. S. Thayer, *Organometallic Chemistry*, (VCH Publisher, Inc: New York, 1988) pp.31-38.
10. U. Bergman, V. Reimer, and B. Atakan, *Phys. Stat. Sol. (a)* 176, 719 (1999).
11. A. Demchuk, J. Cahill, S. Simpson and B. Koplitz, *Chem. Phys. Lett.* 348, 217 (2001).

### High-Mobility Ga-Polarity GaN achieved by NH<sub>3</sub>-MBE

J. X. Wang, X. L. Wang, D. Z. Sun, J. M. Li, Y. P. Zeng, G. X. Hu, H. X. Liu, L. Y. Lin  
Materials Center, Institute of Semiconductors, Chinese Academy of Sciences,  
P. O. Box 912, Beijing 100083, People's Republic of China

#### ABSTRACT

GaN epilayers were grown on (0001) sapphire substrates by NH<sub>3</sub>-MBE and RF-MBE (radio frequency plasma). The polarities of the epilayers were investigated by *in-situ* RHEED, chemical solution etching and AFM surface examination. By using a RF-MBE grown GaN layer as template to deposit GaN epilayer by NH<sub>3</sub>-MBE method, we found that not only Ga-polarity GaN films were repeatedly obtained, but also the electron mobility of these Ga-polarity films was significantly improved with a best value of 290 cm<sup>2</sup>/V.s at room temperature. Experimental results show it is an easy and stable way for growth of high quality Ga-polarity GaN films.

#### INTRODUCTION

III-Nitrides have been studied intensively in recent years because of their excellent properties for potential applications in optical and electronic devices [1-3]. Many important characters of the materials were explored by researchers to improve the quality of the material and further more the performance of the device. Among these characters, the polarity of GaN epilayer has become a hot topic due to its crucial influence on both materials and devices [4-6].

Since the first paper about the polarity of GaN was reported by Sasaki and Matsuoka [7], subsequent research results clearly show its huge effects on surface morphology[8], RHEED pattern[9-10], selectivity of chemical reagent[11-12], material electrical and optical properties, and two-dimensional electron gas (2DEG) sheet density and mobility of AlGaIn/GaN heterostructure. Generally speaking, Ga-polarity or Ga-face epilayer has distinct differences with N-polarity one. For example, Surface of Ga-polarity epilayer is usually much smoother than that of N-polarity epilayer as observed by atomic force microscope (AFM) [8]. With *in situ* RHEED, a 2×2 pattern was usually appeared indicating a Ga-polarity during growth interruption or at a substrate temperature below 400°C after growth. However, a N-polarity only showed 1×1 or 1×3 RHEED patterns during this period[9-10]. Additionally, Seelmann-Eggebert *et al*[13] found that GaN films having N-polarity were etched in a solution of KOH while films having Ga-polarity were resistant to etching in the same solution. So, it was easy to distinguish the polarity of GaN epilayer by etching. Excepting above methods, some other important techniques were used to clarify polarity such as coaxial impact collision ion scattering spectroscopy[14-15], converged beam electron diffraction (CBED)[16], x-ray photoemission spectroscopy[7], hot (160 °C) H<sub>3</sub>PO<sub>4</sub> solution[17], and hemispherically scanned x-ray photoelectron diffraction (HSXPD)[13].

Between two polarities of GaN layer, Ga-polarity is desired for both material growth and device fabrication because it has better properties than N-polarity. It has been proven that

N-polarity will deteriorate the performance of HEMT device by degrading the 2DEG properties in active layer. But with molecular beam epitaxy (MBE), which is an important technique to precisely deposit device structures, the polarity control of the GaN film is still an unresolved problem and a hot researching subject currently. Moreover, the low mobility of the GaN films remains to be improved. These factors have hindered the development of GaN based devices. Some researcher already developed the skills like changing growth rate[17], buffer layer, V/III ratio *et al* to control the polarity of GaN. In this letter, we investigated the polarity of GaN films grown by NH<sub>3</sub>-MBE and RF-MBE on (0001) sapphire substrates. We found that the polarity of GaN films grown by NH<sub>3</sub>-MBE is difficult to be controlled, strongly depending on the growth rate[17], buffer layer *et al*, however, using a RF-MBE grown GaN layer on (0001) sapphire as template, Ga-polarity GaN films can be repeatedly realized by NH<sub>3</sub>-MBE. Additionally, the electron mobility of this Ga-polarity film was significantly improved with a best value of 290 cm<sup>2</sup>/V.s at room temperature. This value can be comparable with that of best GaN grown by MBE [18-19].

## EXPERIMENTS

The GaN samples were grown using a home-made MBE system with two growth chambers equipped with *in situ* RHEED. One growth chamber was designed for NH<sub>3</sub>-MBE using ammonia as N source and the other was for RF-MBE using radio frequency activated N as N source. Conventional Knudsen effusion cells charged with 7N-grade Ga and Al was employed as Ga and Al source in both MBE chambers. Two growth chambers are connected by an ultrahigh vacuum chamber so that the grown samples can move from one growth chamber to another without exposing to air. This system can ensure the grown RF-MBE GaN template out of contamination.

Three different groups of GaN epilayers were grown and their polarities were investigated (see table I). Group I samples were grown by NH<sub>3</sub>-MBE, group II samples were grown by RF-MBE and group III samples were grown by NH<sub>3</sub>-MBE using RF-MBE template.

Prior to growth of the three groups of GaN films, the (0001) sapphire substrates were outgassed for one hour at 300°C~500°C in the preparation chamber of the MBE system and then nitridated using ammonia in NH<sub>3</sub>-MBE growth chamber. The growth of group I samples was performed using NH<sub>3</sub>-MBE. After a low temperature of 600°C AlN buffer was deposited on the nitridated sapphire substrate, the GaN epilayer was grown at a high temperature of 730°C. During growth interruption, a 1×1 RHEED pattern was typically observed. The group II samples was grown by RF-MBE except the nitridation of the sapphire substrate which were performed in NH<sub>3</sub>-MBE growth chamber. A high temperature of 750°C AlN buffer layer was deposited followed by a GaN layer at the same temperature. A 2×2 RHEED pattern was usually observed when the substrate temperature decreased below 400°C. For the group III samples, the growth was carried out on in NH<sub>3</sub>-MBE growth chamber using a RF-MBE GaN template. The RF-MBE template was a typical group II sample with a GaN epilayer of different thickness from 0.5 μm to 1 μm. Observed RHEED pattern was identical with that of group II sample. For all three group samples, the GaN epilayers were about 1 μm thick.

**Table I.** Experimental results of three groups samples.

Group	I	II	III
Growth technique	NH <sub>3</sub> -MBE	RF-MBE	NH <sub>3</sub> -MBE
Buffer	LT AlN	HT AlN	RF-MBE GaN template
Etching result in KOH solution	Dissolvable	Resistant	Resistant
RMS (nm)	15	2	5.8 6.5
Mobility (cm <sup>2</sup> /V.s)	84 94	150 220	259 290
Polarity	N-polarity	Ga-polarity	Ga-polarity

Polarity identification was performed by *in situ* RHEED observation, chemical solution etching and AFM surface examination. KOH aqueous solution with concentration of 1:1 was used as etchant to dissolve GaN epilayer at room temperature. After one hour etching, samples were pick up and rinsed in DI water for further characterization. Surface morphology of as-grown and etched film was investigated by Olympus microscope and contacting-mode Digital Instrument Nanoscope IIIa AFM equipment. The electronic properties of these films were obtained by Hall measurements using the Van de Pauw configuration.

## RESULTS AND DISCUSSIONS

*In situ* RHEED observation firstly helps us to identify the polarity of the three group films. Based on above literatures[9-10], 1×1 RHEED pattern indicated N-polarity and 2×2 RHEED pattern indicated Ga-polarity. We preliminarily conclude that group I samples were of N-polarity and group II, III were of Ga-polarity.

Chemical etching was employed to confirm the polarity of the grown samples. We observed that group I films were easily dissolved in the KOH etchant and the surface of the etched films became very dim when seen with bare eyes. The surface of the films was too rough to be examined by AFM. These results showed that these films were of N-polarity. For group II films, no obvious differences can be found between before and after etching using bare eyes, optical microscope and AFM observation. We believed that these films had Ga-polarity and that the main reason of the formation of the Ga-polarity films was the employment of a high temperature AlN nucleation buffer. These results agree with the conclusion made by former researchers [20-21]. Chemical etching results for group III samples were the same as those of group II films, which indicates that the polarity of the GaN layer grown by NH<sub>3</sub>-MBE on

RF-MBE GaN template was also Ga-polarity.

AFM examination further confirmed the experimental results made by etching and RHEED patterns. For convenience to compare, all AFM images had same  $5\ \mu\text{m} \times 5\ \mu\text{m}$  dimensions. Figure 1 shows a typical surface morphology of Group I films. The surface is rough with a RMS (root mean square) of 15 nm. Figure 2 shows a typical surface morphology of Group II films. The surface is smooth with a RMS of 2 nm. Obviously, the surface of Ga-polarity film was much smoother than that of N-polarity film. Figure 3a, Figure 3b are the contrastive AFM images of a typical group III film before and after etching, we can find that there is no obvious difference in surface morphologies with a RMS of 5.8 nm and 6.5 nm respectively. The resistibility to the etchant of the films indicated that Ga-polarity films were produced.

The mobility of the grown GaN films was list in table I. It can be seen that Ga-polarity films have higher mobility than N-polarity ones. The highest value of  $290\ \text{cm}^2/\text{V.s}$  was achieved in group III films, which showed that employment of RF-MBE template would significantly improve the electron mobility of GaN films by  $\text{NH}_3$ -MBE.

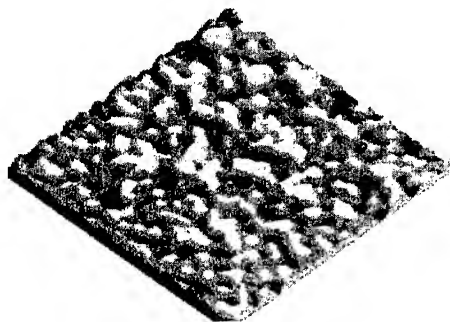


**Figure 1.** A typical  $5\ \mu\text{m} \times 5\ \mu\text{m}$  AFM image of the surface morphology for group I films grown by  $\text{NH}_3$ -MBE. Its surface is rough with a RMS of 15 nm. It is believed to be N-polarity.

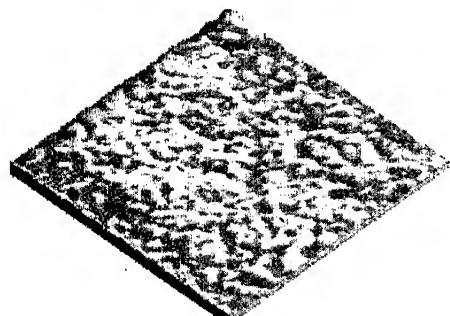


**Figure 2.** A typical  $5\ \mu\text{m} \times 5\ \mu\text{m}$  AFM image of the surface morphology for group II films grown by RF-MBE. Its surface is smooth with a RMS of 2 nm. It is believed to be Ga-polarity.

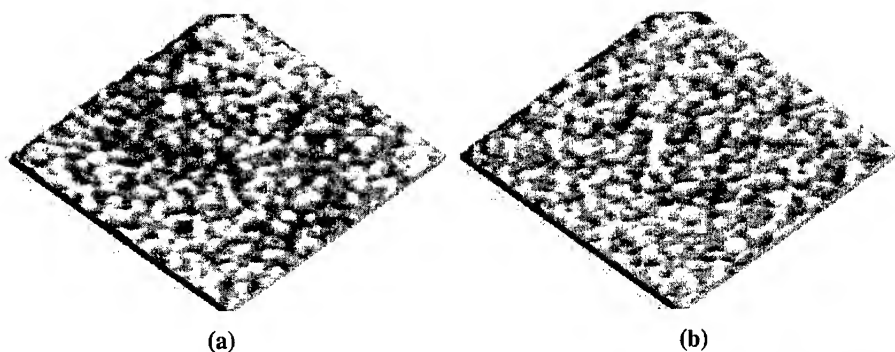


**Figure 3.** The typical  $5\ \mu\text{m} \times 5\ \mu\text{m}$  AFM image of group III films grown by  $\text{NH}_3$ -MBE on RF-MBE GaN template (a) before and (b) after etching. The RMS of the surface is 5.8 nm and 6.5 nm respectively, which shows that the film is resistant to etchant therefore it is believed to be Ga-polarity.

As mentioned above, group I films have N-polarity with low mobility. It is well known that the buffer layer plays a very important role for the growth of high quality GaN. Poor quality of nucleation layer was the main reason of the poor qualities of group I samples. For group II films, employment of a high temperature AlN buffer by RF-MBE method was proven by us and former researchers[20-21] an efficient way to achieve Ga-polarity and smooth surface. The mobility of the films was correspondingly increased indicating the improved material quality. As for group III films which have Ga-polarity and the highest mobility. RF-MBE grown GaN template provided a good Ga-face substrate to subsequent growth of Ga-polarity GaN film. Moreover, growing GaN using  $\text{NH}_3$  as N source can obtain higher growth rates and reduce ion damage that leads to deep levels and semi-insulating electrical properties. As a result, the electron mobility is further improved to  $290\ \text{cm}^2/\text{V.s}$ . Our experimental results show it is an easy and stable way for growth of high quality Ga-polarity GaN films.

## CONCLUSIONS

In conclusion, Ga-polarity GaN was achieved by  $\text{NH}_3$ -MBE on (0001) sapphire substrate using a RF-MBE grown GaN as template. As a result, not only the polarity of GaN film was successfully controlled, but also the electron mobility of this Ga-polarity film was significantly improved with a best value at room temperature reached  $290\ \text{cm}^2/\text{V.s}$ .

## ACKNOWLEDGEMENTS

The author would like to acknowledge Dr. Li Hui for AFM examination. This work was supported by National Natural Science Foundation and Special Funds for Major State Basic Research Project G20000683.

## REFERENCES

- [1] S. Strite, H. Morkoc, J. Vac. Sci. & Technol. **B10**,1237 (1992) .
- [2] S. Nakamura, M. Senoh, N. Iwasa, S. Nagahama, T. Yamada, T. Mukai, Jpn. J. Appl. Phys. **34** ,L1332 (1995)
- [3] S. Nakamura, M. Senoh, S. Nagahama, N. Iwasa, T. Yamada, T. Matsushita, Y. Sugimoto, H. Kiyoku, Appl. Phys. Lett. **70**, 2753 (1997)
- [4] E. S. Hellman, MRS Internet J. Nitride Semicond. Res. **3**, 11(1998)
- [5] F. Bernardini, V. Fiorentini, D. Vanderbilt, Phys. Rev. B **56**, R10024 (1997)
- [6] O. Aktas, Z. F. Fan, A. Botchkarev, S. N. Mohammad, M. roth, T. Jenkins, L. Kehias, H. Morkoc, IEEE Electron Dev. Lett. **18**, 293 (1997)
- [7] T. Sasaki T. Matsuoka, J. Appl. Phys. **64**, 4531 (1998)
- [8] J. L. Weyher, S. Muller, I. Grzegory, S. Porowski, J. Cryst. Growth **17-22**, 182 (1997)
- [9] A. R. Smith, R. M. Feenstra, D. W. Greve, M. S. Shin, M. Skowronski, J. Neugebauer, J. E. Northrup, Appl. Phys. Lett. **72**, 2114 (1998)
- [10] A. R. Smith, R. M. Feenstra, D. W. Greve, M. S. Shin, M. Skowronski, J. Neugebauer, J. E. Northrup, J. Vac. Sci. Technol. B **16**, 2242 (1998)
- [11] J. L. Rouviere, J. L. Weyher, M. Seelmann-Eggebert, S. Porowski, Appl. Phys. Lett. **73**, 668 (1998)
- [12] X. Q. Shen, T. Ide, S. H. Cho, M. Shimizu, S. Hara, H. Okumura, J. Appl. Phys. **77**, 4013 (2000)
- [13] M. Seelmann-Eggebert, J. L. Weyher, H. Obloh, H. Zimmermann, A. Rar, S. Porowski, Appl. Phys. Lett. **71**, 2635 (1997)
- [14] S. Sonoda, S. Shimizu, Y. Suzuki, K. Balakrishnan, J. Shirakashi, H. Okumura, T. Nishihara, M. Shinohara, Jpn. J. Appl. Phys. **38**, L1219 (1999)
- [15] T. Ohnishi, A. Ohtomo, M. Kawasaki, K. Takahashi, M. Yoshimoto, H. Koinuma, Appl. Phys. Lett. **72**, 824 (1998)
- [16] F. A. Ponce, D. P. Bour, W. T. Young, M. Saunders, J. W. Steeds, Appl. Phys. Lett. **69**, 337 (1996)
- [17] D. Huang, P. Visconti, K. M. Jones, M. A. Reshchikov, F. Yun, A. A. Baski, T. King, H. Morkoc, Appl. Phys. Lett. **78**, 4145 (2001)
- [18] H. Morkoc, IEEE J.Sel.Top.Quantum Electron.**4**, 537 (1998)
- [19] H. M. Ng, D. Doppalapudi, T. D. Moustakas, N. G. Weimann, L. F. Eastman, Appl. Phys. Lett. **73**, 821 (1998)
- [20] M. J. Murphy, K. Chu, H. Wu, W. J. Schaff, O. Ambacher, L. F. Eastman, T. J. Eustis, J. Silcox, R. Dimitrov, M. Stutzmann, Appl. Phys. Lett. **75**, 3653 (1999)
- [21] E. C. Piquette, P. M. Bridger, R. A. Beach, T. C. McGill, MRS Internet J. Nitride Semicond. Res. **4S1**, G3.77 (1999)

### Phase Transitions on GaN Surfaces

C. Adelmann<sup>1</sup>, L. Lymperakis<sup>2</sup>, J. Brault<sup>1</sup>, G. Mula<sup>1</sup>, J. Neugebauer<sup>2</sup>, B. Daudin<sup>1</sup>

<sup>1</sup>Equipe mixte CEA-CNRS-UJF Nanophysique et Semiconducteurs, Département de Recherche Fondamentale sur la Matière Condensée, SP2M/PSC, CEA-Grenoble, 17 rue des Martyrs, 38054-Grenoble Cedex 9, France

<sup>2</sup>Fritz-Haber-Institut, Faradayweg 4-6, 14195 Berlin, Germany

#### ABSTRACT

Recent experimental and theoretical studies highlighted the importance of the growing surface structure on the final morphology of GaN. Actually, optimum morphology is achieved by growth in presence of a Ga bilayer adsorbed on the GaN surface. The threshold fluxes limiting the region of the Ga bilayer adsorption have been measured as a function of the GaN substrate temperature, giving rise to a Ga adsorption phase diagram. The Ga flux limiting the regions in the adsorption phase diagram exhibit a linear behavior in an Arrhenius plot. However, both energy activation (about 5 eV) and prefactor (in the  $10^{25}$  range) are surprisingly high. These questions were addressed by studying the adsorption/desorption of Ga adatoms and small islands (consisting of 2 and 3 Ga adatoms) on the Ga bilayer surface employing first principle density functional theory calculations. We find a desorption barrier of 2.1 eV and a binding energy between two Ga atoms of approximately 0.3 eV. Using these numbers we derived a simple growth model (based on rate equations). An analysis of the experimental data with the model revealed the origin of the large difference in the activation energies and the unusually large prefactor. We find that the nucleation of the droplets cannot be described by a simple Arrhenius behavior (as commonly assumed to fit experimental data) but that the nucleation energy is temperature dependent.

#### INTRODUCTION

The potentialities of GaN-based devices as light emitters at wavelength ranging from visible to UV strongly depend on the ability to control growth in order to optimise both optical and structural properties of the material. This is particularly true for plasma assisted molecular beam epitaxy (PAMBE) of nitrides. The ability to control the growth of nitride heterostructures at the monolayer scale, which is a prominent advantage of molecular beam epitaxy (MBE), is somewhat balanced by a rather low growth temperature, compared to metalorganic chemical vapor deposition (MOCVD). Low growth temperature results in a relatively weak diffusion of adatoms which may be detrimental to the structural properties of nitride material. Alternately, the strong dependence of surface morphology to metal/N ratio value makes the optimisation of PAMBE of nitride materials delicate, as N-rich conditions lead to rough surface whereas metal-rich conditions lead, in the general case, to metal droplet accumulation. Surfactants provide solutions to overcome the difficulties mentioned above, which are partly inherent to the relatively low growth temperature in MBE. It has been demonstrated that In acts as a surfactant for growth of GaN and prevents Ga droplet formation, allowing for a smooth growth front for Ga/N ratio values lower than unity [1,2]. Recently, it has been shown that the role of In as a surfactant can be extended to the case of AlGaIn alloys [3]. Furthermore, it has been found that Ga acts as a self-surfactant when growing GaN. In particular, it has been shown that, at high growth temperatures, a wide range of Ga fluxes exists, for which a finite amount of

excess Ga is present on the GaN surface whose quantity is independent of the value of the Ga flux [4]. Such conditions may provide a “growth window” for GaN PAMBE, i.e. a region, where the growth mechanisms and the surface morphology are independent of fluctuations of Ga flux and growth temperature [4,5].

However, the quantitative description of a GaN “growth diagram”, which describes the Ga surface coverage during growth as a function of Ga flux and growth temperature, has not yet been achieved: the results on the temperature dependence of the critical excess Ga flux at the onset of Ga droplet formation are contradictory, yielding activation energies of 2.8 eV (Ref. 5) and 4.8 eV (Ref. 4), respectively. This suggests that the underlying mechanisms of Ga accumulation are not yet understood.

It is the goal of the present work to establish a GaN “growth diagram” and to understand the physical meaning of activation energies involved in such a diagram which describes the Ga coverage of a GaN surface as a function of Ga flux and growth temperature.

## EXPERIMENTAL

The adsorption experiments were performed in a conventional MECA 2000 molecular-beam epitaxy chamber equipped with standard effusion cells. Active nitrogen for GaN growth was provided by an rf plasma cell. The substrates were 2  $\mu\text{m}$  thick (0001) (Ga-polarity) GaN layers grown by MOCVD on sapphire. The substrate temperature,  $T_s$ , was measured by a thermocouple in mechanical contact to the backside of the molybdenum sample holder and shielded from direct heating. Prior to all experiments, a 100 nm thick GaN layer was grown under Ga-rich conditions on the MOCVD GaN material to remove the influence of a possible surface contamination layer.

Ga fluxes,  $\Phi$ , have been calibrated to Ga effusion cell temperatures by reflection high-energy electron diffraction (RHEED) intensity oscillations during N-rich GaN growth at a substrate temperature of  $T_s = 620^\circ\text{C}$ . For such a low substrate temperature, it is reasonable to assume a Ga adatom sticking coefficient equal to unity and a growth rate proportional to the impinging Ga flux. It is worth stressing that this calibration procedure permits an absolute calibration of the Ga flux *in terms of the GaN surface site density*.

Ga coverage was determined by measuring the transient of the specular spot intensity in the RHEED pattern when letting evolve the surface under vacuum after exposing it to Ga flux during a fixed time. It has been shown that the duration of the transients following exposure to Ga flux or to vacuum can be qualitatively related to the amount of adsorbing or desorbing Ga [6,7]. In particular the duration of the transient occurring during Ga desorption can be used to qualitatively estimate the amount of Ga adsorbed on the surface. We will show below that further quantitative calibration can be performed in order to relate the Ga desorption transient time to absolute Ga surface coverages.

## RESULTS

Figure 1 shows the variation of RHEED transients under vacuum, after exposure of the (0001) GaN surface to Ga flux during one minute. The duration of the transient,  $t_{\text{des}}$ , was defined as the time between shuttering of the Ga cell (time 0) and the last inflexion point.

Next, the transient duration was measured as a function of impinging Ga flux for various substrate temperatures. The result for  $T_s = 740^\circ\text{C}$  is shown in figure 2. Three regions, labeled 1, 2 and 3 can be identified. Region 1 and 2 correspond to the steady state regime mentioned above. In regime 3, by contrast, transient duration increases with exposure time to Ga flux, as an

indication of Ga accumulation. Note that the transition between regime 1 and 2 is very sharp, corresponding to less than 1°C variation in the Ga cell temperature.

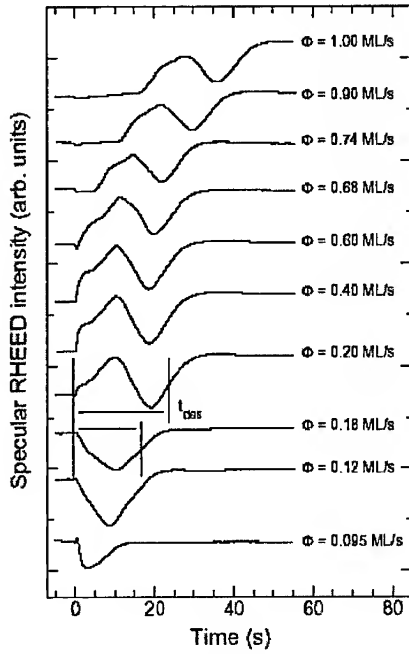


**Figure 1.** Specular RHEED intensity during Ga desorption from a (0001) GaN surface. Beforehand, Ga adsorption has been carried out at Ga fluxes  $\Phi$  as indicated. For  $\Phi < 0.68$  ML/s, the desorption transients do not change as a function of the previous adsorption time, corresponding to a steady state regime. By contrast, for  $\Phi > 0.68$  ML/s, the desorption transients depend on the adsorption time (here 1 min). The substrate temperature is  $T_S = 740$  °C.

In a further step, data in figure 2 were quantitatively calibrated taking into account that the Ga desorption rate,  $\Phi_{des}$ , is given by:

$$\Phi_{des}(c) = \frac{dc}{dt}, \quad (1)$$

with the initial condition  $c(t = -t_{des}) = c_{eq}$ , which denotes the amount of Ga adsorbed in equilibrium conditions, i.e., before Ga desorption sets in. Details of the quantitative procedure will be fully described elsewhere [8]. It was based on the remark that in equilibrium, the impinging Ga flux  $\Phi$  must exactly balance the evaporation rate, hence  $\Phi_{des}(c_{eq}) = -\Phi(c_{eq}[t_{des}])$ . Integrating equation (1), taking the first derivative with respect to  $t_{des}$ , and using the above substitution leads to

$$c_{eq}(\Phi) = \int_0^{\Phi} \Phi' \frac{\partial t_{des}}{\partial \Phi'} d\Phi'. \quad (2)$$

This expression allows the computation of  $c_{eq}$  from  $t_{des}$  as a function of  $\Phi$  (which is known from the experimental data) and can be evaluated numerically.

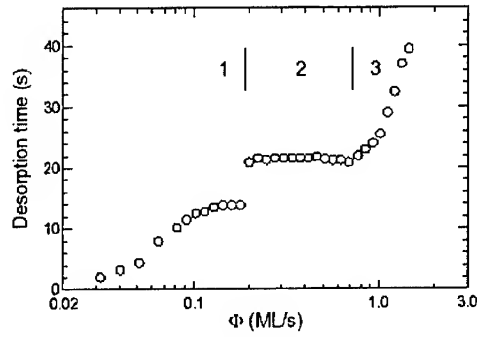


**Figure 2.** Ga desorption time as a function of impinging Ga flux  $\Phi$  after equilibrium has been attained for regions 1 and 2, and after 1 min of Ga adsorption in region 3. The substrate temperature is  $T_S = 740$  °C.

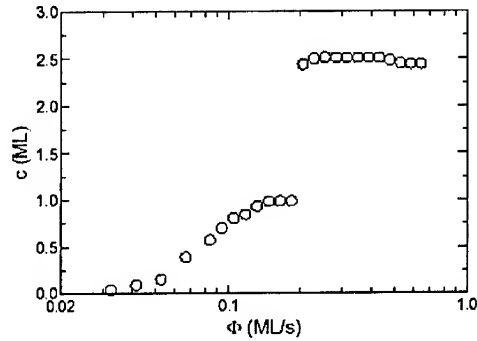


**Figure 3.** Calibrated Ga adsorption isotherm at  $T_S = 740$  °C using Eq. (2). The data are derived from figure 2. As the method can only be applied to equilibrium coverages, only regions 1 and 2 are represented.

The result is shown in figure 3. It suggests that, in regime 1, Ga coverage evolves from 0 to about 1 monolayer (ML) of Ga matched to GaN surface. The abrupt transition to regime 2 corresponds to adsorption of an extra 1.5 Ga MLs. These results are consistent with calculations predicting the

formation of a laterally-contracted Ga bilayer, with the first ML matched to GaN while the second one contains the equivalent of 1.3 MLs of Ga in terms of GaN surface site density [9].

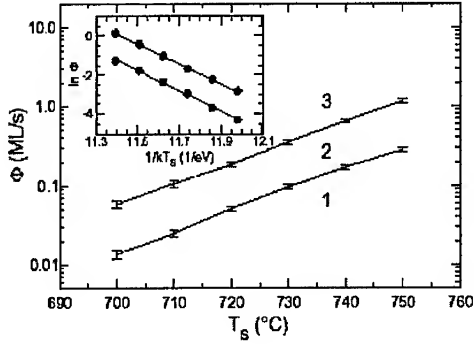


**Figure 4.** Ga adsorption phase diagram indicating the Ga surface coverage as a function of impinging Ga flux  $\Phi$  and substrate temperature  $T_s$ . The definition of regions 1-3 follows Fig. 3. The inset shows an Arrhenius plot of the data.

In figure 4, the Ga flux at boundary between regime 1, 2 and 3 has been plotted as a function of  $T_s$ . In the inset data are displayed in an Arrhenius plot, yielding activation energies of  $E_A^{(12)} = 5.2 \pm 0.1$  eV and  $E_A^{(23)} = 5.1 \pm 0.05$  eV for the 1 $\rightarrow$ 2 and 2 $\rightarrow$ 3 transition, respectively. These values, the prefactors, and the corresponding values of the growth phase diagram in Refs. 4 (1 $\rightarrow$ 2 corresponds to B $\rightarrow$ C and 2 $\rightarrow$ 3 corresponds to C $\rightarrow$ D) and 5 (discussing the 2 $\rightarrow$ 3 transition only) are summarized in table 1.

Reference	Transition	$E_A^{\text{exp}}$ (eV)	$\nu_{\text{des}}^{\text{exp}}$ (Hz)	$\nu$ (ML/s)	$\alpha$ (meV/K)	$\nu_{\text{des}}^{\text{ren}}$ (Hz)
This work	1 $\rightarrow$ 2	5.2	$3 \times 10^{25}$	0	-2.3	$4.7 \times 10^{25}$
This work	2 $\rightarrow$ 3	5.1	$2 \times 10^{25}$	0	-2.2	$1.5 \times 10^{25}$
Ref. 4	1 $\rightarrow$ 2	3.7	$5 \times 10^{17}$	0.28	-0.8	$1.6 \times 10^{18}$
Ref. 4	2 $\rightarrow$ 3	4.8	$1 \times 10^{24}$	0.28	-1.9	$4.8 \times 10^{23}$
Ref. 5	2 $\rightarrow$ 3	2.8	$1 \times 10^{14}$	1.1	> -0.1	$5.5 \times 10^{13}$

**Table 1:** Experimental activation energies  $E_A^{\text{exp}}$  and prefactors  $\nu_{\text{des}}^{\text{exp}}$  for the transition fluxes between different Ga coverage regimes as obtained from the adsorption (this work, Fig. 4) and growth phase diagrams (from Refs. as indicated).  $\nu$  denotes the GaN growth rate (the N-flux),  $\alpha$  the linear temperature coefficient of the adsorption energy, and  $\nu_{\text{des}}^{\text{ren}}$  the renormalized prefactor (see discussion section).

## DISCUSSION

It appears clearly in table 1 that energy and prefactor are *not* constant but vary largely with the growth conditions. As a general trend, one finds that the activation energy and the prefactor decrease with increasing growth rate (N flux). It is also interesting to note that only in

the case of high growth rate ( $v = 1.1$  ML/s) the prefactor ( $1 \times 10^{14}$  Hz) is close to the typical attempt frequencies observed/expected for desorption, i.e. in the  $10^{12}$ - $10^{13}$  Hz range. For conditions where growth is slow ( $v = 0.28$  ML/s) or absent (adsorption), prefactors are found which are many orders of magnitude larger.

In order to identify the origin of these apparent discrepancies, we have explicitly calculated the desorption and the formation of small Ga clusters on the Ga bilayer surface employing density functional theory. Details of the calculation are extensively reported elsewhere [8]. To summarize, a temperature dependence of the activation energy,  $E_A = E_0 + \alpha(T - T_0)$  was assumed with  $E_0$  the temperature independent contribution (equal to 2.75 eV, from first principles calculations [8]),  $T_0$  the temperature offset, and  $\alpha$  the linear temperature coefficient. Then, a renormalized prefactor,  $\nu_{\text{des}}^{\text{ren}} = \nu_{\text{des}} e^{-\alpha/k_B}$ , with  $\nu_{\text{des}} = 3 \times 10^{13}$  Hz, was calculated. Results are reported in table 1 and account well for the large range of  $\nu_{\text{des}}^{\text{exp}}$  experimentally observed.

## CONCLUSION

The main conclusion of this work is the quantitative determination of the Ga coverage on the GaN (0001) surface during adsorption as a function of Ga flux and substrate temperature. Furthermore, a model has been derived, which consistently describes the adsorption of Ga on GaN surfaces as well as the accumulation of Ga during Ga-rich GaN growth. The discrepancies in previous measurements of the activation energy characterizing the critical Ga flux for the onset of Ga droplet formation during GaN growth [4,5] have been clarified.

The origin of the experimentally-observed unphysically high prefactors has been accounted for by a temperature dependent desorption barrier. At the moment, we can only speculate about possible mechanisms which would reduce the activation barrier at higher temperatures. As the number of atoms in the compressed Ga layer of the bilayer structure and thus the lateral lattice constant of the top Ga layer significantly changes with temperature, we tentatively suggest that the concomitant change in the surface geometry could have an important effect on the island formation energy.

## REFERENCES

- 1 F. Widmann, B. Daudin, G. Feuillet, N. Pelekanos, and J. L. Rouvière, Appl. Phys. Lett. 73, 2642 (1998).
- 2 C. Kruse, S. Einfeldt, T. Böttcher, and D. Hommel, Appl. Phys. Lett. 79, 3425 (2001)
- 3 E. Monroy, B. Daudin, E. Bellet-Amalric, N. Gogneau, D. Jalabert, F. Enjalbert, J. Brault, J. Barjon, and Le Si Dang, J. Appl. Physics, in press
- 4 C. Adelmann, J. Brault, D. Jalabert, P. Gentile, H. Mariette, G. Mula, and B. Daudin, J. Appl. Phys. 91, 9638 (2002)
- 5 B. Heying, R. Averbek, L. F. Chen, E. Haus, H. Riechert, and J. S. Speck, J. Appl. Phys. 88, 1855 (2000)
- 6 G. Mula, C. Adelmann, S. Moehl, J. Oullier, and B. Daudin, Phys. Rev. B 64, 195406 (2001)
- 7 L. X. Zheng, M. H. Xie, and S. Y. Tong, Phys. Rev. B 61, 4890 (2001)
- 8 C. Adelmann, J. Brault, Guido Mula, B. Daudin, L. Lymperakis, J. Neugebauer, unpublished
- 9 J. E. Northrup, J. Neugebauer, R. M. Feenstra, and A. R. Smith, Phys. Rev. B 61, 9932 (2000).

### Nitrogen Gas-Cluster Ion Beam – A New Nitrogen Source for GaN Growth

Y. Shao<sup>(1)</sup>, T.C. Chen<sup>(2)</sup>, D.B. Fenner<sup>(1)</sup>, T.D. Moustakas<sup>(2)</sup>, and George Chu<sup>(3)</sup>

(1) Epion Corporation of JDS Uniphase, 37 Manning Rd., Billerica, MA 01821

(2) Boston Univ. Dept. Electrical & Computer Eng., 8 Saint Mary's St., Boston, MA 02215

(3) Agere System corp., Bell Lab, Murray Hill, NJ 07974

#### ABSTRACT

In this paper we report sapphire nitridation and GaN film growth by using ionized nitrogen clusters as a nitrogen source. The clusters, typically 2000-3000 molecules/charge, are generated by a prototype GCIB source. The clusters are accelerated to 10-25 kV and disintegrate upon impact with the substrate surface where they react with Ga atoms to form GaN. The efficiency of this novel nitrogen source was tested by studying the nitridation of (0001) sapphire substrates at relatively low temperatures of 200 - 400°C. The effect of exposure of the substrate to the nitrogen cluster-ion beam was examined by XPS, RHEED and AFM. It was found that the amount of retained surface nitrogen increases nonlinearly with increasing beam energy. There exists a threshold energy, ~ 20 kV, above which nitrogen retention is significantly enhanced.

GaN films were grown with such nitrogen clusters heteroepitaxially on sapphire/AlN-buffer (MBE grown) and homoepitaxially on thick GaN on sapphire (HVPE grown). TEM cross-section images indicate that the heteroepitaxial GaN films had defect density similar to that of MBE and MOCVD grown films. The homoepitaxially-grown GaN films were found to replicate the GaN templates and show strong cathodoluminescence (CL) emission at 363 nm with FWHM of 9 nm. Furthermore, the spectra show no evidence of yellow band emission.

#### INTRODUCTION

GaN and other III-V nitrides have been successfully used in optical and electrical devices, such as blue light-emitting diodes, laser diodes and high electron mobility transistors [1, 2]. In the absence of suitable GaN or AlN substrates, c-plane sapphire ( $\text{Al}_2\text{O}_3$ ) has become the preferred substrate material for group III nitride heteroepitaxy. The active nitrogen needed for nitridation and subsequent nitride layer growth comes from several sources, such as decomposition of ammonia on sapphire surface at high temperature in the case of MOCVD or GSMBE, or generated by radio frequency (RF) or electron cyclotron resonance (ECR)  $\text{N}_2$  plasma sources in molecular beam epitaxy (MBE). In this article, we report the result of sapphire nitridation and GaN growth by using a new nitrogen source: the nitrogen gas cluster ion beam (GCIB) [3].

A cluster contains thousands of gas atoms or molecules which are weakly held together by Van der Waals forces. Unlike a monomer ion, the cluster ion has very large mass to charge ratio and much lower average energy per atom than a monomer ion carrying the same total energy. Upon impinging the target surface, all of the energy carried by the cluster ion (in the keV range) is instantly deposited onto an extremely small volume at the impact site during a period of about  $10^{-12}$  second. Computer simulation [4] suggested instantaneous temperature rise on the order of  $10^5$  °K at the cluster impact site, together with mega-bar instantaneous pressure increase. The extreme instantaneous temperature and pressure conditions make nitrogen molecules crack into active species at relatively low temperature possible.

Energetic gas cluster ion beam has been used for surface modifications such as smoothing and cleaning [5, 6, 7], as well as for the production of high quality thin films. Investigations have

been conducted to grow thin films, such as SiO<sub>2</sub> dielectric layers, ultra-smooth PbO films onto glass, high conductivity ITO films onto plastic [8,9] and group-III nitride films on GaAs substrate [10] using cluster ion beam. The source gas used in those investigations were reactive gases, such as oxygen, CO<sub>2</sub> and ammonia. In this work, we use ultra pure nitrogen as the cluster beam source gas, and study the nitridation of sapphire substrates at relatively low temperatures of 200-400 °C and the growth of GaN film.

## EXPERIMENTAL METHODS AND RESULTS

The nitridation and GaN film growth was carried out in a MBE system with GCIB nitrogen source. The schematics of GCIB source and the process chamber is shown in Fig. 1. A neutral cluster jet is generated by adiabatic expansion of compressed source gas through a small quartz nozzle into vacuum. After passing through the skimmer, the cluster enters the ionizer and acceleration stacks, where it is ionized by electron bombardment, and extracted and accelerated to the desired energy. A permanent magnet is used to filter out monomers and dimers. After this filtering, the cluster ion beam passes through a neutralizer, to eliminate possible charging of the substrate, before reaching the substrate surface. The base pressure of the process chamber was around  $2 \times 10^{-10}$  Torr. During the process, the pressure rises to  $\sim 7 \times 10^{-6}$  Torr. A Ga effusion cell was incorporated into the process chamber, making GaN growth possible.

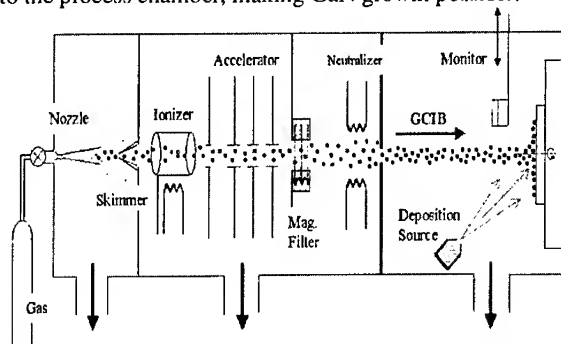


Fig. 1. Schematic diagram of Gas Cluster Ion Beam (GCIB) assisted GaN growth system

The energy of the cluster ions used in the nitridation and GaN growth ranged from 15-25 kV. The clusters have a size distribution from several hundred to 10,000 atoms per cluster, with the most probable size around 1700 molecules/cluster under the current operation condition as measured by Time of Flight (TOF) in a separate experiment. A movable Faraday cup is used to measure the cluster beam flux. Typical beam current density was around 600 nA/cm<sup>2</sup>.

### a. Sapphire Nitridation

Nitridation was carried out at substrate temperature of 200-400 °C. Samples were first degassed at 400 °C for 1 hour before nitridation. The total cluster ion dose was  $1 \times 10^{16}$  ions/cm<sup>2</sup>. The nitridation time was around 2 hours per sample. After nitridation, the samples were evaluated by X-ray Photoelectron Spectroscopy (XPS), Atomic Force Microscopy (AFM) and Reflection High Energy Electron Diffraction (RHEED) for their chemical bonding, surface morphology and microstructure, respectively.

Each of three samples was processed at energy of 15, 20 and 25 kV, respectively. XPS was used to study the surface chemical bonding of the sample nitridated at 400 °C. The XPS spectra were acquired at 90° take off angle with Al K $\alpha$  line irradiation. All scans have been shifted in such a way that the strongest C<sub>1s</sub> peak was at 285 eV. High resolution scans were used for individual peak analysis. A distinct N<sub>1s</sub> peak was observed for all the samples, indicating that nitrogen was incorporated onto the sapphire surface. Table 1 shows the change of N<sub>1s</sub>/Al<sub>2p</sub> ratio with beam energy. The amount of surface nitride was found to increase with increasing beam energy. A sharp increase in nitrogen with beam energy above 20 kV suggests that the cracking of nitrogen was dramatically enhanced in this region.

Table 1. Relative intensity of N<sub>1s</sub>/Al<sub>2p</sub> XPS peaks for sapphire substrates nitridated under different cluster beam energy.

Energy (kV)	15	20	25
N <sub>1s</sub> /Al <sub>2p</sub> ratio (%)	0.28	0.86	15.45

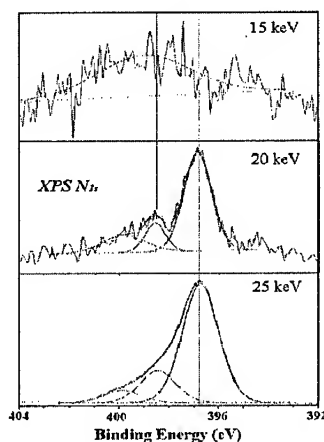


Fig. 2. High resolution N<sub>1s</sub> XPS scans for sample nitridated at different beam energy.

Specifically, for the samples treated with 20 and 25 keV nitrogen beam, the N<sub>1s</sub> peaks can be deconvolved into three components centered at 396.8 eV (Al-N bonds), and 399.3eV (N-O bonds) [11]. The peak at 398.6 eV may result from some sub-stoichiometry of N<sub>x</sub>O. Shown in Fig. 2 are the high resolution N<sub>1s</sub> XPS scans from the three samples nitridated at 15, 20 and 25 kV at 400 °C. The much higher N<sub>1s</sub>/Al<sub>2p</sub> ratio and the strong AlN bond shown in the high resolution N<sub>1s</sub> scan of the sample nitridated with 25 kV beam indicates that there is a threshold, around 20 kV, above which the activation of molecular nitrogen is enhanced. Given the fact that the mass to charge ratio of the cluster is about 2000 molecules per cluster, a 20 kV beam indicates that each nitrogen atom will have about 10 eV, consistent with the binding energy of nitrogen molecules, which is about 9.6 eV.

RHEED images also confirmed the change of surface structure upon nitridation both in the [1  $\bar{1}$  00] and [2  $\bar{1}$   $\bar{1}$  0] direction of the c-plane sapphire surface. In Fig. 3, the RHEED patterns of nitridation at 200 °C substrate temperature with 15 and 25 kV beam are compared. The sharp vertical rods seen on the pattern indicate good flatness and high crystal quality of the nitridated surface. The broadness of the diffraction lines suggests that the AlN film is very thin and maybe

highly strained. Again, the sample nitridated with 25 kV beam shows more complete nitridation from the RHEED pattern.

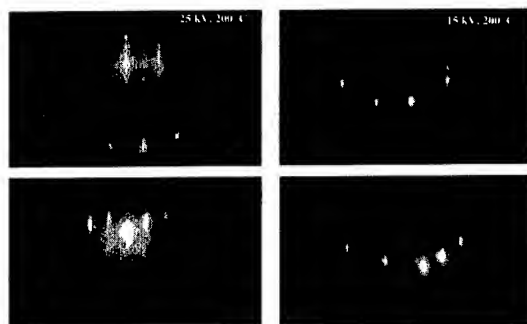


Fig. 3. Comparison of RHEED patterns along the  $\langle 1100 \rangle$  azimuth (top) and  $\langle 1120 \rangle$  azimuth (bottom) for sapphire substrate nitridated at 25 and 15 kV.

Nitridation was also characterized by AFM measurement. The original substrate surface had a roughness ( $R_a$ ) of around 1.3 Å on a 10 µm scale. After 15 kV GCIB nitridation, the surface roughness went up to 2.9 Å. With higher cluster beam energy, the surface became rougher, up to 5.0 Å for the 25 kV beam at 200 °C substrate temperature. Similar results were also found for 400 °C substrate temperature processes.

#### b. GaN Film Growth

Because of the large lattice mismatch between the sapphire substrate and GaN, substrate nitridation followed by the deposition of a low temperature AlN or GaN buffer layer is proven to be critical for subsequent GaN growth by MBE and MOCVD methods. At the current stage, our growth of GaN was limited to growing these films on AlN buffers prepared by plasma assisted MBE or thick GaN films grown by HVPE. Growing GaN or AlN buffer layers directly on GCIB nitridated sapphire substrates by using GCIB source is still under investigation.

Several growth conditions were tested with the nitrogen cluster beam ranging from 15-25 kV and Ga cell temperature from 850-900 °C. The substrates were 300 Å AlN buffer on sapphire. Temperature was maintained at 850 °C. Depending on the nitrogen cluster beam energy and current, the GaN growth rate varied from ~ 1000 Å/hour for a 15 kV beam to over 3000 Å/hour at 25 kV as measured by cross section SEM. It was noticed that higher beam energy ( $\geq 20$  kV) leads to N-rich growth, which agrees with the sapphire nitridation tests where we showed that the cracking efficiency of nitrogen is greatly increased with beam energy above 20 keV. By increasing the Ga cell temperature to 900 °C, the growth converted into Ga-rich growth.

Fig. 4 is the room temperature CL spectrum of a GaN film grown with 15 kV cluster beam and 855 °C cell temperature (a), and 20 kV cluster beam and 870 °C cell temperature (b). Since the films were only about 3000 Å thick, a 5 keV electron beam was used for the analysis. Both spectra show band edge emission at around 363 nm and broad yellow emission. The origin of such yellow band emission is believed to be related to native defects and/or residual impurities. Since the films were only around 3000 Å thick, the defect density is expected to be high, even for films grown by the MBE methods. A large number of threading defects tend to annihilate as the films get thicker and we expect reduction in yellow luminescence.

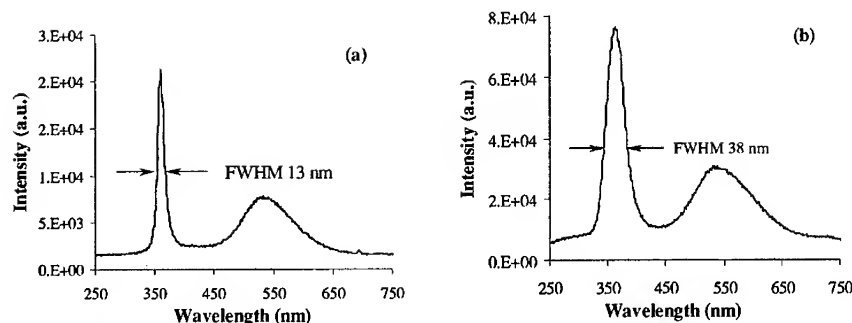


Fig. 4 Cathodoluminescence analysis of GaN films grown heteroepitaxially on MBE grown AlN-buffer on sapphire with GCIB nitrogen source.

A cross section TEM of the GaN film grown at 850 °C with 15 kV nitrogen cluster beam is shown in Fig. 5. It is clearly seen that at the interface of AlN buffer layer, the GaN film has high density of defects. Many of the dislocations in the GaN annihilate each other as they propagate upwards in the film. The defect morphologies are similar to those of MBE and MOCVD grown GaN films.



Fig. 5. Cross section TEM image of a GaN film grown with GCIB Nitrogen beam at 15 kV.

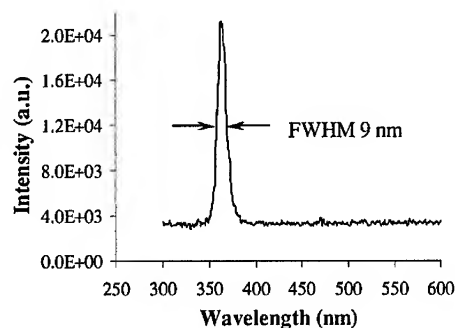


Fig. 6. CL analysis of GaN films grown homoepitaxially on HVPE GaN on sapphire.

Using a mixture of 5%  $\text{NH}_3$  in nitrogen as source gas, GaN films were also grown homoepitaxially on 5- $\mu\text{m}$  thick GaN "seed" (base) layer on sapphire substrate. The GaN base was prepared by HVPE growth. For GCIB growth, both the substrate temperature and Ga cell temperature were maintained at 900 °C during growth with 25 kV cluster beam. The growth rate was around 1200 Å/hour. Most likely the relatively low growth rate is the result of low beam current observed when using  $\text{NH}_3$  gas mixture. The beam current was only around 25% of that with pure nitrogen source. Nevertheless, the GaN film grown under such condition were found to replicate the GaN templates and show strong CL emission at 363 nm with FWHM of 9 nm, as shown in Fig. 6. Furthermore, the spectra show no evidence of yellow band emission.

## SUMMARY

In summary, sapphire nitridation and GaN growth have been carried out by using a new nitrogen source, GCIB nitrogen cluster beam. Such a cluster beam has a high mass to charge ratio and low average energy per molecule,  $\sim 10$  eV. Sapphire nitridation was carried out at relatively low temperature of 200–400 °C. The nitrogen cluster beam energy was found to have a strong effect on the amount of nitrogen retained on the surface of the substrate. It was found that there exist a threshold energy,  $\sim 20$  keV, above which the amount of nitrogen bonded with Al was greatly enhanced.

GaN films were grown with nitrogen clusters heteroepitaxially on MBE grown AlN-buffer on sapphire and homoepitaxially on 5- $\mu\text{m}$  thick HVPE grown GaN on sapphire. The growth rate varied between 1000–3000 Å/hour, which was limited by the cluster beam current and energy. Most of the GaN film thicknesses grown in this studies were around 3000 Å. We found that the heteroepitaxial GaN films showed defect density similar to that of MBE and MOCVD grown films of similar thickness, with room-temperature CL emission at 363 nm together with high yellow band emission. Whereas there is no evidence of yellow band emission in the CL measurement of the homoepitaxially-grown GaN films.

## ACKNOWLEDGEMENT

We would like to thank Dr. Lisa Allen and Dr. Dick Torti for their stimulating suggestions. Special thanks to Marwan Manassah and Bill Butts for the design, modification and maintenance of the GCIB system, and to Allen Kirkpatrick for his continual encouragement throughout the work. We would also like to thank Mr. Sandeep Iyer for help with the RHEED analysis. Work at Epion was supported by DoD-BMDO, SBIR Phase-II contract DTRA01-00-C0035. Work at Boston University was supported by ONR and was monitored by Dr Colin Wood.

## REFERENCE

1. S. Nakamura and G. Fasol, *The Blue Laser Diode* (Springer, Berlin, 1997).
2. G.E. Bulman, K. Doverspike, S.T. Sheppard, T.W. Weeks, H.S. Kong, H.M. Dieringer, J.A. Edmond, J.D. Brown, J.T. Swindell, and J.F. Schetzana, *Electron. Lett.* **33**, 1556 (1997).
3. Y. Shao, T.C. Chen, D.B. Fenner and T.D. Moustakas, "Growth of GaN by Ion Beam Cluster Deposition", *Nitride Semiconductor Workshop*, Richmond, March 2002, (unpublished).
4. W.K. Chu, Y.P. Li, J.R. Liu, J.Z. Wu, S.C. Tidrow, N. Toyoda, J. Matsuo and I. Yamada, *Appl. Phys. Lett.* **72**, 246 (1998).
5. D.B. Fenner, R.P. Torti, L.P. Allen, N. Toyota, A.R. Kirkpatrick, J.A. Greer, V. DiFilippo, and J. Hautala, *MRS Symp. Proceedings*, vol. **585**, (2000).
6. N. Toyoda, N. Hagiwara, J. Matsuo, and I. Yamada, *Nucl. Inst. And Methods in Phys. Res. B* **161-163**, 980, (2000).
7. L.P. Allen, D.B. Fenner, N. Toyota, W.J. Skinner, R. Chandonnet, S.E. Deziel, R.P. Torti, *Proc. of the 1999 IEEE Int. Silicon-on-Insulator Conference*, 117, (1999).
8. H. Katsumata, J. Matsuo, T. Nishihara, T. Tachibana, K. Yamada, M. Adachi, E. Minami and I. Yamada, *Applications of Accelerators in Research and Industry*, edited by J.L. Duggan and I.L. Morgan, AIP Press. 409, (1999).
9. E. Minami, J. Matsuo and I. Yamada, *Application of Accelerators in Research and Industry*, edited by J.D. Duggan and I. L. Morgan, AIP Press. 435, (1999).
10. H. Saito, T. Kato, M. Yoneta, M. Ohishi, J. Matsuo and I. Yamada, *Phys. Stat. Sol. (a)*, **180**, 251 (2000).
11. R.M. Ormerod, K.L. Peat, W.J. Wytenburg and R.M. Lambert, *Surf. Sci.*, **269-270**, 506 (1992).

### Growth of Oriented Gallium Nitride Films on Amorphous Substrates by Self Assembly

Hongwei Li, Mahendra K. Sunkara\*,  
Department of Chemical Engineering, University of Louisville,  
Louisville, KY 40292, U.S.A.

\*E-mail: mahendra@louisville.edu

#### ABSTRACT

C-plane oriented thin films of gallium nitride (GaN) were grown on both amorphous quartz substrates and single crystalline c-sapphire substrates at sub-atmospheric pressures by exposing molten gallium thin films to electron cyclotron resonance (ECR) microwave generated nitrogen plasma. Gallium nitride crystals nucleated from molten gallium and self-aligned with respect to each other due to the mobility of nitrogenated gallium and formed textured film directly on amorphous substrates. Scanning electron microscopy (SEM) images and X-ray Diffraction (XRD) spectra confirmed the orientation among crystals. Micro-Raman spectra exhibited a FWHM of  $3\text{ cm}^{-1}$ . Self-assembled, nanocrystalline GaN thin films were obtained when spin-coated gallium thin films ( $< 1\text{ }\mu\text{m}$ ) on quartz substrates were nitrided.

#### INTRODUCTION

Gallium nitride (GaN) is a direct, wide band gap semiconductor that finds applications in light emitting diodes (LED)[1-2], laser diodes (LD)[3-4], high temperature/power field effect transistors (FET)[5] and UV optical devices. Since both GaN substrates and lattice matched substrates are unavailable, hetero-epitaxy on substrates such as sapphire or SiC is currently employed using metal organic chemical vapor deposition (MOCVD)[6-7], Molecular beam epitaxy (MBE)[8-9] or Hydride vapor phase epitaxy (HVPE)[10-11] techniques. The lattice mismatch and different thermal expansion coefficients between GaN and substrates cause high density of dislocations and stresses in the film [12-13]. Lateral Epitaxial Overgrowth (LEO) [14] and Pendeo-epitaxy [15] have achieved significant reduction in the dislocation density, however homoepitaxy on high quality GaN substrates would be preferred [16].

Bulk gallium nitride growth under high nitrogen pressure ( $\sim 15\text{ kbars}$ ) from gallium melt has low dislocation densities ( $10^6\text{ cm}^{-2}$ ), but the area of these crystals remains at about  $3\text{ cm}^2$  [17]. Bulk nucleation and growth of GaN from gallium melt at sub atmospheric pressure had been demonstrated using atomic nitrogen [18]. However this process produced epitaxial growth on (0001) single crystal sapphire substrate and has dislocation density in excess of  $10^{10}\text{ cm}^{-2}$  [19].

Here, we report a different approach that uses low pressure bulk synthesis to get large area, self-oriented, high quality thin film GaN which avoids epitaxy using either thin molten gallium film as a buffer layer or directly growing on an amorphous substrate.

Thin films of liquid gallium are spread onto a single crystalline, polycrystalline or amorphous substrate, and then nitrided in an ECR-MW nitrogen plasma environment. Since nitrogen containing gallium melts wet solid surfaces very well [20-21], the flow of nitrided gallium melts will allow growing GaN platelets crystals to self-orient with respect to each other. The self-alignment of GaN crystals occurs parallel to the flow direction and the growing platelets join

together by self-assembly process (Fig.1). As mentioned above, this process is essentially independent of substrates.

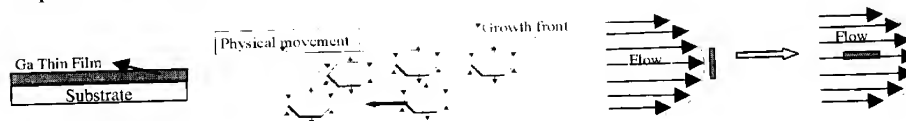


**Figure1.** The self-oriented growth of GaN platelet shaped crystals in flowing Ga melts.

Earlier, we demonstrated this concept of self-assembled GaN growth over bulk pool of molten gallium and also on pyrolytic boron nitride (pBN) substrates [22]. Here we report further investigation of this method on amorphous, fused silica (quartz) and single crystalline c-sapphire substrates using a Boralectric™ heater with uniform temperature distribution.

## EXPERIMENT

Fused quartz and single crystalline c-sapphire substrates were cleaned using hot KOH and acetone and then blown dry with argon. Around 10 μm thick gallium was spread onto the substrates. The experiments were performed in a water-cooled double wall vacuum chamber with an ASTeX® Model AX4500 ECR plasma source. H<sub>2</sub> plasma at room temperature was used for about 30 minutes to remove oxide. Subsequently, the gallium film was exposed to N<sub>2</sub> plasma and heated to 900-1000°C by the Boralectric™ heater for 1-3 hours at a pressure of 100mTorr.

About 1 μm thick gallium was also spin-coated on 2-inches quartz wafers. Similar conditions were performed except that the temperature used for this spin-coated gallium was about 800 °C and the pressure was 140mtorr.

The synthesized gallium nitride films were characterized using Scanning Electron Microscopy (SEM), X-ray Diffraction (XRD) and Raman spectroscopy to study the morphology, orientation and quality, respectively. High resolution TEM was done to study the very thin film of nanocrystalline GaN.

## RESULTS AND DISCUSSION

### Self-oriented GaN growth on the amorphous quartz substrates

The film of gallium on quartz substrates agglomerated into droplets with a considerable size distribution during ramping-up of the substrate temperature. These gallium droplets started to spread due to good wetting characteristic after about 10 minutes at 950°C in nitrogen plasma. Gradually, the nitrogenated melts covered entire substrate and eventually formed a thin gray colored film. The X-ray diffraction spectrum showed primary reflections of (0002) and (0004) planes of wurtzite GaN. See Fig.2 (a). This indicates that the GaN film is c-plane textured. SEM image in Fig. 2(b) also confirmed that the platelet-shaped crystals are oriented in c-plane.

Gallium nitride crystals nucleated from molten gallium and self-oriented with respect to each other due to the mobility of molten gallium. Crystals grew laterally and joined together to form oriented film. The boundaries between some platelets were hardly seen due to complete joining.

as shown in Fig. 2(b). The joining of adjacent crystals was clearly shown in the top view and cross sectional images of the GaN film in Fig.3.

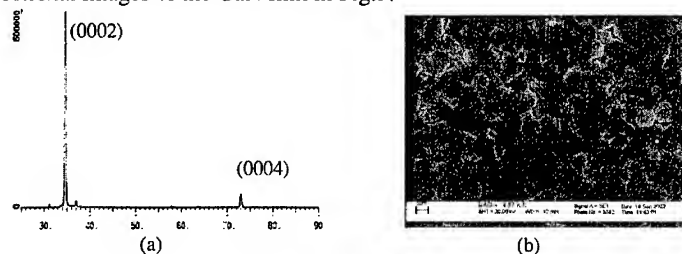


**Figure 2.** (a) XRD spectrum and (b) SEM image of oriented GaN on Quartz

A Raman spectrum in Figure 4(a) was obtained from the thin film on quartz substrates and showed predominant  $E_2^{(2)}$  peak at  $568\text{ cm}^{-1}$  corresponding to wurtzite GaN. This indicates that there is low concentration of structural defects or internal stress. The FWHM of  $3\text{ cm}^{-1}$  of this  $E_2^{(2)}$  peak compares very well with the reported value of  $3.5\text{ cm}^{-1}$ [23].

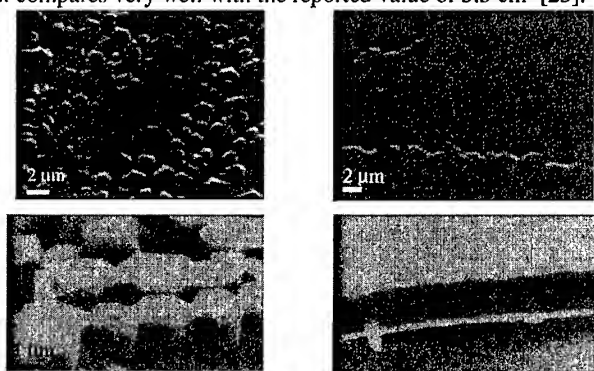


**Figure 3.** Sequential growth of self-oriented GaN film on Quartz substrates

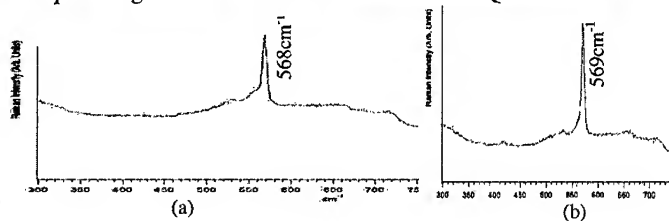


**Figure 4.** Raman spectra of self-oriented GaN film on (a) amorphous quartz and (b) sapphire

#### Single crystal quality GaN on Sapphire substrates

Similar results were obtained with bulk GaN growth on single crystalline sapphire substrates. The gray layer formed on the sapphire became transparent after excess gallium was dissolved

away in aqua regia. X-ray diffraction spectra in Fig.5 (a) showing dominant peaks of hexagonal GaN (0002) and (0004) indicated textured GaN film. SEM images in Fig. 5(b) also confirmed that the crystals are very well oriented with respect to each other.

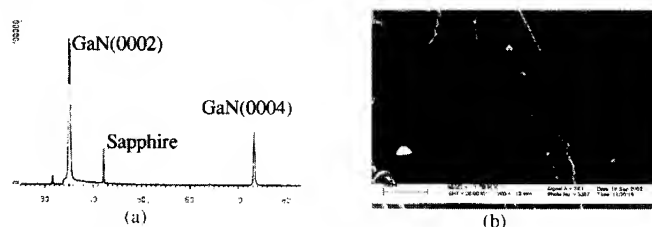


**Figure 5.** (a) XRD spectrum and (b) SEM image of GaN on sapphire substrate.

As shown by the SEM image in Fig.5 (b), most gallium nitride platelet shaped crystals grew and aligned along the fast growing direction. Some crystals aligned with respect to each other very well with no discernible boundaries between them. A Raman spectrum in Fig.4 (b) also indicated good quality of the resulting wurtzite GaN. The seemingly perfect orientation on the sapphire substrates could be due to two reasons. The first reason could be due to uniform lateral temperature distribution because sapphire has higher thermal conductivity (0.35w/cm-K) compared to quartz (0.014w/cm-K). The second reason could be due to occasional epitaxy of GaN crystals with sapphire substrate. Currently, TEM studies are being carried out to determine whether there was any sort of epitaxy of GaN with the substrate.

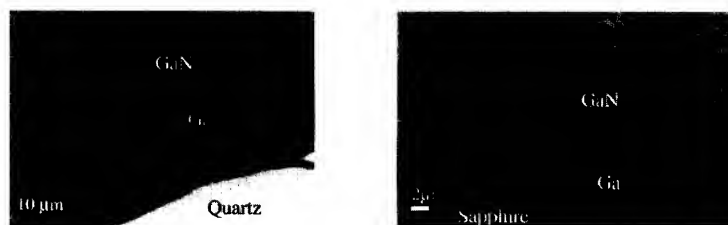


**Figure 6.** Oriented GaN film on Top of gallium

Very thin layer of gallium was found to be present in between the gallium nitride film and the substrate on both quartz and sapphire substrates. See the cross-sectional SEM images in Fig. 6. This indicates gallium nitride crystals nucleated out of molten gallium and assembled freely during growth to form oriented gallium nitride film which is independent of the substrate used.

#### **Nanocrystalline GaN thin film on Quartz substrates**

Around 1 μm thick gallium was coated on a 2-inch quartz wafer by spinning (Shown in Fig. 7(a)). A yellowish thin film formed on the substrate after nitridation in ECR-MW generated nitrogen plasma (Shown in Fig. 7 (b)). SEM pictures in Fig. 7(c) showed the size of the crystals in the film was around 85nm. X-ray diffraction in Fig. 7(d) indicates the film is textured. The possible reason of forming nanocrystalline GaN is the high nucleation density due to thinness of molten Ga film.

together by self-assembly process (Fig.1). As mentioned above, this process is essentially independent of substrates.

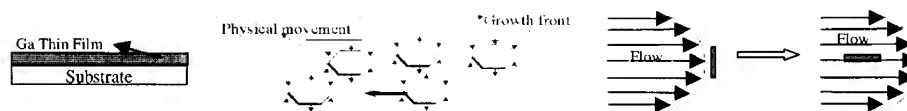


**Figure1.** The self-oriented growth of GaN platelet shaped crystals in flowing Ga melts.

Earlier, we demonstrated this concept of self-assembled GaN growth over bulk pool of molten gallium and also on pyrolytic boron nitride (pBN) substrates [22]. Here we report further investigation of this method on amorphous, fused silica (quartz) and single crystalline c-sapphire substrates using a Boralectric<sup>TM</sup> heater with uniform temperature distribution.

## EXPERIMENT

Fused quartz and single crystalline c-sapphire substrates were cleaned using hot KOH and acetone and then blown dry with argon. Around 10 $\mu$ m thick gallium was spread onto the substrates. The experiments were performed in a water-cooled double wall vacuum chamber with an ASTeX<sup>®</sup> Model AX4500 ECR plasma source. H<sub>2</sub> plasma at room temperature was used for about 30 minutes to remove oxide. Subsequently, the gallium film was exposed to N<sub>2</sub> plasma and heated to 900-1000°C by the Boralectric<sup>TM</sup> heater for 1-3 hours at a pressure of 100mTorr.

About 1 $\mu$ m thick gallium was also spin-coated on 2-inches quartz wafers. Similar conditions were performed except that the temperature used for this spin-coated gallium was about 800 °C and the pressure was 140mTorr.

The synthesized gallium nitride films were characterized using Scanning Electron Microscopy (SEM), X-ray Diffraction (XRD) and Raman spectroscopy to study the morphology, orientation and quality, respectively. High resolution TEM was done to study the very thin film of nanocrystalline GaN.

## RESULTS AND DISCUSSION

### Self-oriented GaN growth on the amorphous quartz substrates

The film of gallium on quartz substrates agglomerated into droplets with a considerable size distribution during ramping-up of the substrate temperature. These gallium droplets started to spread due to good wetting characteristic after about 10 minutes at 950°C in nitrogen plasma. Gradually, the nitrogenated melts covered entire substrate and eventually formed a thin gray colored film. The X-ray diffraction spectrum showed primary reflections of (0002) and (0004) planes of wurtzite GaN. See Fig.2 (a). This indicates that the GaN film is c-plane textured. SEM image in Fig. 2(b) also confirmed that the platelet-shaped crystals are oriented in c-plane.

Gallium nitride crystals nucleated from molten gallium and self-oriented with respect to each other due to the mobility of molten gallium. Crystals grew laterally and joined together to form oriented film. The boundaries between some platelets were hardly seen due to complete joining.

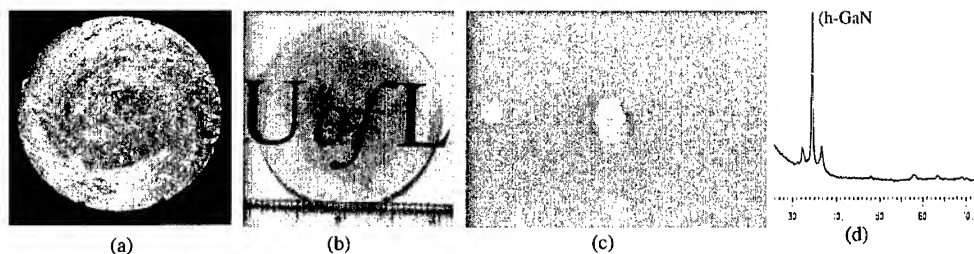


**Figure 7.** Nanocrystalline GaN film on quartz wafer. (a) Spin-coated Ga on quartz, (b) Yellowish GaN film on quartz, (c) SEM image, (d) XRD spectrum

Cross sectional, high-resolution TEM images and selected area diffraction (SAD) patterns of the film were shown in Fig.8. From SAD of (a) and (b) it was shown that the crystal size increased after re-growth on top of one time grown GaN thin film. A sharp GaN-quartz interface was shown in Fig. 8 (c) indicates no epitaxial relationship with the substrates.

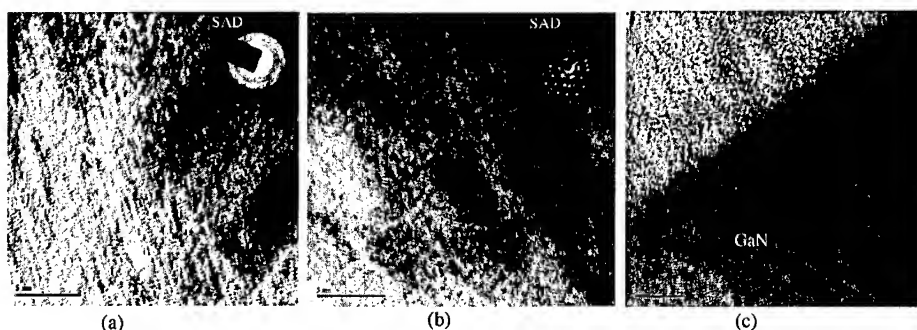


**Figure 8.** HRTEM images of the nanocrystalline GaN film: (a) One time growth sample; (b) Three times growth sample; and (c) Three times growth sample.

## CONCLUSION

Self-oriented GaN films were obtained by direct nitridation at low pressures on both fused quartz and single crystalline sapphire substrates covered with gallium melt. Gallium nitride crystals nucleated out of the nitrogenated gallium and self-aligned with respect to each other during the flow of gallium melts leading to the self-oriented GaN film. This process of using a very thin molten gallium layer as a buffer makes this process uniquely substrates independent. Raman active optical phonon modes were observed for wurtzite gallium nitride with a FWHM 3  $\text{cm}^{-1}$ . Nanocrystalline gallium nitride thin film formed on top of quartz wafer due to high

nucleation density in very thin spin-coated gallium. Cross section HRTEM showed a sharp interface between gallium nitride and quartz substrates.

## ACKNOWLEDGEMENT

We would like to acknowledge US Air Force Research to fund this research through AFOSR Program (Dr.Gerald Witt) and NSF for Career Grant (CTS 9876251). We also thank Dr Apparao Rao at Clemson University for the Raman studies.

## REFERENCES

- [1] S. Nakamura, M Senoh, T. Mukai, *Appl. Phys. Lett.* **62**, 2390 (1993)
- [2] H. Morkoc, S. N. Mohammad, *Science* **267**, 51(1995)
- [3] S. Nakamura, *Mat. Sci. Eng. B-Solid* **43**, 258(1997)
- [4] F.A. Ponce, D. P. Bour, *Nature* **386**, 351 (1997)
- [5] M.A. Khan, M.S. Shur, *Mat. Sci. Eng. B-Solid* **46**, 69(1997)
- [6] C. R. Lee, I. -H. Lee, et al., *J. Cryst. Growth*, **182**, 11(1997)
- [7] C. I. Park, K. Y. Lim, et al., *Thin Solid Films* **401**, 60 (2001)
- [8] M.H. Xie, S.Y. Tong, et al., *Phy. Rev. Letters*, **82**, 2749, (1999)
- [9] E. Kim, A. Bensaoula, et al., *J. Cryst. Growth*, **243**,456(2002)
- [10] I.P. Nikitina, A.E. Nikolaev, Y.V.Melnik, *Diam. Relat. Mat.*, **6**, 1532(1997)
- [11] K. Motoki, T. Okahisa, H. kimura, Y. Kimagai, H. Seki, *J. Cryst. Growth*, **237-239**, 912 (2002)
- [12] S. Porowski, I. Grzegoty, *J. Cryst. Growth*, **178**, 174(1997)
- [13] L. Liu and J. H. Edgar, *Mat. Sci. Eng. R*, **37**, 61, (2002)
- [14] T. S. Zheleva, O. Nam, W. M. Ashmawi, J. D. Griffin, R F. Davis, *J. Cryst. Growth*, **222** 706(2001)
- [15] R. F. Davis, T. Gehrke, K. J. Linthicum, T. S. Zheleva, E. A. Preble, P. Rajagopal, M Mehregany, *J. Cryst. Growth*, **225**,134(2001)
- [16] A.R.A. Zauner, E. Aret, W.J.P. van Enkevort, J.L. Weyher, S. Porowski, J.J. Schermer, *J Cryst. Growth*, **240**, 14(2002)
- [17] S. Porowski, *J. Cryst. Growth*, **166**, 583(1996)
- [18] J.S. Dyck, J.C. Angus, et al., *Appl. Phys. Lett.*, **70**, 179(1997)
- [19] J.C. Angus, et al., *MRS Internet J Nitride research*, **4S1**, G3.23 (1999)
- [20] R. Madar, G. Jacob, J. hallais, R. Fruchart, *J. Cryst. Growth*, **31**, 197(1975)
- [21] D. Elwell, R.S. Feigelson, M.M. Simkins, W.A. Tiller, *J. Cryst. Growth*, **66**, 45(1984)
- [22] H. Chandrasekaran, M. K. Sunkara in *GaN and Related Alloys*, edited by J. E. Northrup, J Neugebauer, D. C. Look, S. F. Chichibu, H. Riechert, (MRS Symp. Proc., **693**, Boston, MA 2001) pp. 159-164
- [23] C.M. Balkas, Z. Sitar, et.al, *J. Cryst. Growth*, **208**, 100(2000)

### Raman Mapping and Finite Element Analysis of Epitaxial Lateral Overgrown GaN on Sapphire Substrates

M. Benyoucef,<sup>1</sup> M. Kuball,<sup>1</sup> B. Beaumont,<sup>2</sup> V. Bousquet,<sup>2</sup> and P. Gibart<sup>2</sup>.

<sup>1</sup> H. H. Wills Physics Laboratory, University of Bristol, Bristol BS8 1TL, United Kingdom.

<sup>2</sup> Centre de Recherches sur l'Hétéroépitaxie et ses Applications (CRHEA-CNRS), Rue Bernard Grégory, Parc Sophia Antipolis, 06560 Valbonne, France.

#### ABSTRACT

Using micro-Raman scattering and finite element (FE) analysis, stress fields in epitaxial lateral overgrown (ELO) GaN fabricated by metalorganic vapor phase epitaxy (MOVPE) on sapphire substrates using a two-step growth method were investigated. Nearly full stress relaxation at the top ELO GaN surface can be achieved by increasing the thickness of ELO GaN to about 50  $\mu\text{m}$ . Reductions in stress variation between window and overgrown regions can be achieved by using a double ELO GaN growth at a much smaller ELO thickness. Increased compressive stress at the coalescence boundary of two adjacent wings of ELO GaN was related to the presence of voids in this area. In the double ELO growth, stress near the top surface was mainly attributed to the presence of voids on top of the upper dielectric mask.

#### INTRODUCTION

GaN and related compounds are the most promising materials for ultraviolet optoelectronics as well as high-power electronic devices. Due to the lack of large area GaN single crystals, the growth of GaN has been developed on foreign substrates such as sapphire, SiC, and Si. Large differences in lattice parameters and thermal expansion coefficients exist between GaN and these substrates, which result in high defect densities ranging from  $10^9$  to  $10^{10}$   $\text{cm}^{-2}$  [1]. Epitaxial lateral overgrowth (ELO) has proven to be a powerful technique for reducing this dislocation density by 3-4 orders of magnitude. This technique allowed the fabrication of blue laser diodes (LDs) with lifetimes of 10 000 hours at room temperature in continuous wave operation [2]. The ELO technique has been applied in both metalorganic vapor phase epitaxy (MOVPE) [3-5] and hydride vapor phase epitaxy (HVPE) [6, 7].

Knowledge of stress fields in ELO GaN is of importance for the understanding of dislocation generation and propagation in ELO GaN, and consequently, for improvements of the process procedures. We report on the Raman scattering and finite element (FE) analysis of stress fields in ELO GaN substrates. Nearly full stress relaxation can be achieved by increasing the thickness of ELO GaN to about 50  $\mu\text{m}$ . Stress variations between window and overgrown regions can be reduced by using a double ELO GaN (D-ELO GaN) growth at a much smaller ELO thickness.

#### EXPERIMENTAL DETAILS

Micro-Raman mapping experiments were performed on single and D-ELO GaN samples using a confocal Renishaw micro-Raman system, with the 488 nm-line of an Ar-laser as

excitation source. Micro-Raman spectra were recorded in  $Z(X,\cdot)\bar{Z}$  back-scattering geometry from the top surface of the ELO GaN. A 50x objective was used to focus and collect the scattered laser light with 1–2  $\mu\text{m}$  spatial and ~2–4  $\mu\text{m}$  depth resolution. Frequency shift resolutions of better than 0.05–0.1  $\text{cm}^{-1}$  were achieved.

The investigated two-step single ELO GaN is grown by MOVPE as follows, illustrated in figure 1 [8]. In the first step, a 2  $\mu\text{m}$  thick GaN layer is grown at a temperature of 1040°C on a sapphire (0001) substrate followed by depositing a 3 nm thick SiN dielectric mask. A set of parallel stripes oriented along the  $[10\bar{1}0]$  direction separated by windows is opened in the mask using standard photolithography and etching techniques. Triangular shaped-GaN stripes are then grown in the mask openings at 1040°C (figure 1(a)). In the second step, growth conditions are modified to achieve coalescence by increasing growth temperature to 1120°C. This second step of the process is characterized by a slow vertical growth rate (figure 1(b)). The empty volume between the triangular GaN seeds formed during the first step (figure 1(a)) is filled by lateral extension during the second step (figure 1(b)). The dislocations propagate through the window first vertically then bend by 90° (figure 1(b)). This results in large sample areas with low dislocation density (figure 1(c)). Thickness of overgrowth for the investigated sample was about 8  $\mu\text{m}$ .

The studied D-ELO GaN structure was grown as follows. The start is the growth of single ELO GaN as described above. In the next step, mask stripes are fabricated in the openings of the first mask which are then overgrown with GaN (a ~6  $\mu\text{m}$ -thick GaN film for the investigated sample). A schematic of the ideal D-ELO process is shown in figure 2. In all cases window and stripe widths of 5  $\mu\text{m}$  were used.

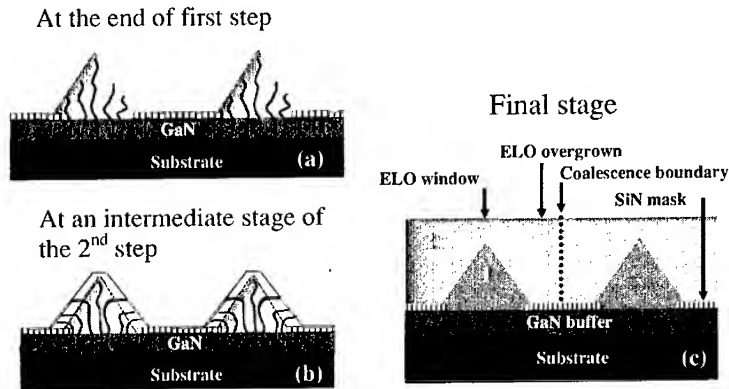


**Figure 1:** A schematic of the two-step single-ELO GaN process: a) at the end of first step, b) at a intermediate stage of the second step, before coalescence. Dashed lines represent the shape at the end of the first step. c) The final stage: high-defect density GaN (1), low-defect density GaN (2), coalescence boundary (dashed line), sapphire substrate (black), silicon nitride mask (striped).

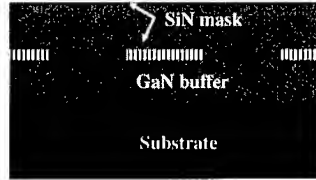


**Figure 2:** A schematic of double ELO GaN.

## RESULTS AND DISCUSSION

### Stress variations in single ELO GaN

Figure 3 shows a line scan of the  $E_2$  frequency obtained by Raman mapping for the single ELO GaN. The inset of figure 3 shows an SEM image of this sample near the coalescence boundary displaying a void formed on top of the dielectric mask. The Raman spectra were taken from near the top surface. Maxima in the  $E_2$  phonon frequency of  $\approx 569.9 \text{ cm}^{-1}$  are evident in the window regions of the ELO GaN. Compressive stress, which is known to increase the  $E_2$  phonon frequency [9], is present and decreases from the window to the ELO GaN wing. In the ELO GaN wing a stress of about 0.86 GPa is present ( $2.9 \text{ cm}^{-1}/\text{GPa}$  for biaxial stress) [9]. Note that GaN grown on sapphire substrates is under compressive biaxial stress. A difference in compressive biaxial stress of  $\Delta\sigma \approx 0.14 \text{ GPa}$  was determined from the  $E_2$  phonon frequency difference of  $0.4 \text{ cm}^{-1}$  between ELO GaN window and overgrown region. Increased stress is visible at the

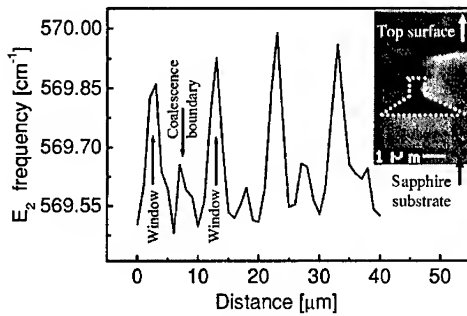


**Figure 3:** Line scan of  $E_2$  phonon frequency of ELO GaN recorded near the top surface. The inset shows an SEM micrograph of the void present at the coalescence boundary between two adjacent wings (overgrown region). Its shape is indicated by a dotted line.

coalescence boundary with a rise in the  $E_2$  phonon frequency of  $\sim 0.1 \text{ cm}^{-1}$  corresponding to compressive uniaxial stress of 0.07 GPa due to the presence of voids at the coalescence boundary (inset of figure 3).

#### **Reduction in stress: increasing the thickness of single ELO GaN**

Studying stress distributions near the ELO GaN top surface is of importance. This stress can influence piezoelectric field effects and therefore the performance of device structures grown on such areas. In order to obtain the optimum ELO thickness to reach full stress relaxation, finite element (FE) analysis was performed, using the code ABAQUS [10]. The simulation applied a static thermal load of  $-1100^\circ\text{C}$ , i.e. the ELO GaN structures were heated to  $1120^\circ\text{C}$ , then cooled to room temperature ( $20^\circ\text{C}$ ). More details about FE analysis of ELO GaN can be found in [11,12]. Stress near the top surface in the overgrown region versus ELO GaN thickness is shown in figure 4. Stress near the ELO top surface decreases with increasing ELO thickness. As example, a reduced stress of  $\sim -0.05 \text{ GPa}$  near the top surface in the overgrown region was found for a sample with  $50 \mu\text{m}$  ELO GaN overgrowth, whilst a significantly larger stress of  $\sim -0.29 \text{ GPa}$  was determined for a similar sample with only  $8 \mu\text{m}$  ELO GaN overgrowth. This is on the same order of magnitude as found for the investigated single ELO GaN sample (figure 3). ELO GaN growth of about  $50 \mu\text{m}$  thickness is necessary to achieve nearly full stress relaxation near the top surface.

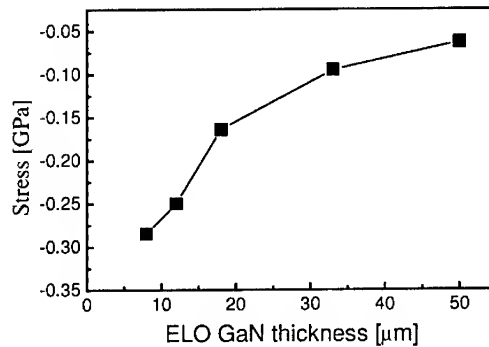


**Figure 4:** Stress in the overgrown region near top surface as function of ELO GaN thickness obtained by finite element analysis.

#### **Reduction in stress variations: using double ELO GaN growth**

A large difference in stress between window and overgrown regions was found for single ELO GaN (figure 3). An alternative growth method to reduce this stress variation is D-ELO-GaN. A schematic of the ideal D-ELO process is shown in figure 2. An SEM micro-graph of the investigated sample is depicted in figure 5(a). Small voids were present on top of both masks. Alignment of the second ELO mask was approximately achieved. Figure 5(b) illustrates a typical

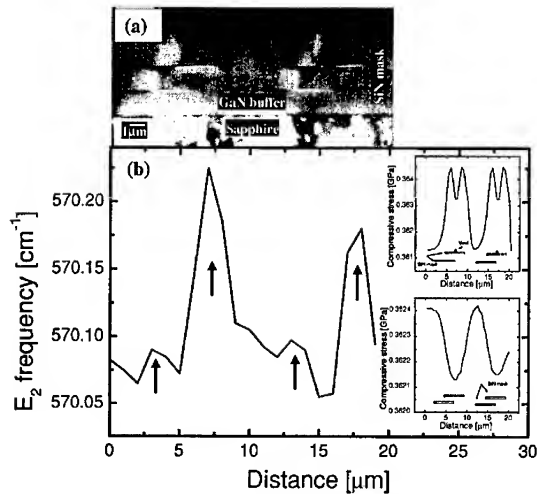


**Figure 5:** (a) Scanning electron microscopy (SEM) micrograph of double ELO (D-ELO) GaN grown on sapphire substrate, (b) line scan of  $E_2$  phonon frequency of ELO GaN recorded near the top surface. The inset in (b) shows stress variations in GPa near the top surface obtained by FE analysis: double mask with voids only on the upper mask and double mask without voids.

variation in  $E_2$  phonon frequency found near the top surface of the D-ELO GaN. Two maxima in  $E_2$  phonon frequency, i.e., compressive stress within the 10 μm period of the D-ELO GaN are visible (marked by arrows), different in magnitude, repeating with the D-ELO period. Only a small difference in stress of ~0.04 GPa between the window (between SiN masks of upper mask) and wing regions (on top of upper SiN mask) was found. This is significantly smaller than values of ~0.14 GPa for single ELO GaN (figure 3).

To understand the origin of the two maxima in compressive stress in D-ELO GaN, FE analysis was performed. Layer thickness, void shapes and void sizes very similar to the investigated sample were used in the simulation. The lower inset in figure 5(b) shows the result of the FE analysis of a D-ELO structure where the voids on top of the upper and the lower mask were neglected. A distinctly different stress field than the experimentally measured one is visible. A FE analysis only with voids on the upper mask was also performed. The result of this simulation is shown in the upper inset of figure 5(b). The graph shows two maxima in compressive stress similar to the Raman results of figure 5(b), although, more symmetric in intensity than experiment. This illustrates that mainly the presence of the upper voids is responsible for the stress distribution visible in the investigated D-ELO GaN sample with its characteristic two maxima in compressive stress. We note that the asymmetry in intensity of the two maxima was found to be induced by the additional presence of voids on the lower mask.

## CONCLUSIONS

Using micro-Raman scattering and FE analysis, we have evaluated single and double ELO GaN on sapphire substrates. Nearly full stress relaxation at the top ELO GaN surface can be achieved by increasing the thickness of ELO GaN to about 50  $\mu\text{m}$ . As example, a reduced stress of  $\sim -0.05$  GPa near the top surface in the overgrown region was found for a sample with 50  $\mu\text{m}$  ELO GaN overgrowth, whilst a significantly larger stress of  $\sim -0.29$  GPa was determined for a similar sample with only 8  $\mu\text{m}$  ELO GaN overgrowth. Reduction in stress variations between window and overgrown regions can be achieved by using a double ELO GaN growth method at a much smaller ELO GaN thickness.

## REFERENCES

1. T. S. Zheleva, O. -H. Nam, W. M. Ashmawi, J. D. Griffin, R. F. Davis, *J. Cryst. Growth*, **222**, 706 (2001).
2. S. Nakamura, M. Senoh, S. Nagahama, N. Iwasa, T. Matsushita, and T. Mukai, *MRS Internet J. Nitride Semicond.* **4S1**, G1.1 (1999).
3. H. Marchand, X. H. Wu, J. P. Ibbetson, P. T. Fini, P. Kozodoy, S. Keller, J. S. Speck, S. P. DenBaars, and U. K. Mishra, *Appl. Phys. Lett.* **73**, 747 (1998).
4. O. -H. Nam, M. D. Bremser, T. S. Zheleva, and R. F. Davis, *Appl. Phys. Lett.* **71**, 2638 (1997).
5. D. Kapolnek, S. Keller, R. Vetury, R. D. Underwood, P. Kozodoy, S.P. Denbaars, and U. K. Mishra, *Appl. Phys. Lett.* **71**, 1204 (1997).
6. A. Usui, H. Sunakawa, A. Sakai, and A. A. Yamaguchi, *Jpn. J. Appl. Phys., Part 2* **36**, L899 (1997).
7. A. Sakai, H. Sunakawa, and A.Usui, *Appl. Phys. Lett.* **71**, 2259 (1997).
8. P. Vennéguès, B. Beaumont, V. Bousquet, M. Vaille, and P. Gibart, *J. Appl. Phys.* **87**, 4175 (2000).
9. F. Demangeot, J. Frandon, M. A. Renucci, O. Briot, B. Gil, and R. L. Aulombard, *Solid State Commun.* **100**, 207 (1996).
10. ABAQUS Standard V.6.0, Hibbitt, Karlsson & Sorensen Inc., 1080 Main Street, Pawtucket, R.I. 02860, U.S.A.
11. M. Benyoucef, M. Kuball, G. Hill, M. Wisnom, B. Beaumont, and P. Gibart, *Appl. Phys. Lett.* **79**, 4127 (2001).
12. M. Benyoucef, M. Kuball, B. Beaumont, and P. Gibart, *Appl. Phys. Lett.* **80**, 2275 (2002)

### Characterization of Dark-Block Defects in Cantilever Epitaxial GaN on Sapphire

P. P. Provencio, D. M. Follstaedt, N. A. Missert, D. D. Koleske, C. C. Mitchell, A. A. Allerman and C. I. H. Ashby  
Sandia National Laboratories, Albuquerque, NM 87185-1056

#### ABSTRACT

Cantilever epitaxy of GaN on sapphire has been augmented by the use of initial faceted GaN growth on narrow sapphire mesas ( $< 1\mu\text{m}$ ) in order to turn remaining threading dislocations from vertical to horizontal, and thus reduce the overall dislocation density at the surface where devices would be placed. With this modification, isolated non-radiative block-like defect areas have been introduced that hinder optical and electronic material performance. Here we characterize these defects with microscopy, and show that they are arrays of lateral dislocations, with cracks and voids along their centerlines. We deduce that they result when tilted GaN is joined to neighboring oriented material. Their presence is independent of the type of nucleation layer used.

#### INTRODUCTION

The favorable semiconductor properties of GaN make it an important material for optical and electronic applications. Hetero-epitaxial growth of hexagonal GaN results in a high density of vertical threading dislocations (VTDs) that limit device performance [1]. Lateral growth methods have been developed to reduce VTDs. Methods such as ELO [2], LEO [3] and FACELO [4] seed vertical GaN growth through openings in  $\text{SiO}_2$  or  $\text{Si}_3\text{N}_4$  masking layers, and then laterally grow GaN with low dislocation densities over the masks. Pendeo-epitaxy [5] uses mesas patterned into GaN previously grown on a substrate to seed lateral growth of material suspended over trenches between the mesas; the suspended GaN also has low dislocation density. Cantilever epitaxy (CE) [6] was developed to reduce VTDs by initiating growth on mesas patterned directly on (0001) sapphire substrate followed by lateral growth of GaN suspended over trenches etched into the sapphire as in Fig. 1. CE has an important advantage over the other methods in that it requires only a single growth sequence in the metallorganic chemical vapor deposition reactor. Details of our growth techniques are given in Ref. [7]. Using an AlN nucleation layer and substrates etched to produce narrow mesas ( $< 1\mu\text{m}$ ) extending in the  $[1-100]$  GaN direction, we compared CE-GaN microstructures for two different initial vertical growths [8]: 1) at  $1050^\circ\text{C}$  with nearly vertical  $\{11-20\}$  sidewall facets and a (0001) top facet, and 2) at  $950^\circ\text{C}$  for slanted  $\{11-22\}$  facets as in Fig. 1. The temperature was then increased to  $1100^\circ\text{C}$  for lateral growth of the cantilevers. The slanted facets turned VTDs emerging from the mesas to horizontal (onto the basal plane), giving a lower overall density at the surface. Most recently, we have combined a low-VTD GaN nucleation layer [9] (instead of AlN) with this faceted CE growth to reduced the overall density of VTDs to  $2-3 \times 10^7/\text{cm}^2$  [10].

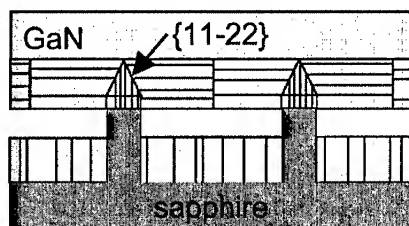


**Figure 1.** Cross-section schematic of CE-GaN with faceted growth initiated on mesas and extended laterally to form cantilevers over trenches etched in sapphire. Unwanted GaN also grows in the trenches.

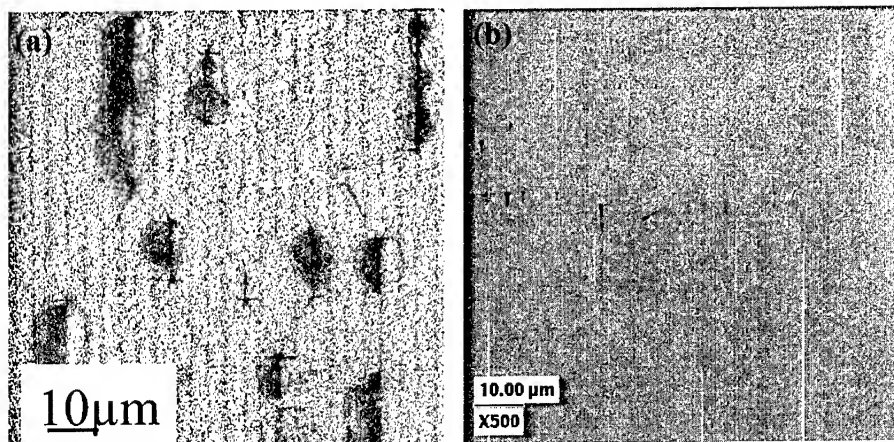


**Figure 2.** (a) Scanning broadband CL and (b) SEM images of CE-GaN grown with the low-VTD nucleation layer in an area with dark-block defects. Image (b) (slightly shifted from (a)) shows bright-contrast ridges in one-to-one correspondence with the centerline of each dark defect in (a). Dark circular loops are resolved at some defects in (a), indicating dislocations bowing laterally in the growth plane are present. Dark lines emerging from the ends of the defects are also seen.

Characterizations of our CE GaN by scanning cathodoluminescence (CL), scanning electron microscopy (SEM), atomic force microscopy (AFM), plan-view transmission electron microscopy (TEM), and cross-sectional TEM (XTEM) demonstrated the low VTD density, but also found isolated defect regions. Given the desirable low densities achieved with these methods, it is important to determine the origin of the defects and eliminate them. In Fig. 2, CL and SEM were done on the same area of CE-GaN. The CL image in Fig. 2a shows dark-contrast regions with low light emission, where each region has similar width and a dark central line with lines bowing outward along the length. Such non-radiating regions were also seen in the earlier material grown with faceting and the AlN nucleation layer. In many images these regions are rectangular, and we refer to them as “dark-block” defects. The SEM image in Fig. 2b shows vertical edges parallel to the mesas that have a one-to-one correspondence with the dark centerlines in the CL image.

To diagnose the origin of these defects, a faceted CE-GaN growth with low-VTD nucleation layer was stopped before cantilever coalescence and examined by SEM. Figure 3 shows stripes of GaN with un-coalesced cantilevers centered over the mesas. Also seen are dark and light lines running perpendicular across the stripes. An AFM image of a dark line across a stripe like that in Fig. 4 indicates a tilt along the direction of the mesa, and shows a step of 120 nm height. This tilted material and step configuration correspond to the light and dark lines in SEM.

Figure 5 shows a SEM image taken from CE-GaN grown to coalescence and cleaved. The image gives both cross-sectional and planar views and shows a crack at the coalescence. The left cantilever is flat and has overgrown the right cantilever, leaving a ridge and crack. The top of the image shows that the crack goes along the cantilever coalescence and ends with a void. Beyond the void there is flat GaN, and the image shows a ridge running nearly perpendicular to the crack that makes the transition from tilted to flat GaN. The ridge, crack, and void accommodate this

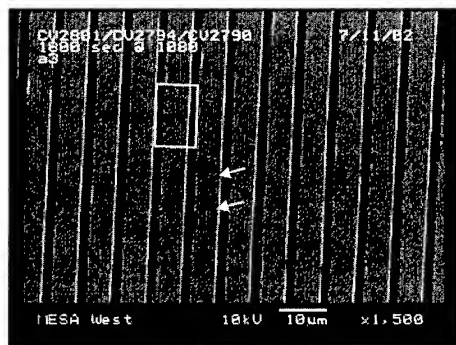


**Figure 3.** SEM image of GaN cantilever/mesa stripes before coalescence. Note the lines crossing the stripes, and in one instance two lines (arrowed) with opposite contrast.

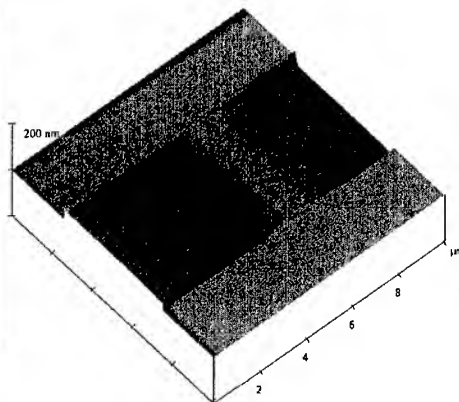


**Figure 4.** AFM image of dark line across a stripe (like that in the area outlined in Fig. 2), showing a 120-nm high step.

transition from flat to tilted regions and form a rectangular region similar to defects in some CL images. Similar cracks along coalescences are seen in CE-GaN with the AlN nucleation layer.

Both plan-view TEM and XTEM were used to characterize the microstructure and tilt configuration of dark-block defects. Figure 6 shows XTEM of a defected cantilever coalescence. There is a partial crack through the coalescence; in other instances, cracks extend completely through the material. The left cantilever has overgrown the right one and is 30 nm higher than the right. The crack curves to the right, i.e., toward the overgrowth direction at the surface, just as seen with SEM in Fig. 5. Centers of dark contrast are seen along the coalescence crack and indicate strain, and lateral dislocations are observed in the cantilevers halfway up and near the surface. The two cantilevers show marked difference in contrast indicating orientation difference, and therefore selected area diffraction (SAD) patterns were obtained from each side. When the left cantilever was oriented along the [1-100] zone (highly symmetric, centered pattern), the SAD pattern from the right cantilever indicated a  $1.7^\circ$  tilt toward the  $c$  direction (vertically in Fig. 5). This tilt along the stripe direction that was also indicated in the SEM and AFM images of Figs. 3 and 4. Examination of several defected coalescences gave tilt differences of  $0.5$ - $2.0^\circ$  with the same direction. Such tilting is not found between cantilevers across non-defected coalescences.

Isolated dark-contrast blocks are found in plan-view TEM over large areas. Images like Figs. 7, 8 and 9 show that these blocks are made up of lateral dislocation arrays bowing outward from a cantilever coalescence. These dislocations often bow laterally as far as the next coalescence. The centerline along the coalescence is a crack, at least partially continuous, and voids are usually found at each end. Figure 8 shows low and higher magnification views of the end of a dark-block defect. The line extending perpendicular to the crack appears to be made of multiple dislocations. The overall shape of the defect appears rectangular because at the center is a straight crack with the lateral dislocations bowing to the next coalescence, and the perpendicular dislocations come out of each end. Two additional dislocations extend outward in a "Vee" from the void. Both they and the perpendicular dislocations are seen in the CL image of dark-block defects in Fig. 2a; thus we know they are inherent defect features and not artifacts of TEM specimen preparation.

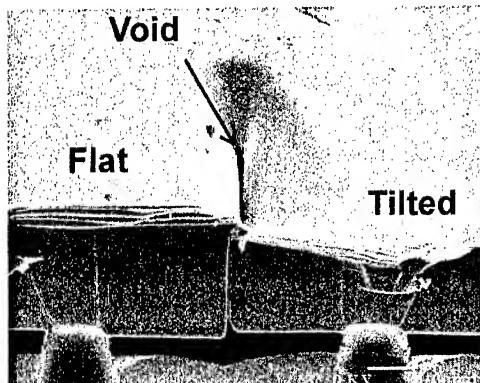


**Figure 5.** Cross-section SEM image of CE-GaN at a defected coalescence of two cantilevers.

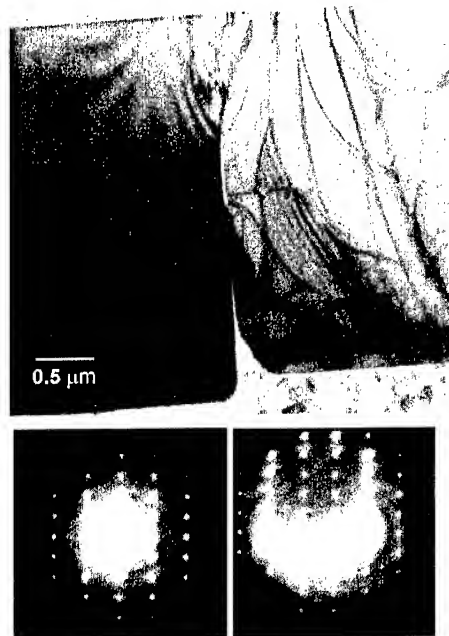


**Figure 6.** Top: XTEM showing a crack at the coalescence between two cantilevers. Below: Diffraction patterns from the cantilevers; the right one is tilted by  $1.7^\circ$  toward the  $c$  axis.



**Figure 7.** Plan-view TEM of a dark-block defect with voids at each end and an array of lateral dislocations bowing from centerline.

The general microstructural features seen in many dark-block defects are shown in the schematic in Fig. 9. These include a partially continuous crack along the centerline at a cantilever coalescence with voids at each end, dislocations bowing outward from the centerline, and perpendicular and “Vee” dislocations at the ends. These features seen with TEM are consistent with all the defect features noted with SEM, AFM, and CL. The non-radiative defects seen with CL thus result from the coalescence of a flat and a tilted cantilever. Since dark-block defects were also observed in CE GaN grown with both GaN and AlN nucleation layers, this layer does not appear responsible for them. Since non-radiative dark-block defects limit optical emission and electronic properties of GaN, their elimination can be expected to improve material quality and device performance.

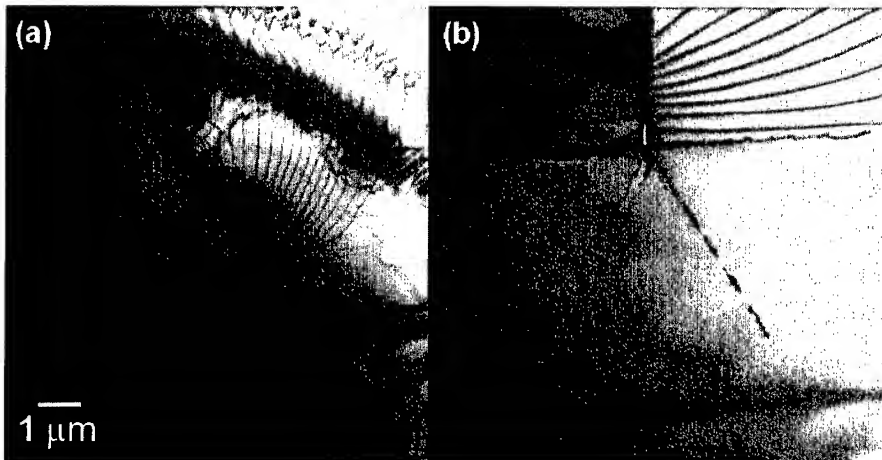


**Figure 8.** (a) Plan-view TEM image of the end of a dark-block defect showing lateral dislocations bowing outward from the centerline. (b) Enlargement of the end of the centerline showing a void, a perpendicular defect line, and dislocations pointing outward in a "Vee".



**Figure 9.** Plan-view TEM showing two dark-block defects (lower center and lower right) whose dislocations overlap and perhaps interact. Note the voids at the ends of the centerline, and Vee dislocations and perpendicular defect lines emerging from the ends. VTDs over mesas and at coalescences are seen in the upper part of the image away from the dark-block defects. Some VTDs interact with a lateral dislocation in the defect (left of center).

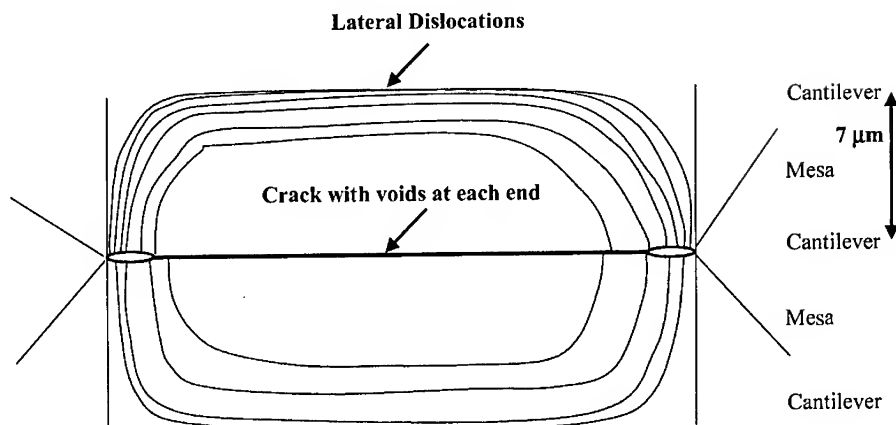


**Figure 10.** Schematic of microstructural features in typical dark-block defects: a centerline crack with voids at each end, lateral dislocations bowing outward, perpendicular dislocation lines at each end, and dislocations emerging in a Vee. These give an overall rectangular shape.

## ACKNOWLEDGEMENTS

We thank Mike Moran and Adam Norman for developing TEM specimen preparations for these difficult CE-GaN on sapphire materials. Sandia is a multiprogram laboratory operated by Sandia Corporation, a Lockheed Martin Company, for the United States Department of Energy under Contract DE-AC04-94AI85000.

## REFERENCES

1. J. S. Speck and S. J. Rosner, *Physica B* **273-274**, 24 (1999).
2. T. S. Zheleva, O.-H. Nam, M. D. Bremser and R. F. Davis, *Appl. Phys. Lett.* **71**, 2472 (1997).
3. D. Kapolnek, S. Keller, R. Vetury, R. D. Underwood, P. Kozodoy, S. P. DenBaars and U. K. Mishra, *Appl. Phys. Lett.* **71**, 1024 (1997).
4. K. Hiramatsu, K. Nishiyama, M. Onishi, H. Mizutani, M. Narukawa, A. Motogaito, H. Miyake, Y. Iyechika and T. Maeda, *J. Cryst. Gro.* **221**, 316 (2000).
5. K. Linthicum, T. Gehrke, D. Thomson, E. Carlson, P. Rajagopal, T. Smith, D. Batchelor and R. Davis, *Appl. Phys. Lett.* **75**, 196 (1999).
6. C. I. H. Ashby, C. C. Mitchell, J. Han, N. A. Missert, P. P. Provencio, D. M. Follstaedt, G. M. Peake and L. Griego, *Appl. Phys. Lett.* **77**, 3233 (2000).
7. M. E. Coultrin, C. C. Willan, M. E. Bartram, J. Han, N. A. Missert, M. H. Crawford and A. G. Baca, *MRS Internet J. Nitride Semicond. Res.* **4S1**, G6.9 (1999).
8. D. M. Follstaedt, P. P. Provencio, N. A. Missert, C. C. Mitchell, D. D. Koleske, A. A. Allerman and C. I. H. Ashby, *Appl. Phys. Lett.* **81**, 2758 (2002).
9. D. D. Koleske, A. J. Fischer, A. A. Allerman, C. C. Mitchell, K. C. Cross, S. R. Kurtz, J. J. Figel, K. W. Fullmer and W. G. Breiland, *Appl. Phys. Lett.* **81**, 1940 (2002).
10. D. M. Follstaedt, P. P. Provencio, D. D. Koleske, C. C. Mitchell, A. A. Allerman, N. A. Missert and C. I. H. Ashby, paper L1.8 in these proceedings.

## Study of the Origin of Misorientation in GaN Grown by Pendeo-Epitaxy

D.N. Zakharov<sup>1</sup>, Z. Liliental-Weber<sup>1</sup>, A. M. Roskowski<sup>2</sup>, S. Einfeldt<sup>3</sup>, and R.F. Davis<sup>2</sup>

<sup>1</sup>Lawrence Berkeley National Laboratory, MS 62-203, Berkeley, CA 94720

<sup>2</sup>North Carolina State University, Department of Materials Science and Engineering, Campus Box 7907, Raleigh, NC 27695

<sup>3</sup>University of Bremen, Institute of Solid State Physics, P.O. Box 330440, 28334 Bremen, Germany

### ABSTRACT

Growth of pendeo-epitaxial (PE) layers introduces misorientation between the seed layers and the overgrown wing layers. The origin of this misorientation has been studied by Transmission Electron Microscopy (TEM) using a set of samples in which subsequent procedures utilized in PE were applied, i.e. growth of GaN template, stripe etching, annealing at the growth temperature of the PE layers and final PE growth. It was shown that etching of seed-strips did not change the type of defects or their distribution. However, heating to the PE growth temperature drastically modified the surface and V-shaped pits were formed. The surface became smooth again after the PE growth took place. Overgrowth of the V-shaped pits resulted in formation of edge threading dislocations over a seed-stripe region with a dislocation density of  $8.0 \times 10^8 \text{ cm}^{-2}$ . Formation of new edge dislocations over the seed can have an influence on the misorientation between the PE grown regions.

### INTRODUCTION

GaN layers are usually grown on sapphire or SiC substrates with either an AlN or a GaN buffer layer. The large misfit in lattice parameters and in thermal expansion coefficients results in a high density of misfit and threading dislocations in the GaN layers ( $10^9$ - $10^{10} \text{ cm}^{-2}$ ). Although light emitting diodes with high efficiency have been produced despite the high dislocation density in this material, other applications such as lasers require dislocation reduction. Methods to reduce dislocation density include lateral epitaxial overgrowth (LEO) [1-3] or pendeo-epitaxy (PE) [4-6]. Both these methods result in a much lower dislocation density in the overgrown areas, but at coalescence fronts (CF) the dislocation density often exceeds or is comparable to the dislocation density observed using conventional growth on SiC or  $\text{Al}_2\text{O}_3$  substrates. Misorientation (such as tilt/twist) between the seed and overgrown wings has been reported [3, 6-8]. Typical values of misorientation are 1-2° for LEO or PE with mask applied on the seed-strips and 0.05-0.3° for mask-free PE. In order to further reduce dislocations in material grown by PE and understand what leads to the wing misorientation, structural studies were performed for each step of the PE process using TEM.

### EXPERIMENTAL

1  $\mu\text{m}$  GaN layers were grown by metalorganic vapor phase epitaxy on 6H-SiC (0001) substrates with a 0.1  $\mu\text{m}$  thick AlN buffer layer. GaN stripes along [1100] were fabricated by etching through the epitaxial layers into the substrate with an inductively coupled plasma. The stripe width and the stripe period were 3-5  $\mu\text{m}$  and 5-12  $\mu\text{m}$ , respectively. Subsequent mask-free

pendeoepitaxial growth was performed (Fig.1) at temperatures between 1080 and 1100 °C using a V/III ratio of 6200 and 1300, respectively. These growth conditions resulted in either coalesced or uncoalesced films. Further details on the growth process can be found in [9].

The set of samples from different stages of PE growth included: GaN template, followed by samples which underwent the etching procedure to form the stripes, and then subsequently samples where annealing for 10 min at 1000 °C and 20 Torr under a mixture of ammonia and hydrogen was performed. The annealing atmosphere corresponded to the standard gas flow conditions used for PE growth, whereas the annealing temperature was slightly lower than the PE growth temperature to limit the degradation of the GaN surface due to decomposition. The annealing time is significantly longer than the time used to stabilize the temperature prior to the PE growth, and it is assumed to be sufficiently long to simulate the thermal load on the stripes during PE growth. Finally samples with PE growth were also studied.

Samples were studied by transmission electron microscopy (TEM) using a JEOL 3010 and Topcon 002B microscopes operated at 300kV and 200kV respectively. Cross-sectional samples for TEM were prepared in a direction perpendicular to the seed-stripe. A standard bright or dark field method for determination of dislocation Burgers vectors was utilized.

## RESULTS AND DISCUSSION

The starting GaN sample used for the PE process had a smooth surface (Fig.2a). Bright field images in two-beam conditions obtained for two perpendicular sets of diffraction vectors ( $g$ ) revealed the presence of pure screw ( $s$ ) and pure edge ( $e$ ) dislocations. Occasionally mixed-type dislocations ( $m$ ) were observed. In Fig.2a, taken with  $g=1\bar{1}20$ , where edge and mixed dislocations should be in a contrast, much higher dislocation density was observed in the area close to the GaN/AlN interface compared to the area near the GaN surface, as observed earlier [10]. The dislocation density measured within the GaN thicknesses  $0 < t < 0.5\mu\text{m}$  was  $19 \times 10^8 \text{cm}^{-2}$ , whereas for thicknesses  $0.5 < t < 1.0\mu\text{m}$  it was  $5.4 \times 10^8 \text{cm}^{-2}$ .

The next step in the PE process was etching of seed-stripes. As a result seed-stripes with width of  $4.9\mu\text{m}$  and separation of  $5.5\mu\text{m}$  were obtained. The etching did not change the GaN layer thickness, or the surface morphology and dislocation density (Fig.2b).

The sample with etched stripes was used for further growth of GaN. In order to learn if this process step introduces any changes to the GaN seeds via the thermal load during PE growth, the sample with etched stripes was annealed for 10min at 1000°C. TEM studies of a cross-section sample show that the annealing process drastically changed the surface morphology of the GaN seeds. The surface became rough and V-shaped pits were formed. The peak-to-valley roughness of the GaN surface was about 150nm (Fig.2c). The angle between walls of the V-shaped pits was measured to be about 60°. This value is very close to the angle of

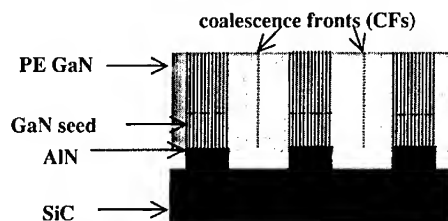


**Fig1.** Schematic diagram of the pendeo-epitaxial layer. Dislocations are shown by vertical lines.

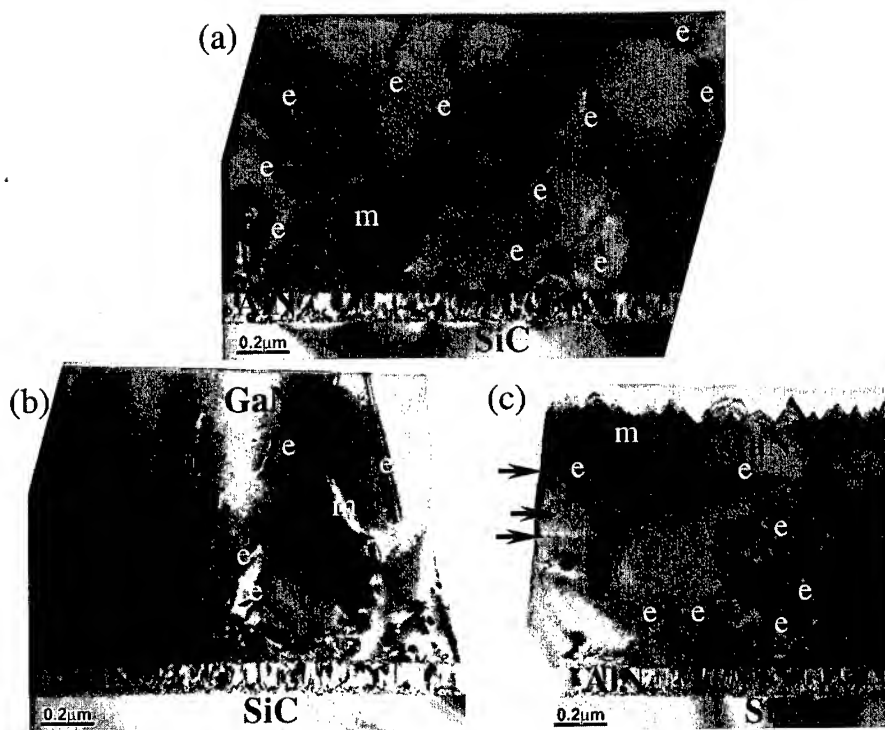


**Fig.2.** Bright field images obtained in two beam condition with  $g=1\bar{1}20$ . (a) as deposited, (b) etched, (c) etched and annealed samples. Some edge (e) and mixed (m) dislocations are marked. Note appearance of edge dislocations with dislocation lines close to GaN c-plane in the annealed sample (marked by arrows).

$56.1^\circ$  formed between  $(10\bar{1}1)$  and  $(101\bar{1})$  planes in GaN. It is concluded that walls of the pit are formed by the set of six  $\{10\bar{1}1\}$  planes making an inverse pyramid with six fold symmetry. Such V-shaped inverted pyramids are often observed on the surface of GaN layers [11]. It was suggested [11] that growth on  $\{10\bar{1}1\}$  planes is the slowest compared to on  $\{1\bar{1}00\}$ ,  $\{1\bar{2}10\}$  and  $\{0001\}$ . It appears from this study that the etching process on these planes is faster. From the measurement of the average layer thickness ( $0.9\mu\text{m}$ ) it appears that some loss of material took place during annealing. It is noted that a degradation of the stripe surface is only observed for the annealing but not for PE growth. In the latter case the decomposition of the GaN is overcompensated by the growth such that an atomically smooth surface is maintained [9].

Dislocation density in the annealed sample remained almost the same at the area close to the AlN buffer layer ( $23 \times 10^8 \text{ cm}^{-2}$ ,  $0 < t < 0.5\mu\text{m}$ ); however it increased to the  $17 \times 10^8 \text{ cm}^{-2}$  for the thickness region of  $0.5 < t < 0.9\mu\text{m}$ . The increase in dislocation density occurred mainly due to a new type of defects observed in the upper part of the sample (marked by arrows on Fig.2c). The dislocations are in contrast for  $g=1\bar{1}20$  and out of contrast for  $g=0002$  which suggest that they are edge dislocations with dislocation line lying in the GaN c-plane with Burgers vectors

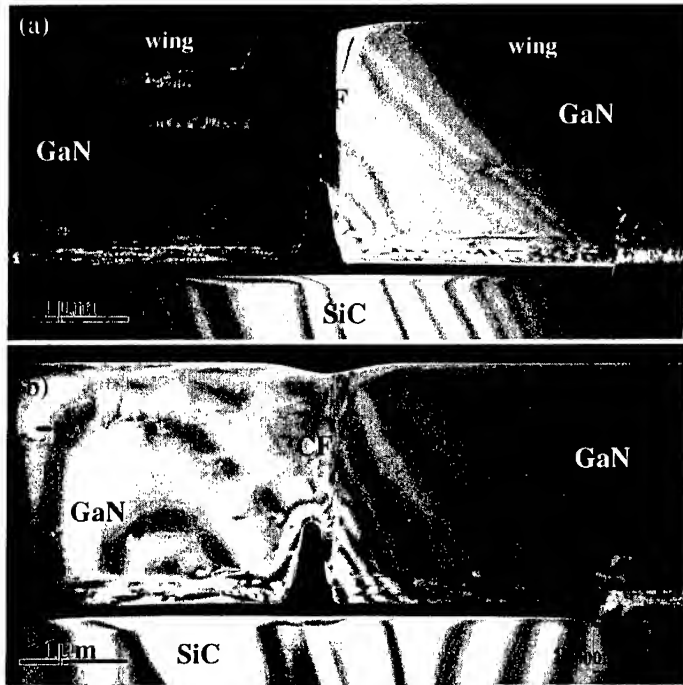


**Fig.3.** Cross-section dark field images from the PE sample taken with  $g$ -vectors (a)  $g=1120$ , different contrast showing an evidence of wings misorientation, (b)  $g=0002$ . There is a crack formation at the coalescence front (CF).

$b=1/3\langle 1120 \rangle$ .

The final sample, with PE growth performed, had a total GaN thickness of  $2.26\mu\text{m}$ . After the growth the sample surface was smooth. There were no V-shape pits observed. This suggests that any V-shaped defects formed previously were overgrown. Dark field images (Fig.3a,b) taken with two perpendicular  $g$ -vectors ( $1120$  and  $0002$ ) revealed a characteristic void and crack formation at the CF. However, it is not clear yet if the cracks were formed during growth or during the TEM sample preparation procedure. Almost all dislocations observed in wing areas were edge type. The dislocation density in wing regions was about  $8.3 \times 10^7 \text{ cm}^{-2}$ , except for the highly defected area  $\sim 250\text{nm}$  from the bottom surface of the overgrown material. Change of contrast along defect lines from dark to bright on the image obtained with  $g=1120$  suggests that this is a dislocation with line direction lying in the GaN  $c$ -plane at a specific angle to  $[1100]$ . Taking into account absence of contrast from the dislocations in  $g=0002$  and six fold symmetry of  $(0001)$  GaN one can conclude that this is Shockley partial dislocations bordering a stacking fault in the crystal. Observation of such defects in two beams condition for  $g=1010$  revealed the contrast from stacking faults. Some of them propagate from the sidewall inside a wing and are terminated by the above-mentioned Shockley partial dislocations with Burgers vectors  $b=1/3\langle 1100 \rangle$  [12,13]. Some probably begins at AlN/GaN interface to accommodate mismatch in  $c$  lattice parameters.

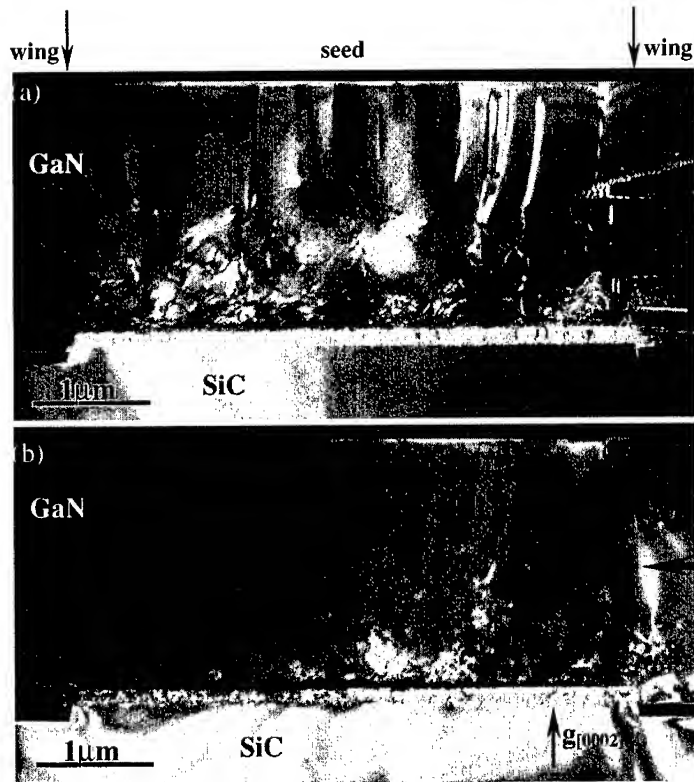


**Fig.4.** Cross-section dark field images from the PE sample (seed region) taken with two perpendicular  $g$ -vectors: (a)  $g=1120$ , edge and mixed dislocations are visible, (b)  $g=0002$ , screw and mixed dislocations are visible. Large arrows show the surface level for the seed-stripe before overgrowth.

The difference in contrast between the wings in Fig.3a suggests an angular misorientation. A change of contrast was also observed between the seed and the wing (see right side of the Fig.3a). This suggests that the wing bends with respect to the seed. From this study it is clear that there are two misorientations in the sample: one between the two wings and the second between a wing and adjacent seed-stripe region. X-ray diffraction indicated a wing tilt of  $0.26^\circ$  for this sample.

Since the surface of the final sample, where PE growth was completed, was smooth over the seed-stripe suggests that during the growth V-shaped pits were overgrown. Based on dark field images taken with two perpendicular  $g$ -vectors (Fig.4a,b) there are dislocations in the overgrown seed region. Most of them are edge dislocations. The density of the edge dislocations was about  $8.0 \times 10^6 \text{ cm}^{-2}$ , which is approximately one order of magnitude more, than the density of dislocations in the wing areas ( $8.3 \times 10^7 \text{ cm}^{-2}$ ). Two large arrows show the level of 1μm thick GaN seed before PE process. One can clearly see that the edge dislocations appear approximately at

the level where V-shaped pits were observed in the annealed sample. Therefore, these pits probably act as a source of edge dislocations. Formation of additional edge dislocations, e.g. inserting (or removing) of half planes in the upper part of the layer grown over the seed would lead to the deformation (such as tilt) of the adjacent wing areas. Since this deformation might be different in different areas of the sample tilt/twist can be introduced between the wings and also between the seeds and the wings. Then it might affect tilt arising due to elastic relief of thermally induced stress described in [8].

It should be stressed that edge dislocations observed earlier in the annealed sample with etched seed-strips (marked by arrows in Fig.2c) were not present in seed-stripe regions of PE overgrown sample.

In summary, we investigated a set of samples from at each step of the PE process. It was found that etching of a GaN layer into seed-strips does not change the layer's surface morphology, or the dislocation distribution. However, annealing of the etched sample at a temperature comparable to GaN growth temperature resulted in formation of V-shapes pits on the surface and edge dislocations in the upper part of the GaN layer. V-shape pits probably acts as a source of edge threading dislocations observed over the seed-stripe region in the PE overgrown sample. These edge dislocations may influence observed misorientation at seed/wing and wing/wing interfaces.

## ACKNOWLEDGMENTS

This work was supported by AFOSR, Order No. FQ86710200852, through the U.S. Department of Energy under Contract No. DE-AC03-76SF00098. The authors would like to thank W. Swider for TEM sample preparation and the National Center for Electron Microscopy at LBNL for the opportunity to use its facilities.

## REFERENCES

1. O. Nam, T. Zheleva, M. Bremser, and R.F. Davis, *J. Electron Matter.* **27**, 333 (1998)
2. H. Marhard, X.H. Wu, J.P. Ibbetson, P.T. Fini, P. Kozodoy, J.S. Peck, S.P. DenBaars, and U.K. Mishra, *Appl. Phys. Lett.* **73**, 747 (1998)
3. Z. Liliental-Weber and D. Cherns, *J. Appl. Phys.*, **89**, 7833 (2001)
4. T. Zeleva, S. Smith, D. Thomson, K. Linthicum, P. Rajagopal, and R.F. Davis, *J. Electron Matter.* **28**, L5 (1999)
5. K. Linthicum, T. Gehrke, D. Thomson, E. Carlson, P. Rajagopal, T. Smith, D. Batchelor, and R.F. Davis, *Appl. Phys. Lett.* **75**, 196 (1999)
6. Z. Liliental-Weber, J. Jasinski, D. Cherns, M. Baines, and R. Davis, *Mat. Res. Soc. Symp. Proc.* **693**, 309 (2002)
7. P.Q. Miraglia, E.A. Preble, S. Einfeldt, T. Stiles, R.F. Davis, J. Schuck, R. Grober, and U. Schwarz, *Phys. Stat. Sol. (a)* **188**, No.2, 729-732 (2001)
8. S. Einfeldt, A.M. Roskowski, E.A. Preble, and R. Davis, *Appl. Phys. Lett.* **80**, 953 (2002)
9. Amy M. Roskowski, Edward A. Preble, Sven Einfeldt, Peter M. Miraglia, Robert F. Davis, *IEEE J. Quantum Electron.* **38**, 1006 (2002).
10. J. Jasinski and Z. Liliental-Weber, *J. Electron. Mat.* **31**, 429 (2002)
11. Z. Liliental-Weber, Y. Chen, S. Ruvimov, and J. Washburn, *Phys Rev. Lett.* **79**, 2835 1997
12. L.T. Romano, EMIS Datareviews Series No.23, INSPEC, London, UK, p.221 (1999)
13. L.T. Romano, B.S. Krusor, R.J. Molnar, *Appl. Phys. Lett.*, **71**, 2283 (1997)

## Effect of growth temperature on the microstructure of the nucleation layers of GaN grown by MOCVD on (11 $\bar{2}$ 0) sapphire

T. Wojtowicz, P. Ruterana\*, M. E. Twigg<sup>1</sup>, R. L. Henry<sup>1</sup>, D.D. Koleske<sup>1,2</sup>, A.E. Wickenden<sup>1,3</sup>  
LERMAT, ISMRA, 6 Bd Maréchal Juin, 14050 Caen, France

<sup>1</sup>Electronics Science and Technology Division, Naval Research Laboratory, Washington, D.C., 20375-5320 USA

### Abstract

Most of the work done on GaN has taken into account layers grown on the (0001) sapphire plane. However one would expect the growth on the (11 $\bar{2}$ 0) plane to lead to different structural defects. As has been shown, in one direction, the mismatch is rather small. In this work, we have carried out structural analysis of nucleation layers grown at temperatures ranging from 600°C to 1100°C. It is shown that for many of the structural parameters, such as the orientation relationships, the layer morphology and the nucleation mechanism critically depend on the growth temperature. At the lowest temperatures, the growth is completely three dimensional with a mixture of the two traditional orientation relationships, but the coalescence thickness is small. In a next step, the A orientation relationship predominates and the layer roughness tends to slightly decrease. This orientation is never perfect, and there is always 1.5° misorientation to the same direction in sapphire, whereas the B orientation is always perfect. At an intermediate temperature, island growth is predominant, whereas towards the high temperature end the B orientation becomes predominant. For the highest growth temperatures, the nucleated layers are completely flat and with the B orientation, although they contain a quite large number of defects such as inversion domains.

### Introduction

The growth of high quality GaN growth is a major research topic for the fabrication of commercial devices such as light emitting diodes [1], lasers[2] and high power electronic devices[3]. In the late eighties, one of the main breakthrough was the use of a low temperature nucleation layer to initiate the growth of the GaN active layers. Although the best results were obtained from layers grown on (0001) sapphire, which exhibits large lattice and thermal misfits. Due to the important potential applications, work is going on for other growth processes and new substrates with some success [4,5]. For some time now, efforts have been going on in order to produce similar quality GaN layers on (11 $\bar{2}$ 0) sapphire [6]. This was done by optimizing the nucleation layer [7] and even by moving on to a miscut substrate surface, leading to enhancement of electrical properties, and layers with larger mosaic grains in the few micron range [8]. Of course, if we consider only the symmetries of the surfaces, one would expect rather different growth of GaN on such surface of sapphire. The already

\* Author for correspondence: Tel 33 2 31 45 26 53 Fax 33 2 31 45 26 60 email ruterana@ismra.fr

<sup>2</sup> Present address: Sandia National Laboratories, Albuquerque, NM 87185

<sup>3</sup> Present address : Army Research Laboratory, Adelphi, MD 20783

numerous reports have shown that GaN grows along its six fold c axis on top of the a surface which exhibits a p2 symmetry[9]. The epitaxial relationships are  $(11\bar{2}0)_{\text{sap}}// (0001)_{\text{GaN}}$ ,  $[0001]_{\text{sap}}// [10\bar{1}0]_{\text{GaN}}$ , whereas  $[10\bar{1}0]_{\text{sap}}// [11\bar{2}0]_{\text{GaN}}$  inside the best layers, but also a rotation of 90° has been reported[10]. Along these directions, the differences in lattice parameters are quite large, which suggests a complex mechanism for lattice matching[11]. In this work, we report the effect of the growth temperature on the microstructure of the nucleation layer. It is shown that the most important structural parameters depend critically on this temperature.

## Experimental

The investigated layers were grown by metal organic vapour phase deposition (MOCVD) in a vertical reactor consisting of an inductively-heated water cooled quartz tube. The sapphire substrate was annealed for 10 min minutes in H<sub>2</sub> at high temperature (> 1080°C) before growth. Subsequently the substrates were cooled down to the nucleation layer temperature while not altering the other parameters. Seven nucleation layers were grown for 30 min at temperatures varying from 585 to 1100°C, as shown in table 1. All the other parameters, such as the chamber pressure and organo-metallic fluxes, were kept constant. The samples and their respective temperatures are S1: 595, S2: 667, S3: 739, S4: 812, S5: 884, S6: 956, S7: 1028, S8: 1100°C

Transmission electron microscopy cross-sections of all the samples were thinned down to 100 µm by mechanical grinding and dimpled down to 10 µm. Electron transparency was achieved by ion milling at 5 kV. TEM and HRTEM observations were performed on a Topcon 002B electron microscope operating at 200 kV with a point-to-point resolution of 0.18 nm.

## Results

Systematic optical microscopy observations show either continuous layers or islands at the sapphire surfaces. Inside the transmission electron microscope the different microstructures become more obvious. As can be seen on figure 1, recorded along the  $[11\bar{2}0]$  for sample S1, there is a huge surface roughness and almost polycrystalline growth. The two epitaxial relationships A:  $[10\bar{1}0]_{\text{sap}}/[11\bar{2}0]_{\text{GaN}}$  and B:  $[10\bar{1}0]_{\text{sap}}/[10\bar{1}0]_{\text{GaN}}$  are equally present. However, the B epitaxial relationship is never perfect, and the islands always have a small misorientation (1-4°).



Figure 1. Morphology of the 595°C nucleation layer, large roughness and polycrystalline growth, with slight predominance of the A epitaxial orientation relationship

When the nucleation temperature is increased to 667°C, the layer is continuous and the surface has a smoother morphology in comparison to the lower temperature sample shown in figure 1. The B epitaxial relationship is the only present in the observed areas. The next observed sample is S3 deposited at 739°C. In this case, there is again a mixture of the A and B orientation relationships in a complex fashion: a layer can start to grown with the epitaxial relationship A, and finish in B (figure 2)

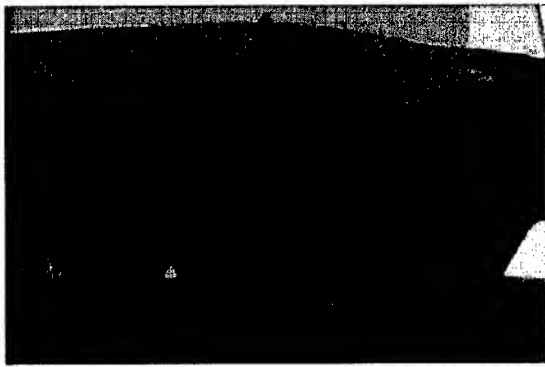


Fig. 2: Voids at the GaN/sapphire interface and mixture of A and B epitaxial relationships

At the interface, voids are visible and many of them form at boundaries between A and B oriented crystallites. When the nucleation temperature is increased further, there is no more coalescence; from S4 to S6, we have a completely three dimensional growth. At the lowest temperatures (S4), there is some lateral growth which may be connected to the voids as shown on figure 2. The center of island has the largest densities of defects and the sides are almost defect free towards the top of the islands (fig. 3). There is a mixture of the two predominant orientations, but the B orientation is always a few degrees off (1-2).

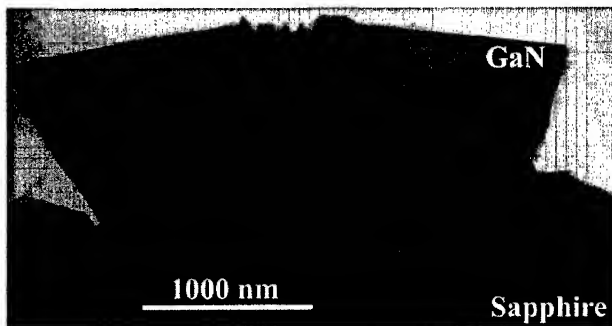


Fig. 3: Lateral growth in sample S4. The center of the island contains the largest defect density

At the next higher temperature (S5), the growth is still three dimensional, but the island morphology changes completely. The growth rate along the [0001] direction is still high but lateral growth becomes competitive as well, and the {10 $\bar{1}$ l} facets terminate the sides of the

islands (fig. 4). We now have the highest and largest islands in this series, where nucleation only takes place at limited sites, thereby delaying coalescence.

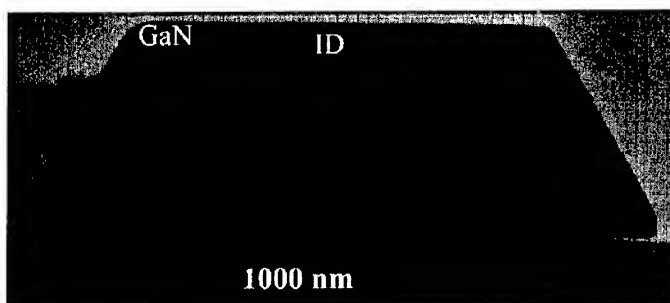


Fig. 4: Lateral island growth in samples S6.

Towards the centers of these flat islands, inversion domains are present. When the temperature is increased further, the growth along the  $c$  axis slows down and the lateral extension which dominates is compensated by a large decrease in the island height as shown in figure 5 taken from sample S6. Again the island is limited by the top (0001) surface and the side  $\{10\bar{1}1\}$  facets, and also contains inversion domains. Moreover, closer examination of the interface shows that at these high temperatures, a 2 nm interface layer was formed between the GaN and the sapphire. This layer has the same structure as the nucleated GaN with a lighter contrast. It is not atomically abrupt, meaning that at these deposition temperatures, some reaction took place between the nitrogen and the substrate so that a layer rich in Al has formed. Further work is in progress in order to determine its composition.



Figure 5. Flat and large islands in sample S7

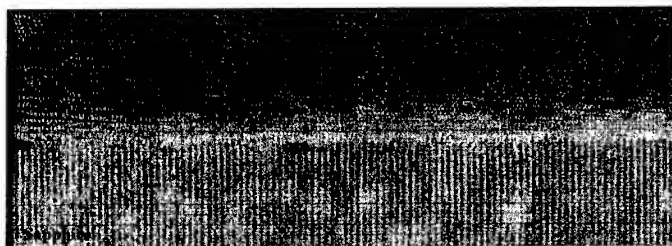


Fig. 6 The GaN/sapphire interface layer in sample S6. The interfacial reaction layer is marked by arrows

At these temperatures, only the A epitaxial orientation forms, but often with a small misorientation. At the highest investigated temperature S7, the growth has given rise to a continuous thin layer with a perfect A orientation relationship as shown on figure 7. The grown layer is flat with inversion domains which originate from the sapphire surface and cross the whole GaN layer to the surface.

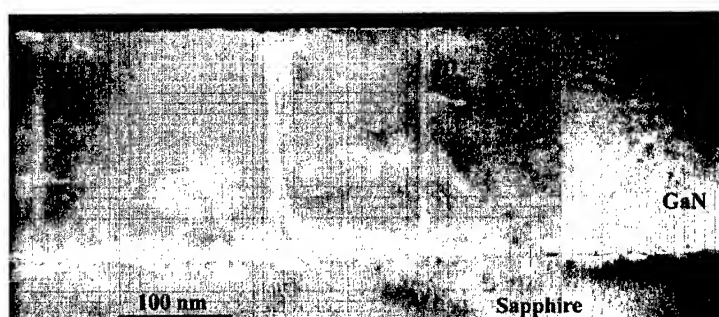


Fig.8 The flat and continuous GaN layer grown at 1100°C with inversion domains

A close examination of the interfacial area shows that there is also an intermediate layer. Again its boundaries are not abrupt and it is much more well-defined than in the 1028° (S6) sample. Its thickness is larger (up to 3nm) and has the same structure than the overgrown GaN.

### Conclusion

This investigation finds that the nucleation of GaN on  $(1\bar{1}20)$  sapphire critically depends on the growth temperature. As reported on figure 8, the fastest growth is obtained at intermediate temperatures where we have the smallest coverage of the substrate surface and a solely three dimensional growth mode on isolated spots of the sapphire surface. Three temperature domains can be pointed out D1: 550-700, D2: 700-950, D3: 950-1100°C. D1 and D3 are characterised by a decrease in growth rate which results in the formation of continuous layers.

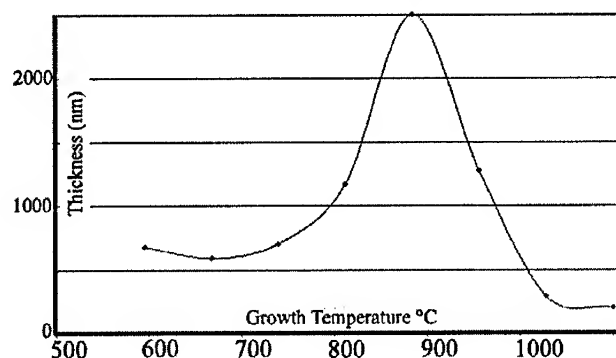


Fig. 8 Film thickness versus nucleation temperature.

D2 is characterized by a fast 3 dimensional growth mode and the formation of islands, whose height increases with the temperature. It is interesting to note that within D2 the voids as seen on figure 2, and that lateral facets on figure 3 are characteristic features of the growth. It seems the number of nucleation sites in D2 are rather smaller than in D1, and that the deposited GaN contributes to the growth mostly along the c axis, although the (0001) plane is not completely settled in order to limit this vertical growth mode as seen on figure 3. Just below 1000°C, although we still have a 3D growth mode, the (10 $\bar{1}$ 1) orientation is quickly established and the lateral growth takes over with the (0001) becoming the limiting plane. This growth mechanism leads to the formation of a completely well-oriented and continuous layer at the highest investigated growth temperature.

#### Acknowledgements

TW and PR acknowledges the support of the EU under contract number HPRN-CT-2001-00297

#### References

1. S. Nakamura, M. Senoh, and T. Mukai, Appl. Phys. Lett., 64, 1687(1994)
2. S. Nakamura, M. Senoh, S. Nagahama, N. Iwasa, T. Yamada, T. Matsushita, H. Kiyoku, Y. Sugimoto, Jpn. J. Appl. Phys. 35, L74 (1996)
3. S.N. Mohammad, A. Salvador, and H. Morkoc, Proc. IEEE 83, 1306(1995)
4. P. Venneegues, B. Beaumont, and P. Gibart, J. Appl. Phys. 87, 4175(2000)
5. T.S. Zheleva, W.M. Ashmawi, K.A. Jones, Phys. Stat. Sol. 176, 545(1999)
6. D.D. Koleske, A.E. Wickenden, R.L. Henry, W.J. DeSisto, and R.J. Norman, J. Appl. Phys. 84, 1998(1998)
7. A.E. Wickenden, D.D. Koleske, R.L. Henry, R.J. Norman, J. C. Culbertson, and M.E. Twigg, J. Electronic Mater. 28, 301(1999)
8. M. Fatemi, A.E. Wickenden, D.D. Koleske, M.E. Twigg, J.A. Freitas, Jr. R. Henry, and R.J. Norman, Appl. Phys. Lett. 73, 608(1998)
9. K. Dovidenko, S. Oktyabrsky, J. Narajan, and M. Razeghi J. Appl. Phys. 79, 2439(1996)
10. M.E. Twigg, R.L. Henry, A.E. Wickenden, D.D. Koleske, M. Fatemi, and J.C. Culbertson in Microscopy of Semiconducting Materials, ed. A.G. Cullis and R. Beanland, I.O.P. Conf. Ser. 164, 367(1999)
11. R. Beanland, C.J. Kiely and R.C. Pond Handbook on Semiconductors, edited by S. Mahajan (North Holland, Amsterdam), Vol. 3a, Chap. 15 (1994)

### Growth and Characterization of non-polar (11-20) GaN and AlGaIn/GaN MQWs on R-plane (10-12) sapphire

Sandeep Iyer, David J. Smith<sup>1</sup>, A. Bhattacharyya, K. Ludwig Jr.<sup>2</sup>, T.D. Moustakas  
Department of Electrical and Computer Engineering and Center for Photonics Research, Boston University, Boston, MA 02215

<sup>1</sup> Center for Solid State Science and Department of Physics and Astronomy, Arizona State University, Tempe, AZ

<sup>2</sup> Physics Department, Boston University, Boston, MA 02215

#### ABSTRACT

The majority of GaN films and related devices have been grown along the polar [0001] direction, and epitaxial growth along non-polar directions has received much less attention. In this paper we report the study of material properties of GaN and AlGaIn/GaN multiple quantum wells (MQWs) deposited on R-plane (10-12) sapphire substrates using RF plasma-assisted molecular beam epitaxy (MBE). In this growth direction, III-Nitrides grow along the non-polar [11-20] direction, with the *c*-axis in the plane of growth. Various nucleation steps such as surface nitridation, as well as GaN and AlN buffer layers were investigated. Our results indicate that surface nitridation of R-plane sapphire is an undesirable nucleation step, contrary to what has been observed in the case of (0001) sapphire. The AlN buffer layer leads to well-oriented films along the [11-20] direction with many threading defects and faceted surface morphology whereas the GaN buffer leads to the formation of mis-oriented domains close to the buffer region. However, these domains are overgrown and the films have smoother surface morphology with fewer threading defects. These structural findings are supported by photoluminescence and Hall effect measurements done on the same films. Photoluminescence (PL) measurements of (11-20) AlGaIn/GaN MQWs show much higher intensity than for similar structures grown on the C-plane sapphire, consistent with the absence of internal fields in the non-polar direction.

#### INTRODUCTION

The majority of epitaxial growth of III-Nitride material and devices was achieved along the [0001] direction by growing on (0001) sapphire and 6H-SiC substrates [1]. This direction of growth is polar, due to the non-centrosymmetric nature of the wurtzite structure. Recently, there have been reports on the growth of GaN and related MQWs along the [1-100] direction on (100) LiAlO<sub>2</sub> [2]. There are also a few reports on the growth of GaN along the [11-20] direction using (10-12) sapphire substrates [3-4]. These reports indicate more intense PL intensity from MQW structure grown along non-polar directions, compared to those grown along the polar direction. These findings are consistent with the elimination of internal fields due to polarization effects.

In this paper we report a detailed study on the growth, microstructure and optoelectronic properties of GaN films and AlGaIn/GaN MQWs grown on the R-plane sapphire substrate using various nucleation steps.

## EXPERIMENTAL METHODS

The GaN films and AlGaIn/GaN MQWs were grown on R-plane sapphire substrates by RF plasma-assisted MBE. The deposition system consists of a Varian Gen-II unit, which employs standard effusion cells for group III elements and dopants and Applied Epi Uni-bulb RF plasma source for nitrogen activation. Nitridation of the substrates was carried out at 600 °C at 450 watts of RF power in the plasma source for 20 mins. The GaN buffer (approx. 50nm) was deposited at 600 °C, and the AlN buffer (approx. 35nm) was deposited at 750 °C. The bulk films and MQWs were deposited at 770 °C using the same power in the RF discharge. Some of the films were doped with Si while others were unintentionally doped n-type.

The films were characterized *insitu* by RHEED and *exsitu* by atomic force microscopy (AFM), X-ray diffraction (XRD), transmission electron microscopy (TEM), photoluminescence (PL) and cathodoluminescence (CL) and Hall effect measurements. AFM was done using a Nanoscope III in the tapping mode. XRD was carried out in a four circle diffractometer and TEM observations used a JEOL-4000EX high-resolution electron microscope operated at 400 keV. The PL was excited with a He-Cd laser and CL was done using a Oxford mono CL2 system. Hall effect measurements were made using the standard Van-der-Pauw method with soldered indium contacts.

## EXPERIMENTAL RESULTS AND DISCUSSIONS

The R-plane sapphire substrates, after outgassing at 800 °C, were examined by reflection high-energy electron diffraction (RHEED) with the electron beam along various azimuths. The results indicated that the substrate surface was smooth and of good crystallinity.

### A. Investigation of Bulk GaN films

A number of GaN films were grown using an AlN or a GaN buffer as described previously. In some of these films the substrate was nitridated and some it was not nitridated. This study was intended to investigate the role of nitridation as well as the nature of buffer during growth on this substrate. Figure 1 shows the  $\theta$ -2 $\theta$  XRD scans for two Si-doped GaN films using an AlN buffer. One of the films (Fig.1a) was grown without nitridation, while the other (Fig.1b) was grown with nitridation. In both cases, GaN was grown in the (11-20) plane, as indicated by the diffraction peak at  $2\theta = 57.7^\circ$ . However, the FWHM of the (11-20) GaN peak in Fig.1b is six times narrower than the corresponding peak in Fig.1a. These results are analyzed using Scherrer's formula. According to this formula, the FWHM of the peak is given by:

$$\delta \theta \approx \frac{\lambda}{2D \cos \theta} + \epsilon_m \tan \theta \quad (1)$$

Where,  $\lambda$  = Wavelength of X-rays used (1.54 Å)

D = Average size of domain

$\epsilon_m$  = Inhomogeneous strain

BEST AVAILABLE COPY

According to Eq.1, the narrower FWHM of the film with the nitridated substrate, can be accounted for either by larger domain size or smaller inhomogeneous strain in these films. However, according to Fig. 1, the (11-20) peak occurs at the same angle suggesting that the inhomogeneous strain is approximately the same in both films. Thus it appears that nitridation promotes larger domain sizes. The FWHM of the on-axis rocking curve of the (11-20) GaN peak for the film grown without nitridation was found to be 590 arcsec and that with nitridation was found to be 1000 arcsec. This result suggests that although nitridation promotes larger grain size, the domains are more mis-oriented with respect to the substrate.

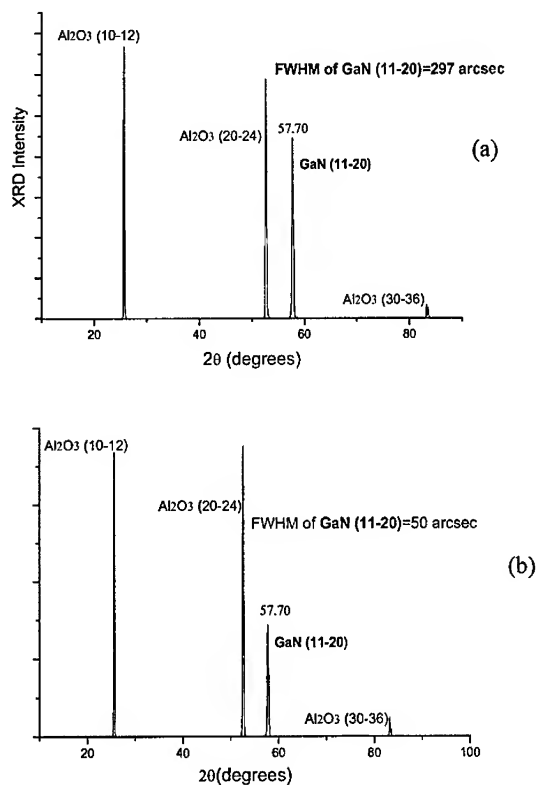


**Figure 1** -  $\theta$ - $2\theta$  XRD scans of Si-doped GaN films grown on R-plane sapphire with AlN buffer. (a) Film grown without substrate nitridation; (b) Film grown with substrate nitridation.

Room temperature PL spectra of the films described in Fig. 1, measured under identical conditions, are shown in Fig. 2. The data from both samples show a single peak at 364 nm with FWHM of about 9nm. However, the PL intensity is significantly larger for the film, which was grown on the non-nitridated substrate, which is consistent with the narrower rocking curve for

this sample. Correspondingly, the Hall effect measurements show that the films grown on non-nitridated substrates show higher electron mobilities for the same carrier concentration.

We conclude from these results that nitridation of the R-plane sapphire does not have the same beneficial effects in the growth of GaN as it does in C-plane sapphire. We attribute this result to the fact that, unlike the C-plane sapphire, which is terminated by oxygen atoms, the R-plane sapphire substrate is terminated by a mixture of oxygen and nitrogen atoms [5].

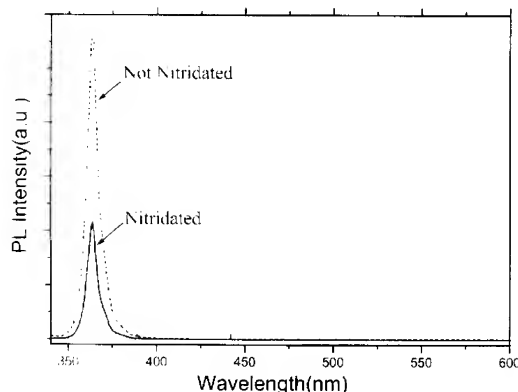


**Figure 2** – PL Spectra of GaN film grown on R-plane sapphire substrate on AlN buffer.

The effect of the AlN or GaN buffers on the growth of GaN films was investigated by detailed electron microscopy studies. Figure 3 shows cross-sectional TEM images of Si-doped GaN films. The sample in Fig. 3a was grown using a GaN buffer, whereas the sample in Fig. 3b was grown using an AlN buffer layer. It is clear from Fig. 3b that the AlN buffer layer is not flat, and the top GaN surface is faceted with a relatively large number of threading defects all the way through the GaN film. In contrast to the sample in Fig. 3b, the sample in Fig. 3a has relatively flat top surfaces and much fewer threading dislocations. Similar observations were made by Craven and co-workers [6]. It is important to note that competing growth directions are nucleated at the substrate in the case of the sample with the GaN buffer (Fig. 3a) and the domains are mis-oriented with respect to each other, whereas the sample with the AlN buffer shows well-oriented domains, in spite of the large number of defects. These results are well supported by our Hall effect and PL results. The mobility for the film with the GaN buffer is almost 40 times larger and the PL intensity is 3 times greater than the film, which had the AlN buffer layer. Preliminary XRD results show that films with an AlN buffer have several orders of magnitude higher intensity than films with the GaN buffer, which is consistent with the TEM results.

BEST AVAILABLE COPY



**Figure 3** – Cross sectional TEM images of Si-doped GaN films: (a) Film grown with GaN buffer; (b) Film grown with AlN buffer.

### B. Investigation of AlGaIn/GaN MQWs

As mentioned earlier, III-Nitride materials and devices grown in the polar [0001] direction exhibit spontaneous and piezoelectric polarization due to the non-centrosymmetric nature of the crystal. The [11-20] direction of GaN is a non-polar direction and materials grown in this direction would be devoid of internal fields arising due to polarization effects. To investigate the effect of polarization fields on the recombination mechanisms, AlGaIn/GaN MQWs were grown along the [0001] and [11-20] directions.

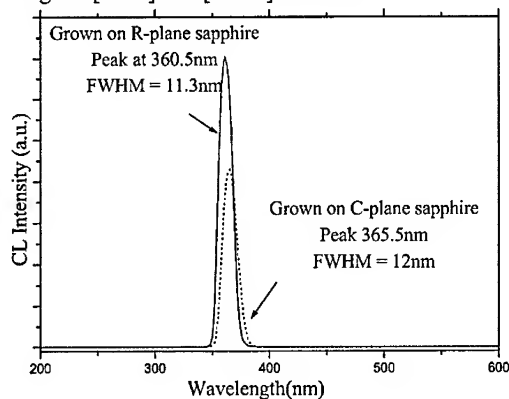


**Figure 4** – Comparison of room temperature CL from MQWs grown on R-plane and C-plane sapphire substrates.

The structure grown on C-plane sapphire substrate was grown on top of 5  $\mu\text{m}$  thick HVPE (Hydride vapor phase epitaxy) grown GaN and the structure grown on R-plane sapphire was grown on 2  $\mu\text{m}$  thick MBE grown GaN. Both had 10 periods of  $\text{Al}_{0.1}\text{Ga}_{0.9}\text{N}/\text{GaN}$  MQWs with a

barrier width of 75 Å and well width of 75 Å. Figure 4 shows a comparison of the CL from MQWs grown on C-plane and R-plane sapphire substrates. The CL intensity from the MQWs grown on R-plane sapphire was found to be 2 times greater than the MQWs grown on C-plane sapphire. This difference is in spite of the fact that the structure on C-plane was grown on a thick HVPE GaN layer, which reduces the defect density significantly and the barriers had a small percentage of In, which has been observed to improve the luminescence intensity by a factor of 5 [7]. The higher CL intensity can be attributed to the effect of built-in electric fields, which causes charge separation in the quantum wells, hence reducing the radiative transition probability [8]. The emission from the MQWs grown on R-plane sapphire shows a peak at 360.5nm with a FWHM of 11nm, and the one grown on C-plane sapphire shows a peak at 365.5nm with a FWHM of 12nm. The peak emission from the structure grown on C-plane (365.5nm) is found to be red-shifted compared to the structure grown on R-plane (360.5nm). This difference can be attributed to the absence of quantum-confined Stark Effect (QCSE) in MQWs grown on R-plane sapphire substrates [9].

## CONCLUSIONS

GaN and AlGaIn/GaN MQWs were grown on R-plane sapphire substrates. Surface nitridation of R-plane sapphire causes the domains to be mis-oriented with respect to the substrate, decrease the electron mobility and decrease the PL intensity, although it promotes larger grain size. Use of a GaN buffer results in better mobility, higher PL intensity and lower number of threading defects compared to films grown on AlN buffer layer. CL intensity of AlGaIn/GaN MQWs grown on R-plane sapphire was found to be significantly higher than those grown on C-plane sapphire.

**Acknowledgements:** The work was supported by the co-operative program of the ARL and BL Photonics center, and was monitored by Drs G. Simonis and M. Wraback.

## REFERENCES

1. D.Doppalapudi and T.D.Moustakas, "Epitaxial Growth of III-Nitrides Thin Films", "Handbook of Thin Film Materials", ed. H.S.Nalwa, 4, 57 (2001)
2. P. Waltereit, O. Brandt, M.Ramsteiner, A.Trampert, H.T.Grahn, J.Menniger, M.Reiche and K.H.Ploog, J.Crystal Growth, 227-228, 437, (2001)
3. C.R.Eddy,Jr and T.D.Moustakas, J. Appl. Phy. 73, 448 (1993)
4. H.M.Ng, Appl.Phy.Lett.80, 4369 (2002)
5. C.J.Sun, P.Kung, A.Saxler, K.Haritos, and M.Razeghi, J. Appl. Lett. 75, 3964, (1994)
6. M.D.Craven, S.H.Lim, F.Wu, J.S.Speck, S.P.Denbaars, Appl.Phy.Lett. 81,469 (2002)
7. A.Bhattacharyya, I.Friel, Sandeep Iyer, Tai-Chou Chen, W.Li, J.Cabalu, Y.Fedyunin, K.F.Ludwig Jr., and T.D.Moustakas (submitted to Journal of Crystal Growth)
8. J.S.Im, H.Kollmer, J.Off, A.Sohmer, F.Scholz, and A.Hangleiter, Phys. Rev. B 57, R9435 (1998)
9. T.Deguchi, K.Sekiguchi, A.Nakamura, T.Sota, R.Matsuo and S.Nakamura, Jpn. J. Appl.Phys., Part 2 38, L914 (1999)

BEST AVAILABLE COPY

### Epitaxial Growth of AlN on 6H-SiC (11 $\bar{2}$ 0) by Molecular-Beam Epitaxy and Effect of Low-Temperature Buffer Layer

N. Onojima, J. Suda and H. Matsunami

Department of Electronic Science and Engineering, Kyoto University,  
Sakyo-ku, Kyoto 606-8501, Japan

#### ABSTRACT

Aluminum nitride (AlN) has been grown on 6H-silicon carbide (SiC) substrates with the non-polar (11 $\bar{2}$ 0) face using rf plasma-assisted molecular-beam epitaxy (rf-MBE). Reflection high-energy electron diffraction (RHEED) revealed that AlN and 6H-SiC (11 $\bar{2}$ 0) had an exact epitaxial relationship, i.e., [11 $\bar{2}$ 0]<sub>AlN</sub>||[11 $\bar{2}$ 0]<sub>SiC</sub> and [0001]<sub>AlN</sub>||[0001]<sub>SiC</sub>. From the result of microscopic Raman scattering spectroscopy, the stacking structure of the AlN epitaxial layer was suggested to be a 2H structure, not a 6H structure. A directly grown AlN layer and layer with AlN low-temperature (LT) buffer layer were investigated based on atomic force microscopy (AFM) and X-ray diffraction (XRD).

#### INTRODUCTION

AlN/SiC structures are of current importance for the development of high-temperature electronic devices. In most cases, epitaxial growth of AlN on SiC is carried out on commercially available on- or off-axis (0001) substrates and extensive studies of the growth mechanism and crystalline structure are performed [1,2].

Recently, SiC substrates with the non-polar (11 $\bar{2}$ 0) face are shipped from some companies. Exploring a new crystal face is very important to expand the design of the device structure and to develop new functional devices. In addition, to investigate the growth and structure of AlN on a non-polar SiC substrate is scientifically interesting.

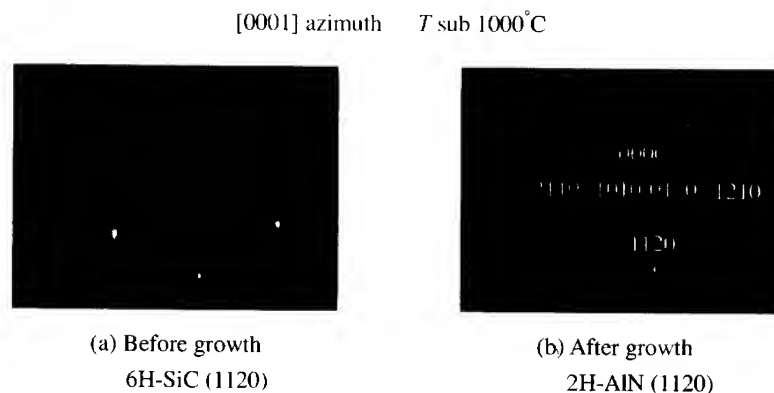
In this study, AlN growth on 6H-SiC (11 $\bar{2}$ 0) substrates has been performed by rf plasma-assisted molecular-beam epitaxy (rf-MBE). AlN epitaxial layers were investigated by *in situ* reflection high-energy electron diffraction (RHEED), atomic force microscopy (AFM), X-ray diffraction (XRD) and microscopic Raman scattering spectroscopy. The epitaxial relationship between AlN and 6H-SiC (11 $\bar{2}$ 0) and the polytype of the AlN layer were examined. A direct growth and two-step growth using an AlN low-temperature (LT) buffer layer were comparatively studied.

## EXPERIMENTAL DETAILS

The substrates used in this study were 6H-SiC wafers with the (1120)-vicinal face from Nippon Steel Corporation. AlN epitaxial layers were grown in an MBE chamber equipped with a standard effusion cell for Al evaporation and an EPI Unibulb rf plasma cell for producing active nitrogen ( $N^*$ ). The substrate was thermally cleaned at 1000°C for 30 min in an ultrahigh vacuum of  $10^{-9}$  Torr, and then an AlN layer was directly grown at 1000°C. Details of the growth condition were reported in [3]. In a two-step growth, a 20-nm-thick AlN LT buffer layer was grown at 600°C prior to the 1000°C -growth mentioned above. The total thickness of AlN layers ranged from 0.4 to 1.0  $\mu\text{m}$ .

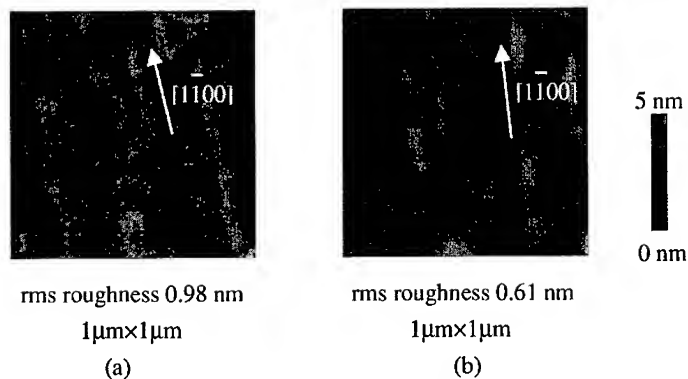
## DISCUSSION

Figure 1(a) shows the RHEED pattern of a 6H-SiC (1120) substrate with the [0001] azimuth. At the initial stage of the direct growth, a spotty pattern of AlN was observed for several minutes, probably due to three-dimensional island growth. After approximately 5 min, the pattern changed to streaky one, indicating two-dimensional growth. Figure 1(b) shows the RHEED pattern with the same azimuth after the AlN growth. In view of RHEED indices, the pattern shown in Fig. 1(b) is that of wurtzite (2H) AlN (1120) with the [0001] azimuth, clearly indicating that AlN and 6H-SiC (1120) have an exact epitaxial relationship, i.e.,  $[11\ 2\ 0]_{\text{AlN}} \parallel [11\ 2\ 0]_{\text{SiC}}$  and  $[0001]_{\text{AlN}} \parallel [0001]_{\text{SiC}}$ . The RHEED pattern of AlN with a LT buffer layer was similar to that shown in Fig. 1(b).



**Figure 1.** RHEED patterns during direct growth of AlN. (a) 6H-SiC (1120) surface, (b) AlN surface after growth (360 nm).

BEST AVAILABLE COPY



**Figure 2.** AFM images of 360-nm-thick AlN epitaxial layers without (a) and with (b) LT buffer layer grown on 6H-SiC (1120) substrates.

Figures 2(a) and 2(b) show the AFM images of 360-nm-thick AlN epitaxial layers without and with a LT buffer layer grown on 6H-SiC (1120) substrates. The surface of AlN with a LT buffer layer was smoother than that without a LT buffer layer. Although the surface roughness of these AlN layers was relatively small (rms roughness < 1 nm), many elongated surface defects expanded along the  $[1\bar{1}00]$  direction of the 6H-SiC substrates. Since these elongated defects were not observed on the substrates before AlN growth, they are probably due to the formation of stacking faults during the growth.

Figures 3(a), (b) and 3(c), (d) show the XRD  $2\theta/\omega$  scan curves of 360-nm-thick AlN epitaxial layers without and with a LT buffer layer grown on 6H-SiC (1120) substrates. Two different X-ray incidence geometries perpendicular to the  $[1100]$  direction ((a), (c)) and parallel to the  $[1100]$  direction ((b), (d)) were examined. The XRD measurements were performed with a triple crystalline X-ray diffractometer. A Cu  $K\alpha_1$  line ( $\lambda=1.540562 \text{ \AA}$ ) was selected using a channel cut Ge (220) monochromator, and an open detector condition was used. A diffraction peak from the AlN (1120) plane ( $2\theta$  angle  $\sim 59.3^\circ$ ) was evidently confirmed, which agrees with the result of RHEED observation. Any diffraction peaks from the AlN (0002) plane ( $2\theta$  angle  $\sim 36.0^\circ$ ) were not detected, indicating that there is no AlN domain grown toward the  $[0001]$  direction. The peak intensities of AlN with a LT buffer layer ((c), (d)) were almost one order of magnitude larger than those without a LT buffer layer ((a), (b)). AlN with a LT buffer layer had a smaller full width at half maximum (FWHM) of (1120) diffraction than AlN without a LT buffer layer. It suggests that using a LT buffer layer enhanced the crystalline quality of AlN grown on a 6H-SiC (1120) substrate. The AlN (1120) diffraction peaks in the X-ray incidence geometry perpendicular to the  $[1100]$  direction ((a), (c)) were considerably weak compared to those parallel

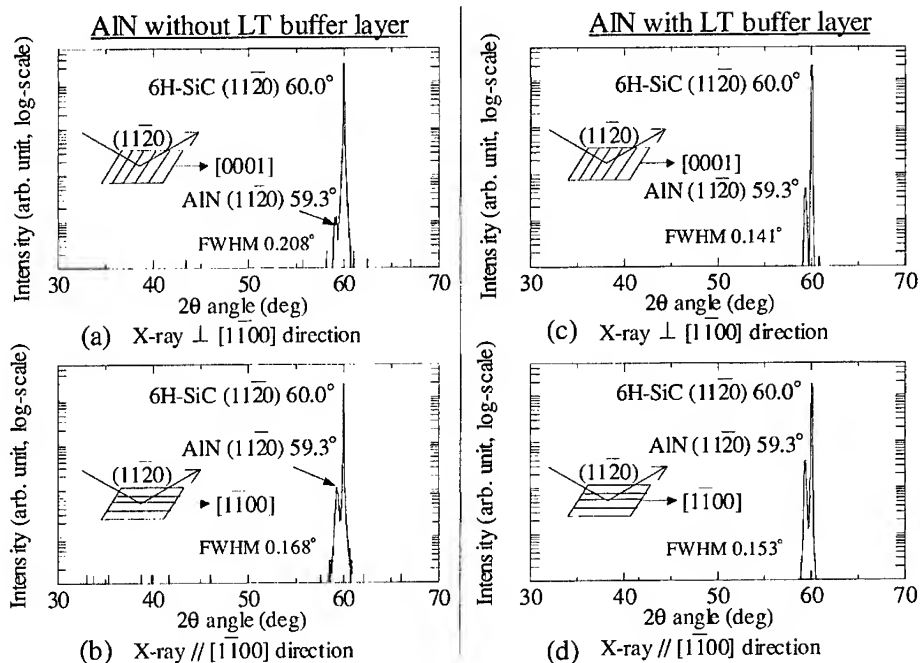


**Figure 3.** XRD  $2\theta/\omega$  scan curves of 360-nm-thick AlN epitaxial layers without (a), (b) and with (c), (d) LT buffer layer grown on 6H-SiC ( $11\bar{2}0$ ) substrates. (a), (c) were measured in X-ray geometry perpendicular to  $[1100]$  direction, and (b), (d) parallel to  $[1100]$  direction.

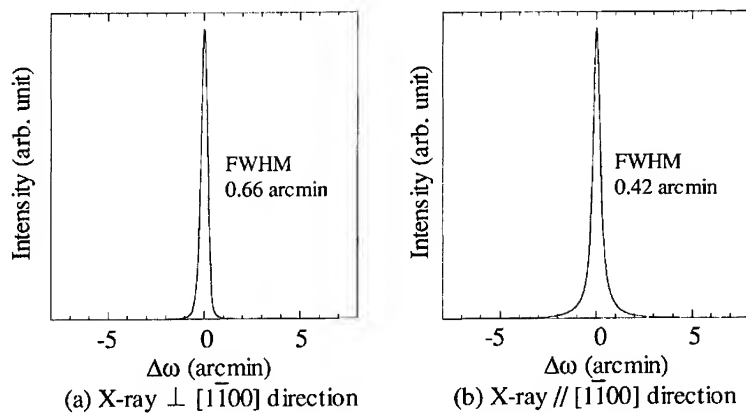


**Figure 4.** X-ray rocking curves of 6H-SiC ( $11\bar{2}0$ ) substrate in X-ray incidence geometry perpendicular (a) and parallel (b) to  $[1100]$  direction.

to the  $[1\bar{1}00]$  direction ((b), (d)). X-ray rocking curves of a 6H-SiC (1120) substrate in the X-ray incidence geometry perpendicular and parallel to the  $[1100]$  direction are shown in Fig. 4(a) and 4(b). There were no large differences of 6H-SiC (1120) diffraction between those two geometries. Therefore, this might be attributed to stacking faults in the AlN layers, which are expanded along the  $[1100]$  direction. Those stacking faults are thought to reduce the spatial coherency of the AlN layers along the  $[1100]$  direction. The peak intensity of AlN shown in Fig. 3(c) was more than 10 times larger than that shown in Fig. 3(a). It suggests that using a LT buffer layer can suppress the formation of stacking faults.

Figure 5 shows the Raman spectra of a 1.0- $\mu\text{m}$ -thick AlN epitaxial layer directly grown on a 6H-SiC (1120) substrate. The Raman spectra were acquired in two different backscattering geometries,  $x(z,-)x$ , and  $x(y,-)x$ , using the 488 nm line (2.54 eV) of an argon-ion laser. In these geometries,  $x$  is the laser incident direction, and  $z$  or  $y$  is the polarization of the incident light; here  $z$  is the direction along the  $\langle 0001 \rangle$  axis of the 6H-SiC substrate. According to Raman selection rules in a backscattering geometry of wurtzite AlN (1120), the observable phonon modes are the  $A_1$  (TO),  $E_1$  (TO) and  $E_2$  modes, where the  $E_2$  mode can be detected only in the polarization direction perpendicular to the  $\langle 0001 \rangle$  axis of AlN (1120) [4]. In the  $x(z,-)x$  geometry, the  $A_1$  (TO) and  $E_1$  (TO) modes were evident, while in the  $x(y,-)x$  geometry, the  $A_1$

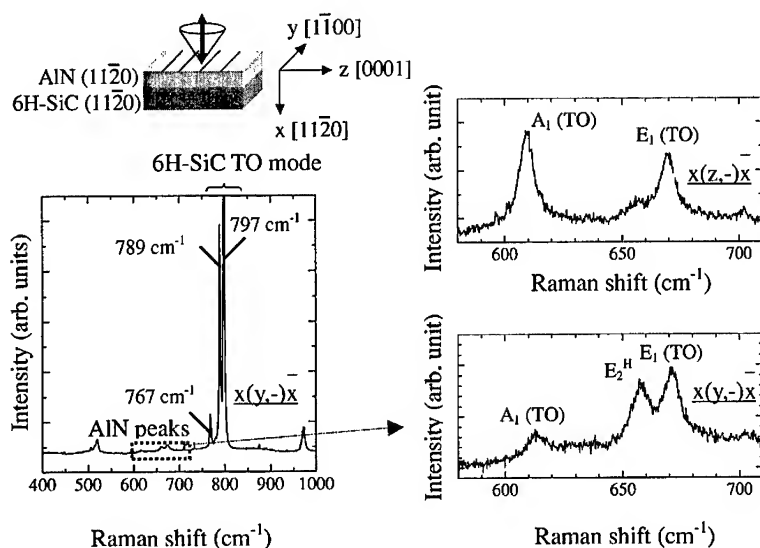


**Figure 5.** Raman scattering of AlN (1120) epitaxial layer in backscattering  $x(z, -)x$  and  $x(y, -)x$  geometries.

(TO),  $E_1$  (TO) and  $E_2^H$  modes were clearly observed. These observations support the parallel in-plane epitaxial relationship,  $[0001]_{\text{AlN}} \parallel [0001]_{\text{SiC}}$ . In general, the stable polytype of AlN grown on (0001) substrates is a wurtzite structure. However, AlN epitaxially grown on a 6H-SiC (1120) substrate is possible to have a 6H structure due to the atomic template of the substrate. In the case of a 6H structure, the phonon modes arising from the zone folding should be detected by Raman scattering spectroscopy. Actually, the phonon modes from the zone folding of the 6H-SiC (1120) substrate were clearly observed. However, the phonon modes related to the zone folding of AlN were not detected, suggesting a 2H structure as mentioned in RHEED indices.

## CONCLUSION

We have studied the structural properties of AlN epitaxial layers on 6H-SiC substrates with the non-polar (1120) face. AlN and 6H-SiC (1120) had an exact epitaxial relationship, i.e.,  $[1120]_{\text{AlN}} \parallel [1120]_{\text{SiC}}$  and  $[0001]_{\text{AlN}} \parallel [0001]_{\text{SiC}}$ . A direct growth and two-step growth using an AlN LT buffer layer were comparatively studied. Using a LT buffer layer, the surface roughness and crystalline quality of AlN grown on a 6H-SiC (1120) substrate were improved. From the result of microscopic Raman scattering spectroscopy, the stacking structure of the AlN epitaxial layer was suggested to be a 2H structure, not a 6H structure.

## ACKNOWLEDGEMENT

This work was supported by the Japan Society for the Promotion of Science, Research for the Future Feasibility Study Program (FY 2001), "Control of Interface Properties in Wide Bandgap Semiconductors and evolution of New Function". One of the authors (J.S.) would like to thank the 2001 Coming Research Grant.

## REFERENCES

1. N. Onojima, J. Suda and H. Matsunami, J. Cryst. Growth **237-239**, 1012 (2002).
2. S. Tanaka, R. S. Kern and R. F. Davis, Appl. Phys. Lett., **66**, 37 (1995).
3. N. Onojima, J. Suda and H. Matsunami, Jpn. J. Appl. Phys., **41**, L002 (2002).
4. V. Y. Davydov, Y. E. Kitaev, I. N. Goncharuk, A. N. Smirnov, J. Graul, O. Semchinova, D. Uffmann, M. B. Smirnov, A. P. Mirgorodsky and R. A. Evarestov, Phys. Rev. B, **58**, 12899 (1998).

### Electrical Properties of GaN/Si Grown by MOCVD

Seikoh Yoshida, Jiang Li, Takahiro Wada, and Hironari Takehara  
Yokohama R&D Laboratories, The Furukawa Electric Co., Ltd  
2-4-3, Okano, Nishi-ku, Yokohama, 220-0073, Japan

#### ABSTRACT

GaN growth on Si substrate is very attractive for realizing low cost electronic devices. We grew a thin GaN film on p-type Si (111) substrate using AlGaIn high temperature buffer without using a conventional low temperature buffer. A homogeneous buffer layer was obtained at 1093 K and a homogenous 500 nm thick GaN layer was also obtained without any crack. Using a transmission electron microscopy (TEM), we observed that the cross-section of GaN and AlGaIn buffer was very smooth and also the surface of GaN was flat although the threading dislocations were observed. Furthermore, we directly fabricated a metal semiconductor field effect transistor (MESFET) using a 500 nm-thick GaN/Si without any high resistive GaN layer. A Schottky electrode was Pt/Au and an ohmic electrode was Al/Ti/Au. A Schottky breakdown voltage was over 100 V. Also, we confirmed a high temperature operation of the MESFET using a thin GaN film on Si substrate at 573 K.

#### INTRODUCTION

III-V nitrides are very promising for high-power, high-frequency, and high-temperature devices [1-8]. GaN and related materials are generally grown using sapphire or SiC substrates. For low-cost device fabrication, a Si substrate is very useful. Si substrates for GaN growth have several advantages compared with other substrates: they can be obtained at low cost, and high-quality Si wafers with a large diameter can be easily obtained. A high-quality very thin GaN film on a Si substrate is required for electronic devices of low-cost mass production. The growth of GaN on Si is very difficult due to the difference of the lattice constant and the thermal-expansion coefficient, resulting in the occurrence of cracks in GaN. Recently, good-quality GaN on a Si substrate has been reported [9-13]. An AlGaIn/GaN heterojunction field effect transistor (HFET) on a Si substrate has been reported. However, there is no report concerning electronic devices such as FETs or Schottky barrier diodes (SBDs) using a thin film GaN below 1000 nm in thickness including high resistive GaN layers on Si substrate. Our purpose is to fabricate electronic devices using very thin GaN and related materials on a Si substrate in order to fabricate low-cost devices. In this paper, we report that by using an AlGaIn buffer, a crack free GaN was obtained on a Si (111) substrate, and that a metal field effect transistor (MESFET) with a breakdown voltage over 100V for a high temperature operation at 573 K was obtained using a 500 nm-thick GaN film on a Si (111) substrate.

## EXPERIMENTAL

We first tried to grow GaN without cracking on a 2-inches p-type Si (111) substrate using metal-organic chemical vapor deposition (MOCVD) in order to fabricate a MESFET using a thin GaN film on the Si substrate. Trimethylgallium (TMG), trimethylaluminium (TMA), and ammonia ( $\text{NH}_3$ ) were used for source gases. A thin AlGaIn buffer was used for GaN growth. The formation condition of AlGaIn buffer on the Si substrate was optimized. After that, the MESFET was directly fabricated using a thin GaN film on p-type Si substrate without a high resistive GaN layer in order to investigate whether or not the thin GaN film can be used as a MESFET. Furthermore, a high temperature operation of the MESFET was investigated.

## RESULTS AND DISCUSSION

The optimum formation temperature condition for an AlGaIn buffer on a p-type Si (111) substrate was investigated. The Al composition of  $\text{Al}_x\text{Ga}_{1-x}\text{N}$  buffer was about 0.05 and its thickness was 40 nm. After that, GaN was grown at 1303 K. When the buffer-formation temperatures were above 1103 K, a GaN layer became an island and a crack was generated, since a grown layer became rough. Figure 1 shows a cross-section transmission electron microscope (TEM) image of GaN/AlGaIn/Si (111) grown at 1123 K. This image shows that a buffer layer was island-like and was composed of both large and small grains. The small grains were composed of inversion or micro crystal domains. The GaN was preferentially grown on the large buffer domain and the grown GaN with a large grain size had a mesa shape with a smooth surface.

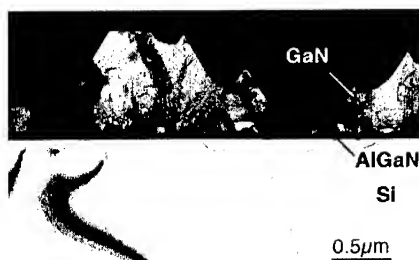


**Figure 1.** Cross-sectional TEM image of grown GaN/Si (111) at an AlGaIn buffer temperature of 1123 K.

When the buffer-formation temperatures were 1073 – 1103 K, an AlGaIn buffer layer with a smooth surface was obtained. As a result, a homogeneous 500 nm thick GaN without any crack was obtained at 1303 K for the growth temperature. Figure 2 also shows a cross-sectional TEM image of GaN/AlGaIn/Si (111). A smooth surface without cracking of GaN was obtained. Furthermore, when the

formation temperatures of the buffer layer were below 1073 K, we observed that the cross-sectional TEM image of GaN/AlGaIn/Si (111) was island-like; a buffer layer was also an island as shown in figure 3, resulting in the occurrence of island growth of GaN. Therefore, the optimum buffer formation-temperature for suppressing the cracking of GaN on the buffer layer was 1073 – 1103 K.

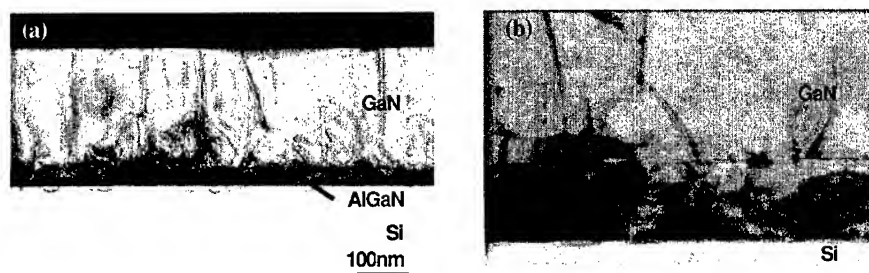


**Figure 2.** Cross-sectional TEM image of grown GaN/Si (111) at AlGaIn buffer temperatures of 1073 – 1103 K (a) and magnified image in the vicinity of the interface of GaN and AlGaIn buffer (b).

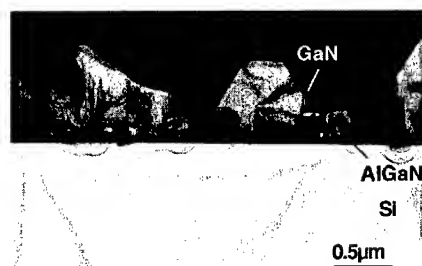


**Figure 3.** Cross-sectional TEM image of grown GaN/Si (111) at AlGaIn buffer temperature below 1073 K.

The Al composition dependence of an  $\text{Al}_x\text{Ga}_{1-x}\text{N}$  buffer at a constant formation temperature (1103 K) was also investigated. When the Al composition of  $\text{Al}_x\text{Ga}_{1-x}\text{N}$  buffer was above 0.3, the surface morphology of thick GaN grown on the buffer layer was rough. That is, it is probable that AlGaIn buffer layer had many grains, including polycrystalline grains, which made it difficult to grow GaN on the surface. When a GaN ( $x = 0$ ) buffer was used for GaN growth, thick GaN was rough and a crack was generated. Therefore, in this case a GaN buffer was not suitable. It was confirmed that the Al composition of an  $\text{Al}_x\text{Ga}_{1-x}\text{N}$  buffer layer for obtaining a smooth surface of thick GaN grown on the surface should be in the range of  $x = 0.05 - 0.3$ . We thus confirmed the optimum growth conditions of  $\text{Al}_x\text{Ga}_{1-x}\text{N}$  buffer for good quality GaN growths on Si (111) by MOCVD.

Photoluminescence (PL) measurement of the 500 nm thick GaN/Si (111) was carried out at 77K. A sharp GaN band edge-emission (365 nm) as well as a broad and weak yellow luminescence (575 nm) was observed. We next investigated the electrical properties. The hall mobility of 500 nm-thick GaN was measured at room temperature. The carrier concentration of undoped GaN was  $5 \times 10^{16} \text{ cm}^{-3}$  and the Hall mobility was  $300 \text{ cm}^2/\text{Vs}$ .

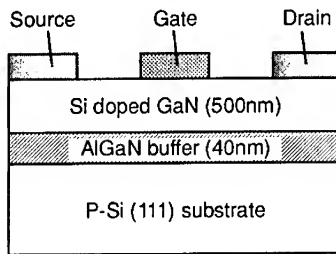
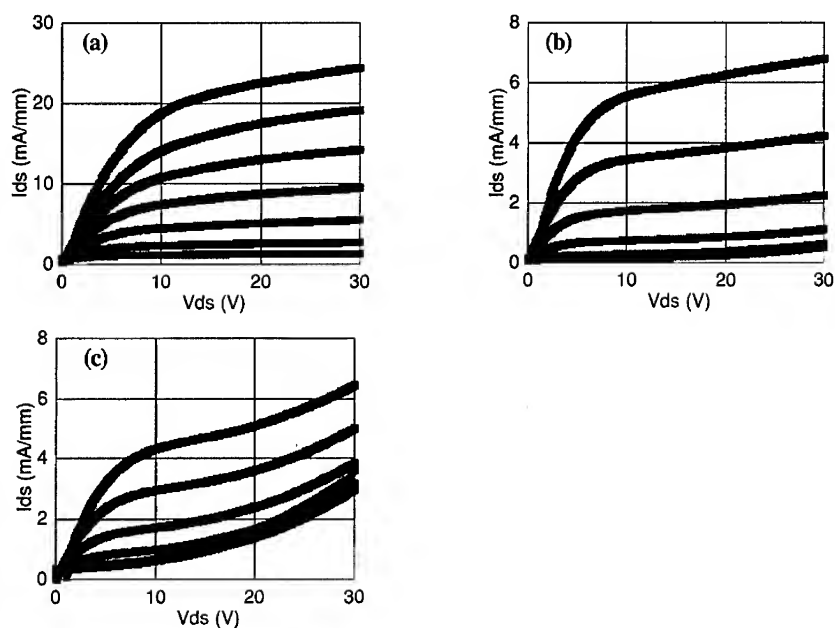


**Figure 4.** Schematic structure of a MESFET using a thin GaN film on P-type Si substrate without a highly resistive Ga layer.

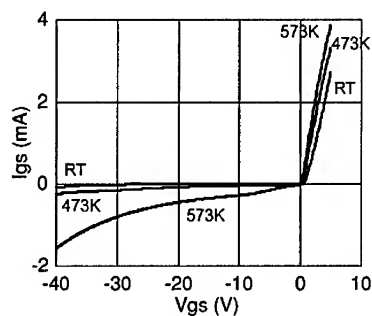
We directly fabricated a MESFET using a thin Si-doped ( $\text{Si}: 2 \times 10^{17} \text{ cm}^{-3}$ ) GaN (500 nm)/AlGaIn buffer (40 nm) on a p-type Si (111) substrate without a highly resistive GaN layer. Etching of the GaN fabrication was carried out by a dry-etching technique using an electron cyclotron resonance (ECR) plasma to make the MESFET. The etching gas was a mixture of  $\text{CH}_4$  (5 sccm), Ar (7 sccm) and  $\text{H}_2$  (15 sccm). The etching rate of the GaN layers was 14 nm/min. The etching depth was 600 nm. The gate length and width were 2000 nm and 0.1 mm, respectively. The distance of the source and drain was 0.01 mm. A scheme of the structure of the MESFET is shown in figure 4. In this case, a contact layer was not formed for the source and drain electrodes. The ohmic electrode material was Al/Ti/Au and the Schottky electrode material was Pt/Au. The Schottky breakdown voltage of the gate and source was over 100 V.

Figure 5 shows the current-voltage (I-V) curve of a MESFET using a thin GaN film without a highly resistive GaN layer at room temperature, 473 K, and 573 K. This MESFET was operated at 573 K, where the leakage current was slightly increased. We consider that the increase in the leakage current at the pinch-off voltage depends on the crystal quality of the interface of the GaN and AlGaIn buffer layer. We confirmed that the measurement is stable at 573 K for over 100 h. When the FET was cooled down to room temperature, the I-V curve was recovered, as shown in figure 5 (a). A transconductance ( $g_m$ ) was about 5 mS/mm and this  $g_m$  can be expected to be improved by forming a contact layer and AlGaIn/GaN heterojunction with a two-dimensional electron gas. Figure 6 shows the temperature dependence of Schottky property of gate and source of the MESFET. The forward current was increased with the increase of the operation temperatures although the backward leakage current was conversely increased. The

increase of reverse current was considered to be due to the crystal quality of the interface between GaN and AlGaN buffer. We consider that this leakage current will be improved by p-type impurity doping for carrier compensation. A high-temperature operation MESFET at 573 K using a thin GaN with a thickness of 500 nm on Si substrate was thus demonstrated.



**Figure 5.** Current-voltage behavior of a MESFET using a thin GaN film on a Si substrate at (a) room temperature, (b) 473 K, (c) 573 K. The start gate bias ( $V_{gs}$ ) was changed from +2V to -10V in steps of -2V.



**Figure 6.** Temperature dependence of Schottky barrier of gate and source of MESFET.

## SUMMARY

A 500 nm thick homogeneous GaN film on a Si (111) substrate was obtained using an AlGaIn high-temperature buffer. A MESFET using a very thin GaN film on a Si (111) substrate was fabricated without a high resistive GaN layer for a low cost mass production. A high-temperature operation of the MESFET at 573 K was confirmed using a 500 nm thick GaN/Si substrate without any highly resistive GaN layer. A Schottky breakdown voltage of a gate and source was over 100 V. We thus demonstrated that a GaN film with a thickness below 1000 nm on a Si substrate can be useful for electronic devices.

## REFERENCES

1. M. A. Khan, M. S. Shur, J. N. Kuzunina, Q. Chin, J. Burn and W. Schaff: Appl. Phys. Lett. **66**, 1083 (1995).
2. O. Akutas, Z. F. Fan, S. N. Mohammad, A. E. Botchkarev and H. Morkoç: Appl. Phys. Lett. **69**, 3872 (1996).
3. N.-Q. Zhang, S. Keller, G. Parish, S. Heikman, S. P. Denbaars and U. K. Mishra: IEEE Electron Device Lett. **21**, 373 (2000).
4. S. Yoshida and J. Suzuki: Jpn. J. Appl. Phys. Lett. **37**, 482 (1998).
5. S. Yoshida and J. Suzuki: Jpn. J. Appl. Phys. Lett. **38**, 851 (1999).
6. S. Yoshida and H. Ishii: Physica Status Solidi (a) **188**, 243 (2001).
7. M. A. Khan, J. N. Kuznia, D. T. Olson, W. J. Schaff, J. W. Burn and M. S. Shur: Appl. Phys. Lett. **65**, 1121 (1994).
8. S. Yoshida, H. Ishii, and J. Li: Materials Science Forum **389-393**, 1527 (2002).
9. S. Guha, N. A. Bojarczuk: Appl. Phys. Lett. **72**, 415 (1998).
10. J. W. Yang, A. Lunev, G. Simin, A. Chitnis, M. Shatalov, M. A. Khan, J. E. van Nostrand and R. Gaska: Appl. Phys. Lett. **76**, 273 (2000).
11. D. Wang, Y. Hiroyama, M. Tamura, M. Ichikawa and S. Yoshida: Appl. Phys. Lett. **77**, 1846 (2000).
12. G. Simin, X. Hu, A. Tarakji, J. Zhang, A. Koudymov, S. Saygi, J. Yang, A. Kahan, M. S. Shur, and R. Gaska, Jpn. J. Appl. Phys. **40**, L1142(2001).
13. N. Vellas, C. Gaquiere, Y. Guhel, M. Werquin, F. Bue, R. Auby, S. Delage, F. Semond, and J. C. De Jaeger IEEE Electron Device Lett. **23**, 461 (2002).

### Studies on Epitaxial Relationship and Interface Structure of AlN/Si(111) and GaN/Si(111) Heterostructures

T. A. Rawdanowicz, H. Wang, A. Kvit and J. Narayan  
Department of Materials Science and Engineering  
North Carolina State University  
Raleigh, NC 27695, USA

#### ABSTRACT

We present the details of epitaxial growth interface structure of single wurtzite AlN thin films on (111) Si substrates by laser-molecular-beam-epitaxy. High quality AlN thin films with atomically sharp interfaces can be obtained by Laser-MBE at a substrate temperature of  $650 \pm 10^\circ\text{C}$ . X-ray diffraction and high resolution transmission electron microscopy was used to study the details of epitaxial growth of AlN on Si(111) substrate. The orientation-relationship of AlN on Si(111) was studied from Si  $\langle 110 \rangle$  and  $\langle 112 \rangle$  zone axis and determined to be AlN  $[2\bar{1}\bar{1}0] \parallel \text{Si}[\bar{1}10]$  and AlN  $[01\bar{1}0] \parallel \text{Si}[\bar{2}11]$ . The atomic structure of the interface was studied by high-resolution transmission electron microscopy and Fourier filtered image of cross-sectional AlN/Si(111) samples from both Si  $\langle 110 \rangle$  and  $\langle 112 \rangle$  zone axis. The results revealed the domain matching epitaxy of 4:5 ratio between the interplanar distances of Si(110) and AlN  $[2\bar{1}\bar{1}0]$ . We also present similarities and differences between the growth mechanism of AlN/Si(111) and GaN/Si(111) heterostructures.

#### INTRODUCTION

There is considerable interest in the growth and characterization of Aluminum Nitride (AlN) and Gallium Nitride (GaN) thin films for application, in optoelectronic and high-temperature devices due to chemical stability at high temperatures, excellent mechanical properties, good thermal conductivity, and a high breakdown field. Particularly, the wide band-gaps of AlN (6.2 eV) and GaN (3.4 eV) make this material promising for ultra-violet (UV) diode emitters.

The lack of suitable single-crystal nitride substrates require these devices to be made through heteroepitaxial growth on substrate materials, such as silicon carbide or sapphire.

However, silicon carbide and sapphire substrate materials are expensive and limited in size. To overcome these disadvantages, the heteroepitaxial processing of high quality AlN and GaN thin films on silicon (Si) has been under considerable investigation, due to its many advantages regarding low cost, large size, high crystal and surface quality, and high electrical and thermal conductivities. Work in this area is further motivated by the potential for co-integration of wide band-gap optoelectronics devices with large-scale silicon-based microelectronic devices.

The Si(111) substrate presents the required hexagonal symmetry for the hexagonal wurtzite epilayers of oriented (0001) AlN and GaN. However, the growth of AlN and GaN directly on Si(111) is presented with several commonly known impediments; large lattice mismatch ( $\sim 19\%$ ), and the difference of thermal expansion coefficient and poor nucleation for GaN on Si(111). Despite these impediments wurtzite AlN and GaN can be grown directly on the Si(111) plane with good structural properties.

The heteroepitaxial growth of AlN and GaN directly on Si(111) and the resulting domain matching epitaxial relationship at the interface is reported using TEM and image analysis.

## EXPERIMENT

The depositions of AlN and GaN were performed in a UHV Laser-MBE chamber with a KrF excimer laser ablating solid source AlN and GaN targets. The chamber deposition parameters were as follows: base pressure –  $2 \times 10^{-9}$  Torr, substrate temperature –  $650 \pm 10^\circ\text{C}$ , laser pulse rate – 10 Hz, laser radiation –  $\lambda = 248$  nm and  $\tau = 25$  nsec, laser pulse energy – 750 mJ for AlN and – 650 mJ for GaN.

The AlN and GaN were deposited on off-axis Si substrates with a nominal tilt of  $2^\circ$ . The Si substrates were P-doped, *n*-type with  $\rho \approx 7.5 \Omega\text{-cm}$ .

Microstructural characterization and interface analysis of these films was performed by high resolution transmission electron microscopy (HRTEM) using a JEOL-2010F analytical electron microscope. The selected area diffractions were performed and compared with simulated diffraction pattern to confirm the orientation relations of AlN and Si substrate. Images based on Fast Fourier Transformation are used to reveal the lattice matching relation of Si and AlN along the interface.

## DISCUSSION

The x-ray diffraction “ $\Theta$ - $2\Theta$ ” scans plotted in figure 1 show the AlN and GaN films to be highly oriented along the [0001] direction.

The interface, in figure 3(a), for AlN deposited on Si(111) remains sharp throughout the film without any indications of interface reactions and inter-diffusions. The corresponding selected-area-diffraction pattern, SAD, from the same area of the  $\langle 110 \rangle$  cross-section sample shows a epitaxial relation of  $\text{AlN}[0002] \parallel \text{Si}[111]$  in figure 2(a). The epitaxial relations from other directions are found to be  $\text{AlN}[2\bar{1}\bar{1}0] \parallel \text{Si}[110]$  and  $\text{AlN}[01\bar{1}0] \parallel \text{Si}[\bar{2}11]$ .<sup>1,3</sup> Figure 2(c) shows the diffraction from  $\text{GaN}[2\bar{1}\bar{1}0] \parallel \text{Si}[\bar{1}10]$  indicating epitaxial growth of GaN film. The slight indication of vertical lines in Figure 2(c) confirms the presence of stacking faults in the GaN basal plane. The simulated diffraction pattern of  $\text{AlN} \langle 2\bar{1}\bar{1}0 \rangle \parallel \text{Si} \langle 110 \rangle$  (see figure 2(b)) confirmed the single crystalline AlN with hex-on-cube epitaxial relationship with  $[2\bar{1}\bar{1}0] \parallel \text{Si}[\bar{1}10]$  and  $[01\bar{1}0] \parallel \text{Si}[\bar{2}11]$  for both AlN and GaN.

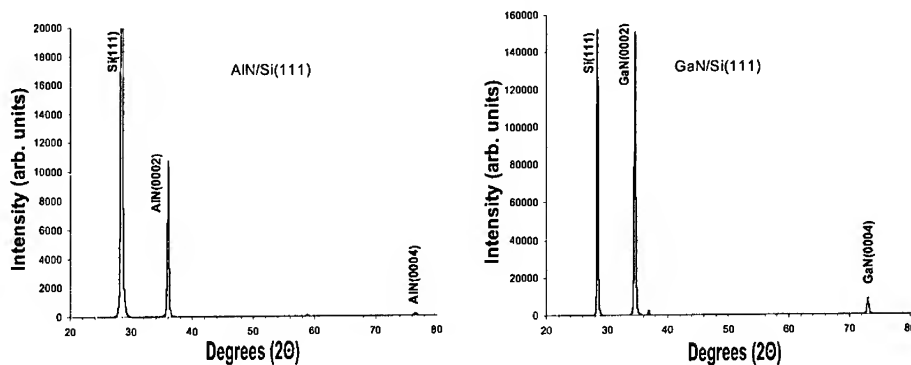


**Figure 1.** X-ray diffraction intensity vs. incident angle plot showing peaks from AlN(0002) and GaN(0002) films on Si(111).

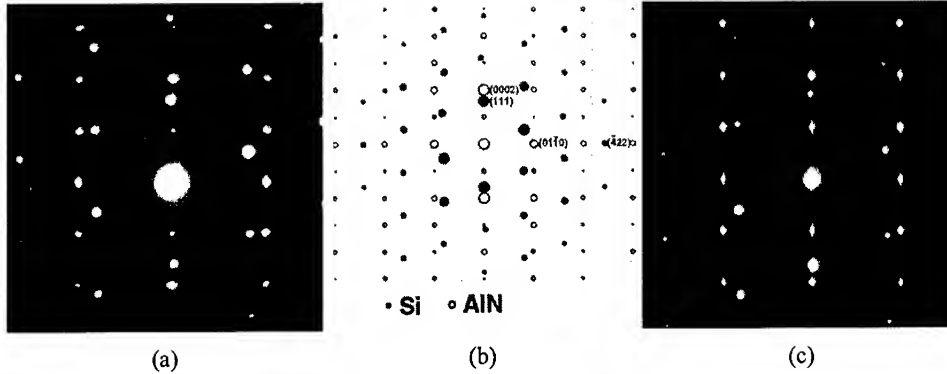


**Figure 2.** (a) Selected-area-diffraction pattern of AlN film on Si (111) in  $\langle 110 \rangle$  zone axis with epitaxial relations:  $\text{AlN}[0002] \parallel \text{Si}[111]$ ,  $\text{AlN}[2\bar{1}\bar{1}0] \parallel \text{Si}[\bar{1}10]$ , and  $\text{AlN}[01\bar{1}0] \parallel \text{Si}[\bar{2}11]$ ; (b) Simulated diffraction pattern showing hex-on-cube AlN epitaxial growth on Si(111); (c) Selected-area-diffraction pattern of GaN film on Si(111) in  $\langle 110 \rangle$  zone axis.

High resolution TEM image from  $\langle 110 \rangle$  cross-section sample of AlN/Si(111) in figure 3 shows a well-defined epilayer of AlN on silicon surface which is free of an amorphous layer. The silicon substrate is atomically flat with some  $\{111\}$  atomic step, which is clearly observed at the interface. The transition from Si to AlN is very sharp from figure 3(b), which is shown in the magnified interface.

It is important to note that the lattice parameters of AlN and Si are quite different. According to the lattice relation  $\text{AlN}[2\bar{1}\bar{1}0] \parallel \text{Si}[110]$ , the lattice mismatch of AlN and Si is about 19% according to the initial misfit strain given by

$$\varepsilon_e = d_f/d_s - 1. \quad (1)$$

Where  $d_f$  and  $d_s$  are the lattice parameter or interplanar distance of film and substrate, respectively. This large lattice mismatch cannot accommodate epitaxy growth within two monolayers of transition.

Researchers<sup>2</sup> have proposed the domain matching epitaxy (DME) in AlN/Si --this large lattice mismatch case 4 to 5 ratio between Si and AlN interplanar distances are estimated. That means 4 interplanar spaces of Si (110) are matching with 5 interplanar spaces of AlN( $2\bar{1}\bar{1}0$ ). Similar analysis was proposed by Bourret et al.<sup>3,4</sup> This matching of integral multiples of lattice planes provides for a lattice misfit of about 1.3% given by

$$\varepsilon_r = md_f/nd_s - 1. \quad (2)$$

The dimensions of the domain are repeated. In each domain, 'm' times lattice interplanar distances in the substrate match with 'n' times lattice interplanar distances in the film, where the 'm' and 'n' are the simple integers based on the lattice mismatch between film and substrate. This DME provides the possible mechanism for epitaxial growth in the AlN/Si system with large lattice misfit by relieving the strain within a couple of monolayers.<sup>5</sup>

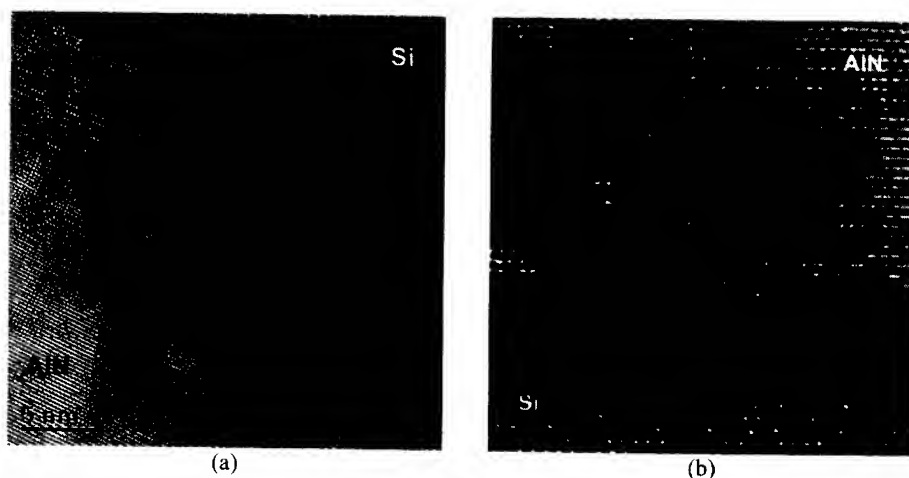


**Figure 3.** High resolution TEM image (a) of cross-section sample of AlN/Si(111) from  $\langle 110 \rangle$  zone axis and magnified image (b) from (a).

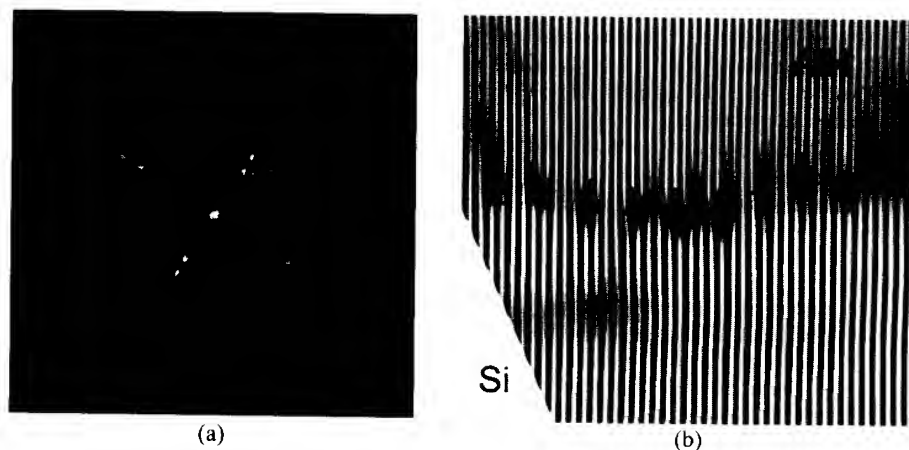


**Figure 4.** FFT of high-resolution image for the AlN  $\langle 01\bar{1}0 \rangle \parallel \text{Si} \langle 211 \rangle$  zone axis (a) with the other directions marked as AlN  $[0002] \parallel \text{Si}[111]$ , AlN  $[2\bar{1}\bar{1}0] \parallel \text{Si}[\bar{1}10]$ , Fourier filtered image of the cross-sectional HRTEM micrograph for the AlN  $\langle 01\bar{1}0 \rangle \parallel \text{Si} \langle 211 \rangle$  zone axis (b), showing a 4:5 ratio matching between Si and AlN.

In order to observe this epitaxy relation of AlN  $[2\bar{1}\bar{1}0] \parallel \text{Si}[\bar{1}10]$ , high resolution images of AlN/Si cross-section sample from  $\langle 422 \rangle$  Si zone axis were obtained. Figure 4(a) shows the corresponding Fast Fourier Transformation (FFT) image from the same area and the diffractions from AlN  $(2\bar{1}\bar{1}0) \parallel \text{Si}(110)$  and AlN(0002)  $\parallel \text{Si}(111)$  are marked. Then one corresponding set of

BEST AVAILABLE COPY

AlN ( $2\bar{1}\bar{1}0$ ) and Si(110) diffractions were masked in the FFT image and the resulting Fourier filtered image is shown in figure 4(b). In this case, only two beams are activated to observe the lattice information only from AlN ( $2\bar{1}\bar{1}0$ ) and Si(110). Along the interface of AlN and Si, the misfit dislocations are generated. The magnified Fourier filtered image shows clear domain matching relation of AlN and Si. The matching follows 5 to 4 ratio with one AlN misfit dislocation, marked as  $\perp$ , which is generated in each domain. Therefore, in each domain, 4 of Si (110) interplanar distances matching with 5 of AlN ( $2\bar{1}\bar{1}0$ ) interplanar distances.

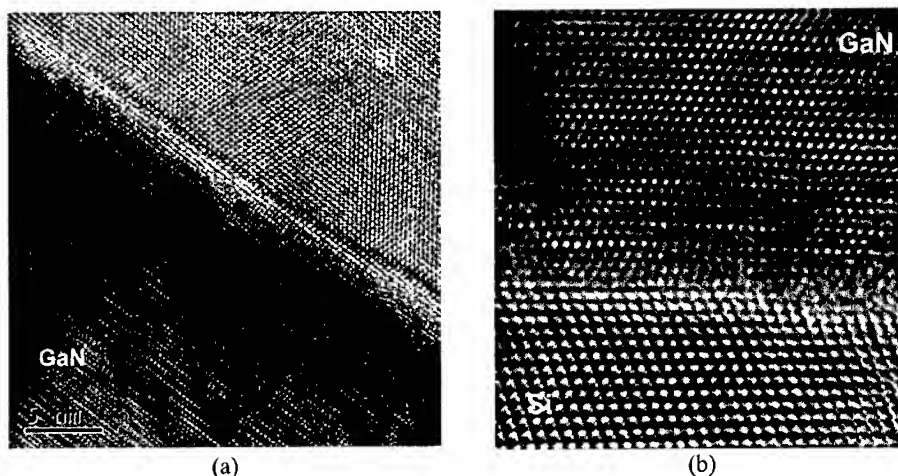


**Figure 5.** High resolution TEM image (a) of cross-section sample of GaN/Si(111) from  $\langle 110 \rangle$  zone axis and magnified image (b) from (a).

The high resolution TEM image from a  $\langle 110 \rangle$  cross-section sample of GaN/Si(111) in figure 5 shows a well-defined epilayer of GaN on the silicon surface. The silicon substrate is atomically flat with some  $\{111\}$  atomic steps, which is clearly observed from the interface in figure 3(b). Similar to the AlN epilayer, the GaN epitaxial growth exhibited DME. Comparison of figures 5(b) and 3(b) show a slight difference in the interface atomic structure for GaN on Si(111).

## CONCLUSIONS

The epitaxial relations of AlN and GaN on Si(111) are revealed as  $[0002] \parallel \text{Si}[111]$ ,  $[2\bar{1}\bar{1}0] \parallel \text{Si}[\bar{1}10]$ , and  $[01\bar{1}0] \parallel \text{Si}[\bar{2}11]$ . An atomically clean interface and a DME of 4:5 ratio between the interplanar distance of Si (110) and AlN ( $2\bar{1}\bar{1}0$ ) is observed, with DME reasoned as the mechanism for epitaxial growth of AlN on Si(111) substrate. DME is suggested as the mechanism for heteroepitaxial growth of GaN directly on Si(111).

---

## ACKNOWLEDGEMENT

We are pleased to acknowledge the partial support from the National Science Foundation under the Center for Advanced Materials and Smart Structures.

## REFERENCES

1. M. Morita, S. Isogai, N. Shimizu, K. Tsubouchi, and N. Mikoshiba, *Jpn. J. Appl. Phys.* **20**, L173 (1981).
2. R. D. Vispute, J. Narayan, Hong Wu, and K. Jagannadham, *J. Appl. Phys.* **77**, 4724 (1995).
3. Bourret, A. Barski, J.L. Rouviere, G. Renaud, and A. Bardier, *J. Appl. Phys.* **83**, 2003 (1998).
4. H. P. D. Schenk, U. Kaiser, G. D. Kipshidze, A. Fizzel, J. Kraußlich, H. Hobert, J. Schulze, and Wo. Richter, *Mat. Sci. Eng.* **B59**, 84 (1999).
5. J. Narayan and B.C. Larson, *J. Appl. Phys.* **93**, 1 (2003).

### Correlation Between the AlN Buffer Layer Thickness and the GaN Polarity in GaN/AlN/Si(111) Grown by MBE

A.M. Sanchez<sup>\*1</sup>, P. Ruterana<sup>1</sup>, P. Vennegues<sup>2</sup>, F. Semond<sup>2</sup>, F.J. Pacheco<sup>3</sup>, S.I. Molina<sup>3</sup>, R. Garcia<sup>3</sup>, M.A. Sanchez-Garcia<sup>4</sup> and E. Calleja<sup>4</sup>

<sup>1</sup> ESCTM-CRISMAT, UMR6508-CNRS, ISMRA. 6, Boulevard Maréchal Juin, 14050 Caen Cedex, France

<sup>2</sup> CRHEA-CNRS, B. Grégory, 06560 Valbonne, France

<sup>3</sup> Departamento de Ciencia de los Materiales e I. M. y Q. I., Universidad de Cadiz. Apdo. 40 E-11510 Puerto Real (Cadiz), Spain

<sup>4</sup> Departamento de Ingenieria Electronica, ETSI Telecomunicacion, Universidad Politecnica, Apdo. 28040 Madrid, Spain

### ABSTRACT

In this work it is shown that thin AlN buffer layers cause N-polarity GaN epilayers, with a high inversion domains density. When the AlN thickness increases, the polarity of the epilayer changes to Ga. The use of a low temperature AlN nucleation layer leads to a flat AlN/Si(111) interface. This contributes to decrease the inversion domains density in the overgrown GaN epilayer with a Ga polarity.

### INTRODUCTION

The III-N semiconductor compounds are of great interest for the fabrication of optoelectronic devices, particularly with short wavelength. Moreover, III-nitrides have excellent electronic properties in comparison with materials frequently used for electronic devices. Moreover, they can be used for high temperature and high power applications.

GaN has been epitaxially grown on a large variety of substrates (6H-SiC, ZnO, GaAs, Si, different mixed oxides, etc) due to the lack of III-N semiconductors wafers. The growth of GaN over Si(111) substrates is an interesting challenge. The realization of GaN-based devices on this substrate would help to combine the optoelectronic and electronic properties of these materials to the well-known silicon technology. Although, the knowledge of heterostructures based on GaN grown over sapphire has considerably advanced, the GaN heteroepitaxy growth on Si(111) has received less attention.

The direct growth of GaN on Si(111) is not possible due to the large lattice mismatch, difference of thermal coefficients as well as the surface chemistry. A thin amorphous layer is generated between both materials because of the reaction of the Si(111) surface with the reactive nitrogen species<sup>1,2</sup>. Due to the poor GaN nucleation on Si(111) it is necessary to introduce a buffer layer in order to obtain an improved GaN epitaxy. An AlN thin layer was found to be an effective buffer for the growth of GaN films over Si(111)<sup>3</sup> and, up to now, it has been the most used buffer layer in this kind of growth<sup>4,5</sup>. In GaN/AlN/Sapphire heterostructures, the control of

\* Corresponding author, Tel. +33 2 31 45 26 53, Fax. +33 2 31 45 26 60, e-mail: ana.sanchez@ismra.fr

the AlN buffer layer thickness is not as critical as in GaN/GaN/Sapphire, and good results have been obtained in a large range of thickness (30-100 nm)<sup>6</sup>.

The anions in GaN wurtzite form a hcp structure in which the cations occupy half of the tetrahedral sites. There are two different kind of tetrahedral sites, at 3/8c above and below each N site respectively, which cannot be occupied simultaneously by the metallic atom, making possible two non-equivalent polarities in III-N semiconductors. Depending on the Ga-N bilayer orientation with respect to the growth direction, we can obtain Ga- or N-polarity.

In the III-N semiconductor thin film heterostructures, it is important to consider the role of the polarity in the structural defects formation. As the extended defects may reduce the device efficiency, a high structural quality of the epilayer is required. Previous reports have shown a higher dislocations density and inversion domains in N-polarity samples than in the Ga-polarity ones<sup>7</sup>. The inversion domains in N-polarity layers that grow faster than the surrounding material and originate pyramids<sup>8</sup>. On the other hand, the majority of flat unipolar GaN films present Ga-polarity<sup>8</sup>, and they have a more stable surface against the exposure to the nitrogen plasma flux than the N-polarity one<sup>9</sup>. A change from N-polarity to Ga-polarity has been determined when the AlN thickness increases<sup>10</sup>. Studies carried out in order to determine the inversion domain origin in the GaN/AlN/Si(111) concluded the existence of two possible factors: the substrate steps and the AlN buffer layer<sup>11</sup>.

In this work, we analyze the influence of the AlN buffer layer thickness on the GaN layer polarity, as well as its influence on the inversion domain formation in the GaN layers. We also point out the growth of AlN/GaN/AlN on the Si substrate previously to the GaN epilayer growth improves considerably the film quality, and a Ga polarity film without inversion domains is obtained.

## EXPERIMENTAL DETAILS

The growth of all the GaN layers was carried out by Molecular Beam Epitaxy (MBE) on Si(111) on axis substrates. Figure 1 shows a scheme of the characterized samples. In the S15 and S35 samples the AlN buffer layers were grown at 820°C and the GaN epilayers at 760-780°C by plasma assisted MBE. In S100 sample, an AlN buffer layer was grown using a nucleation temperature of 620°C followed by a rapid ramping to 920°C. The following GaN growth was carried out at 790°C. After that, a thick high temperature AlN layer is grown before the main GaN epilayer. In this instance the nitrogen source used was ammonia.

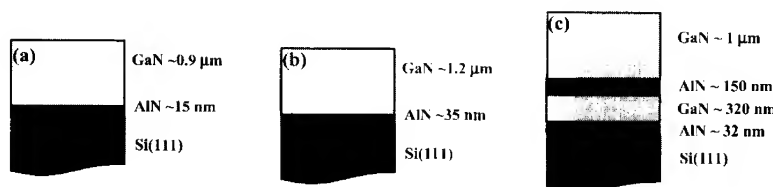


**Figure 1.** Scheme of the characterized samples, (a) S15, (b) S35 and (c) S100

BEST AVAILABLE COPY

Cross-sectional (XTEM) and planar-view (PVTEM) samples were prepared by conventional method. The specimens were thinned down to 100  $\mu\text{m}$  by mechanical grinding and dimpling down to 20  $\mu\text{m}$ , followed by ion milling at 4.5 kV to achieve electron transparency. The defects were conventionally characterized using a Jeol 1200EX and a Jeol 2010EX transmission electron microscopes operating at 120 kV and 200 kV, respectively. Convergent Beam Electron Diffraction (CBED) patterns were recorded in a Jeol 2010EX and High resolution electron microscopy studies (HRTEM) were carried out on a Topcon 002B both operating at 200kV.

## DISCUSSION

The GaN epilayers grown on AlN buffered Si(111) substrates by MBE present different structural defects<sup>12</sup>. These films consist of slightly misoriented subgrains with a high dislocation density. Moreover, stacking faults parallel to the growth plane and prismatic domains have been observed in films grown on Si(111). In our specimens, as deduced from PVTEM and XTEM observations, the typical mosaic structure has been observed, with a dislocation density reaching the GaN surface upper to  $10^9\text{cm}^{-2}$ .

CBED is a useful technique to determine both the epilayer polarity and the establishment of the local polarity in XTEM specimens. The GaN polarity has been determined by CBED applied in different regions inside the epilayer. CBED patterns were recorded along the  $\langle 1\bar{1}00 \rangle$  zone axis, in areas with a homogeneous contrast for all the specimens. The GaN layer polarity was determined by comparing the experimental (0002) and (000 $\bar{2}$ ) diffraction disks with simulations calculated under the same conditions. This study was carried out on S15, S35 and S100 samples. As can be observed in Figure 2, the GaN layer polarity changes with the AlN buffer layer thickness. Sample S15 seems to present a N-polarity, as shown by the fit with the simulated pattern for a GaN layer thickness 100 nm in the specimen. On the other hand, S35 and S100 exhibit a Ga-polarity, the TEM samples thickness is 95 nm and 100 nm, respectively.

Inversion domains have been reported previously in S15 and S35 samples<sup>11</sup>. The density of these defects was higher in the epilayer with smaller buffer layer thickness and N-polarity. A similar study has been realized in the S100 sample using  $g = \pm (0002)$  in order to verify the presence of such inversion domains. Normally, these defects appear as columns of wurtzite GaN having inverse polarity and different contrast to the GaN matrix. They propagate vertically along the epilayer. In this case, we did not find inversion domains arriving to the GaN surface. The threading dislocations crossing the epilayer are the main defects observed in the S100 epilayer (Figure 3a). No vertical domains are present in this image, there is no typical contrast of inversion domain. Therefore, if the inversion domains exist in S100 sample, their density is clearly smaller than in S15 and S35 samples. Figure 3b shows a region near the interface AlN/Si(111) in sample S100. An AlN buffer layer with a thickness of 32 nm can be measured from HRTEM images. Its growth was carried out as follows: the nucleation was initiated at 620°C, then the temperature was increased in two minutes to 920°C.

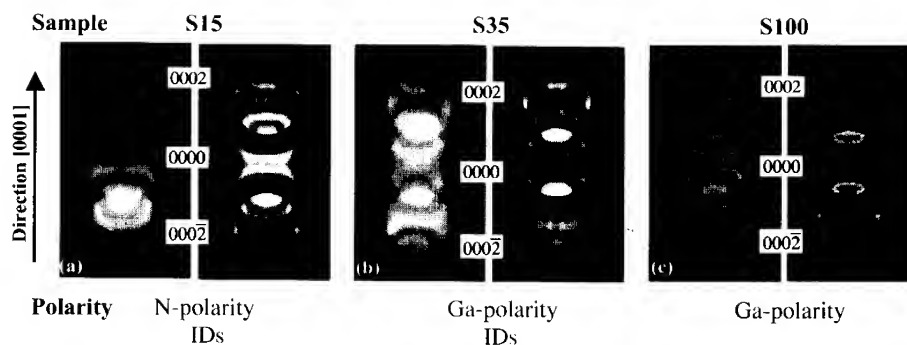


**Figure 2.** CBED patterns taken along the  $\langle 1\bar{1}00 \rangle$  from GaN epilayers of samples (a) S15 (N-polarity), (b) S35 (Ga-polarity) and (c) S100 (Ga-polarity). The experimental pattern are placed on the left and the experimental one on the right.

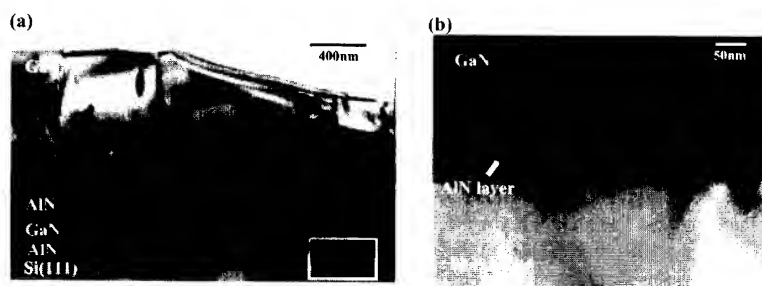


**Figure 3.** (a) Low magnification conventional bright field XTEM image taken in the  $\langle 1\bar{1}00 \rangle$  zone axis. No contrast similar to an inversion domain can be observed. (b) Magnified view (white square in (a))

These results point out that the AlN buffer layer influences the absolute layer polarity and the inversion domain formation inside the GaN epilayer. A buffer layer thickness of 15 nm is not enough to get a Ga-polarity in the overgrown GaN epilayer. When the AlN thickness is larger, we can observe a change in the film polarity. Therefore, a thicker AlN buffer layer leads to Ga-polarity and lower inversion domain density. Moreover, the growth of a low temperature AlN nucleation layer (620°C) in an AlN/GaN/AlN buffer structure previously to the main GaN epilayer provides a film without inversion domains. This is in good agreement with previous observations carried out for GaN grown over sapphire. Stutzmann et al. have studied the effect of a thin AlN buffer layer on the GaN/AlGaIn/GaN heterostructures polarity. The AlGaIn/GaN epilayers were grown on sapphire substrates by plasma induced molecular beam epitaxy (PIMBE), using different AlN buffer layer thickness in order to fabricate novel devices<sup>13</sup>. A

heterostructure with N-polarity is obtained when no buffer layer is incorporated. A change in the layer polarity is obtained when the AlN was integrated in the system. At small AlN thickness a mixed polarity with a large density of inversion domains could be observed. Nevertheless, in the growth over sapphire by PIMBE a thinner AlN buffer layer is required in order to get the polarity inversion of the epilayer. AlN buffer layers with 3 nm of thickness leads to films with mixed polarity with a high inversion domain density. When the AlN thickness exceeds 5 nm the epilayer changes completely to Ga-polarity<sup>13</sup>. In our samples, GaN growth over Si(111) by PAMBE and ammonia, an AlN buffer layer thicker than 15 nm is necessary to obtain Ga-polarity in the film.

In previous reports, various origins of the inversion domains have been observed in GaN epilayer grown on AlN-buffered Si(111) substrates by MBE. It was shown that small inversion domains originate on steps at the Si surface or on the top of misorientated grains in the AlN buffer layers<sup>11</sup>. Thus a flat AlN/Si(111) interface, without many steps, could contribute to get a GaN epilayer with a low inversion domains density. HRTEM images taken along the  $\langle 11\bar{2}0 \rangle$  zone axis in the AlN/Si(111) interface areas have been analyzed. As can be observed in Figure 4, the interface with the substrate does not exhibit any amorphous layer. However, the AlN/Si(111) interface is flatter in the sample S100 than in the other ones.

Although no amorphous layer has been observed in S15 and S35 samples, the interface in these growths were not completely flat. In Figure 4(a), a silicon protuberance penetrating toward the AlN buffer layer is shown (arrow). On the other hand, the interface between the AlN nucleation layer and the Si(111) in the S100 sample provides a flat interface as can be observed in Figure 4(b). When the AlN growth temperature is above 620°C there is outdiffusion of silicon to the GaN epilayer<sup>14</sup>. In S15 and S35 samples the AlN temperature growth was 820°C, promoting the Si diffusion. In this way, the protuberances could correspond to the Si diffusion from the substrate to the epilayer. In the S100 sample (AlN at 620°C) a better AlN/Si(111) interface was then obtained, this seems to decrease the inversion domain density in the GaN epilayer. Therefore, the growth of an AlN nucleation layer at low temperature in GaN samples on Si(111) probably improves the crystalline quality of the epilayer.

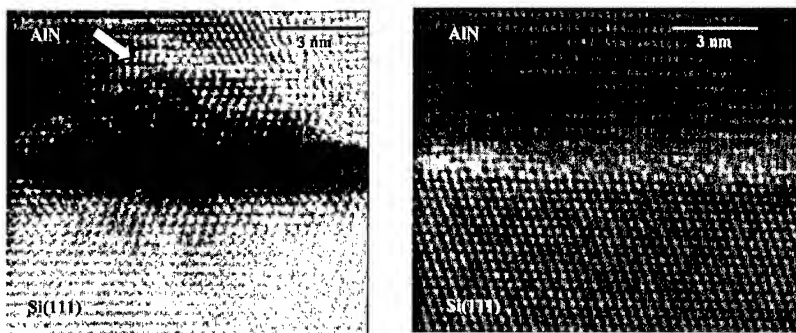


**Figure 4.**  $\langle 11\bar{2}0 \rangle$ -HRTEM images in AlN/Si(111) interface. (a) S35 and (b) S100

## CONCLUSIONS

In summary, we characterized GaN heterostructures grown on Si(111) substrates. The AlN buffer influences both the absolute layer polarity and inversion domains density on the GaN. An AlN buffer layer thicker than 15 nm is necessary to change the epilayer polarity from N- to Ga-. The AlN nucleation layer grown at 620°C, in the first steps of the growth, avoids the outdiffusion from the silicon substrate to the GaN epilayer, providing a flat AlN/Si(111) interface. This contributes to improve the structural quality of the overgrown GaN film.

## ACKNOWLEDGMENTS

The authors acknowledge the support of the EU under contract HPRN-CT-1999-00040. Author from University of Cadiz acknowledge the financial support from the project MAT2000-0478 P4-02 and the Junta de Andalucía (Group TEP-0120).

## REFERENCES

1. A. Ohtani, K.S. Stevens, R. Beresford, *Appl. Phys. Lett.* **65** (1994) 61
2. K.S. Stevens, M. Kinniburgh, A.F. Schwartzman, A. Ohtani, R. Beresford, *Appl. Phys. Lett.* **6** (1995) 3179
3. A. Watanabe, T. Takeuchi, I. K. Hirose, H. Amano, K. Hiramatsu and I. Akasaki, *J. Cryst. Growth* **128** (1993) 391
4. F. Semond, Y. Cordier, N. N. Grandjean, F. Natali, B. Damilano, S. Vezian and J. Massies, *Phys. Stat. Sol.* **188** (2001) 501
5. E. Calleja, M.A. Sanchez-Garcia, F.J. Sanchez, F. Calle, F.B. Naranjo, E. Muñoz, S.I. Molina, A.M. Sanchez, F.J. Pacheco and R. Garcia, *J. Cryst. Growth* **201/202** (1999) 296
6. Group III Nitride semiconductor Compounds, Physics and Applications (1998) Ed. Bernard Gil. Oxford Science Publications.
7. F. Yun, D. Huang, M.A. Reshchikov, T. King, A.A. Baski, C.W. Litton, J. Jasinski, Z. Lilliental-Weber, P. Visconti, H. Morkoç, *Phys. Stat. Sol. B* **228** (2001) 543
8. J.L. Rouviere, M. Arlery, R. Niebuhr, K.H. Bachem and O. Briot, *Mat. Sci. Eng. B* **43** (1997) 161
9. X.Q. Shen, T. Ide, S.H. Cho, M. Shimizu, S. Hara and H. Okumura, *Appl. Phys. Lett.* **77** (2000) 4013
10. A.M. Sanchez, F.J. Pacheco, S.I. Molina, P. Ruterana, F. Calle, T.A. Palacios, M.A. Sanchez-Garcia, E. Calleja and R. Garcia, *Mat. Sci. Eng. B* **93** (2002) 181
11. A.M. Sanchez, P. Ruterana, S.I. Molina, F.J. Pacheco and R. Garcia, *Phys. Stat. Sol.* In press
12. S.I. Molina, A.M. Sanchez, F.J. Pacheco, R. Garcia, M.A. Sanchez-Garcia, F.J. Sanchez and E. Calleja, *Appl. Phys. Lett.* **74** (1999) 3362
13. M. Stutzmann, O. Ambacher, M. Eickhoff, U. Karrer, A. Lima Pimenta, R. Neuberger, J. Schalwig, R. Dimitrov, P.J. Schuck and R.D. Grober, *Phys. Stat. Sol.* **228** (2001) 505
14. E. Calleja, M.A. Sánchez-García, D. Basak, F.J. Sánchez, F. Calle, P. Youinou, E. Muñoz, J.J. Serrano, J.M. Blanco, C. Villar, T. Laine, J. Oila, K. Saarinen, P. Hautajarvi, C.H. Molloy, D.J. Somerford and I. Harrison, *Phys. Rev. B* **58** (1998) 1550

### Single Crystalline InN Films Grown on Si Substrates By Using A Brief Substrate Nitridation Process

**Tomohiro Yamaguchi, Kazuhiro Mizuo, Yoshiki Saito, Takuma Noguchi, Tsutomu Araki and Yasushi Nanishi**

Department of Photonics, Ritsumeikan University, 1-1-1 Noji-Higashi, Kusatsu, Shiga 525-8577, JAPAN.

**Takao Miyajima**

Core Technology Development Center, Core Technology & Network Company, Sony Corporation, 4-14-1 Asahi-cho, Atsugi, Kanagawa 243-0014, JAPAN.

**Yoshihiro Kudo**

Technology Solutions Center, Sony Corporation, 4-16-1 Okata, Atsugi, Kanagawa 243-0021, JAPAN.

#### ABSTRACT

InN films were grown on Si (111) substrates by radio-frequency plasma-excited molecular beam epitaxy. InN films highly oriented to the *c*-axis were obtained by optimizing growth conditions in the direct growth on Si. Growth of single crystalline InN films was realized on Si substrates with substrate nitridation for 3 min. On the other hands, when the substrate nitridation was lasted over 30 min, obtained InN films were polycrystalline due to the amorphous SiN<sub>x</sub> layer formed on a substrate surface. We also studied the local atomic structure in the single crystalline InN film using extended X-ray absorption fine structure measurements.

#### INTRODUCTION

As indicated by its recent research popularity[1-8], InN has a large potential for photonic and electronic applications. InN, including its alloys, would also have a great potential for a new high efficiency solar cell covering the full solar spectrum. However, InN has few suitable substrates due to its large lattice mismatch with most substrates. This means that a good initial growth process is needed for high quality growth. Substrate nitridation is one such initial process that has been studied. Substrate nitridation is well known to improve the crystallinity of InN on sapphire[9-11], GaAs[12], and GaP[12] substrates.

On the other hand, however, the role of nitridation for InN growth on Si is less clear. Yamamoto *et al.* [9] reported that substrate nitridation prevented to grow InN films with metalorganic chemical vapor deposition (MOCVD) because of forming an amorphous SiN<sub>x</sub> layer on Si substrate surface. Therefore, on Si, methods to grow InN films are careful to avoid forming SiN<sub>x</sub> layers [13]. This includes methods that use molecular beam epitaxy (MBE) [14,15]. However, growing single crystalline InN films on Si remains difficult [9,13-18].

Recently, effects of substrate nitridation on Si have been studied. Yodo *et al.* [19] reported that substrate nitridation prevented to contain cubic phases in hexagonal InN films. We succeeded to realize single crystalline hexagonal InN films by using substrate nitridation and a low-temperature buffer layer deposition [20,21]. In this paper, we describe how our use of nitridation allowed us to grow single crystalline hexagonal InN films on Si. We then describe the local atomic structure of this film.

## EXPERIMENTAL DETAILS

InN films were grown on Si (111) substrates by radio-frequency plasma-excited MBE (RF-MBE). The sources used were elemental In from a standard Knudsen effusion cell and excited  $N_2$  gas with 6N purity from an RF plasma source (SVT associates model 4.5). Prior to growth, the Si substrate was cleaned with HF solution and then was thermally cleaned above 800°C for 20 min in vacuum. Following this process, nitridation was carried out at 800°C with a nitrogen flow rate of 1 sccm and an RF power of 380 W. Then, an InN film was grown at 390°C for 1 h. The growth conditions were as follows: an In cell temperature of 775°C, a nitrogen flow rate of 2 sccm, and an RF power of 240 W. An InN film inserted a low-temperature InN buffer layer was also grown on nitridated substrates to improve the crystallinity of the InN film.[21] The low-temperature buffer layer was deposited at 280°C for 10 min. For comparison, an InN film was also directly grown without initial growth processes such as substrate nitridation and low-temperature buffer layer deposition. The obtained InN film thicknesses were approximately 0.25  $\mu\text{m}$ .

The crystal quality of the InN films was characterized by *in situ* reflection high-energy electron diffraction (RHEED), X-ray diffraction (XRD) (Philips X'Pert MRD) and extended X-ray absorption fine structure (EXAFS) measurements. The surface morphologies of these films were examined with scanning electron microscopy (SEM). The nitridated substrate surface before InN growth was investigated by X-ray photoelectron spectroscopy (XPS) measurement.

## RESULTS AND DISCUSSION

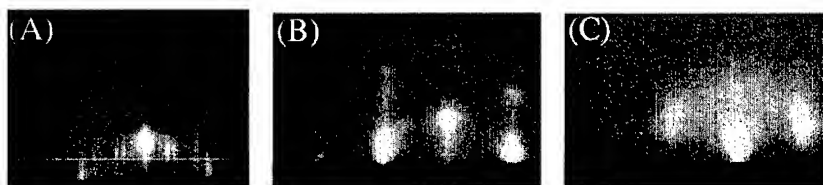
InN films grown directly on Si without initial growth processes are always polycrystalline [9,21]. By optimizing the growth temperature and V/III ratio, an InN film highly oriented to the *c*-axis was obtained. However, the *a*-axis in the film was not well oriented as shown in Fig. 1, indicating that distorted rotation domains were existed.

Figure 2 shows the RHEED patterns of the Si substrates before and after substrate nitridation. Before substrate nitridation, a clear  $7\times 7$ -reconstruction RHEED pattern typical of a clean Si (111) surface was obtained (Fig. 2a). When the Si substrate surface was exposed to the nitrogen plasma, the RHEED pattern changed from  $7\times 7$  to  $1\times 1$ . After a brief substrate nitridation (3 min), the pattern became diffused (Fig. 2b). The in-plane interlayer spacing obtained from the RHEED pattern nearly equaled that of Si, indicating that Si surface almost unchanged crystallographically by the nitridation. We used XPS to determine whether or not  $\text{SiN}_x$  formed on the substrate surface during the 3-min substrate nitridation. Figure 3a shows the Si2p spectra before and after the nitridation; an additional peak representing Si-N bonding appeared in the substrate with nitridation. The N1s spectrum for the substrate without nitridation (Fig. 3b) shows no peak, whereas the peak clearly observed for the substrate with nitridation. The RHEED and XPS results suggest that  $\text{SiN}_x$  formed on the Si substrate even when the nitridation was carried out for only 3 min, and the  $\text{SiN}_x$  would be formed in part on the Si substrate surface. When the substrate nitridation lasted over 30 min (Fig. 2c), the pattern changed to a halo pattern with weak streaks, suggesting that an amorphous  $\text{SiN}_x$  layer formed on the substrate surface.

BEST AVAILABLE COPY



**Figure 1.**  $\{11\bar{2}2\}$  XRD pole-figure of an InN film grown directly without substrate nitridation.



**Figure 2.** RHEED patterns of Si substrates (A) before substrate nitridation, (B) after substrate nitridation for 3min, and (C) after substrate nitridation for 30 min.

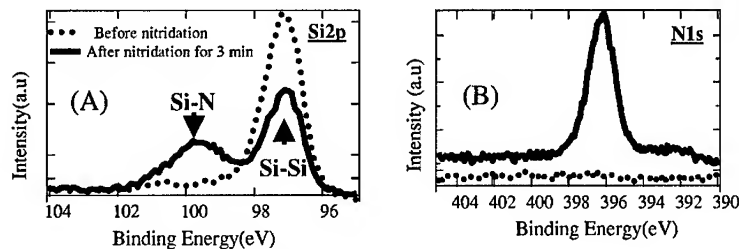


**Figure 3.** (A) Si2p and (B) N1s XPS spectra of Si substrate surface before and after a brief period of nitridation.

Figure 4 shows the RHEED pattern of a hexagonal InN film grown on Si with a brief period of nitridation (3 min). A clear streak pattern appears. Existence of cubic phases in this film was not observed from RHEED and XRD measurements. These results showed a same tendency toward the results by Yodo *et al* [19]. Figure 5 shows an XRD pole figure of this film. Metastable rotation domains, such as that in Fig. 1, were not formed. Furthermore, XRD  $\omega$ -2 $\theta$  spectra of this film showed that metastable tilted domains such as  $(10\bar{1}1)$  were not formed. These results show that single crystalline hexagonal InN film could be grown on Si substrates with a brief substrate nitridation. Figure 6 shows RHEED pattern of an InN film grown on Si substrate with substrate nitridation for 1 h. The diffused ring pattern confirmed that single crystalline InN films could not be grown when nitridation was lasted for 1h. It was indicated that

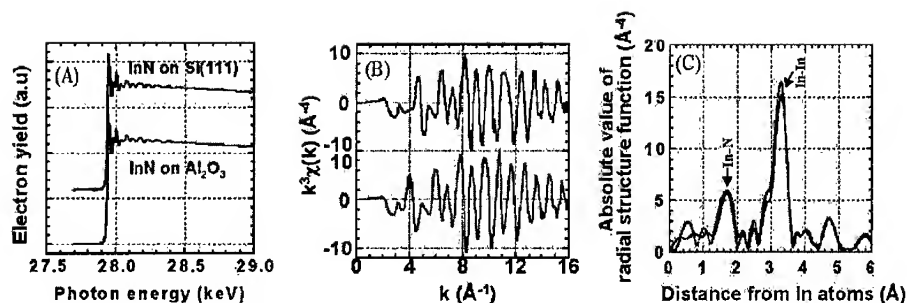


**Figure 8.** (A) Electron-yield spectra, (B)  $k^3$ -weighted In K-edge EXAFS oscillations, and (C) absolute values  $|F(r)|$  of In K-edge radial structure function oscillations, of InN films grown on Si and on sapphire substrates.

The surface morphologies of InN films evaluated by SEM are shown in Fig. 7. Fig. 7a shows that the film grown with the brief nitridation has three-dimensional grains of a few hundred-nanometer sizes. On the other hand, when a low-temperature buffer layer was inserted on a substrate with the same nitridation as that for Fig. 7a, the surface had a two-dimensional growth mode (Fig. 7b). These results indicate that low-temperature buffer layer deposition is a useful way to grow a very flat surface in addition to improve the crystallinity of InN films [21].

Using EXAFS, we studied the local structure in the single crystalline InN film that was grown with the brief nitridation and the low-temperature buffer layer. Figure 8a shows the electron-yield spectra of InN films grown on Si and sapphire substrates. (The data for sapphire is from Ref. 22.) For Fig. 8b, we isolated the  $k^3$ -weighted In K-edge EXAFS oscillation of these films from their electron-yield spectra. In both spectra, the noise level was much lower than the oscillation amplitude for  $k \leq 16$  Å<sup>-1</sup>. We used the Fourier transformation magnitudes for a  $k$  range of 2-14 Å<sup>-1</sup> to obtain the absolute values  $|F(r)|$  of the In K-edge radial structure function (Fig. 8c). The profile of the radial structure function for the Si substrate is similar to that for sapphire. This shows that both the first neighboring distance of In-N pairs and the first neighboring distance of In-In pairs are almost the same for the InN films grown on Si and sapphire substrates. The estimated coordination number for an In atom in InN grown on the Si substrate is 4.0; this value is the ideal coordination number for III-V semiconductors. We conclude, therefore, that the In-N atomic bonding has the ideal  $sp^3$  hybridization in single crystalline InN films grown on Si as well as high quality single crystalline films on sapphire.

## CONCLUSIONS

In the growth of RF-MBE, single crystalline InN films were realized by using an appropriate substrate nitridation. Single crystalline InN films could be grown on Si substrates with a brief substrate nitridation for 3 min. On the other hands, InN films grown on Si substrates nitridated for 1 h, by which amorphous SiN<sub>x</sub> layers were formed on the substrate surfaces, were polycrystalline. The local atomic structures in single crystalline InN films on Si substrates were almost the same as those in high-quality InN films on sapphire.

single crystalline InN films could not be grown on amorphous SiN<sub>x</sub> layer formed by a substrate nitridation lasted for a long time. From these results, we conclude that the nitridation time is an important parameter for the growth of single crystalline InN films on Si substrates. The detail mechanisms of Si substrate nitridation are now being considered.



**Figure 4.** RHEED pattern of an InN film grown on Si with a brief period of substrate nitridation.

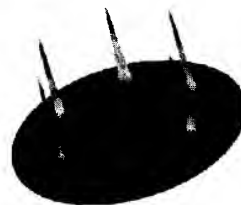


**Figure 5.**  $\{11\bar{2}2\}$  XRD pole-figure of an InN film grown with a brief period of substrate nitridation.



**Figure 6.** RHEED pattern of an InN film grown on Si substrate with substrate nitridation for 1 h.

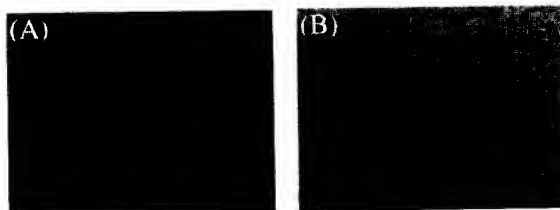


**Figure 7.** SEM images of InN films. (A) InN film grown on substrate with a brief period of nitridation. (B) InN film grown on a low-temperature buffer layer that was grown on substrate with a brief period of nitridation.

BEST AVAILABLE COPY

## ACKNOWLEDGMENTS

We express special thanks to Dr. K. Kamei of Sumitomo Metal Industries, Ltd., Dr. N. Teraguchi of Sharp Corp. and Prof. A. Suzuki of Ritsumeikan Univ. for useful discussions. This work was supported in part by the Ministry of Education, Culture, Sports, Science and Technology, Grant-in-Aid for Scientific Research (B), 13450131, 2002.

## REFERENCES

1. Y. Saito, N. Teraguchi, A. Suzuki, T. Araki and Y. Nanishi, *Jpn. J. Appl. Phys.* **40** (2001) L91.
2. H. Lu, W. J. Schaff, J. Hwang, H. Wu, G. Koley and L. F. Eastman, *Appl. Phys. Lett.* **79** (2001) 1489.
3. M. Higashiwaki and T. Matsui, *Jpn. J. Appl. Phys.* **41** (2002) L540.
4. T. Inushima, V. V. Manutin, V. A. Vekshin, S. V. Ivanov, T. Sakon, and S. Motokawa, *J. Cryst. Growth* **227** (2001) 481.
5. V. Y. Davydov, A. A. Klochikhin, R. P. Seisyan, V. V. Emtsev, S. V. Ivanov, F. Bechstedt, J. Furthmuller, H. Harima, A. V. Mudryi, J. Adhrhold, O. Semchinova, and J. Graul, *phys. stat. sol. (b)* **229** (2002) R1.
6. T. Matsuoka, H. Okamoto, M. Nakao, H. Harima, and E. Kurimoto, *Appl. Phys. Lett.* **81** (2002) 1246.
7. J. Wu, W. Walukiewicz, K. M. Yu, J. W. Arger III, E. E. Haller, H. Lu, W. J. Schaff, Y. Saito, and Y. Nanishi, *Appl. Phys. Lett.* **80** (2002) 3967.
8. Y. Saito, H. Harima, E. Kurimoto, T. Yamaguchi, N. Teraguchi, A. Suzuki, T. Araki, and Y. Nanishi, *phys. stat. sol. (b)* **234** (2002) 796.
9. A. Yamamoto, M. Tsujino, M. Ohkubo and A. Hashimoto, *J. Cryst. Growth* **137** (1994) 415.
10. T. Tsuchiya, H. Yamano, O. Miki, A. Wakahara and A. Yoshida, *Jpn. J. Appl. Phys.* **38** (1999) 1884.
11. T. Yamaguchi, T. Araki, Y. Saito, T. Muramatsu, N. Teraguchi, A. Suzuki and Y. Nanishi, *Inst. Phys. Conf. Ser.* **170** (2001) 765.
12. Q. X. Guo, H. Ogawa, H. Yamano and A. Yoshida, *Appl. Phys. Lett.* **66** (1995) 715.
13. F. H. Yang, J. S. Hwang, K. H. Chen, Y. J. Yang, T. H. Lee, L. G. Hwa and L. C. Chen, *Thin Solid Films* **405** (2002) 194.
14. M. Yoshimoto, T. Nakano, T. Yamashita, K. Suzuki and J. Saraie, *IPAP conf. Series* **1** (2000) 186.
15. F. Agullo-Rueda, E. E. Mendez, B. Bojarczuk and C. Guha, *Sol. Stat. Comm.* **115** (2000) 19.
16. I. Bello, W. M. Lau, R. P. W. Lawson and K. K. Foo, *J. Vac. Sci. Technol A* **10** (1992) 1642.
17. Y. Bu, L. Ma and M. C. Lin, *J. Vac. Sci. Technol A* **11** (1993) 2931.
18. T. Yodo, H. Yona, H. Ando, D. Nosei and Y. Harada, *Appl. Phys. Lett.* **80** (2002) 968-970.
19. T. Yodo, H. Yona, K. Iwaya, N. Toyotomi and Y. Harada, *Extended Abst. of 21<sup>st</sup> Electronic Materials Symposium* (2002) B3.
20. T. Yamaguchi, K. Mizuo, Y. Saito, T. Araki, N. Teraguchi, A. Suzuki and Y. Nanishi, *Extended Abst. of 21<sup>st</sup> Electronic Materials Symposium* (2002) C3.
21. T. Yamaguchi, K. Mizuo, Y. Saito, T. Araki and Y. Nanishi, *Int. Symp. Compound Semicond., Lausanne, Switzerland, 7-10 Oct., (2002) Mo-P-7.* (To be published in *Inst. Phys. Conf. Ser.*).
22. T. Miyajima, Y. Kudo, K.-L. Liu, T. Uruga, T. Honma, Y. Saito, M. Hori, Y. Nanishi, T. Kobayashi and S. Hirata, *phys. stat. sol. (b)* **234** (2002) 801.

BEST AVAILABLE COPY

### Study on Cubic GaN Growth on (001) Rutile TiO<sub>2</sub> Substrates by ECR-MBE

T.Araki, H.Mamiya, K.Kitamura and Y.Nanishi  
Dept. of Photonics, Ritsumeikan University,  
1-1-1 Noji-higashi, Kusatsu, Shiga 525-8577, Japan

#### ABSTRACT

GaN layers were grown on a (001) rutile TiO<sub>2</sub> substrate by electron cyclotron resonance plasma-excited molecular beam epitaxy. For the first time, c-GaN with a preferential growth orientation was obtained. Based on the results from electron diffraction and X-ray diffraction analysis, we found that c-GaN with the growth direction of [110] was grown on the TiO<sub>2</sub> substrate. The formation of c-GaN was also confirmed by cathodoluminescence, in which a luminescence peak was observed at 3.24eV.

#### INTRODUCTION

Nitride semiconductors; GaN, AlN and InN crystallize in both hexagonal wurtzite and cubic zinc-blende crystal structure. Until now, most of all the GaN-based optical and electronic devices are of wurtzite hexagonal GaN (h-GaN) because of both metastable nature of zinc-blende cubic GaN (c-GaN) and a lack of suitable substrates for the c-GaN growth. However, c-GaN has been expected to have various advantages in the physical properties over those of h-GaN due to its higher crystallographic symmetry, resulting in smaller effective mass, lower phonon scattering, higher doping efficiency and so on [1]. Moreover, for the growth of c-GaN on cubic (001) substrates, the absence of piezoelectric polarization fields will help us to understand the emission mechanism of multiple quantum wells [2,3]. As for the device applications, c-GaN grown on appropriate substrates is also superior to h-GaN in the ease of cleaving and the formation of back-side electrode. Thus, a large number of studies to grow c-GaN on various substrates have been carried out [4]. Substrates used in these studies are mainly GaAs [5-7], 3C-SiC [8-10] and Si [11,12]. It has been difficult, however, to grow high quality c-GaN because of the large mismatch with the substrates and the lack of enough stability at growth temperatures, resulting in h-GaN phase mixing. Therefore, further study concerning even about substrate material is still necessary to realize growth of high quality c-GaN.

TiO<sub>2</sub> has rutile (body-centered tetragonal) crystal structure. Figure 1 shows the crystal structure of a TiO<sub>2</sub> unit cell. Lattice constants along *a*-axis and *c*-axis are 4.593 Å and 2.959 Å, respectively. When (001) c-GaN is grown on (001) rutile TiO<sub>2</sub>, lattice mismatch between c-GaN (*a* = 4.531 Å) and the TiO<sub>2</sub> substrate is -1.3%, which is much smaller than those of other substrates; -20 % for (001) GaAs, 4 % for (001) 3C-SiC and 17% for (001) Si. Therefore, TiO<sub>2</sub> is expected as a lattice-matched substrate for the growth of (001) c-GaN. We should consider that TiO<sub>2</sub> substrate is not stable at high temperature and a reducing atmosphere including hydrogen. It

was found that  $\text{TiO}_2$  substrate was reduced during metal organic chemical vapor deposition growth of GaN at around  $1000^\circ\text{C}$  [13]. This result suggests that molecular beam epitaxy (MBE), by which a low growth temperature and a hydrogen free atmosphere are available, should be suitable for the growth of c-GaN on the  $\text{TiO}_2$  substrate. Sitar *et al.* reported the gas source MBE growth of GaN on the (001) rutile  $\text{TiO}_2$  substrate [14]. However, they could obtain only polycrystalline GaN without a preferential orientation.

In this study, we report on the growth of c-GaN on the (001) rutile  $\text{TiO}_2$  substrate by electron cyclotron resonance plasma - excited (ECR-) MBE. For the first time, (110) c-GaN preferentially grown on this substrate was obtained. Structural and optical properties of the c-GaN were also investigated.

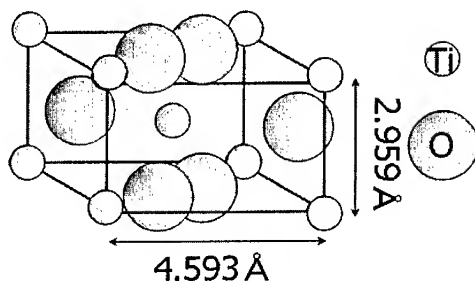


Figure 1. Crystal structure of rutile  $\text{TiO}_2$ .

## EXPERIMENTAL

GaN layers were grown by ECR-MBE. Gallium was effused from the conventional Knudsen cell to the substrates. The  $\text{TiO}_2$  substrate was cleaned by an organic solvent and thermally cleaned at  $750^\circ\text{C}$  for 30 min in the growth chamber just prior to growth. Subsequently, the GaN layer was grown on the  $\text{TiO}_2$  substrate directly. Microwave power and a nitrogen gas flow rate were kept constant at 120 W and 30 sccm, respectively. A temperature of the Ga cell was  $880^\circ\text{C}$ . Only the growth temperature was varied from  $590$  to  $710^\circ\text{C}$ .

Structural characterizations of the GaN layers were performed by reflection high-energy electron diffraction (RHEED), X-ray diffraction (XRD) and scanning electron microscopy (SEM). Optical property was characterized using cathodoluminescence (CL) at room temperature (RT).

## RESULTS AND DISSCUSSION

Figure 2 shows RHEED patterns of the GaN layers grown on the  $\text{TiO}_2$  substrate at various growth temperatures. When the GaN layers were grown under  $600^\circ\text{C}$  or over  $700^\circ\text{C}$ , ring patterns were mainly obtained in the RHEED observation. This means that polycrystalline GaN was obtained at these growth temperatures. On the other hand, spot patterns were clearly appeared from the GaN layers grown at  $620 - 680^\circ\text{C}$ , indicating that the GaN layers had a

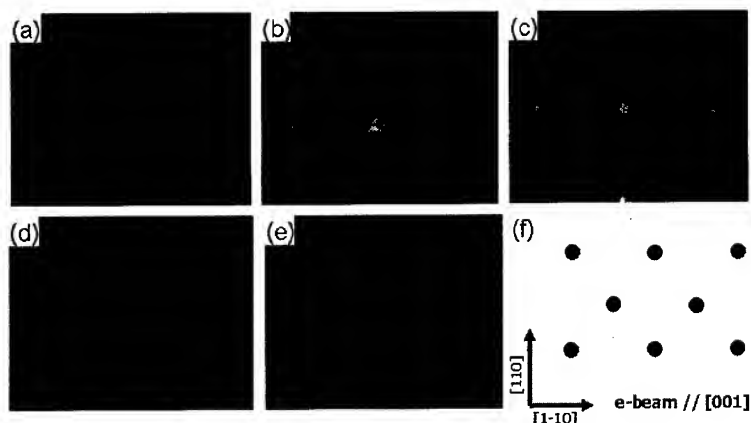


Figure 2. RHEED images of the GaN layers grown on the TiO<sub>2</sub> substrate at (a) 590°C, (b) 620°C, (c) 650°C, (d) 680°C and (e) 720°C. (f) simulated diffraction pattern for c-GaN with a (110) growth orientation.

preferential growth orientation. As shown in Fig. 2(f), the diffraction pattern is corresponding to the simulated pattern for c-GaN with a (110) growth orientation rather than a (001) orientation. In Fig. 2(c), an extra diffraction pattern tilted about 35° from the growth direction was observed as shown by arrows. The pattern was also explained by considering the growth of (110) c-GaN. Figure 3 shows an atomic arrangement of (110) c-GaN. The (111) plane of c-GaN is existed with a tilting angle of 35.3° from [110] direction. Hexagonal phases might be formed on the (111) plane of c-GaN due to the ease of changing atomic stacking sequence from ABCABC~ to ABABAB~. Therefore, the extra pattern is considered to be resulted from h-GaN mixing grown on (111) plane of c-GaN.

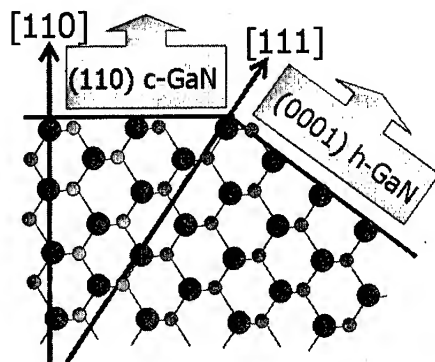


Figure 3. atomic arrangement of (110) c-GaN.

Figure 4 shows an XRD ( $\omega$ -2 $\theta$  mode) profile of the GaN layer grown on the TiO<sub>2</sub> substrate. Strong diffraction peak from (220) c-GaN was observed at 57.5°. Other weak peaks observed at 48.1° and 68.1° are found to be due to (10-12) h-GaN and (11-22) h-GaN, respectively, which means mixing of h-GaN with various growth orientations were existed. These XRD results also confirmed that c-GaN grown on the TiO<sub>2</sub> substrate was oriented along [110] direction of c-GaN.

Surface morphology of the GaN layers grown on the TiO<sub>2</sub> substrate were investigated using

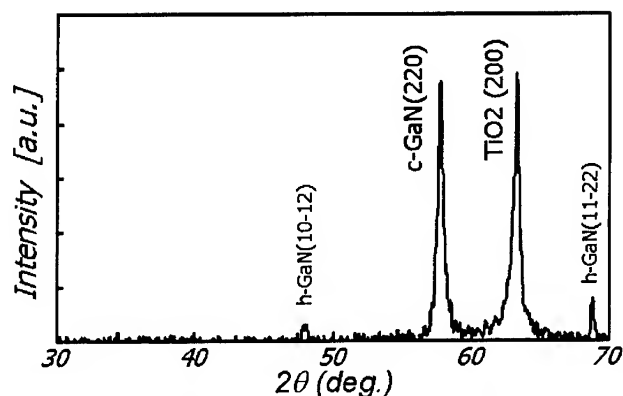


Figure 4. XRD ( $\omega$ - $2\theta$  mode) profile of the GaN layer grown on the  $\text{TiO}_2$  substrate.

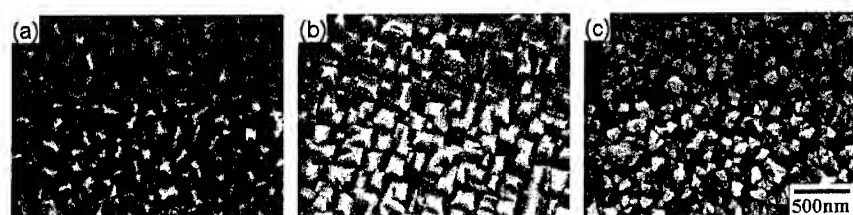


Figure 5. SEM images of the GaN layers grown at (a) 590°C, (b) 650°C and (c) 710°C.

SEM. Figure 5 shows the SEM images of the GaN layers grown at (a) 590°C, (b) 650°C and (c) 710°C, respectively. As shown in Fig. 4(a) and 4(c), the GaN layers grown at 590°C and 710°C exhibited random grain structure without a preferential growth orientation, which agree with the results from the RHEED observation. On the other hands, the GaN layer grown at 650°C seemed to have some kind of ordered grain structure as shown in Fig. 4(b). Almost all the grains showed roof-top surface morphology. This shape is considered to be caused by the crystal

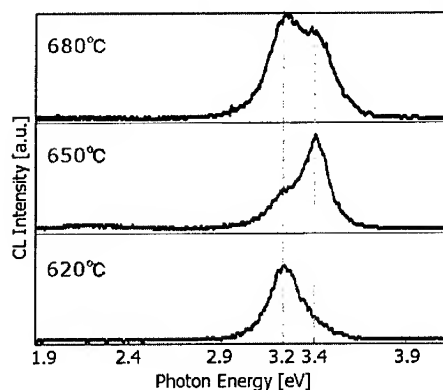


Figure 6. CL profiles of the GaN layers grown at 620°C, 650°C and 680°C.

surface of c-GaN with a (110) growth orientation.

Figure 6 shows CL profiles of the GaN layers observed at RT. All of the GaN layers grown at 620°C, 650°C and 680°C, in which the diffraction pattern of c-GaN was clearly observed in Fig. 2, showed a luminescence peak at 3.24 eV. These results also support that growth of c-GaN was realized on the TiO<sub>2</sub> substrate. However, mixture of hexagonal phase confirmed by a luminescence peak at 3.4 eV was obviously recognized in the GaN layers grown at 650°C and 680°C. Higher growth temperature might enhance the formation of h-GaN which is thermodynamically stable compared to c-GaN.

At this moment, the growth mechanism of (110) c-GaN on the (001) TiO<sub>2</sub> substrate rather than (001) c-GaN, which should have better lattice mismatch for the substrate, is not clear. It seems likely that the difference of crystal structure between zinc-blende of c-GaN and rutile of TiO<sub>2</sub> worked more effectively for the determination of the growth orientation of c-GaN on the TiO<sub>2</sub> substrate than the advantage in the lattice mismatch.

## CONCLUSIONS

We have demonstrated the growth of GaN on the rutile (001) TiO<sub>2</sub> substrate by ECR-MBE. For the first time, c-GaN with a preferential growth orientation was obtained on the TiO<sub>2</sub> substrate. Results from RHEED and XRD confirmed that growth orientation of c-GaN was [110] of c-GaN. CL emission was also observed from c-GaN grown on the TiO<sub>2</sub> substrate although mixture of h-GaN existed.

## ACKNOWLEDGEMENTS

This work was partly supported under the Academic Frontier Promotion Project of the Ministry of Education, Science, Sports and Culture, Japan.

## REFERENCES

1. M. E. Lin, G. Xue, G.L. Zhou, J.E. Greene and H. Morkoc, *Appl. Phys. Lett.* **63**, 932 (1993).
2. T. Koizumi, H. Okumura, K. Balakrishnan, H. Harima, T. Inoue, Y. Ishida, T. Nagatomo, S. Nakashima and S. Yoshida, *J. Cryst. Growth* **201/202**, 341 (1999).
3. T. Kitamura, Y. Suzuki, Y. Ishida, X.Q. Shen, H. Nakanishi, S.F. Chichibu, M. Shimizu and H. Okumura, *phys. stat. sol. (a)* **188**, 705 (2001).
4. H. Okumura, K. Ohta, G. Feuillet, K. Balakrishnan, S. Chichibu, H. Hamaguchi, P. Hacke and S. Yoshida, *J. Cryst. Growth* **178**, 113 (1997).
5. S. Strite, J. Ruan, Z. Li, N. Manning, A. Salvador, H. Chen, D.J. Smith, W.J. Choyke, H. Morkoc, *J. Vac. Sci. Technol.* **B9**, 1924 (1991).
6. H. Okumura, S. Misawa and S. Yoshida, *Appl. Phys. Lett.* **59**, 1058 (1991).

- 
7. S. Fujieda and Y. Matsumoto, *Jpn. J. Appl. Phys.* **30**, L1665 (1991).
  8. M.J. Paisley, Z. Sitar, J.B. Posthill and R.F. Davis, *J. Vac. Sci. Technol.* **A7**, 701 (1989).
  9. H. Okumura, S. Miwasa, T. Okahisa and S. Yoshida, *J. Cryst. Growth* **136**, 361 (1994).
  10. H. Liu, A.C. Frenkel, J.G. Kim and R.M. Park, *J. Appl. Phys.* **74**, 6124 (1993).
  11. T. Lei, T.D. Moustakas, R.J. Graham, Y. He and S.J. Berkowitz, *J. Appl. Phys.* **71**, 4933 (1992).
  12. A. Barski, U. Rossner, J.L. Rouviere and M. Arlery, *Mat. Res. Soc. Int. J. Nitride Semicond. Res.* **1**, 21 (1996).
  13. H. Tanaka, unpublished.
  14. Z. Sitar, M.J. Paisley, B. Yan and R.F. Davis, *Mat. Res. Soc. Symp. Proc.* **162**, 537 (1990).

**Characterization of Cubic GaN Films Using  
An AlN/GaN Ordered Alloy on GaAs (100) by RF-MBE**

Junichi Shike, Atsushi Shigemori, Koichi Ishida, Kiyoshi Takahashi and Ryuhei Kimura  
High-Tech Research Center, Faculty of Science and Engineering,  
Teikyo University of Science and Technology  
2525 Yatsuzawa, Uenohara, Kitatsuru-gun, Yamanashi, 409-0193, Japan

**ABSTRACT**

High quality cubic GaN films were successfully grown on an AlN/GaN ordered alloy by RF-MBE. AlN/GaN ordered alloy is here employed instead of a AlGa<sub>N</sub> nucleation layer formed by nitridation of an AlGaAs buffer layer. Dominant cubic GaN epilayer (1.0 μm) growth was confirmed by insitu RHEED observations, AFM, TEM, PL and X-ray diffraction measurements.

**INTRODUCTION**

Cubic GaN (c-GaN) is expected to have many advantages in physical properties over those of the hexagonal phase due to its higher crystallographic symmetry. We earlier reported that using an AlGa<sub>N</sub> layer formed by nitridation of an Al<sub>0.17</sub>Ga<sub>0.83</sub>As buffer was an efficient process for ensuring growth of a highly pure c-GaN film growth [1,2]. However, there still remain some problems regarding AlGaAs growth. The first relates to fluctuations in Al concentration, which in turn significantly affects the purity of the structural phase of the epilayer. The second is the difficulty of maintaining high quality stoichiometric growth for extend periods of time due to the careful control of the beam fluxes (Al, Ga and As) required.

To improve the efficiency of our research, an AlN/GaN ordered alloy (OA) was employed instead of an AlGaAs buffer layer for c-GaN films growth. It is expected that uniform effective Al molar content can be obtained by using an OA layer. Precise control of the Al molar content can be achieved by varying the ratio of alternate layer thickness. This process makes it easy to maintain high quality stoichiometric growth for extended periods as all constituent layers are binary materials. In our previous work, evidence for the

presence of a polycrystalline component was confirmed for a c-GaN film (0.4  $\mu\text{m}$ ) by high resolution X-ray diffraction (HRXRD) and photoluminescence (PL) [3,4].

In this work, a significant improvement in the crystallinity of the c-GaN epilayer was achieved by optimizing the nitridation conditions. Crystallographic properties were characterized by reflection high-energy electron diffraction (RHEED), transmission electron microscopy (TEM) and HRXRD. Atomic force microscopy (AFM) and low temperature PL measurements were carried out in order to characterize the surface morphology and optical properties, respectively.

## EXPERIMENTAL DETAILS

C-GaN films were grown on semi-insulating GaAs (100) substrates by plasma assisted molecular beam epitaxy (RF-MBE) using a radio frequency (13.56 MHz) plasma cell (Oxford Applied Research, model MPD21) to produce active nitrogen. After thermal annealing under As over pressure conditions ( $4.0 \times 10^{-6}$  Torr), a GaAs buffer layer was deposited at 650°C (0.2  $\mu\text{m}$ ). The surface structure was investigated to confirm the presence of the (2x4) reconstruction pattern (indicating the well known As terminated surface) by in-situ RHEED observation. Nitridation was carried out for 5-10 seconds using N-plasma exposure at 850°C to form a wetting layer on the GaAs surface. Subsequent to nitridation, an alternating supply of Al and Ga flux was introduced to order to form an  $(\text{AlN})_m(\text{GaN})_n$  OA ( $m$  and  $n$  represent the number of monolayers). As there is a large lattice mismatch between AlN, GaN and GaAs, it is necessary to limit each layer to below the critical thickness in order to grow an epitaxial, defect-free OA layer. The OA layer structure, therefore, is typically  $(\text{AlN})_1(\text{GaN})_4 \times 5$  periods (total layer thickness = 0.05  $\mu\text{m}$ ). The crystal quality of the OA layer is strongly dependent on the ratio of constituent layer thickness ( $d_{\text{GaN}}/d_{\text{AlN}}$ ) and the number of periods. The detailed characteristics of OA layer have been reported elsewhere [3,4]. The final c-GaN epilayer (1.0  $\mu\text{m}$ ) was grown at 850°C. RHEED observations were carried out during the entire growth process in order to confirm the crystallinity of the growing films. The crystallinity of epilayer was characterized by a HRXRD (Philips, X'pert MRD system) equipped with a hybrid monochromator (an integrated multilayer X-ray mirror in combination with a Ge 220 channel cut crystal and double detector with Cu 0.1 mm slit). The PL spectra were measured using the 325 nm line of a He-Cd laser (10 mW) as an excitation source (12 K). The surface morphology was observed by AFM (Digital Equipments, Nanoscope III a, Dimension 3100 system).

## DISCUSSION

The key point of this work is the achievement of the successful thicker epitaxial growth of the c-GaN epilayer (1.0  $\mu\text{m}$ ) with higher crystal quality than that of our previous work [3,4] by careful optimization of the nitridation process. Figure 1 (a) and (b) show RHEED patterns and (c) an AFM image of the nitridation GaAs buffer layer surface. The nitridation time of the GaAs buffer layer surface was reduced from 4 minutes to 10 seconds in order to form a uniform wetting layer prior to OA layer growth. During the nitridation process, the RHEED pattern changed from streaky to spotty pattern for nitridation times over about 20 seconds. The characteristic (3x3) reconstruction pattern was observed for the first time in our group for nitridation time between 5-10 seconds. Zsebök et al. reported [5] the same results in the initial growth stage of GaN grown directly on GaAs. They concluded that the (3x3) pattern indicated the formation of a complete N-terminated monolayer on the GaAs surface under stoichiometric growth conditions. The difference between this work and Zsebök's work is the Ga flux condition (slight Ga rich conditions were used in this work). It is speculated that the formation of a complete N-terminated monolayer in the initial growth stage of GaN is essential in order to obtain subsequent epitaxial III-nitride layers. The RMS roughness value calculated from figure 1 (c) was 1.01 nm.

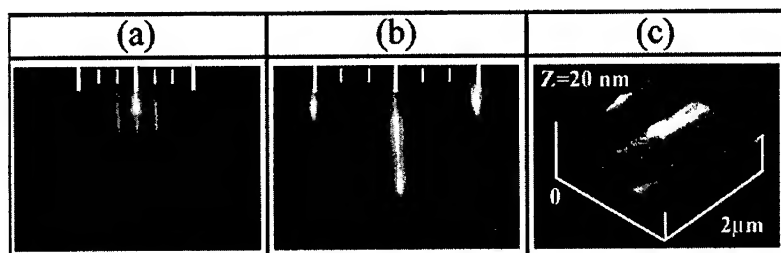


Figure 1. RHEED patterns of (3x3) reconstruction on the nitridation GaAs (a), (b) and AFM image(c). The incident electron beam direction was (a) [011], (b) [011̄].

Figure 2 shows XRD results using  $2\theta$ - $\omega$  scan along the [001] axis for c-GaN epilayer samples. As shown in this figure, c-GaN diffraction (FWHM=66.0 arcmin.) was

dominantly observed indicating that c-GaN was successfully grown. We also carried out XRD pole figure measurement for h-GaN {0002}. Four peaks ( $\phi=54.7^\circ$ ) with four-fold symmetry were observed. It is strongly suggested that these peaks can be attributed to cubic (111) diffraction because there are no diffraction related h-GaN crystal peaks observed in a X-ray reciprocal space area map measurement.

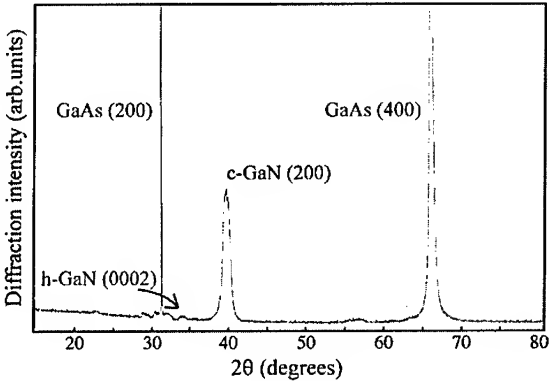


Figure 2. 2θ-ω XRD scans for an epilayer sample (1.0 μm) grown on an OA layer.

Figure 3 (a) shows RHEED pattern for a c-GaN epilayer during growth, and figure 3 (b) is the simulation results reported by Balakrishnan et al. [6] with c-GaN/GaAs (001). They reported that their epilayer included cubic (001), hexagonal (0002) or twinned cubic (111), cubic (111) crystal. Figure 3 (a) agrees very well with figure 3 (b) so that, the epilayer in this work has a similar structural composition. These results consistent with XRD measurement result previously described.

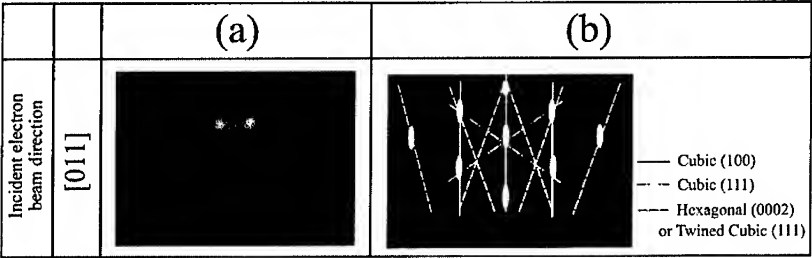


Figure 3. RHEED pattern for c-GaN epitaxial growth.

Figure 4 shows a bright field TEM micrograph and corresponding diffraction pattern for the c-GaN epilayer sample. In the micrograph, thin lamella regions on the  $\{111\}$  planes are noticeable. The diffraction pattern is predominantly c-GaN but near some reflections, satellite diffraction spots and streaks along the  $\langle 111 \rangle$  directions were observed. These results together with XRD data suggest that the thin lamella regions correspond to the remaining hexagonal phase. Reduction of these regions is required to get a perfect c-GaN epilayer.



Figure 4. Bright field TEM image and transmission electron diffraction (TED) pattern for GaN epilayer.

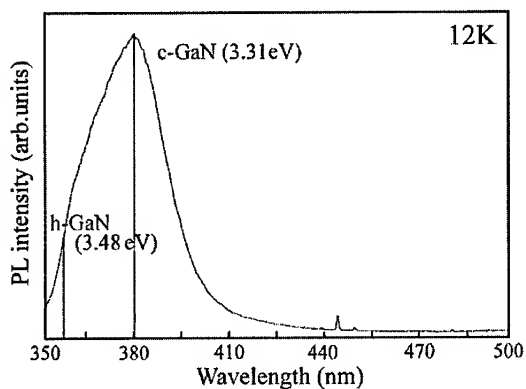


Figure 5. Low temperature PL spectra for c-GaN epilayer on AlN/GaN OA layer sample. The FWHM value of c-GaN emission (3.31 eV) is 269 meV

Figure 5 shows PL spectra for a c-GaN epilayer on an AlN/GaN OA layer sample. Near band edge emission originating from cubic phase was observed, with a FWHM value of 269 meV. A shoulder was observed on the short wavelength side of the peak, indicating mixing of h-GaN phase into the epilayer. Considering XRD, TEM, PL results, epilayer seems to include high density crystal defects, but it is expected that the defects will reduce with thicker epilayer growth as shown in TEM photograph (figure 4).

## CONCLUSIONS

A significant improvement of the crystal quality and growth stability of the c-GaN epilayer on AlN/GaN OA was achieved by optimization of the nitridation conditions, leading to the realization of thicker epilayer growth. Although it is suspected that high density defects including h-GaN crystal remains from PL and TEM measurements, it is thought that c-GaN growth is dominant during the entire growth process.

## ACKNOWLEDGEMENTS

This work was conducted and supported by the High-Tech Research Center Program, Future Materials Research Center.

## REFERENCES

1. R.Kimura and K.Takahashi, J. Crystal Growth. **227/228** (2001), 395.
2. R.Kimura, K.Takahashi and H. T. Grahn, Proc. of MRS Fall Meeting Vol **639** (2001), G3.46.1.
3. R.Kimura, J.Shike, A.Shigemori, K.Ishida and K.Takahashi, Proc. of ICNS-4 (2001), phys.stat.sol.(a) **188** (2001), 687.
4. A.Shigemori, J.Shike, K.Ishida, K.Takahashi and R.Kimura, Proc. of IWN2002 (2002), 267.
5. O.Zsebök, J.V.Thordson and T.G.Andersson, Jpn.J.Appl.Phys. Vol.**40** (2001), 472.
6. K.Balakrishnan, G.Feuillet, K.Ohta, H.Hamaguchi, H.Okumura and S.Yoshida, Jpn.J.Appl.Phys. Vol.**36** (1997), 6221.

### Aluminum Nitride Crystal Growth by Halide Vapor Transport Epitaxy

V. L. Tassev<sup>2</sup>, D. F. Bliss<sup>1</sup>, D. Weyburne<sup>1</sup>, J. S. Bailey<sup>2</sup>, S.-Q. Wang<sup>2</sup>

<sup>1</sup>Air Force Research Laboratory, Sensors Directorate, 80 Scott Road, Hanscom AFB MA 01731  
Tel: (781) 377-4247; Fax: (781) 377-3717; E-mail: Vladimir.Tassev@hanscom.af.mil

<sup>2</sup>Solid State Scientific Corporation, Hollis, NH 03049

#### Abstract

Halide vapor transport epitaxy (HVTE) is demonstrated for growth of AlN layers with thickness up to 50  $\mu\text{m}$  at deposition rates up to 60  $\mu\text{m}/\text{h}$ . The HVTE process uses an aluminum chloride amine adduct as the aluminum source of both aluminum and nitrogen. This new technique eliminates the main difficulties of the conventional hydride VPE growth, where aluminum oxidation and the strong reactivity of aluminum chloride with fused silica create the potential for oxygen contamination. This study shows the effect of temperature, gas flow velocities, and reactor pressure on the growth rate and layer quality. It is found that the growth rate and the layer quality strongly depend on the gas ratio. The species of carrier gas, the flow rates and partial pressures can be used as tools to optimize growth rate and to avoid any etching effects resulting from reverse chemical reactions. The crystalline layer quality as determined by x-ray rocking curve measurement shows FWHM of 300-900 and 500-1300 arc-sec for (002) and (102) planes, respectively.

PACS: 81.05.Ea; 81.15.Kk; 68.55.Jk.

#### 1. Introduction

Thick-film aluminum nitride on sapphire can be used as a substrate material for a wide range of optical and electronic applications from UV sensors to high power RF devices. The properties that make it attractive are its high thermal and low (insulating) electrical conductivity [1], high UV transparency [2], high acoustic wave velocity [3], and its excellent lattice and thermal expansion match with GaN [4].

The choice of a VPE process for growth of aluminum nitride layers is dictated by the possibility of high growth rates compared with other methods, including reactive sputtering [6], MBE [7], MOCVD [8] and VPE [9]. Only VPE has a high growth rate for well-oriented AlN film growth. This paper covers the most recent results of AlN film growth by the HVTE process.

Our approach uses a pre-synthesized aluminum chloride adduct as the source material. Several authors have discussed adduct preparation [11,12] and the adduct properties [13,14,15]. The use of the aluminum chloride amine adduct circumvents the high affinity of pure aluminum for oxygen and the strong reactivity of aluminum chloride to the quartz reactor walls. At the same time, the adduct contains within itself both sources – of aluminum and nitrogen. Thus, the deposition can be easily controlled by the temperature and gas flow rate. In what follows, we present the results of AlN film growth by the HVTE process using the preformed adduct.

## 2. Experimental

The halide vapor transport epitaxy (HVTE) system for III-nitride layer growth is designed to include: 1) 3-zone furnace with computer controlled independent power supplies for each zone; 2) quartz tube reactor 1200 mm long and 50 mm in diameter. 3) mass flow controllers working in the range 1-850 sccm for each source of gas - ammonia, nitrogen and hydrogen, with the possibility for precise gas mixing either outside or inside the reactor. At the outlet: 4) an automatic control butterfly valve MKS type 153; 5) a programmable MKS pressure reader for an accuracy of 1 Torr in the pressure range 1-1000 Torr; 6) a mechanical pump; and 7) oil and water air locks.

Before each run the quartz tube of the reactor was evacuated and heated for 12 h at 500 °C. After that the substrate (sapphire template with 1  $\mu$ m thick MOCVD AlN or GaN layer) and the adduct boat were placed in proper positions and the system was maintained for another 12 h at 100 °C in vacuum. An RGA chemical test for water vapor, oxygen, nitrogen and ammonia contamination followed. When the RGA chemical analysis indicated less than  $10^{-5}$  Torr the epitaxial growth process was initiated in the pressure range 50-760 Torr, deposition temperature 1000-1100°C, adduct temperature 250-360°C, and gas flow rates 170-400 sccm for N<sub>2</sub> and H<sub>2</sub> and 5-100 sccm for NH<sub>3</sub>.

For the HVTE process, adducts of the type  $\text{AlCl}_3 \cdot x \cdot \text{NH}_3$  ( $x=1-6$ ) are produced. The adduct was prepared at low temperature, taking precautions against any possible oxygen contamination. The weights of the initial chemical components were recorded, and after each synthesis run the complex was analyzed by x-ray diffractometer *Philips APD 3720*. The equilibrium vapor pressure over this adduct at different temperatures was investigated and compared to the literature (see Fig. 1). By comparison, the adduct partial pressure is considerably lower than the vapor pressure of either  $\text{AlCl}_3$  or ammonium chloride  $\text{NH}_4\text{Cl}$ .

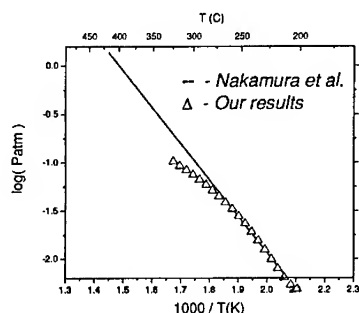


Fig. 1. Adduct partial pressure versus the adduct temperature - a comparison of recent results with some previously published data [10].

## 3. Results

Experiments were conducted under various growth conditions using GaN and AlN 1  $\mu$ m thick MOCVD templates on (0001) sapphire substrates. The growth

temperature, the relative flow rates of gases, and the proximity of the substrate to the aluminum source were studied to determine the optimum growth conditions. AlN layers were grown up to 50  $\mu\text{m}$  thick with good crystal quality at a growth rate from 5 to 40  $\mu\text{m}/\text{h}$ . The results illustrate the following points:

1. The growth rate increases with substrate temperature and with proximity of the substrate to the source. Figure 2 illustrates the point, showing thickness of AlN growth after one hour vs. distance of the wafer from the source. At a furnace temperature of 1100°C the growth rate for a wafer placed near the furnace vestibule was 40  $\mu\text{m}/\text{hr}$ . However, the goals of achieving higher substrate temperature and closer proximity to the source are contradictory. There is a steep thermal gradient between the source temperature and the deposition temperature. A high wafer temperature cannot be maintained as the position approaches the source. On the other hand, when the wafer is placed deep inside the hot zone, very little growth occurs. The adduct molecules decompose and deposit on the quartz chamber during prolonged exposure to the high temperature of the hot zone. A high deposition temperature is also favorable for AlN crystalline quality. Although high temperature growth is not appropriate for hetero-epitaxial growth on GaN templates because of sublimation, higher substrate temperature is not a problem when AlN instead GaN templates are used.

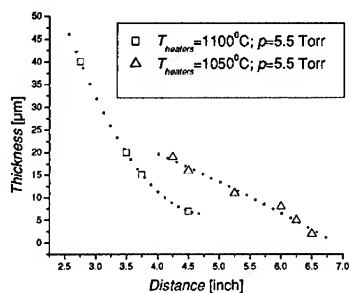


**Fig. 2.** Thickness of AlN layer after 1 hour of growth vs. distance from the source boat.

2. The growth rate depends not only on the adduct temperature, but also the ammonia overpressure. The  $\text{N}_2/\text{NH}_3$  ratio and the temperature of the adduct control the partial pressure of aluminum over the substrate. The presence of ammonia over the aluminum-containing adduct suppresses sublimation (or evaporation if a liquid) at all temperatures. A pure nitrogen atmosphere enhances sublimation and increased growth rate. Figure 3 shows the relationship between growth rate and the gas ratio for a given set of AlN growth conditions. At the limit where ammonia concentration is in balance with nitrogen pressure, the growth rate becomes very slow. Slow growth rates also correspond with improved crystal structure as measured by the x-ray rocking curve FWHM. At the other extreme, the growth rate exceeds 40  $\mu\text{m}/\text{hr}$ , but at a sacrifice of crystalline quality.

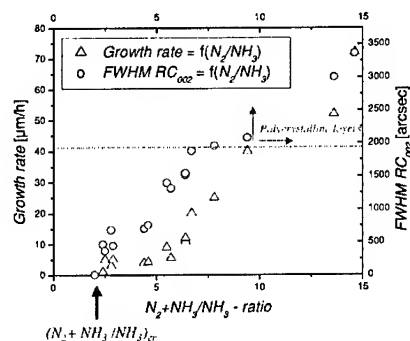


**Fig. 3.** Plot of growth rate vs. nitrogen-ammonia ratio for several conditions.

A high resolution x-ray rocking curve technique is employed to analyze the crystalline quality of epitaxial AlN. The best samples exhibited an x-ray rocking curve FWHM in the range of 300 and 500 arc-sec for reflection (002) and (102), respectively (see Table I). A significant improvement of the crystal quality in comparison to the MOCVD templates was also observed.

Run No	GROWTH CONDITIONS			RESULTS		
	temperatures [°C]	pressure [Torr]	flow rates [sccm]	gr.rate [μm/h]	x-ray RC [arc sec]	
	T <sub>dep</sub>	T <sub>add.</sub>	N <sub>2</sub>	NH <sub>3</sub>		002 102
124	1050	360	777	300	4.7	467 795
125	1050	360	781	300	5	366 512
138	1125	255	19.6	340	26	1503 2104
147	1050	280	5.5	400	16	619 2424
148	1050	250	5.5	400	12	1151 2400

**Table 1.** A series of runs comparing the rocking curves for MOCVD-templates with HVPE layers grown upon them.

#### 4. Discussion

In order to compare the efficiency of different growth methods, we need a criterion that factors out the deposition area. One possibility is to compare the growth rate of the material on the substrate in units of moles per unit time per unit area to the molar flow rate, essentially number of molecules flowing per unit time. According to Chen *et al.* [16], typical growth efficiencies of several thousand micrometer per mole indicate minimal parasitic reactions while growth efficiencies less than several hundreds micrometer per mole suggest parasitic reactions. This criterion will allow us to compare the growth efficiency of different materials. By comparing the efficiency, one can get an idea whether competing factors such as gas phase nucleation, deposition on the sidewalls, and/or deposition downstream are important.

For a bubbler temperature of 250°C (see Fig. 1) and an ambient pressure of 4 torr, the molar flow rate of  $\text{AlCl}_3 \cdot \text{NH}_3$  is:

$$\begin{aligned} \text{Molar Flow Rate of } \text{AlCl}_3 \cdot \text{NH}_3 &= F_{\text{carrier}} \times \frac{P_{\text{Adduct}}}{P_{\text{total}}} \times \frac{1}{22,400 \text{ cm}^3 / \text{mole}} \\ &= F_{\text{carrier}} \times \frac{24}{19.6} \times \frac{1}{22,400 \text{ cm}^3 / \text{mole}} \\ &= F_{\text{carrier}} \times 5.47 \times 10^{-5} \text{ mole/cm}^3 \end{aligned}$$

Taking one of the faster AlN growth rates of 26  $\mu\text{m/hr}$  from Table 1, and a carrier flow rate of 340 sccm of  $\text{N}_2$  through the  $\text{AlCl}_3 \cdot \text{NH}_3$  bubbler, the growth efficiency is calculated,

$$\begin{aligned} \text{Growth Efficiency} &= \frac{26 \mu\text{m/hr}}{F_{\text{carrier}} \times 1.45 \times 10^{-4} \text{ cm}^3 / \text{mole}} \\ &= 1390 \mu\text{m/mole} \end{aligned}$$

This value is consistent with that achieved in other low pressure HVPE processes, such as epitaxial growth of GaAs at 700°C. Such a high efficiency stands in stark contrast to previously reported HVPE growth of AlN [16], where the growth efficiency fell to zero as the substrate temperature was increased. Therefore, we can infer that by using an adduct as the aluminum source, the growth process is relatively efficient. That is, there are few parasitic reactions occurring (wall adsorption, gas phase decomposition, etc.). However, as illustrated in Fig.3, a trade-off must be made between growth efficiency and crystalline quality. At very high growth rates the layer quality is degraded, and becomes polycrystalline. The addition of ammonia to the carrier gas is one means to improve the layer quality while reducing the growth rate.

An optimized system for growth of AlN – using the adduct  $\text{AlCl}_3 \cdot \text{NH}_3$  – is designed to heat the compound to its decomposition temperature at or near the substrate surface, in order to ensure an efficient reaction. The advantage of such a process is that, using a narrow heater with a sharp temperature profile, one can adjust the deposition conditions near the substrate. The rest of the reactor tube is held at a relatively low temperature, sufficient to prevent adduct vapor condensation during the gas transport.

## 5. Summary

High quality AlN layers with thickness up to 50  $\mu\text{m}$  have been grown by HVTE. The deposition temperature and the total reactor pressure were in the range of 1000-1100°C and 5 -760 Torr, respectively. This new technique eliminates the main difficulties of conventional HVPE growth, where aluminum oxidation and the strong reactivity of aluminum chloride with quartz create the potential for oxygen contamination.

The layer quality, as determined by x-ray rocking curve measurements (with a high resolution Philips instrument using omega scan), shows a FWHM of about 300 and 500 arc-sec for (002) and (102) planes, respectively. Trace element impurity measurements by GDMS depth profile analysis indicate about  $10^{19}/\text{cm}^3$  oxygen. Tests are under way to evaluate this material as a substrate for GaN-based devices.

#### Acknowledgements

This work was funded by the Air Force Office of Scientific Research.

#### References

- [1] G. A. Slack, J. Phys. Chem. Solids 34 (1973) 321.
- [2] W. M. Yim, E. J. Stofko, P. J. Zanzucchi, J. I. Pankove, M. Ettenberg and S. L. Gilbert, J. Appl. Phys. 44/1 (1973) 292.
- [3] E. Stern, *ibid.* MTT-17 (1967) 927.
- [4] L. Liu and J. Edgar, Mat. Sci. and Eng. R37 (2002) 61.
- [5] J. Rojo, L. Schowalter, R. Gaska, M. Shur, M. Khan, J. Yang, and D. Koleske, J. Crystal Growth 240 (2002) 508.
- [6] A. J. Shuskus, T. M. Reeder and E. L. Paradis, Appl. Phys. Lett. 24 (1974) 155.
- [7] S. Yoshida, M. Misawa, Y. Fujii, S. Takeda, H. Hayakawa, S. Gonda and A. Iton, J. Vac. Sci. Technol. 16 (1979) 990.
- [8] F. Hasegawa, T. Takahashi, K. Kubo and Y. Nannichi, Jap. J. Appl. Phys. 26 (1987) 1555.
- [9] H. Komiyama and O. Osawa, Jap. J. Appl. Phys 24 (1985) L795.
- [10] K. Nakamura, T. Ostvold and H. Oye, Phys. Chem. 90 (1986) 141.
- [11] T. L. Chu and R. W. Kelm, Jr, J. Electrochem. Soc. 122 (1975) 995.
- [12] T. Goto, J. Tsuneyoshi, K. Kaya, and T. Hirai, J. Mat. Sci. 27 (1992) 247.
- [13] T. Ostvold, E. Rytter and G. N. Papatheododou, Polyhedron 5/3 (1986) 821.
- [14] K. Nakamura, T. Ostvold and H. Oye, Yoyuen 27 (1984) 7.
- [15] I. N. Przhivalskii, S. Yu. Karpov and Yu. N. Makarov, MRS Internet J. Nitride Semicond. Res. 3, 30 (1998) 1.
- [16] C. Chen, *et. al.* J. Elect. Mater., 25 (1996) 1004.

### Experimental and Theoretical Analysis of Heat and Mass Transport in the System for AlN Bulk Crystal Growth

M.V. Bogdanov<sup>1</sup>, S.Yu. Karpov<sup>1</sup>, A.V. Kulik<sup>1</sup>, M.S. Ramm<sup>1</sup>, Yu.N. Makarov<sup>1</sup>, R. Schlessner<sup>2</sup>,  
R.F. Dalmau<sup>2</sup>, Z. Sitar<sup>2</sup>

<sup>1</sup> Semiconductor Technology Research, Inc., P.O.Box 70604, Richmond, VA 23255-0604, USA

<sup>2</sup> Dept. Mat. Sci. Eng., North Carolina State University, 1001 Capability Dr., Raleigh, NC  
27695 -7919, USA

#### ABSTRACT

Bulk AlN crystal growth by Physical Vapor Transport (PVT) is studied both experimentally and numerically. This paper presents the analysis of heat and mass transport mechanisms in closed and partially open crucible geometries. The heat transfer in the growth system used at North Carolina State University (NCSU) is simulated. The computed temperature profiles are used in the analysis of mass transport in the growth cell to gain understanding of the effect of species exchange between the crucible and environment on the AlN growth rate. The model predictions are in reasonable agreement with observations.

#### INTRODUCTION

Bulk aluminum nitride, a promising substrate material for nitride-based high-power electronics and ultra-violet optoelectronics, is normally grown by the sublimation (PVT) technique suggested by Slack and co-workers in the mid '70s [1,2]. A specific feature of the PVT growth is that temperature distribution in a furnace controls the crystal growth rate, the shape of the crystallization front, the stability of AlN powder source, the thermoelastic stress, and, eventually, the quality of the grown material. In the temperature range of interest (1800-2300°C), it is problematic to monitor experimentally the thermal field inside the growth system. Measurements of the temperature distribution, obtained with the crucible removed from the hot zone, do not provide sufficiently accurate information because the crucible considerably disturbs the thermal field.

Another important issue is the control of the V/III ratio in the growth system. In a tightly closed crucible, this ratio is nearly equal to unity due to congruent AlN powder sublimation. The V/III ratio can change due to species exchange between the crucible and its environment, occurring through narrow openings. This, however, results in additional material losses and it is unclear how critical the effect of species exchange on the AlN growth is.

In this paper, we simulate the heat transfer in the growth system used at North Carolina State University (NCSU) [3,4]. The data on axial temperature distribution obtained experimentally in the system with the crucible removed are used for adjustment of the unknown model parameters. Then, the model is applied to predict the temperature perturbations due to crucible insertion into the growth chamber.

The computed temperature profiles are used as a basis for studying the mass transport in the growth cavity with the focus on the effect of species exchange between the crucible and ambient on the material losses and the AlN growth rate. The theoretical predictions are compared with observations.

## HEAT TRANSFER IN THE GROWTH SYSTEM

We model the global heat transfer in the system for bulk AlN growth used at NCSU which is shown schematically in Figure 1. The simulations are carried out with dedicated "Virtual Reactor" software [5]. The computations account for the anisotropy of the heat conductivity in solid components and for both conductive and radiative mechanisms of heat transfer in the gas domains. Special attention was given to the evaluation of thermal conductivity of the graphite felt-insulation that affects dramatically the thermal field. Data on felt conductivity were derived by fitting the axial, experimental temperature profiles which were obtained in the growth system using type C thermocouples which could be moved along the vertical centerline of the growth chamber. Three temperature distributions have been measured for different electric power levels dissipated in the heater. In the computations, we vary the felt conductivity as a function of temperature to provide best fitting with the measured values. The resulting axial temperature distributions computed for the empty container are compared in Figure 2 with the measurements.

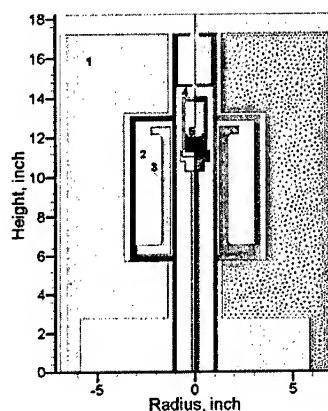


**Figure 1.** Schematic view of the growth system: (1) graphite felt insulation, (2) container, (3) heater, (4) crucible, (5) AlN powder charge. Typical computational grid is shown in the right part.

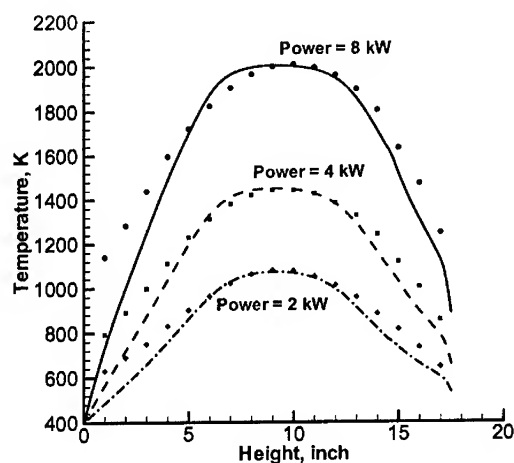


**Figure 2.** Axial temperature distributions in the NCSU growth system. Lines are computations with adjusted felt conductivity. Dots are measured values. Corresponding heater powers are indicated in the legend.

Once the felt conductivity was determined, we performed the modeling of the entire growth system, in order to find the changes in the temperature distribution caused by the crucible insertion. The heat transfer in

the AlN powder charge was simulated with the advanced model of effective heat conductivity  $\lambda_{\text{eff}}(T)$  of the porous media [6,7] accounting for the heat conduction through the granule contact spots, pores and the granule bulk. The computations of  $\lambda_{\text{eff}}(T)$  have been made for the following parameters: powder porosity of 0.6, mean granule diameter of 600  $\mu\text{m}$ , and nitrogen pressure of 400 Torr.

The two-dimensional temperature distribution around the crucible placed in the highest position is shown in Figure 3. It is seen that the thermal field in the crucible is remarkably disturbed especially near its bottom where the powder is located. Figure 4 compares the one-dimensional distributions obtained for the growth system with and without crucible inside. The panels (a), (b), (c), and (d) plot the temperature distributions across the seed holder (line AB in Figure 3), powder surface (line CD), powder bottom (line EF), and along the crucible axis (line GHK), respectively. These data clearly show that the crucible insertion results in a higher temperature of the powder top and in a lower temperature of the powder bottom, thus increasing the axial temperature gradient in the powder. In addition, the crucible introduces considerable radial gradients, which may affect the thermoelastic stress in a growing AlN crystal. A non-uniform temperature distribution in the powder is generally unfavorable for the source utilization efficiency and operation stability, as found recently for SiC sublimation growth [8].

Figure 5 presents the axial temperature drop in the powder and in the gaseous gap between the powder and seed, as a function of the crucible position. Positive displacement corresponds to an upward movement of the crucible. It can be seen from the figure that temperature gradients computed/measured in the empty growth system may considerably differ from those observed in a real growth process when the crucible is inserted into the container. As a result, temperature measurements performed in an empty system can be used only to assess the temperature in the growth zone, but they are inapplicable to evaluate the radial and axial temperature gradients in the growth cell.

## MASS TRANSPORT IN THE GROWTH CELL

The data on temperature distribution in the growth cell discussed in the previous section are used in the analysis of mass transfer in AlN PVT growth. We consider two cases: (i) tightly closed crucible, where there is no species exchange with the environment, and (ii) an open crucible, where the species exchange is performed through a circular opening  $1.55 \cdot 10^{-3}$  inch thick located in the gap between the source and seed.

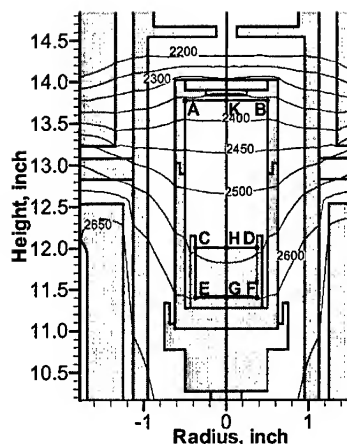


**Figure 3.** Computed isotherms in the crucible zone. The heater power was adjusted to get  $T = 2370\text{K}$  at the seed center (point K).

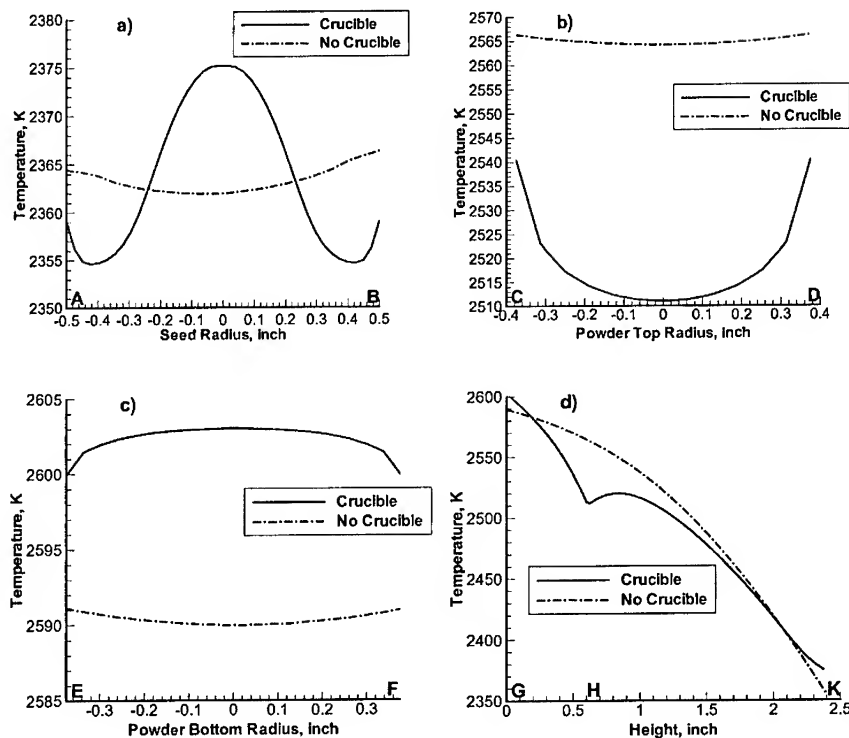


**Figure 4.** Temperature distribution along (a) the seed (AB); (b) the powder surface (CD); (c) the powder bottom (EF); (d) the crucible axis (GHK). The letters correspond to the points marked in Figure 3.

The AlN growth, carried out at 400 Torr and temperature varied between 2050°C and 2150°C, is simulated using the models suggested in [9-10]. In accordance with the experimental setup, the gap between the source and seed is taken as 0.59 inch. Figure 6 compares the computed AlN growth rate as a function of temperature with measurements performed at NCSU. The theory predicts a significant reduction of the growth rate in the open crucible as compared to the closed one. This is due to considerable material losses through the opening at high temperatures. The results of the computations show the same trend as the experimental data. The use of the open crucible allows increasing the V/III ratio in the growth cell up to 30 at 2180 °C and even higher values at lower temperatures.

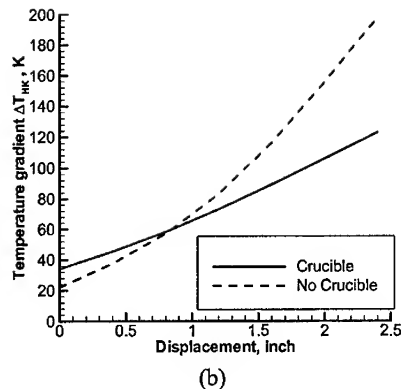
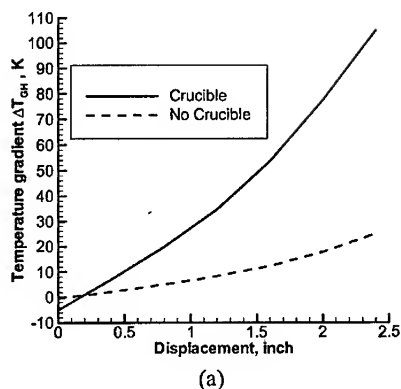


**Figure 5.** The axial temperature drop in the (a) powder ( $\Delta T_{GH}$ ) and (b) gas gap ( $\Delta T_{HK}$ ) as a function of the crucible position. A displacement of 2.4 inch corresponds to the crucible position shown in Figure 1.

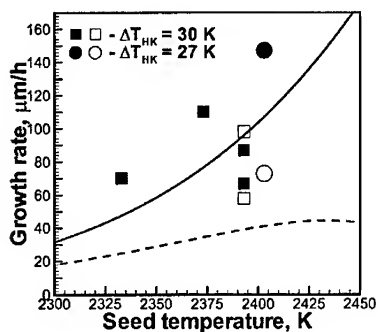


**Figure 6.** Growth rate versus seed temperature. Symbols are experimental points for tightly closed (solid circles and squares) and open (empty circles and squares) crucible. Solid and dashed curves are theoretical predictions for the closed and open crucible, respectively. Temperature drop in the gaseous gap is  $\Delta T_{HK} = 30$  K.

## CONCLUSION

Growth of bulk AlN crystals in the growth system used at NCSU was studied both experimentally and numerically. The heat transfer in the growth system was analyzed with the focus on the perturbations of the temperature distribution caused by the crucible insertion inside the reaction zone. It has been found that the crucible modifies remarkably the temperature profiles in the reactor so that the gradients measured in an empty system cannot be used straightforwardly for estimation of the process parameters. The computed temperature profiles have been used to simulate the species transport in the growth cell and to analyze the effect of a small opening in the crucible on the AlN growth rate and V/III ratio. The computations predict a substantial decrease of the AlN growth rate because of the material losses through the opening. The theoretical predictions agree well with experimental observations.

## REFERENCES

1. G. A. Slack, T. F. McNelly, *J. Crystal Growth* **34**, 263 (1976).
2. G. A. Slack, T. F. McNelly, *J. Crystal Growth* **42**, 560 (1977).
3. R. Schlessler and Z. Sitar, *J. Cryst. Growth* **234**, 349 (2002).
4. R. Schlessler, R. Dalmau, and Z. Sitar, *J. Cryst. Growth* **241**, 416 (2002).
5. M.V. Bogdanov, A.O. Galyukov, S.Yu. Karpov, S.K. Kochuguev, D.Kh. Ofengeim, A.V. Tsiryulnikov, M.S. Ramm, A.I. Zhmakin, and Yu.N. Makarov, *J. Cryst. Growth* **225**, 307 (2001).
6. E.L. Kitanin, V.V. Ris, A.A. Schmidt, S.Yu. Karpov, and M.S. Ramm, Submitted to *Mat. Sci. Eng. B* (2002).
7. E.L. Kitanin, V.V. Ris, M.S. Ramm, and A.A. Schmidt, *Mat. Sci. Eng. B* **55**, 174 (1998).
8. D.S. Karpov, O.V. Bord, S.Yu. Karpov, A.I. Zhmakin, M.S. Ramm, and Yu.N. Makarov, *Mat. Sci. Forum.* **353-356**, 37 (2001).
9. A.S. Segal, S.Yu. Karpov, Yu.N. Makarov, E.N. Mokhov, A.D. Roenkov, M.G. Ramm, and Yu.A. Vodakov, *J. Cryst. Growth* **211**, 68 (2000).
10. S.Yu. Karpov, A.V. Kulik, A.S. Segal, M.S. Ramm, and Yu.N. Makarov, *Phys. Stat. Sol. (a)* **188**, 763 (2001).

### The Influence of Substrate Surface Polarity on Optical Properties of GaN Grown on Single Crystal Bulk AlN

G. Tamulaitis<sup>1,5</sup>, I. Yilmaz<sup>1</sup>, M. S. Shur<sup>1</sup>, R. Gaska<sup>2</sup>, C. Chen<sup>3</sup>, J. Yang<sup>3</sup>, E. Kuokstis<sup>3</sup>, A. Khan<sup>3</sup>, J. C. Rojo<sup>4</sup>, L. J. Schowalter<sup>4</sup>

<sup>1</sup>Department of ECE and CIE, Rensselaer Polytechnic Institute, Troy, NY 12180, U.S.A

<sup>2</sup>Sensor Electronic Technology, Inc., Latham, NY 12110, U.S.A.

<sup>3</sup>Department of EE, University of South Carolina, Columbia, SC 29208, U.S.A.

<sup>4</sup>Crystal IS, Inc., Latham, NY 12110, U.S.A.

<sup>5</sup>IMSAR, Vilnius University, Sauletekio 9-III, Vilnius, Lithuania

#### ABSTRACT

Photoluminescence of the GaN layers grown both on N-face and Al-face bulk AlN is studied under CW and pulsed laser excitation in the temperature range from 8 K to 300 K. We compare localization of excitons, residual strain, and activation energies for thermally activated transfer of carriers to nonradiative recombination. At high excitation intensities, conditions for carrier heating, which is important for the threshold of stimulated emission, are also investigated.

#### INTRODUCTION

Large lattice mismatch of GaN epilayers with available substrate materials is one of the most problematic issues in GaN/AlN/InN based technology. Growth of GaN on c-plane of the sapphire substrates (lattice mismatch ~15%) is made possible by the deposition of AlN or low-temperature GaN buffer layers serving for nucleation of the subsequent GaN epilayer of comparatively high structural quality. 6H SiC has a smaller but still substantial lattice mismatch of 3.5%. The most radical solution of the problem is homoepitaxy. Homoepitaxial GaN layers deposited on bulk GaN substrates exhibit outstanding structural and optical quality [1] and allow fabrication of heterostructures with high mobility [2]. The conventional high-pressure method of bulk GaN growth [3] is still an expensive technology allowing production of only small-size single crystals. Recent development of large free-standing GaN substrates grown by hydride vapor phase epitaxy [4] brought in a new impact to homoepitaxy of GaN.

The need for deep-UV light emitters and detectors for chemical and biological sensing, photochemistry, and nanotechnology stimulates homoepitaxy on AlN, which has considerably a much larger band gap (6.2 eV) than that of GaN (3.41 eV). Passing more than two decades of stagnation after early development [5, 6], the growth technology for bulk AlN recently advanced its capacity to produce larger-size single crystals. AlN single crystals exceeding 1 cm size and having a density of dislocations less than  $10^4 \text{ cm}^{-2}$  have been produced [7] and utilized as substrates to deposit  $\text{Al}_{0.5}\text{Ga}_{0.5}\text{N}$  epilayers of high structural quality [8].

The further development of fabrication of multilayered structures on bulk AlN substrates requires deeper understanding of structural properties of interfaces and study of optical properties of layers deposited on this novel substrate material. The lattices of wurtzite-structure AlN and GaN have the space group  $P6_3mc$  ( $C_{6v}^4$ ) and are compatible with a spontaneous polarization along the hexagonal c-axis, which is usually the growth axis of epitaxial layers of AlN and GaN. The direction of the spontaneous polarization depends on polarity of the layers. AlN layers grown in (0001) direction, which are defined as Al-face or +c plane AlN, have the

top surface composed of three dangling bonds of nitrogen that point up toward the c-plane surface, while the  $(000\bar{1})$  AlN layers are defined as N-face or  $-c$  plane AlN and has a single dangling bond that points upward. The polarization influences the surface morphology [9], causes different surface band bending [10] and results in peculiarities of photoluminescence [11]

In this paper, we present a photoluminescence study of the GaN layers grown both on N-face and Al-face bulk AlN. CW and pulsed laser excitation were used to cover a wide range of excitation power densities. The temperature dependence of photoluminescence spectra and intensities were also studied.

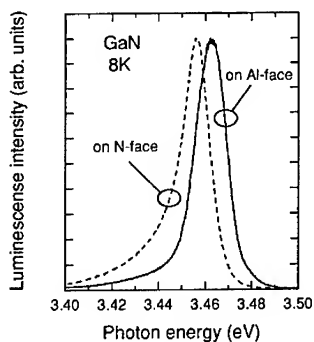
## EXPERIMENTAL DETAILS

The GaN layers, 1  $\mu\text{m}$  thick, were deposited by using low-temperature Metalorganic Chemical Vapor Deposition (MOCVD) on substrates of Al-face and N-face AlN single crystals [7].

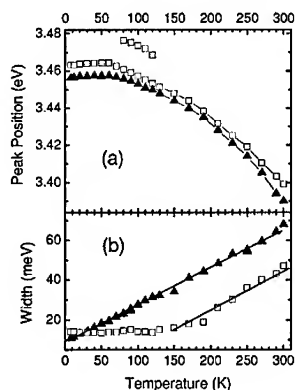
The luminescence spectra were measured by using TRIAX 550 spectrometer and recorded by a UV-enhanced intensified CCD camera. A closed-cycle helium cryostat cooled the samples down to 8 K. He-Cd laser emitting at 325 nm was used as a source for CW excitation. To avoid the sample heating, high excitation intensities were applied in a pulsed mode by using 4-ns-long pulses of the fourth harmonic of Nd:YAG laser radiation at 266 nm (4.66 eV).

## RESULTS AND DISCUSSION

Photoluminescence spectra of the samples of GaN grown on N- and Al-face bulk AlN under weak CW excitation at 8 K temperature are presented in figure 1. Both spectra are dominated by a single band peaked at 3.463 eV and 3.456 eV for the samples on Al-face and N-face AlN, respectively. The absence of narrow lines usually observed in PL spectra of GaN at low temperatures indicates a high free-electron concentration [12].



**Figure 1.** Normalized photoluminescence spectra of GaN layers on Al-face (solid line) and N-face (dashed line) bulk AlN measured under CW excitation at 8 K temperature.



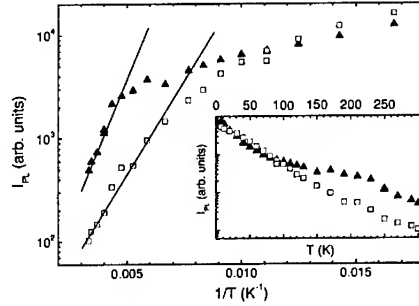
**Figure 2.** Photoluminescence peak position (a) and bandwidth (b) as a function of lattice temperature for the GaN layers on the N-face (triangles) and Al-face (squares) bulk AlN.

Figure 2 shows the temperature dependences of the peak position and width of the bands. In GaN on Al-face AlN, the peak position of the PL band at low temperatures corresponds to the peak of the strongest PL line (due to bound excitons), which was observed at 3.465 eV in homoepitaxial Ga-face GaN [11]. We also observe a weak band which emerges at ~60 K with the peak at 3.478 eV and merges with the main band at temperatures above ~120 K. The position of the band corresponds to the PL line due to free A exciton in homoepitaxial GaN (3.4789 eV) [11]. The bandwidth of the main peak (see figure 2b) is constant up to ~120 K and broadens at elevated temperatures. Even though the band is pretty broad, it is reasonable to assume that the PL observed in GaN on Al-face AlN is mainly caused by recombination of bound excitons at low temperature, while recombination of free excitons dominates in the spectrum at temperatures above ~150 K.

The PL band in GaN grown on N-face AlN is redshifted in respect to that in the sample with Al-face substrate and monotonously broadens in the entire temperature range from 8 to 300 K. This probably points out to localization effects, which are in line with increased probability of intrinsic donor generation or easier donor incorporation in N-face GaN [12]. However, the redshift remains also at high excitation intensities when all local states should be saturated and no blue shift of PL band with increasing pump intensity is observed.

The temperature dependence of the PL intensity is usually governed by thermally activated transfer of carriers to the centers of nonradiative recombination. A semilog plot of the PL intensity versus the reciprocal temperature is presented in figure 3. The slope of the Arrhenius-type dependence in the high-energy region corresponds to activation energies of 31 meV and 46 meV for GaN on Al- and N-face AlN, respectively.

The luminescence spectra measured at elevated pump intensities under pulsed laser excitation are presented in figure 4a for the sample with GaN on N-face AlN and in figure 4b for the sample with GaN on Al-face AlN. The spectra contain a single band peaked at 3.395 eV and 3.4 eV at room temperature for the two samples, respectively. The positions nearly coincide with the peaks under CW excitation (3.39 eV and 3.4 eV, respectively).



**Figure 3.** Photoluminescence intensity versus lattice temperature in a semilog plot and in the whole temperature range from 8 K to 300 K (insert) for the GaN layers on the N-face (triangles) and Al-face (squares) bulk AlN.

Increasing pump intensity causes formation of a narrow band shifted approximately by 80 meV to the long-wavelength side from the main peak. This narrow band corresponds to stimulated emission. Though the excitation depth ( $\sim 0.1 \mu\text{m}$ ) is too small for the light propagating perpendicularly to the sample surface to be considerably amplified due to stimulated transitions, a part of light amplified in the course of propagation along the sample surface (diameter of the spot was  $200 \mu\text{m}$ ) might be easily scattered through the sample surface. Meanwhile, the broad band seems to be caused by spontaneous band-to-band transitions.

Note that the short-wavelength slope of the main broad band is nearly constant in the spectra of the sample on the N-face AlN, but decreases considerably with increasing pump intensity in the sample on the Al-face AlN. The slope is exponential, as it should be expected for the luminescence band caused by recombination in electron hole plasma. The slope is mainly governed by carrier distribution function and its change is most probably caused by carrier heating. For parabolic energy bands, the short-wavelength side of the luminescence band is fairly well described by a simple expression:

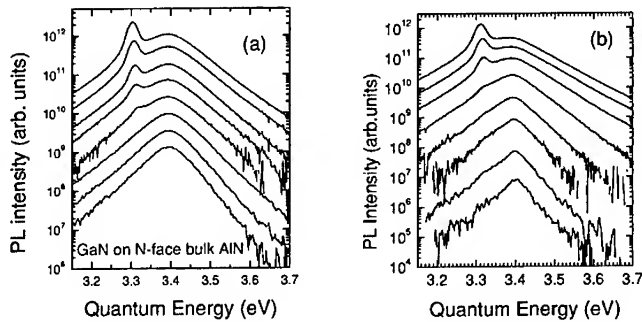


**Figure 4.** Photoluminescence spectra of the GaN layer on the N-face (a) and Al-face (b) bulk AlN at the room temperature under different excitation power densities: 0.0017, 0.0036, 0.0078, 0.03, 0.078, 0.26, 0.84, 2  $\text{MW}/\text{cm}^2$  from bottom to top for (a); 0.004, 0.0082, 0.018, 0.042, 0.13, 0.42, 0.96, 2  $\text{MW}/\text{cm}^2$  from bottom to top for (b).

$$I_{LUM}(h\nu) \propto (h\nu - \tilde{E}_g)^\beta \exp\left(-\frac{h\nu - \tilde{E}_g}{k_B T}\right) \quad (1)$$

Here,  $h\nu$  is the energy of the emitted photon,  $\tilde{E}_g$  is the normalized band gap,  $k_B$  is the Boltzmann constant, and the Boltzmann's distribution of carriers is assumed. The weak pre-exponent factor with exponent  $\beta$ , which equals 2 or 0.5 for transitions without and with momentum conservation, respectively, has a weak influence on practically exponential band slope far from the peak. The excitation power density dependence of the carrier temperature  $T_C$ , which was determined according to equation 1, is presented in figure 5 by points. At moderate carrier densities,  $T_C$  equals the quasi-temperature ( $T_{ph}$ ) of nonequilibrium long-wavelength LO phonons produced predominantly via their successive emission by photogenerated electrons with large excess energy [13]. The solid line in figure 5 depicts the pump intensity ( $I_p$ ) dependence of the carrier temperature under assumptions that  $T_C = T_{ph}$  and

$$[N(T_C) - N(T_L)] \propto I_p \quad (2)$$

where

$$N(T_{C,L}) = \frac{1}{\exp(\hbar\omega_{LO}/kT_{C,L}) - 1} \quad (3)$$

are the Bose-Einstein distribution functions for LO phonons (phonon energy  $\hbar\omega_{LO} = 92$  meV for GaN [14]) for  $T_C$  and  $T_L = 300$  K. The experimentally determined electron temperature follows equation 2 at moderate pump intensities but lags behind at elevated  $I_p$ . The deviation correlates with appearance of the band of stimulated emission, which indicates high density of photogenerated carriers and a change in balance between carrier generation rate and their decay.

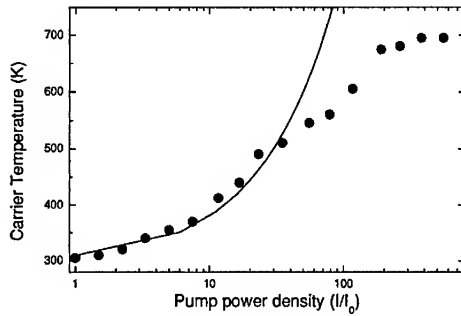


**Figure 5.** Pump power density dependence of carrier temperature in GaN layer on Al-face bulk AlN at the room temperature (dots) and approximation of this dependence by using equation 2;  $I_0 = 4 \text{ kW/cm}^2$ .

The carrier heating is an important phenomenon inhibiting the stimulated emission. Since the intensity of stimulated emission collected from the surface of the excited spot depends not only on real intensity of stimulated luminescence but also on the fraction of it, which is scattered outside, study of photoluminescence emitted from the edge of the photoexcited sample is under way.

## CONCLUSIONS

GaN layers grown on Al- and N-face bulk AlN substrates exhibit certain specific features in photoluminescence. At low excitation intensities, PL spectra of GaN on Al-face AlN are dominated by bound exciton emission, while GaN on N-face AlN have higher contribution of free excitons. The samples have different residual strain resulting in a 5 meV blue shift of photoluminescence bands in GaN on Al-face AlN in respect to GaN on N-face AlN. Activation energies of 31 meV and 46 meV for GaN on Al- and N-face AlN, respectively, were observed for thermally activated transfer of carriers to the centers of nonradiative recombination at elevated temperatures. Different carrier heating and its correlation with stimulated emission were demonstrated at high excitation intensities.

## ACKNOWLEDGMENT

The work at Crystal IS, Inc. has been partially supported by ONR. The authors would gratefully like to acknowledge the support of our contract monitor Dr. C.E.C. Wood. The work at RPI was supported by DARPA (Project Monitor Dr. J. Carrano). The work at SET, Inc. was supported by NASA under contract NAG5-10322.

## REFERENCES

1. M. Leszczynski, B. Beaumont, E. Frayssinet, W. Knap, P. Prystawko, T. Suski, I. Grzegory, and S. Porowski, *Appl. Phys. Lett.* **75**, 1 (1999)
2. E. Frayssinet, W. Knap, P. Lorenzini, N. Grandjean, J. Massies, C. Skierbiszewski, T. Suski, I. Grzegory, S. Porowski, G. Simin, X. Hu, M. Asif Khan, M. S. Shur, R. Gaska, and D. Maude, *Appl. Phys. Lett.* **77**, 2551 (2000)
3. S. Porowski, I. Grzegory, and J. Jun, in *High Pressure Chemical Synthesis*, edited by J. Jurczak and B. Baranowski (Elsevier, Amsterdam, 1989), p. 21
4. K. Motoki, T. Okahisa, N. Matsumoto, M. Matsushima, H. Kimura, H. Kasai, K. Takemoto, K. Uematsu, T. Hirano, M. Nakayama, S. Nakahata, M. Ueno, D. Hara, Y. Kumagai, A. Koukitu, and H. Seki, *Jpn. J. Appl. Phys.* **40**, L140 (2001)
5. G. A. Slack, *J. Phys Chem. Solids* **34**, 321 (1973).
6. G. A. Slack and T. McNelly, *J. Cryst. Growth* **34**, 263 (1976); **42**, 560 (1977).
7. J. C. Rojo, G. A. Slack, K. Morgan, B. Raghoeamachar, M. Dudley, and L. J. Schowalter, *J. Cryst. Growth* **231**, 317 (2001).
8. L. J. Schowalter, Y. Shusterman, R. Wang, I. Bhat, G. Arunmozhi, and G. A. Slack, *Appl. Phys. Lett.* **76**, 985 (2000).
9. M. Sumiya, K. Yoshimura, T. Ito, K. Ohsuka, S. Fuke, K. Mizuno, M. Yoshimoto, H. Koinuma, A. Ohtomo, M. Kawasaki, *J. Appl. Phys.* **88**, 1158 (2000).

- 
10. H. W. Jang, J. H. Lee, J. L. Lee, Appl. Phys. Lett. **80**, 3955 (2002).
  11. V. Kirilyuk, A. R. A. Zauner, P. C. M. Christianen, J. L. Weyher, P. R. Hageman, P. K. Larsen, Appl. Phys. Lett. **75**, 2355 (2000).
  12. P. Prystawko, M. Leszczynski, B. Beaumont, P. Gibart, E. Frayssinet, W. Knap, P. Wisniewski, M. Bockowski, T. Suski, S. Porowski, Phys. Status Solidi B **210**, 437 (1998).
  13. A. Zukauskas, Sov. Phys.-JETP **70**, 1099 (1990).
  14. *Properties of Advanced Semiconductor Materials*, Edited by M. E. Levinshtein, S. L. Rumyantsev, M. S. Shur. John Wiley & Sons, Inc., 2001.

### Optical Characterization of Bulk GaN Grown from a Na/Ga Flux

K. Palle, L. Chen, H.X. Liu, B.J. Skromme, H. Yamane<sup>1</sup>, M. Aoki<sup>1</sup>, C.B. Hoffman<sup>2</sup>, and F.J. DiSalvo<sup>2</sup>

Dept of Electrical Engineering and Center for Solid State Electronics Research, Arizona State University, Tempe, AZ, 85287-5706, U.S.A.

<sup>1</sup>Institute for Advanced Materials Processing, Tohoku University, Sendai 980-8577, Japan

<sup>2</sup>Dept of Chemistry and Chemical Biology, Cornell University, Ithaca, NY, 14853, U.S.A.

#### ABSTRACT

Bulk GaN crystals up to several mm in size, grown by a Na/Ga flux method, have been characterized using room and low temperature photoluminescence (PL) and panchromatic cathodoluminescence (CL) imaging. Highly resolved excitonic PL spectra are obtained for material grown in a new, large-scale reactor. The crystal polarity affects the incorporation of residual Zn and Mg or Si acceptors and the deep level luminescence bands in *c*-oriented platelets. A Zn ( $A^{\circ},X$ ) triplet structure with unusual thermalization properties and a highly resolved structural defect related PL peak are observed. Striations are found in some of the smaller platelets by CL imaging, but are absent in the prismatic crystals.

#### INTRODUCTION

Heteroepitaxial GaN films grown on SiC or sapphire have large lattice and thermal mismatches with their substrates, which leads to the formation of defects. These defects affect the optical and electrical characteristics of the material and of devices made from it. In order to reduce the defect density, true bulk GaN substrates of high quality suitable for homoepitaxy would be desirable. Conventional GaN crystals grown by the high-pressure solution method [1-2] have attained maximum sizes of ~15 mm, but this method requires very high growth temperature (1500 °C) and N<sub>2</sub> pressures (~1 GPa). Recently, bulk GaN platelets grown by the Na/Ga flux method have reached sizes up to ~10 mm [3-7]. This method uses a relatively low growth temperature of 700 °C and a N<sub>2</sub> pressure of only 5 MPa. These crystals show X-ray rocking curves with full width at half maxima (FWHM's) of 45-55 arc-sec for the (0002) reflection, suggesting good structural quality [3]. Previously, we discussed the highly resolved (down to ~0.22 meV FWHM) excitonic photoluminescence (PL) properties and low doping levels (mid 10<sup>16</sup>-low 10<sup>17</sup> cm<sup>-3</sup>, determined by Raman scattering) of material grown in a medium-scale growth reactor [8,9]. We also showed that different growth conditions produced different crystal habits, with correspondingly different PL spectra.

Here, we extend this study to include material grown in a new, large-scale reactor at Cornell, and we perform more detailed studies of material grown in both reactors. Impurity and deep level incorporation is shown to differ significantly on the opposite Ga-polar or N-polar sides of *c*-axis platelets grown in both reactors. We study fine structure of the Zn neutral acceptor-bound exciton ( $A^{\circ},X$ ) system and a structural defect-related peak. Cathodoluminescence imaging is used to compare the uniformity of the luminescence emission to that of heteroepitaxial material.

## EXPERIMENTAL PROCEDURE

Growth conditions for the bulk GaN crystals grown in the medium scale reactor were discussed in detail elsewhere [8]. The GaN platelets grown in the new, large-scale reactor were grown in a 50 mm diameter BN crucible at 700 °C, using a Na mole fraction ( $r_{\text{Na}}$ ) of 0.55. The growth run in this reactor was performed under 5 MPa of >99.995% pure  $\text{N}_2$  gas for 300 hours. The smaller platelets from both reactors generally exhibit one rough, stepped face and one smooth face. These faces were determined to correspond to Ga-polar (0001) and N-polar (000 $\bar{1}$ ) planes, respectively, using anomalous X-ray dispersion [10]. Room and low temperature photoluminescence (PL) measurements were performed using about 6 mW of tightly focused 3.694 eV UV excitation from an  $\text{Ar}^+$  laser and a 1.0 m double spectrometer. The samples were mounted strain-free in superfluid liquid He for the low temperature measurements. All spectra are corrected for the spectral response of the measurement system. The room temperature, panchromatic cathodoluminescence (CL) was performed at an accelerating voltage of 10 kV.

## RESULTS

A low temperature excitonic PL spectrum is shown in Figure 1 for a bulk GaN platelet grown in the large-scale reactor. The main neutral donor bound exciton ( $\text{D}^0, \text{X}$ ) $_{n=1}$  peak at 3.4718 eV has a full width at half maximum (FWHM) of 0.45 meV. While this is one of the first runs in this reactor, this linewidth is already approaching the best value (0.22 meV) observed to date in material grown in the medium-scale reactor [8], showing that the growth process can yield comparable quality in different systems. The ( $\text{D}^0, \text{X}$ ) $_{n=1}$  position closely matches that (3.4709 eV [11]) in unstrained homoepitaxial material grown on high pressure solution grown-substrates, implying that there is negligible strain. The 3.4724 eV peak may be a second ( $\text{D}^0, \text{X}$ ) $_{n=1}$  peak for a shallower donor, possibly the unidentified 31.2 meV donor discussed by Freitas et al. [12]. An excited state of the ( $\text{D}^0, \text{X}$ ) complex is resolved at 3.373 eV. Both A and B free exciton peaks are observed at 3.4786 and 3.4844 eV (denoted as  $\text{X}_A^{n=1}$  and  $\text{X}_B^{n=1}$ , respectively). The  $n=2$  excited state of the A free exciton (denoted as  $\text{X}_A^{n=2}$ ) is present at 3.3955 eV, and several bound  $n=2$  A excitons (denoted  $\text{BX}^{n=2}$  [13-15]) are also observed. A two-electron replica of the ( $\text{D}^0, \text{X}$ ) $_{n=1}$  peak is observed at 3.4466 eV, denoted ( $\text{D}^0, \text{X}$ ) $_{n=2}$ , and corresponds to an  $n=2$  excited final state of a residual donor species with a 33.6 meV binding energy. The same donor species, which has been attributed to  $\text{O}_\text{N}$  [12], was observed in material grown in the medium scale reactor [11]. We also observe strong neutral acceptor-bound exciton peaks involving residual Mg [16, 17] or Si [18] acceptors at 3.467 eV, and a Zn acceptor doublet with components at 3.4545 and 3.4552 eV

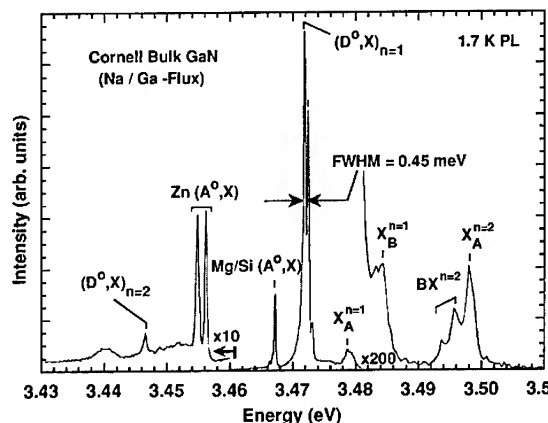


**Figure 1.** Low temperature (1.7 K) excitonic PL spectra of platelet bulk GaN crystals grown from a Na-Ga melt in a new, large scale reactor

[16,19]. A lower energy peak at 3.44 eV may involve excitons bound to closely-spaced pairs of Zn acceptors, an  $(A^\circ-A^\circ,X)$  complex.

Figure 2 shows the room temperature PL spectra of a *c*-oriented platelet grown in the medium-scale reactor on both its Ga-polar (rough, (0001)) and N-polar (smooth,  $(000\bar{1})$ ) faces. Marked differences are observed in these spectra. The residual Zn incorporation is very different on the opposite faces. The residual Zn acceptor PL peaks are always stronger in absolute intensity on the Ga-polar side, by factors ranging from 1.2 to very large. The overall integrated PL intensity is also usually 2-8X higher on the Ga-polar side compared to the N-polar side. The

band edge peak is often sharper on the Ga-polar side, suggesting less donor incorporation there. The true yellow (2.2 eV) band was absent in most (but not all) of these samples; instead, we typically observe a band around ~2.34 eV on the rough (Ga-polar) sides and another band around 1.98 eV on the smooth (N-polar) sides at 300 K. Details of this behavior will be discussed elsewhere.

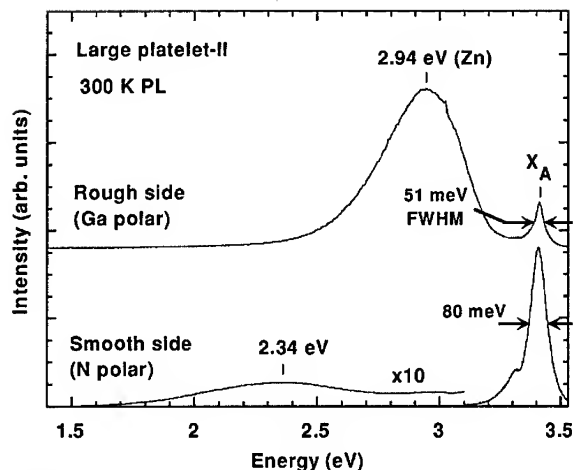


Figure 2. Room temperature PL spectra of both Ga- and N-polar surfaces of a platelet grown in the medium scale reactor.

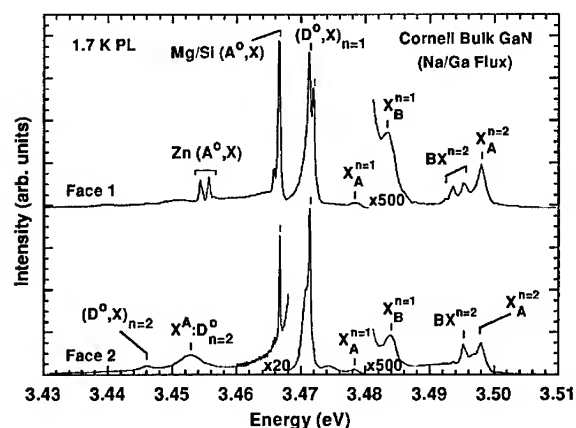
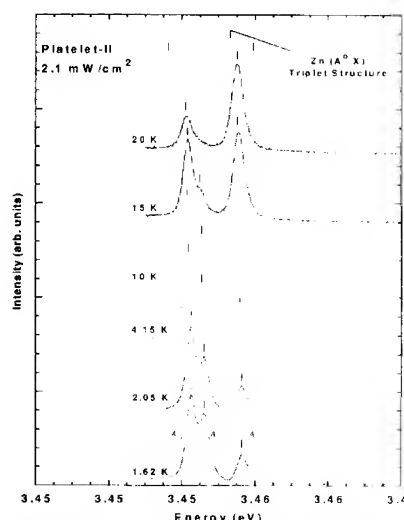


Figure 3. Low temperature excitonic PL spectra of both Ga and N-polar faces of platelets grown in the large-scale reactor.

A similar polarity effect is observed for platelets grown in the large-scale reactor, as shown in Figure 3. Marked differences in the intensities of various bound excitons are observed on the Ga-polar side and N-polar side. The  $(D^\circ,X)_{n=1}$  peaks thought to involve two different donor species show a reversal in their relative intensities on the two faces. This may be due to reduced O incorporation on the Ga-polar face, as is well-known in solution-grown material [1]. The residual Mg or Si acceptor  $(A^\circ,X)$  peak is strong on the Ga-polar side (rough side) and weak on the N-polar side (smooth side). (Note the various vertical expansion factors in Figure 4.) The Zn  $(A^\circ,X)$  peak



**Figure 4.** Thermalization behavior of the Zn ( $A^{\circ}X$ ) triplet structure in a small platelet grown from a Na-Ga melt in the medium-scale reactor.

shown). The  $A_1$  and  $A_3$  components can tentatively be attributed to recombination from different components of the initial ( $A^{\circ}X$ ) complex, which must involve an excitation of a hole. The anomalous quenching of the middle component is not yet understood, however.

Some of the small platelets exhibit a PL band around 3.40-3.42 eV [8]. A broad, unstructured feature in this region has generally been attributed to structural defects, namely stacking faults [20,21]. In the present samples, this feature shows complex resolved fine structure, as shown in Figure 5 for a small platelet grown in the medium scale reactor. Up to nine different components have been observed in the range from 3.319-3.434 eV. The behavior of these features as a function of measurement conditions will be discussed elsewhere, and appears to be consistent with an assignment to polytype 3C quantum

shows a similar behavior, and is pronounced on the Ga-polar side and completely absent on the N-polar side. However, this behavior differs in some samples, and the ( $A^{\circ}X$ ) intensity does not appear to vary the same way as that of the corresponding ( $D^{\circ}-A^{\circ}$ ) peaks in the same samples. More extensive investigations are in progress to clarify this behavior, and to establish whether the Zn-bound exciton and ( $D^{\circ}-A^{\circ}$ ) peak involve the same centers.

A fully-resolved Zn ( $A^{\circ}X$ ) triplet and its thermalization behavior are shown in Figure 4. The three components are observed at 3.4543, 3.4546, and 3.4556 eV in some of the small platelets grown in the medium scale reactor, as reported earlier [8,9]. The intensity of the highest energy component (denoted  $A_3$ ) increases with increasing temperature, but the intermediate component quenches relative to the lowest energy component ( $A_1$ ). Similar behavior is observed as a function of

excitation intensity at low temperature (not

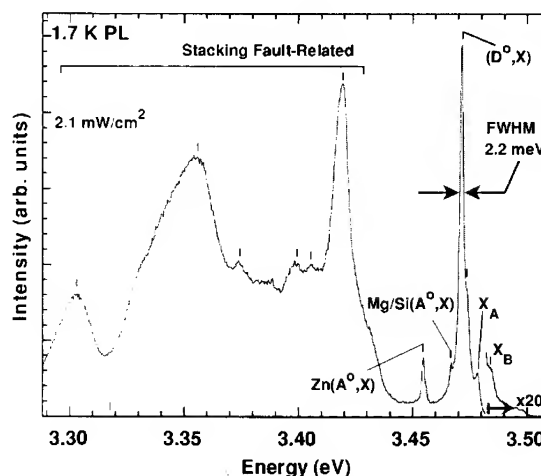


**Figure 5.** Low temperature PL spectrum of a small platelet from Batch I in the medium-scale reactor showing structural defect-related emissions in the range from 3.319-3.434 eV.

BEST AVAILABLE COPY

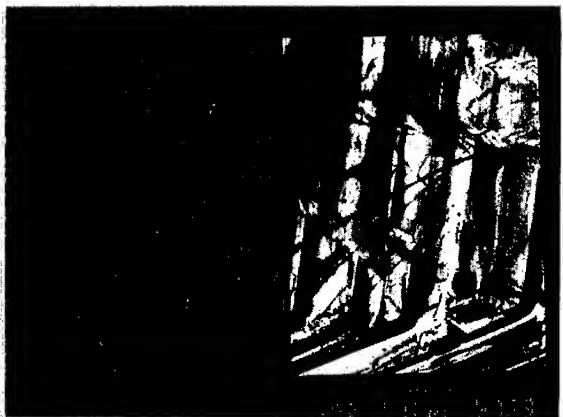


**Figure 6.** Secondary electron image (left) and panchromatic 300 K CL image (right) of a small platelet, both at an accelerating voltage of 10 kV.

observed. These bands form a zigzag pattern and may be associated with growth striations. It remains to be determined if these have any relation to the stacking fault-related PL bands discussed above. These features are not observed in the prismatic crystals, which exhibit uniform CL except for certain types of surface features (not shown). Further work is necessary to understand and control the origins of the striations.

wells in the bulk 2H-GaN matrix. Such wells are highly effective in trapping electrons and holes from the surrounding material. These features are generally absent in prismatic crystals, which implies that the prisms may be of better quality, perhaps due to a different growth mode. These features have not been observed to date in the larger platelets.

A secondary electron image and panchromatic 300 K CL image of a small platelet sample are shown in Figure 6. Some dark (nonradiative) areas are associated with surface scratches, but in addition striated bands are

## CONCLUSIONS

Optical characterization of bulk GaN crystals grown from a Na-Ga melt in a new, large-scale reactor shows that the material is of high optical quality and has low residual doping. The main residual donor species has a 33.6 meV binding energy, which may be  $O_N$ , but a second, shallower donor may be present. A pronounced polarity dependence is evident in the incorporation of impurities and deep levels in *c*-oriented platelets. The Zn and usually Mg or Si incorporation is much stronger on the rough side (Ga-polar) than on the smooth side (N-Polar). Thermalization of the Zn ( $A^0, X$ ) triplet structure and fine structure in the stacking fault-related luminescence near 3.4-3.42 eV has been studied.

## ACKNOWLEDGMENTS

This work was supported by the Office of Naval Research Multidisciplinary University Research Initiative on III-Nitride Crystal Growth and Wafering, Grant No. N00014-01-1-0716, monitored by Dr. C.E.C. Wood. The ASU portion of this work was also supported by the Materials Research Science and Engineering Center at ASU, under Grant No. DMR 96-32635 from the National Science Foundation.

## REFERENCES

1. S. Porowski, MRS Internet J. Nitride Semicond. Res. **4S1**, G1.3.1-G1.3.11 (1999).
2. T. Inoue, Y. Seki, O. Oda, S. Kurai, Y. Yamada, and T. Taguchi, Phys. Stat. Sol. (b) **223**, 15-27 (2001).
3. M. Aoki, H. Yamane, M. Shimada, S. Sarayama, and F.J. DiSalvo, J. Crystal Growth **242**, 70-76 (2002).
4. H. Yamane, M. Shimada, T. Sekiguchi, and F.J. DiSalvo, J. Crystal Growth **186**, 8-12 (1998).
5. M. Aoki, H. Yamane, M. Shimada, T. Sekiguchi, T. Hanada, T. Yao, S. Sarayama, and F.J. DiSalvo, J. Crystal Growth **218**, 7-12 (2000).
6. M. Aoki, H. Yamane, M. Shimada, S. Sarayama, and F.J. DiSalvo, Crystal Growth Des. **1**, 119-122 (2001).
7. M. Aoki, H. Yamane, M. Shimada, T. Kajiware, S. Sarayama, and F.J. DiSalvo, Crystal Growth & Design **2**, 55-59 (2002).
8. B. J. Skromme, K. Palle, C. D. Poweleit, H. Yamane, M. Aoki and F. J. DiSalvo, J. Crystal Growth **246**, 299-306 (2002).
9. B.J. Skromme, K.C. Palle, C.D. Poweleit, H. Yamane, M. Aoki, and F.J. DiSalvo, Appl. Phys. Lett. **81**, 3765-3767 (2002).
10. H. Yamane, M. Shimada, and F.J. DiSalvo, Mater. Sci. Forum **325-326**, 21-24 (2000).
11. K. Kornitzer, T. Ebner, M. Grehl, K. Thonke, R. Sauer, C. Kirchner, V. Schwegler, M. Kamp, M. Leszczynski, I. Grzegory, and S. Porowski, Phys. Stat. Sol. (b) **216**, 5-9 (1999).
12. J.A. Freitas Jr., W.J. Moore, B.V. Shanabrook, G.C.B. Braga, S.K. Lee, S.S. Park, J.Y. Han, and D.D. Koleske, J. Crystal Growth **246**, 307 (2002).
13. B.J. Skromme, MRS Internet J. Nitride Semicond. Res. **4**, 15 (1999).
14. B.J. Skromme, Mater. Sci. Engrg. B **50**, 117-125 (1997).
15. B.J. Skromme, J. Jayapalan, R.P. Vaudo, and V.M. Phanse, Appl. Phys. Lett. **74**, 2358-2360 (1999).
16. B.J. Skromme and G.L. Martinez, MRS Internet J. Nitride Semicond. Res. **5S1**, W9.8 (2000).
17. M. Leroux, B. Beaumont, N. Grandjean, P. Lorenzini, S. Haffouz, P. Vennéguès, J. Massies, and P. Gibart, Mater. Sci. Engrg. B **50**, 97-104 (1997).
18. J. Jayapalan, B.J. Skromme, R.P. Vaudo, and V.M. Phanse, Appl. Phys. Lett. **73**, 1188-1190 (1998).
19. H. Amano, K. Hiramatsu, and I. Akasaki, Jpn. J. Appl. Phys. **27**, L1384-L1386 (1988).
20. S. Fischer, C. Wetzel, W. Walukiewicz, and E.E. Haller, in Gallium Nitride and Related Materials, ed. F.A. Ponce, R.D. Dupuis, S. Nakamura, and J.A. Edmond (Mater. Res. Soc., Warrendale, PA, 1996) p. 571-576.
21. S. Fischer, G. Steude, D.M. Hofmann, F. Kurth, F. Anders, M. Topf, B.K. Meyer, F. Bertram, M. Schmidt, J. Christen, L. Eckey, J. Holst, A. Hoffmann, B. Mensching, and B. Rauschenbach, J. Crystal Growth **189/190**, 556-560 (1998).

### Background Impurity Reduction and Iron Doping of Gallium Nitride Wafers

Robert P. Vaudo, Xueping Xu, Allan D. Salant, Joseph A. Malcame, Edward L. Hutchins, and George R. Brandes

ATMI, Inc., Danbury, CT 06810, U.S.A.

#### ABSTRACT

Background impurities and the resulting electrical characteristics were studied for GaN wafers grown using hydride vapor phase epitaxy at various growth conditions. The electron concentration was found to decrease with increasing GaN thickness, by orders of magnitude in the first few microns of growth, but continuing gradually for thousands of microns. Physical removal of the backside degenerate layer enabled improved analysis of the electrical properties. Secondary ion mass spectroscopy was used to determine that the presence of oxygen and silicon accounted for the electron concentration for unintentionally *n*-type doped material. The concentration of oxygen was found to vary more than that of silicon and increased with decreasing growth temperature. The resistivity was measured to be as high as 1 ohm-cm, corresponding to a carrier concentration of  $10^{16} \text{ cm}^{-3}$ . Iron was demonstrated to effectively compensate the residual donors and increased the resistivity to greater than  $10^9$  ohm-cm at room temperature and greater than  $3 \times 10^5$  ohm-cm at 250 °C. An activation energy for the iron-doped GaN was determined by variable temperature resistivity measurements to be 0.51 eV.

#### INTRODUCTION

A promising pathway for improving the reliability of GaN-based electronic devices is to form the device on low defect density GaN substrates, which can be produced by hydride vapor phase epitaxy (HVPE). In addition to low defect density [1,2], the HVPE approach is inherently scalable to very large wafer area. Early reports of GaN growth by HVPE [3,4] produced material that was heavily *n*-type with a carrier concentration in excess of  $10^{18} \text{ cm}^{-3}$ . Since that time, the background impurities have been reduced. The current state-of-the-art HVPE growth of unintentionally doped GaN exhibits an electron concentration on the order of  $10^{16} \text{ cm}^{-3}$  [5-7]. Motoki [8] reports a background level of  $5 \times 10^{18} \text{ cm}^{-3}$  due to auto-doping from the  $\text{SiO}_2$  mask used. While the background electrical concentration has been reduced by several orders of magnitude since the 1970s, the purity of the material must be further increased and/or a deep level compensating impurity must be incorporated to make the material suitable for high frequency electronic applications. Kuznetsov [9] reported 0.2-0.4  $\mu\text{m}$  thick Zn-doped GaN layers by HVPE and calculated a specific resistivity as high as  $10^{12}$  ohm-cm. Activation energies of 0.18 and 0.7 eV were found in low and high temperature regimes, respectively.

In this work, we grew unintentionally doped GaN under a variety of growth conditions and studied how the background impurity concentration changed with process conditions. Iron doping was employed to compensate the residual donors to make thick, semi-insulating GaN with a room temperature resistivity in excess of  $10^9$  ohm-cm.

## EXPERIMENTAL DETAILS

The HVPE growth conditions used to make the GaN for electrical and impurity analysis are detailed in Table I. While a wide range of each parameter was explored, in some cases cracking of the GaN precluded reliable electrical measurements or poor material quality limited the utility of the material for electrical applications. For instance, GaN grown with a growth temperature less than 950 °C was polycrystalline. The concentration of background impurities was determined using secondary ion mass spectroscopy (SIMS), and in cases where additional sensitivity was required, glow discharge mass spectroscopy (GDMS). Resistivity and Hall effect measurements were used to assess carrier type, carrier concentration and mobility.

**Table I.** HVPE growth parameters used to make samples for subsequent electrical and impurity characterization.

Growth parameter	Range
Temperature (°C)	900-1070
Pressure (Torr)	25-700
Growth rate (μm/hr)	50-250
Thickness (μm)	50-3000
V/III ratio	10-50

## RESULTS

### Interface region

As has been reported previously for GaN films grown by HVPE on sapphire [7], the electrical characteristics of the bulk material were confounded by a degenerate *n*-type layer at the GaN-sapphire interface. This is understandable based on the defect structure in the first layers

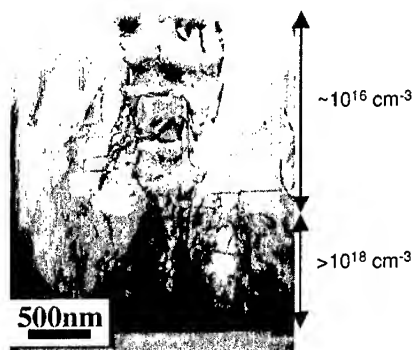


**Figure 1.** Cross-sectional TEM image of the interface of an HVPE GaN-sapphire interface, showing the more than 0.5 μm thick defective layer.

closest to the sapphire. Fig. 1 shows a cross-section transmission electron microscope image of a representative GaN-sapphire interface. Additional structural analysis of the early stages of HVPE growth [10] shows that island coalescence is not complete until 1-2 μm into film growth. SIMS measurements indicated greater than  $10^{20} \text{ cm}^{-3}$  oxygen atoms at the interface, which was reduced abruptly over 1 μm. The lack of an increased Al signal confirms that the oxygen measurement does not derive from pinholes to the sapphire. In contrast, Gotz [7] reported an interface layer only 300 nm thick. Nevertheless, the thicker conductive interface layer in the current work provides a similar parallel conduction path and prohibits direct measurement of the relatively low impurity bulk portion of the material.

The impact of the interface layer on the carrier concentration and mobility was measured directly. Figure 2 shows the marked change in Hall effect results obtained before and after removal of the interface layer from three typical 300  $\mu\text{m}$  thick freestanding GaN samples. The measured room temperature electron concentration decreased from approximately  $10^{18} \text{ cm}^{-3}$  with the interface present to  $10^{16} \text{ cm}^{-3}$ . Correspondingly, the room temperature mobility increased from less than  $100 \text{ cm}^2/\text{V-s}$  with the degenerate layer to in excess of  $500 \text{ cm}^2/\text{V-s}$  after removal of the degenerate layer. To decouple the effects of the degenerate layer from the electrical analysis, the remainder of the work presented here is for freestanding GaN material that has had the interface layer removed by either mechanical lapping or slicing with a wire saw (for thicker material).

### Bulk region

The reduction in electron concentration was abrupt in the first few microns of growth, but continues for much longer. Figure 3 displays the Hall characteristics measured from subsequent slices fabricated from a  $\sim 3 \text{ mm}$  long boule. The electron concentration clearly decreased over the length of the boule, while the mobility correspondingly increased. This trend was attributed to a gradual reduction of impurities in the growth ambient.

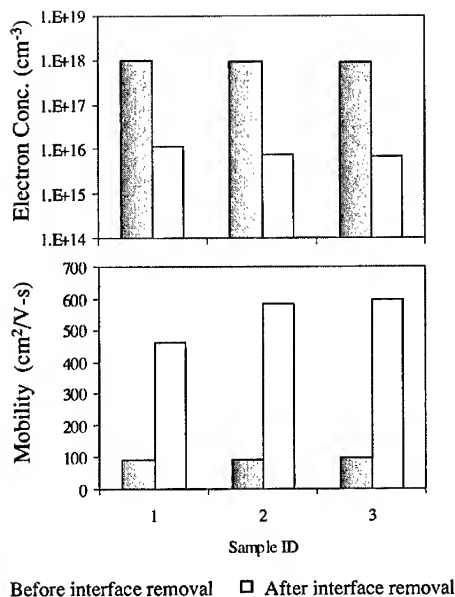


**Figure 2.** Room temperature Hall effect measurements taken before and after removal of the degenerate interface layer. Electron concentration decreased by two orders of magnitude, while mobility increased more than five-fold.

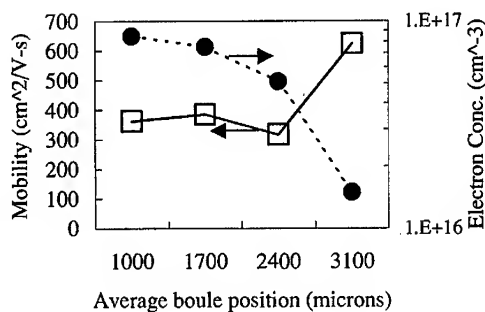


**Figure 3.** Hall characteristics measured from subsequent slices fabricated from a GaN boule.

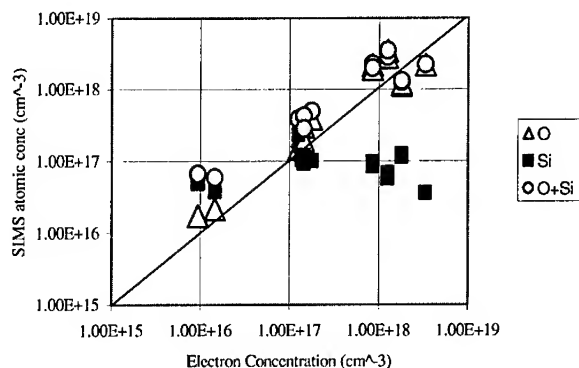


**Figure 4.** Electron concentration vs. shallow impurity concentrations (Si, O, and O+Si). The O concentration shows greater variability.

The primary impurities present in the GaN wafers were Si, O, C, H, and Cl, depending on growth conditions. Of these impurities, Si and O are known to act as shallow donors in GaN. Figure 4 shows the electron concentration as a function of oxygen, silicon and sum of oxygen and silicon concentrations, as measured by SIMS. The films were grown with varied temperature, pressure and V/III ratio, as described in Table I. The silicon concentration was low, near the SIMS detection limits ( $2\text{--}10 \times 10^{16} \text{ cm}^{-3}$ ). The oxygen concentration varied with growth conditions, particularly growth temperature. However, the oxygen concentration also varied from run to run with identical growth condition. In the low carrier concentration samples the silicon concentration was higher than oxygen concentration, while in the higher carrier concentration materials the oxygen concentration was higher and the samples were typically grown at temperatures less than  $1000^\circ\text{C}$ . Thus, variation in the electron background may be kinetically controlled, consistent with the temperature dependence. Likely sources of silicon and oxygen during HVPE growth include virtual leaks, quartz reactor hardware and source materials. Further background reduction will require controlling both the kinetics and impurity sources.

### Resistivity increase

Figure 5a shows the electron concentration vs. electron mobility measured at room temperature for a large number of samples grown under varied growth conditions, including samples intentionally doped with oxygen. As expected from reduced ionized impurity scattering, a reduction in electron concentration corresponded to increased mobility. Electron concentrations as low as  $10^{16} \text{ cm}^{-3}$  corresponded to Hall mobilities from  $600\text{--}1000 \text{ cm}^2/\text{V}\cdot\text{s}$ . Figure 5b shows the room temperature resistivity vs. carrier concentration. The increased mobility with reduced carriers makes it more difficult to make semi-insulating material by impurity reduction alone. Several orders of magnitude more background reduction would be needed to achieve desired levels for an electronic device substrate.

Based on these results, iron doping was investigated as a means of compensating residual donors and increasing resistivity. The iron was introduced into the growth ambient as iron

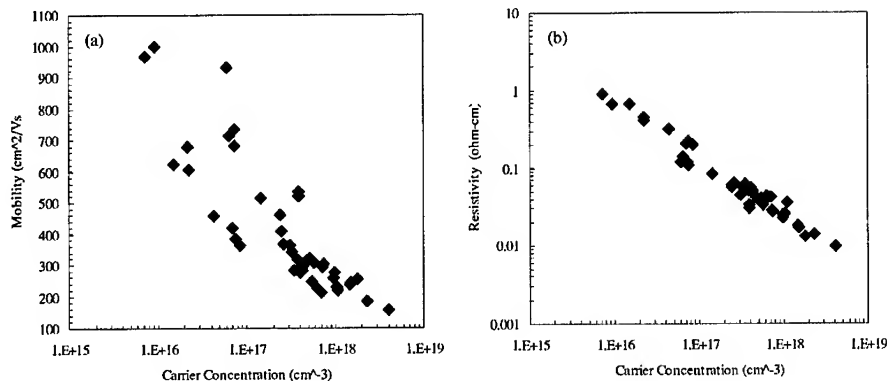


**Figure 5.** Room temperature mobility (a) and resistivity (b) as a function of Hall carrier concentration.

chloride. The growths were successfully completed and the crystal quality based on x-ray rocking curve was consistent with that produced without the iron present. Typical GaN wafers had full width at half maximum (FWHM) of 100 to 300 arcsec, and an iron doped sample had FWHM of  $172 \pm 24$  arcsec. To make characterization straightforward, the sapphire template and backside GaN layers were removed before characterization. One iron doped sample had an iron concentration of  $6 \times 10^{16} \text{ cm}^{-3}$  as measured by SIMS and  $4 \times 10^{16} \text{ cm}^{-3}$  as measured by GDMS. This level of iron is sufficient to compensate for the residual oxygen and silicon present in the sample. The resistivity of the GaN:Fe sample was measured as a function of temperature by forming annealed InSn contacts. Figure 6 shows the resistivity data as a function of sample

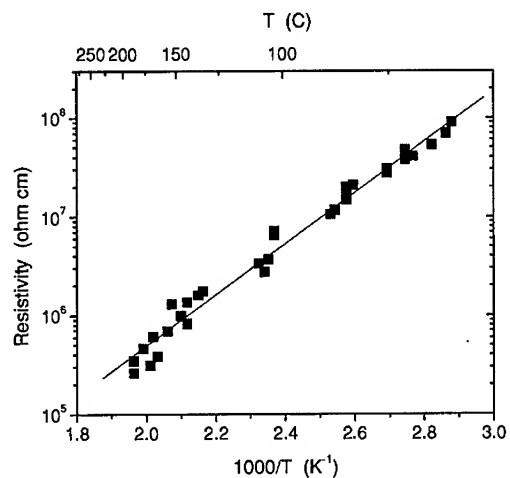


**Figure 6.** Plot of resistivity as a function of inverse temperature for an iron-doped GaN wafer.

temperature. The resistivity at 250 °C was  $3 \times 10^5$  ohm-cm and the resistivity at room temperature was determined by extrapolation to be  $2 \times 10^9$  ohm-cm. The activation energy for Fe-doped GaN was 0.51 eV, as shown in Figure 6. The semi-insulating behavior is promising for application in GaN:Fe substrates.

## CONCLUSIONS

Oxygen and silicon were the major impurities in the freestanding HVPE GaN wafer, resulting in the *n*-type conductivity in the unintentionally doped materials. In the high carrier concentration samples oxygen was the major impurity while in the low carrier concentration samples silicon was the major impurity. The source of impurities is less clear, but is speculated that silicon is likely originated from quartz reactor hardware and oxygen is probably associated with problems related to reactor seal and virtual leaks. Introducing iron into HVPE GaN was found effective to compensate the residual donors without crystal quality degradation. Room temperature resistivity greater than  $10^9$  ohm-cm was demonstrated. The structural and electronic properties of the impurity defects in the semi-insulating GaN will be further investigated. This work offers a pathway for evaluating low defect density, semi-insulating GaN as a substrate for electronic applications.

## ACKNOWLEDGEMENTS

The authors thank DARPA for partial financial support for this work under contract number N00014-02-C-0321.

## REFERENCES

1. X. Xu, R. P. Vaudo, G. R. Brandes and J. S. Flynn, *J. Electron. Mater.* **31**, 402 (2002).
2. A. Usui, H. Sunakawa, A. Sakai, and A. A. Yamaguchi, *Jpn. J. Appl. Phys.* **36**, L899 (1997).
3. H. P. Maruska and J. J. Tietjen, *Appl. Phys. Lett.* **15**, 327 (1969).
4. J. J. Nickl, W. Just, and R. Bertinger, *Mat. Res. Bull.* **9**, 1413 (1974).
5. D. C. Look and J. R. Sizelove, *Appl. Phys. Lett.* **79**, 1133 (2001).
6. R. P. Vaudo, G. R. Brandes, J. S. Flynn, X. Xu, M. F. Chriss, C. S. Christos, D. M. Keogh, and F. D. Tamweber, *Proc. Int. Workshop on Nitride Semiconductors, IPAP Conf. Series 1*, 15 (2000).
7. W. Gotz, J. Walker, L. T. Romano, N. M. Johnson, and R. J. Molnar, *Mat. Res. Soc. Symp. Proc.* **449**, 525 (1997).
8. K. Motoki, T. Okahisa, N. Matsumoto, M. Matsushima, H. Kimura, H. Kasai, K. Takemoto, K. Uematsu, T. Hirano, M. Nakayama, S. Nakahata, M. Ueno, D. Hara, Y. Kumagai, A. Koukitu, and H. Seki, *Jpn. J. Appl. Phys.* **40**, L140 (2001).
9. N. I. Kuznetsov, A. E. Nikolaev, A. S. Zubrilov, Y. V. Melnik, and V. A. Dimitriev, *Appl. Phys. Lett.* **75**, 3138 (1999).
10. Y. Golan, X. H. Wu, J. S. Speck, R. P. Vaudo and V. M. Phanse, *Appl. Phys. Lett.* **74**, 1498 (1999).

### Low-Electron-Energy Cathodoluminescence Study Of Polishing And Etching Effects On The Optical Properties Of Bulk Single-Crystal Gallium Nitride

Lawrence H. Robins and Bruce Steiner

National Institute of Standards and Technology, Gaithersburg, MD 20899, U.S.A.

Norman A. Sanford

National Institute of Standards and Technology, Boulder, CO 80305, U.S.A.

Carmen Menoni

Colorado State University, Fort Collins, CO 80523, U.S.A.

#### ABSTRACT

Low electron energy cathodoluminescence (LEECL) was used to examine polishing-induced damage in a bulk high-pressure grown GaN single-crystal platelet. The Ga-polarity face of the platelet was mechanically polished; chemically-assisted ion-beam etching (CAIBE) to a depth of 200 nm was performed on a portion of this face. Low-temperature (15 K) CL spectra of the polished-only and polished+CAIBE regions of the Ga-face were taken at 2.8 kV, 5.4 kV, and 10.6 kV (corresponding to average electron penetration depths of 19 nm, 56 nm, and 170 nm). The low-temperature CL spectrum of the unpolished, N-polarity face was taken at 10.6 kV. In the near-band-edge region, all the CL spectra from the Ga-polarity face show a narrow peak near 3.47 eV, ascribed to donor-bound exciton recombination, and several overlapping peaks at lower energy (3.1 eV to 3.4 eV), ascribed to defect-related levels or to donor-acceptor pair recombination. Functional curve-fitting analysis enabled deconvolution of the spectra into the sum of an asymmetric peak (the donor-bound exciton) and several symmetric Gaussian peaks (the lower energy, defect-related or donor-acceptor peaks). The linewidth of the donor-bound exciton peak decreased with increasing penetration depth, and also decreased on going from the polished-only to the polished+CAIBE region. The relative intensity of a defect-related peak at  $\approx 3.325$  eV showed a similar decreasing trend with increasing penetration depth or with CAIBE treatment. The LEECL results suggest that the thickness of the polishing damage layer is approximately 400 nm; the 200 nm CAIBE step is thus insufficient to completely remove the damage.

#### INTRODUCTION

Bulk free-standing high-pressure grown GaN crystals are promising substrates for homoepitaxial growth of GaN and related alloys. Particularly attractive is the reported absence of threading dislocations that may, if present, propagate into epitaxial films.[1] However, thin-film growth on the native {0001} faces of the bulk GaN crystals has proven problematic since the faces, although atomically flat on a scale of roughly 100  $\mu\text{m}$ , are often textured on longer length scales, with hillocks and terraced growth. The {0001} surfaces must therefore be prepared by mechanical or chemical-mechanical polishing before homoepitaxial growth can take place.[2,3] In the present study, a bulk high-pressure grown GaN platelet was examined by low electron energy cathodoluminescence (LEECL) spectroscopy. The LEECL results lend insight into the nature and depth of the subsurface damage induced by mechanical polishing.

## EXPERIMENTAL DETAILS

The sample, designated #I-JRM-2, was provided by the High Pressure Research Center, Polish Academy of Sciences. The sample was in the form of an irregular hexagonal platelet measuring  $\approx 0.1$  mm along [0001] and 3 mm to 5 mm along [11 $\bar{2}$ 0]. LEECL measurements were performed in a scanning electron microscope (SEM) equipped with a liquid-helium cold stage and a CL port (consisting of collection optics, a monochromator, and an intensified photodiode array detector). In the LEECL experiment, the electron beam axis is vertical, the CL collection axis is horizontal, and the sample surface is tilted at 45° to the vertical axis. For these measurements, the wavelength resolution of the monochromator was approximately 1 nm, corresponding to a photon energy resolution of 0.009 eV at 3.4 eV (band gap of GaN). LEECL spectra were acquired with the sample cooled to 15 K, at three electron beam voltages, 2.8 kV, 5.4 kV and 10.6 kV. The calculated maximum electron penetration depths into the GaN platelet at these voltages, taking into account the 45° angle of incidence of the electron beam on the sample surface, which reduces the penetration depth by a cosine factor, are 56 nm, 170 nm, and 510 nm respectively. The corresponding calculated average penetration depths, representing the mean of the electron energy dissipation vs. depth distribution function[4], are 19 nm, 56 nm, and 170 nm respectively. (Note that the ratio of the maximum penetration depth to the average penetration depth at each voltage is approximately equal to 3.)

It should be mentioned that sample #I-JRM-2 and other GaN samples from the High Pressure Research Center were also characterized by full-sample, monochromatic (8 keV to 10 keV) high-resolution x-ray diffraction imaging (HRXRD) at the NIST topography station at the National Synchrotron Light Source, Brookhaven National Laboratory. The HRXRD results will be reported in another publication.[5]

## DISCUSSION

CL spectra from the mechanically-polished-only region of the Ga-terminated face, taken at the three electron beam voltages of 2.8 kV, 5.4 kV and 10.6 kV, corresponding to mean electron penetration depths of 19 nm, 56 nm and 170 nm respectively, are shown in Fig. 1(a), and the corresponding CL spectra from the polished+CAIBE region are shown in Fig. 1(b). Only the near-band-edge spectral region, including photon energies from 2.9 eV to 3.8 eV, is displayed in Fig. 1. The deep-level CL spectrum, at lower energies than 2.9 eV, was dominated by the well-known “yellow” luminescence band[6] of GaN at  $\approx 2.2$  eV. The deep-level CL was found to be less sensitive to surface treatment and penetration depth (incident electron energy) than the near-band-edge CL, therefore our analysis is limited to the near-band-edge region. Arrows in Fig. 12 indicate the donor-bound exciton or free exciton emission at  $\approx 3.475$  eV, and a defect-related peak at  $\approx 3.325$  eV.

The 10.6 kV spectrum of the polished+CAIBE region (the Ga-face spectrum least affected by polishing damage) is compared to the 10.6 kV spectrum of the unpolished, N-terminated face in Fig. 2. The exciton or band-edge peak is seen to occur at 3.535 eV for the N-face,  $\approx 0.05$  eV higher in energy than for the Ga-face; also, the full width at half maximum (FWHM) of the peak is significantly larger for the N-face. These effects are ascribed to free carrier conduction band filling induced by unintentional donor impurities. In GaN, the band-edge emission energy has been observed to shift upward with increasing carrier

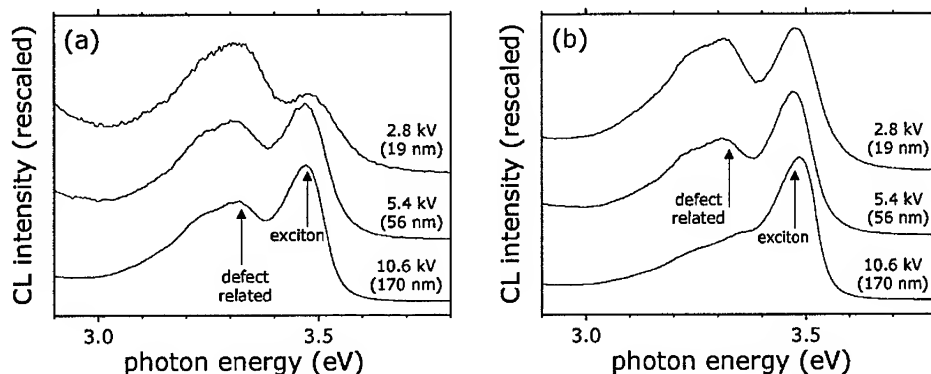


**Figure 1.** (a) Low-temperature CL spectra from the mechanically-polished-only region of the Ga-terminated face of sample #I-JRM-2, taken at different electron beam voltages and mean penetration depths. Arrows indicate the donor-bound exciton or free exciton emission at  $\approx 3.475$  eV, and a defect-related peak at  $\approx 3.325$  eV. (b) Low-temperature CL spectra from the polished+CAIBE region of the Ga-terminated face.

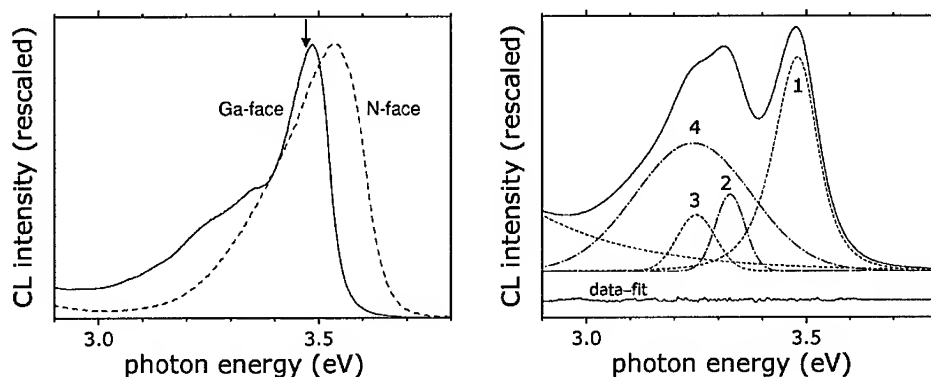


**Figure 2.** Low-temperature CL spectra of the polished+CAIBE region of the Ga-terminated face (solid curve) and the unpolished N-terminated face (dashed curve), taken at a beam voltage of 10.6 kV. The arrow indicates the position of the donor-bound exciton peak[9] in pure, unstrained GaN (3.471 eV).

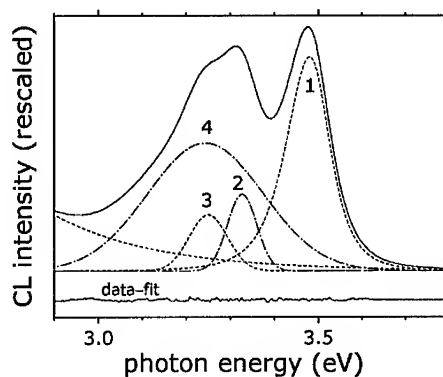


**Figure 3.** Curve-fitting results for the 2.8 kV spectrum from the polished+CAIBE region of the Ga-terminated face. Overall fit to data: solid curve, toward top of figure. The five components of the fit: dashed and dash-dotted curves, including asymmetric bell-shaped peak ascribed to donor-bound exciton (#1), three symmetric Gaussian peaks (#2, #3, and #4), and exponential function. Deviation between overall fit and data: solid curve, bottom of figure.

concentration[7] in the degenerate semiconductor regime ( $>10^{19} \text{ cm}^{-3}$ ). Other studies of bulk high-pressure grown GaN have shown that this material typically contains a very high free carrier concentration[8] ( $\approx 6 \times 10^{19} \text{ cm}^{-3}$ ), induced by unintentionally added donor impurities such as oxygen and silicon, and/or donor-like point defects. It should be pointed out that in high-purity, unstrained GaN, the low-temperature CL spectrum is usually dominated by donor-bound exciton recombination[9] at 3.471 eV. The shift of the exciton peak from 3.471 eV to energies as high as 3.489 eV on the Ga-face of sample #I-JRM-2 may also be caused by free-carrier band filling. From the results of Fig. 2, it appears that the electron concentration is much smaller near the Ga-face than near the N-face of the same sample.

It can be seen in Fig. 1(a) that the width of the exciton emission peak increases, and the intensity ratio of the exciton peak to the defect ( $\approx 3.325 \text{ eV}$  and lower energy) peaks decreases, with decreasing penetration depth beneath the mechanically polished surface. A similar trend is observed for the polished+CAIBE surface, Fig. 1(b), but the change in the shape of the spectrum from the largest to the smallest penetration depth is less pronounced for the polished+CAIBE surface than for the polished-only surface. This comparison indicates that the CAIBE processing was partially successful in removing the polishing-induced damage layer.

The subsurface polishing damage precluded HRXRD visualization of the native defect structure of either the polished-only region or the polished+CAIBE region. In both regions, the HRXRD was primarily sensitive to the surface morphology.[5] The diffracted intensity was greater from the polished+CAIBE region than from the polished-only region, indicated partial removal of the polishing damage by CAIBE, in agreement with the LEECL results.

Curve-fitting to a sum of bell-shaped peaks was performed to analyze the CL spectra in more detail. The exciton component was represented by an asymmetric (skewed) bell-shaped peak, with a lineshape intermediate between Gaussian and Lorentzian<sup>2</sup>. The defect emission in the 3.0 eV to 3.4 eV range was represented by a sum of three symmetric Gaussians, and the high-energy tail of the deep-level emission (which is most pronounced in the top spectrum of Fig. 1(a)) was represented by an exponential function. This multi-component model yielded a good fit to the data. The fitting results for the 2.8 kV spectrum from the polished+CAIBE surface (top curve in Fig. 1(b)) are illustrated in Fig. 3, including the overall fitting function, the five components, and the deviation between the fit and the data. Table I lists the values of several fitting parameters for the donor-bound exciton peak (component #1 in Fig. 3) and the defect-related peak at  $\approx 3.325 \text{ eV}$  (component #2 in Fig. 3): the peak energy, FWHM, and fractional integrated intensity. (The fractional integrated intensity is defined as the ratio of the integrated intensity of the given peak to the sum of the integrated intensities of all four peaks.)

The variation of the fitting parameters listed in Table I suggests some conclusions that are not as readily apparent by inspection of the spectra in Fig. 1. First, on going from the 2.8 kV spectrum of the polished-only surface (most affected by polishing damage) to the 10.6 kV nm spectrum of the polished+CAIBE surface (least affected by polishing damage), there is no systematic variation of the fractional integrated intensity of the exciton peak, or the peak energy. In other words, the polishing damage does not appear to quench the exciton CL. Rather, the decrease in the peak intensity of the exciton CL with polishing damage is a consequence of the increase in FWHM. There is no increase in the exciton FWHM from the 10.6 kV spectrum to the 5.4 kV spectrum of the polished+CAIBE surface. Thus, the effect of the polishing on the exciton CL lineshape is negligible at a depth of more than 56 nm from the polished+CAIBE surface, or  $\approx 260 \text{ nm}$  from the polished-only surface (the CAIBE etching depth is  $\approx 200 \text{ nm}$ ).

**Table I.** Selected numerical parameters obtained from curve-fitting (as shown in Fig. 3) of the low-temperature CL spectra of the Ga-terminated face of sample #I-JRM-2. The stated  $2\sigma$  uncertainties were obtained from a covariance analysis of the fitting parameters, based on the magnitude of the deviation between the data and the fitted function.

Surface treatment	Beam voltage (kV), mean penetration depth (nm)	Peak number	Peak energy (eV)	FWHM of peak (eV)	Fractional integrated intensity
mechanical polishing	2.8 kV 19 nm	1	3.482 $\pm 0.0012$	0.146 $\pm 0.009$	0.333 $\pm 0.107$
mechanical polishing	5.4 kV 56 nm	1	3.472 $\pm 0.0017$	0.124 $\pm 0.007$	0.413 $\pm 0.045$
mechanical polishing	10.6 kV 170 nm	1	3.475 $\pm 0.0007$	0.108 $\pm 0.004$	0.376 $\pm 0.025$
polishing + CAIBE	2.8 kV 19 nm	1	3.480 $\pm 0.0007$	0.118 $\pm 0.003$	0.362 $\pm 0.014$
polishing + CAIBE	5.4 kV 56 nm	1	3.476 $\pm 0.0005$	0.100 $\pm 0.001$	0.333 $\pm 0.009$
polishing + CAIBE	10.6 kV 170 nm	1	3.489 $\pm 0.0002$	0.101 $\pm 0.001$	0.434 $\pm 0.007$
mechanical polishing	2.8 kV 19 nm	2	3.343 $\pm 0.0070$	0.104 $\pm 0.017$	0.196 $\pm 0.125$
mechanical polishing	5.4 kV 56 nm	2	3.320 $\pm 0.0025$	0.093 $\pm 0.010$	0.099 $\pm 0.028$
mechanical polishing	10.6 kV 170 nm	2	3.325 $\pm 0.0014$	0.083 $\pm 0.002$	0.075 $\pm 0.007$
polishing + CAIBE	2.8 kV 19 nm	2	3.326 $\pm 0.0012$	0.078 $\pm 0.003$	0.074 $\pm 0.007$
polishing + CAIBE	5.4 kV 56 nm	2	3.318 $\pm 0.0016$	0.080 $\pm 0.003$	0.059 $\pm 0.004$
polishing + CAIBE	10.6 kV 170 nm	2	3.348 $\pm 0.0010$	0.057 $\pm 0.003$	0.012 $\pm 0.001$

In contrast to the exciton peak, the fractional integrated intensity of the  $\approx 3.325$  eV defect peak is seen to increase dramatically on going from the weakest to strongest polishing damage effect (reading Table I from bottom to top). Further, the FWHM of this peak increases with increasing polishing damage. The  $\approx 3.325$  eV peak is barely observable in the 10.6 kV spectrum of the polished+CAIBE surface, but the fractional integrated intensity of this peak increases by a factor of 5 when the mean penetration depth is reduced from 170 nm to 56 nm (10.6 kV to 5.4 kV). If the  $\approx 3.325$  eV peak is taken to be an indicator of polishing damage, it can be concluded from these observations that the polishing damage extends to a depth of  $\approx 170$  nm below the polished+CAIBE surface, or  $\approx 400$  nm below the polished-only surface.

## CONCLUSIONS

An increase in the FWHM of the exciton ( $\approx 3.475$  eV) emission peak, and the appearance of a defect peak at  $\approx 3.325$  eV, were found to be indicators of polishing damage in low-temperature CL spectroscopy of the Ga-terminated face of a bulk high-pressure grown single-crystal GaN platelet designated #I-JRM-2. Regions of the Ga-terminated face prepared by mechanical polishing only, and by mechanical polishing + CAIBE to a depth of 200 nm, were compared. The  $\approx 3.325$  eV peak appears to be the more sensitive damage indicator. From the variation of the  $\approx 3.325$  eV peak intensity with electron penetration depth in the CL spectra of the polished+CAIBE and polished-only surfaces, the total thickness of the polishing damage layer was estimated to be 400 nm.

## REFERENCES

1. Z. Liliental-Weber, in *Semicond. and Semimet.* 57 (Academic Press, New York, 1999), pp. 129-156
2. S. Porowski and I. Grzegory, in *Semicond. and Semimet.* 55 (Academic Press, New York, 1998), pp. 353-379
3. M. Asif Khan, J. W. Yang, W. Knap, E. Frayssinet, X. Hu, G. Simin, P. Prystawko, Mleszczyski, I. Grzegory, S. Porowski, R. Gaska, M. S. Shur, B. Beaumont, M. Teisseire, and G. Neu, *Appl. Phys. Lett.* 76, 3807 (2000)
4. L.H. Robins, J.R. Lowney and D.K. Wickenden, *J. Mater. Res.* 13, 2480 (1998)
5. B. Steiner, N.A. Sanford, L.H. Robins, C. Menoni, unpublished
6. S. C. Jain, M. Willander, J. Narayan, and R. Van Overstraeten, *J. Appl. Phys.* 87, 965 (2000)
7. M. Yoshikawa, M. Kunzer, J. Wagner, H. Obloh, P. Schlotter, R. Schmidt, N. Herres, and U. Kaufmann, *J. Appl. Phys.* 86, 4400 (1999)
8. P. Perlin, E. Litwin-Staszewska, B. Suchanek, W. Knap, J. Camassel, T. Suski, R. Piotrzkowski, I. Grzegory, S. Porowski, E. Kaminska, and J. C. Chervin, *Appl. Phys. Lett.* 68, 1114 (1995)
9. K. Kornitzer, T. Ebner, K. Thonke, R. Sauer, C. Kirchner, V. Schwegler, M. Kamp, M. Leszczynski, I. Grzegory, and S. Porowski, *Phys. Rev. B* 60, 1471 (1999)

### Production of Sapphire Blanks and Substrates for Blue LEDs and LDs

Chandra P. Khattak, Frederick Schmid, Paul J. Guggenheim  
Maynard B. Smith, Henry H. Rogers, and Kurt Schmid  
Crystal Systems Inc., 27 Congress Street  
Salem, MA 01970

#### ABSTRACT

The Heat Exchanger Method (HEM) of crystal growing was combined with the Fixed Abrasive Slicing Technology (FAST) to produce low-cost, high-quality sapphire substrates for deposition of the GaN family of compounds. Production quantities of 2-inch diameter blanks have been supplied, and 3-inch diameter material has been qualified. Current technology can be used to prepare sapphire blanks up to 6-inch diameter.

#### INTRODUCTION

Gallium nitride (GaN) and related compound semiconductors are among the most attractive materials for blue, violet and ultraviolet light emitting diodes (LEDs), laser diodes (LDs) and high speed, high power transistors [1-3]. Considerable progress has been made with these devices operating with long lifetime and high brightness. A key issue for the growth of GaN has been the lack of a suitable substrate, since GaN substrates are not readily available. While several new substrates, such as AlN [4,5], LaAlO<sub>3</sub> [6], LiGaO<sub>3</sub> [7] bulk GaN or self-supported film by ELO [8] or Pendeo epitaxy [9], etc., are being explored the most common substrates being used are sapphire ( $\alpha$ -Al<sub>2</sub>O<sub>3</sub>) and single crystal silicon carbide (SiC). In addition to meeting technical requirements to produce the devices, it is important that the components used in the manufacture be available in large quantities in a manufacturing environment so that low-cost devices can be produced and their full potential realized. Therefore, while novel substrates may find niche applications the real competition is between sapphire and SiC substrates for high volume, widespread use in laser diodes, LEDs and lighting applications.

This paper discusses two unique technologies for the production of high quality sapphire substrates in high volume not only to meet current requirements, but also to meet future applications without requiring changes in the basic technologies. These two key technologies are the Heat Exchanger Method (HEM) of crystal growth and the Fixed Abrasive Slicing Technology (FAST) for wafering of sapphire rods. The current requirement of 2-inch diameter substrates is being met in production. However, wafers up to 6-inch diameter size can be produced by modification of production procedures without developing new technologies.

#### HEAT EXCHANGER METHOD

The Heat Exchanger Method (HEM<sup>TM</sup>) is a solidification technique [10,11] that has been utilized for more than 30 years for growth of sapphire crystals from the melt by controlling the heat input and heat extraction, as shown on Figure 1. A crucible with a single crystal seed centered at the bottom is loaded with sapphire crackle (meltstock) and placed on a high-temperature, helium-cooled heat exchanger. After evacuation of the heat zone, heat is applied and the charge is melted. The seed is prevented from melting by flowing helium gas through the heat exchanger.

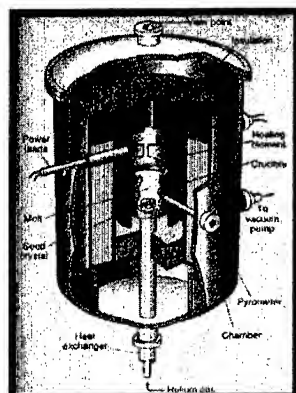


**Figure 1.** Schematic of a Heat Exchanger Method (HEM) furnace.

After meltback of the seed is achieved, growth is initiated and progressed by increasing the helium flow through the heat exchanger and/or decreasing the furnace temperature. After complete solidification of the charge is achieved, the furnace temperature is reduced below the melting point of sapphire and the helium flow through the heat exchanger is reduced to achieve *in situ* annealing of the boule. Thereafter, the furnace temperature is reduced in a controlled manner for cooldown of the boule.

Growth during HEM is achieved under stabilizing temperature gradients as the hot melt is near the top of the crucible and the colder solid is at the bottom of the crucible, thereby minimizing convection. The crystal growth parameters have been optimized to ensure that the solid-liquid interface during growth is submerged below the liquid during most of the growth cycle. Under these conditions, the thermal and mechanical perturbations are damped out by the surrounding liquid before they reach the interface. The submerged interface also produces low temperature gradients at the growth site. This minimizes the propensity for spurious nucleation and growth under low temperature gradients and produces higher quality crystals. In HEM sapphire growth, the last material to solidify is along the crucible wall. Most impurities have a low segregation coefficient and therefore are segregated near the crucible wall in the last material to solidify. The material near the surface of the boule containing a higher level of impurities can easily be removed, and the remainder of the boule is significantly purer than the starting meltstock.

After HEM crystal growth is completed, the crystal is still in the heat zone below the melt temperature but under a temperature gradient and susceptible to cracking. The temperature gradient and stress on the boule can be decreased by reducing the helium flow through the heat exchanger. The unique feature of *in situ* annealing of HEM can be utilized to reduce temperature gradients on the crystal and relieve solidification stresses. The reduction in stresses aids in achieving higher crystal perfection. After annealing, the crystal can be cooled at a rate preventing cracking of the boule. Figure 2 shows a typical 34-cm diameter, 65-kg production sapphire boule, and Figure 3 shows a 38-cm diameter, 83-kg sapphire boule in development.



**Figure 2.** A typical 34-cm diameter, 65-kg production HEM sapphire boule.

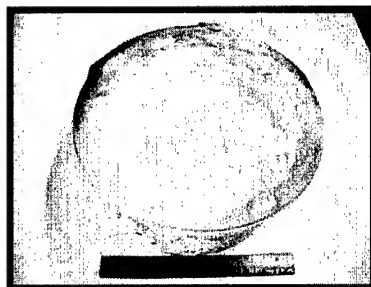


**Figure 3.** A 38-cm diameter, 83-kg HEM sapphire boule grown in development.

#### CHARACTERISTICS OF HEM SAPPHIRE

The world's largest sapphire boules are produced using HEM [12]. The melting point of sapphire is 2040°C, and HEM furnaces are designed to operate in excess of 2200°C for extended periods. Crystal growth is carried out under a vacuum so that the volatile impurities and reaction products are removed from the heat zone, thereby reducing the probability of these impurities being incorporated in the growing crystal. Typical impurity analysis of HEM sapphire is shown in Table I. It should be noted that impurities close to the detection limits of analysis, and impurities, such as titanium, are low for HEM sapphire; titanium is usually observed when a lower cost meltstock is used for crystal growth.

To achieve growth of high-quality sapphire boules, it is essential that growth take places under low temperature gradients. The heat zone of the HEM furnace is designed with no built-in temperature gradients. Resistive heating of HEM furnaces for sapphire growth maintains low temperature gradients in the heat zone. Using low enough temperature gradients in the liquid to minimize constitutional supercooling and maintaining low temperature gradients in the solid ensure that high quality sapphire crystals are grown.

**Table I.** Typical impurity analyses of different sapphire meltstock and HEM sapphire boules using spark source mass spectroscopy (SSMS) and inductively coupled plasma (ICP) methods.

Sample	Analysis Method	Na	Si	Fe	Ca	Mg	Ga	Cr	Ni	Ti	Mn	Cu	Mo	Li	Zn	Zr
Meltstock	SSMS	2	3	1	6	1	0.7	0.3	0.4	<0.5	0.1	0.2	<0.5	<1	1	0.5
Meltstock	SSMS	5	20	2	5	1	0.7	0.5	0.3	<0.5	0.3	0.3	<0.5	0.1	0.3	0.5
HEM Sapphire	SSMS	1	4	0.6	2	2	2	0.2	0.3	<0.3	0.5	0.1	<0.5		1	1
Meltstock	ICP	<4	9	2	3	<1	<4	<1	<1	<1	<1	<1	<4	<1	<1	<1
Meltstock	ICP	<4	7	1	3	<1	<4	<1	<1	<1	<1	<1	<4	<1	<1	<1
HEM Sapphire	ICP	<4	4	5	3	<1	<4	<1	<1	<1	<1	<1	<4	<1	<1	2

Even when sapphire crystal growth is carried out under low temperature gradients, stresses are generated in the crystal. These stresses degrade crystal quality unless they are annealed after growth before cooldown to room temperature. The unique feature of *in situ* annealing with HEM allows relieving of solidification stresses after growth. This can be carried out to temperatures close to the melting point after growth.

The combination of large-size of HEM sapphire crystals and low thermal conductivity of sapphire material requires that sapphire boules be cooled at a slow rate to minimize stresses and defect density in the boules.

#### FIXED ABRASIVE SLICING TECHNOLOGY (FAST)

FAST has been developed as a multiwire slicing technique [13,14] in which wires plated with diamonds are used to cut the workpiece. It was necessary to minimize the contact areas between the wire and the workpiece so that higher feed forces could be achieved at the cutting edge of the diamonds on the wire. To achieve high surface speed of wire, FAST was modified to incorporate high-speed rotation of the workpiece, as shown in Figure 4. Diamond-plated wires are held in a multiwire pack with equal spacing and tension. The wirepack is stretched to high tension in the bladehead of the slicer. A cylindrical workpiece is rotated at high speeds up to 5,000 rpm and advanced at a controlled feed rate against the wires which are reciprocated. Grooved rollers are placed on either side of the workpiece below the wirepack to minimize wire wander and improve wafer accuracy. High speed rotation results in high surface speed and minimizes the contact length between the workpiece and the wires. The effective feed force on the diamond tip against the workpiece is thereby increased and allows diamonds to plow into the workpiece to achieve effective slicing. In this configuration, slicing is achieved from the circumference of the cylinder toward the interior. The diamonds on the side of the wires are still contacting the cut surface of sapphire resulting in a lapping action to give smooth cut surfaces.

FAST slicing combines all the major advantages of other slicing processes. For example, kerf was minimized, as with multiwire slicing (MWS), low expendable material costs were achieved, as with internal diameter (ID) slicing, and the equipment is simple, as with outside diameter (OD) slicing. In addition, thin slices are produced with high wafer accuracy. FAST slicing is carried out using low feed forces to achieve high wafer quality.

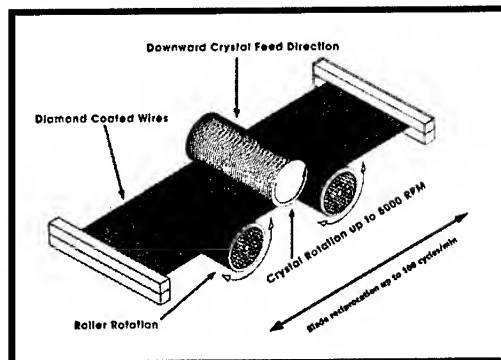


Figure 4. Schematic of a FAST slicer showing high-speed rotation of the workpiece.

With these improvements, FAST slicing is three times faster than MWS for slicing sapphire with one-third of the consumable cost. As the hardness of the material increases, the rotation rates for the crystal can be increased. The size of the workpiece that can be sliced will be limited by the degradation of diamonds on the wirepack. These improvements in FAST have opened a new era of slicing many crystals more efficiently and particularly large hard crystals that could not be sliced effectively with existing technology.

## PRODUCTION OF SAPPHIRE SUBSTRATES

Sapphire has a rhombohedral crystal structure that results in anisotropic properties. It is a uniaxial crystal, and this axis is referred to as the *c*-axis or [0001]. The properties of sapphire relative to the *c*-axis are quite different from those along the *c*-axis. For example, the *a*-axis [11  $\bar{2}$ 0] and *m*-axis [10  $\bar{1}$ 0] are quite similar, but the properties along the *c*-axis or [0001] are quite different. The *c*-axis is commonly referred to as 0° orientation and *a*- and *m*-axis as 90° orientation. The most common sapphire substrates for LED application are specified as *c*-axis, however, high quality growth of sapphire boules is achieved for the 90° orientations. Therefore, HEM sapphire boules are grown with *a*- or *m*-axis orientations, *c*-axis is located orthogonal to the growth direction and rods of the desired orientation are cored from the boules as shown in Figure 5. The cored sapphire rods are characterized and oriented, and appropriate flats are put on and prepared for FAST slicing. The cycle time for slicing 2-inch diameter sapphire rods is less than 8 hours. The following specifications are met for FAST-sliced, HEM sapphire blanks:

Crystal: HEMCOR single crystal sapphire  
Orientation: (0001) *c*-axis  $\pm$  0.2 degrees  
Diameter:  $50.8 \pm 0.20$  mm, fine grind OD  
Thickness:  $0.635 \pm 0.040$  mm  
Primary Flat: [11  $\bar{2}$ 0] *a*-axis  $\pm$  0.3 degrees  
Flat Length:  $16.0 \pm 0.8$  mm

Front Side Surface:  $R_a < 1.0 \mu\text{m}$   
Back Surface Roughness:  $R_a < 1.0 \mu\text{m}$   
TTV:  $< 30.0 \mu\text{m}$   
Bow:  $< 30.0 \mu\text{m}$   
Packaging: Shipped in jars of 50

These blanks have been supplied to the industry on production basis for over two years. Even though the bulk of shipments has been 2-inch diameter blanks, 3-inch diameter sapphire blanks have also been supplied. Figure 6 shows a representative sample of 3-inch diameter sapphire blanks.

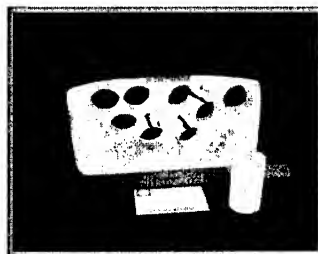


**Figure 5.** A section of an *a*-axis HEM sapphire boule; *c*-axis is located orthogonal to the growth direction, and rods of desired size are cored from the section. A 2-inch diameter as-cored rod is also shown.

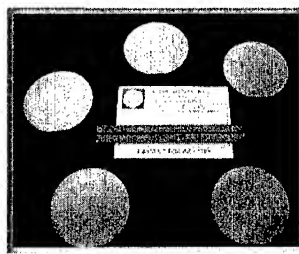


**Figure 6.** A representative sample of 3-inch diameter sapphire blanks.

## CONCLUSIONS

The combination of two unique technologies – HEM for sapphire boule growth and FAST slicing – has resulted in production of high quality sapphire substrates at low cost for deposition of GaN family of compounds for laser diode (LD) and light emitting diode (LED) applications. Production quantities of 2-inch diameter blanks have been supplied to the industry, and 3-inch diameter material has been qualified. The large diameter HEM boules facilitate multiple small diameter rod fabrication from the same boule. Present production of sapphire boules allow rods larger than 6-inch diameter to be fabricated. While FAST slicing has been tested for crystals up to 3-inch diameter, increasing the diameter of workpiece has not shown significant problems. Therefore, sapphire blanks up to 6-inch diameter can be produced using current technology and production practices.

## REFERENCES

1. S. Nakamura, M. Senoh and T. Mukai, *Appl. Phys. Lett.* **64**, 1687 (1994).
2. S. Nakamura, M. Senoh, S. Nagahama, N. Iwasa, T. Yamada, T. Matsushita, H. Kiyoku, Y. Sugimoto, *Jpn. J. Appl. Phys.* **35**, L74 (1996).
3. S. N. Mohammad, A. Salvador and H. Morkov, *Proc. IEEE* **83**, 1306 (1995).
4. G. A. Slack and T. F. McNelly, *J. Crystal Growth* **42**, 560 (1977).
5. M. Tanaka, S. Nakahata, K. Sogabe, H. Nakata and M. Tobioka, *J. Appl. Phys.* **36**, L106 (1997).
6. E. S. Hellmann, Z. Lilientha-Weber, D. N. E. Buchanan, *MRS Internet J. Nitride Semicond. Res.* **2**, 30 (1997).
7. P. Kung, A. Saxler, X. Zhang, D. Walker, R. Lavado and M. Razeghi, *Appl. Phys. Lett.* **69**, 2116 (1996).
8. P. Vennegues, B. Beaumont and P. Gibart, *J. Appl. Phys.* **87**, 4175 (2000).
9. T. S. Zheleva, W. M. Ashmawi, K. A. Jones, *Phys. Stat. Sol.* **176**, 545 (1999).
10. F. Schmid and D. Viechnicki, *J. Am. Ceramic Soc.* **53** (9), 528 (1970).
11. C. P. Khattak and F. Schmid, *Proc. SPIE* **505**, 4 (1984).
12. C. P. Khattak and F. Schmid, *J. Crystal Growth* **225**, 572 (2001).
13. C. P. Khattak and F. Schmid, *Proc. E.C. Photovoltaic Specialists Conf.*, D. Reidel Publ. Co., p. 106 (1979).
14. F. Schmid and C. P. Khattak, *Optical Spectra* **15** (5) 65 (1981).

## Transport and Chemical Mechanisms in GaN Hydride Vapor Phase Epitaxy

Sergey Yu. Karpov<sup>1</sup>, Alexander S. Segal<sup>1</sup>, Darya V. Zimina<sup>1</sup>, Sergey A. Smirnov<sup>1</sup>, Alexander P. Sid'ko<sup>1</sup>, Alexey V. Kondratyev<sup>1</sup>, Yuri N. Makarov<sup>2</sup>, Denis Martin<sup>3</sup>, Volker Wagner<sup>3</sup>, and Marc Illegems<sup>3</sup>

<sup>1</sup> Soft-Impact Ltd, P.O.Box 33, 27 Engels av., 194156 St. Petersburg, Russia

<sup>2</sup> STR Inc, P.O.Box 70604, Richmond, VA 23255, USA

<sup>3</sup> Institute for Quantum Electronics and Photonics, Swiss Federal Institute of Technology, CH-1015 Lausanne, Switzerland

### ABSTRACT

On the basis of both experimental and theoretical studies, a simple quasi-thermodynamic model of surface kinetics is suggested for Hydride Vapor Phase Epitaxy (HVPE) of GaN, working in a wide range of growth conditions. Coupled with detailed 3D modeling of species transport in a horizontal reactor, the model provides quantitative predictions for the GaN growth rate as a function of process parameters. Significance of transport effects on growth rate uniformity is demonstrated.

### INTRODUCTION

The development and production of advanced group-III nitride opto- and microelectronic devices, UV light emitting diodes (LEDs) for white solid-state lightning, high-brightness LEDs, laser diodes, high-power field-effect transistors, etc., strongly require a reduced dislocation density in the epitaxial heterostructures. Due to the lack of commercially available GaN and AlN homoepitaxial substrates, alternative approaches based on the growth of these quasi-bulk wafers by HVPE have been widely employed [1]. Much progress has been recently made in fabrication of the quasi-bulk wafers by using the epitaxial lateral overgrowth technique [2-6]. However, despite this progress, the basic mechanisms underlying GaN HVPE are still obscure. In [7], a first kinetic model of surface chemistry was suggested, giving a qualitative interpretation of the effects of carrier gas (hydrogen *versus* helium) and temperature on the GaN growth rate. A thermodynamic analysis of GaN HVPE neglecting N<sub>2</sub> production due to surface reactions was performed in [8] in order to provide an equilibrium vapor composition at the growth surface and to estimate the thermodynamic driving force for growth. An elaborated kinetic model of heterogeneous processes was suggested by Cadoret et al. (see [9] and references therein) where two distinct growth mechanisms were presented to explain the data of Ref.[7]. The quasi-thermodynamic approach to surface chemistry combined with 3D simulations of GaN HVPE in a reactor of realistic geometry has revealed the essential effects of gas dynamics and species transport on the growth rate and V/III ratio distribution across the wafer [10]. However, the lack of systematic data at that time did not allow developing of a quantitative HVPE model workable in a wide range of growth conditions.

This paper reports on a coupled experimental and theoretical study of GaN HVPE in a horizontal tube reactor aimed at further understanding the basic growth mechanisms. We suggest here a simple quasi-thermodynamic model of surface chemistry providing quantitative predictions of

the growth rate as a function of process parameters. The transport effects on the GaN growth rate and V/III ratio near the growth surface are discussed on the basis of 3D simulations.

## EXPERIMENT

The horizontal reactor and growth procedure used in the experiments were described in detail in [2,3]. Growth was performed on a sapphire (0001) substrate at atmospheric pressure with a  $N_2/H_2$  mixture as carrier gas. For the data reported here,  $(NH_3 + N_2)$  is supplied by two quartz injector tubes placed on each side of the substrate holder with their outlets oriented towards the substrate, while the  $(GaCl + N_2)$  outlet is situated just upstream and slightly above the substrate. The total area of the reactor tube cross-section is about  $145 \text{ cm}^2$ . The substrate rotation rate was maintained at 30 rpm and the growth temperature was varied between  $1010^\circ\text{C}$  and  $1080^\circ\text{C}$ . A wide-range variation of  $NH_3$ ,  $H_2$ , and  $HCl$  flow rates was used for parametric study of HVPE. The GaN growth rate at the center of the wafer was monitored by a laser reflectometer operating at  $670 \text{ nm}$  [11].

## THEORY

Detailed 3D modeling considers both diffusive and convective species transport in the reactor. According to the mass-spectrometry data [12] and thermodynamic analysis [8], we select five species essential for growth –  $GaCl$ ,  $NH_3$ ,  $H_2$ ,  $HCl$ , and  $N_2$ . The  $HCl$  introduced into the source chamber containing a boat of liquid  $Ga$  transforms almost totally into  $GaCl$  and  $H_2$ . Thus, the  $HCl$  observed in the reactor is largely produced by surface reactions involved in the GaN growth. Ammonia gas-phase decomposition is negligible under the HVPE conditions employed here [13] and  $GaCl_3$  formation from  $GaCl$  and  $HCl$  is found to be thermodynamically unfavorable. Hence, gas-phase reactions between the selected species can be entirely neglected in the HVPE model.

Consider now the surface reactions. It was shown in [14,15] that the reactions involving molecular nitrogen (for instance,  $NH_3$  decomposition into  $N_2$  and  $H_2$ ) are essentially suppressed because of a low probability of  $N_2$  sticking on a GaN surface. The sticking probability can be additionally reduced in a reactive gaseous environment [16] due to formation of a protective adsorption layer. We suppose, that this is the case in HVPE where chlorine adsorbed on the Ga sites of the GaN surface may affect the  $N_2$  adsorption and desorption rates. This assumption is, in part, confirmed by the fact that GaN decomposition into gaseous  $Ga$  and  $N_2$  is insignificant under typical HVPE conditions, in contrast to high-temperature growth of GaN by other techniques [14,15]. Indeed, the principal channel of  $Ga$  removal from the growth surface is  $GaCl$  desorption, while no atomic  $Ga$  is produced in HVPE, according to the observations [12] and thermodynamic analysis [8]. All this allows us to consider molecular nitrogen as a nearly inert gas, neglecting its chemical reactions with the other species. Taking this into account, we can conclude that the only surface reaction occurring on the growth surface is



In this paper, we use the quasi-thermodynamic model of surface kinetics described in detail in [15]. The model is based on the Hertz-Knudsen equations

$$J_i = \beta_i (P_i - P_i^e) \quad , \quad i = GaCl, NH_3, H_2, \text{ and } HCl \quad (2)$$

relating the normal projections  $J_i$  of the species fluxes to their partial pressures  $P_i$  at the growth surface and to their thermodynamic pressures  $P_i^e$ , the mass balance equations

$$J_{\text{GaCl}} = V_g (\rho_{\text{GaN}} / M_{\text{GaN}}) \quad (3a)$$

$$J_{\text{NH}_3} = V_g (\rho_{\text{GaN}} / M_{\text{GaN}}) \quad (3b)$$

$$J_{\text{GaCl}} + J_{\text{HCl}} = 0 \quad (3c)$$

$$3J_{\text{NH}_3} + 2J_{\text{H}_2} + J_{\text{HCl}} = 0 \quad (3d)$$

and the mass action law equation for reaction (1)

$$P_{\text{GaCl}}^e \cdot P_{\text{NH}_3}^e = K_{\text{GaN}} \cdot P_{\text{HCl}}^e \cdot P_{\text{H}_2}^e \quad (4)$$

Here,  $\beta_i$  is the Hertz-Knudsen factor of the  $i$ -th species,  $V_g$  is the growth rate,  $\rho_{\text{GaN}}$  and  $M_{\text{GaN}}$  are the density and molar mass of GaN, respectively, and  $K_{\text{GaN}}$  is the equilibrium constant of the reaction (1) computed from the thermochemical properties of the relevant species [17]. The sum of the species partial pressures, including  $\text{N}_2$ , is equal to the total gas pressure in the reactor.

Eqs.(2)-(4) serve as boundary conditions for the mass transport equations set on the wafer and reactor walls covered with parasitic deposits. It is important to note that the model does not use any fitting parameters.

## PARAMETRIC STUDY ON GaN HVPE

First of all, we have performed the parametric study of the GaN growth. In Fig.1, the experimental data are compared with 3D computations accounting for the actual reactor geometry. We do not consider here the parasitic deposition of polycrystalline GaN on the quartz reactor walls, which is found experimentally to be rather low and located entirely downstream from the substrate holder.

It is seen that the GaN growth rate weakly decreases with temperature (Fig.1a), indicating surface kinetic effects to be insignificant in the temperature range of interest. The growth rate is proportional to the HCl flow rate through the GaCl source (Fig.1b). However, this is not the evidence for mass transport-limited (MTL) growth because the slope of the curve depends on the V/III ratio at the GaN surface. This conclusion is also confirmed by the distinct sublinear growth rate dependence on the  $\text{NH}_3$  flow rate, shown in Fig.1c (under MTL conditions and  $V/\text{III} > 1$  the growth rate would be nearly independent of ammonia supply). To understand this behavior, we mention that for MTL growth, the adsorption of a growth rate limiting species, here GaCl, dominates over its desorption, i.e.  $P_{\text{GaCl}} \gg P_{\text{GaCl}}^e$  in Eq.(2). In HVPE,  $P_{\text{GaCl}}$  is typically comparable with  $P_{\text{GaCl}}^e$ . Therefore, the growth rate dependence both on the HCl and  $\text{NH}_3$  flow rates is controlled by the interplay of the thermodynamic pressures of these species, in accordance with the mass action law (4). This situation is similar, for instance, to high-temperature metal-organic vapor phase epitaxy of GaN where the growth rate is controlled by Ga desorption from the surface, which, in turn, primarily depends on V/III ratio [15].

By the same reason, the GaN HVPE becomes sensitive to the  $\text{H}_2$  flow rate. According to the mass action law (4), the GaCl thermodynamic pressure may be expected to increase

monotonically with an increase in the  $H_2$  pressure. Hence, a higher  $H_2$  flow rate generally results in a lower growth rate (Fig. 1d). At the moment, we are not able to interpret the non-monotonic behavior of the growth rate observed experimentally at low  $H_2$  flow rates, which needs further investigations. Nevertheless, it is generally seen that the computations are quantitatively consistent with the experimental data. This indicates the basic chemical and transport mechanisms of HVPE to be properly accounted for in the model.

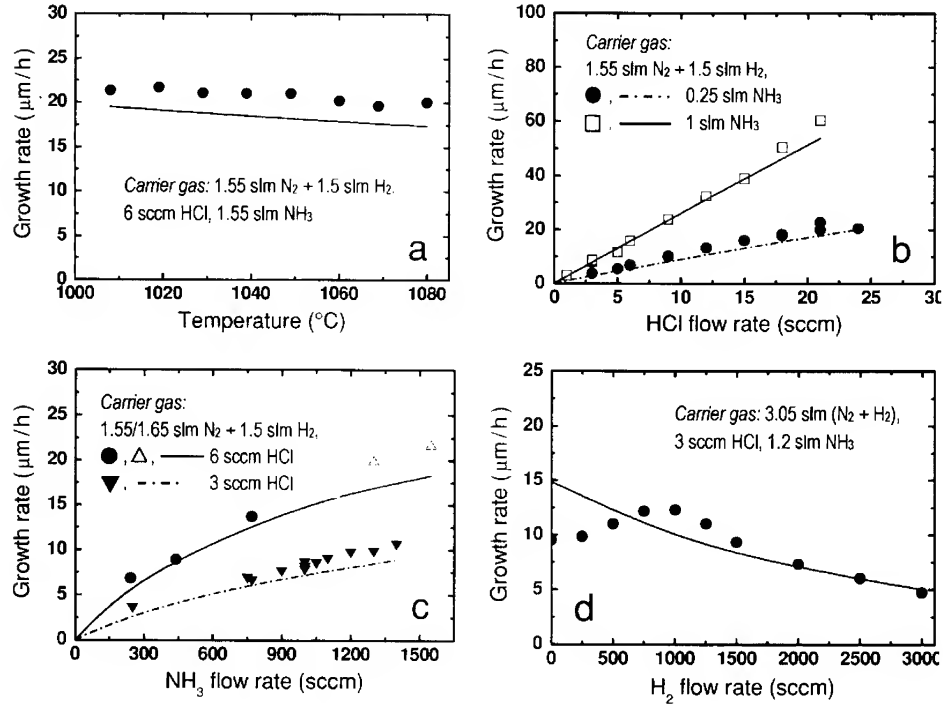


**Figure 1.** Growth rate as a function of (a) temperature, (b)  $HCl$  flow rate, (c)  $NH_3$  flow rate, and (d)  $H_2$  flow rate. Symbols are experimental points, lines are computations, temperature is 1050  $^{\circ}\text{C}$  in b-d,  $\bullet$  and  $\Delta$  correspond to 1.55 and 1.65 slm of the carrier  $N_2$  in c.

#### TRANSPORT EFFECT ON GROWTH RATE

A specific feature of GaN HVPE is that the growth is strongly affected by the species transport in the reactor [10]. First, due to high flow rates, the precursors,  $NH_3$  and  $GaCl$ , are injected in the form of jets which do not relax completely before reaching the substrate. Second, the computations show that a complex vortex-like gas motion is generated near the susceptor due to natural concentration convection. This effect originates from the considerable difference in the species partial densities. Third, due to a relatively high pressure, the distribution of species concentrations is controlled not only by their diffusion but also by the convective gas flow. Fig.2

shows that GaCl and NH<sub>3</sub> supplied through different injectors are non-uniformly distributed over the substrate, reflecting the positions of the gas injectors. A slow substrate rotation makes their distributions somewhat asymmetric. The drop of the precursor concentrations near the circular slit seen in Fig.2 is due to the N<sub>2</sub> injection through the slit, necessary for the wafer rotation. The N<sub>2</sub> flow, however, is rather weak here and does not normally affect the species transport over the wafer.

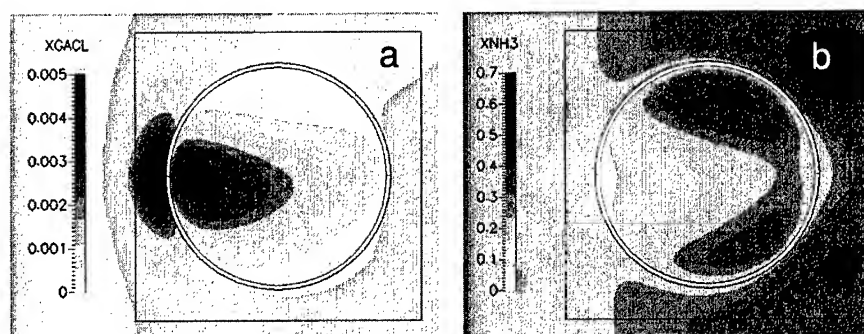


**Figure 2.** Distributions of the GaCl (a) and NH<sub>3</sub> (b) molar fractions in the horizontal plane located at the substrate height (the rotation rate is 30 rpm).

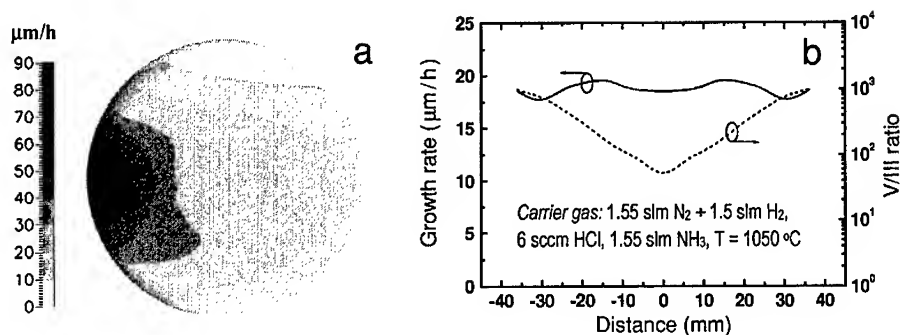


**Figure 3.** Instantaneous growth rate distribution across the wafer (a) and the radial angle-averaged growth rate and V/III ratio distributions (b) (the rotation rate is 30 rpm).

The non-uniformity in the precursor supply produces a non-uniform instantaneous growth rate distribution on the rotating surface, shown in Fig.3a. Since both GaCl and NH<sub>3</sub> determine the GaN growth rate, its distribution does not follow that of each precursor. The substrate rotation makes the mean growth rate much more uniform due to the angle averaging (Fig.3b). Here, the sharp upstream maximum in the instantaneous growth rate is compensated by its minimum on the periphery and, therefore, does not manifest itself in the average growth rate.

Comparison of the NH<sub>3</sub> and GaCl molar fraction distributions in Fig.2 shows the values of the V/III ratio in the upstream and downstream regions to be significantly different. Hence, far from

the center of the wafer, GaN actually grows under modulated GaCl and NH<sub>3</sub> flows, in contrast to the material growing near the center. This may induce a radial variation of GaN surface morphology.

## CONCLUSIONS

In this paper, basic mechanisms of GaN HVPE have been studied both experimentally and theoretically. The simple surface chemistry model without fitting parameters, coupled with a detailed 3E modeling of species transport in a horizontal reactor provides quantitative predictions for the GaN growth rate in a wide range of operating conditions. The model interprets the particular growth rate dependence on GaCl and NH<sub>3</sub> flow rates observed in experiment and, generally, the growth rate variation with other parameters. Further efforts are still necessary to understand in more detail the hydrogen effect on the growth rate. The computations have demonstrated the importance of species transport phenomena for growth rate uniformity.

## REFERENCES

1. R.J. Molnar, W. Gotz, L.T. Romano, and N.M. Johnson, *J. Cryst. Growth* **178**, 147 (1997).
2. O. Parillaud, V. Wagner, H.J. Buehlmann, and M. Illegems, *Internet J. Nitride Semicond. Res.* **3**, 40 (1998).
3. V. Wagner, O. Parillaud, H.J. Buehlmann, M. Illegems, S. Gradecak, P. Stadelmann, T. Riemann, and J. Christen, *J. Appl. Phys.* **92**, 1307 (2002).
4. M.K. Kelly, R.P. Vaudo, V.M. Phanse, L. Gorgens, O. Ambacher, and M. Stutzmann, *Jpn. J. Appl. Phys.* **38**, L217 (1999).
5. O. Oda, T. Inoue, Y. Seki, K. Kainosho, S. Yaegashi, A. Wakahara, A. Yoshida, S. Kurai, Y. Yamada, and T. Taguchi, *Phys. Stat. Solidi (a)* **180**, 51 (2000).
6. S.S. Park, I.-W. Park, and S.H. Choh, *Jpn. J. Appl. Phys.* **39**, L1141 (2000).
7. W. Seifert, G. Fitzl and E. Butter, *J. Cryst. Growth* **52**, 257 (1981).
8. A. Koukitu, Sh. Hama, T. Taki and H. Seki, *Jpn. J. Appl. Phys.* **37**, 762 (1998).
9. R. Cadoret and A. Trassoudaine, *J. Phys.: Condens. Matter* **13**, 6893 (2001).
10. S.Yu. Karpov, D.V. Zimina, Yu.N. Makarov, B. Beaumont, G. Nataf, P. Gibart, M. Heuken, H. Jurgensen and A. Krishnan, *Phys. Stat. Sol. (a)* **176**, 439 (1999).
11. D. Martin, J. F. Carlin, V. Wagner, H. J. Buehlmann, and M. Illegems, *Phys. Stat. Sol. (b)* (2002) (in press).
12. V. Ban, *J. Electrochem. Soc.* **119**, 761 (1972).
13. S.S. Liu and D.A. Stevenson, *J. Electrochem. Soc.* **125**, 1161 (1978).
14. S.Yu. Karpov, Yu.N. Makarov, and M.S. Ramm, *Internet J. Nitride Semicond. Res.* **2**, 45 (1997).
15. S.Yu. Karpov, V.G. Prokofyev, E.V. Yakovlev, R.A. Talalaev, and Yu.N. Makarov, *Internet J. Nitride Semicond. Res.* **4**, 4 (1999).
16. N. Grandjean, J. Massies, F. Semond, S.Yu. Karpov, and R.A. Talalaev, *Appl. Phys. Lett.* **74**, 1854 (1999).
17. I.N. Przhivalskii, S.Yu. Karpov, and Yu.N. Makarov, *Internet J. Nitride Semicond. Res.* **3**, 30 (1998).

BEST AVAILABLE COPY

### Lattice constant variation in GaN:Si layers grown by HVPE

A. Usikov, O.V. Kovalenkov, M.M. Mastro, D.V. Tsvetkov, A.I. Pechnikov, V.A. Soukhoveev, Y.V. Shapovalova, G.H. Gainer  
Technologies and Devices International, Inc., 12214 Plum Orchard Dr.,  
Silver Spring, MD 20904, USA

#### ABSTRACT

The structural, optical, and electrical properties of HVPE-grown GaN-on-sapphire templates were studied. The  $c$  and  $a$  lattice constants of the GaN layers were measured by x-ray diffraction. It was observed that the  $c$  and  $a$  lattice constants vary non-monotonically with Si-doping. The proper selection of Si-doping level and growth conditions resulted in controllable strain relaxation, and thus, influenced defect formation in GaN-on-sapphire templates. It was also observed that HVPE homoepitaxial GaN layers grown on the templates have better crystal quality and surface morphology than the initial templates.

#### INTRODUCTION

One of the challenges remaining in the epitaxial growth of III-N materials is the absence of a suitable lattice-matched substrate. Currently, sapphire and SiC substrates are widely used in nitride-based technology [1,2]. Device quality III-nitride materials are commonly grown on sapphire by metal organic chemical vapor deposition (MOCVD). Blue, green and white light emitting diodes (LEDs), violet laser diodes (LDs), field effect transistors, and ultraviolet photodiodes have been developed. These structures, however, suffer from a high density of threading dislocations and strain-induced problems that strongly affect device performance. GaN grown on sapphire with a low temperature nucleation layer still has a dislocation density as high as  $10^9$  to  $10^{10}$  cm<sup>-2</sup>. These dislocations are a major cause of device degradation, particularly for LDs, which operate at high current density [3].

Due its high growth rate and high material quality, hydride vapor phase epitaxy (HVPE) is the method of choice for fabricating GaN quasi-bulk material and GaN templates for use as substrates for III-N device structure growth.

The homoepitaxial growth of GaN-based device structures on GaN templates can improve the crystal quality, and thus, device performance. Other benefits of GaN and AlGaN templates are reduced growth time and precursor consumption, reduced downtime and maintenance, and increased productivity of the MOCVD reactors. The purpose of this work is to study the optical and structural properties of HVPE-grown GaN-on-sapphire templates and HVPE GaN layers grown homoepitaxially on the templates. The influence of Si-doping on the structural properties of GaN templates was also studied. This is important because structural defects can penetrate from the template to the upper growth structure.

#### EXPERIMENTAL DETAILS

Details of the HVPE technique for fabricating GaN-on-sapphire templates were previously reported [4]. The GaN-on-sapphire templates consist of a 2.5 to 30  $\mu$ m-thick GaN layer grown on c-plane 2" diameter sapphire substrates at 1000 to 1100 °C at atmospheric pressure. The flow

rates of GaCl and ammonia were controlled to establish a growth rate of 20 to 30  $\mu\text{m/h}$ . A silane mixture consisting of 50 ppm silane in argon was used for n-type doping. As measured by a mercury probe on satellite wafers, the  $\text{N}_\text{d}-\text{N}_\text{a}$  concentration varied from  $3 \times 10^{16} \text{ cm}^{-3}$  to  $3 \times 10^{18} \text{ cm}^{-3}$  for different templates. All samples were crack-free.

Template structural properties were studied with a Rigaku ATX-E x-ray diffractometer. Lattice constant measurements were performed in a double crystal geometry using the Bond method with an accuracy of  $\pm 0.0001 \text{ \AA}$ . Lattice constant  $c$  was measured using the symmetric refl. (00.6), and the constant  $a$  was evaluated using the asymmetric refl. (20.5).

Optical, structural and electrical properties of the templates were also studied by means of SEM, photoluminescence (PL) and C-V mercury probe. An optical microscope was used for surface morphology evaluation.

Homoeptaxial GaN layers with a thickness of 0.1 to 1.7  $\mu\text{m}$  were grown in a standard HVPE growth system on GaN-on-sapphire templates. After loading the template into the reactor, the procedure for homoeptaxial HVPE growth included two steps. The first step was template surface cleaning inside HVPE growth machine and second was the homoeptaxial growth step.

## RESULTS AND DISCUSSION

It was observed for thick GaN films grown by HVPE that most of the strain relaxation occurs within the first five microns of growth [5]. The remainder of the GaN has a nearly constant strain. During MBE growth, it was observed that Si incorporation disturbs the GaN layer stoichiometry and decreases the  $c$  lattice constant [6].

Figure 1 shows the full width at half maximum (FWHM) of the X-ray rocking curve ( $\omega$ -scan, (00.2) reflection) as a function of the GaN thickness and the Si-doping level. The FWHM is a figure of merit for crystal quality. The template structural quality improves with increasing layer thickness and decreasing Si doping. A hyperbola-like dependence is seen in Figure 1. For GaN

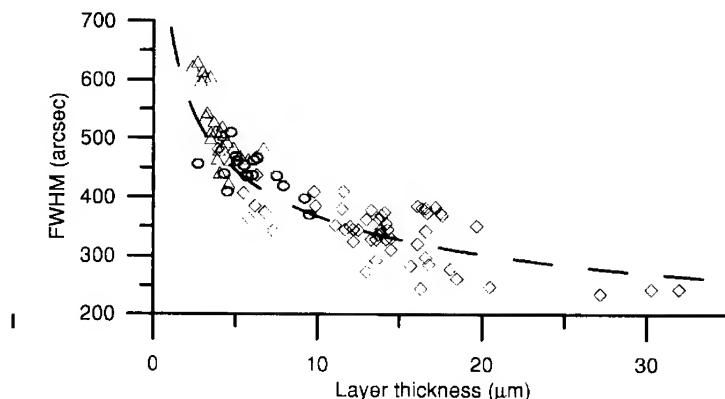


**Figure 1.** Variation of the FWHM of the x-ray (00.2) reflection with GaN layer thickness for no Si-doping (◇), and Si-doping with a silane mixture flow of 350 sccm (Δ) and 150 sccm (○). The dotted line is a guide for the eye.

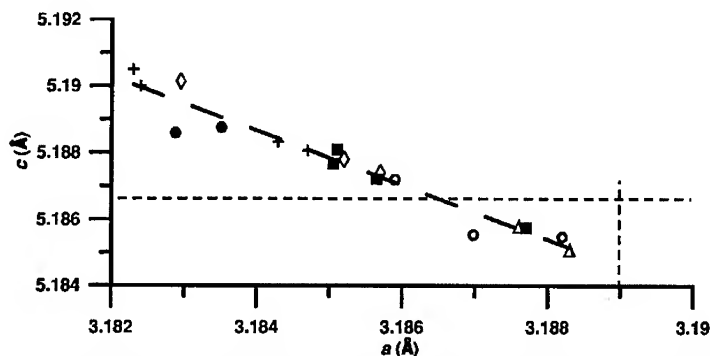
BEST AVAILABLE COPY

layers in the range from 4  $\mu\text{m}$  to than 6 or thinner, small changes in layer thickness (due to unexpected variation in growth conditions, for example) result in noticeable variation of  $\omega$ -scan FWHM. This leads to non-reproducibility and scatter of structural properties of the grown layers. Also, template bending for GaN layers thicker than 10  $\mu\text{m}$  influences the reliability of XRD data. For all other measurement conditions being the same (slit width, reflection used, measurement point etc.), the bending can effectively increase the sample region where x-ray diffraction takes place, leading to variations in rocking curve parameters. This explains the data scatter in Figure 1 beyond normal error due to instability in growth conditions, particularly for layer thickness greater than 10  $\mu\text{m}$ .

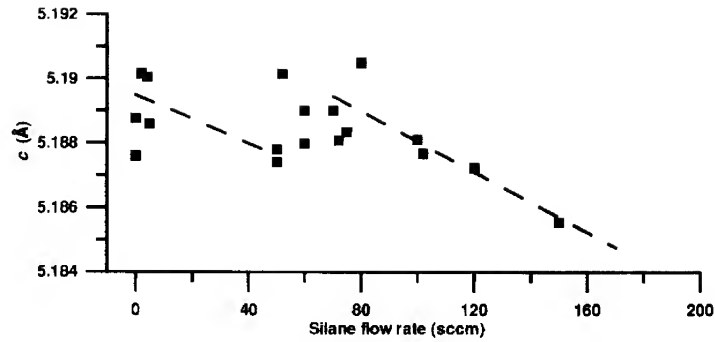
The critical thickness for crack formation is reduced from 30  $\mu\text{m}$  for undoped GaN to 2 to 4  $\mu\text{m}$  for heavily Si-doped GaN with a  $N_D-N_A$  concentration higher than  $3 \times 10^{18} \text{ cm}^{-3}$ . This is due to the influence of Si doping level on strain in HVPE-grown GaN layers. To clarify the influence Si-doping,  $c$  and  $a$  lattice constants were measured in GaN layers with a thickness in the range from 2 to 7  $\mu\text{m}$ . No noticeable relation between lattice constants and total layer thickness was observed.

Figure 2 shows the relation between the  $c$  and  $a$  lattice constants for both undoped and doped GaN layers. Experimental data agrees well with a linear approximation. Moreover, it was found that the  $c/a$  ratio deviates little from the average value of 1.629. This is indicative that these layers have a volume conserving distortion of the unit cell and is mainly under biaxial compressive stress. Some scatter, however, was found in the experimental data as can be observed in Figure 2. It was more pronounced for undoped GaN layers with larger  $c$ - and lower  $a$ - parameters. These deviations can be attributed to the presence of a hydrostatic stress component in the form of point defects (for undoped GaN layers) and dopant (for Si-doped GaN layers). The dashed-line in Figure 2 denotes the  $c$  lattice constant for bulk GaN (typically,  $c=5.1864 \text{ \AA}$  and  $a=3.189 \text{ \AA}$ ) [7]. It is seen that biaxial stress can reverse sign in heavily Si doped GaN layers ( $N_D-N_A > 6 \times 10^{17} \text{ cm}^{-3}$ ). This fact can explain the low critical thickness for crack formation in Si-doped layers.

The relationship for  $c$  lattice constant to silane mixture flow is given in Figure 3. A non-monotonic or kink-like behavior is seen. As in Figure 2, noticeable scattering of experimental data is observed for undoped and lightly Si doped GaN layers. Si doping decreases the  $c$  parameter and increases the  $a$  parameter. At silane mixture flow greater than 100 sccm



**Figure 2.** Relation between  $a$  and  $c$  lattice constants. Dotted line is linear fit. Dashed lines intersection point corresponds to the  $c$  and  $a$  parameters for bulk GaN [7]. Silane mixture flow: ● - 0 sccm, ◇ - 50 sccm, + - 75 sccm, ■ - 100 sccm, ○ - 160 sccm, △ - 300 sccm.



**Figure 3.** Variation of  $c$  lattice constant with doping level of Si-doped GaN layers. Dotted lines are linear fits in the range of silane flow from 0 to 50 sccm and from 70 to 170 sccm.

( $N_D - N_A \sim 6 \times 10^{17} \text{ cm}^{-3}$ ), the  $c$  parameter is less than bulk material indicating a change in the sign of the stress. Proper selection of Si-doping concentration and growth conditions is useful for strain engineering and defect minimization in GaN:Si templates.

Based on results in Figures 1, 2 and 3, it is concluded that the optimal thickness of crack-free GaN on sapphire template in terms of reliability and reproducibility in structural properties lies in the range from 5 to 10  $\mu\text{m}$ . By proper selection of initial growth conditions, this range can be expanded toward larger thickness. To grow heavily Si doped GaN layers on sapphire substrates with improved structural properties, one can combine a thick undoped GaN layer with a thinner GaN cap layer doped with Si.

Figure 4 shows typical PL spectra measured for a GaN-on-sapphire template. The PL spectrum contains two peaks in the 360 to 380 nm wavelength range. A peak at approximately

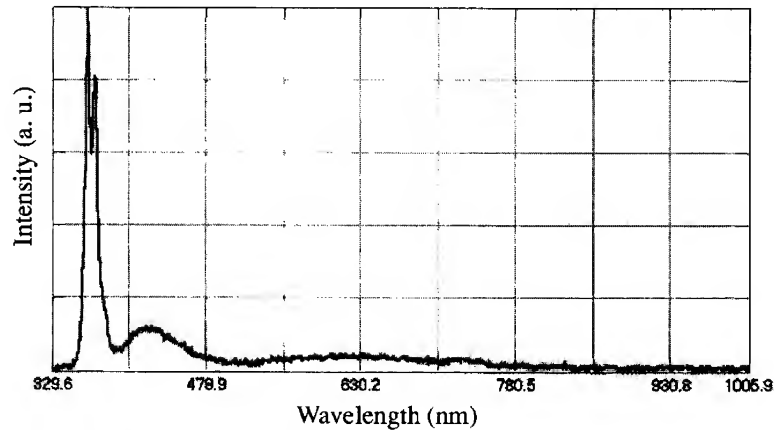


**Figure 4.** PL spectrum of Si-doped GaN-on-sapphire template at 300 K.  $N_D - N_A \sim 3 \times 10^{17} \text{ cm}^{-3}$ .

364 nm corresponds to neutral-donor-bound exciton recombination (the FWHM for this peak is 50 to 56 meV at 300 K), whereas the peak approximately 371 nm can be attributed to Si-donor bound-exciton transitions. Depending on the doping level, the intensity of this peak varies. For heavily doped templates ( $N_D - N_A \sim (1.8-2) \times 10^{18} \text{ cm}^{-3}$ ), this transition with a FWHM of approximately 83 meV became dominant over the near-band edge emission. Si-doped templates do not exhibit noticeable yellow defect luminescence but they do show a weak blue defect band at 420 to 430 nm.

Hexagonal-pyramids with dimensions in the tens of microns are clearly observed by optical microscopy on the surface of moderately Si-doped templates ( $N_D - N_A \sim 3 \times 10^{17} \text{ cm}^{-3}$ ). These growth features become noticeably smaller in size for heavily doped templates ( $N_D - N_A > 1.8 \times 10^{18} \text{ cm}^{-3}$ ).

A similar tendency was observed for GaN homoepitaxy by HVPE on GaN templates. Growth on heavily doped templates resulted in hexagonal-pyramids on the surface of the GaN homoepitaxial layer similar to that observed on the undoped template surface. Growth on moderately doped templates resulted in a homoepitaxial GaN undoped layer with less dense but larger size hexagonal-pyramids. In general, a 1 to 3  $\mu\text{m}$  thick undoped HVPE homoepitaxial layer improves the morphology of the template. In some cases, however, large size morphological defects were still observed on the homoepitaxial layer surfaces. The nature of these defects and mechanism of their formation are still unclear.

PL spectra of undoped homoepitaxial layers are similar to that of undoped GaN templates. In addition to the intensive exciton-related near band-edge emission at approximately 364 nm (the FWHM is approximately 43 meV at 300 K) and Si-related emission at approximately 370 nm, a wide yellow band with a peak at 630 to 650 nm is seen in the PL spectrum. This yellow band was not observed in the PL spectra of a doped GaN:Si templates layer.

Figure 5 shows comparative results of the x-ray rocking curve FWHM for GaN templates and GaN homoepitaxial layers grown on templates. It was observed that the FWHM values for homoepitaxial structures of a certain total thickness are narrower than the FWHM values measured for GaN layers with the same thickness grown in a single epitaxial run. This implies that the HVPE homoepitaxial process improves the structure crystal quality of grown GaN.

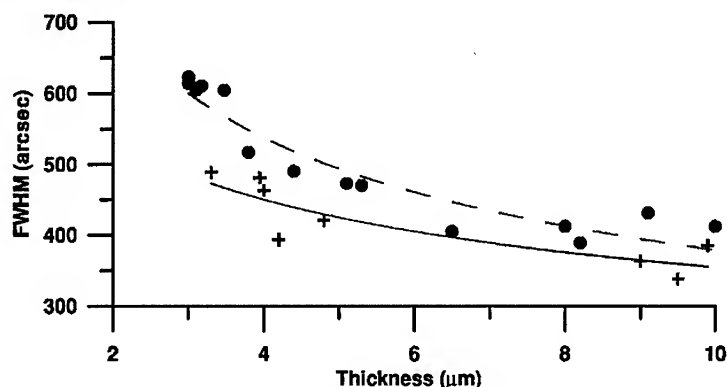


Figure 5. Variation of FWHM of the (00.2) reflection with total GaN thickness for: (●) GaN-on-sapphire templates; (+) homoepitaxial GaN layer grown on template. Dotted and solid lines are guided for eye.

However, defect formation and material contamination during GaN homoepitaxial growth must be further investigated.

## CONCLUSIONS

In this work, X-ray diffraction studies revealed that  $c$ - and  $a$ - lattice constants in GaN layers vary non-monotonically with Si-doping. In heavily Si doped GaN layers ( $N_D - N_A > 6 \times 10^{17} \text{ cm}^{-3}$ ) biaxial stress can reverse sign.

Optimal thickness of a crack-free GaN-on-sapphire template in terms of reliability and reproducibility in structural properties lies in the range from 5 to 10  $\mu\text{m}$ . By proper selection of the initial growth conditions, this range can be extended toward larger thickness.

HVPE homoepitaxial growth of undoped GaN layers on GaN-on-sapphire templates improves the structural crystal quality and surface morphology. To grow heavily Si-doped GaN layers on sapphire substrates with improved structural properties, a thick undoped GaN layer can be combined with the thin GaN cap layer doped with Si.

## ACKNOWLEDGMENTS

The authors would like to thank Dr. Yuriy Melnik for his valuable comments. This work at TDI was supported by the MDA and monitored through the ONR by contract monitor Colin Wood.

## REFERENCES

1. T.W. Weeks, Jr. M.D. Bremser, K.S. Ailey, E. Carlson, W.G. Perry, R.F. Davides, *Appl. Phys. Lett.*, **67**, 401 (1995).
2. S. Nakamura, M. Senoh, S. Nagahama, N. Iwasa, T. Yamada, T. Matsushita, H. Kiyoku, Y. Sugimoto, T. Kozaki, H. Umemoto, M. Sano, and K. Chocho, *Jpn. J. Appl. Phys.*, **36**, L1568 (1997).
3. T. Tojyo, T. Asano, K. Yanashima, M. Takeya, T. Hino, S. Kijuima, S. Ikeda, *IPAP Conf. Series 1*, Proc. Int. Workshop on Nitride Semiconductors, Nagoya, 878 (2000).
4. Yu. Melnik, D. Tsvetkov, A. Davydov, A. Shapiro, O. Kovalenkov, J.B. Lam, J.J. Song and V. Dmitriev, *Phys. Stat. Sol. (a)*, **188**, 429 (2001).
5. E. Valcheva, T. Paskova, P.O.A. Persson, L. Hultman and B. Monemar, *Appl. Phys. Lett.*, **80**, 1550 (2002).
6. G.S. Sudhir, Y. Peyrot, J. Kruger, Y. Kim, R. Klockenbrink, C. Kisilewski, M.D. Rubin and E.R. Weber, W. Kriegseis and B.K. Meyer, *Nitride Semiconductors*, ed. F.A. Ponce, S.P. DenBaars, B.K. Meyer, S. Nakamura, S. Strite, Mater. Res. Soc. Proc. **482**, 525 (1998).
7. M. Leszczynski, H. Teisseyre, T. Suski, I. Gregory, M. Bockowski, J. Jun, S. Porowski, K. Pakula, J. M. Baranowski, C. T. Foxon, T.S. Cheng, *Appl. Phys. Lett.* **69**, 73 (1996).

### Theoretical analysis of $\langle 0001 \rangle$ tilt grain boundaries in GaN at the atomic scale

Jun Chen<sup>1</sup>, Pierre Ruterana and Gérard Nouet

Laboratoire d'Etude et de Recherche sur les Matériaux, FRE 2149 CNRS, Institut des Sciences de la Matière et du Rayonnement, 6 Boulevard du Maréchal Juin, 14050 Caen Cedex, France.

<sup>1</sup>Laboratoire Universitaire de Recherche Scientifique d'Alençon, Institut Universitaire de Technologie, 61250 Damigny, France.

#### ABSTRACT

Epitaxial layers of GaN contain a very high density of threading dislocations. In the first stage of growth they may form low and high angle grain boundaries. Energetic calculations of  $\langle 0001 \rangle$  tilt grain boundaries have been performed with the Stillinger-Weber potential modified to take into account the wrong bonds Ga-Ga and N-N. The variation of the energy has been calculated as a function of the rotation angle. Two minima exist with special atomic structures based on a limited number of structural units. They are used to describe the other misorientations in terms of dislocation cores.

#### INTRODUCTION

The III-V nitride semiconductors have known a very fast evolution for the last decade with the fabrication of LED's and LDs [1]. These semiconductors, GaN, AlN and InN are characterised by direct band gaps ranging from less than 1.0 eV for InN, to 6.2 eV for AlN. They are highly promising in devices active from infrared to the ultraviolet range. They are grown by heteroepitaxy due to the lack of suitable bulk crystals for substrates. The layers contain large densities of threading dislocations which can reach  $10^{10} \text{ cm}^{-2}$ . Other crystallographic defects such as prismatic stacking faults, inversion domain boundaries, nanopipes are also present. The origin of this very high density of threading dislocations is connected to the growth process resulting in a mosaic structure of slightly misoriented grains [2]. Thus, low-angle and high-angle grain boundaries may form and their atomic structures have been analysed by high resolution transmission electron microscopy (HREM) [3]. Energetic calculations have been performed on special grain boundaries described in terms of the coincidence site lattice concept [4]. In the case of wurtzite structure, high resolution electron microscopy analysis of special grain boundaries was performed in zinc oxide [5] and gallium nitride [3]. It was shown that the atomic structure of  $\langle 0001 \rangle$  tilt grain boundaries in gallium nitride is based on periodic structure involving different cores of the  $1/3\langle 11\bar{2}0 \rangle$  edge dislocations. Atomistic simulation of these dislocation cores [6,7] and of some coincidence grain boundaries was undertaken to determine their relative stability [8,9]. The aim of this study is the systematic calculation of the energy of  $\langle 0001 \rangle$  tilt grain boundaries in the  $0^\circ$ - $60^\circ$  range.

## INTERATOMIC POTENTIAL

The energetic calculations in nitride semiconductors dealt with the core structure of edge and screw threading dislocations by using ab initio local- density functional cluster method or a density functional based on tight binding method [10,11] and density-functional-pseudopotential approach for stacking faults [12,13]. These methods give very precise and reliable results but they use cells containing less than one hundred atoms, which is not enough to analyse extended defects such as grain boundaries. For the later, cells containing a large number of atoms, 500 to 6000, are necessary due to the length of the period of the coincidence cell unit, and empirical potentials are still the most appropriate.

The treatment of compound semiconductors rises the problem of the wrong bonds, which form in the crystallographic defects. Among available empirical potentials used to calculate the potential energy of defects and grain boundaries in semiconductors [14-17], the Stillinger-Weber [16] and Tersoff [17] potentials accept any atomic surrounding. We have defined a new parameterisation of the Stillinger-Weber potential in order to allow a complete calculation of any atomic configuration, dangling bonds, wrong bonds and excess bonds [18]. The optimisation of the parameters was carried out for the Ga-N bonds on the elastic constants to fit with the experimental data obtained by Polian et al [19]. For the wrong bonds, the interaction parameters were obtained after fitting with the ab initio calculation of inversion domain boundaries (IDB) involving wrong bonds, Holt model [20]. The final set is reported in table1[18].

Table 1: Parameters of Stillinger –Weber potential adapted to GaN

Parameters	Ga-N	Ga-Ga	N-N
$\epsilon(\text{eV})$	2.17	0.665	0.665
$\sigma(\text{nm})$	0.1695	0.2038	0.1302
$\lambda$	32.5	26.76	26.76
A	7.917		
B	0.720		
a	1.8		

In fact, three sets are used according to the type of bonds. In these conditions, the values obtained with the Stillinger-Weber potential are acceptable by comparison with those deduced from ab initio calculation (table 2).

Table 2: Energy values ( mJ/m<sup>2</sup> )

	Ab initio [21]	This work
IDB with wrong bonds	2663	2361
IDB without wrong bonds	400	567

Although the capacities of empirical potentials are limited, it was previously shown that the hierarchy and understanding of the energy behaviour for grain boundaries versus the rotation angle are correct [22]. The relaxation was performed with the Verlet molecular dynamic scheme [23] and the energy was calculated as an excess of energy with respect to the energy of the bulk crystal and by subtracting the energy of each bond in the perfect crystal. Each super-cell contains two identical grain boundaries and the periodic condition is applied in the three directions. The size of the cells varies from 416 atoms to more than 5500 atoms.

## COINCIDENCE GRAIN BOUNDARIES

Two adjacent grains may be described by a geometrical transformation such as a rotation. For specific values, common site lattices (CSL) are formed. They are characterised by an index  $\Sigma$  corresponding to the ratio of the unit cells of the crystal and CSL. Knowing the orientation relationship describing two adjacent grains, the dichromatic complex may be drawn [24]. For the wurtzite structure, the space group is  $P6_3mc$  and the space group of the dichromatic complexes corresponding to coincidence orientations around [0001] is  $P6_3m'c'$ . The final step of the construction of the bicrystal consists in introducing the boundary plane in the dichromatic complex before deleting one half of each crystal. The introduction of the boundary plane needs some care because the wurtzite structure exhibits corrugated planes that have two spacings, the interface can thus be located in the shuffle  $a$ , glide position  $b$ , or a combination of both. Therefore, three atomic configurations must be built:  $a/a$ ,  $b/b$  and  $a/b$  [25].

The lowest energy configuration was calculated by considering the  $\gamma$  surface taking into account the translations parallel and normal to the grain boundary plane [26]. These translations are limited to the Wigner-Seitz cell of the Displacement Shift Lattice equivalent to the cell of non-identical displacements [27]. The translations were carried out along  $Ox$ , in the boundary plane and along  $Oz$ , parallel to [0001]. The steps were  $0.1a_0$ ,  $a_0 = 0.318$  nm and  $0.1c$ ,  $c = 0.519$  nm, respectively. In the third direction,  $Oy$  normal to the boundary plane, the configuration is relaxed.

## RESULTS

### Atomic configuration of the grain boundaries

In the range,  $0^\circ < \Theta < 21^\circ 79'$ , six coincidence grain boundaries have been analysed. All of them from  $\Sigma = 91$  ( $\Theta = 6.01^\circ$ ) to  $\Sigma = 19$  ( $\Theta = 13.17^\circ$ ), except  $\Sigma = 7$ , may be regarded as low-angle grain boundaries formed by the introduction of one 57 core of the edge dislocation  $1/3[11\bar{2}0]$  or  $a_1$ . The next coincidence orientation,  $\Sigma = 49$  ( $\Theta = 16.43^\circ$ ), needs two edge dislocations per period, 57576, thus the Burgers vector of this period is  $b = 2a_1$  instead of  $b = a_1$  for the previous  $\Sigma$ s. For  $\Sigma = 7$ , the grain boundary is built up with the same 57 atom ring. Its period is the shortest, 0.831 nm and the interaction between the cores due to their overlapping is expected. The result is that the energy of the grain boundary is no longer described by the

continuum elastic theory, its energy ( $E_p = 820 \text{ mJ/m}^2$ ) is lower than that of  $\Sigma = 49$ . If we consider that 6 is the basic structural unit for the perfect crystal and 57 that for  $\Sigma = 7$ , the intermediate coincidence grain boundaries may be described by a combination of these two basic units with the lowest energies, 0 and  $820 \text{ mJ/m}^2$ , respectively. These grain boundaries are symmetric with respect to the grain boundary plane.

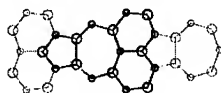


**Figure1.** Atomic configuration of  $\Sigma = 7$

Beyond  $\Sigma = 7$ ,  $21^\circ 79' < \Theta < 32^\circ 20'$ , we deal with a new configuration based on two classical 57 atom rings, one shifted with respect to the other by  $d_{hkl}$ , the reticular distance of the grain boundary plane, leading to a zig-zag configuration, (57/57). These grain boundaries are no more symmetric. The  $\Sigma = 79$  and 97 are a mixture of the previous core, 57, and of this new unit, (57/57). The Burgers vector is the same for both cores of this new unit, and thus its total Burgers vector is  $2a_1$ . The period contents are  $4a_1$  and  $5a_1$  for  $\Sigma = 79$  and 97, respectively. For the  $32.20^\circ$  tilt angle,  $\Sigma = 13$ , a second minima energy configuration appears,  $753 \text{ mJ/m}^2$ . It is only made by the new structural unit (57/57). If a  $c/2$  component is added a new configuration is obtained: (57<sup>+</sup>57<sup>-</sup>). The main difference with the previous one is the occurrence of Ga-Ga and N-N wrong bonds in the same  $c$  plane. Its energy is about the same:  $764 \text{ mJ/m}^2$ . Each atom ring, 57<sup>+</sup> and 57<sup>-</sup>, is characterized by a different Burgers vector,  $-a_1$  and  $a_2$ , which are not normal to the grain boundary plane, and the total Burgers vector is  $[01\bar{1}0]$  with magnitude  $a(3)^{1/2}$ . The Burgers vectors  $b$  of both units, (57/57) and (57<sup>+</sup>57<sup>-</sup>) are  $2a$  and  $a(3)^{1/2}$ , respectively. Since the length of the period is the same for the two descriptions,  $d = 0.1136 \text{ nm}$ , by using the equation  $2\sin(\Theta/2) = b/d$ ,  $b/d$  is equal to 0.561 and 0.486 whereas the first term is 0.480, thus the second atomic ring, (57<sup>+</sup>57<sup>-</sup>), fits best the rotation and may be used to describe  $\Sigma = 13$  (Figure 2).



**Figure 2.** Atomic configuration of  $\Sigma = 13$ : (57/57), left, and (57<sup>+</sup>57<sup>-</sup>), right.

The last range,  $32^\circ 20' < \Theta < 60^\circ$ , is characterized by the systematic introduction of the component  $\Delta z = 0.5$  which gives rise to the structural unit (57<sup>+</sup>57<sup>-</sup>). The next boundary,  $\Sigma = 67$ , is based on two units of  $\Sigma = 13$  plus one 6 atom ring, so the magnitude of the associated Burgers vector is still  $2a(3)^{1/2}$ . The other configurations up to  $60^\circ$  are described by the introduction of a variable number of 6 atom rings leading to configurations of the type: (57<sup>+</sup> x 6 57<sup>-</sup> y 6) with  $x$  and  $y$  in the range 1 – 3 depending on the  $\Sigma$  value. Since only one unit (57<sup>+</sup>57<sup>-</sup>) is involved for each  $\Sigma$ , all Burgers vectors are  $[10\bar{1}0]$  with the magnitude  $a(3)^{1/2}$ . These grain boundaries may be considered as low-angle grain boundaries with respect to  $\Sigma = 1$  ( $\Theta = 60^\circ$ ). The  $60^\circ$  rotation also needs the addition of the  $c/2$  component to restore the perfect crystal of the wurtzite structure which is connected to  $\Sigma = 1$  ( $\Theta = 60^\circ$ ) by a rotoinversion.

### Boundary energy

The variation of the energy as a function of the rotation angle presents two well-pronounced minima or energy cups corresponding to  $\Sigma = 7$  ( $\Theta = 21^\circ 78'$ ) and  $13$  ( $\Theta = 32^\circ 20'$ ) as shown in figure 3. For the angles close to  $0^\circ$  and  $60^\circ$  the continuum elasticity theory may be used to calculate the boundary energy. A good agreement is obtained in the ranges  $0^\circ$ - $18^\circ$  and  $42^\circ$ - $60^\circ$  which correspond to the formation of low-angle grain boundaries with respect to the perfect crystal,  $0^\circ$ , and to a perfect crystal after a rotation of  $60^\circ$ . The formation of energy cups corresponds to well-defined atomic structures of the grain boundaries with the shortest period.

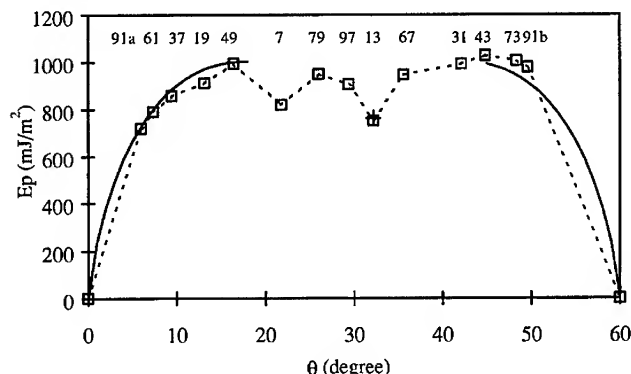


Figure 3. Variation of the energy as a function of the rotation angle.

In these cases, the atomic structure of the grain boundary is well ordered and its coherence is highest. The overlapping of the cores leads to the minimization of the dislocation strain fields.

### DISCUSSION AND CONCLUSION

Using an adapted Stillinger-Weber empirical potential, it is shown that the atomic structure of  $[0001]$  tilt grain boundaries can be described by a limited number of structural units corresponding to the core of  $1/3\langle 11\bar{2}0 \rangle$  edge dislocations. The reconstruction of the atomic structure of the grain boundaries was carried out by using the 57 configuration, in combination with the 6 atom ring of the hexagonal unit. Until  $\Sigma = 7$  ( $22^\circ 71'$ ), it is shown that linear combinations of the two atom cycles leads to stable configurations. Beyond  $\Sigma = 7$ , the configurations of minimum energy are shown to have a zigzag structure, with no translation along the  $c$  axis. In this case, the total Burgers vector of the CSL depends on the number of these structural units. The turning point is hit with  $\Sigma = 13$ . Above, the reconstruction of the boundaries needs the introduction of a  $c/2$  translation and two variants (57+ and 57-) are found to lead to minimum energy configurations. It is then shown that in wurtzite GaN, the potential energy of  $[0001]$  tilt grain boundaries exhibits a similar behavior that in cubic semiconductors [4] with two cups in energy for  $\Sigma = 7$  and 13. This is in contrast to

the results which were very recently reported following a rather similar procedure, in which no energy cups was found in particular for  $\Sigma = 7$ [28].

## ACKNOWLEDGMENTS

The authors acknowledge the support of the UE under contract HPRN-CT-2001-00297.

## REFERENCES

1. S. Nakamura, M. Senoh, N. Iwasa, S. Nagahama, *Jpn. J. Appl. Phys.* **34**, 1797 (1995)
2. X. J. Ning, F.R. Chien, P. Pirouz, J.W. Wang and M.A Khan, *J. Mater. Sci.* **3**, 580 (1996)
3. V. Potin, P. Ruterana, G. Nouet, R.C. Pond and H. Morkoç, *Phys. Rev. B* **61**, 5587 (2000)
4. M. Kohyama, Modelling Simul. *Mater. Sci. Eng.* **10**, R31 (2002)
5. F. Sarrazit, E.A. Stepanov, E. Olsson, T. Claeson, V.I. Bondarenko, R.C. Pond and N.A. Kiselev, *Philos. Mag.* **A76**, 633 (1997)
6. J. Chen, P. Ruterana and G. Nouet, *Mater. Sci. Eng.* **B82**, 117 (2001)
7. A. Béré and A. Serra, *Phys. Rev. B* **65**, 205323 (2002)
8. J. Chen, G. Nouet and P. Ruterana, *Phys. Stat. Sol. (b)* **228**, 411 (2001)
9. A. Béré and A. Serra, *Interf. Sci.* **9**, 149 (2001)
10. J. Elsner, R. Jones, P.K. Sitch, V.D. Porezag, M. Elstner, Th. Frauenheim, M.I. Heggie, S. Oberg, and P.R. Briddon, *Phys. Rev. Lett.* **79**, 3672 (1997)
11. A.F. Wright and U. Grossner, *Appl. Phys. Lett.* **73**, 2751 (1998)
12. C. Stampfl and C.G. Van de Walle, *Phys. Rev. B* **57**, R15 052 (1998)
13. J.A. Chislom and P.D. Bristowe, *J. Phys.: Condens. Matter* **11**, 5067 (1999)
14. P.N. Keating, *Phys. Rev.* **145**, 637 (1966),
15. G.A. Baraff, E.D. Kane and M. Schluter, *Phys. Rev. B* **21**, 5665 (1980)
16. F.H. Stillinger and T.A. Weber, *Phys. Rev. B* **31**, 5262 (1985),
17. J. Tersoff, *Phys. Rev. B* **37**, 6991 (1988); **B38**, 9902 (1988); **B39**, 5566 (1989); *Phys. Rev. Lett.*, **61**, 2879 (1988)
18. N. Aïchoune, V. Potin, P. Ruterana, A. Hairie, G. Nouet and E. Paumier, *Comput. Mater. Sci.* **17**, 380 (2000)
19. A. Polian, M. Grimsditch and J. Grzegory, *J. Appl. Phys.* **76**, 3343 (1996)
20. D.B. Holt, *J. Phys. Chem. Solids* **30**, 1297 (1969)
21. J.E. Northrup, J. Neugebauer and L.T. Romano, *Phys. Rev. Lett.* **77**, 103 (1996)
22. J.T. Wetzell, A.A. Levi, D.A. Smith, *Trans. Jpn. Inst. Met. Suppl.* **27**, 1060 (1986)
23. L. Verlet, *Phys. Rev.* **159**, 98 (1967)
24. R.C. Pond and D.S. Vlachavas, *Proc. Roy. Soc. London A* **386**, 95 (1983)
25. F. Oba, I. Tanaka, S.R. Nishitani, H. Adachi, B. Slater and D. H. Gay, *Philos. Mag.* **A 80**, 1567 (2000)
26. V. Vitek, *Crystal Lattice Defects*, **5**, 1 (1974)
27. V. Vitek, A.P. Sutton, D.A. Smith and R.C. Pond, *Grain Boundary Structure and Kinetics*, Ed. R.W. Balluffi, ASM, Metals Park, OH, 115 (1980)
28. A. Béré and A. Serra, *Phys. Rev. B* **66**, 085330 (2002)

### Screw Dislocations in MBE GaN Layers Grown on Top of HVPE Layers: Are They Different?

Z. Liliental-Weber, D. Zakharov, J. Jasinski, and J. Washburn, M.A. O'Keefe and H. Morkoc<sup>a</sup>  
Lawrence Berkeley National Laboratory, Berkeley, CA 94720 m/s 62/203

<sup>a</sup> Virginia Commonwealth University, Richmond, VA

#### ABSTRACT

Transmission Electron Microscopy was applied to study HVPE template and MBE overlayers in plan-view and cross-section. It was observed that screw dislocations in the HVPE layers are decorated by small voids arranged along the screw axis. However, no voids were observed along screw dislocations in MBE overlayers grown with excess Ga, despite the fact that Ga droplets were observed on the layer surface as well as imbedded in the layer. By applying a direct reconstruction of the phase and amplitude of the scattered electron wave from a focal series of high-resolution images, the core structures of screw dislocations in both materials have been studied and show that all screw dislocations have filled cores. Dislocation cores in MBE samples grown Ga-rich and N-rich show no substantial differences and no stoichiometric change compared to the matrix. However, in HVPE materials, single atomic columns show substantial differences in intensities and indicate the possibility of Ga presence. These Ga-rich cores might be responsible for the attraction impurities forming voids in their close vicinity.

#### INTRODUCTION

Epitaxial growth of (0001) GaN on Al<sub>2</sub>O<sub>3</sub> leads to high concentrations (typically 10<sup>9</sup>-10<sup>11</sup> cm<sup>-2</sup>) of threading edge, screw and mixed dislocations which propagate vertically from the GaN/Al<sub>2</sub>O<sub>3</sub> interface to the GaN surface [1-2]. Despite this high density of dislocations, a high emitting efficiency has been achieved for optical devices such as light-emitting diodes (LEDs) and laser diodes (LDs) [3]. This behavior may be contrasted with that of GaAs-based LDs where a value of dislocation density of about 10<sup>4</sup> cm<sup>-2</sup> is usually sufficient to prevent laser action [4]. The most common explanation for this phenomenon is that the threading dislocations in GaN do not have electronic states in the band gap. However, this is still a controversial issue, and there is no agreement on this subject between different scientific groups [5-8].

Density functional theoretical calculations [8] and early experimental work [4] suggested that threading dislocations in GaN are not non-radiative recombination centers. However, the increase in optical properties that is achieved [3] by reducing the threading dislocation density by use of the epitaxial lateral overgrowth method [9] provides circumstantial evidence that dislocations do have some deleterious effect. Atomic force microscopy (AFM) combined with cathodoluminescence (CL) [10], and plan-view transmission electron microscopy (TEM) combined with CL [11], clearly show threading dislocations to be related to dark spots in band edge emission CL images. This effect is consistent with theoretical calculations suggesting that dislocations can be charged depending on doping and growth conditions [12].

Look and Sizelove [13] developed a model for charged dislocation scattering in GaN, and have applied it to temperature-dependent mobility and electron-concentration data for two samples grown by MBE, with low and high dislocation densities, respectively. The model fits the data very well over the full temperature range for both samples.

There are also discrepancies concerning the nature of dislocation cores in GaN. Some investigators claim that GaN dislocations have open cores [14], but the work of Arslan and Browning suggests that screw dislocations have full cores [15]. Our experimental observations show that other void-type defects exist in GaN: nanotubes and pinholes [16-17]. The density of these defects was estimated to be in the range of  $10^5$  -  $10^7$  cm<sup>-2</sup> and their radii in the range 3–1500 nm. We suggested [16-17] that these two types of defects are related to the impurity presence in the material, supporting theoretical work by Elsner et al [6], who showed that O and O-related defect complexes can be formed on the walls of nanopipes in GaN. Cherns [18] suggested that nanopipes form under non-equilibrium conditions and are influenced by growth factors.

Scanning current-voltage microscopy (SIVM) studies showed leakage spots at screw/mixed dislocations but not at pure edge dislocations. The authors [19] concluded that the reverse bias current in GaN was carried by dislocations with a screw component, with Ga accumulated at or near screw dislocations and that Ga affects the dislocation electrical activity. These experimental studies were in agreement with the work of Northrup [20,21], indicating the Ga-filled screw dislocation core to be stable in Ga-rich growth conditions using first-principles total energy calculations. The aim of this work was to find if screw dislocations have full or empty core and determine the core stoichiometry in the case of full core.

## EXPERIMENTAL

Two sets of samples were grown by two different growth methods: Hydride Vapor Phase Epitaxy (HVPE) and Molecular Beam Epitaxy (MBE). MBE samples were grown using Ga rich and N rich conditions, as in earlier experiments [19]. Transmission Electron Microscopy (TEM) has been applied to study these layers in electron-transparent samples in plan-view and cross-section. Determination of dislocation core structure from plan-view samples was carried out using a modified 300keV field emission Philips electron microscope (OAM) to obtain high resolution focal series with a constant defocus step. The electron exit wave from the crystal structure was obtained by numerical reconstruction [22] from the full focal series of 20 images.

## RESULTS AND DISCUSSION

Samples grown by two different growth methods (HVPE and MBE) were studied in cross-section. Under  $g \cdot b = 0$  diffraction conditions, for which screw dislocations are out of contrast, small voids along dislocation lines were observed for HVPE grown samples (Fig. 1a,b). These voids were not observed for edge dislocations in the same material and not at all in the MBE (Figs. 1c,d) or MOCVD (Fig. 1e,f) overlayer samples grown on top of the HVPE template.

In order to obtain information about dislocation core structures, observations were performed in plan-view configuration. No displacement vector can be observed around screw dislocations in plan-view configuration; this result is expected for screw dislocations since the displacement vector is along the c-axis. (Fig.2a,b) shows that indeed this applies for dislocations in both HVPE and MBE samples. When a high-resolution image is taken at Scherzer defocus, it can be seen that only part of the image has an on-axis orientation (Fig.-2a-right hand side). The remaining part of the image has some tilt, which is caused by the tilted lattice planes surrounding the screw dislocation. This tilt makes this study experimentally very demanding.

BEST AVAILABLE COPY

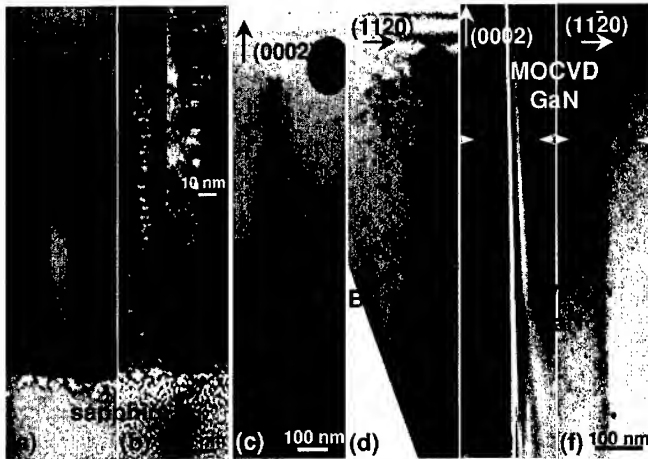


Fig. 1. Cross-section images show screw dislocations in HVPE-grown material; (a)-dislocation in contrast for  $g=(0002)$  and (b)-out of contrast for  $g=(1120)$ . Note voids stacked vertically. The inset in (b) shows that voids with pyramidal shape can have their tips slightly shifted from the dislocation line. (c,d) Screw dislocations in the MBE overlayer sample grown on top of the HVPE material. Note lack of voids and the dark spot representing a Ga droplet imbedded in the layer. (e,f) Area near the interface between HVPE template and the MOCVD overlayer. Note voids along screw dislocation in the HVPE material and lack of them in the MOCVD material.

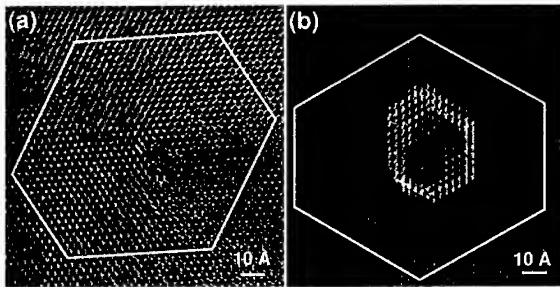


Fig. 2. Plan view images of screw dislocations in MBE (a) and HVPE (b) GaN. Burgers circuits have no displacement, as expected. Note tilted c-planes around dislocation in (a) and void in (b).

As expected from the cross-sectioned samples, voids are observed surrounding the dislocation in the HVPE sample. These voids have a hexagonal shape (lighter contrast in the central part of Fig. 2b). To obtain structural information at higher resolution, 20 micrographs were obtained from each screw dislocation at large values of defocus and the complex electron wave reconstructed numerically [22]. An image of the phase of the exit-surface wave gives information on the distribution of atomic columns. Usually additional micrographs were taken at Scherzer defocus before the series of 20 images and after, to check on image drift during this long exposure time. Only low-drift images were further interpreted.

We looked for missing atomic columns expected for the empty core model (Fig. 3a) and for changes in intensity of particular columns to indicate the possibility of a nonstoichiometric core. Calculations show that atomic column intensity can change with specimen tilt and stoichiometry. For the perfectly aligned stoichiometric sample, each atomic column has the same intensity and the pattern has six-fold symmetry. Small specimen tilts (4 milliradian) can change the relative intensity of two adjacent atomic columns by up to 4%, but this can be easily detected since pattern symmetry then changes to two-fold. Larger tilts change the image pattern so drastically that they are easy to recognize visually without column intensity measurement.

Primary and diffracted beam intensities forming the image change with sample thickness as well as with stoichiometry. To avoid partially-reversed image contrast, sample thickness must be such that all contributing beams have the same sign of phase. This is particularly important where different dislocation core stoichiometry is considered. Calculations (not shown for lack of space) of images from the Ga-rich dislocation core model of Northrup [20,21] with no N atoms at the core (6:0 model), show the ranges of thickness within which the distinction between a stoichiometric and a Ga-rich core is clearly possible using our approach.

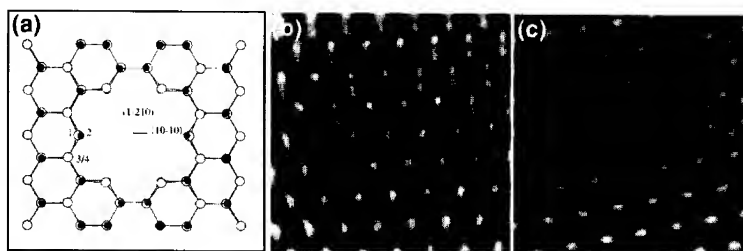


Fig. 3. (a) Model of open core screw dislocation (after Elsner et al [8]). (b) Full core of screw dislocation in Ga-rich MBE grown GaN and (c) in the N-rich GaN. Lack of difference in atomic column intensity between center image and surrounding matrix indicates stoichiometric cores.

The focal-series reconstruction technique described above was applied to Ga-rich MBE grown samples in [0001] projection where atomic columns are separated by  $1.84\text{\AA}$ . No change in intensity between atomic columns can be observed for the Ga rich or N rich samples (Fig. 3b and c), suggesting that dislocation cores studied in these samples were stoichiometric and also have full cores. This result is in agreement with early work [15].

Similar focal-series reconstructions were obtained for [0001] projections of screw dislocations accompanied by voids in HVPE samples (Fig. 4a). In the dislocation core area, one atomic column appears to be very weak (Fig. 4a- column circled in the upper-left corner) and another column very bright (Fig. 4a- column circled in the center). These columns are not adjacent to one other, but separated by  $8\text{\AA}$ , a distance comparable to that between a dislocation line and the tip of the pyramidal voids observed in cross-section samples. The intensities of the highest-intensity and lowest-intensity atomic columns lie more than three standard deviations from the mean atomic column peak intensity in the matrix (Fig. 4b). Therefore, the intensity difference between the highest-intensity and lowest-intensity atomic columns is about six standard deviations. The observed change in intensity between the highest-intensity and lowest-intensity atomic columns cannot be obtained simply by sample tilt, therefore this difference in their intensity can be assigned only to the stoichiometry of the particular columns. It also does

not appear that this large intensity fluctuation (6 standard deviations) could be an artifact of electron beam damage, since such fluctuations were not observed in the matrix or at the dislocation cores in the samples grown by MBE.

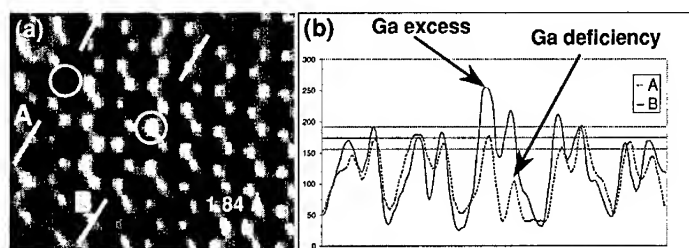


Fig. 4. (a) Image reconstruction of screw dislocation in HVPE sample. (b) Intensity profiles show reduced (A) and enhanced (B) image intensity, indicating Ga excess and deficiency.

Observation of all the atomic columns in the HVPE samples revealed that the screw dislocations in these samples are also full-core dislocations but they are decorated by voids. The column with the lowest intensity can be attributed to the tip of the void since the small sample thickness and possibility of the light atom presence would be expected, as suggested earlier [16]. The highest intensity column with the significant change of intensity could be assigned to the stoichiometry change and the excess of Ga atoms. Based on comparison with cross-section images it is clear that location of the tip of the void does not need to overlap with a dislocation line, but intensity difference with the surrounding matrix suggests that the dislocation core might have more Ga atoms as suggested by Northrup [21]. It is possible that not only strain at dislocation but also an excess of Ga within the core may attract the impurities (light elements) giving the reason for formation of voids close to the dislocation line.

## CONCLUSIONS

High-resolution reconstructions of the phase and amplitude of the complex electron exit wave scattered from HVPE and MBE grown sample were carried out using focal series consisting of 20 under-focused images. The reconstructed phase images showed that screw dislocations in GaN grown by these two methods are different. The main difference appears in the formation of voids with pyramidal shape stacked on top of each other along a dislocation line. These voids are never observed in MBE grown material even when MBE samples were grown directly on HVPE substrates. They were never observed along edge dislocations. All observed screw dislocations had full cores independent of the growth method. In MBE grown materials dislocation cores appear to be stoichiometric. However, in the HVPE grown material some high intensity columns were observed within the dislocation core. Based on the comparison with image calculations from model structures, it was concluded that Ga presence could be assigned to these atomic positions. Another column associated with the tip of the pyramidal void had very low intensity suggesting the possibility of the presence of light atoms and much lower sample thickness. It is speculated that Ga-rich atomic columns along screw dislocations can attract impurities present in the sample. From comparison between the samples grown by different methods it was clear that MBE method (and machine used for this growth) is much cleaner and not so many impurities are introduced in comparison with the HVPE grown samples.

## ACKNOWLEDGEMENT

Work supported by the U.S. Department of Energy under contract DE-AC03-76SF00098. The authors would like to express our gratitude to Dr. J. Northrup for sharing his models for screw dislocations with different stoichiometry; details will be published elsewhere. Use of the OAM facility at the National Center for Electron Microscopy at the LBNL is greatly appreciated.

## REFERENCES:

1. B. Heying, X. H. Wu, S. Keller, Y. Li, D. Kapolnek, B. P. Keller, S. P. DenBaars, and J. Speck, *Appl. Phys. Lett.* 68, 643 (1996).
2. F. A. Ponce, D. Cherns, W. T. Young, and J. W. Steeds, *Appl. Phys. Lett.* 69, 770 (1996).
3. S. Nakamura, M. Senoh, S. Nagahama, N. Iwasa, T. Yamada, T. Matsushita, H. Kiyoku, Y. Sugimoto, T. Kozaki, H. Umemoto, M. Sano, and K. Chocho, *Appl. Phys. Lett.* 72, 211 (1998).
4. S.D. Lester, F. A. Ponce, M.G. Craford, and D.A. Steigewald, *Appl. Phys. Lett.* 66, 1249 (1995).
5. A. F. Wright and J. Furthmuller, *Appl. Phys. Lett.* 72, 3467 (1998).
6. J. Elsner, R. Jones, M. I. Heggie, P. K. Stich, M. Haugk, Th. Frauenheim, S. Öberg, and P. R. Briddon, *Phys. Rev. B* 58, 12 571 (1998).
7. S. Keller, B. P. Keller, Y-F. Wu, B. Heying, D. Kapolnek, J. S. Speck, U. K. Mishra, and S. P. DenBaars, *Appl. Phys. Lett.* 68, 1525 (1996).
8. J. Elsner, R. Jones, P. K. Stich, V. D. Porezag, M. Elstner, Th. Frauenheim, M. I. Heggie, S. Öberg, and P. R. Briddon, *Phys. Rev. Lett.* 79, 3672 (1997).
9. O. Nam, M.D. Bremser, and R.F. Davis, *Appl. Phys. Lett.* 71, 2638 (1997).
10. S.J. Rosner, E.C. Carr, M. J. Ludowise, G. Giromali, and H.I. Erikson, *Appl. Phys.*, 70, 420 (1997).
11. T. Sugahara, H. Sato, M.S. Hao, Y. Naoi, S. Kurai, S. Tottori, K. Yamashita, K. Nishino, L.T. Romano, and S. Sakai, *Jpn. J. Appl. Phys* 37, L398 (1998).
12. A. F. Wright and U. Grossner, *Appl. Phys. Lett.* 73, 2751 (1998).
13. D.C. Look and J.R. Sizelowe, *Phys. Rev. Lett.* 82, 1237 (1999).
14. W. Qian, G. S. Rohrer, M. Skowronski, K. Doverspike, L. B. Rowland, and D. K. Gaskill, *Appl. Phys. Lett.* 67, 2284 (1995).
15. I. Arslan and N.D. Browning, *Phys. Rev. B* 65, 075310 (2002).
16. Z. Liliental-Weber, Y. Chen, S. Ruvimov, and J. Washburn, *Phys. Rev. Lett.* 79, 2835 (1997).
17. Z. Liliental-Weber, J. Washburn, K. Pakula, and J. Baranowski, *Microscopy and Microanalysis the J. Electr. Microsc. Soc. Am.* 3, 436 (1997).
18. D. Cherns, *J. Phys. Condens. Matter* 12, 10205 (2000).
19. J.W.P. Hsu, M.J. Manfra, S.N.G. Chu, C.H. Chen, L.N. Pfeiffer, and R.J. Molnar, *Appl. Phys. Lett.*, 78, 3980 (2001).
20. J.E. Northrup, *Appl. Phys. Lett.* 78, 2286 (2001).
21. J.E. Northrup, *Phys. Rev.B.* 66, 045204 (2002).
22. A. Thust, W.M.J. Coene, et al, *Ultramicroscopy* 64, 211, (1996).

# PHOTOREFLECTANCE PROBING OF BELOW GAP STATES IN GaN/AlGaN HIGH ELECTRON MOBILITY TRANSISTOR STRUCTURES

D.K. Gaskill, O.J. Glembocki, B. Peres\*, R. Henry, D. Koleske\*\*, and A. Wickenden\*\*\*  
Naval Research Laboratory, Washington, D.C. 20375

\* EMCORE, Somerset, NJ 08873

\*\* Sandia National Laboratories, Albuquerque, NM 87185-0601

\*\*\* Army Research Laboratory, Adelphi, MD 20783-1197

## ABSTRACT

Optical Impedance Spectroscopy of GaN/AlGaN high electron mobility transistor structures (HEMTs) using photoreflectance exhibit a photoreflectance lags – the component of the modulated reflectance out of phase with the chopper – ranging from 0.1 to 0.5. Photoreflectance was performed using below gap pumping on various samples. Samples that do exhibit appreciable photoreflectance lag for above gap pumping show significantly enhanced photoreflectance signals for below gap pumping. Yet, samples that do not exhibit appreciable photoreflectance lag for above gap pumping do not exhibit a signal for below gap pumping. This implies that the photoreflectance phase lag is due to mid-gap trap states. At least 2 types of traps are found, above and below about 2.5 eV. This result means that that photoreflectance can be used as a probe of HEMT device quality.

## INTRODUCTION

GaN and its alloys are of great interest for RF-based devices because of desirable electronic transport and thermal dissipation properties inherent to these material systems. [1] Currently, investigations have focused on devices made from high electron mobility transistors (HEMT). It has been found in this laboratory, and others that HEMT device performance is often associated with defects in the GaN and AlGaN layers. These defects may be due to a combination of factors such as substrate lattice mismatch, nucleation layer formation and growth parameters. For example, the commonly referred-to yellow band photoluminescence in GaN may be due to more than one type of defect and it has been demonstrated that the intensity of the yellow band can be controlled during the epitaxial layer synthesis.

In this paper, we use photoreflectance (PR) as an optical impedance spectroscopy to probe the material properties of GaN/AlGaN HEMT structures. The photoreflectance signal consists of two portions, that portion of the change in reflectance which is in-phase with the chopped pump light and the portion that is out-of-phase with the chopped pump. The out-of-phase portion contains information about how the sample responds to the pump light. [2] Sample doping geometry and electron barriers and traps all affect the out-of-phase portion of the PR signal.

## THEORETICAL CONSIDERATIONS

The photoreflectance technique has traditionally been used to study interband transitions in various semiconductors. The technique produces derivative like line shapes for transitions at various critical points in the Brillouin zone. The derivative nature of PR comes from the Franz-Keldysh effect, which results in the reflectivity and absorption of a material being dependent on an applied or built-in electric field. In general, the relationship between the electric field,  $F$ , its modulation (through a change in surface potential,  $\Delta V$ ) and the optical reflectivity,  $R$ , can be expressed in a simple manner:

$$\frac{\Delta R}{R} = \frac{1}{R} [R(F + \delta F) - R(F)] \approx \frac{1}{R} \frac{dR(F)}{dF} \frac{\partial F}{\partial V} \Delta V \quad (1)$$

In the case of photoreflectance, the surface potential modulation,  $\Delta V$ , is through a photovoltage,  $\Delta V_p$ . This shows that the intensity of measured PR signal will be directly proportional to the modulation of the electric field.

In addition, because the reflectivity is a function of band gap of the material being probed,  $E_g$ , the broadening parameter,  $\Gamma$ , and the photon energy,  $E$ , of the probe light, we can rewrite Eq. (1) in a more familiar form:

$$\frac{\Delta R}{R} = V_p(\Omega_m) AL(E, E_g, \Gamma) \quad (2)$$

where  $A$  is a constant,  $L$  is a spectral line shape function, which defines the observed spectral feature. In Eq. (2), we have assumed that the field or surface potential modulation is produced by a photovoltage,  $V_p(\Omega_m)$  that is induced by a monochromatic pump beam that illuminates the surface with frequency  $\Omega_m$ . The reflectivity which is measured by a second probe light and contains in it a component with frequency,  $\Omega_m$ , which is just the derivative-like photoreflectance signal of Eq.(2). As can be seen from Eq.(2), the intensity of this component is proportional to the photovoltage,  $V_p(\Omega_m)$ . Because  $V_p(\Omega_m)$  can have both in-phase and out-of-phase (often termed quadrature) components it will strongly depend on the presence of defects in the region where light is absorbed.

Consider the PR optical impedance spectroscopic investigation of an undoped layer between two doped layers of opposite sign. The reflectance is found to have an exponential rise and fall time with time constant consistent with the RC time constant of the layer structure. It can be shown that the ratio of the out-of-phase component to the in-phase components of the PR signal, called the photoreflectance lag, is directly related to the RC time constant by,

$$\text{PR Lag} = 2\pi\Omega_m\tau, \quad (3)$$

where  $\Omega_m$  is the frequency that the pump beam is chopped. [3] It is interpreted that the time constant,  $\tau$ , is the characteristic time of charge currents that arise in the sample to return it to equilibrium when the pump light is incident upon the sample and also then subsequently when it is turned off. The time responses of these currents are dominated by capacitive charging time of the depleted region.

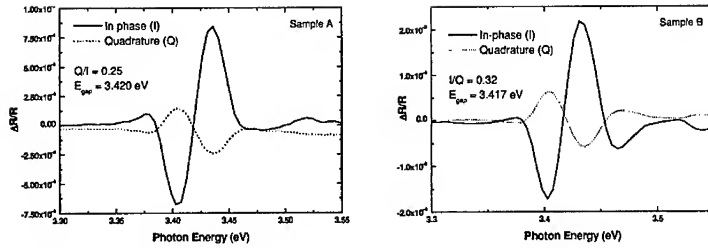


Figure 1 Photoreflectance spectra of HEMT samples A and B using 351 nm pump. Sample A has the photoreflectance lag of the two.

For the case of (electron) traps in a semiconductor structure the response of the sample is more complex. The photoreflectance lag will depend up the probability of electron trapping, that is the electron capture cross section, as well as the diffusion of holes to the physical location of the trap for recombination to take place. The characteristic time for this process is not, in general, a simple exponential. But the PR signal amplitude, proportional to the photovoltage, should be approximately proportional to the number of electrons trapped.

## EXPERIMENTAL DETAILS

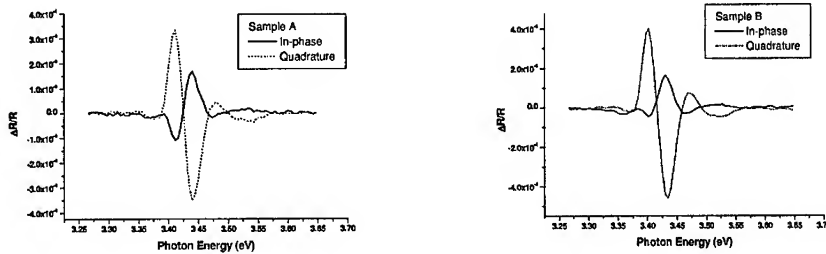


Figure 2 The photoreflectance spectra obtained from Samples A and B using 488.0 nm pump with intensity 72 mW.

The photoreflectance apparatus used has been described previously. [4] An Ar<sup>+</sup>-ion laser was used as the pump source having wavelengths of 351, 459.9, 476.5, 488.0, 501.7, and 514.5 nm. The laser power of the uv-line was about 5 mW and the powers of the other lines are noted in the text. A HeNe laser was also used for some measurements with emission at 632.8 nm with intensity of about 5 mW. The probe beam originated from a Xe arc lamp passed through a 0.25m SPEX spectrometer with 0.5 mm entrance and exit slits.

Samples were grown by organometallic vapor phase epitaxy on sapphire or 4H-SiC wafers. After the nucleation layer was deposited, an undoped, high resistivity GaN layer was grown with thickness 1-2  $\mu\text{m}$ . This was followed by a 100-200 Å AlGaIn layer having a nominal bandgap of 4 eV.

For the samples investigated, the photoreflectance lag was found to range from about 0.1 to 0.5. Figure 1 shows the PR signal near the fundamental gap for above gap pump illumination for two samples, A and B. Both samples have the same structure but were grown in different locations of a multi-wafer platter. Both samples exhibit a fundamental gap shifted about 20 meV above bulk values. The reasons for this shift are unclear at this time. Sample A and B exhibit a photoreflectance lag of 0.25 and 0.32, respectively. The difference in photoreflectance lag between the two samples is considered experimentally significant as repeated measurements of these samples indicate an experimental uncertainty is about 5%.

If the photoreflectance lag were due to mid-gap trapping states, PR performed using below gap pumping should yield a signal. Figure 2 shows the PR signal obtained from samples A and B where 488.0 nm pump light was used with intensity 72 mW. Note that the out-of-phase (quadrature) components of the spectra in Fig. 2 are very large compared to the in-phase components. The photoreflectance lags for A and B are 2.5 and 4.1, respectively. It is noted that samples having small ( $\sim 0.1$ ) photoreflectance lag under uv-pumping did not have a PR signal when below gap pump illumination was used. Figure 3 shows the PR intensity dependence as a function of 488.0 nm pump power for samples A and B. Note that sample B has the steeper slope than sample A.

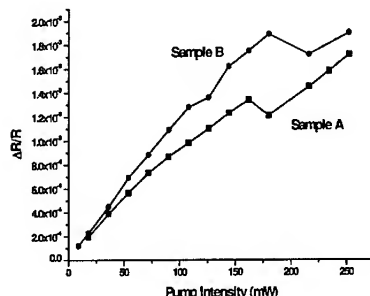


Figure 3 The photoreflectance intensity as a function of 488.0 nm pump intensity.

Figure 4 shows the photoreflectance lag for sample B for different pump photon energies where the pump intensity was held constant at 36 mW. Note that the photoreflectance lag abruptly changes from values near 3 to values above 4.5 above 2.55 eV.

The photoreflectance lag for sample B starts out at values near 3 for low pump intensities and becomes approximately constant and equal to 4.3 for 488.0 nm pump powers of ranging from 100 to 250 mW, as shown in Figure 5. But for sample A, the photoreflectance lag was found to be approximately constant at 2.3 for the same range of pump powers.

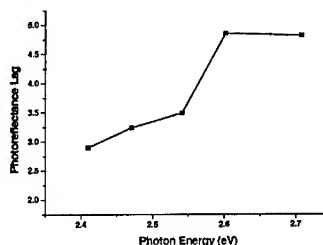


Figure 4 The photoreflectance lag for different pump photon energies.

## DISCUSSION

For sample B, the data in Figure 4 imply that at least two traps are present, above and below 2.55 eV, since the photoreflectance lag is significantly different for the two ranges of pump wavelength. The difference probably lies in

differing capture cross sections for the two traps. Sample A has the least number of traps since the PR intensity dependence on pump power has the shallowest slope as shown in Figure 3 and is dominated by the low energy trap. Sample B has a larger number of traps, as seen by both the higher slope in Figure 3 and that both high and low energy trap are present, as shown in Figure 4.

Klein *et al* using photoionization energy spectroscopy have previously observed two traps in GAN HEMT structures. [5] The two traps had absorption edge onsets of 1.8 and 2.85 eV. That work showed that trap concentrations were dependent upon growth conditions, suggesting that carbon impurities were responsible for the higher energy trap and that extended defects were responsible for the lower energy trap.

Since the photorefectance lag is a measure of the trap concentration in HEMT structures, this technique may find utility in non-destructively probing HEMT wafers before fabrication of device structures; to “weed out” potentially poor performing devices. Recently, we have observed a correlation between samples having large photorefectance lag using uv-pump illumination and gate lag in fabricated devices. Although additional work to investigate this correlation is needed, based upon the results presented herein, it is suggested that below gap pumping would be the most sensitive way of performing these measurements.

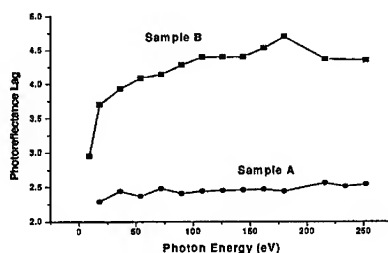


Figure 5 Photorelectance lag as a function of pump photon energy.

## ACKNOWLEDGEMENTS

The Office of Naval Research and DARPA supported this work.

## REFERENCES

- [1] S.J. Pearton, F. Ren, A.P. Zhang and K.P. Lee, *Mat.Sci.Eng.Rep* R30, 55(2000).
- [2] H. Shen and M. Dutta, *J. Appl. Phys.* 78, 2152 (1995).
- [3] D.K. Gaskill, R.T. Holm, and O.J. Glembocki, *Rev. Sci. Instrum.* 71, 1, (2000).
- [4] D.K. Gaskill, O.J. Glembocki, R.T. Holm, and A. Giordana, *J. Electron. Mater.* 28, 1424 (1999).
- [5] P.B. Klein, S.C. Binari, K. Ikossi, A.E. Wickenden, D.D. Koleske, and R.L. Henry, *Appl. Phys. Lett.*, 79, 3527 (2001).

### Compositional Fluctuations in $\text{Al}_x\text{Ga}_{1-x}\text{N}$ Layers grown on 6H-SiC (0001) by Metal Organic Vapor Phase Epitaxy

R. Kröger<sup>1</sup>, S. Einfeldt<sup>1</sup>, Z. J. Reitmeier<sup>2</sup>, R. Chierchia<sup>1</sup>, P. Ryder<sup>1</sup>, D. Hommel<sup>1</sup>, and R.F. Davis<sup>2</sup>

<sup>1</sup>Institute of Solid State Physics, University of Bremen, P.O. Box 330440, 28334 Bremen, Germany

<sup>2</sup>North Carolina State University, Dept. of Materials Science and Engineering, Campus Box 7907, Raleigh, NC 27695

#### ABSTRACT

The microstructural evolution of  $\text{Al}_x\text{Ga}_{1-x}\text{N}$  films grown by metalorganic vapor phase epitaxy on 6H-SiC (0001) was studied by means of X-ray diffraction, atomic force microscopy and transmission electron microscopy in conjunction with energy dispersive X-ray spectroscopy. A significant spatial variation of composition was found in 100 nm thick layers the nature of which could be traced back to the initial stage of film formation. Upon nucleation two phases are formed: a wetting layer and isolated islands of high and low aluminum content, respectively. The observed results are discussed in terms of strain and growth rates.

#### INTRODUCTION

In contrast to GaN, AlGaN reasonably wets SiC and can be used as a buffer layer for the epitaxial growth of group-III nitrides on SiC substrates. If the Al mole fraction of the AlGaN stays low, the buffer can be sufficiently doped such that vertical devices on conductive SiC substrates can be made [1-3]. However, AlGaN harbors a number of difficulties regarding the nucleation process on SiC as it does not grow in a two-dimensional mode from the very beginning, and it shows chemical fluctuations [4,5]. In this work the focus is set on the nucleation and evolution of AlGaN layers on 6H-SiC (0001) substrates via the investigation of the microstructure and the chemical composition of such films. A comprehensive study of these properties was performed on AlGaN layers with thicknesses between 20 nm and 1  $\mu\text{m}$ .

#### EXPERIMENTAL DETAILS

$\text{Al}_x\text{Ga}_{1-x}\text{N}$  layers with a nominal aluminum mole fraction of ~0.15 and nominal thicknesses of 20 nm, 60 nm, 100 nm and 1  $\mu\text{m}$  were grown on 6H-SiC (0001) substrates using metal organic vapor phase epitaxy (MOVPE). The growth temperature and the V/III ratio were 1010 °C and 4600, respectively. The chosen growth conditions led to a growth rate of ~0.6  $\mu\text{m}/\text{h}$ . It is noted that if 100 nm thick AlGaN layers grown in this way were used as buffer layers for subsequent growth of GaN, state-of-the-art GaN layers with atomically smooth surfaces could be obtained. The microstructure and the chemical composition of the AlGaN films were studied by a variety of tools. Atomic force microscopy (AFM) was used to study the topology. High resolution X-ray diffraction (XRD) was performed in to investigate the composition and strain. Transmission electron microscopy (TEM) in conjunction with energy-dispersive X-ray spectroscopy (EDS) served to examine the microstructure in high resolution as well as the chemical composition.

## DISCUSSION

Figure 1 shows AFM images taken from the  $\text{Al}_x\text{Ga}_{1-x}\text{N}$  films of varying thickness. The 20 and 60 nm thick layers consist of three-dimensional islands which are of low density and well-separated for the first case but of higher density and partially coalesced for the second case. At a film thickness of  $\sim 100$  nm trench-like features can be observed, which disappear during further growth and are rarely visible for the 1000 nm thick layer.

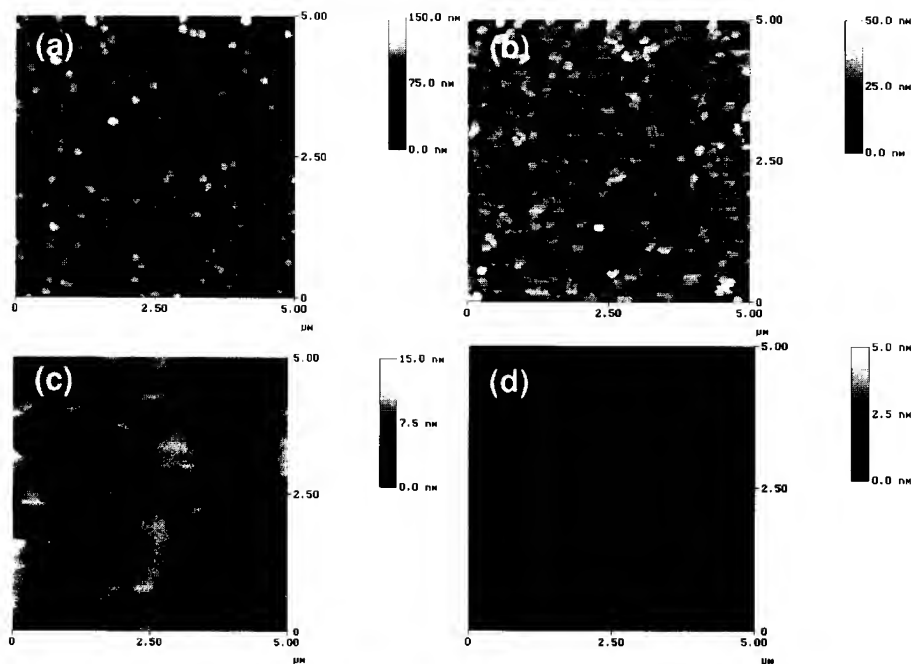


**Figure 1:** AFM images of AlGaIn layers having a nominal thickness of (a) 20 nm, (b) 60 nm, (c) 100 nm and (d) 1000 nm, respectively.

To study the microstructure of the trench evolution TEM analysis was performed on the 20 nm layer. A high resolution TEM image taken along the  $[10\bar{1}0]$  zone axis is shown in figure 2. A large three-dimensional island with a stepped edge can be seen on the left side of the image, whereas an  $\sim 10$  nm thick layer is found on its right side, both separated by a trench. A "wetting layer" of the latter type was already reported by others [5]. The authors found this layer to consist of nearly pure AlN, which tends to grow in a two-dimensional mode due to its low lattice mismatch to SiC whereas the islands were claimed to be almost pure GaN.

BEST AVAILABLE COPY



**Figure 2:** High resolution TEM image of the nominally 20 nm thick AlGaIn layer showing a three dimensional island on the left and the "wetting" layer on the right side.

The EDS mapping of the GaK $\alpha$  signal, shown in figure 3, reveals that both the island and the wetting layer contain gallium, i.e. there is no phase separation into nearly pure GaN and AlN as was previously reported [5]. A quantitative evaluation of EDS point analysis for the AlK $\alpha$  signal reveals Al mole fractions of ~3.5% and 18 % for the island and the wetting layer, respectively.

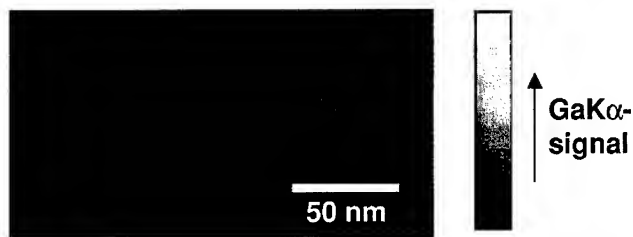


**Figure 3:** EDS map taken from the 20 nm thick AlGaIn layer using the GaK $\alpha$  signal for the area indicated by a rectangle in figure 2.

An evaluation of the average composition and strain in the 100 nm thick layer was performed by XRD. Figure 4 shows the reciprocal space map containing the Al $_x$ Ga $_{1-x}$ N (105) and SiC (1015) reflections. At least two peaks are found for the Al $_x$ Ga $_{1-x}$ N indicating phases of different composition in the layer. Based on literature values for the lattice constants and stiffness constants of both GaN and AlN, the Al mole fractions of the two phases can be estimated to  $x = 0.10$  and  $x = 0.18$ , respectively [6]. The tail structures toward lower and higher values of the out-of-plane component  $q_z$  of the scattering vector could possibly arise from areas of even lower or higher Al contents, respectively. Since the Al $_x$ Ga $_{1-x}$ N peaks in figure 4 all have the same in-plane component  $q_x$  of the scattering vector, the phases are fully strained with respect to each other. In average, however, the Al $_x$ Ga $_{1-x}$ N is not significantly strained by the SiC substrate as the peaks are close to the positions of fully relaxed Al $_x$ Ga $_{1-x}$ N.

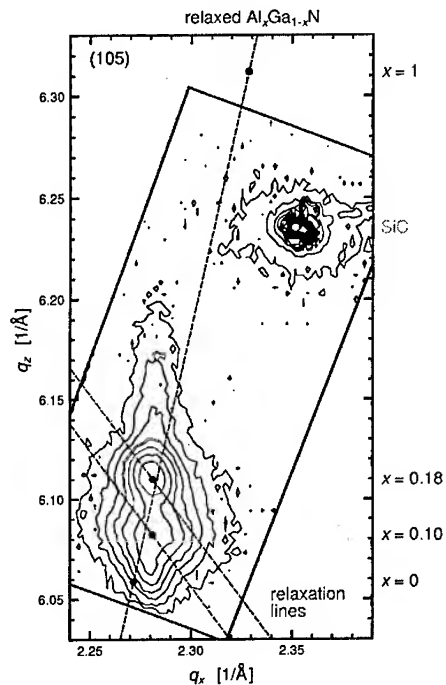


**Figure 4:** Reciprocal space map of the nominally 100 nm thick  $\text{Al}_x\text{Ga}_{1-x}\text{N}$  film showing two distinct maxima for the AlGa $\text{N}$  (105) reflection corresponding to values of  $x = 0.10$  and  $0.18$ . The dashed lines correspond to the expected position of the AlGa $\text{N}$  (105) reflection for fully relaxed AlGa $\text{N}$  of varying composition and for AlGa $\text{N}$  with  $x = 0.10$  and  $x = 0.18$  of variable biaxial strain.

The EDS maps for the 100 nm thick film are shown in figure 5 together with the scanning TEM image of the analyzed region containing a trench. Aluminum-rich regions can be identified at the layer/substrate interface as well as close to the surface of the film. These domains appear to alternate with respect to each other. It is assumed that the aluminum-rich areas close to the SiC in figure 5 coincide with the “wetting” layer in figure 3, whereas the aluminum-poor regions are attributed to the three-dimensional islands. The trench seen in the images is found close to the edge of an aluminum-rich region leading to the conclusion that it was formed between the “wetting” layer and the island upon nucleation. The appearance of a second layer of aluminum-rich regions at a film thickness of  $\sim 100$  nm is not yet understood and needs further investigations. However, AFM images show that at film thickness of  $\sim 60$  nm the film is not yet fully coalesced such that the formation of aluminum-rich regions could be connected with the coalescence process and local strain variations during this stage of growth.

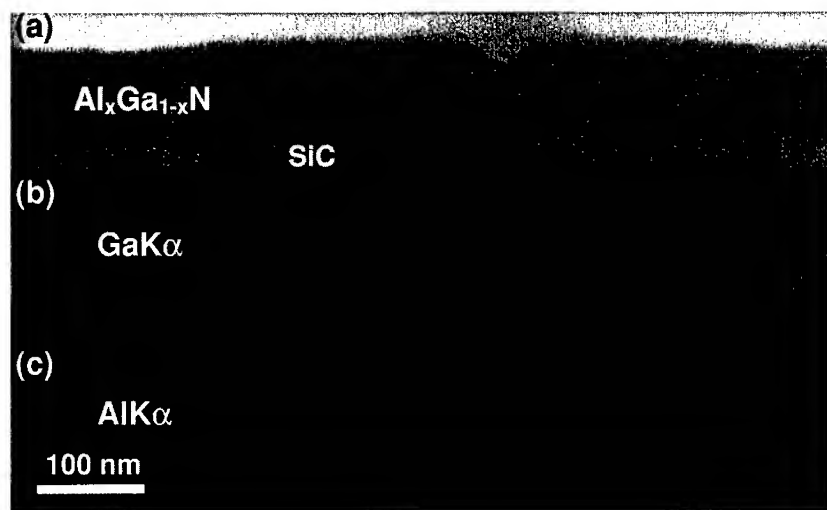


**Figure 5:** (a) Scanning TEM image and corresponding gray scale maps of the (b) GaK $\alpha$  and (c) AlK $\alpha$  signal intensities. The scans were performed in a trench region.

Based on the data gained from the microstructural and chemical characterization it is concluded that the trench formation takes place during the initial stage of growth upon nucleation. A phase separation occurs, which leads to areas of significantly different aluminum content. The aluminum-poor islands grow faster in vertical direction than the aluminum-rich phase up to a critical thickness when they start to laterally overgrow the latter phase. This growth mechanism leads to the formation of aluminum-rich and aluminum-poor domains close to the substrate interface.

## CONCLUSIONS

The microstructural and chemical analysis of Al $_x$ Ga $_{1-x}$ N layers grown on SiC reveals that the phase separation between Al-rich and Al-poor areas leads to the formation of trenches, which are gradually overgrown upon further deposition. Two layers of alternating Al rich regions are found at the interface with the SiC and between at 60 nm and 100 nm film thickness, which is possibly connected with local strain variations during coalescence. The different phases are found to be pseudomorphic with respect to each other and relaxed with respect to the SiC substrate.

## REFERENCES

1. B. Moran, M. Hansen, M.D. Craven, J.S. Speck, S.P. DenBaars, J. Cryst. Growth **221**, 301 (2000).
2. H. Lahrèche, P. Vennéguès, M. Vaille, B. Beaumont, M. Laiigt, P. Lorenzini, P. Gibart, Semicond. Sci. Technol. **14**, L33 (1999).
3. J.A. Smart, A.T. Schremer, N.G. Weimann, O. Ambacher, L.F. Eastman, J.R. Shealy, Appl. Phys. Lett. **75**, 388 (1999).
4. M.D. Bremser, W.G. Perry, T. Zheleva, N.V. Edwards, O.H. Nam, N. Parikh, D.E. Aspnes, R.F. Davis, MRS Internet J. Nitride Semicond. Res. **1**, 8 (1996).
5. P. Vennéguès, H. Lahrèche, Appl. Phys. Lett. **77**, 4310 (2000).
6. H. Heinke, M.O. Möller, D. Hommel, G. Landwehr, J. Cryst. Growth **135**, 41 (1994).

### High-Spatial-Resolution Cathodoluminescence Measurement of InGaN

Hisashi Kanie, Hiroaki Okado, Takaya Yoshimura  
Dept. of Applied Electronics, Tokyo Univ. of Science,  
Noda, Chiba, 278-8510, JAPAN.

#### ABSTRACT

This paper described observation of cathodoluminescence (CL) of microcrystalline InGaN bulk crystals under a scanning electron microscope (SEM) with a high-spatial-resolution (HR) CL measuring apparatus. HR-CL spectra from facets of InGaN crystals vary from facet to facet and are single peaked. Histogram analysis of the CL peak positions of HR spectra from the facets of the crystals in the area scanned during a low-resolution CL measurement shows a two-peaked form with comparable peak wavelengths. The diffusion length of a generated electron-hole pair or an exciton from the recombination centers with a higher-energy-level state to that with a lower state is estimated to be 500 nm at the longest by the comparison of two monochromatic HR-CL images of adjoining facets.

#### INTRODUCTION

InGaN active layers play an important role in a high efficiency light emitting diode ranging from violet to amber, however, its microscopic structure of luminescence center is not well understood yet [1,2]. Because almost all the samples studied are epilayers grown by metal organic chemical vapor deposition stresses within them caused by the large lattice misfit between an epilayer and a substrate modulate luminescence properties through piezoelectric field or band gap modulation. As we synthesize free standing and stress free microcrystalline InGaN [3], we study luminescence properties of InGaN without a nuisance of stresses or piezoelectric field.

When we measure photoluminescence we often observed two peaked spectra. As we use a laser the excitation beam diameter of the laser is 1 mm a measured emission band is an integration of each emission band of the crystals under excitation. The intensity profile of the band may be explained by a summation of the product of the bulk density of the crystals showing a certain emission band in the observed area and the intensity of the band. As we can probe with an electron beam with a diameter of subnanometers for CL measurement, we observe CL properties for GaN microcrystals.

From HR-CL images dark lines running in the  $\langle 11\bar{2}0 \rangle$  or  $\langle 1\bar{1}00 \rangle$  directions from a (0001)

basal plane of GaN microcrystals are observed [4]. The dark lines terminated on the surface of  $\{11-2x\}$  or  $\{1-10y\}$  facets as dark spots. Although there is few report which associated the CL dark lines with threading dislocations [5], these dark lines are assigned to threading dislocations in GaN crystals, because their crystallographic orientation have the feature of the threading dislocation and density of the dark spots is comparable to that of the threading dislocation [4].

This paper describes the CL spectra from each facet of InGaN microcrystals and CL mapping images studied under the HR-CL SEM at room temperature.

## EXPERIMENT

InGaN micorcrystals were grown by a two-step method described in Ref. 3. In the first step, GaN microcrystals were synthesized by the nitridation of  $Ga_2S_3$  with ammonia at 1120°C; in the second step InGaN microcrystals were synthesized by the nitridation of a mixture of obtained GaN microcrystals and ground  $In_2S_3$  with ammonia at 850 - 950 °C. The size of InGaN crystals ranged from 1 to 20  $\mu m$ .

HR-CL was observed under an in-lens scanning electron microscope (Topcon DS130S) equipped with a monochromator directly coupled to an optical port. Detail of the equipment is described in Ref. 4. HR-CL measurement conditions are as follows: A beam diameter of 10 nm and an accelerating voltage of 5 kV. Low-spatial-resolution CL (LR-CL) spectra to compare with HR-CL spectra were measured under an electron probe micro analyzer (Shimazu EPMA 8705) with an electron beam of 1  $\mu m$  in diameter.

## RESULTS AND DISCUSSIONS

A nanoscale CL image of nonradiative defects are observed with a HR-CL apparatus. Dark lines with a width of 30 nm and dark spots with a diameter of 30 nm are observed in a monochromatic image at 390 nm from a (0001) basal plane of an InGaN microcrystal synthesized at 950 °C as shown in Fig. 1. Dark lines stretching in  $\langle 11-20 \rangle$  or  $\langle 1-100 \rangle$  directions through the c-plane are observed. We assign dark lines and dark spots to threading dislocations as is the case with GaN microcrystals, although the dark spots on the c-plane were not observed for GaN samples [4].

Emission spectra from an area with sides of several tens nanometers can be observed in HR-CL measurement. The CL spectra from each facet of an InGaN crystal in Fig. 2 are summarized in Fig. 3. Areas marked in Fig. 2 are selected to minimize the mixing of emission from the adjoining facets. The alphabetic order of the spectrum in Fig. 3 corresponds to the ordinal number of the scanned area. Most of the HR-CL spectra are single peaked. When there is

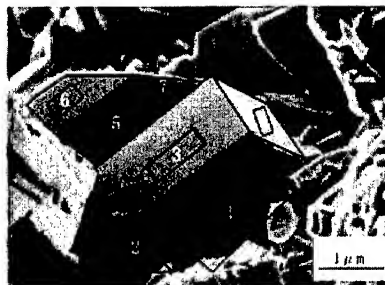
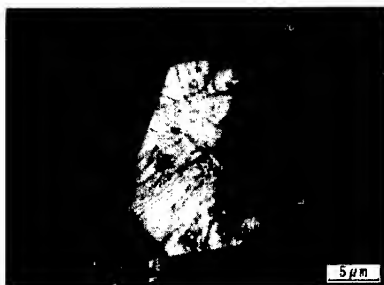


Figure 1. Dark spots and lines on (0001) plain of InGaN in a monochromatic CL image at 390 nm.

Figure 2. SEM image of an InGaN crystal

a small hump in the HR-CL spectra, the location of the hump is near the peak position of the adjacent facet, see the spectra in Fig. 3 (b) and (e). Peak positions of CL spectra range from 420 to 460 nm. The facet where the area 1 is located is a (0001) basal plane and the peak position of the c-plane is in a group with the shortest peak wavelength. By the CL peak position the In content  $x$  of  $\text{In}_x\text{Ga}_{1-x}\text{N}$  for each facet is estimated if we apply the relationship equation between the PL peak energy and the In content in Ref.6. Estimated In contents in the facet range from 0.07 to 0.15 for the InGaN crystal in Fig. 3. The reason why the In concentration varies so abruptly from facet to facet is still under investigation.

By the comparison of SEM images in Fig. 2 and monochromatic HR-CL images at 420 and 460 nm in Figs. 4 (a) and (b), the diffusion distance of a generated electron-hole pair or an exciton before recombination at the center assigned to the emission band at 420 nm in a facet to that at 460 nm in the adjoining facet is estimated. The diffusion length is estimated to be in the range from 300 to 500 nm at the longest, which is twice as large as that of MOCVD grown GaN [7]. No reverse diffusion process occurred from the lower state to the higher state.

In LR-CL measurement a two-peaked emission spectrum was sometimes observed from the area with a side of few micrometers of InGaN microcrystals, as shown in Fig. 5.

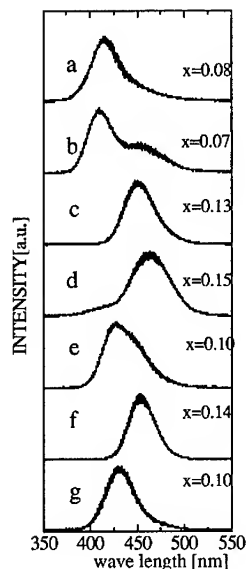


Figure 3. HR-CL spectra of the facets of an InGaN crystal (a) scanned at the area 1, (b) 2, (c) 3, (d) 4, (e) 5, (f) 6, and (g) 7.



(a) at 420 nm



(b) at 460 nm

Figure 4. Monochromatic HR-CL images (a) at 420 nm and (b) at 460 nm. The width from the edge of a bright band in the circle labeled A of Fig. 4 (b) is 500 nm and that in the circle B is 300 nm. The diffusion length of an electron-hole pair or an exciton from the higher-energy state to the lower-energy state of In recombination centers is estimated to be 300 to 500 nm. The width of a dark band in the circle A in Fig. 4 (a) is 200 nm and that is in definable in the circle B. The observation indicates that no reverse diffusion of an electron-hole pair or an exciton occurred from the lower energy state to the higher state.

Histogram of the HR-CL peak position of obtained spectra shows two peaks at 420 and 450 nm classes, as shown in Fig. 6, which agrees well to the CL peaks in Fig. 5. The spectrum profile of LR-CL is an integration of HR-CL spectra from all the facets in the LR-CL scanning area. A single-peaked spectrum or single-peaked one with a shoulder or hump measured in a HR-CL spectrum is another cause of a two-peaked emission spectrum.

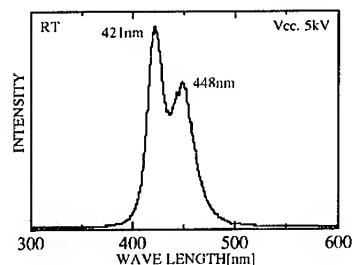


Figure 5. LR-CL spectrum of an InGaN crystal.

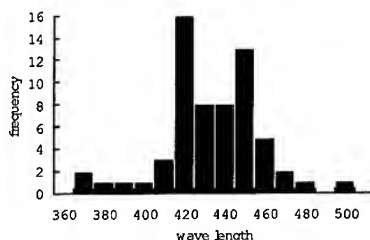


Figure 6. Histogram of the peak positions of the HR-CL spectrum for facet of InGaN.

## CONCLUSION

High-spatial resolution CL measurements showed that a CL spectrum varies for each facet of a InGaN crystal. Peak positions of CL spectra from facets range from 420 to 460 nm. Estimated In contents from the HR-CL peak positions range from 0.07 to 0.15. The excitation energy transfer from the higher energy level state to the lower energy level state of the In luminescence center is observed. The estimated diffusion length of an excited electron-hole pair or an exciton is 500 nm at the longest.

## ACKNOWLEDGEMENT

This study is partly supported by Futaba Natural Science Foundation. The authors specially thank to Mr. SHIKANO for his help.

## REFERENCES

1. S.Chichibu, T. Azuhata, T. Sata, and S. Nakamura, Appl. Phys. Lett. **70**, 2822 (1997).
2. Y. Narukawa, Y. Kawakami, M. Funato, Sz. Fujita, Sg. Fujita, and S. Nakamura, Appl. Phys. Lett. **70**, 891 (1997).
3. H. Kanie, K. Sugimoto, and H. Okado, Mat. Res. Soc. Proc. **639** G6.18.1 (2001).
4. H. Kanie, K. Sugimoto, H. Okado, phys. stat. sol. (a) **188** 481 (2001).
5. Tomoya Sugahara, Hisao Sato, Maosheng Hao, Yoshiki Naoi, Satoshi Kurai, Satoru Tottori, Kenji Yamashita, Katushi Nishino, Rinda T.Romano, and Shiro Sakai, Jpn. J. Appl. Phys. **37** L398 (1998).
6. C.A.Paker, J.C.Roberts, S.M.Bedair, M.J.Reed, S.X.Liu, N.A.El-Masry, and L.H. Robins, Appl. Phys. Lett. **75** 2566 (1999).
7. S. J. Rosner, G. Girolami, H. Marchand, P. T. Fini, J. P. Ibbetson, L. Zhao, S. Keller, U. K. Mishra, S. P. DenBaars, and J. S. Speck, Appl. Phys. Lett. **74** 2035 (1999).

### Comparisons of Gallium Nitride and Indium Nitride Properties after CF<sub>4</sub>/ Argon Reactive Ion Etching

Marie WINTREBERT-FOUQUET, K. Scott A. BUTCHER, Physics Department, Macquarie University, Sydney NSW 2109, Australia  
and Simon K H Lam, CSIRO Telecommunications & Industrial Physics, PO Box 218, Lindfield, NSW 2070, Australia

#### ABSTRACT

We present a comparative study of the effects of low power reactive ion etching (RIE) on GaN and InN. This new, highly chemical, dry etching, using CF<sub>4</sub> and Ar, has been developed for thin nitride films grown at low temperature in our laboratories. GaN films were grown by remote plasma enhanced-laser induced chemical vapor deposition and InN films were grown by radio-frequency RF reactive sputtering. Commercial GaN samples were also examined. Optical and electrical characteristics of the films are reported before and after removing 100 to 200 nm of the film surface by RIE. We have previously shown that the GaN films, although polycrystalline after growth, may be re-crystallized below the growth temperature. Removal of the surface oxide has been found to be imperative since a polycrystalline residue remains on the surface after re-crystallization.

#### INTRODUCTION

III-V nitrides have some unique properties, such as wide band gap, high thermal conductivity and chemical stability, which make them ideal materials for optoelectronic and high power devices. III-V nitrides have high bond energies compared to conventional III-V semiconductors and are therefore more difficult to process for device applications. Dry etching of nitrides has been extensively investigated using numerous plasma-based machines and sources[1]. However, only a few studies on etching damage have been published. A large number of high-density plasma dry etch processes have been developed to obtain vertical and smooth sidewall profiles for nitride optoelectronics devices[2]. In addition to etch anisotropy, an important consideration for device fabrication is the elimination of ion damage. Achieving high anisotropy generally requires high, ion assisted etch rates. In this work we report on the RIE of our thin nitride films performed using CF<sub>4</sub>/Ar chemistries. These thin GaN and InN films are grown in our lab at low temperature. We investigate the effect of the rf plasma power as a function of etch rate and surface contamination. We also present the results of an investigation into the cause of etch-induced damage for this chemistry. The GaN and InN films exposed to RIE were examined electrically, chemically and optically to identify the effects of various treatments.

#### EXPERIMENTAL DETAILS

GaN films were grown by remote plasma enhanced-laser induced chemical vapor deposition at 550-600 °C on Si (100) and Sapphire substrates. Although the GaN was polycrystalline after growth, it may be re-crystallized below the growth temperature[3]. InN films were grown by radio-frequency reactive sputtering at 80 °C on borosilicate glass, sapphire and Si(100) substrates.

The RIE was performed in a conventional RF-power reactor. Ar gas was added in order to stabilize the plasma and enhance the physical etching process. The total pressure was held at 10 Pa with partial pressures of 2 Pa and 8 Pa for Ar and  $\text{CF}_4$  respectively. Microwave powers of 15-200 W were used. Silastic as well as metals were used for masking. All etch experiments were performed at room temperature. The etch depth was measured with an Alpha-step Tencor surface profiler.

The surface morphology of the unprocessed and processed samples was examined by scanning electron microscopy (SEM) and atomic force microscopy (AFM). AFM was performed in one by one micron scans using a silicon tip in the contact mode.

The structural morphology of GaN and InN were investigated using X-ray diffraction after sequential surface removal of layers 200 nm thick by low power RIE.

Some individual samples were cut into 0.4 by 0.4  $\text{cm}^2$  samples and evaluated using Hall measurements, this was done with or without RIE. Thermally evaporated Ti/Al/Au alloy and Au contacts were deposited at the corners of GaN and InN un-etched and etched samples to serve as ohmic contacts. The Hall measurements were collected at room temperature. For Hall measurements on GaN, commercial samples were used.

A Cary UV-Vis double beam transmission spectrophotometer was used to collect optical transmission spectra for band-gap measurements of the etched and un-etched samples.

Chemical information of the un-etched and etched surfaces was obtained by secondary ion mass microscopy (SIMS) and X-ray photoelectron microscopy (XPS).

## RESULTS AND DISCUSSION

Figure 1 shows the results of the etch rate of GaN and InN in  $\text{CF}_4/\text{Ar}$  as a function of the power of the rf plasma. The etch rate of GaN increases linearly with the power of the rf plasma. This is twice the etch rate of GaN presented by H. Lee et al with  $\text{CHF}_3/\text{Ar}$  chemistries[4]. The etch rate of the InN increases linearly and follows closely the GaN etch rates up to 70 W then decreases and saturates at 180 W. The most straightforward explanation for such an observation is to assume that there is an incomplete chemical reaction with partial creation of the volatile species where the F radicals are incorporated in the InN surface by implantation before they have a chance to react. Similar dependences have been noticed when etching SiGe with  $\text{CF}_4/\text{Ar}$  chemistries where the etch rates increase linearly and then decrease and saturate[5]. Figure 2 shows the AFM measurements on the InN before and after etching 200 nm down at a RIE power of 70 W.

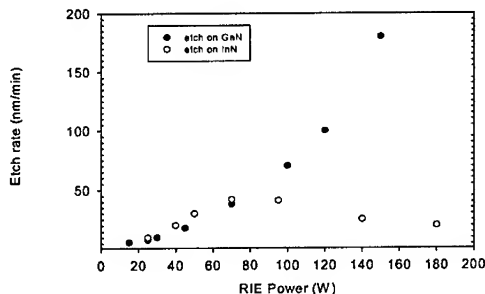
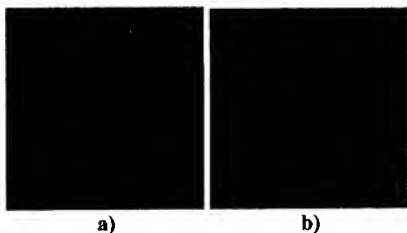


Figure 1. Etch rates of the nitrides as a function of RIE power.



**Figure 2.** Taping-mode AFM  $1\ \mu\text{m}^2$  images of InN sample surfaces. (a) Unprocessed and (b) 200 nm removed by RIE at 70 W



**Figure 3.** SEM cross-section of GaN film that has been re-crystallized. A residue of 100-200 nm is also visible near the top of the film.

The surface morphologies show that the size of the InN crystals decreases from a root-mean-square surface roughness of 4 nm to 3.2 nm with RIE treatment. AFM for the GaN reveals that the crystal sizes at the surface before and after etching were very similar; the only variation noticed was sample related as previously noted for GaN samples grown at different temperature[6]. SEM cross-sectional micrographs reveal that smoother etched surfaces and sharper edges were obtained for a RIE power of 70 W. Figure 3 is the cross sectional image of a GaN film, grown on (100)Si, that has undergone re-crystallization processing. XRD were taken for this sample before any etching and then after removing 200 nm of the top layer where there is a polycrystalline residue remaining at the surface after re-crystallization. Figure 4 presents the XRD results on GaN, before and after two steps of RIE. We note a change in the orientation of the crystal along the etch. At the surface (graph 1), there are 3 prominent peaks  $2\theta = 32.4^\circ$ ,  $35^\circ$  and  $36.96^\circ$  indicating polycrystalline material with multiple orientation which can be GaN

(10 $\bar{1}$ 0), Ga<sub>2</sub>O<sub>3</sub> (111) and GaN (10 $\bar{1}$ 1) orientations respectively. After removing 200 nm from top surface (graph 2) the middle peak corresponding to Ga<sub>2</sub>O<sub>3</sub> is gone and the GaN peaks decreased. After removing 300nm more from top surface (graph 3), a single strong peak is evident at  $2\theta = 34.6^\circ$ , which is a GaN (0002) reflection. The presence of this reflection indicates predominantly (0001) oriented material with the hexagonal structure c-axis aligned normal to the (100) cubic silicon surface. The XRD measurements on InN films un-etched and etched show the same characteristics, with a preferred (0001) orientation indicating again the c-axis of the hexagonal InN structure perpendicular to the substrate. Figure 5 shows a typical XRD of an InN film, well oriented with all crystallites having (0002) and (0004) planes parallel to the growth surface.

The influence of various etch conditions on the electrical properties are summarized in Table I. The resistivity, carrier concentration and mobility are given before any etch (un-etched samples:  $\rho_u$ ,  $n_u$ ,  $\mu_u$ ) and after plasma etching (etched samples:  $\rho_e$ ,  $n_e$ ,  $\mu_e$ ).

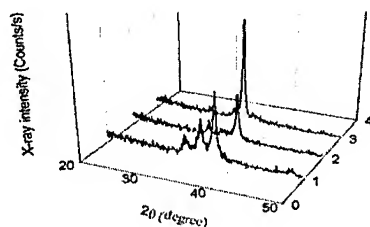


**Figure 4.** XRD measurements of GaN film  
Graph1: on surface  
Graph 2: after removing 200 nm film  
Graph 3: after removing 300 nm more of the surface.

For the InN samples, the deposited contacts were good for etched and un-etched, the mobility decreases when using a RIE power of 140 W, and remains nearly the same as the un-etched sample when using a RIE power of 70 W. For the GaN samples, a dead layer was evident for the deposited contacts on etched surfaces and a current of 2 mA and 3 mA had to be applied on the 140 W etched sample and 200 W etched sample respectively to break through the dead layer and allow the Hall measurements. The mobility decreases slightly as the RIE power used on the sample increases. C.R. Eddy, et al observed similar decreases in mobility on GaN using different plasma chemistries[7]. However, the same sample and same ohmic contacts were used before and after etching.

**Table I.** Room temperature Hall measurements on un-etched samples (resistivity:  $\rho_u$ , carrier concentration:  $n_u$ , mobility:  $\mu_u$ ) and etched samples( $\rho_e$ ,  $n_e$ ,  $\mu_e$ ).

Sample	RIE Power (W)	Etch time (min)	$\rho_u$ ( $\Omega$ .cm)	$n_u$ ( $\text{cm}^{-3}$ )	$\mu_u$ ( $\text{cm}^2/\text{V.s}$ )	$\rho_e$ ( $\Omega$ .cm)	$n_e$ ( $\text{cm}^{-3}$ )	$\mu_e$ ( $\text{cm}^2/\text{V.s}$ )
GaN	70	3	$5.04 \times 10^{-2}$	$4.8 \times 10^{17}$	259.4	$4.05 \times 10^{-2}$	$6 \times 10^{17}$	254.7
GaN	140	2	$5.04 \times 10^{-2}$	$4.8 \times 10^{17}$	259.4	$2.88 \times 10^{-2}$	$8.66 \times 10^{17}$	249.5
GaN	200	1.5	$5.04 \times 10^{-2}$	$4.8 \times 10^{17}$	259.4	$4.6 \times 10^{-2}$	$5.8 \times 10^{17}$	234
InN	140	2	$3.1 \times 10^{-3}$	$4 \times 10^{19}$	43	$3.07 \times 10^{-3}$	$2.7 \times 10^{20}$	5
InN	70	5	$4.2 \times 10^{-3}$	$2.07 \times 10^{20}$	7.3	$4.63 \times 10^{-3}$	$1.94 \times 10^{20}$	6.9

There were no significant changes of band-gap measurements on InN and GaN un-etched and etched samples. The InN is highly degenerate with band-gap values within 2.0-2.1 eV and the GaN has a band-gap of 3.4 eV.

XPS has been performed to determine the surface composition of all the samples un-etched and etched at different rf power. Table II shows atomic concentration ratio of F/Ga for GaN samples and F/In for InN samples from XPS analysis. In general these ratios increase when increasing the power of the RIE and more dramatically for GaN samples than for InN samples.

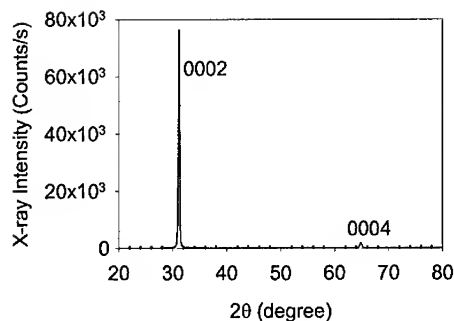


Figure 5. Typical XRD measurements of InN film

Table II. Atomic concentration ratio of F(1s) / Ga(2p<sub>3/2</sub>) and F(1s) / In(3d<sub>5</sub>), determined by XPS

GaN samples				InN samples			
RIE power	Un-etched	30 W	70 W	RIE power	Un-etched	140 W	200 W
F/Ga ratio	0	1.38	2.16	F/In ratio	0	0.5	0.52

SIMS measurements show that the F radicals get deeper into InN samples than GaN samples. SIMS results were only regarded as qualitative. Figure 6 shows the F radical penetration in InN and GaN samples for RIE power of 140 W and 200 W. For the InN samples, the F gets deeper into the etched surface (around 30 nm) and is in strong concentration. In GaN samples, there is not much difference between samples etched at 140 W and 200 W and the presence of F is seen only in nm at the surface.

## CONCLUSION

This work is an investigation of a new reactive ion etching using CF<sub>4</sub> and Ar chemistries for our GaN and InN thin films grown at low temperatures. We noticed that the etch rate increases linearly with the RIE power and RIE powers below 70 W have less damaging effects than higher powers. In InN case, the etch rate decreased dramatically when the power is higher than 70 W and saturated around 140 W. The role of ion bombardment does not play the only role in creating etch-induced damage in InN. There is evidence of fluorine incorporation on the InN surface exposed to this plasma. SIMS measurements were in accordance with this result showing high concentration of fluorine in the first 30 nm of the treated surface. Furthermore this saturation of the etching rate in InN compared to GaN at high RIE power can be used for selective etching, however the strong incorporation of F in the InN films should be taken into consideration.

The surface morphology of the treated surfaces analyzed by AFM and SEM were similar when using RIE power up to 70 W. Less etch-induced damages were seen beyond RIE power of 70 W. The effect of plasma etching on the electrical properties was demonstrated with Hall effect measurements. In the GaN samples, small variation of the mobilities and carrier concentrations were reported, with small decrease of the mobility as the RIE power increases. However a dead layer was remarked when contacting on etched GaN surfaces. This dead layer can be explain with XPS results showing a stronger F/Ga ratio at the surface and SIMS results showing that the presence of F as a function of depth profile is just in the first few nm of the GaN treated surface.

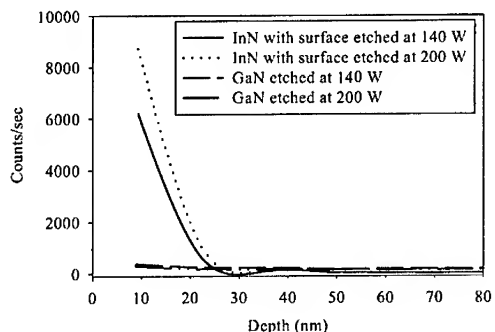


**Figure 6.** SIMS measurements showing the F contamination along the depth of GaN and InN treated at different RIE power.

Further work is being undertaken to find out a technique to remove this dead layer at the surface of GaN by changing the gas ratio in the RIE chamber and doing a quick etch *in situ* after RIE. Other possible techniques for removing the influence of the dead layer could be to use different alloy techniques for contacting just after RIE treatment. SIMS and XPS measurements on InN showed that there is more F incorporation within the InN and less F at the surface. Also, as InN is highly conductive, very good contacts were also possible on the RIE treated surfaces.

A gentle RIE at power of 40-70 W was successful for removing the residual polycrystalline film at the surface of the re-crystallized GaN without damaging the crystal.

This study has also shown that the most effective ion-assisted etching using this chemistry is for RIE power of 70 W or lower on both GaN and InN films. As the F incorporation is very strong in InN films, a chlorine-based discharge should be considered.

## ACKNOWLEDGMENTS

The authors would like to acknowledge the support of the Australian Research Council through a Large ARC grant.

## REFERENCES

1. S.J. Pearton, R.J. Shul and Fan Ren, *Internet J. Nitride Semicond. Res.* **5**, 11 (2000).
2. F. Karouta, B. Jacobs, P. Vreugdewater, N.G.H.V. Melick, Oschon, H. Protzmann, and M.Heuken, *Electrochem. and Solid State*, **2**, 5, 240 (1999).
3. K.S.A. Butcher, Afifuddin, P. P. -T. Chen, M. Godlewski, A. Szczerbakow, E.M. Goldys and T. L. Tansley, *J.Crys.Growth* (in press)
4. H. Lee, D.B. Oberman and J.S.Harris, Jr., *Appl. Phys. Lett.* **67** (12) 1754 (1995).
5. S.J. Chang, Y.Z. Juand, D.K. Nayak and Y.Shiraki, *Mater. Chem.and Phys.* **60**, 22 (1999).
6. K.S.A. Butcher, H. Timmers, Afifuddin, , P. P. -T. Chen, T.D.M. Weijers, E.M. Goldys and T. L. Tansley, R.G. Elliman, and J.A. Freitas, Jr., *J. Appl. Phys.*, **92**, 6, 3397 (2002).
7. C.R. Eddy, Jr and B. Molnar, *J. of Electronics and Mat.*, **28**, 3, 314 (1999).

## PHOTOREFLECTANCE CHARACTERIZATION AND CONTROL OF DEFECTS IN GaN BY ETCHING WITH AN INDUCTIVELY COUPLED PLASMA

O.J. GLEBOCKI,\* D.K. GASKILL,\* S.M. PROKES\* and S.W. PEARTON,\*\*

Naval Research Laboratory, Code 6862, Washington, D.C. , 20375

\*Department of Material Science and Engineering, University of Florida, Gainesville, FL 32611

### ABSTRACT

Photoreflectance (PR) is used to detect and characterize the electronic effects etch-induced defects in GaN that is exposed to an Ar or Ar/Cl inductively coupled plasma (ICP). Because of the sensitivity of PR we can follow the formation of etch-induced defects as a function of ion energies and densities. We show that at low RF powers, below 100W, the surface improves in electronic quality, but as the power is increased beyond 200W, etch-induced defects, are formed. The use of an Ar/Cl mixture plays a critical role in control of etch-induced defects.

### INTRODUCTION

GaN and its alloys are of great interest because of desirable electronic transport properties inherent to these material systems as well as their good thermal dissipation characteristics. Devices that are made from GaN based materials often involve the formation of recessed gates, which are formed through dry etch removal of material.[1] The etching scheme of choice is inductively coupled plasma etching, which utilizes an inert species such as Ar to provide directional sputtering and a reactive species such as Cl<sub>2</sub> to enhance the etch rate and in many cases control the effects of etch-induced damage. A trade-off occurs because the energetic ions can penetrate well below the surface and create defects such as vacancies or interstitials. In GaAs, it was found that a careful balance of ion energy and reactive gas pressure can control the process-induced defects, and in-situ post etch treatments could be used to remove any other residual defects.[2] In the case of GaN, however, such control over defects in processing does not exist, and the only recourse for defect removal is post-etch annealing, which is found to be incomplete.

Previous studies of GaN based devices that were exposed to a ICP plasma have shown that the etch damage can have a deleterious effect on device performance.[1] This included reduced Schottky barrier heights as well as motion of the Fermi energy at the surfaces of GaN toward mid gap.[3] These results suggest significant changes to the surface electronic properties of GaN that is exposed to a plasma.

In this paper, we take advantage of the fact the photoreflectance spectroscopy (PR) is based on the ability to photomodulate the built-in surface electric field. This ties in directly into the fact that the photomodulation is just a photovoltage. The AC nature of the modulation allows us to explore in a contactless manner the response of the surface states that pin the Fermi-level. Thus changes in the surface potential will directly lead to changes in the PR signal. In addition, the surface photovoltage will also be sensitive to formation of subsurface defects. We show that

we can follow the formation of defects that are induced by ICP etching of GaN from the initial changes to the surface potential to the formation of subsurface defects that act as trap centers.

## THEORETICAL CONSIDERATIONS

The photoreflectance technique has traditionally been used to study interband transitions in various semiconductors. The technique produces derivative like line shapes for transitions at various critical points in the Brillouin zone. The derivative nature of PR comes from the Franz-Keldysh effect, which results in the reflectivity and absorption of a material being dependent on an applied or built-in electric field.[4] In general, the relationship between the electric field,  $F$ , its modulation (through a change in surface potential,  $\Delta V$ ) and the optical reflectivity,  $R$ , can be expressed in a simple manner:

$$\frac{\Delta R}{R} = \frac{1}{R} [R(F + \delta F) - R(F)] \approx \frac{1}{R} \frac{dR(F)}{dF} \frac{\partial F}{\partial V} \Delta V \quad (1)$$

This shows that the intensity of measured PR signal will be directly proportional to the modulation of the electric field. In the case of photoreflectance, the surface potential modulation,  $\Delta V$ , is through a photovoltage,  $\Delta V_p$ .

In addition, because the reflectivity is a function of band gap of the material being probed,  $E_g$ , the broadening parameter,  $\Gamma$ , and the photon energy,  $E$ , of the probe light, we can rewrite Eq. (1) in a more familiar form:

$$\frac{\Delta R}{R} = V_p(\Omega_m) AL(E, E_g, \Gamma) \quad (2)$$

where  $A$  is a constant,  $L$  is a spectral line shape function, which defines the observed spectral feature. In Eq. (2), we have assumed that the field or surface potential modulation is produced by a photovoltage,  $V_p(\Omega_m)$  which is induced by a monochromatic pump beam that illuminates the surface. The reflectivity which is measured by a second probe light and contains in it a component with frequency,  $\Omega_m$ , which is just the derivative-like photoreflectance signal of Eq.(2). As can be seen from Eq.(2), the intensity of this component is proportional to the photovoltage,  $V_p(\Omega_m)$ . Because  $V_p(\Omega_m)$  can have both in-phase and quadrature components it will depend strongly on the presence of defects in the near surface region. Thus, the intensity of the photoreflectance signal becomes a contactless optical probe of the surface photovoltage. Therefore, any change in surface state density and pinning position will manifest themselves through concomitant changes in the PR intensity.

In general,  $V_p$  will have real and imaginary components ( $V_p = V_{p, re} + iV_{p, im}$ ), whose ratio we define as the PR lag ( $= V_{p, im} / V_{p, re}$ ). This is equivalent to the complex impedance analysis of a simple RC network, in which one measures a complex response, whose phase angle is directly related to the capacitance in the network [ $\tan(\phi) = R C \Omega_m$ ]. Thus, one can view the PR lag a direct measure of the capacitance of semiconductor surfaces or interfaces.

Finally, it is important to note that any photovoltage depends on an induced photocurrent, which requires the presence of either an applied or built-in electric field. Thus,  $V_p$  will follow

BEST AVAILABLE COPY

the photovoltaic behavior in which  $V_p \sim A \ln[ B I_0 \exp(-qV_f/kT) + 1 ]$ . [5,6] Here,  $V_f$  is the position of the Fermi-level at the surface,  $I_0$  is the incident photon flux and  $B$  is a term containing the Richardson constant and the arial density of surface states.

## EXPERIMENTAL DETAILS

The samples that were used in these experiments were 1.5  $\mu\text{m}$  thick MBE grown p-GaN and commercially purchased from SVT. Unfortunately, the surfaces of the pre-etch GaN samples can vary significantly between one growth run and another. Shown in Figure 1 are two atomic force microscopy (AFM) images of such a variation in sequentially grown MBE wafers. Wafer (a) is smoother and shows small spherical features, while wafer (b) is characterized by V-defects. Between the V-defects of sample (b), the surface is much smoother. In our experiments, we used mostly wafer (a), as it was the one that was most readily available. In addition, all of our samples

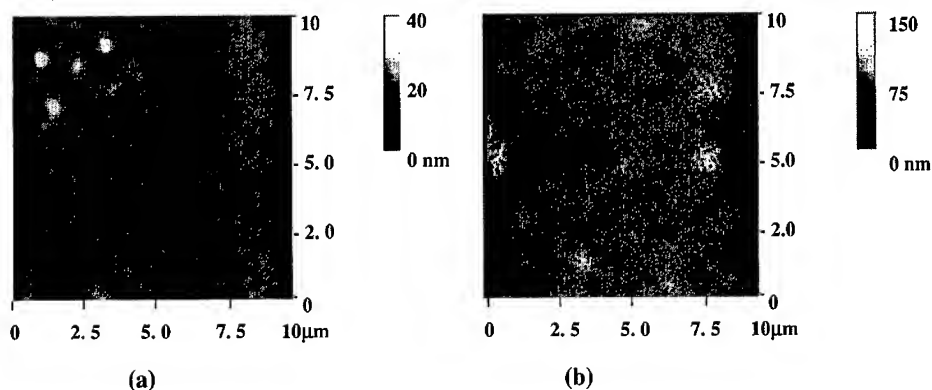


**Figure 1.** AFM images of two different MBE grown p-GaN samples. The surface of wafer (a) has a puffy texture, while wafer (b) is riddled with defects that show up as holes.

were screened using AFM to ensure that only one type was etched.

Prior to etching, the samples were water rinsed and blown dry in filtered  $\text{N}_2$ . The samples were then etched in a 300 W ICP system that had a flow rate of 15 sccm, with a mixture of 10 sccm of  $\text{Cl}_2$  and 5 sccm of Ar the process pressure was 5 mTorr. The ion energies were varied from 40 V to 400 V by changing the RF power to the sample chuck from 40 W to 300 W. The etch times were 1 minute for each samples. This led to etch depths varying from 40 nm for Ar/ $\text{Cl}_2$  to 10nm for Ar only. It is important to note that while for flow rates, gas mixtures and microwave power contribute to the etch rates it is the RF power that is variable and produces energetic ions which will produce damage.

The photorefectance measurements were performed using the typical apparatus described in the literature. In this case, however, we used the 351nm line of the Ar ion laser as our pump for producing the photovoltaic modulation. The laser was mechanically chopped at a frequency of 390Hz. The reflectivity was measured with a 150W Xenon lamp that was dispersed through a Spex  $\frac{1}{4}$  monochromator and the reflected light was detected with a UV enhanced Si

photodiode. The PR signal was extracted from the reflectivity with a lock-in amplifier tuned to 390Hz.

## RESULTS AND DISCUSSION

Shown in Figure 2, are a series of photoreflectance spectra for GaN that was exposed to an Ar/Cl<sub>2</sub> ICP plasma. Both the in-phase and quadrature components of the PR signal are shown. The first thing to note about the spectra is the variation in signal intensity. The control sample had a very small signal compared to the etched samples, which were about 50 times more intense. The initial etch with 40 W RF power dramatically increases the PR signal intensity. Subsequent etching with 200 W RF power is seen to reduce the PR intensity. In addition to the effects of etching on the PR intensity, we also see that there are significant changes in the ratio of the in-phase and quadrature PR components (PR lag).

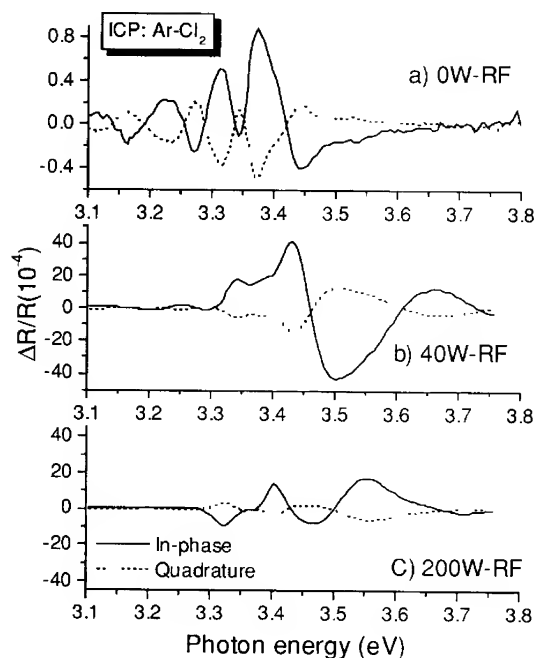


**Figure 2.** Photoreflectance spectra for a) the control p-GaN sample and for samples etched with b) 40 W and c) 200 W of RF power. The in-phase (solid) and quadrature (dotted) components of the PR signal are shown.

The control sample has a quadrature signal that is 54% of the in-phase signal, while the etched samples have lower values near 30%.

In addition to changes in the signal intensity and the PR lag, it is evident that the line shape is also effected by the etch process. The control sample has a very low PR intensity and also has a simple line shape near 3.4 eV. The oscillations below 3.4 eV are due to optical interference between light reflected from the surface of the sample and the substrate/epitaxial interface. They are small and only seen when the PR signal is very weak.

The structure between 3.35 and 3.5 eV comprises the PR signal. For the sample that was etched at 40 W, the PR lines increase in intensity, broaden and we see additional oscillations above the gap. These oscillations are due to the Franz-Keldysh effect and are known as the Franz-Keldysh Oscillations (FKO). The period of the FKO is a direct measure of the built-in electric field. Clearly, the period of the FKO in Fig. 2b is much larger than that of Fig. 2a

BEST AVAILABLE COPY

indicating that the etching increased the electric field. This behavior is consistent with a shift of the Fermi-level from near the valence band to mid gap. Further etching at 200 W of RF power, reduces the period of the FKO indicating a decreased the electric field.

The results for the Ar etching are similar to those obtained for the Ar/Cl<sub>2</sub> case, with one exception. The increases in the PR intensity at low RF powers are a factor of 4 smaller than for the Ar/Cl<sub>2</sub> case. In addition, the

period of the FKO from those samples indicates a smaller electric field, one similar to that of the 200 W ArCl<sub>2</sub>.

The results for the PR intensity and PR lag for both etching scenarios are summarized in Figures 3 and 4. We will use this information below to form a picture of the effects of ICP etching on the electronic properties of the GaN surfaces.

The initial surfaces of the GaN are heavily pinned near the valence band. This is indicated by the small PR intensity and the large PR lag of 0.54 as shown in Fig.4. Any initial exposure to either a reactive (with Cl<sub>2</sub>) or nonreactive plasma at low ion energies improves the surface by removing the defects responsible for the initial pinning. This is indicated by the fact that both types of etching reduce the PR lag.

The FKO's and PR intensity indicate different pinning sites for the Ar and Ar/Cl<sub>2</sub> etches, with the Fermi-level moving toward mid gap. In the case of Ar, the new pinning position is closer to the valence band, while for the case of an Ar/Cl<sub>2</sub> plasma, it is much closer to mid gap.

Etching at higher RF powers reduces the PR intensity (Fig. 3) and the FKO period for Ar/Cl<sub>2</sub> and has no major effect on the Ar etched samples. In

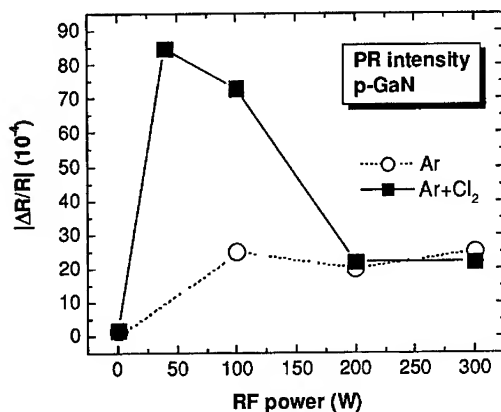


**Figure 3.** Photorefectance intensity as a function of RF power for Ar (open circles) and Ar/Cl<sub>2</sub> etches. The intensity was obtained from the extrema near 3.4 eV.

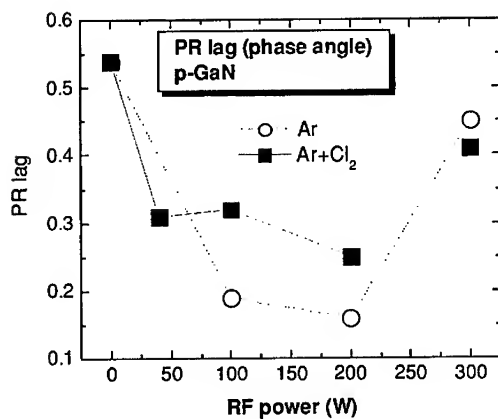


**Figure 4.** Photorefectance lag as a function of RF power for Ar (open circles) and Ar/Cl<sub>2</sub> etches.

addition, in both cases etching beyond 200 W significantly increases the PR lag, despite no changes in PR intensity or electric field.

The results for higher powers can be understood in terms of the onset of subsurface damage. At higher RF powers, ions from the Ar only plasma not only sputter surface atoms, but also penetrate below the surface, where collisions with lattice atoms produces a variety of point defects. In the Ar plasma, there is no effective method of removing these defects, since increased ion energies only leads to deeper penetration into the lattice. In the case of the Ar/Cl<sub>2</sub> plasma, the chemical reactivity of Cl<sub>2</sub> increases the etch rate and allows for effective removal of the defects. In addition, in GaAs work it has been shown that Cl<sub>2</sub> may also have a passivating effect on defects that are formed.

At some increased ion energy, however, the sputtering and deep penetration outpaces the chemical removal and the defects begin to form. This is the case in our experiments for 200 W and above. At this point, the PR lag increases significantly indicating the formation of slow subsurface traps, which act as an added capacitance to that of the surface field. Because of this, our results suggest that damage free etching occurs below 200W of RF power. These results are consistent with previous work for ECR of GaAs in an Ar/Cl<sub>2</sub> plasma.[2,7] In that case, subsurface damage was observed at ion energies of 200 V compared to 300 V in our case for GaN.

In conclusion, we have used photoreflectance spectroscopy to study the effects of ICP etching on the electronic properties of GaN surfaces. We have shown that important information can be obtained about the effects of etching and in a contactless manner.

#### ACKNOWLEDGEMENTS

This work was in part supported by the Office of Naval Research.

#### REFERENCES

1. S.J.Pearson, F.Ren, A.P.Zhang and K.P.Lee, Mat.Sci.Eng.Rep.,vol R30 pp55-212(2000).
2. O. J. Glembocki, J. A. Tuchman, J. A. Dagata, K. K. Ko, S. W. Pang and C. E. Stutz, Appl. Phys. Lett., **73**, 114(1998).
3. V.M. Bermudez, Appl. Surf. Sci. **119**, 147 (1997).
4. D.E. Aspnes, Surf. Sci. **37**, 418(1973).
5. J.M. Woodall, Proc. MRS, **324**, 141(1994) and references therein.
6. X. Yin, H.-M Chen, F.H. Pollak, Y. Chan, P.A. Montano, P.D. Kirchner, G. Petitt and J.M. Woodall, J. Vac. Sci Technol., **A10**, 131(1992).
7. D. Leonhardt, C.R. Eddy, Jr., V.A. Shamamian, R.T. Holm, O.J. Glembocki, J.E. Butler, J. Vac. Sci Technol., **A16**, 1547(1998).

### Electroreflectance and Photorefectance Studies of Electric Fields in Pt/GaN Schottky Diodes and AlGaIn/GaN Heterostructures

S. Shokhovets<sup>1</sup>, R. Goldhahn<sup>1</sup>, G. Gobsch<sup>1</sup>, O. Ambacher<sup>2</sup>, I.P. Smorchkova<sup>3</sup>, J.S. Speck<sup>3</sup>, U. Mishra<sup>3</sup>, A. Link<sup>4</sup>, M. Hermann<sup>4</sup> and M. Eickhoff<sup>4</sup>

<sup>1</sup>Institute of Physics and <sup>2</sup>Center for Micro- and Nanotechnologies, Technical University Ilmenau, 98684 Ilmenau, Germany

<sup>3</sup>Electrical and Computer Engineering Department and Materials Department, University of California, Santa Barbara, CA 93106, U.S.A.

<sup>4</sup>Walter Schottky Institute, Technical University Munich, 85748 Garching, Germany

#### ABSTRACT

We have performed electroreflectance and photorefectance studies of Pt/GaN Schottky diodes with Ga- and N-face polarity as well as AlGaIn/GaN based transistor heterostructures. The experimental data were analyzed using electric field-dependent dielectric functions of GaN and AlGaIn. Inhomogeneities in the electric fields were taken into account by application of a multi-layer formalism. We observed an increase of the electric field strength underneath the Schottky contact and in the AlGaIn barrier with increasing temperature. The results are explained in terms of temperature dependent densities of ionized impurities and surface charges.

#### INTRODUCTION

A detailed investigation of electric fields caused by Schottky contacts as well as the piezoelectric and spontaneous polarization of wurtzite group III nitrides is crucial to understand the performance of GaN based devices. Among the methods suitable for a direct measurement of the electric field strength, electroreflectance (ER) and photorefectance (PR) have proven their high sensitivity and usefulness [1]. These methods utilize the dependence of the dielectric function (DF) of a material on the electric field strength  $F$ . However, investigations of particular mechanisms of electro-optical response and systematic applications of ER and PR methods to nitrides are rare up to date. In most cases, Franz-Keldysh oscillations (FKO) are employed for optical determination of the electric field strength [2-4]. It should be noted that strong excitonic effects are characteristic of nitrides which are not included into the one-electron FKO picture. A more general approach must be used which takes into account the electric field-dependent contributions of discrete excitons and excitonic continuum to the DF [5-9]. Quenching of discrete excitons in high electric fields leads to the formation of an exciton dead layer (EDL). Recently [9] it has been shown that the resulting spatial changes of optical constants along a depletion region determine the shape of ER spectra for GaN Schottky diodes leading to so-called "rotation" ER spectra. In addition, the linear electro-optic (LEO) effect has been found to dominate below the band gap [10]. In this paper, we focus on the determination of electric fields in Pt/GaN Schottky diodes and in barriers of AlGaIn/GaN heterostructures using the electric field-dependent DF.

## SAMPLES AND EXPERIMENTAL DETAILS

The diodes were formed on 1.5  $\mu\text{m}$  Si-doped GaN layers grown on *c*-plane sapphire substrates by plasma-induced molecular-beam epitaxy (PIMBE). The layers of Ga- and N-face polarity were obtained with and without deposition of a 10 nm AlN nucleation layer, respectively, before the GaN layer growth. For semi-transparent Schottky gates, Pt was electron-beam evaporated with a thickness of 5 nm on a circular contact area with a diameter of 800  $\mu\text{m}$ . Ohmic contacts were processed by evaporation of Ti/Al (30/70 nm) and subsequent annealing at 800°C for 1 min under vacuum. For AlGaIn/GaN high electron mobility transistor (HEMT) heterostructures, first a 2  $\mu\text{m}$  thick unintentionally doped GaN layer was grown on (0001) sapphire substrates by metal organic chemical vapour deposition. Then a 250 nm thick GaN channel layer and an  $\text{Al}_x\text{Ga}_{1-x}\text{N}$  barrier with a thickness of about 20 nm were deposited by PIMBE. The samples were of Ga-face polarity. Further details can be found elsewhere [11, 12].

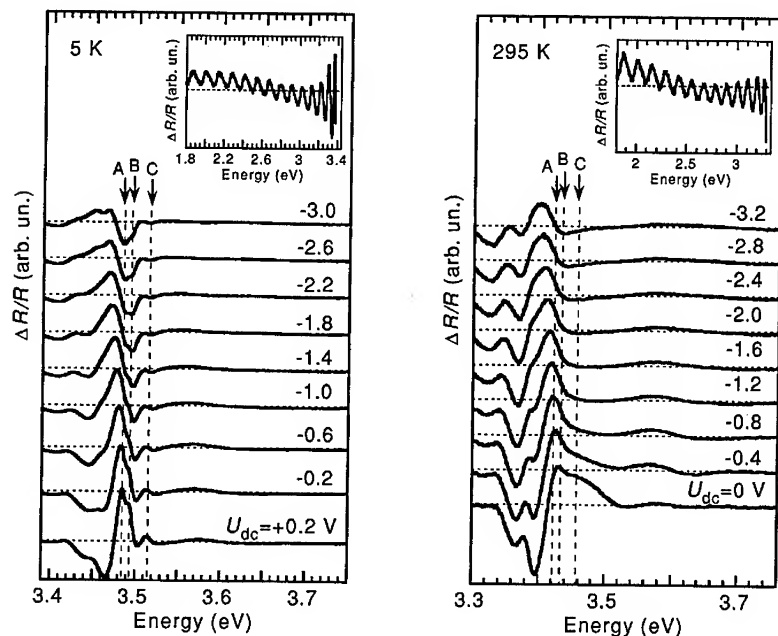
ER and PR were investigated under nearly normal incidence of the probe beam which was provided by the emission of a 100 W xenon arc lamp dispersed with a 2 m focal length grating monochromator. ER spectra were studied as a function of the dc bias voltage  $U_{\text{dc}}$ . To modulate the internal electric fields in the samples, either a square wave modulation voltage with a peak-to-peak amplitude of  $U_{\text{mod}} = 0.2$  V at a frequency of 180 Hz or a 325 nm line of a HeCd laser with a power of 100  $\mu\text{W}$  were used for ER and PR measurements, respectively. The resulting reflectance change was detected by standard lock-in technique.

## RESULTS AND DISCUSSION

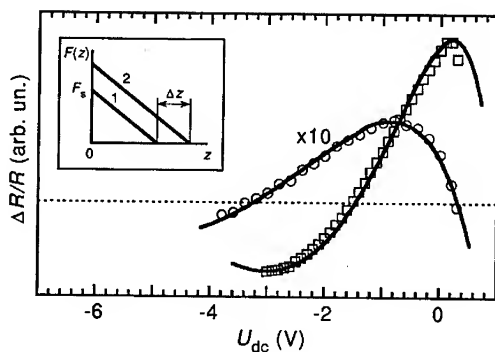
### Pt/GaN Schottky diodes

Figure 1 shows low-temperature (left) and room-temperature (right) ER spectra of a Ga-face diode for a range of bias voltages. In the low-temperature ER, sharp structures around 3.5 eV due to the free A, B, and C excitons are well resolved while the features resembling FKOs are observed above 3.55 eV. It indicates that all parts of the depletion region contribute to the ER signal, i.e. deeper lying low-field parts with relatively weakly perturbed discrete excitons and shallower lying higher-field parts where discrete exciton states are significantly broadened (intermediate fields) or quenched (EDL) by the electric field. This is why the ER spectra are strongly dependent on the bias voltage as it changes the electric field strength and the width of the depletion region. Examples of such data are shown in figure 2 ("rotation" ER spectra). At elevated temperatures excitons become weaker pronounced (figure 1, right) due to the phonon broadening. For instance, the magnitude of excitonic ER at 295 K is about 20 times smaller than that for 5 K. Just below the excitonic band gap we observe an ER signal which originates from the absorption by the band tail states and the LEO effect, with the latter being dominant in the transparent region (insets of figure 1). The spectral modulation is due to interference fringes in the reflectance. The signal size is approximately independent of the temperature and relatively weak, more than two order smaller than the excitonic ER at 5 K. Like the excitonic ER, it also demonstrates the "rotation" in dependence upon the bias voltage.

The experimental data were analyzed using a Schottky model (inset of figure 2) and a multi-layer formalism. The electric field-dependent DF was obtained by parameterization of numerical data for Wannier excitons and excitonic continuum [5-7]. The characteristic field unit for these



**Figure 1.** Electroreflectance spectra of a Ga-face diode. The arrows indicate the exciton energies for the zero-field limit. Insets show ER spectra in the transparent spectral region ( $U_{dc} = -0.1$  V).



**Figure 2.** "Rotation" electroreflectance spectra of a Ga-face diode at the photon energy of the A exciton for 5 K (squares) and 295 K (circles). The solid lines represent fits to the experimental data. The inset shows the electric field profiles underneath the gate for zero bias (1) and negative bias (2) voltage.

calculations is the exciton ionization field  $F_i$ . Using  $\epsilon = 9.5$  as the static dielectric constant and the electron and hole effective masses of 0.19 and 1.19 [13], respectively, we obtained  $F_i = 81$  kV/cm for GaN. The Rydberg energy and the oscillator strength ratio for A, B, and C excitons were set to 25 meV [13, 14] and 1:0.8:0.2 [15], respectively. The LEO effect was included by an expression [10]

$$n = \frac{n_o}{(1 + n_o^2 r_{13} F)^{1/2}} \quad (1)$$

where  $n$  is the electric field-dependent refractive index,  $n_o$  is the zero-field ordinary refractive index, and  $r_{13}$  is the LEO coefficient. Two sets of spectra, ER versus photon energy and ER versus bias voltage ("rotation" ER spectra) were calculated and compared with the corresponding experimental data. The adjusted parameters were the surface band bending  $V_b$  and the ionized impurity concentration  $N_i$ , as well as the exciton energies and the broadening parameter for the zero-field limit. Examples and results of fits are shown in figure 2 and table I, respectively. We found that electric fields increase with increasing temperature which is mainly due to the increasing ionized impurity concentration. Such behavior qualitatively agrees with results of Hall measurements on GaN doped with Si [16]. In addition, our studies revealed differences in ionized impurity concentration, surface band bending, electric field strength and their temperature dependence for diodes with different polarity while elastic recoil detection and secondary ion mass spectroscopy yielded approximately equal Si-concentrations of about  $8 \times 10^{17} \text{ cm}^{-3}$  for both samples. Note, however, that ER probes only a thin region close to the sample surface (the width of the space charge region varied in a range of 25-70 nm for our experimental conditions). It means that the impurity incorporation in the vicinity of the surface and the density of surface charges are different for Ga- and N-face polarity. These effects can be related to an opposite sign of the spontaneous polarization and differences in the microstructure of samples with Ga- and N-face polarity which, for example, can influence the electric field-induced or local strain-induced impurity diffusion.

**Table I.** Ionized impurity concentration, surface band bending, and zero bias surface electric field strength  $F_s$  for Pt/GaN Schottky diodes with different polarity.

Polarity	5 K			295 K			$\Delta F_s^a)$ (kV/cm)
	$N_i$ ( $10^{17} \text{ cm}^{-3}$ )	$V_b$ (eV)	$F_s$ (kV/cm)	$N_i$ ( $10^{17} \text{ cm}^{-3}$ )	$V_b$ (eV)	$F_s$ (kV/cm)	
Ga-face	8.3	1.78	750	11	1.45	780	30
N-face	6.2	0.93	469	8.4	0.95	554	85

<sup>a)</sup> Change of the surface electric field strength between room and helium temperature

### AlGaIn/GaN heterostructures

Figure 3 shows PR spectra at 5 K and 295 K for a heterostructure with Al content of the barrier of  $x=0.06$ . Contributions at lower photon energies and at higher ones are clearly resolved which arise from the MBE grown GaN layer and the AlGaIn barrier layer, respectively. The latter signal is related to the Franz-Keldysh effect allowing for the determination of the barrier field strength  $F_B$  using the asymptotic expression [17]

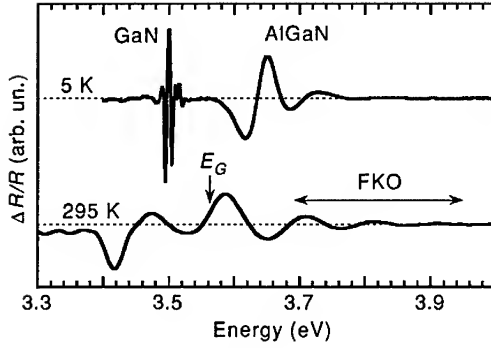


**Figure 3.** Photoreflectance spectra for a Ga-face  $\text{Al}_{0.06}\text{Ga}_{0.94}\text{N}/\text{GaN}$  HEMT heterostructure.

$$\frac{\Delta R}{R} \sim \frac{1}{E^2(E-E_G)} \exp\left[\frac{-2\Gamma(E-E_G)^{1/2}}{(\hbar\theta)^{3/2}}\right] \cos\left[\frac{4}{3}\left(\frac{E-E_G}{\hbar\theta}\right)^{3/2} + \varphi\right] \quad (2)$$

where  $E$  is the photon energy,  $E_G$  is the band gap of AlGaN,  $\Gamma$  is the broadening energy,  $(\hbar\theta)^{3/2} = F_B e \hbar / (2m_r)^{1/2}$ ,  $m_r$  is the electron-hole reduced effective mass, and  $\varphi$  is a phase angle. As it can be seen from figure 3, the splitting between adjacent extrema of the FKOs decreases with temperature indicating a lowering of the field strength. Such behavior has been verified in a temperature range from 150 K to 295 K for all heterostructures. At low temperatures, the analysis based on equation (2) was possible not for all samples because of the observed strong damping of FKOs. The results are summarized in table II. We found significantly larger changes of electric fields in the barriers of AlGaN/GaN heterostructures compared to the diodes. This is related to a strong temperature dependence of piezoelectric induced surface charges because the strains in the GaN buffer layer and the AlGaN barrier layer are temperature dependent as indicated by energetic positions of free exciton lines [18].

**Table II.** Sheet carrier density, mobility, barrier thickness, and barrier electric field strength for AlGaN/GaN heterostructures.

Al content	$n_s$ ( $10^{12} \text{ cm}^{-2}$ )	$\mu$ ( $\text{cm}^2 \text{ V}^{-1} \text{ s}^{-1}$ )	$d_B^a)$ (nm)	$F_B$ (kV/cm)		$\Delta F_B^b)$ (kV/cm)
				5 K	295 K	
0.06	1.0 <sup>c)</sup>	8900 <sup>c)</sup>	16	205	335	130
0.09	3.7 <sup>c)</sup>	9100 <sup>c)</sup>	30	-	260	-
0.10	1.85 <sup>c)</sup>	17200 <sup>c)</sup>	18	-	305	-
0.10	2.25 <sup>d)</sup>	25660 <sup>d)</sup>	23	-	255	-

<sup>a)</sup> Data of spectroscopic ellipsometry study

<sup>c)</sup> Change of barrier electric field between room and helium temperature

<sup>b)</sup> Hall effect measurements at  $T = 77 \text{ K}$

<sup>d)</sup> Hall effect measurements at  $T = 330 \text{ mK}$

In conclusion, we have demonstrated that three mechanisms of electro-optical response, (a) electric field-dependent contribution of discrete excitons and excitonic continuum to the DF, (b) LEO effect, and (c) Franz-Keldysh effect (in the high-field regime) determine the ER and PR of Pt/GaN Schottky diodes and AlGaIn/GaN HEMT heterostructures. Analysis of experimental data in dependence on photon energy and bias voltage using the electric field-dependent DF provides the possibility to determine the electric field strength and parameters of the depletion region, such as ionized impurity concentration and surface band bending. The electric fields in the diodes and barriers of the heterostructures were found to increase with temperature which is related to temperature dependent densities of ionized impurities and surface charges.

## ACKNOWLEDGMENTS

The groups from Ilmenau University acknowledge financial support by the Thuringia Ministry of Science, Research, and Art under contract No. B609-02004. Part of the work was supported by the Deutsche Forschungsgemeinschaft (STU139/2).

## REFERENCES

1. H. Shen and M. Dutta, *J. Appl. Phys.* **78**, 2151 (1995).
2. C. Wetzel, T. Takeuchi, H. Amano, and I. Akasaki, *J. Appl. Phys.* **85**, 3786 (1999).
3. Y.T. Hou, K.L. Teo, M.F. Li, K. Uchida, H. Tokunaga, N. Akutsu, and K. Matsumoto, *Appl. Phys. Lett.* **76**, 1033 (2000).
4. S.R. Kurtz, A.A. Allerman, D.D. Koleske, and G.M. Peake, *Appl. Phys. Lett.* **80**, 4549 (2002).
5. J.D. Dow and D. Redfield, *Phys. Rev. B* **1**, 3358 (1970).
6. F. Blossey, *Phys. Rev. B* **2**, 3976 (1970).
7. F. Blossey, *Phys. Rev. B* **3**, 1382 (1971).
8. F. Binet, J.Y. Duboz, E. Rosencher, F. Scholz, and V. Härle, *Phys. Rev. B* **54**, 8116 (1996).
9. S. Shokhovets *et al.*, *Phys. Status Solidi B* (in press).
10. S. Shokhovets, R. Goldhahn, and G. Gobsch, *Mater. Sci. Eng. B* **93**, 215 (2002).
11. U. Karrer, O. Ambacher, and M. Stutzmann, *Appl. Phys. Lett.* **77**, 2012 (2000).
12. I.P. Smorchkova, C.R. Elsass, J.P. Ibbetson, R. Vetury, B. Heying, P. Fini, E. Haus, S.P. DenBaars, J.S. Speck, and U.K. Mishra, *J. Appl. Phys.* **86**, 4520 (1999).
13. G. Martínez-Criado, C.R. Miskys, A. Cros, O. Ambacher, A. Cantarero, and M. Stutzmann, *J. Appl. Phys.* **90**, 5627 (2001).
14. K. Kornitzer, T. Ebner, K. Thonke, R. Sauer, C. Kirchner, V. Schwegler, M. Kamp, M. Leszczynski, I. Grzegory, and S. Porowski, *Phys. Rev. B* **60**, 1471 (1999).
15. B. Gil, in *Semiconductors and Semimetals*, v. 57, Volume Editors J.I. Pankove and T.D. Moustakas (Academic Press, San Diego, USA, 1999), p. 209.
16. W. Götz, N.M. Johnson, C. Chen, H. Liu, C. Kuo, and W. Imler, *Appl. Phys. Lett.* **68**, 3144 (1996).
17. D.E. Aspnes, *Phys. Rev. B* **10**, 4228 (1974).
18. R. Goldhahn *et al.*, *Phys. Status Solidi B* (in press).

### EFFECT OF OXYGEN PRESSURE ON MAGNESIUM OXIDE DIELECTRICS GROWN ON GaN BY PLASMA ASSISTED GAS SOURCE MOLECULAR BEAM EPITAXY

A. H. Onstine<sup>1</sup>, B. P. Gila<sup>1</sup>, J. Kim<sup>2</sup>, D. Stodilka<sup>1</sup>, K. Allums<sup>1</sup>, C. R. Abernathy<sup>1</sup>, F. Ren<sup>2</sup> and S. J. Pearton<sup>1</sup>

<sup>1</sup> Department of Materials Science and Engineering, University of Florida, Gainesville, FL 32611

<sup>2</sup> Department of Chemical Engineering, University of Florida, Gainesville, FL 32611

#### ABSTRACT

The effect of oxygen pressure on MgO grown by RF plasma assisted gas-source molecular beam epitaxy was investigated. Increasing oxygen pressure was found to decrease the growth rate, improve the morphology and reduce the Mg/O ratio to near that obtained from bulk single crystal MgO. By contrast, the electrical characteristics of MgO/GaN diodes showed continual improvement in breakdown field and interface state density as the pressure was decreased. The lowest pressure tested,  $1 \times 10^{-5}$  Torr, produced the lowest  $D_{it}$ ,  $3 \times 10^{11} \text{ eV}^{-1} \text{ cm}^{-2}$ , and the highest  $V_{BD}$ , 4.4 MV/cm. Cross sectional transmission electron microscopy of the MgO grown at the lowest pressure showed the initial 40 monolayers to be epitaxial, with the remainder of the layer appearing to be fine grained poly-crystal. Comparisons with films grown using an electron cyclotron resonance (ECR) plasma suggest that higher ion energies are desirable for obtaining the best electrical characteristics.

#### INTRODUCTION

MgO is a rock salt dielectric which has been explored as an intermediate buffer layer for growth of ferroelectric materials on semiconductors [1,2] or as a potential gate dielectric for GaAs [3,4] or Si.[2] While MgO deposition by MBE has been successfully demonstrated by a number of groups, the crystal quality of the films deposited on GaAs and Si has been poor due to the large lattice mismatch between the MgO and the semiconductor substrate. GaN has a smaller lattice constant than GaAs and is thus a much closer match to MgO. [5,6] An additional advantage of this system is the large bandgap and thus large band offsets that are expected relative to either an n- or p-type semiconductor. Further, the dielectric constant for MgO, 9.8, is substantially higher than for SiO<sub>2</sub>. We have previously reported on the feasibility of using MgO as a gate dielectric for GaN [7,8] and as a field passivation dielectric for GaN HFET power devices [9]. In this paper we will discuss the optimization of the plasma conditions for growth of MgO dielectrics on GaN.

#### EXPERIMENTAL

MgO films were deposited using a RIBER 2300 MBE equipped with a reflection high-energy electron diffraction (RHEED) system and an Oxford radio frequency (RF) oxygen plasma source operating at 13.56 MHz. The RF power was set at 300W. For comparison, some films were also grown with a Wavemat MPDR electron cyclotron resonance (ECR) oxygen plasma source. In all cases, two-micron thick GaN layers grown on sapphire (0001) by MOCVD were

used as substrates. Elemental Mg from a standard effusion cell at 380°C supplied the Mg. Films were grown using a variety of oxygen pressures,  $1 \times 10^{-5}$  -  $1 \times 10^{-4}$  Torr, in order to evaluate the effect of oxygen pressure. The substrate temperature was measured using a backside thermocouple. All MgO layers were grown with a substrate temperature of 100°C. The MgO layers grow with a (111) orientation relative to the GaN basal plane as determined by both RHEED and XRD.

The GaN substrate preparation began with a wet chemical etch of HCl:H<sub>2</sub>O (1:1) for 3 minutes, followed by a DI rinse, for an initial cleaning of the substrate surface. Next, a UV-ozone exposure for 25 minutes in a UV Cleaner model 42-220 was used to assist in the removal of the carbon contamination. Finally a dip in buffered oxide etch (6:1, ammonium fluoride: hydrofluoric acid) for 5 minutes was used to remove most of the surface oxide. At room temperature, the surfaces of the substrates were polycrystalline according to RHEED images. Upon heating the GaN to 700°C, a streaky (1x3) pattern appears. This was the starting surface for all the films grown in this study. Structural and chemical characterization of the MgO was obtained using reflection high-energy electron diffraction (RHEED), scanning electron microscopy (SEM), cross-sectional transmission electron microscopy (XTEM), atomic force microscopy (AFM) and depth profiling Auger electron spectroscopy (AES). Electrical characterization consisted of I-V and C-V analysis of 80 micron diodes fabricated using Ti/Al/Pt/Au (20nm/70nm/40nm/100nm) Ohmic contacts and Pt/Au (20nm/100nm) Schottky gate contacts.

## RESULTS AND DISCUSSION

To study the effect of oxygen pressure on the properties of the MgO, several different pressures,  $1 \times 10^{-5}$ ,  $3 \times 10^{-5}$ ,  $7 \times 10^{-5}$  and  $1 \times 10^{-4}$  Torr as measured by the beam flux gauge, were investigated. The higher pressures produced a decrease in the growth rate, as shown in Figure 1. From AES, the films were shown to contain only Mg and oxygen, with the Mg/O ratio decreasing from 0.72 to 0.63 as the pressure was increased. By comparison, the ratio of Mg/O peak heights of a standard single crystalline sample of MgO was measured and showed the ratio to be 0.60. The reduction in growth rates at higher pressures may be an indication of a lack of reactive oxygen species at the surface or of site blocking due to the higher concentration of oxygen absorbed on the surface. Both would result in a reduction in the Mg sticking coefficient. The lower Mg/O ratio at the higher pressures would seem to favor the site blocking explanation.

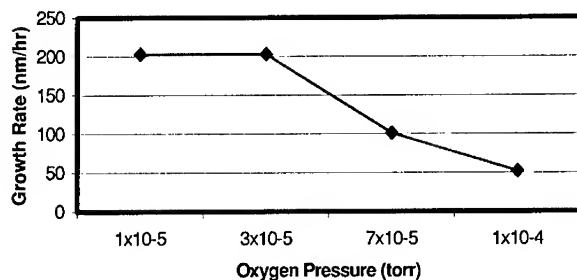
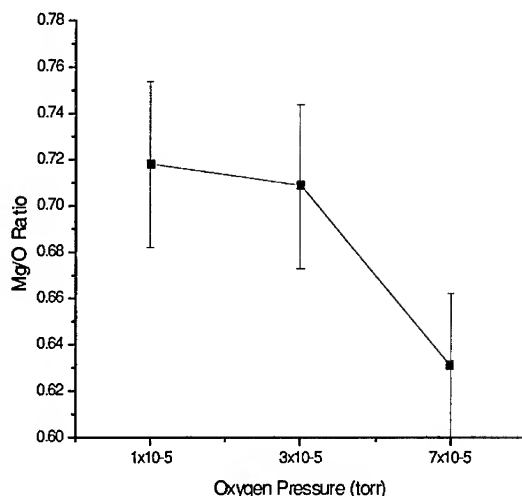


Figure 1. Dependence of growth rate on oxygen pressure.



**Figure 2.** Mg/O ratio as determined by AES as a function of oxygen pressure.

AFM analysis, shown in Figure 3, indicated that as the pressure was increased the surface morphology became smoother, as evidenced by the decrease in RMS roughness from 0.998nm at a pressure of  $1 \times 10^{-5}$  Torr to 0.247 nm at  $1 \times 10^{-4}$  Torr. All of the films appeared smooth when examined by SEM. XTEM of the MgO grown at the lowest pressure showed the initial 40 monolayers to be epitaxial, with the remainder of the layer appearing to be fine-grained polycrystal. The precise microstructure of the films grown at higher pressures is not yet known. It is quite likely that given the superior morphology these films retained their single crystal nature for a greater percentage of their thickness before becoming polycrystalline.

From the structural and compositional analysis it would appear that higher oxygen pressures are beneficial to the growth of the MgO layers. However, electrical characterization of MgO/GaN diodes suggests the opposite. As shown in Table I, the breakdown field,  $V_{BD}$ , and interface state density,  $D_{it}$ , improve with decreasing oxygen pressure. It was also found that the fixed oxide charge decreases with decreasing pressure. Ironically, the reduction in dielectric strength may be due to superior microstructure in the films grown at higher pressures. Previous work with other dielectrics such as  $Gd_2O_3$  has shown that if the layer does not contain a substantial polycrystalline region, then the breakdown field will be substantially lowered due to leakage through the defects, which propagate through the layer. The presence of a nanocrystalline layer on top of the single crystal material at the interface appears to improve the breakdown strength of the layer in spite of the presence of numerous grain boundaries.

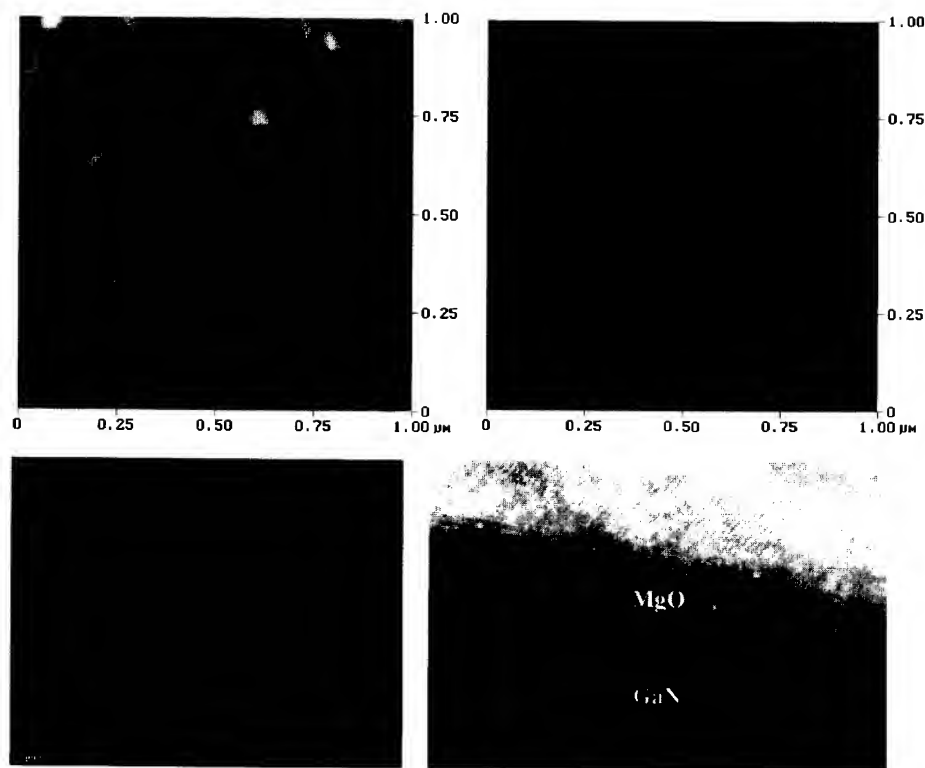


**Figure 3.** AFM scans of MgO grown at 100C using an oxygen pressure of (at left)  $1 \times 10^{-5}$  Torr, or (at right)  $1 \times 10^{-4}$  Torr. The RMS roughnesses were 0.998 nm and 0.247 nm respectively. An SEM image (10,000x) of the MgO layer grown at  $1 \times 10^{-5}$  Torr is shown at bottom left and an XTEM image of the same layer is shown at bottom right.

The effect of pressure on interface and bulk charge densities suggests that the electrical behavior of the layer is enhanced by the presence of higher ion energy species at the surface. Since the total power to the plasma is fixed, increasing the oxygen flow will decrease the average energy per ion, and possibly the concentration of ionized species as well. Studies with electron cyclotron resonance (ECR) plasmas suggest that the average ion energy is a critical parameter. ECR plasmas typically exhibit very low ion energies. MgO films grown using an ECR plasma with similar oxygen pressures to those used in the RF grown films exhibit breakdown fields which are up to four times lower than those obtained with RF plasmas. Work is in progress to further explore the role of ion energy by depositing layers at fixed oxygen pressure with a variety of RF powers. It is likely that as the ion energy is increased, damage of the interface will eventually become a factor and begin to increase the interface state density. Clearly, however, this does not occur at standard pressures and powers making RF plasmas the optimum choice for deposition of MgO dielectrics on GaN.

**Table I.** Electrical characterization of MgO/GaN diodes.  $V_{BD}$  was the applied voltage, which produced a leakage current of  $1\text{ mA/cm}^2$ .  $D_{it}$  was the defect value at  $0.4\text{ eV}$  below the conduction band calculated using the Terman method. The diode grown at  $1 \times 10^{-4}$  Torr was too leaky to be measured.

Oxygen Pressure (Torr)	$V_{BD}$ (MV/cm)	$D_{it}$ ( $\text{eV}^{-1}\text{cm}^{-2}$ )
$1 \times 10^{-5}$	4.4	$3.4 \times 10^{11}$
$3 \times 10^{-5}$	4	$7.1 \times 10^{11}$
$7 \times 10^{-5}$	1.2	$1.8 \times 10^{12}$

## CONCLUSION

Increasing the oxygen pressure during growth of MgO was found to improve the morphology and produced an MgO closer to that obtained for single crystal MgO. By contrast, electrical characterization of MgO/GaN diodes showed the best breakdown field and interface state density in films grown at lower oxygen pressures. It is believed that the superior electrical behavior at lower oxygen pressures is due to the higher ion energy obtained at the lower pressures. This is in agreement with the poorer electrical characteristics obtained using ECR oxygen plasmas, which produce significantly lower ion energies than RF plasmas. Further work investigating the role of ion energy at fixed oxygen pressure is in progress.

## ACKNOWLEDGEMENTS

The authors gratefully acknowledge the support of this work by the U. S. Office of Naval Research under grant no. US Navy N00014-98-1-0204 and by the U. S. Air Force Office of Scientific Research under grant no. U. S. Air Force F49620-02-1-0366

## REFERENCES

1. E. S. Hellman and E. H. Hartford, *Appl. Phys. Lett.*, **64**, 1341 (1994).
2. F. Niu, B. H. Hoerman and B. W. Wessels, *J. Vac. Sci. and Technol. B*, **18**, 2146 (2000).
3. E. J. Tarsa, X. H. Wu, J. P. Ibbetson, J. S. Speck, J. J. Zinck, *Appl. Phys. Lett.*, **66**, 3588 (1995).
4. M. Hong, M. Passlack, J. P. Mannaerts, J. Kwo, S. N. G. Chu, N. Moriya, S. Y. Hou and V. Fratello, *J. Vac. Sci. Technol. B*, **14**, 2297 (1996).
5. N. Daude, C. Jouanin and C. Gout, *Phys. Rev. B*, **15**, 2399 (1977).
6. G. V. Samsonov, *The Oxide Handbook*, Plenum, New York, 1973, and references therein.
7. J. Kim, B. Gila, R. Mehandru, J. W. Johnson, J. H. Shin, K. P. Lee, B. Luo, A. Onstine, C. R. Abernathy, S. J. Pearton, F. Ren, *Journal of The Electrochemical Society*, **149** (8) G482 (2002).
8. J. Kim, R. Mehandru, B. Luo, F. Ren, B.P. Gila, A.H. Onstine, C.R. Abernathy, S.J. Pearton, Y. Irokawa, *Appl. Phys. Lett.*, **80**, 4555 (2002).

- 
9. J.K. Gillespie, R.C. Fitch, J. Sewell, R. Dettmer, G.D. Via, A. Crespo, T.J. Jenkins, B. Luo, R. Mehandru, J. Kim, F. Ren, B.P. Gila, A.H. Onstine, C.R. Abernathy, S.J. Pearton, *IEEE Electron Device Letters*, **23**(9), 505 (2002)

---

## **Epitaxy—Nonpolar Orientations and Alloys**

### Morphology and surface reconstructions of m-plane GaN

C. D. Lee,<sup>1</sup> R. M. Feenstra,<sup>1</sup> J. E. Northrup,<sup>2</sup> L. Lymerakis,<sup>3</sup> J. Neugebauer<sup>3</sup>

<sup>1</sup>Department of Physics, Carnegie Mellon University, Pittsburgh, PA 15213

<sup>2</sup>Palo Alto Research Center, 3333 Coyote Hill Road, Palo Alto, CA 94304

<sup>3</sup>Fritz-Haber-Institut der Max-Planck-Gesellschaft, Faradayweg 4-6, D-14195 Berlin, Germany

#### ABSTRACT

M-plane GaN(1 $\bar{1}$ 00) is grown by plasma assisted molecular beam epitaxy on ZnO(1 $\bar{1}$ 00) substrates. A low-temperature GaN buffer layer is found to be necessary to obtain good structural quality of the films. Well oriented (1 $\bar{1}$ 00) GaN films are obtained, with a slate like surface morphology. On the GaN(1 $\bar{1}$ 00) surfaces, reconstructions with symmetry of c(2x2) and approximate "4x5" are found under N- and Ga-rich conditions, respectively. We propose a model for Ga-rich conditions with the "4x5" structure consisting of  $\geq 2$  monolayers of Ga terminating the GaN surface.

#### INTRODUCTION

Wurtzite GaN heteroepitaxy and surface reconstructions have been extensively studied in the past 5-10 years [1,2]. It is well known that GaN films with (0001) and (000 $\bar{1}$ ) surface orientations have pyroelectric and piezoelectric properties [3,4], leading to strong electric fields along the crystal c-axis which have useful device applications such as the formation of a two-dimensional electron gas near a heterointerface. However these strong electric fields also produce a shift in the wavelength of emission lines and reduced quantum efficiency because of the spatial separation of electrons and holes in quantum wells. Thus, several growth studies of (1 $\bar{1}$ 00) oriented (m-plane) GaN have been performed, since for this orientation the crystal symmetry precludes pyroelectric and piezoelectric effects (at least in the absence of shear stresses in the growth plane) [5-7].

In this work we have used plasma assisted molecular beam epitaxy (PAMBE) to grow GaN films on ZnO(1 $\bar{1}$ 00) substrates. We find that a low temperature ( $\sim 500^\circ\text{C}$ ) buffer layer is needed to obtain smooth morphology. Several reconstructions on the GaN(1 $\bar{1}$ 00) surfaces are observed for both Ga- and N-rich conditions. The most dominant of these occurs under Ga-rich conditions and it has an approximate surface unit cell of 4x5. We propose a model for this structure in which it consists of a contracted and distorted arrangement of a Ga bilayer on the surface.

#### EXPERIMENTAL

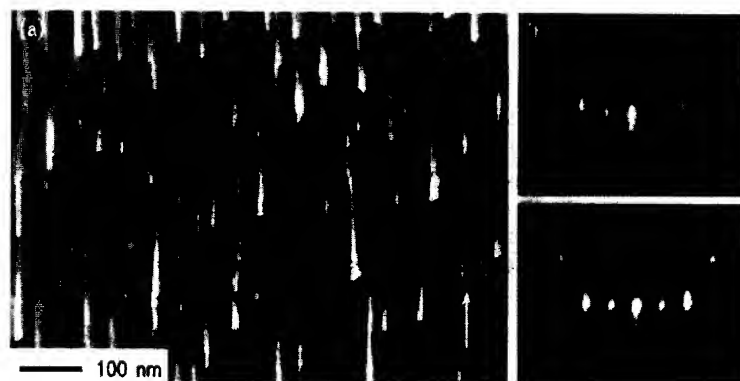
ZnO(1 $\bar{1}$ 00) substrates were obtained from Cermet, Inc. The substrates were prepared by mechanical polishing; atomic force microscopy (AFM) revealed many scratches and polishing marks on the substrate surfaces. The MBE growth and subsequent scanning tunneling microscopy (STM) were performed using a system previously described [1,2]. The ZnO substrates were cleaned inside the growth chamber prior to growth simply by heating them to about  $550^\circ\text{C}$  for 20 min. Growth was initiated by exposing the ZnO surface simultaneously to

incident Ga and N fluxes. A  $\approx 20$  nm thick GaN layer is grown at a relatively low temperature of about  $500^{\circ}\text{C}$ , and subsequent growth was performed at about  $700\text{--}750^{\circ}\text{C}$ . If growth is performed in the absence of the low temperature buffer layer, a very spotty RHEED pattern forms during the initial stages of growth, indicating a rough morphology. Similar spotty RHEED patterns are obtained whenever the ZnO is exposed to the Ga beam at a temperature of  $>550^{\circ}\text{C}$  (i.e. in the absence of the low temperature buffer), possibly indicating a reaction between Ga atoms and O atoms leading to the dissociation of ZnO. Although we do not know the detailed chemical reactions occurring on the substrate, the low temperature ( $\sim 500^{\circ}\text{C}$ ) growth certainly results in a significant improvement of surface morphology. During and following the growth the surface is characterized by reflection high energy electron diffraction (RHEED). After the growth the samples were cooled and transferred under ultra high vacuum to an adjoining analysis chamber for STM study.

## RESULTS & DISCUSSION

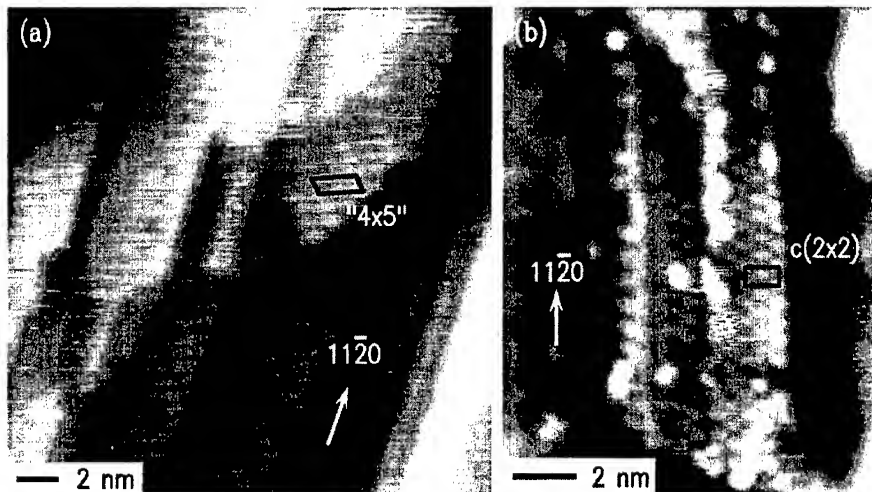
### Experiment

Figure 1(a) shows a typical surface morphology for our m-plane GaN films, grown with thicknesses of about  $0.5\text{ }\mu\text{m}$  grown and generally under similar Ga-rich growth conditions as used for our c-plane growth [8]. RHEED study reveals that the films have the same in-plane orientation as the substrate, i.e. with GaN(0001)//ZnO(0001) and GaN( $11\bar{2}0$ )//ZnO( $11\bar{2}0$ ), thereby demonstrating the ( $1\bar{1}00$ ) orientation of the films. The substrates have an unintentional miscut of several degrees oriented primarily towards the [0001] direction, thus producing the steps seen extending vertically in the image. In Fig 1(a), large flat GaN( $1\bar{1}00$ ) terraces are found. The terraces tend to be elongated in the  $[11\bar{2}0]$  direction, forming a slate like morphology. The surface morphology and the lattice constants obtained from RHEED are similar to that reported by Waltereit et al. [5]. RHEED patterns of the films are streaky, as shown in Fig. 1(b), consistent with the flat terraces observed in the morphology. The RHEED shows a streaky  $1\times 1$  pattern throughout the entire growth sequence when Ga-rich conditions are used. Consistent with our prior c-plane GaN growth on SiC [8], growth under N-rich conditions results



**FIG 1** (a) STM image of GaN film grown on ZnO ( $1\bar{1}00$ ) substrate. (b) and (c) RHEED patterns (with electron beam along  $[11\bar{2}0]$ ) acquired under Ga-rich and N-rich conditions, respectively.

BEST AVAILABLE COPY



**FIG 2** (a) STM image of Ga-rich GaN( $1\bar{1}00$ ) surface. The image was acquired with a sample voltage of  $-2.0$  V and is displayed with a gray scale range of  $8.5$  Å. (b) STM image of nitrided surface showing reconstruction with  $c(2\times 2)$  unit cell. The image was acquired with a sample voltage of  $-1.0$  V and is displayed with a gray scale range of  $3.0$  Å.

in spotty RHEED patterns indicative of 3-dimensional growth as shown in Fig. 1(c). For thicker films the RHEED patterns display a clear evidence of facetting, as described elsewhere [7].

We have observed several reconstructions on the GaN( $1\bar{1}00$ ) terraces, with our clearest observations being for films grown under Ga-rich conditions as pictured in Fig. 2(a). Terraces extending in the  $[11\bar{2}0]$  direction are seen there separated by narrow trenches and/or raised rows of atoms. The triangular shape of step edges seen in Fig. 2(a) are often observed. We note that the elongation along the  $[11\bar{2}0]$  direction is the same as recently reported for films grown by metal-organic chemical vapor deposition. [8]. This anisotropic morphology may arise from an anisotropy in the migration lengths of adatoms. A reconstruction of the surface is visible in Fig. 2(a); the slightly brighter rows of atoms seen there extend at angles of  $\pm 22^\circ$  away from the  $[11\bar{2}0]$  direction (these angles are slightly distorted in Fig. 2(a), due to drift). A unit cell is indicated in the image. As discussed in the following section, and described in detail elsewhere [7], the basis vectors for this unit cell are  $4\mathbf{a} + \mathbf{c}$  and  $-\mathbf{a} + 5\mathbf{c}$ , where  $\mathbf{a}$  and  $\mathbf{c}$  span the  $1\times 1$  surface unit cell. The structure thus contains  $21\ 1\times 1$  cells. This surface unit cell can be constructed from a  $4\mathbf{a}\times 5\mathbf{c}$  cell by slightly rotating and shearing it, and so for a shorthand notation we refer to our observed structure as " $4\times 5$ " (including quotation marks to indicate an approximate symmetry). This surface appears to be metallic since relatively little difference is found between the empty and filled states images, and imaging at low voltages of  $\pm 0.1$  V is found to be possible [7].

Figure 2(b) shows an STM image obtained from the surface which had been nitrided for 1 min following growth. A different reconstruction is observed here than in Fig. 2(a). We find a

$c(2\times 2)$  unit cell as indicated in the image. RHEED patterns for this film display weak  $2\times$  streaks for both the  $[0001]$  and  $[11\bar{2}0]$  azimuths. This type of structure has been observed reproducibly on surfaces prepared under N-rich conditions, but we have not investigated in detail its voltage dependence nor the underlying geometric arrangement of atoms.

### Theory

Theoretical studies on  $\text{GaN}(1\bar{1}00)$  surfaces have been reported in previous studies [7,9]. Initially, the focus was on structural models similar to those found on cubic III-V  $(110)$  surfaces, i.e., models which have a  $1\times 1$  surface unit cell and obey electron counting [9]. These structures are characterized by two threefold coordinated surface atoms in each  $1\times 1$  cell. In the stoichiometric case the two atoms are a Ga and a N atom, and the surface is stabilized by a charge transfer from the cation to the anion dangling bond and a subsequent rehybridization causing the N to move slightly outward and the Ga to move slightly inward. This surface, which would be expected to be present following cleavage or cracking, has been found to be energetically favorable over a large range of the thermodynamically allowed chemical potentials. However, when going to rather Ga-rich conditions (i.e., to conditions realized in the experiments described here) structures with excess Ga atoms become more stable [7,9]. These structures are formed from the stoichiometric structure by (i) replacing the N surface atom in the  $1\times 1$  surface cell by a Ga atom and/or (ii) by adding two monolayers (ML, defined as one atom per  $1\times 1$  cell) Ga on top of this surface. Since the Ga-Ga spacing in the Ga adlayer is slightly larger than in Ga bulk, an additional lowering of the surface energy might be achieved by compressing the Ga atoms in the top layer such that their density approaches something close to that of Ga bulk. In Ref. [7] we have briefly discussed the energetics of such a structure without giving details regarding the calculational approach, geometry or construction of the surface. Below we provide this additional information.

To set up the structure we combined the structural information from the STM data regarding size, symmetry and orientation of the surface unit cell and with the energetical considerations from the *ab initio* calculations. Specifically, we constructed a surface which has the experimentally observed " $4\times 5$ " unit cell and in which the rows of Ga atoms in the adlayer follow the outline of this cell. The structure is pictured in Fig. 3. It consists of the stoichiometric surface containing 21 Ga-N dimers, on top of which is placed a compressed Ga adlayer consisting of 45 atoms (see Fig. 3(a)). The adlayer thus corresponds to a Ga coverage of  $45/21=2.14$  ML.

A direct calculation of this structure using the same pseudopotentials (LDA Troullier Martins pseudopotentials with Ga  $3d$  in the valence), plane wave energy cutoff (60 Ry), and slab thickness (4 layers) as for the  $1\times 1$  structures [9] turned out to be computationally too expensive. We have therefore performed careful convergence checks to identify a parameter set which minimizes the computational effort but still allows to obtain accurate surface geometries and energies. Based on these results we found that using PBE-GGA Troullier Martins pseudopotentials where the Ga  $3d$  orbitals are treated in the non-linear core approximation, an energy cutoff of 30 Ry and a slab thickness of 2 GaN layers plus the Ga adlayer are sufficient to describe the surface energy with an accuracy of better than  $0.005$  eV/ $\text{\AA}^2$ , and the surface geometry better than  $0.027$   $\text{\AA}$ , for Ga-rich surface structures. We note that e.g. for stoichiometric surface structures significantly larger error bars result. To be more specific, let us consider the

BEST AVAILABLE COPY

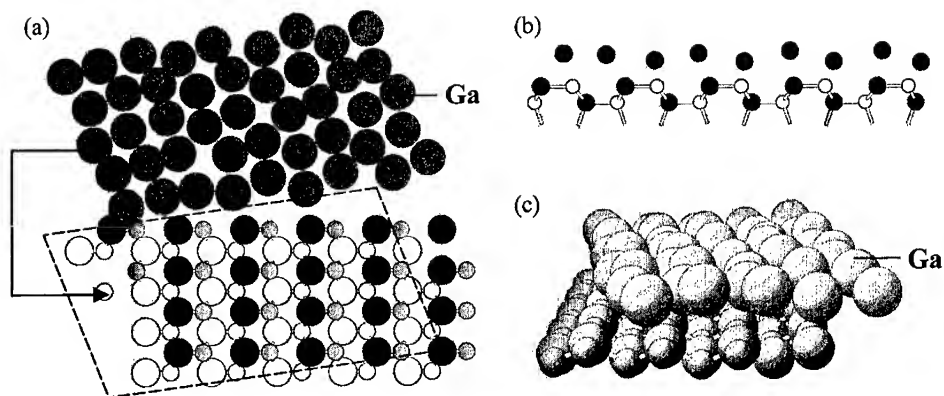


**FIG 3** (color) Schematic view of the reconstructed and compressed Ga adlayer GaN( $1\bar{1}00$ ) surface. (a) top view with "4x5" cell shown by the dashed line, (b) side view and (c) perspective view. In (a), large black or small gray filled circles mark the Ga or N atoms, respectively, in the top surface layer. The large green (or grey, if not viewed in color) filled circles mark the positions of the Ga atoms in the Ga adlayer, as indicated.

convergence of the surface energy with respect to the slab thickness for the stoichiometric (SD) and the adlayer (SD+2) structure (SD indicates here a single GaN dimer, +2 stands for adding 2 ML of Ga). We find that the energy of the stoichiometric surface significantly increases when going from a two to a four layer slab (by more than  $0.025 \text{ eV}/\text{\AA}^2$ ) while it changes less than  $0.005 \text{ eV}/\text{\AA}^2$  for the adlayer structure. An analysis showed that the origin of the different convergence behavior lies in the presence/absence of nitrogen dangling bond states. The presence of N dangling bond states causes (as described above) charge transfer, rehybridization and eventually a rather strong atomic relaxation of the N bond. Since the N forms stiff bonds with the neighboring Ga atoms this effect causes considerable strain in the lattice which decays only slowly with increasing slab thickness. On the other hand, adding a Ga adlayer prevents the formation of N dangling bonds and the N atoms stay close to their bulk positions. In this case strain effects in the GaN layer turn out to be negligible.

Using the above described parameter set we have performed a geometry optimization for the structure. To destroy the initially high symmetry of the surface we adsorbed a single adatom and removed it after performing a few atomic steps. The resulting equilibrium geometry is shown in Figs. 3(a-c). As can be seen the Ga adlayer buckles and forms a low symmetry structure. The underlying Ga-N layer, however, is virtually not affected and the atoms are close to their corresponding bulk positions. A closer analysis showed that the low symmetry of the Ga adlayer and the large buckling ( $\sim 0.8 \text{ \AA}$ ) is related to the fact that the Ga atoms in the Ga adlayer are out of registry to the underlying Ga-N surface layer.

The out of registry arrangement of the Ga adlayer also affects the stability of this surface: While the compression of the Ga adlayer is expected to strengthen the Ga-Ga bonds and thus the stability of the surface, the out of registry arrangement weakens the Ga-N bonds. Our total energy calculations show that the two effects almost cancel each other – the energy of the compressed Ga-adlayer structure under very Ga-rich conditions is practically the same as the

energy of the uncompressed 2 ML Ga adlayer structures considered previously [7]. It is possible that further optimization of the geometry (i.e. considering other arrangements and/or other densities of the adlayer) may produce a reduction in energy. In any case, judging from the experimental STM images, the arrangement of the adlayer must indeed be a rather complicated one. The investigation described here establishes the energetic feasibility of such structures containing >2 ML of Ga, and further work is required to definitively determine the complete structural arrangement.

## CONCLUSION

In conclusion, we have grown (1  $\bar{1}$  00) oriented GaN films on ZnO. Under Ga rich conditions a "4×5" reconstruction is observed. Experimentally this structure appears to be metallic, indicating that it consists of an adlayer of Ga on the surface, in analogy with the known structures of (000  $\bar{1}$ ) and (0001) surfaces [1,2]. Theoretical computations indicate that  $\geq 2$  monolayers of Ga terminating the GaN crystal is energetically favorable, under Ga-rich conditions. We have investigated in detail a distorted, compressed adlayer structure containing 2.14 ML of Ga, and find that its energy is nearly the same as that of the uncompressed 2 ML adlayer.

## ACKNOWLEDGMENTS

This work has been supported by the Office of Naval Research under grant N00014-96-1-0214 (program monitor, C. Wood), the Deutsche Forschungsgemeinschaft SFB "296", and the EU TMR program IPAM.

## REFERENCES

- [1] A. R. Smith, R. M. Feenstra, D. W. Greve, J. Neugebauer, J. E. Northrup, Phys. Rev. Lett. **79**, 3934 (1997).
- [2] A. R. Smith, R. M. Feenstra, D. W. Greve, M.-S. Shin, M. Skowronski, J. Neugebauer, J. E. Northrup, Surf. Sci. **423**, 70 (1999).
- [3] A. Bykhovski, B. Gelmont, and M. Shur, J. Appl. Phys. **74**, 6734 (1993).
- [4] F. Bernardini, V. Fiorentini, and D. Vanderbilt, Phys. Rev. B **56**, R10024 (1997).
- [5] P. Waltereit, O. Brandt, M. Ramsteiner, A. Trampert, H. T. Grahn, J. Menniger, M. Reiche, R. Uecker, P. Reiche, and K. H. Ploog, Phys. Stat. Sol. (a) **180**, 133 (2000).
- [6] C. Q. Chen, M. E. Gaevski, W. H. Sun, E. Kuokstis, J. P. Zhang, R. S. Q. Fareed, H.M. Wang, J. W. Yang, G. Simin, M. A. Khan, H.-P. Maruska, D. W. Hill, M. M. C. Chou, and B. Chai, Appl. Phys. Lett. **81**, 3194 (2002).
- [7] C. D. Lee, R. M. Feenstra, J. E. Northrup, L. Lymperakis, and J. Neugebauer, submitted to Appl. Phys. Lett.
- [8] C. D. Lee, V. Ramachandran, A. Sagar, R. M. Feenstra, D. W. Greve, W. L. Sarney, L. Salamanca-Riba, D. C. Look, S. Bai, W. J. Choyke, and R. P. Devaty, J. Electron. Mater. **30**, 162 (2001).
- [9] J. E. Northrup and J. E. Neugebauer, Phys. Rev. B **53**, R10477 (1996).

BEST AVAILABLE COPY

## GaN epilayers and AlGaN/GaN multiple quantum wells grown on freestanding [1 $\bar{1}$ 00] oriented GaN substrates

C. Q. Chen,\* M. E. Gaevski,\* W. H. Sun,\* E. Kuokstis,\* J. W. Yang,\* G. Simin,\* M. A. Khan,\* H.P. Maruska,\*\* D. W. Hill,\*\* M. M. C. Chou,\*\* J. J. Gallagher,\*\* B. H. Chai,\*\* J. H. Song,\*\*\* M. Y. Ryu,\*\*\* P. W. Yu\*\*\*

\*Depart. of Electr. Engineering, University of South Carolina, Columbia, SC29208, USA

\*\*Crystal Photonics, Inc., Sanford, FL 32773, USA

\*\*\*Dept. of Information and Communications, Kwangju Institute of Science and Technology, Kwangju, 500-712, Republic of Korea

### Abstract

We report on the homoepitaxial growth of GaN on freestanding [1 $\bar{1}$ 00] oriented GaN substrates using metalorganic chemical vapor deposition. A proper pretreatment of the substrates was found to be essential for the GaN homoepitaxy. The influence of growth conditions such as V/III molar-ratio and temperature on the surface morphology and optical properties of epilayers was investigated. Optimized pretreatment and growth conditions led to high quality [1 $\bar{1}$ 00] oriented GaN epilayers with a smooth surface morphology and strong band-edge emission. These layers also exhibited strong room temperature stimulated emission under high intensity pulsed optical pumping. Based on these GaN epilayer, AlGaN/GaN multiple quantum wells have been grown on the freestanding M-plane GaN. Photoluminescence data confirm that built-in electric field for M-plane structures is very weak, and this situation results in a stronger PL intensity in comparison with C-plane multiple quantum wells in tests at low excitation level.

### Introduction

Recently excellent progress has been made in the development of high-quality III-nitride optoelectronic and electronic devices.<sup>1,2</sup> Nearly all the reported light emitting diodes (LEDs), laser diodes and high temperature and high power transistors employed III-nitride heterojunctions, which were deposited on the C-plane (0001) sapphire, 6H or 4H-SiC, or free-standing GaN substrates. All of these deposited (III-nitride) films and heterostructures feature the polar (0001) orientation, and hence they exhibit strong piezoelectric and spontaneous polarization induced fields.<sup>3,4</sup> These polarization fields give rise to a significant band bending and thus reduce the overlap of the electron-hole wave functions. This situation significantly reduces the optical emission from quantum wells. To avoid these polarization effects, R-plane sapphire substrates have been used for III-nitride optical devices.<sup>5,6</sup> Heteroepitaxy on sapphire, however, results in a large number ( $> 10^8/\text{cm}^2$ ) of threading dislocations, which counteract the beneficial effect of polarization field reduction on the optical emission intensity. Homoepitaxy of GaN and III-nitride heterostructures on non-polar M-plane [1 $\bar{1}$ 00] oriented bulk GaN substrates should in principle eliminate these problems.<sup>7-9</sup> This serves as the motivation for our work reported here.

## Experiment

Boules of  $\text{LiAlO}_2$  up to 200 mm long were pulled from the melt by the Czochralski method. GaN bulk crystals with  $(1\bar{1}00)$  surface (M-plane) were grown by halide vapor phase epitaxy (HVPE)<sup>10</sup> at 875 °C on the closely lattice matched (100) plane of  $\text{LiAlO}_2$  wafers sawed from these boules. No buffer layers were employed on the chemically polished wafer surfaces, but pre-growth nitriding in ammonia was used. After depositing about 350  $\mu\text{m}$ -thick GaN, the  $\text{LiAlO}_2$  substrate was removed with wet acid etching. Thus freestanding  $[1\bar{1}00]$  oriented GaN templates were obtained, which served as the starting substrates for our study. The phase purity of the GaN templates was examined by X-ray diffraction (XRD). The  $2\theta$ - $\omega$  XRD scans exhibit only two sharp GaN  $(1\bar{1}00)$  and  $(2\bar{2}00)$  peaks.

The growth of GaN layers and AlGaIn/GaN multiple quantum wells (MQWs) were carried out by low-pressure metalorganic chemical vapor deposition (MOCVD). Triethylgallium (TEG), Triethylaluminum (TEA) and  $\text{NH}_3$  were used as the precursors for Ga, Al and N, respectively. The six period AlGaIn/GaN MQWs were simultaneously deposited on the M-plane GaN homoepitaxial layers and thick C-plane GaN epilayers under identical conditions for comparison. TEA has been chosen as the Al source to obtain a sharp interface because of the small vapor pressure. During the growth, the reactor pressure and temperature were kept at 76 Torr and 1000 °C and  $\text{H}_2$  was used as carrier gas. The GaN homoepilayers were grown with thicknesses ranging from 2 to 4  $\mu\text{m}$ . The AlGaIn/GaN MQWs have a well width  $L_w = 5$  nm and a barrier width  $L_b = 10$  nm, respectively. The surface morphologies of these samples were studied using a Nomarsky optical microscope, scanning electron microscopy (SEM) and an atomic force microscope (AFM). The room and low-temperature (10 K) PL spectra were measured using a CW He-Cd laser (operating at 325 nm) as a low-intensity excitation source and a pulsed ( $\tau = 0.4$  ns) nitrogen laser (at 337 nm) for a high-excitation intensity source.

## Results and Discussion

For the GaN homoepitaxy, the pretreatment before growth was found to be essential and have been reported by several groups for  $[1000]$  oriented GaN substrate.

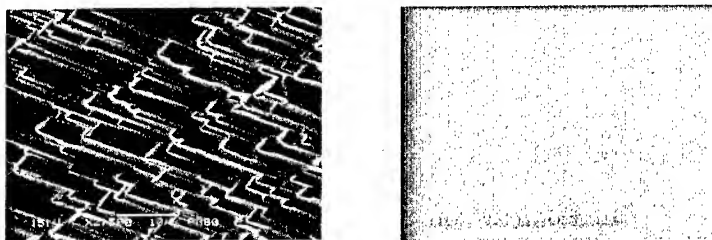


Fig.1 Plane-view SEM images of homoepitaxial layers on GaN templates with different pretreatment procedures: (a) heat treatment after polishing; (b) chemical and heat treatment after polishing.

Similarly, for the homoepitaxy on  $[1\bar{1}00]$  oriented GaN, a proper pretreatment is an important starting point. Since the surfaces of the M-plane GaN substrates were rough, the freestanding GaN templates were polished with diamond paste until the RMS roughness was as low as 2 nm. Although we obtained reasonable smooth surfaces after polishing, a thin layer under the surface has been already damaged by the mechanical polish procedure. We used a chemical treatment process by  $H_3PO_4$  etching at 150 °C to remove this damaged thin layer.<sup>11</sup>

Fig. 1 shows the top-view SEM images of the homoepitaxial GaN layers grown on the GaN templates by two different treatments: (a) heat treatment after polishing (b) chemical and heat treatment after polishing. The GaN layers grown on as-polished or only heat treatment after polish GaN substrates have very rough surfaces. However, the surface was greatly improved and shows a smooth morphology by the addition of chemical treatment procedure. It indicates that the damage layer during polishing was removed by chemical etching.

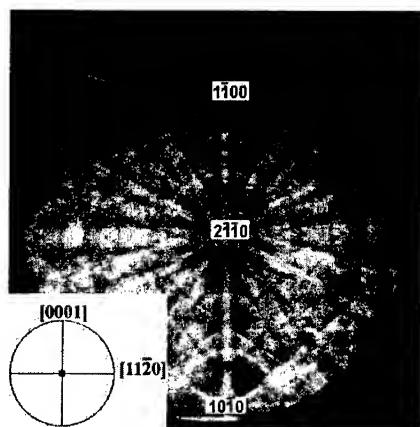


Fig.2 EBSD pattern obtained from GaN homoepitaxial epilayers. Inset shows the  $\{1\bar{1}00\}$  pole-figure. Black square on the pole-figure indicates the layer surface orientation, which is exactly  $[1\bar{1}00]$ .

The crystal orientation of GaN homoepitaxial layer was studied by electron backscattered-diffraction technique (EBSD).<sup>12</sup> Using an accelerating voltage of 20 kV and a sample tilt of 70 degrees, assures the EBSD-signal to originate from the top 1  $\mu\text{m}$  of the examined sample. Since the thickness of the homoepitaxial GaN epilayers were larger than 2  $\mu\text{m}$ , there is no contribution to the EBSD-signal from the GaN substrate templates. Therefore a careful indexing of all Kikuchi lines using the commercial Opal Inc. software allows a precise identification of our sample surface orientation. Fig. 2 shows a typical diffraction pattern obtained from the epilayer where the numbers indicate crystallographic directions. Taking into account the sample tilt angle 70 degrees, one can find that normal direction to the sample surface will exactly coincide with  $[1\bar{1}00]$ . Thus surface orientation was determined to be  $[1\bar{1}00]$ . On the XRD data we also only observed  $(1\bar{1}00)$  and  $(2\bar{2}00)$  peaks, which confirm the  $[1\bar{1}00]$  orientation of the GaN epilayers.

The surface morphology of GaN homoepitaxial layers were also affected by the V/III molar-ratio and temperatures. At a growth temperature of 1000°C, we found that the root-mean-squares (RMS) roughness increases with increasing the V/III molar-ratio.

Fig. 3 shows the surface AFM scans for 4  $\mu\text{m}$  thick homoepitaxial GaN epilayers grown using V/III ratios of 2500 and 5000. At the lower ratio, the layers exhibited a relatively smoother surface with RMS value around 0.7 nm. At the higher ratio, the RMS roughness increases to about 2.0 nm. On the other hand, we also note that the RMS value increases with increasing growth temperatures from 1000 to 1050°C for a fixed V/III ratio. AFM scans of Fig. 3 reveal stripe-like growth features aligned along the  $[1\bar{1}20]$  direction. These stripe features may result from the different migration lengths of adatoms along  $[0001]$  and  $[1\bar{1}20]$  directions.

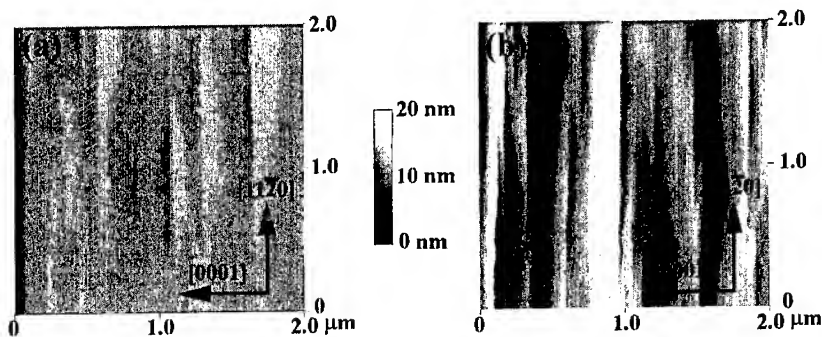


Fig. 3 AFM images of  $(1\bar{1}00)$  oriented GaN homoepitaxial layers. The stripes in images run along  $[1\bar{1}20]$  direction. The films were grown at V/III molar ratios of (a): 2500 and (b): 5000.

The influence of V/III molar ratio and growth temperature on the luminescent properties of the homoepitaxial GaN films was also studied. The data for the two films of Fig. 3 are shown in Fig. 4. In addition to the band-edge emission peak at 3.4 eV, a strong yellow band around 2.1 eV is also observed. This yellow emission band decreases with increasing the V/III molar ratio or growth temperature. In inset to Fig.3 we include the near band-edge luminescence at (10 K) from the M-plane GaN film. As seen, the low temperature PL spectra exhibits an emission structure arising from the free and bound excitons. This behavior is similar to what is typically observed for the high quality GaN grown over C-plane oriented substrates.<sup>13</sup> To further establish the high optical quality of the homoepitaxial  $[1\bar{1}00]$  oriented GaN epilayers, PL excited by a pulsed nitrogen laser was measured at room temperature. At the low excitation levels, the PL is dominated by a broad band, presumably arising from an electron-hole plasma emission. At high pump excitations, a strong and narrow stimulated emission line at 3.34 eV appears on the spectrum. This behavior is very similar to that for high quality C-plane deposited GaN films.<sup>14</sup>

We now turn to one of the most interesting properties predicted from this  $[1\bar{1}00]$  orientation: the absence of polarization effect along the growth direction. The six period AlGaIn/GaN MQWs were deposited on top of the  $[1\bar{1}00]$  GaN homoepitaxial layers and

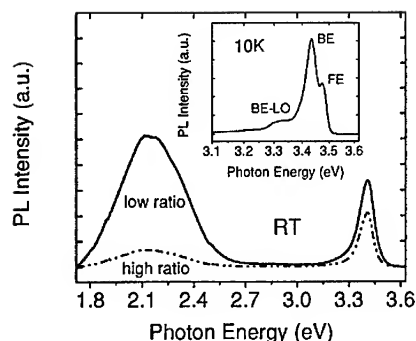


Fig. 4 PL spectra of M-plane GaN epilayers under different V/III molar ratios. The inset shows the near band-edge emission at 10 K.

epilayers, the polarization effect could be avoided since the M-planes contain an equal number of Ga and N atoms. From the PL measurements, we observed, at the low laser excitation level of  $1\text{ kW/cm}^2$ , PL intensity for M-plane MQWs was found to be 30 times higher than that for C-plane MQWs. Also, due to QCSE, C-plane MQWs have a PL peak position around 3.28 eV which is lower than the bandgap of GaN (3.4 eV). For M-plane MQWs, PL peak position situates at 3.42 eV.

Dependence of peak position of the PL spectra on excitation power density has been measured for C- and M-plane AlGaIn/GaN MQWs. Strong PL peak blueshifts (up to 140 meV) were observed for C-plane MQWs whereas no shifts were observed for M-plane MQWs. The excitation-induced blueshift of the PL peaks is due to the screening of the polarization electric field by photoinjected carriers. This also confirms that the polarization field for C-plane structures is much stronger than that for M-plane MQWs. The effect of the electrostatic fields on the electron-hole overlap is also evident from time-resolved photoluminescence measurement at 9 K. The striking difference between the decay times for M-plane (0.48 ns) and C-plane (3.64 ns) wells is a direct evidence of the presence of electrostatic fields in the later wells. At the low temperature, the decay time corresponds to the value for the radiative lifetime, which is

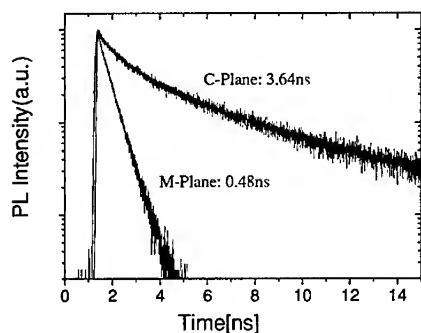


Fig.5 PL decay profiles measured at 9 K for AlGaIn/GaN MQWs grown on C- and M-plane GaN layers.

[0001] GaN epilayers in order to investigate the influence of polarization effect on the PL emission. As we know, for MQWs grown on [0001] oriented GaN, the strong polarization induced electrostatic field bends energy bands of quantum wells and then results in quantum confined stark effect (QCSE). The QCSE is undesirable in LEDs because this build-in field gives rise to a spatial separation of electrons and holes and a significant reduction of emission intensity. For MQWs grown on non-polar  $[1\bar{1}00]$  oriented GaN

epilayers, the polarization effect could be avoided since the M-planes contain an equal number of Ga and N atoms. From the PL measurements, we observed, at the low laser excitation level of  $1\text{ kW/cm}^2$ , PL intensity for M-plane MQWs was found to be 30 times higher than that for C-plane MQWs. Also, due to QCSE, C-plane MQWs have a PL peak position around 3.28 eV which is lower than the bandgap of GaN (3.4 eV). For M-plane MQWs, PL peak position situates at 3.42 eV.

inversely proportional to the wavefunction overlap integral.<sup>8</sup>

### Summary

We report low-pressure MOCVD growth of GaN epilayers and AlGaIn/GaN MQWs on  $[1\bar{1}00]$  oriented freestanding HVPE grown GaN substrates. Data is presented showing the effect of growth conditions such as V/III molar ratio and temperature on their surface morphology and optical properties. Room temperature stimulated emission under pulsed optical pumping confirms the high optical quality. High quality AlGaIn/GaN MQWs can be grown on these homoepitaxial M-plane GaN films which contain very weak built-in electric fields. Therefore, the quantum efficiency of AlGaIn/GaN MQWs can be improved by using  $[1\bar{1}00]$  crystal orientation.

### Acknowledgements

The authors gratefully acknowledge the help from Ms. Q. H. Zhang. The work was partially supported by DARPA contracts number DAAD19-02-10282, monitored by Dr. J. Zavada and Dr. J. Carrano, and number F19628-02-C-0057, monitored by Dr. J. Lorenzo and Dr. J. Carrano.

### References

- 1) S. Nakamura and G. Fasol, *The blue Laser Diode* (Spring, Heidelberg, 1997).
- 2) S. J. Pearton, J. C. Zolper, R. J. Shul, and F. Ren, *J. Appl. Phys.* **86**, 1 (1999).
- 3) F. Bernardini, V. Fiorentini and D. Vanderbilt, *Phys. Rev. B* **56**, 10024 (1997).
- 4) T. Deguchi, K. Sekiguchi, A. Nakamura, T. Sota, R. Matsuo, S. Chichibu and S. Nakamura, *Jpn. J. Appl. Phys., Part 2* **38**, L914 (1999).
- 5) S. Tripathy, R. K. Soni, H. Asahi, K. Iwata, R. Kuroiwa, K. Asami and S. Gonda, *J. Appl. Phys.* **85**, 8386 (1999).
- 6) M. D. Craven, S. H. Lim, F. Wu, J. S. Speck and S. P. DenBaars, *Appl. Phys. Lett.* **81**, 469 (2002).
- 7) C.R. Miskys, M. K. Kelly, O. Ambacher, G. Martinez-Criado, and M. Stutzmann, *Appl. Phys. Lett.* **77**, 1858 (2000).
- 8) P. Waltereit, O. Brandt, A. Trampert, H. T. Grahn, J. Menniger, M. Ramsteiner, M. Reiche, and K. H. Ploog, *Nature (London)* **406**, 865 (2000).
- 9) P. Waltereit, O. Brandt, M. Ramsteiner, A. Trampert, H. T. Grahn, J. Menniger, M. Reiche and K. H. Ploog, *J. Cryst. Growth* **227**, 437 (2001).
- 10) H. P. Maruska and J. J. Tietjen, *Appl. Phys. Lett.* **15**, 327 (1969).
- 11) H. Sato, T. Sugahara, M. Hao, Y. Naoi, S. Kurai, K. Yamashita, K. Nishino and S. Sakai, *Jpn. J. Appl. Phys.* **37**, 626 (1998).
- 12) C. Trager-Cowan, S. K. Manson-Smith, D. A. Cowan, F. Sweeney, D. McColl, A. Mohammed, R. Timm, P. G. Middleton, K. P. O. Donnell, D. Zubia and S. D. Hersee, *Mater. Sci. Eng., B* **82**, 19 (2001).
- 13) E. Felton, B. Beaumont, M. Luigt and P. De Mierry, P. Vennegues, M. Leroux and P. Gibart, *Phys. Status Solidi A* **188**, 531 (2001).
- 14) H. Amano, T. Asahi and I. Akasaki, *Jpn. J. Appl. Phys., Part 1* **29**, 205 (1990).

### Growth of Quaternary AlInGaN/GaN Heterostructures by Plasma Assisted MBE

E. Monroy<sup>1</sup>, N. Gogneau<sup>1</sup>, D. Jalabert<sup>1</sup>, F. Enjalbert<sup>2</sup>, E. Bellet-Amalric<sup>1</sup>, Y. Hori<sup>1</sup>, Le Si Dang<sup>2</sup>, and B. Daudin<sup>1</sup>

Equipe mixte CEA-CNRS-UJF Nanophysique et Semiconducteurs

<sup>1</sup> Dépt. de Recherche Fondamentale sur la Matière Condensée, SP2M/PSC, CEA-Grenoble, 17 rue des Martyrs, 38054-Grenoble cedex 9, France

<sup>2</sup> Laboratoire de Spectrométrie Physique, Université Joseph Fourier, Grenoble, France

#### ABSTRACT

Epitaxial growth of quaternary AlGaInN compounds by plasma-assisted molecular beam epitaxy has been demonstrated. Two-dimensional growth is achieved under In excess, with a monolayer of In segregating at the growth front. The maximum In incorporation is significantly affected by the substrate temperature and the Al mole fraction of the alloy. This behavior has been attributed to the enhancement of In segregation due to the high binding energy of AlN compared to InN and GaN.

#### INTRODUCTION

Quaternary AlGaInN compounds have meant a breakthrough in research towards III-nitride based deep-UV emitters. Their use as emitting medium reduces the strain and the electric field in the heterostructure, and enhances radiative efficiency in comparison to the AlGaIn/GaN system [1,2]. Furthermore, the controlled growth of AlGaInN should make possible to vary independently the lattice constant and the bandgap, which is interesting to tailor the strong piezoelectric and spontaneous polarization present in III-nitride heterostructures.

Growth of quaternary AlGaInN is a challenge due to the different binding energy of the binary compounds, and the different mobility and desorption temperature of the growing species. The feasibility of AlGaInN has been demonstrated [3-6] by sophisticated growth procedures using metalorganic vapor phase epitaxy (MOVPE). The capability of molecular beam epitaxy (MBE) for low temperature growth opens new possibilities for the fabrication of quaternary-based heterostructures in a wide composition range [7]. In this work we demonstrate the controlled growth of quaternary  $\text{Al}_x\text{Ga}_{1-x-y}\text{In}_y\text{N}$  by plasma-assisted MBE, and we study the incorporation of In as a function of metal fluxes and substrate temperature.

#### EXPERIMENTAL

AlGaInN epilayers (0.5-0.7  $\mu\text{m}$  thick) were grown on GaN templates grown on c-sapphire by MOVPE. After chemical degreasing and acid cleaning, the substrates were introduced in a Meca 2000 MBE chamber equipped with standard effusion cells for Ga and In. A water-cooled-tip cell from Addon was used for Al. Active nitrogen was supplied by a radio-frequency plasma cell. The mass fluxes in monolayers per second (ML/s) were deduced from the growth rate of GaN, AlN and InN measured at low temperature, to prevent a possible overestimation due to metal desorption. Prior to AlGaInN growth, a thin (~10 nm) GaN buffer layer was deposited at 730°C. Quaternary compounds were grown in the range of substrate temperatures between 650°C and

610°C. Growth rate was fixed at 0.20 ML/s.

The composition of the alloys was determined by Rutherford Backscattering Spectrometry (RBS). The growth kinetics and the structure of the layers were analyzed by reflection high-energy electron diffraction (RHEED), atomic force microscopy (AFM), and high resolution X-ray diffraction (HRXRD). Photoluminescence (PL) was measured by exciting with the fourth frequency of a pulsed Nd-YAG laser (266 nm) with a peak power of 500 kW/cm<sup>2</sup> and a mean power of 10 mW.

## RESULTS AND DISCUSSION

The determination of the growth conditions of quaternary nitrides consists of the delimiting the adequate range of substrate temperatures and metal fluxes. In our case, the nitrogen flux remains constant and determines the growth rate. The proper definition of these parameters requires to gain in-depth in the growth kinetics of AlGaInN.

The growth of III-nitrides should be performed at the highest possible temperature, to maintain sufficient diffusion length of Al and Ga species during epitaxy. The maximum growth temperature for Al<sub>x</sub>Ga<sub>1-x-y</sub>In<sub>y</sub>N is determined by the incorporation limit of In in AlGaInN ( $T_s \leq 650^\circ\text{C}$ ).

At the low substrate temperatures required to achieve a significant In incorporation, Al and Ga re-evaporation is negligible, i.e. the sticking coefficients of Ga and Al are unity. In contrast, In shows a high desorption rate for temperatures higher than 530°C, and a tendency to segregate on the growing surface. Thus, to incorporate In in the alloy, it is necessary that the sum of Ga and Al fluxes,  $\Phi_{\text{Ga}} + \Phi_{\text{Al}}$ , remains lower than the nitrogen flux,  $\Phi_{\text{N}}$ , and growth must proceed in presence of an excess of In at the surface. In summary, metal fluxes must satisfy the relations:  $\Phi_{\text{N}} > \Phi_{\text{Ga}} + \Phi_{\text{Al}}$  and  $\Phi_{\text{N}} < \Phi_{\text{Ga}} + \Phi_{\text{Al}} + \Phi_{\text{In}}$ .

More precisely, In flux should be high enough to generate an In layer on the growing surface, which guarantees In-rich growth, but low enough to prevent In accumulation and droplet formation. For compounds with low In contents, we can determine the adequate growth conditions by studying the wetting of the AlGaInN surface with In. In a previous work [8], we demonstrated the existence of two self-regulated regimes in which an In film is dynamically-stable on GaN, corresponding to an In coverage of 1 ML and 2 ML, in agreement with first-principle calculations [9]. On AlGaInN, the presence of Al modifies the growth kinetics so that the <1 ML to 1 ML boundary shifts to higher In fluxes, while the 1 ML to 2 ML boundary remains approximately unchanged [8]. Based on this remark, the 1 ML / 2 ML boundary can be considered as an upper limit of the In flux required for AlGaInN growth in the 610–650°C range, in order to maintain In-rich growth and prevent In accumulation. These conditions correspond to In fluxes in the 0.03–0.06 ML/s range.

Information about growth kinetics can be extracted by analyzing the RHEED pattern. Figure 1 shows the variation of the RHEED specular intensity when starting the growth of AlGaInN and AlGaIn at the same substrate temperature and with the same N, Ga and Al fluxes. In the case of the quaternary alloy, we observe some transient oscillations that correspond to the formation of the In film at the surface. Then, metals and N diffuse through this film and growth proceeds layer by layer, as demonstrated by the presence of RHEED oscillations. After growth, the adsorbed In film is removed by keeping the sample under vacuum for about one minute at a substrate temperature of 650°C.

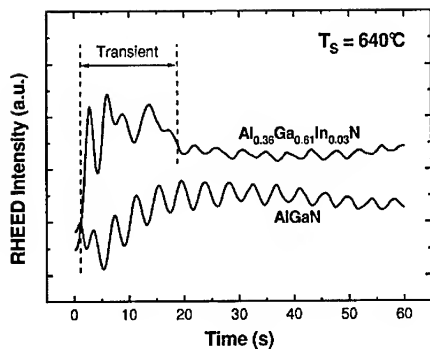


**Figure 1.** Evolution of the RHEED intensity when starting the growth of ternary and quaternary alloys at a substrate temperature  $T_s = 640^\circ\text{C}$ , using the same Al, Ga and N fluxes.

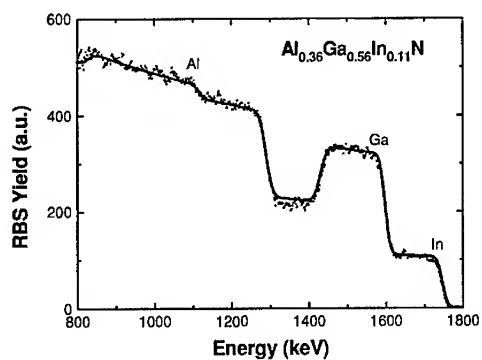


**Figure 2.** Measured and simulated (solid line) RBS spectrum of an  $\text{AlGaInN}$  sample grown on  $\text{GaN/sapphire}$  at a substrate temperature of  $630^\circ\text{C}$ . The surface channels are marked by the corresponding element.

The homogeneity of the alloy was checked by RBS, as shown in Figure 2 for an  $\text{Al}_{0.36}\text{Ga}_{0.53}\text{In}_{0.11}\text{N}$  layer. The simulation fits accurately the experimental data. In addition, the structural quality of the layers was analyzed by HRXRD. The full width at half maximum (FWHM) of symmetric (002)  $\omega$ -scans of  $\text{Al}_x\text{Ga}_{1-x-y}\text{In}_y\text{N}$  samples ( $0 \leq x \leq 0.50$ ,  $0 \leq y \leq 0.15$ ) lies in the range from 300 arcsec to 700 arcsec, whereas the FWHM of asymmetric (-102)  $\omega$ -scans remains in the 600-750 arcsec range. The surface roughness measured by AFM increases with In content from 0.7 nm to 2 nm (rms), in samples with an Al content of about 40%.

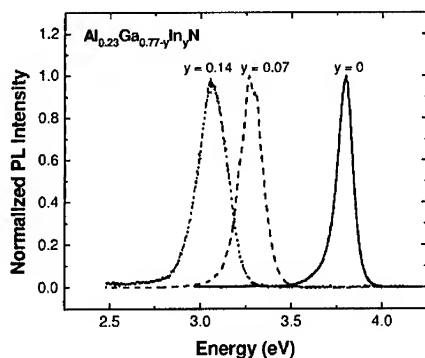


**Figure 3.** Photoluminescence spectra of AlGaInN layers with  $x = 0.23$ , and  $y = 0, 0.07$ , and  $0.14$ .

Figure 3 shows the room temperature photoluminescence spectra of quaternary samples with the same Al content and different In mole fraction. Together with the strong red-shift, characteristic of In incorporation, we observe a broadening of the main line.

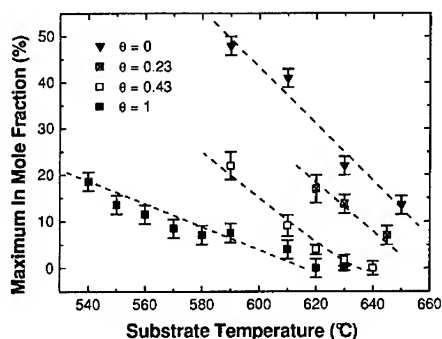


**Figure 4.** Maximum In incorporation in the quaternary compound as a function of the substrate temperature and the  $\theta = \text{Al}/(\text{Al} + \text{Ga})$  ratio.

Previous experimental results demonstrate that In incorporation in InGaN [9,10] and AlGaInN [7] depends on substrate temperature, although the physical origin of that dependence is still under debate. In Figure 4, we present an study of the In incorporation limit as a function of substrate temperature and Al mole fraction. In order to determine this limit, the Ga flux is reduced until observing a reduction of the growth rate, evidenced *in situ* by RHEED oscillations. Under these conditions, there is an excess of In at the layer surface, which manifests in a diffuse RHEED pattern that recovers brightness when stopping the In flux. However, this excess segregates at the surface, and only a limited amount of In contributes to the growth. Higher In fluxes result in a darker RHEED pattern that evidences the accumulation of In on the surface, but the growth rate does not increase and the growth front remains rough. Experimental results in Figure 4 indicate that, apart from the effect of  $(\text{Al} + \text{Ga}) / \text{N}$  ratio, there is a second limit to In incorporation, which is a function not only of the substrate temperature, but also of the Al mole fraction of the alloy.

From our experiments we can assert the mechanism that limits In incorporation is not the re-evaporation of adsorbed In atoms, since the In flux was adjusted to guarantee In-rich conditions in all the temperature range. The predicted immiscibility of InN and GaN should neither be the origin of this phenomenon, since it should be attenuated by temperature, in contrast with our observations. In contrast, In loss should be due to the thermal decomposition of In-N bonds, which is supported by the measurement of an InN decomposition temperature of 530°C in our MBE chamber. Above this temperature, In-N bonds are thermally unstable, and the In mole fraction of the alloy is thus determined by growth kinetics. At the growing surface, the exchange of In atoms with Ga or Al is energetically favorable, due to the different binding energies of InN, GaN and AlN. Thus, In tends to segregate at the growth front, and the higher binding energy of AlN in comparison to GaN is most likely the origin of the segregation enhancement for higher Al mole fractions.

## CONCLUSION

Controlled growth of quaternary AlGaInN compounds by PAMBE has been demonstrated, achieving homogeneous layers with good structural and optical properties. It has been shown for the first time that the maximum incorporation of In is significantly affected by the Al mole fraction. This behavior is attributed to the enhancement of In segregation due to the high binding energy of AlN compared to InN and GaN.

## ACKNOWLEDGEMENTS

Thanks are due to Y. Genuist and M. Falco for technical support. Financial support from TIPEL Project (DiGITIP 3 / STSI/SDCO) is acknowledged.

## REFERENCES

1. J. Han and A. V. Nurmikko, IEEE J. Quantum Electron. 8, 289 (2002).
2. Chitnis, R. Pachipulusu, V. Mandavilli, M. Shatalov, E. Kuokstis, J. P. Zhang, V. Adivarahan, S. Wu, G. Simin, M. A. Khan, Appl. Phys. Lett. 81, 2938 (2002).
3. F. G. McIntosh, K. S. Boutros, J. C. Roberts, S. M. Bedair, E. L. Piner, and N. A. El-Masry, Appl. Phys. Lett. 68, 40 (1996).

- 
4. S. Yamaguchi, M. Kariya, S. Nitta, H. Kato, T. Takeuchi, C. Wetzel, H. Amano, and I. Akasaki, *J. Cryst. Growth* 195, 309 (1998).
  5. J. Han, J. J. Figiel, G. A. Petersen, S. M. Meyers, M. H. Crawford, and M. A. Banas, *Jpn. J. Appl. Phys.* 39, 2372 (2000).
  6. M. A. Khan, V. Adivarahan, J. P. Zhang, C. Chen, E. Kuokstis, A. Chitnis, M. Shatalov, J. W. Yang, and G. Simin, *Jpn. J. Appl. Phys.* 40, L1308 (2001).
  7. P. Lima, C. R. Miskys, U. Karrer, O. Ambacher, A. Wenzel, B. Rauschenbach, and M. Stutzmann, *J. Cryst. Growth* 220, 341 (2000).
  8. E. Monroy, B. Daudin, E. Bellet-Amalric, N. Gogneau, D. Jalabert, F. Enjalbert, J. Brault, J. Barjon, and Le Si Dang, *J. Appl. Phys.* (To be published).
  9. H. Chen, R. M. Feenstra, J. Northrup, J. Neugebauer, and D. W. Greve, *MRS Internet J. Nitride Semicond. Res.* 6, 11 (2001).
  10. C. Adelmann, R. Langer, G. Feuillet, and B. Daudin, *Appl. Phys. Lett.* 75, 3518 (1999).

### **Lattice Relaxation of AlN Buffer on Surface-Treated SiC in Molecular-Beam Epitaxy for Growth of High-Quality GaN**

Jun Suda, Kouhei Miura, Misako Honaga, Norio Onojima, Yusuke Nishi  
and Hiroyuki Matsunami  
Department of Electronic Science and Engineering, Kyoto University,  
Sakyo-ku, Kyoto 606-8501, Japan

#### **ABSTRACT**

The effects of SiC surface treatment on the lattice relaxation of AlN buffer layers and the crystalline quality of GaN layers grown on the buffer layers were studied. AlN buffer layers and GaN main layers were grown by plasma-assisted molecular-beam epitaxy on on-axis 6H-SiC (0001)<sub>Si</sub> substrates. High-temperature HCl-gas etching resulted in an atomically flat SiC surface with ( $\sqrt{3}\times\sqrt{3}$ )R30° surface reconstruction, while HCl-gas etching followed by HF chemical treatment resulted in an atomically flat surface with (1×1) structure. The AlN layer grown on the (1×1) surface showed slower lattice relaxation. GaN grown on the AlN buffer layer exhibited a (0002) X-ray rocking curve of 70 arcsec and  $10^7\text{ cm}^{-2}$  of screw-type dislocation density, which was superior than that of GaN grown on ( $\sqrt{3}\times\sqrt{3}$ )R30° surface.

#### **INTRODUCTION**

Growth of high-quality GaN on SiC is one of key issues to realize high-frequency high-power transistors. We have reported molecular-beam epitaxial (MBE) growth of AlN on 6H-SiC (0001)<sub>Si</sub> substrates pretreated by high-temperature HCl-gas etching [1,2]. HCl-gas etching resulted in an atomically flat SiC surface [3]. The crystalline quality and surface roughness of AlN grown layers were greatly improved compared to AlN grown on an as-received SiC substrate, suggesting that HCl-gas etching is an effective pretreatment to grow high-quality AlN. In this study, the AlN layer was used as a buffer layer for GaN growth. We discuss the correlation between the lattice relaxation process of AlN buffer, which depends on surface reconstruction of SiC substrates, and the quality of GaN layer grown on the AlN buffer. It was revealed that surface reconstruction of 6H-SiC has strong effects on the lattice relaxation process of AlN buffer layers and the crystalline quality of GaN.

## EXPERIMENTAL DETAILS

AlN and GaN layers were grown by plasma-assisted MBE using elemental Ga and Al, and active nitrogen (N\*) generated by an EPI Unibulb radio-frequency plasma cell. Commercially available on-axis 6H-SiC (0001)<sub>Si</sub> substrates were used.

In this study, three different pretreatments for 6H-SiC substrates were investigated. They were combinations of two methods, a wet chemical process and high-temperature HCl-gas etching. First, all substrates were cleaned by a wet chemical process: dipping into aqua regia, HCl solution and HF solution for removal of contamination and natural oxide. These substrates were referred as as-received substrates. As shown in figure 1(a), many polishing scratches were observed by AFM on the as-received substrate. Second, some of the substrates were etched by HCl/H<sub>2</sub> gas at 1300°C to remove the damaged layer caused by polishing, which were referred as HCl-treated substrates. The surface exhibited clear step-and-terrace structure without scratches as shown in figure 1(b). Most of the steps had 6 monolayer (ML) height [3]. The terrace widths were 200-600 nm, corresponding to a misorientation of 0.1-0.4°. Finally, some of the HCl-treated substrates were successively cleaned by the same wet chemical process as described above for surface modification. The substrates were referred as HF/HCl-treated substrates. As shown in figure 1(c), the step-and-terrace structure was also observed on the substrate, indicating that the wet chemical process doesn't affect surface flatness.

After surface pretreatment described above, the substrate was loaded into the MBE system. Thermal cleaning at 1000°C for 30 min in an ultra high vacuum was followed by growth of 60-nm-thick AlN at 1000°C under a nearly stoichiometric condition, which resulted in a smooth grown surface. And then, 1-μm-thick GaN was grown at 850°C under a slightly Ga-rich condition. The growth rates of AlN and GaN were 0.36 μm/h and 0.5 μm/h, respectively. The growth process of AlN buffer layer was studied by *in situ* reflection high-energy electron diffraction (RHEED) observation and the quality of GaN grown layer was characterized by atomic force microscope (AFM) and X-ray diffraction (XRD) measurements.

## DISCUSSION

In figure 1, RHEED patterns are shown for the three 6H-SiC substrates after thermal cleaning. A diffused streak pattern was observed on the as-received substrate (figure 1(a)), while sharp and intense streak patterns with clear Kikuchi lines were observed on the HCl-treated and HF/HCl-treated substrates (figures 1(b) and 1(c)). The as-received substrate exhibited (1×1)

## BEST AVAILABLE COPY

structure. On the HCl-treated substrate,  $(\sqrt{3} \times \sqrt{3})R30^\circ$  surface reconstruction was evident. On the other hand,  $(1 \times 1)$  structure was observed on the HF/HCl-treated substrate.

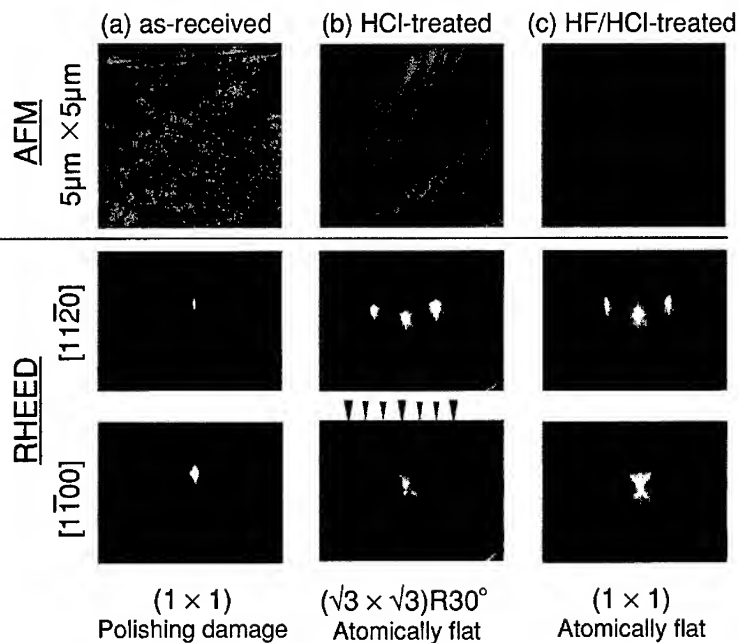


**Figure 1.** AFM images and RHEED patterns of 6H-SiC substrates after thermal cleaning. (a) as-received substrate, (b) HCl-treated substrate and (c) HF/HCl-treated substrate.

AlN buffer layers were grown on these surfaces. Just after the growth of AlN, the RHEED pattern became faint. Then, a streak pattern appeared gradually. The evolution of a-axis lattice constant calculated from the spacing of streaks is shown in figure 2. Two dashed lines indicate the a-axis lattice constants of bulk AlN and SiC, corresponding to fully relaxed and coherent growth of AlN on SiC, respectively. During the initial stage of growth, the lattice constant could not be calculated because of the faint RHEED pattern. In all cases, lattice relaxation due to the 1% lattice mismatch between AlN and SiC was observed, but the relaxation processes were different. On the as-received substrate, the lattice constant increases slowly. Even after 600 s growth (60 nm), the lattice constant still remained at the middle of fully relaxed and coherent conditions, indicating that the AlN layer has a compressive strain (the a-axis lattice constant of

grown layer is smaller than that of bulk AlN). On the other hand, the lattice constant on the HCl-treated substrate approaches that of fully relaxed AlN within 200 s growth (20 nm). The evolution of lattice constant on the HF/HCl-treated substrate was similar to that observed on the as-received substrates, but the AlN layer has a larger compressive strain. These results clearly indicate that the strain relaxation process of AlN was strongly affected by 6H-SiC substrate pretreatment. It is thought that the SiC initial surface with  $(\sqrt{3}\times\sqrt{3})R30^\circ$  resulted in fast relaxation of AlN layer.

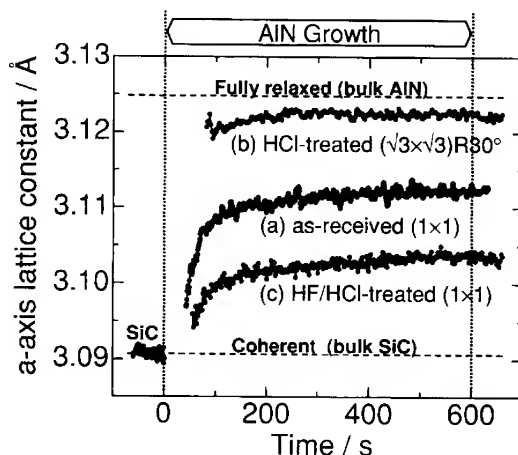


**Figure 2.** Evolution of a-axis lattice constant during AlN buffer layer growth on three different substrates; (a) as-received substrate, (b) HCl-treated substrate and (c) HF/HCl-treated substrate.

A 1- $\mu\text{m}$ -thick GaN main layer was grown after the growth of AlN buffer layer. During and after the growth of GaN, RHEED exhibited a streak pattern for all samples. The X-ray rocking curves (XRCs) of GaN (0002) are shown in figures 3(a)-(c). GaN grown on the as-received substrate exhibits relatively good full width at half maximum (FWHM) value, 272 arcsec. As clearly seen, the FWHM value on the HCl-treated substrate is 977 arcsec, significantly larger than those on the other two substrates, indicating poor crystalline quality of GaN. On the HF/HCl-treated substrates, 149 arcsec (the best value of 70 arcsec) was obtained, which is a considerably small value for MBE-grown GaN on SiC [4,5].

Figures 3(d)-(f) show AFM images of GaN layers. On the as-received substrate, a lot of spiral hillocks were observed as shown in figure 3(d). These hillocks originate from spiral growth at screw-type (pure screw or mixed) dislocations [6]. The density of hillocks was  $\sim 10^9$

BEST AVAILABLE COPY

$\text{cm}^{-2}$ . On the HCl-treated substrate, irregular steps and many small holes were observed as shown in figure 3(e), showing the poor crystalline quality of GaN. On the HF/HCl-treated substrate, hillocks were also observed with a large scan range (not shown here), but its density was  $\sim 10^7 \text{ cm}^{-2}$ , two orders of magnitude smaller than that on the as-received substrate. Between hillocks, a clear step-and-terrace structure was observed as shown in figure 3(f). These results suggest that HF/HCl-treatment resulted in a remarkable reduction of screw-type dislocations in GaN grown layers. However, the presence of dark spots (pits) in the AFM image may indicate the presence of other defects such as pure-edge dislocations. The total density of dislocations should be confirmed by transmission electron microscopy in future.

Although both of HCl-treated and HF/HCl-treated SiC substrates have a very flat surface, the crystalline quality of GaN grown on these substrates was very different as discussed above. These two SiC substrates have different surface reconstruction (or surface chemical composition), which resulted in the different relaxation process of AlN buffer layer. Detailed studies on

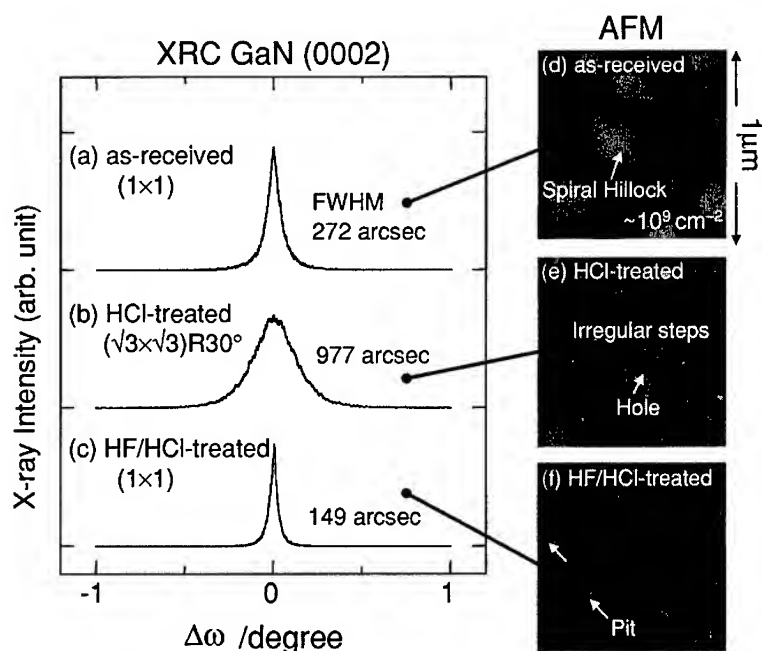


**Figure 3.** X-ray rocking curves for (0002) diffraction and AFM images from GaN layers grown on 6H-SiC substrates with three different pretreatments; (a),(d) as-received substrate, (b),(e) HCl-treated substrate and (c),(f) HF/HCl-treated substrate.

quality of the AlN buffer layer will be a key to understand why the quality of GaN is so different. It is also expected that precise control of SiC surface will result in further improvement of crystalline quality of GaN.

## CONCLUSIONS

We proposed high-temperature HCl-gas etching followed by chemical treatment as a new SiC substrate pretreatment, which resulted in (1×1) structure with an atomically flat surface. On the surface-pretreated SiC substrate, the AlN layer exhibited slow lattice relaxation. AlN had a compressive strain even after 60 nm-thick growth. GaN layers grown on the AlN buffer layer exhibited a XRC (0002) diffraction of 70 arcsec and  $10^7 \text{ cm}^{-2}$  of screw-type dislocation density, which is two orders of magnitude smaller than that of GaN grown on as-received substrates.

## ACKNOWLEDGMENTS

This work was supported by the Japan Society for the Promotion of Science, Research for the Future Feasibility Study Program (FY2001), "Control of Interface Properties in Wide Bandgap Semiconductors and Evolution of New Function". One of authors (J.S.) would like to thank the Sasagawa Grants for Science Fellows from the Japan Science Society.

## REFERENCES

1. N. Onojima, J. Suda and H. Matsunami, *Appl. Phys. Lett.* **80**, 76 (2002).
2. N. Onojima, J. Suda and H. Matsunami, *J. Crystal Growth* **237-239**, 1012 (2002).
3. S. Nakamura, T. Kimoto, H. Matsunami, S. Tanaka, N. Teraguchi and A. Suzuki, *Appl. Phys. Lett.* **76**, 3412 (2000).
4. O. Brandt, R. Muralidharan, P. Waltereit, A. Thamm, A. Trampert, H. von Kiedrowski and K. H. Ploog, *Appl. Phys. Lett.* **75**, 4019 (1999).
5. M. H. Xie, L. X. Zheng, S. H. Cheung, Y. F. Ng, H. Wu, S. Y. Tong and N. Otani, *Appl. Phys. Lett.* **77**, 1105 (2000).
6. B. Heying, E. J. Tarsa, C. R. Elsass, P. Fini, S. P. DenBaars and J. S. Speck, *J. Appl. Phys.* **85**, 6470 (1999).

### Growth of Thick InN by Molecular Beam Epitaxy

Hai Lu, William J. Schaff and Lester F. Eastman  
Department of Electrical and Computer Engineering, Cornell University  
Ithaca, NY 14853

J. Wu, Wladek Walukiewicz  
Lawrence Berkeley National Laboratory, Berkeley, CA 94720

David C. Look  
Semiconductor Research Center, Wright State University, Dayton, OH 45435

Richard J. Molnar  
MIT Lincoln Laboratory, Lexington, MA 02420

#### ABSTRACT

In this study, InN films with thickness up to 7.5 micron were prepared by molecular beam epitaxy (MBE) on (0001) sapphire and quasi-bulk GaN templates. Previously it has been challenging to grow InN film much beyond 1 micron because the growing surface tended to become rough. Techniques to overcome this limit have been developed. Various buffer techniques were used and compared to optimize the epitaxial growth. It was found that with increasing film thickness, Hall mobility will monotonically increase, while carrier concentration decreases. Hall mobility beyond 2100 cm<sup>2</sup>/Vs with carrier concentration close to  $3 \times 10^{17}$  cm<sup>-3</sup> was obtained at room temperature. Compared with the lowest carrier concentration  $\sim 2 \times 10^{18}$  cm<sup>-3</sup> obtained on thin InN films grown at the same condition, the conclusion is that impurities from the growth environment are not responsible for the high background doping of InN. Instead, some structural defects or substrate/buffer impurities may be the major source of the unintentional doping, which can be reduced by growing thicker films.

Some results on Mg and Be doping of InN will be reported as well. To date, all Mg and Be doping attempts have resulted in n-type material.

#### INTRODUCTION

Indium nitride, as an essential component in the III-nitride system, has attracted much attention recently. Knowing more about this material is very helpful to the design of novel III-nitride devices based on the concept of band-gap and strain engineering. During the past few years, many important improvements on the research of this material have been achieved. InN films with room temperature Hall mobility more than 1000 cm<sup>2</sup>/Vs and carrier concentration in the order of  $10^{18}$  cm<sup>-3</sup> have been produced by several groups in the world. [1,2] What more significant is the successful demonstration of the narrow bandgap (0.7 eV) of InN.[3-5] This discovery has two important implications. First, many theoretical studies and experimental explanations based on the predominantly reported bandgap (1.9 eV) of InN have to be updated. Second, InN and its related In-rich nitrides can be utilized in a new domain of applications. In

the field of opto-electronics, III-nitride-based light emitters can be made over a broader wavelength range from infrared to ultraviolet.

In our previous study, it was found that by increasing InN film thickness, the electrical properties of InN can be improved.[1] However, at the same time, it was also found that it is quite challenging to grow InN film much beyond 1 micron because the growing surface tends to become rough near 1 micron of thickness. As a result of the rough surface, the electrical properties of InN can not be improved further and even degrade. Since there is an urgent need to synthesize high quality InN for the extraction of its fundamental parameters, in this study we focused on the optimization of the InN growth conditions. Techniques to overcome the smooth surface thickness limit of InN have been developed. InN films with thickness up to 7.5 micron and smooth surface morphology were prepared on (0001) sapphire and quasi-bulk GaN templates. Hall mobility beyond  $2100 \text{ cm}^2/\text{Vs}$  with carrier concentration close to  $3 \times 10^{17} \text{ cm}^{-3}$  was obtained at room temperature. It is determined that impurities from the growth environment are not responsible for the high background doping of InN. Instead, some structural defects or substrate/buffer impurities may be the major source of the unintentional doping. In this paper, some results on Mg and Be doping of InN will be reported as well.

## EXPERIMENTAL

A Varian GEN-II remote RF-plasma MBE system was used for the growth of InN. The details of the system have been described elsewhere.[1] The substrates used were (0001) sapphire and HVPE GaN:Zn quasi-bulk templates on sapphire. The backsides of the substrates were sputter-coated by TiW alloy for efficient heat absorption during the growth. For InN films grown on sapphire, an AlN or GaN layer was grown prior to InN growth to serve as a buffer layer. Unless specified, the whole growth process can be separated into three steps. In the first step, (0001) sapphire wafer was nitridated by nitrogen plasma; then an AlN or GaN buffer layer was deposited at high temperature by the conventional MBE technique. Finally, the substrate was cooled down slowly to the desired temperature and then InN growth began. For InN films grown on HVPE GaN, the substrate was directly heated to the InN growth temperature and then the growth was started. The HVPE GaN template has been compensated with Zn introduced during growth to suppress unintentional n-type conductivity. Its thickness is around  $16 \mu\text{m}$  with 300K resistivity up to  $10^9 \Omega\cdot\text{cm}$  and dislocation density around  $5 \times 10^8 \text{ cm}^{-2}$ . [6]

All InN films were grown by the conventional MBE technique in this study. The growth rate is about  $0.7 \mu\text{m/h}$ . Previously the main challenge for growing thick InN was the degradation of surface morphology. Two possible reasons may lead to the degradation. One is over-heating of the InN film. Due to the narrow bandgap of InN, the film will absorb black body radiation from the furnace and RF plasma efficiently. As a result, even though a constant power is supplied to the substrate heater, the actual film temperature may go up as the film thickness increases. Since the optimum temperature we used to grow InN is close to the dissociation temperature of InN to maximize the surface mobility of group-III atoms, the absorption heating effect may increase the actual film temperature up to the dissociation temperature, which leads to the degradation. The other reason is the deviation from the optimum III/V ratio. It has been found that the optimum III/V ratio for InN growth lies close to the In-stable region. During the InN growth, the  $\text{N}_2$  Plasma density is relatively stable while the In flux will decrease at the same furnace temperature for prolonged growth due to the depletion of In charge. If this continues, the

growth condition may shift from near In-stable region to N-stable region. Growth of InN in the N-rich condition is unfavorable which usually results in poor surface morphology and high carrier density.

Precise control to maintain an optimum growth condition is critical for growing thick InN. In this study, we modified and computerized our growth system. Various parameters, such as substrate temperature and furnace temperature, were measured and adjusted by computer in a feedback mode throughout the growth. InN films with thickness up to 7.5  $\mu\text{m}$  have been successfully produced. The growth conditions of Mg or Be doped InN are similar to those of undoped InN. The Mg or Be shutter was opened directly after the InN growth began.

The electrical properties were determined by Hall measurements with Van der Pauw geometry using In contacts. To improve the precision of Hall measurements, standard Hall patterns defined by optical lithography and plasma etching were used.

## RESULTS AND DISCUSSIONS

### Electrical properties of thick InN films

Figure 1 shows a summary of electrical properties of many epitaxial InN growths. The InN samples were prepared by either MEE [7] or conventional MBE. Various buffer techniques and growth temperatures have been tried. The progress in our InN study is clearly shown in this figure. Before year 2001, the thickest InN we could produce was about 1  $\mu\text{m}$ . Accordingly the highest room temperature Hall mobility obtained was about 1300  $\text{cm}^2/\text{Vs}$  with carrier density around  $2 \times 10^{18} \text{ cm}^{-3}$ . With the development of our growth technique, much better electrical properties were achieved in our thick InN films. The highest 300K Hall mobility obtained until today is 2160  $\text{cm}^2/\text{Vs}$  with carrier density  $3.15 \times 10^{17} \text{ cm}^{-3}$ . These are the highest mobility and lowest electron density reported in single crystal InN to date.

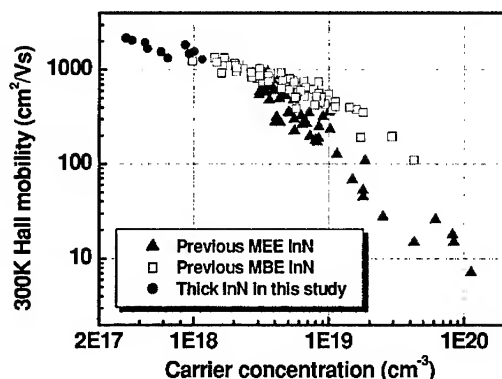


**Figure 1.** A summary of electrical properties of many InN growths. The InN samples were either prepared by MEE or conventional MBE with different buffer techniques and growth temperatures.

The effect of film thickness on the electrical properties of InN was studied by preparing a series of InN films with different film thickness. Figure 2 shows the evolution of their 300K Hall mobility and carrier density as a function of film thickness. It is found that with increasing film thickness, the Hall mobility of InN films will continuously increase while carrier concentration decreases. The enhancement of Hall mobility can be explained by the reduced defect density away from the lattice-mismatched buffer. Since the lattice mismatch between InN and GaN buffer is still more than 11%, high densities of dislocations are expected. Based on our previous TEM study on thin InN film, the dislocation density near the InN/buffer interface is on the order of  $10^{10} \text{ cm}^{-2}$ . [8] At this dislocation density level, charged dislocation scattering should be one of the major scattering mechanisms. With increasing film thickness, dislocation annihilation occurs, which results in an enhanced Hall mobility. Here it is worth noting that for a thick InN film, the Hall mobility obtained is a weighted average value of the whole film. The actual Hall mobility of the upper layer of the film should be higher than the average, which raises the expectation that InN can achieve a mobility suitable for high-speed electronics.

From the same figure, it is surprising to observe that the carrier concentration of InN films decreases at the same time. Such effect does not strongly occur for growing undoped GaN, which is partially due to the fact that dislocations are acceptor-like in GaN. [9] Since the film was prepared at the same growth environment throughout the growth, this result means that impurities from the growth environment are not responsible for the high background doping of InN. Instead, some structural defects or substrate/buffer impurities may be the major source of the unintentional doping, which can be reduced by growing thicker films.

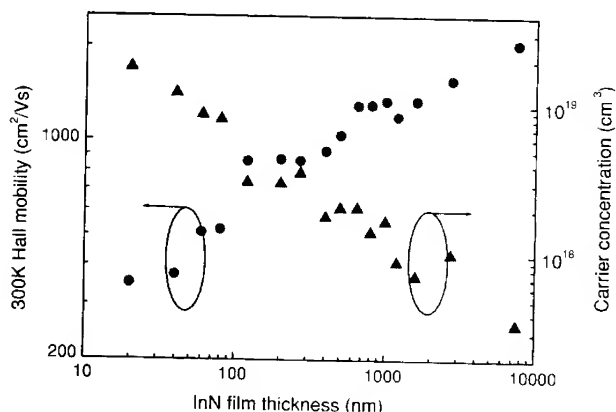


**Figure 2.** Room temperature Hall mobility and electron concentration of InN films as a function of film thickness. InN samples were grown under the same conditions on 220nm GaN buffers.

We also prepared thick InN films on HVPE GaN templates. The purpose for this experiment is to determine whether a high quality GaN buffer improves InN growth. The normal dislocation density in our thin MBE-grown GaN buffer layers is on the order of high  $10^9 \text{ cm}^{-2}$ . Meanwhile, the dislocation density of the HVPE GaN templates is around  $5 \times 10^8 \text{ cm}^{-2}$ . The surface morphologies of both kinds of GaN films are similar. Figure 3 shows the electrical properties of InN films grown on HVPE GaN as a function of film thickness. The 300K Hall

BEST AVAILABLE COPY

mobility and carrier concentration show similar trends as what observed in InN films grown on MBE GaN buffers, which again confirms that impurities from the growth environment are not responsible for the high background doping. By comparing fig.2 and fig.3, it is found that at the same film thickness, Hall mobility and carrier concentration of InN films on both buffers are quite similar, which means that lower dislocation HVPE GaN buffer does not significantly improve InN growth. It is further suggested that lattice mismatch is the dominant factor in controlling the following InN quality. A graded composition buffer might improve InN growth.

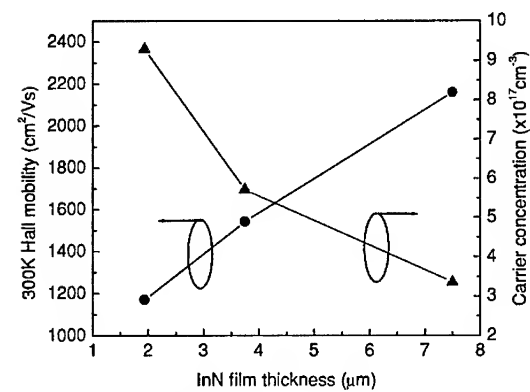


**Figure 3.** Room temperature Hall mobility and electron concentration of InN films as a function of film thickness. These samples were prepared on HVPE GaN templates.

### Electrical properties of Mg and Be doped InN

Developing insulating and p-type InN is critical for InN-based device applications. Mg and Be atoms might be acceptors in InN if they can occupy the right lattice sites. By doping InN by Mg or Be, we hope that we can further reduce the carrier concentration, or produce p-type InN. Our previous attempt on Mg-doping of InN resulted in higher electron concentration than undoped materials, which was explained by the structural degradation. [10] In this study, we prepared Mg and Be doped InN under our optimized growth conditions. However, to date, all Mg and Be doping attempts still resulted in n-type material.

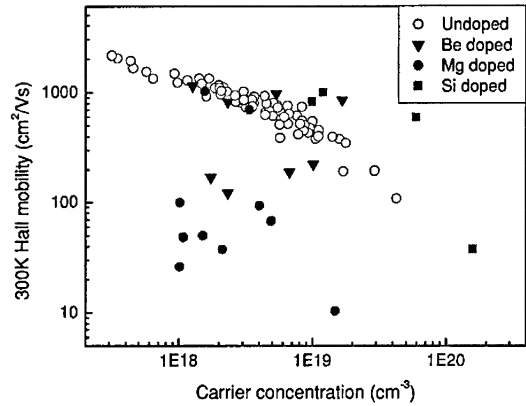


**Figure 4.** A summary of electrical properties of Mg and Be doped InN. Some data on undoped and Si doped InN are also shown in this figure for comparison.

Figure 4 summarizes the electrical properties of Mg and Be-doped InN. Some results on undoped and Si-doped InN are also shown in this figure for comparison. The thickness of these Mg and Be doped InN film range from 200 nm to 1  $\mu$ m. Different Mg and Be doping levels have been attempted. Fig.4 shows that for a given Hall mobility, Mg or Be doped InN usually has lower electron concentration than undoped samples. This observation might be explained by the partial compensation of background electrons by ionized Mg or Be dopants. The Hall measurements of Mg and Be doped samples vary much more widely than undoped or Si doped InN which, to date, makes interpretation of electrical activity unreliable.

## SUMMARY

Thick InN films with high purity and mobility have been made by MBE under optimized growth conditions. It is found that with increasing the film thickness, the Hall mobility will monotonically increase while carrier concentration decreases. Hall mobility beyond 2100  $\text{cm}^2/\text{Vs}$  with carrier concentration close to  $3 \times 10^{17} \text{ cm}^{-3}$  was obtained at room temperature. It is determined that impurities from the growth environment are not responsible for the high background doping of InN. Some results on Mg and Be doping of InN were also reported.

## ACKNOWLEDGEMENTS

This work at Cornell University is supported by ONR contract No. N000149910936 monitored by Dr. Colin Wood.

## REFERENCES

1. H. Lu, W. J. Schaff, J. Hwang, H. Wu, K. Goutam and L. F. Eastman, *Appl. Phys. Lett.* **79**, 1489 (2001).
2. M. Higashiwaki and T. Matsui, *Jpn. J. Appl. Phys.* **41**, L540 (2002).
3. V. Yu. Davydov, A. A. Klochikhin, R. P. Seisyan, V. V. Emtsev, S. V. Ivanov, F. Bechstedt, J. Furthmuller, H. Harima, A. V. Mudryi, J. Aderhold, O. Semchinova, and J. Graul, *Phys. Stat. Solidi (b)*, **229**, R1 (2002).
4. J. Wu, W. Walukiewicz, K. M. Yu, J. W. Auger III, E. E. Haller, H. Lu, W. J. Schaff, Y. Saito and Y. Nanishi, *Appl. Phys. Lett.* **80**, 3967 (2002).
5. T. Matsuoka, H. Okamoto, M. Nakao and E. Kurimoto, *Appl. Phys. Lett.* **81**, 1246 (2002).
6. M. J. Manfra, N. G. Weimann, J. W. P. Hsu, L. N. Pfeiffer, K. W. West, S. Syed, H. L. Stormer, W. Pan, D. V. Lang, S. N. G. Chu, G. Kowash, A. W. Sargent, J. Caissie, K. M. Molvar, L. J. Mahoney and R. J. Molnar, *J. Appl. Phys.* **92**, 338 (2002).
7. H. Lu, W. J. Schaff, J. Hwang, H. Wu, W. Yeo, A. Pharkya, and L. F. Eastman, *Appl. Phys. Lett.* **77**, 2548 (2000).
8. D. C. Look, H. Lu, W. J. Schaff, J. Jasinski and Z. Liliental-weber, *Appl. Phys. Lett.* **80**, 258 (2002).
9. J. Cai and F. A. Ponce, *Phys. Stat. Sol. (a)*, **192**, 407 (2002).
10. H. Lu, W. J. Schaff, J. Hwang and L. F. Eastman, *MRS Spring Meeting* (April 16-20, 2001, San Francisco, CA), on *Mater. Res. Soc. Symp.* (2001), 680E, E3.2.

BEST AVAILABLE COPY

### Optical Characterization of High Quality GaN Produced by High Rate Magnetron Sputter Epitaxy

Minseo Park, E. Carlson<sup>3</sup>, Y. C. Chang<sup>1</sup>, J. F. Muth<sup>1</sup>, J. Bumgarner<sup>3</sup>, R. M. Kolbas<sup>1</sup>, J. J. Cuomo, R. J. Nemanich<sup>2</sup>

Department of Materials Science and Engineering, North Carolina State University, Raleigh, NC 27695

<sup>1</sup>Department of Electrical and Computer Engineering, North Carolina State University, Raleigh, NC 27695

<sup>2</sup>Department of Physics, North Carolina State University, Raleigh, NC 27695

<sup>3</sup>Kyma Technologies, Inc., 8829 Midway West Road, Raleigh, NC 27617

#### ABSTRACT

The thick films of GaN were investigated using X-ray diffraction, micro-Raman spectroscopy and photoluminescence spectroscopy. The thick films of GaN were prepared on (0001) sapphire using high rate magnetron sputter epitaxy with growth rates as high as 10-60  $\mu\text{m}/\text{min}$ . The width of the X-ray rocking curve ((0002) reflection) for the sample produced by this method is  $\sim 300$  arc-sec. Only the allowed modes were observed in the polarized Raman spectra. The background electron concentration is lower than  $3 \times 10^{16} \text{ cm}^{-3}$ , which was determined from the Raman spectra. The phonon lifetime determined from Raman  $E_2^{(2)}$  mode was 1.6 ps, which is comparable to that of bulk single crystal GaN grown by sublimation (1.4 ps). The full-width-at-half-maximum of the near band-edge photoluminescence peak obtained at 77K is  $\sim 100$  meV.

#### INTRODUCTION

Wide band gap III-V nitrides semiconductors such as gallium nitride (GaN) are important materials for optoelectronic applications in the short-wavelength spectral region. GaN can be prepared using a variety of techniques such as organometallic vapor phase epitaxy (OMVPE) and molecular beam epitaxy (MBE). It can also be produced using sputtering, but the sputtering process has not been considered as a method to produce high quality epitaxial films of GaN. After the sputtered GaN was synthesized by Hovel and Cuomo [1], only a few workers have reported on sputter epitaxy of GaN [2-7].

Recently, we have demonstrated that high quality GaN films can be grown using sputtering, and the full-width-at-half-maximum of X-ray rocking-curve for this sample is  $\sim 300$  arc-sec. The smallest value reported until now was 620 arc-sec, which was produced by Webb *et al.* using magnetron sputter epitaxy [7]. Values for the FWHM of (0002) rocking curves for thin GaN films grown *via* HVPE directly on sapphire have been previously reported in the range of 200 to 600 arc-sec [8, 9, 10]. Note that FWHM for GaN grown by OMVPE can be as low as  $\sim 30$  arc-sec [11].

In the present investigation, we have used X-ray diffraction, micro-Raman scattering, and photoluminescence spectroscopy to assess the crystal quality of the sputtered GaN.

## EXPERIMENTAL

Thick films of GaN were prepared on sapphire substrates using high-rate DC reactive magnetron sputter epitaxy. As a target, pure gallium (99.9999%) was contained in a large area stainless steel cup (6 in.). This sputtering technique allows the growth of high quality GaN layers on large area substrates (up to 4 in.) with growth rates as high as 10-60  $\mu\text{m}/\text{min}$ . The deposition chamber was pumped to a pressure of  $1 \times 10^{-6}$  Torr and backfilled with a gas mixture of argon and nitrogen. The GaN layers were deposited on single crystal (0001) sapphire substrates (2 in.) that were heated up to 1200  $^{\circ}\text{C}$  using a graphite filament. The layers were grown under a variety of conditions of sputtering atmosphere and substrate temperature. The thickness of the film is 20  $\mu\text{m}$ .

X-ray rocking curve measurements were carried out using the Bede 200 double crystal X-ray diffractometer. Micro-Raman spectroscopy was performed at room temperature using backscattering geometry with the 514.5 nm line of an  $\text{Ar}^+$  laser and an ISA U-1000 scanning double monochromator to disperse the Stokes Raman scattering spectra. The excitation laser beam was focused to a small spot (2  $\mu\text{m}$  in diameter) with a microscope objective, and the power of the laser was fixed to 140 mW. The frequency-tripled output of a pulsed Ti: Sapphire laser (280 nm and 250 fs at 76 MHz) was used as the UV excitation source for photoluminescence spectroscopy. The sample was mounted on an oxygen-free highly conductive copper plug and placed on the cold finger of a liquid nitrogen dewar. The photoluminescence (PL) signal was collected, collimated and focused on to the entrance slits of a 0.32 m spectrometer, and the emission was detected using a cooled GaAs photomultiplier dc coupled to an electrometer.

## RESULTS AND DISCUSSION

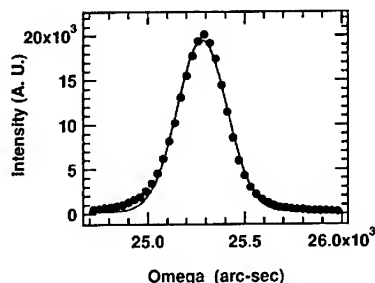


FIGURE 1. X-ray rocking curve from (0002) reflection

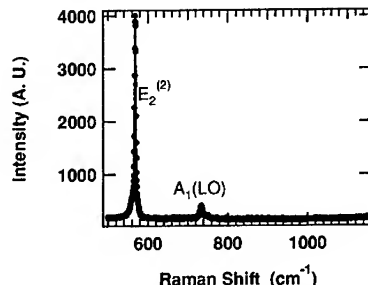


FIGURE 2. Raman spectrum of sputtered GaN

Figure 1 presents an X-ray rocking-curve for GaN film deposited on (0001) sapphire. The FWHM of the (0002) rocking curve for the sample which was used for this investigation is  $\sim 300$  arc-sec. Hexagonal GaN has a wurtzite structure which belongs to the  $C_{6v}^4$  space group. According to group theory,  $A_1(z) + 2B_1 + E_1(x,y) + 2E_2$  optical modes occur at the  $\Gamma$  point of the Brillouin zone of GaN [17]. Among these optical modes, the two  $E_2$  modes are Raman active, the  $A_1$  and  $E_1$  modes are both Raman and

infrared active, and the two  $B_1$  modes are neither Raman nor infrared active. The  $A_1$  and  $E_1$  modes split into longitudinal optical (LO) and transverse optical (TO) components due to their polar nature. Only the  $E_2^{(1)}$ ,  $E_2^{(2)}$ , and  $A_1(\text{LO})$  modes are allowed with the  $z(x,-)z$  scattering geometry of our experiment. Figure 2 shows polarized Raman spectra of the GaN grown on sapphire. As can be seen from the figure, only the allowed phonon modes were observed. A high-resolution spectrum of the  $E_2^{(2)}$  mode is shown in Figure 3(a).

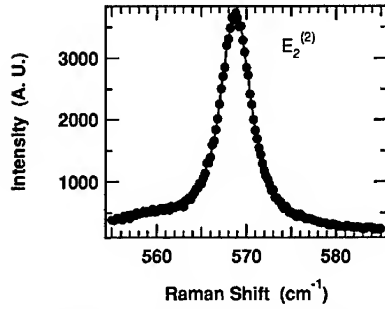


FIGURE 3(a). High resolution Raman spectrum of  $E_2^{(2)}$  mode.

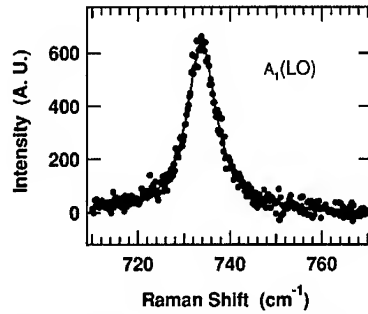


FIGURE 3(b). High resolution Raman spectrum of  $A_1(\text{LO})$  mode.

A longitudinal optical (LO) phonon couples with a plasmon through the macroscopic electric field in the case of polar semiconductors such as GaAs and GaN [12]. The coupling is via the macroscopic electric fields of the phonons and plasmons. The coupling between the plasmons and the LO phonon generates two coupled LO phonon-plasmon (LPP) modes, which are referred to as  $\omega_+$  (LPP<sup>+</sup>) and  $\omega_-$  (LPP<sup>-</sup>) [13]. The frequency of these coupled modes varies as a function of the free carrier concentration. This effect was suggested by Varga [14], and first experimentally observed in GaAs by Mooradian and Wright [13]. In the case of GaN where plasmon damping is substantial, the coupling will be manifested as a shift of the LO phonon mode. The plasma frequency can be obtained by fitting the coupled mode to the following formula [15]:

$$I_A = \text{Constant} \cdot A(\omega) \cdot \text{Im}\{-1/\epsilon(\omega)\} \quad (2)$$

where  $\omega$  is the Raman shift,  $\epsilon(\omega)$  is the dielectric function which has a phonon and a plasmon contribution, and  $A(\omega)$  is the interference term which contains Faust-Henry coefficient. The  $A(\omega)$  is expressed as

$$A(\omega) = 1 + 2C \frac{\omega_{\text{TO}}^2}{\Delta} [\omega_p^2 \gamma (\omega_{\text{TO}}^2 - \omega^2) - \omega^2 \Gamma (\omega^2 + \gamma^2 - \omega_p^2)] + C^2 \left\{ \omega_p^2 [\gamma (\omega_{\text{LO}}^2 - \omega_{\text{TO}}^2) + \Gamma (\omega_p^2 - 2\omega^2)] + \omega^2 \Gamma (\omega^2 + \gamma^2) \right\} \left( \frac{\omega_{\text{TO}}^4}{\Delta (\omega_{\text{LO}}^2 - \omega_{\text{TO}}^2)} \right) \quad (3)$$

where

$$\Delta = \omega_p^2 \gamma \{ (\omega \Gamma)^2 + (\omega_{\text{TO}}^2 - \omega^2)^2 \} + \omega^2 \Gamma (\omega^2 + \gamma^2) (\omega_{\text{LO}}^2 - \omega_{\text{TO}}^2), \quad (4)$$

and  $C$  is the Faust-Henry coefficient [16],  $\omega_p$  is the plasma frequency,  $\omega_{\text{TO}}$  and  $\omega_{\text{LO}}$  are the TO and LO phonon frequencies, respectively, and  $\Gamma$  and  $\gamma$  are the phonon and plasmon damping constants, respectively. The parameter  $\omega_p$ ,  $\Gamma$ ,  $\gamma$ , and  $C$  can be obtained

from least-square fitting. Finally, the free carrier concentration is calculated from the plasma frequency by using

$$\omega_p = \left( \frac{4\pi n e^2}{\epsilon_\infty m^*} \right)^{\frac{1}{2}}, \quad (5)$$

where  $n$  is the free carrier concentration and  $m^*$  is the effective mass of the free carriers.

Figure 3(b) shows the high resolution Raman spectrum of the coupled  $A_1(\text{LO})$ -plasmon mode. Note that the spectrum from sapphire was removed by collecting Raman spectrum from the backside of the sample, followed by spectral subtraction. By fitting the spectrum with eq. (2), a plasma frequency of  $\omega_p = 50.6 \text{ cm}^{-1}$  was obtained. By using eq. (5), the calculated free carrier concentration of the sputtered GaN is  $< 3 \times 10^{16} \text{ cm}^{-3}$ . This value is considered as maximum since this is the detection limit for this method.

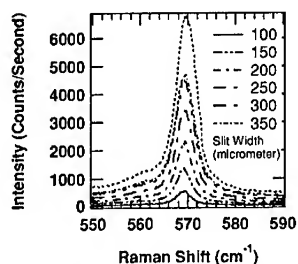


**FIGURE 4.** Raman spectrum of  $E_2^{(2)}$  mode as a function of the monochromator slit width.

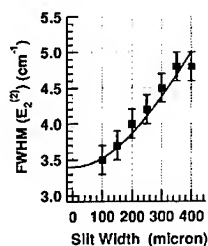


**FIGURE 5.** The plot of FWHM of the  $E_2^{(2)}$  mode vs. slit width.

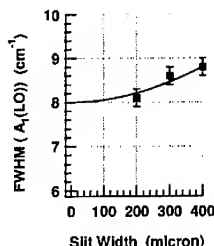


**FIGURE 6.** The plot of FWHM of the  $A_1(\text{LO})$  mode vs. slit width.

Figure 4 shows the Raman spectra of the  $E_2$  mode as a function of the spectrometer slit width. The plot of FWHM vs. spectrometer slit width is shown in Figure 5. The "zero-slit width" of  $3.4 \text{ cm}^{-1}$  was determined using the method used by Bergman *et al.*, and the detailed procedure can be found elsewhere [17]. According to the uncertainty relation,

$$\Delta E \cdot \tau \sim \hbar \quad (6)$$

where  $\tau$  is the phonon lifetime, and  $\Delta E$  is the Raman line width. The phonon lifetime of the sputtered GaN can be calculated using eq. (6) [18]. The phonon lifetime of the sputtered GaN (1.6 ps) is comparable to that of single crystal GaN grown by sublimation (1.4 ps) [15]. It is well recognized that incorporation of impurities and point defects substantially reduces phonon lifetimes, broadening the Raman peak. Note that the Raman  $E_2$  mode in GaN is not affected by variation in the free carrier concentration. Similarly, phonon lifetime of  $A_1(\text{LO})$  mode was determined to be 0.7 ps (Figure 6).

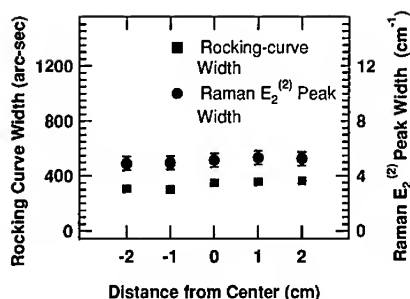


**FIGURE 7.** X-ray rocking curve width and FWHM of  $E_2^{(2)}$  mode collected from different region of the GaN film.

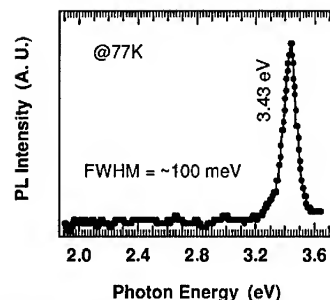


**FIGURE 8.** Photoluminescence spectrum of the sputtered GaN.

Figure 7 shows the X-ray rocking curve width and FWHM of the Raman  $E_2^{(2)}$  peak for different regions on the sputtered GaN films. No substantial variation in X-ray rocking curve width or FWHM of the Raman peak was found, which implies that the quality of the film was uniform across the wafer. Figure 8 shows the photoluminescence spectrum of the same film. The “yellow luminescence” peak was not detected from the spectrum. The FWHM of the near band-edge photoluminescence peak obtained at 77K is  $\sim 100$  meV. For comparison, the FWHM of the PL peak for samples grown by OMVPE is  $\sim 40$  meV.

## CONCLUSIONS

The thick films of GaN were investigated using X-ray diffraction, micro-Raman spectroscopy and photoluminescence spectroscopy. The thick films of GaN were prepared on (0001) sapphire using high rate magnetron sputter epitaxy with growth rates as high as  $10\text{--}60\text{ }\mu\text{m/min}$ . The width of the X-ray rocking curve ((0002) reflection) for the sample produced by this method is  $\sim 300$  arc-sec. Only the allowed modes were observed in the polarized Raman spectra. The background electron concentration is lower than  $3 \times 10^{16}\text{ cm}^{-3}$ , which was determined from the Raman spectra. The phonon lifetime determined from Raman  $E_2^{(2)}$  mode was 1.6 ps, which is comparable to that of bulk single crystal GaN grown by sublimation (1.4 ps). The full-width-at-half-maximum of the near band-edge photoluminescence peak obtained at 77K is  $\sim 100$  meV.

## ACKNOWLEDGEMENTS

We would like to thank Mr. E. Pupa, CEO of Kyma Technologies, Inc., for financial support for this work. We also appreciate Mr. M. Reed and Dr. N. El-Masry for X-ray rocking curve measurements.

## REFERENCES

1. H. J. Hovel and J. J. Cuomo, *Appl. Phys. Lett.*, **20**, 71 (1972).
2. H. Tang, J. Webb, J. Bardwell, B. Leathem, S. Charbonneau, and S. Raymond, *J. Electron. Mater.* **29**, 268 (2000).
3. K. Kubota, Y. Kobayashi, and K. Fujimoto, *J. Appl. Phys.* **66**, 2984 (1989).
4. P. Singh, J. M. Corbett, J. B. Webb, S. Charbonneau, F. Yang, and M. D. Robertson, *J. Vac. Sci. Technol.* **A16**, 786 (1998).
5. J. Ross and M. Rubin, *J. Mater. Res.*, **8**, 2613 (1993).
6. T. L. Tansley and R. J. Egan, *Thin Solid Films*, **164**, 441 (1988).
7. J. B. Webb, D. Northcott, S. Charbonneau, F. Yang, D. J. Lockwood, O. Malvezin, P. Singh and J. Corbett, *Materials Science Forum*, **264**, 1229 (1998).
8. L. T. Romano, B. S. Krusor, and R. J. Molnar, *Appl. Phys. Lett.*, **71**, 2283 (1997).
9. P. R. Tavernier and D. R. Clarke, *J. Am. Ceram. Soc.*, **85**, 49 (2002).
10. E. Valcheva, T. Paskova, P. O. Å. Persson, L. Hultman, and B. Monemar, *Appl. Phys. Lett.*, **80**, 1550 (2002).
11. M. A. di Forte-Poisson, F. Huet, A. Romann, M. Tordjman, D. Lancefield, E. Pereira, J. Di Persio, and B. Pecz, *J. Cryst. Growth* **195**, 314 (1998).
12. M. V. Klein in: *Light Scattering in Solids*, Ed. M. Cardona, Springer-Verlag, Berlin, Heidelberg, New York 1975.
13. A. Mooradian and G. B. Wright, *Phys. Rev. Lett.*, **16**, 999 (1966).
14. B. B. Varga, *Phys. Rev.* **A137**, 1896 (1965).
15. H. Yugami, S. Nakashima, and A. Mitsuishi, *J. Appl. Phys.* **61**, 354 (1987).
16. W. L. Faust and C. H. Henry, *Phys. Rev. Lett.* **17**, 1265 (1966).
17. L. Bergman, D. Alexon, P. L. Murphy, R. J. Nemanich, M. Dutta, M. A. Stroschio, C. Balkas, H. Shin, and R. F. Davis, *Phys. Rev.* **B59**, 12977 (1999).
18. M. Kuball, J. M. Hayes, Y. Shi, and J. H. Edgar, *Appl. Phys. Lett.* **77**, 1958 (2000).

---

## **Optical Properties**

### Role of polarization in the photoluminescence of C- and M-plane oriented GaN/AlGaIn multiple quantum wells

E. Kuokstis, C. Q. Chen, M. E. Gaevski, W. H. Sun, J. W. Yang, G. Simin, M. Asif Khan, H. P. Maruska,<sup>1</sup> D. W. Hill,<sup>1</sup> M. M. C. Chou,<sup>1</sup> J. J. Gallagher,<sup>1</sup> and B. H. Chai<sup>1</sup>  
Department of Electrical Engineering, University of South Carolina,  
Columbia, SC 29208, U.S.A.  
<sup>1</sup>Crystal Photonics, Inc.,  
Sanford, FL 32773, U.S.A.

#### ABSTRACT

The comparative study of photoluminescence (PL) dynamics of wurtzite-type GaN/AlGaIn multiple quantum wells (MQWs) fabricated using low-pressure metalorganic chemical vapor deposition technique over GaN coated [0001]-sapphire (C-plane) and single crystalline [1 $\bar{1}$ 00]-oriented freestanding GaN (M-plane) substrates is presented. The MQWs on C-plane sapphire at low excitation exhibited much lower (~30 times) PL intensity in comparison with M-plane samples. The C-plane MQWs showed a strong excitation intensity-induced PL spectrum line blueshift (up to 140 meV). Meanwhile identical MQW structures on M-plane substrates demonstrated no PL peak shifts indicating an absence of polarization fields. At higher excitation (>50 kW/cm<sup>2</sup>) the PL intensity and spectra peak positions for both the C- and the M-plane MQWs become nearly the same and do not differ with subsequent increase of pumping. Theoretical analysis and comparison with PL experimental data revealed strong (up to ~1.2-1.3 MV/cm) built-in electrostatic fields in the C-plane structures whereas M-plane structures are almost non-polar.

#### INTRODUCTION

Thin films of N-based wurtzite (WZ) compounds grown along the *c*-axis ([0001] direction) usually have strong built-in electrostatic field as a result of spontaneous and piezo-electric polarization, due to the noncentrosymmetric nature of WZ C-plane oriented layers[1]. In quantum wells, these electrostatic fields tend to bend the energy bands, and electrons and holes typically become situated in nearly triangular potential wells. The modulation of the conduction and valence band edges due to large internal electrostatic fields leads to the Quantum Confined Stark Effect (QCSE) which is undesirable in light-emitting devices because the fields across the individual quantum wells give rise to a spatial separation of electrons and holes [2]. This results in a reduced oscillator strength and lower quantum efficiency for radiative transitions. Furthermore, in multiple quantum well (MQW) structures designed for deep UV emission, QCSE causes an undesirable red shift in the emission spectra [3].

A useful approach for reducing the deleterious effects of built-in fields is to fabricate GaN-based structures along non-polar directions, e.g., to grow [1 $\bar{1}$ 00]-oriented M-plane films since these surfaces contain equal number of Ga and N atoms and therefore are non-polar [4].

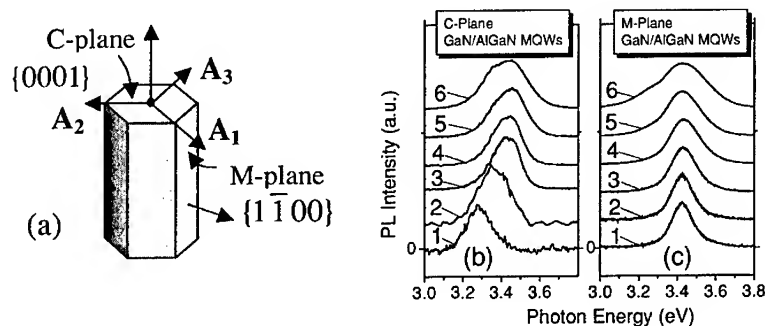
In the present study, we demonstrate fabrication of non-polar N-based WZ layers and analyze the dynamics of photoluminescence (PL) in highly excited GaN/AlGaIn MQWs with C- and M-plane surfaces, seeking to gain control over the built-in electrostatic field and while determining the properties of quantum structures.

## EXPERIMENTAL DETAILS

The six-period of GaN/AlGaIn MQWs were deposited simultaneously on the two types of substrates using low-pressure metalorganic chemical vapor deposition. The  $[1\bar{1}00]$ -oriented M-plane GaN templates were grown by halide vapor phase epitaxy (HVPE) on the closely lattice matched (100) plane of LiAlO<sub>2</sub>. After depositing a 350- $\mu\text{m}$ -thick layer of GaN, the original LiAlO<sub>2</sub> substrate was removed with wet acid etching. Thus freestanding  $[1\bar{1}00]$ -oriented GaN templates were obtained, which served as the starting substrates for our study. The  $[0001]$ -oriented C-plane AlGaIn/GaN MQWs were grown on 3- $\mu\text{m}$ -thick GaN layers which were deposited on C-plane sapphire substrates. The quality and parameters of MQWs was checked by X-Ray measurements, as well as Nomarsky optical microscopy and scanning electron microscopy. The barrier alloy contained 18% of Al. The quantum well and barrier widths were  $L_w = 5$  nm and  $L_b = 10$  nm, respectively. The PL spectra were measured using excitation from a pulsed ArF excimer laser ( $\lambda = 193$  nm,  $\tau = 8$  ns,  $f_{\text{rep}} = 10$ -100 Hz). The laser beam was focused on the surface of the samples to a spot of about 0.2 mm diameter. A maximum pump power density of  $\sim 2$  MW/cm<sup>2</sup> could thus be reached. Excitation intensity could be reduced by a set of neutral density filters. Luminescence was measured in a back-scattering geometry using a TRIAX550 monochromator with a UV-enhanced charge-coupled device array.

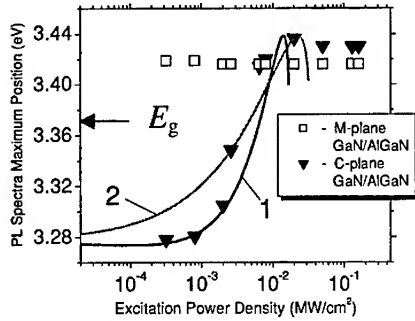
## DISCUSSION

Figure 1 illustrates room temperature PL experimental results in the two types of GaN/AlGaIn MQWs under different excitation levels. In both cases [figure 1(b),(c)], the



**Figure 1.** Crystallographic orientation of WZ films (a) and PL spectra for C-plane (b) and M-plane (c) GaN/Al<sub>0.18</sub>Ga<sub>0.82</sub>N MQWs as a function of excitation power density: 1 – 3, 2 – 10, 3 – 30, 4 – 80, 5 – 190, and 6 – 640 kW/cm<sup>2</sup>, respectively.

near band-edge emission spectrum consists of one band; however, for the C-plane sample the peak undergoes a blueshift with excitation intensity whereas for M-plane its position remains unchanged. The experimental points in figure 2 show the peak energies of the PL spectra as a function of excitation power density  $P$  with more detail.



**Figure 2.** PL spectra maximum position as a function of excitation power density. Symbols correspond to experimental data and solid curves show theoretical dependencies. Arrow  $E_g$  shows the forbidden gap position of bulk well material.

Note that for  $P > 50 \text{ kW/cm}^2$ , PL spectral positions in both cases become very close and remain nearly the same with further increases in excitation intensity. The observed PL dependencies may be explained taking into account the built-in electrostatic field, the strength of which is reduced with increasing excitation, due to field screening by the carriers. In order to evaluate the magnitude of the electrostatic field in the MQWs, we applied a simple model based on a triangular potential well resulting from the presence of both the total built-in field as well as the photo-generated carriers with carrier density  $n$ . We assumed that those carriers accumulate at GaN/AlGaIn interfaces, thereby reducing the field  $F_w$ , which can be approximately evaluated as [5]

$$F_w(n) = F_0 - neL_bL_w / [\epsilon_0(L_w\epsilon_b + L_b\epsilon_w)] \quad (1)$$

Here  $F_0$  is built-in electrostatic field strength in unexcited wells. All the parameters used in our calculations are taken from the literature [1,6-8]. Since the position of the PL peak energy  $h\nu_{\text{max}}$  for near band-edge emission (electron-hole band-to-band and/or excitonic recombination) is determined by the ground level energy, we can obtain [9]

$$h\nu_{\text{max}} = \tilde{E}_g - eF_w(n)L_w + \left[ \frac{9ehF_w(n)}{16\sqrt{2}} \right]^{2/3} \left[ \left( \frac{1}{m_e^*} \right)^{1/3} + \left( \frac{1}{m_h^*} \right)^{1/3} \right] \quad (2)$$

Her  $\tilde{E}_g$  is carrier density-dependent forbidden gap due to many-body effects in high-density carrier system [10].

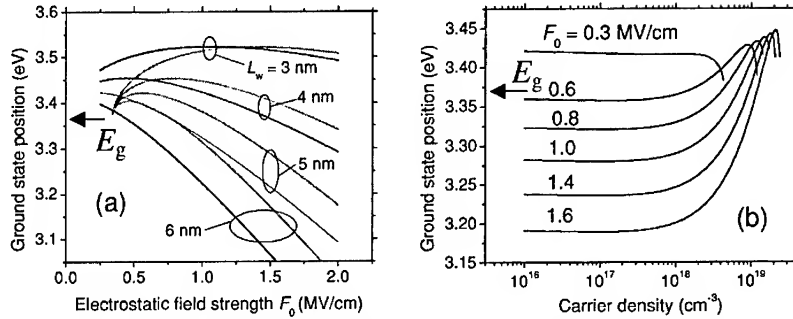


**Figure 3.** Ground level position of GaN/Al<sub>0.18</sub>Ga<sub>0.82</sub>N quantum well as a function of electrostatic field strength for different well widths (a), and carrier density for different electrostatic field strength (b). In (a), light lines correspond to carrier concentration  $5 \times 10^{18} \text{ cm}^{-3}$ , whereas black ones correspond to  $10^{16} \text{ cm}^{-3}$ . Arrows  $E_g$  show the forbidden gap position of unexcited bulk material.

Figure 3 illustrates ground level position calculation as a function of built-in electrostatic field (a) and photo-injected carrier concentration (b) for several parameters. Note, that our triangular potential model is valid for total built-in fields which are stronger than  $\sim 0.3 \text{ MV/cm}$ . As can be seen, there is a considerable ground state shift due to QCSE, especially for wells with larger widths [more than  $\sim 4 \text{ nm}$ , see figure 3(a)]. On the other hand in our quantum structures, effective screening of the built-in fields just starts at carrier densities exceeding  $\sim 10^{18} \text{ cm}^{-3}$  [see figure 3(b)].

In order to compare our experimental PL results with calculations, we have to express  $\hbar\nu_{\text{max}}$  as a function of excitation power density  $P$ . We have used two approaches: (i) assuming constant carrier lifetime  $\tau$  (this situation is expected for lower carrier injection level), or (ii) assuming predominantly bimolecular recombination (higher excitation). In the former case, the carrier density  $n = \alpha P \tau / \hbar\nu_{\text{las}}$ , whereas in the latter case

$$n = \sqrt{\frac{P\alpha}{\hbar\nu_{\text{las}}\gamma}}. \text{ Here } \alpha \text{ is the absorption coefficient for the laser emission at } \hbar\nu_{\text{las}} \text{ and } \gamma \text{ is}$$

the bimolecular recombination coefficient. The results of calculations are shown in figure 2. It can be seen that our model can be rather successfully applied for C-plane MQWs assuming the built-in electrostatic field is around  $1.23 \text{ MV/cm}$ , whereas for M-plane MQWs the initial field values need to be much lower ( $< 300 \text{ kV/cm}$ ). We can also confirm that the constant lifetime approach describes experiment results better for lower excitation levels (curve 1), while bimolecular recombination presumably starts to appear at  $P > 10 - 20 \text{ kW/cm}^2$  (curve 2).

We have evaluated the built-in electrostatic field  $F_0$  in the case of spontaneous and piezoelectric polarization in GaN/Al<sub>0.18</sub>Ga<sub>0.82</sub>N MQWs (C-plane orientation) independently, just taking into account the material parameters relevant to those quantum structures [5]:

$$F_0 = (P_{sp}^w - P_{sp}^b - P_{pc}^b)L_b / [\epsilon_0(L_w\epsilon_b + L_b\epsilon_w)] \quad (3)$$

In this model, we have neglected piezo-polarization in the wells since the well material is GaN and is free from in-plane deformation due to the thick (therefore relaxed) GaN buffer layer included in the structures. However, the  $\text{Al}_{0.18}\text{Ga}_{0.82}\text{N}$  barrier is under the tension  $\sigma_{\parallel}$  due to in-plane mismatch with GaN, and hence barrier piezoelectric charge can be calculated as  $P_{pe}^b = -2\sigma_{\parallel}(e_{33}C_{11}/C_{33} - e_{31})$ , where  $e_{ij}$  and  $C_{ij}$  are piezoelectric tensor components and the elastic constants [1,5], respectively. The field value evaluated according to (3) for C-plane MQWs is found to be 1.27 MV/cm. It agrees well with the value 1.23 MV/cm obtained from our earlier theoretical and experimental PL data fitting in figure 2.

In addition, we have analyzed the PL integrated intensity dependence on excitation for both M- and C-plane MQWs over a wide range of intensities. Figure 4 shows integrated PL intensity as a function of excitation power density.

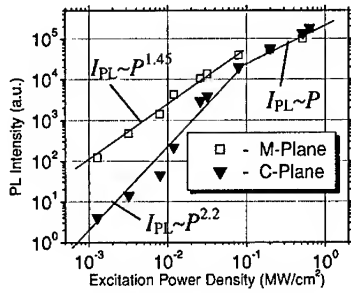


**Figure 4.** Integrated PL intensity versus excitation power density in M- and C-oriented GaN/AlGaIn MQWs.

Note that under higher excitation levels ( $P > 50 \text{ kW/cm}^2$ ), absolute PL intensity is very close for both C- and M-plane MQWs and then increases linearly with excitation ( $I \sim P$ ), whereas at low excitation levels the situation is quite different. At low excitation the PL intensity for C-plane MQWs increases strongly superlinearly ( $I \sim P^{2.2}$ ), whereas for M-plane MQWs the dependence is weaker ( $I \sim P^{1.45}$ ). At the excitation level of  $\sim 1 \text{ kW/cm}^2$  the PL intensity from MQWs with M-plane orientation is about 30 times higher in comparison to those with C-plane orientation. A similar difference in PL intensities was reported recently in quantum well structures with R-plane orientation using CW laser excitation [11]. These observations can be understood by taking into account the strong built-in electrostatic field in C-plane MQWs in contrast to M-plane MQWs which exhibit much lower field strength. Indeed, spatial separation of carriers in triangular wells due to the QCSE in C-plane MQWs with the characteristic strong built-in fields, which exist at low excitation intensities, leads to poor overlapping of the wave functions of electrons and holes. This process leads to the major reduction of electron-hole radiative recombination traffic as compared to M-plane MQWs under these conditions. Typically, when nonradiative channels predominate (low excitation and constant lifetime regime), the band-to-band or excitonic radiative recombination rate is expected to change with excitation as  $I \sim P^2$ . There will be a transformation to  $I \sim P$  when nonradiative channels

saturate and radiative recombination predominates at elevated excitation (high excitation and bimolecular recombination regime). A power index 2.2 for C-plane MQWs indicates that there must be some additional reason for a steeper PL intensity dependence on excitation. We suggest that the reason is based on screening of the built-in electrostatic field by injected carriers at elevated excitation levels, whereby the reduction of the field strength leads to stronger overlap of the carrier wave functions and consequently an additional increase of PL intensity.

## CONCLUSIONS

The comparative study of PL for C- and M- plane GaN/AlGaIn MQWs showed strong differences in excitation-induced behavior of PL in these quantum structures. The PL spectrum peak position of C-plane MQWs undergoes a strong blueshift with increasing excitation intensity, whereas that of M-plane MQWs remains unchanged. We observed much weaker PL intensity for C-plane MQWs in comparison to M-plane MQWs at low excitation levels. These results indicate the existence of much stronger built-in electrostatic fields in C-plane quantum structures in comparison with M-plane MQWs. Analysis of the experimental results along with theoretical data fitting shows that the electrostatic field strength in C-plane MQWs reaches the value of 1.2-1.3 MV/cm. Clearly, the growth of GaN/AlGaIn MQWs with a non-polar orientation can lead to a significant increase in the quantum efficiency of these nitride-based emitters, especially at low and medium excitation levels (e.g. for light emitting diodes).

## ACKNOWLEDGEMENTS

The work was partially supported by DARPA contract number DAAD19-02-10282, monitored by Dr. J. Zavada and Dr. J. Carrano, and DARPA contract number F19628-02-C-0057, monitored by Dr. J. Lorenzo and Dr. J. Carrano.

## REFERENCES

1. F. Bernardini, V. Fiorentini, and D. Vanderbilt, *Phys. Rev. B* **56**, R10024 (1997).
2. J. S. Im, H. Kollmer, J. Off, A. Sohmer, F. Scholz, and A. Hangleiter, *Phys. Rev. B* **57**, R9435 (1998).
3. G. Vaschenko, D. Patel, C. S. Menoni, N. F. Gardner, J. Sun, W. Götz, C. N. Toné, and B. Clausen, *Phys. Rev. B* **64**, 241308 (2001).
4. J. E. Northrup and J. Neugebauer, *Phys. Rev. B* **53**, R10477 (1996).
5. R. Cingolani, A. Botchkarev, H. Tang, and H. Markoç, *Phys. Rev. B* **61**, 2711 (2000).
6. D. W. PALMER, [www.semiconductors.co.uk](http://www.semiconductors.co.uk), 2001.04.
7. S. C. Jain, M. Willander, J. Narayan, and R. Van Overstraeten, *J. Appl. Phys.* **87**, 965 (2000).
8. A. Dmitriev and A. Oruzhenikov, *J. Appl. Phys.* **86**, 3241 (1999).
9. C. Weisbuch, B. Vinter, *Quantum Semiconductor Structures*, Academic Press, 1991.
10. W. F. Brinkman and T. M. Rice, *Phys. Rev. B*, **7**, 1508 (1973).
11. H. M. Ng, *Appl. Phys. Lett.* **80**, 4369 (2002).

### Cathodoluminescence of MBE-grown cubic AlGa<sub>x</sub>N/GaN multi-quantum wells on GaAs (001) substrates

D. J. As, S. Potthast, U. Köhler, A. Khartchenko and K. Lischka,  
University of Paderborn, Faculty of Science, Department of Physics, Warburger Strasse 100,  
D-33095 Paderborn, Germany, [d.as@uni-paderborn.de](mailto:d.as@uni-paderborn.de)

#### ABSTRACT

Cubic phase GaN/Al<sub>x</sub>Ga<sub>1-x</sub>N Multi Quantum Well structures were grown by rf-plasma assisted molecular beam epitaxy (MBE) on GaAs (001) substrates. X-ray measurements showed a high phase purity of the epilayers and revealed an Aluminum incorporation between 9 % and 49 %, respectively. The QW luminescence was tuned between 3.25 eV and 3.4 eV by means of the variation of QW barrier Aluminum content and QW width. Strong Cathodoluminescence (CL) from the GaN QWs and the underlying cubic Al<sub>x</sub>Ga<sub>1-x</sub>N bulk material was observed at room temperature. The spatial localization of the QW emission was unambiguously determined by depth-resolved CL measurements. Combined with a model of energy-dependent penetration, diffusion, and recombination, these variations indicate a value of about 20 nm for the minority carrier diffusion length within the Al<sub>x</sub>Ga<sub>1-x</sub>N confinement layer. The assignment of Al<sub>x</sub>Ga<sub>1-x</sub>N bulk and GaN luminescence was further supported by employing a simple effective-mass quantum mechanical model.

#### INTRODUCTION

In optoelectronic and microelectronic applications of group-III nitrides, heterostructures incorporating Al<sub>x</sub>Ga<sub>1-x</sub>N and GaN epilayers are important ingredients in, e.g. lasers, LEDs and high electron mobility transistors (HEMTs). However, the commonly used hexagonal Al<sub>x</sub>Ga<sub>1-x</sub>N/GaN heterostructures show an inherently strong spontaneous polarisation oriented along the hexagonal c-axis as well as strain induced piezoelectric polarization. Such polarization induced electric fields have a detrimental effect on the electrical and optical characteristics of GaN-based quantum well (QW) devices with wurtzite lattice configuration and increases the threshold current and redshifts the emission wavelength in laser diodes [1-3]. The absence of built-in field in these structures will improve the performance and will significantly simplify the design of such devices. The metastable cubic phase of group III nitrides offers the possibility to avoid these problems by growing the samples on (001) oriented substrates.

In this contribution we report on the optical properties of cubic Al<sub>x</sub>Ga<sub>1-x</sub>N/GaN multi quantum well (MQW) structures. The samples were grown by radio-frequency plasma-assisted molecular beam epitaxy (MBE) on GaAs (001) substrates and depth resolved cathodoluminescence (CL) was used for optical characterization. The spatial localization of the QW emission as well as the minority diffusion length were unambiguously determined by depth-resolved CL measurements.

## EXPERIMENTAL

Multi Quantum Well (MQW) structures of cubic phase  $\text{Al}_x\text{Ga}_{1-x}\text{N}$  barriers and GaN wells were grown on GaAs (001) substrates in a Riber 32 MBE system using a RF plasma-assisted Nitrogen source. Solid source Knudsen cells were used in order to supply Al and Ga in elemental form.

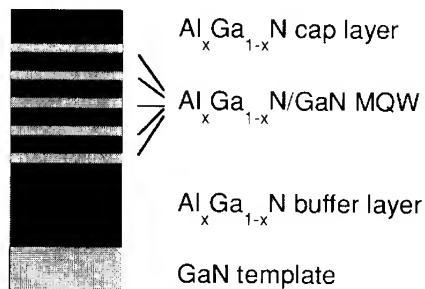


**Figure 1.** Schematic structure of the cubic  $\text{AlGaIn/GaN}$  MQWs

The epilayers were deposited at a substrate temperature  $T_S = 720^\circ\text{C}$ . During growth, the process was continuously controlled by means of reflection high-energy electron diffraction (RHEED). Details of the growth procedure have been published elsewhere [4].

A sketch of the vertical structure of the investigated MQWs is schematically shown in Fig. 1. The sample consisted of a 300 nm GaN buffer layer on a GaAs (001) substrate, followed by a 350 nm  $\text{Al}_x\text{Ga}_{1-x}\text{N}$  layer, whose thickness was chosen such as to ensure that it was relaxed [5]. On top of this structure, MQWs consisting of 5 GaN wells with  $\text{Al}_x\text{Ga}_{1-x}\text{N}$  barriers of the same Al content  $x$  were grown. Finally, a cap layer of about 70 nm  $\text{Al}_x\text{Ga}_{1-x}\text{N}$  was deposited. The well width was varied between 2 nm, 5 nm, and 10

nm and the Aluminum content was changed between  $x=0.09$ ,  $x = 0.25$  and  $0.49$ , respectively.

The cubic nature, the phase purity and crystalline quality of the  $c\text{-Al}_x\text{Ga}_{1-x}\text{N/GaN}$  layers were verified by high-resolution X-ray diffraction (HRXRD) experiments and transmission electron microscopy (TEM). Cross-section TEM images showed well resolved, abrupt interfaces and an excellent periodicity of the quantum well structures [6]. The thickness variation in the lateral direction was estimated to be a few monolayers. However, at the coalescence of submicron-size grains a wavy structure was observed in TEM. A severe broadening of the XRD reflection was observed due to the high dislocation density in cubic III nitrides and superlattice satellite peaks were only weakly indicated.

CL experiments were performed in a Zeiss DSM 950 scanning electron microscope (SEM) equipped with an Oxford CL sample stage. The light emitted from the sample was collected by an elliptical mirror and focused onto a UV-transparent glass fiber. The light was analyzed spectrally by a 0.5 m Spex monochromator and detected by a 1P28 photomultiplier operating in photon counting mode [7]. Depth-resolved CL measurements were performed by varying the electron acceleration voltage between 1 kV and 15 kV. The spectral resolution was 2 nm.

## RESULTS AND DISCUSSION

Strong luminescence from the GaN QWs and the cubic  $\text{Al}_{0.25}\text{Ga}_{0.75}\text{N}$  bulk material is measured by Cathodoluminescence at room temperature. In Fig. 2 spectra of a fivefold GaN QW with a well width of 5 nm and a barrier width of 10 nm are shown at different electron beam acceleration voltages. The energy of the e-beam has been varied between 3 keV and 10 keV. The CL spectra are dominated by two emission bands at 3.409 eV and 3.638 eV, respectively. The

BEST AVAILABLE COPY

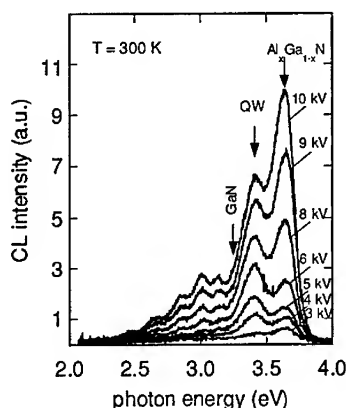


**Figure 2.** Plot of room temperature CL spectra as function of energy, measured on a sample with Aluminum mole ratio  $x_{Al}=0.25$  and a well width of 5 nm. The spectra were recorded for different electron beam acceleration energies 10keV, 8keV, 6keV, 5keV, and 3keV, ordered from top to bottom.

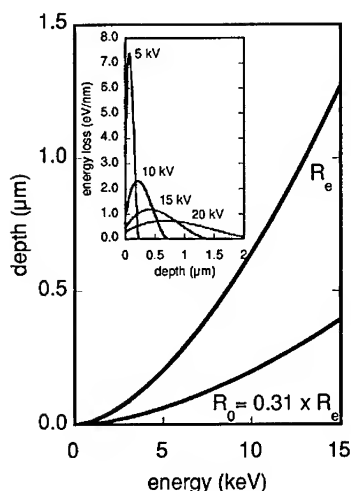


**Figure 3.** Maximum penetration depth  $R_e$  and depth of maximum energy loss  $R_0$  versus e-beam energy calculated for cubic GaN. The inset shows characteristic energy loss  $dE/dx$  versus depth.

high energy peak is due to emission from the cubic  $Al_{0.25}Ga_{0.75}N$  [8] whereas the lower one is due to emission of quantized states from GaN QWs. Using the linear increase of the band gap energy with Al-content  $E_{gap}(x) = 3.20 + 1.85 \cdot x$  [eV] [9] an Al-content of 0.24 is found. This is in excellent agreement with the value estimated on  $c-Al_xGa_{1-x}N$  bulk material by x-ray measurements and spectroscopic ellipsometry [10].

For shallow excitation energy ( $E_{beam} = 3$  keV) luminescence is excited only in the  $Al_{0.25}Ga_{0.75}N$  capping layer. With increasing electron beam acceleration voltage, first the emission of the GaN QW luminescence increases and then, at higher e-beam energies, that of the  $Al_{0.25}Ga_{0.75}N$  bulk luminescence. Obviously the emission from the MQW region is dominating at intermediate e-beam energies whereas at large electron beam energies most of the luminescence stems from the underlying  $Al_{0.25}Ga_{0.75}N$  layer.

For a more quantitative analysis of the emission as a function of the electron beam energy the production of free electron-hole pairs by the incident electron beam has to be considered in detail. Electrons incident on a semiconductor generate a cascade of secondaries with energies decreasing with increasing penetration depth. The rate of energy loss reaches a maximum at an intermediate depth that increases with incident beam energy. Figure 3 illustrates the depth of maximum energy loss  $R_0$  and the depth of maximum penetration  $R_e$  (Bohr-Bethe depth) as a function of incident e-beam energy in GaN. The inset contains several curves of energy loss per unit length,  $dE/dx$ , as a function of depth into the solid. These curves are generated using a polynomial function fit to the Everhart-Hoff depth-dose relation [11, 12]. The curves are normalized in area to reflect relative differences in carriers generated with constant beam current.  $R_0$  is approximated as 0.31 times the maximum range of energy dissipation  $R_e$  which has been calculated using a model of Kanaya and Okayama [13].

In Figure 4 the intensity ratio of the QW emission at 3.409 eV to the emission of the  $Al_{0.25}Ga_{0.75}N$  layer at 3.638 eV is plotted versus depth  $R_0$ . In particular, the ratio of quantum well to  $Al_xGa_{1-x}N$

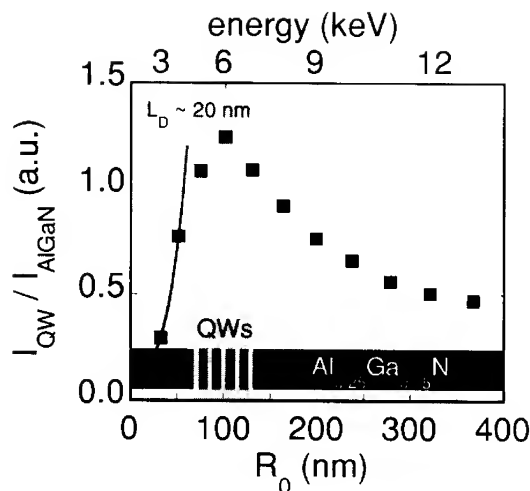


**Figure 4.** Ratio of QW-emission to  $\text{AlGaIn-N}$  emission versus depth of maximum energy loss  $R_0$ . At the bottom a schematic drawing of the sample is inserted. The full curve represents the exponential intensity decay due to the diffusion of the minority carriers into the QW.

diffusion length of about 20 nm is determined from the slope of the rightmost data points. This value is comparable to the minority carrier diffusion length estimated for a hexagonal GaN/InGaN/GaN QW, which was 25-28 nm [15].

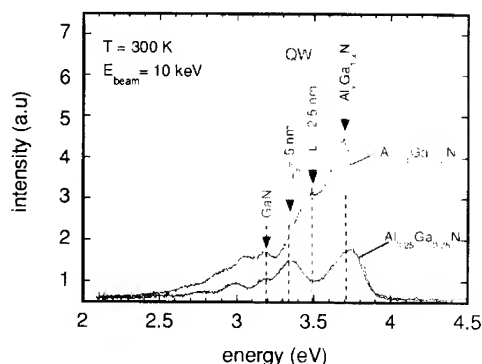


**Figure 5.** Room temperature CL spectra versus photon energy for two samples with an Aluminum mole fraction  $x_{\text{Al}}$  of 0.25 and with well widths of 5 nm and 2.5 nm, respectively.

near band edge emission displays a clear maximum for incident beam energies at about 6 keV. An excellent correlation between the spatial localization of the QWs estimated from the measured growth rate and the maximum in intensity ratio is found. This allows the unambiguous assignment of the 3.409 eV band to the emission from the  $\text{Al}_{0.25}\text{Ga}_{0.75}\text{N}/\text{GaN}$  MQW structure.

Since the intensity of QW emission is proportional to the recombination of free electrons and holes excited either within the QW or within a diffusion length of the QW, the pronounced onset and maximum in the intensity ratio of the QW to barrier emission can be used to measure the minority carrier diffusion length  $L_D$ . Using  $I_{\text{QW}} \sim I_{\text{max}} \cdot \exp(-x/L_D)$  [14] a

A clear proof for the correctness of our attribution is given by the shift of the QW emission with varying QW thickness. Figure 5 shows CL spectra of two cubic GaN QW of well thicknesses of 2.5 nm and 5 nm, respectively. A clear shift to higher energies with thinner well width is observed whereas the emission from the barrier material is unchanged. A shift to higher emission energies is also observed if the well width was held constant and the Al content of the barrier material was increased. In addition the intensity of luminescence assigned to GaN QWs is clearly increasing with the number of

BEST AVAILABLE COPY

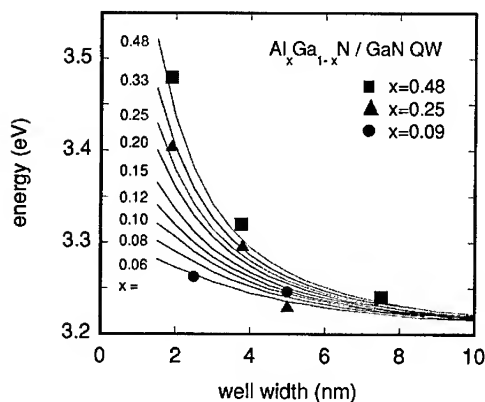


**Figure 6.** Plot of Quantum Well transition energies for GaN/Al<sub>x</sub>Ga<sub>1-x</sub>N QWs at room temperature in dependence of GaN well width for different barrier Aluminum content. The lines depict results of calculations, as detailed in the text, while the points represent experimental data from RT CL measurements.

emitting lasers or in quantum cascade lasers, where thin and thick QW layers are needed simultaneously in the injection regions [17]. A first support that in cubic GaN quantum wells the efficiency of transition in thin QWs ( $L_z = 2$  nm) is similar to that of thick QWs ( $L_z = 7.5$  nm) is clearly observed in our samples, where the intensities of wide and narrow QW emission is comparable under equal excitation conditions.

To confirm the assignment of the observed QW emission energies the transition energy of quantum wells has been calculated as a function of the well width  $L_z$ . In this calculation a ratio of conduction band discontinuity  $\Delta E_c$  to valence band discontinuity  $\Delta E_v$  of 60 to 40 is assumed [18]. In addition we take into account that the GaN wells are pseudomorphic strained [19]. The band gap discontinuity  $\Delta E_{Gap}$  is given by the experimentally determined variation of the gap energy  $\Delta E_{Gap}(y) = 1.85 \cdot y$  [eV] at RT [10]. For the effective masses of the electron and heavy hole in GaN we used  $m_e^* = 0.15 m_0$  and  $m_{hh}^* = 0.80 m_0$ , for the elastic constants  $c_{11} = 296$  GPa,  $c_{12} = 154$  GPa, and for the deformation potentials  $a = -6.4$  eV and  $b = -2.67$  eV, respectively [20]. Figure 6 shows the results of the calculations as full lines for an Al-content varying between 0.06 to 0.48. The points, triangles and squares represent experimental data from room temperature CL measurements on samples with various Al contents and well widths, respectively. One clearly sees that for all different Al mole fractions the measured data follow exactly the corresponding calculated curve.

## CONCLUSION

Multi Quantum Well structures of cubic phase GaN/Al<sub>x</sub>Ga<sub>1-x</sub>N with varying well widths and barrier heights were grown by rf-plasma assisted molecular beam epitaxy (MBE) on GaAs (001) substrates. The Al mole fraction of the barrier material was varied between 9% and 48% as determined by X-ray analysis and the c-GaN well width was changed between 2 nm and 7.5 nm,

incorporated QWs (not shown).

One advantage of cubic QWs in comparison to hexagonal QW is the slight variation of oscillator strength due to the absence of the internal electric field. Whereas for cubic QWs the oscillation strength varies by a factor of 2 only, in hexagonal Al<sub>0.27</sub>Ga<sub>0.73</sub>N/GaN QWs the presence of a typical electric field due to the spontaneous polarization  $F = 1.1$  MV/cm results in an reduction of oscillator strength by five orders of magnitudes from narrow wells to 30 monolayers (1ML = 0.26 nm) wide QWs [16]. Thus radiative lifetime is nearly insensitive to well width in cubic QWs, which enables the usage of wide QW structures for conventional edge

respectively. In this way the energy of the QW luminescence was tunable between 3.25 eV and 3.5 eV as measured by cathodoluminescence at room temperature. Depth-resolved CL measurements allowed the unambiguously spatial localization of the QW emission and enabled the estimation of the minority carrier diffusion length of about 20 nm. The assignment of the  $\text{Al}_x\text{Ga}_{1-x}\text{N}$  bulk and GaN luminescence was supported by employing a simple effective-mass quantum mechanical model.

## ACKNOWLEDGEMENTS

This paper was supported by Deutsche Forschungsgemeinschaft (DFG) under project number As 107/1-3.

## REFERENCES

1. H. Morkoç, in *"Nitride Semiconductors and Devices"*, Springer, Berlin (1999)
2. O. Ambacher, *J. Phys. D: Appl. Phys.* **31**, 2653 (1998).
3. V. Fiorentini, F. Bernardini, F.D. Sala, A.D. Carlo and P. Lugli, *Phys. Rev. B* **60**, 8849 (1999).
4. D. Schikora, M. Hankeln, D.J. As, K. Lischka, T. Litz, A. Waag, T. Buhrow and F. Henneberger, *Phys. Rev. B* **54** (12), R8381 (1996).
5. T. Frey, D.J. As, M. Bartels, A. Pawlis, K. Lischka, A. Tabata, J.R.L. Fernandez, M.T.O. Silva, J.R. Leite, C. Haug and R. Brenn, *J. Appl. Phys.* **89** (5), 2631 (2001).
6. D.J. As, U. Köhler, S. Potthast, A. Khartchenko, K. Lischka, V. Potin and D. Gerthsen, *phys. stat. sol. (c)*, (to be published) (2003).
7. C. Wang, D.J. As, B. Schöttker, D. Schikora and K. Lischka, *Semicond. Sci. Technol.* **14**, 161 (1999).
8. D.J. As, T. Frey, M. Bartels, K. Lischka, R. Goldhahn, S. Shokhovets, A. Tabata, J.R.L. Fernandez and J.R. Leite, *J. Crystal Growth* **230** (3-4), 421 (2001).
9. T. Koizumi, H. Okumura, K. Balakrishnan, H. Harima, I. Inoue, Y. Ishida, T. Nagatomo, S. Nakashima and S. Yoshida, *J. Crystal Growth* **201/202**, 341 (1999).
10. D.J. As, T. Frey, A. Khartchenko, D. Schikora, K. Lischka, R. Goldhahn and S. Shokhovets, *Mat. Res. Soc. Symp. Proc.* **639**, G5.9 (2001).
11. T.E. Everhart and P.H. Hoff, *J. Appl. Phys.* **42**, 5837 (1971).
12. L.J. Brillson, *J. Vac. Sci. and Technol. B* **19** (5), 1762 (2001).
13. K. Kanaya and S. Okayama, *J. Phys. D: Appl. Phys.* **5** (1), 43 (1972).
14. H.J. Leamy, *J. Appl. Phys.* **53** (6), R51 (1982).
15. T.M. Levin, G.H. Jessen, F.A. Ponce and L.J. Brillson, *J. Vac. Sci. and Technol. B* **17** (6), 2545 (1999).
16. P. Bigenwald, P. Lefebvre, T. Bretagnon and B. Gil, *phys. stat. sol. (b)* **216**, 371 (1999).
17. H.M. Ng, C. Gmachl, J.D. Heber, J.W.P. Hsu, S.N.G. Chu and A.Y. Cho, *phys. stat. sol. (c)*, (to be published) (2003).
18. J.A. Majewski, G. Zandler and P. Vogl, *Semicond. Sci. Technol.* **13**, A90 (1998).
19. S.L. Chuang, in *"Physics of Optoelectronic Devices"*, Wiley & Sons, New York (1995)
20. D.J. As, "Growth and characterization of MBE-grown cubic GaN,  $\text{In}_x\text{Ga}_{1-x}\text{N}$ , and  $\text{Al}_y\text{Ga}_{1-y}\text{N}$ ", in *Optoelectronic Properties of Semiconductors and Superlattices*, Vol.19, edited by M.O. Manasreh and I. Ferguson, (Gordon and Breach, 2002) pp.323

### Microscopic Description of Radiative Recombinations in InGaN/GaN Quantum Systems

Aurelien Morel, Pierre Lefebvre, Thierry Taliercio, Bernard Gil, Nicolas Grandjean<sup>1</sup>, Benjamin Damilano<sup>1</sup>, and Jean Massies<sup>1</sup>.

Groupe d'Etude des Semiconducteurs, CNRS, Université Montpellier II, CC 074, 34095  
Montpellier Cedex 5, France.

<sup>1</sup>Centre de Recherche sur l'Hétéro-Epitaxie et ses Applications, CNRS, rue Bernard Grégory,  
06560 Valbonne, France.

### ABSTRACT

Recombination dynamics in a variety of InGaN/GaN quantum systems has been studied by time resolved photoluminescence (PL). We have discovered that the time-decay of PL exhibits a scaling law: the nonexponential shape of this decay is preserved for quantum wells and quantum boxes of various sizes while their decay time varies over several orders of magnitude. To explain these results, we propose an original model for electron-hole pair recombination in these systems, combining the effects of internal electric fields and of carrier localization on a nanometer-scale. These two intricate effects imply a separate localization of electrons and holes. Such a microscopic description accounts very well for both the decays shape and the scaling law.

### 1. INTRODUCTION

Optical recombination processes in InGaN/GaN quantum systems are one of the central issues of light-emitting devices based on group-III nitrides. Previous studies have shown that radiative recombination in these systems is influenced by huge internal electric fields and by local potential fluctuations [1]. Envelope-function calculations of transition energies and oscillator strengths, including internal electric fields [2], account very well for experimental results, yielding an electric field value of ~2.5 MV/cm along the growth axis. On the other hand, the local potential fluctuations, together with large carrier effective masses in group-III nitrides, induce the localization of carrier wave-functions on nanometric scales [3], which prevents their efficient capture by nonradiative centers, related to the high density of threading dislocations. This ensures purely radiative recombination at low temperature.

The two intricate effects of electric field and localization imply a complex recombination dynamics. By performing time resolved photoluminescence (PL), we have determined how these two effects influence respectively the recombination dynamics. We recall, in a first part, the experimental results; then we present our nanoscopic model of recombination mechanisms.

### 2. EXPERIMENTAL RESULTS

We have performed time-resolved PL experiments at varying temperature on series of  $\text{In}_x\text{Ga}_{1-x}\text{N}/\text{GaN}$  quantum well (QW) and quantum box (QB) samples of similar compositions ( $0.15 < x < 0.20$ ). The samples are grown by molecular beam epitaxy on sapphire substrates. The QB size is typically of 10 nm in diameter and 2-5 nm in height. As the lateral dimension of QBs

is larger than the exciton Bohr radius (for GaN, we can estimate  $\sim 3$  nm, from the exciton binding energy and the effective masses [4]), the effects of lateral confinement are negligible and QBs behave essentially like QWs concerning electric field effects [5]: the larger the vertical size, the smaller the emission energy and the larger the characteristic time. In practice, by varying the vertical size between 2 and 6 nm, the emission energy covers the entire visible spectrum and the characteristic decay time covers four orders of magnitude.

Now, it has been understood, too, that the carriers are localized in deep valleys induced by strong potential fluctuations in the volume of the ternary alloy. One can probe such carrier localization by temperature-dependent spectroscopy [3]. For InGaN epilayers, large Stokes shifts have been assigned to carrier localization, possibly in self-formed In-rich quantum dots [6]. But we remark that the random distribution of In atoms can localize the carriers near small groups of them, not necessarily organized into nano-clusters. From our results, there is basically no difference between InGaN QWs and QBs, which indicates that localization takes place at scales which are much smaller than the size of our QBs ( $\sim 10 \times 2$  nm typically).

The large variety of localization centers, with different transition energy and oscillator strength, implies a nonexponential shape of the time-decay of the PL intensity. We have observed such nonexponential decays for both InGaN/GaN QWs and planes of QBs (Fig. 1).

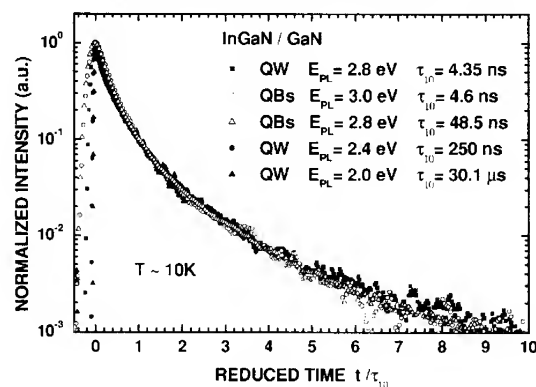


**Figure 1:** PL intensity decays plotted against a reduced time-scale, obtained from various InGaN/GaN QW and QB samples. The corresponding characteristic times are listed in the figure.

Due to the nonexponential behavior, we characterize these decays by the delay  $\tau_{10}$  after which the intensity is decreased by a factor of 10. To compare the shapes of the decays for different emission energies, we have plotted them on a reduced time scale (the time  $t$  divided by  $\tau_{10}$ ). All decays are superimposed almost exactly. We ascribe this behavior to the constancy of the properties of local potential fluctuations, among the different samples. To explain this nonexponential behavior, we can discard a temporary screening of the electric field by high densities of electron-hole pairs. Indeed, given the power density of our laser, the injected charge density is not sufficient to produce any variation of radiative decay time. As a proof of this, we observed no effect when changing the power density over several orders of magnitude. Another important result is the preservation of the decay shape when we examine small energy intervals within the PL linewidth. As shown in Fig. 2, for an InGaN/GaN QW, the characteristic decay time increases when we shift toward low energy, but the decay shape is always the same.

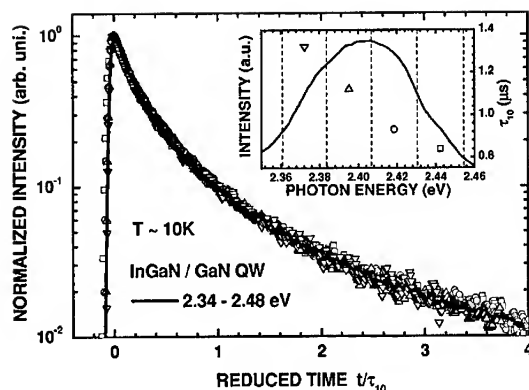


**Figure 2:** PL intensity decays plotted against a reduced time-scale, from different regions of the spectrum of an InGaN/GaN QW sample, as shown in the inset.

This increase of the characteristic decay time with decreasing PL energy can be attributed to the combination of fluctuations of (i) the QW width and (ii) the shape (size and depth) of local potential fluctuations. To explain the decay shape, we can therefore discard a summation of exponential contributions which would exhibit a variety of decay times as shown in the inset of Fig. 2.

Rather, we will show that we can describe the recombination dynamics in InGaN/GaN quantum systems, on a nanometer scale, by using a model based on the recombination process of two-dimensional “pseudo-donor-acceptor-pairs” (“pseudo-DAPs”).

### 3. NANOSCOPIC MODEL

To introduce our model, we will explain in what sense we have an analogy with the recombination dynamics of DAPs. The first important point is the large localization energy of each individual carrier in the ternary alloy, compared to the Coulomb attraction between the electron and the hole which constitute a Wannier exciton. Indeed, from experimental Stokes shifts for InGaN epilayers, the localization energy can be estimated at  $\sim 0.2$  eV, for an indium concentrations of 15-20 %, whereas the exciton binding energy is only of  $\sim 25$  meV. Moreover, the electric field separates electrons and holes along the growth axis so that, in a QW, electrons are localized near one interface and holes near the other one. Thus, Coulomb attraction is not sufficient to avoid a separate localization of the two types of carriers. Considering electrons and holes localized separately near the QW interfaces, for each electron-hole pair configuration, the separation along the growth axis is nearly the same (which corresponds to an emission energy “controlled” by the electric field, with small deviation due to variation in the shape of local traps). On the other hand, the electron-hole pair separation along the plane depends on the relative positions of carriers at interfaces (Fig. 3).

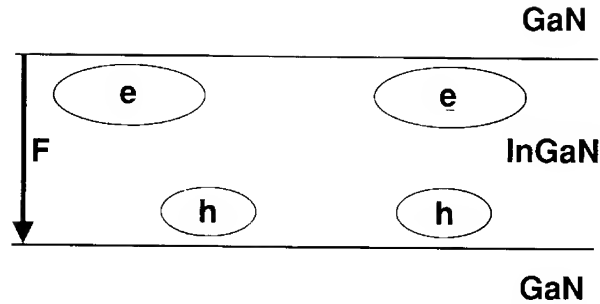


**Figure 3:** Schematic representation of electron-hole pair localization in an InGaN/GaN QW.

The larger the in-plane separation, the longer recombination times. Summing all possible configurations explains the nonexponential decay, quite similarly to what is observed for DAPs [7]: when the separation between the impurities increases, the electron-hole recombination probability decreases. We had already proposed such an analogy with DAP after the observation of the increase of the coupling of electron-hole pairs with polar phonons, when increasing the vertical size of InGaN/GaN QWs and QBs [8].

In the present case, contrary to the situation of donors or acceptors, the attracting potential is not Coulombic (long-range). Instead, the fluctuations of In content act as isoelectronic traps, but, because of the electric field, those near one interface capture electrons ("pseudo-donors") and those near the other interface capture holes ("pseudo-acceptors"). The recombination dynamics of such a system is similar to that of two-dimensional (2D) DAPs. In this case, the well width controls the time scale and the distribution of in-plane separation between electrons and holes influences the decay shape. Indeed, the electron-hole distance along the growth axis increases with the well width. But the distribution of in-plane relative distances between electrons and holes remains constant. This can also explain the universal character of the decay shape. Thomas et al. [7] have developed a model that can reproduce the nonexponential decay of the PL of DAP in bulk crystals. Particularly interesting, their model needs only two parameters: the first one influences the decay shape and the other one is a scaling factor. We have adapted this model for "pseudo-donors" and "pseudo-acceptors" located along a plane.

First, we need to know the decay rate for an isolated pair. The calculation of the radiative recombination rate  $W(r)$  of an electron bound to a "pseudo-donor" with a hole bound to a "pseudo-acceptor" at a distance  $r$  from the "pseudo-donor", involves the optical momentum element  $M$  between the state with the electron and hole present and the state with them absent. Considering  $W(r)$  proportional to  $|M|^2$  itself proportional to  $|I_{e-h}|^2$  where  $I_{e-h}$  is the in-plane overlap integral between the electron and the hole envelope functions, the problem is to find an adequate planar electron-hole wave function. We do not know the shapes of the potential drops near the traps, but they are not induced by an electrostatic charge, like for a true donor or acceptor. Therefore we have a short-range attractive potential, induced by the potential drop between Ga-N and In-N bonds, instead of a long-range Coulombic potential, which would yield an exponential (hydrogen-like) wave-function. As a first approximation, we assume harmonic potentials, with two-dimensional Gaussian wave-functions. In this case,



$$W(r) = W_{\max} e^{-\frac{r^2}{a^2}} \quad (1)$$

The  $a$  parameter is a *characteristic distance* for the extension of the wave-functions. Now, we can calculate the total light decay for 2D “pseudo-DAPs”. We consider a random distribution of “pseudo-donors” and “pseudo-acceptors” in a plane, all initially occupied and we assume one type of traps in excess. Following the procedure given in [7], the intensity  $I(t)$  is

$$I(t) = \left\{ 2\pi n \int_0^\infty W(r) \exp[-W(r)t] r dr \right\} \times \left\{ \exp \left[ 2\pi n \int_0^\infty \{ \exp[-W(r)t] - 1 \} r dr \right] \right\} \quad (2)$$

where  $n$  is the surface density of the majority constituent (“pseudo-acceptor” or “pseudo-donor”). Within the above assumptions,  $I(t)/I(0)$  is a function of only two parameters,  $W_{\max} \times t$  and  $\eta = n \times a^2$ . Particularly important, only one parameter sets the time scale, namely  $W_{\max}$ , so that a necessary scaling law exists between  $I(t)$  and  $W_{\max}$ . In InGaN/GaN QWs, due to the huge electric field which separates the carriers along the growth axis, we may assume that the carrier motions along the growth axis and along the plane are uncoupled. We know that the electron-hole overlap along the growth axis varies nearly exponentially with the QW width [2], but the shape of  $I(t)$  is preserved. In other words, the electron-hole overlap along the growth axis defines the time scale, thus  $W_{\max}$ . Finally, only the parameter  $\eta$  influences the decay shape. We have computed equation (2) and the results are presented in Fig. 4.

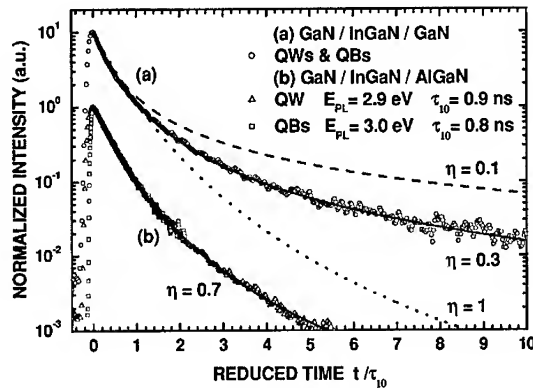


**Figure 4:** (a) Theoretical PL decays in the case of a 2D “pseudo-DAP” model, compared with the decay shape of Fig. 1. (b) PL intensity decays for GaN/InGaN/AlGaIn nano-objects.

For a comparison, we have added the decay shape of Fig. 1 (Fig. 4-a). In the limit of a large ratio of “pseudo-donor” and “pseudo-acceptor” concentrations and for a value of  $\eta$  equal to 0.3, the shape of  $I(t)$  remarkably fits the experimental decay. We obtain a lesser quality of the fit, if we place the model in the “compensated” case [7]. In fact, the assumption that a large ratio exists between the surface densities of “pseudo-acceptors” and “pseudo-donors”, can be justified by the fact that the hole effective mass is approximately six times larger than the electron mass. This

means that holes can be trapped on much smaller traps than electrons, whence the larger surface density of "hole traps". The value of  $\eta$  does not give any direct information on localization centers since we cannot separate  $n$  from  $a$  ( $\eta = n \times a^2$ ).  $\eta$  simply defines the ratio of the surface occupied by the majority constituent (probably "hole traps"). In other words,  $\eta$  is characteristic of the "nanotexture". For example, in Fig. 4-b, we show the decays obtained for GaN/InGaN/AlGaN QW and plane of QBs samples. The indium concentrations are always of the order of 15-20 % and the aluminum concentrations are in the same range. In this case, the parameter  $\eta$  is equal to 0.7, indicating a different "nanotexture" than for GaN/InGaN/GaN quantum systems studied here.

#### 4. CONCLUSION

In summary, we propose a model for the recombination mechanism of electron-hole pairs in InGaN/GaN quantum systems. Based on the joint effects of internal electric fields and of carrier localization on a nanometer-scale, this model accounts very well for the nonexponential decay shape and for the scaling law exhibited by the PL time-decay of QWs and QBs of various sizes. In this model, the decay time simply depends on the electric field, whereas the shape of the decay can be reproduced by using a single parameter which accounts for the local "nanotexture" of the ternary alloy. The excellent agreement between experimental results and this model supports the idea that optical recombinations in these quantum systems do not involve localized excitons, in the usual sense, but rather separately localized electrons and holes.

#### ACKNOWLEDGEMENTS

The authors acknowledge the financial support provided through the European Community's Human Potential Programme (contract HPRN-CT-1999-00132, "CLERMONT"). They also acknowledge support from the French Ministry of Education, Research and Technology through the "BOQUANT", "NANILUB" and "INTRANIT" Research Programs.

#### REFERENCES

1. P. Lefebvre, A. Morel, M. Gallart, T. Taliencio, B. Gil, J. Allègre, H. Mathieu, N. Grandjean, B. Damilano, J. Massies, MRS Symposium Proceedings Vol. **639**, Article G10.1 (2001).
2. P. Lefebvre, A. Morel, M. Gallart, T. Taliencio, J. Allègre, B. Gil, H. Mathieu, B. Damilano, N. Grandjean, J. Massies, Appl. Phys. Lett. **78**, 1252 (2001).
3. P. Lefebvre, T. Taliencio, A. Morel, J. Allègre, M. Gallart, B. Gil, H. Mathieu, B. Damilano, N. Grandjean, J. Massies, Appl. Phys. Lett. **78**, 1538 (2001).
4. I. Vurgaftman, J.R. Meyer and L.R. Ram-Mohan, J. Appl. Phys. **89**, 5815 (2001).
5. T. Taliencio, P. Lefebvre, M. Gallart, A. Morel, J. Phys.: Condens. Matter **13**, 7027 (2001).
6. K.P. O'Donnell, R.W. Martin, P.G. Middleton, Phys. Rev. Lett. **82**, 237 (1999).
7. D.G. Thomas, J.J. Hopfield, W.M. Augustyniak, Phys. Rev. **140**, A202 (1965).
8. S. Kalliakos, X.B. Zhang, T. Taliencio, P. Lefebvre, B. Gil, N. Grandjean, B. Damilano, J. Massies, Appl. Phys. Lett. **80**, 428 (2002).

**BEST AVAILABLE COPY**

### **Subpicosecond Luminescence Studies of Carrier Dynamics in Nitride Semiconductors Grown Homoepitaxially By MBE On GaN Templates**

G.A. Garrett, A.V. Sampath, C.J. Collins, F. Semendy, K. Aliberti, H. Shen, M. Wraback, \*Y. Fedyunin and \*T.D. Moustakas

U.S. Army Research Laboratory, Sensors and Electron Devices Directorate, AMSRL-SE-EM,  
2800 Powder Mill Road, Adelphi, MD 20783

\*ECE Department, Photonics Center, Boston University, 8. St. Mary's Street, Boston MA,  
02215

#### **ABSTRACT**

A new technique is presented that employs luminescence downconversion using an ultrashort gating pulse to enable the characterization of UV light emission from III-nitride semiconductors with subpicosecond temporal resolution. This technique also allows one to measure PL rise times and fast components of multiple decays in the subsequent time evolution of the PL intensity. Comparison of luminescence emission intensity and lifetime in GaN and AlGaIn with ~0.1 Al content grown homoepitaxially on GaN templates with the same quantities measured in heteroepitaxial layers grown on sapphire indicate significant improvement in the homoepitaxial layers due to reduction in dislocation density. Fast (<15 ps) initial decays in the AlGaIn are attributed to localization associated with alloy fluctuations and subsequent recombination through gap states.

#### **INTRODUCTION**

One of the most important issues in the development of high quality III-nitride semiconductors is the lack of native substrates for epitaxial growth. Most devices are fabricated on either sapphire or SiC substrates, with the resulting material quality often dictated by the control of threading dislocations produced by the lattice mismatch between the III-nitride epilayers and these substrates. These threading dislocations lead to enhancement of nonradiative recombination that reduces radiative efficiency in ultraviolet light emitters [1], as well as degradation of the reliability of high sensitivity avalanche photodiodes [2]. Moreover, carrier localization associated with alloy fluctuations in the AlGaIn alloys required for operation in the important 280 nm to 340 nm spectral region can also lead to nonradiative recombination in UV emitters and reduced out of band rejection associated with broadening of the absorption edge in detectors [3-5]. Time-resolved photoluminescence (TRPL) provides information about radiative lifetimes and nonradiative recombination mechanisms in III-nitride semiconductors crucial to the design of UV light emitters and detectors. Moreover, it has been shown that reduction of dislocations in GaN leads to both longer PL [6-7] and longer carrier lifetimes [8]. These results imply that

homoepitaxial growth of III-nitride materials on low defect density GaN templates should lead to improved radiative efficiency and concomitant longer PL lifetimes at room temperature, and it is therefore important to evaluate the extent to which this is the case in both GaN and AlGaIn, for which it has been suggested that alloy fluctuations lead to ultrafast carrier localization [3]. Such studies have been hampered to date by the temporal resolution ( $\sim 10$  ps or larger) of current UV optoelectronic spectroscopic techniques involving streak cameras and time-correlated photon counting [4-7].

In this paper we present a new technique that employs luminescence downconversion using an ultrashort gating pulse to enable the characterization of UV light emission from III-nitride semiconductors with subpicosecond temporal resolution. This technique also allows one to measure PL rise times and fast components of multiple decays in the subsequent time evolution of the PL intensity. Comparison of luminescence emission intensity and lifetime in GaN and AlGaIn with  $\sim 0.1$  Al content grown homoepitaxially on GaN templates with the same quantities measured in heteroepitaxial layers grown on sapphire indicate significant improvement in the homoepitaxial layers due to reduction in dislocation density. Observation of fast ( $< 15$  ps) initial decays in the AlGaIn irrespective of substrate suggests that localization associated with alloy fluctuations and subsequent recombination through gap states is the dominant decay mechanism in this material.

## EXPERIMENTAL METHOD

The samples for the optical studies were grown by molecular beam epitaxy using standard techniques on either c-plane sapphire substrates or thick ( $\sim 5$ -10mm) GaN templates deposited by hydride vapor phase epitaxy (HVPE) on sapphire substrates. In the absence of bulk substrates the use of thick templates is employed because threading dislocations propagating from the GaN-sapphire interface tend to annihilate with increasing film thickness, leading to improved optical properties of the GaN [6]. The dislocation density for these thin GaN templates was estimated to be in the mid- $10^8/\text{cm}^2$  range. In contrast, typical dislocation densities in thin GaN epilayers deposited by MBE directly on sapphire are greater than  $10^9 \text{ cm}^{-2}$ .

The time-resolved experiments were performed using a 250 kHz Ti:sapphire regenerative amplifier-pumped optical parametric amplifier that produces ultrashort pulses frequency doubled to obtain a source of UV pulses tunable between 225 nm and 375 nm. Photoluminescence (PL) was measured with subpicosecond resolution using a novel PL downconversion technique that provides one to two orders of magnitude better temporal resolution than standard ultraviolet time-resolved PL measurement techniques such as time-correlated photon counting or use of a streak camera and spectrometer [4-7]. In a downconversion experiment, the PL created by the radiative recombination of electron-hole pairs excited by an ultrafast ultraviolet pulse is time-resolved through gating of the PL in a nonlinear crystal with a synchronized  $\sim 800$  nm pulse derived from the same source, the regenerative amplifier. Since the nonlinear process,

**BEST AVAILABLE COPY**

downconversion, is nonresonant, it only occurs within the temporal slice of the luminescence coincident in time with the gating pulse. In this way, the time dependence of the PL can be mapped out with subpicosecond resolution by varying the timing of the gating pulse with respect to that of the excitation pulse using a mechanical delay line. While this experiment is quite similar to PL upconversion studies performed on infrared emitting materials [9], the lack of efficient detectors in the deep UV for detection of the upconverted UV PL dictates that downconversion of this PL to the visible is required.

## RESULTS AND DISCUSSION

The temporal resolution of our apparatus is demonstrated in fig. 1, which shows the rise time of the spectrally integrated bandedge PL from a GaN epilayer on an HVPE template photoexcited by a pump pulse centered at 348 nm. The system response, obtained by downconversion of pump light scattered from a frosted glass, is illustrated in the cross-correlation trace, which shows a full width at half maximum limited by the dispersion in the collection optics to  $\sim 250$  fs. The PL intensity increases abruptly at first, but then transitions to a slower rise that reaches a plateau at  $\sim 1.5$  ps. The fact that the rise time of the data is both significantly slower than the time integral of the cross-correlation and possesses multiple time scales indicates that the rise of the PL is temporally resolved for the first time. In this case the PL rise time contains information primarily about hot carrier thermalization and energy relaxation through carrier-LO phonon and carrier-carrier scattering.

Another important aspect of this temporal resolution is that it allows one to resolve fast components of multiple decays in the subsequent time evolution of the PL intensity that may

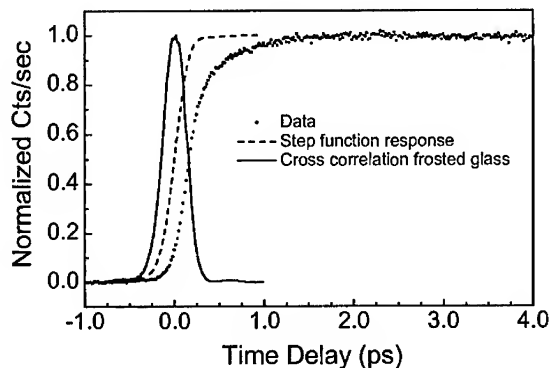


Fig. 1. Temporal resolution of the luminescence downconversion technique. The data provide a measure of the rise time of the spectrally integrated bandedge photoluminescence from GaN for excitation at 348 nm. The system resolution is obtained by downconversion of the pump pulse scattered from frosted glass.

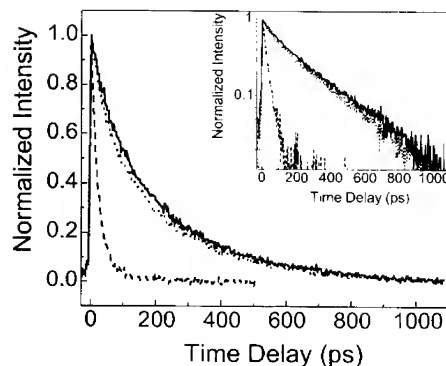


Fig. 2. Downconverted photoluminescence signal as a function of time delay for 364 nm excitation of GaN on HVPE GaN template (solid line), GaN on sapphire (dashed line), and GaN template (dotted line). Inset: data on log scale.

provide information about the effect of ultrafast trapping on radiative recombination. Figure 2 shows a comparison of the room temperature PL decays for bandedge (364 nm) excitation of GaN grown homoepitaxially on a thick, low defect density HVPE GaN template, and GaN grown heteroepitaxially on sapphire. The excitation density in these samples was in the mid- $10^{18}$ - $10^{19}/\text{cm}^3$  range. The linear plot shows that the PL lifetime in the homoepitaxially grown sample is significantly longer than that in its heteroepitaxially grown counterpart, and about the same as that in the GaN template itself. This result is consistent with the fact that the CW PL is nearly 20 times brighter for the homoepitaxial sample than for the heteroepitaxial one, while the linewidth is  $\sim 6$  meV narrower (32 meV for GaN on template versus 38 meV for GaN on sapphire). The semilog plot in the inset indicates that while the GaN on sapphire data may be characterized primarily by a single exponential decay of  $\sim 20$  ps, the GaN on template data possess both a fast ( $\sim 65$  ps) and a more dominant slow ( $\sim 300$  ps) decay. The fast decay in both samples may be associated with trapping and subsequent nonradiative recombination at defect-related states in the gap, with the longer decays in the homoepitaxial sample indicative of a lower defect density and saturation of these deep states. These results are consistent with ones obtained for high quality and low quality MOCVD-grown GaN on sapphire in which the dislocation densities were measured to be close to what we expect for our samples [7]. The PL decay in the high quality undoped material possessed time constants of 50 ps and 250 ps for a dislocation density of  $4 \times 10^8/\text{cm}^2$ , while that in the low quality undoped sample was characterized by a single 30 ps decay time for a dislocation density of  $2 \times 10^9/\text{cm}^2$ . Moreover, the fact that PL decay times of 530 ps for a 63 mm-thick HVPE template [6] and 860 ps for an 80mm-thick quasi-

**BEST AVAILABLE COPY**

substrate [10] suggests that even better results should be obtained for growth on thicker templates with lower defect densities.

Figure 3 shows a comparison of room temperature PL decays in AlGa<sub>0.1</sub>N with ~ 0.1 Al content for 330 nm excitation. The PL decays for both AlGa<sub>0.1</sub>N samples possess both a slow and a fast decay. The fast decay in both samples is ~ 13 ps, while the slow decay is longer (~61 ps) in the AlGa<sub>0.1</sub>N on template than for the sample on sapphire (~39 ps), but still shorter than that for the GaN template (~ 83 ps). The fast PL decay, which has not been observed before due to lack of

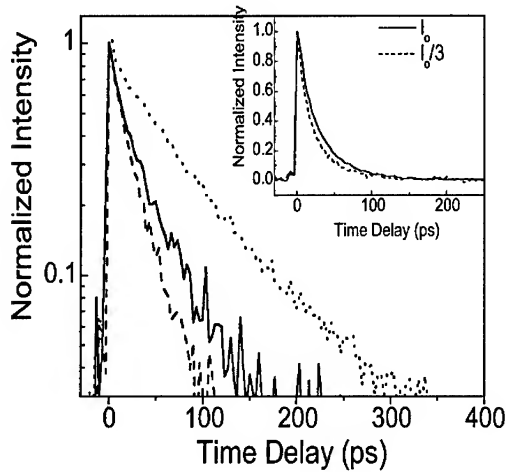


Fig. 3. Downconverted photoluminescence signal as a function of time delay for 330 nm excitation of Al<sub>0.1</sub>Ga<sub>0.9</sub>N on HVPE GaN template (solid line), Al<sub>0.1</sub>Ga<sub>0.9</sub>N on sapphire (dashed line), and GaN template (dotted line). Inset: Intensity dependence of PL decays in Al<sub>0.1</sub>Ga<sub>0.9</sub>N on sapphire.

temporal resolution [5] and occurs regardless of template/substrate, may be due to localization in shallow levels and subsequent nonradiative recombination associated with alloy fluctuations, with the decays becoming faster with decreasing intensity in the sample on sapphire (inset), as observed in time-resolved reflectivity experiments [3]. Low temperature CW PL measurements show an alloy broadening of ~23 meV in the PL linewidth when moving from GaN to AlGa<sub>0.1</sub>N with 0.1 Al content [11]. These results are consistent with the measured room temperature linewidths of 55 meV and 61 meV for our homo- and heteroepitaxial AlGa<sub>0.1</sub>N, respectively, when viewed in the context of our GaN PL linewidths reported earlier. The discrepancy in light emission dynamics between the homoepitaxial AlGa<sub>0.1</sub>N and the GaN template may also be due to the combination of carrier localization and nonradiative recombination associated with alloy fluctuations in the AlGa<sub>0.1</sub>N. The longer decays in these AlGa<sub>0.1</sub>N samples may be associated with

trapping and nonradiative recombination through deep states related to dislocations and other defects, as in GaN. Viewed in this way, the time-resolved PL data suggest that homoepitaxial growth of AlGaIn on GaN templates leads to improved material quality, even though the TRPL on the GaN template employed in this case indicates that this template is of poorer structural quality than the one employed for the GaN homoepitaxial growth.

## CONCLUSION

In conclusion, we have demonstrated a unique luminescence downconversion technique for the measurement of UV PL from III-nitride semiconductors with subpicosecond temporal resolution. The ability of this technique to resolve both PL rise times and fast components of multiple decays in the subsequent time evolution of the PL intensity enables the study of carrier relaxation and the effect of ultrafast trapping on radiative recombination. Comparison of luminescence emission intensity and carrier lifetime in GaN and AlGaIn with ~0.1 Al content grown homoepitaxially on GaN templates with the same quantities measured in heteroepitaxial layers grown on sapphire indicate significant improvement in the homoepitaxial layers due to reduction in defect density. Fast (<15 ps) initial decays in the AlGaIn are attributed to localization associated with alloy fluctuations and subsequent recombination through gap states.

## REFERENCES

1. S. Nakamura., and G. Fasol. *The Blue Laser Diode*. Springer, Berlin, 1997.
2. J.C. Carrano., D.J.H. Lambert, C.J. Eiting, C. J. Collins, T. Li, S. Wang, B. Yang, A.L. Beck, R.D. Dupuis, and J.C. Campbell, *Appl. Phys. Lett.* 76, 924 (2000).
3. M. Wraback, F. Semendy, H. Shen, U. Chowdhury, D.J.H. Lambert, M.M. Wong, and R.D. Dupuis, *Phys. Stat. Sol. (a)* 188, 807 (2001).
4. H.S. Kim, R.A. Mair, J. Li, J.Y. Lin, and H.X. Jiang, *Appl. Phys. Lett.* 76, 1252 (2000).
5. Y. H. Chow, G.H. Gainer, J.B. Lam, and J.J. Song, *Phys. Rev. B* 61, 7203 (2000).
6. G.E. Bunea, W.D. Herzog, M.S. Unlu, B.B. Goldberg, and R.J. Molnar, *Appl. Phys. Lett.* 75, 838 (1999).
7. H.K. Kwon, C.J. Eiting, D.J.H. Lambert, M.M. Wong, R.D. Dupuis, Z. Liliental-Weber, and M. Benamara, *Appl. Phys. Lett.* 77, 2503 (2000).
8. M. Wraback, H. Shen, C.J. Eiting, J.C. Carrano, and R.D. Dupuis, *MRS Internet J. Nitride Semicond. Res.* 5S1, W11.55 (2000).
9. J. Shah, *IEEE J. Quantum Electron.* 24, 276 (1988).
10. S.F. Chichibu, H. Marchand, M.S. Minsky, S. Keller, P.T. Fini, J.P. Ibbetson, S.B. Fleischer, J.S. Speck, J.E. Bowers, E. Hu, U.K. Mishra, S.P. DenBaars, T. Deguchi, T. Sota, and S. Nakamura, *Appl. Phys. Lett.* 74, 1460 (1999).
11. G. Steude, T. Christmann, B.K. Meyer, A. Goeldner, A. Hoffmann, F. Bertram, J. Christen, H. Amano, and I. Akasaki, *MRS Internet J. Nitride Semicond. Res.* 4S1, G3.26 (1999).

**BEST AVAILABLE COPY**

### Deep Donor-Acceptor Pair Luminescence in Codoped GaN

Bing Han, Joel M. Gregie, Melville P. Ulmer,<sup>1</sup> and Bruce W. Wessels

Department of Materials Science and Engineering and Materials Research Center, Northwestern University, Evanston, IL 60208, USA

<sup>1</sup>Department of Physics and Astronomy, Northwestern University, Evanston, IL 60208, USA

#### ABSTRACT

Deep level defects formed in *p*-type GaN:Mg codoped with shallow donors have been investigated by photoluminescence (PL) spectroscopy. A donor-acceptor pair (DAP) luminescence band peaked at 2.45 eV dominates the room temperature PL spectrum in heavily codoped epilayers. A superlinear dependence of PL intensity on excitation density is observed for this band, with an exponent of 1.4~1.7. The intensity of this band increases with increasing temperature with a maximum at 264K. To explain the luminescent behavior a DAP model was developed whereby the recombination involves a deep donor and shallow Mg acceptor. The deep donor is tentatively attributed to a *DX* center.

#### INTRODUCTION

Advances in the epitaxial deposition of group III-V nitrides have led to high efficiency solid state devices such as UV-blue lasers and solar-blind UV detectors [1,2]. Despite their importance, much is still unknown about deep recombination centers and their properties in these materials and devices. For example, metastable defects have been observed in *p*-type GaN:Mg whose origin remains controversial [3-7]. Persistent photoconductivity effect has been observed in *p*-type GaN and attributed to the bistable Mg center [3,4]. Evidence for deep level defect formation has also been obtained from photoluminescence measurements. Deep level green luminescence [5-7] is often observed in *p*-type GaN:Mg, which has been attributed to transitions involving deep Mg complexes [6].

In the present study, codoping of *p*-type GaN with Mg and Si or O was investigated to determine its effect on the luminescent properties and in particular deep-level formation. In the codoped material, a broad DAP emission band at 2.45 eV was observed at room temperature. The band is tentatively attributed to recombination involving a deep *DX* state and a shallow Mg acceptor.

#### EXPERIMENTAL DETAILS

Co-doped *p*-type GaN films were grown by atmospheric pressure metal-organic vapor phase epitaxy (MOVPE) on *c*-plane sapphire substrates [10,11]. Film growth was initiated with a low temperature GaN nucleation layer, followed by a 0.5-1.0  $\mu\text{m}$  semi-insulating ( $>100\Omega\text{cm}$ ) GaN:Mg buffer layer. Films were then doped with Mg and the donor O or Si. The codoped layer, 0.5-1  $\mu\text{m}$  thick, was grown at 1030°C. The as-grown films were annealed for 15 minutes in  $\text{N}_2$  at 850°C to activate the Mg acceptors through the removal of hydrogen.

Photoluminescence measurements were made between 18K and 300K using a closed-cycle He cryostat. A He-Cd laser was used as the above bandgap excitation source and the excitation intensity was varied over the range  $10^{-5}$ -1.2  $\text{W}/\text{cm}^2$  using calibrated neutral density filters. Van der Pauw measurements were conducted at room temperature to determine the electrical properties. Either In or Ni/Au were used as ohmic contacts.

## EXPERIMENTAL RESULTS

**Table I.** Electrical characteristics of Mg doped and Si codoped samples

Sample No.	Mg ( $\mu\text{mol/min}$ )	Si (nmol/min)	O (Ppm)	$p$ ( $\times 10^{17} \text{cm}^{-3}$ )	$\rho$ ( $\Omega\text{cm}$ )
I	0.09	0	0	1.6	4.0
II	0.09	2.24	0	2.3	2.9
III	0.09	0	4	4.0	2.4

The growth conditions and the electrical characteristics for (i) Mg doped, (ii) Mg-O codoped, and (iii) Mg-Si codoped films are summarized in Table I.

The room temperature PL spectra of these films are shown in Fig. 1. A blue band peaked around 2.73 eV was observed in the Mg-doped GaN. The origin of the blue band was previously attributed to the DAP emission involving a  $\text{Mg}_{\text{Ga}}$  acceptor and a nitrogen vacancy related donor complex [11-13]. It's well known that the blue band redshifts with increasing temperature. Its peak position varies significantly for different samples [11-13]. Upon codoping of Si or O, the blue band quenches [10,11], and a broad emission band is observed with the peak at 2.45 eV. This band dominates the PL spectrum at room temperature. The green band has been previously observed in  $p$ -type GaN:Mg although its origin remains controversial [5-7].

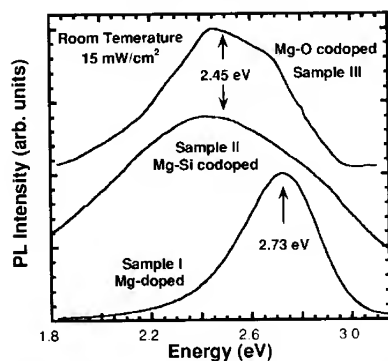


**Figure 1.** Room temperature PL spectra of Mg-doped, Mg-Si codoped and Mg-O codoped  $p$ -type GaN films. The excitation density was fixed at  $15 \text{ mW/cm}^2$ .

The excitation density dependence of the green band peak intensity was studied. Fig. 2 shows the PL intensity of the green band (in Mg-Si/O codoped films) and blue band (in a Mg doped film) as a function of the excitation density at room temperature. For simple bimolecular recombination involving electrons and holes, a linear dependence of PL intensity on excitation density is expected for DAP transitions. Furthermore, sublinear, saturation behavior at high excitation densities is often observed because of the finite concentrations of donors and/or acceptors in a material [12]. As shown in Fig. 2, the room temperature PL intensity of the blue band is linearly dependent on the excitation density ( $I_{\text{exc}}$ ) up to  $1.2 \text{ W/cm}^2$ , which is consistent with the assignment of this emission to DAP recombination.

In contrast, a superlinear dependence of the PL intensity on excitation density was observed for the green band in codoped samples ( $\propto I_{\text{exc}}^n$ ), with the exponent  $n$  between 1.4 (Sample II) and 1.7 (Sample III).

BEST AVAILABLE COPY

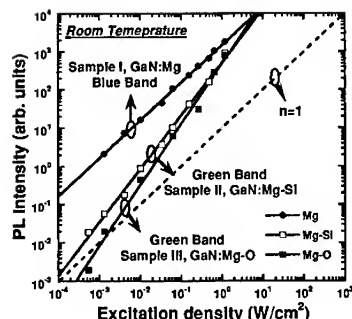


Figure 2. Excitation density dependence of the PL intensities for the blue and green PL bands in Mg-doped and codoped *p*-type GaN films.

A complex temperature dependence of the green band intensity was also observed in the codoped films. The dependence of the PL spectra on temperature is shown in Fig. 3 for one representative sample (Sample II). As shown in Fig. 3(a), the blue DAP band dominates at low temperature and a second band at 3.3 eV appears as a shoulder. When  $T < 181\text{K}$ , the blue band slowly redshifts and quenches with increasing temperature. Its peak shape and FWHM are roughly invariant up to 150K. However, in the temperature range between 181K and 293K [Fig. 3(b)], striking changes in the PL spectra were observed. The dominant band redshifts by more than 400 meV between 205K and 293K. Moreover, above 200K the PL intensity of the dominant peak increases with increasing temperature and reaches a maximum at 264K. The shape of the dominant PL band also noticeably changes with increasing temperature. The unusually large redshift and band widths, together with the shape change of this band with increasing temperature, suggest that more than one recombination channel is involved in the luminescence band.

The luminescence band at high temperatures was resolved into two Gaussian peaks around 2.5 eV and 2.9 eV. One of the fitted spectra ( $T=264\text{K}$ ) is shown in Fig. 4(a) (the solid line represents the PL data, and the dotted lines show the fitted spectra). The intensities of the resolved

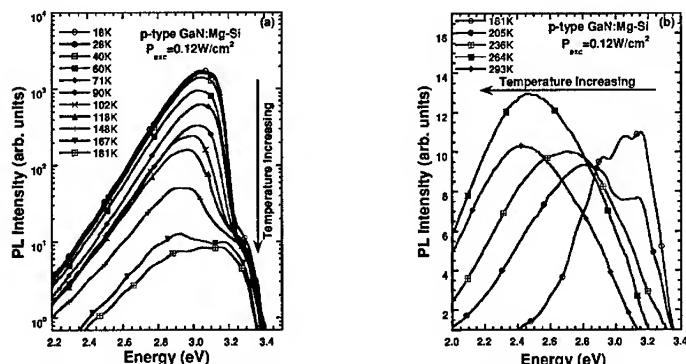
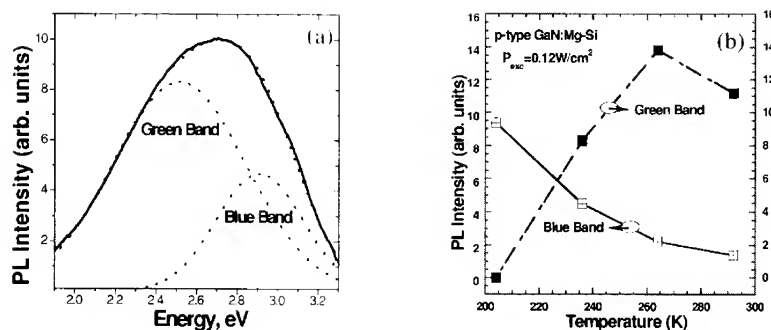


Figure 3. PL spectra of the Mg-Si codoped film at different temperatures. (a)  $T \leq 181\text{K}$ , (b)  $T \geq 181\text{K}$ . The high temperature ( $T > 200\text{K}$ ) PL spectra can be resolved into two Gaussian peaks at  $\sim 2.5\text{ eV}$  and  $\sim 2.9\text{ eV}$ .



**Figure 4.** (a) Two bands with Gaussian line shapes are used in the fitting of the broad band. The shown spectrum was measured at 264K. (b) shows the temperature dependent intensities of the resolved 2.5 eV and 2.9 eV PL bands. The green PL band intensity increases with temperature with a maximum at 264K.

green and blue bands are plotted in Fig. 4(b) as a function of the temperature. No green band was resolved when  $T < 181 \text{ K}$ . For  $T \geq 205 \text{ K}$ , however, the green band emerges and its intensity increases with temperature up to 264K, accompanied by a significant quenching of the blue band. When resolving the luminescence band, the Gaussian peak positions were not fixed, whose values are determined to be 2.53eV (2.93eV), 2.50eV (2.92eV), and 2.45eV (2.89eV) for the resolved green (blue) band at 236K, 264K and 292K, respectively. Both the blue and green bands redshift with increasing temperature. Note the fitted positions can only be regarded as approximate since the blue band is actually asymmetric instead of Gaussian [12].

## DISCUSSION

To explain the excitation and temperature dependent behaviors of the 2.5 eV luminescence band, a DAP model is proposed. The green band is attributed to radiative transitions involving a deep donor like state and a shallow Mg acceptor. The deep donor is tentatively attributed to a  $DX$  center. These  $DX$  centers are highly localized deep level defects formed by a large lattice relaxation (LLR) [14-16]. The ground state of the  $DX^-$  centers is a negatively charged two electron state, showing the distinguishing "negative U" character [14]. The configuration coordinate diagram of the proposed deep  $DX$  state is illustrated in Fig. 5 [14-16]. The lowest parabola with energy minima near  $Q_{DX}$  represents the  $DX^-$  state, which is occupied by two electrons. This state has experienced a LLR and is the stable ground state. The parabola above this state represents the excited  $DX^0$  state plus one electron in the conduction band. The parabolas with energy minima near  $Q_d$  represent the substitutional configuration, with the upper parabola showing the total energy of the ionized donor ( $d^+$ ) state with two electrons in the conduction band, while the lower one shows the total energy of the neutral donor ( $d^0$ ) state with one electron in the conduction band. Since simultaneous trapping of two electrons is highly improbable, thermal transitions of electrons between the substitutional states and the  $DX$  centers can only occur as indicated by the dashed arrows [17,18].

The observed thermal behavior of the green band is consistent with the proposed  $DX$  model. When cooling the sample in the dark, the system remains in its ground state; substitutional and  $DX$  states are empty of electrons in  $p$ -type films [19]. Upon laser excitation at low temperature

**BEST AVAILABLE COPY**

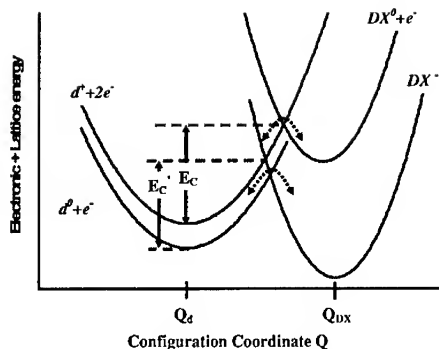


**Figure 5.** Configuration diagram for the proposed deep  $DX$  center in codoped  $p$ -type GaN:Mg.

with photon energy larger than the bandgap, photo-generated electrons in the conduction band (the total energy is represented by the curve  $d^+ + 2e^-$ ) can only be captured by the effective mass substitutional donors ( $d^0 + e^-$ ). No electrons can be captured by the  $DX$  states ( $DX^0 + e^-$  or  $DX^-$ ) due to the large thermal barriers indicated by  $E_c$  and  $E_c'$  (Fig. 5). Consequently, no  $DX^-$  state related DAP green luminescence can be observed at low temperature.

At higher temperatures, however, capture of electrons from the conduction band to the  $DX^-$  states via the neutral one-electron state  $DX^0$  or  $d^0$  are more probable since the photogenerated electrons have enough thermal energy to surmount the energy barriers  $E_c$  or  $E_c'$ . Since the  $DX^-$  is the lower energy state, most of the photogenerated electrons will be trapped by these states. The electrons at charged  $DX^-$  centers can subsequently recombine with the holes bound to neutral  $(Mg_{Ga})^0$  acceptors, resulting in increased green DAP luminescence intensity at high temperature.

Since the hole capture cross-section of the  $DX$  center is very large [20], the blue luminescence intensity is greatly reduced at high temperature because most holes bound to the neutral  $(Mg_{Ga})^0$  acceptors recombine with electrons in the  $DX^-$  centers. Consequently, a strong concurrent quenching of the blue band was observed with the increase of the green band intensity, as shown in Fig. 4(b).

It is important to note that the photogenerated electrons are involved in a two-step luminescence process. This process for converting the ionized  $d^+$  state to  $DX^-$  state is illustrated in Fig. 5, assuming simultaneous trapping of two photoelectrons is highly unlikely [17,18]. As shown in Fig. 5, electrons recharge the ionized  $d^+$  states first, converting them to the one electron  $DX^0$  or  $d^0$  state. The  $DX^-$  state is then formed by capturing a second electron [16]. Since two photons are involved in forming one  $DX^-$  center, a superlinear dependence on excitation density is expected for the green luminescence band [19]. This is consistent with our excitation density dependent PL results (Fig. 2), where  $I \propto I_{ex}^n$  with  $n=1.4-1.7$  was observed. This superlinearity is a fingerprint of  $DX$  center involvement in the recombination process, i.e., the ground  $DX^-$  state captures two electrons.

Luminescence with optical properties (temperature and/or excitation dependence) similar to those of the green band have been observed in other systems including AlGaAs [19], InGaP:S [21], and for the 3.27 eV band in  $p$ -type GaN [22].

## CONCLUSIONS

In summary, the DAP luminescence present in *p*-type GaN:Mg codoped with shallow donors (oxygen or silicon) has been investigated. In addition to the often observed blue band, a second PL band at 2.5 eV emerges in the heavily codoped epilayers. Complex temperature and excitation density dependencies are observed for the green band. The luminescence behavior is attributed to a donor-acceptor pair recombination whereby the donor is a *DX* center and Mg is the shallow acceptor.

## ACKNOWLEDGMENTS

The authors thank Dr. M. Reshchikov of Virginia Commonwealth University for helpful discussions regarding the manuscript. This work is supported by an NASA grant NAG5-1147 (P. Crane, contract monitor). JMG acknowledges the support by a National Defense Science and Engineering Graduate Fellowship.

## REFERENCES

1. S. Nakamura, S. Pearton, and G. Fasol, *The Blue Laser Diode: The Complete Story* (Springer, New York, 2000).
2. F. S. Shahedipour, M. P. Ulmer, B. W. Wessels, C. L. Joseph, and T. Nishashi, *IEEE J. Quantum Elect.*, **38**, 333 (2002).
3. C. Johnson, J. Y. Lin, H. X. Jiang, M. Asif Kahn, and C. Sun, *Appl. Phys. Lett.*, **68**, 1808 (1996).
4. J. Z. Li, J. Y. Lin, H. X. Jiang, A. Salvador, A. Botchkarev, and H. Morkoc, *Appl. Phys. Lett.*, **69**, 1474 (1996).
5. H. Amano, M. Kitoh, K. Hiramatsu, and I. Akasaki, *J. Electrochem. Soc.* **137**, 1639 (1990).
6. J. M. Myoung, K. H. Shim, C. Kim, O. Gluschenkov, K. Kim, S. Kim, D. A. Turnbull, and S. G. Bishop, *Appl. Phys. Lett.*, **69**, 2722 (1996).
7. R. K. Korotkov, J. M. Gregie, and B. W. Wessels, *Mat. Res. Soc. Symp.*, **639**, G6.39.1 (2001).
8. C. H. Park and D. J. Chadi, *Phys. Rev. B*, **55**, 12995 (1997).
9. C. G. Van de Walle, C. Stampfl, J. Neugebauer, *J. Cryst. Growth*, **189/190**, 505 (1998).
10. R. K. Korotkov, J. M. Gregie, and B. W. Wessels, *Mat. Res. Soc. Symp.*, **639**, G6.39.1 (2001).
11. B. Han, J. M. Gregie, and B. W. Wessels, to be published.
12. M. A. Reshchikov, G.-C. Yi, and B. W. Wessels, *Phys. Rev. B* **59**, 13176 (1999).
13. F. Shahedipour and B. W. Wessels, *Appl. Phys. Lett.* **76**, 3011 (2000).
14. D. J. Chadi and K. J. Chang, *Phys. Rev. Lett.*, **671**, 873 (1988).
15. D. V. Lang and R. A. Logan, *Phys. Rev. Lett.*, **39**, 635 (1977).
16. P. M. Mooney, *J. Appl. Phys.*, **67**, R1 (1990).
17. T. N. Theis, *Proc. Symp. On Defects in Materials*, Materials Research Society Fall Meeting, Boston, Nov 26-Dec 1, 1990 (1991).
18. T. N. Theis and P. M. Mooney, *Mater. Res. Soc. Symp. Proc.* **163**, 729 (1990).
19. D. P. Gladkov and K. Zdansky, *J. Appl. Phys.* **80**, 3004 (1996).
20. G. Brunthaler, K. Ploog and W. Jantsch, *Phys. Rev. Lett.* **63**, 2276 (1989).
21. N. Y. Lee, I. Hwang, J. E. Kim, H. Y. Park, H. K. Kwon, B. D. Choe, and H. Lim, *Solid State Commun.*, **105**, 1 (1998).
22. T. W. Kang, S. H. Park, H. Song, T. W. Kim, G. S. Yoon and C. O. Kim, *J. Appl. Phys.*, **84**, 2082 (1998).

**BEST AVAILABLE COPY**

### Dielectric Function of "Narrow" Band Gap InN

R. Goldhahn<sup>1</sup>, S. Shokhovets<sup>1</sup>, V. Cimalla<sup>2</sup>, L. Spiess<sup>2</sup>, G. Ecke<sup>2</sup>, O. Ambacher<sup>2</sup>,  
J. Furthmüller<sup>3</sup>, F. Bechstedt<sup>3</sup>, H. Lu<sup>4</sup> and W.J. Schaff<sup>4</sup>

<sup>1</sup>Institute of Physics and <sup>2</sup>Center for Micro- and Nanotechnologies,  
Technical University Ilmenau, 98684 Ilmenau, Germany

<sup>3</sup>Institut of Solid State Theory and Theoretical Optics, Friedrich Schiller University,  
07743 Jena, Germany

<sup>4</sup>Department of Electrical and Computer Engineering, Cornell University, Ithaca, NY 14853,  
U.S.A.

#### ABSTRACT

Spectroscopic ellipsometry studies in the energy range from 0.7 up to 5.5 eV were carried out in order to determine the dielectric function (DF) of 'narrow' band gap ( $< 1$  eV) single-crystalline InN films grown by molecular beam epitaxy on sapphire substrates. The imaginary part of the DF is characterized by a strong increase immediately above the band gap and then by a nearly constant value up to 4 eV. Pronounced structures above 4 eV are attributed to transitions along the L-M direction in the Brillouin-zone as a comparison with *first-principles* calculations indicates. In contrast, sputtered layers (band gap  $\sim 1.9$  eV) studied for comparison show a completely different spectral shape of the DF. Finally, DF's of high In-content InGaN alloys are presented, providing further evidence that InN is a "narrow" band gap semiconductor.

#### INTRODUCTION

Among the group-III nitride semiconductor compounds, the physical properties of InN are known rather poorly. This is mainly attributed to the difficulties in growing high-quality crystals. A discussion of optical properties of InN demands to differentiate between investigations employing either sputtered films or epitaxial layers deposited by molecular beam epitaxy (MBE) and metalorganic vapor-phase epitaxy (MOVPE). Interband optical absorption measurements of sputtered polycrystalline InN films yield a band gap of  $E_g \sim 1.9$  eV at room temperature [1-4]. This value of the band gap has been accepted for a long time and was frequently used as the end-point value for the extrapolation of the band gap in  $\text{In}_x\text{Ga}_{1-x}\text{N}$  alloys. In contrast, recent studies of epitaxial layers grown by MBE [5-7] or MOVPE [8] revealed a narrow gap of  $E_g < 1$  eV.

For both types of films, reports on the dielectric function (DF) covering an extended energy range are scarce. Refractive index and extinction coefficient of sputtered layers were obtained from transmittance/reflectance [3] and spectroscopic ellipsometry (SE) [9] studies. However, the applied single-layer model neglects the influence of roughness and interface layers on the spectra [10]. Guo *et al.* reported optical constants for MOVPE grown InN determined from reflectance investigations followed by Kramers-Kronig analysis. These data suffer from the relatively low InN layer thickness ( $\sim 300$  nm) and the neglect of sample surface roughness. However, both effects require the application of a multi-layer model.

In this work, we present a comprehensive SE data analysis based on multi-layer models in order to determine the InN DF's for both single-crystalline MBE grown and sputtered films with high reliability. The extracted data are compared with the results of *first-principles* calculations.

## EXPERIMENTAL DETAILS

The single-crystalline InN films were grown on (0001) sapphire by MBE as described elsewhere [12]. For two samples the InN layers of 120 nm (#M1) and 250 nm (#M2) thickness (nominal) were directly deposited on top of an 230 nm AlN buffer layer. The third sample (#M3) consists of a 10 nm AlN nucleation layer followed by a 310 nm GaN buffer layer and the final 960 nm InN film. Structural properties of the films were examined by high resolution x-ray diffraction (HRXRD) measurements. For all samples, the optical axis ( $c$ ) is oriented normal to the surface. From reciprocal space maps of the symmetric (002) and the asymmetric (20.5) Bragg reflexes the InN lattice constants were determined. For sample #M3 we found  $c = 5.686 \text{ \AA}$  and  $a = 3.552 \text{ \AA}$  which is in excellent agreement with previous studies of thick InN films deposited on GaN [13]. The lattice constants of the other two samples deviate only slightly from these values. The root-mean-square (rms) surface roughness  $\delta$  was obtained by atomic force microscopy (AFM) yielding  $\delta = 9, 1.5$ , and  $12 \text{ nm}$  for samples #M1, #M2, and #M3, respectively. Hall measurements at room temperature evidenced for the thinner samples electron densities (mobilities) of  $\sim 2 \times 10^{18} \text{ cm}^{-3}$  ( $\sim 850 \text{ cm}^2/\text{Vs}$ ) and for the thicker sample of  $8 \times 10^{17} \text{ cm}^{-3}$  ( $1500 \text{ cm}^2/\text{Vs}$ ).

In order to demonstrate the systematic change of the DF with increasing Ga-content, three  $\text{In}_{1-x}\text{Ga}_x\text{N}$  alloys ( $x = 0.22, 0.32$ , and  $0.43$ ) with thickness of  $\sim 250 \text{ nm}$  were grown by MBE on sapphire substrates with an AlN buffer layer ( $\sim 250 \text{ nm}$ ) [4]. The growth temperature was in the range of  $470$  to  $570^\circ\text{C}$ . The Ga atomic fraction was determined by XRD assuming a complete lattice relaxation.

The polycrystalline InN layers under investigation were provided by the Tansley group. They were deposited by magnetron sputtering of a nitrided indium target in a reactive nitrogen plasma [3] either on glass (#S1) or Si (#S2) substrates with a thickness of  $975 \text{ nm}$  and  $1210 \text{ nm}$ , respectively. The layers are composed of needle-like crystallites with diameters in the range of  $10\text{--}30 \text{ nm}$ . The lattice constants of #S1 (#S2) are  $c = 5.821 \text{ \AA}$  ( $5.786 \text{ \AA}$ ) and  $a = 3.622 \text{ \AA}$  ( $3.58 \text{ \AA}$ ). For both samples the roughness amounts to  $\delta \sim 8 \text{ nm}$ .

The optical properties of the films were investigated by SE. In order to minimize the correlation between DF's and layer thickness, the ellipsometric parameters  $\Psi$  and  $\Delta$  were measured at different angles of incidence ( $60^\circ, 68^\circ$ , and  $74^\circ$ ).

## RESULTS AND DISCUSSION

The dots in Fig. 1(a) and (b) represent typical examples for the spectral dependence of the ellipsometric parameter  $\Psi$  taken at different angles of incidence for the thick single-crystalline film #M3 and the sputtered layer on Si substrate #S2. Remarkable differences are observed. For the sputtered layer in Fig. 1(b),  $\Psi$  shows oscillatory behavior below  $\sim 2 \text{ eV}$  due to interference, but a smooth dependence on the photon energy at higher energy. Obviously, the film is transparent in the low-energy range and strongly absorbing above  $2 \text{ eV}$ . In contrast, for the MBE grown film oscillations start to evolve only below  $\sim 1 \text{ eV}$  indicating a much smaller band gap for this film. It is worth noting that  $\Delta$ , not presented here, shows similar features.

A multi-layer model has been established for determining the real ( $\epsilon_1$ ) and imaginary ( $\epsilon_2$ ) part of the complex DF ( $\bar{\epsilon} = \epsilon_1 + i\epsilon_2$ ) from the experimental data. For the MBE samples, it consists of the substrate, buffer layer, InN film, and a surface layer. The latter takes into account the sample surface roughness. Its optical constants are modeled by an effective medium theory

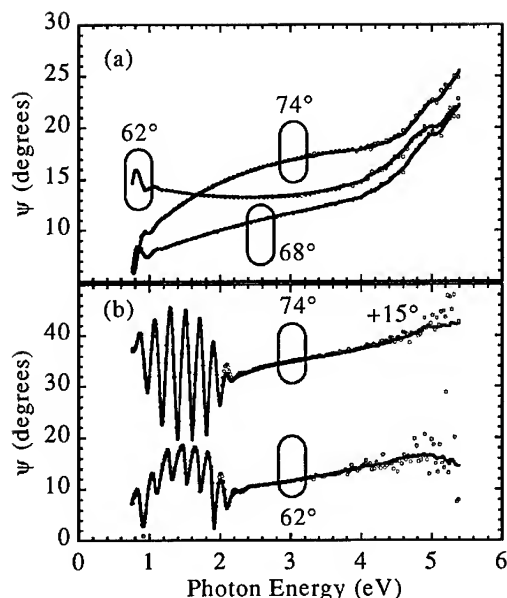


**Figure 1.**

Fit (full lines) of ellipsometric data (dots) taken at different angles of incidence. (a) and (b) refer to the MBE grown single-crystalline InN film (#M3) and InN obtained by sputtering techniques (#S2), respectively. Data taken at 74° in (b) are shifted by 15° for clarity.

assuming a 1/1 mixture of InN with voids. The applicability of this method has been demonstrated in Ref. 10. Furthermore, we assumed that the DF of InN should be identical for all samples of the M series, i.e. the data of all samples ( $\Psi$  and  $\Delta$  at various angles of incidence) are fitted together for determining one pair of  $\epsilon_1$  and  $\epsilon_2$  values at each photon energy yielding an averaged DF. The layer thicknesses were allowed to vary with respect to the nominal values. Such an approach (point-by-point multi-sample fit) increases the reliability of the  $\bar{\epsilon}$  data because it minimizes the correlation to the layer thickness and removes the noise in the high-energy range. It should be noticed again that we did not make any assumption concerning the shape of the DF (dielectric function model). The fit results for  $\Psi$  of sample #M3 are indicated by the full lines in Fig. 1(a). In this example as well as for the other spectra, excellent agreement is obtained over the full investigated range although the averaged DF is employed. It emphasizes the assumption of a, within the experimental uncertainty, sample independent DF. For the sputtered layers the multi-sample fit yields similar good agreement with the experimental data as the example in Fig. 1(b) demonstrates.

Before discussing the extracted DF's, a few details of the theoretical calculations are given in the following. The properties of wurtzite InN have been calculated within the framework of density functional theory (DFT) in its local density approximation (LDA) employing the Vienna ab-initio Simulation Package [14]. The In4d electrons are treated as valence electrons. It guarantees correct structural properties, and lattice constants of  $c = 5.688 \text{ \AA}$  and  $a = 3.523 \text{ \AA}$  were calculated. Besides the strain aspects, these values agree well with the data obtained for the MBE grown layers. This DFT-LDA procedure, however, gives a negative fundamental energy gap of InN because  $p$ - $d$  repulsion is strongly overestimated. In the case of calculations of the optical properties, we therefore used another type of pseudopotentials which account for self-

interaction corrections of the 4d electrons in the underlying atomic calculation but freeze the In4d electrons in the core [15]. Already in the DFT-LDA case this opens artificially a gap. Therefore, additional quasi-particle corrections (overestimating the gap) were not taken into account in the calculations of optical properties. The independent-particle approximation and the projector-augmented-wave (PAW) method [16] are applied to calculate at first the imaginary part of the dielectric function [17]. The real part of the dielectric function is obtained via a Kramers-Kronig transform.

Fig. 2 summarizes the optical properties for InN concerning the real (a) and imaginary (b) parts of the DF as well as for the corresponding absorption coefficient  $\alpha$  (c). The full and dashed lines are obtained by the point-by-point multi-sample fits of the MBE grown (M series) and sputtered (S series) films, respectively, while the long-dashed lines represent the results of the DFT-LDA calculations. Let us first focus on the absorption coefficient (c). Our results for the sputtered films are in excellent agreement with previous investigations [2]. Those layers show only weak absorption in the energy range between 1 and 2 eV. For single-crystalline InN, however, the absorption coefficient increases continuously with the photon energy.

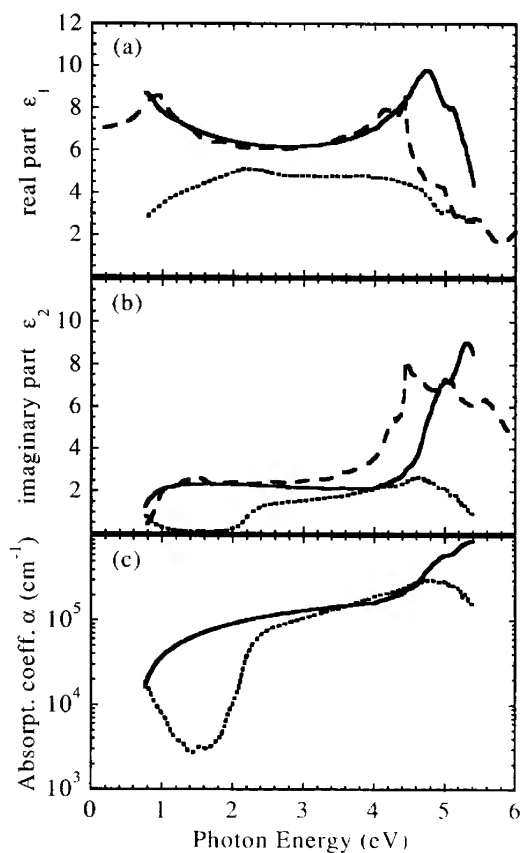


**Figure 2.**

Comparison of the real (a) and imaginary (b) part of the DF and the absorption coefficient for InN. The full and dashed lines are obtained from the by point-by-point multi-sample fits of the MBE grown (M series) and sputtered (S series) layers, respectively. The long-dashed lines represent the results of the calculations without quasi-particle corrections.

**BEST AVAILABLE COPY**

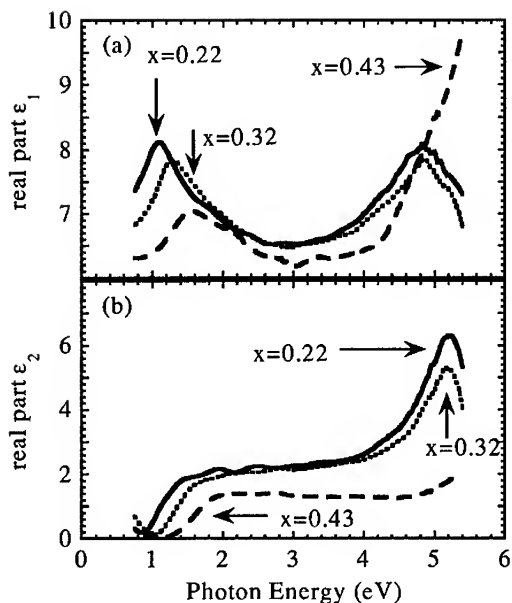


**Figure 3.** Real (a) and imaginary (b) part of the DF for  $\text{In}_{1-x}\text{Ga}_x\text{N}$  alloys obtained from fitting ellipsometric data.

The main result of this work is shown in Fig. 2(b) where the imaginary parts of the DF's are compared. The MBE grown films exhibit a spectral dependence of  $\epsilon_2$  which coincides in essential features with the theoretical results. Above the band gap ( $E_g \approx 0.75$  eV) the imaginary part increases very sharply indicating a non-parabolic band structure and remains nearly constant above the band gap up to energies of about 4 eV. The strong increase at higher energies arise from transitions along the L-M direction in the Brillouin-zone and was also calculated in Ref. [18]. However, its energetic position depends on the assumptions made in the DFT-LDA procedure. For the sputtered films such a strong increase around 4 eV is not observed, i.e. the two types of InN films differ not only in their band gap values but in addition in the higher-energetic parts of the DF. Therefore we conclude that only the MBE grown films represent bulk-like InN in the wurtzite structure.

Preliminary results of ellipsometry studies on  $\text{In}_{1-x}\text{Ga}_x\text{N}$  films shown in Fig. 3 emphasize this conclusion. As expected for an alloy system the spectral shape of both parts of the DF does not change very much if a low amount of Ga atoms replace In atoms in the InN lattice. With increasing Ga-content the step-like structure of  $\epsilon_2$  found between 1 and 2 eV shifts continuously to higher energies reflecting the rising band gaps. But even for 43% Ga composition, the gap energy is unambiguously below 1.9 eV, the value reported for sputtered films

In summary, applying spectroscopic ellipsometry and using multi-layer models for data analysis, we have determined the complex dielectric function from the near infra-red up to the near ultra-violet spectral region for single-crystalline InN films grown by MBE as well as of sputtered polycrystalline InN layers. Striking differences of the optical properties were found. MBE grown InN films show a 'narrow' band gap of around 0.75 eV, a nearly photon energy

independent imaginary part of the DF between 1 and 4 eV, and a strongly enhanced transition probability above 4 eV. The qualitative behavior agrees in essential features with the presented results of theoretical predictions. In contrast, sputtered layers with a gap energy around 1.9 eV do not show the increase of  $\epsilon_2$  at higher energies. Therefore, we conclude that 'narrow' band gap InN obtained by epitaxial growth techniques represents InN in the wurtzite structure with bulk-like properties. The clarification of the deviating properties of sputtered films requires further studies.

## ACKNOWLEDGEMENTS

The authors would like to thank the group of T.L. Tansley for providing the sputtered InN film for optical studies. The groups from Ilmenau University acknowledge financial support by the Thuringia Ministry of Science, Research, and Art under contract No. B609-02004. The work at Cornell University is supported by ONR Contract No. N000149910936 monitored by Dr. C. Wood.

## REFERENCES

1. K. Osamura, K. Nakajima, Y. Murakami, P. S. Shingu and A. Ohtsuki, *Solid State Commun.* **11**, 617 (1972); K. Osamura, S. Naka and Y. Murakami, *J. Appl. Phys.* **46**, 3432 (1975).
2. T.L. Tansley and C.P. Fowley, *J. Appl. Phys.* **59**, 3241 (1986).
3. R.T. Shamrell and C. Parman, *Optical Materials* **13**, 289 (1999).
4. W. Z. Shen *et al.*, *Appl. Phys. Lett.* **80**, 2063 (2002); H. F. Yang *et al.*, *J. Appl. Phys.* **91**, 9803 (2002).
5. T. Inushima, V. V. Mamutin, V.A. Vekshin, S. V. Ivanov, T. Sakon, M. Motokawa and S. Ohoya, *J. Crystal Growth* **227-228**, 481 (2001).
6. V. Yu. Davydov *et al.*, *phys. stat. sol. (b)* **229**, R1 (2002).
7. J. Wu *et al.*, *Appl. Phys. Lett.* **80**, 3967 (2002); J. Wu *et al.*, *ibid.* **80**, 4741 (2002).
8. T. Matsuoka, H. Okamoto, M. Nakao, H. Harima and E. Kurimoto, *Appl. Phys. Lett.* **81**, 1246 (2002).
9. F. Li, D. Mo, C. B. Cao, Y. L. Zhang, H. L. Chan and C. L. Choy, *J. Mat. Science: Mat. in Electronics* **12**, 725 (2001).
10. R. Goldhahn *et al.*, *phys. stat. sol. (a)* **177**, 107 (2001).
11. Q. Guo, O. Kato, M. Fujisawa and A. Yoshida, *Solid State Commun.* **83**, 721 (1992); Q. Guo, H. Ogawa and A. Yoshida, *J. Electron Spectrosc. Relat. Phenom.* **79**, 9 (1996).
12. H. Lu, W. J. Schaff, J. Hwang, H. Wu, G. Koley and L. F. Eastman, *Appl. Phys. Lett.* **79**, 1489 (2001).
13. S. Yamaguchi, M. Kariya, S. Nitta, T. Takeuchi, C. Wetzel, H. Amano and I. Akasaki, *J. Appl. Phys.* **85**, 7682 (1999).
14. G. Kresse and J. Furthmüller, *Comput. Mater. Sci.* **6**, 15 (1996); *Phys. Rev. B* **54**, 11169 (1996).
15. M. M. Rieger and P. Vogl, *Phys. Rev. B* **52**, 16567 (1995).
16. G. Kresse and D. Joubert, *Phys. Rev. B* **59**, 1758 (1999).
17. B. Adolph, J. Furthmüller and F. Bechstedt, *Phys. Rev. B* **63**, 125108 (2001).
18. C. Persson, R. Ahuja, A. Ferreira da Silva and B. Johansson, *J. Phys.: Condens. Matter* **13**, 8945 (2001).

**BEST AVAILABLE COPY**

---

## **Poster Session**

**In as a Surfactant for the Growth of AlGaIn/GaN Heterostructures by Plasma Assisted MBE**

E. Monroy<sup>1</sup>, N. Gogneau<sup>1</sup>, E. Bellet-Amalric<sup>1</sup>, F. Enjalbert<sup>2</sup>, J. Barjon<sup>1</sup>, D. Jalabert<sup>1</sup>, J. Brault<sup>1</sup>, Le Si Dang<sup>2</sup>, and B. Daudin<sup>1</sup>

Equipe mixte CEA-CNRS-UJF Nanophysique et Semiconducteurs

<sup>1</sup>Dépt. de Recherche Fondamentale sur la Matière Condensée, SP2M/PSC, CEA-Grenoble, 17 rue des Martyrs, 38054-Grenoble cedex 9, France

<sup>2</sup>Laboratoire de Spectrométrie Physique, Université Joseph Fourier, Grenoble, France

**ABSTRACT**

In this paper, we study the surfactant capability of In for the growth of AlGaIn/GaN heterostructures by plasma-assisted molecular beam epitaxy. Growth conditions were determined to have a self-regulated 1×1 In adlayer on Al<sub>x</sub>Ga<sub>1-x</sub>N (0001). The presence of this In film favors two dimensional growth of AlGaIn under stoichiometric conditions, and inhibits the formation of metal droplets on the surface. The quality of these layers was assessed by high resolution X-ray diffraction, atomic force microscopy and photoluminescence.

**INTRODUCTION**

Reliable low-power ultraviolet emitters are demanded for applications like optical detection of biological agents in the range from 340 nm to 250 nm, low-power communication links in the solar-blind spectral region (below 280 nm), or high-density data storage systems. Devices using AlGaIn as active media present much lower efficiency than their InGaIn/GaN-based counterparts in the green and blue range [1]. It is thus important to develop growth procedures that improve the quality of AlGaIn alloys.

Specific difficulties are faced when growing AlGaIn by molecular beam epitaxy (MBE) [2,3], due to the low mobility of Al species in comparison to Ga, which results in preferential Al incorporation and accumulation of Ga on the surface. The use of In as a surfactant appears as an attractive possibility to improve the material quality [4,5]. In this work, we report the assessment of In as a surfactant for the growth of AlGaIn/GaN heterostructures by plasma-assisted MBE.

**EXPERIMENTAL**

AlGaIn epilayers (0.5-0.7 μm thick) were grown on templates consisting of 1 μm thick GaN or AlN layers grown on sapphire by metalorganic vapor phase epitaxy (MOVPE). After a standard chemical degreasing procedure and acid cleaning, the substrates were introduced in a Meca 2000 MBE chamber equipped with standard effusion cells for Ga, In and Al. Active nitrogen was supplied by a radio-frequency plasma cell. The mass fluxes in monolayers per second (ML/s) were deduced from the stoichiometric growth rate of GaN, AlN and InN, measured at low temperature to prevent overestimation due to metal desorption. Prior to AlGaIn growth, a thin (~10 nm) GaN or AlN buffer layer was deposited at 730°C.

The Al mole fraction of the alloys was determined by Rutherford backscattering spectrometry (RBS). The growth kinetics and the structure of the layers were analyzed by reflection high-energy electron diffraction (RHEED), atomic force microscopy (AFM) in tapping mode, and high resolution X-ray diffraction (HRXRD). HRXRD measurements were carried out in a SEIFERT

XRD 3003 PTS-HR system with a beam concentrator prior to the Ge(220) 4-bounce monochromator and a Ge(220) 2-bounce analyzer in front of the detector. Photoluminescence (PL) was measured by exciting with the fourth frequency of a pulsed Nd-YAG laser (266 nm) with a peak power of 500 kW/cm<sup>2</sup> and a mean power of 10 mW.

## RESULTS AND DISCUSSION

The In wetting of the GaN and AlGaN surface was evaluated by exposing the surface to an In flux for a given time, and studying the oscillatory transient in RHEED intensity during In desorption under vacuum [5,6]. For In fluxes lower than about 1 ML/s, the desorption time remains constant for In expositions longer than 20 s (see inset of Figure 1), which confirms the deposition of a dynamically-stable In film.

From the duration of the desorption transient, we can calculate precisely the quantity of In deposited on the substrate surface. Figure 1 presents the results obtained on GaN at a substrate temperature of 680°C. This graph indicates that there are two regimes corresponding to a self-regulated In coverage of 1 ML and 2 ML (i.e. 1.7 ML in terms of InN surface sites [5]). Remarkably, these results correspond to the stable In surface structures during InGaN growth under In-rich conditions, predicted by *ab initio* calculations [7,8] and identified by scanning tunneling microscopy [8]. Varying the In flux and the substrate temperature, we can draw a phase diagram of In adsorbed on GaN, as shown in Figure 2(a).

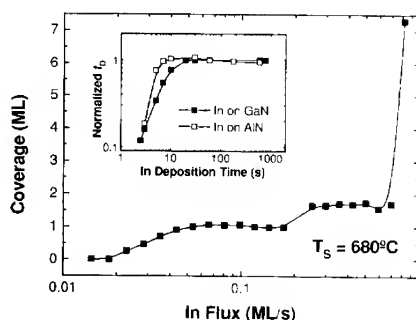


**Figure 1.** In coverage as a function of the impinging In flux, measured on a GaN layer at 680°C. In the inset, In desorption time,  $t_D$ , from GaN and AlN layers as a function of the In deposition time, measured in the same conditions. In both cases, the In coverage becomes stable after about 20 s.

We have also analyzed the In wetting as a function of the Al mole fraction of the epilayer at a substrate temperature  $T_S = 680^\circ\text{C}$ . As shown in Figure 2(b), only the In coverage of 1 ML is self-regulated on  $\text{Al}_x\text{Ga}_{1-x}\text{N}$  ( $x \geq 0.15$ ), and the flux window becomes narrower for higher Al contents, no self-regulated window being observed for AlN. A remarkable result from this diagram is the fact that at 680°C and with an In flux of  $\sim 0.08$  ML/s we can generate a 1 ML self-regulated In film, independent of the Al mole fraction of the underlying substrate. At this temperature, In does not incorporate in AlGaN, so that the In film will segregate at the growth front, modifying the growth kinetics. It is therefore possible to grow a complete GaN/AlGaN heterostructure in presence of a constant In flux.

**BEST AVAILABLE COPY**

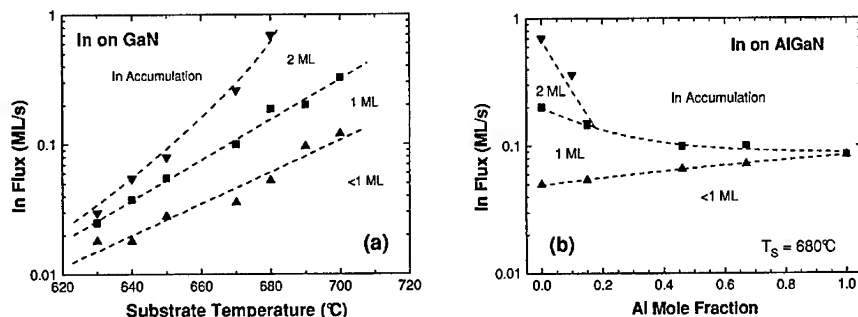


**Figure 2.** (a) Diagram of In coverage on GaN as a function of substrate temperature and impinging In flux. (b) Variation of the In coverage as a function of the impinging In flux and the Al mole fraction, measured on AlGaIn layers at 680°C.

To assess the surfactant effect of In,  $\sim 0.5 \mu\text{m}$  thick  $\text{Al}_x\text{Ga}_{1-x}\text{N}$  layers ( $x = 0.08$  to  $0.70$ ) were grown at 680°C on GaN and AlN MOCVD templates, in presence of an In flux of  $\Phi_{\text{In}} = 0.08$  ML/s. In presence of indium, 2D growth can be achieved under slightly N-rich conditions, which prevents Al or Ga accumulation on the surface. A streaky  $1 \times 1$  reconstruction was visible throughout the growth process. This pattern is slightly diffuse during growth due to the presence of the In layer, but recovers brightness about 1 min after stopping growth, which confirms the desorption of the In adlayer. Samples present mirror-like surfaces, with an average surface roughness of  $\sim 10 \text{ \AA}$  (rms) measured by AFM in a surface of  $1 \mu\text{m} \times 1 \mu\text{m}$ . No droplets or macroscopic defects are observed.

The structural quality of the AlGaIn layers was evaluated by HRXRD. The full width at half maximum (FWHM) of (0002)  $\omega$  and  $\theta-2\theta$  scans of samples grown with and without In surfactant are summarized in Figure 3. The low broadening values in surfactant-assisted growth indicate a low density of screw dislocations and demonstrate the structural quality of the material.

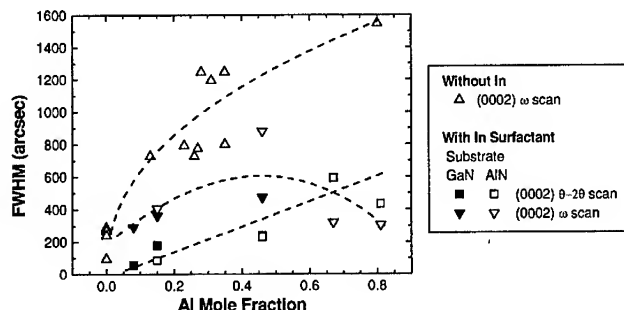


**Figure 3.** Variation of the full width at half maximum (FWHM) of HRXRD as a function of the Al mole fraction, measured in AlGaIn samples with and without In surfactant.

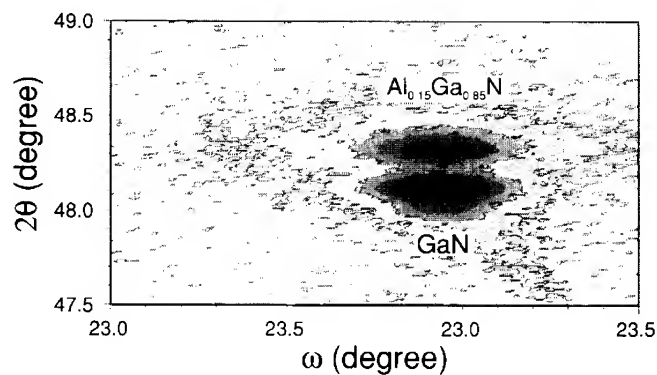


**Figure 4.** Reciprocal space map of the (-102) reflection of an  $\text{Al}_{0.15}\text{Ga}_{0.85}\text{N}$  layer grown on GaN.

(0001)-oriented III-nitride epilayers present a columnar structure characterized by the average tilt and twist of the columnar domains. The symmetric (0002) rocking curve is only sensitive to the column tilt, since it is broadened by screw and mixed dislocations. The twist, however, is only accessible by asymmetric reflections, which are also broadened by threading edge dislocations. Thus, to evaluate the quality of AlGaN layers, it is necessary to measure broadening of both symmetric and asymmetric reflections. Figure 4 presents the reciprocal space map of the (-102) reflection of an  $\text{Al}_{0.15}\text{Ga}_{0.85}\text{N}$  layer grown on GaN, which shows that the broadening value registered in the asymmetric reflection of AlGaN is comparable to the value of the template (430 arcsec for the AlGaN layer and 370 arcsec for the GaN template).

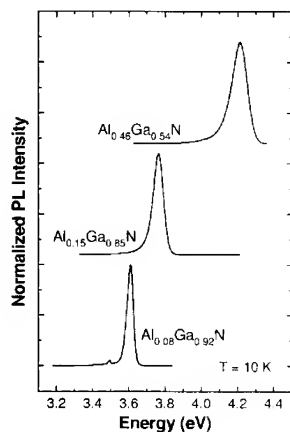


**Figure 5.** Low temperature photoluminescence of AlGaN layers with different Al content.

**BEST AVAILABLE COPY**

Low temperature PL spectra of the samples are shown in Figure 5. As expected, the emission shifts to higher energy for increasing Al contents. For low Al contents ( $x < 0.4$ ) deep transitions are not observed, and no relevant differences were found between samples grown on GaN and AlN templates, from an optical viewpoint. However, for Al contents  $x > 0.4$ , samples grown on GaN present extended cracks that obey a six fold symmetry. These observations agree with studies of strain relaxation in AlGaIn under tensile stress [9]. An additional deep emission ( $\sim 400$  meV below the main line) appears in the photoluminescence and cathodoluminescence spectra of cracked samples. On the contrary, the compressive strain in the layers grown on AlN prevents cracking whatever the Al composition, for the layer thickness considered in this study ( $\sim 0.5 \mu\text{m}$ ).

The improved structural quality and reduced roughness of these AlGaIn layers are promising parameters for the development of III-nitride based heterostructures. To validate the use of these alloys in the active region of light emitters, we have analyzed their effect on the photoluminescence of GaN quantum wells. Figure 6 shows the room temperature photoluminescence (PL) spectra of two structures consisting of ten 1-nm-thick GaN quantum wells (QW) separated by 10-nm-thick  $\text{Al}_{0.30}\text{Ga}_{0.70}\text{N}$  barriers, grown with and without In surfactant. Both samples were grown on NOVASIC-polished 6H-SiC substrates, using an AlN buffer layer. To improve as much as possible the quality of the ternary alloy, AlGaIn grown without In was deposited at higher substrate temperature ( $T_s = 730^\circ\text{C}$ ) and under Ga-rich conditions. The RHEED pattern remained streaky during the growth of both heterostructures, indicating two-dimensional growth.

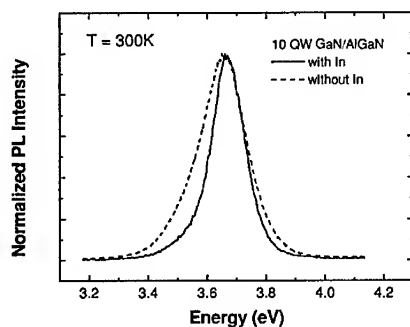


**Figure 6.** Room temperature photoluminescence of 10 QW of GaN in  $\text{Al}_{0.30}\text{Ga}_{0.70}\text{N}$  with and without In surfactant. Growth temperature was  $680^\circ\text{C}$  and  $730^\circ\text{C}$ , respectively.

Emission from the barrier is not observed in any of the structures, which indicates a good transfer of carriers from the barrier to the QWs. Structures grown with In surfactant present thinner PL lines, both at room temperature and at 10 K. This feature is likely related to better AlGaIn/GaN interfaces, and improved structural quality.

## CONCLUSION

We have determined the range of In fluxes at which  $1 \times 1$  In adlayer is dynamically-stable on  $\text{Al}_x\text{Ga}_{1-x}\text{N}$  (0001) at  $680^\circ\text{C}$ . More precisely, we have demonstrated the possibility of growing

GaN/AlGaIn heterostructures in presence of a self-regulated In film, independent of the Al content of the underlying AlGaIn layer. The presence of this In layer, which segregates at the growth front, modifies the surface energy and growth kinetics, enabling 2D-growth of AlGaIn under stoichiometric and slightly N-rich conditions. The quality of AlGaIn layers grown with In as a surfactant is demonstrated by high-resolution X-ray diffraction, atomic force microscopy, and photoluminescence.

#### ACKNOWLEDGEMENTS

Thanks are due to Y. Genuist and M. Falco for technical support. Financial support from TIPEL Project (DiGITIP 3 / STS / SDCO) is acknowledged.

#### REFERENCES

1. J. Han and A. V. Nurmikko, IEEE J. Quantum Electron. 8, 289 (2002).
2. E. Iliopoulos and T. D. Moustakas, Appl. Phys. Lett. 81, 295 (2002).
3. J. R. Jenny, J. E. Van Nostrand, and R. Kaspi, Appl. Phys. Lett. 72, 85 (1998).
4. F. Widmann, B. Daudin, G. Feuillet, N. Pelekanos, and J. L. Rouvière, Appl. Phys. Lett. 73, 2642 (1998).
5. E. Monroy, B. Daudin, E. Bellet-Amalric, N. Gogneau, D. Jalabert, F. Enjalbert, J. Brault, J. Barjon, and Le Si Dang, J. Appl. Phys. 93, 1550 (2003).
6. G. Mula, C. Adelmann, S. Moehl, J. Oullier, and B. Daudin, Phys. Rev. B 64, 5406 (2001).
7. J. E. Northrup and J. Neugebauer, Phys. Rev. B 60, R8473 (1999).
8. H. Chen, R. M. Feenstra, J. Northrup, J. Neugebauer, and D. W. Greve, MRS Internet J. Nitride Semicond. Res. 6, 11 (2001).
9. S. Einfeldt, V. Kirchner, H. Heinke, M. DieBelberg, S. Figge, K. Vogeler, and D. Hommel, J. Appl. Phys. 88, 7029 (2000).

BEST AVAILABLE COPY

**BEST AVAILABLE COPY**

### **Molecular Beam Epitaxial Growth of AlN/GaN Multiple Quantum Wells**

Hong Wu, William J. Schaff, and Goutam Koley  
School of Electrical and Computer Engineering, Cornell University,  
Ithaca, NY 14853, U.S.A.

Madalina Furis and A. N. Cartwright  
Department of Electrical Engineering, State University of New York at Buffalo,  
Buffalo, NY 14260, U.S.A.

Karen A. Mkhoyan and John Silcox  
School of Applied and Engineering Physics, Cornell University,  
Ithaca, NY 14853, U.S.A.

Walter Henderson and W. Alan Doolittle  
School of Electrical and Computer Engineering, Georgia Institute of Technology,  
Atlanta, GA 30332, U.S.A.

A.V. Osinsky  
Science and Technology, Corning Inc.,  
Corning, NY 14831, U.S.A.

#### **ABSTRACT**

AlN/GaN multiple quantum wells (MQWs) were grown on sapphire substrates by plasma-assisted molecular beam epitaxy. Growth temperature, III/V ratio, growth rate, and other growth parameters were optimized for the buffer layer and the MQWs, separately. The growth of AlN buffer was kept as Al-rich as possible while the formation of Al droplets was avoided. A GaN buffer layer was also tried but proved to be inferior to AlN buffer probably due to its larger surface roughness, higher dislocation density, and larger lattice mismatch with the AlN barrier layers in the MQWs. Very flat surfaces with a RMS roughness of 0.7nm were observed by atomic force microscopy (AFM) on the samples with both AlN buffer layer and 20 MQWs deposited under the optimized growth conditions. Abrupt interfaces and excellent periodicities of the MQWs were confirmed by X-ray diffraction (XRD) and reflectivity measurements with MQWs' satellite peaks clearly visible up to the 10th order. Room-temperature intense ultraviolet (UV) photoluminescence (PL) emission with wavelength in the range of 320-350nm was also observed from the MQWs with well width ranging from 1.0 to 1.5nm. These MQW structures can potentially be used for UV light emitters and quantum cascade lasers.

#### **INTRODUCTION**

There have been considerable interests in group III-nitrides for their applications in the ultraviolet (UV) light emitter diodes (LEDs) and laser diodes (LDs) [1-3]. Until recently, most of the efforts had been focused on InGaN-based light emitters [1,2]. But to achieve light emission with even shorter wavelength, AlGaN-based light emitting structures need to be used. Due to the fact that low-dimensional heterostructures can provide carrier confinement and therefore

improve the optical efficiency, AlGaIn/GaN quantum wells with low aluminum concentration AlGaIn barriers have been used to make UV LEDs [4]. In order to further shorten the emission wavelength, higher aluminum concentration AlGaIn or even AlN barriers should be used in the quantum well structures. Besides the applications using intraband transitions, AlGaIn/GaN quantum well system is also a potential candidate for quantum cascade lasers due to the recent realization of intersubband transitions (absorption, so far) [5]. High aluminum concentration AlGaIn or AlN barriers are also needed in this case to maximize the intersubband transition energy for potential applications in short wavelength quantum cascade lasers.

In this study, we fabricated AlN/GaN MQWs by molecular beam epitaxy and optimized the growth conditions. Strong room-temperature UV PL emission was observed from the MQWs.

## EXPERIMENT

The structures used in this study were grown in a Varian Gen II molecular beam epitaxy (MBE) system which used standard effusion cells for the group III elements and an EPI Unibulb rf plasma source to supply nitrogen radicals. The MQWs were grown typically with the rf power and growth chamber pressure at approximately 250 W and  $1.5 \times 10^{-5}$  torr, respectively. All the growths took place on 2 inch c-plane sapphire substrates which were backside coated with TiW for more efficient heating. The wafer pretreatment process included a one-hour outgassing step at 450°C and a following 30-minute low temperature nitridation step at 160°C with the rf power set at 500 W. Growth temperatures were monitored by a pyrometer calibrated to measure the temperature of the TiW on the backside of the substrates.

The epitaxial structures consisted of a buffer layer of 0.3-0.5  $\mu\text{m}$ , which was either AlN or GaN, and 20 AlN/GaN quantum wells on all the samples in this study. Different growth conditions were experimented in an attempt to achieve the best quality of the MQWs. For all the samples studied, the AlN barrier thickness was kept at 60 Å, while the thickness of GaN wells varied from 9 to 15 Å. The nominal thickness of each layer was calculated by the growth rates of equivalent bulk samples. No growth interruptions occurred during the deposition of MQWs.

## RESULTS AND DISCUSSION

### Growth Optimization

The growth optimization process was made by the comparisons of the MQWs' quality among the samples grown under different conditions (see Table I.). The entire epitaxial structure of all the samples listed in Table I was undoped. Also listed in the table is the RMS surface roughness measured by AFM for each sample with both the buffer and MQWs already deposited. None of the samples listed in Table I exhibited cracks on the surface. The first thing to optimize in this study was the material of the buffer layer. In our case, for simplicity, only AlN and GaN buffer layers were tried. The growth conditions we used for the GaN buffer layer were expected to produce the GaN epitaxial layer of the best quality in our MBE system, based on our previous experience. But according to the surface roughness measurements, the MQW sample with GaN buffer (sample "E") had the poorest surface morphology with an RMS roughness of 4.9 nm, which was higher than any of the MQW samples grown on AlN buffer. Besides AFM measurements, the quality of the MQWs on some of these samples was also evaluated by X-ray diffraction and reflectivity measurements. A comparison of X-ray diffraction pattern was made

**Table I.** Structures of the samples for growth optimization and the measured surface roughness.

Sample	Buffer	Growth temperature of buffer (°C)	Growth temperature of MQWs (°C)	Nominal thickness of GaN wells (Å)	Surface RMS roughness (nm)
A	AlN	700	700	10	2.8
B	AlN	700	700	14	3.3
C	AlN	800	700	12	0.7
D	AlN	800	800	14	3.2
E	GaN	800	800	14	4.9
F	AlN	800	700	14	1.3

between sample “E” and sample “D”, which had the same structures and growth conditions except for the buffer. The X-ray pattern of sample “E” showed almost no satellite peaks of MQWs, while satellite peaks up to the 3<sup>rd</sup> order were clearly resolved in the case of sample “D”, which indicated that the MQWs on sample “D” had more abrupt interfaces, better periodicities, and probably a flatter surface of buffer layer to start with. This, along with the AFM results, proved that the GaN buffer was probably inferior to the AlN buffer for the growth of AlN/GaN MQWs possibly due to its larger surface roughness, higher dislocation density, and larger lattice mismatch with the AlN barrier layers in the MQWs. The second parameter optimized was the growth temperature of the AlN buffer layer. Based on the surface roughness results, the samples with the high temperature (800°C) buffer (“C” and “F”) had consistently much smoother surface than the samples with low temperature (700°C) buffer (“A” and “B”), if the MQWs were grown at the same temperature (700°C in this study). This suggested that a high temperature AlN buffer should be a preferred candidate for the growth of AlN/GaN MQWs due to its flatter surface and possibly lower dislocation density. Both X-ray diffraction and reflectivity measurements confirmed this finding. The X-ray diffraction profile of sample “C” exhibited more and also much stronger satellite peaks than that of sample “A” or “B”, while the X-ray reflectivity measurements gave similar results on sample “C” and “B” (see Figure 1.). The next very

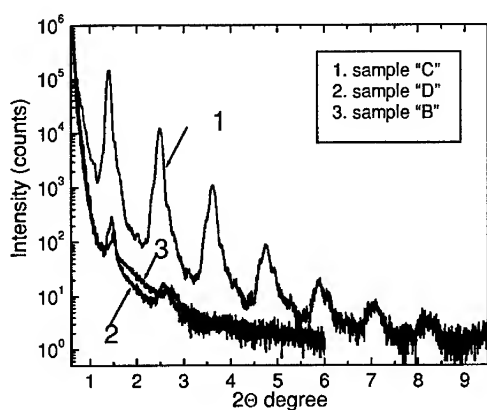


**Figure 1.** X-ray reflectivity measurements of AlN/GaN MQW samples.

important growth parameter was the growth temperature of the AlN/GaN MQWs. The results of AFM (sample "C", "D", and "F" in Table I.), X-ray diffraction (much more and stronger satellite peaks on sample "C" and "F" than on sample "D"), and X-ray reflectivity (sample "C" and "D" in Figure 1.) measurements all pointed to the same conclusion that AlN/GaN MQWs grown at low temperature (700°C) had much better quality and flatter surface than those grown at high temperature (800°C). One possible explanation is the growth mode dependence on the substrate temperature when GaN is grown on AlN [6]. However, so far, no solid evidence has been observed in reflection high energy electron diffraction (RHEED) or other measurements to support this explanation. Further study is required. Another observation worth mentioning is that according to the data in Table I, the thickness of the GaN wells did not seem to affect as much the surface roughness as the growth temperatures or the buffer material.

In order to have more precise control of the thickness of MQW layers, we grew the MQWs at a growth rate of 0.3-0.4  $\mu\text{m}$  per hour, instead of 0.5-0.6  $\mu\text{m}$  per hour which is typical and probably optimum (to get the best material qualities, based on our previous experiences) for the buffer layer growth. This was done by using relatively lower group-III fluxes and rf power of nitrogen plasma during the MQW growth. It is not clear at this point whether such a reduced growth rate is optimum or not for the MQWs in terms of material qualities.

Apart from the growth parameters mentioned above, we also found that during the AlN buffer growth, the more Al-rich the III/V ratio was, the better the AlN quality we obtained. In order to make the growth as Al-rich as possible without forming Al droplets, we adjusted the III/V ratio so that the 2" wafer was covered by Al droplets except for the central area about 1" in diameter due to the radial nonuniformity of the plasma density and substrate heating efficiency. In doing so, the AlN buffer layer grown in the central area of the wafer usually had flatter surface and lower dislocation density than those grown without using this method.

### **Optimizedly-grown MQWs**

A series of AlN/GaN MQWs with different well thickness were grown under the optimized

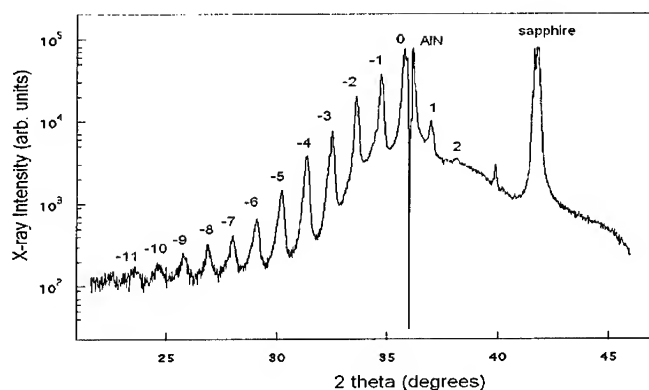


**Figure 2.** X-ray diffraction profile ( $\theta$ - $2\theta$  scan) of AlN/GaN MQWs. The kinks (sharp decrease in signal) at the peaks of AlN and sapphire were due to the saturation of X-ray detector.

conditions which were used in the growths of sample "C" and "F" listed in Table I. A typical X-ray diffraction pattern of these MQWs is shown in Figure 2. Well resolved satellite peaks up to the 10<sup>th</sup> order were observed, which indicated that abrupt interfaces and excellent periodicities of the MQWs were achieved. Surface RMS roughness of 1.0nm or smaller was obtained on these samples. The high quality of MQWs was also confirmed by transmission electron microscopy (TEM) measurements. In Figure 3, the TEM image exhibits near monolayer-abrupt interfaces between GaN wells and AlN barriers, considering the fact that the quantum wells, except the first one, shown in the figure were only approximately 5-monolayer-thick. It is interesting to note that the first quantum well was unexpectedly thin, which was probably due to the excess Al from the Al-rich buffer forming high Al concentration AlGa<sub>0.2</sub>N by competing with Ga to react with nitrogen radicals when the growth of the first GaN well started. This could have been avoided if the wafer had been exposed to the nitrogen plasma for a short period of time immediately after the AlN buffer growth was finished. Besides, the comparisons between the simulated X-ray diffraction profile (not shown in Figure 2.) and the measured X-ray data showed that the AlN barriers were almost fully relaxed while the GaN wells were almost fully strained, which was expected due to the relatively thick AlN buffer layer.

Finally, room-temperature PL measurements were made on these AlN/GaN MQW samples grown with the optimized conditions [7]. Single-peak strong UV emission with the peak energy in the range of 3.45-3.97eV was observed from the samples with the well width ranging from 0.9 to 1.5nm (see Figure 4.). The well width dependence of the peak energy agrees fairly well with the theoretical calculation when the piezoelectric and spontaneous polarization effects are taken into account.

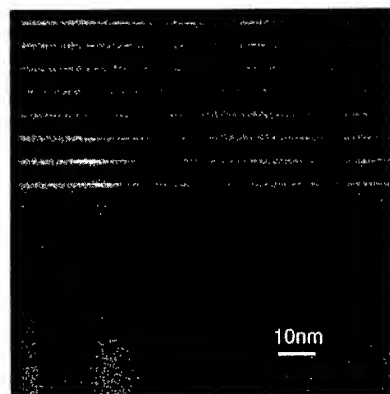


**Figure 3.** TEM image (dark field) of AlN/GaN MQWs. The first 9 quantum wells are shown. The brighter layers are GaN wells and the rest is AlN. The nominal thickness of GaN wells and AlN barriers on this sample is 1.3 and 6.0nm, respectively. The abrupt color change near the bottom of the image was due to the fact that a piece of sample peeled off during TEM sample preparation.

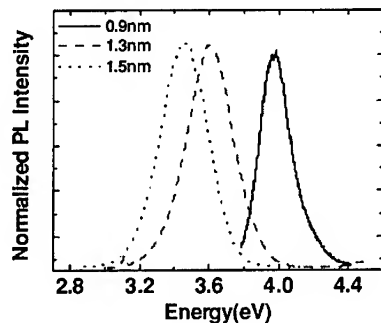


**Figure 4.** Room temperature time-integrated photoluminescence spectra from three AlN/GaN MQW samples with the well thickness of 0.9, 1.3, and 1.5nm, respectively.

## CONCLUSIONS

This study shows the optimization process of the molecular beam epitaxial growth of AlN/GaN MQWs. Grown under the optimum conditions, the MQWs showed near monolayer-abrupt interfaces and coherent periodicities. Room temperature strong UV emission was observed from these MQWs.

## ACKNOWLEDGEMENTS

The authors would like to thank Nikolai Faleev for valuable discussions of the X-ray data. This work is supported by NSF 01-65 Award No. 0123453 and ONR Contract No. N000140210951.

## REFERENCES

1. S. Nakamura, M. Senoh, N. Iwasa, S. Nagahama, T. Yamada, and T. Mukai, *Jpn. J. Appl. Phys., Part 2* **34**, L1332 (1995).
2. S. Nakamura, M. Senoh, S. Nagahama, N. Iwasa, T. Yamada, H. Kiyoku, Y. Sugimoto, T. Kozaki, H. Umemoto, M. Sano, and K. Chocho, *Jpn. J. Appl. Phys., Part 2* **36**, L1568 (1997).
3. S. Nakamura and G. Fasol, *The Blue Laser Diode* (Springer, Berlin, 1997).
4. J. Han, M. H. Crawford, R. J. Shul, J. J. Figiel, M. Banas, L. Zhang, Y. K. Song, H. Zhou, and A. V. Nurmikko, *Appl. Phys. Lett.* **73**, 1688 (1998).
5. C. Gmachl, H. M. Ng, S.-N. G. Chu, and A. Y. Cho, *Appl. Phys. Lett.* **77**, 3722 (2000).
6. B. Daudin, F. Widmann, G. Feuillet, Y. Samson, M. Arlery, and J. L. Rouvière, *Phys. Rev. B* **56**, 7069 (1997).
7. M. Furis, F. Chen, A. N. Cartwright, H. Wu, and W. J. Schaff, *GaN and Related Alloys, MRS Symposium Proceedings of 2002 Fall Meeting* (submitted).

### Evolution of Subgrain Boundaries in Heteroepitaxial GaN/AlN/6H-SiC Grown by Metalorganic Chemical Vapor Deposition

H.X. Liu, G.N. Ali, K.C. Palle, M.K. Mikhov, B.J. Skromme, Z. J. Reitmeyer,<sup>1</sup> and R.F. Davis<sup>1</sup>  
Department of Electrical Engineering and Center for Solid State Electronics Research,  
Arizona State University, Tempe, AZ, 85287-5706, U.S.A.

<sup>1</sup>Department of Materials Science and Engineering, North Carolina State University, Raleigh,  
NC, 27695-7907, U.S.A.

#### ABSTRACT

We have characterized the surface morphology and luminescence properties of GaN/AlN/SiC layers of various thicknesses using secondary electron imaging (SEI), panchromatic room temperature cathodoluminescence (CL), atomic force microscopy (AFM), optical Nomarski microscopy, and room and low temperature photoluminescence (PL). The nominally undoped GaN layers were grown by MOCVD on 0.1  $\mu\text{m}$  thick AlN buffer layers on commercial 6H-SiC(0001) substrates. The GaN layer thicknesses are 0.5, 1.0, 1.6, and 2.6  $\mu\text{m}$ . A second 1.0  $\mu\text{m}$  thick layer was grown by identical procedures on a 6H-SiC substrate that was first etched in  $\text{H}_2$  to remove scratches and damage due to mechanical polishing. Biaxial compressive lattice mismatch stress is present in all layers and decreases with increasing layer thickness, while PL linewidths decrease. The 1  $\mu\text{m}$  layer on the H-etched substrate is as relaxed as the 2.6  $\mu\text{m}$  layer on a non H-etched substrate, however. Pronounced surface structures, apparently corresponding to columnar subgrain boundaries, are observed on the samples on non H-etched SiC. Their typical sizes increase from about 3 to 10  $\mu\text{m}$  with increasing layer thickness. They are absent in the H-etched sample. These structures are generally nonradiative in CL images, although mottled contrast is also observed inside them. Similar layers doped with  $3 \times 10^{18} \text{ cm}^{-3}$  Si do not show these features, suggesting a different microstructure.

#### INTRODUCTION

Gallium nitride and related semiconductors have attracted more and more attention in recent years, mainly due to their promising applications in short-wave light-emitting devices and photodetectors, as well as in radiation-hard, high frequency and high power electronic devices [1]. To date, it is still very hard to grow bulk GaN crystals, so heteroepitaxial growth of high quality GaN thin films is the premise for the development of GaN-based devices. Compared with the more common growth on sapphire, epitaxial growth of GaN on SiC substrates offers advantages such as high electrical conductivity, smaller lattice mismatch, and higher thermal conductivity [2, 3]. In this sense, better material quality and subsequent device performance should be expected for GaN grown on SiC. However, the quality of GaN on SiC reported to date does not very much surpass that of GaN on sapphire [4], and the effect of structural properties on luminescence has not yet been widely studied.

In this work, we report characterization of the surface morphology and luminescence properties of GaN/AlN/SiC layers of various thicknesses. The characterization techniques include the secondary electron imaging (SEI) mode of a scanning electron microscope, panchromatic room temperature CL, AFM, optical Nomarski microscopy, room and low temperature PL, and low temperature reflectance. We study the effects on the structure and

luminescence properties of the GaN layers of processing the SiC substrates by hydrogen etching prior to growth, and of Si doping the GaN epilayers.

## EXPERIMENTAL PROCEDURE

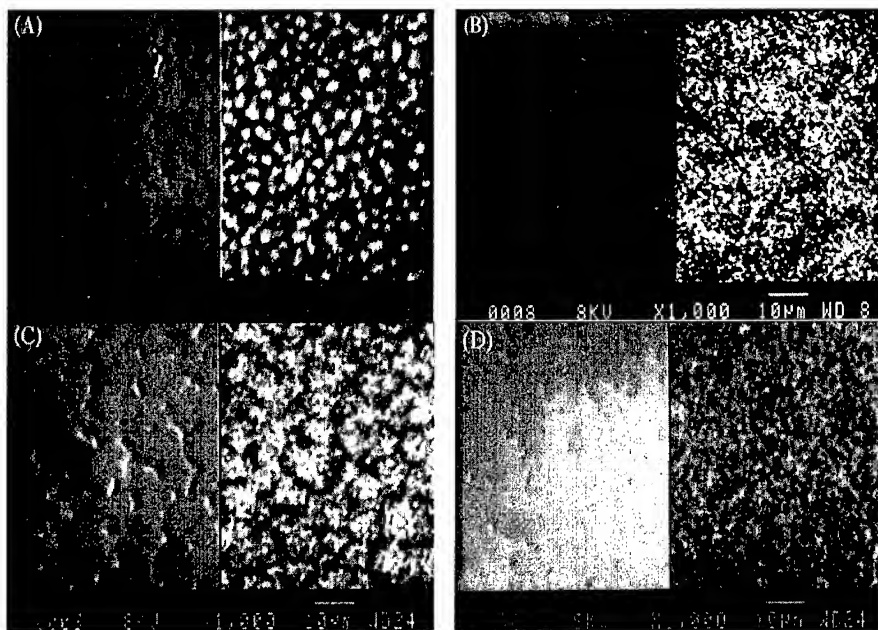
The GaN epilayers were grown by MOVCD using an AlN buffer layer on the Si-face of on-axis 6H-SiC (0001) wafers (Cree, Inc.). The MOCVD reactor was a cold-walled vertical pancake-style system. The base pressure was  $\sim 10^{-6}$  Torr. Trimethylaluminum, triethylgallium, and ammonia were used as the precursors, with hydrogen as both the carrier and diluent gas. The temperature of the SiC-coated graphite susceptor was measured by a single wavelength optical pyrometer. Prior to loading into the reactor, the substrates were etched at room temperature in a HF:H<sub>2</sub>O (1:10) solution for 10 min to remove native oxides, rinsed in deionized water, and blown dry with nitrogen. For the hydrogen-etched samples, after chemical etching, the SiC substrates were transferred to a cold-walled vertical system with a flow of 8 slm H<sub>2</sub>(25%):He(75%) mixture for 20 min at 1600 °C and 1 atm pressure. All epitaxial layers were grown at a pressure of 20 Torr, using a V/III ratio of 24,000 for AlN, and a V/III ratio of 1,300 for GaN. The AlN buffer layer was grown at a temperature of 1115 °C, with a thickness of 0.1  $\mu\text{m}$  for each run. The GaN epilayers were grown at a temperature of 1015 °C, with thicknesses of 0.5, 1.0, 1.6, and 2.6  $\mu\text{m}$ . The Si-doped samples have a doping level of  $3 \times 10^{18} \text{ cm}^{-3}$ , as determined from Hall effect measurements.

The SEI and panchromatic room temperature CL imaging were performed on a JEOL JXA 840 SEM. The AFM was performed on a Digital Instruments Multimode AFM. The PL measurements were performed at 1.7 and 300 K with an unfocused, 8 mW beam from an Ar<sup>+</sup> laser operating at 305.5 nm.

## RESULTS

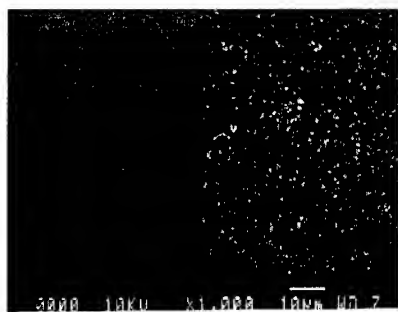
Typical SEI and panchromatic room temperature CL images of GaN grown on non H-etched SiC are shown in Figure 1. Pronounced surface structures corresponding to columnar subgrain boundaries are observed by SEI on all the samples, although they are not uniformly present in all regions. The typical sizes increase from about 3 to 10  $\mu\text{m}$  as the GaN film thickness increases from 0.5 to 2.6  $\mu\text{m}$ . The CL images show dark areas at the borders of the columns, indicating that these boundaries are generally nonradiative. Some mottled contrast is also observed inside the columns, presumably due to isolated threading dislocations. As the film thickness increases, the CL becomes relatively more homogeneous. At a layer thickness of 2.6  $\mu\text{m}$ , the CL image shows similar contrast to that observed inside the columns of thinner samples, although portions of faint grain boundaries remain detectable. Figure 2 shows the SEI and CL images of a 1.0  $\mu\text{m}$  thick GaN layer grown on a H-etched SiC substrate. It shows a quite flat surface morphology and does not have the columnar structure observed in the layer grown on non H-etched SiC. The CL image shows a mottled contrast, presumably due to individual dislocations. Figure 3 compares deflection-mode AFM images of the 1.0  $\mu\text{m}$  thick GaN layers grown on non H-etched and H-etched SiC. These images show the presence of grain boundaries in the non H-etched case and their absence in the H-etched case, confirming the SEI observations.

The difference in the surface structures of GaN on non H-etched and H-etched substrates can partly be explained in terms of the initial nucleation of GaN, and reflects different growth mechanisms. In the non H-etched case, a separate study of the initial phases of growth has

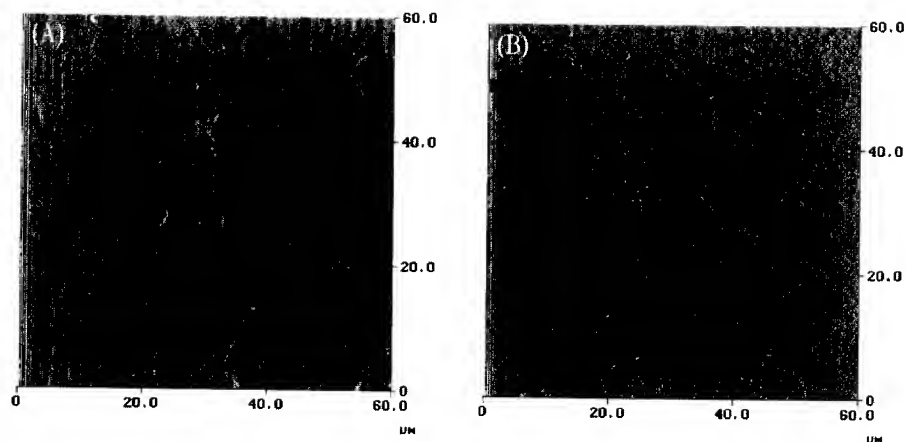


**Figure 1.** SEI (left) and panchromatic 300 K CL (right) images of GaN grown on non H-etched SiC. GaN layer thickness is (A) 0.5  $\mu\text{m}$ , (B) 1.0  $\mu\text{m}$ , (C) 1.6  $\mu\text{m}$ , (D) 2.6  $\mu\text{m}$ .

shown that the bare AlN buffer layer exhibits many undulations and deep pits arranged along lines, which are believed to be associated with polishing scratches on the SiC [3]. Subsequent GaN growth was found to occur by a Stranski-Krastanov growth mode. It starts with the growth of a 1 to 1.5 nm thick continuous wetting layer and continues with the formation of GaN islands, which form preferentially at the bottoms of the undulations. These islands coalesce after about 100 nm of growth [3]. We believe that the three-dimensional growth mode and undulant surface



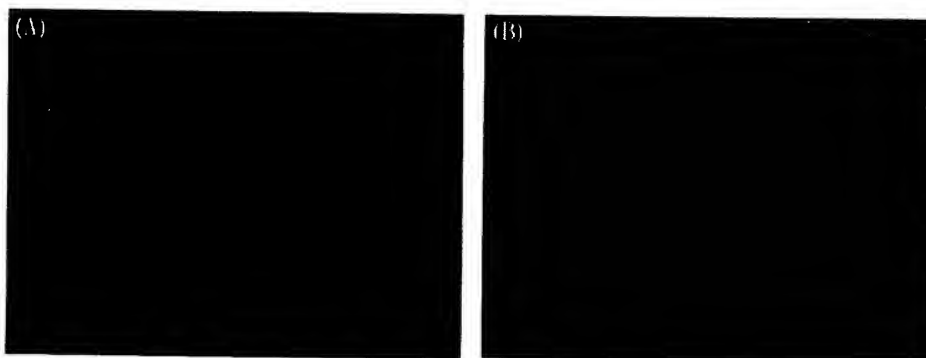
**Figure 2.** SEI (left) and panchromatic 300 K CL (right) images of a 1.0  $\mu\text{m}$  thick GaN layer grown on H-etched SiC (compare to Figure 1B for the corresponding case on non H-etched SiC, grown side by side in the same run.)



**Figure 3.** Deflection-mode AFM images of 1.0  $\mu\text{m}$  thick GaN layers grown on (a) non H-etched and (b) H-etched SiC. Vertical range is 30 nm; average depth of grain boundary depressions in (a) is 7-10 nm (determined from height mode images).

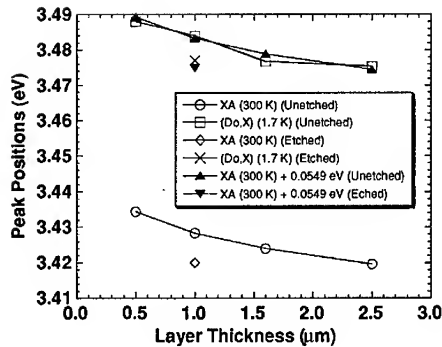
structure on non H-etched SiC contributes to the eventual polygonization of some of the threading dislocations into subgrain boundaries. As observed in the SEI images, the columnar grain size increases with thickness. In the H-etched case, we attribute the flatter surface morphology to a step-mediated layer-by-layer growth mechanism, which probably results from the etching process. This process efficiently removes the scratches and damaged surface layer due to polishing, and creates an atomically smooth surface with steps having primarily unit cell heights [5-8]. The more two-dimensional growth that occurs in this case is less likely to generate strain fields which stimulate the formation of grain boundaries.

Figure 4 shows SEI and CL images of two 1.0  $\mu\text{m}$  thick GaN layers doped with a Si concentration of  $3 \times 10^{18} \text{ cm}^{-3}$  on both non H-etched and H-etched SiC. In contrast to the



**Figure 4.** SEI (left) and panchromatic 300 K CL (right) images of 1.0  $\mu\text{m}$  thick Si-doped GaN layers grown on (a) non H-etched and (b) H-etched SiC.

**BEST AVAILABLE COPY**



**Figure 5.** PL peak positions as a function of (undoped) GaN layer thickness on both non H-etched and H-etched SiC.

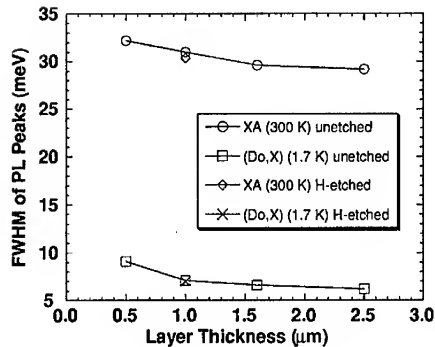


**Figure 6.** PL linewidths as a function of (undoped) GaN layer thickness on both non H-etched and H-etched SiC.

undoped case, the Si-doped layer exhibits a flat surface, even on the non H-etched substrate. The CL images of both samples show contrast similar to that of the undoped sample on the H-etched substrate, suggesting a random arrangement of dislocations and the absence of subgrain boundaries. This behavior is quite similar to that observed by S. Ruvimov *et al.* for growth of undoped and Si-doped GaN layers on sapphire [9,10]. They attributed the large difference in morphology to the presence of small-angle grain boundaries in the undoped case, and a lower-density, random distribution of dislocations in the Si-doped case, as determined by plan-view TEM. We speculate that Si doping promotes a more two-dimensional growth mode, similar to that obtained by H etching of the substrate. More detailed studies of the initial phases of growth will be required to confirm this assumption, however.

Room temperature and low temperature PL measurements were also performed on all samples. Figure 5 shows band-edge PL peak positions as a function of GaN layer thickness. The band-edge peaks involve A free exciton ( $X_A$ ) recombination at 300 K, and neutral donor-bound ( $D^0,X$ ) recombination at 1.7 K. They are both shifted 4-17 meV higher in energy compared to the corresponding peaks in unstrained bulk GaN. These shifts imply biaxial compressive strain in all of these samples. Unstrained GaN has a ( $D^0,X$ ) position of 3.4711 eV at 1.7 K [11]. The A free exciton ( $X_A$ ) positions at 300 K are also shown shifted 54.9 meV higher in energy to compensate for the difference in 1.7 and 300 K band gaps and the localization energy of excitons to neutral donors. The shifted values track the low temperature ( $D^0,X$ ) values well, although the latter are more precise. As the GaN layer thickness increases, the band edge peak shifts lower in energy, indicating that thicker samples have relatively more relaxed compressive strain. The 0.5  $\mu\text{m}$  thick layer has  $\Delta a/a \sim -2.1 \times 10^{-3}$ , and the 2.6  $\mu\text{m}$  thick layer has  $\Delta a/a \sim -5.7 \times 10^{-4}$ , based on the 1.7 K ( $D^0,X$ ) positions and the previous strain calibration by Perry *et al.* [12].

In GaN grown on H-etched SiC, the ( $D^0,X$ ) position is lower by about 7 meV in energy compared to the same layer thickness grown on a non H-etched substrate, and nearly matches the position in the 2.6  $\mu\text{m}$  thick layer on non H-etched SiC. This indicates greater relaxation of compressive strain in GaN grown on the H-etched SiC. The more rapid relaxation may again be due to the more two-dimensional growth mode, in which lateral elastic relaxation of the

undulating surface structure present in the non-etched case must be replaced by plastic deformation processes.

Linewidths of the main band-edge peaks are plotted in Figure 6 as a function of GaN layer thickness. They range from 29.1 to 32 meV at room temperature and from 6.2-9.1 meV at 1.7 K. They decrease monotonically with increasing layer thickness, due to a larger distance from the interfacial extended defects and their inhomogeneous strain fields. Little difference is observed between the samples on non-etched and H-etched substrates, presumably because the very high density of dislocations near the interface is similar in both cases.

## CONCLUSIONS

Heteroepitaxial GaN layers grown on non H-etched SiC substrates show pronounced subgrain boundary structures formed by dislocations. Their typical sizes increase from 3 to 10  $\mu\text{m}$  as the GaN film thickness increases. Compressive strain exists in all films and decreases with increasing layer thickness. GaN grown on H-etched SiC does not have the grain boundary structure, and shows greater relaxation of the compressive strain found in thin layers. Silicon-doped samples show flat surface morphologies with no grain boundaries. Both Si-doping and H-etching are believed to contribute to a more two-dimensional growth mode.

## ACKNOWLEDGMENT

The ASU portion of this work was supported by the National Science Foundation under Grant No. ECS 0080719 and by the MRSEC at ASU under NSF DMR 96-32635.

## REFERENCES

1. H. Morkoç, S. Strite, G.B. Gao, M.E. Lin, B. Sverdlov, and M. Burns, *J. Appl. Phys.* **76**, 1363 (1994).
2. S. Strite, M.E. Lin, and H. Morkoç, *Thin Solid Films* **231**, 197 (1993).
3. S. Einfeldt, Z.J. Reitmeier, and R.F. Davis, submitted to *J. Crystal Growth*.
4. R.F. Davis, T.W. Weeks, M.D. Bremser, S. Tanka, R.S. Kern, Z. Sitar, K.S. Ailey, W.G. Perry, and C. Wang, *Mater. Res. Soc. Symp. Proc.* **395**, 3 (1996).
5. C. Hallin, F. Owman, P. Martensson, A. Ellison, A. Konstantinov, O. Kordina, and E. Janzen, *J. Crystal Growth* **181**, 241 (1997).
6. T.L. Chu and R.B. Campbell, *J. Electrochem. Soc.* **112**, 955 (1965).
7. F. Owman, C. Hallin, P. Martensson, and E. Janzen, *J. Crystal Growth* **167**, 391 (1996).
8. V. Ramachandran, M.F. Brady, A.R. Smith, R.M. Feenstra, and D.W. Greve, *J. Electron. Mater.* **27**, 308 (1998).
9. S. Ruvimov, Z. Liliental-Weber, T. Suski, J.W. Ager III, J. Washburn, J. Krueger, C. Kisielowski, E.R. Weber, H. Amano, and I. Akasaki, *Appl. Phys. Lett.* **69**, 990 (1996).
10. Z. Liliental-Weber, S. Ruvimov, T. Suski, J.W. Ager III, W. Swider, Y. Chen, Ch. Kisielowski, J. Washburn, I. Akasaki, H. Amano, C. Kuo, and W. Imler, *Mater. Res. Soc. Symp. Proc.* **423**, 487 (1996).
11. B.J. Skromme, K.C. Palle, C.D. Poweleit, H. Yamane, M. Aoki, and F.J. DiSalvo, *Appl. Phys. Lett.* **81**, 3765 (2002).
12. W.G. Perry, T. Zheleva, M.D. Bremser, R.F. Davis, W. Shan, and J.J. Song, *J. Electron. Mater.* **26**, 224 (1997).

### Segregation effects and bandgap engineering in InGaN quantum-well heterostructures

Kirill A. Bulashevich, Sergey Yu. Karpov, Roman A. Talalaev, Igor Yu. Evstratov, Yuri N. Makarov<sup>1</sup>

Soft-Impact Ltd, P.O.Box 33, 194156 St. Petersburg, Russia

<sup>1</sup> STR Inc, P.O.Box 70604, Richmond, VA 23255, USA

#### ABSTRACT

The analysis of In surface segregation and its impact on the composition profile and light emission spectra of the InGaN single quantum well heterostructures grown by Metalorganic Vapor Phase Epitaxy (MOVPE) is carried out by coupled solution of the Poisson and Schrödinger equations. Effective methods of controlling the composition profile, indium predeposition and temperature ramping during the cap layer growth are considered in terms of surface segregation model. General trends in spectra transformation upon the forward bias variation and their correlations with the quantum well electronic structure are discussed.

#### INTRODUCTION

Recently, In surface segregation has been recognized as a factor critical to control of the composition profiles in III-nitride light emitting diode (LED) quantum well (QW) heterostructures. Much effort was made to find correlations between the growth recipes, segregation effects, and emission characteristics of the grown diodes. Along with variation of growth parameters (temperature, pressure, precursor flow rates, etc.), specific procedures – growth interruption at the QW interfaces [1], indium predeposition [2,3], and temperature ramping during barrier or cap layer growth [4] – were suggested to improve the composition profiles in InGaN QWs, normally serving as active regions in blue and green LEDs. Recent theoretical studies [5,6] considered basic mechanisms of In surface segregation in the multi-layer structures grown by MOVPE and some approaches to control of the composition distributions in the InGaN QW. However, the interrelation between the segregation effects and the characteristics of light emitted from the LED structures still remains poorly understood.

In this paper, we report on the quantum-mechanical study of segregation effects on the composition profiles and emission spectra of MOVPE-grown InGaN single-quantum-well (SQW) structures. Special attention is given to the most effective ways of controlling the front and back QW interfaces – indium predeposition and temperature ramping during the cap layer growth.

#### CONTROL OF COMPOSITION PROFILE IN InGaN-SQW HETEROSTRUCTURES

Consider a simple heterostructure that consists of an undoped InGaN SQW between n- and p-doped thick GaN layers, grown by MOVPE at 730°C in a vertical rotating-disk reactor under the conditions reported in [1]: pressure of 200 Torr, flow rates of TMGa, NH<sub>3</sub>, and N<sub>2</sub> (carrier gas) of 10.8 μmole/min, 406 mmole/min, and 196 mmole/min, respectively. TMIn flow rate was adjusted

to obtain steady-state indium composition of 0.27. We will distinguish between (i) the ideal structure, which can be projected from the steady-state calibration of the precursor flow rates, (ii) the real structure with profile affected by In surface segregation, and (iii) the structure grown with the temperature jump from 730°C to 800°C at the onset of the GaN cap layer deposition (hereafter referred to as T-ramping). Figure 1a compares the composition profiles of these structures computed by using the model suggested in [5,6]. Because of delayed In incorporation into the crystal at the onset of the InGa<sub>N</sub> QW growth, the InN fraction does not reach its steady-state value in the real structure and exhibits the presence of indium (In “tail”) in the cap layer. The application of T-ramping reduces considerably the In incorporation into the cap layer due to intensive In desorption observed at elevated temperatures.

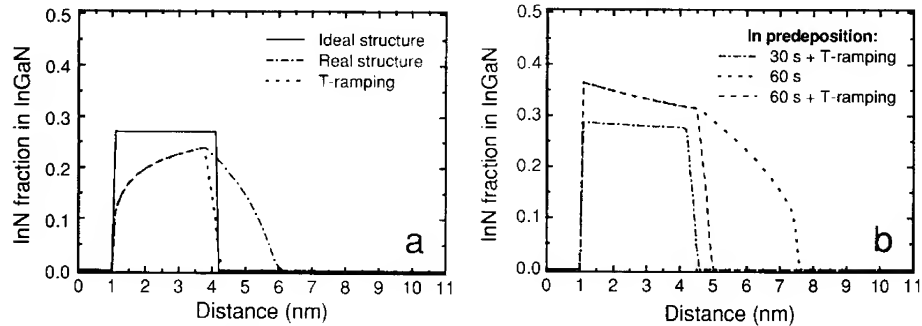


**Figure 1** Composition profiles in GaN/InGa<sub>N</sub>/GaN SQW heterostructures grown under various conditions (see text for more detail).

TMIn deposition on the GaN surface prior to InGa<sub>N</sub> growth proves to be quite effective for improving the abruptness of the QW front interface. The variation of the TMIn exposure combined with the T-ramping during the cap layer growth allows one to control the entire InGa<sub>N</sub> QW composition profile (Figure 1b). In particular, the In predeposition for 30 s followed by T-ramping results in the nearly rectangular profile very close to that of the ideal heterostructure.

## COMPUTATION OF BAND DIAGRAMS AND LIGHT EMISSION SPECTRA

The band diagrams of the InGa<sub>N</sub> SQW structures are found from self-consistent solution of the Poisson and Schrödinger equations. To calculate the space/surface charges due to piezoeffect and spontaneous polarization as a function of the QW composition, we use the non-linear approximations suggested in [7]. The donor and acceptor concentrations in the n- and p-GaN cladding layers are assumed to be  $3 \times 10^{18} \text{ cm}^{-3}$  and  $2 \times 10^{19} \text{ cm}^{-3}$ , respectively. The ionization energies of donor and magnesium acceptors are chosen to be, correspondingly, of 13 meV and 170 meV. Inside the QW, we take into account only the contribution of confined electrons and holes in the space charge. Outside the well, we use the local three-dimensional statistics relating the carrier concentrations to the separations of their quasi-Fermi levels,  $F_n$  and  $F_p$ , from the conduction band bottom  $E_C$  and the valence band top  $E_V$ . The concentrations of the ionised donors and acceptors are calculated via the quasi-Fermi levels in a conventional way. We assume here that

**BEST AVAILABLE COPY**

the quasi-Fermi levels are nearly constant throughout the heterostructure, neglecting the effects of carrier injection on band diagram. The quasi-Fermi levels at the edges of the structures are found from the electro-neutrality conditions, while their separation equals the forward bias applied, i.e.  $U_b = F_n - F_p$ . The band diagrams of the above SQW heterostructures computed for the bias of 3.0 V are shown in Figure 2a.

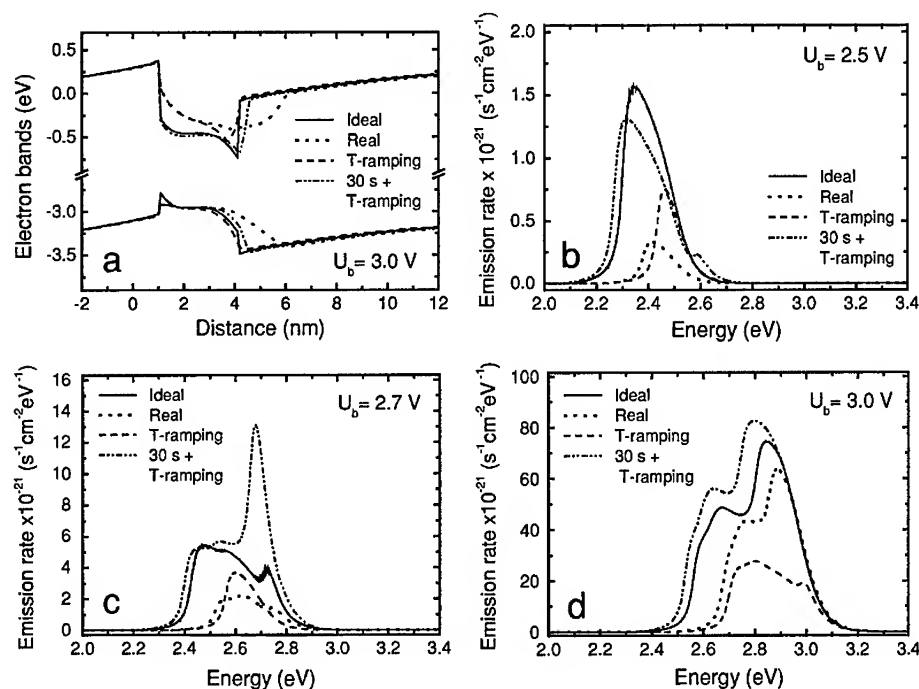


**Figure 2** Band diagrams of InGaN SQWs (a) and their electroluminescence spectra (b-d) computed for different forward biases.

The spectra of electroluminescence (EL) are computed by accounting for only the spontaneous recombination between the electrons and holes confined in the QW. We neglect the radiative recombination through the donor and acceptor levels assuming the carrier injection into the QW to be sufficiently high at the biases of interest. The effect of indium composition fluctuations on the luminescence spectra is also neglected in this study. The Luttinger-Kohn approach is used to consider the complex valence band structure of nitrides [8]. The carrier effective masses, spin-orbital and crystal-field splittings are borrowed from [8,9]. The bowing parameter for the energy gap variation with InGaN composition is chosen to be 2.5 eV after [10]. The angle-averaged EL spectra are computed assuming a uniform electron level broadening  $\Gamma$  to be equal to 20 meV, the value typical for other III-V compounds.

## RESULTS

Without broadening, an EL spectrum consists of several sharp peaks corresponding to the transitions between various electron and hole levels. The peak intensities depend on the filling of the levels with carriers and on the overlap of the electron and hole wave functions, which are spatially separated within the QW due to high build-in polarization field. The heavy holes (HH) and light holes (LH) in InGaN have rather similar effective masses in the [0001] direction and their spin-orbital splitting is small. Hence, they give rise into the nearly the same range of the EL spectrum. However, the heavy holes provide a higher contribution into the light intensity due to a larger effective mass in the lateral direction and, respectively, a higher density of states. Because of a small effective mass of the crystal-field split-off holes (CH) in the [0001] direction and of a large crystal field splitting, the CH energy levels are shifted down from the HH and LH levels. Thus, the concentration of the crystal-field split-off holes and their contribution to the EL spectra is relatively small.

In our computations, the separation between the hole levels in the QW turns out to be less or comparable with the broadening  $\Gamma$ . Therefore the fine structure of the hole levels is not resolved in the EL spectra. That is not the case for electrons, where the level separation exceeds the broadening remarkably. Therefore, the EL spectra become of a multi-peak character when new electron levels are produced by the QW transformation and filled by the carriers due to the bias increase (see Figure 2c,d).

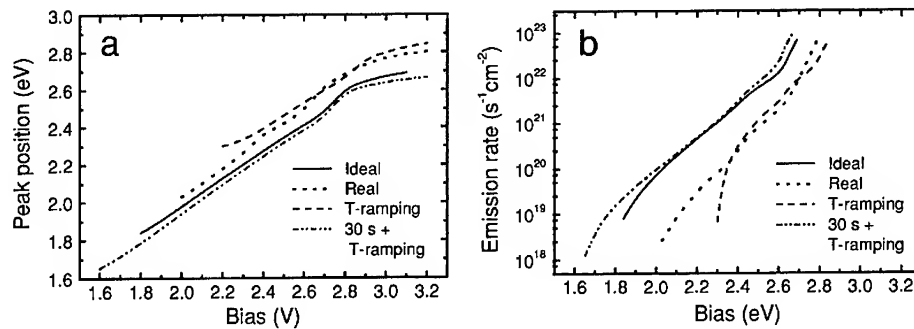


**Figure 3** First EL peak spectral position (a) and its intensity (b) as a function of forward bias.

### Electroluminescence spectra as a function of bias

At a small bias, there is practically no light emission from these heterostructures due to negligible carrier concentration in the QW. The concentration of electrons and holes gradually rises with bias, resulting in a more intensive light emission. In addition, a higher carrier concentration favours the screening of the polarization field inside the QW. Thus, the overlap of the wave functions corresponding to the ground electron and hole states increases, giving additional contribution to the light emission. First, there is the only peak in the EL spectra, with the energy close to separation of the electron and hole levels. The increasing forward bias produces the

second electron level and, respectively, the second peak in the EL spectra. This results in a blue shift of the whole luminescence spectra. An additional blue shift originates from the screening of the polarization field inside the QW, which produces a higher separation of the electron and hole energy levels (Figure 3a).

### **Segregation effects on the band diagram and emission spectra**

As discussed above, the In surface segregation produces a remarkable difference between the composition profiles in the ideal and real InGa<sub>N</sub> SQW structures. The real QW has a smaller depth than the ideal one because of a lower peak composition, but it is wider due to the In tail in the cap layer. As a result, the EL spectra of the real structure are systematically blue-shifted by 50-100 meV compared to the ideal SQW (see Figure 3). T-ramping makes the QW narrower that leads to further blue shift in the spectra. As mentioned above, the combination of the 30 s indium predeposition with the T-ramping allows getting the structure very close to the ideal one by its shape. So, it is no wonder that the EL spectra of such a structure are quite similar to those of the ideal SQW. For all the structures considered here the first peak spectral position exhibits a nearly linear dependence with approximately the same slope until the bias of ~2.8 V is reached. This is due to the fact that under low biases, the effect of electron and hole injection into the QW on the space charge in the whole structure is negligible. At higher injection level, ( $U_b > 2.8$  V) the electron and holes screen the build-in electric field, which makes the separation of their energy levels much less dependent on the applied bias.

The intensity of the first emission peak increases exponentially with bias  $U_b$ . This correlates well with the tendency reported in literature [11]. In [11], the first maximum in the EL spectra was associated with the “tunnel recombination” between unconfined electrons and holes. Our computations show that this peak may come from the recombination of electron and holes occupying the ground states in the QW.

### **Discussion**

The most critical assumption made in our analysis of the luminescence spectra is neglecting the effects of In composition fluctuations on the light emission from the InGa<sub>N</sub> QWs. Normally, the fluctuation result in additional broadening of the emission spectra (~50-60 meV as measured in [11]) and in additional red shift of the spectra due to carrier localization in the In-rich regions. The account of the fluctuations, nevertheless, could not change the general trends in the EL spectra behavior predicted by our analysis. In particular, the second peak in the luminescence spectra also should be resolved as the separation between the first and second electron levels in the QW (~120-140 meV) is still larger than the fluctuation-related broadening.

### **CONCLUSION**

In this work, we have studied theoretically the effect of In surface segregation on the composition profiles, band diagrams, and light emission spectra in the InGa<sub>N</sub> SQWs. The most effective approaches to control of the abruptness of front and back interfaces in the SQW – indium predeposition and temperature ramping during the cap layer growth – are considered by using the

model [5,6]. It is shown that the combination of the In predeposition with the temperature ramping allows getting the SQWs with the composition profile very close to the desirable one (here, to that of the ideal rectangular QW).

Assuming a uniform broadening of the electron energy levels, we have computed the EL spectra from the SQW structures with different degrees of segregation impact. It is shown that In surface segregation normally results in a systematic blue shift of the EL spectra (~50-100 meV) due to incomplete In incorporation into the crystal in unsteady MOVPE growth. The bias variation produces the transformation of the QW band diagram in such a way as new electron and hole states are formed at high biases. The latter phenomenon results in a multi-peak structure of the EL spectra and, consequently, in additional blue-shift of the emission wavelength. Besides, the secondary peaks provide a higher broadening of the spectra, which is undesirable for practical applications.

Generally, this work demonstrates that the detailed analysis of a device structure growth, accounting for unsteady effects like surface segregation, coupled with the computations of light emission spectra is a powerful tool for bandgap engineering of the nitride LEDs. Further efforts should be made to consider fluctuations of In composition in an InGaN QW as well as the specificity of the active region doping.

## REFERENCES

1. Y.T. Moon, D.J. Kim, K.M. Song, C.J. Choi, S.H. Han, T.Y. Seong, and S.J. Park, *J. Appl. Phys.* **89**, 6514 (2001).
2. S.-J. Leem, M.-H. Kim, J. Shin, Y. Choi and J. Jeong, *Jpn. J. Appl. Phys.* **40**, L371 (2001).
3. J.S. Park, Y.T. Moon, D.J. Kim, J.T. Oh, and S.J. Park, presentation at ICNS-4, Denver, 2001.
4. S. Kim, K. Lee, K. Park, C.-S. Kim, *J. Cryst. Growth* **247**, 62 (2003).
5. S.Yu. Karpov, R.A. Talalaev, I.Yu. Evstratov, and Yu.N. Makarov, *Phys. Stat. Sol. (a)* **192**, 417 (2002).
6. R.A. Talalaev, S.Yu. Karpov, I.Yu. Evstratov, and Yu.N. Makarov, accepted for publication in *Phys. Stat. Sol.*, (2002).
7. V. Fiorentini, F. Bernardini and O. Ambacher, *Appl. Phys. Lett.* **80**, 1204 (2002).
8. S.-H. Park and S.-L. Chuang, *J. Appl. Phys.* **87**, 353 (2000).
9. V. Bougrov, M. Levinshtein, S. Rumyantsev, and A. Zubrilov, in *Properties of Advanced Semiconductor Materials: GaN, AlN, InN, BN, SiC, SiGe*, edited by M.E. Levinshtein, S.L. Rumyantsev, M.S. Shur (John Wiley & Sons, Inc., New York, 2001), Ch.1-3.
10. S. Stepanov, W.N.Wang, B.S.Yavich, V. Bougrov, Y.T.Rebane, and Y.G.Shreter, *MRS Internet J. Nitride Semicond. Res.* **6**, 6 (2001).
11. V.E.Kudryashov, K.G.Zolin, A.N.Turkin, A.E. Yunovich, A.N. Kovalev and F.I. Manyakhin, *Fiz. Tekn. Poluprovodn.*, **31**, 3104 (1997) [*Semiconductors*, **31**, 1123 (1997)].

**Indium distribution inside quantum wells: The effect of growth interruption in MBE**

A.M. Sanchez<sup>1</sup>, P. Ruterana<sup>1</sup>, S. Kret<sup>2</sup>, P. Dłużewski<sup>3</sup>, G. Maciejewski<sup>3</sup>, N. Grandjean<sup>4</sup>, B. Damilano<sup>4</sup>

<sup>1</sup> ESCTM-CRISMAT, UMR6508-CNRS, ISMRA. 6, Boulevard Maréchal Juin, 14050 Caen Cedex, France

<sup>2</sup> Institute of Physics, PAS, Al. Lotników 32/46, 02-668 WARSAW, Poland

<sup>3</sup> IFTR PAS, Świętokrzyska 21, 00-049 WARSAW, Poland

<sup>4</sup> CRHEA, UPR 10 CNRS, 1 rue Bernard Gregory, 06560 VALBONNE, France

**ABSTRACT**

Quantitative analysis of high resolution electron microscopy image has been carried out to measure the indium distribution inside InGaN/GaN quantum well. The analyzed samples were nominally grown with 15% indium composition by molecular beam epitaxy with interruptions during the  $\text{In}_x\text{Ga}_{1-x}\text{N}$  layer growth. The strain distribution is not homogeneous inside the quantum wells, and indium rich clusters can be observed. Areas with almost no indium concentration were observed corresponding to the growth interruption. A comparison with samples grown by metalorganic chemical vapor deposition is attempted.

**INTRODUCTION**

The III-N semiconductor materials technology is progressing rapidly with many practical applications in optoelectronic. GaN and related materials have been intensively used in recent years for super-bright blue and green light emission diodes and laser diodes. InGaN/GaN quantum wells constitute the active structures in these devices. They exhibit better efficiency than GaAs-based devices in spite of the huge densities of defects observed in the layers ( $10^8$ - $10^{10}$   $\text{cm}^{-2}$  dislocations). The first explanation implied that the emission takes place inside InGaN quantum dots due to indium segregation in metalorganic chemical vapor deposition (MOCVD) grown devices<sup>1</sup>. The recombination of localized excitons in In rich nanometers islands play an important role in the strong emission from InGaN/GaN multiple quantum wells (MQW). The presence of In rich regions could be related to the poor miscibility between InN and GaN at the growth temperature. At 800°C the alloy is unstable in a wide composition range ( $0.04 < x < 0.88$ )<sup>2</sup>. Phase separation during the InGaN growth has been previously reported<sup>3,4</sup>. The mismatch between InN and GaN is probably the leading factor behind the In segregation inside the InGaN quantum wells.

The In clusters have been observed by different experimental techniques. By Conventional Transmission Electron Microscopy (CTEM) a dark contrast corresponds to In rich islands. The local composition can be determined by Scanning Transmission Electron Microscopy (STEM) with Energy Dispersive X-Ray (EDX) or Electron Energy Loss Spectroscopy (EELS). High Resolution Transmission Electron Microscopy (HRTEM) can also be used to analyze the structure at nanometer scale and obtain information about chemical

composition, interdiffusion and segregation in such ternary systems as InGaN. Previous work, carried out in InGaN/GaN structure using pattern recognition on HRTEM images, has demonstrated that indium rich clusters are present in this MQW<sup>5</sup>.

Recently, nearly constant indium composition in InGaN wells has been determined in samples with growth interruption by MOCVD whereas composition fluctuations were observed when no interruption was used<sup>6</sup>.

In this work, we analyze the indium composition fluctuations inside InGaN/GaN quantum wells grown by molecular beam epitaxy (MBE). We compare the results with those published in samples grown by MOCVD<sup>6</sup>.

HRTEM images obtained from cross sectional were used to measure the local strain. The indium concentration was calculated from the strain field after modelling by finite elements analysis.

## EXPERIMENTAL DETAILS

The samples were grown by MBE in a Riber reactor modified for the use of ammonia as nitrogen precursor. Ga and In were evaporated by double-filament effusion cells. Before the growth of the InGaN/GaN quantum wells, a few microns of GaN are deposited on sapphire substrate with standard GaN growth conditions<sup>7</sup>. The temperature was then decreased to 550°C for the growth of the  $\text{In}_x\text{Ga}_{1-x}\text{N}$  ( $x=0.15$ ) thin layer<sup>8</sup>. The peculiarity of these samples is that the InGaN layer is not grown continuously. One or several growth interruptions are realized. During this interruption step the temperature was raised to 650°C and brought back at the growth temperature in one minute. For N4 sample, a growth interruption was performed every 1 nm and for N2, only one interruption between the 1.5 nm and 3.0 nm thick InGaN layers. After the last InGaN layer, the temperature is increased to 800°C for the growth of the GaN barrier layer (300 Å), this increase is done in one minute which corresponds to an additional temperature cycle. Figure 1 shows a scheme of the characterized samples.

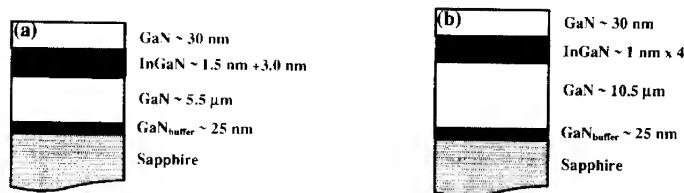


Figure 1. Scheme of the characterized samples, (a) N2 and (b) N4

Cross-sectional (XTEM) specimens were prepared by thinning down to 100 μm by mechanical grinding and dimpling down to 5 μm. Ion milling at 5 kV was used to achieve electron transparency. HRTEM studies were carried out on a Topcon 002B microscope operating at 200kV.

In order to investigate the effect of the growth interruption on the strain distribution in InGaN quantum wells, typical high-resolution images of thin areas have been used to evaluate

**BEST AVAILABLE COPY**

the composition in the different specimens. The quantitative analyses of HRTEM images were carried out using routines written in analytical language for images of Optimas graphical environment. The local lattice distortion measurements were obtained by the peak finding procedure. Firstly, we applied a Wiener filter on the image to reduce the noise level of the area of interest and the localization of the intensity maxima by 4 parabolas. A reference area was chosen outside of deformed regions and we determined the basis vectors. Using this reference system, the lattice were extrapolated on the whole image, including the quantum well region. The lattice distortion components parallel to the growth direction can be obtained from the derivatives of the discrete displacement field.

## RESULTS AND DISCUSSION

Cross-sectional bright field TEM images were recorded in  $\langle 11\bar{2}0 \rangle$  zone axis in both samples (Figure 2). The InGaN quantum well exhibits a darker contrast with respect to the GaN layer. This contrast is not completely homogeneous. A detailed observation of these quantum wells shows discontinuities in the InGaN contrast along the growth direction. In Figure 2a a brighter contrast can be observed in the middle of the quantum well (sample N2), whereas there is an alternate bright/dark in the image corresponding to sample N4 (Figure 2b). The brighter areas inside the InGaN quantum well correspond to the growth interruption. During the interruption, the temperature is raised to 650°C to eliminate the indium excess and a layer poor in this element is obtained. Figure 2b shows four brighter fringes in the InGaN quantum well corresponding to the four interruption for one minute carried out during the discontinuous growth of this sample.

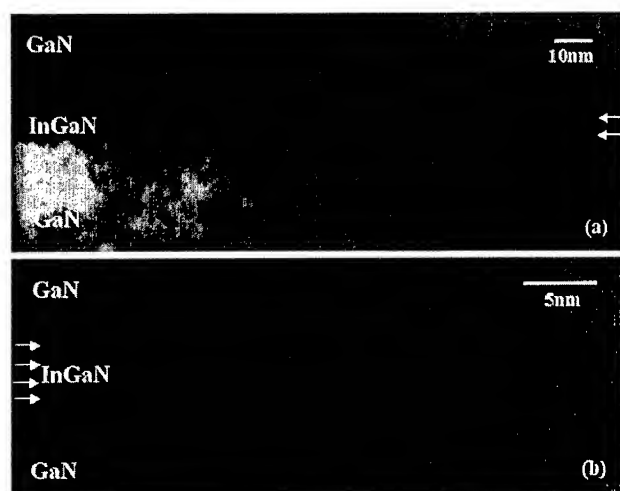


**Figure 2.** High magnification CTEM images recorded along the  $\langle 11\bar{2}0 \rangle$  zone axis showing the alternated contrasts inside the InGaN quantum well, (a) N2 and (b) N4. Quantum wells are shown by white arrows.

In order to analyze the strain distribution in the InGaN quantum wells, we performed lattice distortion measurements from high resolution images. Only areas with relatively slow rise of thickness were considered for quantitative evaluation.

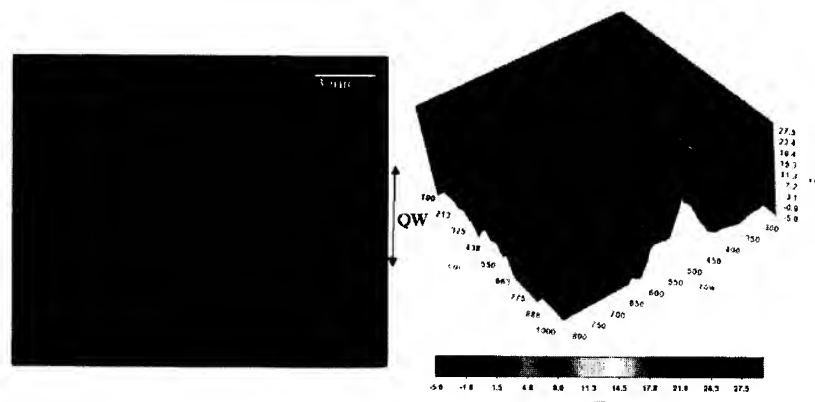


**Figure 3.** (a) Superposition of the experimental HRTEM image and strain map in sample N2. A non-homogeneous indium distribution can be determined. (b) Surface plot with the indium concentration inside the quantum well.

Figure 3a shows the superposition of the experimental HRTEM image and the strain distribution calculated in this area corresponding to the N2 sample. This image is in good agreement with the previous one shown in Figure 2a. As can be observed, the InGaN quantum well is not continuous along the growth direction. The total nominal thickness of this quantum well was 4.5 nm grown in two steps with a growth interruption of 1 min (see experimental part). The strain distribution measurements results can be seen in Figure 3. The superposition of experimental and calculated images, Figure 3a, shows three different areas inside the quantum well. In the first 1.3 nm a positive strain can be measured (green color) which corresponds to an  $\text{In}_x\text{Ga}_{1-x}\text{N}$  area. If we continue along the [0001] direction a strain decrease is visible. This blue area has lost indium atoms during the growth interruption. We observe again a green zone of 2.3 nm grown in the second step. The strain distribution is also inhomogeneous along [01 $\bar{1}$ 0] direction inside the quantum well. The  $\text{In}_x\text{Ga}_{1-x}\text{N}$  quantum well exhibits a lateral variation in the strain distribution. Figure 3a clearly shows maxima which suggest the presence of indium rich clusters. Areas with strain higher than 2.5% (red in the picture) are presented which means that the composition inside the quantum well is not homogeneous. The thickness of the HRTEM specimen in this area is estimated to be between 5 and 10 nm and thus we calculated the indium composition (Figure 3b). As can be clearly seen the indium concentration fluctuates in the quantum well inside N2 sample. The maxima of indium in red areas are higher than 20%, in spite of the nominal indium concentration was in the range 15%. In the area corresponding to the growth interruption the indium composition drops to lower than 5%.

**BEST AVAILABLE COPY**

Figure 4 shows the HRTEM image and the calculated strain distribution for N4 sample with four 60s interruptions which took place every 1 nm of InGaN. In this image we can observe that the strain distribution is not homogeneous neither in the growth direction nor in the perpendicular. As in Figure 3, areas poor in indium inside the quantum well are visible corresponding to the growth interruptions. As the total thickness of the quantum well is 4.5 nm, and we have three growth interruptions and four indium rich areas, this leads to an individual layer of less than 1 nm in thickness. Inside the indium rich layers we clearly observe strong local strain field fluctuations. The observed maxima are in the range of 3-6% corresponding to indium peak concentration above 40%.

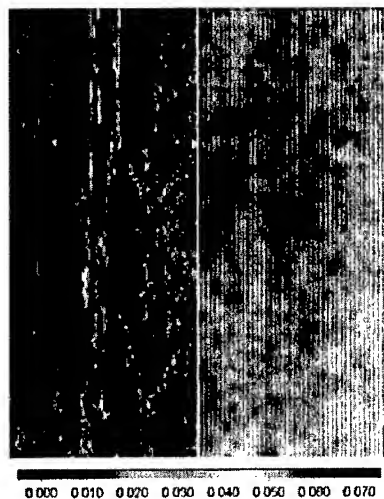


**Figure 4.** Experimental HRTEM image and strain map in sample N4. A non-homogeneous strain distribution can be observed.

Cho et al.<sup>6,9</sup> carried out a study about the effect of growth interruption on the indium clustering of InGaN/GaN quantum wells grown by MOCVD. The samples were grown on sapphire substrates. Their samples were made for six periods of InGaN/GaN. The MQW structure was grown at 750°C. After a 2-μm GaN overgrown layer was obtained at 1130°. In these samples grown by MOCVD, a strain relaxation is obtained with the growth interruption period. As the interruption times was increases a more homogeneous indium concentration distribution was obtained inside the quantum well. The attributed it to the indium desorption due to thermal annealing.

In our MBE samples, the growth interruption took place during the growth of the InGaN quantum well and also at the end of the growth as in the case of MOCVD samples. Temperature was raised to 650°C and brought back at the growth temperature in one minute in order to

eliminate the indium excess. We have observed rich indium areas, corresponding to the maxima of strain distribution in the InGaN.

In MOCVD samples with 5 and 30 s interruption time the average indium composition in the InGaN well was 31% and 24% respectively, while no growth interruption the indium composition fluctuations were between 5% and 40%. It means that the interruption leads to a more homogeneous indium distribution in the quantum well.

In summary, we have investigated indium composition inside InGaN ultra-thin layers (4.5 nm) grown by MBE, with one and three growth interruptions. It is shown that the growth interruption eliminate the possible indium accumulation at the growth and leaves a layer whose composition is close to GaN. Moreover, for the quantum well with three growth interruption, we have individual layers and indium composition fluctuations are shown at a scale below 1 nm. Our result are at variance with those reported for MOCVD growth but the different growth kinetics may probably explain the observed different behaviour.

#### ACKNOWLEDGMENTS

The authors acknowledge the support of the EU under contract HPRN-CT-1999-00040 as well as the MRT under 'action incitative Boquani'. SK acknowledges the partial support of EU under contract N° ICA1-CT-2000-70018

#### REFERENCES

1. Y. Narukawa, Y. Kawakami, M. Funato, S. Fujita and S. Nakamura, Appl. Phys. Lett. **70** (1997) 981
2. T. Saito and Y. Arakawa, Phys. Rev. B **60** (1999) 1701
3. R. Singh, D. Doppalapudi, T.D. Moustakas and L.T. Romano, Appl. Phys. Lett. **70** (1997) 1089
4. M.D. McClukey, L.T. Romano, B.S. Krusar, D. P. Bour, N. M. Johnson, and S. Brennan, Appl. Phys. Lett. **72** (1998) 1730
5. C. Kisielowski, Z. Liliental Weber and S. Nakamura, Jpn. J. Appl. Phys., Part 1 **36** (1997) 6932
6. H.K. Cho, J.Y. Lee, N. Sharma, C.J. Humphreys, G.M. Yang, C.S. Kim, J.H. Song and P.W. Yu, Appl. Phys. Lett. **79** (2001) 2594
7. N. Grandjean, M. Leroux, J. Massies, M. Mesrine and M. Lügt, Jpn. J. Appl. Phys. **38** (1999) 618
8. B. Damilano, N. Grandjean, J. Massies, L. Siozade and J. Leymarie, Appl. Phys. Lett. **77** (2000) 1268
9. H.K. Cho, J.Y. Lee, C.S. Kim and G.M. Yang, J. Appl. Phys. **91** (2002) 1166

**BEST AVAILABLE COPY**

### Thermoelectric properties of III-nitrides and III-oxynitrides prepared by reactive rf-sputtering: targetting a thermopower device

S. Yamaguchi <sup>1,2</sup>, Y. Iwamura <sup>1,2</sup>, A. Yamamoto <sup>2</sup>

<sup>1</sup>Department of Electrical, Electronic and Information Engineering, Kanagawa University,  
3-27-1 Rokkakubashi, Kanagawa-ku, Yokohama, 221-8686, Japan

<sup>2</sup>Energy Electronics Institute, National Institute of Advanced Industrial Science and Technology,  
AIST Tsukuba Central 2 Umezono 1-1-1, Tsukuba, Japan, 305-8568

#### ABSTRACT

We have studied thermoelectric properties of III-nitrides of  $\text{Al}_{1-x}\text{In}_x\text{N}$  and III-oxynitrides of  $\text{Al}_{1-x}\text{In}_x\text{O}_y\text{N}_z$  and  $\text{InO}_y\text{N}_z$  prepared by radio-frequency sputtering with the aim of fabricating a thermoelectric power device based on III-nitride semiconductors. For  $\text{Al}_{0.55}\text{In}_{0.45}\text{N}$ , the maximum value of power factor was  $3.63 \times 10^{-4} \text{ W/mK}^2$  at 873K. For  $\text{Al}_{0.02}\text{In}_{0.98}\text{O}_{1.14}\text{N}_{0.49}$  and  $\text{Al}_{0.14}\text{In}_{0.86}\text{O}_{1.30}\text{N}_{0.67}$ , the maximum power factor was  $2.82 \times 10^{-4} \text{ W/mK}^2$  and  $4.73 \times 10^{-4} \text{ W/mK}^2$  at 873 K, respectively. For  $\text{InO}_{0.82}\text{N}_{0.86}$ , it was  $3.75 \times 10^{-4} \text{ W/mK}^2$  at 973 K.

#### INTRODUCTION

Thermoelectric phenomena in solids can cause thermoelectric generation, which directly converts heat energy into electric energy without both using moving parts and producing emissions such as carbon dioxide gas and radioactive substances. This is basically important from the standpoints of environmental and energy-saving issues [1,2], and there has recently been large increase in the research and development of thermoelectric power generation systems that are designed to employ the vast resources of waste heat [3] and environmentally sound cooling [4]. Realization of any practical applications associated with them requires the achievement of a high efficiency (i.e., large figure of merit) characterized by electric conductivity, thermoelectric Seebeck coefficient and thermal conductivity.

However, since no binary compounds better than  $\text{Bi}_2\text{Te}_3$ ,  $\text{PbTe}$  and  $\text{Si}_{1-x}\text{Ge}_x$  have been found for room-temperature applications [6]. However, because Te is scarce, volatile, and toxic, the application of  $\text{Bi}_2\text{Te}_3$  and  $\text{PbTe}$  has been limited for commercial use, and  $\text{Si}_{1-x}\text{Ge}_x$  is only used at 1000 °C in vacuum. In the search for any new thermoelectric materials, much effort has been directed toward the development of thermoelectric materials with improved characteristics. The thermoelectric materials have been evaluated using the figure of merit  $Z$ . There are many reports regarding the improvement of the figure of merit  $Z$ . The figure of merit  $Z$ , which signifies the thermal to electrical energy conversion efficiency of the material, is defined by  $Z = P/\kappa$ ,

$$P = \alpha^2/\rho, \quad (1)$$

where  $P$ ,  $\alpha$ ,  $\rho$  and  $\kappa$  are the power factor, thermoelectric power, electrical resistivity and thermal conductivity, respectively. One of the criteria for the practical application of thermoelectric materials can be expressed as  $ZT > \text{or} = 1$ , where  $T$  is the absolute temperature. Generally, it is difficult to decrease  $\rho$  and  $\kappa$ , and increase  $\alpha$  simultaneously, because  $\alpha$  and  $\rho$  completely depend on many parameters such as the carrier concentration, carrier mobility and effective carrier mass. The power factor  $P$  indicates the electrical power generation capability, and is commonly used for materials of which the thermal conductivity is difficult to measure. Instead of using  $Z$ , in a given temperature gradient, the power factor,  $\alpha^2/\rho$ , is often used as a good measure of the thermoelectric properties. In this study, we used  $P$  for assessment of our samples as a thermoelectric material.

Currently, III-nitrides semiconductors (GaN, AlN, InN, and their alloys) have high prospects for applications in optical devices such as light-emitting devices. However, no work has been carried out in terms of targeting a thermopower device using the materials based on III-nitrides. The nitrides have advantages for such target mainly since they are composed of Al, Ga, In and N, which do not stress the environment.

We have paid attention to the properties of  $\text{Al}_{1-x}\text{In}_x\text{N}$  [7]. We have most recently studied the thermoelectric properties of III-nitrides ternary  $\text{Al}_{1-x}\text{In}_x\text{N}$ , and, in addition, III-oxynitrides of  $\text{Al}_{1-x}\text{In}_x\text{O}_y\text{N}_t$  and  $\text{InO}_s\text{N}_t$  to open a new device field using III-nitrides, the field of thermoelectricity. In this letter, we report on the thermoelectric properties of III-nitrides of  $\text{Al}_{0.35}\text{In}_{0.65}\text{N}$ , III-oxynitrides of  $\text{Al}_{0.02}\text{In}_{0.98}\text{O}_{1.14}\text{N}_{0.49}$ , and  $\text{InO}_{0.82}\text{N}_{0.86}$  targeting a thermoelectric power device..

### Experiments

The samples studied here were prepared by the reactive radio-frequency (RF) sputtering method. They were grown on  $\text{SiO}_2$  glass substrates at 100 °C using  $\text{N}_2$  and Ar gases. The content of the elements was estimated using an energy-dispersive X-ray spectrometer (EDX). In addition, electrical resistivity and Seebeck coefficient were measured by the dc method with a temperature gradient of 4K in the temperature range of 100-700 °C. All samples assessed here showed n-type conductivity.

### RESULTS AND DISCUSSION

Figure 1(a) shows the temperature dependence of absolute values of Seebeck coefficient of  $\text{Al}_{0.55}\text{In}_{0.45}\text{N}$ . With increasing temperature, Seebeck coefficient increases, while the resistivity decreased with increasing temperature (not shown here). Moreover, with increasing temperature, the Seebeck coefficient increases monotonically. In general, with decreasing resistivity, probably caused by an increase in carrier concentration, the Seebeck coefficient should decrease.

**BEST AVAILABLE COPY**

However, our data show the reverse trend, the Seebeck coefficient increases regardless of decrease in resistivity. We consider that the phenomenon is due to the hopping conductance at higher temperatures.

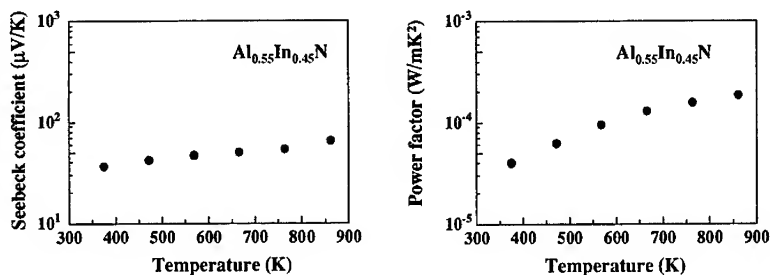


Figure 1. (a) (left): Temperature dependence of absolute values of Seebeck coefficient of Al<sub>0.55</sub>In<sub>0.45</sub>N. (b) (right): Temperature dependence of power factor of Al<sub>0.55</sub>In<sub>0.45</sub>N.

Using the data of Seebeck coefficient and resistivity, the power factor was derived according to equation (1). Figure 1(b) shows the temperature dependence of power factor of Al<sub>0.55</sub>In<sub>0.45</sub>N. With increasing temperature, the power factor increases monotonically, and is 1.84 × 10<sup>-4</sup> W/mK<sup>2</sup> at 873K for Al<sub>0.55</sub>In<sub>0.45</sub>N.

Figure 2(a) shows the temperature dependence of absolute values of Seebeck coefficient of Al<sub>0.02</sub>In<sub>0.98</sub>O<sub>1.14</sub>N<sub>0.49</sub> and Al<sub>0.14</sub>In<sub>0.86</sub>O<sub>1.30</sub>N<sub>0.67</sub>.

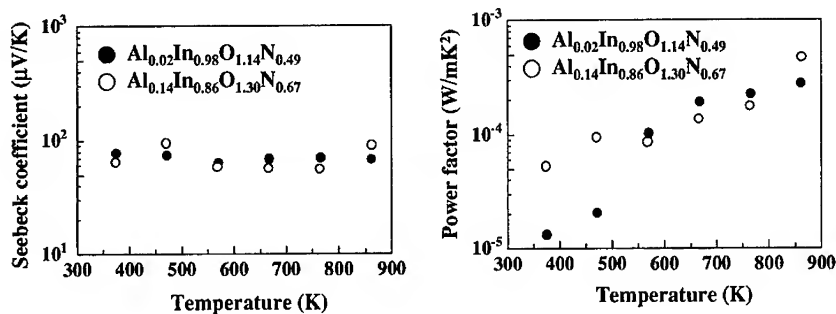


Figure 2. (a) (left): Temperature dependence of absolute values of Seebeck coefficient and (b) (right): Temperature dependence of power factor of Al<sub>0.02</sub>In<sub>0.98</sub>O<sub>1.14</sub>N<sub>0.49</sub> (closed circles) and Al<sub>0.14</sub>In<sub>0.86</sub>O<sub>1.30</sub>N<sub>0.67</sub> (open circles).

In both cases, the Seebeck coefficient remains almost constant, while the resistivity decreased with increasing temperature (not shown). Figure 2(b) shows the temperature dependence of power factor of  $\text{Al}_{0.02}\text{In}_{0.98}\text{O}_{1.14}\text{N}_{0.49}$  and  $\text{Al}_{0.14}\text{In}_{0.86}\text{O}_{1.30}\text{N}_{0.67}$ . We obtained a maximum value of  $2.82 \times 10^{-4} \text{ W/mK}^2$  and  $4.73 \times 10^{-4} \text{ W/mK}^2$  at 873 K, respectively.

Figure 3(a) shows the temperature dependence of absolute values of Seebeck coefficient of  $\text{InO}_{0.82}\text{N}_{0.86}$ . With increasing temperature, the Seebeck coefficient increases monotonically. Figure 3(b) shows the temperature dependence of power factor of  $\text{InO}_{0.82}\text{N}_{0.86}$ . We obtained a maximum value of  $3.75 \times 10^{-4} \text{ W/mK}^2$  at 973 K. For  $\text{Al}_{0.02}\text{In}_{0.98}\text{O}_{1.14}\text{N}_{0.49}$ , the power factor was saturated over 600 K, while for  $\text{InO}_{0.82}\text{N}_{0.86}$  it increased almost linearly.

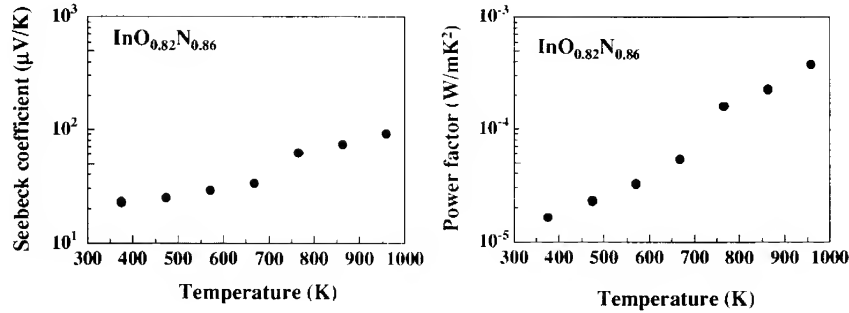


Figure 3. (a) (left): Temperature dependence of absolute values of Seebeck coefficient of  $\text{InO}_{0.82}\text{N}_{0.86}$ . (b) (right): Temperature dependence of power factor of  $\text{InO}_{0.82}\text{N}_{0.86}$ .

For reference, the Seebeck coefficient and power factor of InN as a function of temperature are shown in Fig.4(a) and Fig.4(b), respectively.

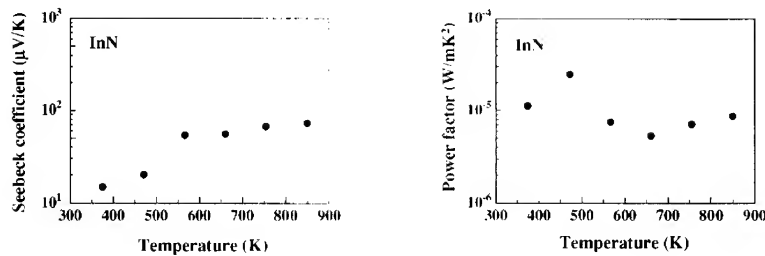


Figure 4. (a) (left): Temperature dependence of absolute values of Seebeck coefficient of InN. (b) (right): Temperature dependence of power factor of InN.

**BEST AVAILABLE COPY**

The unstable behaviour of the thermoelectric properties are considered to be due to the thermal instability of InN itself. Consequently, the incorporation of oxygen into InN is expected to be effective for thermally stable of crystal.

Considering the situation that a power factor value of the order of  $10^{-3}$  W/mK<sup>2</sup> has been aimed at using many compounds other than III-nitrides, our data in this study demonstrate that III-nitrides and III-oxynitrides are one of the suitable candidate materials for thermopower devices.

## CONCLUSION

Thermoelectric properties of III-nitrides of Al<sub>0.55</sub>In<sub>0.45</sub>N and III-oxynitrides of Al<sub>0.02</sub>In<sub>0.98</sub>O<sub>1.14</sub>N<sub>0.49</sub> and InO<sub>0.82</sub>N<sub>0.86</sub> prepared by radio-frequency sputtering. For Al<sub>0.55</sub>In<sub>0.45</sub>N, the maximum value of power factor was  $3.63 \times 10^{-4}$  W/mK<sup>2</sup>. For Al<sub>0.02</sub>In<sub>0.98</sub>O<sub>1.14</sub>N<sub>0.49</sub> and Al<sub>0.14</sub>In<sub>0.86</sub>O<sub>1.30</sub>N<sub>0.67</sub>, the maximum power factor was  $2.82 \times 10^{-4}$  W/mK<sup>2</sup> and  $4.73 \times 10^{-4}$  W/mK<sup>2</sup> at 873 K, respectively. For InO<sub>0.82</sub>N<sub>0.86</sub>, it was  $3.75 \times 10^{-4}$  W/mK<sup>2</sup> at 973 K.

## ACKNOWLEDGEMENTS

This work was partly supported by the Izumi Science and Technology Foundation.

## REFERENCES

1. G. Mahan, B. Sales, and J. Sharp, Phys. Today **50**, 42 (1997).
2. G. D. Mahan, Solid State Phys. **51**, 81 (1998).
3. W. Shin, M. Murayama, K. Ikeda, and S. Sago, Jpn. J. Appl. Phys. **39**, 1254 (2000).
4. S. Bhattacharya, A. L. Pope, R. T. Littleton, T. M. Tritt, V. Ponnambalam, Y. Xia, and S. J. Poon, Appl. Phys. Lett. **77**, 2476 (2000).
5. J. P. Dismukes, L. Ekstrom, E. F. Steigmeier, I. Kudman, and D. S. Beers, J. Appl. Phys. **35**, 2899 (1964).
6. B. C. Sales, D. Mandrus, and R. K. Williams, Science **272**, 1325 (1996).
7. S. Yamaguchi, M. Kariya, S. Nitta, H. Amano, and I. Akasaki, Appl. Phys. Lett. **76**, 876 (2000).

**X-Ray Diffraction Analysis of GaN and AlGaN**

H. Kang, N. Spencer, D. Nicol, Z.C. Feng, and I. Ferguson\*

School of Electrical and Computer Engineering,  
Georgia Institute of Technology, Atlanta, GA 30332, U.S.A

\*ianf@ece.gatech.edu

S. P. Guo, M. Pophristic, and B. Peres

EMCORE Corporation, 145 Belmont Drive, Somerst, NJ 08873, U.S.A

**ABSTRACT**

In this paper, threading dislocation densities in GaN and AlGaN epitaxial layers have been evaluated using two different X-ray analysis techniques; a Williamson Hall (WH) plot and reciprocal space mapping (RSM). GaN and AlGaN have crystalline growth composed of columnar structures that can be estimated by coherence length and angular misorientation measured by X-ray. A WH plot can provide information about coherence length and tilt angle from a linear fit to the linewidth of the triple axis rocking curve (000 $l$ ) symmetric reflections. RSM is typically used to obtain this data, but it is more involved in technique. The two dominant components of threading dislocation densities (screw and edge types) in the GaN and AlGaN epitaxial layers were found to be similar by both techniques. The threading dislocation density correlates to the size of columnar structure as determined by coherence length, tilt angle, and twist angle. The effect of Al composition in AlGaN alloys on these dislocation densities was investigated and found to depend strongly on the type of nucleation layer, GaN or AlN.

**INTRODUCTION**

GaN-based materials have attracted much attention for optoelectronic device applications where there is a need to operate in the blue-green regime.[1] However, the high threading dislocation density in the III-Nitrides is an issue that encumbers their further development as optoelectronic devices in the ultraviolet.[2] The threading dislocation (TD) density is normally determined using plan view transmission electron microscopy (TEM), however this technique is destructive and typically requires a few days before the this data can be obtained.[3] X-Ray Diffraction (XRD) has been used to obtain functionally equivalent data from some average measurements of crystal microstructure. Since XRD is non-destructive and rapid characterization technique it is the most common technique used to optimize crystalline quality growth parameters. GaN is different to other compound semiconductor materials because it is formed with large areas of crystalline material that are misaligned to each other, a columnar structure (i.e. mosaic structure).[4] Thus an estimate of size of those domains, the average misorientation between them and dislocation density is important in optimizing material growth. High-resolution XRD reciprocal space mapping (RSM) is normally utilized for detailed characterization of such crystalline structures. However, a much quicker and simpler method to obtain similar information utilizes the Williamson-Hall (WH) plot.

In this study of GaN and AlGaN, RSM and WH plot techniques were used to characterize the columnar structures and to evaluate the threading dislocation densities of thin layers grown by MOCVD. These two methods are compared for consistency and to investigate the effect Al composition in AlGaN alloys on dislocation density.

## THEORY

Reciprocal space mapping (RSM) of a reflection plane can be plotted by recording equivalent intensities from a series of  $\Omega$  scans each having different detector position with respect to  $2\theta$  direction ( $\Omega$ - $2\theta$  scans). Since the linewidth of these scans for RSM are broadened by size (coherence lengths) and angular misorientation (tilt and twist angles) of the columnar structure, the RSM is used to obtain information of the columnar structure. As illustrated in Fig. 1, the lateral coherence length ( $L_{||}$ ) is the reciprocal of the component of the FWHM parallel to surface ( $L_{coh}$ ) in the RSM of an asymmetric reflection.[5] On the other hand, from the RSM of a symmetric (000 $l$ ) reflection plane, the tilt angle ( $\alpha_{tilt}$ ) is the vertical component of the FWHM ellipse. Lastly, from the RSM of reflection planes in the  $a$ -axis direction, the vertical component of the FWHM ellipse is twist angle ( $\alpha_{twist}$ ). [6,7,8]

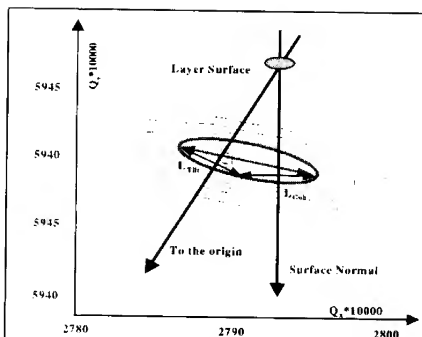


Fig. 1 (1104) RSM of GaN #1.  $L_{coh}$  is the length of the FWHM component parallel to surface, and  $L_{||}$  is the reciprocal of  $L_{coh}$ .  $\alpha_{tilt}$  is derived by the length of component perpendicular to origin direction. In addition,  $\alpha_{tilt}$  can be obtained from (0004) RSM.

Another technique for obtaining  $L_{||}$  and  $\alpha_{tilt}$  is through the use of Williamson-Hall (WH) plots. For this technique, the broadening of the  $\Omega$  scan (rocking curve) of the symmetric reflections is affected only by the tilt and the coherence length parallel to the reflection surface. WH plots make it possible to distinguish these two broadening mechanisms.[9] When  $\beta_w(\sin\theta)/\lambda$  is plotted against  $(\sin\theta)/\lambda$  for each reflection and a straight line is fitted, the y-intersect ( $Y_o$ ) of the fitted line is used to estimate the lateral coherence length,  $L_{||} (= 0.9 / 2Y_o)$  [2,10,11,12], where  $\beta_w$ ,  $\theta$ , and  $\lambda$  are the integral width of the measured profile, the Bragg reflection angle, and X-Ray wavelength, respectively. In addition, the slope of the fitted line corresponds to the tilt angle,  $\alpha_{tilt}$ . Additionally,  $\alpha_{twist}$  is found from  $\Phi$ -scan on asymmetric reflections. In this work, it is assumed that columnar structure does not abruptly change over the reflection planes, so the information from a specific reflection by using RSM method can be compared to the mean values obtained from the WH method.

Using the data obtained from RSM or WH method, different dislocation densities can be determined. This is done through the use of Burgers vectors and the calculations given below. GaN layers have three main types of threading dislocation (TD) densities; screw dislocation along the  $c$ -axis [0001], edge dislocation in the  $a$ -axis  $[11\bar{2}0]$  and mixed screw and edge dislocations. In this work the mixed dislocations are ignored because they should have much lower densities than pure screw or edge dislocation. Screw and edge dislocation densities are distinguished by Burgers vectors  $b_c = [0001]$  and  $b_a = \frac{1}{3} [11\bar{2}0]$  respectively. The tilt angle is used to determine the screw dislocation density,  $N_{screw}$ , with the Burgers vector  $|b_c|$  by [2,11]

$$N_{screw} = \alpha_{tilt}^2 / (4.35 |b_c|^2) \quad (2)$$

The same is done with twist angle to determine the edge dislocation density,  $N_{edge}$ , with the Burgers vector  $|b_a|$ , the majority of the dislocations occur at the small angle grain boundaries, [2]

**BEST AVAILABLE COPY**

$$N_{\text{edge}} = \alpha_{\text{twist}} / (2.1 |b_a| L_{\parallel}) \quad (3)$$

These dislocation density is a function of Burgers vector that is directly expressed by lattice constant of the films. For dislocation densities of  $\text{Al}_x\text{Ga}_{1-x}\text{N}$  layers, therefore it is necessary to find their lattice constants. Lattice constant of an alloy can be derived using Vegard's law ( $a_{\text{AlN}} \cdot x\text{Ga}_x\text{N} = xa_{\text{AlN}} + (1-x)a_{\text{GaN}}$ ) which is a relation between composition and lattice constant.[13]

## EXPERIMENT

In this work, all samples were grown by Metalorganic Chemical Vapor Deposition (MOCVD) in an EMCORE D180 short jar system on (0001) on sapphire. TMGa, TMAI and  $\text{NH}_3$  were used as the source precursors for Ga, Al, and N, respectively. A 30nm low-temp (540 °C at 300 Torr) GaN nucleation layer was used for undoped GaN samples #1, #2, and #3; 2.2, 1.9 and 2.2  $\mu\text{m}$  thick, respectively. The GaN epilayers were grown at 1050 °C with a V/III ratio of 4000 and a growth rate of  $\sim 2\mu\text{m/h}$ . a 25 nm low-temperature (590 °C at 300 Torr) AlN nucleation layer was used for AlGa epilayers.  $\text{Al}_{0.15}\text{Ga}_{0.85}\text{N}$  #4 was grown at 900 °C on 2 m GaN buffer layer with a V/III ratio of 33000 and a growth rate of  $\sim 0.15$  m/h.  $\text{Al}_{0.4}\text{Ga}_{0.6}\text{N}$  #5,  $\text{Al}_{0.62}\text{Ga}_{0.38}\text{N}$  #6 and AlN sample were grown at 1080 °C on low-temperature AlN nucleation layers with a V/III ratio of 4000 and a growth rate of 0.5, 0.3 and 0.2  $\mu\text{m/h}$ , respectively. In-situ reflectometry was used to monitor the growth rate and the surface morphology.

XRD measurements were performed with the Philips X'pert MRD triple-axis diffractometer equipped with a four bounce Ge (022) monochromator and a Cu sealed anode.  $\Omega$  scan and  $2\Theta$ - $\Omega$  scan on the symmetric (0002), (0004), and (0006) reflection planes as well as RSMs on (0004),  $(1\bar{1}04)$ , and  $(1\bar{2}11)$  reflection planes were performed. In addition,  $\Phi$ -scans were completed on each sample.

## RESULTS

### Undoped GaN

A reciprocal space mapping (RSM) of GaN #1 is shown in Figure 1, from which lateral coherence length is determined as the reciprocal of  $L_{\text{coh}}$ . In addition, the  $\alpha_{\text{tilt}}$  and  $\alpha_{\text{twist}}$  are given by (0004) and  $(1\bar{2}11)$  RSMs (not shown here), respectively. Furthermore,  $L_{\parallel}$ ,  $\alpha_{\text{tilt}}$ , and  $\alpha_{\text{twist}}$  are determined in the same manner for GaN #2 and #3.

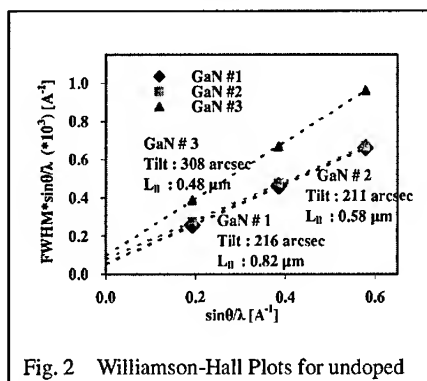


Fig. 2 Williamson-Hall Plots for undoped

WH plots have also been used to extract values for  $L_{\parallel}$  and  $\alpha_{\text{tilt}}$  for these samples in Fig. 2. Values for  $\alpha_{\text{twist}}$  were obtained directly from  $\Phi$ -scans on asymmetric reflections.

The data for GaN obtained by both these techniques is summarized in Table 1. The mean  $N_{\text{screw}}$  with the Burgers vector ( $|b_c|=5.185$  Å) and  $N_{\text{edge}}$  with the Burgers vector ( $|b_a|=3.189$  Å) obtained using a WH plot have been compared with these obtained using RSM. The  $\alpha_{\text{tilt}}$  values by WH are larger than these by RSM methods. This may be explained by annihilation of the defects with respect to the growth direction (i.e. c-axis)

during the growth process.[14, 15] Since the tilt angle along the c-axis is relaxed during growth, the average  $\alpha_{\text{tilt}}$  by WH is smaller than a transition  $\alpha_{\text{tilt}}$  value by RSM. While the mean  $L_{\text{||}}$  by WH is smaller than a transition  $L_{\text{||}}$  value by RSM, since  $L_{\text{||}}$ , a component length with respect to

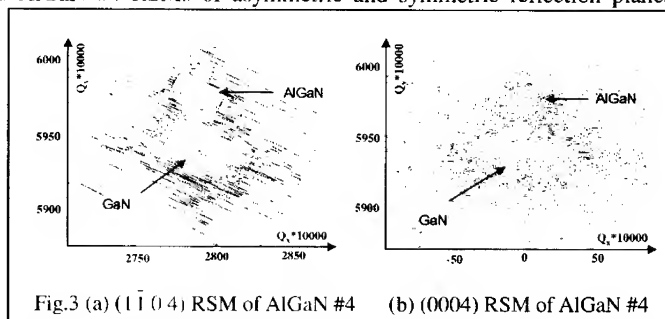
	Method	GaN #1	GaN #2	GaN #3
$L_{\text{  }}$ [um]	WH plot	0.82	0.58	0.48
	RSM	0.33	0.25	0.28
Tilt [aresec]	WH plot	216	211	308
	RSM	274	266	335
Twist [arcsec]	$\Phi$ scan	835	662	792
	RSM	792	655	702
$N_{\text{scw}}$ [cm <sup>-2</sup> ]	WH plot	9.4E+07	9.0E+07	1.9E+08
	RSM	1.5E+08	1.4E+08	2.3E+08
$N_{\text{edge}}$ [cm <sup>-2</sup> ]	WH plot	7.4E+08	8.3E+08	1.2E+09
	RSM	1.7E+09	1.9E+09	1.8E+09

Table 1. Summary of the mosaic structure factors of GaN samples #1, #2, and #3 by various methods

parallel to surface, is smaller as  $\alpha_{\text{tilt}}$  is larger. These differences lead to dissimilarity between two methods for  $N_{\text{scw}}$  and  $N_{\text{edge}}$  due to relaxation of defect during growth. The WH plot provides the mean size and angular distribution of the columnar structure from a combination of the (0002), (0004), and (0006) reflections, while RSM provides a specific value from a specific reflection. Therefore, the WH plot may be expected to provide a more reliable estimate of the average values for the columnar structure of GaN, even though RSM measurements will provide more accurate information. It should be noted that the values obtained for  $N_{\text{scw}}$  and  $N_{\text{edge}}$  are less accurate than those typically measured by TEM and this is being investigated.[3] However, both the WH plot and RSM still allow a relative measure of material quality.

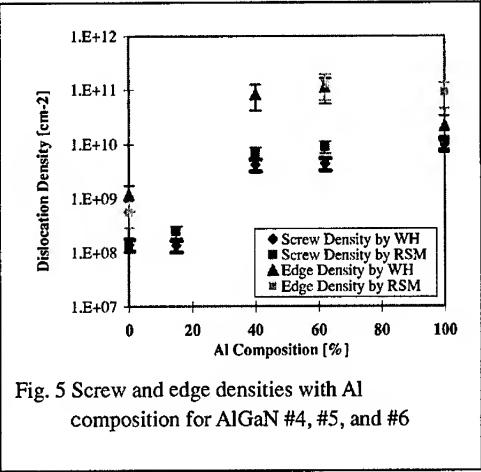
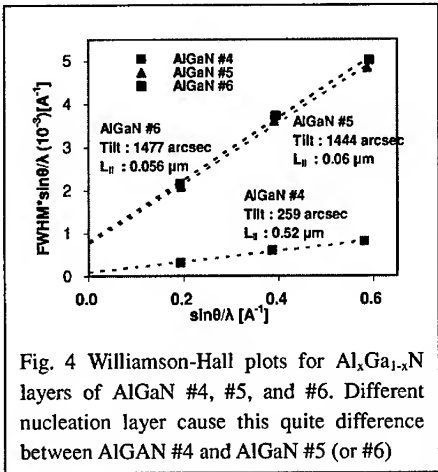
#### Al<sub>x</sub>Ga<sub>1-x</sub>N/Nucleation layer on Al<sub>2</sub>O<sub>3</sub>

Based on the previous two methods for GaN samples, AlGaN epitaxial layers have also been investigated. Fig.3 exhibits AlGaN #4 RSMs of asymmetric and symmetric reflection planes which provide  $L_{\text{||}}$  and  $\alpha_{\text{tilt}}$ . While  $\alpha_{\text{twist}}$  is given by (1 $\bar{2}$ 11) RSMs (not shown here). AlGaN #5 and #6 were also performed in the same way. These RSMs have two peaks corresponding to GaN layer and AlGaN layer, respectively. It can be observed that the GaN peak is stronger than the diffraction corresponding to the AlGaN layer in Fig. 3 (a). A thicker



**BEST AVAILABLE COPY**

layer (2  $\mu\text{m}$  GaN > 0.2  $\mu\text{m}$   $\text{Al}_{0.15}\text{Ga}_{0.85}\text{N}$ ) leads to stronger XRD intensity as well as sharper peak. It is shown in Fig. 4 that WH plots provide  $L_{\parallel}$  and  $\alpha_{\text{tilt}}$ .  $\text{Al}_{0.15}\text{Ga}_{0.85}\text{N}$  layer of AlGa#4 on



GaN nucleation layer seems to have values similar to those of GaN samples. Whereas, AlGa#5 and #6 grown AlN nucleation layer have quite different values from the AlGa#4. The difference is probably caused by relaxation of the underlying layer. This relaxation associated with layer thickness can be influence on the columnar structure of the AlGa#N layer and also cracking in this layer.[16] In addition, AlGa#N samples have larger tilt angles and smaller coherence lengths as the Al composition increases.

Dislocation density is a function of Burgers vector that is directly indicated by lattice constant of the layer. 2 $\theta$  scans on (0004) reflection are measured to evaluate lattice constants of AlGa#4, #5, and #6. Thus, from the measurement data, the Burgers vectors of c-axis and a-axis for  $\text{Al}_x\text{Ga}_{1-x}\text{N}$  alloys can be easily determined as  $|b_c|=5.153$  and  $|b_a|=3.177$  Å,  $|b_c|=5.101$  and

	Methods	AlGa#4 GaN layer	AlGa#5 $\text{Al}_{0.15}\text{Ga}_{0.85}\text{N}$ layer	AlGa#6 $\text{Al}_{0.4}\text{Ga}_{0.6}\text{N}$ layer	AlGa#6 $\text{Al}_{0.62}\text{Ga}_{0.38}\text{N}$ layer	AlN AlN layer
$L_{\parallel}$ [um]	WH plot	0.51	0.52	0.06	0.056	0.27
	RSM	0.62	0.46	0.05	0.054	0.06
Tilt [arcsec]	WH plot	265	259	1444	1477	2140
	RSM	256	349	1857	2120	2232
Twist[arcsec]	$\Phi$ scan	831	NA	6804	8496	8028
	RSM	493	NA	NA	9457	7380
$N_{\text{screw}}$ [cm <sup>-2</sup> ]	WH plot	1.4E+08	1.4E+08	4.3E+09	4.4E+09	1.0E+10
	RSM	1.3E+08	2.5E+08	7.2E+09	9.5E+09	1.1E+10
$N_{\text{edge}}$ [cm <sup>-2</sup> ]	WH plot	1.2E+09	NA	8.3E+10	1.1E+11	2.2E+10
	RSM	5.8E+08	NA	NA	1.3E+11	9.0E+10

Table 2. Summary of the mosaic structure factors of AlGa# samples #4, #5, and #6 by various methods

$|b_a|=3.158$  Å, and  $|b_c|=5.055$  and  $|b_a|=3.141$  Å for AlGaIn samples #4, #5, and #6, respectively.

The variation of the screw and edge densities with Al composition measured by WH and RSM is shown in Figure 5. It is apparent that AlGaIn grown on the GaN nucleation layer (< 40% Al) shows lower densities of screw and edge dislocations than those grown on AlN nucleation layers (> 40% Al). Moreover, it appears that the screw density increase with Al composition in Al<sub>x</sub>Ga<sub>1-x</sub>In layer (> 40% Al) shows a systematic increase with Al composition. It could be expected that the growth mechanism could change with increasing Al however further measurements are needed before this conclusion can be reached.

Table 2 shows mean geometric size of columnar structures as well as dislocation densities for the epitaxial AlGaIn layers. Some values are not reported due to the weak XRD intensity and, as a consequence, the large error on these measurements. Moreover, the values obtained for  $L_{||}$ ,  $\alpha_{||}$  and  $\alpha_{twist}$  by WH and RSM are in closer agreement than GaN; i.e. specific values aren't much varied since defects are less relaxed due to smaller thickness and different type of nucleation layers.

## CONCLUSION

In this work, we have studied the typical mosaic structures of GaN on sapphire with WH and RSM methods by XRD measurements. The effects of not only the columnar structure's size and angular uniformity, but Al composition in the epitaxial AlGaIn layers on TD density have been investigated. In Addition, TD is influence by the type and thickness of nucleation layer

## Acknowledgements

This work was funded by DARPA (John Carrano) and ONR (Yoon-Soo Park) under contract number N00014-02-1-0596 as part of the SUVOS program.

## REFERENCES

- [1] C. Kim, and J. Je, Mat.Res. Soc. Symp.**595**, W3.52.1 (2000)
- [2] T. Metzger, R. Hopler, E. Born, and O. Ambacher, Phil. Mag. A, **77**, 1013 (1998)
- [3] F. Ponce, *Microstructure of Epitaxial III-V Nitride Thin Films*, 1997, p.141
- [4] T. Cheng, L. Jenkins, S. Hooper, and C. Foxon, Appl. Phys. Lett. **66**, 1509 (1995)
- [5] P.F. Fewster, X-Ray Scattering from semiconductors 263 (2000)
- [6] P.F. Fewster, *X-Ray and Neutron Dynamical Diffraction: Theory and Applications*, NATO ASI Series B: Physics **357** (1996) p.287
- [7] P.R. Fewster, N. L. Andrew, and C.T. Foxon. J. Crys. Growth **230**, 404, (2001)
- [8] D.K. Bowen, *High Resolution X-ray Diffractometry and Topography*, 149 (2001)
- [9] G.K. Williamson and W.H. Hall, Acta. Metall. **1**, 22 (1953)
- [10] T. Metzger, R. Hopler, E. Born, and S. Christiansen, Phys. Stat. Sol. A **162**, 529 (1997)
- [11] H.Wang, J. Zhang, C. Chen, Q. Fareed, and J. Yang, Appl. Phys. Lett., **81**, 605 (2002)
- [12] H. Heinke, V. Kirchner, S. Einfeldt, and D. Hommel, Phys. Stat. Sol. A **172**, 391 (1999)
- [13] P.Bhattacharya, *Semiconductor Optoelectronic Devices*, (1997), p.5
- [14] S. Molina, A. Sanchez, F. Pacheco, and R. Garcia, Appl. Phys. Lett. **74**, 3362 (1999)
- [15] L. Kirste, D. Ebling, C. Haug, and K. Tillmann, Mater. Sci. Eng., B **82** 9 (2001)
- [16] B. Bennett, Appl. Phys. Lett. **73**, 3736 (1998)

## BEST AVAILABLE COPY

## ELECTRON MICROPROBE AND PHOTOLUMINESCENCE ANALYSIS OF EUROPIUM-DOPED GALLIUM NITRIDE LIGHT EMITTERS

R.W. Martin<sup>a</sup>, S. Dalmaso<sup>a</sup>, K.P. O'Donnell<sup>a</sup>, Y. Nakanishi<sup>b</sup>, A. Wakahara<sup>b</sup>, A. Yoshida<sup>b</sup> & the RENIBEI Network

<sup>a</sup>Department of Physics, Strathclyde University, Glasgow, G4 0NG, U.K.

<sup>b</sup>Toyohashi University of Technology, Tenpaku, Toyohashi, 441-8580, Japan

### ABSTRACT

Rare-earth doped GaN structures offer potential for optical devices emitting in the visible region [1,2]. We describe a study of MOVPE grown GaN-on-sapphire epilayers implanted with Europium ions, producing characteristic red emission lines between 540 and 680 nm due to intra-4f(n) electron transitions. As-implanted and subsequently annealed samples are investigated using a combination of wavelength dispersive x-ray analysis (WDX), electron microscopy, cathodoluminescence (CL) and photoluminescence (PL). WDX is shown to be a powerful technique for quantifying rare-earth concentrations in GaN, with varying electron beam voltages allowing a degree of depth profiling, further enhanced by the simultaneous collection of room temperature luminescence (CL) from the analysed region [3]. The intensities of the sharp lines observed in the luminescence spectrum are compared to the doping density (between  $10^{14} - 10^{15} \text{ cm}^{-2}$ ) and the Eu content measured by WDX, using a Eu-doped glass standard. Differences observed in the luminescence spectra produced by laser and electron beam excitation will be discussed along with the importance of the annealing conditions, which "heal" defects visible in the electron micrographs.

### INTRODUCTION

Rare earth (RE) ions, such as Nd, Er and Eu, are found in a range of important optoelectronic applications, including solid state lasers and phosphors. They have a partially filled 4f shell shielded by completely filled outer 5s and 5p levels, resulting in very sharp optical emissions due to 4f-4f electron transitions with energies largely independent of the host material. For example, doping with europium, erbium and thulium, respectively, can generate red, green and blue emissions. The host material does play an important role in the thermal quenching of the luminescence and wide band-gap semiconductors, such as GaN, have been shown to be particularly good in this respect [1,4]. Alongside this low thermal quenching additional attractions of investigations into RE:GaN include its high radiation hardness [4] and the proven success of nitride (mainly InGaN based) based optoelectronic devices.

In this paper we describe experiments on Eu doped GaN thin films and relate measurements of the Eu composition to the optical properties, measured with laser and electron beam excitations. The samples are annealed to repair damage resulting from the Eu implantation and the effects of this on the optical and structural properties are explored.

## SAMPLE DETAILS AND EXPERIMENTAL TECHNIQUES

GaN on sapphire epilayers grown by MOVPE were implanted with 200 keV Eu ions at doses of  $10^{14}$  and  $10^{15}$  cm<sup>-2</sup>, as described previously [4,5]. Following implantation the samples were annealed at 1050°C for 30 minutes in a nitrogen/ammonia atmosphere (ratio 9:1).

The as-implanted and annealed samples were investigated using a Cameca electron probe micro-analyser (EPMA), equipped with three WDX spectrometers, secondary electron and back-scattered electron detectors and cathodoluminescence spectroscopy [3]. The Eu content was quantified by detecting the L<sub>α</sub> X-rays diffracted by a large area pentaerythritol (PET, 2d = 8.75 Å) crystal in comparison with a Eu-doped glass standard. A thick undoped GaN epilayer was used as a standard for both the Ga and N determinations. Thallium acid phthalate (TAP, 2d = 25.75 Å) and a synthetic pseudocrystal (PC1, 2d = 60 Å), respectively, were employed to diffract the Ga L<sub>α</sub> and N K<sub>α</sub> X-rays. For the measurements the electron beam current was typically set to 30 nA, and controlled by a beam regulator, with beam energies in the range 5 to 20 keV. Generation of the Eu L<sub>α</sub> X-rays has a energy threshold of approximately 7 keV, for which the depth corresponding to deposition of 90% of the electron beam energy is ~200 nm in GaN. A simulation of 200 keV Eu implantation using TRIM2000 [6] indicates that the implanted ions reside in a layer of thickness between 50 and 80 nm. Thus it is not possible to confine the Eu measurement to the Eu-containing layer and measurements as a function of beam energy are used in combination with software that simulates electron beam excitation of a layered structure.

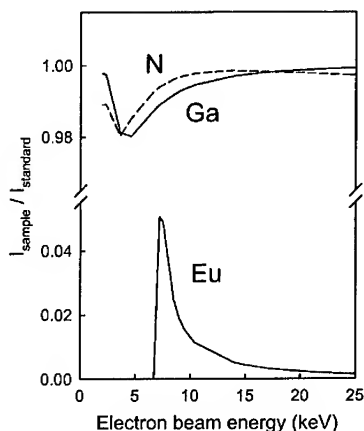


Figure 1. X-ray intensity ratios estimated for Eu, Ga and N for a 40 nm Eu:GaN layer at the surface of GaN. The signals are compared with Eu-doped glass and GaN standards.

Figure 1 shows the calculated intensity ratios (X-ray counts from the sample divided by those from the appropriate standard) for 40 nm of Eu:GaN, containing 0.4% by weight of Eu, at the surface of a thick GaN layer. The 7 keV threshold for the generation of Eu X-rays is clearly seen along with the rapid decrease of sensitivity as the beam energy increases and more of the energy is deposited in the underlying undoped GaN. The Ga and N signals are always very close to unity

due to the similarity of the sample and standard, but the effect of the Eu in the surface layer can be seen at low energies.

Room temperature CL spectra were measured *at the same time as the WDX analyses* using a CCD spectrograph to collect light from the region of electron impact through the optical microscope on the EPMA. In addition temperature-dependent PL measurements were performed using low power excitation by 351 nm light from an Argon ion laser. The samples were mounted within a closed cycle cooler allowing the temperature to be varied between 20 and 300K.

## EXPERIMENTAL RESULTS AND DISCUSSION

The as-implanted  $10^{15} \text{ cm}^{-2}$  sample has a dark appearance and surface damage is visible using an optical microscope. Secondary electron imaging reveals the  $\sim$ micron-sized hexagonal features shown in Fig. 2. These features disappear completely upon annealing and are not observed at all in the  $10^{14} \text{ cm}^{-2}$  samples.

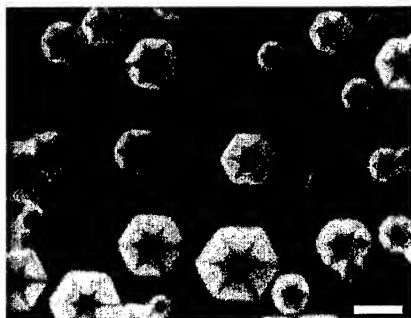


Figure 2. Secondary electron image (10 kV, 1nA) showing surface damage for the  $10^{15} \text{ cm}^{-2}$  as-implanted Eu:GaN sample.

The concentrations of Eu, Ga and N were quantified using the wavelength dispersive X-ray spectrometers as described above. In all cases apart from the as-implanted  $10^{15} \text{ cm}^{-2}$  sample the measured Ga and N compositions were always in the range  $(50 \pm 1 \text{ atomic } \%)$ . For the  $10^{15} \text{ cm}^{-2}$  as-implanted samples the measurements were taken in the regions between the hexagonal crystallites, although there is indication at low beam voltages (below 10kV) that these, or other, features are compromising the data. In this case the total measured weight percent is  $\sim 90\%$ , rather than  $(100 \pm 1)\%$ , and a slight deviation from stoichiometry (2.5 atomic %) is suggested but may be an artefact of the data fitting. The Eu concentration ranges from 0 to 0.13 atomic % but the sampled volume goes beyond the implanted layer, as described earlier, and measurements as a function of electron beam energy are required in order to extract details of the Eu compositional profile.

Fig. 3 plots the ratio of the Eu X-ray intensity measured from the sample to that in the standard for beam energies from 8 to 20 keV along with line fits generated assuming a single layer with uniform Eu content. Although the assumption of a uniform layer is clearly too simple for a single energy implantation the "thickness – composition" product is reasonably well

defined and the fitted lines provide important information on the relative implantation depth and peak concentration.

As expected the as-implanted " $10^{15}\text{cm}^{-2}$ " sample shows the largest amount of Eu and the data can be fitted assuming a 100 nm layer of 0.5 weight % Eu in GaN, as shown in Fig. 3(a). Reasonable fits can also be achieved by varying the layer thickness by 20% and making commensurate changes in Eu content and an alternative fit to 120 nm of 0.4 weight % Eu in GaN is also shown. The error bars represent the random error in the measured points, typically numbering 12, and not the full uncertainty in the measurement. After annealing there has been a noticeable loss of Eu and the thickness-composition product has dropped by a factor of  $\sim 3$ , with a good fit now possible for 0.35 weight % Eu in 40 nm. Fig. 3(b) shows that a sensible trend with beam energy is still obtained for the " $10^{14}\text{cm}^{-2}$ " sample, although the Eu concentrations are lower and approaching the detection limit of the instrument. There is no evidence of a change upon annealing in this case and both sets of data can be well fitted by the assumption of a single 40 nm layer of between 0.15 and 0.2 weight % Eu.

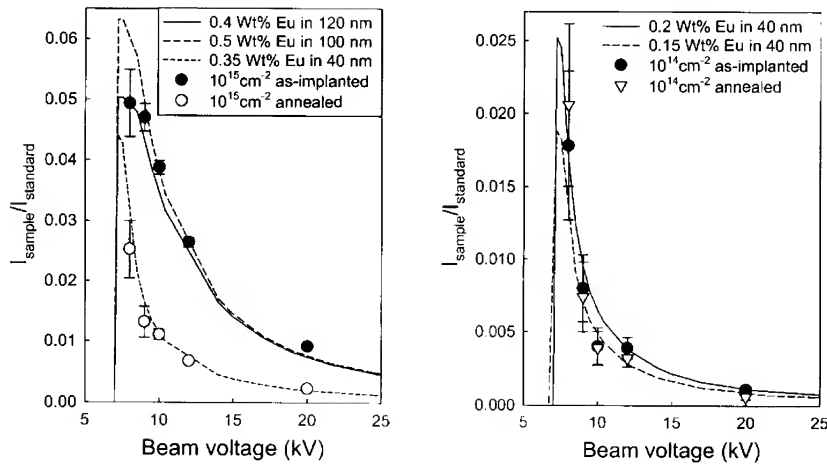


Figure 3. WDX data measured as a function of beam voltage for (a)  $10^{15}\text{cm}^{-2}$  and (b)  $10^{14}\text{cm}^{-2}$  Eu:GaN samples. The lines are the theoretical profiles assuming a single uniform layer of Eu:GaN as described in the text.

An Eu weight % value of 0.5 corresponds to approximately 0.14 atomic % and a concentration of  $1.2 \times 10^{20}\text{cm}^{-3}$ . Taken over a thickness of 100 nm this agrees very well with the actual implanted dose for the  $10^{15}\text{cm}^{-2}$  sample. The measured composition for the  $10^{14}\text{cm}^{-2}$  sample corresponds to approximately 0.05 atomic %, a concentration of  $\sim 4 \times 10^{19}\text{cm}^{-3}$  and a sheet density of  $\sim 1.5 \times 10^{14}\text{cm}^{-2}$  over a thickness of 40 nm. The WDX data for the Eu concentrations within these samples agree well with results from Rutherford Back-scattering Spectrometry [7].

Room temperature CL spectra measured using a 10 kV, 40 nA electron beam are shown in Fig. 4. For both as-implanted samples no  $\text{Eu}^{3+}$  or GaN luminescence is detected but the repair of implantation induced damage is seen in the spectra for the annealed samples. The sharp transitions observed in the red spectral region are associated with intra-4f shell transitions of  $\text{Eu}^{3+}$  ions [1,8]. The strongest line, at 621 nm, is due to the  ${}^5\text{D}_0 \rightarrow {}^7\text{F}_2$  transition and other lines

**BEST AVAILABLE COPY**

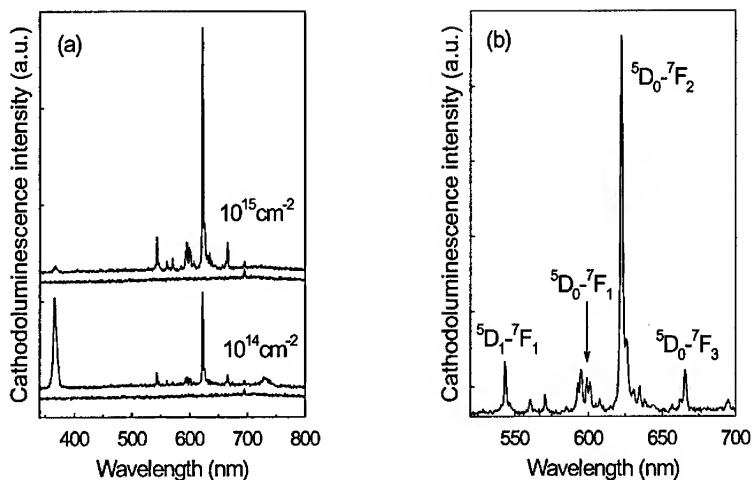


Figure 4. (a) Room temperature CL spectra from the annealed Eu:GaN samples. The traces are offset vertically for clarity and shown in pairs with the trace from the annealed sample above that from the as-implanted sample (b) An expanded version of the room temperature CL from the  $10^{15}\text{cm}^{-2}$  sample, showing the  $\text{Eu}^{3+}$ -related emission.

are identified in Fig. 4(b). Following the anneal the CL spectra also show the characteristic GaN band-edge luminescence in the region of 360 nm. The fact that this is stronger in the  $10^{14}\text{cm}^{-2}$  sample, coupled with the relatively higher intensity of the  $\text{Eu}^{3+}$  luminescence in the lower doped sample, indicates that some damage remains in the  $10^{15}\text{cm}^{-2}$  sample. The CL results should be compared with PL spectra, excited using low intensity excitation by 351 nm laser radiation as

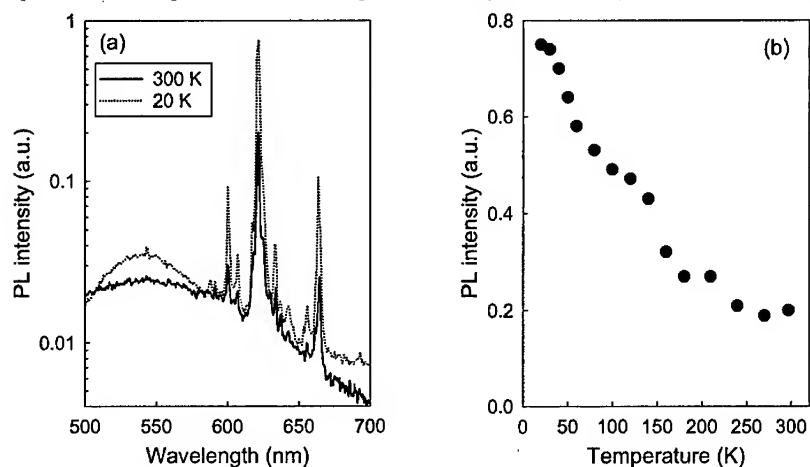


Figure 5. (a) PL spectra from the annealed  $10^{15}\text{cm}^{-2}$  Eu:GaN sample measured at room temperature and 20 K. (b) The intensity of the 621 nm peak plotted as a function of temperature, showing the slow fall-off with temperature.

shown in Fig. 5 for the annealed  $10^{15}\text{cm}^{-2}$  sample. Spectra measured at room temperature and 20 K are shown along with the temperature dependence of the main  $\text{Eu}^{3+}$ -related line. The low temperature quenching of the rare earth luminescence can be seen, with a fall off of less than a factor of four up to room temperature. As reported in Ref [4] this is considerably less (by  $\sim \times 7$ ) than the fall off for the GaN luminescence.

Differences between the CL and PL spectra are the subject of a continuing investigation.

## CONCLUSIONS

An investigation of the composition and optical emission of a pair of Eu-implanted GaN epilayers has been described. Annealing is shown to be necessary for the observation of rare earth related luminescence but is also shown to have an impact on the density of rare earth ions. Wavelength dispersive X-ray has been shown to be a useful technique for the measurement of Eu down to densities of  $\sim 0.05$  atomic % in layers of only 40 nm thickness. The electron micro-probe permits the measurement of CL spectra at the same time and location on the sample as the WDX analysis, paving the way to further studies relating the luminescence and composition.

## ACKNOWLEDGEMENTS

This work has been supported by the EU HPRN-CT-2001-00297 RENiBEI project.

## REFERENCES

1. A.J. Steckl, J. Heikenfeld, D.S. Lee and M.J. Garter, C.C. Baker, Y.Q. Wang, and R. Jones IEEE J. Sel. Top. Quant. Elect. **8** 749 (2002)
2. E. Alves, K. Lorenz, R. Vianden, C. Boemare, M.J. Soares, T. Monteiro, Mod. Phys. Lett. **B** **15** 1281 (2001)
3. R.W. Martin, P. R. Edwards, K. P. O'Donnell, E. G. Mackay, and I. M. Watson, phys. stat. sol. (a) **192** 117 (2002)
4. Y. Nakanishi, A. Wakahara, H. Okada, A. Yoshida, T. Ohshima and H. Itoh, Appl. Phys. Lett. **81**, 1943 (2002)
5. Y. Nakanishi et al. Proceedings of International workshop on Nitride Semiconductors 2000 p486 (2001)
6. J. F. Ziegler, J. P. Biersack and U. Littmark, *The Stopping and Range of Ions in Solids*, (Pergamon Press, New York, 1985)
7. B. Pipeleers and A. Vantomme (unpublished)
8. T. Monteiro, C. Boemare, M.J. Soares, R.A. Sa Ferreira, L.D. Carlos, K. Lorenz, R. Vianden, E. Alves, Physica **B** **308-310** 22 (2001)

**BEST AVAILABLE COPY**

### Lattice Location and Cathodoluminescence Studies of Ytterbium/Thulium Implanted 2H-Aluminium Nitride

U. Vetter<sup>1</sup>, M. F. Reid<sup>2</sup>, H. Hofsäss<sup>1</sup>, C. Ronning<sup>1</sup>, J. Zenneck<sup>1</sup>, M. Dietrich<sup>3</sup>, ISOLDE Collaboration<sup>3</sup>

<sup>1</sup>2. Physikalisches Institut, Universität Göttingen, Bunsenstr. 7-9, D-37073 Göttingen, Germany

<sup>2</sup>Department of Physics and Astronomy, University of Canterbury, Christchurch, New Zealand

<sup>3</sup>CERN, 1211 Geneva 23, Switzerland

#### ABSTRACT

Lattice location studies of radioactive  $^{169}\text{Yb}$  ions, implanted at an energy of 60 keV into 2H-AlN at the on-line isotope separator ISOLDE at CERN, were performed using the emission channeling technique. The measurements, which yield a substitutional Al lattice site for the implanted ions, were recorded for annealing temperatures ranging from 293 K to 1273 K. After complete decay of  $^{169}\text{Yb}$  to  $^{169}\text{Tm}$  cathodoluminescence measurements were performed in the range 12 K – 300 K. The samples show a strong visible luminescence at 460 - 470 nm at room temperature, which is attributed to the  $^1\text{D}_2\text{-}^3\text{F}_4$  intra-4f electron transition of  $\text{Tm}^{3+}$ . At 12 K the luminescence is dominated by transitions starting from the  $^1\text{H}_6$  multiplet. Time resolved as well as temperature dependent cathodoluminescence measurements are presented and discussed.

The lattice location as well as the time resolved cathodoluminescence measurements suggest that there is only one pronounced site of the implanted ions in the AlN lattice and that this is the substitutional aluminium site.

#### INTRODUCTION

2H-aluminium nitride (AlN), with its large band gap of 6.2 eV is, among the wide band gap semiconductors, a very promising candidate for the study of intra-4f electron transitions of triply ionised lanthanides and for the implementation of efficient light emitters in the near infrared, visible and ultraviolet spectrum [1-4]. However, fundamental investigations of luminescence spectra of lanthanide implanted wide band gap semiconductors are difficult because comparative absorption or reflection or selective excitation spectroscopy is not applicable due to the limited implantation fluence. A common problem is therefore the unknown site of the implanted ions. To overcome these problems direct lattice location studies are very useful. In recent years the electron emission channeling method [5] using radioactive isotopes has been very successfully applied to the determination of lattice sites of lanthanides implanted into semiconductors.

#### EXPERIMENTAL DETAILS

We implanted radioactive  $^{169}\text{Lu}$  ions into AlN (grown by metal-organic vapor phase epitaxy on 6H-SiC, as described in Ref. [6]) at an energy of 60 keV and fluences of  $1 \cdot 10^{13}$  ions/cm<sup>2</sup> at the online isotope separator ISOLDE [7] at CERN. The ions are produced by irradiation of a tantalum target with protons accelerated to 1.6 GeV and are extracted via surface ionisation and mass separation, followed by implantation at 60 keV. After complete decay of  $^{169}\text{Lu}$  ( $T_{1/2} = 35$  h) to  $^{169}\text{Yb}$  ( $T_{1/2} = 32.0$  d), electron emission channeling spectra were recorded using the conversion electrons arising in the decay  $^{169}\text{Yb}$ - $^{169}\text{Tm}$ . The measurements were performed by mounting a

sample on a three axes goniometer monitoring the electron flux with a fixed surface barrier silicon diode, while tilting the sample with respect to the detector around certain axes of interest in the 2H-AlN lattice. The angular resolutions of the setup was  $\sigma = 0.3^\circ$ . Isochronal annealing (10 min.) up to 1273 K using a radiation heater was performed without dismounting the sample from the goniometer. To identify the lattice location of the implanted ions, experimental EC channeling spectra were fitted against spectra simulated using the *manybeam* code [5] to determine the lattice location of the implanted ions.

After complete decay of  $^{169}\text{Yb}$  to  $^{169}\text{Tm}$  cathodoluminescence (CL) spectra were recorded in the temperature range 12 K – 300 K. The samples were mounted on the head of a closed cycle refrigerator and irradiated with a 5 keV electron beam (Spectra EQ-22). The luminescence light was focussed into a Czerny-Turner spectrograph (Jobin Yvon 1000M) and detected by either a photomultiplier (Hamamatsu R928) or a CCD camera. Time resolved CL measurements were performed by pulsing the electron beam and counting the pulses generated by a constant fraction discriminator (Ortec 473A) with a multichannel scaler (FastCOM 7882, minimum dwell timer of 125 ns).

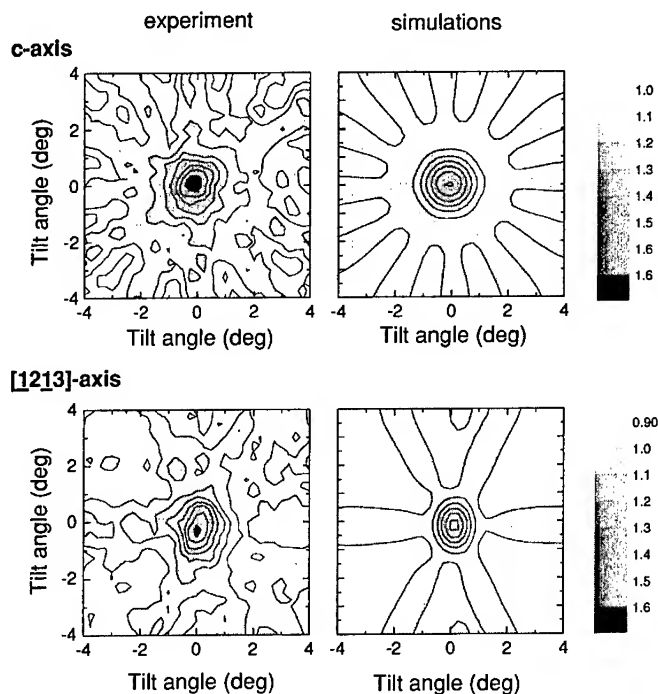


**Figure 1.** (left) Normalized 2-dimensional channeling spectra of conversion electrons from  $^{169}\text{Tm}$  in 2H-AlN as implanted, for the c-axis as well as the [1213]-axis. (right) Best fits to experimental spectra correspond to a fraction of 69 (5) % of emitter atoms on substitutional Al sites, with a mean static displacement of 0.24 Å. The remainder of the emitter atoms is assumed to be located on sites of low symmetry.

## EXPERIMENTAL RESULTS AND DISCUSSION

Figure 1 shows the normalized 2-dimensional EC spectra of conversion electrons from  $^{169}\text{Tm}$  in 2H-AlN as implanted, for the c-axis as well as for the [1213]-axis. On the right side the simulated pattern applying the *manybeam* formalism are shown, whereas best fitting results are obtained by assuming that 69 (5) % of the emitter atoms are located on substitutional Al lattice sites with a mean static displacement of 0.24 Å. The remainder of the emitter atoms is assumed to be located on sites of low symmetry, so called "random" sites. Upon annealing of the sample up to 1273 K the substitutional fraction did slightly increase to 78 (5) %. This behaviour is similar to lanthanide implanted GaN where after implantation a large fraction of the implanted ions is located on substitutional Ga sites and this fraction stays nearly constant upon annealing [8,9]. It should be kept in mind that lattice location studies never reflect the local symmetry of the ions. The annealing behaviour of ion implanted AlN using radioactive  $^{111}\text{In}$  as probe atoms was recently given [10] showing that about 50 % of the probe atoms are on undisturbed hexagonal sites after annealing the samples up to a temperature of at least 1073 K.

After complete decay of the  $^{169}\text{Yb}$  ions, CL measurements were performed in the temperature range 12 K – 300 K. Figure 2 shows the CL spectra of  $^{169}\text{Tm}$  in AlN. At room temperature a strong visible blue luminescence at around 465 nm is observed, while at 12 K many transitions are detected. For the assignment of the luminescence lines with radiative transitions between individual Stark levels we performed preliminary calculations including the mean free ion parameters for  $\text{Tm}^{3+}$  taken from Ref. [11] as well as crystal field parameters  $B_{q,k}$  for symmetry  $C_{3v}$  and lower. The free ion energy levels of  $\text{Tm}^{3+}$  are shown figure 3, except the

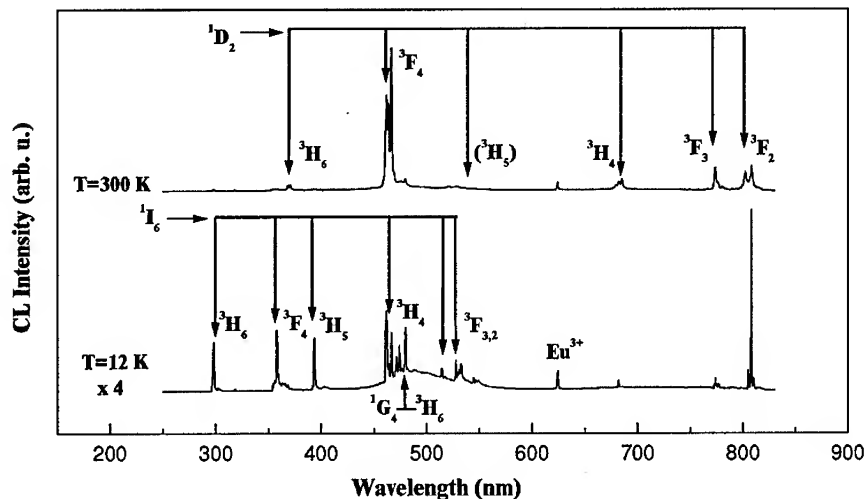


**Figure 2.** CL spectra of Tm-doped 2H-AlN, annealed at 1273 K under vacuum conditions, measured at 300 K (upper graph) and 12 K (lower graph) under 5 keV, 0.3 W/cm<sup>2</sup> electron excitation. The strong luminescence at 805 nm is either due to  $^3\text{H}_4 - ^3\text{H}_6$  or the  $^1\text{G}_4 - ^3\text{F}_4$  intra-4f electron transition.

$^1S_0$  level which is located far above ( $\sim 74,000 \text{ cm}^{-1}$ ). The magnitude of the band gap of AlN is indicated as well. The final assignment of the observed groups of lines to transitions between individual  $^{2S+1}L_J$  multiplets is however difficult because of overlapping transitions between different pairs of multiplets and because of an unknown population of the multiplets. The discussion given here is based on the assumption that transitions starting from the  $^3P_J$  levels are absent. Based on preliminary calculations, lifetime measurements and studies of  $\text{Tm}^{3+}$  related luminescence data found in the literature [12-14], most observed transitions at 12 K in the ultraviolet and visible can be attributed to transitions starting from the  $^1I_6$  multiplet. Transitions starting from the  $^1D_2$  multiplet are, except  $^1D_2 \rightarrow ^3F_4$ , almost absent. The  $^1G_4 \rightarrow ^3H_6$  transition which is the dominant transition in the blue in case of  $\text{Tm}^{3+}$  doped GaN [15,16] and is identified via life time measurements in our case, seems to play no significant role. At 300 K luminescence originating from radiative intra-4f electron transitions between the  $^1D_2$  and energetically lower lying multiplets such as  $^1H_6$ ,  $^3F_4$ ,  $^3H_4$ ,  $^3F_3$ ,  $^3F_2$  dominate the spectrum from the ultraviolet to the near infrared region. There are additional lines that do not originate from intra-4f electron transitions of  $\text{Tm}^{3+}$  rather than from  $\text{Eu}^{3+}$ . The contamination with  $\text{Eu}^{3+}$  can be explained with the implantation process at the online isotope separator. Conditional on the surface ionisation process "contaminations" of lanthanide monoxides pass the mass separation process. These monoxides are of the form  $^{153}\text{Ln}^{16}\text{O}$ , and these lanthanides decay to  $^{153}\text{Eu}$ . The contaminations are supposed to be in the order of 5 % and are not expected to have any influence on the  $\text{Tm}^{3+}$

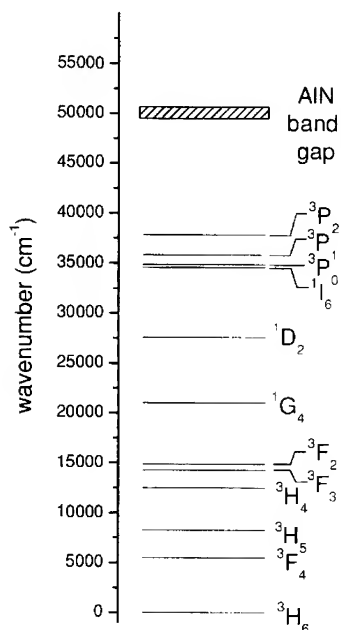


**Figure 3.**  $\text{Tm}^{3+}$  free ion energy levels and the magnitude of the AlN band gap.

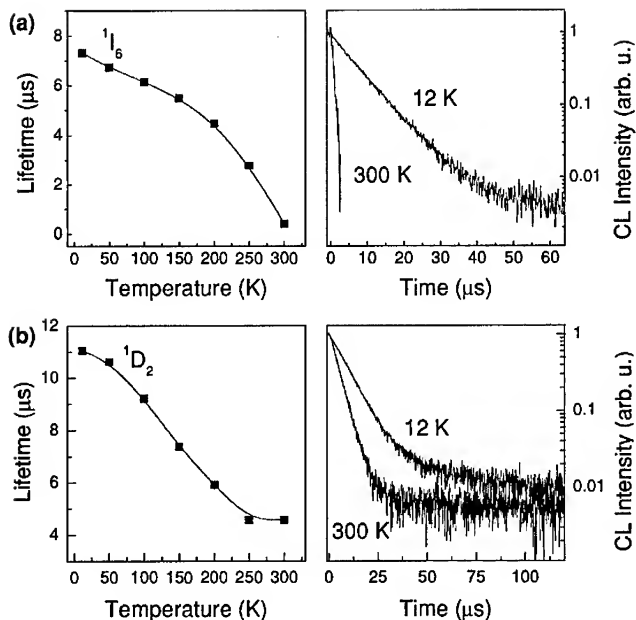
spectrum. The spectra discussed here have been reproduced by implanting stable  $^{169}\text{Tm}$  ions into different AlN substrates with varying implantation doses and energies and for different annealing conditions.

Figure 4 shows the temperature dependent lifetimes for both the  $^1I_6$  and  $^1D_2$  levels. The decay curves shown on the right of Figure 4 (a) show a simple exponential behaviour. It is found that with increasing temperature the lifetime of the  $^1I_6$  level drops down from its initial value of  $7.3 \mu\text{s}$  at 12 K to approx.  $0.4 \mu\text{s}$  at 300 K. The decay curves of the  $^1D_2$  level are non-exponential in the beginning and are reasonably described by assuming that the  $^1D_2$  level is partially populated by the upper  $^1I_6$  level leading to the simple rate equation

$$dN_1/dt = -\tau_1^{-1}N_1 + \tau_2^{-1}N_2 \quad (1)$$

where  $N_1$  (normalized to one) corresponds to the number of excited atoms on level  $^1D_2$  (lifetime  $\tau_1$ ) and  $N_2$  is proportional to the number of excited atoms on level  $^1I_6$  (lifetime  $\tau_2$ ). Both  $N_1$  and  $N_2$  are unknown but introduced to fit the decay curves of the  $^1D_2$  level to the integral version of equation (1). Using the measured lifetime of the  $^1I_6$  level, the lifetime of the  $^1D_2$  level is extracted as shown in figure 4 (b). The

**BEST AVAILABLE COPY**



**Figure 4.** Temperature dependent lifetimes of the (a)  $^1I_6$  and the (b)  $^1D_2$  levels monitored at 298 nm ( $^1I_6 - ^3H_6$ ) and 465 nm ( $^1D_2 - ^3F_4$ ) respectively, measured under 4 keV, 0.24 W/cm<sup>2</sup> electron excitation. On the right side the decay curves shown for the temperatures T=12 K as well as T=300 K.

lifetime of the  $^1D_2$  level itself decreases with increasing temperature from 11.1  $\mu\text{s}$  at 12 K to 4.6  $\mu\text{s}$  at 300 K. In figure 5 the integral intensity of the  $^1D_2 - ^3F_4$  intra-4f electron transition is shown over the temperature range 12 K – 300 K. With increasing temperature the intensity increases linearly, the curve changes its slope at around 200 K. The CL intensity shown in figure 5 seems to be related to the lifetime of the  $^1I_6$  level shown in figure 4 (a) and we may conclude that the increase of intensity of transitions starting from the  $^1D_2$  level are due to a population of this level by the upper  $^1I_6$  level due to a cross-relaxation process.

Finally we summarize in table 1 the lifetimes of the  $^1I_6$ ,  $^1D_2$  and  $^1G_4$  levels.

**Table 1.** Lifetimes  $\tau$  of the  $^1I_6$ ,  $^1D_2$  and  $^1G_4$  levels of  $\text{Tm}^{3+}$  in AlN, measured at 12 K and 300 K respectively. All values are in  $\mu\text{s}$ .

	$^1I_6$	$^1D_2$	$^1G_4$
12 K	7.3	11.1	106
300 K	~0.4	4.6	100

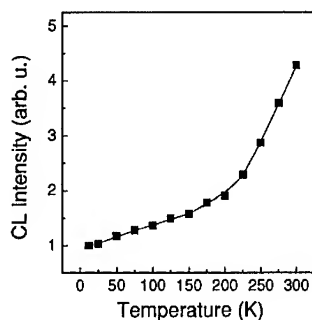


**Figure 5.** Dependence of the integral CL intensity of the luminescence arising from the  $^1D_2 - ^3F_4$  intra-4f electron transition on the sample temperature.

## CONCLUSION

We have shown that  $^{169}\text{Yb}$  ions, implanted into 2H-AlN, are located on substitutional Al lattice sites. A fraction of 69 (5) % of the implanted ions is located on these Al sites directly after implantation. Annealing the samples up to 1273 K under vacuum conditions leads to a slight increase of the fraction of  $^{169}\text{Yb}$  atoms on substitutional Al lattice sites up to 78 (5) %.

Cathodoluminescence measurements of the same samples were recorded after complete decay of  $^{169}\text{Yb}$  to  $^{169}\text{Tm}$ . At 12 K the luminescence is dominated by transitions starting from the  $^1\text{I}_6$  level. At 300 K the spectrum in the range 200 nm – 820 nm is dominated by a bright blue luminescence at 460 - 470 nm which is attributed to the  $^1\text{D}_2\text{-}^3\text{F}_4$  intra-4f electron transition of  $\text{Tm}^{3+}$ . The increase of this blue luminescence with increasing temperature was, based on lifetime measurements, attributed to a population of the  $^1\text{D}_2$  level through the upper  $^1\text{I}_6$  level.

A complete crystal field analysis of  $\text{Tm}^{3+}$  in AlN based on transitions between individual Stark levels and the site determined for the  $\text{Tm}^{3+}$  ions is currently under investigation and will prove whether the assignment of the transitions is correct or has to be modified.

## ACKNOWLEDGEMENTS

Partial financial support by the German Bundesminister für Forschung und Technologie is gratefully acknowledged.

## REFERENCES

1. R. G. Wilson *et al.*, Appl. Phys. Lett. **65**, 992-994 (1994).
2. X. Wu *et al.*, Appl. Phys. Lett. **70**, 2126-2128 (1997).
3. X. Wu *et al.*, J. Luminescence **72-74**, 284-286 (1997).
4. W. M. Jadwisieniczak *et al.*, J. Appl. Phys. **89**, 4384-4390 (2001).
5. H. Hofsäss and G. Lindner, Phys. Rep. **210**, 121 (1991).
6. T. W. Weeks Jr. *et al.*, J. Mater. Res. **11**, 1011 (1996).
7. E. Kugler, Hyperfine Interact. **129**, 23 (2000).
8. M. Dalmer *et al.*, Mater. Res. Soc. Symp. Proc. **482**, 1021 (1998).
9. U. Wahl *et al.*, J. Appl. Phys. **88**, 1319-1324 (2000).
10. C. Ronning *et al.*, J. Appl. Phys. **87**, 2149-2157 (2000).
11. C. Görller-Walrand and K. Binnemans, in *Handbook on the Physics and Chemistry of Rare Earths; Vol. 23*, edited by J. K. A. Gschneidner and L. Eyring (Elsevier Science B. V., 1996), p. 121.
12. S. V. J. Lakshman and C. K. Jayasankar, J. Phys. C. **17**, 2967-2980 (1984).
13. J. M. Chwalek and G. R. Paz-Pujalt, Appl. Phys. Lett. **66**, 410-412 (1995).
14. S. Tanabe, K. Tamai, K. Hirao, and N. Soga, Phys. Rev. B. **53**, 8358-8362 (1996).
15. A. J. Steckl, M. Garter, D. S. Lee, J. Heikenfeld, and R. Birkhahn, Appl. Phys. Lett. **75**, 2184-2186 (1999).
16. H. J. Lozykowski, W. M. Jadwisieniczak, and I. Brown, Appl. Phys. Lett. **74**, 1129-1131 (1999).

**BEST AVAILABLE COPY**

### The Properties of a P-Implanted GaN Light-Emitting Diode

J. Kikawa, S. Yoshida, and Y. Itoh

Yokohama R&D Laboratories, The Furukawa Electric Co., Ltd.

2-4-3, Okano, Nishi-ku, Yokohama, 220-0073, Japan

#### ABSTRACT

Electroluminescence measurements of P-implanted GaN light-emitting diodes were performed. The measured peak densities of P in the GaN were  $5 \times 10^{20} \text{ cm}^{-3}$  and  $4 \times 10^{21} \text{ cm}^{-3}$  based on secondary ion mass spectroscopy. The EL spectra had a broad blue-band emission at the peak energy from around 2.8 eV to 3.3 eV and yellow-band emission at an energy centered at 2.2 eV. The blue-band emission could decompose into two components at energy positions of 2.9 eV and 3.2 eV. The former component is considered to be emission due to the recombination of the bounding exciton by P atoms, known as an isoelectronic trap in GaN.

#### INTRODUCTION

Gallium nitride (GaN) and its cation mixed alloys offer a host of important applications in optoelectronic devices. Recently, there has been considerable interest in mixed-anion nitride alloys, such as  $\text{Ga}_{1-x}\text{As}_x$  or  $\text{Ga}_{1-x}\text{P}_x$ , and related quaternary semiconductor compounds, because they have a gigantic band-gap bowing compared with mixed-cation GaN. There is a possibility for applications in optoelectronic devices operating at wavelengths from ultraviolet to infrared. It has been reported that N-rich hexagonal  $\text{Ga}_{1-x}\text{P}_x$  could be grown on a sapphire substrate by gas-source molecular-beam epitaxy (GS-MBE) [1] and metal-organic chemical vapor deposition (MOCVD) [2]. There have also been several experimental reports concerning luminescence originating from As atoms in GaN. Li et al [3] observed emission at an energy position of 2.583 eV from As-doped GaN grown by metal organic vapor phase epitaxy (MOVPE); Winsor et al [4] also observed strong blue emission at an energy of around 2.6 eV from As-doped GaN by MBE. On the other hand, Pankove et al [5] and Jadwisienczk et al [6] reported on the luminescence of P atoms implanted in GaN. Thus as though there have been many studies on the luminescence of these compounds, on the electro-luminescence (EL) studies have been few. In this paper, it is reported that we tried to make a  $\text{Ga}_{1-x}\text{P}_x$  active layer light emitting diode (LED) using a P-atom implanting technique, and performed EL measurements.

#### EXPERIMENTAL

In these studies we used a single crystal of GaN epitaxial wafers grown by an ordinary metal organic chemical vapour deposition (MOCVD) technique on the basal plane of sapphire substrates. The GaN wafers were high quality p-type with the yellowing structure: GaN: Mg  $2.5 \mu\text{m}$  / undoped GaN  $0.5 \mu\text{m}$  / undoped AlN  $0.04 \mu\text{m}$  / sapphire. The concentration of Mg was  $1 \times 10^{19} \text{ cm}^{-3}$ . The wafers were implanted at room temperature with  $\text{P}^+$  ions with a dose of  $2 \times 10^{15} \text{ ions/cm}^2$  at 35 keV for sample #390

and with a dose  $4 \times 10^{14}$  ions/cm<sup>2</sup> at 30 keV for sample #387. The implanting ion beam was inclined at 7 degrees to the normal to the GaN epitaxial layers to prevent channeling. Wafers were then grown on a Si-doped GaN epitaxial layer by ordinary MOCVD with 0.15  $\mu$ m thickness and a dose of  $2 \times 10^{19}$  cm<sup>-3</sup>. Post-implant annealing at temperature of 1050°C for 5 minutes was done with coating a SiO<sub>2</sub> film on the surface of a epitaxial films. LEDs were fabricated by an electron cyclotron resonance (ECR) plasma etching process using Ar/CH<sub>4</sub>/H<sub>2</sub>. The etching rate of n and p-type GaN were 10 nm/min and 6 nm/min, respectively. The Ohmic contacts to the p-n junction were then formed using Ti/Al/Au for n-type and Pt/Au for p-type metals. LEDs were characterized using a voltage-current (I-V) curve and an EL method, respectively.

## RESULTS AND DISCUSSION

Figure 1 shows the depth profile of secondary ion mass spectroscopy (SIMS) for a sample #390. The peak concentration of P atoms is  $5 \times 10^{20}$  atoms/cm<sup>3</sup> and the projected range is around 50 nm. The diffusion of Mg atoms was observed in the region of the Si-doped GaN epitaxial layer, but no diffusion of Si atoms was observed in the region of the Mg-doped epitaxial layer. The depth profile of SIMS for sample #387 was similar to sample #390, and the peak concentration of P atoms was  $4 \times 10^{21}$  atoms/cm<sup>3</sup>.

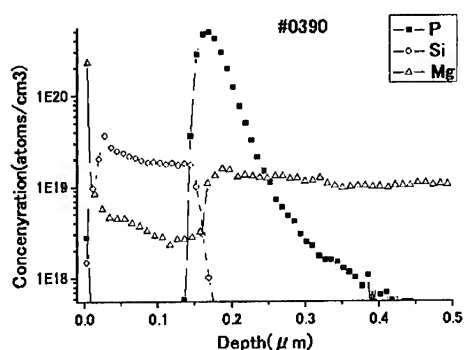


Figure 1. SIMS profile of P implanted GaN LED epitaxial structure.

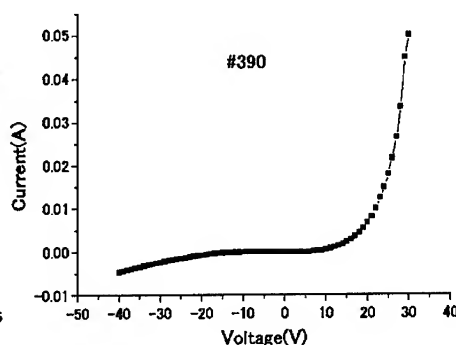


Figure 2. I-V curve of a sample #390 LED.

Figure 2 shows the I-V curve of the sample #390 LED at room temperature. The forward bias part of this curve is good fitting to an exponential function, but the ideal factor ( $n$ ) is unrealistic, being over 100. We also reported on a similar large value of a GaN<sub>1-x</sub>P<sub>x</sub> LED, which was made by the laser-assisted metal-organic vapor-deposition method. These  $n$  values can adjust to about less than 100 by taking account of the series resistances, which were estimated by extrapolating the  $dV/dI$  versus  $1/I$  characteristic. Also, the turn-on voltage of the forward current rising was high. These  $n$  values and the

turn-on voltage would suggest the quality of the  $\text{GaN}_{1-x}\text{P}_x$  film. The reverse bias current of this LED is -0.3 mA at 10 V. Because of its large band-gap energy, the reverse bias saturation current due to minority carrier diffusion would be immeasurably small in an ideal GaN p-n diode. There are many candidates to explain the origin of this large current, for example the tunneling effect or the path through dislocation, but further investigation is necessary.

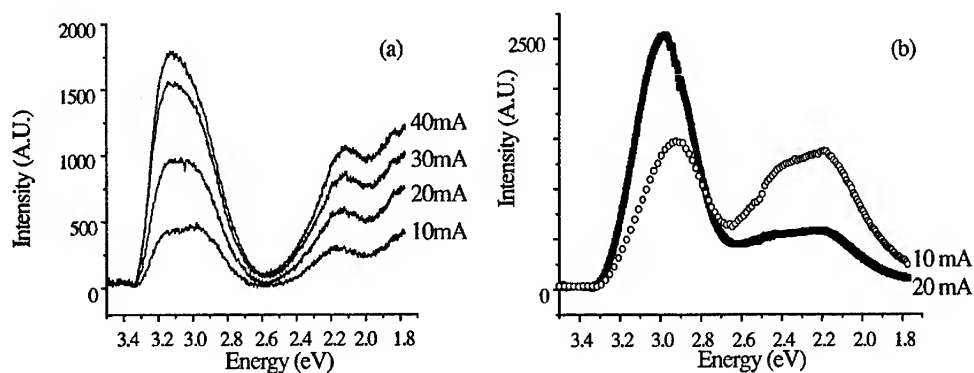


Figure 3. The EL spectra of a sample #387(a) and a sample #390(b).

The EL spectra of sample #387 shown in figure 3(a) were obtained for continuous forward currents ranging from 10 mA to 40 mA at room temperature. A broad blue emission band can be seen in the region of 2.8-3.3 eV and a broad yellow emission band in the region of 2.0-2.3 eV. The blue band can be decomposed to 2.9 eV and 3.2 eV peaks. The 2.9 eV peak is close to the energy position of the photo-luminescence peak, which has been observed by many authors in GaN incorporated P atoms. Jadwisnienczk et al [6] also observed and determined that it was due to the recombination of bound exciton to P-hole isoelectronic traps. We have already reported on the EL spectra of a LED having an active layer of N-rich hexagonal  $\text{GaN}_{1-x}\text{P}_x$  by using LA-MOCVD. The blue band of its spectra was dominated by the 2.9 eV peak [7]. We thus assumed the origin of the 2.9 eV peak to be P atoms, which substitute for N atoms. The origin of the 3.2 eV peak is unknown. The ratio of the 3.2 eV to 2.9 eV peak increased with increasing the drive currents, and the 3.2 eV peak dominated above 20 mA. Similarly, the EL spectra of sample #390 in figure 3(b) have a blue emission band and a yellow emission band. In the blue band, the peak energy position appears as a blue shift though this is due to an increasing 3.2 eV peak with increasing drive currents. The full at width half maximum (FWHM) of the blue band in sample #390 was less than that of sample #387. This was due to the difference in the concentration of implanted P atoms between sample #387 and sample #390. Since the recombination center of the 2.9 eV peak might be related to P atoms, which substitute N atoms, it is superior in the blue band of sample #390 compare with sample #387.

## SUMMARY

We fabricated N-rich  $\text{GaN}_{1-x}\text{P}_x$  active layer LEDs using P-atom implantation. The EL spectra of these LEDs were measured. They had a blue band and a yellow band; in the blue band peaks at 2.9 eV and 3.2 eV were observed. The former peak was related to P atoms, which substituted N atoms;  $\text{P}_\text{N}$  might act as an isoelectronic trap. These properties of the EL spectrum are the same to those of the  $\text{GaN}_{1-x}\text{P}_x$  LED, which was made from light-assisted metal organic chemical deposition (LAMOCVD), as reported before. This shows that the role of P atoms as a radiative recombination center does not depend on the procedure of introducing P atoms in the GaN that is by LAMOCVD or by ion implantation.

## ACKNOWLEDGMENTS

This work was supported by NEDO/JRCM's "The light for the 21<sup>st</sup> century" Japanese national project. The authors also gratefully acknowledge Prof. K. Onabe at University of Tokyo and Prof. Y. Shiraki at RCAST of University of Tokyo for their useful discussions concerning GaNP (III-V-N) research, and further thank Prof. T. Taguchi at Yamaguchi University and Prof. T. Okumura at University of Tokyo Metropolitan for their helpful advice and encouragement regarding our research. They thank Dr. H. Ishii for discussion about the PL.

## REFERENCES

1. K. Iwata, H. Asahi, K. Asami, R. Kuroiwa, and S. Gonda, *Jpn. Appl.* 37, 1436 (1998).
2. J. Kikawa, S. Yoshida, and Y. Itoh, *Proc. Int'l Workshop on Nitride Semicon. IPAP Conf. Ser.* 1, 429 (2000) Dec.
3. X. Li, S. kin, E. E. Reuter, S. G. Bishop, and J. J. Coleman, *Appl. Phys. Lett.* 72, 1990 (1998).
4. A. J. Winsor, S. V. Novikov, C. S. Davis, T. S. Cheng, and C. T. Foxon, *Appl. Phys. Lett.* 77, 2506 (2000).
5. J. I. Pankove and J. A. Hutchby, *J. Appl. Phys.*, 47, 5387 (1976).
6. W. M. Jadwisienzak and H. J. Izykowski, *Mat. Res. Soc. Symp. Proc.* 482, 1033 (1998).
7. J. Kikawa, Y. Itoh, and S. Yoshida, *Mat. Res. Soc. Symp. Proc. Vol.693*, 213 (2002).

## EFFECT OF THICKNESS VARIATION IN HIGH-EFFICIENCY InGaN/GaN LIGHT EMITTING DIODES

J. Narayan and H. Wang

Department of Materials Science and Engineering  
North Carolina State University, Raleigh, NC 27695

Jinlin Ye, Schang-Jing Hon, Kenneth Fox, Jyh Chia Chen, H. K. Choi, and John C.C. Fan  
Kopin Corporation, 695 Myles Standish Blvd. Taunton, MA 02780

### ABSTRACT

We have found that  $\text{In}_x\text{Ga}_{(1-x)}\text{N}/\text{GaN}$  multi-quantum-well (MQW) light emitting diodes (LEDs) having periodic thickness variation (TV) in  $\text{In}_x\text{Ga}_{(1-x)}\text{N}$  active layers exhibit substantially higher optical efficiency than LEDs with uniform  $\text{In}_x\text{Ga}_{(1-x)}\text{N}$  layers. In these nano-structured LEDs, the thickness variation of the active layers is shown to be more important than In composition fluctuation in quantum confinement of excitons (carriers). Detailed STEM-Z contrast analysis, where image contrast is proportional to  $Z^2$  (atomic number)<sup>2</sup>, was carried out to investigate the thickness variation as well as the spatial distribution of In. In the nanostructured LEDs, there are short-range (SR-TV, 3 to 4 nm) and long-range thickness variations (LR-TV, 50 to 100 nm) in  $\text{In}_x\text{Ga}_{(1-x)}\text{N}$  layers. It is envisaged that LR-TV is the key to quantum confinement of the carriers and enhancing the optical efficiency. We propose that the LR-TV thickness variation is caused by two-dimensional strain in the  $\text{In}_x\text{Ga}_{(1-x)}\text{N}$  layer below its critical thickness. The SR-TV may be caused by In composition fluctuation. The observations on thickness variation are in good agreement with model calculations based upon strain effects.

### INTRODUCTION

The AlN-GaN-InN and their alloys have assumed a special importance due to their tremendous potential for fabricating the light emitting devices operating in the red to ultraviolet (UV) energy range.<sup>1-5</sup> The In incorporation in the active layer with a composition of  $\text{In}_x\text{Ga}_{(1-x)}\text{N}$  has been the key to obtaining a high optical efficiency despite high dislocation density ( $\sim 10^{10}\text{cm}^{-2}$ ). However, its role has not been clarified. Some studies have suggested In composition fluctuation leading to a phase separation to be responsible for high optical efficiency. Since the In content controls the band gap in  $\text{In}_x\text{Ga}_{(1-x)}\text{N}$  alloys, it is envisaged that the composition fluctuation leads to quantum-confined (QC) regions whose size is smaller than the dislocation separation (DS). These QC regions trap the bound excitons, and thus the recombination of excitons would not be affected by the presence of defects such as dislocations.<sup>3, 6, 7</sup>

The evidence for In composition fluctuation in  $\text{In}_x\text{Ga}_{(1-x)}\text{N}$  layers in multiple-quantum-well (MQW) structures has been largely circumstantial. Some authors found the evidence for phase separation (In-rich and In-poor phases) in  $\text{In}_x\text{Ga}_{(1-x)}\text{N}$  ( $x > 0.3$ ) only in relatively thick layers (3000-4000 Å), which were grown by molecular beam epitaxy.<sup>8, 9</sup> However, they did not observe any phase separation in thin GaN/ $\text{In}_x\text{Ga}_{(1-x)}\text{N}/\text{GaN}$  double heterostructures with  $x > 0.3$ , grown under similar conditions. Similarly, in MOCVD (metalorganic chemical vapor deposition)-grown samples, phase separation was reported

only in thick  $\text{In}_x\text{Ga}_{(1-x)}\text{N}$  layers for  $x > 0.28$ .<sup>10</sup> The formation of InGa $\text{N}$  quantum dots in single-quantum-well structures has been reported only when additional layers of  $\text{Si}$ <sup>11</sup> and  $\text{In}$ <sup>12</sup> are introduced as anti-surfactant to promote three-dimensional growth. In the case of MQW structures (sapphire/4,000-nm Ga $\text{N}$ : $\text{Si}$ /10-period 2-nm InGa $\text{N}$  and 4-nm Ga $\text{N}$ /200-nm Ga $\text{N}$ : $\text{Mg}$ ), phase separation was observed only after prolonged (40 h) post annealing above 950°C.<sup>13</sup> The phase separation was also observed in  $\text{In}_x\text{Ga}_{(1-x)}\text{N}$ /Ga $\text{N}$  MQW structures after annealing at 950°C in a hydrostatic pressure of 5 kbar in  $\text{N}_2$  for 4 h.<sup>14</sup> Some authors have reported the formation of In-rich and In-poor regions (2-5 nm size) in as-grown MOCVD-grown MQW structures using diffraction contrast transmission electron microscopy (TEM) techniques. Since the image contrast in these techniques is sensitive to diffraction of atomic planes, these observations do not provide reliable information on composition fluctuation.<sup>15, 16</sup> Thus, there is an urgent need to clarify the role of In composition fluctuation or any other effects leading to the formation of quantum-confined regions.

In this study, we have used high-resolution TEM and STEM-Z (scanning transmission electron microscopy-atomic number) contrast techniques,<sup>17, 18</sup> where contrast is proportional to atomic number ( $Z$ )<sup>2</sup>, to investigate the In composition fluctuation and thickness variation and to correlate them with optical efficiencies. We have found that high-efficiency LEDs contain MQW structures with periodic thickness variations, which we call nano-structured LEDs. The characteristics for the thickness variation are related to growth conditions. We envisage that the introduction of In leads to compressive stresses in the film, which are relieved by a periodic thickness variation, similar to the Ge film growth on Si.<sup>19-21</sup>

## EXPERIMENTAL

$\text{In}_x\text{Ga}_{(1-x)}\text{N}$ /Ga $\text{N}$  MQW LED structures were grown by the MOCVD technique on sapphire substrates. The growth temperatures for n-Ga $\text{N}$ , MQW, and p-Ga $\text{N}$  capping layers were ~1000°C, between 700 and 900°C, and 950°C, respectively. The details of growth conditions for these structures will be reported elsewhere. The LED chips were fabricated by using standard processing steps, and were packaged in T-1 ¾ packages for power measurements. We compare the results using two representative wafers A and B. Figure 1 shows the output power vs dc forward current of LEDs from the two wafers. The output power of LEDs fabricated from wafer A showed 8 mW at 20 mA, which is comparable to the state-of-the-art LED power. However, the power of LEDs from wafer B was only 3.8 mW at 20 mA.

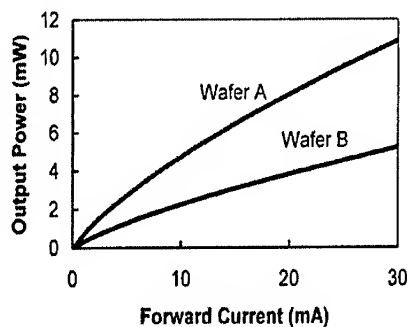


Fig. 1. Output power as a function of dc forward current for LEDs from wafer A and wafer B.

For TEM studies, cross-section specimens from the above wafers were prepared by a standard ion milling procedure. A special care was necessary in terms of low-temperature, low-voltage and shallow-angle thinning to minimize the surface damage for STEM-Z studies. For STEM-Z contrast studies, we used atomic-resolution JEOL 2010 field emission electron microscope with GIF (Gatan Image Filter) attachment. In the STEM-Z mode, a small electron probe (1.6 nm) is scanned across the thin cross-section specimen, and the Z-contrast image results from mapping the intensity of electrons reaching the annular detector. The detector performs the function of Lord Rayleigh's condenser lens. It enforces high scattering angles, so that Rutherford scattering dominates and atoms contribute to the image with a brightness determined by their mean square atomic number ( $Z^2$ ) and with a resolution of the probe size (1.6 nm). Since the atomic number of In (49) is much higher than that of Ga (31), the image contrast is dictated by In concentration.<sup>17, 18</sup>

## RESULTS AND DISCUSSION

Figure 2 shows STEM-Z contrast images from wafer A. The InGa<sub>N</sub> active layer is typically ~2 nm thick and the GaN barriers 7 nm thick. Figure 2(a) shows all the ten active layers, where thickness variation of the active layers is quite apparent. At higher magnifications (Fig. 2 (b) and Fig. 2 (c)), these thickness variations become quite clear as shown by the brightness contrast, which is proportional to  $Z^2$ . Figure 3 shows these thickness variations at a still higher magnification, where short-range thickness variation (SR-TV) with a period of about 3 to 4 nm and a long-range thickness variation (LR-TV) with a period of about 50 to 100 nm are clearly observed. As the brightness contrast is proportional to  $Z^2$ , there is no evidence for separate In phases in the active InGa<sub>N</sub> layers, although from the contrast variation less than 10% fluctuation in In concentration may exist. The results from wafer B with a lower optical efficiency are shown in Fig. 4. A uniform thickness of the active layers as well as uniform In concentration is clearly delineated. There are no thickness variations either short range or long range present in these samples with relatively low optical efficiencies.

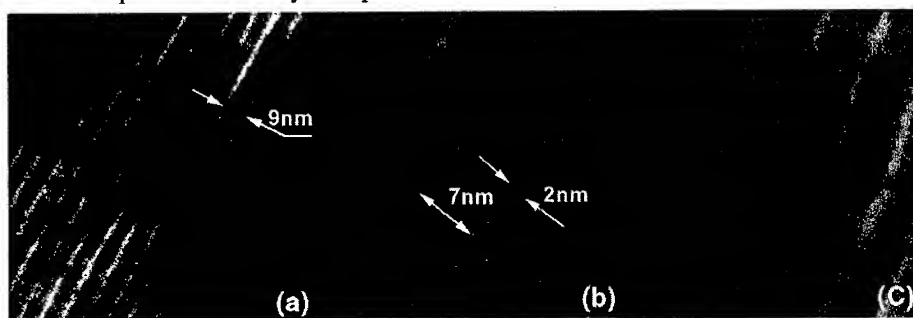


Fig. 2. (a) STEM-Z contrast image in cross-section showing thickness variation in all ten active MQW InGa<sub>N</sub> layers in high-efficiency LED structures (wafer A); (b) & (c) STEM-Z contrast images showing characteristic thickness variations at a higher magnification from the same sample.

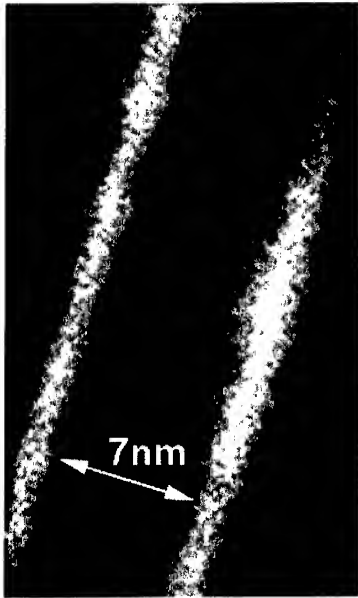


Fig. 3. STEM-Z contrast image in cross-section showing the details of thickness variation in two of the InGaN layers from a high-efficiency LED (sample from wafer A).

Thus our experimental results on a comparative study of high- and low-efficiency LEDs demonstrate that the thickness variation coupled with In concentration variation is clearly related to enhancing the optical efficiencies in LEDs. The QC regions resulting from variations in thickness or In composition trap excitons whose radiative recombination is responsible for efficient spontaneous emission in MWQ LEDs. High optical efficiency results despite high dislocation density ( $\sim 10^{10} \text{ cm}^{-2}$ ) if the localization of excitons is within a region smaller than DS in these structures. The DS is given by  $p^{-1/2}$ , where  $p$  is the density of dislocations (number/cm<sup>2</sup>). Thus, the loss of excitons due to nonradiative

recombination at the dislocations is avoided, resulting in a high optical efficiency of LEDs.

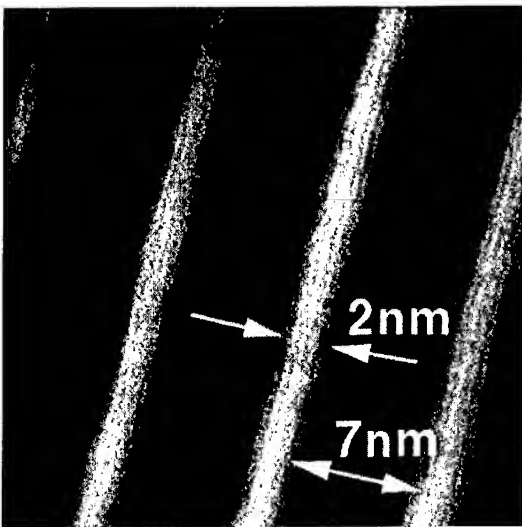


Fig. 4. STEM-Z contrast image at a higher magnification showing extreme uniformity in thickness and indium concentration from a low-efficiency sample (wafer B).

The change in band gap of  $\text{In}_x\text{Ga}_{(1-x)}\text{N}/\text{GaN}$  MQW structures can occur with variations in the composition 'x' or the thickness ' $L_z$ ' of the quantum well. For a typical active layer composition ( $x = 0.4$ ), experimentally observed composition fluctuations are less than  $\pm 2\%$ . The corresponding change in band

gap is less than 0.07 eV. On the other hand, a thickness variation in InGaN layers can create an even bigger change in the band gap. Calculations show that a band gap change

of  $\sim 0.07$  eV is obtained for a thickness variation of  $\text{In}_{0.4}\text{Ga}_{0.6}\text{N}$  layers from 1.8 to 2.2 nm, or  $\sim 0.15$  eV from 1.5 to 2.5 nm. Experimentally observed LR-TV is in the range of 20 to 50%, and SR-TV is less than 10%. It is envisaged that the LR-TV is the key to quantum confinement of the carriers and enhancing the optical efficiency.

We propose that the thickness variation is caused by two-dimensional strain in the  $\text{In}_x\text{Ga}_{(1-x)}\text{N}$  layer below its critical thickness.<sup>19-21</sup> A balance between the elastic energy released and the surface energy expended provides a condition for a minimum wavelength for which the thickness fluctuation is stable.<sup>22,23</sup> Since strain energy increases with thickness, the uniform thickness breaks into a periodic variation by which the free energy of the system can be lowered. Since the strain also increases with In concentration, some fluctuation in In concentration is also expected. However, this phenomenon of thickness variation has been well documented for pure Ge film growth on (100) Si<sup>20,21</sup> as well as for InAs and GaInAs on (100) GaAs<sup>24</sup> below the critical thickness where no composition fluctuation is involved. The thickness variation period  $\lambda$  is given by the following relation:

$$\lambda = \pi\gamma(1-\nu)/[2(1+\nu)^2\mu\epsilon^2], \quad (1)$$

where  $\gamma$  is the surface energy,  $\nu$  is the Poisson's ratio,  $\mu$  is the shear modulus of the film, and  $\epsilon$  is the strain normal to the film surface. To avoid nonradiative recombination at the dislocations, DS should be larger than  $\lambda$ :

$$\rho^{-1/2} > \pi\gamma(1-\nu)/[2(1+\nu)^2\mu\epsilon^2] \text{ or } \rho < \{\pi\gamma(1-\nu)/[2(1+\nu)^2\mu\epsilon^2]\}^{-2}. \quad (2)$$

We have estimated a typical value of  $\lambda$  using the following parameters for our growth conditions. For  $\text{In}_{0.4}\text{Ga}_{0.6}\text{N}$ , shear modulus is estimated to be 82 GPa, Poisson's ratio to be 0.3, surface energy 4,000 ergs/cm<sup>2</sup>, and strain 2%. This results in  $\lambda$  of  $\sim 80$  nm, which is in good agreement with the observed LR-TV. It should be mentioned that to fully develop the observed TV structures, film and substrate variables need to be optimized so that strain relaxation and associated mass transport can occur during growth at high temperatures.

## CONCLUSION

In summary, we have fabricated  $\text{In}_x\text{Ga}_{(1-x)}\text{N}/\text{GaN}$  MQW LEDs and shown that the LEDs with thickness variation of  $\text{In}_x\text{Ga}_{(1-x)}\text{N}$  active layers exhibit substantially higher optical efficiency than the ones with uniform thickness. The thickness variation has two periods, one short range (SR-TV, 3 to 4 nm) and other long-range (LR-TV, 50 to 100 nm). It is envisaged that the LR-TV is the key to quantum confinement of the carriers and enhancing the optical efficiency. The SR-TV may be caused by the In composition fluctuation. It was also found that the variation in In concentration is not very large in the LED structures which exhibit high optical efficiency.

## REFERENCES

1. S. Strite and H. Morkoc, *J. Vac. Sci. Technol. B* **10**, 1237 (1992).
2. GaN and Related Alloys- 1998 MRS Proceedings Volume **537**, ed by S. J. Pearton, C. P. Kao, A. F. Wright, and T. Uenoyama( MRS Internet J. Nitride Semi Res, **4S1**, 1999).
3. S. Nakamura, *Science* **281**, 956 (1998).
4. S.C. Jain, M. Willander, J. Narayan, R. Van Overstraeten, *J. Appl. Phys.* **87**, 965 (2000).
5. Introduction to Nitride Semiconductor Blue Lasers and Light Emitting Diodes, ed. S. Nakamura, S. F. Chichibu, Taylor and Fancis, New York (2000).
6. S. Chichibu, K. Wada, and S. Nakamura, *Appl. Phys. Lett.* **71**, 2346 (1997).
7. Y. Narukawa, Y. Kawakami, S. Fujita, and S. Nakamura, *Phys Rev B* **59**, 10283 (1999).
8. R. Singh, D. Doppalapudi, T. D. Moustakas, and L. T. Romano, *Appl. Phys. Lett.* **70**, 1089 (1997).
9. F. B. Naranjo, M. A. Sanchez-Garcia, F. Calle, and E. Calleja, *Appl. Phys. Lett.* **80**, 231 (2002).
10. N. A. El-Masry, E. L. Piner, S. X. Liu, and S. M. Bedair, *Appl. Phys. Lett.* **72**, 40 (1998).
11. H. Hirayama, S. Tanaka, P. Ramvall, and Y. Aoyagi, *Appl. Phys. Lett.* **72**, 1736 (1998).
12. J. Zhang, M. Hao, P. Li, and S. J. Chua, *Appl. Phys. Lett.* **80**, 485 (2002).
13. M. D. McCluskey, L. T. Romano, B. S. Krusor, D. P. Bour, N. M. Johnson, and S. Brennan, *Appl. Phys. Lett.* **72**, 1730 (1998).
14. L. T. Romano, M. D. McCluskey, C. G. Van de Walle, J. E. Northrup, D. P. Bour, M. Kneissi, T. Suski, and J. Jun, *Appl. Phys. Lett.* **75**, 3950 (1999).
15. Y. Narukawa, Y. Kawakami, M. Funato, S. Fujita, S. Nakamura, *Appl. Phys. Lett.* **70**, 981 (1997).
16. Y-S. Lin, K-J. Ma, C. Hsu, S-W. Feng, Y-C. Cheng, *Appl. Phys. Lett.* **77**, 2988 (2000).
17. S. J. Pennycook and J. Narayan, *Phys. Rev. Lett.* **54**, 1543 (1985).
18. S. J. Pennycook and D. E. Jesson, *Ultramicroscopy* **37**, 14 (1991).
19. D. J. Eaglesham and M. Cerullo, *Phys. Rev. Lett.* **64**, 1943 (1990).
20. S. Oktyabrsky, H. Wu, R. D. Vispute, and J. Narayan, *Phil. Mag.* **A71**, 537 (1995).
21. D. E. Jesson, K. M. Chen, S. J. Pennycook, T. Thundat and R. J. Warmack, *Phys. Rev. Lett* **77**, 1330 (1996).
22. R. J. Asaro and W. A. Tiller, *Metall. Trans.* **3**, 1789 (1972).
23. J. K. Lee, *Int. Mater. Rev.* **43**, 221 (1997).
24. N. P. Kobayashi, T. R. Ramchandran, P. Chen, and A. Madhukar, *Appl. Phys Lett.* **68**, 3299 (1996).

## Efficient GaN-based Micro-LED Arrays

H.W. Choi, C.W. Jeon, M.D. Dawson, P.R. Edwards<sup>1</sup> and R.W. Martin<sup>1</sup>  
Institute of Photonics, University of Strathclyde, Glasgow G4 0NW, UK  
<sup>1</sup> Department of Physics, University of Strathclyde, Glasgow G4 0NG, UK

### ABSTRACT

Highly efficient, two-dimensional arrays of parallel-addressed InGaN blue micro-LEDs with individual element diameters of 8, 12 and 20  $\mu\text{m}$  have been fabricated. In order to overcome the difficulty of interconnecting multiple device elements with sufficient step-height coverage for contact metallisation, a novel scheme involving the etching of sloped-sidewalls has been developed. The devices have I-V characteristics similar to those of broad-area reference LEDs fabricated from the same wafer, and give superior (3mW) light output in the forward direction to the reference LEDs, despite much lower active area. The external efficiencies of the micro-LED arrays improve as the dimensions of the individual elements are scaled down. This is attributed to scattering at the etched sidewalls of in-plane propagating photons into the forward direction.

### INTRODUCTION

As GaN-based light-emitting diode (LED) technology grows in maturity, the focus of many research groups has shifted towards the fabrication of higher power and higher efficiency LEDs. The improvement of output power to date from these devices has been achieved via a number of techniques, including optimisation of epitaxy and processing [1], improved current spreading [2] or through resonant cavity structures [3]. The overall performance of such LEDs is, in addition, strongly dependent on the extraction efficiency of the devices. Due to total internal reflections occurring at the LED-ambient interface, as much as several tens percent of the light emitted from the active region may be confined within the device. In the case of InGaN/GaN LEDs, the novel approaches adopted to allow more light to be extracted include formation by etching of microdisks within the LEDs, to increase the overall surface area [4]. In this manner, apart from benefitting from an enhanced level of light extraction, an enhancement of quantum efficiency was also reported, attributed to micro-size effects as well as to a more efficient usage of the injected current.

We investigate here further development of the pattern-etching approach, where arrays of isolated pillar-like micro-size LEDs are formed, sharing a common broad-area metallisation. We use the term "parallel-addressed" micro-LEDs for this type of device. They offer enhancement in surface area to volume ratio, and ready flexibility in number and size of emitting elements. We report on the fabrication of these devices and on their performance compared to conventional broad-area LED's fabricated from the same wafer. The major issue involved in the fabrication is the interconnection of each individual element, via metallization, as a result of the non-planar device topology. In order to overcome this difficulty involving metal step-height coverage, the sidewalls of the micro-LEDs are made to be non-vertical.

**Table I.** Summary of device information and characteristics

Elemental diameter ( $\mu\text{m}$ )	Chip area ( $\mu\text{m}^2$ )	Number of elements	Total active area ( $\mu\text{m}^2$ )	Turn-on voltage (Volts)	Operation voltage @20mA
8	240000	625 (25x25)	31416	7.62	7.48
12	240000	400 (20x20)	45239	4.64	4.60
20	240000	256 (16x16)	80425	3.12	3.49
Broad Area	240000	1	160000	3.42	3.80

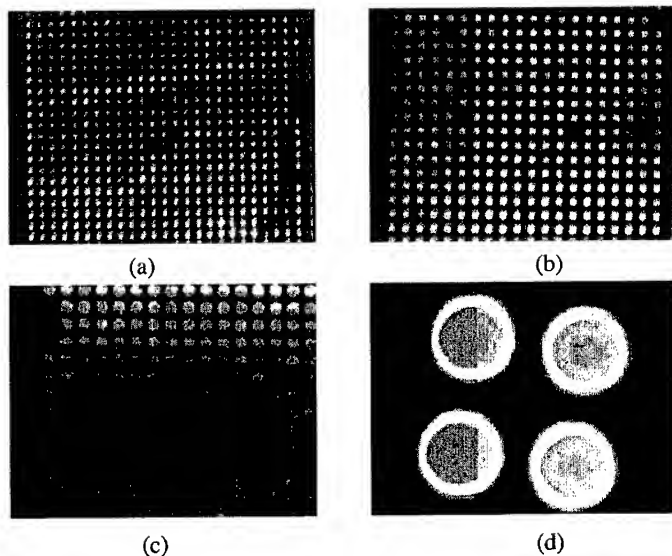
## DEVICE FABRICATION

The micro- and broad area- devices are fabricated on an LED wafer grown on the c-plane of a sapphire substrate. The LED structure consists of a 25 nm GaN buffer layer, 3.2  $\mu\text{m}$  of Si-doped GaN, a 3-period InGaN/GaN multi-quantum well (MQW) for emission at  $\sim 470\text{nm}$ , topped with a 0.25  $\mu\text{m}$  Mg-doped GaN epi-layer. Activation of the Mg dopant was carried out by rapid thermal annealing (RTA) at  $950^\circ\text{C}$  for 30sec in a  $\text{N}_2$  ambient. Processing of the devices begins with the formation of mesa structures using inductively-coupled plasma (ICP) dry etching. The plasma comprised 30 sccm of  $\text{Cl}_2$  and 10 sccm of Ar at a process temperature and pressure of  $25^\circ\text{C}$  and 20mTorr, respectively. Operating parameters were 400W of ICP power and 200W of RIE power, yielding a dc bias voltage of 650V and an etch rate of more than 0.5  $\mu\text{m}/\text{min}$ . An additional masking step was needed to form the pillar-like structure of the individual micro-LED elements, whose diameters ranged from 8 to 20 $\mu\text{m}$ , respectively, for a series of processed samples. In order to achieve non-vertical sidewalls, an anisotropic etch recipe has been employed. The sidewalls can be made to have an inclination of  $30^\circ$  to the vertical, which allows for conformal metal step-coverage of up to 3 $\mu\text{m}$ .

Prior to metal deposition, a 40nm-thick  $\text{SiO}_2$  layer was deposited onto the sample by electron-beam deposition, which acts as an isolation layer. Finally, the metal layers, including the spreading and pad layers, were deposited by electron-beam evaporation patterned by a lift-off procedure. The choice of metal is Ti/Al (20/200nm) for the n-contact pad and Ni/Au (30/30nm for spreading, 20/200nm for pad) for the p-contact. A pre-metallisation HCl treatment was applied, and the contacts were alloyed by rapid thermal annealing in air for 5 min at  $550^\circ\text{C}$ . The I-V characteristics of the devices were measured with an HP4145 parametric analyser, whilst the room-temperature electroluminescence (EL) data were collected with a coupled spectrometer and cooled charge coupled device (CCD) detection system (0.4nm resolution). The light output power measurements were performed using a calibrated power meter with the Si detector (detector area  $3\times 3\text{mm}^2$ ) approximately 8mm above the device, collecting light emitted in the forward direction. An electron microprobe system was used for cathodoluminescence studies.

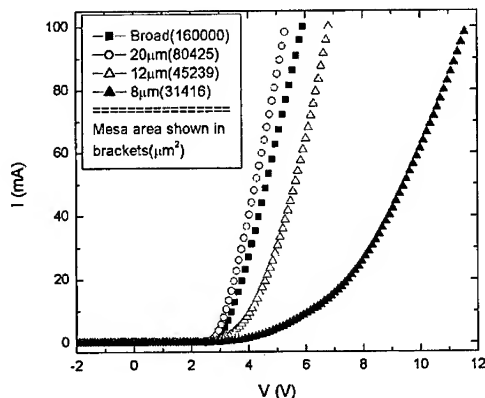
## RESULTS AND DISCUSSION

Figure 1 shows optical microscope images of operating device arrays of individual element size 8 $\mu\text{m}$ , 12 $\mu\text{m}$  and 20 $\mu\text{m}$ , respectively (Fig.1 (a)-(c)), and also a



**Figure 1.** Optical microscope images of operating arrays of (a) 8 $\mu\text{m}$ , (b) 12 $\mu\text{m}$  and (c) 20 $\mu\text{m}$  element diameter, and (d) optical image of cathodoluminescence under broad-beam excitation of a cluster of four 12 $\mu\text{m}$  micro-LED elements.

optical image, referred to later, of a cluster of four of the 12 $\mu\text{m}$  devices excited under broad-area electron beam excitation (Fig.1(d)). The I-V curves (Figure 2) for the micro-LED arrays and reference broad-area LEDs show that the turn-on and operating voltages increase as the size of the micro-LEDs are reduced. These values are summarized in Table I, as are the respective element diameters and quantities, overall areas of the respective chips and their respective total active areas. As the current spreading layer in each case covers the entire micro-LED array, a smaller element will also have a smaller contact area. The contact resistance is sensitive to the actual contact area [5], which is the most likely explanation of higher voltage drops developed across the p-contact as the dimensions of the micro-LEDs are scaled down.



**Figure 2.** I-V characteristics of micro-LEDs compared to a macro-LED.

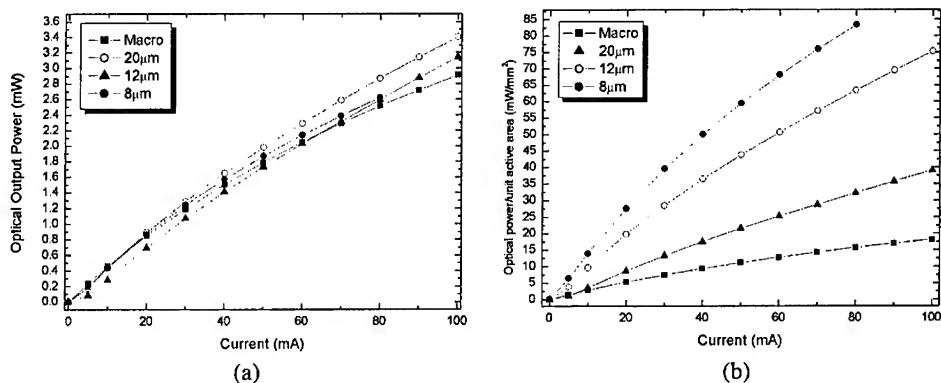


**Figure 3.** (a) L-I plots of micro-LED devices, and (b) active-area-normalized L-I plots for comparison between the external efficiencies of micro-LEDs with different dimensions.

The optical output power characteristics of the micro-LEDs (measured in the forward direction, and note that the chips are unencapsulated) as a function of current are plotted in Figure 3(a). In passing, we note that the gradient of the broad-area LED plot decreases at a slightly faster rate than the micro-LEDs at higher injection currents, implying that the greater surface area of micro-LEDs offers some improvement in heat dissipation. While the different devices appear to emit similar amounts of light, their total active emission area varies greatly (Table 1). For comparison purposes, the light output powers are normalized to their respective total active areas, and are re-plotted in Figure 3(b). The effect of scaling down the size of the individual elements becomes immediately apparent, with the highest power density of emission coming from the smallest devices, despite their suffering some degradation in electrical characteristics.

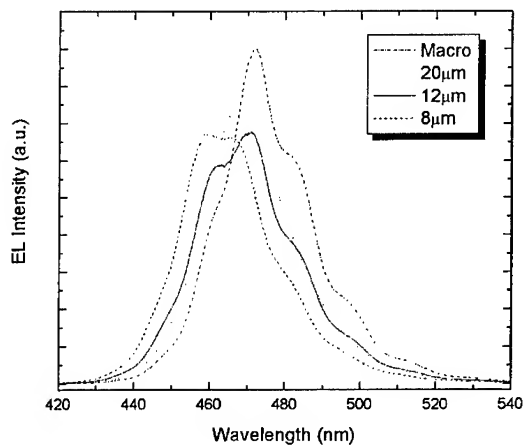


**Figure 4.** EL spectra of the respective devices operated at 10mA.

The light output of the devices is seen to be a strong function of the pillar size. In the recent literature, the mechanism of such enhancements in related structures has been attributed to various sources. Dai et al. [6] proposed an enhancement of internal quantum efficiency in InGaN micro-LEDs due to partial strain relaxation in the microstructures. However, in a Raman study carried out by F. Demangeot et al. [7] on reactive-ion etched (non-device) GaN pillars, the observation of strain relief was shown to be limited to sub-micron structures, which are of smaller scale than the microstructures in [6] and those considered here. Thus, an increase in light extraction efficiency appears to be the more likely cause. However, the exact mechanism is unclear from the earlier reports, particularly as the increased light output emitted in the forward direction is unaccounted for.

A detailed investigations of this increase in efficiency will be reported elsewhere [8]. In short, we attribute a major cause as being the scattering of in-plane propagating light at the etched sidewalls into the forward direction. Strong evidence for this is provided by optical images of cathodoluminescence taken under broad-area e-beam excitation (Fig.1(d)), which show a bright ring of light at the periphery of each element. A contribution to this scattering may be attributed to resonant modes [9,10] supported by the micro-disk geometry, whose presence is inferred from our analysis [8] of the substructure of the electroluminescence spectral data (Fig.4) and our previous work [11]. Further contributions to the increase in extraction efficiency include reduced absorption in the semiconductor material. Since photons in micro-LEDs may travel shorter distances before escaping from the mesa, the likelihood of (re)absorption is also reduced. The absorption coefficient of GaN at 470nm is reported [12] to be approximately  $10^3 \text{ cm}^{-1}$ , which correspond to an absorption length of  $\sim 10\mu\text{m}$ . Consequently, we can expect lower absorption in micro-LEDs, particularly those with radius of less than  $10\mu\text{m}$ .

## CONCLUSION

In summary, high-performance InGaN parallel-addressed micro-LED arrays have been fabricated and characterised. The basis of the fabrication procedure is the formation of sloped sidewalls, which allows the individual elements of the device to be straightforwardly interconnected (for addressing in parallel) via metallisation. Whilst the I-V characteristics of the micro-LEDs suffer minor degradation as they are scaled down in size, the devices offer superior extraction of output power in the forward direction as a result of increased surface area and surface scattering.

## REFERENCES

1. S. Nakamura, M. Senoh, S. Nagahama, N. Iwasa, T. Yamada, T. Matsushita, H. Kiyoyoku and Y. Sugimoto, "InGaN-based multi-quantum-well-structure laser diodes", *Jpn. J. Appl. Phys.* **35**, pp.L74-L76, 1996.
2. S.R. Jeon, Y.H. Song, H.J. Jang, G.Y. Yang, S.W. Hwang and S.J. Son, "Lateral current spreading in GaN-based light-emitting diodes utilizing tunnel contact junctions", *Appl. Phys. Lett.* **78**, pp.3265-3267, 2001.
3. M. Diagne, Y. He, E. Makarona, A.V. Nurmikko, J. Han, K.E. Waldrip, J.J. Figiel, T. Takeuchi and M. Krames, "Vertical cavity violet light emitting diode incorporating an aluminum gallium nitride distributed Bragg mirror and a tunnel junction", *Appl. Phys. Lett.* **79**, pp.3720-3722, 2001.

4. S.X. Jin, J. Li, J.Y. Lin and H.X. Jiang, "InGaN/GaN quantum well interconnected microdisk light emitting diodes", *Appl. Phys. Lett.* **77**, pp.3236-3238, 2000.
5. N. Blanc, P. Gueret, P. Buchmann, K. Datwyler and P. Vettiger, "Conductance statistics of small-area ohmic contacts on GaAs", *Appl. Phys. Lett.* **56**, pp.2216-2218, 1990.
6. L. Dai, B. Zhang, J.Y. Lin and H.X. Jiang, "Comparison of optical transitions in InGaN quantum well structures and microdisks", *J. Appl. Phys.* **89**, pp.4951-4954, 2001.
7. F. Demangeot, J. Gleize, J. Frandon, M.A. Renucci, M. Kuball, D. Peyrade, L. Manin-Ferlazzo, Y. Chen and N. Grandjean, "Optical investigation of micrometer and nanometer-size individual GaN pillars fabricated by reactive ion etching", *J. Appl. Phys.* **91**, pp.6520-6523, 2002.
8. H.W. Choi, C.W. Jeon, M.D. Dawson, P.R. Edwards, and R.W. Martin, "Mechanism of enhanced light output efficiency in InGaN-based micro-LEDs", submitted to *J. Appl. Phys.*
9. A. Onischenko and J. Sarma, "Estimation of in-plane superluminescence in vertical-cavity surface-emitting lasers", *IEEE Proc. Optoelectron.* **143**, pp.67-70, 1996.
10. R.A. Mair, K.C. Zeng, J.Y. Lin, H.X. Jiang, B. Zhang, L. Dai, A. Botchkarev, W. Kim, H. Morkoc and M.A. Khan, "Optical modes within III-nitride multiple quantum well microdisk cavities", *Appl. Phys. Lett.* **72**, pp.1530-1532, 1998.
11. K.-S. Kim, P.R. Edwards, H.-S. Kim, R.W. Martin, I.M. Watson, and M.D. Dawson, "Characterisation of optical properties in micro-patterned InGaN quantum wells", *phys. stat. sol (b)*, vol. 228, pp.169-172, 2001.
12. O. Ambacher, W. Rieger, P. Ansmann, H. Angerer, T.D. Moustakas, M. Stutzmann, "Sub-bandgap absorption of gallium nitride determined by photothermal deflection spectroscopy", *Solid State Comms.* **97**, pp.365-370, 1996.

### Growth and Characterization of Deep UV Emitter Structures Grown on Single Crystal Bulk AlN Substrates

X. Hu<sup>1</sup>, R. Gaska<sup>1</sup>, C. Chen<sup>2</sup>, J. Yang<sup>2</sup>, E. Kuokstis<sup>2</sup>, A. Khan<sup>2</sup>, G. Tamulaitis<sup>3,5</sup>, I. Yilmaz<sup>3</sup>, M. S. Shur<sup>3</sup>, J. C. Rojo<sup>4</sup>, L. J. Schowalter<sup>4</sup>

<sup>1</sup>Sensor Electronic Technology, Inc., Latham, NY 12110, U.S.A.

<sup>2</sup>Department of EE, University of South Carolina, Columbia, SC 29208, U.S.A.

<sup>3</sup>Department of ECE and CIE, Rensselaer Polytechnic Institute, Troy, NY 12180, U.S.A.

<sup>4</sup>Crystal IS, Inc., Latham, NY 12110, U.S.A.

<sup>5</sup>IMSAR, Vilnius University, Sauletekio 9-III, Vilnius, Lithuania

#### ABSTRACT

We report on high Al-content AlGa<sub>0.5</sub>N-based deep UV emitter structures grown over single crystal, slightly off c-axis (5.8 degrees) bulk AlN substrates. AlN/AlGa<sub>0.5</sub>N multiple quantum well (MQW) structures with up to 50% of Al in the well material were grown by using low-pressure MOCVD and characterized by using X-ray, AFM, SEM and photoluminescence techniques. Two light sources, one at 213 nm wavelength for selective excitation of quantum well layers and another one at 193 nm to excite both wells and barriers, were exploited. A weak temperature dependence (from 8 K to 300 K) of the luminescence intensity and the absence of blue-shift of the luminescence peak with increasing excitation intensity pointed to a low density of localized states, in a good agreement with the X-ray data, which indicated very high quality of these MQW structures.

The most striking result was observation of stimulated emission at wavelength as short as 258 nm in Al<sub>0.5</sub>Ga<sub>0.5</sub>N/AlN MQWs grown on bulk AlN single crystals.

#### INTRODUCTION

Deep-ultraviolet (UV) emitters have potential applications in chemical and biological agent detection, solid-state lighting, lithography and short range telecommunications. III-nitrides are the most promising candidates for the UV emitters. Penetration deeper into the UV region requires high molar fractions of Al in AlGa<sub>0.5</sub>N structures. However, a higher aluminum content in AlGa<sub>0.5</sub>N layers causes more defects, which result in the emitter performance degradation. These defects are mainly caused by strain induced by the lattice mismatch at the interfaces between the substrate and the epilayers and between the well and barrier materials in multi-quantum well (MQW) structures. In order to reduce the defect formation in these structures several methods such as growing lattice-matched heterostructures with AlInGa<sub>0.5</sub>N compounds and using AlN/AlGa<sub>0.5</sub>N superlattices on c-face sapphire substrate are utilized [1,2]. In this paper, we report on the growth and characterization of structural and optical properties of the AlN/AlGa<sub>0.5</sub>N MQW structures grown on single crystal bulk AlN substrate. Bulk AlN is a perfect candidate as a substrate for III-nitrides due to its structural, thermal and chemical compatibility. Recently, this material has been used as a substrate in deposition of Al<sub>0.5</sub>Ga<sub>0.5</sub>N epilayers of high structural quality [3].

## EXPERIMENTAL DETAILS

AlN/AlGa<sub>N</sub> MQW structures which contain Al<sub>x</sub>Ga<sub>1-x</sub>N wells with the Al- content up to 50% were grown using low-pressure metal-organic chemical vapor deposition (MOCVD). The structures containing three quantum wells were fabricated by depositing 5 nm thick Al<sub>0.5</sub>Ga<sub>0.5</sub>N layers separated by 20 nm wide AlN barriers by using conventional MOCVD. The crystalline quality of these structures was checked by X-ray diffraction. The MQW structure was grown over an AlN epilayer deposited on bulk substrate. Silicon carbide was also used as a substrate to fabricate a sample for comparison by maintaining the same fabrication conditions as for the sample grown on bulk AlN.

The photoluminescence (PL) measurements were performed in two different photoexcitation modes. An ArF excimer laser with pulse duration of 8 ns at 193 nm (6.42 eV) was utilized to excite the carriers not only in the wells but also in the barriers (The bandgap equals 6.2 eV for AlN). In order to generate the carriers only in the quantum wells, the fifth harmonic of Nd:YAG laser radiation with pulse duration of 4 ns at 213 nm is used as a selective excitation source. The laser beam was focused onto the samples to a spot size of  $\approx 0.1$  mm in diameter. The PL spectrum was measured by using TRIAX 550 spectrometer. The spectra in the band-to-band excitation were recorded by using a UV-enhanced CCD camera. A UV enhanced intensified CCD camera was utilized to record spectra under selective excitation. The spectra for stimulated emission were detected from the sample edge along the direction of 30  $\mu$ m wide stripe by using the variable stripe length technique.

## RESULTS AND DISCUSSION

An X-ray rocking curve of the AlN/Al<sub>0.5</sub>Ga<sub>0.5</sub>N MQW structure, which is presented in figure 1, shows that the three quantum wells (see their structure in the insert of figure 1) are crystalline structures of very high quality. The estimated growth defect density in the structures was in the range from  $10^6\text{cm}^{-2}$  to  $10^7\text{cm}^{-2}$ . This is about the three orders of magnitude higher than that in the initial bulk AlN substrates [4] and about the three orders of magnitude lower than that

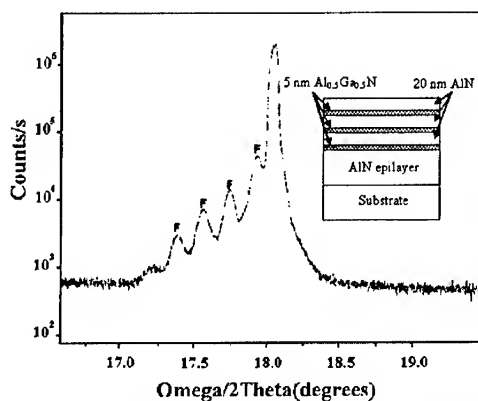
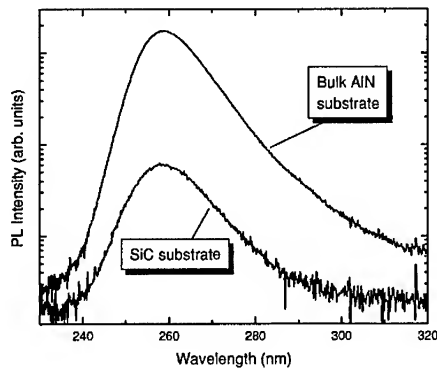


**Figure 1.** X-ray rocking curve of multiple quantum well Al<sub>0.5</sub>Ga<sub>0.5</sub>N/AlN structure depicted in the insert.

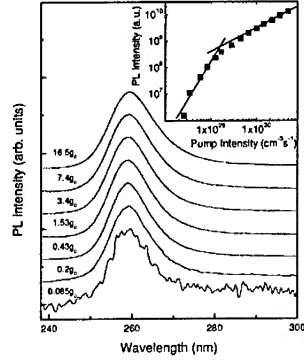
in AlInGaN-based structures grown on sapphire and SiC substrates.

Figure 2 demonstrates that the PL intensity of the structures grown on bulk AlN substrate is higher than that of the identical structure grown on SiC by nearly a factor of 30. This huge enhancement provides strong evidence that bulk AlN substrate makes real difference in the quality of the MQW structures. The high PL intensity of the samples grown on bulk AlN substrate is consistent with the high structural quality evidenced by X-ray diffraction technique.

Figure 3 illustrates the pump intensity dependence of PL spectra of the MQWs under pulsed excitation at 213 nm. The generation rates indicated in figure 3 were estimated according to the measured power densities. The absorption coefficients  $\alpha$  were estimated to be  $1.6 \times 10^5 \text{ cm}^{-1}$  at 213 nm by assuming a square root dependence of  $\alpha$  on quantum energy above the effective band gap energy of 4.43 eV [5]. Initially the PL intensity  $I_{PL}$  increases with increasing pump intensity  $I_p$  approximately as  $I_{PL} \propto I_p^3$  (see insert in figure 3). At elevated excitation intensities, this dependence transforms into a linear dependence  $I_{PL} \propto I_p$  indicating prevalence of band-to-band transitions. The increase of PL intensity as a function  $I_{PL} \propto I_p^3$  is faster than it could be expected for any recombination mechanism in a rectangular quantum well. Thus the carriers are probably confined in a triangular quantum well, which is formed due to piezoelectric field. Screening of the piezoelectric field improves the overlap of wavefunctions of electrons and holes and thus increases the probability of radiative recombination and enhances the growth of luminescence intensity with increasing pump intensity. The PL band shows no significant blue shift with increased pump intensity under selective excitation with low excess energy. Such a shift is a typical feature both in structures with high density of localized states, which are being gradually populated from the lowest to the highest states, and in quantum wells with a triangle shape due to piezoelectric field, which is being screened by increasing density of photoexcited carriers. The absence of a significant blue shift of the PL band indicates that the strain-induced electric field in our structures is relatively small.



**Figure 2.** Room-temperature photoluminescence spectra of identical multiple quantum well structures grown on conventional SiC substrate and on bulk AlN substrate (excitation at 193 nm).



**Figure 3.** The pump intensity dependence of photoluminescence spectra and spectrally integrated intensity (insert) of the MQW under pulsed excitation at 213 nm. The pump intensity is indicated in terms of carrier generation rate  $g_0 = 5.7 \times 10^{29} \text{ cm}^{-3} \text{ s}^{-1}$ .

Figure 4a shows spectra of emission measured from the edge of the sample containing  $\text{Al}_{0.5}\text{Ga}_{0.5}\text{N}/\text{AlN}$  quantum wells on bulk AlN. Stripes of 30  $\mu\text{m}$  in width and with different lengths from 400 to 700  $\mu\text{m}$  were excited at the sample edge to a power density of  $7.5 \text{ MWcm}^{-2}$ . The evolution the spectrum with increasing pump intensity at the stripe length fixed at 420  $\mu\text{m}$  is presented in figure 4b.

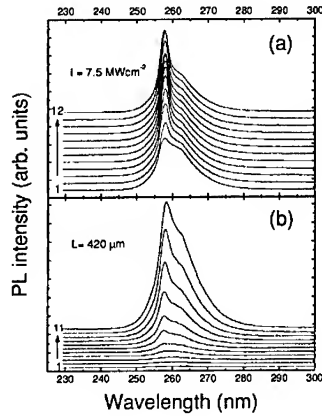


**Figure 4.** Photoluminescence spectra of edge emission at different stripe lengths  $L$  ( $\mu\text{m}$ ): 1  $\rightarrow$  12; 400, 420, 440, 460, 480, 500, 520, 550, 560, 600, 650, 700 (a), and pump intensities  $I$  ( $\text{MWcm}^{-2}$ ): 1  $\rightarrow$  11; 0.25, 0.38, 0.50, 0.75, 1.1, 1.9, 2.8, 4.1, 6.0, 8.7, 12.4 (b) from  $\text{Al}_{0.5}\text{Ga}_{0.5}\text{N}/\text{AlN}$  quantum wells on bulk AlN under pulsed excitation at 213 nm. The spectra were measured from sample edge along the direction of a 30  $\mu\text{m}$  wide excited stripe. The base lines of the spectra are vertically shifted.

The most striking feature is the appearance of a new, narrow band at 258 nm when the stripe length or pump intensity is increased. A superlinear increase of this band with increasing pump intensity and exponential dependence of its intensity on the stripe length prove the stimulated origin of the emission responsible for this narrow band. Meanwhile the background of spontaneous emission resulting in the broad band in the spectrum is very strong in this sample.

The spontaneous luminescence dominates over the stimulated emission at short stripe lengths and makes application of variable stripe length method to reveal the gain spectrum very difficult. Thus, we estimated the value of gain coefficient  $g$  from the observed saturation effect, which occurs at the stripe length  $L$  of approximately 500  $\mu\text{m}$ . An assumption that (as in most other semiconductors) the stimulated emission saturates at  $gL \approx 5$ , gives the value of 100  $\text{cm}^{-1}$  as an estimate for the observed gain coefficient. The value of the gain coefficient might probably be enhanced by improving the fabrication technology. The stimulated emission at the wavelength as short as 258 nm evidences a strong potential of growing high aluminum content MQWs with AlN barriers on bulk AlN substrates for laser diodes in deep UV region.

## CONCLUSIONS

X-ray analysis and photoluminescence spectroscopy confirm high quality of MQW structures consisting of  $\text{Al}_{0.5}\text{Ga}_{0.5}\text{N}$  wells and AlN barrier layers deposited on AlN single crystal substrates. The homoepitaxial growth of AlN epilayers on bulk AlN substrates allows us to avoid lattice mismatch and many resulting structural defects in subsequent multiple layers. Stimulated emission at 258 nm was observed and demonstrates good prospective for this approach in production of UV lasers based on heterostructures with high aluminum content.

## ACKNOWLEDGMENTS

This work has been partially supported by ARO, ONR and MDA (formerly BMDO). The authors would gratefully like to acknowledge the support of our contract monitors Dr. Bill Clark, C.E.C. Wood (ONR) and Dr. C. Litton (AFRL). The work at RPI was supported by DARPA (Project Monitor Dr. J. Carrano).

## REFERENCES

1. M. Asif Khan, J. W. Yang, G. Simin, R. Gaska, M. S. Shur, H.-C. zur Loye, G. Tamulaitis, A. Zukauskas, D. J. Smith, D. Chandrasekhar, and R. Bicknell-Tassius, *Appl. Phys. Lett.* **76**, 1161 (2000).
2. J. P. Zhang, H. M. Wang, M. E. Gaevski, C. Q. Chen, Q. Fareed, J. W. Yang, G. Simin, and M. Asif Khan, *Appl. Phys. Lett.* **80**, 3542 (2002).
3. L. J. Schowalter, Y. Shusterman, R. Wang, I. Bhat, G. Arunmozhi, and G. A. Slack, *Appl. Phys. Lett.* **76**, 985 (2000); J.C. Rojo, L.J. Schowalter, R. Gaska, M. S. Shur, M.A. Khan, J. Yang, D.D. Koleske, *J. Cryst. Growth* **240**, 508 (2002).
4. J. C. Rojo, G. A. Slack, K. Morgan, B. Raghothamachar, M. Dudley, and L. J. Schowalter, *J. Cryst. Growth* **231**, 317 (2001).
5. D. Brunner, H. Angerer, E. Bustarret, F. Freudenberger, R. Höppler, R. Dimitrov, O. Ambacher, and M. Stutzmann, *J. Appl. Phys.* **82**, 5090 (1997)

## Deposition of GaN Films on Glass Substrate and Its Application to UV Electroluminescent Devices

Tohru HONDA, Kenichi IGA and Hideo KAWANISHI

*Department of Electronic Engineering, Kohgakuin University, 2665-1 Nakano-machi, Hachiohji, Tokyo 192-0015, JAPAN*

Takahiro SAKAGUCHI and Fumio KOYAMA

*P&I Lab., Tokyo Institute of Technology, 4259 Nagatsuta, Midori-ku, Yokohama 226-8503, JAPAN*

### Abstract

GaN films were deposited on glass substrates using a compound-source molecular beam epitaxy technique. Electroluminescent devices with a double-insulator structure were also fabricated using the deposited films. When the devices were operated using a sine-wave voltage, one of the emission peaks was located in the UV spectral region. Introducing a small ammonia flow increased the deposition rate.

### 1. Introduction

Deposition of GaN at lower substrate temperature than 600 °C is suitable for the application to low-cost and large-area light emitting devices such as flat display panels [1] or photo detectors [2]. Nevertheless synthesis of GaN required higher deposition temperatures than 700 °C [3], we consider that low substrate temperature will be realized using GaN powder as a source material and its sublimation [4]. The sublimation of GaN has already been reported [5]. However, hydrogen atoms remained in the GaN powder act as transport assistance during the sublimation. The quantity of remained hydrogen atoms is decreased during the deposition. Thus the sublimation rate is decreased during the sublimation [6]. It is not suitable for the fabrication of light emitting devices, because the deposition rate and quality of deposited films is changed during the deposition. To obtain the constant deposition rate, GaN source powders were pre-annealed in vacuum before the deposition. Although the deposition using compound source molecular beam epitaxy (CS-MBE) technique and no additional nitrogen source was performed, the layers deposited at room temperature were Ga-rich amorphous GaN. The N/Ga ratio in the film was able to control by changing the substrate temperature [7].

Although the control of substrate temperature is effective to obtain high light intensity of photoluminescence spectra, the deposition rate was decreased as increasing the substrate temperature, because of the re-evaporation of Ga metal in the surface. The low deposition rate of 80 nm/h is not enough to the device fabrication. In this paper, the fabrication of electroluminescent devices (ELDs) using deposited GaN films at the substrate temperature of 450 °C is reported. The introduction of ammonia during the growth is discussed in the view of deposition rate and optical properties.

## 2. Deposition of GaN films

For the deposition, GaN powder (5N) was used as the source material. This GaN, which was synthesized from Ga metal and ammonia, was kept at 960 °C in a Knudsen cell (K-cell) during the deposition. Because it contained hydrogen, the source was annealed in vacuum at 900°C for more than 10 hours to reduce the hydrogen contamination. The GaN powder was yellow before annealing, but became white after annealing. Ammonia was supplied during film deposition, at a flow rate of less than 0.1 sccm. SiO<sub>2</sub>-fused glass substrates were used for the deposition. The substrate temperatures were varied from RT to 500°C, respectively. The back of the substrates was coated with indium to obtain uniform substrate temperature. The N/Ga ratio was estimated from Auger electron spectroscopy (AES) spectra. The atomic concentrations of N and Ga on the surface were estimated using AES peak-to-peak widths and sensitivity parameters. All deposited films were Ga-rich, that was estimated using the N/Ga ratio of GaN deposited by metal-organic vapor phase epitaxy (MOVPE). Although the N/Ga ratio does not perfectly reflect the stoichiometry in the layers, it is a very valuable parameter that reflects the nitrogen concentration in the layers.

## 3. Fabrication of electroluminescent devices

The ELDs were fabricated using a-GaN as the emission layer deposited at RT and 450 °C with no additional nitrogen sources. ELDs were fabricated using a-GaN as emitting layers. Double insulators were adopted for the device structure [1]. The

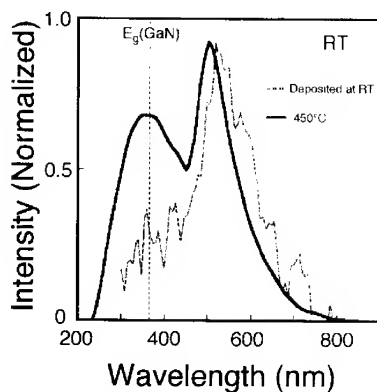


Fig. 1 Electroluminescent spectra of GaN-based ELDs. GaN films were deposited at different substrate temperatures.

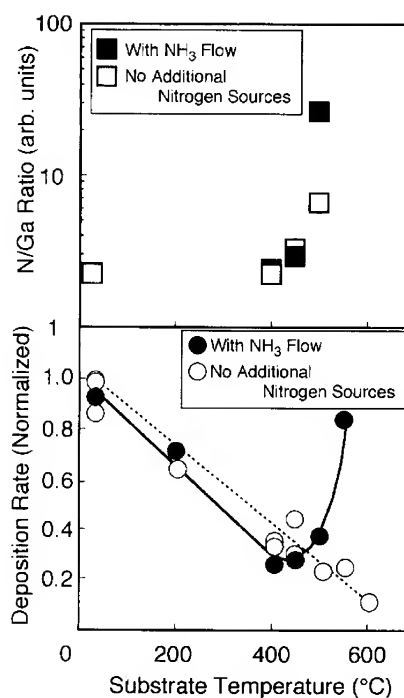


Fig. 2 The N/Ga ratio and normalized deposition rate of GaN films deposited at different substrate temperatures.

BEST AVAILABLE COPY

structure of the ELDs is like a capacitor. The devices were operated under the driving conditions of a sine wave, a maximum applied voltage of 80 V, and a frequency of 0.9 kHz.

The electroluminescent (EL) spectra of the ELDs using a-GaN as the emission layer deposited at the substrate temperatures of RT and 450 °C are shown in Fig. 1. The EL spectra at room temperature were detected using a multichannel spectrometer, with accumulation time of 500 seconds. The UV emission peak was observed from the devices deposited at 450 °C, although no UV peaks were observed from that deposited at RT. The spectral different of the samples between deposited at RT and 450 °C is due to the N/Ga ratio in the deposited layers.

#### 4. Deposition rate and ammonia flow

The thickness of deposited layers depends on the substrate temperature during the deposition, as shown in Fig. 2 (open circles). On the other hand, the N/Ga ratio of deposited layers increased with increasing the substrate temperature due to the re-evaporation of excess Ga metal on the surface of substrates. In order to increase the deposition rate, it is effective to take the excess Ga metal in the films by reaction with a nitrogen source. Thus a small amount of ammonia gas was introduced during film deposition. The deposition rate was increased upon introducing the ammonia flow at a substrate temperature higher than 400 °C, due to the catalytic reaction between Ga metal and ammonia [8]. The N/Ga ratio was also increased upon introducing the ammonia flow.

### 5. Discussion

#### 4-1 Electroluminescent devices

The spectrum of the device deposited at 450 °C consisted of 360 nm (UV) and 550 nm (visible) peaks. Although the origins of these emissions are unclear at present, the 550 nm emission peak tends to increase gradually with operation time. The emission peak at 360 nm is very interesting, because part of the emission energy is higher than the band-gap energy of the hexagonal GaN crystal. We consider that some clusters are formed in the a-GaN films and that the UV peak is related to the bond-gap energies of the clusters, because the bond-gap energy is higher than the band-gap energy of its crystal [8]. The lifetime of the device deposited at 450 °C was several minutes, which was longer than that deposited at RT (a few seconds). Although comparison of the intensities is impossible because of their lifetime, the emission intensity of the device deposited at 450 °C

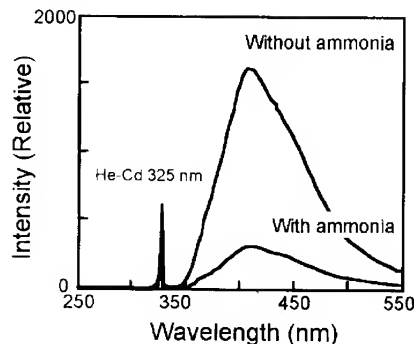


Fig. 3 Photoluminescence spectra of GaN films deposited with and without ammonia flow.

**BEST AVAILABLE COPY**

looks like stronger than that deposited at room temperature.

The high N/Ga ratio of deposited films indicates the close to the stoichiometry. The vapor pressure of Ga is higher than that of nitrogen under a Ga-rich condition [9]. Increase of substrate temperature and additional ammonia flow are effective to recover the stoichiometry of the deposited films, which lead to the increase of the UV emission peak.

#### *4-2 Deposition rate and ammonia flow*

The UV emission peak was observed from the a-GaN-based ELD under sine-wave operation. Because its structure is simple and a glass substrate can be used, the a-GaN-based ELD is a suitable light emitter for light-emitting systems requiring large-area, low cost fabrication, such as flat displays. For this application, a high deposition rate is required. However, the deposition rate in the CS-MBE technique using GaN powder with no additional gas is around 0.3  $\mu\text{m/h}$ . In this study, it is clarified that the introduction of a small amount of ammonia is effective for the realization of a high deposition rate. However, the introduction of ammonia affects the intensity of photoluminescence spectra shown in Fig 4. The intensity is decreased as introducing the ammonia flow. It indicates that the hydrogen involved in the film increases some non-radiative centers.

#### **Summary**

GaN films were deposited by the CS-MBE technique. Using the deposited GaN films, ELDs were fabricated. The UV emission peak was observed from the ELDs under sine-wave operation at room temperature, although the visible emission was also observed. Increase of substrate temperature, which leads to improvement of the N/Ga ratio, is effective to obtain the UV emission. Introduction of ammonia during the deposition also improved the N/Ga ratio. The results indicate that these GaN films are one of the suitable light-emitting materials for the light emitting devices, such as flat display panels.

#### **References**

- [1] T. HONDA, K. MAKI and H. KAWANISHI, IPAP Conf. Series **1**, 644 (2000).
- [2] S. YAGI, Jpn. J. Appl. Phys. **38**, L792 (1999).
- [3] H. TAMPO, H. ASAH, M. HIROKI, Y. IMANISHI, K. ASAMI and S. GONDA, J. Cryst. Growth **189/190**, 218 (1998).
- [4] T. HONDA, K. SATO, T. HASHIMOTO, M. SHINOHARA and H. KAWANISHI, Phys. Stat. Sol. **188**, 587 (2001).
- [5] S. KURAI, Y. NAOI, T. ABE, S. OHMI and S. SAKAI, Jpn. J. Appl. Phys. **35**, L77 (1996).
- [6] K. NISHINO and S. SAKAI, Gallium Nitride and Related Semiconductors, eds. J. H. Edgar, S. Stride, I. Akasaki, H. Amano and C. Wetzel, INSPEC, London 1999 (p 367).
- [7] T. HONDA, Y. INAO, K. KONNO, K. MINEO, S. KUMABE and H. KAWANISHI, Phys. Stat. Sol., in press.
- [8] M. KAMP, M. MAYER, A. PELEZMANN and K. J. EBEILING, Mat. Res. Soc. Symp. Proc. **449**, 191 (1997).
- [9] W. A. HARRISON, *Electronic Structure and The Properties of Solids* (Dover, New York, 1989) p. 66.
- [10] A. KOUKITU and H. SEKI, Jpn. J. Appl. Phys. **36**, L750 (1997).

**BEST AVAILABLE COPY**

### GROWTH AND FABRICATION OF HIGH REVERSE BREAKDOWN HETEROJUNCTION n-GaN: p- 6H-SiC DIODES

A.V. Sampath, A. Bhattacharyya, R. Singh, C.R. Eddy, P. Lamarre\*, W.F. Stacey\*, R.S. Morris\*, T.D. Moustakas  
ECE Department, Boston University, 8. St. Mary's Street, Boston MA, 02215

\*Viatronix Inc., 40 Amherst Avenue, Waltham, MA 02451

#### ABSTRACT

Wide band gap semiconductors are attractive for developing high power switching devices because of their ability to operate at both higher temperatures as well as higher frequencies than conventional Si. In this paper we report on the growth and fabrication of GaN/SiC np heterojunction diodes by depositing Si doped n-GaN films by plasma-assisted molecular beam epitaxy directly on SiC without the use of GaN or AlN buffers. Careful ex-situ and in-situ preparation of the Si terminated 6H- SiC surface was necessary to produce high quality diodes. Vertical circular diodes were fabricated with sizes varying from 200 microns to 1mm in diameter. Mesas were formed by ICP etching of the MBE deposited n- GaN layer using Cl<sub>2</sub>. A Ti/Al/Ni/Au metal stack was employed as an n-ohmic contact to the GaN layer and an Al/Ti/Au metal stack was employed as a backside p-ohmic contact to the 6H- SiC layer. The diodes were characterized by I-V and C-V measurements. The 1 mm diameter diodes exhibited almost ideal behavior under forward bias with an ideality factor of 1.6, and a reverse saturation current of 10-19 A/cm<sup>2</sup>. Under reverse bias, these devices were driven up to 1000 V with a measured leakage current of 5x 10<sup>-7</sup> A. and a dynamic resistance varying from 1010 to 109 ohms with increasing reverse bias. The built-in potential in these n-p heterojunctions was determined from C-V measurements to be 2.25 V. From these values we determined that the heterojunction is of Type II with conduction and valence bands offsets calculated to be 0.65 and 1.1 eV respectively.

#### INTRODUCTION

The III-Nitrides are an attractive family of semiconductors for the development of high power electronic devices due to the high breakdown fields and large saturation velocities found in these materials. However, these films are generally deposited on sapphire or 6H-SiC substrates due to the lack of a readily available and large area GaN substrates. 6H SiC substrates are advantageous for the growth of III-Nitrides power electronic devices due to their small lattice mismatch with GaN, ~ 4%, and high thermal and electrical conductivity. As a result, these devices can be fabricated as vertical diodes in contrast to the case of a GaN homojunction deposited on c-plane sapphire. Torkiv et al have reported on GaN/SiC n-p heterojunctions fabricated by depositing n-GaN by molecular beam epitaxy (MBE) directly on 6H-SiC substrates [1]. The authors demonstrated 100x100 mm area diodes with nearly ideal forward IV characteristics,  $h = 1.2$ , and low reverse saturation current,  $I_{sat} = 10^{-32}$  A/cm<sup>2</sup> but high reverse leakage currents  $\sim 5 \times 10^{-8}$  A/cm<sup>2</sup> at -10V. Danielsson et al reported on similar diodes fabricated by depositing n-GaN by hydride vapor phase epitaxy (HVPE) on p-p 4H-SiC substrates [2]. These devices showed greatly reduced reverse leakage current of  $\sim 5 \times 10^{-9}$  A/cm<sup>2</sup> at -200V bias

for a 196 mm diameter diode. In addition, the authors determined that the heterojunction has a type II band alignment that should suppress minority carrier injection.

In this paper we report on the fabrication of GaN/SiC np heterojunctions having a high reverse breakdown voltage that are fabricated by depositing n-GaN by molecular beam epitaxy directly on a p-p 6H-SiC substrate.

## EXPERIMENTAL METHODS

The Si doped n-GaN films were deposited by plasma assisted molecular beam epitaxy (PA-MBE) using a Varian GenII MBE system. Active nitrogen was supplied by an ASTeX compact ECR source. All of the films were deposited on 6H-SiC substrates acquired from Cree Inc. consisting of a 13 mm thick p-SiC epitaxial layer (doped  $1 \times 10^{16} \text{ cm}^{-3}$ ) deposited on a 405 mm thick p-type SiC substrate polished  $3^\circ$  off Si-face. The n-GaN films epitaxial films were grown at a substrate temperature of  $750^\circ\text{C}$  using a 100W microwave plasma and a  $\text{N}_2$  flow rate of 10 sccm. The epi-layers were deposited directly on the SiC substrates without the use of a buffer layer [3] by initially covering the substrate surface with Ga metal while at the growth temperature and subsequently initiating epitaxial growth.

Discrete circular devices with diameters varying from 100  $\mu\text{m}$  to 1 mm were fabricated by etching away the MBE deposited n-GaN layer by inductive coupled plasma etching (ICP). This layer was etched at a rate of  $\sim 180 \text{ nm/min}$  using a  $\text{Cl}_2$  plasma with a forward power of 350W and a DC bias of  $-900 \text{ V}$ . The p+-SiC ohmic contact consisted of a Al/Ti/Au (50/50/300 nm) stack e-beam deposited on the backside of the substrate. The n+-GaN ohmic contact consisted of an e-beam deposited Ti/Al/Ni/Au (20/50/20/200 nm) stack that was lift-off using standard lithographic techniques.

The forward bias I-V characteristics of the fabricated devices were measured using a Hewlett Packard 4155A Semiconductor Parameter Analyzer. The reverse bias I-V characteristics were investigated using a high voltage power supply as a voltage source, a HP 34401A voltmeter to measure the voltage output of the supply and a HP 3457A picoammeter to measure the current through the diode. A 10 MW resistor was placed in series with the diode to current limit the device. C-V measurements were performed using a Hewlett Packard 4284 LCR meter using an AC frequency of 1MHz and a signal voltage of 0.1 V.

## RESULTS AND DISCUSSION

Figure 1. shows a typical IV characteristic of a 1mm diameter diode. These devices were driven to a reverse bias of 830 V without observing the onset of breakdown. This is consistent with the theoretically expected breakdown of this junction that should occur by avalanche at reverse biases in excess of 1000V based on the calculated avalanche break-down voltage (BVPP) and depletion width at breakdown for the p-- 6H-SiC layer given by Chow and coworkers [4]. In addition, these diodes were found to have a differential resistance of  $1010 \text{ W}$  at biases below 700V that is comparable to what has been reported for other GaN based homojunctions at zero bias.

**BEST AVAILABLE COPY**

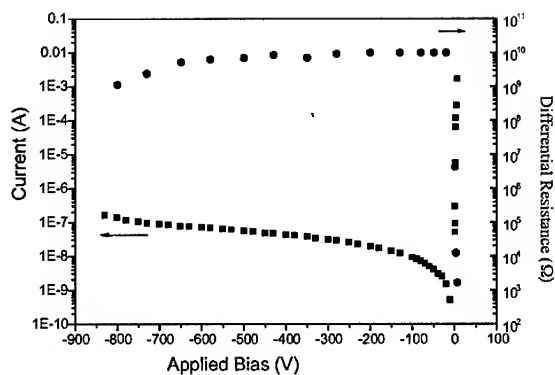


Figure 1. IV characteristics of a GaN/SiC np heterojunction. Reverse breakdown occurs at over 830V. Nearly constant differential resistance is observed for bias less than 700V.

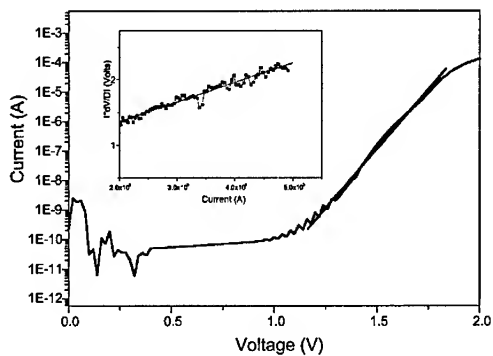
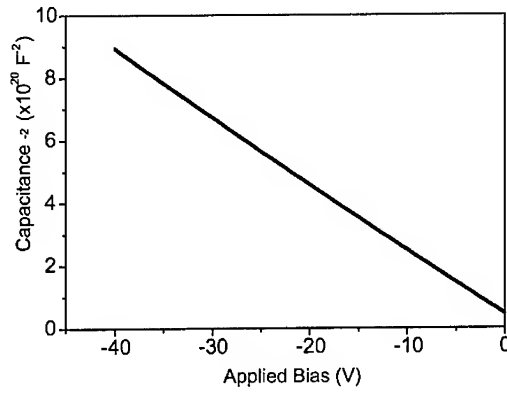


Figure 2. Forward IV characteristics of 1 mm diameter GaN/SiC np heterojunction. The insert shows a plot of  $I \cdot dV/dI$  vs.  $I$  for the 1 mm diameter heterojunction. The slope of the plot is the on-state resistance ( $R_{on}$ ) of the diode.

The forward IV characteristic of a 1 mm diameter diode is shown in Figure 2. Under forward bias, these diodes show nearly ideal behavior over 5 decades in current and the calculated ideality factor and reverse saturation current were 1.6 and  $3.9 \times 10^{-19}$  A/cm<sup>2</sup>. However, a large on-state series resistance ( $R_{on}$ ) of  $\sim 297$   $\Omega$  was extrapolated from a plot of  $I \, dV/dI$  vs.  $I$  for these diodes (inset of Figure 2). Possible sources for this resistance include the bulk p-type SiC substrate as well as the ohmic contacts to the p-SiC and n-GaN layers. Based on specifications provided by Cree Inc, we calculated the contribution of the substrate to be  $\sim 0.5$   $\Omega$ . As a result, we conclude that the metal contacts are primarily responsible for the large on-state resistance. Since no annealing was performed on these devices, it is likely that the series resistance of both contacts can be improved through refinement of the processing.



**Figure 3.** Plot of  $1/C^2$  vs.  $V$  for 1mm diameter GaN/SiC np heterojunction.  $V_{bi} = 2.2$  V and  $p = 1.2 \times 10^{16}$  cm<sup>-3</sup> extrapolated from the linear plot.

The quality of the diodes was investigated by C-V measurements and a typical  $1/C^2$  vs.  $V$  plot is shown in Figure 3. A linear dependence was observed for reverse bias up to 40V. The doping of the epitaxial p-SiC layer was determined to be  $1.2 \times 10^{16}$  cm<sup>-3</sup> from the slope of the plot that agrees well with the specifications provided by Cree Inc. In addition, the extrapolated built in voltage ( $V_{bi}$ ) for the diode was determined to be 2.2V that agrees well with theoretical calculations as well as experimental results that have been reported in the literature [1].

Using the following expressions given by Sze [5], the band offsets and the type of heterojunction can be determined.

$$\Delta E_c = E_{g, SiC} - [(E_F - E_V)_{SiC} + \Phi_{bi} - (E_F - E_C)_{GaN}]$$

$$\Delta E_v = [(E_F - E_V)_{SiC} + \Phi_{bi} - (E_F - E_C)_{GaN}] - E_{g, GaN}$$

Based on the built in potential determined from C-V measurements we conclude that the heterojunction is of Type II with conduction and valence bands offsets calculated to be 0.65 and 1.1 eV respectively. While Torvik et al make similar conclusions about the type of heterojunction, the authors determined considerably smaller numbers for the conduction and valence band offsets, 0.11 and 0.46 eV respectively [1]. This may be attributed to the larger range of applied bias with which our diodes were investigated (0- 40V in contrast to 0-4V) due to greatly reduced leakage currents observed for these devices. Figure 4 illustrates the GaN/SiC band alignments based upon these results.

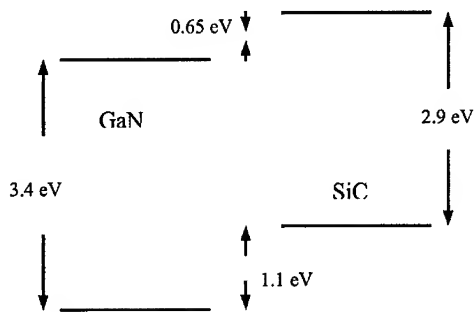


**Figure 4.** Calculated band alignments for GaN and 6H-SiC. The heterojunction is determined to be Type II.

A common figure-of-merit for a power diode is  $V_{2RB}/R_{ON}$ , that is the ratio of the reverse breakdown voltage squared divided by the on-state resistance. A value greater 3.2 MW/cm<sup>2</sup> was calculated for these 1 mm diameter diode, based on the extrapolated on- state series resistance ( $R_{on}$ ), that is about 1 order of magnitude poorer than what has been reported for SiC homojunctions based power diodes. However, considerable improvement is expected with optimization of the ohmic contacts.

## CONCLUSIONS

In conclusion, we have demonstrated large area GaN/SiC np junctions with reverse breakdown voltage greater than 830 V reverse bias. These devices show nearly ideal behavior under forward bias but are presently limited by a large on-state series resistance. The built in potential for these heterojunctions was determined to be 2.2 V by C-V measurements. Based on this result, we have determined that the np GaN/ SiC heterojunction is Type II and calculated the conduction and valence band offsets to be 0.65 and 1.1 eV respectively.

## ACKNOWLEDGEMENTS:

This work was supported by ONR under grant # N00014-01-M-0231, monitored by Dr. Colin Wood.

---

## REFERENCES

- [1] J. Torkiv, M. Leksono, J.I. Pankove, B. Van Zeghbroeck, H.M. Ng, T.D. Moustakas, Appl. Phys. Lett., 72, 1371 (1998)
- [2] E. Danielsson, C. Zetterling, M. Ostling, A. Nikolaev, I. P. Nikitina, V. Dimitriev, IEEE Trans Electron Devices, 48, 44 (2001)
- [3] D. Korakakis, A. Sampath, H.M. Ng, G. Morales, I.D. Goepfert and T. D. Moustakas, MRS Proc., 395, 151, (1996).
- [4] T.P. Chow, V. Khemka, J. Fedison, N. Ramungul, K. Matocha, Y. Tang, R.J. Gutmann, Solid State Electronics, 44, 227 (2000)
- [5] Sze S.M, Physics of Semiconductor Devices, John Wiley and Sons, NY, NY (1981)

### Properties of Surface Acoustic Waves in AlN And GaN

Jianguo Deng<sup>1</sup>, Daumantas Ciplys<sup>2,3</sup>, Gang Bu<sup>3</sup>, Michael Shur<sup>3</sup>, Remis Gaska<sup>1</sup>

<sup>1</sup>Sensor Electronic Technology, Inc., 1195 Atlas Road, Columbia, SC 29209, U.S.A.

<sup>2</sup>Department of Radiophysics, Vilnius University, Vilnius 2040, Lithuania

<sup>3</sup>Department of Electrical, Computer, and Systems Engineering and Center for Integrated Elelectronics, Rensselaer Polytechnic Institute, Troy, NY 12180, U.S.A.

#### ABSTRACT

The surface acoustic wave velocities, electromechanical coupling coefficients, and the spatial distributions of both elastic displacement and electric potential have been calculated for various configurations of gallium nitride and aluminum nitride. The electromechanical coupling coefficient values of 0.13 % in GaN and 0.29 % in AlN have been predicted. The maximum electromechanical coupling coefficient values of 0.24 % at Euler angles (0, 54°, 90°) in GaN and 1.08 % at (0, 53°, 90°) in AlN have been found. For GaN layer-on- sapphire substrate structures, the SAW velocity and electromechanical coupling coefficient have been calculated as functions of layer thickness and acoustic wavelength. The experimentally measured values of the surface acoustic wave velocity and electromechanical coupling coefficient are in satisfactory agreement with the calculation results.

#### INTRODUCTION

Recent results on remote solar-blind sensors [1] and demonstration of acousto-optic diffraction [2] using surface acoustic wave (SAWs) have highlighted the importance of SAW in nitrides for novel acousto-opto-electronic device applications. The emergence of bulk AlN and GaN substrates has opened up a possibility to launch SAWs in GaN and AlN-based films with different crystallographic orientations. The calculation of basic SAW parameters such as velocity and electromechanical coupling coefficient for various orientations is of great importance for the design of AlGaN- based acousto-opto-electronic devices. In particular, the orientations of maximum SAW efficiency can be determined. In guided wave acoustooptics, the knowledge of the spatial distribution of elastic displacement and electric potential of the wave is necessary for the calculation of overlapping between acoustic and optical waves and finding conditions for the optimization of their interaction. We solved the wave propagation equations with appropriate boundary conditions and calculated the SAW velocity and electromechanical coupling coefficient in GaN and AlN substrates for various crystal orientations. For the GaN layer-on-sapphire structure, the SAW velocity and electromechanical coupling coefficient have been calculated as functions of layer thickness and acoustic wavelength. The spatial variations of the SAW elastic displacement and electric potential have been calculated for both single substrate and layer-on-substrate configurations. The SAW velocity and electromechanical coupling coefficient have been measured in GaN-on-sapphire structure and are in good agreement with the calculated values.

## CALCULATION METHOD

Consider the structure consisting of a piezoelectric layer (AlN or GaN) of thickness  $h$  over a semi-infinite non-piezoelectric substrate (sapphire) as shown in figure 1. The surface acoustic velocity and the electromechanical coupling coefficient in such a system are calculated using the method described in Ref.3. The propagation of elastic wave in a piezoelectric film is described by the following set of equations:

$$\begin{aligned} \rho \frac{\partial^2 u_j}{\partial t^2} - c_{ijkl} \frac{\partial^2 u_k}{\partial x_i \partial x_l} - e_{kij} \frac{\partial^2 \phi}{\partial x_i \partial x_k} &= 0 \\ e_{ikl} \frac{\partial^2 u_k}{\partial x_i \partial x_l} - \epsilon_{ik} \frac{\partial^2 \phi}{\partial x_i \partial x_k} &= 0, \quad i, j, k, l = 1, 2, 3 \end{aligned} \quad (1)$$

where  $\rho$  is the mass density of the material,  $c_{ijkl}$ ,  $e_{ijk}$  and  $\epsilon_{ij}$  are the elastic stiffness, the piezoelectric, and the dielectric permittivity tensors, respectively,  $u_i$  is the elastic displacement vector, and  $\phi$  is the electric potential. For a non-piezoelectric substrate, the system (1) is simplified by  $e_{ijk} \equiv 0$ . The boundary conditions are: (1) continuity of the mechanical displacement,  $u_i = u'_i$ , and stress,  $T_{3i} = T'_{3i}$ , at the interface,  $x_3 = 0$ ; (2) vanishing of the stress,  $T'_{3i} = 0$ , at the free surface,  $x_3 = h$ ; (3) continuity of the normal component of the electrical displacement,  $D_3 = D'_3$ , and potential,  $\phi = \phi'$ , at the interface,  $x_3 = 0$ . Concerning the electric boundary condition for the top surface,  $x_3 = h$ , two cases can be considered: (4a) continuity of the normal component of the electrical displacement,  $D'_3 = k\epsilon\phi'$ , for the free surface (the potential above the top surface must satisfy the Laplace's equation in the free space), and (4b) vanishing of the potential,  $\phi' = 0$ , for the surface covered with the infinitely thin perfect conductor. (Here, the symbols with apostrophes represent material properties of the layer, and those without apostrophes represent substrate properties). The electromechanical coupling coefficient is obtained from the relation

$$\frac{K^2}{2} = \frac{V_f - V_c}{V_f} \quad (2)$$

where  $V_f$  and  $V_c$  are the SAW velocities on a free and conducting surface, respectively.

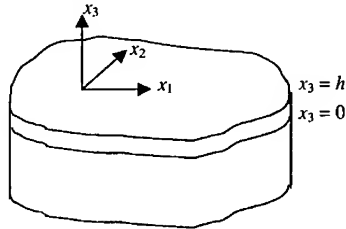


**Figure 1.** Layer-on-substrate structure and coordinate system used in calculations. Surface acoustic wave propagates along  $x_1$  axis.

## SAWs ON SEMI-INFINITE SUBSTRATE

First, we performed calculations for infinitely thick GaN and AlN layers (as if they were semi-infinite substrates themselves). These solutions also apply for homoepitaxy on bulk GaN and AlN substrates. AlN and GaN belong to hexagonal class 6mm. The values of the elastic constants  $c_{ij}$ , piezoelectric constants  $e_{ij}$  and dielectric permittivities  $\epsilon_{ij}$  were taken from Ref. 4. The crystal cut and the SAW propagation direction are conventionally described by the set of Euler rotation angles  $(\lambda, \mu, \theta)$ . We calculated the velocity  $V$  and coupling coefficient  $K^2$  for SAWs propagating along crystallographic  $[1\bar{1}00]$  direction by rotating the propagation surface orientation around the SAW propagation direction. The corresponding Euler angles were  $(0, 0 \leq \mu \leq 90^\circ, 0)$ . The results are shown in figure 2 (a) for GaN, and in figure 2 (b) for AlN. Angle  $\mu = 0$  corresponds to the direction of surface normal along  $[0001]$  crystal axis. The maximum  $K^2$  values are attained for the Z-cut and they are 0.13 % for GaN and 0.29 % for AlN. Because of symmetry, the phase velocity does not depend on the propagation direction on the Z-plane. For Y-cut,  $K^2$  drops to zero. It was interesting to examine the possibilities of obtaining the larger values of the electromechanical coupling coefficient by varying the SAW propagation orientation with respect to the crystal axes. We found that the maximum  $K^2$  of 0.24 % is achieved at Euler angles  $(0, 54^\circ, 90^\circ)$  in GaN substrate, and 1.08 % is achieved at  $(0, 53^\circ, 90^\circ)$  in AlN. The calculated depth variations of the elastic displacement and electric potential amplitudes are plotted in Figure 3 for the free and metallized surface of AlN. It should be noted that displacement contains only sagittal components,  $u_1$  and  $u_3$ .

For comparison, the electromechanical coupling value of 0.06-0.07 % has been reported for GaAs, and up to 5.6 % in  $\text{LiNbO}_3$  [5,7].

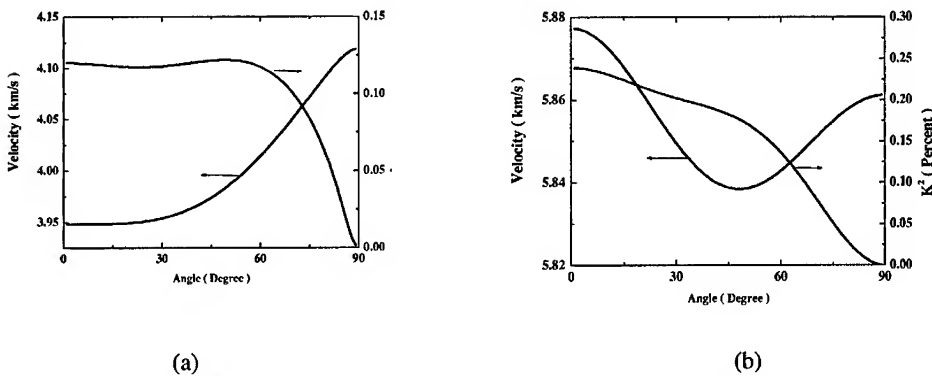


**Figure 2.** Phase velocity and electromechanical coupling coefficient as a function of angle  $\mu$  between surface normal and  $[0001]$  axis in the  $(1\bar{1}00)$  plane for SAW propagating along  $[1\bar{1}00]$  axis in (a) GaN and (b) AlN substrate.

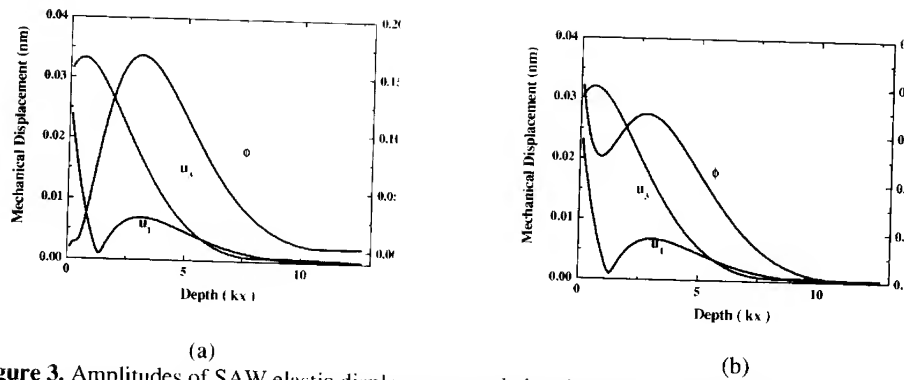


**Figure 3.** Amplitudes of SAW elastic displacement and electric potential as functions of distance from surface for (a) conducting and (b) free surface of AlN substrate at Euler angles (0, 53°, 90°)

### SAWs IN LAYER ON SUBSTRATE STRUCTURE

Most of the GaN crystals are grown as thin layers on sapphire substrates. In this section, we present the results of calculations for this configuration (see figure 1). Sapphire ( $\text{Al}_2\text{O}_3$ ) belongs to the point symmetry class  $\bar{3}m$  of the trigonal crystal system. We took its parameters from [5].

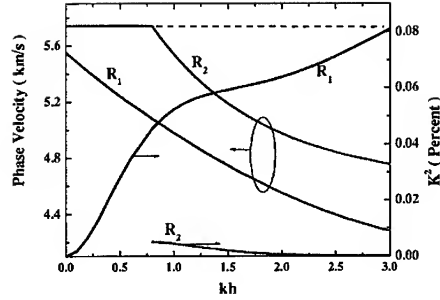
The Rayleigh velocity in sapphire (5528 m/s at the Euler angles (0,0,0)) is much higher than the transverse bulk wave velocity in GaN 4132 m/s. The transverse bulk wave velocity in the sapphire substrate is 5743 m/s. Thus, the conditions for appearance of higher-order surface acoustic modes in the layer-substrate configuration are satisfied, provided the product  $kh$  is sufficiently large (i. e. sufficiently thick or the SAW frequency is sufficiently high).

Figure 4 shows the velocities of the first two modes and the electromechanical coupling coefficients calculated for GaN layer and sapphire surfaces normal to [0001] crystallographic direction. The second-order mode appears when  $kh$  product is larger than about 0.7. The third-order mode appears at  $kh$  beyond 4 and it is not shown in the figure. We can see that the second mode-order has a much smaller  $K^2$  value than the fundamental one.

As the thickness of the GaN layer increases, the  $K^2$  becomes larger. However, it does not increase beyond the  $K^2$  for GaN substrate in figure 2. This result does not coincide with the results of calculation reported in Ref. 6, where a similar velocity drop range for the first-order mode was obtained but a higher value of  $K^2$  (~0.33%) was reported. The reason for this discrepancy is still under investigation.

Comparing figure 5(a) and figure 5(b), we can see that the major difference between  $R_1$  and  $R_2$  is the dominance of the transverse horizontal component  $u_2$ , of the elastic wave. In the fundamental mode, it is the transverse vertical component  $u_3$  which is dominant.

BEST AVAILABLE COPY



**Figure 4.** Phase velocities and electromechanical coupling coefficients as functions of product  $kh$  for SAWs propagating in the structure consisting of (0001) GaN layer on (0001) sapphire substrate, (Euler angles: 0, 0, 0).

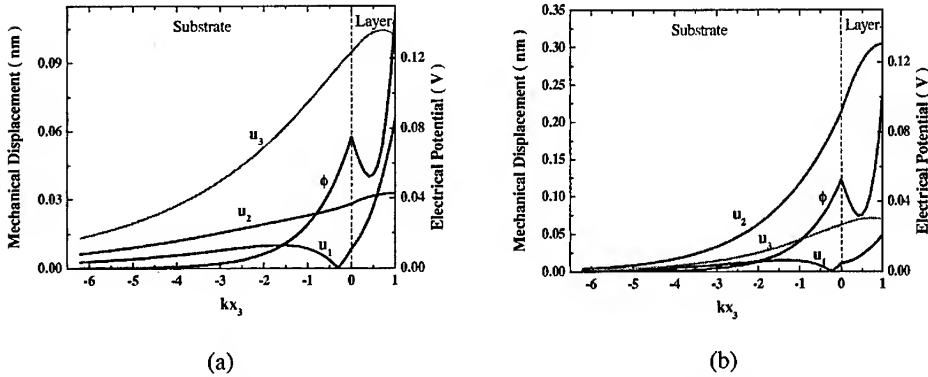


**Figure 5.** Amplitudes of SAW elastic displacement and electric potential as functions of distance from surface (in  $kx_3$  units) for (a) first-order and (b) second-order surface acoustic modes in the structure consisting of (0001) GaN layer on (0001) sapphire substrate.

## EXPERIMENTAL RESULTS FOR GaN ON SAPPHIRE

The 2.6  $\mu\text{m}$  thick GaN layer grown by MOCVD on (0001) sapphire substrate has been used in experiment. An Al interdigital transducer (IDT) with 16  $\mu\text{m}$  period has been deposited on the sample and its  $S_{11}$  parameter was measured by the network analyzer. The extracted frequency dependence of IDT radiation conductance is shown in figure 6. From the resonant IDT frequency  $f_0 = 310$  MHz at the SAW wavelength 16  $\mu\text{m}$ , we obtain the SAW velocity value 4960 m/s. The  $K^2$  value 0.058% is found from the relation

$$G_a(f_0) = 8K^2 f_0 C_T N, \quad (2)$$

where the number of digits  $N = 90$ , and the transducer static intrinsic capacitance  $C_T = 9$  pF. The

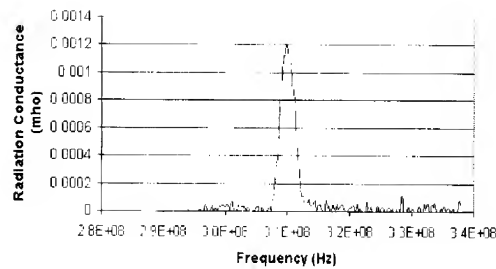


**Figure 6.** Experimentally measured radiation conductance of interdigital transducer vs frequency

experimental SAW velocity and  $K^2$  values agree well with the calculated values 4980m/s and 0.052%, respectively, corresponding to  $kh=1$  in figure 4.

## CONCLUSION

The surface acoustic wave velocities, electromechanical coupling coefficients, and the spatial distributions of both elastic displacement and electric potential have been calculated for GaN and AlN substrates and GaN layer-on-sapphire substrate structure. The  $K^2$  value as large as 1 % have been predicted for a specific orientation in AlN. The experimentally measured values of the surface acoustic wave velocity and electromechanical coupling coefficient in GaN layer-on-sapphire are in satisfactory agreement with the calculation results.

**ACKNOWLEDGMENT** The work at RPI was supported by DARPA under a subcontract from Crystal IS, Inc. (Project Monitor Dr. E. Martinez). The work at SET, Inc. was supported by NASA under contract NAG5-10322

## REFERENCES

1. D. Ciplys, R. Rimeika, M. S. Shur, S. Rumyantsev, R. Gaska, A. Sereika, J. Yang, M. A. Khan, *Appl.Phys.Lett.* **80**, 2020 (2002)
2. D. Ciplys, R. Rimeika, M. S. Shur, R.Gaska, J. Deng, J. W. Yang, M. A. Khan, *Appl.Phys.Lett.* **80**, 1701 (2002)
3. G. W. Farnell, E. L. Adler, *Elastic Wave Propagation in Thin Layers*, Physical Acoustics, Principles and Methods, edited by W. P. Mason, R. N. Thurston, Vol. IX (Academic Press, 1972)
4. M. E. Levinshtein, S. L. Rumyantsev, M. S. Shur, *Properties of Advanced Semiconductor Materials, GaN, ALN, InN, BN, SiC, SiGe* (John Wiley & Sons, 2001)
5. D. Royer, E. Dieulesaint, *Elastic Waves in Solids I, Free and Guided Propagation*, (Springer, 1996).
6. S. Camou, Th. Pastureauud, H. P. D. Schenk, S. Ballandra, V. Laude, Guided Elastic Waves in GaN-on-Sapphire. *Electron. Lett.* **37**, 1053 (2001).
7. C. K. Campbell, *Surface Acoustic Wave Devices for Mobile and Wireless Communication*, pp125-6 (Academic Press, San Diego, 1998).

**BEST AVAILABLE COPY**

### Surface acoustic wave resonator from thick MOVPE-grown layers of GaN(0001) on sapphire

Sverre V. Pettersen<sup>1</sup>, Thomas Tybell<sup>1</sup>, Arne Rønnekleiv<sup>1</sup>, Stig Rooth<sup>2</sup>, Veit Schwegler<sup>3</sup>, and Jostein K. Grepstad<sup>1</sup>

<sup>1</sup>Department of Physical Electronics, Norwegian University of Science and Technology, O.S. Bragstads Plass 2A, N-7491 Trondheim, NORWAY

<sup>2</sup>Alcatel Space Norway AS, Knudsrødveien 7, N-3190 Horten, NORWAY

<sup>3</sup>Department of Optoelectronics, University of Ulm, Albert Einstein Allee 45, D-89081 Ulm, GERMANY.

#### ABSTRACT

We report on fabrication and measurement of a surface acoustic wave resonator prepared on ~10µm thick GaN(0001) films. The films were grown by metal-organic vapor phase epitaxy on a c-plane sapphire substrate. The surface morphology of the films were examined with scanning electron and atomic force microscopy. A metallic bilayer of Al/Ti was subsequently evaporated on the nitride film surface. Definition of the resonator interdigital transducers, designed for a wavelength of  $\lambda=7.76\mu\text{m}$ , was accomplished with standard UV lithography and lift-off. S-parameter measurements showed a resonator center frequency  $f_0=495\text{MHz}$  at room temperature, corresponding to a surface acoustic wave velocity of 3844m/s. The insertion loss at center frequency was measured at 8.2dB, and the loaded Q-factor was estimated at 2200. Finally, measurements of the resonator center frequency for temperatures in the range 25-155°C showed a temperature coefficient of -18ppm/°C. The intrinsic GaN SAW velocity and electromechanical coupling coefficient were estimated at  $v_{\text{SAW}}=3831\text{m/s}$  and  $K^2=1.8\pm0.4\cdot10^{-3}$ .

#### INTRODUCTION

The wide bandgap semiconductor gallium nitride has frequently made it to the headlines in the semiconductor science community during the last decade, mainly because of successful applications in short wavelength optical emitters such as blue laser diodes and light emitting diodes spanning the entire optical spectrum [1]. Moreover, the piezoelectric properties of the group III-nitrides render this material system an interesting option for surface acoustic wave (SAW) devices [2]. The GaN/sapphire system is of particular interest from an engineering point of view, with the sapphire substrate featuring a high and anisotropic SAW velocity, ranging from 5548m/s in the  $[1\bar{1}20]$  direction to 5687m/s in the  $[1\bar{1}00]$  direction [3]. This provides rich opportunities for engineering the propagation properties of the SAW device by controlling the GaN film thickness and the orientation of the SAW device with respect to the in-plane crystalline axes of the sapphire substrate, as well as the SAW wavelength [3-5].

In order to take full advantage of the engineering potential of the GaN/sapphire system, it is important to establish the intrinsic GaN SAW propagation properties. An important engineering challenge in this regard is to grow thick epitaxial films with semi-insulating conduction properties, essential to SAW applications [6]. Recent advances in materials growth now render this a feasible endeavor. In the present paper, we have investigated the performance of a SAW resonator fabricated on thick GaN films in order to obtain the intrinsic SAW velocity, temperature coefficient of frequency (TCF), and electromechanical coupling coefficient  $K^2$ .

## EXPERIMENTAL

A 10 $\mu\text{m}$  thick film of wurtzite GaN(0001) was grown without intentional doping on a two inch wafer of c-plane sapphire using metal-organic vapor phase epitaxy (MOVPE). Room temperature Hall-effect measurements showed a carrier density  $\leq 10^{16}\text{cm}^{-3}$ , which is adequate for SAW generation with metallic interdigital transducers (IDTs). Examination of the GaN film with both scanning electron and atomic force microscopy showed a smooth film surface with a typical root-mean-square roughness of 11 Å for a 5 $\mu\text{m}$   $\times$  5 $\mu\text{m}$  scan, and scattered defects in the form of  $\sim 0.5\mu\text{m}$  diameter pinholes with a density less than one per 25 $\mu\text{m}^2$ .

The SAW resonator measured and analyzed in this study had two identical IDTs placed between a pair of reflector arrays, as depicted in figure 1. Both transducer and reflector structures were made from a metallic bilayer of Al (300 $\pm$ 30nm) / Ti (15 $\pm$ 2nm) evaporated on the GaN film surface, which had been precleaned by a 3 $\times$ 5 min ultrasonic rinse in trichloroethylene, acetone and methanol, respectively. The IDT geometry was defined by standard UV lithography and lift-off. To improve adhesion between the IDTs and the GaN film surface, the samples were annealed for 30 min in air at 130°C. This was the only annealing adopted in the processing of the IDTs to ensure minimal nitrogen out-diffusion, which may cause unwanted n-type doping of the GaN film. Each transducer had 25 pairs of equally spaced interdigital electrodes, 1567 $\mu\text{m}$  long and 1.94 $\mu\text{m}$  wide, with a pitch corresponding to a SAW wavelength of  $\lambda=7.76\mu\text{m}$ . The separation between the nearest finger electrodes of the two transducers was 76.1 $\mu\text{m}$ , and the two reflectors were composed of 479 disconnected fingers each, with a width and pitch identical to that of the two IDT's. The separation of the reflectors from the outer finger electrodes of the two IDTs was 7.0 $\mu\text{m}$ .

The transmission and reflection parameters (S-parameters) of the resonator were measured with a HP8703A Lightwave Component Analyzer. The input power in the reported measurements was fixed at  $P=1\text{mW}$ .

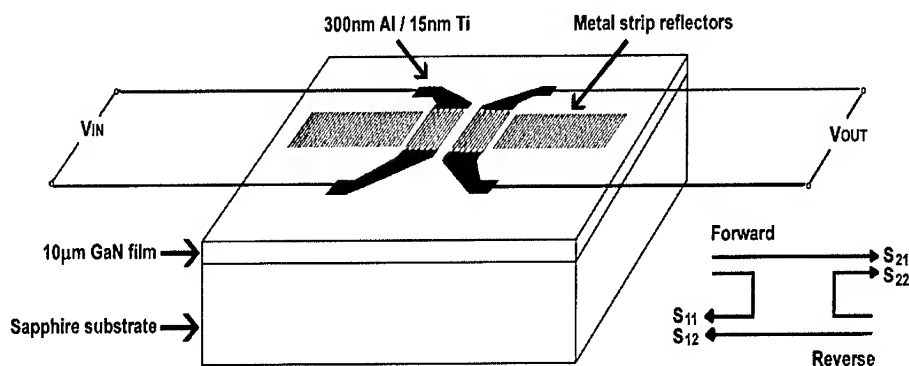


**Figure 1.** Schematic of the SAW resonator reported in this paper, with the notation adopted for the forward and reverse S-parameter measurements.

## RESULTS AND DISCUSSION

Figure 2 shows the measured amplitude response  $S_{21}$  in the time domain (a) and the frequency domain (b) for the SAW resonator. Figure 2b shows a resonance superimposed on the SAW transducer passband, with a center frequency  $f_0=495\text{MHz}$  at room temperature for the resonance and the IDT passband alike. Note that the direct electromagnetic feedthrough, marked “direct EM” in figure 2a, has been gated out of the amplitude response displayed, which also shows the simulated response of the ideal resonator. The insertion loss at the center frequency was measured at 8.2dB, and the resonator Q-factor was estimated at 2200. The insertion loss of the SAW transducer passband was measured at 23.7dB with a Q-factor of 41, and the suppression of the first order side lobes with respect to that of the passband was 23.5dB and 25.5dB, respectively. This data shows that adequate reflection properties for a SAW resonator can be achieved with IDTs and reflectors prepared from a simple Al/Ti bilayer.

The SAW velocity for this GaN/sapphire resonator was obtained from the equation relating the Rayleigh wave velocity to its frequency,

$$v = f_0 \cdot \lambda \quad (1)$$

and was estimated at 3844m/s. Equation (1) is derived for transducers without SAW reflections from the IDT fingers. From the measured S-parameters, we estimate a reflection coefficient of  $r=0.004$  per finger, which given the limited number of fingers in the two IDTs is sufficiently small to merit the use of this equation.

Several studies have addressed the issue of how to account for the GaN SAW velocity when designing transducers that take advantage of the favorable propagation properties in a sapphire substrate. Deger *et al.* [3] and Kahn *et al.* [5] have studied the variations in SAW velocity for thin films with small wavenumber–thickness products  $kd$ ,  $k$  being the wavenumber

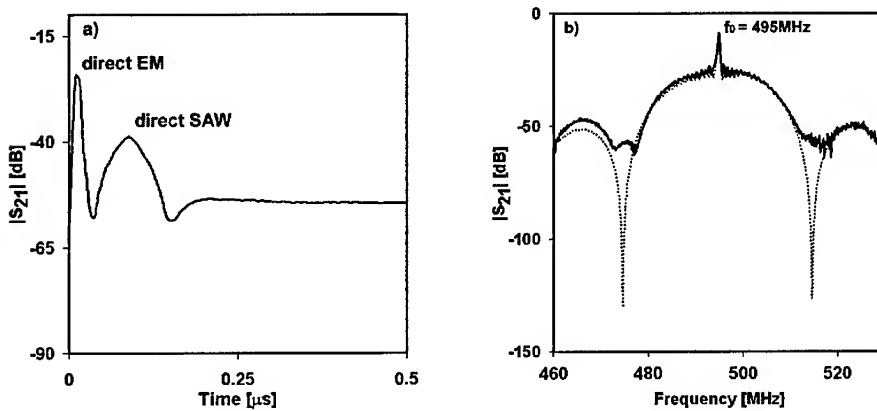


**Figure 2.** Measured amplitude response  $S_{21}$  of the SAW resonator; a) in the time domain. b) in the frequency domain with the direct electromagnetic coupling gated out. The dotted line in b) represents the simulated response of the ideal resonator.

$2\pi\lambda$  and  $d$  the film thickness, for which a substantial part of the signal propagates in the substrate. For  $kd$  numbers less than  $\sim 2$ , the SAW velocity was found to be strongly dependent on the device orientation with respect to the symmetry axes of the sapphire substrate. For higher values of  $kd$ , the SAW velocity was virtually independent of the device orientation, decreasing with growing  $kd$  numbers towards what appeared to be the intrinsic SAW velocity of GaN for  $kd > 2\pi$ , i.e.,  $d > \lambda$ . These studies extrapolate the SAW velocity of bulk GaN to 3700m/s [3] and 3689m/s [5], respectively.

In the present study, carried out with thick GaN films, we chose to work with  $kd=8.07$ , in excess of  $2\pi$ , in order to be in a regime with SAW propagation properties characteristic of the GaN film [8]. The measured SAW velocity of 3844m/s exceeds the conjectured value for bulk GaN as previously published [3,5]. With the thick metallic bilayer used in the IDTs and reflectors of our resonator, we should expect an even higher value for the free surface SAW velocity than the measured 3844m/s, due to partial short-circuiting of the SAW at the GaN film surface and mechanical loading [9].

In order to estimate the impact of the electrodes and the sapphire substrate on the measured SAW velocity, we have performed numerical simulations using reported experimental values for the mass density, the dielectric, elastic and piezoelectric constants of GaN and sapphire [10-14]. Following the analysis by Rooth *et al.* [15], the simulations were based on deriving the SAW solutions of the vectorial wave equation. For reasons of simplicity, identical material properties were assumed for the Ti and the Al layers, thus performing the actual computation for a 315nm Al layer on top of a 10 $\mu$ m thick GaN film. The simulations were found to be highly sensitive to uncertainties in the elasticity tensor components. Thus, calculations were made both with the nominal and the minimum values for the components of this tensor. The simulations gave estimates for the SAW velocities  $v_f$  of the GaN free surface,  $v_s$  of the short-circuited surface and  $v_{Al}$  of the surface covered with aluminium. The actual resonator SAW velocity  $v_r$  was determined from [15]:

$$v_r = v_f + 0.73(v_s - v_f) + 0.5(v_{Al} - v_s) \quad (2)$$

where the factor 0.73 derives from partial short-circuiting of the electrostatic potential at the GaN surface in an IDT structure with finger thickness and gap equal to  $\lambda/4$ , and the factor 0.5 is due to the 50% surface metal coverage of the resonator structure.

The orientation of the device with respect to the symmetry directions of the sapphire substrate gives a maximum change in SAW velocity of 0.3m/s, which renders the anisotropy of the SAW velocity in sapphire immaterial. However, taking the nominal and minimum values of the elasticity tensor components we compute an increase in the SAW velocity of this resonator due to the sapphire substrate of 26m/s and 33m/s, respectively. Taking an average of these estimates, we obtain a correction to the measured SAW velocity of our resonator of  $30 \pm 1$ m/s.

Similarly, for the nominal and minimum values of the elasticity tensor components we estimate reductions in the GaN free surface SAW velocity due to the metal electrodes of 18m/s and 16.5m/s, respectively. From the calculated contributions of terms two and three in equation (2), we conclude that the mechanical loading is approximately 10 times more effective in reducing the SAW velocity than the electrical short-circuiting of the GaN film surface in this case. We take the average correction in SAW velocity of  $-17 \pm 1$ m/s to be a good estimate for this resonator. The two contributions are the same order of magnitude and of opposite sign. The intrinsic GaN SAW velocity is estimated at 3831m/s.

The change in SAW velocity due to the metal IDTs and reflectors is related to a loss of electrical energy from the wave. The electromechanical coupling coefficient  $K^2$  was estimated by fitting of a simulated SAW transducer response to the measured direct SAW response, depicted in figure 2a, by variation of  $(v_f - v_s)/v_f$ . The best fit gave an electromechanical coupling coefficient of:

$$K^2 \approx 2 \frac{v_f - v_s}{v_f} = (1.8 \pm 0.4) \cdot 10^{-3} \quad (3)$$

We note that this value is one order of magnitude smaller than what was previously reported by Lee *et al.* [16] for a 2 $\mu$ m thick film of Mg-doped GaN with Al IDTs, but comparable to the  $K^2$  reported by Čiplys *et al.* [9] for 1.1 $\mu$ m and 5.8 $\mu$ m films of GaN on sapphire, both with Al metallizations.

Another important figure of merit for materials to be used in SAW devices is the stability of the center frequency upon changes in temperature. In order to investigate this, we measured the amplitude response of our resonator as a function of temperature, which was measured with a thermocouple placed inside the sample heater. As the temperature was increased from 25°C to 155°C, the center frequency shifted from 495MHz to 494MHz, as shown in figure 3. A linear fit to this data renders a frequency shift of  $\Delta f = -9\text{kHz}/^\circ\text{C}$ , corresponding to a TCF of  $-18\text{ppm}/^\circ\text{C}$ . Several groups have measured the TCF for GaN thin films, [16-17]. Jeong *et al.* [17] showed that the TCF of a 2.4 $\mu$ m film of GaN on sapphire depends on the wavenumber–thickness product  $kd$  much in the same way as the SAW velocity. Since sapphire has a TCF of  $-60\text{ppm}/^\circ\text{C}$  [18], good temperature stability for SAW devices prepared from GaN/sapphire calls for devices with large wavenumber–thickness products.

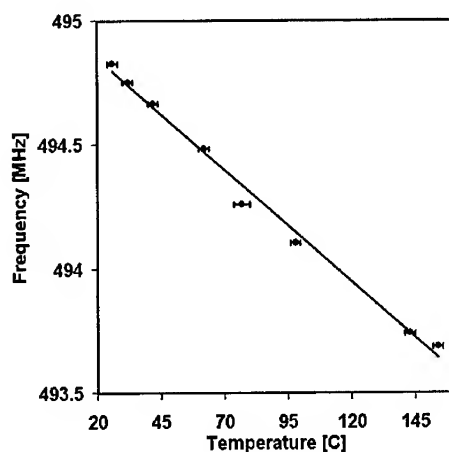


**Figure 3.** Temperature dependence of the resonator center frequency,  $f_0$ . The TCF was determined by linear regression (solid line).

## CONCLUSIONS

In this study we have demonstrated the possibility of manufacturing working SAW devices on thick MOVPE-grown GaN epilayers. The SAW velocity of our resonator was measured at 3844m/s, from which the intrinsic SAW velocity of the GaN films was estimated at 3831m/s. The resonator showed good temperature stability with a measured TCF of -18ppm/°C. The electromechanical coupling coefficient  $K^2$  was estimated at  $1.8 \pm 0.4 \cdot 10^{-3}$ .

## ACKNOWLEDGMENTS

Einar Myhre is gratefully acknowledged for his assistance with the SEM. The project was funded by the Norwegian Research Council under contract no. 114114/410.

## REFERENCES

1. S. Nakamura and G. Fasol, *The Blue Laser Diode*, Springer-Verlag, Berlin Heidelberg (1997).
2. G. D. O'Clock Jr. and M. T. Duffy, *Appl. Phys. Lett.* **23**, 55 (1973).
3. C. Deger, E. Born, H. Angerer, O. Ambacher, M. Stutzmann, J. Hornsteiner, E. Riha and G. Fischerauer, *Appl. Phys. Lett.* **72**, 2400 (1998).
4. W. R. Smith, *J. Appl. Phys.* **42**, 3016 (1971).
5. A. Khan, R. Rimeika, D. Čiplys, R. Gaska and M. S. Shur, *Phys. Stat. Sol. (B)*, **216**, 477 (1999).
6. B. Gil (ed.), *Group III Nitride Semiconductor Compounds - Physics and Applications*, Oxford University Press, Oxford (1998).
7. C. K. Campbell, *Surface Acoustic Wave Devices for Mobile and Wireless Communications*, Academic Press, New York (1998).
8. J. Vollmer and D. Gandolfo, *Science*, **175**, 129 (1972).
9. D. Čiplys, R. Rimeika, R. Gaska, M. S. Shur, A. Khan and J.W. Yang, *Electron. Lett.* **36**, 591 (2000).
10. V. W. Chin, T. L. Tansley and T. Osotchan, *J. Appl. Phys.* **75**, 7365 (1994).
11. A. Polian, M. Grimsditch, I. Grzegory, *J. Appl. Phys.* **79**, 3343 (1996).
12. A. D. Bykhovski, B. L. Gelmont and M. S. Shur, *J. Appl. Phys.* **81**, 6332 (1997).
13. J. H. Edgar (ed.), *Properties of group III-Nitrides*, EMIS data reviews series vol. 11, INSPEC (1994).
14. B. A. Auld, *Acoustic Fields and Waves in Solids*, John Wiley & Sons, New York (1973).
15. S. Rooth, E. Halvorsen, S. Bardal and E.D. Tuset, *IEEE Ultrason. Symp. Proc.* **1**, 329 (2000).
16. S.-H. Lee, H.-H. Jeong, S.-B. Bae, H.-C. Choi, J.-H. Lee and Y.-H. Lee, *IEEE Trans. on Electron. Dev.* **48**, 524 (2001).
17. H.-H. Jeong, S.-K. Kim, Y.-C. Jung, H.-C. Choi, J.-H. Lee and Y.-H. Lee, *Phys. Stat. Sol. (A)*, **188**, 247 (2001).
18. T. Mitsuyu, S. Ono and K. Wasa, *J. Appl. Phys.* **51**, 2464 (1980).

---

## **UV Emitters and Detectors**

### A GaN-free LED Structure for High UV-light Extraction

Toshio Nishida, Tomoyuki Ban,<sup>1</sup> and Naoki Kobayashi

NTT Basic Research Laboratories, NTT Corporation,

Atsugi, Kanagawa, 243-0198, Japan

<sup>1</sup>NEL Technosupport

Atsugi, Kanagawa, 243-0198, Japan

#### ABSTRACT

We improved the extraction of ultraviolet light from AlGaIn-based light emitting diodes (LEDs) at the wavelength of about 350 nm, by introducing a transparent structure that is free from binary GaN. We used an AlN-template layer on a sapphire substrate as starting medium of the metal organic vapor phase epitaxial growth. The buffer layer is an Al<sub>0.2</sub>Ga<sub>0.8</sub>N alloy. We also used a short period alloy superlattice as transparent and conductive p-type cladding and p-type contact layers. The resultant epitaxial structure is confirmed to be transparent with the transmittance of about 90% within the wavelength range of 340 – 400 nm. The crystal quality of the Al<sub>0.2</sub>Ga<sub>0.8</sub>N buffer layer was estimated by the transmission electron microscope (TEM) observation. The dislocation density of AlGaIn buffer layer was highly reduced on the AlN template layer, both of which have a low density of screw and mixed-type dislocations, of the order of 10<sup>8</sup>cm<sup>-2</sup>. We also found that light extraction is improved by a factor of 6 by introducing the transparent LED structure and a p-contact mirror. The resultant LED shows high performance under RT-CW operation, where 1 mW output power at 348 nm with 20 mA injection corresponds to the external quantum efficiency of 1.4 %. The maximum power was 7 mW at 220 mA. The emission spectrum is highly monochromatic with the UV-to-visible intensity ratio of about 1000. We also demonstrate the application of this transparent UV-LED to white light source in a bottom-emission geometry.

#### INTRODUCTION

Nitride semiconductors with sufficient Al content, such as AlGaIn, provide short band-gap wavelengths of 200 - 360 nm in the ultraviolet (UV) range. Light sources of such UV range are promising as efficient solid-state excitation sources in wavelength conversion technologies for lighting equipment and displays, where ultraviolet lights are converted to visible light by using fluorescence dyes. They are also promising in the application field of spectro-chemical analyses and photo-catalytic chemical reactions. Therefore, clarifying their

potential is a very important issue. We have already demonstrated a highly efficient AlGa<sub>0.2</sub>N active layer[1,2] grown on a bulk GaN substrate[3] at the emission wavelength of 353 nm. However, the extraction efficiency of the device was as low as 1 %. The drawback of this system is the light absorption by binary GaN layers. GaN layers are conventionally used as buffer layers for high-quality crystal growth and as p-type layers for conductive cladding and metal contact. To improve extraction of UV light shorter than GaN band-gap wavelength of 363 nm, transparent buffer layers including transparent substrates and transparent p-type layers, are indispensable. In this study, we fabricated transparent LED structures that are free from optically absorptive GaN layers (hereafter, referred to as the GaN-free structure), and demonstrated its potential for highly efficient ultraviolet light sources.

## EXPERIMENT

We grew device structures by low-pressure metalorganic vapor phase epitaxy (LP-MOVPE) at 300 Torr. The inset of Fig. 1 is a schematic drawing of the device structure. In this study, we used an AlN template layer on sapphire substrates (NGK Insulators, Ltd.).[4] We grew an AlN homoepitaxial layer (30 nm), an undoped Al<sub>0.2</sub>Ga<sub>0.8</sub>N buffer layer (0.7 micron), a Si-doped n- Al<sub>0.2</sub>Ga<sub>0.8</sub>N conductive layer (2.3 micron), and LED device structure. The active layer of the UV-LEDs is a 2-nm-thick Al<sub>0.04</sub>Ga<sub>0.96</sub>N/ Al<sub>0.08</sub>Ga<sub>0.92</sub>N single quantum well (SQW) layer sandwiched by Al<sub>0.3</sub>Ga<sub>0.7</sub>N blocking layers (30 nm) and cladding layers consisting of the

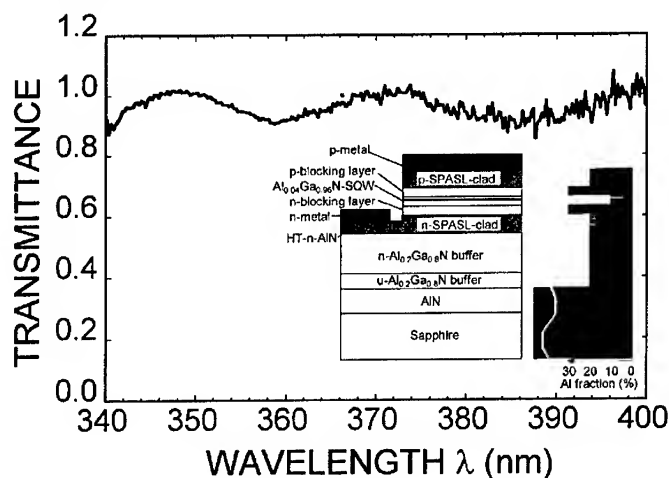


Figure 1 Transmittance spectrum of AlGa<sub>0.2</sub>N-LED wafer. The inset shows a schematic drawing of the device structure.

$\text{Al}_{0.16}\text{Ga}_{0.84}\text{N}(1.5\text{ nm})/\text{Al}_{0.2}\text{Ga}_{0.8}\text{N}(1.5\text{ nm})$  short period alloy superlattice (SPASL).[5,6] The n-type doping and p-type doping were performed using Si and Mg, respectively. In other words, we used transparent materials to the 350-nm emission light, except for the active layer. To fabricate LED devices, we used Pd as p-type ohmic contact metal. The n-type contact is obtained by dry etching the LED sample down to the n-type layers beneath the active layer by electron cyclotron resonance plasma reactive ion etching using  $\text{Cl}_2$  gas. We deposited Ti/Al on the n-type layers as contact metal. The output power of the LED device was measured by a Si-pin photodiode placed above or under the sample.

## RESULT AND DISCUSSION

Figure 1 shows the result of the evaluation of the transparency of the LED structure. Here, we used an AlGaIn-SQW-LED as a probe light source (peak wavelength: 354 nm) for transparency measurement in the ultraviolet range. The transmittance of the epitaxially grown wafer was obtained by normalization using a raw substrate with an AlN-template layer. The result indicates the transparency is higher than 90 %, although there is a residual fringe due to optical interference. This confirms the formation of the transparent UV-LED structure consisting of AlGaIn layers free from binary GaN.

Figure 2 shows a transmission electron micrograph (TEM) of the  $\text{Al}_{0.2}\text{Ga}_{0.8}\text{N}$  layer grown on the AlN-template layer on the sapphire substrate. The brightest layer is the

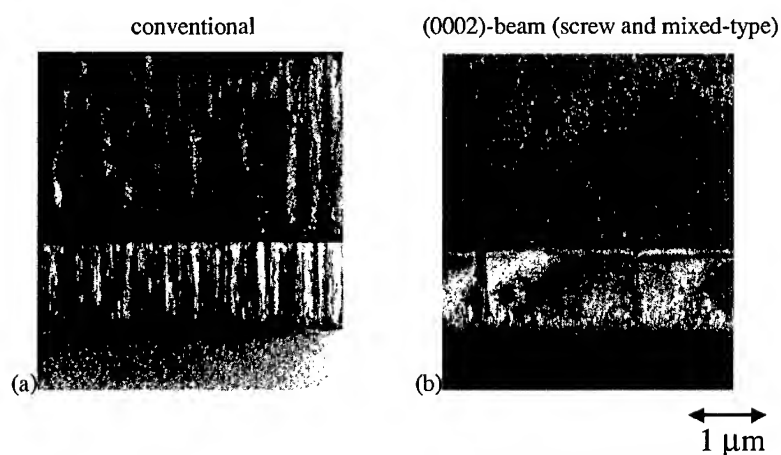


Figure 2 TEM micrographs obtained using a (a) conventional bright field, and (b) a  $(0002)$  beam, which highlights screw and mixed-type dislocations.

Table I Comparison of the output power of different types of AlGaIn-SQW-LEDs

epi-structure	GaN-free LED (A)	GaN-free LED (B)	GaN-buffer LED (C)
p-contact metal	thick mirror	semitransparent	semitransparent
top emission	-	2	1
bottom emission	6	4	~ 0

AlN-template layer. Figure 2(a) shows the conventional bright field TEM image, which clearly shows the significant reduction of dislocation density from the AlN-template layer ( $> 10^{10} \text{ cm}^{-2}$ ) to the AlGaIn buffer layer ( $\sim 10^9 \text{ cm}^{-2}$ ). Figure 2(b) shows the TEM image obtained under (0002)-beam excitation. In this condition, only screw- and mixed-type dislocations are observed and it is clear that both the AlGaIn buffer layer and AlN-template layer have low densities of these types of dislocations, about  $2 \times 10^8 \text{ cm}^{-2}$ . We attribute the reduction in Fig. 2(a), which is mainly due to the reduction of the edge-type dislocations, to the nature of the low density of the screw- and mixed-type dislocations in the AlN-template layers.

Table I compares the emission intensity of three types of AlGaIn-SQW-LEDs: (A) A GaN-free LED with a thick p-contact metal (Pd) as a reflecting mirror, with which the emission is from the bottom of the device (LED A); A GaN-free LED with a semi-transparent p-type electrode, with which emissions from the top and the bottom are possible (LED B); a GaN-buffer LED with the semitransparent p-type contact metal as a reference device (LED C). As shown in the table, LED A achieved the highest output power. This is due to the reflection enhancement by the Pd metal mirror. The emission from the bottom side of the LED B is twice of that from the top side. This is due to a low transparency ( $\sim 50\%$ ) of the p-type semitransparent electrode. The emission from LED C has lower emission intensity than LED B. This is perhaps due to the lack of the extraction enhancement caused by the internal reflection of the LED device. Therefore, we conclude that light extraction is enhanced by a factor of 6 by introducing the transparent, i.e. GaN-free, LED structure and p-type mirror electrode.

Figure 3 shows the characteristics of the output power versus injection current of the LED C. The emission from the substrate side of the output power is 1 mW at the injection current of 20 mA, and the external quantum efficiency is about 1.4 %. In spite of the existence of dislocations (Fig. 2), these values are superior to those we reported for the LED grown on high-quality bulk GaN substrate,[3] which is due to the light extraction improvement by introducing the transparent device structure. The maximum output power is 7 mW at the injection current of 220 mA. This saturation current is smaller than that of the LED on GaN substrate. This is due to the heating effect caused by the poor thermal conductivity of sapphire substrate. Therefore, we expect that the output can be improved by changing the chip shape and through

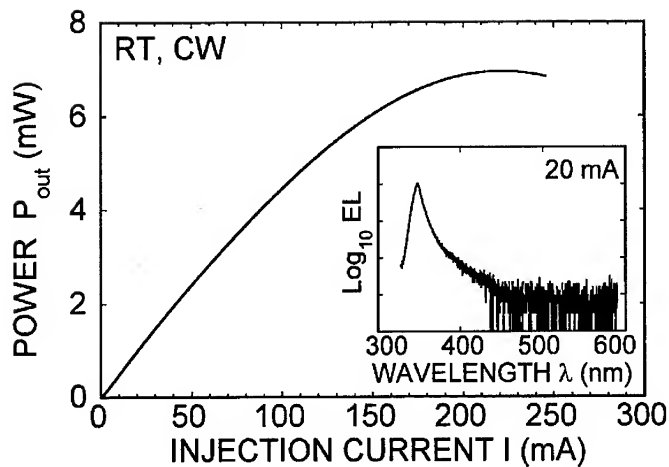


Figure 3 Output characteristics of the AlGaIn-SQW LED. The inset shows the output power of the transparent LED

package design. As shown in the inset of Fig. 3, the emission spectra is highly monochromatic due to the separate confinement structure achieved by using the SPASL and current blocking layers.[5,6] The EL peak intensity at 348-351 nm is 1000 times as large as those of the visible emission. Such a monochromatic UV light source is very useful for spectrochemical analyses.

Further, we demonstrate the UV-LED application to the excitation of white fluorescence dye. The GaN-free LED with a semitransparent contact (B) is placed on a fluorescence board.

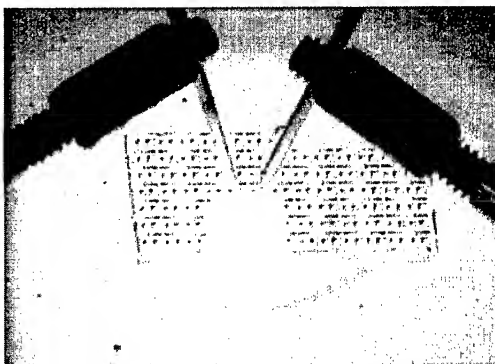


Figure 4 White light excitation by UV light from the GaN-free UV-LED from a fluorescence board beneath the LED wafer.

The fluorescence dyes were excited by UV light that came through the epi-layers and the substrate. This result indicates the potential applicability of the AlGaIn-based LED to the wavelength conversion technologies similarly.

## CONCLUSIONS

In conclusion, we demonstrated the possibility of the fabrication of transparent UV-LEDs and their potential for high power extraction. The GaN-free UV-LEDs consist of AlGaIn-buffer-layers, a short-period-alloy-superlattice for the cladding and contact layers, and an AlGaIn-SQW active layer. We confirmed the transparency of this LED structure from its transmittance spectra measured by using an AlGaIn-based UV-LED. The output power from the substrate side of the transparent LED is 1 mW at the injection current of 20 mA. The external quantum efficiency is about 1.4 %, due to extraction enhancement achieved by introducing the transparent device structure. This efficiency is higher than even that of a UV-LED grown on bulk-GaN substrate, although the crystal quality of the bulk GaN is much better.

## ACKNOWLEDGEMENTS

The authors express special thanks to Dr. Tetsuya Akasaka for his collaboration.

## REFERENCES

- 1 T. Nishida, H. Saito, and N. Kobayashi, Appl. Phys. Lett. **79**, 711 (2001).
- 2 T. Nishida and N. Kobayashi, Phys. Stat. (a) **188**, 113 (2001)
- 3 K. Motoki, T. Okahisa, N. Matsumoto, M. Matsushima, H. Kimura, H. Kasai, K. Takemoto, K. Uematsu, T. Hirano, M. Nakayama, S. Nakahata, M. Ueno, D. Hara, Y. Kumagai, A. Koukitu, and H. Seki, Jpn. J. Appl. Phys. **40**, L140 (2001).
- 4 T. Shibata, Y. Kida, T. Nagai, S. Sumiya, M. Tanaka, O. Oda, H. Miyake, H. Hiramatsu, MRS Fall Meeting, **19**.3 (2001).
- 5 T. Nishida, H. Saito, K. Kumakura, T. Makimoto, and N. Kobayashi, IPAP Conf. Ser., **1**, 872 (2000).
- 6 T. Nishida, H. Saito, and N. Kobayashi, Appl. Phys. Lett. **78**, 399 (2001).

**BEST AVAILABLE COPY**

### Room and Cryogenic Temperature Operation of 280 nm Deep Ultraviolet Light Emitting Diodes

Maxim Shatalov, Vinod Adivarahan, Jian Ping Zhang, Ashay Chitnis, Shuai Wu, Radhika Pachipulusu, Vasavi Mandavilli, and M. Asif Khan  
Department of Electrical Engineering, University of South Carolina,  
Columbia, SC 29208, U.S.A.

#### ABSTRACT

We present a study of the electrical and optical characteristics of 280 nm emission deep ultraviolet light emitting diodes (LED) at room and cryogenic temperatures. At low bias the defect assisted carrier tunneling primarily determines the current conduction. The room-temperature spectral performance and optical power are limited mostly by pronounced deep level defect assisted radiative and non-radiative recombination as well as poor electron confinement in the active region. At temperatures below 100 K the electroluminescence peak intensity increases by more than one order of magnitude due to suppression of non-radiative recombination channels indicating that with a proper device design and improved material quality, milliwatt power 280 nm LED are viable.

#### INTRODUCTION

Due to their enormous potential applications several research groups are actively developing deep ultraviolet (UV) light-emitting diodes (LEDs). Nishida et al. have reported on milliwatt power UV LEDs with emission at 352 nm over hydride vapor phase epitaxial (HVPE) GaN substrates [1]. Recently using sapphire substrates, we have also reported on deep UV LEDs with peak emission at 325 nm and 280 nm [2,3]. Our reported devices utilized an innovative  $\text{AlN}/\text{Al}_{0.5}\text{Ga}_{0.5}\text{N}$  superlattice (SL) approach for deposition of 2  $\mu\text{m}$  thick  $\text{Al}_x\text{Ga}_{1-x}\text{N}$  ( $x>0.35$ ) buffer layers with significantly lower defect levels [4,5]. In addition we also employed a  $\text{p}^+\text{-GaN/p-AlGaN}$  hole accumulation layer for improving the p-doping and thereby hole injection into the active region, which, for the initial design of 285 nm LED, comprised of an  $\text{Al}_{0.46}\text{Ga}_{0.54}\text{N}/\text{Al}_{0.42}\text{Ga}_{0.58}\text{N}$  single quantum well [3,6]. The emission spectra of these 280 nm LEDs contained a sharp quantum well band edge peak at 280 nm and a deep level assisted emission band at 330 nm.

Our recent studies show that at very low pump currents the 330 nm emission is stronger than that at 280 nm [7,8]. At higher currents it rapidly saturates with a simultaneous increase in the 280 nm peak, which then dominates the spectra at pump currents in excess of 200 mA. For the 280 nm emission, we previously reported room temperature powers as high as 0.25 mW for a pulsed pump current of 650 mA [9]. The number of nonradiative defects is a key factor that controls the quantum efficiency of LED devices [3]. The number of nonradiative defects is itself a strong function of the buffer and the active layers material quality. Additionally, our studies indicated that the emission band at 330 nm results from a recombination of the electrons via deep neutral acceptor levels in the p-AlGaIn layer of our device structure [8, 9]. This data also suggests that the weak carrier confinement not only resulted in the long wavelength emission (at 330 nm), but also reduced the 280 nm emitted powers [9]. Now, we present experimental results

confirming the origin of long wavelength band of the electroluminescence spectra due to recombination in p-AlGaN layers due to tunneling nature of conduction mechanism. We also discuss a new design of deep UV LED using  $\text{Al}_x\text{Ga}_{1-x}\text{N}$  multiple-quantum-wells (MQWs) in the active region. This design results in a more efficient carrier confinement and thereby reduces the long wavelength emission band at 330 nm. In addition we have further improved the  $\text{n}^+\text{-Al}_{0.5}\text{Ga}_{0.5}\text{N}$  buffer layer quality grown over the  $\text{AlN}/\text{Al}_{0.85}\text{Ga}_{0.15}\text{N}$  superlattice by using a unique pulsed atomic layer epitaxy (PALE) deposition process [10]. These design and deposition process increases the 278 nm pulse powers as high as 3 mW at a pump current of 1 A.

## STRUCTURE DETAILS

The epilayer structure of the 285 nm LED of initial design consisted of a 0.2  $\mu\text{m}$  thick  $\text{Al}_{0.5}\text{Ga}_{0.5}\text{N}$  layer that is deposited over basal plane sapphire using conventional low-pressure metalorganic chemical vapor deposition [3]. This is followed by a 10 period  $\text{AlN}$  (20 Å) /  $\text{Al}_{0.5}\text{Ga}_{0.5}\text{N}$  (300 Å) SL for strain relief and dislocation filtering and a 1.8  $\mu\text{m}$  thick Si-doped  $\text{n}^+\text{-Al}_{0.5}\text{Ga}_{0.5}\text{N}$  buffer layer. This approach reduces the threading dislocation density and thus enables the deposition of the 1.8  $\mu\text{m}$  thick  $\text{n}^+\text{-Al}_{0.5}\text{Ga}_{0.5}\text{N}$  layers without cracking [4,5]. In addition, it improves the emission characteristics of the active layers by a reduction of the nonradiative recombination. The device active region consisted of an  $\text{Al}_x\text{Ga}_{1-x}\text{N}$  ( $x = 0.46$ , 100 Å) /  $\text{Al}_x\text{Ga}_{1-x}\text{N}$  ( $x = 0.42$ , 30 Å) /  $\text{Al}_x\text{Ga}_{1-x}\text{N}$  ( $x = 0.46$ , 100 Å) single quantum well (SQW) which was capped with a Mg-doped p- $\text{Al}_{0.5}\text{Ga}_{0.5}\text{N}$  (200 Å) and a p $^+\text{-GaN}$  (500 Å) layer. All layers of the structure were deposited at 1050 °C and 76 torr.

For the experimental study, square geometry p-n junction devices were fabricated using a reactive ion etched mesa to access the bottom  $\text{n}^+\text{-Al}_{0.4}\text{Ga}_{0.8}\text{N}$  layer. As before,  $\text{Ti}$ (20 Å)/ $\text{Al}$ (100 Å)/ $\text{Ti}$ (200 Å)/ $\text{Au}$ (2000 Å) and  $\text{Ni}$ (20 Å)/ $\text{Au}$ (200 Å) were used for the n- and p- contact metals. The contact anneal procedures were identical to our earlier reports [9]. For the temperature dependent measurements the sample was mounted in the close-cycle He cryostat. The electrical characteristics were measured over the temperature range from 10 K to 300 K using Agilent 4155C semiconductor parametric analyzer. A single pass TRIAX-550 spectrometer with UV enhanced cooled CCD detector was used for the electroluminescence (EL) and photoluminescence (PL) spectra measurements.

## EXPERIMENT AND DISCUSSION

In Figure 1 we plotted the current vs. voltage (I-V) characteristics of the LED in the temperature range of 10-300 K. At 10 mA of forward current the LED operating voltage increases from 5.2 V at room temperature to 6.7 V at 10 K. The turn-on voltage of about 4.9 V at 300 K is somewhat larger than that expected from the active layer bandgap of 4.35 eV showing additional voltage drop at the heterointerfaces. The increase of turn-on and operating voltage is

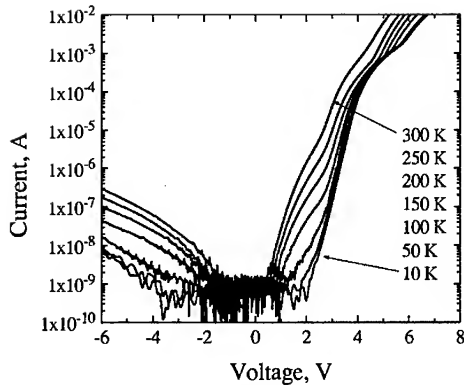


**Figure 1.** The LED I-V curves at different temperatures.

much larger than that expected from the active layer bandgap change with temperature. We believe it could be associated with contact degradation with temperature. At low currents the I-V characteristics can be described by tunneling current associated with tunneling of high energy electrons from active layer into the p-barrier layers followed by non-radiative and radiative recombination with deep impurity-related levels. From the I-V curves of Figure 1 the characteristics energy of tunneling process was found to be about 151 meV at 10 K increasing up to 194 meV at room temperature. This weak dependence of the I-V slope on the temperature is typical for the tunneling related excess current at low bias levels.

The device differential resistance was measured at 50 mA to reduce the p-n junction contribution to the resistance. In order to avoid the device self-heating by the applied bias the high current measurements ( $I > 30$  mA) were done under pulse pumping of 500 ns pulses with 0.5 % duty cycle. As follows from Figure 1 the resistance changes from  $24 \Omega$  at 300 K up to only  $32 \Omega$  at 10 K. The increase of the resistance and the absence of the freeze-out effect at low temperatures are related to the electron hopping transport along the impurity states in highly doped n-layers. The p-layer contribution to the differential resistance is small and temperature independent due to hole accumulation at the AlGaIn/GaN interface and small p-GaN layer thickness.

The EL spectra at different temperatures under 200 mA pulsed pump current are plotted in Figure 2. As seen the intensity of QW band-to-band emission peak located at around 280 nm increases fast with the reduction of temperature from 300 K down to 10 K. The main peak intensity increases at low temperature by more than 10 times. Note that increase is a function of the pump current and at lower bias this intensity goes up by a factor of 100 from 300 K to 10 K. The intensity of the parasitic peak centered at about 330 nm significantly reduces as the temperature decreases. This parasitic peak is associated with the recombination through the deep levels, which are about 0.5-0.6 eV within the band gap of p-AlGaIn layer.

In Figure 3 we plotted the photoluminescence (PL) spectra on the same structure measured in the same temperature range. For PL study we used the pulsed excimer laser emitting at 193 nm with the pulse duration of 8 ns and the repetition frequency of 100 Hz. As seen from Figure 3 the PL spectra show similar increase in main QW peak intensity as a function of temperature.

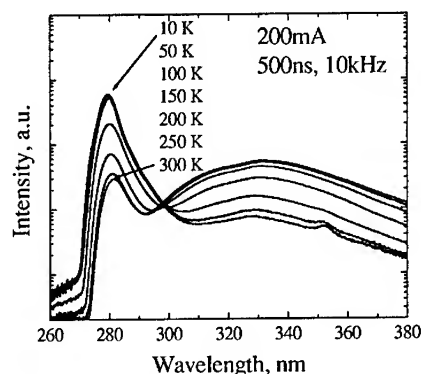


**Figure 2.** Electroluminescence spectra of 280 nm LED as a function of temperature.

The deep level emission peak is not seen in the PL spectrum since the characteristic time of deep levels is much longer than the excitation pulse width of 8 ns. This is confirmed by time resolved EL measurements, which showed the characteristic time for long wavelength peak to build up is about 75 ns [8]. From this study we also found that the transitions between the band and deep level are responsible for the long wavelength emission. These are speculated to be transitions between the conduction band and deep neutral acceptor levels in p-AlGaIn induced by Mg-doping.

The comparison of EL and PL peak increase with reduction of temperature clearly shows that the hole injection into the QW remains the same even at temperatures as low as 10 K. This shows the defect related recombination and carrier confinement in the QW but not the hole injection to be the key factors controlling the room temperature LED performance. Also this implies the power level of few milliwatts at 280 nm can be obtained at room temperatures.

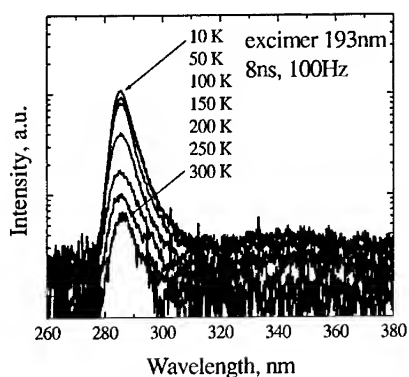


**Figure 3.** Photoluminescence spectra of LED structure as a function of temperature.

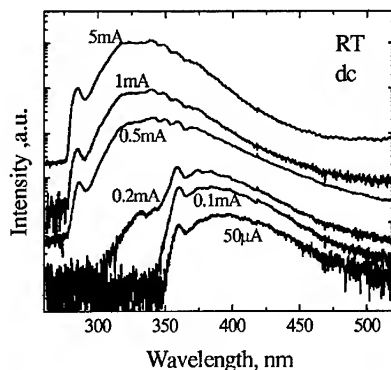


**Figure 4.** LED electroluminescence spectra under low forward bias.

The EL spectra at room temperature in low current range ( $50\ \mu\text{A} - 5\ \text{mA}$ ) corresponding to the turn-on of the I-V curve are plotted in Figure 4. As seen at  $50\ \mu\text{A}$  (3.8 V) the EL spectrum shows distinct peak at 360 nm and broad band centered around 400 nm, which are characteristic for p-GaN band-to-band and band-to-acceptor recombination. This points out to a pronounced electron tunneling current from n-AlGaN into p-GaN followed by the recombination in p-GaN layer. At higher bias other peaks start to appear. In particular, a 330 nm broad peak arises first followed by main 280nm peak, which is seen only at 0.5 mA (5.1V) and above. This spectral behavior clearly indicates deep levels in p-AlGaN to be responsible for long-wavelength emission.

In order to reduce non-radiative and long wavelength radiative recombination we modified the design of the LED structure and growth process. We used newly developed pulsed atomic layer epitaxy (PALE) to grow the high quality AlN buffer layer and AlN/ $\text{Al}_{0.85}\text{Ga}_{0.15}\text{N}$  SL layers [10]. This allowed us to improve the quality of the bottom n- $\text{Al}_{0.5}\text{Ga}_{0.5}\text{N}$  layer. Also in contrast to our previous design of the active layer with single quantum well we now use two  $\text{Al}_{0.47}\text{Ga}_{0.53}\text{N}/\text{Al}_{0.44}\text{Ga}_{0.56}\text{N}$  quantum wells. This MQW active region increases the carrier confinement results in significant reduction of the long wavelength emission band. Improved carrier confinement, reduced defects and efficient hole injection led to devices with dc powers as high as 0.47 mW at 260 mA and pulsed powers of 3 mW at 1 A at room temperature [11]. These to date are the highest reported powers at the shortest wavelength for III-N UV LEDs.

## CONCLUSIONS

We report on low temperature study of deep UV AlGaIn SQW LEDs emitting at 280 nm. The I-V curves show small increase of differential resistance with reduction of the temperature showing small contribution from p-layers due to good p-doping by strain-induced hole accumulation at AlGaIn/GaN interface. Temperature independent tunneling carrier transport is seen at low bias levels. The increase of QW emission peak by more than one order of magnitude is shown at 100 K and below. These experiments show the room temperature LED performance to be limited mostly by poor electron confinement in the QW region as well as large deep level

assisted recombination in p-AlGaIn layers. The modification of the structure design led to significant suppression of the long wavelength emission band at 330 nm. Improved carrier confinement, reduced defects and efficient hole injection resulted in devices emitting at 278 nm with dc powers as high as 0.47 mW at 260 mA and pulsed powers of 3 mW at 1 A.

#### ACKNOWLEDGMENT

This work was supported by DARPA grant No. DAAD19-02-10282, monitored by J. Zavada and J. Carrano. This work was also partially supported by US Army SMDC grant No. DASG60-00-10003, monitored by F. Clarke, and by NASA contract No. NAG5-10322.

#### REFERENCES

1. T. Nishida, H. Saito, and N. Kobayashi, *Appl. Phys. Lett.* **79**, 711 (2001).
2. A. Chitnis, J. P. Zhang, V. Adivarahan, S. Wu, J. Sun, M. Shatalov, J. Yang, G. Simin, and M. Asif Khan, *Jpn. J. Appl. Phys.* **41**, L450 (2002).
3. V. Adivarahan, J. P. Zhang, A. Chitnis, S. Wu, J. Sun, R. Pachipulusu, M. Shatalov, and M. Asif Khan, *Jpn. J. Appl. Phys.* **41**, L435 (2002).
4. J. P. Zhang, H. M. Wang, M. E. Gaevski, C. Q. Chen, Q. Fareed, J. W. Yang, G. Simin, and M. Asif Khan, *Appl. Phys. Lett.* **80**, 3542 (2002).
5. H. M. Wang, J. P. Zhang, C. Q. Chen, Q. Fareed, J. W. Yang, and M. Asif Khan, *Appl. Phys. Lett.* **81**, 604 (2002).
6. M. Shatalov, G. Simin, J. P. Zhang, V. Adivarahan, A. Koudymov, R. Pachipulusu, and M. A. Khan, *IEEE Electron Device Lett.* **23**, 452 (2002).
7. A. Chitnis, R. Pachipulusu, V. Mandavilli, M. Shatalov, E. Kuokstis, J. P. Zhang, V. Adivarahan, S. Wu, G. Simin, and M. Asif Khan, *Appl. Phys. Lett.* **81**, 2938 (2002).
8. M. Shatalov, A. Chitnis, V. Mandavilli, R. Pachipulusu, J. P. Zhang, V. Adivarahan, S. Wu, G. Simin, M. Asif Khan, G. Tamulaitis, A. Sereika, I. Yilmaz, M. S. Shur, and R. Gaska, *Appl. Phys. Lett.* to be published.
9. V. Adivarahan, S. Wu, A. Chitnis, R. Pachipulusu, V. Mandavilli, M. Shatalov, J. P. Zhang, M. Asif Khan, G. Tamulaitis, A. Sereika, I. Yilmaz, M. S. Shur, and R. Gaska, *Appl. Phys. Lett.* **81**, 3666 (2002).
10. J. P. Zhang, M. Asif Khan, W. H. Sun, H. M. Wang, C. Q. Chen, Q. Fareed, E. Kuokstis, and J. W. Yang, *Appl. Phys. Lett.* **81**, 4392 (2002).
11. J. P. Zhang, A. Chitnis, V. Adivarahan, S. Wu, V. Mandavilli, R. Pachipulusu, M. Shatalov, G. Simin, J. W. Yang, and M. Asif Khan, *Appl. Phys. Lett.* **81**, 4910 (2002).

### **New UV Light Emitter Based on AlGa<sub>N</sub> Heterostructures with Graded Electron and Hole Injectors**

M.A.L. Johnson, J.P Long<sup>1</sup> and J.F. Schetzina<sup>2</sup>  
Department of Material Science and Engineering  
NC State University  
Raleigh, NC 27695-7907

<sup>1</sup> Department of Physics, NC State University

<sup>2</sup> Department of Electrical and Computer Engineering, NC State University

#### **ABSTRACT**

New ultraviolet (UV) light emitting device structures address the problems of small carrier concentrations and large band-offsets in wide bandgap Aluminum Gallium Nitride (AlGa<sub>N</sub>) heterostructures through the use of graded epilayers for electron and hole injection. For light emission at 280-290 nm, a multiple-quantum-well separate confinement heterostructure (MQWSCH) employs a graded AlGa<sub>N</sub> structure for the injection of majority carriers from the metal-semiconductor contact layers into the space-charge region of the pn-junction with a higher bandgap energy. Sample LED mesa devices were fabricated and have shown light emission of 289 nm under a forward bias of 12V (20mA). These results provide a 'proof-of-concept' for this new graded device structure which can be employed for the development of both UV-LEDs and laser diodes.

#### **INTRODUCTION**

Research in wide bandgap semiconductors for optoelectronic devices has yielded tremendous advances in the past decade including the commercial introduction of LED across the blue and green wavelength range (400-525 nm) as well as the demonstration of UV-LEDs near 370nm for fluorescence based white general illumination. [1,2,3] These devices have been based on indium gallium nitride (InGa<sub>N</sub>) and gallium nitride (Ga<sub>N</sub>) heterostructures thereby limiting usage to wavelengths longer than 365 nm (3.41 eV). The demonstration of optoelectronic devices at shorter UV wavelengths have used AlGa<sub>N</sub> or quaternary AlGaInN based heterostructures to achieve direct bandgap transition energies higher than 3.41eV [4]. UV optoelectronic devices based on this approach have included UV light emitters and p-i-n photodiodes for both visible blind and solar blind UV detection and imaging [5,6].

A recent potential application to be identified for wide bandgap semiconductors is UV light emitters for optical sources to be used in the fluorescence detection of biomolecules including the tryptophan, tyrosine and phenylalanine. It is well known from biochemistry that the aromatic structure of these amino acids provides a resonance for UV fluorescence spectroscopy. With an optical excitation source for fluorescence spectroscopy of 265-280nm (4.42- 4.67eV), characteristic luminescence is emitted at longer wavelengths for each compound [7]. AlGa<sub>N</sub> based UV light emitters are expected to form the technological basis of compact fluorescence detectors of such biomolecules.

Our work identifies two specific issues to be addressed in the development of AlGa<sub>N</sub> based light emitters. The first is the unavailability of a suitable p-type acceptor dopant for AlGa<sub>N</sub> at bandgap energies needed for UV emission. The second is the

significant role of conduction and valence band offsets in the vertical transport of majority carriers in pn junction LED structures. Magnesium (Mg) is the most common p-type dopant used for  $\text{Al}_x\text{Ga}_{1-x}\text{N}$  semiconductors. The acceptor ionization energy for Mg is approximately 185 eV for GaN ( $x=0.0$ ) which corresponds to a hole concentration of less than  $[h^+] < 5 \times 10^{17} \text{ cm}^{-3}$  for an acceptor concentration exceeding  $[\text{Mg}] > 10^{19} \text{ cm}^{-3}$ . Despite this very low hole ionization efficiency, Mg doping is a quite successful for the GaN based devices previously described [8]. Unfortunately, the acceptor ionization efficiency increases with Al composition in  $\text{Al}_x\text{Ga}_{1-x}\text{N}$  to an estimated 430-495 meV at  $x=0.45$  which corresponds to 280nm (4.42eV) when using a band-bowing parameter of 1.0eV. Such high acceptor ionization efficiencies precludes the thermal generation of an acceptable number of holes. While less pronounced than in the p-type layers, a similar effect of increased donor ionization energy with Al composition has also been observed in n-type AlGaIn. Approaches to circumvent low majority carrier concentrations have included the use of strained AlGaIn/GaN superlattice structures where spontaneous and piezoelectric polarization fields induce the production of free holes in the valence band [9,10]. Such techniques have shown success particularly in Hall Effect measurements where carrier transport is perpendicular to the polarization field direction.

A concern for the band-offsets inherent in these heterostructures for devices where carrier transport is in the direction of the strain induced field, has motivated this work in using graded interfaces for the injection of excess majority carriers across low energy barriers into the pn junction of UV light emitters. Graded injection has generally been recognized to minimize the influence of band-offsets on carrier transport [11]. Graded structures for carrier transport have previously been demonstrated as an effective means of injecting majority carriers for LEDs made from wide bandgap II-VI semiconductors [12]. Our structure uses a similar approach for AlGaIn devices, where the majority carriers at the metal-semiconductor contact layers are injected across graded barriers with minimized offsets in both the valence and conduction bands. As shown in Figure 1, LED structures without graded injection will not only have high donor ionization energies, but

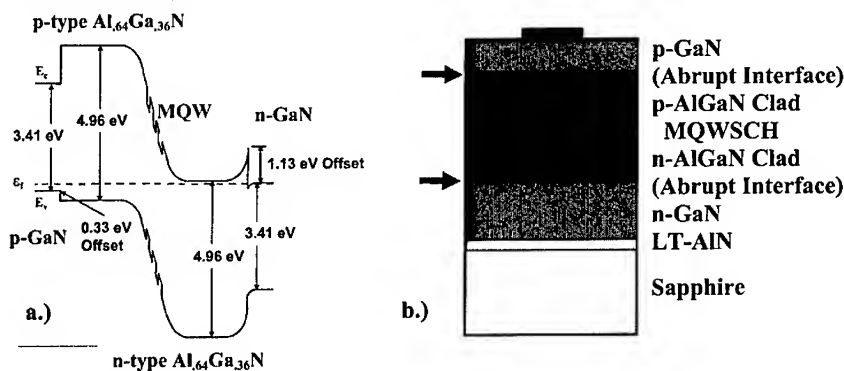


**Figure 1.** (a) Band energies and (b) typical epitaxial layer design for MQW light emitting devices containing traditional abrupt interfaces. Note the barriers to carrier transport due to band offsets at the GaN-AlGaIn interfaces. Abrupt interfaces block the injection of majority carriers from the metal/semiconductor contacts into the pn-junction.

will also possess substantial band-offsets across both the n-type ( $\sim 1.13$  eV) and p-type ( $\sim 0.33$  eV) layers. Band offsets give rise to the need for a substantial electric field to generate a current normal to the interface as necessary for p-n junction diodes. This electric field manifests itself as a high operating voltage for the LED or laser diode. Such high voltage operation is undesirable and leads to premature failure for devices. Figure 2 displays a MQWSCH light emitter structure with graded AlGaIn layers between the GaN contacts and the AlGaIn cladding layers. Note the absence of band offsets on either the p-type or n-type side of the diode. When biased, a graded structure should allow the injection of majority carriers from the contact layers into the space charge region of the diode, and result in the emission of light at the shorter wavelength of the MQW structure. Forward voltages for LEDs operating at 20mA are typically about 1.0-1.4V higher than the voltage corresponding to the bandgap energy at the emission wavelength. The additional voltage drop often occurs due to contact resistances in series. Following this approximation, a UV LED emitting at 280 nm should ultimately operate at a forward bias of 5.3-5.7 V at an injected current of 20mA. This work will demonstrate the use of these graded AlGaIn structures for light emission in the 280nm wavelength range.

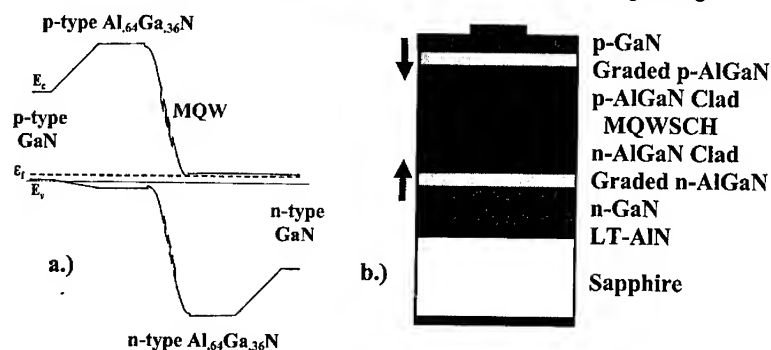


**Figure 2.** (a) Band energies and (b) epitaxial layer design for MQW light emitting devices containing graded interfaces. Note the graded interfaces eliminate band offsets and allow for majority carrier transport across the GaN-AlGaIn heterostructures.

## EXPERIMENTAL DETAILS

Metal Organic Chemical Vapor Deposition (MOCVD) of the epitaxially grown AlGaIn based heterostructures in this study was performed in a downward vertical flow, high-speed rotating reactor that has been previously described [13]. The metal-organic sources were trimethylaluminum (TMA) and triethylgallium (TEG) which were injected to the MOCVD reactor separately from the ammonia to avoid gas phase pre-reaction. Double sided 50mm sapphire was used as the heteroepitaxial substrate and employed a standard low temperature Aluminum Nitride (AlN) buffer layer for the 2D nucleation and growth of the subsequent AlGaIn epitaxial films.

LED test structures used a 1  $\mu\text{m}$  thick silicon (Si) doped GaN buffer layer with a carrier concentration of  $1 \times 10^{18} \text{ cm}^{-3}$  as measured by CV. The composition of  $\text{Al}_x\text{Ga}_{1-x}\text{N}$  is graded across 80nm to the  $x=0.65$  cladding. The 120nm thick n-AlGaIn ( $x=0.65$ )

cladding and 120nm thick n-AlGaIn ( $x=0.55$ ) light-guide layers were doped with a silane molar flow equivalent to the doping in the n-GaN layer. CV profiling of separate Si doped AlGaIn layers ( $x=0.57$ ) achieved a concentration of  $1.3-1.5 \times 10^{18} \text{ cm}^{-3}$  at a 1kHz test frequency and  $3-4 \times 10^{17} \text{ cm}^{-3}$  at a 1 MHz test frequency. For dopant energies substantially higher than  $kT$ , the CV measurements correspond to donor state and free carrier concentrations respectively. Three quantum wells ( $x=0.45$ ) were separated by barriers ( $x=0.54$ ) with thicknesses of 3.5nm and 15nm respectively as estimated by growth rate. Changes in UV emission wavelength were accomplished by changing Al composition of the quantum wells. P-type light guiding and cladding layers were doped with Mg with compositions and thicknesses identical to the n-type layers. Following the cladding layer, p-AlGaIn was graded from  $x=0.65$  to  $x=0.0$  for p-type GaN. Mg doping in GaN was typically  $2-3 \times 10^{19} \text{ cm}^{-3}$  acceptor and  $4-5 \times 10^{17} \text{ cm}^{-3}$  hole concentration using low frequency (1 kHz) and high frequency (1 MHz) CV as described above. The p-AlGaIn layers were doped using  $\text{Cp}_2\text{Mg}$  molar flows to achieve Mg concentrations similar to that of the p-GaN top layer. As acceptor energy increases with Al composition, we were unable to separately measure high mole fraction p-AlGaIn by CV. Contact metals were Ti/Al and Ni/Au for n-type and p-type respectively.

LEDs were tested using a two-contact probe station modified to accept fiber-optic collection of emitted light. The fiber was positioned to detect light emitted from the edge of the LED mesas. Care was taken to maximize the collection of electroluminescent light directly from the edge of the mesa structure and minimized light which is re-emitted by photoluminescence from heterostructures in the presence of an internal UV source. Light collected by the fiber system was fed into an Acton Research monochromator with computer controlled CCD detection. Current-voltage (I-V) measurements were taken in the same configuration using a curve tracing oscilloscope.

## DISCUSSION

The MQW-SCH test structures were fabricated with two separate active layer compositions, the first group targeted for UV emission at 330-340nm and the second group targeted for 280-290nm. Representative spectra from each set of devices are shown in figure 3a and 3b. The spectra were typically recorded at forward injection current of less than 10mA for  $100\mu\text{m} \times 100\mu\text{m}$  mesa structures which had been configured to maximize the electroluminescence collected by the fiberoptic system. Note the slight emission at the long wavelength side of the peak in figure 3a. We attribute this addition emission at longer wavelengths to photoluminescence generated by contact layers internal to the device with electroluminescence at a shorter wavelength. We expect further improvement with graded layer structures employing an optical design to minimize this photoluminescence effect for UV-LEDs. This work clearly demonstrates light emission in the 280nm wavelength range using graded injector device structure.

A parallel requirement for UV-LEDs is low voltage operation. I-V 25V. Samples grown without graded layers exhibit significantly higher forward voltages curves for the LED devices tested in electroluminescence experiments display the typical rectifying behavior of a diode, with a minimum forward voltage of approximately 12V at a current of 20mA. In addition, the reverse bias does not exhibit breakdown at voltages exceeding (>100V) at equivalent injection current levels. These I-V results demonstrate the lower forward voltages observed by using a graded carrier injector design on UV-LEDs made

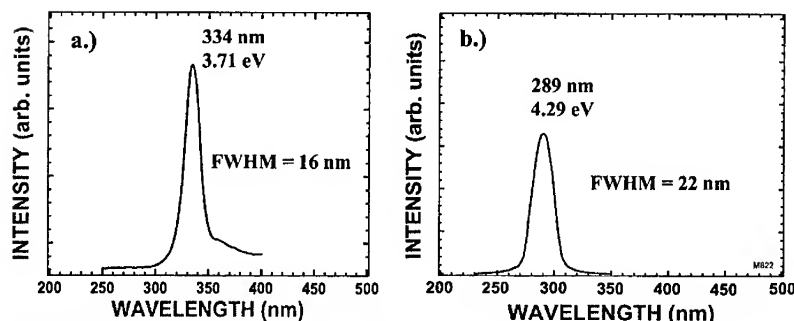


**Figure 3** (a) Electroluminescence spectrum from an LED test structure emitting at 334nm with a forward injection current of 2mA. The emission wavelength corresponds to an  $\text{Al}_x\text{Ga}_{1-x}\text{N}$  composition of  $x=0.15$ . (b) Electroluminescence spectrum from an LED test structure emitting at 289nm with a forward injection current of 7mA. The emission corresponds to an aluminum composition of  $x=0.40$ .

of wide bandgap AlGaIn semiconductor material.

While the graded structure offers a substantial reduction in series resistance relative to non-graded structures, this voltage is still approximately 50% higher than is desired for an optimum LED structure. Factors which may introduce this higher voltage drop include series resistance due to metal-semiconductor contact interfaces, parallel current flow through dislocations or other defects in the III-N epilayers and non-optimized graded interface structures. The metal-semiconductor contacts in this study followed a standard metal selection and rapid thermal anneal activation procedure. A metallization procedure optimized for these structures, including contact metals optimized for contact to n-type AlGaIn are expected to reduce this series resistance. III-nitride semiconductors are notorious for having high concentration of dislocations. A graded structure in combination with an epitaxially overgrown buffer layer should minimize parallel current flow requiring high forward voltages [14]. In addition to dislocations, differences in lattice constant and thermal expansion coefficients often leads to brittle fracture or crack formation in epitaxial layers containing high mole fraction AlGaIn. While unexplored to date, minimizing crack density should have an effect similar to the minimization of dislocation density. Finally, the graded structures for this study were not specifically optimized for minimum series resistance across the diode. A layer thickness of 100nm was used for the graded layers. Changes in the layer design such as grading rate, linear vs. non-linear grading, and MQW SCH layer thicknesses may be optimized to further reduce the series resistance for UV-LEDs at 280nm.

Finally, we have demonstrated that emission wavelength may be adjusted by changing AlGaIn composition in the MQW layer of these UV-LEDs. Future efforts include LEDs with higher AlGaIn compositions to match the UV-LED emission with the 265-280nm wavelengths needed for the fluorescence detection of biochemicals. A final goal of this effort is to provide biochemists with the UV solid-state devices operating at voltages and wavelengths necessary to utilize the tools of UV-spectroscopy in a compact system suitable for use beyond the confines of a traditional biochemistry laboratory.

## CONCLUSIONS

This study demonstrates the use of graded  $\text{Al}_x\text{Ga}_{1-x}\text{N}$  for injecting of majority carriers from p-type and n-type GaN contact layers into wider bandgap AlGaIn layers. This approach circumvents difficulties related to high dopant ionization energies and substantial band-offsets in high Al content wide bandgap LEDs. Earlier work demonstrated graded injection for wide bandgap II-VI LEDs. This work demonstrates the effectiveness graded interfaces in wide bandgap AlGaIn based light emitters, particularly at the compositions needed for solid-state devices emitting in 280nm UV wavelengths. Electroluminescence under forward bias conditions demonstrated the effectiveness of the graded structure as a means of injecting majority carriers into the pn junction of the LED for radiant recombination. A relatively low voltage of 12V at 20mA is evidence of graded interfaces as an effective means to minimize band offsets in LED structures. Additional work to optimize graded interfaces and improve ohmic contacts is expected to yield practical devices for detecting biochemicals by UV fluorescence.

## ACKNOWLEDGEMENTS

The authors thank Joe Matthews for his essential contributions to lab operations. This work has been supported by DARPA/MTO (J. Carrano, Program Manager).

## REFERENCES

1. S. Strite and H. Morkoç, *J. Vac. Sci. Technol. B.*, **10**, 1237 (1992)
2. S. Nakamura, G. Fasol, *The Blue Laser Diode - GaN based Light Emitters and Lasers* (Springer-Verlag, Heidelberg, 1997).
3. M.G. Crawford *MRS Bulletin* (Oct. 2000) p27.
4. J. Han, J. Figiel, G. Petersen, S. Myers, M. Crawford, M. Banas and S. Hearne, *MRS Internet J. Nitride Semicond. Res.* **5S1**, W6.2 (2000).
5. A. Chitnis, P. Z. Jain, V. Adivarahan, S. Wu, S. Jie, M. Shatalov, J.W. Yang; G. Simin, M.A. Khan *Japanese J. Appl. Phys.* **41**.L450 (2002)
6. J. D. Brown, J. Matthews, S. Harney, J. C. Boney, J. F. Schetzina, J. D. Benson, K. V. Dang, T. Nohava, W. Yang, S. Krishnakutty *MRS Internet J. Nitride Semicond. Res.* **5S1**, W1.9 (2000).
7. S. Pine, J. Hendrickson, D. Cram and G. Hammond *Organic Chemistry*, 4<sup>th</sup> Ed. McGraw-Hill: New York (1980) p789-794.
8. J. Li, T.N. Oder, M.L. Nakarmi, J.Y. Lin and H.X. Jiang, *Appl. Phys. Lett.*, **80**, 1210 (2002).
9. E.F. Schubert, W. Grieshaber and I.D. Goepfert, *Appl. Phys. Lett.* **69** (24) 3737 (1996).
10. A. Yasan, R. McClintock, S.R. Darvish, Z. Lin, K. Mi, P. Kung, M. Razeghi, *Appl. Phys. Lett.*, **80**, 2108 (2002).
11. CL Allyn, AC Gossard, and W. Wiegmann, *Appl. Phys. Lett.*, **36**, 373 (1980).
12. M.C. Phillips, M.W. Wang, J.F. Swenberg, J.O. McCaldin and T.C. McGill, *Appl. Phys. Lett.* **61**, 1962 (1992).
13. M.A.L. Johnson, Zh. Yu, J.D. Brown, F.A. Koeck, N.A. El-Masry, H.S. Kong, J.A. Edmond, J.W. Cook, Jr., J.F. Schetzina, *MRS Internet J. Nitride Semicond. Res.* **4S1**, G5.10 (1999).
14. O-H Nam, MD Bremser, TS Zheleva, RF Davis, *Appl. Phys. Lett.*, **71**, 2638 (1997).

### High Power 325 Light Emitting Diode Arrays by Flip-Chip Packaging

Ashay Chitnis, Maxim Shatalov, Vinod Adivarahan, Jian Ping Zhang, Shuai Wu, Jie Sun, and M. Asif Khan  
Department of Electrical Engineering, University of South Carolina,  
Columbia, SC 29208, U.S.A.

#### ABSTRACT

We report flip-chip 325 nm emission light emitting diodes over sapphire with dc powers as high as 0.84 mW at 180mA and pulse powers as high as 6.68 mW at 1A. These values to date are the highest reported powers for such short wavelength emitters. Our data shows the device output power under dc operation to be limited by the package heat dissipation. A study is presented to determine the role of thermal management in controlling the power output for the reported 325 nm ultraviolet light emitting diodes.

#### INTRODUCTION

Recently, there have been a number of reports of deep ultraviolet (UV) ( $280\text{ nm} < \lambda < 350\text{ nm}$ ) III-N quantum well light-emitting diodes (LEDs) on sapphire, SiC and bulk GaN substrates [1-9]. In these substrate choices, SiC and HVPE GaN have superior thermal conductivity and they also allow for vertical conduction device geometry. However, both of these substrate types are highly absorbing in the deep ultraviolet wavelength region and thus require the output power extraction through the top p-contact and the p<sup>+</sup>-GaN contact layer. In contrast, we have shown sapphire to be a good substrate choice for deep UV LEDs with efficient light extraction through the substrate [5,6,8-10]. However, under dc operation, sapphire substrate based deep UV LEDs suffer from excessive self-heating due to its lower thermal conductivity and relatively high operating voltages. Recently, using micro-Raman spectroscopy and electroluminescence (EL), we have reported that the self-heating in 325 nm emission UV LEDs can increase the device temperature by about 70°C for a dc bias current of 50 mA [10]. We now report a significant improvement in the performance of the sapphire substrate based 325 nm LEDs by the use of a low thermal resistance package. A customized silver (Ag) plated copper header and flip-chip packaging enabled us to obtain record dc and pulsed powers of 0.84 mW and 6.68 mW for room temperature operation.

#### EXPERIMENTAL DETAILS

The epilayer structure for the LEDs of our study was grown over basal plane sapphire substrates using the low-pressure metal organic chemical vapor deposition technique. Similar to our previous report a 10 period AlN (20 Å)/Al<sub>0.2</sub>Ga<sub>0.8</sub>N (300 Å) superlattice (SL) and a 2 μm thick n<sup>+</sup>-Al<sub>0.2</sub>Ga<sub>0.8</sub>N over layer were used to reduce the threading dislocation density by a factor of five [11]. The device active layers consisted of three Al<sub>0.18</sub>Ga<sub>0.82</sub>N (110 Å)/Al<sub>0.12</sub>Ga<sub>0.88</sub>N (35 Å) quantum wells. These were capped with a 200 Å thick Mg-doped p-Al<sub>0.3</sub>Ga<sub>0.7</sub>N and a 500 Å thick p<sup>+</sup>-GaN layer. Square geometry mesa devices with edge dimensions ranging from

100  $\mu\text{m}$  to 300  $\mu\text{m}$  were then fabricated. The mesa etching, contact metalization and annealing procedures were identical to those reported earlier [5-7].

## DISCUSSION

The fabricated wafer was diced and identical 200  $\mu\text{m}$  x 200  $\mu\text{m}$  LED chips were selected for this study. These single chips were then mounted in flip-chip configuration on high thermal conductivity (175 W/mK) insulating AlN carriers by thermo-compression gold bonding. The AlN carriers with the flip-chip LEDs were mounted on a custom designed silver coated header and on a standard gold-coated TO-39 header. In addition, using an identical procedure, a parallel combination of four 200  $\mu\text{m}$  x 200  $\mu\text{m}$  LEDs were also flip-chip mounted in the custom copper header, which we refer to as the array-package. Figure 1 shows the electro-luminescence spectrum at dc pump current for a single 200  $\mu\text{m}$  x 200  $\mu\text{m}$  LED. As seen, the peak emission wavelength is at 325 nm with a FWHM of 8 nm.

Figure 2a shows the dc optical powers as a function of pump currents (L-I) for the single flip-chip LEDs in the TO-39 and the custom copper header package. An integrating sphere with a calibrated UV-enhanced Si detector was used for these measurements. It is clear from Figure 2a that for the device packaged on the copper header the saturation dc-current increases by about 20 mA along with an increase in the output optical power. The operating voltage of 6.6 V at 70 mA dc was measured for the single device mounted on either the TO-39 or the custom copper header package. From the low current optical power data, where the heating effects are minimal, we estimated the light extraction to be improved by 30 % for the copper package. The improvement at the higher pump currents is attributed to both a better thermal management and an increased light extraction. Figure 2a also shows the L-I characteristics of the 2x2 array-package. A record optical power of 0.84 mW at 180 mA dc bias was measured for this package configuration. We attribute this improved performance to the lower differential resistance and the better heat removal resulting from the 2x2 package configuration.

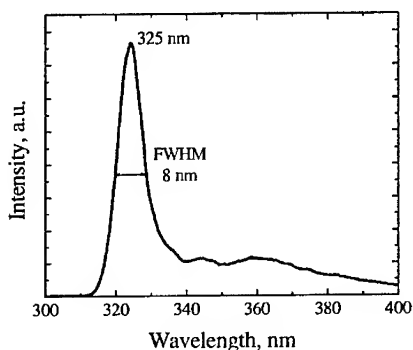
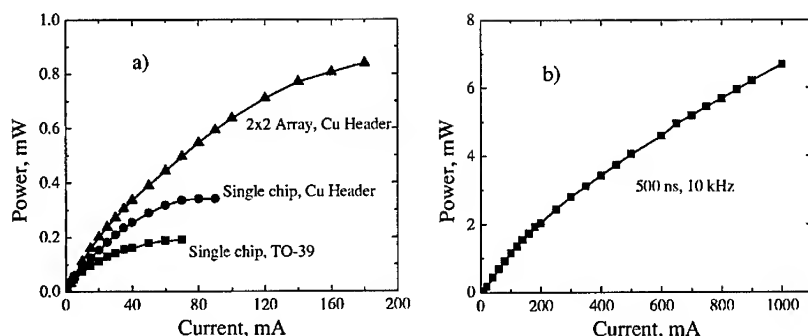


Figure 1. LED EL spectrum at 100 mA dc.



**Figure 2a.** dc output power for different flip-chip package configurations.  
**b.** Pulse power of the 2x2 LED array.

Figure 2b shows the pulsed (500 ns, 10 kHz) L-I for the 2x2 LED array package. As seen an output power as high as 6.7 mW was measured for a pulsed pump current of 1 A. To the best of our knowledge, these dc and pulsed powers are to date the highest reported values for a 325 nm emission LED device.

Figure 3 shows the DC L-I characteristics as a function of the package temperature for the 2x2 LED array. For these measurements the package was mounted on a thermo-electric cooler. From the data of Figure 3 we see that the saturation current increase significantly when the total package is cooled. At 10°C and 180 mA of dc pump current, the optical power increases by 0.36 mW from its room temperature value. In addition, the saturation point of the L-I characteristics increases from about 200 mA to 350 mA. Finally the maximum dc output power of 1.5 mW at 350 mA dc was measured when the package was maintained at 10 °C. These data clearly establish that thermal management and in particular package heat-sinking still to be a critical limiting factor for the dc operation of sapphire based deep UV LEDs.

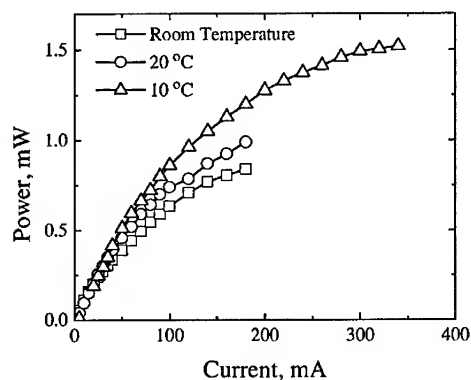


**Figure 3.** dc output power for LED array package at different package temperatures.

We then estimated the temperature rise with dc bias current for the custom copper header. These measurements were carried out using a micro-thermocouple assembly. Type-T thermocouples were mounted on the top of sapphire substrate (for flip-chip configuration) as well as on the copper header. The thermal loss in the TC wire was estimated to be smaller than the measured temperature increase and thus was neglected in these measurements. Figure 4a shows the temporal temperature rise for the sapphire substrate and the copper header when the dc bias current was switched from zero to 40 mA. The dc current was kept steady for 1000 sec and then switched off. As seen from Figure 4a, it takes approximately 600 sec for the package temperature to reach its steady-state value. We also measured the emitted power at 325 nm and the operation voltage as a function of time with the device under a steady dc bias of 40mA. These data are plotted in Figure 4b. As seen, in about 600 sec after the application of the steady-state 40mA dc bias, the optical power reduces to 60% of its initial value while the operating voltage remains nearly constant. However, as evidenced from the repeated measurements on the same device, these power and voltage changes were not permanent. They are a consequence of the device temperature rise [10]. Note that the degradation time constant of 600 sec is also very close to the rise time for the packaged device temperature to reach a steady state. Better heat extraction from the package should therefore reduce the device operating temperatures and thus increase the output powers.

We also estimated the device steady state temperature rise from the shift of EL spectrum peak position as a function of applied dc bias current [12]. The procedure used was similar to the one described in our earlier report [10] From these temperature measurements, we determined the effective thermal resistance for the 2x2 array-package at steady state to be about 80 °C/W at 40 mA. Thus, at the saturation current of 180 mA, we estimate the device temperature rise to be about 90 °C.

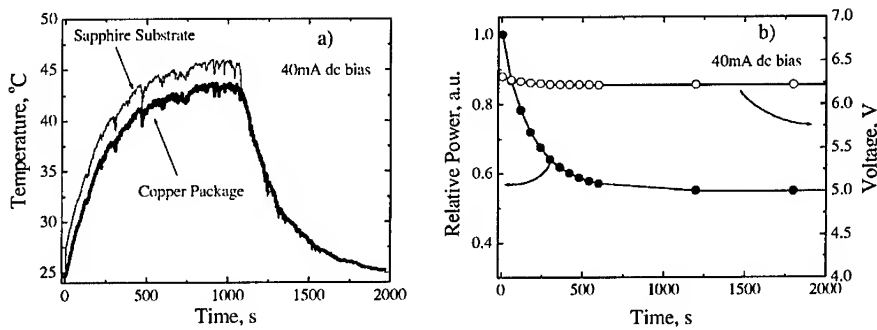


**Figure 4a.** Temporal evolution of the LED array package temperature at 40mA dc bias.  
**b.** Relative optical power and operating voltage change of the LED array package under 40mA dc bias as a function of time.

## CONCLUSION

In summary, we report record performance of flip-chip packaged 324 nm UV LEDs on sapphire substrates. A total dc optical power of 0.84 mW at 180 mA and a pulsed power as high as 6.68 mW at 1 A was measured for room temperature operation. At 10 °C the maximum dc power increases to 1.5 mW for 350 mA of dc pump current. Our results therefore show that with proper thermal management, 324 nm deep UV LEDs on sapphire substrates are fully capable of milliwatt power operation.

## ACKNOWLEDGEMENT

This work was supported by DARPA grant No. DAAD19-02-10282, monitored by J. Zavada and J. Carrano. This work was also partially supported by US Army SMDC grant No. DASG60-00-10003, monitored by F. Clarke, and by NASA contract No. NAG5-10322.

## REFERENCES

1. T. Nishida, H. Saito, and N. Kobayashi, *Appl. Phys. Lett.* **78**, 3927 (2001).
2. Kinoshita, H. Hirayama, M. Ainoya, Y. Aoyagi, A. Hirata, *Appl. Phys. Lett.* **77**, 175 (2000).
3. N. Otsuka, A. Tsujimura, Y. Hasegawa, G. Sugahara, M. Kume, Y. Ban, *Jpn. J. Appl. Phys.* **39**, L445 (2000).
4. M. Iwaya, S. Terao, T. Sano, S. Takanami, T. Ukai, R. Nakamura, S. Kamiyama, H. Amano, I. Akasaki, *Phys. Stat. Sol. (a)* **188**, 117 (2001).
5. V. Adivarahan, A. Chitnis, J. P. Zhang, M. Shatalov, J. W. Yang, G. Simin, M. Asif Khan, M. Shur, R. Gaska, *Appl. Phys. Lett.* **79**, 4240 (2001).
6. M. Asif Khan, V. Adivarahan, J. P. Zhang, C. Chen, E. Kuokstis, A. Chitnis, M. Shatalov, J. W. Yang, G. Simin, *Jpn. J. Appl. Phys.* **40**, L1308 (2001).
7. J. P. Zhang, V. Adivarahan, H. M. Wang, Q. Fareed, E. Koukstis, A. Chitnis, M. Shatalov, J. W. Yang, G. Simin, M. Asif Khan, M. Shur, R. Gaska, *Jpn. J. Appl. Phys.* **40**, L921 (2001).
8. A. Chitnis, J. P. Zhang, V. Adivarahan, W. Shuai, J. Sun, M. Shatalov, J. W. Yang, G. Simin, M. Asif Khan, *Jpn. J. Appl. Phys.* **41**, L450 (2002).
9. V. Adivarahan, J. Zhang, A. Chitnis, W. Shuai, J. Sun, R. Pachipulusu, M. Shatalov, M. Asif Khan, *Jpn. J. Appl. Phys.* **41**, L435 (2002).
10. A. Chitnis, S. Jason, V. Mandavilli, R. Pachipulusu, S. Wu, M. Gaevski, V. Adivarahan, J. P. Zhang, M. Asif Khan, A. Sarua, M. Kuball, *Appl. Phys. Lett.* **81**, 3491 (2002).
11. J. P. Zhang, H.M. Wang, M.E. Gaevski, C.Q. Chen, Q. Fareed, J.W. Yang, G. Simin, M. A. Khan, *Appl. Phys. Lett.* **80**, 3542 (2002).
12. A. Chitnis, V. Adivarahan, J. P. Zhang, S. Wu, J. Sun, R. Pachipulusu, V. Mandavalli, M. Gaevski, M. Shatalov, and M. Asif Khan, *Electron. Lett.* **25**, 1709 (2002).

### Micro-Raman Spectroscopy: Self-Heating Effects In Deep UV Light Emitting Diodes

A. Sarua<sup>1</sup>, M. Kuball<sup>1</sup>, M. J. Uren<sup>2</sup>, A. Chitnis<sup>3</sup>, J. P. Zhang<sup>3</sup>, V. Adivarahan<sup>3</sup>, M. Shatalov<sup>3</sup>, and M. Asif Khan<sup>3</sup>

<sup>1</sup>H. H. Wills Physics Laboratory, University of Bristol, Bristol BS8 1TL, United Kingdom

<sup>2</sup>QinetiQ Ltd, Malvern WR14 3PS, United Kingdom

<sup>3</sup>Department of Electrical Engineering, University of South Carolina, Columbia, South Carolina 29208

#### ABSTRACT

Ultraviolet light emitting diodes (LED) based on GaN and its ternary alloy AlGaIn are key devices for applications such as solid state white lighting and chemical sensing. Ultraviolet LEDs are prone to self-heating effects, i.e., temperature rises during operation, contributing significantly to the commonly observed saturation of light output power at relatively low input currents. Rather little, however, is known about the actual device temperature of an operating ultraviolet LED. Using micro-Raman spectroscopy temperature measurements were performed as a function of input current on 325nm-Al<sub>0.18</sub>Ga<sub>0.82</sub>N/Al<sub>0.12</sub>Ga<sub>0.88</sub>N multiple quantum wells LEDs grown on sapphire substrates, flip-chip mounted on SiC for heat-sinking. Temperature maps were recorded over the active device area. Temperature rises of about 65 °C were measured at input currents as low as 50mA (at 8V) for 200 µm x 200 µm size LEDs despite flip-chip mounting the devices. Temperature rises at the device edges were found to be higher than in the device center, due to combined heat sinking and current crowding effects. Finite difference heat dissipation simulations were performed and compared to the experimental results.

#### INTRODUCTION

Wide bandgap materials, such as GaN, AlN, InN and their alloys offer a range of key properties such as the possibility to cover a bandgap range from 0.9eV up to 6.2eV, high breakdown electric field, high mobility, and high temperature and chemical stability. Development of nitride based LEDs has recently been targeted towards low power consumption white light illumination as well as light sources for chemical and biological sensor applications. Starting from high-efficiency blue-LEDs based on InGaIn/GaN demonstrated in the early 90's<sup>1</sup>, there has recently been a major breakthrough into the deep UV (below 350nm) range with the introduction of quantum well structures based on ternary and quaternary nitride alloys (Al,In)GaIn<sup>2-9</sup>. Recently, LEDs with main peak emission wavelength as low as 278 nm with milliwatt operation have also been realized<sup>10</sup>. Nevertheless, there are several issues to be resolved before these devices can be introduced into the commercial market. In particular, self-heating effect is known to be responsible for saturation of light output power in nitride based LEDs<sup>11</sup>. The device thermal management is, therefore, of great importance for LED designers. In this work we report on the use of the micro-Raman technique to study self-heating in a deep UV LED based on AlGaIn quantum well active structures operated using DC pump current. Finite difference heat dissipation simulation was used to compare with the experimental results.

## EXPERIMENTAL DETAILS

The LED structure was grown on a double-side polished sapphire (0001) substrate using low-pressure metal organic chemical vapor deposition (MOCVD). To reduce dislocation density caused by the lattice and thermal expansion coefficient mismatch 10 periods of an AlN (20 Å)/Al<sub>0.2</sub>Ga<sub>0.8</sub>N (300 Å) superlattice (SL) and a 2 µm thick Al<sub>0.2</sub>Ga<sub>0.8</sub>N layer were grown. The active region was constructed of three Al<sub>0.18</sub>Ga<sub>0.82</sub>N (110 Å)/Al<sub>0.12</sub>Ga<sub>0.88</sub>N (35 Å) multiple quantum wells. A capping layer of 200 Å thick Mg-doped p-Al<sub>0.3</sub>Ga<sub>0.7</sub>N and a 500 Å thick p<sup>+</sup>-GaN layer was used. The 200 µm x 200 µm diode was diced from the wafer and then flip-chip mounted onto a SiC thermal conductor for efficient heat-sinking and then fixed onto a gold coated TO-39 holder. This structure gives improved heat extraction from the active region, since sapphire alone is a poor thermal conductor ( $\kappa_{\text{sapphire}} = 0.35 \text{ Wcm}^{-1}\text{K}^{-1}$ ,  $\kappa_{\text{SiC}} = 4.5 \text{ Wcm}^{-1}\text{K}^{-1}$ ). Flip-chip mounting also allows efficient UV light extraction from the sapphire side, which avoids the use of semi-transparent metal contacts for p-contacting.

Actual device temperature was monitored by micro-Raman measurements using the 488 nm Ar<sup>+</sup>-ion laser line and a Renishaw micro-Raman system in confocal mode with a shift spectral resolution of about 0.1-0.2 cm<sup>-1</sup> and a spot collection size of about 1 µm diameter. 2D Raman maps were recorded using a motorized XY-stage attached to the microscope with minimum step size as low as 0.1 µm. The 488 nm (2.54 eV) excitation used in measurement is far below the bandgap of AlGa<sub>x</sub>N material, thus no laser heating of the device occurs.

## DISCUSSION

Fig.1 shows a typical IV curve of an UV LED measured at DC. The turn-on voltage is about 5V for the given device. The mean emission peak was about 325 nm with 100 µW output power at 20 mA DC. The sapphire substrate is transparent for visible and UV radiation and allows direct optical access to the active device region and the micro-Raman technique can, therefore, be effectively applied for monitoring the device temperature during device operation<sup>12</sup>. To monitor the actual device temperature the position of the non-polar E<sub>2</sub>(high) phonon mode of AlGa<sub>x</sub>N was followed. The position of the E<sub>2</sub>(high) phonon mode measured at zero voltage was 574.2 cm<sup>-1</sup>, which is in a good agreement with the position reported for Al<sub>0.20</sub>Ga<sub>0.80</sub>N<sup>13</sup>. To calibrate the temperature measurements the dependence of the phonon position as a function of the temperature was measured by placing the device on a heating stage. The measured temperature dependence was assumed to be linear in the range between 300K and 500K. A

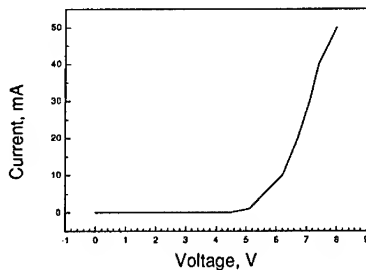
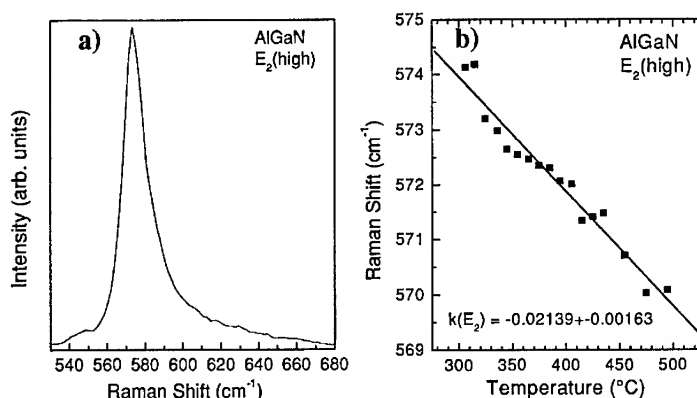
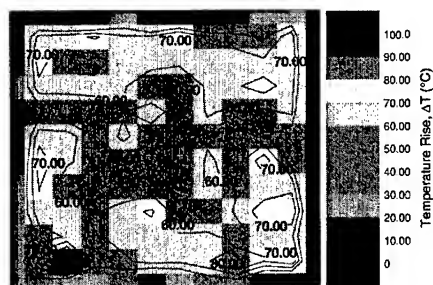


Figure 1. IV curve of investigated UV LED operating in DC pumping mode.

temperature coefficient  $k(E_2)$  of  $0.0214 \text{ cm}^{-1}/\text{K}$  was found (Fig. 2). This is similar to the value reported on GaN material<sup>14</sup>, i.e. approximately the temperature dependence of the GaN phonon modes could be used without the need for prior calibration. The accuracy for the temperature determination is limited by the spectral resolution of the system and accuracy of the  $k(E_2)$  determination. Estimated temperature accuracy was about  $10^\circ\text{C}$  in our case. To eliminate other effects affecting the position of the  $E_2(\text{high})$  phonon mode (stress, inhomogeneity) 2D Raman maps were recorded at zero voltage over the active device area. These were used as a reference to the maps measured at applied voltage to obtain the temperature rise. Fig. 3 shows the result of the obtained temperature distribution recorded at 50mA (8V) corresponding to a power of 0.4 W for the chip area. The average temperature rise  $\Delta T_{\text{av}}$  for the LED chip measured was about  $65^\circ\text{C}$ . Line profiles across a similar chip (Fig. 4) and temperature point measurements (Fig. 5) in different places on the chip were performed to reveal the temperature rise as a function of applied electrical power. Device temperature was found to be 10-15 degrees higher towards the device edges than the average temperature in the middle of the device. This difference becomes



**Figure 2.** a) Raman spectrum of AlGaIn (room temperature). b)  $E_2(\text{high})$  phonon frequency as a function of temperature. Solid line displays a linear fit to the data.  $k(E_2)$  - phonon temperature coefficient.



**Figure 3.** Temperature map obtained from the position of the  $E_2(\text{high})$  phonon mode of AlGaIn: device is operating at 8V, 50mA DC. Each pixel is a square of  $20 \mu\text{m} \times 20 \mu\text{m}$ .

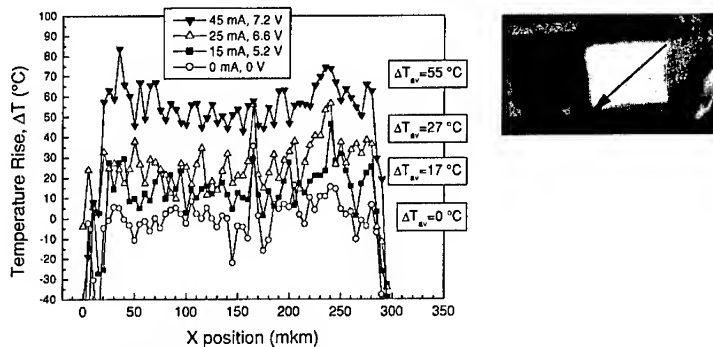


**Figure 4.** Temperature rise recorded in a line scan on an UV LED (see insert). Arrow shows the direction of the scan. For each profile an average temperature rise is given on the right hand side.

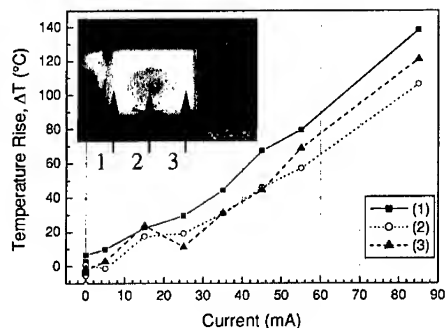


**Figure 5.** Temperature rise recorded from the position of the  $E_2(\text{high})$  phonon mode of AlGaIn b. point measurements on the chip (see insert) as a function of device current.

more apparent at operating currents higher than 50 mA as seen in Fig. 5. Light emission occurring preferentially at the edges of the device indicates that current crowding may be one of the factors contributing to this temperature distribution, but other factors also need to be considered.

Finite difference heat dissipation simulations were performed to simulate temperature distribution in the device. The result is shown in Fig. 6. Simulations (assuming homogeneous current distribution, i.e., neglecting current crowding) show that the metallic p-contact results in a significant temperature drop in the middle of the device, as compared to the device edges. The resulting temperature rise from simulation was about 30–35°C for the middle of the device and about 60–65 °C towards the chip edges. This is in the reasonably good agreement with experimental data obtained, taking into account the large uncertainty in values of heat conductivity for GaN, AlGaIn and SiC materials and the simplified structure used. The following values of thermal conductivities were used in the simulation:  $\kappa_{\text{Sapphire}} = 0.35 \text{ Wcm}^{-1}\text{K}^{-1}$ ,  $\kappa_{\text{SiC}} = 4.5 \text{ Wcm}^{-1}\text{K}^{-1}$ ,  $\kappa_{\text{AlGaIn}} = 0.14 \text{ Wcm}^{-1}\text{K}^{-1}$ ,  $\kappa_{\text{GaN}} = 1.6 \text{ Wcm}^{-1}\text{K}^{-1}$ ,  $\kappa_{\text{AuSn}} = 0.58 \text{ Wcm}^{-1}\text{K}^{-1}$ .

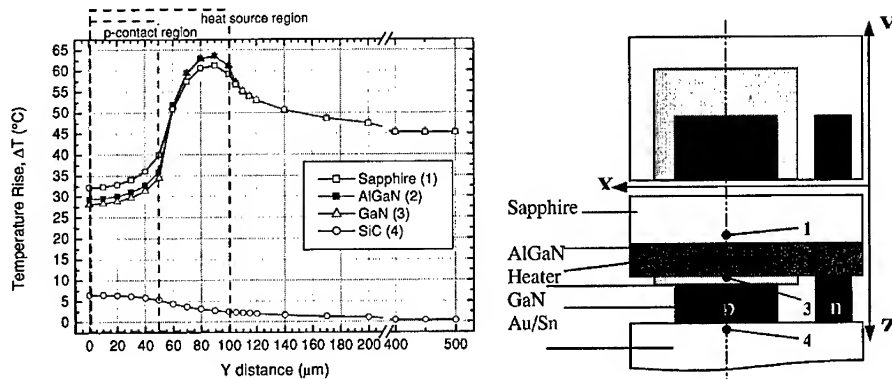


**Figure 6.** Temperature rise simulated using finite difference heat dissipation for a 50mA, 8V DC operating device (half of the chip is modelled). On the right hand side a schematic structure used for simulations is shown. Dash-dotted line indicates the cross-section plane for which the temperature profiles are shown.

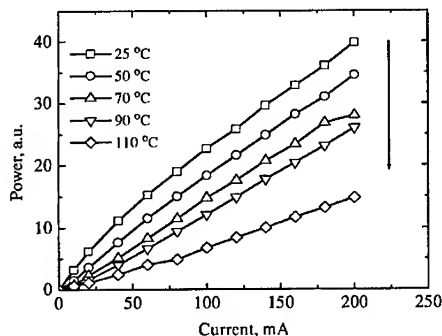


**Figure 7.** Output power vs. pulsed pump current for flip-chip mounted UV LED measured at different temperatures.

The measured temperature rise on the chip edges, therefore, is a consequence of the combined effect of current crowding and better heat extraction through the p-contact in the middle of the chip. Experiments on heating the operating UV LED externally show that elevated temperatures lead to a significant reduction in emitted light intensity (Fig. 7), confirming that self-heating effects contribute significantly to the UV output light saturation observed in operating UV LED devices.

## CONCLUSION

We have shown that 325 nm deep UV LED devices based on  $\text{Al}_{0.18}\text{Ga}_{0.82}\text{N}/\text{Al}_{0.12}\text{Ga}_{0.88}\text{N}$  MQW structures are prone to self-heating effects while operating at DC pumping. The effect of

self-heating is responsible for a reduction in light output power. The temperature of the operating device can be effectively measured by micro-Raman spectroscopy. The temperature rise of about 55 °C in the middle of the device and about 70 °C for the device edges was measured at a power dissipation of 0.4 W for a 200 µm x 200 µm LED device. This temperature profile results from the combined effect of heat-sinking through the flip-chip contact in the middle of the device and current crowding at its edges. Finite difference heat dissipation simulations show fair agreement with the experimental data obtained.

## ACKNOWLEDGEMENTS

The work in Bristol was in part supported by EPSRC and Renishaw plc. The work in University of South Carolina (USC) was supported by Army SMDC contract DASG60-00-10003, monitored by Mr. Terry Bauer. The work in USC was also partially supported by DARPA contract number DAAD19-02-10282, monitored by Dr. J. Zavada and Dr. J. Carrano.

## REFERENCES

1. S. Nakamura and G. Fasol, *The Blue Laser Diode* (Springer, Berlin, 1997).
2. A. Kinoshita, H. Hirayama, M. Ainoya, Y. Aoyagi, and A. Hirata, *Appl. Phys. Lett.*, **77**, 175 (2000).
3. N. Otsuka, A. Tsujimura, Y. Hasegawa, G. Sugahara, M. Kume, and Y. Ban, *Jpn. J. Appl. Phys.*, Part 2 **39**, L445 (2000).
4. M. Iwaya, S. Terao, T. Sano, S. Takanami, T. Ukai, R. Nakamura, S. Kamiyama, H. Amano, and I. Akasaki, *Phys. Status Solidi A*, **188**, 117 (2001).
5. V. Adivarahan, A. Chitnis, J. P. Zhang, M. Shatalov, J. W. Yang, G. Simin, M. Asif Khan, M. Shur, and R. Gaska, *Appl. Phys. Lett.*, **79**, 4240 (2001).
6. M. Asif Khan, V. Adivarahan, J. P. Zhang, C. Chen, E. Kuokstis, A. Chitnis, M. Shatalov, J. W. Yang, and G. Simin, *Jpn. J. Appl. Phys.*, Part 2 **40**, L1308 (2001).
7. J. P. Zhang, V. Adivarahan, H. M. Wang, Q. Fareed, E. Koukstis, A. Chitnis, M. Shatalov, J. W. Yang, G. Simin, M. Asif Khan, M. Shur, and R. Gaska, *Jpn. J. Appl. Phys.*, Part 2 **40**, L921 (2001).
8. A. Chitnis, J. P. Zhang, V. Adivarahan, W. Shuai, J. Sun, M. Shatalov, J. W. Yang, G. Simin, and M. Asif Khan, *Jpn. J. Appl. Phys.*, Part 2 **41**, L450 (2002).
9. V. Adivarahan, J. Zhang, A. Chitnis, W. Shuai, J. Sun, R. Pachipulusu, M. Shatalov, and M. Asif Khan, *Jpn. J. Appl. Phys.*, Part 2 **41**, L435 (2002).
10. J. P. Zhang, A. Chitnis, V. Adivarahan, S. Wu, V. Mandavilli, R. Pachipulusu, M. Shatalov, G. Simin, J. W. Yang, and M. Asif Khan, to be published *Appl. Phys. Lett.*.
11. A. Chitnis, J. Sun, V. Mandavilli, R. Pachipulusu, S. Wu, M. Gaevski, V. Adivarahan, J. P. Zhang, M. Asif Khan, A. Sarua, and M. Kuball, *Appl. Phys. Lett.*, **81**, 3491 (2002).
12. M. Kuball, J. M. Hayes, M. J. Uren, I. Martin, J. C. H. Birbeck, R. S. Balmer, and B. T. Hughes, *IEEE Electron Device Lett.*, **23**, 7 (2002). [INSPEC].
13. F. Demangeout, J. Groenen, J. Frandon, M. A. Renucci, O. Briot, S. Ruffenach-Clur, R. L. Aulombard, *MRS Internet J. Nitride Semicond. Res.*, **2**, 40 (1997).
14. M. S. Liu, L. A. Bursill, S. Pawer, K. W. Nugent, Y. Z. Tong and G. Y. Zhang, *Appl. Phys. Lett.*, **74**, 3125 (1999).

### Epitaxial Growth for Solar-Blind AlGaIn Photodetector Imaging Arrays by Metalorganic Chemical Vapor Deposition

Uttiya Chowdhury; Charles J. Collins; Michael M. Wong; Ting Gang Zhu; Jonathan C. Denyszyn; Jin Ho Choi; Bo Yang; Joe C. Campbell; and Russell D. Dupuis  
10100 Burnet Road, Building 160, Austin, TX 78758 USA  
Phone: +1-512-471-0537, Fax: +1-512-471-0957, e-mail: dupuis@mail.utexas.edu

#### ABSTRACT

Solar-blind imaging arrays based on AlGaIn *p-i-n* structures are of high interest for defense applications. We have studied the material issues involved in development of such imaging arrays and have developed discrete photodetector devices with a high external quantum efficiency (EQE) and imaging arrays of high operability.

For the discrete devices, a record EQE of 58.1% peaking at 274 nm under zero volt bias was obtained without using an anti-reflecting (AR) coating. The EQE was seen to have a slight voltage dependence: going up to 64.5% at -5V reverse bias. The responsivity had a drop-off by one order of magnitude for a wavelength change of 4 nm on both the shorter and longer wavelength side. The material quality and uniformity was found to be very good leading to the development of  $256 \times 256$  arrays. A high yield along with uniform, high EQE was obtained for the detector devices in the array leading to a high operability of 99.8%.

#### INTRODUCTION

The solar-blind spectrum ranging from ~290 nm to shorter wavelength is of interest from a variety of applications. This spectral region is called solar-blind because due to absorption in the terrestrial ozone layer, solar radiation obtained near Earth's surface contains very little radiation of this wavelength range. As a result, a solar-blind photodetector (SBD), sensitive to light of wavelength shorter than ~290 nm, but insensitive to longer-wavelength radiation will be able to operate near the Earth's surface without a large background signal from the solar radiation. As a result, if it is intended to image some object emitting light of wavelength shorter than ~290 nm, a solar-blind photodetector can provide a much higher signal-to-noise ratio compared to photodetectors operating at other spectral ranges. This is very useful for a number of defense applications including missile detection from the radiation of the exhaust plume. Accordingly, there has been a high interest in the defense industry in fabrication of solar-blind imaging arrays.

Semiconductor-based SBDs are of particular interest due to the ease of fabrication into imaging arrays, their compact size, and low voltage operation. Particularly, for convenience of integration, it is desired to flip-chip mount the imaging array on Si based read-out integrated circuit (ROIC). As a result, it is desired to have back-illuminated SBDs capable of operating at low bias voltages. Operability at low bias voltages allows driving of the photodetectors using the same power supply as the one used for the ROIC, obviating the need of additional bulky power supplies. In the present work, we report on development of high external quantum efficiency (EQE) discrete SBDs and high-performance imaging array from the same epitaxial structures.

#### DESIGN OF DEVICE STRUCTURE

$\text{Al}_x\text{Ga}_{1-x}\text{N}$  based *p-i-n* diode structures are ideal candidates for the fabrication of back-

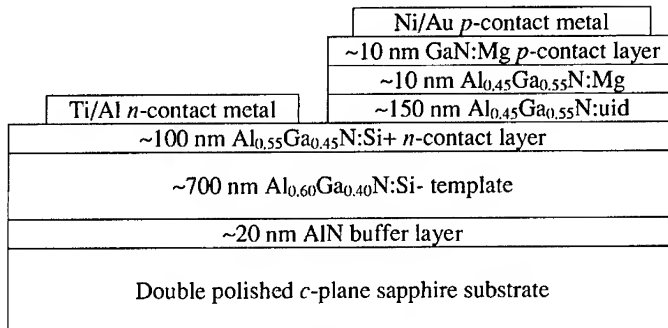


**Figure 1. Device structure used for AlGaN SBD.**

illuminated SBDs. For  $x \sim 0.42$ , the diode will have a photoresponse for photons of energy larger than the bandgap energy, corresponding to a wavelength shorter than  $\sim 290$  nm. The diode will be insensitive to radiation at longer wavelengths because those wavelengths will not be absorbed. Since high-quality AlGaN can be conveniently grown on sapphire substrates, dual-side polished sapphire, being transparent to UV luminescence is an ideal substrate for development of SBD. The diode however, cannot be grown directly on the substrate because of the presence of a high threading dislocation density (TDD) in the first few hundred nanometers of material grown on sapphire. As a result, first a thick AlGaN layer needs to be grown on the substrate before growing the device structure. However, this AlGaN layer will also absorb light and the Al content of the layer must be higher than in the active region because otherwise, all the light of interest will be absorbed in this dislocation-reduction layer before reaching the active region. Also, if the Al-content of the dislocation-reducing “window” layer is increased, this effectively extends the spectral range of the detector device in the shorter wavelength side. However, the Al-content of the dislocation-reduction layer cannot be increased arbitrarily because this will lead to relaxation of the active device layers due to lattice mismatch. Al<sub>0.52</sub>Ga<sub>0.48</sub>N is a convenient composition giving adequate difference in cut-off wavelength and also low enough lattice mismatch for growth of a thick enough *i*-layer for the *p-i-n* device structure.

Commonly, the *n*-side of the diode is grown first (on the substrate-side) to reduce the device impact of the spreading resistance in the relatively high resistivity *p*-material and to reduce the memory effect from Mg, which is the *p*-type dopant of choice for this material system. Since the *n*-layer is also in the path of incident light to the active region, it is desirable to use an Al<sub>0.52</sub>Ga<sub>0.48</sub>N:Si+ layer for this in order to maximize the light getting into the active region. It is to be noted that although the photodetector device operates in reverse-bias under low current conditions, a low series resistance is of high importance for obtaining a high EQE. This is because the measurement of EQE under zero volt bias essentially involves measuring the short-circuit current of a photodetector under illumination. A high series resistance will essentially reduce the short-circuit current, yielding a lower EQE. Transparency to wavelengths of interest and low resistivity are thus to be simultaneously achieved in order to obtain high performance of the photodetector device. Previously, we have demonstrated significant improvement of the EQE in an SBD device by use of an Al<sub>0.52</sub>Ga<sub>0.48</sub>N:Si+ layer where these two conditions were achieved[1]. In the present work, the same design was found to yield even higher EQE through

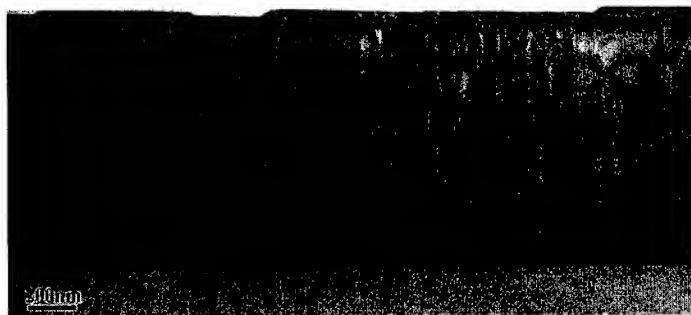


**Figure 2.** Cross sectional TEM image of SBD epitaxial structure.

further optimization of growth conditions. Also, the work was extended to fabricate imaging arrays of SBDs.

## EXPERIMENT

### Growth conditions

The AlGaIn device structures used in this work were grown by low-pressure metalorganic chemical vapor deposition (MOCVD) in an EMCORE Model D125 UTM rotating disk reactor on two-inch diameter *c*-plane (0001) double-polished sapphire substrates. The growth occurs in a H<sub>2</sub> ambient employing the primary precursors trimethylgallium (TMGa) and trimethylaluminum (TMAI) as alkyl sources, and ammonia (NH<sub>3</sub>) as the hydride source. Silane (SiH<sub>4</sub>) is used as a source of Si for *n*-type doping and bis-cyclopentadienyl magnesium (Cp<sub>2</sub>Mg) is used for *p*-type (Mg) doping. The growth pressure ranged from 50 to 200 Torr. A two-step growth was used beginning with a low-temperature AlN nucleation layer grown at ~535C followed by growth at high-temperature: ~1050 to 1070C. After growth, the sample is in-situ annealed in a nitrogen ambient at 850C for 10 min to activate the Mg acceptor impurities.

The device structure is shown in Figure 1. X-ray reciprocal space map of the as-grown epitaxial structure revealed that with the layer thicknesses chosen, the *p-i-n* structure is nearly fully strained to the Al<sub>0.52</sub>Ga<sub>0.48</sub>N window layer underneath. Figure 2 shows a cross-sectional TEM image of an as grown SBD structure. Threading dislocation density was estimated to be  $\sim 4 \times 10^9 / \text{cm}^2$  near the top of the AlGaIn layers.

### Device Processing and Testing

The as-grown crystal was processed into mesa-geometry photodiodes following standard processing techniques. First, diode mesas were defined by etching the AlGaIn layers through window openings patterned in a 200 nm thick SiO<sub>2</sub> mask using reactive ion etching (RIE) employing boron trichloride (BCl<sub>3</sub>) and silicon tetrachloride (SiCl<sub>4</sub>). Then the etch mask was removed and the Mg acceptor atoms were activated using rapid thermal annealing at 850C for 10 min. Through openings defined in the SiO<sub>2</sub> passivation layer, Ti/Al/Ti/Au *n*-contact metal was evaporated which was followed by an *n*-contact anneal at 850C for 30 sec. Then Ni/Au *p*-

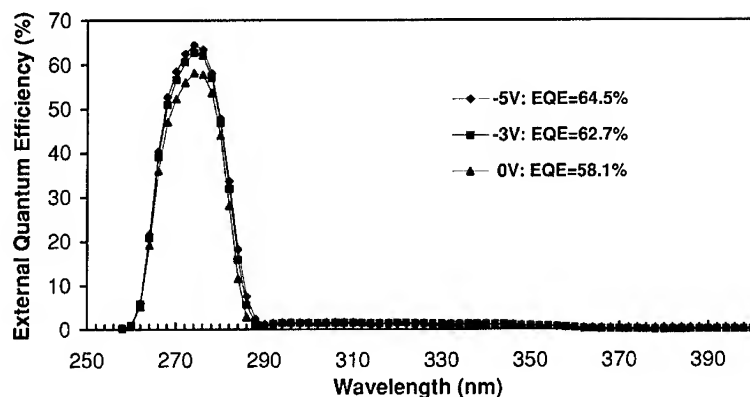


Figure 3. EQE spectrum of discrete SBD device.

metallization was evaporated and the contact was annealed at 675C for 2 min. For the discrete devices, round mesa diodes were fabricated and for the imaging array, a 256×256 array of square photodetectors of 30 μm×30 μm cell dimensions were fabricated.

The fabricated photodetectors were tested using standard semiconductor parameter analyzer hardware. EQE measurement was done in chopped mode using a locking amplifier. EQE was determined from measured photocurrent by comparing with a reference UV enhanced Si-photodetector.

## RESULTS

The EQE spectrum of a discrete SBD device is shown in Figure 3. The peak of EQE was obtained at a wavelength of 274 nm. The peak EQE measured was 58.1% at zero volt bias, which went up to 64.5% at -5V reverse bias without the use of an AR coating. The individual devices of the 256×256 array also showed a high EQE of 44.5% without any AR coating. The devices of the array showed a cut-on wavelength of 262 nm and a cut-off at 278 nm. Uniformity of responsivity was determined by the ratio of standard deviation to mean and the  $\sigma/\mu$  ratio was found to be 6%. The response operability was determined to be 99.8%. The elements of the array also displayed a high zero-volt resistance  $R_0$ . The median value of  $R_0$  was found to be  $4.3 \times 10^{15} \Omega$  leading to a median  $R_0A$  product of  $3.1 \times 10^{10} \Omega\text{-cm}^2$ . This high value of  $R_0$  led to a high detectivity of  $D^* = 1.5 \times 10^{14} \text{ cm-Hz}^{1/2}\text{-W}^{-1}$ . The responsivity map from a fabricated SBD imaging array is given in Figure 4.

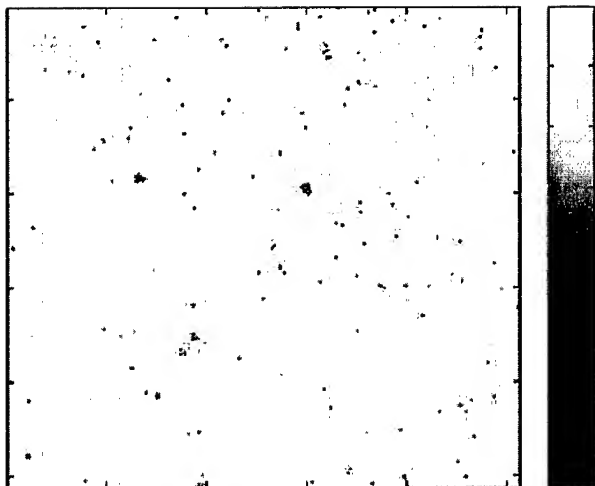


**Figure 4. Responsivity map of an SBD imaging array. The color bar on the right side is in arbitrary linear scale.**

## CONCLUSIONS

We have demonstrated solar-blind operation of AlGaIn *p-i-n* photodiodes with a high EQE of 48.1% at  $\lambda=274$  nm at zero volt bias without any anti-reflection coating. The same epitaxial structure was used to develop a 256×256 imaging array of photodetectors. The individual cells of the array also showed a high EQE of 44.5%. The cells also had a high zero-volt resistance giving a high detectivity of  $D^*=1.5 \times 10^{14}$  cm-Hz<sup>1/2</sup>-W<sup>-1</sup>. In addition, the cells of the array demonstrated a high yield and uniform performance. A response operability of 99.8% was determined for the array. To our knowledge, this performance is the state-of-the art for discrete SBDs and SBD imaging arrays.

## ACKNOWLEDGEMENTS

We thank DARPA/MTO (E. Martinez) and ONR (Y. S. Park) for support of this work. RDD gratefully acknowledges the support of the Judson S. Swearingen Regents Chair in Engineering. We also thank D. N. Zakharov and Z. Liliental-Weber for kindly performing TEM analysis of the device structure. We gratefully acknowledge A. Hairston, P. Lamarre, K. Wong, C. Cooke, J. Mullarkey, and M. Reine of BAE SYSTEMS for fabricating and testing the SBD devices.

## REFERENCES

- [1] U. Chowdhury, M. M. Wong, C. J. Collins, B. Yang, J. C. Denyszyn, J. C. Campbell, and R. D. Dupuis, accepted for publication in *J. Cryst. Growth*.

### Crack Nucleation in AlGa<sub>N</sub>/Ga<sub>N</sub> Heterostructures

Peter J. Parbrook, Malcolm A. Whitehead, Richard J. Lynch and Robert T. Murray<sup>1</sup>

EPSRC National Centre for III-V Technologies,

Department of Electronic and Electrical Engineering, University of Sheffield,  
Mappin Street, Sheffield, S1 3JD, United Kingdom.

<sup>1</sup>Materials Science and Engineering, Department of Engineering, University of Liverpool,  
Liverpool, L69 3GH, United Kingdom.

#### ABSTRACT

The tensile strain in AlGa<sub>N</sub> layers on Ga<sub>N</sub> is well established to lead to cracking if a critical thickness is reached, unless measures such as interlayers are applied to prevent their formation. However in devices, such as HFETs such an approach is impractical. Growth of AlGa<sub>N</sub>-Ga<sub>N</sub> structures was carried out by MOVPE using a standard two stage process for the growth of the Ga<sub>N</sub> on sapphire. The crack structures were examined by optical and atomic force microscopy. Studies on thin AlGa<sub>N</sub> layers on Ga<sub>N</sub> close to the crack critical thickness show the stress centres from which the cracks propagate are threading dislocations with cracks often initially forming to link together these stress centres if they are in close proximity. These cracks then extend and "lock" into the generally observed  $\langle 2\bar{1}10 \rangle$  direction in more highly strained layers. A macroscopically uniform crack array is observed in these thin AlGa<sub>N</sub> samples.

#### INTRODUCTION

The growth of AlGa<sub>N</sub> is required in a wide variety of III-nitride devices. These include violet laser diodes (LDs), heterojunction field effect transistors (HFETs), ultra-violet emitters, photodetectors and also intersubband devices. However the lattice mismatch of around 3% between AlN and Ga<sub>N</sub> limits the thickness of material that can be grown before relaxation occurs. For AlGa<sub>N</sub> layers on Ga<sub>N</sub> the observed relaxation is through the formation of a network of cracks [1,2,3]. These cracks, in addition to relieving strain in themselves, can lead to the formation of misfit dislocations in the basal plane [2]. While such crack networks can be avoided through the use of a low temperature interlayer of AlN at the AlGa<sub>N</sub>-Ga<sub>N</sub> interface for example [4], these strategies are not appropriate in a critical device region (as in an HFET) and can cause an increased threading dislocation density, (which would affect LD performance).

Although the above studies have outlined in some detail the propagation and relaxation induced by cracks, none have to our knowledge discussed their nucleation. In this paper evidence is presented that in single layers of AlGa<sub>N</sub> on Ga<sub>N</sub> a high density of microcracks are nucleated from the dislocations threading up through the Ga<sub>N</sub> epilayer into the AlGa<sub>N</sub>.

#### EXPERIMENTAL

The samples examined in this study were grown by metalorganic vapour phase epitaxy at low pressure in a Thomas-Swan 3x2" close coupled showerhead reactor. They were grown on c-plane sapphire substrates, using a standard two-stage growth process with a Ga<sub>N</sub> nucleation layer grown at 525°C followed by the high temperature Ga<sub>N</sub> buffer at 1030°C. Details of the

nucleation process employed are reported elsewhere [5]. The AlGa<sub>x</sub>N layers were grown on approx. 1  $\mu$ m thick GaN epilayers at the GaN growth temperature.

Analysis of the structures was carried out using a variety of techniques. Imaging of the epilayer surface was carried out using Nomarski interference optical microscopy, scanning electron microscopy (SEM) using a Philips field emission gun system and atomic force microscopy (AFM) employing a Digital Instruments system. Plan view samples for transmission electron microscopy (TEM) were prepared by ion-milling.

The AlGa<sub>x</sub>N layer thickness and composition were estimated from double crystal x-ray diffraction, using a Bede D200 system, and Bede modelling software to simulate the resulting rocking curves. For the purposes of the simulation, in all cases the layers were assumed fully strained to the GaN which was assumed relaxed. The measured values of the samples examined in this study are listed in Table I

## RESULTS

On examination of the samples by AFM clear differences are found in the formation of the defects observed, as shown in Figure 1. In Figure 1(a) for the lowest composition sample (#1) the AFM image of the surface is similar to that observed in GaN epilayers, with step edges clearly visible, with terminations at threading dislocation cores that contain a screw component. In Figure 1(b) an image for sample #2 is shown. In this case the threading dislocation cores are apparently elongated, with a tendency to elongate towards neighbouring cores in cases where they are in close proximity. For sample #3, shown in Figure 1(c) a high density of small, short cracks is observed. It should be noted that in this last case there appear to be no screw or mixed threading dislocation cores observable in the AFM images taken on #3. These cracks were also observed by SEM (Figure 2) but under optical microscopy the features could not be observed. Under SEM examination faint features attributable to the extension of the dislocation cores were observed in the case of #2, giving a qualitatively similar morphology to those observed by AFM.

Plan view TEM was carried out on both samples #2 and #3. In the case of #2 it was difficult to identify extension to the cores, the reason for which is unclear. Cracks were clearly observed in #3, along with some circular features, not apparently participating the crack relaxation mechanism, which may be nanopipes.

## DISCUSSION

The breaking strains for "true" (defect free) single crystals are well known to be extremely large, and not reproduced by experimental results. In most cases some form of defect is required to amplify the stress, allowing cracks to nucleate. Possible stress centres that can act as nucleation sites are reviewed elsewhere [6], but for example may include dislocations as suggested by Olsen et al [7].

Table I: Al<sub>x</sub>Ga<sub>1-x</sub>N composition and thickness values for layers examined

Sample Code	Al <sub>x</sub> Ga <sub>1-x</sub> N Composition, x	Al <sub>x</sub> Ga <sub>1-x</sub> N Thickness, nm
#1	0.241	65.0
#2	0.317	31.5
#3	0.419	23.0

**BEST AVAILABLE COPY**

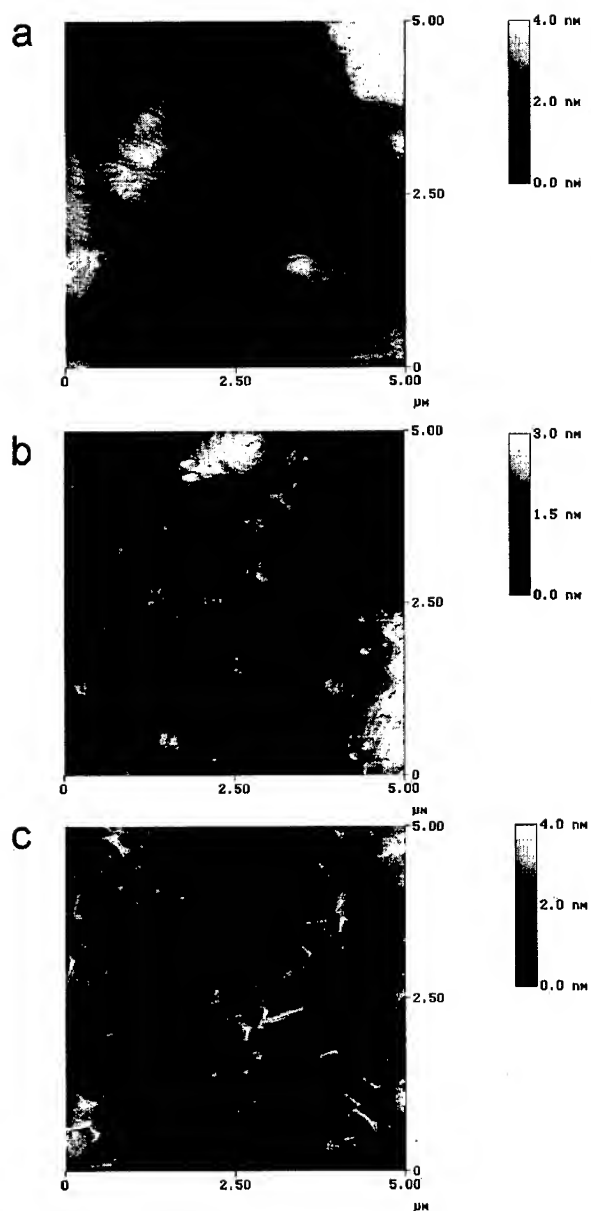


Figure 1: 5μm x 5μm AFM images of the surfaces of samples (a) #1, (b) #2 and (c) #3

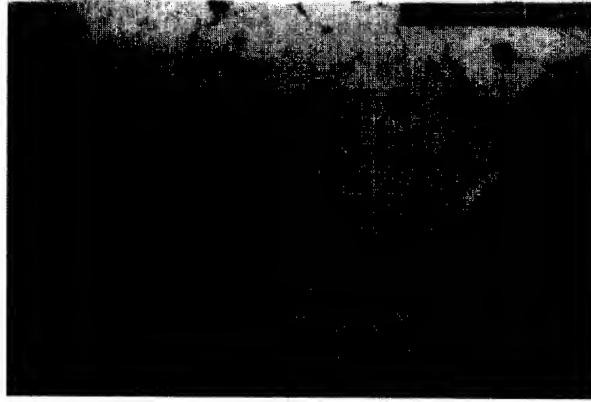


Figure 2: SEM image of the surface of #3, showing a dense array of small cracks. The dark spots are attributed to charging effects.

Based on the AFM images in Figure 1 it is apparent that the initial cracks forming in the AlGaIn epilayers are being nucleated at the cores of the screw and mixed threading dislocations propagating up through the epitaxial layer. It appears that the stress around the core is sufficient to allow the material to start cracking from it, often in a direction towards a neighbouring threading core. As the strain in the epilayer increases these cracks begin to propagate along  $\langle 2\bar{1}10 \rangle$  directions due to breaking of the material along the  $\{1\bar{1}00\}$  planes, as reported elsewhere [3,8]. It appears also that virtually all of the threading dislocations nucleate cracks simultaneously, with the observation that few, if any, threading dislocation cores are observed in sample #3.



Figure 3: Plan view TEM image shown cracks and evidence of defects not nucleating cracks

**BEST AVAILABLE COPY**

It should be noted, however, that based on the AFM data it is difficult to comment on what role pure edge dislocations play in the relaxation. These dislocations do not interact with the surface steps and are therefore difficult to observe by this technique, although in samples grown with other nucleation conditions, we have observed weak features attributable to them. Further, more detailed, studies using TEM are required in order to deal with this question.

The critical thickness,  $t_c$ , for crack formation to become energetically favourable has been given as [8]:

$$t_c = \frac{\Gamma}{Mf^2} \quad (1)$$

where  $\Gamma$  is the surface energy of the crack plane,  $M$  the two-dimensional equivalent of Young's modulus and  $f$  is the in-plane lattice parameter misfit between the two materials. This formula can be reduced to simply the product of a constant and the reciprocal of the misfit squared. Assuming that #2 is a sample located at the critical thickness, this would give a value for the constant of  $1.82 \times 10^{-12}$  m, somewhat lower than that expected using the theoretical parameters for  $\Gamma$ ,  $M$  [8]. A number of reasons for this discrepancy are possible:

- The GaN buffer layer may itself be under stress, causing a reduction in the critical thickness [9], in which case the critical thickness for cracking will be dependent on the growth procedure, and it may be possible to engineer a larger critical thickness by modifying the nucleation and initial buffer layer growth conditions.
- The model is a rather simple one, more detailed treatments, such as used by Hearne et al [2], include a crack driving force term for example.
- Other explanations include the fact that the values are measured at room temperature, rather than the growth temperature, or that there remain errors in the estimation of these parameters for GaN based materials.

A notable feature of the crack distributions in Figure 1(c) is its relatively high density, with many small cracks visible in an area of a few microns<sup>2</sup>. This is in contrast to the apparent situation observed by others [3] and ourselves [8], where the inter-crack spacing is much larger in AlGaIn films well above the crack critical thickness. The reasons for this are not understood at present, although one possibility is that many of these microcracks undergo a healing process with growth, as a network of crack induced misfit dislocations form at the AlGaIn-GaN interface as proposed by Hearne et al [2]. Further work to examine this issue is required.

## DISCUSSION OF OTHER LAYER STRUCTURES

We have also examined a variety of other AlGaIn containing structures, both of thick (>0.5  $\mu$ m) low composition AlGaIn grown directly on GaN buffers, as part of a laser diode type structure, and also AlGaIn-GaN multilayer "Bragg stacks" grown on a thick AlGaIn layer of intermediate composition using an AlN low temperature interlayer to relieve the strain between the AlGaIn strain balanced layer and the GaN buffer [4]. In a number of cases a very low density of cracks propagating across the wafer has been observed, with mm or even cm between cracks propagating in the same direction. There is no evidence of the array of cracks normally observed [3,8]. It therefore appears in this case that a separate nucleation mechanism may be responsible.

In these layers it is noticeable that essentially all the cracks appear to have at least one of their termination points at the wafer edge, and mid-wafer terminations are often associated with the crack meeting a pre-existing crack. In such cases it is likely that defects, or alloy inhomogeneities at the wafer edge may be acting as the nucleation site. Further evidence for this

comes from a sample where two wafers from different manufacturers had the same structure grown simultaneously on them. While one wafer was observed to be crack free, the other exhibited the low density of cracks as described above. In addition to polishing damage at the wafer edge, wafers from different manufacturers may behave differently under heating [10] with the wafer warpage leading to localised alloy non-uniformities at the edge.

## CONCLUSIONS

In conclusion we report the observation of a dense array of small microcracks in thin epitaxial layers of AlGaIn grown on GaN. These microcracks appear to have nucleated from the cores of screw and mixed dislocations propagating up through the layer structure. The density appears high compared to those reported in thicker films, suggesting that crack healing may be occurring at higher layer thicknesses, with the strain relaxation being accommodated from other sources.

## ACKNOWLEDGEMENTS

The authors acknowledge the support of the EPSRC in funding this work, and also to Dr J. Jacobs and Dr G. Hill for their assistance performing the AFM and SEM studies, respectively.

## REFERENCES

1. K. Ito, K. Hiramatsu, H. Amano and I. Akasaki, *J. Crystal Growth* **104** 533 (1990)
2. S. J. Hearne, J. Han, S. R. Lee, J. A. Floro, D. M. Follstaedt, E. Chason, and I. S. T. Tsong, *Appl. Phys. Lett.* **76**, 1534 (2000)
3. S. Einfeldt, V. Kirchner, H. Heinke, M. Dießelberg, S. Figge, K. Vogeler and D. Hommel, *J. Appl. Phys.* **88** 7029 (2000)
4. H. Amano, M. Iwaya, N. Hayashi, T. Kashima, M. Katsuragawa, T. Takeuchi, C. Wetzel and I. Akasaki, *MRS Internet J. Nitride Semicond. Res.* **4S1** G10.1 (1999)
5. D. A. Wood, P. J. Parbrook, R. J. Lynch, M. Lada and A. G. Cullis, *Phys. Stat. Sol. (a)* **188** 641 (2001)
6. R. T. Murray, G. Hill, M. Hopkinson and P. J. Parbrook, *Phil. Mag.*, accepted for publication (2003)
7. G. H. Olsen, M. S. Abraham and T. J. Zamerowski, *J. Electrochem. Soc.* **121** 1650 (1974)
8. R. T. Murray, P. J. Parbrook, D. A. Wood and G. Hill, "*Proc. Microscopy of Semiconducting Materials Conference 2001*", *Inst. Phys. Conf. Ser.* **169** 289 (2001)
9. S. Hearne, E. Chason, J. Han, J. A. Floro, J. Figiel, J. Hunter, H. Amano and I. S. T. Tsong, *Appl. Phys. Lett.* **74** 356 (1999)
10. E. J. Thrush, M. J. Kappers, P. Dawson, D. Graham, J. S. Barnard, M. E. Vickers, L. Considine, J. T. Mullins and C. J. Humphreys, "*Proc. Inter. Symp. Blue Lasers and Light Emitting Diodes*" (Cordoba, March 2002)

**BEST AVAILABLE COPY**

## Solar-Blind AlGa<sub>x</sub>N-based Schottky Photodiodes With High Detectivity and Low Noise

Necmi Biyikli <sup>a)</sup> and Orhan Aytur

Department of Electrical and Electronics Engineering, Bilkent University, Bilkent Ankara 06533, TURKEY

Ibrahim Kimukin, Turgut Tut and Ekmel Ozbay

Department of Physics, Bilkent University, Bilkent Ankara 06533, TURKEY

### Abstract

We report on the design, fabrication and characterization of solar-blind Schottky photodiodes with high detectivity and low noise. The devices were fabricated on *n*+/*n*+ AlGa<sub>x</sub>N/GaN hetero-structures using a microwave compatible fabrication process. Using Al<sub>0.38</sub>Ga<sub>0.62</sub>N absorption layer, true solar-blind operation with a cut-off wavelength of ~274 nm was achieved. The solar-blind detectors exhibited < 400 fA dark current in the 0-25 V reverse bias regime, and a maximum responsivity of 89 mA/W around 267 nm. The photovoltaic detectivity of the devices were in excess of  $2.6 \times 10^{12}$  cmHz<sup>1/2</sup>/W, and the detector noise was 1/*f* limited with a noise power density less than  $3 \times 10^{-29}$  A<sup>2</sup>/Hz at 10 KHz.

### 1. Introduction

Photodetectors that operate only in the  $\lambda < 280$  nm spectrum are named as solar-blind detectors due to their blindness to solar radiation within the atmosphere.<sup>1</sup> Solar-blind photodetectors are essential components for a number of applications including missile plume detection and missile tracking, flame/engine control, chemical/biological agent sensing, UV astronomy, and ozone layer monitoring. Al<sub>x</sub>Ga<sub>1-x</sub>N-based photodetectors potentially offer significant advantages over the current photomultiplier tube and silicon-based solar-blind detector technology in terms of size, complexity, cost, robustness, stability, power demands, and bandwidth.<sup>2</sup> Moreover, its intrinsic solar-blindness (for  $x \geq 0.38$ ) and the ability of operation under harsh conditions (high temperature and high power levels) due to its wide band-gap makes Al<sub>x</sub>Ga<sub>1-x</sub>N-based photodetectors attractive for high-performance solar-blind detection applications. Several research groups have demonstrated successful solar-blind operation with Al<sub>x</sub>Ga<sub>1-x</sub>N photodetectors using photoconductive,<sup>3,4</sup> p-i-n,<sup>5-14</sup> metal-semiconductor-metal (MSM),<sup>15-16</sup> and Schottky<sup>17-20</sup> detector structures. Cut-off wavelengths ( $\lambda_c$ ) as short as ~225 nm, a UV/VIS rejection over 5 orders of magnitude along with responsivities as high as 0.12 A/W at 232 nm were reported using a Al<sub>0.7</sub>Ga<sub>0.3</sub>N p-i-n detector structure.<sup>6,11</sup> Al<sub>0.5</sub>Ga<sub>0.5</sub>N MSM photodiodes with a noise equivalent power (NEP) as low as 30 fW

at 280 nm and detectivity of  $2.5 \times 10^{13}$  cmHz<sup>1/2</sup>/W correspond to the best noise performance achieved for AlGaIn-based solar-blind detectors.<sup>15</sup> Dark currents less than 2 pA at 30 V reverse bias and a 3-dB bandwidth of 100 MHz was reported for a Al<sub>0.4</sub>Ga<sub>0.6</sub>N MSM structure.<sup>16</sup> Al<sub>0.35</sub>Ga<sub>0.65</sub>N p-i-n photodiodes on SiC substrates with low leakage currents were also successfully demonstrated.<sup>12</sup>

When compared with p-i-n photodiodes, AlGaIn Schottky photodiodes have several advantages. Growth of p-type doped AlGaIn layers and formation of low resistance p+ ohmic contacts are two challenging issues for p-i-n photodiodes, while Schottky photodiodes do not face these problems. Besides the ease of growth and fabrication, efficient collection of generated carriers within the junction and better high-frequency characteristics are the other advantages of AlGaIn Schottky photodiodes. However, they lack from low efficiency mainly due to the optical absorption introduced by the thin Schottky metal, and exhibit high leakage currents and poor noise performance. The reported best detector performances obtained with solar-blind AlGaIn Schottky photodiodes include a maximum responsivity of 0.07 A/W at 290 nm along with a NEP of  $6.6 \times 10^{-9}$  W<sup>1/2</sup>,<sup>18</sup> a minimum  $\lambda_c$  of 278 nm and a minimum dark current density of  $6.6 \times 10^{-6}$  A/cm<sup>2</sup>.<sup>19</sup> In this letter, we demonstrate low noise solar-blind AlGaIn-based Schottky photodiodes with high detectivity and very low dark current.

## 2. Design and Fabrication

Figure 1 shows the epitaxial structure of the front-illuminated Schottky detector wafer which was designed to achieve true solar-blindness, low leakage, and high solar-blind/near-UV rejection ratio. In order to meet these requirements, Al<sub>0.38</sub>Ga<sub>0.62</sub>N absorption layer was used to achieve  $\lambda_c < 280$  nm. The Al<sub>x</sub>Ga<sub>1-x</sub>N/GaN epitaxial layers of our hetero-junction Schottky PD wafer were grown on a 2-inch single-side polished (0001) sapphire substrate using metal-organic chemical vapor deposition (MOCVD). A thin AlN nucleation layer was first deposited followed by a 0.5 μm thick unintentionally doped GaN mesa isolation layer. Afterwards a highly doped ( $n^+ = 2 \times 10^{18}$  cm<sup>-3</sup>) ohmic contact layer composed of 0.6 μm thick GaN and 0.2 μm thick Al<sub>0.38</sub>Ga<sub>0.62</sub>N were grown respectively. The growth of the Schottky hetero-structure was completed with the deposition of a 0.8 μm thick undoped Al<sub>0.38</sub>Ga<sub>0.62</sub>N active layer. The highly doped GaN layer was used for ohmic contact region due to the difficulty of obtaining high-quality ohmic contacts with Al<sub>x</sub>Ga<sub>1-x</sub>N layers. The n-type doped 0.2 μm thick Al<sub>0.38</sub>Ga<sub>0.62</sub>N layer was used as a diffusion barrier for the photo-carriers generated in the GaN ohmic contact layer. Such a diffusion barrier is expected to increase the solar-blind/near-UV rejection ratio of the detector.

The samples were fabricated by using a four-step microwave-compatible fabrication process in a class-100 clean room environment. First, the ohmic contact regions were defined via reactive ion etching (RIE) under CCl<sub>2</sub>F<sub>2</sub> plasma, 20 sccm gas flow-rate and 100 W RF power. The etch rates for GaN and Al<sub>0.38</sub>Ga<sub>0.62</sub>N layers

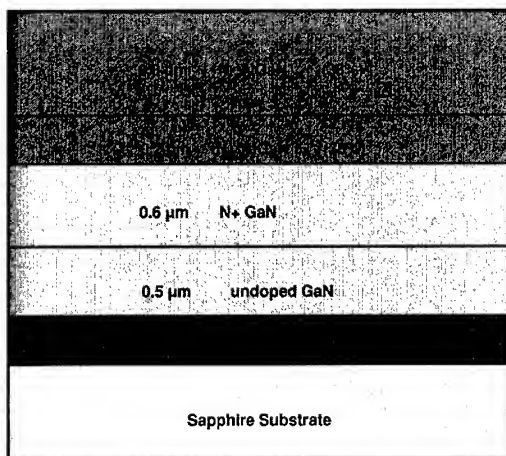


Figure 1. Epitaxial structure of solar-blind Schottky photodiode wafer

were determined as 300 and 80 Å/min respectively. After an ohmic etch of  $\sim 1.3 \mu\text{m}$ , Ti/Al (100 Å/1000 Å) contacts were deposited via thermal evaporation and left in acetone solution for lift-off process. The contacts were annealed at 700 °C for 30 seconds in a rapid thermal annealing (RTA) system. Mesa structures of the devices were formed via the same RIE process, by etching all the layers ( $> 1.6 \mu\text{m}$ ) down to the undoped GaN mesa isolation layer. Then, a  $\sim 100$  Å thick Au film was evaporated to form the Au/AlGaIn Schottky contacts. Finally, a  $\sim 0.7 \mu\text{m}$  thick Ti/Au interconnect metal was deposited and lifted-off to connect the Schottky layers to coplanar waveguide transmission line pads.

### 3. Characterization

The resulting AlGaIn Schottky photodiodes had breakdown voltages above 50 V and turn-on voltages around 2 V. Figure 2 shows the current-voltage (I-V) characteristics of a  $150 \times 150 \mu\text{m}^2$  device. The leakage current of the diodes was lower than 1 pA for reverse bias voltages up to 30 V. As can be observed in the logarithmic plot, the dark current fluctuated within 150-400 fA in the 0-25 V reverse bias range. The actual leakage values in this range could not be measured due to the measurement setup resolution. These leakage values correspond to dark current density values of 0.7-1.8 nA/cm<sup>2</sup>. Hence, we can safely claim that our solar-blind detectors exhibited dark current densities lower than 1.8 nA/cm<sup>2</sup> under reverse bias voltages as high as 25 V. The differential resistance ( $R = dV/dI$ ) of our detectors was calculated and a dark impedance in excess of  $10^{13} \Omega$  was obtained in the 0-25 V range.

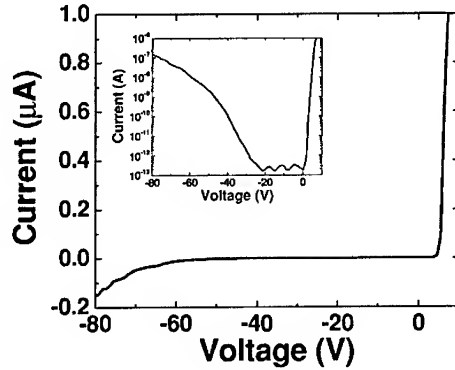


Figure 2. Current-voltage (I-V) characteristics of a 150x150  $\mu\text{m}^2$  solar-blind Schottky photodiode. Inset shows the same data plotted in logarithmic scale.

Spectral photoresponse measurements were done in the 250-350 nm range, using a xenon lamp light source, a single-pass monochromator, a lock-in amplifier, and a calibrated Si photodetector. Figure 3(a) shows the measured spectral quantum efficiency under reverse bias voltages ranging from 0 to 50 V. The quantum efficiency increased with reverse bias and reached a maximum value of  $\sim 42\%$  at 267 nm under 50 V reverse bias. The cut-off wavelength red-shifted with reverse bias, from 266 nm to 274 nm for 0 and 50 V reverse bias respectively. Since  $\lambda_c < 280$  nm was satisfied, true solar-blind detection was successfully demonstrated. The corresponding device responsivity curve under 50 V reverse bias is shown in Fig. 3(b). A peak responsivity of 89 mA/W at 267 nm is measured. The responsivity drops sharply around 270 nm and a solar-blind/near-UV contrast of 4 orders of magnitude is observed within 80 nm. To estimate the detectivity ( $D^*$ ) of our detectors in the photovoltaic mode, we have used the thermal-noise limited detectivity relation  $D^* = R_\lambda / (R_0 A / 4kT)$ , where  $R_\lambda$  is the device responsivity at zero bias,  $R_0$  is the zero volt dark impedance and  $A$  is the detector area. With a 0.01 A/W photovoltaic responsivity at 250 nm, the zero-bias detectivity of our detectors were in excess of  $2.6 \times 10^{12} \text{ cmHz}^{1/2}/\text{W}$ , which corresponds to a set-up limited NEP of  $5.8 \times 10^{-15} \text{ W/Hz}^{1/2}$ .

Finally, noise characterization of the solar-blind Schottky detectors were carried out in the frequency range of 1 Hz – 100 KHz using a fast Fourier transform spectrum analyzer and a microwave probe station. Our low-leakage, high-breakdown voltage solar-blind detectors had noise power densities below the instrument resolution. Even under reverse bias as high as 25 V, the detector noise did not exceed the measurement set-up noise floor of  $3 \times 10^{-29} \text{ A}^2/\text{Hz}$  around 10 KHz. Therefore, we have measured devices with higher leakage currents in order to

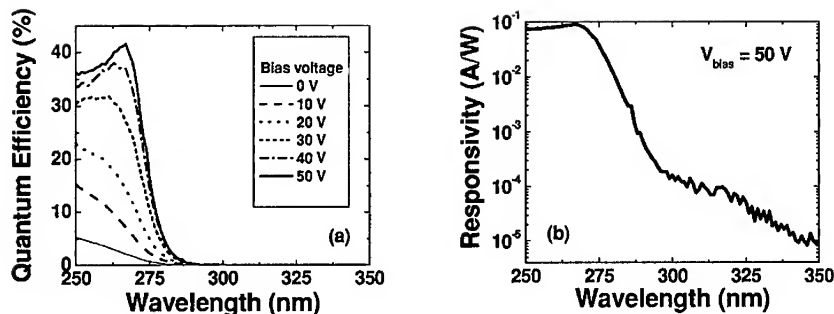


Figure 3. (a) Measured spectral quantum efficiency of the AlGaIn Schottky photodiode. (b) Corresponding responsivity curve of the device under 50 V reverse bias.

observe the bias dependence of the spectral noise density. Figure 4 shows the low-frequency spectral noise density of a 80  $\mu\text{m}$  diameter detector with  $\sim 7$  orders of magnitude larger dark currents ( $>1 \mu\text{A}$  @ 5V) and  $\sim 14$  V breakdown voltage. The spectral noise curves show that  $1/f$ -noise is the dominant noise mechanism in our detectors, as is common for Schottky barrier AlGaIn detectors at low frequencies.  $S_n(f)$  values of  $\sim 8 \times 10^{-23} \text{ A}^2/\text{Hz}$  at 30 Hz under 2 V increased up to  $\sim 10^{-19} \text{ A}^2/\text{Hz}$  for 10 V bias. The noise curves obey the  $S_n = S_0 / f^\gamma$  relation with the fitting parameter  $\gamma$  varying from 0.9 to 1.2.

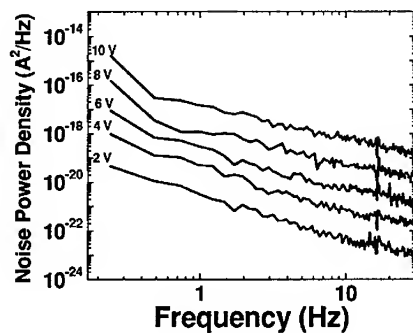


Figure 5. Low-frequency spectral noise measurements of a high-leakage 80  $\mu\text{m}$  diameter Schottky photodiode as a function of applied reverse bias.

#### 4. Conclusion

In summary, we have demonstrated solar-blind AlGaIn-based Schottky photodiodes with low dark current, low noise and high detectivity. Breakdown

voltages larger than 50 V and dark currents less than 400 fA under 25 V reverse bias were achieved. I-V characteristics of the solar-blind detectors led to the lowest dark current density ( $< 1.8 \text{ nA/cm}^2$ ) and the highest detectivity ( $> 2.6 \times 10^{12} \text{ cmHz}^{1/2}/\text{W}$ ) values reported for solar-blind AlGaIn Schottky photodiodes. Device responsivities as high as 89 mA/W were measured under 50 V reverse bias. Detector noise was  $1/f$  limited with spectral noise density values less than  $3 \times 10^{-29} \text{ A}^2/\text{Hz}$  under reverse bias voltages as high as 25 V.

This work was supported by NATO Grant No. SfP971970, Turkish Department of Defense Grant No. KOBRA-001 and Thales JP8.04

## REFERENCES

1. P. Schreiber, T. Dang, G. Smith, T. Pickenpaugh, P. Gehred, and C. Litton, *Proc. SPIE* **3629**, 230 (1999).
2. J. C. Carrano, T. Li, P. A. Grudowski, R. D. Dupuis, and J. C. Campbell, *IEEE Circuits & Devices Mag.* **15**, 15 (1999).
3. D. Walker, X. Zhang, P. Kung, A. Saxler, S. Javapour, J. Xu, and M. Razeghi, *Appl. Phys. Lett.* **68**, 2100 (1996).
4. B. W. Lim, Q. C. Chen, J. Y. Yang, and M. Asif Khan, *Appl. Phys. Lett.* **68**, 3761 (1996).
5. G. Parish, S. Keller, P. Kozodoy, J. P. Ibbetson, H. Marchand, P. T. Fini, S. B. Fleischer, S. P. Denbaars, U. K. Mishra, and E. J. Tarsa, *Appl. Phys. Lett.* **75**, 247 (1999).
6. D. Walker, V. Kumar, K. Mi, P. Sandvik, P. Kung, X. H. Zhang, and M. Razeghi, *Appl. Phys. Lett.* **76**, 403 (2000).
7. E. J. Tarsa, P. Kozodoy, J. Ibbetson, B. P. Keller, G. Parish, and U. Mishra, *Appl. Phys. Lett.* **77**, 316 (2000).
8. D. J. H. Lambert, M. M. Wong, U. Chowdhury, C. Collins, T. Li, H. K. Kwon, B. S. Shelton, T. G. Zhu, J. C. Campbell, and R. D. Dupuis, *Appl. Phys. Lett.* **77**, 1900 (2000).
9. J. D. Brown, J. Li, P. Srinivasan, J. Matthews, and J. F. Schetzina, *MRS Internet J. Nitride Semicond. Res.* **5**, 9 (2000).
10. M. M. Wong, U. Chowdhury, C. J. Collins, B. Yang, J. C. Denyszyn, K. S. Kim, J. C. Campbell, and R. D. Dupuis, *Phys. Stat. Sol. (A)* **188**, 333 (2001).
11. P. Sandvik, K. Mi, F. Shahedipour, R. McClintock, A. Yasan, P. Kung, M. Razeghi, *J. Crystal Growth* **231**, 366 (2001).
12. G. Parish, M. Hansen, B. Moran, S. Keller, S. P. Denbaars, and U. K. Mishra, *Phys. Stat. Sol. (A)* **188**, 297 (2001).
13. A. Hirano, C. Pernot, M. Iwaya, T. Detchprohm, H. Amano, and I. Akasaki, *Phys. Stat. Sol. (A)* **188**, 293 (2001).
14. J. C. Campbell, C. J. Collins, M. M. Wong, U. Chowdhury, A. L. Beck, and R. D. Dupuis, *Phys. Stat. Sol. (A)* **188**, 283 (2001).
15. J. Y. Duboz, J. L. Reverchon, D. Adam, B. Damilano, F. Semond, N. Grandjean, and J. Massies, *Phys. Stat. Sol. (A)* **188**, 325 (2001).
16. T. Li, J. H. Lambert, A. L. Beck, C. J. Collins, B. Yang, M. M. Wong, U. Chowdhury, R. D. Dupuis, and J. C. Campbell, *J. Electronic Materials* **30**, 872 (2001).
17. A. Osinsky, S. Gangopadhyay, B. W. Lim, M. Z. Anwar, M. A. Khan, D. V. Kuksenkov, and H. Temkin, *Appl. Phys. Lett.* **72**, 742 (1998).
18. S. L. Rumyantsev, N. Pala, M. S. Shur, R. Gaska, M. E. Levinstein, V. Adivarahan, J. Yang, G. Simin, and M. Asif Khan, *Appl. Phys. Lett.* **79**, 866 (2001).
19. V. Adivarahan, G. Simin, G. Tamulaitis, R. Srinivasan, J. Yang, M. Asif Khan, M. S. Shur, and R. Gaska, *Appl. Phys. Lett.* **79**, 1903 (2001).
20. E. Monroy, F. Calle, J. L. Pau, F. J. Sanchez, E. Munoz, F. Omnes, B. Beaumont, and P. Gibart, *J. Appl. Phys.* **88**, 2081 (2000).

---

## **Visible Light Emitters**

### Formation of quantum dots by self-rearrangement of metastable 2D GaN

N. Gogneau, D. Jalabert, E. Monroy, C. Adelmann and B. Daudin.  
CEA / CNRS / UJF Research Group "Nanophysique et Semi-conducteurs"  
Dept. de Recherche Fondamentale sur la Matière Condensée, SP2M/PSC  
CEA - Grenoble, 17 rue des Martyrs, 38054 - Grenoble cedex 9, France.

#### ABSTRACT

We propose a new procedure to grow GaN quantum dots (QDs) on AlN by using the Ga surfactant effect in plasma-assisted molecular beam epitaxy. Self-formed GaN islands were spontaneously generated under vacuum from a GaN 2D layer grown under Ga-rich conditions. Island characteristics (size and density) are studied as a function of the GaN coverage. We demonstrate that the QD density can be controlled in the  $10^{10} \text{ cm}^{-2}$  to  $2 \times 10^{11} \text{ cm}^{-2}$  range. It is shown that beyond a given GaN thickness there is a coexistence between elastic and plastic relaxation.

#### INTRODUCTION

The Stranski-Krastanow (SK) growth mode is a widely used method to growth semiconductor self-organized quantum dots. The deposition of a strained two-dimensional (2D) wetting layer is followed by elastic relaxation through three-dimensional (3D) islanding above a given critical thickness ( $\sim 2.0$  monolayers (ML) for GaN on AlN) [1-3]. In the specific case of nitride semiconductors grown by plasma-assisted molecular beam epitaxy (PAMBE), SK mode is observed when growing GaN at high temperature (710 – 750 °C) under N-rich conditions. In contrast, Ga-rich growth conditions inhibit the SK growth mode due to the formation of a self-regulated Ga film, about 2 ML thick, on the growing surface [4].

Taking advantage of Ga surfactant effect, we report in this article a new method to growth GaN QDs. We describe the structural properties of these "modified SK GaN islands" and demonstrate the possibility to control their density and size as a function of the GaN coverage. In addition, it will be shown that beyond a given GaN thickness there is a coexistence between elastic and plastic relaxation.

#### EXPERIMENTAL

Samples were grown on AlN templates deposited by metal-organic chemical vapor deposition (MOCVD) on c-sapphire. After a standard cleaning procedure, they were introduced in a MECA2000 molecular beam epitaxy chamber equipped with standard effusion cells for Al and Ga evaporation. Active nitrogen was produced by dissociation of  $\text{N}_2$  in a radio-frequency plasma cell.

The experimental procedure is schematized in figure 1. Prior to GaN deposition, a thin ( $\sim 100$  nm) AlN buffer layer is deposited on the pseudo-substrate. The GaN layer is grown under Ga-rich conditions, at a fixed substrate temperature of 750 °C and a growth rate of 0.23 ML/s, leading to the formation of a continuous Ga bilayer on the growing surface (figure 1-a). This Ga-

film inhibits the SK growth mode and favors a layer-by layer growth (Frank-Van der Merwe mode). When we shutter the N-flux, while maintaining the Ga flux, the Ga bilayer is regenerated and the surface remains 2D. The RHEED pattern is unchanged (figure 1-b). Under vacuum, the Ga-film desorbs rapidly (figure 1-c). The RHEED pattern becomes spotty with additional lines characteristics of facets (figure 1-d), associated to the formation of 3D islands. Structures were then annealed 2 min under vacuum after the 2D/3D transition.

Surface morphology was studied *ex-situ* by atomic force microscopy (AFM) and the elastic relaxation induced by the 2D/3D transition was measured in-situ by reflection high-energy electron diffraction (RHEED). The GaN quantity deposited on AlN was determined by Rutherford backscattering spectroscopy (RBS)

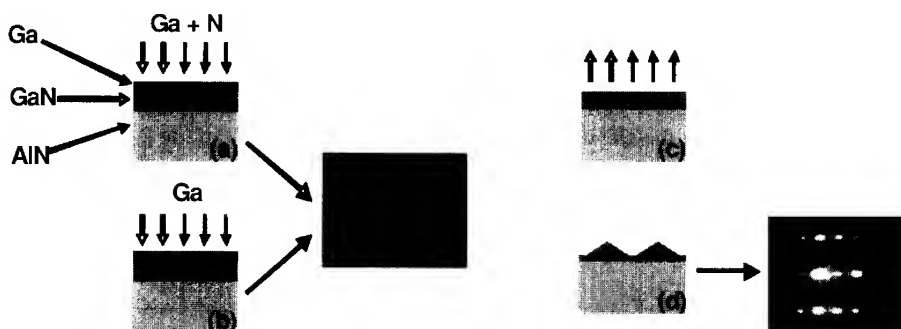


**Figure 1** : Schematic representation of the experimental procedure to growth self-formed GaN islands. (a) GaN growth under Ga-rich conditions. (b) Exposition to Ga-flux alone. (c) Ga evaporation under vacuum. (d) Self re-arrangement of GaN layer into 3D islands.

## RESULTS AND DISCUSSION

GaN QDs formed using the method schematized in figure 1, are hexagonal pyramids with {10-13} facets, the facet angle being equal to  $32^\circ$ . It is remarkable that this geometry is the same as previously observed for GaN islands grown by the SK mode [1]. Moreover it has been shown that a wetting layer is still present, which leads us to name the method described above as "modified SK growth mode". A promising feature of these nanostructures is their intensive cathodoluminescence at room temperature, as show in figure 2.

An important parameter governing the formation of the GaN QDs is the GaN coverage,  $\Theta$  (quantity of GaN deposited before stopping the growth). We have investigated QD characteristics (density, size) for varying GaN coverage from 2.8 ML to 13 ML. Experimental results confirm the existence of a threshold coverage ( $\approx 2.5$  ML) below which no transformation of the 2D GaN layer into 3D facettted islands is observed [5]. AFM images of GaN QDs obtained by varying  $\Theta$  from 2.8 ML to 13 ML are shown in figure 3.

**BEST AVAILABLE COPY**

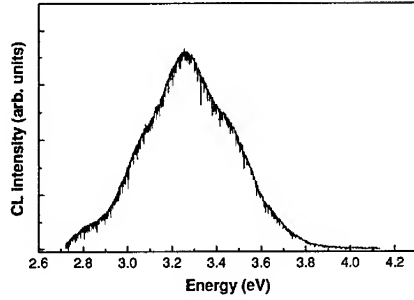


**Figure 2 :** Room temperature cathodoluminescence spectra of GaN QDs grown under Ga-rich conditions on AlN at 750 °C and subsequently annealed 2 minutes under vacuum. The thickness of the initial 2D GaN layer is 6 ML.

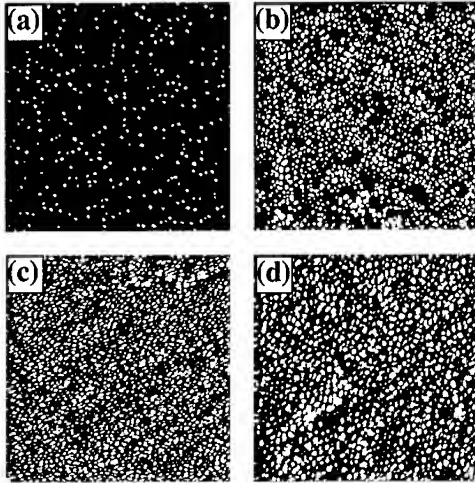


**Figure 3 :** 1  $\mu\text{m}$  x 1  $\mu\text{m}$  AFM images of GaN layers grown at  $T_s = 750$  °C. The GaN coverages are (a)  $\Theta = 2.8$  ML, (b)  $\Theta = 6$  ML, (c)  $\Theta = 10$  ML and (d)  $\Theta = 13$  ML.

In figure 4-a, the island density is plotted as a function of GaN coverage. Interestingly, it appears that QD density can be controlled over more than one decade for coverage varying from 2.8 ML to 6 ML. As a comparison the density of GaN QDs grown in the SK mode saturates at  $2 \times 10^{11} \text{ cm}^{-2}$  for a coverage of only 3 ML [6].

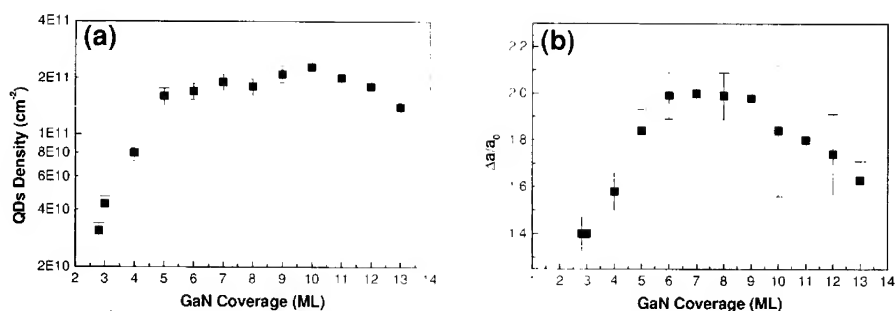


**Figure 4 :** (a) Variation of the total density of GaN QDs and (b) In-plane relative lattice relaxation (with respect to AlN) measured during the rearrangement of the 2D layer into 3D faceted islands as a function of the initial GaN coverage.

The relative variation of the in-plane lattice parameter, during the formation of 2D GaN layer into GaN 3D faceted islands, in-situ determined from the RHEED pattern, is shown in figure 4-b. We can observe that the elastic relaxation increases from 2.8 ML to 8 ML and then decreases slowly. This suggests a modification of the relaxation process of GaN layer when increasing the GaN growth coverage.

The shape of GaN QDs is also affected by GaN coverage. Figure 5 shows the variation of the aspect ratio (defined as islands height / islands diameter), which increases up to 8 ML before markedly decreasing for higher coverages.

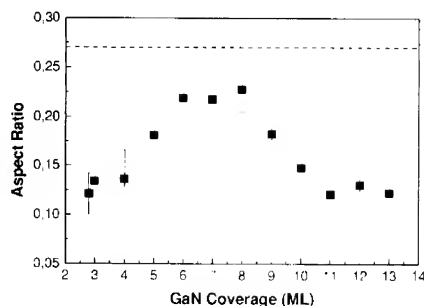


**Figure 5 :** Variation of the aspect ratio as a function of the nominal GaN coverage. The dashed line indicates the aspect ratio of a non-truncated pyramid.

Results displayed in figures 4-b and 5 reveal a correlation between the QD aspect ratio and the elastic strain relaxation of the 2D GaN layer associated with 3D islands formation. Actually, one may wonder what is the strain state of the 2D GaN layer just before islands formation. In

**BEST AVAILABLE COPY**

particular, plastic relaxation associated with formation of misfit dislocations should occur for thick enough 2D GaN layer.

We have demonstrated that for small dots ( $\Theta = 3$  ML) relaxation is purely elastic, without any dislocation [5]. As the elastic relaxation is in first approximation proportional to the aspect ratio of the islands [7], the increasing aspect ratio observed up to 8 ML is consistent with the increase of elastic relaxation observed in figure 4-b. For a GaN coverage greater than 8 ML, the aspect ratio decreases as well as the elastic relaxation (during island formation). Along the views detailed in [7] this suggests that GaN islands experience a decreasing strain when the thickness of the 2D layer exceeds 8 MLs. Above this nominal GaN coverage, we tentatively propose that the slowly decrease of  $(\Delta a/a_0)$  is assigned to an uncomplete transformation of the 2D layer into islands. Thus, the thickness of the 2D layer below the islands excess the 2 MLs corresponding to the so-called wetting layer. Moreover, we propose that this 2D GaN layer is then partially relaxed contrary to the 2 MLs thick wetting layer which is perfectly matched to AlN.

The above hypothesis are strongly supported by a Rutherford backscattering spectroscopy (RBS) analysis of the amount of GaN deposited as a function of the amount of GaN in dots, extracted from AFM data. First of all, biasing of data due to partial decomposition of GaN at 750 °C under vacuum have been discarded by measuring the effective GaN amount as a function of the nominally GaN deposited quantity.

Figure 6-a shows the total GaN quantity measured by RBS as a function of the nominal deposited amount.

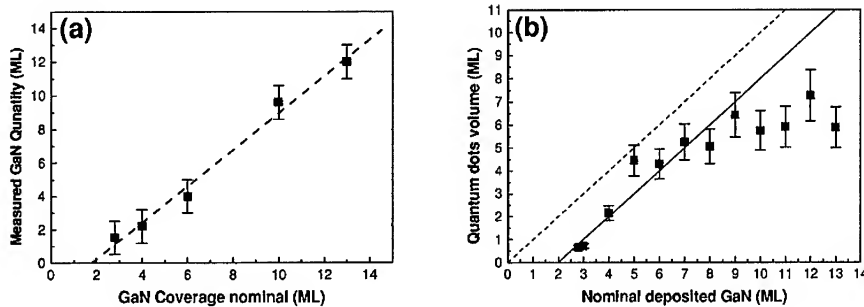


**Figure 6 :** (a) GaN amount contained into the layer, measured by RBS as a function of the nominal GaN deposited. (b) Total volume contained in the GaN islands as a function of the GaN coverage. The solid line indicates 2 ML thick GaN layer and the dash line corresponds to the case without 2D layer.

We establish that there is a linear variation between the amount of GaN nominally deposited and the amount effectively present on AlN. It is deduced from these results that 1.8 MLs of GaN is dissociated / desorbed during annealing under vacuum (2 min after the 2D/3D transition). We have furthermore calculated the total amount of GaN contained into the islands as a function of deposited GaN. The results are plotted in figure 6-b. The solid line indicates the expected behavior assuming that a 2 ML thick 2D GaN layer is present below the islands. The dashed line corresponds to the case when no 2D GaN layer is present. We can observe that for

GaN coverages up to 8 ML, the experimental data are consistent with the presence of a 2 ML thick wetting layer between the AlN buffer and the islands, which is corroborated by the high-resolution transmission electron microscopy (HRTEM) in [5]. In contrast, for GaN coverage higher 8 ML, the deviation from a linear behavior is the signature of the thickening of the non transformed 2D layer, while the amount of GaN contained in dots saturates to about 6 MLs. This amount is limited by geometrical considerations, as the aspect ratio cannot exceed the value corresponding to a full pyramid.

As shown in figure 5, at 8 ML GaN coverage, the aspect ratio is still slightly below its maximum theoretical value. This suggests that regime change in islands formation observed around 8 ML. GaN coverage is rather related to kinetic factor during growth, such as a temperature-dependent capture radius. This is supported by results in figure 3 while shown that even for  $\Theta$  as high as 13 ML, dots are clearly separated one from each other.

In addition, the thickening of the 2D layer observed for high coverages correlated to elastic relaxation results shown in figure 4-b, suggests the occurrence of plastic strain relaxation, through misfit dislocation formation, for  $\Theta > 8$  ML, leading to the conclusion that elastic and plastic relaxation likely coexist for nominal GaN coverage above 8 ML.

## CONCLUSION

We have described a new procedure to grow GaN QDs. Using this method, we have demonstrate the possibility to control the islands density in the  $10^{10} \text{ cm}^{-2}$  to  $2 \times 10^{11} \text{ cm}^{-2}$  range. we have found that a 2D layer is present below the 3D islands. Above a critical GaN coverage, the thickness of this layer exceeds the 2 ML corresponding to the wetting layer thickness in SK growth mode. Thus plastic strain relaxation is expected to occur, simultaneously with 3D islands formation.

## ACKNOWLEDGEMENTS

The authors acknowledge Y. Genuist and M. Falco for technical support.

## REFERENCES :

- 1 B. Daudin, F. Widmann, G. Feuillet, Y. Samson, M. Arlery and J.L. Rouvière, Phys. Rev. B 56, 7069 (1997).
- 2 S. Guha, A. Madhukar and K. C. Rajkuma, Appl. Phys. Lett. 57, 2110 (1990).
- 3 S. Varma, C.M. Reeves, V. Bressler-Hill, S. P. Den Baars and W. H. Weinberg, Surf. Sci. 393, 24 (1997).
- 4 G. Mula, C. Adelmann, S. Mochl, J. Oullier and B. Daudin, Phys. Rev. B 64, 195406 (2001).
- 5 C. Adelmann, N. Gogneau, E. Sarigiannidou, J. L. Rouvière and B. Daudin, Appl. Phys. Lett. 81, 3064 (2002).
- 6 C. Adelmann et al, unpublished.
- 7 R. Kern and P. Müller, Surf. Sci. 392, 103 (1997).

**BEST AVAILABLE COPY**

---

## **Electronic Devices**

### Material and Device Issues of AlGaIn/GaN HEMTs on Silicon Substrates

P. Javorka, A. Alam,<sup>1</sup> M. Marso, M. Wolter, A. Fox, M. Heuken,<sup>1</sup> and P. Kordoš  
Institute of Thin Films and Interfaces, Research Centre Jülich, D-52425 Jülich, Germany.  
<sup>1</sup>Aixtron AG, D-52072 Aachen, Germany.

#### ABSTRACT

Results on the preparation and properties of AlGaIn/GaN HEMTs on silicon substrates are presented and selected issues related to the material structure and device performance devices are discussed. Virtually crack-free AlGaIn/GaN heterostructures ( $x_{\text{AlIn}} \cong 0.25$ ), with low surface roughness (rms of 0.64 nm),  $n_s \cong 1 \times 10^{13} \text{ cm}^{-2}$  and  $\mu \cong 1100 \text{ cm}^2/\text{V s}$  at 300 K, were grown by LP-MOVPE on 2-inch (111)Si substrates. HEMT devices with  $L_g = 0.3\text{--}0.7 \text{ }\mu\text{m}$  were prepared by conventional device processing steps. Photoionization spectroscopy measurements have shown that a trap level of 1.85 eV, additional to two levels of 2.9 and 3.2 eV found before on GaN-based HEMTs on sapphire, is present in the structures investigated. Self-heating effects were studied by means of temperature dependent dc measurements. The channel temperature of a HEMT on Si increases with dissipated power much slower than for similar devices on sapphire substrate (e.g. reaches 95 and 320 °C on Si and sapphire, respectively, for 6 W/mm power). Prepared AlGaIn/GaN/Si HEMTs exhibit saturation currents up to 0.91 A/mm, a good pinch-off, peak extrinsic transconductances up to 150 mS/mm and static heat dissipation capability up to ~16 W/mm. Unity current gain frequencies  $f_T$  up to 21 and 32 GHz were obtained on devices with gate length of 0.7 and 0.5  $\mu\text{m}$ , respectively. The saturation current and  $f_T$  values are comparable to those known for similar devices using sapphire and SiC substrates. Properties of AlGaIn/GaN/Si HEMTs investigated show that this technology brings a prospect for commercial application of high power rf devices.

#### INTRODUCTION

AlGaIn/GaN high electron mobility transistors (HEMTs) have recently been attracting much attention because of their promising uses for high-frequency, -power and -temperature applications. Sapphire and since recently also SiC are commonly used as substrates because of lack of large-area GaN bulk crystals. An output power higher than 100 W at 2 GHz has been achieved on AlGaIn/GaN HEMTs using sapphire thinned down to 50  $\mu\text{m}$  (pulsed operation, 10% duty) [1] as well as high-resistive SiC (cw operation) [2]. However, silicon can be a useful alternative because of its low cost and large area availability, good thermal conductivity and potential integration of GaN power devices with advanced Si electronics. Growth of GaN on Si is more difficult than on sapphire due to the higher lattice constant and thermal expansion coefficient mismatches, which produce higher dislocation density and potential generation of cracks. Nevertheless encouraging results on AlGaIn/GaN/Si HEMTs concerning their high-frequency and -power performance have been presented recently by various groups [3-6]. The device performance is comparable to that known for devices using sapphire and SiC substrate [4]. Thus, GaN-based HEMTs on silicon substrate can be a cost-effective alternative for various applications.

In the present study results concerning the preparation and properties of AlGaIn/GaN HEMTs on silicon substrates are presented and selected issues related to the material structure and device performance are discussed. Prepared devices are characterized by dc, pulsed and rf techniques. Issues related to the heat dissipated power and channel temperature, as well as high temperature operation of devices are analyzed. Photoionization spectroscopy is used to evaluate the traps in the material structure. For comparison also AlGaIn/GaN HEMTs on sapphire substrates were prepared and their performance was investigated.

## SILICON AS A SUBSTRATE FOR GaN GROWTH

The idea to use low cost and large area available silicon as a substrate for GaAs- and InP-based semiconductor devices is known for a long time and many attempts have been made to optimize this procedure [7]. Obtained results, unfortunately, are not very impressive and therefore commercial applications of this technology have not started yet. However, in contradiction to GaAs and InP, this issue is especially important for GaN-based devices because of lack of GaN bulk crystals. Small-area ( $\sim 4 \text{ cm}^2$ ) 'free-standing' GaN templates are available since recently [8], but all results reported on AlGaIn/GaN HEMTs are on structures grown by MOVPE or MBE on sapphire or SiC substrates. Sapphire is high resistive and up to 6-inch substrates are available for mediate price. The main limitation of devices on sapphire is its low thermal conductivity, about 5-times lower than that of GaN (see Table I). Therefore the sapphire substrate needs to be thinned down as possible in order to improve the heat-dissipated power of a HEMT [1]. Thermal conductivity of SiC is more than 10-times higher than that of sapphire and thus SiC is today the main preferable substrate for GaN-based high-power devices. However, high resistive SiC wafers are very expensive (price ratio of 2-inch SiC and Si wafers is more than 100) and their quality is rather poor.

**Table I.** Comparison of some features of GaN, sapphire, SiC and Si substrates ( $\Delta a/a$  and  $\alpha_{th}$  are the lattice mismatch and the thermal expansion coefficient respectively, relative to GaN,  $K_{th}$  is the thermal conductivity).

Substrate	GaN	Al <sub>2</sub> O <sub>3</sub>	SiC	Si
wafer size	$\sim 4 \text{ cm}^2$	6"	3"	12"
cost	high	mediate	high	low
perfection	low	high	mediate	high
$\Delta a/a$ (%)	-	13	3.4	17
$\alpha_{th}$ (%)	-	-34	+25	+100
resistivity	high	high	high	mediate
$K_{th}$ (W/cmK)	1.3	0.3	3.5	1.5

Silicon substrates might be a useful alternative because of some advantages in comparison to sapphire and SiC, as it follows from Table I. They are cheap and available in high quality and in the size up to 12-inches. Their thermal conductivity is partially lower than that of SiC, but still 5-times higher than that of sapphire and slightly higher than that of GaN. However, the lattice constant and the thermal expansion mismatches for GaN on Si are much higher than those for

GaN on sapphire and GaN on SiC. Therefore growth of GaN on silicon is much more difficult, accompanied with higher dislocation density and potential generation of cracks. This is the reason that the number of papers dealing with the growth of GaN on Si highly exceeds the number of those describing GaN-based devices on Si substrates.

Formation of cracks seems to be the basic issue of GaN on silicon technology. Growth by MBE should be preferable because of much lower growth temperature of  $\sim 750^\circ\text{C}$  (i.e. lower thermal strain after cooling) than by MOVPE with a common growth temperature of  $\sim 1050^\circ\text{C}$ . Indeed,  $3\text{ }\mu\text{m}$  thick crack-free GaN layers have been prepared by MBE [9]. On the other hand, several groups have found that the critical thickness for crack-free growth by MOVPE is only about  $0.7\text{--}1\text{ }\mu\text{m}$ . Various buffer layers between GaN and Si, with limited success, have been used to grow thicker GaN layers. However, significant progress in a decrease of the crack density has been achieved recently by various groups [6,10,11]. This improvement saturated with a breakthrough and entirely crack-free GaN layers on 2-inch Si wafers have been obtained. Consequently GaN-on-Si devices with improved performance have been presented. Blue light-emitting diodes on Si(111) substrates, with an optical power up to  $270\text{ }\mu\text{W}$  at  $455\text{ nm}$  wavelength, have been reported [10]. Recently also AlGaIn/GaN HEMTs on Si have been realized by various groups [3-6]. The unity current gain cutoff frequencies fully comparable to those obtained on devices with similar geometry and using sapphire and SiC substrates have been obtained [4]. Power density of  $3.3\text{ W/mm}$  as well as an output power up to  $27\text{ W}$  on large periphery devices, both at  $2\text{ GHz}$ , were also reported recently [12].

## GROWTH AND PROPERTIES OF LAYER STRUCTURE

Low-pressure MOVPE technique was used to grow AlGaIn/GaN heterostructures on 2-inch (111)-oriented p-type Si substrates. A special layer sequence to reduce strain during the growth and to avoid layer cracking after the cooling cycle was deposited on Si substrate first. It consisted of two low-temperature AlN layers and one embedded high-temperature GaN layer with a total thickness of  $\sim 0.4\text{ }\mu\text{m}$  [13]. An  $\sim 1\text{ }\mu\text{m}$  thick high resistive GaN buffer layer was then deposited on top of this 'accommodation' layer sequence. Finally, a  $6\text{ nm}$  nominally undoped AlGaIn spacer, a  $10\text{--}15\text{ nm}$  Si doped ( $2\text{--}5 \times 10^{18}\text{ cm}^{-3}$ ) AlGaIn carrier-supply and a  $6\text{ nm}$  nominally undoped AlGaIn barrier layer were grown. All AlGaIn layers were grown with the mole fraction of AlN  $x = 0.23$  as determined by RBS. For wurtzitic group III-nitride based heterostructures, a high 2DEG channel conductivity can be obtained without doping due to large spontaneous and piezoelectric polarization. Therefore, beside conventionally doped heterostructures, we also prepared undoped AlGaIn/GaN heterostructures for some comparative studies.

Virtually crack-free structures with reduced tensile strain and very good surface morphology were obtained. The surface roughness of  $\text{rms} = 0.64\text{ nm}$  was determined by atomic force microscopy, as shown in Fig. 1a [14]. The scanning electron microscopy photograph of an AlGaIn/GaN heterostructure is shown in Fig. 1b. However, in spite of reduced stress of the layers we would like to mention that a curvature of 2-inch wafers was still observed. A radius of of  $7.8\text{ m}$  was reported for MOCVD grown crack-free GaN on Si(111) substrates [10].

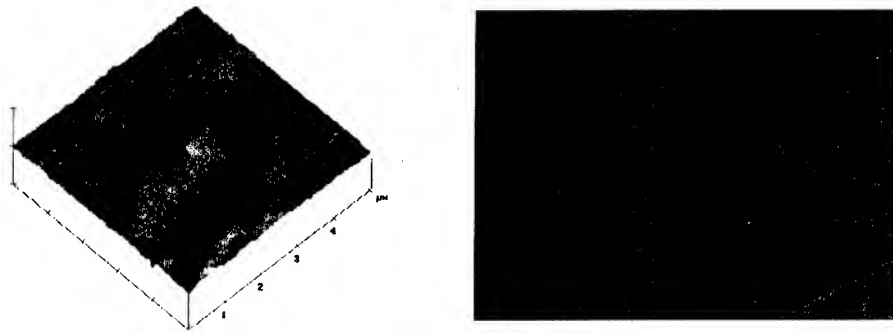


**Figure 1.** AFM (a) and SEM (b) microphotographs of AlGaIn/GaN heterostructure grown on Si(111) substrate.

Temperature dependent Hall-effect measurements on  $\sim 5 \times 5 \text{ mm}^2$  van der Pauw samples with alloyed In-ball contacts were performed to evaluate the properties of prepared heterostructures. Room temperature data yielded the sheet carrier concentration  $n_s = (0.75\text{--}1) \times 10^{13} \text{ cm}^{-2}$  and the carrier mobility of  $950\text{--}1200 \text{ cm}^2/\text{V s}$ . The temperature dependent measurements have shown typical behavior for 2DEG structures with saturated carrier mobility at low temperatures, as it is demonstrated for both doped and undoped AlGaIn/GaN/Si heterostructures in Fig. 2.

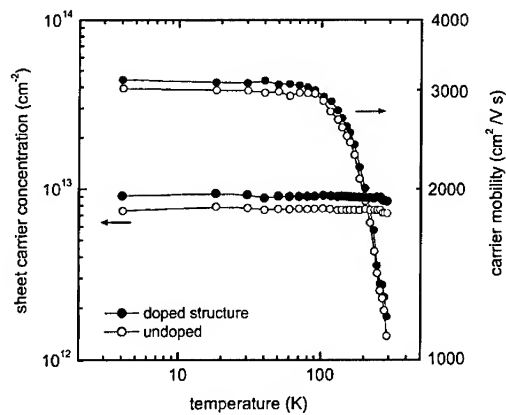


**Figure 2.** Temperature dependent Hall-effect measurement on doped and undoped AlGaIn/GaN heterostructure grown on Si substrate.

## DEVICE FABRICATION

The device processing consisted of conventional HEMT fabrication steps. At first mesa etching isolation using an argon sputtering was performed. After that ohmic contacts were prepared by evaporating multilayered Ti/Al/Ni/Au sequence followed by annealing at 850 °C for 30 s in a N<sub>2</sub> ambient [15]. The ohmic contact resistance of 0.35–0.8 Ωmm with a channel sheet resistivity of 550–900 Ω/sqr were measured using the transmission-line-method. The Schottky gate metallization consisted of a Ni/Au double-layer patterned by e-beam lithography. The Schottky barrier height of 0.98 and 1.11 eV was found from I-V and I-V-T measurement [15]. An improvement of the recessed Schottky contacts can be obtained after annealing at 450 °C [16]. Unpassivated as well as passivated (Si<sub>3</sub>N<sub>4</sub>, SiO<sub>2</sub>) multifinger-gate devices with different source-drain separation, nominal gate lengths of 0.3, 0.5 and 0.7 μm and a finger gate width of 50 μm (2–6 fingers used) were prepared. The existence of the 2DEG in the AlGaIn/GaN/Si heterostructures to be processed was confirmed by C-V measurements.

## DEVICE PERFORMANCE

### DC characterization

The HEMT maximum output rf power relates to the dc parameters as  $P_{rf} = (\Delta V \times \Delta I)/8$ . Here  $\Delta V$  is a difference of a source-drain breakdown voltage and a knee voltage,  $\Delta I$  is given by a maximum drain saturation current. This emphasizes the relevance of the HEMT dc characterization. Typical static output characteristics at different gate voltages from +1 V up to –9 V ( $\Delta V_G = -1$  V) measured up to drain voltage of 20 V on devices with 0.3 μm gate length are shown in Fig. 3a (solid lines). Low output conductance and minimal thermal effects are

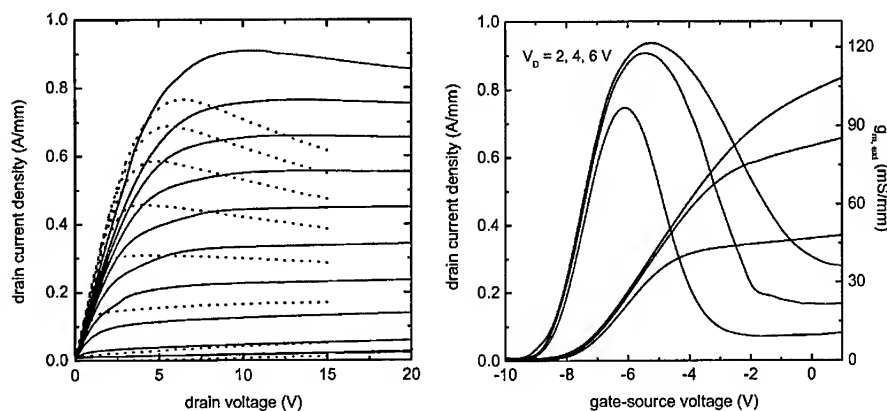


**Figure 3.** I–V (a) and transfer (b) characteristics of AlGaIn/GaN HEMT on Si substrate (dotted lines are for the similar device on sapphire substrate).

observed. A drain saturation current of 0.91 A/mm (0.72 A/mm for devices with 0.5  $\mu\text{m}$  gate length, not shown here) is obtained at +1 V on the gate. This is higher than so far reported for AlGaIn/GaN HEMTs on Si and comparable to values on high performance microwave power HEMTs on SiC substrates. Also presented in Figure 3a are typical I–V output characteristics for devices with a similar layer structure however grown on sapphire substrates (dotted lines). The HEMTs on Si substrates can sustain significantly higher DC power in comparison to similar devices grown on sapphire. The drain current decreases only slightly ( $V_G = 1$  V) or is almost constant ( $V_G \leq 0$  V) with increasing drain voltage for devices on Si. An improvement in heat dissipation because of the higher thermal conductivity of Si compared to sapphire ( $k_{\text{Si}}/k_{\text{sapphire}} \cong 5$ ) is evident. Thus, channel heating effects are significantly reduced and the devices can handle static heat dissipation of up to about 16 W/mm without remarkable degradation of their performance.

The transfer characteristics of the AlGaIn/GaN HEMT on Si are shown in Fig. 3b. The peak extrinsic transconductance of 125 mS/mm was measured at  $V_G = -5$  V. This is only slightly lower than reported for high performance microwave power GaN-based HEMTs on SiC. However, further enhancement may be achieved by optimizing the HEMT dimensions, especially the gate length and the gate drain spacing. Thus transconductances up to 150 mS/mm were achieved. The threshold voltage of these devices is close to  $-9$  V opposed to  $-6$  V observed on similar devices on sapphire. The breakdown voltage at pinch-off is found to be slightly above 40 V.

#### Properties at higher temperatures

The dc characterization of AlGaIn/GaN/Si HEMTs shows good handling capability of static heat dissipation without any degradation of their performance. Consequently smaller degradation in the device performance at higher temperatures is expected if silicon substrate is used (Fig. 4). The saturation current  $I_{D,\text{max}}$  and the peak transconductance  $g_{m,\text{ext}}$  at various temperatures up to

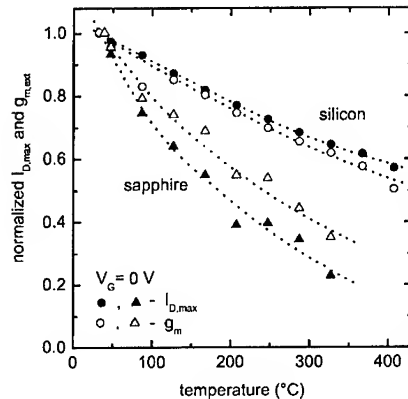


**Figure 4.** Saturation current and peak transconductance as a function of temperature (normalized to their 300 K values) for AlGaIn/GaN HEMTs on Si and sapphire substrates.

400 °C for AlGaIn/GaN HEMTs prepared on Si and sapphire are shown in Fig. 4. It is clear that reduction of the dc performance with increased temperature is much less pronounced for devices on Si compared to those on sapphire substrates.

### Channel temperature

Self-heating effects and temperature rise in AlGaIn/GaN HEMTs were studied in details, exploiting transistor DC characterization methods. We observed that the negative differential conductance in the output characteristics accompanies the HEMT self-heating effect. An analytic formula for a source-drain current drop as a function of parasitic source resistance and the threshold voltage changes is proposed to explain this behavior [17]. The  $R_s$  and  $V_{th}$  were determined experimentally at different elevated temperatures to construct channel temperature versus dissipated power transfer characteristic. Typical result for AlGaIn/GaN HEMTs on Si and sapphire substrates are compared in Fig. 5. The channel temperature increases much rapidly for devices on sapphire reaching 320 °C in comparison to 95 °C for a HEMT on Si at 6 W/mm dissipated power.

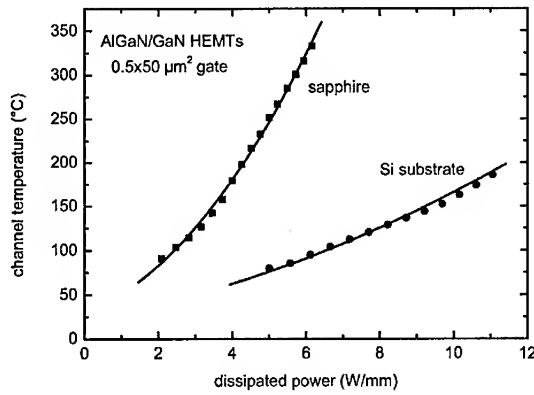


**Figure 5.** Transfer characteristics channel temperature - dissipated power for AlGaIn/GaN HEMT grown on Si and sapphire substrates.

### Photoionization spectroscopy of traps

It is well known that high density of traps present in AlGaIn/GaN heterostructures is responsible for dc/rf dispersion (current collapse), i.e. for lower output power as predicted from the dc properties. We performed photoionization spectroscopy measurements on AlGaIn/GaN HEMTs, which allows to identify the trap signatures. Typical examples of the photoionization cross section as a function of the photon energy for devices prepared on Si and sapphire substrates are shown in Fig. 6. Measured data are evaluated using Lucovsky formula  $\sigma = K(h\nu - E_t)^{3/2}/(h\nu)^3$  and assuming Gaussian broadening of the defect levels (full lines in Fig. 6). Defects with two distinct levels of 3.2 and 2.9 eV are present in all structures independent on the substrate used. Our previous results on AlGaIn/GaN/sapphire HEMTs with different channel-

surface distance indicate that the traps observed are surface related [18]. The third trap level of 1.85 eV is found only in devices prepared on Si. On the other hand, levels of 2.85 and 1.8 eV have been found before on GaN-based FETs on sapphire and are suggested to be present in the high resistive GaN buffer [19]. Thus, further studies are needed in order to identify the origin of observed traps in AlGaIn/GaN HEMTs.

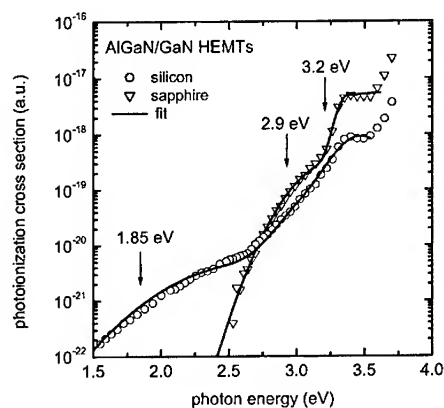


**Figure 6.** Photoionization cross section spectra for AlGaIn/GaN HEMT grown on Si and sapphire substrates.

#### Characterization under pulse conditions

A comparison of the I-V and transfer characteristics measured on the same AlGaIn/GaN HEMT device under dc and pulsed ( $\sim 1.5 \mu\text{s}$ ) conditions are shown in Fig. 7. Characteristics for

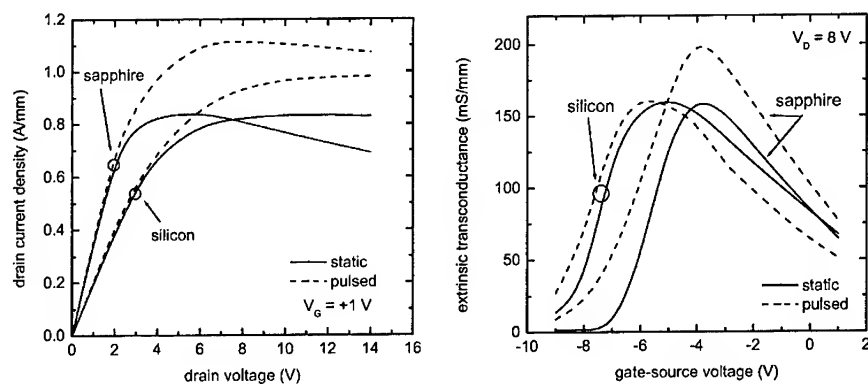


**Figure 7.** I-V and transfer characteristics of AlGaIn/GaN HEMTs on Si and sapphire substrates (full and dashed lines are for DC and pulsed conditions, respectively).

devices with similar geometry prepared on Si and sapphire substrates are shown. The pulsed drain currents (dashed lines) are partially higher, as expected, than those for dc conditions (full lines, both at  $V_G = +1$  V). However, for HEMT on sapphire also the pulsed characteristics show a decrease of the drain current in contradiction to the almost constant current at higher voltages for devices on Si. The pulsed I-V characteristics of HEMT on sapphire exhibits still negative conductance indicating on heating effects. On the other hand, the transconductance as a function of the gate bias for HEMT on Si ( $V_D = 8$  V) shows nearly the same behavior at dc and pulsed conditions. Thus, Si substrate promises better device cooling and brings a prospect of a higher power rf performance.

### Small signal characterization

The small signal characterization of the devices was carried out by on-wafer S-parameters measurements using an HP 8510C network analyzer [4]. Fig. 8a shows the short circuit current gain ( $h_{21}$ ) and unilateral power gain (GU) against frequency for AlGaIn/GaN/Si HEMTs. An extrinsic unity gain cutoff frequency of 32 and 21 GHz and a maximum frequency of oscillation of 27 and 22 GHz are evaluated for devices with 0.5 and 0.7  $\mu\text{m}$  gate length, respectively. These are the highest values reported so far for AlGaIn/GaN HEMTs on Si substrates. Moreover, the unity current gain cutoff frequencies are fully comparable to those obtained on devices with similar geometry and using sapphire and SiC substrates. This is shown in Fig. 8b, in which the best  $f_T$  values found in the literature for various gate lengths (gate width not considered) are plotted together with those reported here. However, the  $f_{\text{max}}/f_T$  of  $\sim 1$  results for AlGaIn/GaN/Si HEMTs prepared. This is similar as reported before [3] and indicates parasitic conduction through the Si substrate.

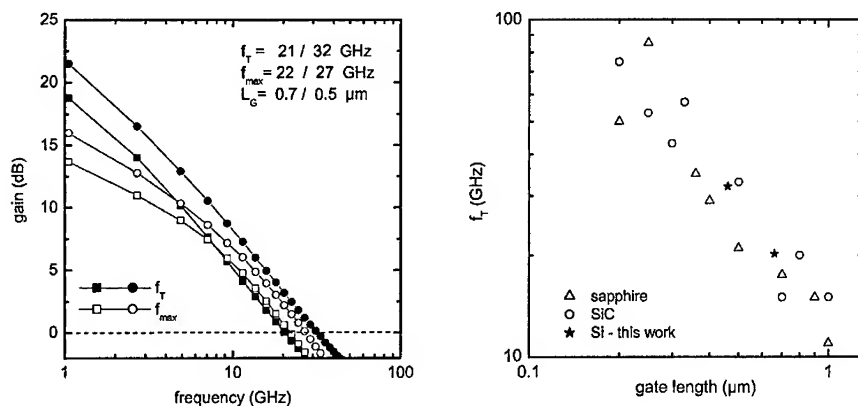


**Figure 8.** Small signal performance of AlGaIn/GaN HEMTs on Si substrates (a) and unity current gain cutoff frequencies for various gate lengths known for devices on sapphire and SiC substrates in comparison with those reported here on Si substrates (b).

## CONCLUSIONS

AlGaIn/GaN HEMTs prepared on (111)Si substrates were characterized by conventional on-wafer dc, pulse and rf methods and their properties were compared with those found on similar devices on sapphire substrates. From the static and pulsed I-V measurements it follows that the use of a Si substrate promises better device cooling and thus higher power performance can be expected. It was shown that degradation of the dc performance at higher temperatures is much less pronounced for devices on Si than on sapphire substrates. Photoionization spectroscopy studies revealed trap level of 1.85 eV, additional to two levels found before on GaN-based HEMTs prepared on sapphire substrate. Properties of AlGaIn/GaN/Si HEMTs show that this technology brings a prospect for commercial application of high power rf devices.

## REFERENCES

1. Y. Ando, Y. Okamoto, H. Miyamoto, N. Hayama, T. Nakayama, K. Kasahara, and M. Kuzuhara, *Internat. Electron Devices Meeting Digest IEDM-2001*, Washington DC, 381 (2001).
2. III-V Review **15**, 17 (2002).
3. E. M. Chumbes, A. T. Schremer, J. A. Smart, Y. Wang, N. C. MacDonald, D. Hogue, J. J. Komiak, S. J. Lichwalla, R. E. Leoni, and J. R. Shealy, *IEEE Trans. Electron Devices* **48**, 420 (2001).
4. P. Javorka, A. Alam, A. Fox, M. Marso, M. Heuken, and P. Kordos, *Electron. Lett.* **38**, 288 (2002).
5. V. Hoel, N. Vellas, C. Gaquière, J. C. De Jaeger, Y. Cordier, F. Semond, F. Natali, and J. Massies, *Electron. Lett.* **38**, 750 (2002).
6. J. D. Brown, R. Borges, E. Piner, A. Vescan, S. Singhal, and R. Therrien, *Solid-St. Electron.* **46**, 1535 (2002).
7. S. F. Fang, K. Adomi, S. Iyer, H. Morkoc, and H. Zabel, *J. Appl. Phys.* **68**, R31 (1990).
8. Advanced Technology Materials, Inc. (2002).
9. F. Semond, P. Lorenzini, N. Grandjean, J. Masies, *Appl. Phys. Lett.* **78**, 335 (2001).
10. A. Dadgar, M. Poschenrieder, J. Bläsing, K. Fehse, A. Diez, and A. Krost, *Appl. Phys. Lett.* **80**, 3670 (2002).
11. Y. Dikme, G. Gerstenbrandt, A. Alam, H. Kalisch, A. Szymakowski, M. Fieger, R. H. Jansen and M. Heuken, *J. Cryst. Growth* (2003) – in press.
12. A. Vescan, J. D. Brown, J. W. Johnson, R. Therrien, T. Gehrke, P. Rajagopal, J. Roberts, S. Singhal, W. Nagy, R. Borges, E. Piner, and K. Lithicum, *phys. stat. solidi* (2002) – in press.
13. P. Javorka, A. Alam, N. Nastase, M. Marso, H. Hardtdegen, M. Heuken, H. Lüth, and P. Kordoš, *Electron. Lett.* **37**, 1364 (2001).
14. P. Javorka, Master Thesis, FZ Jülich (2000).
15. J. Kuzmík, P. Javorka, M. Marso, and P. Kordoš, *Semicond. Sci. Technol.* **17**, L76 (2002).
16. J. Kuzmík, P. Javorka, A. Alam, M. Marso, M. Heuken, and P. Kordos, *IEEE Electron Device Lett.* **49**, 1496 (2002).
17. M. Wolter, P. Javorka, A. Fox, M. Marso, H. Lüth, P. Kordoš, R. Carius, A. Alam, and M. Heuken, *J. Electron. Materials* **31**, No. 12 (2002) – in press.
18. P. B. Klein, *J. Appl. Phys.* **92**, 5498 (2002).

**AlGaIn/GaN Heterostructure Field-Effect Transistors  
with Back-Doping Design for High-Power Applications:  
High Current Density with High Transconductance Characteristics**

Narihiko Maeda<sup>1</sup>, Kotaro Tsubaki<sup>2</sup>, Tadashi Saitoh<sup>1</sup>, Takehiko Tawara<sup>1</sup>, and Naoki Kobayashi<sup>1</sup>

<sup>1</sup>NTT Basic Research Laboratories, NTT Corporation

3-1 Morinosato Wakamiya, Atsugi-shi, Kanagawa, 243-0198, Japan

<sup>2</sup>Department of Electrical & Electronic Engineering, Toyo University

2100 Kujirai, Kawagoe-shi, Saitama, 350-8585, Japan

**ABSTRACT**

Electron transport properties and DC device characteristics have been examined in the AlGaIn/GaN heterostructure field-effect transistors (HFETs) with back-doping design that makes it possible to obtain high two-dimensional electron gas (2DEG) densities even for the devices with thin AlGaIn barrier layers. In the back-doping design, an asymmetric double-heterostructure is employed, and donor atoms are doped not only in the surface-side AlGaIn layer but also in the underlying AlGaIn layer. In this structure, electrons are efficiently supplied also from the back-doped AlGaIn barrier layer to the GaN channel and merged into a single 2DEG layer, with the help of the negative polarization charges at the heterointerface between the GaN channel and the underlying AlGaIn barrier layer. By using back-doping design, very high 2DEG densities around  $3 \times 10^{13} \text{ cm}^{-2}$  has been achieved in the  $\text{Al}_{0.3}\text{Ga}_{0.7}\text{N}/\text{GaN}$  HFET whose barrier layer ( $\text{Al}_{0.3}\text{Ga}_{0.7}\text{N}$ ) is designed to be as thin as 120 Å. An HFET with the gate-length of 1.5 μm has exhibited a high current density of 1.2 A/mm and a high transconductance of 200 mS/mm, which is ascribed to high 2DEG densities and thin barrier layers in these devices. HFETs with the back-doping design are thus promising for high-power applications.

**INTRODUCTION**

AlGaIn/GaN heterostructure field-effect transistors (HFETs) have recently emerged as the attractive transistors suitable for high-temperature and high-power microwave applications [1-12]. For further improving high-power device performance, increasing the two-dimensional electron gas (2DEG) density is effective, which can be attained by using the unrelaxed HFETs with high Al compositions [13-16]. On the other hand, reducing the thickness of the AlGaIn barrier layer is effective to obtain the high transconductance. In this paper, we point out the problem with the conventional doping design that the 2DEG density decreases when the AlGaIn barrier thickness is reduced. As a solution for this problem, we propose the back-doping doping design that makes it possible to obtain high 2DEG densities in the HFETs with the thin barrier thickness. We examine the electron transport properties and DC device characteristics of the HFETs with the back-doping design.

**EXPERIMENTAL DETAILS AND DISCUSSIONS**

**Problem with Conventional Modulation Doping accompanied by Thinning Barrier Layer**

To examine the 2DEG density in modulation doped HFETs with thin AlGaIn layers, we have grown modulation doped HFETs whose barrier thickness is as thin as 120 Å, and, for

comparison, we have also grown modulation doped HFETs with a typical barrier thickness of 200 Å. We have grown these HFET samples on 6H-SiC(0001) substrates by low-pressure metal organic vapor phase epitaxy (MOVPE) at 300 Torr. The structures were as follows: 40 Å undoped  $\text{Al}_{0.3}\text{Ga}_{0.7}\text{N}$ / 130 or 50 Å Si-doped  $\text{Al}_{0.3}\text{Ga}_{0.7}\text{N}$ / 30 Å undoped  $\text{Al}_{0.3}\text{Ga}_{0.7}\text{N}$ / 1  $\mu\text{m}$  GaN/ 1000 Å AlN buffer/ SiC(0001) substrates. Thus, of the 200 (or 120) Å AlGaN barrier layer, the midst part of the 130 (or 50) Å region was doped with Si, and the surface-side 40 Å and the channel-side 30 Å layers were left undoped as the Schottky contact and the spacer layers, respectively. The doping concentration of Si was varied from 0 (undoped) to  $4 \times 10^{19} \text{ cm}^{-3}$  to increase the 2DEG density. For these modulation doped HFET samples, we have performed the Hall effect measurements with Van der Pauw geometry.

Figure 1 shows the relation between the 2DEG mobility and the 2DEG density at 300 K in modulation doped HFETs whose AlGaN thickness is 200 and 120 Å. In both HFETs, the 2DEG density increases with increasing the Si doping, and the 2DEG mobility is shown to decrease with increasing the 2DEG density as the result of the increased impurity scattering by ionized Si atoms in the barrier layer. What is important in Fig. 1 is that the maximum 2DEG density obtained in the HFET with the 120 Å AlGaN layer is only about  $1.5 \times 10^{13} \text{ cm}^{-2}$ , although that obtained in the HFET with the 200 Å AlGaN layer is as high as  $2.2 \times 10^{13} \text{ cm}^{-2}$ . Thus, the 2DEG density that can be obtained in modulation doped HFETs decreases when the AlGaN layer becomes thin. This situation explicitly emerges when the AlGaN thickness is less than about 150 Å. Thus, we cannot fully utilize the large 2DEG capacity of GaN-based HFETs when the thickness of the AlGaN layer is reduced.

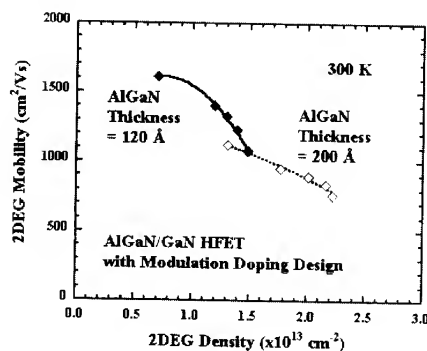


**Figure 1.** Relation between 2DEG mobility and 2DEG density in modulation doped AlGaN/GaN HFETs with different AlGaN thickness of 120 and 200 Å.

The above situation contrasts with the case of (In)GaAs-based HFETs, where the 2DEG capacity is in the order of  $10^{12} \text{ cm}^{-2}$ , and hence, modulation doping in the thin barrier layer is sufficient to fill the 2DEG capacity. Thus, the 2DEG density is not limited by the thickness of the barrier layer in these devices. In contrast, the 2DEG capacity of GaN-based HFETs is in the order of  $10^{13} \text{ cm}^{-2}$ , hence, a critical situation occurs that the electron density that can be realized with modulation doping becomes smaller than the 2DEG capacity when the barrier layer is thin. Therefore, when we reduce the AlGaN barrier thickness to improve the device performance, we need to supply electrons by using doping designs other than the conventional modulation doping.

**BEST AVAILABLE COPY**

### High 2DEG Density in Back-Doped HFETs

As a solution for the above problem we propose the AlGaIn/GaN HFETs with the back-doping design (BD-HFET). In BD-HFETs, an asymmetric double-heterostructure is employed, and donor atoms are doped not only in the surface-side AlGaIn layer but also in the underlying AlGaIn layer whose Al composition is not as high as that of the surface-side AlGaIn layer. In this structure, electrons are efficiently supplied also from the back-doped AlGaIn barrier layer to the GaN channel, with the help of the negative polarization charges at the heterointerface between the GaN channel and the underlying AlGaIn barrier layer. Hence, high 2DEG densities should be obtained even when the thickness of the surface-side AlGaIn layer becomes small and the supply of electrons from this layer becomes small.

We have fabricated BD-HFETs and have examined their 2DEG densities. The samples were grown by low-pressure MOVPE at 300 Torr. The BD-HFETs have the following structure: 40 Å undoped  $\text{Al}_{0.3}\text{Ga}_{0.7}\text{N}$ /50 Å Si-doped  $\text{Al}_{0.3}\text{Ga}_{0.7}\text{N}$ /30 Å undoped  $\text{Al}_{0.3}\text{Ga}_{0.7}\text{N}$ /250 Å GaN/100 Å Si-doped  $\text{Al}_{0.09}\text{Ga}_{0.91}\text{N}$ /1 μm AlGaIn (gradual Al composition)/ 6H-SiC(0001). Thus, the structure of the surface-side  $\text{Al}_{0.3}\text{Ga}_{0.7}\text{N}$  layer in BD-HFETs was completely the same as that in the HFETs with the conventional modulation doping design (MD-HFETs) treated in the previous section. The total thickness of the  $\text{Al}_{0.3}\text{Ga}_{0.7}\text{N}$  layer was thus as thin as 120 Å in both BD and MD-HFETs. In BD-HFETs, the Si concentration in the back-side  $\text{Al}_{0.09}\text{Ga}_{0.91}\text{N}$  barrier layer was  $(0.1) \times 10^{19} \text{ cm}^{-3}$ . No discontinuity of the Al composition was made below the back-side  $\text{Al}_{0.09}\text{Ga}_{0.91}\text{N}$  layer in order to avoid the additional accumulation of the 2DEG. It should be noted that no GaN buffer layer was included in BD-HFETs except for the 250 Å channel layer.

Figure 2 shows the relation between the 2DEG mobility and the 2DEG density at 300 K in BD-HFETs, together with that in conventional MD-HFETs. The maximum 2DEG density in the BD-HFET is shown to be as high as about  $3 \times 10^{13} \text{ cm}^{-2}$ . This value is almost the twice of the maximum 2DEG density obtained in the MD-HFET ( $1.5 \times 10^{13} \text{ cm}^{-2}$ ), although both HFETs have the same barrier structure whose total thickness is as thin as 120 Å. Thus, the 2DEG density can be increased with the back-doping design.

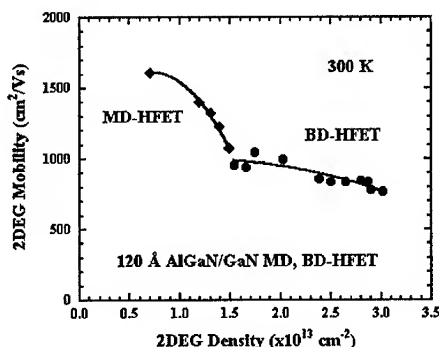
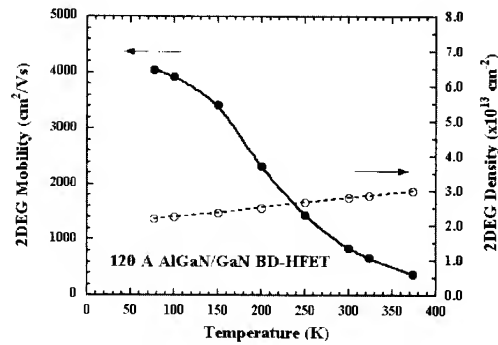


Figure 2. Relation between 2DEG mobility and 2DEG density in MD- and BD-HFETs. The thickness of AlGaIn layer is as thin as 120 Å in both HFETs.

The 2DEG mobility in the BD-HFET is around  $800 \text{ cm}^2/\text{Vs}$ , which is relatively high considering the very high 2DEG density of  $3 \times 10^{13} \text{ cm}^{-2}$ . These values lead to a record value of the mobility-density product of  $2.4 \times 10^{16} (\text{Vs})^{-1}$ . Hence, with BD-HFETs, we can attain high 2DEG densities even when the barrier thickness is reduced to obtain high aspect ratio and high transconductance.

### 2DEG Transport Properties and DC Device Characteristics in BD-HFETs

We have examined the 2DEG transport properties in a BD-HFET sample whose 2DEG density is as high as  $2.8 \times 10^{13} \text{ cm}^{-2}$  at 300 K. Figure 3 shows the temperature dependence of the 2DEG mobility and the 2DEG density from 77 to 400 K. The 2DEG mobility is shown to increase with decreasing the temperature, and the 2DEG mobility at 77 K is about  $4000 \text{ cm}^2/\text{Vs}$ , which is very high considering the high 2DEG density above  $2 \times 10^{13} \text{ cm}^{-2}$ . This indicates that the sample exhibits typical 2DEG transport and no three dimensional conduction in the back-side AlGaIn barrier layer is not involved in the transport. Thus, the BD-HFET with a thin AlGaIn barrier layer exhibits excellent transport properties below and above room temperature.



**Figure 3.** Temperature dependence of 2DEG mobility and 2DEG density in BD-HFETs.

We have fabricated the device structure by using the above BD-HFET substrate. Mesa isolation was performed by low-damage reactive ion etching (RIE) using chlorine-nitrogen mixed plasmas. To form the source and drain ohmic contacts, 200 Å Ti/ 800 Å Al/ 400 Å Ti/ 1200 Å Au layers were annealed at 800 °C for 30 sec. As the Schottky gate metal, 500 Å Ni/ 1200 Å Au layers were used without being annealed. The gate length and width of fabricated HFETs were 2 and 20  $\mu\text{m}$ , respectively. No surface passivation was performed in these devices.

Figures 4 shows the I-V characteristics at room temperature. The gate voltage was stepped from +2 to -8 V in -2 V increments. Excellent pinch-off characteristics are obtained with a threshold voltage of -8 V, indicating that no parallel conduction exists in the back-side AlGaIn barrier and underlying AlGaIn buffer layers. The saturation current density is 1.2 mA/mm, and the maximum transconductance is estimated to be 200 mS/mm. These values are very high considering a relatively long gate length of 1.5  $\mu\text{m}$ . It should be noted that, as shown in Fig. 4, the device exhibits high transconductance not in the low current density region but in the high current region near 1 mA/mm. These characteristics are advantageous for high-power

**BEST AVAILABLE COPY**

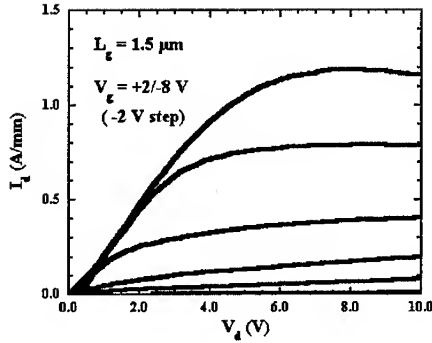


**Figure 4.** I-V characteristics of BD-HFET. The maximum transconductance is 200 mS/mm.

applications, and should be related to the 2DEG transport properties in BD-HFETs that the 2DEG mobility is relatively high even for very high 2DEG densities. Thus, the BD-HFET has exhibited a high current density and a high transconductance, which is attributed to the high 2DEG density and the thin barrier thickness in the BD-HFET.

As we point out in a previous section, the back-doping design is important in GaN-based HFETs in order to fully exploit their high potentiality for the large 2DEG capacity in the order of  $10^{13} \text{ cm}^{-2}$ . We here comment on the difference in the GaN-based BD-HFET and the (In)GaAs-based HFET with double-doping design where the symmetrical double-heterostructure is usually used and the doping is performed in the two barrier layers.

In the case of (In)GaAs-based HFETs with double-doping design, there exist two layers of the 2DEG system existing at each heterointerface, and the electron density is increased by using these separated two layers of the 2DEG system, which is not preferable for device operation in general. In contrast, the GaN-based BD-HFET can be designed to consist of a single layer of the 2DEG system at the surface-side heterointerface, with the help of the negative polarization charges at the back-side heterointerface and the asymmetric double-heterostructure where the back-side barrier is designed to be smaller. A single layer of the 2DEG system is preferable for device operation. The observed pinch-off characteristics and high transconductance in Fig. 4 suggest that such situation is realized in the fabricated device.

Hence, the situations are different in GaN-based and (In)GaAs-based HFETs. In GaN-based HFETs, channel electrons consist of a single layer of the 2DEG system, and we perform the additional doping in order to fully utilize the large 2DEG capacity, because, without additional doping, the actual 2DEG density could be smaller than the 2DEG capacity when the surface-side barrier layer becomes thin. Thus, the back-doping design is important and effective in GaN-based HFETs that have the large 2DEG capacity and the large polarization effects.

## CONCLUSION

As the result of the large 2DEG capacity in the order of  $10^{13} \text{ cm}^{-2}$  in AlGaIn/GaN HFETs, the actual 2DEG density that can be realized with the conventional modulation doping design could be smaller than the inherent 2DEG capacity, when we reduce the barrier thickness to improve the device performance. Thus, we propose the back-doping design that makes it possible to obtain high 2DEG densities even for the devices with thin AlGaIn barrier layers. By

using back-doping design, very high 2DEG densities around  $3 \times 10^{13} \text{ cm}^{-2}$  has been achieved in the  $\text{Al}_{0.3}\text{Ga}_{0.7}\text{N}/\text{GaN}$  HFET whose barrier layer is designed to be as thin as 120 Å. An HFET with the gate-length of 1.5  $\mu\text{m}$  has exhibited a high current density of 1.2 A/mm and a high transconductance of 200 mS/mm, which is ascribed to high 2DEG densities and thin barrier layers in these devices. HFETs with the back-doping design are thus promising for high-power applications.

#### ACKNOWLEDGMENTS

The authors would like to thank Dr. Yoshiro Hirayama and Dr. Sunao Ishihara for their encouragement throughout this work.

#### REFERENCES

1. M.A. Khan, Q. Chen, M.S. Shur, B.T. Medermott, and J.A. Higgins: IEEE Electron Device Lett. **17**, 325 (1996).
2. S.C. Binari, J. M. Redwing, G. Kelner, and W. Krupp: Electron. Lett. **33**, 242 (1997).
3. Y. F. Wu, B. P. Keller, P. Fini, S. Keller, T. J. Jenkins, L. T. Kehias, S. P. Denbaars, and U. K. Mishra: IEEE Electron Device Lett. **19**, 50 (1998).
4. S. T. Sheppard, K. Doverspike, W. L. Pribble, S. T. Allen, J. W. Palmour, L. T. Kehias, and T. J. Jenkins: IEEE Electron Dev. Lett. **20**, 161 (1999).
5. R. Gaska, Q. Chen, J. Yang, A. Osinsky, M. A. Khan, and M. S. Shur: IEEE Electron Device Lett. **18**, 492 (1997).
6. N. Maeda, T. Saitoh, K. Tsubaki, T. Nishida, and N. Kobayashi: Jpn. J. Appl. Phys. **38**, L987 (1999).
7. T. Egawa, H. Ishikawa, M. Umeno, and T. Jimbo: Appl. Phys. Lett. **76**, 121 (2000).
8. N. Maeda, K. Tsubaki, T. Saitoh and N. Kobayashi: Appl. Phys. Lett. **79**, 1634 (2001).
9. N. Maeda, K. Tsubaki, T. Saitoh and N. Kobayashi: Physica Status Solidi(a), **188**, 223 (2001).
10. J. S. Moon, M. Micovic, P. Janke, P. Hashimoto, W. S. Wong, L. M. McCray, A. Kurdoghlian and C. Nguyen: Electron Lett. **37**, 528 (2001).
11. Y. Ando, Y. Okamoto, H. Miyamoto, N. Hayama, T. Nakayama, K. Kasahara and M. Kuzuhara: *Technical Digest of Int. Electron Devices Meeting 2001*, 381 (Electronic Devices Society of IEEE, Washington DC, 2001).
12. V. Kumar, W. Lu, F. A. Khan, R. Schwindt, A. Kuliev, J. Yang, M. Asif Khan and I. Adesida: *Technical Digest of Int. Electron Devices Meeting 2001*, 573 (Electronic Devices Society of IEEE, Washington DC, 2001).
13. N. Maeda, T. Nishida, N. Kobayashi, and M. Tomizawa: Appl. Phys. Lett. **73**, 1856 (1998).
14. B. Shen, T. Someya, and Y. Arakawa: Appl. Phys. Lett. **76**, 2746 (2000).
15. M. Hiroki, N. Maeda, and N. Kobayashi, J. of Cryst. Growth **237-239** Pt2, 956 (2002).
16. Optoelectronic Properties of Semiconductors and Supper Lattices, Vol. 16, *III-V Nitride Semiconductors: Applications and Devices*, 273 (Taylor & Francis Books, Inc. New York, 2002).

**BEST AVAILABLE COPY**

### High-Quality AlGaIn/GaN HFET Structures Grown by MOCVD Using Intermediate High Temperature AlGaIn/GaN Superlattices

Alexander Demchuk, Don Olson, Minseub Shin, Dan Olson, Peter Nussbaum, Andy Strom<sup>1</sup>,  
Simon Bates<sup>2</sup>, Frank Hofmann<sup>2</sup>, and Gordon Munns

APA Optics, Inc., 2950 NE 84<sup>th</sup> Lane, Blaine, MN 55449, U.S.A.

<sup>1</sup> now with Hysitron, Inc., 5251 W. 73rd Street, Minneapolis, MN 55439

<sup>2</sup> Bede Scientific, 14 Inverness Drive East, Suite -100, Englewood, CO 80112, U.S.A.

#### ABSTRACT

We report on device quality  $\text{Al}_{0.28}\text{Ga}_{0.72}\text{N}/\text{GaN}$  heterostructures growth by low-pressure metalorganic chemical vapor deposition (LP-MOCVD) using intermediate  $\text{Al}_x\text{Ga}_{1-x}\text{N}/\text{GaN}$  superlattices (SL) with  $x < 0.15$ . High-quality  $\text{Al}_{0.28}\text{Ga}_{0.72}\text{N}/\text{GaN}$  heterostructures have been confirmed with HRXRD analysis by measurement of mosaic twist and tilt in growth films, SEM with selective etching and Van der Pauw Hall measurements. The edge and threading dislocations were efficiently filtered by the AlGaIn/GaN SL resulting in further reduction dislocation densities at the channel. Additionally, the superlattice served to improve the planarity of the channel heterointerface as evidenced by x-ray and AFM analysis. The increase of 2-DEG mobility from  $\sim 1187 \text{ cm}^2/\text{V s}$  to  $\sim 1443 \text{ cm}^2/\text{V s}$  was obtained at the carrier density of  $1.0$  to  $1.2 \times 10^{13} \text{ cm}^{-2}$  on heterostructures with intermediate AlGaIn/GaN SL grown on sapphire.

#### INTRODUCTION

AlGaIn/GaN heterojunction field effect transistors (HFET) have attracted a great deal of interest due to their potential for high frequency power amplification and resistance to harsh environments [1]. The inherent strong spontaneous polarization and piezo-electric effect at the AlGaIn/GaN heterointerface produce sheet carrier concentrations in excess of  $10^{13} \text{ cm}^{-2}$ , mobilities greater than  $1500 \text{ cm}^2/\text{V s}$  and sheet conductivities above  $2 \times 10^{16} \text{ V}^{-1}\text{s}^{-1}$ . In combination with high breakdown fields and large peak and saturated velocities the result can be state of the art power densities at microwave frequencies [2]. To obtain this level of performance it has been well documented that the planarity of the heterointerface is critical in minimizing the scattering of carriers in the channel of an HFET [3]. Additionally, while there is some evidence that nitride based devices may be tolerant of relatively high threading dislocation densities ( $10^9$ - $10^{10} \text{ cm}^{-2}$ ) inherent to the large substrate/epilayer lattice mismatch, there is clear indication that propagating defects tend to roughen the surface of the system [4,5].

In order to provide a high quality film with minimal thickness, several approaches have been explored. Epitaxial overgrowth [6] has enjoyed very good success in reducing threading dislocations, but it demands increased complexity and may reduce the usable surface area of the wafer. Others have reported growth on patterned substrates (an example is epitaxial lateral overgrowth) [6]. While this approach has been shown to be beneficial, it is at the expense of significantly more complicated processing prior to crystal growth.

In order to improve the planarity of the growth front and filter the threading dislocations the use of strained layer AlGaIn/GaN superlattices (SL) has been investigated in this study. It was shown the intentionally introduced strain field local to the SL not only deflects a significant portion of the defects that would otherwise reach the channel but also planarizes the growth

front. This results in reducing scattering at the channel and is manifested in higher mobility at a given carrier concentration. It is important to note, the SL design must not induce a parasitic parallel conduction path. This is especially important due to the potential for spontaneously generated carriers at any AlGa<sub>x</sub>N/GaN heterointerface. As such the SL is located close to the substrate/epilayer interface where the threading dislocation density is sufficient to disrupt undesirable conduction path parallel competing with the channel. In order to help ensure this, a SL design with a low fraction of aluminum has been used in the AlGa<sub>x</sub>N layers. This differs from other approaches that have used recently such as silicon SL [7] and AlN SL [8] in that semi-insulating behavior of the buffer layer must be maintained in order to preserve high frequency performance.

## EXPERIMENTAL

AlGa<sub>x</sub>N/GaN heterostructures in this study were grown on (0001) basal plane sapphire substrate by low-pressure metalorganic chemical vapor deposition (LP-MOCVD) in a custom built vertical reactor with a RF heater described previously [9]. Figure 1 illustrates the AlGa<sub>x</sub>N/GaN epitaxial design heterostructures. A conventional low-temperature (~350 °C below

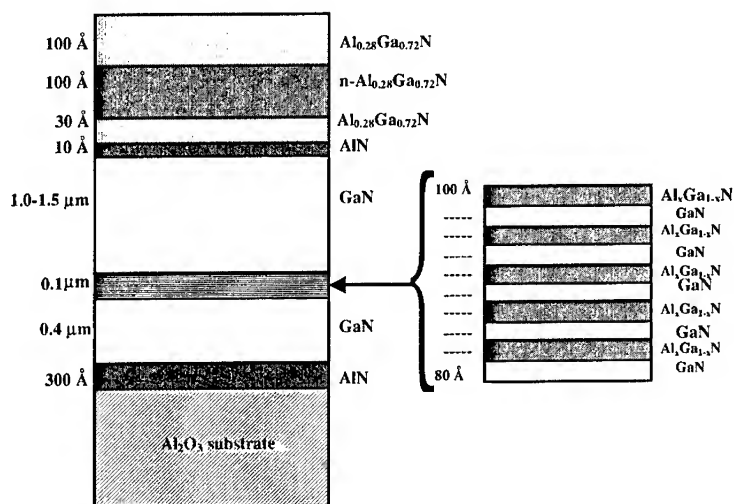


**Figure 1.** Schematic of HFET AlGa<sub>x</sub>N/GaN structure with intermediate AlGa<sub>x</sub>N/GaN SL.

growth temperature) buffer layer of AlN (300 Å) was followed by high-temperature undoped GaN layer (0.5 μm). The 5 periods Al<sub>x</sub>Ga<sub>1-x</sub>N/GaN SL (0.1 μm total thickness) with  $x \leq 0.15$  then was deposited without any growth interruption as shown in Figure 1. After the SL was deposited, an additional 1-1.5 μm of undoped GaN was grown. An AlN/Al<sub>0.28</sub>Ga<sub>0.72</sub>N spacer (10 Å/30 Å)

layer was grown atop the channel. A silicon doped ( $3 \times 10^{18} \text{ cm}^{-3}$ )  $\text{Al}_{0.28}\text{Ga}_{0.72}\text{N}$  layer (200 Å) was then grown.

Several techniques were employed to evaluate the material grown including atomic force microscopy (AFM), scanning electron microscopy (SEM) with selective etching, room temperature van der Pauw Hall measurements, C-V depletion profiling, and high resolution x-ray diffraction (HRXRD). HRXRD measurements were performed using a Bede D1 High Resolution diffractometer. The effect of the threading dislocations on the x-ray diffraction peak in epitaxial GaN films was evaluated in both angular ( $\omega$  scans), radial scans ( $\omega$ - $2\theta$  scans) in a series of symmetric and asymmetric reflections. Grazing incidence x-ray reflection (GIXRR) was used to evaluate the heterointerface planarity. For etch pit density measurements, the samples were selectively photo-electrochemical (PEC) etched in aqueous KOH solution [10].

## RESULTS AND DISCUSSION

Figure 2 shows the measured grazing incidence X-ray reflectivity (GIXRR) data from a sample as shown in Figure 1 with and without SL. Values of layer thickness, interface roughness and density have been extracted from the reflectivity curve using a modeling method which is built around first principles, Maxwell's equations, and Genetic fitting algorithms [11]. The GaN layer was assumed to be the effective substrate due to the limited penetration depth of the GIXRR method (few thousand Angstroms maximum). For the Al concentration of  $\text{Al}_x\text{Ga}_{1-x}\text{N}$  a value of  $x = 25\%$  was used as calculated from the peak separation of the  $\omega$ - $2\theta$  scans (see Fig. 3). A comparison between the samples indicates that the thickness of the  $\text{Al}_{0.25}\text{Ga}_{0.75}\text{N}$  layers is very similar (see table 1). The main differences relate to the level of interface roughness. The sample with SL has sharper interfaces than sample without SL (see table 1).

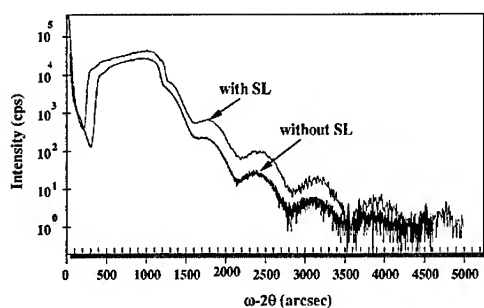


**Figure 2.** GIXRR measurements of the AlGaIn/GaN samples with and without SL.

**Table 1.** Parameters extracted from GIXRR measurements.

Layer	Thickness (Å)		Roughness (Å)		Density (%)	
	no SL	SL	no SL	SL	no SL	SL
Extra top layer (damage, oxide, etc.)	1.0 (fixed)		5.51	9.92	24.86	36.64
$\text{Al}_{0.25}\text{Ga}_{0.75}\text{N}$	193.78	195.76	19.98	11.73	100.0	99.98
AlN	5.70	6.74	11.32	6.56	85.7	99.26
GaN	$\infty$		15.75	9.70	100 (fixed)	

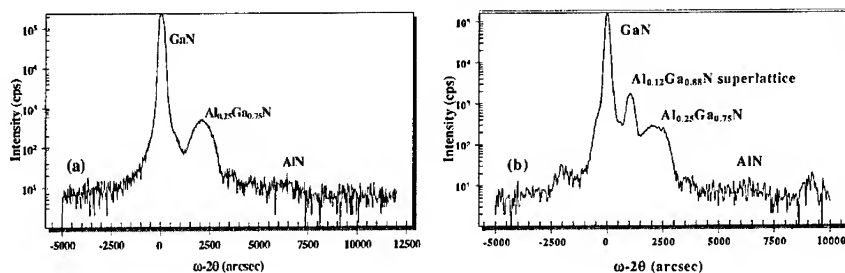


**Figure 3.** The  $\omega-2\theta$  measurements on the (004) reflection of the AlGa/GaN samples (a) without and (b) with SL.

Reciprocal space maps (RSMs), utilizing high-resolution x-ray optics, provide insight into the structural difference between the 2 samples. Figure 4 shows a XRR reciprocal space map for

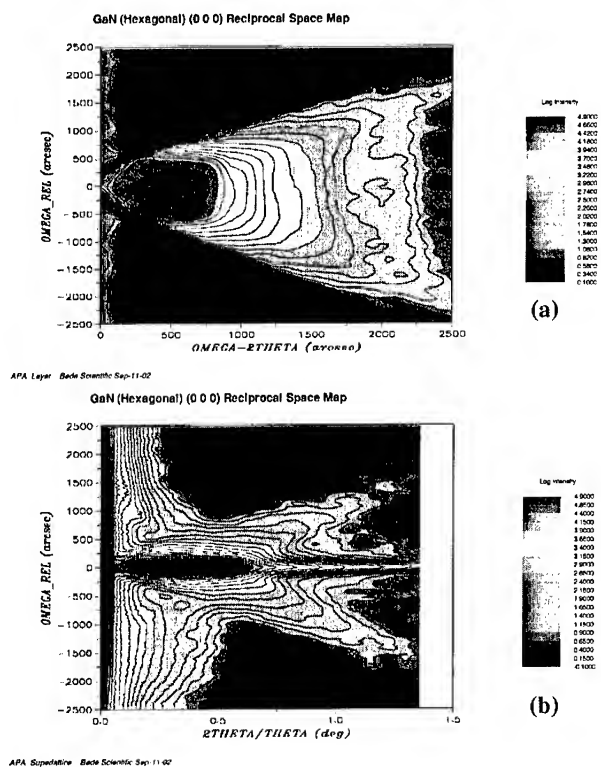


**Figure 4.** XRR (000) RSMs on the AlGa/GaN samples (a) without and (b) with SL.

both samples – with and without the underlying SL. In order to get the solid wedge image the roughness must be uncorrelated – without a well-defined average interface. Sharp interface roughness always produces 2 very well-defined peaks at the Yoneda position as seen in figure 4b along with the well defined central reflection streak. Such a ‘V’ shape with central streak requires a well-defined average interface with correlated or partially correlated roughness [11]. The difference between the interfacial structures of the two samples is very significant, more so than just the difference of 5 Å may suggest. The image in figure 4a shows no central streak and therefore exhibits no average sharp interface. This conclusively shows the AlGaIn/GaN interface is physically sharp for sample with SL. The additional broadening seen for the sample without SL is due to increased tilt and twist of the mosaic blocks of the crystal.

High resolution angular scans ( $\omega$  scans) were performed through symmetric (002) (004) peaks in plane asymmetric (104) (105), (115) peaks and out of plane asymmetric peaks. The angular variations of the peak widths were used to determine the various dislocation densities [12-14]. The summary of these measurements is shown in table 2, along with asymmetric  $\phi$  scans. To note the symmetric peak measurements on both samples yield very similar results. The symmetric peaks, however, are not sensitive to the pure edge dislocations characteristic of threading dislocations in the simple mosaic block model [5,15]. These edge dislocations are equivalent to rotation (twisting of the mosaic blocks about the [001] axis. Since these mosaic blocks are twisted about the [001], they will not contribute any peak broadening for the (002) or (004) reflections. Furthermore, asymmetric reflections like the (104) or (105) will not be sensitive to this broadening – if measured within the diffraction plane. In order to measure this mosaic twist, the asymmetric reflection must be measured out of the diffraction plane; this is accomplished by using CHI tilt motion (90 degree angle with respect to  $\omega$ ). The rocking curve width is then measured with an  $\omega$  scan. The higher the CHI tilt angle used, the greater the expected peak broadening in  $\omega$ . The  $\phi$  scans through asymmetric peaks have often been used to measure the density of edge dislocations, however the reduction in the in plane x-ray correlation length due to the pile up of dislocations at grain boundaries must be first be corrected for [13].

**Table 2.** Analysis summary of XRD measurements

Scans Parameters	no SL	SL
Asymmetric in plane $\omega$ scans (HOL) family of reflections: (102), (104), (105) Screw dislocation density, $N_{SC}$ (cm <sup>-2</sup> ):	$1.42 \times 10^8$	$5.77 \times 10^7$
Asymmetric out of plane $\omega$ scans (HOL) family of reflections: (102), (103), (104), (105) Edge dislocation density, $N_E$ (cm <sup>-2</sup> ):	$6.53 \times 10^8$	$4.69 \times 10^7$
Asymmetric in plane $\phi$ scans (HKL) family of reflections: (104), (115), (105) Edge dislocation density, $N_E$ (cm <sup>-2</sup> ):	$8.51 \times 10^9$	$6.85 \times 10^8$

Room temperature Hall effect measurements were made using van der Pauw technique. The increase of 2-DEG mobility from 1187 cm<sup>2</sup>/V s to 1443 cm<sup>2</sup>/V s was obtained at the carrier density of 1.0 to 1.2  $\times 10^{13}$  cm<sup>-2</sup> (respectively) on heterostructures with SL. This corresponds to a low field conductivity of 1.19 $\times 10^{16}$  V<sup>-1</sup>s<sup>-1</sup> and 1.73 $\times 10^{16}$  V<sup>-1</sup>s<sup>-1</sup> for sample without and with SL, respectively. The trend likely reflects changes in the planarity of the heterointerface. The difference in the RMS surface roughness was confirmed by AFM that showed decrease in roughness from 1.614 nm to 1.223 nm accordingly on the sample with SL. In order to assess the potential for undesirable parallel conduction in the superlattice region depletion CV characteristics were measured. The depletion CV profile indicates that there is no

underlying source of carriers in the region of the superlattice or the interface. Even at the high aluminum mole fraction in  $\text{Al}_x\text{Ga}_{1-x}\text{N}/\text{GaN}$  SL ( $x=0.15$ ) there is no evidence in the depletion CV profile that indicates parallel conduction path due to the presence of the SL [16]. It is possible that the carriers generated by spontaneous polarization are compensated by a high density of threading dislocations at these interfaces.

## CONCLUSIONS

It was found that the dislocation density was reduced by approximately 1 order of magnitude for the sample with SL. Grazing incidence XRR indicated that the surface (RMS) roughness was improved by a minimum 5 Å on the GaN, AlN, and AlGaN layers. The difference in the RMS surface roughness was corroborated by AFM that showed half the roughness when compared to the sample without SL. The significant improvement in the interface roughness is consistent with an improvement in the low field conductivity of ~45%. The critical difference between with and without SL samples appears in both the discrete localized defect density and the apparent buckling within the mosaic nature of the growth.

## REFERENCES

1. M. A. Khan, A. Bhattarai, J. N. Kuznia, D. T. Olson, *Appl. Phys. Lett.*, **63**, 1214 (1993).
2. Y. -F. Wu, D. Kapolnek, J. P. Ibbetson, P. Parikh, B. P. Keller, and U. K. Mishra, *IEEE Electron Device Lett.* **48**, 586, (2001).
3. Y. Zhang and J. Singh, *J. Appl. Phys.* **85**, 587 (1999).
4. S. D. Lester, F. A. Ponce, M. G. Craford, D. A. Steigerwald, *Appl. Phys. Lett.* **66**, 1249 (1995).
5. B. Heying, E. J. Tarsa, C. R. Elsass, P. Fini, S. P. DenBarrs, J. S. Speck, *J. Appl. Phys.* **85**, 6470 (1999).
6. O. Nam, M. D. Bremser, T. S. Zheleva, R. F. Davis, *Appl. Phys. Lett.* **71**, 2638 (1997).
7. H. Hirayama, M. Aino, A. Kinoshita, A. Hirata, Y. Aoyagi, *Appl. Phys. Lett.* **80**, 2057 (2002).
8. K. Kusakabe, K. Kishino, A. Kikuchi, T. Yamada, D. Sugihara, S. Nakamura, *J. Crystal Growth* **230**, 387 (2001).
9. M. A. Khan, J. N. Kuznia, J. M. Van Hove, D. T. Olson, S. Krishnakutty, R. M. Kolbas, *Appl. Phys. Lett.* **58**, 526 (1991).
10. J. L. Weyher, P. D. Brown, J. L. Rouviere, T. Wosinski, A. R. A. Zauner and I. Grzegory, *J. Crystal Growth* **210**, 151 (2000).
11. U.S.A. Patent 6,192,103.
12. G. K. Williamson and W. H. Hall, *Acta Metall.* **1**, 22 (1953).
13. T. Metzger, R. Hoppler, E. Born, O. Ambacher, M. Stutzmann, R. Stommer, M. Schuster, H. Gobel, S. Christiansen, M. Albrecht, and H. P. Strunk, *Phys. Stat. Solid. A* **77**, 1013 (1998).
14. H.-M. Wang, J.-P. Zhang, C.-Q. Chen, Q. Fareed, J.-W. Yang and M. A. Khan, *Appl. Phys. Lett.* **81**, 604 (2002).
15. S. Bates, *J. Appl. Phys.* (2002) will be published.
16. G. Munns et al., *MRS Internet J. Nitride Semicond. Res.* (2003) will be published.

### High Performance HFET Devices on Sapphire and SiC: Passivation with AlN

Jennifer A. Bardwell, Ying Liu, James B. Webb, Haipeng Tang, Stephen J. Rolfe and Jean Lapointe

National Research Council Canada, Institute for Microstructural Sciences, Ottawa, ON, K1A 0R6, Canada

#### ABSTRACT

AlGaIn/GaN two dimensional electron gas (2DEG) heterostructures were grown by ammonia-MBE on sapphire and SiC substrates. Devices fabricated from these optimized HFET layers, with optically defined gates showed excellent characteristics, e.g. a maximum drain current density of 1.3 A/mm, maximum transconductance of 220 mS/mm,  $f_T$  of 15.6 GHz and  $f_{MAX}$  of 58.1 GHz was measured for devices with 0.9  $\mu\text{m}$  gate length and 40  $\mu\text{m}$  gate width. Shorter gate length devices exhibited higher frequency responses:  $f_T$  of 68 GHz and  $f_{MAX}$  of 125 GHz for 0.25  $\mu\text{m}$  gate length and  $f_T$  of 103 GHz and  $f_{MAX}$  of 170 GHz for 0.15  $\mu\text{m}$  gate length. However, these devices showed "current collapse" when subjected to load pull measurements. Current collapse was also observed in sequentially repeated DC measurements in the dark, both on sapphire and SiC substrates, although the degree of collapse varied greatly from one wafer to another. One method of reducing the current collapse was to apply a thin (100 - 6000 Å) magnetron sputtered AlN passivation layer (over the gates) or a 500 Å layer under the gates so that MISFET devices were obtained. The electrical characteristics of the passivated and unpassivated devices are discussed.

#### INTRODUCTION

GaN/AlGaIn HFETs are of great interest for high power, high frequency devices. The mobility and carrier concentration obtained for these structures has improved markedly over the past few years, particularly on substrates such as SiC which offer higher thermal dissipation characteristics and smaller lattice mismatch compared to that of sapphire. HFET structures with electrical performance characteristics comparable to or better than those grown on sapphire substrates have been obtained [1-5]. In this paper we report the use of ammonia-MBE for the growth of AlGaIn/GaN (2DEG) structures on insulating 4H-SiC (0001) and sapphire substrates using a magnetron sputter epitaxy (MSE) deposited AlN buffer layer and carbon doped channel isolation layers [6]. Excellent device performance is routinely obtained; nevertheless, current collapse [5,7,8] remains a problem. The use of room temperature magnetron sputtered AlN passivation layers to alleviate this collapse is discussed.

#### EXPERIMENTAL DETAILS

The HFET structures were grown by ammonia-MBE. The MBE system [9] and the SiC wafer preparation prior to deposition have been described previously [10]. No ex- or in-situ high temperature hydrogen treatment of the substrate was used. The molybdenum back coated SiC wafers were degreased in chloroform vapor for 10 min. followed by a 1 min dip in 1:1 HF:H<sub>2</sub>O and a 10 min. deionized water rinse. The wafers were blown dry in N<sub>2</sub> prior to mounting and loading into the MBE load-lock. They were then heated to 1000°C for 10 min under an NH<sub>3</sub>

flow of 50 sccm. The HFET layers consist of a 200 Å AlN buffer layer deposited by magnetron sputtering at  $\sim 880^\circ\text{C}$ , followed by a series of layers grown by ammonia MBE at  $\sim 910 - 925^\circ\text{C}$ . These consist of a  $2\text{ }\mu\text{m}$  insulating carbon-doped GaN layer, a  $0.2\text{ }\mu\text{m}$  undoped GaN channel layer and about 200 Å undoped AlGaIn barrier layer.

Processing of the HFET structures has been described previously [11,12]. Briefly the steps consisted of mesa isolation by chemically assisted ion beam etching, ohmic metal deposition (Ti/Al/Ti/Au 200/1000/450/550 Å) and rapid thermal annealing at  $700 - 750^\circ\text{C}$  for 30 – 90 s in  $\text{N}_2$ , gate metal deposition (300 Å of sputtered Pt, for adhesion, followed by e-beam deposited Pt/Au 1000/2000 Å). The T-gate process used a three-layer resist stack, patterned by e-beam lithography. The passivation was by reactive magnetron DC sputtering of AlN at room temperature in a 50%  $\text{N}_2$ , 50% Ar atmosphere at 4 mTorr and 100W of power. The AlN layers were deposited in the mesa regions only and patterned by lift-off. A stripe mask made by photoplotting onto a Mylar film was overlaid onto the conventional quartz mask during the patterning for the passivation. This allowed passivated and unpassivated devices located proximally on the wafer surface to be compared. This is necessary because of the smooth, lateral variation in electrical properties of the devices due to a temperature gradient present during the growth.

## RESULTS AND DISCUSSION

Typical DC electrical results obtained for sapphire and SiC substrates are shown in figure 1.

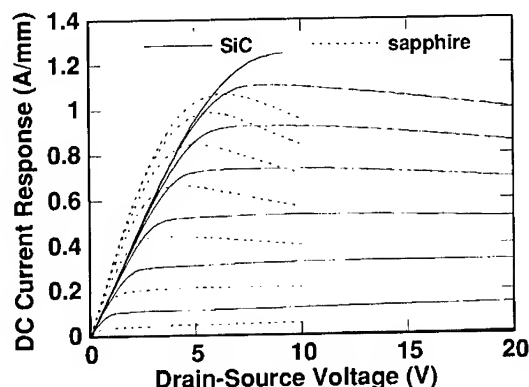
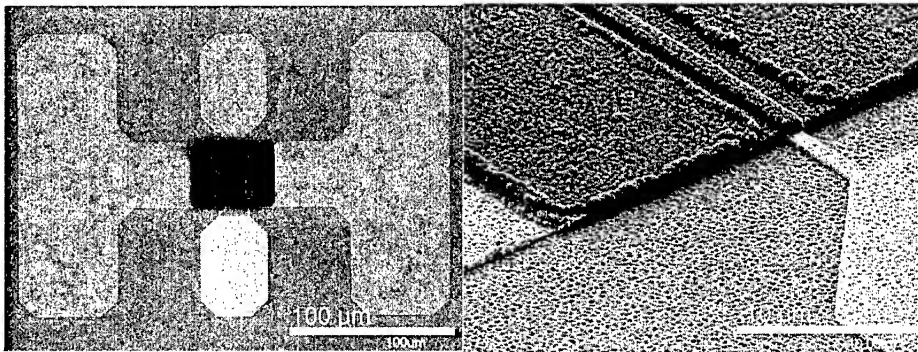


Figure 1. Typical DC response from  $0.9\text{ }\mu\text{m}$  gate length processed HFET devices on SiC and sapphire substrates. The gate voltage was varied from +3 V to -5 V in increments of 1 V.

The gate length was  $0.9\text{ }\mu\text{m}$ , and the width was  $80\text{ }\mu\text{m}$ . The devices on sapphire substrates showed negative differential resistances at high source drain voltages due to self-heating in the channel. This problem was greatly reduced for devices on SiC substrates due to the improvement in the thermal conductivity of the substrate. Both types of devices showed  $g_m(\text{max}) > 220\text{ mS/mm}$ , with  $f_T \sim 12 - 15\text{ GHz}$  and  $f_{\text{MAX}} \sim 40 - 58\text{ GHz}$  for these optically defined gates.

For devices on SiC substrates with shorter gate lengths, improved DC and RF characteristics were observed. For devices of gate length  $0.25\text{ }\mu\text{m}$ , values of  $f_T = 68\text{ GHz}$  and  $f_{\text{MAX}} = 125\text{ GHz}$  were obtained [6]. For  $0.15\text{ }\mu\text{m}$  devices, values of  $f_T = 103\text{ GHz}$  and  $f_{\text{MAX}} = 170\text{ GHz}$  are obtained. These device results are among the highest recorded [1-4]. This device also showed  $g_m(\text{max}) = 250\text{ mS/mm}$  and maximum drain current  $> 1.25\text{ A/mm}$ .

However, despite these encouraging results, all devices showed some degree of current collapse, manifested either in an obvious decrease of the DC current response on repeated scans, or in an unexpectedly low power output in load pull measurements, typically  $\sim 1.2\text{ W/mm}$  for devices on sapphire substrates. We attempted to reduce this current collapse by using an AlN passivation layer deposited over the gates. Figure 5 shows micrographs of the passivation scheme, which covers the mesa of the finished devices. Results using  $500\text{ }\text{\AA}$  AlN thicknesses, over the gates, under the gates, and both under and over the gates to form passivated HFETs, MISFETs and passivated MISFETs have been presented previously [13].



**Figure 5.** Scanning electron micrographs showing the deposited AlN film (dark) in the mesa region of the HFET device.

The room temperature reactively sputtered AlN films were found to have a refractive index of  $\sim 1.8$ , compared to a value of  $1.96$  reported in the literature [14]. The AlN film exhibited stress, when deposited on Si (100) substrates, in the range from  $-150$  to  $-700\text{ MPa}$  (compressive), and RHEED suggested that the films were textured polycrystalline. The characteristics of our films are consistent with those observed in a previous study [15]. In all cases studied, the addition of the AlN layer was found to degrade the measured sheet resistance of the HFET structures. The results for three different HFET growths are shown in figure 5.

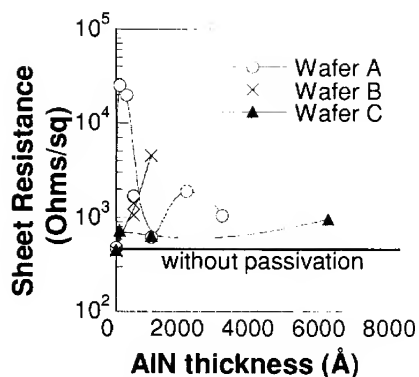


**Figure 5.** Material sheet resistance, measured from passivated transmission line structures, as a function of the deposited AlN thickness for three different wafers. Wafer A is a poor quality HFET layer on sapphire, which showed relatively low current response, even without passivation. Wafer B is a good quality HFET layer on sapphire, which had good current response, but showed clear current collapse during repeated DC scans [13]. Wafer C is a good quality HFET layer on SiC, which showed little current collapse in repeat DC scans.

For Sample A, in most cases the sheet resistance was degraded so severely that the current response of devices was very poor. Even in the case of 1000 Å of AlN passivation, the current collapse was not alleviated by the AlN passivation. For Sample B, the results have been reported previously [13]. For sample C, very little current collapse was exhibited in repeated DC scans, even for unpassivated devices. Thus, stressing of the devices was employed to assess the results of applying the passivation. Figure 6 shows the results. The source-drain voltage was held constant at 20V. The gate voltage was stepped to 0V (saturation conditions) and the current response measured. Then the device was stressed by stepping the gate voltage to -4V (pinch-off conditions) for 10 min. Then the gate voltage was stepped back up to 0V and the current response measured.

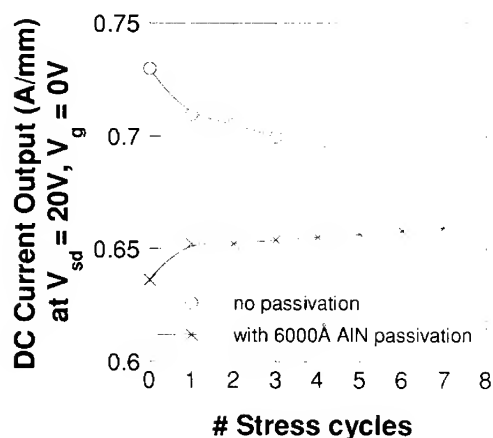


**Figure 6.** DC current output of passivated and unpassivated devices as a function of number of 10 min. stress cycles at  $V_g = -4V$ .

The results show that the passivation with AlN does reverse the pattern of current collapse with number of stress cycles. Instead of a sequentially decreasing DC current output, the passivated sample actually shows an increase in current output. Note that the sheet resistance of

**BEST AVAILABLE COPY**

the passivated devices has been increased by a factor of approximately two from that of the unpassivated devices; however, the output current at saturation is reduced by only about 7%. Load pull measurements have not yet been performed on the passivated devices.

## CONCLUSIONS

High quality AlGaIn/GaN HFET structures have been grown on both sapphire and SiC substrates using ammonia-MBE. These structures have been fabricated into very good quality devices with RF responses among the best reported:  $f_T = 103$  GHz and  $f_{MAX} = 170$  GHz. However, the devices are subject to current collapse. One method of reducing the effect of current collapse was to passivate the devices with a sputtered AlN layer. However, this layer did degrade the sheet resistance of the devices. Nevertheless, the DC current output was not decreased in proportion to the increase in the sheet resistance, with the passivated devices still demonstrating respectable current output. Load pull results will be necessary to confirm the efficacy of the AlN passivation layer.

## REFERENCES

1. M. Micovic, N. X. Nguyen, P. Janke, W.-S. Wong, P. Hashimoto, L.-M. McCray, and C. Nguyen, *Electron. Lett.* **36**, 358 (2000).
2. W. Lu, J. Yang, M. A. Khan, I. Adesida, *IEEE Trans. on Electron Dev.* **48**, 581 (2001).
3. V. Kumar, A. Kuliev, R. Schwindt, G. Simin, J. Yang, M. Asif Khan, and I. Adesida, *Phys. Stat. Sol. (a)* **194**, 456 (2002).
4. L. F. Eastman, V. Tilak, J. Smart, B. M. Green, L. M. Chumbes, R. Dimitrov, H. Kim, O. S. Ambacher, N. Weimann, T. Prunty, M. Murphy, W. J. Schaff and J. R. Shealy, *IEEE Trans. Electron Dev.* **48**, 479 (2001).
5. S. Arulkumaran, T. Egawa, H. Ishikawa and T. Jimbo, *Appl. Phys. Lett.* **81**, 3073 (2002).
6. J. B. Webb, H. Tang, J. A. Bardwell, Y. Liu, J. Lapointe and T. MacElwee, *Phys. Stat. Sol. (a)* **194**, 439 (2002).
7. I. Daumiller, D. Theron, C. Gaquiere, A. Vescan, R. Dietrich, A. Wiesz, H. Leier, R. Ventury, U. K. Mishra, I. P. Smorchkova, S. Keller, N. X. Nguyen, C. Nguyen and E. Kohn, *IEEE Electron. Dev. Lett.* **22**, 62 (2001).
8. T. Mizutani, Y. Ohno, M. Akita, S. Kishimoto and K. Maezawa, *Phys. Stat. Sol. (a)* **194**, 447 (2002).
9. H. Tang and J. B. Webb, *Appl. Phys. Lett.* **74**, 2373 (1999).
10. J. Webb, H. Tang, J. A. Bardwell, S. Rolfe, Y. Liu, J. Lapointe, P. Marshall and T.W. MacElwee, *Phys. Stat. Sol. (a)* **188**, 271 (2001).
11. J. A. Bardwell, I. Foulds, B. Lamontagne, H. Tang, J. B. Webb, P. Marshall, S. J. Rolfe, J. Stapledon, and T. W. MacElwee, *J. Vac. Sci. Technol. A*, **18**, 750-753 (2000).
12. J. A. Bardwell, G. I. Sproule, Y. Liu, H. Tang, J. B. Webb, J. Fraser and P. Marshall, *J. Vac. Sci. Technol. B*, **20**(4), 1444-1447 (2002).
13. Y. Liu, J. A. Bardwell, S. P. McAlister, S. Rolfe, H. Tang, and J. B. Webb, *Phys. Stat. Sol.*, accepted.
14. D. Brunner, H. Angerer, E. Bustarret, F. Freudenberger, R. Hopler, R. Dimitrov, O. Ambacher and M. Stutzmann, *J. Appl. Phys.* **82**, 5090 (1997).
15. K. Kusaka, D. Taniguchi, T. Hanabusa and K. Tominaga, *Vacuum*, **66**, 441 (2002).

### Self-Heating Effects in Multi-Finger AlGaIn/GaN HFETs

M. Kuball<sup>1</sup>, S. Rajasingam<sup>1</sup>, A. Sarua<sup>1</sup>, M.J. Uren<sup>2</sup>, T. Martin<sup>2</sup>, R.S. Balmer<sup>2</sup>, and K. P. Hilton<sup>2</sup>,

<sup>1</sup>University of Bristol, H.H. Wills Physics Laboratory, Bristol BS8 1TL, United Kingdom

<sup>2</sup>QinetiQ Ltd., St. Andrew's Road, Malvern, Worcs WR14 3PS, United Kingdom

#### ABSTRACT

We report on the in-situ measurement of temperature, i.e., self-heating effects, in multi-finger AlGaIn/GaN HFETs grown on SiC substrates. Optical micro-spectroscopy was used to measure temperature with 1  $\mu\text{m}$  spatial resolution. Thermal resistance (temperature rise per W/mm) was measured as a function of device pitch and gate finger width. There is significant thermal cross talk in multi-finger AlGaIn/GaN HFETs and this needs to be seriously considered for device performance and ultimately device reliability. A comparison with theoretical modeling is presented. Uncertainties in modeling parameters currently make modeling less reliable than experimental temperature assessment of devices.

#### INTRODUCTION

Wide transistor widths arranged in compact multi-finger layout are required for high-power high-frequency AlGaIn/GaN heterostructure field effect transistors (HFETs). In these multi-finger designs, self-heating induced "thermal" cross-talk between individual gate fingers becomes very important, affecting channel temperatures, and ultimately device performance and device reliability. Spatial resolutions on the order of 1  $\mu\text{m}$  are required to accurately measure the temperature in AlGaIn/GaN HFETs with their narrow source-drain openings. Such spatial resolutions can be achieved by using micro-Raman spectroscopy [1]. Infrared techniques often employed to measure the temperature of an active device are not adequate for AlGaIn/GaN HFETs due to their limited spatial resolution. We report here on the use of micro-Raman spectroscopy to measure accurately temperature in multi-finger AlGaIn/GaN HFETs with 1  $\mu\text{m}$  spatial resolution as a function of device pitch and gate finger width. Comparison of the experimental results with theoretical modeling is presented.

#### EXPERIMENTAL DETAILS

HFETs were fabricated from heterostructures consisting of 28nm of  $\text{Al}_{0.23}\text{Ga}_{0.77}\text{N}$  on 1.2  $\mu\text{m}$  thick GaN grown by metalorganic vapor phase epitaxy (MOVPE) on insulating SiC (0001) substrates. Conventional mesa-isolated device technology with Ti/Al/Ti/Au ohmic contacts, Ni/Au Schottky gates, and silicon nitride surface passivation were employed. Four multi-finger HFET layouts were studied, designed for operation at S-band (2-4GHz) with 4 or 8 fingers, with a finger spacing (device pitch) of 50 or 25  $\mu\text{m}$ , respectively, each finger either 250 or 500  $\mu\text{m}$  wide. The devices had 5  $\mu\text{m}$  wide source-drain gaps with 0.8  $\mu\text{m}$  electron beam drawn gates. The inset of Figure 1 shows a photograph of an  $8 \times 250 \mu\text{m}$  device with 25  $\mu\text{m}$  finger pitch. Three (for 250  $\mu\text{m}$ -wide devices) or six (for 500  $\mu\text{m}$ -wide devices) equidistantly spaced broad gold airbridges have been used to interconnect the source contacts.

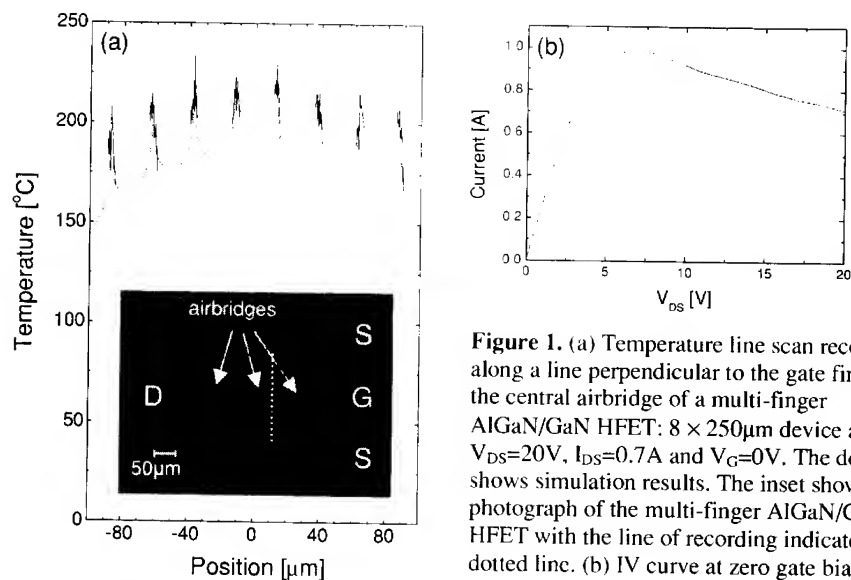


**Figure 1.** (a) Temperature line scan recorded along a line perpendicular to the gate fingers near the central airbridge of a multi-finger AlGaIn/GaN HFET:  $8 \times 250 \mu\text{m}$  device at  $V_{DS}=20\text{V}$ ,  $I_{DS}=0.7\text{A}$  and  $V_G=0\text{V}$ . The dotted line shows simulation results. The inset shows a photograph of the multi-finger AlGaIn/GaN HFET with the line of recording indicated by a dotted line. (b) IV curve at zero gate bias.

To measure temperature with high spatial resolution, micro-Raman spectroscopy measurements were performed between the airbridges using a Renishaw micro-Raman system. Backscattering geometry with unpolarized detection, i.e.,  $z(x..)z$  scattering geometry [2], with the 488nm-line of an Ar-laser as excitation source was employed in the Raman measurements. Shifts in the  $E_2(\text{high})$  phonon frequency of GaN induced by passing a current through the device allow the measurement of the device temperature taking advantage of the well-known temperature dependence of the  $E_2(\text{high})$  phonon frequency of GaN [3]. To obtain  $E_2(\text{high})$  phonon frequency maps and therefore temperature maps, the device was scanned underneath the laser beam using a computer-controlled XY-stage with step sizes as small as  $0.1\text{-}1 \mu\text{m}$ . The laser spot size was  $\approx 1 \mu\text{m}$ , i.e., temperature is measured with  $\approx 1 \mu\text{m}$  spatial resolution. The laser power at the sample was approximately 3mW. Phonon frequency shift resolutions of better than  $0.1 \text{cm}^{-1}$  were achieved corresponding to a temperature accuracy of better than  $10^\circ\text{C}$ . Use of a laser excitation below the GaN bandgap (below band gap excitation of 488nm) prevents any significant laser light absorption in the device, i.e., effects of laser heating of the device can be neglected. More details about the experimental procedure have been published elsewhere [1].

## RESULTS AND DISCUSSION

Figure 1 shows a temperature cross-section through the center of the  $8 \times 250 \mu\text{m}$  AlGaIn/GaN HFET device recorded in a direction perpendicular to the gate fingers. Temperature in the multiple source-drain openings of the device is shown. The peak temperature occurs in the device center decreasing towards the device edges. Also shown is the result of a simulation of the device temperature using a three dimensional finite difference code. The thermal

**BEST AVAILABLE COPY**

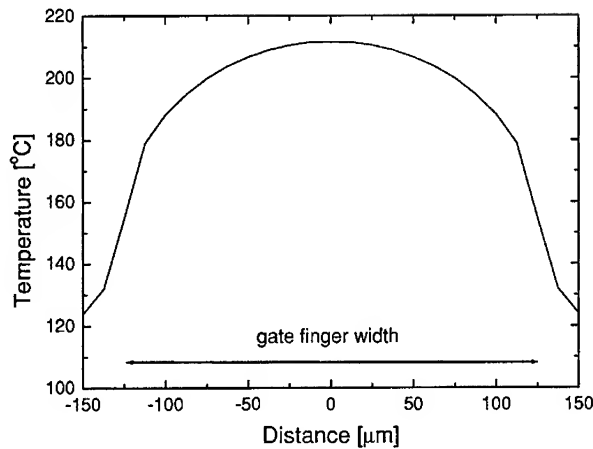


**Figure 2.** Simulated temperature in device center along central gate finger for  $8 \times 250 \mu\text{m}$  AlGaIn/GaN device. Simulation parameters are the same as those used for the simulation results of Figure 1(a).

conductivity values at room temperature of the GaN layer used were  $\kappa_{\text{GaN}} = 1.6 \text{ Wcm}^{-1}\text{K}^{-1}$  [4] and  $\kappa_{\text{SiC}} = 3.3 \text{ Wcm}^{-1}\text{K}^{-1}$  for a SiC substrate [5]. Both were taken to vary as  $T^{-1}$  due to phonon-phonon scattering, as often assumed in device modeling. The thermal resistance of the package was included in the simulation using the experimentally measured value. This was done by using micro-Raman spectroscopy to measure the temperature at the extreme edge of the chip, and then assuming that this was characteristic of the temperature of the top of the package under the heat generating region of the chip. Reasonably good agreement between experiment and three dimensional finite difference modeling was achieved, with both showing clearly the peak in temperature at the center of the device. Simulation results along the width of the central gate finger of the device of Figure 1 are shown in Figure 2. There is a significant temperature variation along the length of the gate finger with a maximum temperature in the device center.

Temperature in the device center, i.e., peak device temperature, was measured for different device designs. Figure 3 shows this temperature for a 4 and 8 finger device, with  $50 \mu\text{m}$  and  $25 \mu\text{m}$  device pitch, respectively, both with a finger width of  $250 \mu\text{m}$ . The faster temperature rise with increasing power dissipation for the 8 finger device is apparent. This indicates the significant thermal cross talk between individual gate fingers for a  $25 \mu\text{m}$  device pitch. Also shown are simulation results. Fair agreement between simulation and experiment was achieved, although simulation overestimates device temperature in this case.

An exponential relationship between device temperature and power density results when assuming a  $T^{-1}$  temperature dependence of thermal conductivities in the simulation [6]. Thermal resistance of the devices at room temperature, i.e., temperature rise per  $\text{W/mm}$ , was therefore determined by fitting an exponential curve to the experimental data, and taking the linear part of this exponential curve. Table I gives the results for the thermal resistance for the different investigated device designs. Also displayed are the results of the finite difference modeling. The more densely packed layouts with  $25 \mu\text{m}$  spacings have severe thermal cross-talk giving a much

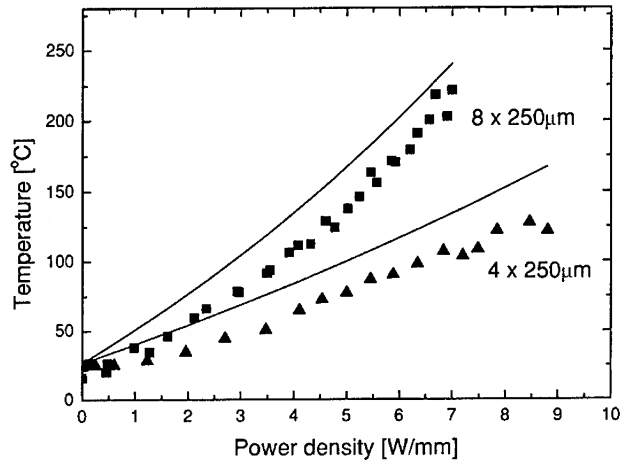


**Figure 3.** Temperature measured at fixed location in center of multi-finger AlGaIn/GaN HFET as function of power density for 4x250μm and 8x250μm device. Full line represents finite difference heat dissipation results.

	4 × 250 μm (50μm pitch)	8 × 250 μm (25μm pitch)	4 × 500 μm (50μm pitch)	8 × 500 μm (25μm pitch)
$K_{exp}$ °C/(W/mm)	10.7	21.3	19.4	30.6
$K_{modeling}$ °C/(W/mm)	13.1	23.0	18.0	32.8

**Table I.** Thermal resistance (temperature rise per W/mm) in center of multi-finger AlGaIn/GaN HFETs: comparison of experiment and simulation results.

higher thermal resistance than the 50μm spacing as already seen in Figure 3. Also increasing the device width from 250μm to 500μm for the same gate finger spacing increases thermal resistance. The smallest thermal cross-talk is naturally achieved for the 50μm spacing 250μm wide device. Fair agreement between experiment and modeling was achieved for all layouts, with the trends accurately captured. Although thermal resistance of the device packaging was taken into account in the simulation, simulated thermal resistance appears to be in most cases slightly larger than the experimentally measured one.

Finite difference modeling has been proven to work well e.g. for GaAs and Si-based devices, however, it is in some sense surprising how good the agreement is for the AlGaIn/GaN devices studied here. There are currently large uncertainties in thermal conductivity values for the AlGaIn/GaN/SiC material system. Thermal conductivity of GaN reported in the literature for example can range from  $\kappa_{GaN}=0.5$  to  $2\text{Wcm}^{-1}\text{K}^{-1}$  dependent on growth conditions [4,7]. Similar

variations have been reported for SiC [8]. Also the temperature dependence of the thermal conductivity can be different from a  $T^{-1}$  relationship. The high Debye temperature of these material systems (GaN:  $\theta_D=600\text{K}$ , SiC:  $\theta_D=1200\text{K}$  [9]) compared to the actual device temperature may result in a temperature dependence of the thermal conductivity stronger than  $T^{-1}$  [10]. A high defect density on the other hand may “weaken” such a relationship to  $T^{-\alpha}$ ,  $\alpha < 1$  [11] due to phonon-defect scattering. Factors such as local defect concentrations, especially in the SiC substrate, may also contribute. Also uncertainties in the thermal resistance of the device packaging may play a role. Unless thermal properties have been characterized for a specific SiC substrate, device structure and device packaging, one needs to be aware of this uncertainty in thermal properties when considering the results of an AlGaIn/GaN/SiC thermal device simulation. Although general guidance on device design can obviously be obtained from simulation, experimental assessment of device temperature is therefore required to obtain reliable temperature information for a specific AlGaIn/GaN device at present.

## CONCLUSIONS

We have demonstrated the use of micro-Raman spectroscopy to measure temperature in active high-power multi-finger AlGaIn/GaN transistors with  $\approx 1\mu\text{m}$  spatial resolution and a temperature accuracy of better than  $10^\circ\text{C}$ . Thermal cross-talk between individual gate fingers was found to be significant for  $250\mu\text{m}/500\mu\text{m}$ -wide devices with  $25\mu\text{m}$  pitch. Thermal simulation results need to be considered with caution since there are still significant uncertainties in thermal properties for the investigated device system. Experimental assessment of device temperature is therefore required to obtain reliable temperature information for a specific AlGaIn/GaN device at present.

## ACKNOWLEDGEMENTS

The work in Bristol was supported by QinetiQ Ltd, Renishaw plc and EPSRC. The QinetiQ contribution to this work was funded by the UK MoD Corporate Research Program. The thermal simulation software was written by R. G. Davis whilst at QinetiQ.

## REFERENCES

1. M. Kuball, J.M. Hayes, M.J. Uren, T. Martin, J.C.H. Birbeck, R.S. Balmer, and B.T. Hughes, *IEEE Electron Dev. Lett.* **23**, 7 (2001).
2. M. Kuball, *Surf. Interface Anal.* **31**, 987 (2001).
3. M.S. Liu, L.A. Bursill, S. Prawer, K.W. Nugent, Y.Z. Tong, and G.Y. Zhang, *Appl. Phys. Lett.* **74**, 3125 (1999).
4. D.I. Florescu, V.M. Asnin, F.H. Pollak, A.M. Jones, J.C. Ramer, M.J. Schurman, and I. Ferguson, *Appl. Phys. Lett.* **77**, 1464 (2000).
5. S.T. Allen, S.T. Sheppard, W.L. Pribble, R.A. Sadler, T.S. Alcorn, Z. Ring, and J.W. Palmour, *Mat. Res. Soc. Symp. Proc.* **572**, 15 (1999).

- 
6. H. S. Carslaw and J. C. Jaeger, *Conduction of Heat in Solids*, Oxford Clarendon Press, Oxford, 2nd ed., 1959.
  7. D. I. Florescu, V. M. Asnin, and F. H. Pollak, *Compound Semiconductor* **7**, no.2, 62 (2001).
  8. C.H. Carter, Jr., V.F. Tsvetkov, R.C. Glass, D. Henshall, M. Brady, St.G. Müller, O. Kordina, K. Irvine, J.A. Edmond, H.-S. Kong, R. Singh, S.T. Allen, and J.W. Palmour, *Mat. Sci. Engin. B* **61-62**, 1 (1999).
  9. Landolt-Börnstein, *Numerical Data and Functional Relationships in Science and Technology*, New Series, Vol. 17a (Springer, Berlin, 1982).
  10. N.W. Ashcroft and N.D Mermin, "Solid State Physics" (Saunders, New York, 1976).
  11. B. C. Daly, H. J. Maris, A. V. Nurmikko, M. Kuball, and J. Han, *J. Appl. Phys.* **92**, 3820 (2002).

### Gate Current Modeling for Insulating Gate III-N Heterostructure Field-Effect Transistors

Frederick W. Clarke<sup>1</sup>, Fat Duen Ho<sup>2</sup>, M. Asif Khan<sup>3</sup>, Grigory Simin<sup>3</sup>, J. Yang<sup>3</sup>, Remis Gaska<sup>4</sup>,  
Michael S. Shur<sup>5</sup>, Jianyu Deng<sup>4</sup>, S. Karmalkar<sup>6</sup>

<sup>1</sup> U.S. Army Space and Missile Defense Command Technical Center, Huntsville, AL.

<sup>2</sup> Department of Electrical and Computer Engineering, University of Alabama in Huntsville

<sup>3</sup> Department of Electrical Engineering, University of South Carolina

<sup>4</sup> Sensor Electronic Technology Inc., Columbia, SC 29209

<sup>5</sup> Broadband Center and ECSE Department, Rensselaer Polytechnic Institute, Troy, NY 12180

<sup>6</sup> Department of Electrical Engineering, Indian Institute of Technology, Madras, India

#### Abstract:

Gate current plays an important role in determining the characteristics and limiting performance of GaN-based field effect transistors. In GaN-based HFETs, the gate current limits the gate voltage swing and, hence, the maximum device current. Since the electron transport across the wide band gap barrier layer involves trapping, under certain bias conditions, the gate current leads to the threshold voltage shifts and causes reliability problems. Under reverse bias, the gate leakage in GaN-based HFET dominates the minimum (pinch-off) drain current. Insulating gate HFETs (i.e. Metal Oxide Heterostructure Field Effect Transistors – MOSHFETs) have the gate leakage currents 4 – 6 orders of magnitude lower than HFETs, even at elevated temperatures up to 300 °C. In this paper, we report on the gate current characteristics in these devices at room and elevated temperatures. We propose a semi-empirical model for the current-voltage characteristics in these devices, which is in good agreement with experimental data. Our data also show that both tunneling and temperature activation are important factors in MOSHFETs. These results are important for possible applications of GaN MOSHFETs in high power amplifiers and power switches as well as in non-volatile memory devices and integrated circuits that will operate in a much wider temperature range than conventional silicon and GaAs devices.

#### Introduction:

With the successful growth of high quality insulators such as SiO<sub>2</sub> and Si<sub>3</sub>N<sub>4</sub> over AlGaIn barrier, MISHFETs and MOSHFETs have emerged as a beneficial addition to modern GaN-based transistor technology<sup>1</sup>. The low interface charge density at insulator/semiconductor interface makes these devices operate using the same principle as AlGaIn/GaN HFETs while enjoying higher dynamic range and much lower gate current, which come from better gate isolation.

---

The gate current is a good indicator of the insulator quality and interface surface charge density. Gate leakage current determines the dynamic operation regime for microwave power transistors. MOSHFETs have larger dynamic range than conventional HFET and often can operate at large forward gate bias ( $>+5V$ ) with a drain-source current increase up to fifty percent.<sup>2</sup> Lower gate leakage current also produces lower  $1/f$  noise and phase noise, which are important in mixer and oscillator applications.<sup>3</sup> Gate leakage current determines the harmonic distortion level for GaN transistors.<sup>4</sup> It is thus important to understand the physics of gate leakage in insulating gate HFETs.

In this paper, we attempt to create a model for the MOSHFET gate leakage current for different temperatures. This model has its origin in previous research in Si MOSFETs. We believe that good modeling technique will help us suppress gate current and optimize the device structure.

#### Gate Leakage Model:

Ultra thin oxides and tunneling processes have been actively researched in MOSFETs since the 1970's. In reference<sup>5</sup>, a model derived for p-type silicon was discussed. The model considered different current components such as the tunneling currents through oxide and the current through the surface states. We will discuss the model in more technical detail and adapt it to our n type substrate in the next section. It is also worth mentioning that gate current becomes more important as device dimensions scale down and leakage begins to influence the oxide reliability.<sup>6</sup>

In GaN-based devices, not much modeling effort has been put into gate leakage although its influence is well known. In reference<sup>7</sup>, it was found that under reverse bias conditions, the gate leakage current increased rapidly below the threshold voltage ( $V_{th} < V_g < 0$ ) while the rate of increase became much slower above the threshold voltage. Hence, it was proposed that vertical tunneling from the metal to the channel dominates the leakage below threshold. However, when the gate voltage is above threshold, lateral tunneling from the source to the drain/source contact dominates (the source was actually floating in these measurements<sup>7</sup>).  $I_{gs}$  behavior (similar to  $I_{gd}$  because of the symmetry between source and drain) also becomes an important process due to the dramatic increase in the lateral electric field in the cutoff region. Also, it is proposed in<sup>7</sup> that tunneling through the defects states is another mechanism that we will have to consider.

Recent paper by Karmalkar et al.<sup>8</sup>, stressed the importance of trap-assisted tunneling for applications below 500K. For even higher temperatures, direct tunneling will be the controlling mechanism. With a parameter fitting procedure, the trap density can be extracted from the leakage current dependence on the gate voltage.

In this paper, we first study the temperature dependence of both MOSHFETs and HFETs. We will propose a semi-empirical model to give us insight into the device behavior.

## Experimental Results:

In Table I, we compare gate current density for different devices. As can be seen, the leakage current in conventional GaN HEMTs can vary a lot depending on materials quality and fabrication technology and is comparable to that in GaAs HFETs. The gate leakage current in GaN MOSHFETs is the lowest compared to other compound semiconductor technologies.

Technology	Gate Current Density	Reference
GaAs Insulated Gate PHEMT	$10^{-4}$ A/cm <sup>2</sup>	9
GaAs HFET	$10^{-1}$ A/cm <sup>2</sup> $10^{-2}$ A/cm <sup>2</sup>	10 9
GaN HFET	$10^{-2}$ A/cm <sup>2</sup> $10^{-1} \sim 10^{-2}$ A/cm <sup>2</sup> $10^{-2} \sim 10^{-3}$ A/cm <sup>2</sup>	11 7 USC/SET/RPI Group
GaN MOSHFET	$10^{-7} \sim 10^{-5}$ A/cm <sup>2</sup>	USC/SET/RPI group
GaN MISHFET	$10^{-5}$ A/cm <sup>2</sup>	1

Table I. Comparison of Gate Leakage Current Density for Different Technologies

Fig. 1 compares the gate current density at different temperatures for several GaN-based HFETs. The results by Mizuno clearly show the importance of the fabrication technology in determining the leakage current. The gate leakage current is temperature activated. GaN MOSHFETs have a much larger activation energy. This points out that the barrier controlling the leakage in these devices is different from that in GaN HFETs (i.e. SiO<sub>2</sub> rather than AlGaIn.)

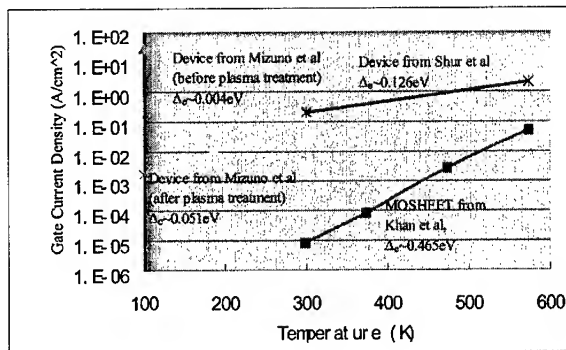


Fig. 1. Comparison of the current density for several different devices at different temperatures. The activation energy  $\Delta_0$  was extracted from  $I = I_0 \exp(-\Delta_0/kT)$ , using results in Mizuno et al<sup>12</sup>. Shur et al<sup>13</sup>

Fig.2 compares the leakage current gate voltage dependences for GaN HFETs and MOSHFETs.

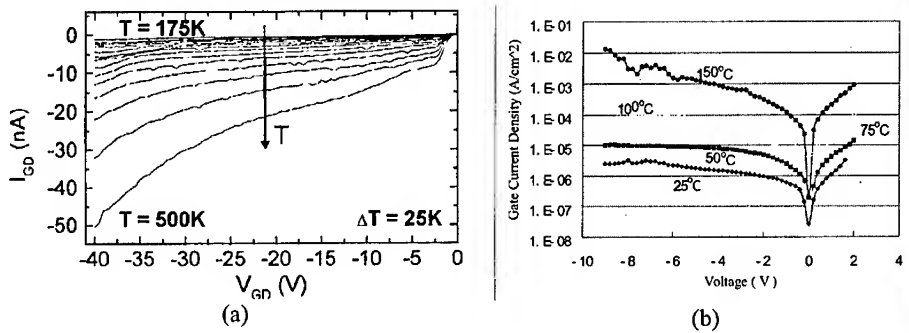


Fig. 2. Comparison of the leakage current gate voltage dependences for GaN HFETs <sup>7</sup>(a) and MOSHFETs (b).

Fig. 2 clearly shows that in the MOSHFET, the gate current behavior is different than in the conventional HFET. The gate current does not saturate at the threshold voltage, as was discussed by Miller et al. <sup>7</sup> and Karmalkar et al. <sup>8</sup>. As mentioned above, the activation energy is much higher in MOSHFETs. The measured MOSHFET leakage current characteristics are similar to Stress Induced Leakage Current (SILC) characteristics in Si MOSFETs.

The reason for this difference can be understood from the equivalent circuit of the gate leakage current in MOSHFETs shown in Fig. 3.

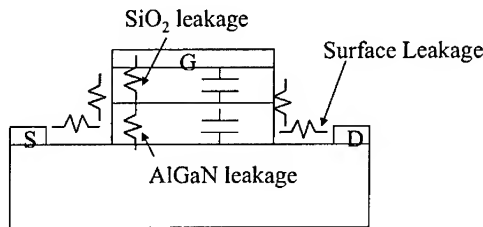


Fig. 3 Equivalent circuit showing the important components contributing to the gate leakage current

At measurement frequencies ( $\sim 0.1$  Hz), AlGaIn behaves as an active impedance and  $SiO_2$  as a capacitive impedance. Hence, the equivalent circuit becomes very similar to that of a MOSFET.

Model:

Based on the equivalent circuit of Fig. 3, we propose the following semi-empirical model for the gate leakage in GaN MOSHFETs

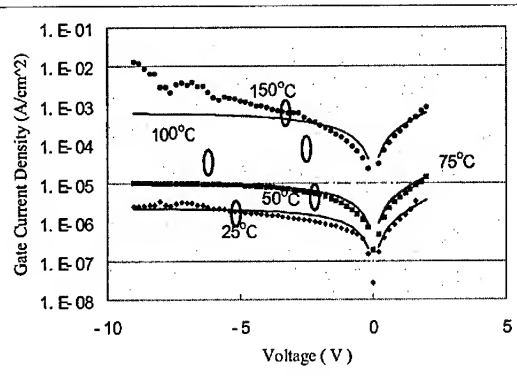


Fig. 4. Comparison between experimental and the semi-empirical model proposed in this paper. Symbols: Experimental results, Lines: Model results

$$I_g = I_o \exp\left(-\frac{q\Delta}{kT}\right) \left( \exp\left(\frac{qV_g}{nkT}\right) - 1 \right)$$

The resulting fitting to the experimental data is shown in Fig. 4. The parameters are:  $\Delta=0.496\text{eV}$ ,  $I_o=490\text{A/cm}^2$ ,  $n=80$ . A large value of the constant  $n$  indicates that tunneling is a very important mechanism in the gate leakage current. (In a more general case,  $n$  might depend on temperature (especially at cryogenic temperatures) but this dependence was not important in the investigated temperature range from 25 C to 150 C.)

As seen, the model is in excellent agreement with experimental data.

Conclusions:

In this paper, we propose and validate a semi-empirical model to explain the gate leakage current in MOSHFETs. We found that leakage current in MOSHFETs is limited by the silicon dioxide layer. Both tunneling and thermal activation are important in the mechanisms of the gate current. The model is suitable for parameter extraction and for the implementation in circuit simulators.

Acknowledgement:

The authors wish to thank Mr. Alexei Koudymov for useful discussions. The work at SET was supported by MDA. The work at RPI was partially supported by ONR and monitored by Dr. H. Dietrich.

# References:

- <sup>1</sup> M. Asif Khan, G. Simin, J. Yang, J. Zhang, A. Koudymov, M. S. Shur, R. Gaska, X. Hu, and A. Tarakji, Insulating Gate III-N Heterostructure Field-Effect Transistors for High Power Microwave and Switching Applications, Submitted
- <sup>2</sup> M. A. Khan, X. Hu, A. Tarakji, G. Simin, J. Yang, R. Gaska, M. S. Shur, AlGaIn/GaN Metal-Oxide-Semiconductor Field Effect Transistor on SiC Substrates, Applied Physics Letters, Vol. 77, No. 9, pp. 1339-1341, 2000
- <sup>3</sup> N. Pala, R. Gaska, M. S. Shur, J. Yang and M. A. Khan, Low-Frequency Noise in SiO<sub>2</sub>/AlGaIn/GaN Heterostructures on SiC and Sapphire Substrates, Mat. Res. Soc. Proc, vol. 595, pp. W11.9.1-W11.9.6, T. H. Myers, R. M. Feenstra, M. S. Shur, H. Amano, Editors, MRS, Warrenton, PA, (2000), MRS Internet J. Nitride Semicond. Res. 5S1, W11.9 (2000).
- <sup>4</sup> R. Caverly, Distortion in Gallium Nitride Microwave and RF Switch Control Circuits
- <sup>5</sup> M. Y. Doghish, F. D. Ho, A Comprehensive Analytical Model for Metal-Insulator-Semiconductor (MIS) Devices, IEEE Transactions on Electron Devices, v. 39, No. 12, p.2771, Dec. 1992
- <sup>6</sup> Y.-C. Yeo, Q. Lu, and C. Hu, "Gate Oxide Reliability: Anode Hole Injection Model and its Applications", Chapter 5 of Selected Topics in Electronics and Systems, vol. 23, Oxide Reliability- A Summary of Silicon Oxide Wearout, Breakdown, and Reliability, Ed. D. J. Dumin, World Scientific, pp. 233-270, 2002. ISBN 981-02-4842-3
- <sup>7</sup> E. J. Miller, X. Z. Dang and E. T. Yu, Gate leakage current mechanisms in AlGaIn/GaN heterostructure field-effect transistors, JOURNAL OF APPLIED PHYSICS VOLUME 88, NUMBER 10, NOVEMBER 15, 2000
- <sup>8</sup> Shreepad Karmalkar, D. Mahaveer Sathaiya, M. S. Shur, Mechanism of the Reverse Gate Leakage in AlGaIn / GaN HEMTs, Submitted to APL
- <sup>9</sup> Xie, et al, A Novel InGaAs/InAlAs Insulated Gate Pseudomorphic HEMT with a Silicon Interface Control Layer Showing High DC and RF Performance, IEEE EDL, Vol. 22, No. 7, pp312-314
- <sup>10</sup> C.B. Demelo, et al, High Electron Mobility InGaAs-GaAs FET with thermally Oxidized AlAs Gate Insulator, Electronics Letters, Vol. 36, No. 1, pp84-86
- <sup>11</sup> Zhifang Fan, S. N. Mohammad, O. Aktas, A. E. Botchkarev, A. Salvador and Hadis Morkoc, Suppression of leakage currents and their effect on the electrical performance of AlGaIn/GaN modulation doped field-effect transistors. Appl. Phys. Lett. 69 (9), 26 August 1996
- <sup>12</sup> S. Mizuno, Y. Ohno, S. Kishimoto, K. Maezawa and T. Mizutani, "Large Gate Leakage Current in AlGaIn/GaN High Electron Mobility Transistors", Jpn. J. Appl. Phys. vol. 41, Part 1, No. 8, pp. 5125-5126, 2002.
- <sup>13</sup> M. S. Shur, A. D. Bykhovski, R. Gaska, and A. Khan, GaN-based Pyroelectronics and Piezoelectronics, in Handbook of Thin Film Devices, Volume 1: Hetero-structures for High Performance Devices, Edited by Colin E.C. Wood, Handbook edited by Maurice H. Francombe, Academic Press, San Diego, 299 (2000).

**BEST AVAILABLE COPY**

### AlGaN/GaN Metal-Oxide-Semiconductor Heterostructure Field-Effect Transistors (MOSHFETs) with the Delta-Doped Barrier Layer

Z. Y. Fan, J. Li, J. Y. Lin, and H. X. Jiang<sup>a)</sup>

Department of Physics, Kansas State University, Manhattan, Kansas 66506-2601, USA

Y. Liu, J. A. Bardwell, J. B. Webb, and H. Tang

Institute for Microstructural Sciences, National Research Council, Ottawa, ON, K1A 0R6, Canada

#### ABSTRACT:

The fabrication and characterization of AlGaN/GaN metal-oxide-semiconductor heterostructure field-effect transistors (MOSHFETs) with the  $\delta$ -doped barrier are reported. The incorporation of the SiO<sub>2</sub> insulated-gate and the  $\delta$ -doped barrier into HFET structures reduces the gate leakage and improves the 2D channel carrier mobility. The device has a high drain-current-driving and gate-control capabilities as well as a very high gate-drain breakdown voltage of 200 V, a cutoff frequency of 15 GHz and a maximum frequency of oscillation of 34 GHz for a gate length of 1  $\mu$ m. These characteristics indicate a great potential of this structure for high-power-microwave applications.

#### INTRODUCTION

With a great potential for applications in the area of high power and high temperature microwave electronics [1, 2], the power and voltage handling ability of AlGaN/GaN heterostructure field-effect transistors (HFETs) has been considerably improved in recent years, with the state-of-art power density of 6.6 W/mm (6 GHz) on sapphire substrates [3], 10.7 W/mm (10GHz) [4] and 5 W/mm (26 GHz) [5] on SiC substrates. However, it has been observed that the Schottky gate of HFET tends to degrade with enhanced gate leakage current and insufficient pinch-off characteristics, especially when the HFETs are operating under high power conditions. The degradation of the gate leads to the premature breakdown and hence a deficient device performance with a reduction of output power, the RF efficiency and noise figure [6]. It is believed that the premature breakdown is caused by the traditional gate-drain diode breakdown as a result of the thermionic emission [7], or the thermal effect as a consequence of the surface hopping conduction of gate leakage current [8]. HFETs with insulated gate structure, especially by incorporating a thin SiO<sub>2</sub> or AlN layer under the gate have been employed to tackle the gate leakage problem by increasing the energy barrier, and the leakage current was dramatically reduced by several orders [9,10]. The insulation layer also has the effect to reduce the electrical field in the underlying nitride semiconductor and hence, and increase the gate breakdown voltage [11].

To further reduce the vertical tunneling current [12] and hence increase the gate-drain breakdown voltage, we have proposed to replace the uniformly doping scheme in the AlGaN barrier with a  $\delta$ -doping profile [13]. With the dopants farther away from the gate, the gate leakage current would be reduced. Moreover, with an optimized separation distance between the

dopants and the AlGaN/GaN interface, carrier-impurity scattering can be minimized and hence carrier mobility would be enhanced. In this paper, we report the fabrication, DC and RF small signal characterization of  $\delta$ -doped AlGaN/GaN MOSHFETs.

## EXPERIMENT

Figure 1 shows a schematic diagram of the metal-oxide-semiconductor HFET (MOSHFET) layer structure used in this study. The AlGaN/GaN heterostructures were grown by metal organic chemical vapor deposition (MOCVD) on sapphire substrates. Following a 50 nm GaN nucleation layer on the substrate, 1  $\mu\text{m}$  highly resistive GaN layer was deposited. A very thin AlN interfacial layer ( $\sim 1$  nm) was subsequently deposited above GaN to separate the channel from the AlGaN barrier layer and to improve the sheet charge density and mobility by increasing the confinement of electrons in the channel and decreasing the alloy scattering [14, 15]. The heterostructure was then capped by a Si  $\delta$ -doped  $\text{Al}_{0.35}\text{Ga}_{0.65}\text{N}$  barrier layer with a thickness of 20 nm, grown at 1050  $^{\circ}\text{C}$ . The  $\delta$ -doping profile was implemented by interrupting the usual crystal-growth mode by closing the Ga (trimethylgallium) and Al (trimethylaluminum) flows, while the Si impurities ( $\text{SiH}_4$ ) are introduced into the growth chamber. The as grown structure typically exhibits an electron mobility and sheet carrier density of about  $1300 \text{ cm}^2/\text{Vs}$  and  $1.3 \times 10^{13}$ , respectively, as obtained by Hall measurement. The device fabrication started from the mesa isolation performed by chlorine-based inductively coupled plasma (ICP) etching. The ohmic metal stack of Ti(20 nm)/Al(150 nm)/Ti(30 nm)/Au(50 nm) was deposited by e-beam evaporator, and followed by lift-off, ohmic contacts were formed by rapid thermal annealing of the sample in nitrogen atmosphere at 850  $^{\circ}\text{C}$  for 30 s. A  $\sim 6$  nm thick  $\text{SiO}_2$  layer and gate metal stack of Ni/Au were then deposited to form insulated gate. DC characteristics and RF small signal performance were measured.

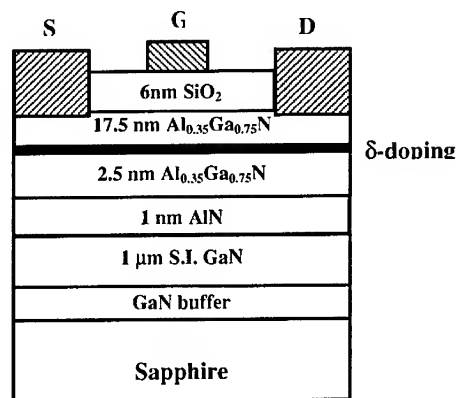
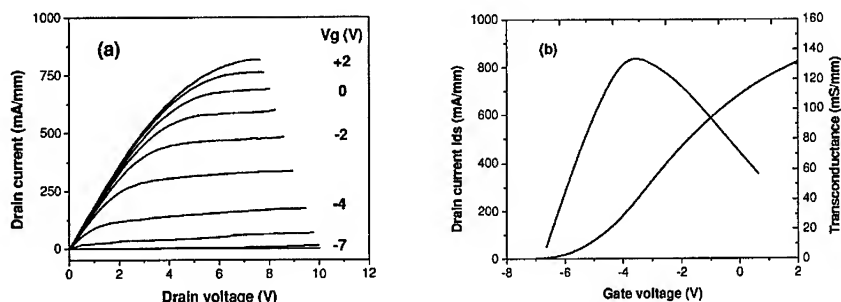


Figure. 1. The schematic diagram of the  $\delta$ -doped AlGaN/GaN MOSHFET layer structure.

## RESULTS AND DISCUSSIONS

The on-wafer measured drain-source dc current-voltage ( $I - V$ ) characteristics of a MOSHFET device with  $\delta$ -doped  $\text{Al}_{0.35}\text{Ga}_{0.65}\text{N}$  barrier are shown in Fig. 2. The device exhibits a high drain current driving ability and excellent pinch-off property. The drain current arrives a maximum value of  $\sim 0.82$  A/mm at a gate bias of 2 V and drain bias of 8 V. The slightly larger knee voltage (6 V) could be attributed to the  $\delta$  doping scheme in the  $\text{Al}_{0.3}\text{Ga}_{0.7}\text{N}$  barrier, because the source and the drain were directly formed on the undoped  $\text{Al}_{0.3}\text{Ga}_{0.7}\text{N}$  without recessing etch, leading to a larger contact resistance. The device was completely pinched off at a gate bias of  $-7$  V. In this off state, the drain current was less than 0.5 mA/mm at a drain bias of 8 V, implying a ratio exceeding  $10^3$  for the on/off state current control capability. A peak extrinsic transconductance  $g_m$  of 130 mS/mm was achieved at a gate bias of  $-3.5$  V. The performance was much improved over that of a uniformly doped HFET with a similar current density that was found to be difficult to pinch off due to its much higher leakage current.



**Figure 2.** DC  $I - V$  characteristics (a) and transfer characteristics (b) for a  $2 \times 40 \mu\text{m} \times 1 \mu\text{m}$  AlGaIn/GaN MOSHFET with  $\delta$ -doped barrier. In (a) the gate was biased from 2 V to  $-7$  V in a step of  $-1$  V; in (b) the drain bias was 8 V. A maximum drain saturation current of 0.82 A/mm, a peak extrinsic transconductance of 130 mS/mm, and a threshold voltage of  $-7$  V were achieved.

With the  $\text{SiO}_2$  insulation layer under the gate and a  $\delta$ -doping scheme, the device has a very large gate-drain breakdown voltage with a typical value about 200 V for  $1 \mu\text{m}$  gate length, as shown in Fig 3(a), and the breakdown voltages for devices with different doping level and doping profile are compared in Fig 3(b). As we can see, for the  $\delta$ -doping scheme, the gate-drain breakdown voltage was reduced from 200 V to 65 V as the effective Si dopant concentration was increased from  $5 \times 10^{12} \text{ cm}^{-2}$  to  $1.25 \times 10^{13} \text{ cm}^{-2}$ . At higher sheet densities, electrons may spill over from the 2D channel into the barrier region, demonstrated by numerical simulations. The electrons spilling into the barrier layer would enhance the gate leakage current and decrease the breakdown voltage between the drain and the gate. Included in the figure is also the breakdown voltage of one device fabricated from a uniformly doped  $\text{Al}_{0.35}\text{Ga}_{0.65}\text{N}$ /GaIn HFET structure with an effective Si dopant concentration of about  $1 \times 10^{13} \text{ cm}^{-2}$ . It can be seen that at this dopant concentration the uniformly doped device withstands a much lower breakdown voltage ( $\sim 60$  V) than a value of 100 V for the  $\delta$ -doped device, demonstrating the advantage of the  $\delta$ -doping

scheme over uniform doping.

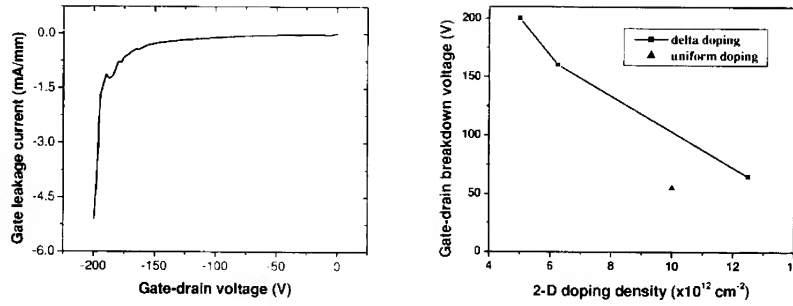


**Figure 3.** (a) The gate leakage current vs. gate-drain voltage of a AlGaIn/GaN MOSHFET with  $\delta$ -doped AlGaIn barrier. A very high gate-drain breakdown voltage ( $\sim 200$  V) is observed. (b) Compares the gate-drain breakdown voltage at different Si-dopants concentration and different doping scheme.

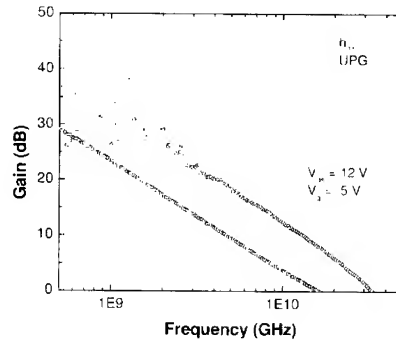


**Figure 4.** Short-circuit current gain ( $|h_{21}|$ ) and unilateral power gain (UPG) as a function of frequency for a  $2 \times 80 \mu\text{m} \times 1 \mu\text{m}$  device.

The RF performance of the  $\delta$ -doped MOSHFET devices was characterized by on-wafer probing. In Fig. 4, the as-measured small signal short-circuit current gain ( $|h_{21}|$ ) and unilateral power gain (UPG) as a function of frequency for the  $1 \mu\text{m}$  gate length device are shown. The measurement was taken at a drain bias of 12 V and a gate bias of  $-5$  V. A unity current gain cutoff frequency ( $f_T$ ) of 15 GHz and a maximum frequency of oscillation ( $f_{\text{max}}$ ) of 34 GHz were measured. These are the as-measured results without de-embedding the influence of pad parasitics. For the  $1 \mu\text{m}$  gate length, these values are considerably high, which is attributed to the enhanced high electron mobility by optimizing the doping scheme and the good confinement of electrons in the channel.

**BEST AVAILABLE COPY**

## CONCLUSIONS

We have fabricated AlGaIn/GaN based MOSHFETs with high drain-current-driving and gate-control capabilities, with a very high gate-drain breakdown voltage of 200 V, a cutoff frequency of 15 GHz and a maximum frequency of oscillation of 34 GHz for a 1  $\mu\text{m}$  gate length devices. The improved characteristics were obtained by incorporating insulating gate oxide and  $\delta$ -doped AlGaIn barrier layers. These characteristics indicate a great potential of this structure for high power microwave applications.

## ACKNOWLEDGMENTS

This research is supported by BMDO (Dr. Kepi Wu) monitored by USASMDC (Mr. Fred Clarke and Terry Bauer) and DOE (DE-FG03-96ER45604).

## REFERENCE:

- a). Electronic mail: [jiang@phys.ksu.edu](mailto:jiang@phys.ksu.edu)
1. T. P. Chow and R. Tyagi, IEEE Electron Devices **41**, 1481 (1994).
  2. M. Asif Khan, Q. Chen, J. W. Yang, M. S. Shur, B. T. Dermott, and J. A. Higgins, IEEE Electron Device Lett. **17**, 325 (1996).
  3. S. Keller, Y. F. Wu, G. Parish, N. Ziang, J. J. Xu, B. P. Keller, s. P. Denbarra, and U. K. Mishra, IEEE Electron Device Lett. **48**, 552 (2001).
  4. V. Tilak, B. Green, V. Kaper, H. Kim, T. Prunty, J. Smart, J. Shealy, and L. Eastman, IEEE Electron Device Lett. **22**, 504 (2001).
  5. C. Lee, H. Wang, J. Yang, L. Witkowski, M. Muir, M. A. Khan, and P. Saunier, Electron Lett. **38**, 924 (2002).
  6. N. Maeda, T. Saitoh, K. Tsubaki, T. Nishida, and N. Kobayash, Jpn. J. Appl. Phys., Part 2 **38**, L987 (1999).
  7. E. Alekseev, P. Nguyen-Tan, D. Pavlidis, M. Micovic, D. Wong, and C. Nguyen, Proc. 17<sup>th</sup> IEEE/Cornell Conf., Ithaca, NY, August, 2000, P84.
  8. W. S. Tan, P. A. Houston, P. J. Parbrook, D. A. Wood, G. Hill, and C. R. Whitehouse, Appl. Phys. Lett. **80**, 3207 (2002).
  9. M. Asif Khan, X. Hu, A. Tarakji, G. Simin, J. Yang, R. Gaska, and M. S. Shur, Appl. Phys. Lett. **77**, 1339 (2000).
  10. D. H. Cho, M. Shimizu, T. Ide, H. Ookita, and H. Okumura, Jpn. J. Appl. Phys. **41**, 4481 (2002).
  11. B. Gaffey, L. J. Guido, X. W. Wang, and T. P. Ma, IEEE Trans. Electron Devices **48**, 458 (2001).
  12. E. J. Miller, X. Z. Dang, and E. T. Yu, J. Appl. Phys. **88**, 5951 (2000).
  13. Z. Y. Fan, J. Li, J. Y. Lin, and H. X. Jiang, Appl. Phys. Lett. **81** (2002) (being published on Dec. 9 issue).
  14. L. Hsu and W. Walukiewicz, J. Appl. Phys. **89**, 1783 (2001).
  15. L. Shen, S. Heikman, B. Moran, R. Coffie, N.-Q. Zhang, D. Buttari, I. P. Smorchkova, S. Keller, S. P. DenBaars, and U. K. Mishra, IEEE Electron Device Lett. **22**, 457 (2001).

---

## **Characterization of Defects and Transport**

**Electrical, Optical, Structural, and Analytical Properties of Very Pure GaN**

D.C. Look

Semiconductor Research Center, Wright State University, Dayton, OH 45435

J.R. Sizelove

Air Force Research Laboratory, AFRL/MLPS, Wright-Patterson AFB, OH 45433

J. Jasinski and Z. Liliental-Weber

Lawrence Berkeley National Laboratory, 1 Cyclotron Road, Berkeley, CA 94720

K. Saarinen

Helsinki University of Technology, P.O. Box 1100, FIN-02015, Espoo, Finland

S.S. Park and J.H. Han

Samsung Advanced Institute of Technology, P.O. Box 111, Suwon, Korea, 440-600

**ABSTRACT**

Present hydride vapor phase epitaxial growth of GaN on  $\text{Al}_2\text{O}_3$  can produce material of very high quality, especially in regions of the crystal far from the substrate/epilayer interface. In the present study, we characterize a 248- $\mu\text{m}$ -thick epilayer, which had been separated from its  $\text{Al}_2\text{O}_3$  substrate and etched on top and bottom to produce flat surfaces. Temperature-dependent Hall-effect data have been fitted to give the following parameters: mobility  $\mu(300) = 1320 \text{ cm}^2/\text{V-s}$ ;  $\mu(\text{peak}) = 12,000 \text{ cm}^2/\text{V-s}$ ; carrier concentration  $n(300) = 6.27 \times 10^{15} \text{ cm}^{-3}$ ; donor concentration  $N_D = 7.8 \times 10^{15} \text{ cm}^{-3}$ ; acceptor concentration  $N_A = 1.3 \times 10^{15} \text{ cm}^{-3}$ ; and effective donor activation energy  $E_D = 28.1 \text{ meV}$ . These mobilities are the highest ever reported in GaN, and the acceptor concentration, the lowest. Positron annihilation measurements give a Ga vacancy concentration very close to  $N_A$ , showing that the dominant acceptors are likely native defects. Secondary ion mass spectroscopic measurements show that  $N_D$  is probably composed of the common donors O and Si, with  $[\text{O}] > [\text{Si}]$ . Transmission electron microscopy measurements yield threading dislocation densities of about  $1 \times 10^7 \text{ cm}^{-2}$  on the bottom (N) face, and  $< 5 \times 10^5 \text{ cm}^{-2}$  on the top (Ga) face. Photoluminescence (PL) spectra show a strong donor-bound exciton ( $\text{D}^0\text{X}$ ) line at 3.47225 eV, and a weaker one at 3.47305 eV; each has a linewidth of about 0.4 meV. In the two-electron satellite region, a strong line appears at 3.44686 eV, and a weaker one at 3.44792 eV. If the two strong lines represent the same donor, then  $E_{D,n=1} - E_{D,n=2} = 25.4 \text{ meV}$  for that donor, and the ground-state activation energy ( $E_C - E_{D,n=1}$ ) is  $(4/3)25.4 = 33.9 \text{ meV}$  in a hydrogenic

model, and 32.7 meV in a somewhat modified model. The measured Hall-effect donor energy, 28.1 meV, is smaller than the PL donor energy, as is nearly always found in semiconductors. We show that the difference in the Hall and PL donor energies can be explained by donor-band conduction via overlapping donor excited states, and the effects of non-overlapping excited states which should be included in the  $n$  vs.  $T$  data analysis (charge balance equation).

## INTRODUCTION

Although GaN growth techniques have been developing over a period of more than thirty years [1], the high incorporation of impurities and defects still remains a major issue. Perhaps the dominant reason is that most of the growths are carried out on mismatched substrates, such as  $\text{Al}_2\text{O}_3$ , leading to a high strain and a strong diffusion of both impurities and point defects from the substrate [2]. Threading dislocations are also extremely dense ( $> 10^{10} \text{ cm}^{-2}$ ) near the substrate/epilayer interface, but diminish toward the surface because of annihilation processes [3]. Thus, the average quality of a typical layer is nearly always dependent upon thickness. Hydride vapor phase epitaxy (HVPE) has a high growth rate ( $\sim 100 \mu\text{m}$  per hr), and thus is capable of growing thick material, up to  $1000 \mu\text{m}$  in some cases [4-6]. For such a thick layer, a standard surface-sensitive characterization technique, such as photoluminescence (PL), will find a large difference in the quality of the top and bottom surface regions. Hall-effect measurements, on the other hand, will sample the whole crystal, and, in fact, will be strongly influenced by a thin, very conductive epilayer/substrate interface region, which always appears in HVPE GaN layers grown on  $\text{Al}_2\text{O}_3$  [2,7]. Corrections for the interface region can be easily implemented if the sample can be modeled as two parallel layers, bulk and interface, and if the interface layer is totally degenerate [7]. Although this model has attained some success, and is widely used, still it is an approximation. Thus, for example, the donor activation energy  $E_D$ , obtained from a fit of the corrected temperature-dependent Hall-effect (T-Hall) data, may suffer from the inaccuracy of the two-layer model. In particular, a reliable comparison of the Hall and PL donor energies, long an issue in semiconductor circles, is made difficult.

Recently, such HVPE wafers have been proposed as a solution to the GaN substrate problem because, unlike the cases in Si, GaAs, SiC, and ZnO, large-area wafers of GaN cannot be obtained by bulk-growth techniques. However, since thick HVPE GaN layers can be grown on  $\text{Al}_2\text{O}_3$  substrates, and since they can be easily separated from the  $\text{Al}_2\text{O}_3$  substrates by a laser irradiation technique [5,6], they can possibly serve as GaN substrates for further GaN epitaxial growth. However, one problem with these separated wafers is a strong bow, due to the strain caused by the mismatched growth. This bow necessitates lapping, etching, and polishing both top and bottom surfaces in order to produce a flat wafer. In the Samsung procedure, the GaN layer is grown to a thickness of about 500  $\mu\text{m}$ , and then about 100  $\mu\text{m}$  of material are removed from each of the surfaces. From a characterization point of view, removal of 100  $\mu\text{m}$  from the bottom surface eliminates the conductive interface layer, and a large portion of the dislocations and diffused impurities and point defects. Thus, the Hall-effect measurements on the final wafer are representative of the true, bulk material, and can be meaningfully compared with the PL results. Here, we examine the structural, analytical, optical, and electrical properties of a 248- $\mu\text{m}$  Samsung wafer, S417, which exhibits the highest mobility ever reported in GaN. We also show that a rather simple model can reconcile the differences found between Hall and PL donor activation energies in this sample, and that this same model should be applicable to other samples and materials, also.

## SECONDARY-ION MASS SPECTROSCOPY - IMPURITIES

Secondary-ion mass spectroscopy (SIMS) measurements [8] have been carried out on a GaN sample very similar to S417, but having a slightly inferior quality. These measurements give Si and O concentrations in the low-to-mid  $10^{16} \text{ cm}^{-3}$ , with  $[\text{O}] > [\text{Si}]$ . Another group has studied donors in Samsung material by far-IR absorption and SIMS techniques, and they have also concluded that O is the dominant donor [9]. Later, we will show that the total shallow, hydrogenic donor concentration  $N_D$  in S417 is  $7.8 \times 10^{15} \text{ cm}^{-3}$ , a somewhat lower value than  $[\text{O}] + [\text{Si}]$ , as determined by SIMS. However, SIMS measurements are not always accurate at these low concentrations, and, also, some of the O and Si may not be electrically active.

## POSITRON ANNIHILATION SPECTROSCOPY - VACANCIES

Positrons injected into defect-free GaN are annihilated by electrons in a mean time of 160 – 165 ps. However, if there are negatively charged vacancies present, some of the positrons will become trapped at those locations, and will have longer lifetimes, because of the reduced electron density at vacancies. In the case of GaN, Ga vacancies (but not N vacancies) would be expected to fill this role, and indeed, PAS has been used to identify and quantify  $V_{Ga}$ -related defects [10]. In fact, comparisons of  $V_{Ga}$  concentrations with acceptor concentrations  $N_A$  in a series of undoped, n-type HVPE GaN samples, with  $N_A$  ranging from  $10^{15}$  to  $10^{19}$  cm<sup>-3</sup>, show that  $[V_{Ga}] \approx N_A$ , to within experimental error [2,10]. In particular, a Samsung HVPE GaN sample with properties very similar to those of S417 has been shown to have  $[V_{Ga}] \approx 2 \times 10^{15}$  cm<sup>-3</sup> [11], very close to our value of  $N_A$  determined by Hall-effect measurements, discussed below. Thus, it appears that  $V_{Ga}$ , and not any impurity, is the dominant acceptor in HVPE GaN, and probably in other types of undoped GaN, also. Indeed, theory predicts that  $V_{Ga}$  centers should be abundant in n-type GaN[12].

## TRANSMISSION ELECTRON MICROSCOPY - DISLOCATIONS

Convergent beam electron diffraction analysis shows that the bottom surface (closest to the Al<sub>2</sub>O<sub>3</sub>) is the N face, and the top surface, the Ga face. This, in fact, turns out to be the case for most HVPE-grown GaN/Al<sub>2</sub>O<sub>3</sub> layers. Transmission electron microscopy results for the Ga face, shown in Fig. 1, show very few threading dislocations, with  $N_{dis} < 5 \times 10^5$  cm<sup>-2</sup>. This is one of the lowest results ever reported in heteroepitaxial GaN, and suggests that such wafers could be used for many commercial purposes. On the N face, the number is somewhat higher:  $N_{dis} \leq 1 \times 10^7$  cm<sup>-2</sup>, but it is likely that the Ga face would be used for most subsequent epitaxial growth.

## PHOTOLUMINESCENCE - DONORS

A 4-K PL spectrum of the near-band-edge (exciton) region, 3.465 – 3.480 eV, is shown in Fig. 2. The sharp lines at 3.47123, 3.47225, and 3.47305 eV are likely neutral donor-bound A excitons ( $D^0X_{AS}$ ), while the broader line at 3.47921 eV is the free A exciton  $X_A$ . The line at 3.47609 eV may be an excited (rotator) state of a  $D^0X_A$ , or possibly a  $D^0X_B$  transition. It has been reported that the  $D^0X_A$  line in unstrained material should lie at 3.471 - 3.472 eV, a result that suggests immediately that the present Samsung wafer does not have a high strain. This is expected, since strain decreases with thickness. The full width at half maximum (FWHM) for each of the  $D^0X$  lines is about 0.4 meV, which indicates excellent material; however, for *homoepitaxial* layers, even better FWHM values, 0.1 meV, have been reported [13]. Another group of PL lines appears in the region 3.440 – 3.455 eV, with a strong line at 3.44686 eV and a weaker one at 3.44792 eV. This region should include two-electron satellite (TES) replicas of the  $D^0X$  transitions. That is, if the collapse of an exciton bound to a neutral donor leaves the donor in an  $n=2$  state, rather than the usual  $n=1$  state, then the difference in energy should be  $E_{D,n=2} - E_{D,n=1} = 3R/4$ , where  $R$  is the Rydberg for GaN ( $R = 13.6m^*/\epsilon_0^2$  eV). By shifting the entire spectrum up by 25.4 meV, in order to overlay the strongest  $D^0X$  line onto the strongest TES line, we see in Fig. 3 that these two lines have very similar shapes and thus probably correspond to the same donor. If so, the GaN Rydberg should be about  $4(25.4)/3 = 33.9$  meV. However, this calculation presumes that the donor is fully hydrogenic, which is often not true in semiconductors, especially for the ground state ( $n=1$ ). For a more accurate determination of  $R$ , Moore et al. [9] have compared 2p and 3p states, seen in absorption, because these states should be nearly hydrogenic, i.e., they should have small central-cell corrections. From the fact that the energy difference between the 2p and 3p states in the hydrogenic model is  $(1/4 - 1/9)R$ , Moore et al. have determined that  $R = 29.1$  meV. If this value of  $R$  is correct, then the true ground state of our main donor is  $E_{D,n=1} - E_{D,n=2} + R/4 = 32.7$  meV, i.e., 3.6 meV above the Rydberg. This means that there must be an additional attractive force acting in conjunction with the donor core. However, we must reserve judgment on this issue, because the positions of some weaker (3s and 4s) TES lines, compared with that of the strongest (2s) TES line, is more consistent with an energy of 33.9 meV, rather than 32.7 meV. Below, we will compare the PL-derived donor energy with that determined by Hall-effect analysis.

## HALL-EFFECT MEASUREMENTS – DONORS AND ACCEPTORS

The basic equations for Hall-effect analysis, allowing for the energy  $\mathcal{E}$  dependence of the electrons, are as follows [14]:

$$j_x = \frac{ne^2 \langle \tau \rangle}{m^*} E_x \equiv -ne\mu_c E_x \quad (1)$$

$$R_H = \frac{E_y}{j_x B} = -\frac{1}{ne} \frac{\langle \tau^2 \rangle}{\langle \tau \rangle^2} = -\frac{r}{ne} \quad (2)$$

where  $j_x$  is the current density,  $E_x$  and  $E_y$  are the electric field vectors,  $B_z = B$ , the magnetic field strength,  $\tau$  the relaxation time,  $R_H$ , the Hall coefficient, and

$$\langle \tau^n(E) \rangle = \frac{\int_0^\infty \tau^n(E) E^{3/2} \frac{\partial f_0}{\partial E} dE}{\int_0^\infty E^{3/2} \frac{\partial f_0}{\partial E} dE} \rightarrow \frac{\int_0^\infty \tau^n(E) E^{3/2} e^{-E/kT} dE}{\int_0^\infty E^{3/2} e^{-E/kT} dE} \quad (3)$$

This formulation is called the relaxation-time approximation to the Boltzmann Transport Equation. Here  $f_0$  is the Fermi-Dirac distribution function and the second equality in Eq. 3 holds for non-degenerate electrons, i.e., those describable by Boltzmann statistics. The quantity  $\mu_c = e\langle \tau \rangle / m^*$  is known as the “conductivity” mobility, since the quantity  $ne\mu_c$  is just the conductivity  $\sigma$ . We define the “Hall” mobility as  $\mu_H = R_H \sigma = r\mu_c$ , and the “Hall” concentration as  $n_H = n/r = -1/eR_H$ . Thus, a combined Hall-effect and conductivity measurement gives  $n_H$  and  $\mu_H$ , although we would prefer to know  $n$ , not  $n_H$ ; fortunately, however,  $r$  is usually within 20% of unity, and is almost never as large as two. In any case,  $r$  can often be calculated or measured so that an accurate value of  $n$  can usually be determined.

The relaxation time,  $\tau(\mathcal{E})$ , depends upon how the electrons interact with the lattice vibrations as well as with extrinsic elements, such as charged impurities and defects. For example, acoustical-mode lattice vibrations scatter electrons through the deformation potential ( $\tau_{ac}$ ) and piezoelectric potential ( $\tau_{pe}$ ); optical-mode vibrations through the polar potential ( $\tau_{po}$ ); ionized impurities and defects through the screened coulomb potential ( $\tau_{ii}$ ); and charged dislocations, also through the coulomb potential ( $\tau_{dis}$ ). The strengths of these various scattering mechanisms depend upon certain lattice parameters, such as

dielectric constants and deformation potentials, and extrinsic factors, such as donor, acceptor, and dislocation concentrations,  $N_D$ ,  $N_A$ , and  $N_{dis}$ , respectively [14-16]. The total momentum scattering rate, or inverse relaxation time, is

$$\tau^{-1}(\mathcal{E}) = \tau_{ac}^{-1}(\mathcal{E}) + \tau_{pe}^{-1}(\mathcal{E}) + \tau_{po}^{-1}(\mathcal{E}) + \tau_{ii}^{-1}(\mathcal{E}) + \tau_{dis}^{-1}(\mathcal{E}) \quad (4)$$

and this expression is then used to determine  $\langle \tau^n(\mathcal{E}) \rangle$  via Eq. 3, and thence,  $\mu_H = e\langle \tau^2 \rangle / m^* \langle \tau \rangle$ . Formulas for  $\tau_{ac}$ ,  $\tau_{pe}$ ,  $\tau_{po}$ ,  $\tau_{ii}$ , and  $\tau_{dis}$ , can be found in the literature, and, fortunately, the only unknowns in Eq. 1-4, are  $N_D$ ,  $N_A$ , and  $N_{dis}$ . For our sample,  $N_{dis}$  is very small, and furthermore,  $N_D$  can be written in terms of  $n$  and  $N_A$ . Thus, the only unknown in the  $\mu_H$  vs.  $T$  fit is  $N_A$ .

The fitting of  $\mu_H$  vs.  $T$  data should be carried out in conjunction with the fitting of  $n$  vs.  $T$  data, and the relevant expression here is the charge-balance equation (CBE) [14]:

$$n + N_A = \frac{N_D}{1 + n / \phi_D} \quad (5)$$

where we have assumed only one type of donor, with a single charge state, and where

$$\phi_D = \frac{g_0}{g_1} e^{\frac{\alpha_D}{k}} N_C' T^{3/2} e^{-\frac{E_{D0}}{kT}} \quad (6)$$

Here,  $g_0/g_1$  is a degeneracy factor,  $N_C' = 2(2\pi m_n^* k)^{3/2} / h^3$  is the effective conduction-band density of states at 1K,  $h$  is Planck's constant,  $E_D$  is the donor ground-state energy, and  $E_{D0}$  and  $\alpha_D$  are defined by  $E_D = E_{D0} - \alpha_D T$ . If more than one donor is needed to fit the data, then equivalent terms are added on the right hand side of Eq. 5. Examples of common, single-charge-state donors in GaN are Si on a Ga site, and O on an N site. If there are double or triple donors, or more than one acceptor, proper variations of Eq. 5 can be found in the literature [14].

If the donors are effective-mass-like, they will have a set of excited states, much like those of hydrogen. Using standard statistical analysis, we can add hydrogenic-type excited states ( $j = 2, 3, \dots, m$ ) to the analysis by modifying  $\phi_D$  [14,17].

$$\phi_D = \frac{g_0}{g_1} e^{\frac{\alpha_D}{k}} N_C T^{3/2} \frac{e^{-\frac{E_{D0}}{kT}}}{1 + \sum_{j=2}^m j^2 e^{-\left(1 - \frac{1}{j^2}\right) \frac{E_{D0}}{kT}}} \quad (7)$$

where we have assumed that  $g_j/g_0 = j^2$ , as is the case for the hydrogen atom, and also that  $\alpha_D$  is the same for each state. (Actually, in any case,  $\alpha_D$  should be small for an effective-mass-like donor state.) At low temperatures, only the ground state will be occupied, and the additional term in the denominator of Eq. 7 will be small. However, at higher temperatures, the  $n$  vs.  $T$  curve will be modified. To see the effects of excited states in GaN, we plot  $\ln(n)$  vs.  $1/T$  for the case of 0, 2, and 10 excited states. Here, we have assumed parameters appropriate for the present sample:  $E_{D0} = 32.7$  meV ( $O_N$ ),  $g_0 = 1$ ,  $g_1 = 2$ ,  $\alpha_D = 0$ ,  $m^* = 0.22 m_0$ ,  $N_D = 7.8 \times 10^{15} \text{ cm}^{-3}$ , and  $N_A = 1.3 \times 10^{15} \text{ cm}^{-3}$ . As seen in Fig. 4, two excited states have only a small effect on the curve, but ten have a very large effect. However, is it reasonable to include ten or more excited states in the analysis? The answer is no, as argued below.

In the hydrogenic model, the orbital radius of the  $m^{\text{th}}$  excited state is  $r_m = m^2 a_0$ , where  $a_0$  is the Bohr radius,  $a_0 = 0.529 \epsilon_0 / m^*$ . For GaN,  $m^*$  is well determined at  $0.22 m_0$ , and we can then get  $\epsilon_0 = 10.14$  from Moore's determination [9] of the Rydberg,  $R = 0.0291 \text{ eV} = 13.6 m^* / \epsilon_0^2$ . So,  $a_0 \approx 24 \text{ \AA}$  for GaN. For a given donor density  $N_D$ , the  $m^{\text{th}}$  orbitals will begin to overlap at the approximate condition  $(4/3) \pi r_m^3 N_D = 1$ . The energy of the  $m^{\text{th}}$  excited state, with respect to the conduction band, is  $E_C - R/m^2 = E_C - R a_0 / r_m = E_C - [(1.16 \times 10^{-4}) / \epsilon_0] N_D^{1/3} \text{ meV}$ . For  $\epsilon_0 = 10.14$ , in GaN, this expression becomes  $E_C - (1.14 \times 10^{-5}) N_D^{1/3} \text{ meV}$ . Because of the wavefunction overlap in the  $m^{\text{th}}$  orbital, donor-band conduction will begin to take place, so that the *effective* conduction-band minimum is lowered by  $R/m^2$ , at least from a conductivity point of view. Or, equivalently, the effective donor energy is reduced by  $R/m^2$ , or approximately  $E_{D0}/m^2$ . We can now also see that it doesn't make sense to include excited states higher than  $m$ , because they are essentially in the conduction continuum [18]. For our sample,  $N_D = 7.8 \times 10^{15} \text{ cm}^{-3}$ , so that  $r_m \approx 313 \text{ \AA}$ , and thus  $m = (r_m/a_0)^{1/2} \approx 3.58$ . Allowing  $m$  to remain a non-integer, we

can then calculate the *predicted* Hall-effect donor energy in our example to be  $32.7 - 29.1/12.83 = 30.4$  meV.

The Hall mobility  $\mu_H$  data, and the theoretical fit are plotted vs. temperature in Fig. 5. From these data, an acceptor concentration  $N_A = 1.3 \times 10^{15} \text{ cm}^{-3}$  is deduced, the lowest ever determined in GaN. The carrier concentration data, corrected for the Hall r-factor, are plotted in Fig. 6, along with the theoretical fit (Eq. 5). Here two donors are found from the fit:  $N_{D1} = 7.8 \times 10^{15} \text{ cm}^{-3}$ ,  $E_{D1} = 28.1$  meV; and  $N_{D2} = 1.1 \times 10^{15} \text{ cm}^{-3}$ ,  $E_{D1} = 53.2$  meV. Also, the fitted acceptor concentration  $N_A$  is  $7.2 \times 10^{14} \text{ cm}^{-3}$ , a little smaller than the value found from the mobility fit, but not considered to be as accurate as the latter. The main point here is that  $E_D(\text{Hall}) < E_D(\text{PL})$  by a few meV, as predicted from the above analysis. Although the analysis predicts a difference of 2.3 meV, and the actual difference is 4.6 meV, still the crudeness of the wavefunction-overlap model would not be expected to give precise results. For example, the random nature of the donor distribution should be included. Also, there is one more factor to consider, i.e., the effects of *non-overlapping* excited states ( $m = 2$  and 3, in this case).

At low temperatures, Eq. 5 can be written,  $n = (N_D/N_A - 1)\phi_D$ , and the donor activation energy is often determined by plotting  $\ln(n/T^{3/2})$  vs.  $1/T$ . Including excited states in  $\phi_D$  (Eq. 7), and ignoring the small difference between  $E_D$  and  $R$ , we can show that the slope of this plot is

$$\frac{d[\ln(n/T^{3/2})]}{d(1/T)} = -\frac{E_D}{k} \left\{ \frac{1 + \sum_2^m e^{-E_D(1-1/j^2)/kT}}{1 + \sum_2^m j^2 e^{-E_D(1-1/j^2)/kT}} \right\} \quad (8)$$

Clearly, the magnitude of the slope will be less than the typically assumed value,  $E_D/k$ ; however, the question is, how much less? In the present case, with wavefunction overlap predicted at  $m = 3.58$ , we should include only the  $m = 2$  and 3 excited states in the analysis. Still, the value of the bracketed term in Eq. 8 cannot be calculated precisely, because it depends upon temperature. For  $E_D = 30$  meV, the bracketed term is about 0.987 at  $T = 40$  K, 0.969 at 50 K, and 0.923 at 60 K. For our sample, the low-temperature slope would best be determined at  $T = 40$  K, and the existence of excited states would lower the measured slope here by about 1.3% of 29.1 meV, or about 0.4 meV. However,

fitting algorithms generally fit the whole curve, not just the low-temperature part; thus, it is difficult to predict the final fitted value of  $E_D$ , except that it will be too low if excited states are not properly included in the analysis.

## CONCLUSIONS

The analysis of thick GaN layers grown by HVPE demonstrates that donor and acceptor concentrations below  $10^{16} \text{ cm}^{-3}$ , and 300-K mobilities above  $1200 \text{ cm}^2/\text{V-s}$ , can be reproducibly achieved [19]. The high purity is most likely due to the lower dislocation density in thick material, because dislocations can promote the diffusion of point defects and impurities from the substrate. Such high-quality material allows us to gain insight into the difference between the donor energies as measured by Hall-effect and photoluminescence measurements, a difference which is nearly universal in semiconductor research. By consideration of the two-electron satellite transitions seen in the PL measurements, and the value of the Rydberg in GaN, determined by another group [9], we find that the dominant donor (probably  $\text{O}_N$ , but possibly Si) has a ground-state energy of between 32.7 and 33.9 meV. The *measured* Hall-effect energy  $E_D(\text{Hall})$ , on the other hand, is expected to be less than the *true* ground-state energy, because: (1) donor-band conduction, which can occur as the excited-state orbitals begin to overlap, reduces the activation energy necessary for strong, band-type conductivity; and (2) non-overlapping excited states are typically (and wrongly) excluded when fitting  $n$  vs.  $T$  with the charge-balance equation (CBE). We calculate that the overlap effect should reduce  $E_D(\text{Hall})$  by about 2.3 meV, for  $N_D = 7.8 \times 10^{15} \text{ cm}^{-3}$ , and that the failure to include excited states in the CBE analysis should further reduce  $E_D(\text{Hall})$  by at least 0.4 meV, and perhaps more. (Note that care must be taken to include in the CBE only *non-overlapping* excited states,  $m = 2$  and 3 in this case.) A conclusion of this investigation is that a true ground-state energy can, in principle, be found from PL data, but not from Hall data, unless  $N_D$  is very low and excited states are properly included in the analysis. However, the PL determination requires the observation of one or more TES lines, and also a good value for the GaN Rydberg, presently thought to be about 29.1 meV, but possibly higher.

There are also other explanations of why  $E_D(\text{Hall}) < E_D(\text{PL})$ . Perhaps the most common of these is that PL will mainly sample the lowest- $N_D$  (highest  $E_D$ ) parts of the sample, because those parts give the sharpest, most intense spectral lines, whereas Hall-effect measurements will sample the highest- $N_D$  (lowest  $E_D$ ) parts, because those parts conduct the most current. While this mechanism may be valid for samples with high inhomogeneity, the model we have proposed is valid in all cases, and indeed, is fundamental. An interesting corollary of our analysis is that when  $N_D$  is high enough that the  $m=2$  orbitals began to overlap, then the PL TES lines (which usually derive from the  $m=2$  orbitals) may be affected, and it may no longer be possible to get an accurate ground-state energy from PL data. From our analysis, this condition should occur at  $N_D = 2.6 \times 10^{17} \text{ cm}^{-3}$  in GaN. Further research on these ideas should be conducted, especially on samples with different values of  $N_D$ .

## ACKNOWLEDGMENTS

We wish to thank T.A. Cooper for the Hall-effect measurements, W. Rice for the PL measurements, W. Swider for TEM sample preparation, and the NCEM in Berkeley for the use of the TEM facility. We also would like to thank W.J. Moore for helpful discussions. DCL was supported under AFOSR Grant F49620-00-1-0347 and ONR Grant N00014-02-1-0606, and most of his work was carried out at the Air Force Research Laboratory, Wright-Patterson AFB, Ohio. JJ and ZL-W were supported by AFOSR, Order No. FQ86710200652, through the U.S. Department of Energy under Contract No. DE-AC03-76F00098.

## REFERENCES

1. H.P. Maruska and J.J. Tietjen, Appl. Phys. Lett. **15**, 327 (1969).
2. D.C. Look, C.E. Stutz, R.J. Molnar, K. Saarinen, and Z. Liliental-Weber, Solid State Commun. **117**, 571 (2001).
3. J. Jasinski and Z. Liliental-Weber, J. Electron. Mater. **31**, 429 (2002).
4. R.J. Molnar, K.B. Nichols, P. Makai, E.R. Brown, and I. Melngailis, Mater. Res. Soc. Symp. Proc. **378**, 479 (1995).
5. S.S. Park, I-W. Park, and S.H. Choh, Jpn. J. Appl. Phys., Part 2 **39**, L1141 (2000).
6. E. Oh, S.K. Lee, S.S. Park, K.Y. Lee, I.J. Song, and J.Y. Han, Appl. Phys. Lett. **78**, 273 (2001).
7. D.C. Look and R.J. Molnar, Appl. Phys. Lett. **70**, 3377 (1997).
8. Evans East, 104 Windsor Center, East Windsor, NJ, 08520
9. W.J. Moore, J.A. Freitas, Jr., S.K. Lee, S.S. Park, and J.Y. Han, Phys. Rev. B **65**, 081201 (2002).
10. K. Saarinen, J. Nissilä, P. Hautojärvi, J. Likonen, T. Suski, I. Grzegory, B. Lucznik, and S. Porowski, Appl. Phys. Lett. **75**, 2441 (1999).
11. J. Oila, J. Kivioja, V. Ranki, K. Saarinen, D.C. Look, R.J. Molnar, and S.S. Park (to be published).
12. J. Neugebauer and C.G. Van de Walle, Phys. Rev. B **50**, 8067 (1994).
13. K. Kornitzer, T. Ebner, K. Thonke, R. Sauer, C. Kirchner, V. Schwegler, M. Kamp, M. Leszczynski, I. Grzegory, and S. Porowski, Phys. Rev. B **60**, 1471 (1999).
14. D.C. Look, *Electrical Characterization of GaAs Materials and Devices* (Wiley, New York, 1989), Ch.1.
15. D.L. Rode, Semicond. Semimetals **10**,1 (1975).
16. B.R. Nag, *Electron Transport in Compound Semiconductors* (Springer, Berlin, 1980).
17. D.V. Eddolls, J.R. Knight, and B.L.H. Wilson, in *Proc. Int. Symp. on GaAs*, ed. by J. Franks and W.G. Moore (Inst. Phys., London, 1967) pp.3-9.
18. G.E. Stillman and C.M. Wolfe, Thin Solid Films **31**, 69 (1976).
19. D.C. Look and J.R. Sizelove, Appl. Phys. Lett. **79**, 1133 (2001).

Fig. 1. Cross-sectional TEM micrograph of the region near the Ga face. Note the lack of dislocation features.



Fig. 2. Photoluminescence spectrum in exciton region. The portion of the spectrum above 3.475 eV has been multiplied by a factor 10, to emphasize the weak lines.

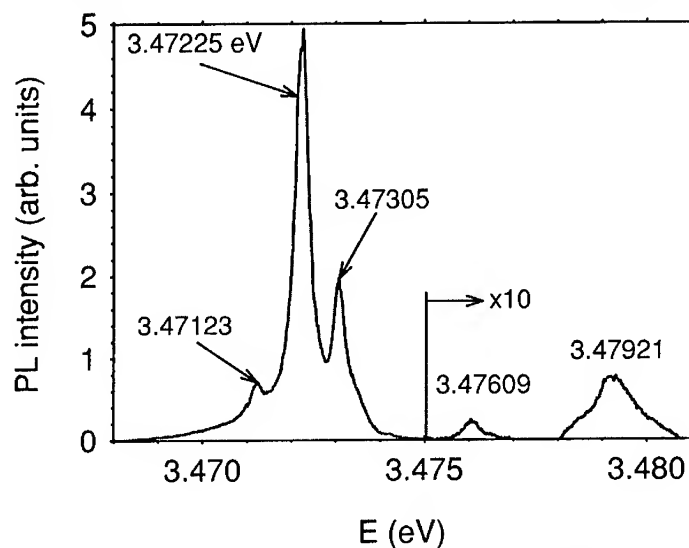


Fig. 3. Comparison of exciton lines (solid curve – unshifted), and TES lines (dashed curve – shifted up by 25.4 meV). The dashed curve has been multiplied by a factor 89 over the full range, while a portion of the solid curve, from 3.475 – 3.481 eV, has been multiplied by a factor 10.

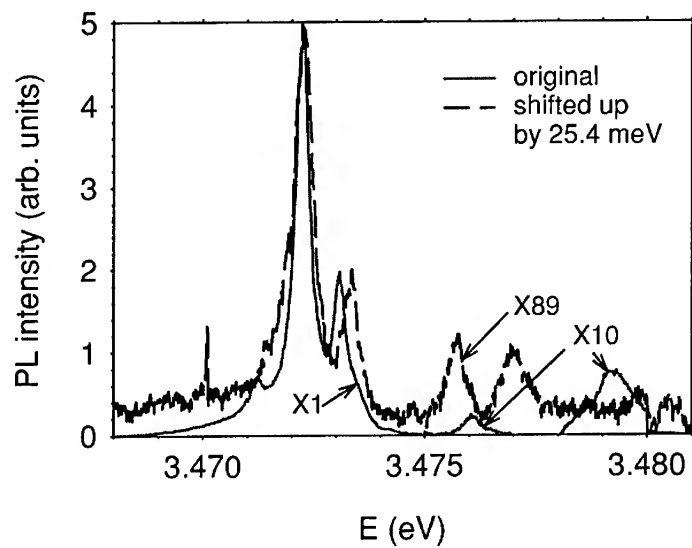


Fig. 4. Effects of donor excited states on simulated Hall-effect data.

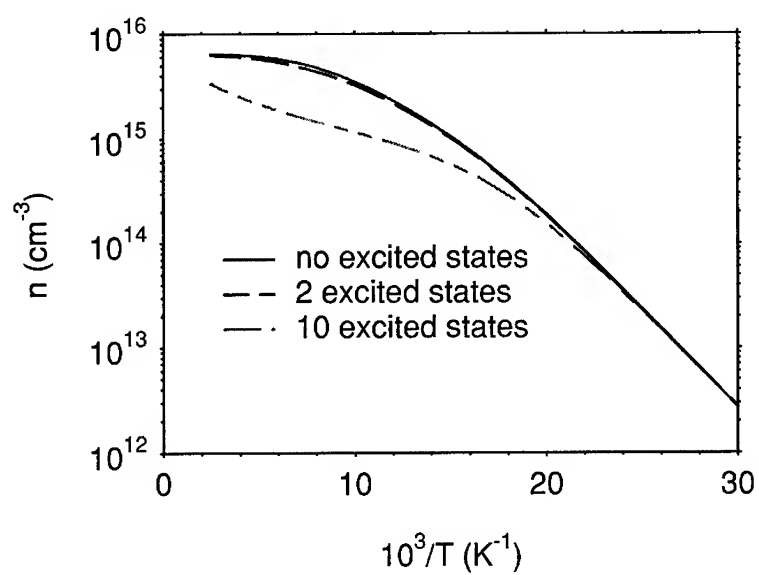


Fig. 5. Experimental and theoretical Hall mobility plots.

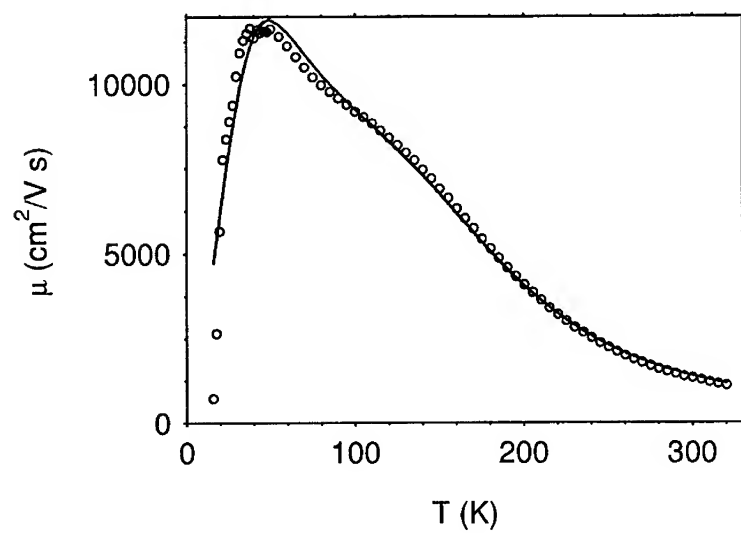
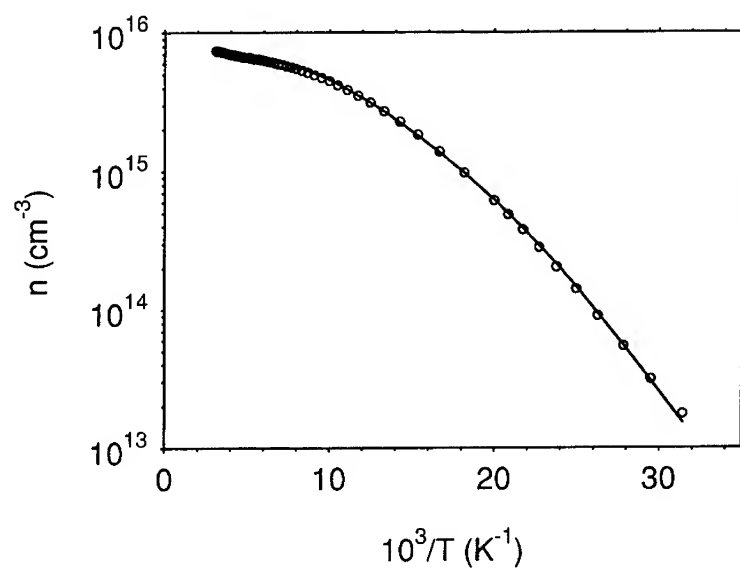


Fig 6. Experimental and theoretical carrier concentration plots.



## Observations of electron velocity overshoot during high-field transport in AlN

Ramón Collazo, Raoul Schlessler, Amy Roskowski, Robert F. Davis and Z. Sitar  
Department of Materials Science and Engineering, North Carolina State University,  
Raleigh, N.C. 27695-7919

### ABSTRACT

The energy distribution of electrons transported through an intrinsic AlN film was directly measured as a function of the applied electric field. Following the transport, electrons were extracted into vacuum through a semitransparent Au electrode and their energy distribution was measured using an electron spectrometer. The electron energy distribution featured kinetic energies higher than that of completely thermalized electrons. Transport through 80 nm thick layers indicated the onset of quasi-ballistic transport. This was evidenced by symmetric energy distributions centered at energies above the conduction band minimum for fields greater than 530 kV/cm. Drifted Fermi-Dirac energy distributions were fitted to the measured energy distributions, with the energy scale referenced to the bottom of the AlN conduction band. The drift energy and the carrier temperature were obtained as fitting parameters. Overshoots as high as five times the saturation velocity were observed and a transient length of less than 80 nm was deduced. In addition, the velocity-field characteristic was derived from these observations. This is the first experimental demonstration of this kind of transport in AlN.

### INTRODUCTION

Transient transport is characterized by the onset of ballistic or velocity overshoot phenomena. It takes place in spatial lengths in the sub-micron range, and occurs in rapidly changing applied fields or immediately after the application of a field. In AlN, this phenomenon is expected to occur for transport lengths of less than 100 nm, and field strengths greater than 450 kV/cm.<sup>1</sup> Ballistic transport can be simply described by the acceleration of an electron immediately after the application of a field: inertial effects limit the acceleration of the electron, while subsequent scattering events start randomizing the momentum and limiting the energy, thus causing the system to eventually reach a steady state. Nevertheless, a velocity overshoot with respect to the steady-state velocity is obtained before the steady state is reached. The energy relaxation time characterizes the time scale of this overshoot<sup>2</sup>, which is usually of the order of tenths of picoseconds.

Transport with velocity overshoot occurs between the limit of the ballistic transport and before it reaches a steady-state transport condition. The velocity in this regime is still higher than the steady-state velocity but slightly smaller than the ballistic velocity. In this transient regime, the energy increases progressively from the equilibrium energy (thermal energy) towards its steady-state value.<sup>2</sup> The overshoot effect can be explained in the following way: the electron mobility decreases with increasing average

carrier energy for most semiconductors; as a result, the instantaneous drift velocity reaches higher values at the beginning of the motion when the average carrier energy is close to the thermal energy ( $w_0$ ) and thus the mobility will keep a value higher than that of the steady state.<sup>2</sup>

Hot-electron and ballistic transport have been observed in several materials, including AlN, ZnS and GaAs.<sup>3,4,5</sup> The experimental procedure consists of extracting hot electrons into vacuum through a semitransparent electrode and performing direct measurements of their kinetic energy by means of an electron spectrometer. Measured energy spectra allow one to distinguish between the aforementioned types of electron transport. In this letter, we present experimental evidence for the presence of velocity overshoot during the electron transport in AlN thin films at high fields. From these measurements, we estimate important parameters related to transient transport, e.g., overshoot drift velocity and drift energy.

## EXPERIMENT

The nature of electron transport can be determined using an electron spectrometer to directly measure electron energy distribution (EED) of electrons extracted into vacuum, following their transport through a thin film. The experimental device structure that allows such measurements consists in our case of the semiconducting layer to be investigated, sandwiched between a semitransparent Au top electrode and an Ohmic back contact ( $n^+$ -SiC/Ti/Au). Electrons can be transported through the semiconductor and emitted into vacuum by the application of an electric potential between these two contacts, thus establishing an internal electric field that can be easily deduced from the thickness of the semiconducting layer in this planar structure. The bands of the semiconducting layer are bent due to the presence of the applied electric field. The position of the conduction band at the surface can be used as an absolute reference to measure the kinetic energy of the electrons prior to their extraction into vacuum. A complete description of the experimental procedure, details on the bandstructure of the device and current-voltage characterization along with a schematic of the test structure under an applied electric field can be found elsewhere.<sup>3,6</sup>

During the experiments, the potential across the AlN sample was applied using a Keithley 238 High Current Source Measure Unit. All measurements were performed inside a Surface Analysis Chamber with a base pressure of  $1 \times 10^{-10}$  Torr, equipped with a VG Clam II semi-hemispherical electron analyzer. After the deposition of the contacts, the sample was prepared for the experiments and introduced into the vacuum system. The sample was heated in a UHV cleaning chamber for a few hours at 250°C before being transferred in vacuo to the surface analysis chamber. All energy distribution measurements were taken at a spectrometer pass energy of 5 eV, providing a spectral resolution of 0.2 eV.

## RESULTS AND DISCUSSION

Energy distribution of electrons which traversed an 80 nm thick AlN film was measured. Figure 1 shows a cascade plot of energy distributions for different applied electric fields. In a first order approximation, under an applied field  $E$ , a carrier

momentum distribution function is given by  $f_p = f_p^0(\mathbf{p} - e\tau\mathbf{E})$ , where  $\tau$  is the momentum relaxation time, and  $\mathbf{p}$  is the electron momentum. If the distribution is of Maxwellian type, the carrier energy is given by  $w = 3kT_e/2 + m^*v_d^2/2$ , where the first term represents the thermal component at an electron temperature  $T_e$  and the second term the drift component corresponding to the electron drift velocity  $v_d$  and an effective mass  $m^*$ . In a thermal distribution, the drift component of the energy is negligible as compared to the thermal component, especially if the carrier temperature is higher than the lattice temperature. A symmetric energy distribution, however, indicates that the drift component of the carrier energy cannot be neglected, even though some carrier thermalization may have occurred. Usually, this condition is observed as a transient effect, leading to a drift velocity overshoot or, as an extreme case, ballistic transport. The electron energy distributions corresponding to fields greater than 560 kV/cm were clearly symmetric around a specific energy above the conduction band minimum and shifted towards higher energies as the field was increased. These symmetric distributions were not observed for thicker AlN layers in the same range of applied fields.<sup>6</sup>

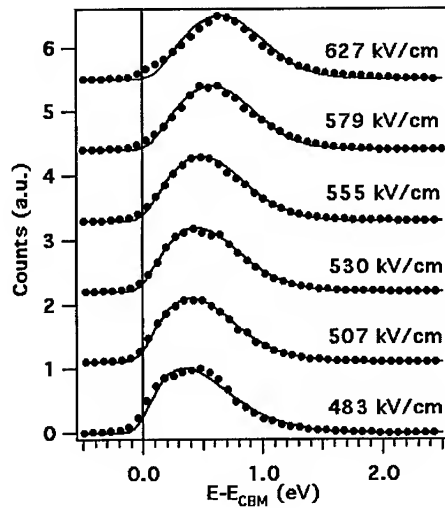


**Figure 1.** Cascade plot showing normalized electron energy distributions taken at different fields across the sample for an AlN layer 80 nm thick. The solid lines represent the best fits of the experimental data to the drifted Fermi-Dirac distribution.

The relaxation time approximation can be used to characterize the drift component of the distribution. The drifted, or displaced, momentum distribution is  $f_p = f_p^0(\mathbf{p} - m^*\mathbf{v}_d)$  in the first order approximation. Considering a Fermi-Dirac distribution and a parabolic band approximation, the energy distribution can be written as

$$(1) \quad f(\varepsilon, \cos\theta) = \left[ \exp\left( \frac{w_d + \varepsilon - 2\cos\theta\sqrt{\varepsilon w_d}}{k_B T_e} \right) + 1 \right]^{-1},$$

where  $\varepsilon$  is the electron energy and the drift component of the energy is given by  $w_d = m^* v_d^2 / 2$ . The distribution depends on the angle between the carrier momentum and its drift component,  $\theta$ . As the drift component becomes considerable with respect to the thermal component, the energy distribution will become more pronounced in the forward direction. A completely thermal distribution will have spherical symmetry. Under our experimental conditions, angle-dependence could not be measured; instead, angle-averaged electron energy distributions were recorded. If the drift component of the energy is at least half as large as the thermal component, the distribution can be assumed to be completely oriented in the forward direction,<sup>7</sup> thus  $\langle \cos \theta \rangle \approx 1$ . Moreover, the metallic top contact and the electron analyzer act as electron lenses, averaging the actual angular distribution. Considering this angle averaging, the energy distribution becomes

$$(2) \quad f(\varepsilon) = f(\varepsilon, \langle \cos \theta \rangle) = \left[ \exp \left( \frac{w_d + \varepsilon - 2\sqrt{\varepsilon w_d}}{k_B T_c} \right) + 1 \right]^{-1}.$$

Using this expression, we fitted the experimental electron energy distributions obtained from an 80 nm thick AlN layer; results are shown in Figure 1. The fitting procedure, which takes into account the conduction band density of states and a peak broadening induced by the finite resolution of the spectrometer, is described elsewhere.<sup>6</sup> For all the experiments, the energy scale was referenced to the bottom of the AlN conduction band. The drift energy and the carrier temperature were obtained as fitting parameters.

In all the measurements, the average angle  $\theta$  was close to  $0^\circ$ , as the value of the drift energy was comparable to the thermal component of the average carrier energy. Figure 2 shows the field strength dependence of the drift and the thermal energy. The average carrier energy as a function of field strength is also shown.

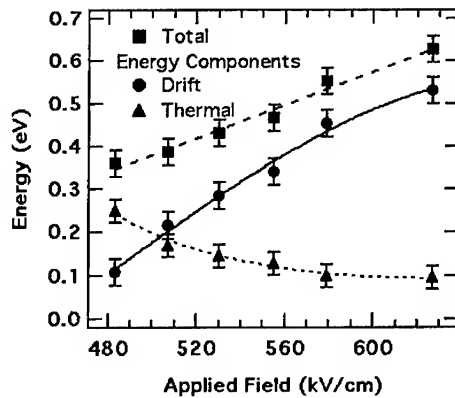


**Figure 2.** Drift and thermal component of the average carrier energy as a function of field strength for the energy distributions shown in Figure 1. The total average carrier energy is the sum of both energy components. The lines are visual guidelines only.

For low fields, and in particular in the case of steady-state distributions, the drift component is smaller than the thermal component. As can be seen in Figure 2, the total average carrier energy increases monotonically with the applied field and the drift component becomes higher than the thermal component for fields greater than  $\sim 510$  kV/cm. This is a signature of velocity overshoot. Figure 3 shows the drift velocity characteristic curves for this field range. Data points are calculated for the two values of effective electron mass used in previously published Monte Carlo simulations.<sup>8,9</sup> The error bars are estimated from the  $\pm 0.03$  eV uncertainty in the drift energy fit parameter.

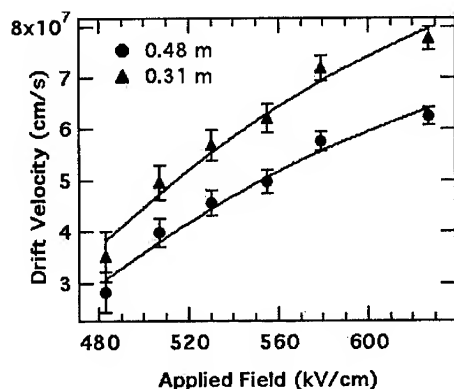


**Figure 3.** Drift velocity characteristic curves for a transport length of 80 nm. Effective electron masses of 0.48 and 0.31 are used for this curve. The solid lines are visual guidelines only.

In transient effects, the effective mass plays an important role in determining the overshoot velocity. For example, at a field of 627 kV/cm, the drift velocity is  $6 \times 10^7$  cm/s for an effective electron mass of 0.48<sup>8</sup>, while an effective electron mass of 0.31<sup>9</sup> yields a drift velocity of  $7.7 \times 10^7$  cm/s, or 30 % higher. These values are approximately five times higher than the saturation velocities estimated for each of the effective masses.<sup>8,9</sup> We do not expect the drift velocities reported here to be the maximum overshoot velocities; it is likely that the transient length in AlN, defined as  $\ell_E \approx v_d \tau_E$ , is smaller than the layer thickness of 80 nm investigated here. Experiments using thicker samples indicated that for transport lengths of 100 nm steady-state transport was already realized.<sup>6</sup>

## CONCLUSION

Transient transport under high electric fields was identified to occur in AlN. Velocity overshoot, a characteristic of transient transport, was recognized from a large drift component of the average carrier energy. These parameters were determined by fitting the experimental energy distributions to a drifted Fermi-Dirac distribution. Overshoot drift velocity characteristic curves were estimated from the drift component of the energy for two different values of the effective electron mass. Overshoot as high as five times the expected saturation velocity<sup>8,9</sup> was observed for the highest applied

electric fields. From these observations, we determined that the transient length for AlN is likely to be shorter than the transport length used for these experiments, i.e. 80 nm.

#### ACKNOWLEDGMENTS

The authors acknowledge Dr. Amy Roskowski and Prof. R. F. Davis for supplying the samples used in this work. Financial assistance from the Office of Naval Research, under the auspices of the MURI program, is gratefully acknowledged: Grant No. N00014-98-1-0654. (Monitored by Drs. J. Zolper and H. Dietrich)

#### REFERENCES

- <sup>1</sup> B. E. Foutz, S. K. O'Leary, M. S. Shur, and L. F. Eastman, *J. Appl. Phys.* **85**, 7727 (1999).
- <sup>2</sup> E. Constant, in *Topics in Applied Physics: Hot-Electron Transport in Semiconductors*, 1st edition, edited by L. Reggiani (Springer-Verlag, Berlin, 1985), Vol. **58**, Chap. 8, p.227.
- <sup>3</sup> R. Collazo, R. Schlessner, A. Roskowski, R. F. Davis, and Z. Sitar, *J. Appl. Phys.* **88**, 5865 (2000).
- <sup>4</sup> H. J. Fitting, G. O. Müller, R. Mach, G. U. Reinsperger, Th. Hingst, and E. Schreiber, *Phys. Status Solidi A* **121**, 305 (1990).
- <sup>5</sup> H. J. Fitting, Th. Hingst, E. Schreiber, and E. Geib, *J. Vac. Sci. Technol. B* **14**, 2087 (1996).
- <sup>6</sup> R. Collazo, R. Schlessner, A. Roskowski, P. Miraglia, R.F. Davis, and Z. Sitar, to be published in *J. Appl. Phys.*
- <sup>7</sup> R. Collazo, Ph.D. Dissertation, North Carolina State Univ. (2002).
- <sup>8</sup> S. K. O'Leary, B. E. Foutz, M. S. Shur, U. V. Bhapkar, and L. F. Eastman, *Solid State Commun.* **105**, 621 (1998).
- <sup>9</sup> J. D. Albrecht, R. P. Wang, P. P. Ruden, M. Farahmand, and K. F. Brennan, *J. Appl. Phys.* **83**, 1446 (1998).

### Determination of AlGaIn/GaN HFET Electric Fields using Electroreflectance

S. R. Kurtz, A. A. Allerman, D. D. Koleske, A. G. Baca, and R. D. Briggs  
Sandia National Laboratories  
Albuquerque, NM 87185-0601, U.S.A.

#### Abstract

A contacted electroreflectance technique was used to characterize the electronic properties of AlGaIn/GaN heterostructure field-effect transistors (HFETs). By studying variations in the electroreflectance with applied electric field, spectral features associated with the AlGaIn barrier, the 2-dimensional electron gas at the interface, and bulk GaN were observed. Barrier-layer composition and electric field were determined from the AlGaIn Franz-Keldysh oscillations. Comparing HFETs grown on SiC and sapphire substrates, the measured AlGaIn polarization electric field ( $0.25 \pm 0.05$  MV/cm) approached that predicted by a standard model (0.33 MV/cm) for the higher mobility HFET grown on SiC.

#### Introduction

Large piezoelectric and spontaneous polarization fields occurring in AlGaIn/GaN heterostructures can generate a 2-dimensional electron gas (2DEG) without doping. The unusually large 2DEG carrier densities ( $>1 \times 10^{13}/\text{cm}^2$ ), electron saturation velocities, breakdown fields, and thermal conductivities found in these structures make them attractive as heterostructure-field-effect-transistors (HFETs) for high voltage, high power microwave amplifiers.[1-5] In this work, we use a contacted electroreflectance measurement technique to identify distinct spectral features associated with the 2DEG and the AlGaIn barrier. We show that electroreflectance augments conventional electrical characterization of GaN-based HFETs by providing a direct measurement of the electric field in the AlGaIn barrier.

#### Experiment

AlGaIn/GaN samples were grown by metal-organic chemical vapor deposition (MOCVD). An AlN nucleation layer was used to initiate GaN growth on sapphire or SiC substrates. Thickness of the top AlGaIn barrier, the 2DEG sheet concentration, and the 2DEG depletion or pinch-off voltage were determined from Hall mobility and capacitance measurements for each sample. Gated van der Pauw contacts ( $1-4 \text{ mm}^2$ ) were used for electroreflectance. Ohmic Ti/Al/Ni/Au source and drain contacts at corners of the sample penetrated to contact the 2DEG. Oxidized Ni(75 Å)/Au(75 Å) formed an optically transparent, Schottky-barrier gate contact. Electroreflectance measurements were performed with a 150W Xe lamp. Typical gate voltage modulation amplitudes were  $0.2 V_{pp}$  @ 100 Hz, with grounded source and drain.

## Results and Discussion

An electroreflectance spectrum for an AlGaIn/GaN HFET, grown on sapphire, is shown in Fig. 1. As reported previously for thicker InGaIn [6] and AlGaIn [7] layers, Franz-Keldysh oscillations (FKOs) from the AlGaIn barrier, polarization-induced electric field were clearly observed. The period of the FKO increased as the barrier electric field increased with negative gate bias, enabling unambiguous identification of those features associated with the AlGaIn barrier.[8] In addition, a broad 2DEG feature appeared at energies just above the bandgap of GaN.[8-10] As the 2DEG was depleted, the broad feature narrowed and converged with the GaN band-edge feature. [8]

Experimental AlGaIn FKO spectra were least-squares fit to the Airy function formula for a single band-edge, [11] and this fit (see Fig. 1, solid line) produced AlGaIn electric-field (0.50 MV/cm, assuming an electron-hole reduced mass of  $0.2 m_e$ ), bandgap (3.85 eV), and linewidth ( $25 \pm 22$  meV) values close to those obtained from analysis of the high order FKOs with the simple asymptotic expression.[8] As previously discussed, this measured electric field was much larger than the value (0.33 MV/cm) predicted by a "standard model" of this AlGaIn/GaN heterostructure.[5] We speculated that the electric field anomaly may be due to material quality issues such as trapped space charge in the barrier. [8] Our fitting of the AlGaIn FKOs revealed a broad, first-derivative lineshape for the 2DEG in the energy range,  $\approx 3.4$ -3.8 eV. The 2DEG electroreflectance can be modeled using a golden-rule calculation of the dielectric function for the measured 2DEG density,  $5.9 \times 10^{12} \text{ e/cm}^2$ . [12] (see Fig. 1 dashed line)

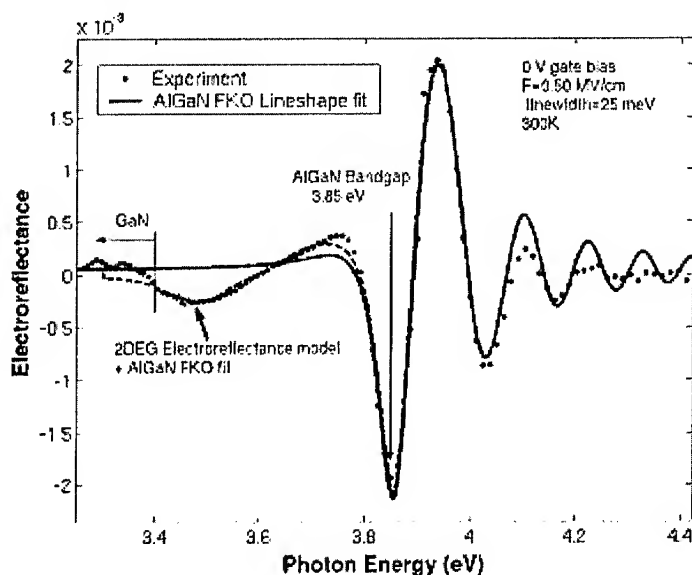


**Figure 1** – Electroreflectance spectrum of an AlGaIn/GaN HFET (0V gate bias) grown on a sapphire substrate. Combined models of the AlGaIn FKO and 2DEG lineshapes are indicated by the dashed line.

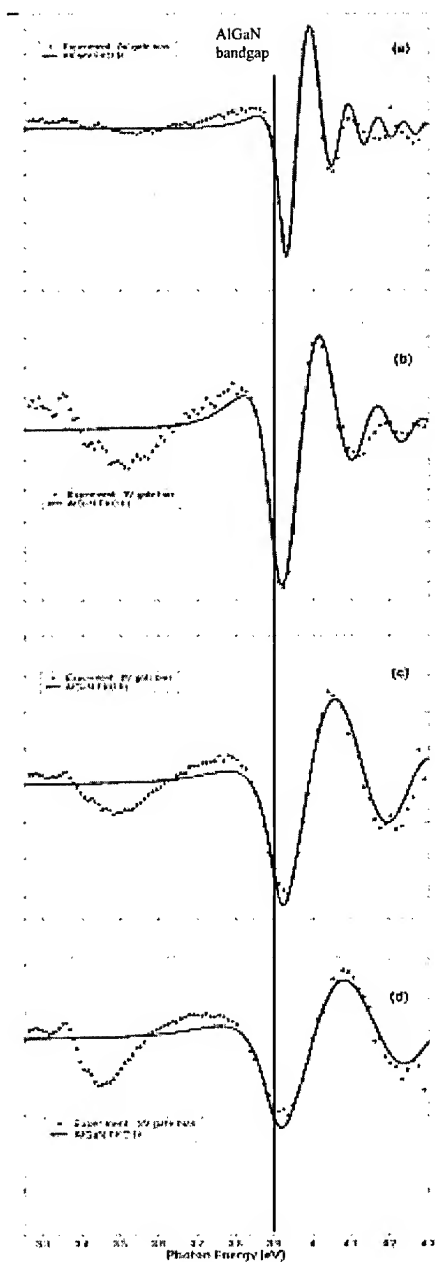


**Figure 2 – (a-d)** Electoreflectance spectra of an AlGaIn/GaN HFET on SiC (300 K) and AlGaIn FKO lineshape fits for 0, -1, -2, and -3 V gate bias.

Overall, the material quality of AlGaIn/GaN HFETs grown on SiC was improved over that obtained for HFETs grown on sapphire. Typically our HFETs on SiC displayed 300K Hall mobilities  $>1000 \text{ cm}^2/\text{V s}$  over a 2DEG density range  $3.5 \times 10^{12} - 1.1 \times 10^{13} \text{ e/cm}^2$ , with the mobility weakly increasing with decreasing 2DEG density over much of that range. For our electroreflectance device on SiC, peak 300K mobility was  $1400 \text{ cm}^2/\text{V s}$  @  $7.4 \times 10^{12} \text{ e/cm}^2$ . However, the 2DEG mobility (300K) for HFETs on sapphire, like that in Fig.1, peaked at  $900 \text{ cm}^2/\text{V s}$  and decreased with decreasing 2DEG density, dropping to  $200 \text{ cm}^2/\text{V s}$  @  $4 \times 10^{12} \text{ e/cm}^2$ . These Hall results indicate that 2DEG mobility was limited by high dislocation densities for our HFETs grown on sapphire, and dislocation densities were reduced in HFETs grown on SiC to levels where scattering in the AlGaIn barrier limited 2DEG mobility.[13,14]

The variation of electroreflectance with gate-bias is shown in Figs. 2(a)-(d) for an AlGaIn/GaN HFET grown on SiC. Clearly the period of the AlGaIn FKO increased with negative bias on the gate and increasing electric field in the AlGaIn. Comparing 0V bias spectra (Figs. 1 and 2(a)), the AlGaIn electric field was lower in the HFET grown on SiC. Best lineshape fits of the FKO spectra in Fig. 2 were obtained with an AlGaIn bandgap of  $3.905 \pm 0.025 \text{ eV}$ . This value was in reasonable agreement with a photoconductivity estimate of the AlGaIn bandgap,  $3.96 \text{ eV}$ . From the bandgap energy, we estimated an  $\text{Al}_x\text{Ga}_{1-x}\text{N}$  composition,  $x=0.19 \pm 0.01$ , based on reflectance data for the bulk alloy.[15,16] Although we infer some improvement in material quality for this HFET on SiC, the AlGaIn electroreflectance linewidth ( $\approx 30 \text{ meV}$ ) was comparable to that observed for devices grown on sapphire.

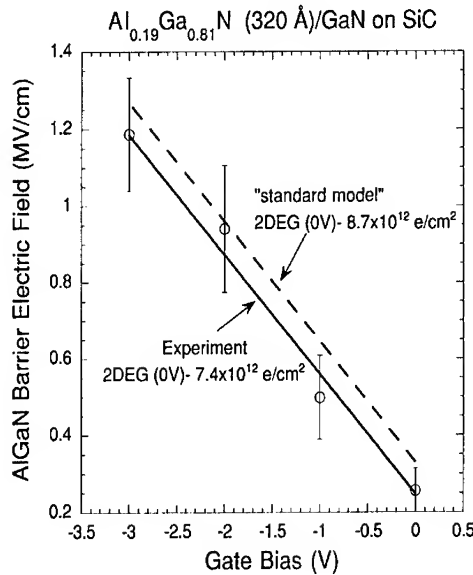


**Figure 3** – AlGaIn barrier electric field obtained from FKOs of HFETs on SiC. Solid line is a weighted linear fit to the data. Electric field predicted by the “standard model” of this heterostructure is indicated by dashed line.

Electric fields determined from the FKO period in Figs. 2(a)-(d) are plotted in Fig. 3. The electric field was roughly linear versus gate bias with the slope indicating  $\approx 100\%$  of the bias dropped across the AlGa<sub>N</sub> barrier, not the source/drain contacts or channel. Thickness of the AlGa<sub>N</sub> barrier (320 Å) was determined from capacitance measurements on the electroreflectance device. Averaging over the data in Fig. 3, we measured a 0V bias, AlGa<sub>N</sub> polarization electric field of  $0.25 \pm 0.05$  MV/cm. Hall and capacitance-voltage measurements both produced a 2DEG density of  $7.4 \times 10^{12}$  e/cm<sup>2</sup> @ 0V bias for this device. The AlGa<sub>N</sub> electric field predicted by the “standard model” for an Al<sub>0.19</sub>Ga<sub>0.81</sub>N (320 Å)/Ga<sub>N</sub> heterostructure (doping mid- $10^{16}$ /cm<sup>3</sup>) is also shown in Fig. 3 (dashed line). [5] The model predicted an electric field of 0.33 MV/cm and 2DEG density of  $8.7 \times 10^{12}$  e/cm<sup>2</sup> @ 0V bias.

Although the model produced electric field and 2DEG density values which remain slightly outside our range of experimental error, we found that agreement between measured and theoretical electric field values was greatly improved in the higher quality HFET grown on SiC. Of course, we could further improve agreement between theory and experiment by adjusting model and sample parameters, but that may be premature because “nonidealities” may still contribute to the results presented for the HFET on SiC. We are attempting to correlate material morphology and electrical properties with the observation of large field anomalies like those for devices grown on sapphire.

### Acknowledgement

The authors thank J. Figiel, T. Bauer, and C. Sanchez for technical support. Sandia is a multiprogram laboratory operated by Sandia Corporation, a Lockheed Martin Company, for the U.S. Dept. of Energy under contract DE-AC04-94AL85000.

### References

- [1] M. A. Khan, J. N. Kuznia, J. M. Van Hove, N. Pan, and J. Carter, Appl. Phys. Lett. **60**, 3027 (1992).
- [2] M. A. Khan, J. N. Kuznia, D. T. Olsen, W. J. Schaff, J. W. Burm, and M. S. Shur, Appl. Phys. Lett. **65**, 1121 (1994).
- [3] S. N. Mohammad, A. A. Salvador, and H. Morkoc, Proc. IEEE **83**, 1306 (1995).
- [4] J. M. Redwing, M. A. Tischler, J. S. Flynn, S. Elhamri, M. Ahoujja, R. S. Newrock, and W. C. Mitchel, Appl. Phys. Lett. **69**, 963 (1996).
- [5] O. Ambacher, J. Smart, J. R. Shealy, N. G. Weimann, K. Chu, M. Murphy, W. J. Schaff, L. F. Eastman, R. Dimitrov, L. Wittmer, M. Stutzmann, W. Rieger, and J. Hilsenbeck, J. Appl. Phys. **85**, 3222 (1999), and references therein.
- [6] C. Wetzel, T. Takeuchi, H. Amano, and I. Akasaki, J. Appl. Phys. **85**, 3786 (1999).
- [7] Y.T. Hou, K. L. Teo, M. F. Li, K. Uchida, H. Tokunaga, N. Akutsu, and K. Matsumoto, Appl. Phys. Lett. **76**, 1033 (2000).
- [8] S. R. Kurtz, A. A. Allerman, D. D. Koleske, and G. M. Peake, Appl. Phys. Lett. **80**, 4549 (2002).
- [9] D. Y. Lin, Y. S. Huang, Y.F. Chen, and K. K. Tiong, Solid State Comm. **107**, 533 (1999).
- [10] E. S. Snow, O. J. Glembocki, and B. V. Shanabrook, Phys. Rev. B **38**, 12483 (1988).

- [11] D. J. Hall, T. J. C. Hosea, and D. Lancefield, *J. Appl. Phys.* 82, 3092 (1997).
- [12] S. R. Kurtz, to be published.
- [13] X. Z. Dang, P. M. Ashbeck, E. T. Yu, G. J. Sullivan, M. Y. Chen, B. T. McDermott, K. S. Boutros, and J. M. Redwing, *Appl. Phys. Lett.* 74, 3890 (1999).
- [14] Debdeep Jena, Arthur C. Gossard, and Umesh K. Mishra, *Appl. Phys. Lett.* 76, 1707 (2000).
- [15] T. J. Ochalski, B. Gil, P. Lefebvre, N. Grandjean, M. Leroux, J. Massies, S. Nakamura, and H. Morkoc, *Appl. Phys. Lett.* 74, 3353 (1999).
- [16] H. Jiang, G. Y. Zhao, H. Isikawa, T. Egawa, T. Jimbo, and M. Umeno, *J. Appl. Phys.* 89, 1046 (2001).

**Optical and electrical properties of semi-insulating GaN:C grown by MBE**R. Armitage<sup>1,2</sup>, Qing Yang<sup>1,2</sup>, H. Feick<sup>3</sup>, S.Y. Tzeng<sup>1,2</sup>, J. Lim<sup>1,2</sup>, and E.R. Weber<sup>1,2</sup><sup>1</sup> Dept. of Materials Science and Engineering, University of California, Berkeley CA 94720<sup>2</sup> Materials Sciences Division, Lawrence Berkeley National Laboratory, Berkeley, CA 94720<sup>3</sup> Center of Advanced European Studies and Research (caesar), Bonn, Germany**ABSTRACT**

Semi-insulating wurtzite GaN:C of high optical quality is obtained with CCl<sub>4</sub> or CS<sub>2</sub> doping sources in plasma-assisted molecular-beam epitaxy in Ga-rich growth conditions. The highest resistivity ( $10^7 \Omega\text{-cm}$ ) is found for [C] in the low  $10^{18} \text{ cm}^{-3}$  range. An increasing fraction of carbon appears to form electrically inactive pair defects for higher doping levels causing the concentration of uncompensated residual donors to be higher in films with [C] in the  $10^{19} \text{ cm}^{-3}$  range compared with [C] in the  $10^{18} \text{ cm}^{-3}$  range. Blue (2.9 eV) and yellow (2.2 eV) luminescence bands are associated with carbon-related defects, and additional support is provided for the association of the blue luminescence with the carbon-acceptor deactivating pair defect. Finally, the temperature dependence of the resistivity is described within the grain-boundary controlled transport model of Salzman *et al.*, *Appl. Phys. Lett.* **76**, 1431 (2000).

**INTRODUCTION**

Carbon is a major residual impurity in GaN grown by metal-organic vapor phase epitaxy (MOVPE), and found practical use as an intentional dopant for semi-insulating GaN [1] and in p-type conducting zincblende GaN [2]. Despite this, understanding of the influence of carbon defects on GaN properties remains limited.

Carbon could conceivably introduce several defect species: C<sub>N</sub>, C<sub>Ga</sub>, and C<sub>i</sub> (interstitial). The calculated formation energies of these different defects are in fact similar [3]. Theory and experiment indicate that at low concentrations carbon forms predominately C<sub>N</sub> acceptors in n-type GaN [3,4]. However, some evidence suggests that a fraction of carbon exists as deep-level defects related to technologically important phenomena such as current collapse in field-effect transistors [5] and parasitic luminescence bands [6].

Few systematic studies were reported for carbon concentrations above  $10^{18} \text{ cm}^{-3}$ . These either involved the metastable zincblende GaN phase [2], or utilized relatively poor-quality wurtzite material [7], obscuring the influence of carbon defects on GaN properties.

**EXPERIMENTAL DETAILS**

GaN epilayers of thickness  $\sim 1 \mu\text{m}$  were grown by MBE in a modified Riber 1000 system equipped with a gallium effusion cell and dc nitrogen plasma source. Semi-insulating ( $10^9 \Omega\text{-cm}$ ) MOVPE-GaN/sapphire templates were used as substrates. The carbon concentration was controlled by injecting CCl<sub>4</sub> or CS<sub>2</sub> vapor (Sigma Aldrich, 99.9%) into the chamber through a needle valve. The growth temperature was 750°C. Ga-rich conditions were maintained for all samples, confirmed by the presence of Ga droplets around the edges of the samples. The N-

limited growth rates studied varied from 120-250 nm/hour. No obvious differences in film properties were found for different growth rates within this range.

The quality of reference MBE films without carbon doping was assessed by Hall effect measurements using indium contacts in the van der Pauw-geometry with a B-field of 0.28 T. A typical electron mobility of 400 cm<sup>2</sup>/V-sec was obtained for  $n \sim 1 \times 10^{17}$  cm<sup>-3</sup>. Samples were characterized by secondary ion mass spectroscopy (SIMS) at Applied Microanalysis Labs (Santa Clara, CA) to determine concentrations of C and residual impurities (Cl, S, O, Si, H).

The GaN:C film resistivity was evaluated by two-point probe current-voltage (I-V) measurements from -5 V to 5 V using Ti/Al or Ti/Au contacts. To obtain resistor structures, the metal was e-beam evaporated over the entire sample except for a narrow (1-2 mm) masked stripe across the center. Spreading resistance is expected to be negligible for such a geometry. The I-V curves observed were linear, suggesting contact resistance did not significantly affect the measured resistivity. The measurement temperature was varied from -60° to 200°C.

Photoluminescence (PL) was excited by a HeCd laser at 325 nm with an estimated power density of 20 W/cm<sup>2</sup>. The light was diffracted by a double-grating monochromator and detected with a multi-alkali photo-multiplier using the standard lock-in technique. The temperature was varied from 12 K to 300 K using a closed-cycle helium cryostat. The data were corrected for the wavelength dependence of the sensitivity of the optical system.

## DISCUSSION

### Influence of doping sources on GaN growth

Previously, we showed that CCl<sub>4</sub> increased the desorption of Ga from the growth surface, presumably as volatile GaCl species [8]. Although increasing the Ga flux made possible normal growth rates despite this parasitic reaction, the high flux needed to maintain Ga-rich conditions led to rapid depletion of the charge in the effusion cell. Therefore CS<sub>2</sub> vapor was investigated as an alternative. No parasitic reaction was observed for CS<sub>2</sub> and the film properties were similar to those grown with CCl<sub>4</sub>.

Table I. Impurity Concentrations Determined by SIMS (cm<sup>-3</sup>)

	[C]	[O]	[Cl] or [S]	[Si]	[H]
Si-doped reference	$6 \times 10^{16}$	$4 \times 10^{16}$	$< 2 \times 10^{15}$	$1 \times 10^{17}$	$3 \times 10^{17}$
C-doped with CCl <sub>4</sub>	$3 \times 10^{19}$	$3 \times 10^{17}$	$4 \times 10^{16}$	$5 \times 10^{16}$	$3 \times 10^{17}$
C-doped with CS <sub>2</sub>	$2 \times 10^{19}$	$2 \times 10^{17}$	$2 \times 10^{16}$	$5 \times 10^{16}$	$5 \times 10^{17}$

SIMS impurity concentrations for representative films are shown in Table I. For both sources, Cl or S contamination increased with dopant flow. Films with [C]  $\sim 10^{18}$  cm<sup>-3</sup> had lower Cl or S concentrations than indicated in Table I. Dopant flow rates higher than  $\sim 0.1$  sccm gave dramatically increased residual impurity levels and nonuniform film properties. This limited the maximum carbon concentration that could be achieved to about  $5 \times 10^{19}$  cm<sup>-3</sup>.

## Photoluminescence

Low-temperature PL spectra for three representative films are shown in Fig. 1. The spectra have not been normalized and were measured under identical conditions to ensure a

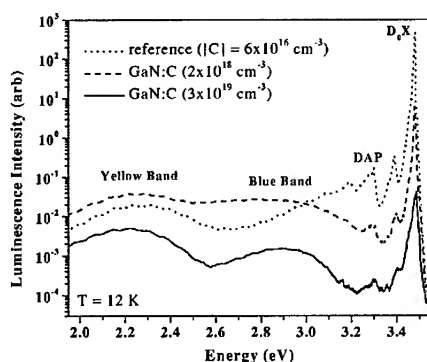


Fig. 1 PL spectra at 12 K for representative GaN:C and reference samples. The intensity data are not normalized and the same arbitrary units are used for all three samples.

meaningful comparison of the absolute intensities between samples. The reference sample is dominated by bound exciton and shallow donor-acceptor pair (DAP) luminescence, but the commonly observed yellow luminescence (YL) at ~2.2 eV is also present. The sample with  $[C] = 2 \times 10^{18} \text{ cm}^{-3}$  shows much weaker band-edge emission but somewhat stronger YL. The shallow DAP emission is absent and instead a blue (~2.9 eV) band is observed. In the  $[C] = 3 \times 10^{19} \text{ cm}^{-3}$  sample the overall luminescence intensity is reduced by several orders of magnitude compared to the reference sample, yet the YL is still comparatively strong.

The heavily carbon-doped spectrum in Fig. 1 is markedly different from that reported by Tang *et al.* [1] for MBE GaN of similar carbon concentration doped using a methane ion gun. In their material only YL was observed and band-edge emission was completely absent even at low temperatures (5 K). The PL results in this work are qualitatively similar to the electroluminescence spectra of Seager *et al.* [4] for carbon-contaminated MOVPE GaN.

The temperature dependence of the blue band has yet to be studied in detail, though it has been found to persist up to 400 K. Excitation-density dependent measurements from 0.02-20 W/cm<sup>2</sup> (not shown) gave no shift of the blue band peak position. The blue band saturated at much higher excitation than the YL, indicating that the defect responsible for the blue band has a higher concentration but lower radiative efficiency. The blue emission was suggested by Seager *et al.* [4] to result from recombination between a C<sub>N</sub> acceptor and C<sub>Ga</sub> donor, each of which has a calculated ionization energy of 0.2-0.3 eV. Our results are consistent with this model provided that the C<sub>N</sub> and C<sub>Ga</sub> defects exist in the form of near-neighbor complexes, which would account for the lack of peak shift with excitation power.

The strong YL in GaN:C films of poor overall luminescence efficiency suggests a causal relationship between carbon and YL. There is much evidence supporting a gallium vacancy mechanism for the YL [9]. However, we observed strong YL in GaN:C films of very low gallium vacancy concentration as determined by positron annihilation spectroscopy. This observation combined with analysis of the thermal quenching of the YL in GaN:C and reference samples strongly supports the hypothesis that *both* gallium vacancies and carbon-related deep levels contribute to YL in GaN. Details of this investigation will be published elsewhere [10].

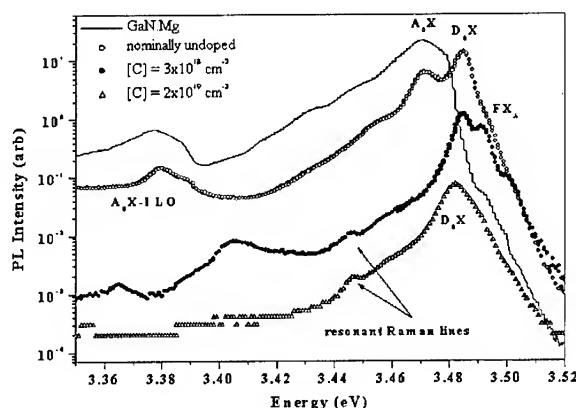


Fig. 2 Near band-edge region of the 12 K PL spectra for GaN:C and reference samples. Resonant Raman lines indicate the 4<sup>th</sup> replica of the LO phonon scattered laser light (3.81 eV).

Figure 2 shows highly resolved PL in the near band-edge region for several GaN:C and reference samples (not the same samples as Fig. 1). The GaN:Mg film is shown to demonstrate the correct assignment of the acceptor-bound exciton peak. Nominally undoped GaN shows both donor- and acceptor-bound exciton lines, but GaN:C films show no  $A_0X$  peaks. This is surprising since GaN:C films must contain more acceptors than undoped films. The most likely explanation is that  $C_N$  acceptors in GaN of high carbon concentration exist mainly as complexes with donors. Such complexes would not cause excitonic luminescence. Since carbon is the dominant impurity in the films, most  $C_N$  acceptors must be in complexes such as  $C_N-C_{Ga}$  or possibly  $C_N-C_i$ . This is consistent with the assignment of the blue band to recombination from  $C_N-C_{Ga}$  complexes. The film electrical properties (next section) also suggest the majority of  $C_N$  exists in the form of electrically inactive carbon complexes.

### Electrical Properties

Films with carbon concentration exceeding the residual donor concentration were highly resistive, in agreement with the observations of Seager *et al.* [4]. For  $[C]$  in the low  $10^{18} \text{ cm}^{-3}$  range the room temperature resistivity was  $\sim 10^7 \Omega\text{-cm}$ , while for an order of magnitude higher  $[C]$  the resistivity fell to  $\sim 10^5 \Omega\text{-cm}$ . Note that the SIMS residual donor (O + Si) concentrations in both samples are approximately equal ( $3 \times 10^{17} \text{ cm}^{-3}$ ).

Given the absence of acceptor-bound exciton lines in PL, the lower resistivity for heavier doping cannot be due to p-type conduction from  $C_N$  acceptors. To understand the compensation mechanism, temperature-dependent resistivity measurements were carried out. The results are shown in Fig. 3. If the films were uncompensated p-type, a conduction activation energy of 0.2 eV or lower (the  $C_N$  optical ionization energy) would be expected. A higher value could indicate the energetic position of a compensating deep level. However, the value of 0.55 eV is quite far from any predicted carbon defect energy level, a result difficult to explain if the conduction followed a normal semiconductor transport model.

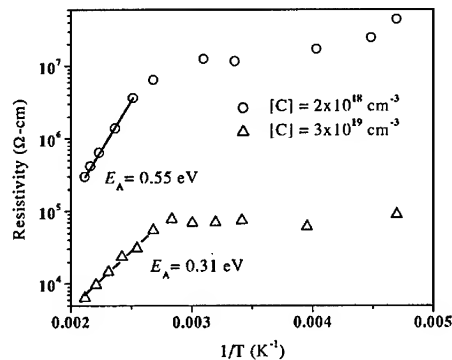


Fig. 3 Temperature dependence of the resistivity of GaN:C films.

Tang *et al.* reported a conduction activation energy of 0.9 eV in GaN:C [1], equal to the energy found in semi-insulating GaN obtained by alpha particle irradiation [11]. For highly compensated GaN it was shown by Salzman *et al.* [11] that the conduction can be described by the grain-boundary controlled transport (GBCT) model. Details of this model and its implications are discussed in ref. 11.

Following the GBCT model, the lower activation energy (0.31 eV) indicates that  $(N_D - N_A)$  in heavily doped GaN:C is *larger* than the net donor concentration in moderately doped films (0.55 eV). As  $C_N$  is the energetically favored defect in n-type GaN, this result is surprising. It can be explained if carbon on the growth surface tends to form pair defects; formation of pairs is statistically more likely for higher doping. The work of Birkle *et al.* also suggests formation of carbon pairs on the growth surface [7]. According to first principles calculations,  $C_N$ - $C_{Ga}$  pairs in GaN are expected to be stable for all values of the Fermi energy [3]. These pair defects should be electrically inactive and fail to compensate the residual donors.

The conduction activation energy of 0.9 eV found by Tang *et al.* compared to the lower energies in this work suggests their samples were more completely compensated and/or had smaller grain sizes. They grew by ammonia MBE rather than plasma-assisted MBE and used a different carbon source (200 eV methane ion gun), so different results are not entirely unexpected. It is emphasized that the conduction activation energies of 0.31 eV, 0.55 eV, and 0.9 eV discussed here should *not* correspond to carbon defect energy levels. These are rather proposed to be the heights of potential barriers existing at structural defects such as grain boundaries or dislocations, as suggested in ref. 11. Following GBCT theory, the barrier height

depends on ( $N_D - N_A$ ), which would account for the several different activation energies observed in GaN:C samples.

## CONCLUSIONS

Semi-insulating GaN films were obtained in Ga-rich MBE growth using  $\text{CCl}_4$  or  $\text{CS}_2$  as carbon doping sources. For doping levels below  $5 \times 10^{19} \text{ cm}^{-3}$  the carbon concentration is controlled without introducing significant levels of other impurities. The optical quality of these films is superior to results previously reported for wurtzite GaN:C. Carbon defects contribute to blue (2.9 eV) and yellow (2.2 eV) luminescence bands. However, more than one mechanism is likely responsible for the 2.2 eV band.

A maximum room-temperature resistivity of  $\sim 10^7 \Omega\text{-cm}$  was found for [C] in the low  $10^{11} \text{ cm}^{-3}$  range. The resistivity decreases for heavier doping. The electrical properties of GaN:C are well described by the grain-boundary controlled transport model. Application of this model combined with PL analysis showed that the lower resistivity in heavily doped GaN:C is due to a higher net donor concentration, not p-type conduction.

The carbon concentration dependence of the film properties is consistent with the hypothesis that electrically inactive pair defects ( $\text{C}_\text{N}-\text{C}_\text{Ga}$ ) form on the growth surface. Such pairs are statistically more likely to form for higher C fluxes, which explains the less efficient carbon acceptor incorporation and compensation of residual donors for higher doping levels.

## ACKNOWLEDGMENTS

This work was supported by the Air Force Office of Scientific Research, grant No. F49620-98-1-0135 (program manager Dr. Gerald Witt). The authors thank Michael Cich for suggesting the use of  $\text{CS}_2$  vapor as a C-doping source.

## REFERENCES

1. H. Tang, J.B. Webb, J.A. Bardwell, S. Raymond, J. Salzman, and C. Uzan-Saguy, *Appl. Phys. Lett.* **78**, 757 (2001).
2. D.J. As and U. Köhler, *J. Phys. Condens. Matter* **13**, 8923 (2001).
3. A.F. Wright, *J. Appl. Phys.* **92**, 2575 (2002).
4. C.H. Seager, A.F. Wright, J. Yu, and W. Götz, *J. Appl. Phys.* **92**, 6553 (2002).
5. P.B. Klein, S.C. Binari, K. Ikossi, A.E. Wickenden, D.D. Koleske, and R.L. Henry, *Appl. Phys. Lett.* **79**, 3529 (2001).
6. T. Ogino and M. Aoki, *Jpn. J. Appl. Phys.* **19**, 2395 (1980).
7. U. Birkle, M. Fehrer, V. Kirchner, S. Einfeldt, D. Hommel, S. Strauf, P. Michler, and J. Gutowski, *MRS Internet J. Nitride Semicond. Res.* **4S1**, G5.6 (1999).
8. R. Armitage, Q. Yang, H. Feick, Y. Park, and E.R. Weber, *Proc. Mat. Res. Soc. Symp.* **719**, F1.2 (2002).
9. J. Neugebauer and C. Van de Walle, *Appl. Phys. Lett.* **69**, 503 (1996).
10. R. Armitage, W. Hong, Q. Yang, H. Feick, J. Gebauer, E.R. Weber, S. Hautakangas, and K. Saarinen, submitted to *Appl. Phys. Lett.*
11. J. Salzman, C. Uzan-Saguy, R. Kalish, V. Richter, and B. Meyler, *Appl. Phys. Lett.* **76**, 1431 (2000).

### Hollow core dislocations in Mg-doped AlGa<sub>N</sub>

D. Cherns, Y.Q. Wang, R. Liu\*, F.A. Ponce\*, H. Amano\*\* and I. Akasaki\*\*

*H.H. Wills Physics Laboratory, University of Bristol, Bristol BS8 1TL, United Kingdom*

*\*Dept of Physics, Arizona State University, Tempe, AZ 85287-1504, USA*

*\*\*Dept of Mat. Sci and Eng, Meijo University, Nagoya 468-8502, Japan*

#### ABSTRACT

Transmission electron microscopy has been used to investigate the core structure of threading dislocations in heavily Mg-doped ( $10^{20} \text{ cm}^{-3}$ ) Al<sub>0.03</sub>Ga<sub>0.97</sub>N films grown on (0001) sapphire by metal-organic chemical vapour deposition. Evidence is presented that Mg segregates to edge and mixed dislocations, and that these dislocations often have open cores with diameters in the range 1-5nm. The mechanism of hollow core formation and the role of Mg are discussed.

#### INTRODUCTION

Light emitting and electronic devices based on hexagonal (0001)Ga<sub>N</sub> layers often have high densities of threading dislocations,  $10^9 \text{ cm}^{-2}$  or greater, introduced during the early stages of growth. The electronic properties of these dislocations are therefore of great interest. One factor which may affect these properties is whether dislocations have open or closed core structures. This appears to depend on the dislocation type, i.e whether the dislocations are of edge or a-type with Burgers vectors,  $b = 1/3\langle 11\bar{2}0 \rangle$ , mixed or c+a-type with  $b = 1/3\langle 11\bar{2}3 \rangle$  or screw or c-type with  $b = \langle 0001 \rangle$ . In observations of undoped Ga<sub>N</sub> grown by metalorganic chemical vapour deposition (MOCVD), screw dislocations have been reported as open core with diameters of typically 5-30nm, whereas edge and mixed dislocations, which usually predominate in device structures, have closed core configurations [1]. There is evidence that the core structure is affected by impurities and by n-doping. We have found that screw dislocations in heavily Si-doped material can alternate between open core and closed core configurations [2]. Others have reported that the density of nanopipes in n-Ga<sub>N</sub> depends on the level of background impurities during growth [3].

In this paper we report transmission electron microscope (TEM) studies of dislocations in heavily Mg-doped Al<sub>0.03</sub>Ga<sub>0.97</sub>N films grown by MOCVD on (0001) sapphire. It is shown that, in contrast to observations on n-Ga<sub>N</sub>, dislocations of edge and mixed type are found to have open cores with diameters in the range 1-5nm. It is also shown that excess Mg segregates to these dislocations. The possible role of the Mg in generating open core dislocations is discussed.

#### EXPERIMENTAL

Studies were carried out on a 5µm thick Al<sub>0.03</sub>Ga<sub>0.97</sub>N layer doped with Mg ( $10^{20} \text{ cm}^{-3}$ ). The layer was grown on (0001) sapphire by MOCVD at 1100°C. The sapphire substrate was patterned with grooves along a  $\langle 1\bar{1}00 \rangle$  direction although the observations

described here relate to growth on the (0001) seed face. TEM studies were carried out using a 300kV Philips EM430 microscope operating at 250kV on samples prepared in both plan view and cross-sectional orientation. Microanalysis using electron energy loss spectroscopy (EELS) was carried out on a JEOL 3000F microscope.

Fig. 1 shows a cross-sectional sample imaged in two-beam conditions with  $g = 0002$ . Under these conditions, threading dislocations of c- and c+a-type are in contrast, while a-type dislocations are out of contrast. In addition to threading dislocations, a high density of precipitates is also visible. These appear as V-shaped defects in projection, opening out in the [000-1] growth direction. The shape is consistent with that of inverted hexagonal pyramids, indicative of local Mg precipitation, which have been widely reported [e.g. see 4]. The distribution of precipitates is, however, non-isotropic, with denuded regions often visible around threading edge and mixed dislocations. This can be seen in fig. 1. The effect is most marked in area A, which contains edge dislocations that are out of contrast. Denuded regions are also visible around some, but certainly not all, of the dislocations in contrast; this point will be discussed later.

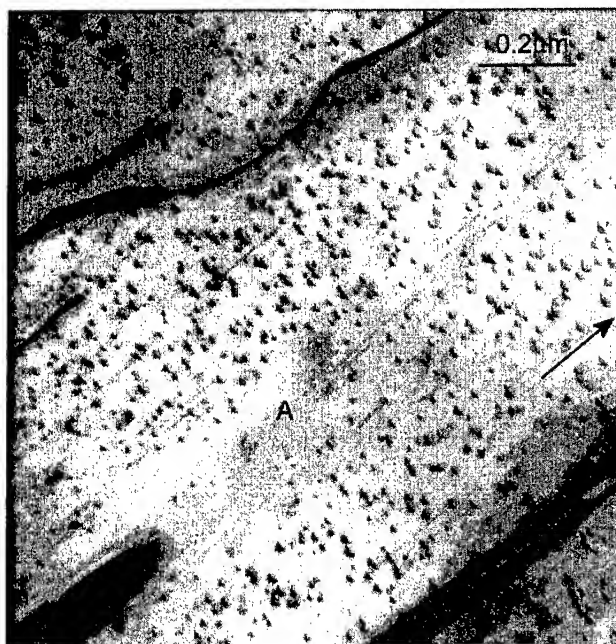


Fig. 1: Bright field micrograph of the AlGaIn layer taken under two-beam imaging conditions with  $g = 0002$ . The growth direction is arrowed. The distribution of precipitates is non-uniform, with few large precipitates in area A. Some faint lines of contrast in area A indicate small precipitates which decorate edge dislocations which are out of contrast.

A close examination of the area A in fig.1 reveals some faint lines of contrast, some of which correspond to edge dislocations that are themselves out of contrast, i.e. since  $g \cdot b = 0$ . The reason for this contrast is seen more clearly in thinner regions of the foil. One such region is shown in fig. 2. In this case, an edge dislocation, A, which is itself out of contrast, is delineated by a line of small defects. A line of much larger defects is also present on the mixed dislocation, B. The defects on both A and B appear as V-shaped defects as do the precipitates seen in the bulk regions. However, the larger defects close to dislocation B clearly differ from the defects in bulk both in the inclined facet planes and in displaying void-like character.

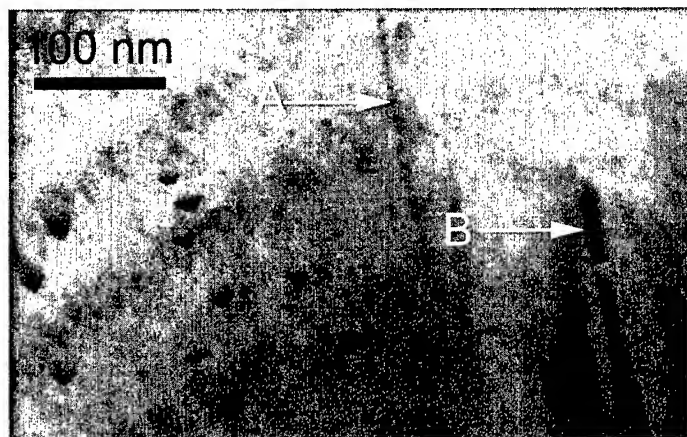


Fig. 2: Bright field micrograph in two-beam conditions with  $g = 0002$ , showing defects decorating the cores of an edge dislocation, A, which is itself out of contrast, and a mixed dislocation, B.

The core structure of edge and mixed dislocations was investigated in more detail using plan view samples. Observation in the near end-on orientation suggested that both types of dislocation had hollow cores. The diameters of the hollow core varied in the range 1-5nm. Some examples are illustrated in figs. 3 and 4. Fig.3 illustrates bright field micrographs showing two edge dislocations (arrowed) in a relatively thick region. In fig. 3(a), the foil is near horizontal with  $[0001]$  a few degrees off the electron beam direction. Although the core structure is not clearly resolved here, bright contrast in the core regions is suggestive of a hollow core structure. This structure is rather clearer in fig. 3(b), where the foil has been tilted up to nearly  $30^\circ$  from the horizontal orientation, such that the dislocations are now obliquely inclined and seen in projection. The dislocations again show bright contrast indicative of hollow cores, with diameters less than 2nm. Periodic fluctuations in the core contrast suggest that the core diameters vary somewhat along the dislocation length.

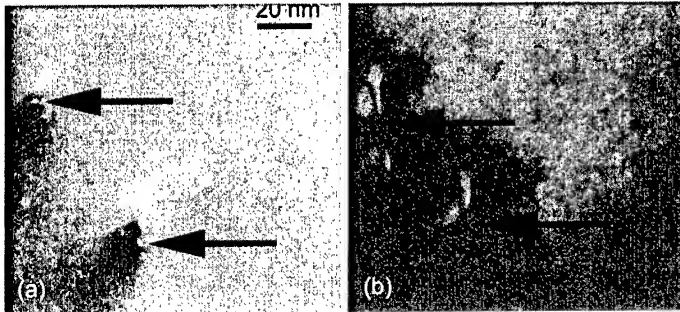


Fig. 3: Bright field micrographs from a plan view sample showing edge dislocations (a) near end-on and (b) obliquely inclined. Both images show contrast consistent with hollow cores in the range 1-2nm in diameter.

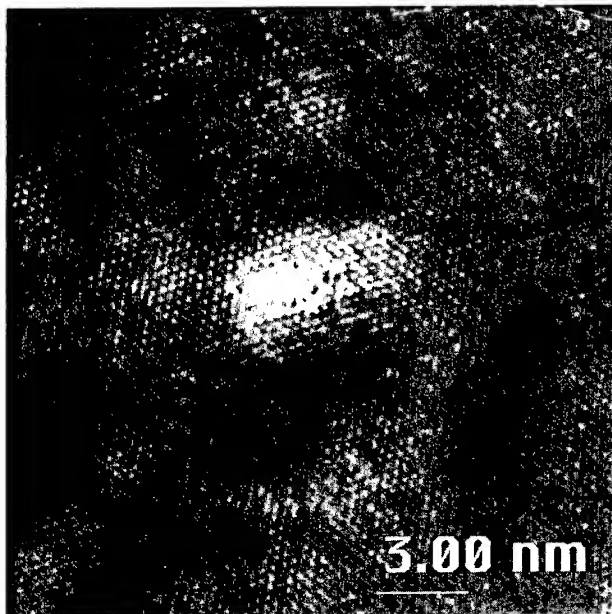


Fig. 4: (0001) lattice image of a hollow core dislocation. A Burgers circuit around the dislocation indicates an edge component of the Burgers vector. Since the presence of a screw component cannot be seen in this orientation, the dislocation is either of edge or mixed type.

The open cores of edge and mixed dislocations can be seen more directly by lattice imaging. Fig. 4 shows a lattice image of an open core dislocation in a relatively thin region of the foil taken with [0001] parallel to the electron beam direction. The core is now clearly seen as hollow, albeit with a diameter of a few atom spacings. The edges of the nanotube are, however, not well defined, consistent with a varying core diameter. The lattice image allows us to construct a Burgers circuit around the open core. Such a circuit (not shown) indicates the presence of an edge component of the Burgers vector, confirming that this is an edge or mixed type dislocation.

The presence of precipitates on the cores of edge and mixed dislocations, and the occurrence of regions denuded of precipitates, believed to be Mg-related, around dislocations suggests strongly that Mg segregation and precipitation on dislocation cores has taken place. EELS was used to investigate the presence of Mg on the dislocation cores directly. EELS studies carried out with a 3nm probe confirmed an increase in the Mg signal on the cores of dislocations compared with the surrounding bulk. Preliminary results are shown in fig. 5. More detailed EELS studies will be reported at a later date.

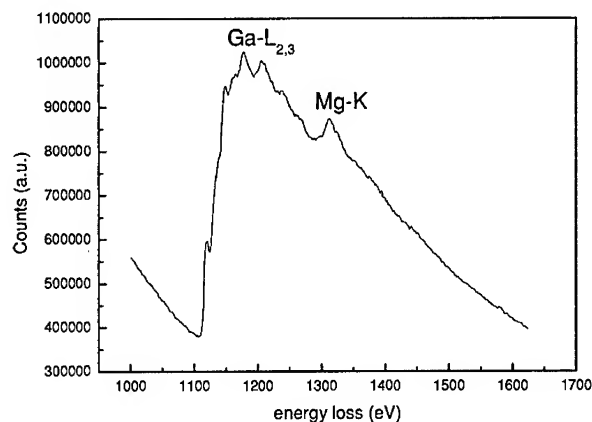


Fig. 5: EELS without background subtraction using a 3nm probe focused on an end-on dislocation. The Mg K signal at around 1300eV loss was an order of magnitude higher than the signal from regions free of dislocations.

## DISCUSSION

TEM observations confirm that the cores of edge and mixed dislocations in our Mg-doped AlGaIn sample are hollow. This is in direct contrast to previous work on undoped and n-doped GaN, which indicates that edge and mixed dislocations are of closed core type while screw dislocations can be open core. The diameters of open core screw dislocations, reported as 5-30nm [1], are also much larger than in the present case. The EELS studies, in agreement with observations of precipitates on dislocation cores, provide good evidence that Mg segregates to edge and mixed dislocations. The distribution of precipitates around dislocations is worth considering. While we expect

denuded regions as a result of segregation, such regions are not consistently observed: c.f. fig. 1. This can be explained if we assume that segregation of Mg depends partly on the dislocation strain field. With the Mg ion some 20% larger in diameter than the Ga ion, we expect preferential segregation of Mg to the dilatational as opposed to the compressional part of the strain field associated with an edge component of the Burgers vector. This might lead to enhanced precipitation of Mg on one side of the core and a denuded region on the other side. Preliminary experiments carried out to examine the spatial distribution of precipitates around edge and mixed dislocations support this general picture [Y.Q. Wang: private communication].

Assuming that Mg precipitates on dislocation cores, hollow core formation could occur through a number of causes. Mg may inhibit growth, perhaps by nucleating more slowly growing N-polar material, as proposed in the growth of Mg precipitates in the bulk [4]. In common with precipitate formation in the bulk, it might be expected that the precipitate is then overgrown such that a void is trapped. Once the Mg concentration is built up again, the process repeats. This might explain the periodic fluctuations seen in fig. 3. An alternative possibility is that Mg segregation generates low energy surfaces, and the formation of hollow cores, which releases strain field energy, becomes energetically favourable [5].

**Acknowledgements:** This work was carried out with the support of a NEDO grant, no 01MB10. The authors are also grateful to Dr CJD Hetherington, Dept of Materials, University of Oxford, for assistance in carrying out the EELS experiment in fig. 5.

## REFERENCES

1. D. Cherns, W.T. Young, J.W. Steeds, F.A. Ponce and S. Nakamura, *J. Cryst. Growth* **178**, 201 (1997).
2. D. Cherns, *J. Phys. Condens. Matter* **12**, 10205 (2000).
3. Z. Liliental-Weber, *J. Electron Microscopy* **49**, 339 (2000).
4. P. Vennegues, M. Benaissa, B. Beaumont, E. Feltin, P. De Mierry, S. Dalmaso, M. Leroux and P. Gibart, *Appl. Phys. Lett.* **77**, 880 (2000).
5. J.E. Northrup, *Appl. Phys. Lett.* **78**, 2288 (2001).

### Development of a High Lateral Resolution Electron Beam Induced Current Technique for Electrical Characterization of InGaN-Based Quantum Well Light Emitting Diodes

Kristin L. Bunker<sup>1</sup>, Juan Carlos Gonzalez<sup>1</sup>, Dale Batchelor<sup>1</sup>, Terrence J. Stark<sup>2</sup>, and Phillip E. Russell<sup>1,2</sup>

<sup>1</sup>Analytical Instrumentation Facility and Materials Science and Engineering Department, North Carolina State University, Box 7531, Raleigh, NC 27695 USA

<sup>2</sup>Materials Analytical Services, 616 Hutton Street, Suite 101, Raleigh, NC 27606 USA

#### ABSTRACT

Electron Beam Induced Current (EBIC) is a Scanning Electron Microscope (SEM)-based technique that can provide information on the electrical properties of semiconductor materials and devices. This work focuses on the design and implementation of an EBIC system in a dedicated Scanning Transmission Electron Microscope (STEM). The STEM-EBIC technique was used in the characterization of an Indium Gallium Nitride (InGaN) quantum well Light Emitting Diode (LED). The conventional "H-bar" Transmission Electron Microscopy (TEM) sample preparation method using Focused Ion Beam Micromachining (FIBM) was adapted to create an electron-transparent membrane approximately 300 nm thick on the sample while preserving the electrical activity of the device. A STEM-EBIC sample holder with two insulated electrical feedthroughs making contact to the thinned LED was designed and custom made for these experiments. The simultaneous collection of Z-contrast images, EBIC images, and In and Al elemental images allowed for the determination of the p-n junction location, AlGaIn and GaN barrier layers, and the thin InGaIn quantum well layer within the device. The relative position of the p-n junction with respect to the thin InGaIn quantum well was found to be  $(19 \pm 3)$  nm from the center of the InGaIn quantum well.

#### INTRODUCTION

As the solid-state electronics industry continues to shrink the dimensions of electronic devices and enter into the nanotechnology era, the field of analytical techniques for materials and device characterization is presented with new and additional challenges. The structural, chemical, electrical, and optical properties have to be studied with nanometer resolution and higher sensitivity. Therefore, nano-characterization techniques are needed to investigate the properties of new materials and the performance and failure of devices formed from these new materials. Scanning Electron Microscope (SEM)-based Electron Beam Induced Current (EBIC) is a technique that can be used for the electrical characterization of materials and devices. EBIC can provide information on electrically active defects, diffusion of carriers, surface recombination mechanism, bulk recombination mechanism, trapping centers, and especially p-n junction width, position, and homogeneity [1,2,3,4]. However, in the SEM-based EBIC technique, the beam excited volume of electron hole pairs (EHPs) limits the spatial resolution. Therefore, there is a need for a high-resolution EBIC technique. The STEM-based EBIC technique combines a thin sample and a high-energy electron beam to reduce the spatial

resolution of STEM analysis to the nanometer level by decreasing the amount of beam spreading to a few nanometers.

The STEM-EBIC technique was first demonstrated in the late 1970's by Sparrow and Valde in the correlation of crystal defects and the electrical properties of Si transistors [5]. A few years later, Petroff et al. used the STEM-EBIC method to obtain information on the relationship between dislocation cores and nonradiative recombination properties in GaAlAsP [6]. In the early 1990's, Cabanel and Laval implemented STEM-EBIC to relate the electrical activity of microstructural defects in polycrystalline Si to the presence of impurities [7]. More recently, Cabanel et al. used cross-sectional STEM-EBIC to relate the inhomogeneities in Si p-n junctions to variations in doping concentrations [8]. In this work, an EBIC system in a HD-2000 dedicated FSTEM has been designed and implemented. The STEM-EBIC method is used to study the cross-section of an InGa<sub>N</sub> quantum well LED in order to determine the p-n junction location with respect to the quantum well of the device.

## EBIC THEORY

In the linescan configuration, the plane of the p-n junction is perpendicular to the sample surface, and the electron beam scans the surface perpendicular to the depletion layer (Figure 1). As the incident electron beam is scanned across the device, EHPs or mobile charge carriers are generated within a small volume at each point. The built-in electric field created by the p-n junction of the device moves the mobile charge carriers. Electrons and holes tend to move in opposite directions, and this motion constitutes a current that can be detected in an external circuit. The EBIC signal is formed by scanning the electron beam across the p-n junction of the device and plotting the short circuit current at each point. The electrical transport mechanism of the carriers towards the p-n junction produces an EBIC curve with a maximum at the p-n junction position and exponentially decaying tails on both sides of the depletion layer due to the

diffusive nature of the electrical transport in those regions. The EBIC signal does not fall to zero outside of the depletion region due to the diffusion of the minority carriers from the bulk to the depletion region of the device.

If an EBIC linescan is obtained in low injection conditions (i.e. the generated minority carrier concentration is less than the majority equilibrium concentration), the tails of the EBIC profile can be used to extract minority carrier diffusion length and surface recombination velocity, and the maximum of the profile identifies the p-n junction location [9]. Calculations confirmed that high injection conditions were used in the STEM-EBIC experiments. Therefore, the carrier transport equations that describe the minority carrier diffusion length and surface recombination velocity are not valid. However, the p-n junction location, as determined by the

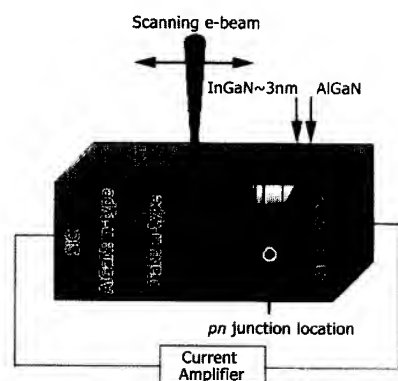


**Figure 1.** Schematic of the cross-section of the InGa<sub>N</sub>-quantum well LED structure and experimental linescan setup used in the STEM-EBIC measurements (Not drawn to scale).

maximum in the EBIC signal, can be resolved with nanometer precision with the STEM-EBIC technique.

## SAMPLE PREPARATION

The sample used in the STEM-EBIC experiments was an InGaN quantum well LED. The general structure of this device is shown in Figure 1. The device was grown by metal-organic chemical-vapor deposition on a (0001) Silicon Carbide (SiC) substrate. An n-type AlGaIn buffer layer was grown on the SiC substrate followed by n-type GaN. A 3 nm InGaIn quantum well was grown on top of the n-type GaN material. This layer was followed by an AlGaIn layer and finally a p-type GaN contact layer. The as-received sample was a 1 mm<sup>2</sup> square piece cleaved from the wafer and mounted unpackaged on the edge of a TO header. The can of the TO header made contact to the backside of the device (i.e. n-type material) and a gold bonded wire made contact to the topside of the device (i.e. p-type material).

The sample preparation was a variation of the traditional 'H-bar' Transmission Electron Microscopy (TEM) method using Focused Ion Beam Micromachining (FIBM). The TO header was embedded in wax and mechanically ground down using diamond lapping films on an Allied Multiprep™ System. The sample was ground down to a final wedge of less than 50  $\mu\text{m}$ , while ensuring that the gold bonded wire was still attached to the p-type material of the device. The backside of the thinned device was attached to a half copper mesh TEM grid with silver paint, while the gold bond wire remained free (Figure 2). The silver paint provided electrical contact between the backside of the device and the TEM grid. In the final step, a FEI 200 TEM with a magnum column and a 30keV Ga<sup>+</sup> beam was used to create a 300 nm thick electron transparent membrane. Figure 3(a) shows a SE image taken on the HD-2000 of the region of the sample thinned by FIBM with respect to the gold wire. Figure 3(b) shows the FIBM area and reveals the 'H-bar' shape of the region.

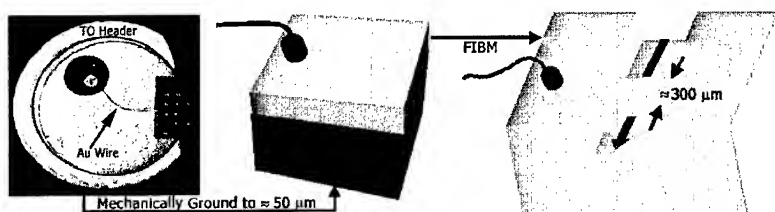


**Figure 2.** Schematic of the steps involved in the STEM-EBIC sample preparation from the as-received sample to the electron transparent membrane created by FIBM.

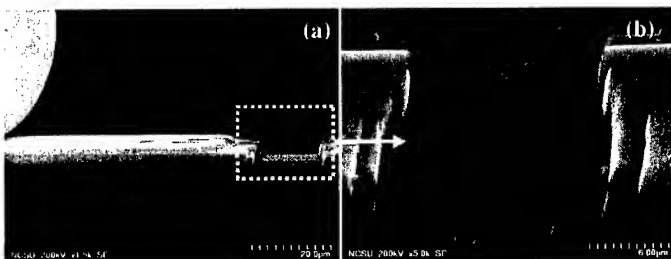


**Figure 3.** (a) and (b) SE images of the FIBM region of the LED taken on the HD-2000 at 200keV.



**Figure 4.** (a) Customized STEM-EBIC holder showing the device connected to the two electrical feedthroughs with silver paint and In solder. (b) Fully prepared LED mounted in STEM-EBIC.

#### CUSTOM SAMPLE HOLDER

The STEM-EBIC specimen holder was designed after a standard single-tilt side-entry HD-2000 FESTEM specimen holder. A ceramic feedthrough was placed in the barrel of a specimen holder and sealed with Torr Seal, a solvent free epoxy resin, to ensure no vacuum leaks

through the barrel. Two shielded coaxial single-stranded and silver-plated copper wires insulated with Kapton® were fed through the ceramic feedthrough and sealed with Torr Seal. On the air-side of the barrel, the two wires were soldered to a subminiature A (SMA) connector that was mounted in a plastic handle. The shielding and the Kapton® insulation were removed from the ends of the two wires on the vacuum-side of the barrel in order to allow electrical connections to be made to the sample.

The tip of the specimen holder is a separate component and attaches to the barrel with setscrews. The tip has a 3mm cup, which holds the specimen, and an isolated jewel bearing that makes mechanical contact to the column of the STEM. A piece of mica was glued down on the tip and a hole was cut in the mica around the 3mm cup. The mica was used to create electrical isolation between the specimen and the specimen rod holder and the 3mm hole in the mica allowed for the transmission of the electron beam through the sample.

The fully prepared LED sample was glued onto the mica surrounding the 3 mm cup, while the gold bonded wire was still allowed to move freely. One of the feedthrough wires was glued to the top of the copper grid and silver paint was used to make the electrical connection between the feedthrough wire and the backside of the sample (Figure 4(a)). The end of the second wire was placed in a strip of Indium that was positioned near the 3 mm cup on the tip. The free gold bonded wire was also placed in the Indium strip, thus making contact between the frontside of the sample and the feedthrough wire (Figure 4(a)). Figure 4(b) shows the fully prepared LED sample, including the FIBM area, mounted in the specimen holder.

#### ANALYSIS AND RESULTS

The goal of the STEM-EBIC experiments was to determine the p-n junction location, defined as the maximum of the built in electric field, with respect to the position of the InGaN quantum well. All EBIC experiments were performed at room temperature in a HD-2000 FESTEM with a 200keV electron beam, a 0.5 nm spot size, and a beam current of 350 pA. Initially, an Oxford ISIS EDS acquisition system was used to obtain Z-contrast and EBIC images simultaneously (Figure 5(a)). In the external acquisition system, the output from a Keithley 614 electrometer was fed directly into the auxiliary port of the imaging system. The EBIC and Z-contrast images were collected with a 12.8 ms dwell time and 128 x 100 resolution. The EBIC

#### BEST AVAILABLE COPY

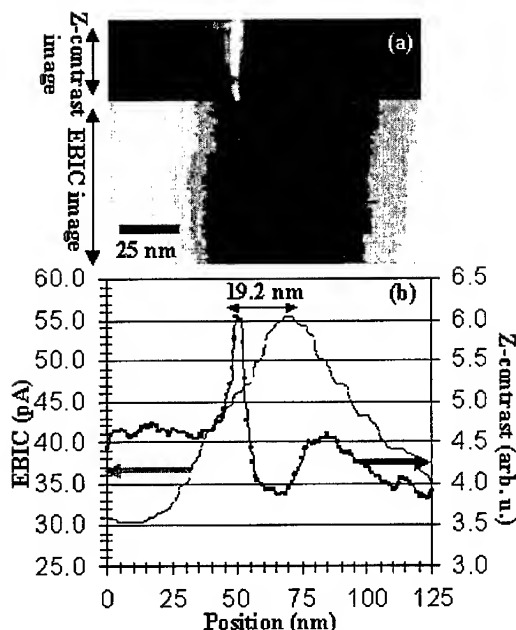


**Figure 5.** (a) EBIC and Z-contrast images acquired with the Oxford ISIS EDS system. (b) Mean Z-contrast and EBIC linescans showing p-n junction is located  $(19 \pm 3)$  nm from center of InGaN QW.

negative output voltage from the electrometer to a positive voltage. The positive voltage signal was converted to a frequency using a Frequency Converter (VFC) and sent to one of the Multichannel Scaler (MCS) ports of the Thermo Noran Vantage Energy Dispersive Spectroscopy (EDS) system. The 90 nm linescans had a total of 100 data points acquired with a 2 second dwell time. These linescans were taken using conditions optimized for the EBIC signal. Typical EDS and Z-contrast linescans optimized for good signal to noise are shown in Figure 6(b). This setup allowed for simultaneous acquisition of large angle scattered electrons (i.e. Z-contrast), EBIC, and EDS images. The elemental In EDS linescan confirmed the position of the InGaN quantum well that was previously determined with the Z-contrast image.

## CONCLUSIONS

The EBIC technique can be implemented in a SEM or a STEM in order to obtain electrical information about electrical transport properties of semiconductor materials and devices. Due to the high energy electron beam (200keV) and the thin specimen (300nm), the STEM-EBIC technique has been shown to be superior in terms of spatial resolution when

signal varied between 30 and 55 pA during the EBIC image acquisitions. The Z-contrast images allowed structural confirmation of the GaN and AlGaIn barrier layers as well as the InGaIn quantum well (Figure 5(a)).

In order to determine the p-n junction location, a mean Z-contrast linescan was obtained by averaging 28 lines in the Z-contrast image and a mean EBIC linescan was obtained by averaging 70 lines in the EBIC image. A comparison of the maximum in the mean Z-contrast linescan to the maximum in the mean EBIC linescan revealed the position of the p-n junction with respect to the center of the InGaIn quantum well. The relative position of the p-n junction with respect to the InGaIn quantum well was found to be  $(19 \pm 3)$  nm from the center of the InGaIn quantum well (Figure 5(b)).

A Noran Vantage EDS system was used to simultaneously obtain Z-Contrast, EDS, and EBIC linescans (Figure 6(a)). The external electronic acquisition system had a Keithley 614 electrometer connected to a low gain voltage amplifier that converted the

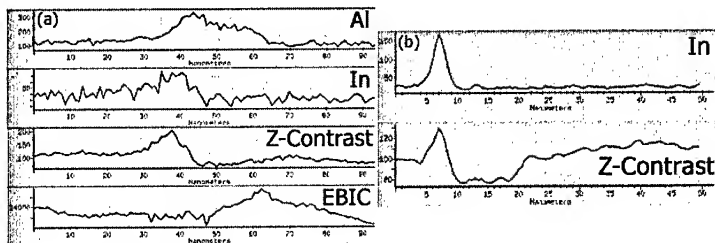


**Figure 6.** (a) EDS linescans of Al, In, and EBIC and Z-Contrast linescans. (b) EDS linescan of In and Z-Contrast linescan optimized for signal to noise. All linescans acquired with the Thermo Noran Vantage EDS system.

compared to the SEM-EBIC technique. The increased resolution is an important feature due to the decreasing size of electronic and optoelectronic devices and the overwhelming need for micro- and nano-characterization techniques in the nanotechnology industry. The sample preparation and electrical connections for STEM-EBIC are challenging. However, the introduction of a novel sample preparation method as well as the design and construction of a custom specimen holder was described here and proved to be a viable solution. The capability of the Hitachi HD-2000 dedicated FSTEM in conjunction with a customized STEM-EBIC holder to simultaneously collect structural (i.e. Z-contrast), chemical (i.e. EDS), and electrical (i.e. EBIC) images of semiconductor samples was also demonstrated. Finally, the STEM-EBIC technique resolved the position of the p-n junction with respect to the InGaN quantum well with nanometer precision. The STEM system is a useful and powerful tool for the nano-characterization of structural, compositional, and electrical properties of semiconductor materials.

## REFERENCES

1. D.B. Holt, *Quantitative Scanning Electron Microscopy: Quantitative Conductive Mode Scanning Electron Microscopy*, edited by D.B. Holt, M.D. Muir, P.R. Grant, and I.M. Boswarva (Academic Press, London 1974) p. 213.
2. L. Reimer, *Scanning Electron Microscopy: Physics of Image Formation and Microanalysis* (Springer, Berlin 1998) p. 253.
3. D.E. Newbury, D.C. Joy, P. Echlin, C. E. Fiori, and J.I. Goldstein, *Advanced Scanning Electron Microscopy and X-Ray Microanalysis* (Plenum Press, New York 1986) p. 61.
4. H.J. Leamy, *J. Appl. Phys.* **53** (6), R51 (1982).
5. T.G. Sparrow and U. Valdre, *Philosophical Magazine* **36** (6), 1517 (1977).
6. P.M. Petroff, R.A. Logan, and A. Savage, *Phys. Rev. Lett.* **44** (4), 287 (1980).
7. C. Cabanel and J.Y. Laval, *J. Appl. Phys.* **67** (3), 1425 (1990).
8. C. Cabanel, H. Maya, and J.Y. Laval, *Phil. Mag. Lett.* **79** (2), 55 (1999).
9. C. Donolato, *Solid State Electronics* **25**, 1077 (1982).

### X-ray Spectroscopic Studies of the Bulk Electronic Structure of InGaN Alloys

Cormac McGuinness, James E. Downes, Philip Ryan\* and Kevin E. Smith\*\*

*Department of Physics, Boston University, Boston, MA 02215*

Dharanipal Doppalapudi and Theodore D. Moustakas

*Electrical and Computer Engineering Department, Boston University, Boston, MA 02215*

#### ABSTRACT

Synchrotron radiation excited soft x-ray emission and soft x-ray absorption spectroscopies are applied to the study of the electronic structure of  $\text{In}_x\text{Ga}_{1-x}\text{N}$  alloys with ( $0 \leq x \leq 0.29$ ). The elementally resolved partial density of states of the valence and conduction bands may be measured using these spectroscopies. The x-ray absorption spectra indicate that the conduction band broadens considerably with increasing indium incorporation. The band gap evolution as a function of indium content derives primarily from this broadening of the conduction band states. The emission spectra indicate that motion of the valence band makes a smaller contribution to the evolution of the band gap. This gap evolution differs from previous studies on the  $\text{Al}_x\text{Ga}_{1-x}\text{N}$  alloy system, which observed a linear valence band shift through the series ( $0 \leq x \leq 1$ ). Instead in the case of  $\text{In}_x\text{Ga}_{1-x}\text{N}$  the valence band exhibits a significant shift between  $x = 0$  and  $x = 0.1$  with minimal movement thereafter. Furthermore, evidence of In  $4d$  - N  $2p$  and Ga  $3d$  - N  $2p$  hybridisation is reported. Finally, the thermal stability of an  $\text{In}_{0.11}\text{Ga}_{0.89}\text{N}$  film was investigated. Both emission and absorption spectra were found to have a temperature dependent shift in energy, but the overall definition of the spectra was unaltered even at annealing temperatures well beyond the growth temperature of the film.

#### INTRODUCTION

It is abundantly clear that nitride based wide band gap semiconductors have great technological potential due to their application in light emitting devices coupled with their extreme hardness and the ability to sustain high temperatures.<sup>1-5</sup> Optoelectronic devices made from alloys of InN, GaN and AlN cover the visible to ultraviolet range of the electromagnetic spectrum as their band gap energies are 1.9 eV, 3.4 eV, and 6.2 eV respectively. However, experimental data on the detailed electronic structure of these alloys is scarce, particularly in the case of  $\text{In}_x\text{Ga}_{1-x}\text{N}$ . Although photoemission spectroscopy is a standard probe of electronic structure in solids, it is difficult to apply to  $\text{In}_x\text{Ga}_{1-x}\text{N}$  since it requires that atomically clean surfaces be prepared before bulk properties can be measured.<sup>6</sup> Successful methods exist for cleaning surfaces of GaN thin films, but obtaining clean surfaces of  $\text{In}_x\text{Ga}_{1-x}\text{N}$  alloys suitable for photoemission studies is very difficult.<sup>7</sup> However soft x-ray emission (SXE) and soft x-ray absorption (SXA) spectroscopies are ideal probes of the valence and conduction band density of states as in these spectroscopies there is a sampling depth of approximately 1000 Å, and they can thus be considered insensitive to atomic contamination or disorder of sample surfaces.<sup>8</sup> The electronic structure of GaN, AlN and  $\text{Al}_x\text{Ga}_{1-x}\text{N}$  alloys have been previously studied by both SXE and SXA where we were able to measure the elementally resolved partial density of states (PDOS), the band gap evolution as a function of  $\text{Al}_x\text{Ga}_{1-x}\text{N}$  composition, and shallow core level hybridization.<sup>9-11</sup> An SXE and SXA study of the electronic structure in  $\text{In}_x\text{Ga}_{1-x}\text{N}$  has been carried out and we report the first full measurement of the elementally resolved valence and conduction band PDOS. The highlights of these studies are presented here while a more complete analysis of this data has been presented elsewhere.<sup>12</sup>

## EXPERIMENT

The samples of  $\text{In}_x\text{Ga}_{1-x}\text{N}$  ( $0 \leq x \leq 0.29$ ) investigated were wurtzite thin films of thickness 1.2, 1.1, 0.5 and  $0.25\mu\text{m}$  thickness for  $x=0, 0.1, 0.2$  and  $0.29$  respectively. All samples were grown in a Varian GenII MBE system which employs a compact electron cyclotron resonance (ECR) microwave plasma source for activating molecular nitrogen. All three samples were grown on sapphire in 3 steps employing AlN and GaN buffer layers with a top layer of InGa $\text{N}$  grown at  $650\text{C}$ - $675\text{C}$ . The films are auto-doped n-type. Full details of the growth conditions and the structure of the films have been reported elsewhere.<sup>13,14</sup> The films were characterized by x-ray diffraction (XRD) and photoluminescence (PL); XRD was also used to obtain the In and Ga ratios and to ascertain whether any phase separation is present.<sup>13</sup> The SXE and SXA experiments were performed on the undulator beamline X1B at the National Synchrotron Light Source, Brookhaven National Laboratory. Absorption spectra were recorded in the total electron yield mode by measuring the sample drain-current with an energy resolutions of  $\sim 0.2\text{ eV}$  at  $400\text{ eV}$  in the vicinity of the N  $1s$  edge. Emission spectra were recorded using a Nordgren-type grazing-incidence grating spectrometer using a  $5\text{m}$ ,  $1200\text{ lines/mm}$  grating in first order of diffraction at a resolution of approximately  $0.31\text{ eV}$  at the N  $1s$  edge. The acquisition time for individual SXE spectra was approximately  $90\text{ min}$ . The base pressure in the experimental system was better than  $1.0 \times 10^{-9}\text{ Torr}$ . Sample surfaces were not processed or cleaned in the vacuum chamber. Details of the energy calibration for the SXE and SXA spectra can be found elsewhere.<sup>9,11</sup>

## RESULTS

### Valence and conduction band PDOS, and band gap evolution.

SXE and SXA spectroscopies at the N  $1s$  edge probe the N  $2p$  occupied and unoccupied states respectively. Figure 1 presents the SXE and SXA spectra for a series of  $\text{In}_x\text{Ga}_{1-x}\text{N}$  alloys where the dashed lines indicate movements of the band edges as a function of indium content. The energy axis is referenced to the valence band maximum (VBM) of GaN. Due to the limits in growing high quality InGa $\text{N}$  with an indium content beyond  $x \sim 0.3$  due to phase segregation, the sample series only extends to  $x=0.29$ .<sup>13</sup> The evolution of the elementally resolved band gap is clearly visible. A shift of  $0.15\text{ eV}$  occurs in the position of the N  $2p$  VBM between the GaN ( $x=0$ ) and  $\text{In}_{0.15}\text{Ga}_{0.85}\text{N}$ , but no further shift in the band edge as the In content is increased differing from the behavior observed in Al $\text{Ga}_{1-x}\text{N}$  alloys.<sup>11</sup> This is found to be consistent with the results of large supercell empirical pseudopotential calculations which predict a large shift of the VBM between  $x=0$  and  $x=0.1$ , with a minimal change thereafter.<sup>15</sup> In contrast to the measured behavior of the VBM, the N  $2p$  conduction band edge shifts continuously with In content and is

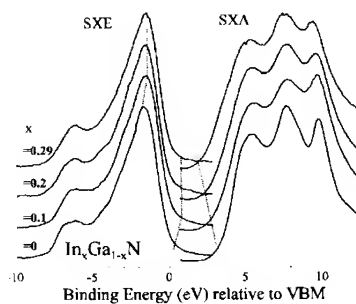


**Figure 1:** N  $2p$  SXE and SXA spectra from a series of  $\text{In}_x\text{Ga}_{1-x}\text{N}$  alloys.

highlighted in Figure 2, where the SXA spectra were recorded at normal incidence. The motion of the conduction band edge with increasing In content is clearly visible, deriving mostly from the broadening of spectral feature A. A arises from the mixing of  $s$  and  $p_z$  atomic orbitals as does C while B is a transition to  $(p_x, p_y)$  final states. Broadening and loss of spectral feature definition is also observed in the SXA spectrum taken at the Ga  $2p_{3/2}$  edge. Further the SXE spectrum

resulting from transitions from Ga 3d states to the Ga 2p<sub>3/2</sub> state were obtained and shows broadening of the FWHM of the Ga 3d states from 3.13 eV to 3.71 eV in GaN and In<sub>0.29</sub>Ga<sub>0.71</sub>N respectively. These changes, and the increase in FWHM of the Ga 3d emission, are consistent with a speculated alloy disordering.<sup>16</sup> The observed behavior of the experimentally measured N 2p band gap derived from the SXE and SXA spectra of Figure 1 is plotted in Figure 3. Theoretically, the behavior of the energy gap in such an alloy system may be described by Vegard's law:<sup>17</sup>

$$E_g(x) = \bar{E}_g + \Delta E_g(x - \frac{1}{2}) - bx(1-x)$$

Here,  $\bar{E}_g$  is the average gap,  $\Delta E_g$  is the difference between the gaps of the pure end-members of the alloy system, and  $b$  is the bowing parameter. The fit to the data presented here gives a value of  $b = 3.68$  eV. As can be seen in Figure 3, the measured band gap for the In<sub>x</sub>Ga<sub>1-x</sub>N alloys ( $x \leq 0.3$ ) exhibit a pseudo-linear dependence on the In fraction,  $x$ . A linear least-squares fit to the band gap data for  $x \leq 0.3$  gives  $E_g = 3.35 - 4.04 \cdot x$

This figure is comparable to a number of recent studies of In<sub>x</sub>Ga<sub>1-x</sub>N epilayers which obtained slopes with values of -3.57, -3.86 and -3.93.<sup>18-21</sup> A review of the band parameters for III-V compound semiconductors and their alloys gives an overview of the theoretical and experimental results obtained for the bowing parameter and provisionally suggests a bowing coefficient of 3.0 eV.<sup>22</sup> Experimental results have varied with band-gap bowing values ranging initially from  $b \approx 1$  eV,<sup>23</sup> to  $b = 2.6 - 4.11$  eV,<sup>20, 24-26</sup> The discrepancy with earlier experimental results has been largely attributed to erroneous estimates of the alloy composition which lead to overestimates of the bowing parameter.<sup>22</sup> A recent study of In<sub>x</sub>Ga<sub>1-x</sub>N alloys using a wide range of experimental techniques resulted in a large spread of gap values for samples with  $x < 0.4$ .<sup>27</sup> The bowing coefficient for the band gap obtained from this data set was  $b = 2.5$  eV. A linear fit to the same data set gives a slope of -3.2 eV for the variation of the calculated band gap with In content. In contrast, our results give a bowing coefficient of  $b = 3.68$  eV and a slope of -4.04 eV. Comparison of the experimental dependence of the band-gap on composition with calculations has often proved unsatisfactory.<sup>15, 21</sup> However the supercell empirical pseudo-potential calculations of Bellaiche *et al* produce a bowing parameter that has a strong composition dependence, with  $b > 5$  eV for small ( $x < 0.1$ ) compositions.<sup>15</sup> The calculations also predict strong shifts in the VBM, particularly at small  $x$ , and much smaller shifts in the conduction band minimum. We report a behavior similar to these predictions. Figure 4 shows a comparison between our estimates of the N 2p VBM and CBM compared to the behavior predicted by the above supercell empirical calculations. It has been suggested that the bowing term  $x(1-x)$  is reasonable only when based on the assumption that the mixed crystal is an ideal

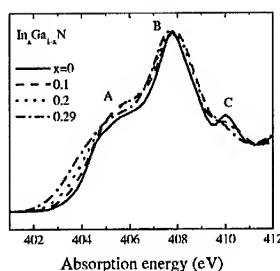


**Figure 2:** Normal incidence SXA spectra for In<sub>x</sub>Ga<sub>1-x</sub>N as a function of In content.

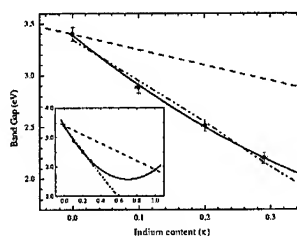


**Figure 3:** Data points indicate the position of the experimentally determined gap from the N 2p SXE and SXA spectra; the solid line is the fit using Vegard's law with constant bowing parameter  $b = 3.68$  eV; the dash-dot line is a straight line fit to the data points for  $0 \leq x \leq 0.29$ , the dashed line joins GaN to InN.

solution and the crystal lattice changes gradually through the ternary alloy system.<sup>28</sup> While phase separation is well documented in  $\text{In}_x\text{Ga}_{1-x}\text{N}$  alloys with high indium content,<sup>13, 29, 30</sup> a valence force-field calculation of a relatively low indium content ( $\text{In}_{0.2}\text{Ga}_{0.8}\text{N}$ ) model alloy revealed random alloying or 'alloy disorder' as opposed to complete phase separation.<sup>16</sup> Due to the In-N and Ga-N bond length difference ( $\sim 10.8\%$ ), the atomic positions are considered to fluctuate from the ideal lattice sites, leaving both bond length and bond angle distortions in the alloy. Others have suggested that the large, composition-dependent band-gap bowing coefficient (along with many other optical anomalies) in  $\text{In}_x\text{Ga}_{1-x}\text{N}$  alloys is due to the localization of hole states in the upper valence band.<sup>15</sup> Bellaiche *et al* point out that, in contrast to conventional alloys, no chemical clustering of In atoms is needed to induce this localization. Thus the results presented here can reasonably be interpreted as obtained from random alloys rather than from the existence of phase separated InN.

#### Hybridisation of N 2p states with Ga 3d and In 4d states in $\text{In}_x\text{Ga}_{1-x}\text{N}$

SXE has been shown to be highly sensitive to hybrid states.<sup>9, 11</sup> This is a consequence of the strong dipole selection rules that govern the transitions, and the dominance of intra-atomic transitions over interatomic transitions. The Ga 3d state lies approximately 19 eV below the valence band maximum. When N 2p to 1s SXE spectra were recorded from GaN, a weak emission feature was observed at this energy, which could be conclusively identified as emission from N 2p states hybridized with the Ga 3d shallow core level.<sup>11</sup> Figure 5 shows a series of N 2p to 1s SXE spectra from  $\text{In}_x\text{Ga}_{1-x}\text{N}$  as previously seen in Figure 1. As can be seen in the spectrum for pure GaN ( $x = 0$ ), there is a clear emission feature  $\sim 19$  eV due to the N 2p - Ga 3d hybridization. As the In content increases, the emission feature at 19 eV decreases, due to the reduction in relative Ga content. The Ga atoms are being substituted by an element that has shallow d states of its own. Thus we also anticipate an increase in hybridization of N 2p states to In 4d states as the In content increases. Such a behavior is evident in Figure 5, where it is clear that as the emission feature at approximately 19 eV decreases with In content, a broad feature at approximately 17 eV increases. As in the case of  $\text{Al}_x\text{Ga}_{1-x}\text{N}$ , this hybridization of the shallow core levels is important, since it must be taken into account when band structure calculations are performed.

#### Thermal Effects.

It is known that  $\text{In}_x\text{Ga}_{1-x}\text{N}$  alloys have a propensity to phase separate, particularly at high indium content<sup>13, 29, 30</sup>. A published growth phase diagram illustrates the growth stability of the InN-GaN quasi-binary system with respect to indium content and growth temperatures.<sup>31, 32</sup> We

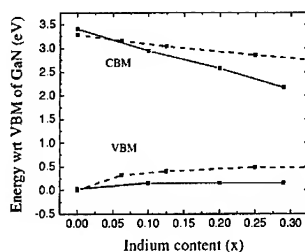


**Figure 4:** Comparison of the present data showing the motion of the elementally resolved N 2p VBM and CBM (solid line) with the results of the supercell calculations (dashed line).

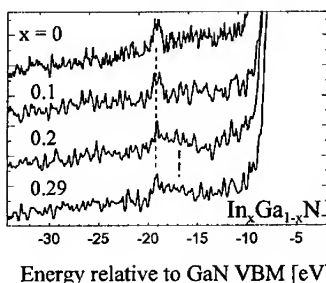


**Figure 5:** N K emission spectra showing N 2p-Ga 3d hybrid peak at 19 eV below the VBM. As x increases a N 2p -In 4d peak at lower binding energy is visible.

used SXE and SXA to study thermal effects on the band structure of a film grown in the stable region of the phase diagram. An additional motivation for this is concerned with studying the effect of the typical annealing performed in connection with preparing atomically clean surfaces of GaN.<sup>7</sup> A sample of  $\text{In}_{0.11}\text{Ga}_{0.89}\text{N}$  was electron beam heated to three separate temperatures: 610°C, 780°C, and 980°C for an hour in vacuum of  $\sim 1 \times 10^{-8}$  Torr. The sample growth temperature was  $\sim 650^\circ\text{C}$ – $675^\circ\text{C}$ ; thus these sample temperatures were respectively below, near, and well above the growth temperature. Figure 6 shows the SXE and SXA spectra of the N 2p valence and conduction band density of states through the annealing series. The qualitative features of the spectra are unaffected, with almost no broadening effects, but upon inspection, a slight shift in both the valence band and conduction band edges is evident and is indicated by the dashed lines. After annealing to 610°C the both spectra exhibit a decrease in energy. Annealing to 780°C resulted in no further spectral shift but another energy shift (to a lesser extent in the absorption spectra) is evident after annealing to 980°C. The stability of the bands at high temperatures is evident from the constant spectral shape. The band shifting sequence or origin is not understood at present but may be related to the diffusion and segregation of indium to the surface at even moderate annealing temperatures as observed in initial photoemission studies.<sup>33</sup>

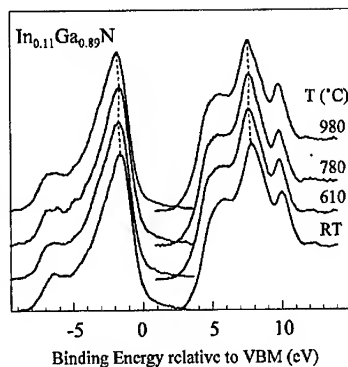


**Figure 6:** SXE and SXA spectra showing the N 2p PDOS of both the valence and conduction bands of an  $\text{In}_{0.11}\text{Ga}_{0.89}\text{N}$  sample as a function of annealing temperature.

## CONCLUSION

The valence band and conduction band electronic structure of  $\text{In}_x\text{Ga}_{1-x}\text{N}$  alloys has been studied using SXA and SXE for  $x$  between 0 and 0.29. The elementally resolved N 2p band gap evolution as a function of In content was measured. The N 2p valence band shows little change with increasing indium content except on going from  $x=0$  to  $x=0.1$  where a 0.15 eV shift of the VBM is observed, but no significant movement thereafter while the CBM showed a linear progression to lower energies. This behavior of the VBM and CBM is in close agreement with calculations which attribute this and the anomalous compositional-dependent band gap bowing to In-localized hole states in the upper valence band.<sup>15</sup> The SXA spectral features broaden with increasing In content, indicating a decrease in the atomic nitrogen localization, primarily caused by the random alloying in the crystal.<sup>11</sup>

## ACKNOWLEDGEMENTS

This work was supported in part by the National Science Foundation under grant number DMR-99-86099 and the U.S. Army Research Office under grant 40126-PH. Our x-ray emission spectrometer is funded by the US Army Research Office under DAAH04-95-0014. Experiments were performed at the NSLS which is supported by the U.S. Department of Energy, Divisions of Materials and Chemical Sciences. PR gratefully acknowledges support from the William V. Shannon Memorial Fellowship. TDM acknowledges the support of DoD/ARPA under grant MDA972-96-3-0014.

\* Permanent Address: Advanced Photon Source, Argonne National Laboratory, Argonne, IL 60439, USA

\*\* Author to whom correspondence should be addressed. Electronic mail: [ksmith@bu.edu](mailto:ksmith@bu.edu).

## REFERENCES

- <sup>1</sup> S. Nakamura and G. Fasol, *The Blue Laser Diode: GaN Based Light Emitters and Lasers* (Springer, Berlin, 1997).
- <sup>2</sup> F. A. Ponce and D. P. Bour, *Nature* **386**, 351 (1997).
- <sup>3</sup> F. A. Ponce, T. D. Moustakas, I. Akasaki, *et al.*, in *Materials Research Society Symposium Proceedings* (Materials Research Society, Pittsburg, 1997), Vol. 449.
- <sup>4</sup> H. Morkoc, S. Strite, G. B. Gao, *et al.*, *Journal of Applied Physics* **76**, 1363 (1994).
- <sup>5</sup> H. Morkoc and S. N. Mohammad, *Science* **267**, 51 (1995).
- <sup>6</sup> S. D. Kevan, *Angle Resolved Photoemission* (Elsevier, Amsterdam, 1991).
- <sup>7</sup> V. M. Bermudez, D. D. Koleske, and A. E. Wickenden, *Applied Surface Science* **126**, 69 (1998).
- <sup>8</sup> J. Nordgren and N. Wassdahl, *Physica Scripta* **T31**, 103 (1990).
- <sup>9</sup> C. B. Stagarescu, L.-C. Duda, K. E. Smith, *et al.*, *Physical Review B* **54**, 17335 (1996).
- <sup>10</sup> K. E. Smith, L.-C. Duda, C. B. Stagarescu, *et al.*, *Journal of Vacuum Science and Technology B* **16**, 2250 (1998).
- <sup>11</sup> L.-C. Duda, C. B. Stagarescu, J. Downes, *et al.*, *Physical Review B* **58**, 1928 (1998).
- <sup>12</sup> P. Ryan, C. McGuinness, J. E. Downes, *et al.*, *Physical Review B* **65**, art. no. (2002).
- <sup>13</sup> D. Doppalapudi, S. N. Basu, K. F. Ludwig, Jr., *et al.*, *J. Appl. Phys.* **84**, 1389 (1998).
- <sup>14</sup> D. Doppalapudi, S. N. Basu, and T. D. Moustakas, *Journal of Applied Physics* **85**, 883 (1999).
- <sup>15</sup> L. Bellaiche, T. Mattila, L. W. Wang, *et al.*, *Applied Physics Letters* **74**, 1842 (1999).
- <sup>16</sup> T. Saito and Y. Arakawa, *Physical Review B* **60**, 1701 (1999).
- <sup>17</sup> E. A. Albanesi, W. R. L. Lambrecht, and B. Segall, *Physical Review B* **48**, 17841 (1993).
- <sup>18</sup> S. Pereira, M. R. Correia, T. Monteiro, *et al.*, *Journal of Crystal Growth* **230**, 448 (2001).
- <sup>19</sup> S. Pereira, M. R. Correia, T. Monteiro, *et al.*, *Applied Physics Letters* **78**, 2137 (2001).
- <sup>20</sup> M. D. McCluskey, C. G. Van de Walle, C. P. Master, *et al.*, *Applied Physics Letters* **72**, 2725 (1998).
- <sup>21</sup> C. G. Van de Walle, M. D. McCluskey, C. P. Master, *et al.*, *Materials Science and Engineering B-Solid State Materials For Advanced Technology* **59**, 274 (1999).
- <sup>22</sup> I. Vurgaftman, J. R. Meyer, and L. R. Ram-Mohan, *Journal of Applied Physics* **89**, 5815 (2001).
- <sup>23</sup> K. Osamura, S. Naka, and Y. Murakami, *Journal of Applied Physics* **46**, 3432 (1975).
- <sup>24</sup> C. Wetzel, T. Takeuchi, S. Yamaguchi, *et al.*, *Applied Physics Letters* **73**, 1994 (1998).
- <sup>25</sup> J. Wagner, A. Ramakrishnan, D. Behr, *et al.*, *MRS Internet Journal of Nitride Semiconductor Research* **4**, U111 (1999).
- <sup>26</sup> M. Goano, E. Bellotti, E. Ghillino, *et al.*, *Journal of Applied Physics* **88**, 6476 (2000).
- <sup>27</sup> K. P. O'Donnell, R. W. Martin, C. Trager-Cowan, *et al.*, *Materials Science and Engineering B-Solid State Materials For Advanced Technology* **82**, 194 (2001).
- <sup>28</sup> E. V. Kalashnikov and V. I. Nikolaev, *Mrs Internet Journal of Nitride Semiconductor Research* **2**, 18 (1997).
- <sup>29</sup> R. Singh, D. Doppalapudi, T. D. Moustakas, *et al.*, *Applied Physics Letters* **70**, 1089 (1997).
- <sup>30</sup> N. A. El-Masry, E. L. Piner, S. X. Liu, *et al.*, *Appl. Phys. Lett.* **72**, 40 (1998).
- <sup>31</sup> I. H. Ho and G. B. Stringfellow, *Mater. Res. Soc. Symp. Proc.* **449**, 871 (1997).
- <sup>32</sup> I. H. Ho and G. B. Stringfellow, *Appl. Phys. Lett.* **69**, 2701 (1996).
- <sup>33</sup> J. E. Downes, K. E. Smith, A. Y. Matsuura, *et al.*, (MAX-lab Activity Report, Lund, 2000), p. 74.

---

## **Poster Session**

### Blue Luminescence in Undoped and Zn-doped GaN

**M. A. Reshchikov and H. Morkoç**

Virginia Commonwealth University, Richmond, VA 23284, U.S.A.

**R. J. Molnar**

MIT Lincoln Laboratory, Lexington, MA 02420, U.S.A.

**D. Tsvetkov and V. Dmitriev**

TDI, Inc., Silver Spring, MD 20904, U.S.A.

#### ABSTRACT

A broad band with a maximum at about 2.9 eV (blue band) is widely observed in the photoluminescence (PL) and cathodoluminescence (CL) spectra of unintentionally doped GaN grown by metalorganic chemical vapor deposition (MOCVD) or by hydride vapor phase epitaxy (HVPE). In some samples this band exhibits fine structure attributed to electron-phonon coupling, in others it appears featureless. Different defect origin and recombination mechanisms responsible for the blue band have been suggested in the past. The situation is complicated by the fact that bands similar in shape and position were observed also in Zn- and Mg-doped GaN, as well as in undoped GaN after dry or wet etching. We investigated PL in HVPE-grown undoped, Si- and Zn-doped GaN layers in wide temperature and excitation intensity ranges. We have found that the shape, temperature and excitation intensity dependencies of the blue band in undoped GaN are almost identical to those in GaN lightly doped with Zn. Moreover, in both undoped and Zn-doped samples we observed a distinctive set of peaks related to an exciton bound to the Zn acceptor. Although the exact structure of the Zn acceptor is still unknown, our experimental results unambiguously demonstrate that Zn impurity is responsible for the blue band in unintentionally doped GaN. The results of transient PL study are also consistent with the above attribution.

#### INTRODUCTION

A blue luminescence (BL) band peaking at 2.9 eV is often observed in PL and CL spectrum of undoped and Si-doped GaN [1-10]. Kaufman *et al.* [7] attributed the BL band in undoped GaN to deep donor-acceptor pair (DAP) transitions involving residual Mg impurity as acceptor and the  $V_N\text{Mg}$  complex as a deep donor. More recently, detailed studies of the BL band in undoped GaN at different temperatures and excitation intensities revealed that it is related to transitions from a shallow donor (or from the conduction band at elevated temperatures) to a deep acceptor [10,11]. Thermal activation energy of the acceptor was estimated as 0.34 eV [11]. Various proposals have been made as to the nature of the defect responsible for the 2.9 eV band in undoped GaN. Besides the above-mentioned assignment of this band to residual Mg, it was also attributed to a gallium vacancy ( $V_{Ga}$ )-related complex [9,11,12], in particular to  $V_{Ga}O_N$  [9] and  $V_{Ga}H_n$  [12]. Note that in a few studies a similar band centered at about 3.0 eV has been observed that exhibited a strong fatigue effect [13-15]. We also observed a broad blue band with a similar fatigue effect in a GaN epilayer grown by molecular beam epitaxy (MBE). With etching experiments using hot phosphoric acid, we attributed this feature to manifestation of the surface states [16]. To elucidate the origin of the 2.9 eV band in undoped GaN, we have studied temperature and excitation intensity dependencies of the BL band in undoped GaN and compared its behavior with that in Mg-, Si- and Zn-doped GaN. Our results suggest that the 2.9 eV band often observed in undoped GaN is caused by Zn contamination.

## EXPERIMENTAL DETAILS

Epitaxial GaN layers with thicknesses ranging from 6 to 15  $\mu\text{m}$  were grown onto the *c*-plane of sapphire substrates by the HVPE method. Room-temperature concentration of free electrons and their mobility were about  $1 \times 10^{17} \text{ cm}^{-3}$  ( $1 \times 10^{18} \text{ cm}^{-3}$ ) and  $360 \text{ cm}^2 \text{ V}^{-1} \text{ sec}^{-1}$  ( $370 \text{ cm}^2 \text{ V}^{-1} \text{ sec}^{-1}$ ), respectively, in undoped (Si-doped) GaN. Zn-doped GaN layers were semi-insulating with a room-temperature resistivity of about  $10^9 \Omega \text{ cm}$  and a concentration of Zn ranging from  $\sim 10^{17}$  to  $10^{18} \text{ cm}^{-3}$ . Steady-state and time-resolved PL was excited with HeCd and nitrogen lasers, respectively. The emission was dispersed by a 0.5 m grating monochromator and detected by a photomultiplier tube. Excitation density was varied over the range of  $10^{-5}$  -  $200 \text{ W/cm}^2$  by means of neutral density filters. The temperature of the sample was varied from 15 to 330 K using a closed cycle optical cryostat.

## RESULTS AND DISCUSSION

The PL spectra of the undoped, Si- and Zn-doped GaN layers are shown in Fig. 1.

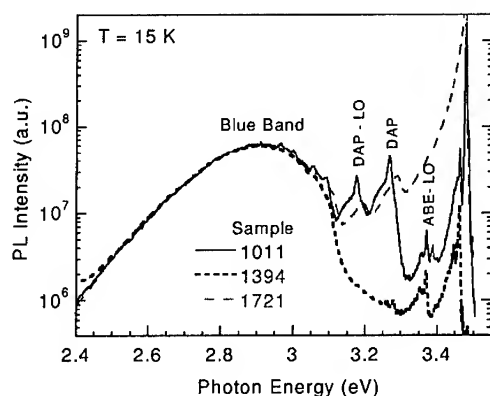


**Figure 1.** Low-temperature PL spectrum of undoped (#1011), Si-doped (#1721) and Zn-doped (#1394) GaN layers grown on sapphire. The intensity is normalized at maximum of the BL band.

In all these samples the BL dominated among the defect-related bands in the PL spectrum. The internal quantum efficiency of the BL band was about 5% in all studied samples, although the efficiency of the exciton emission differed substantially. The shape and position of the BL band were similar in undoped, Si- and Zn-doped GaN (Fig. 1). Even the fine structure, observed earlier in the MOCVD-grown undoped GaN and attributed to electron-phonon coupling with LO and local (or pseudo-local) phonon modes [10], was similar in these samples, although in Si- and Zn-doped GaN it was blurred.

Another supporting evidence that the BL bands in undoped and Zn-doped GaN samples have the same origin follows from an analysis of the excitonic part of the PL spectrum (Fig. 2). The peaks at 3.486 and 3.479 eV are attributed to the free exciton and the exciton bound to a shallow donor, respectively. A peak at 3.463 eV is very strong in the Zn-doped layer, and its shape and position coincide with the corresponding peak in undoped layer. Previously, the peak with the binding energy of 23 - 25 meV in Zn-doped GaN has been attributed to the exciton bound to a Zn acceptor [17,18].

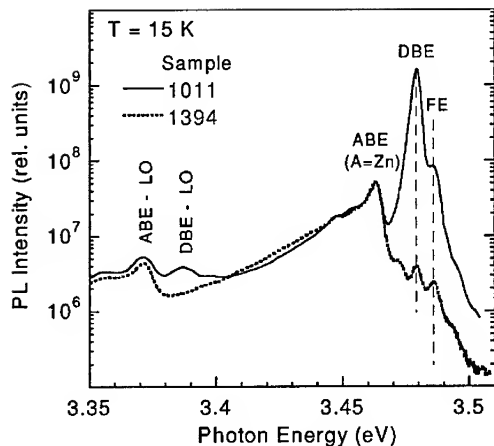


**Figure 2.** Excitonic part of the PL spectrum of undoped (#1011) and Zn-doped (#1394) GaN. The spectrum of the Zn-doped sample is shifted by 4 meV to higher energies to compensate the difference in strain-related shifts.

We did not notice any shift of the BL band in undoped and Si-doped GaN to an accuracy of 10 meV with an increase of excitation density from  $10^{-5}$  to  $10^2$  W/cm<sup>2</sup>. The blue band in Zn-doped samples shifted by at most 70 meV in this range of excitation intensities. Moreover, the character of the shift and position of the BL band were sample-dependent in semi-insulating GaN (Fig. 3).

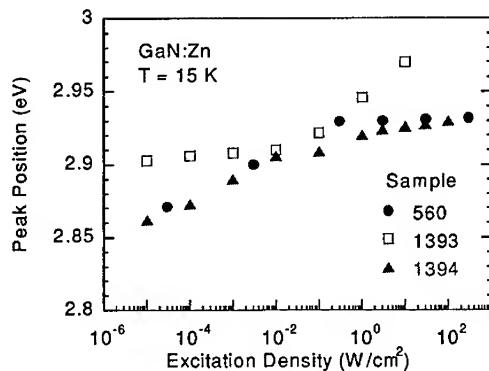


**Figure 3.** Position of the BL band in semi-insulating Zn-doped GaN samples at different excitation intensities. The shape of the band was nearly the same in all samples and at any excitation intensity.

Earlier we attributed this fact to pinning of Zn acceptors to dislocations [18]. However similar behavior was observed in dislocation-free bulk GaN [19]. We suggest that DAP-type recombination involving several donors and the same Zn acceptor may be responsible for the observed shifts. Indeed, in undoped or Si-doped GaN the Fermi level is close to the conduction band and shallow donors are partially filled in equilibrium at low temperatures. Probability of the DAP-type transition decreases exponentially for deeper donors due to smaller overlap of the electron and hole wavefunctions. Note also high concentration of the shallow donors in these samples. Therefore contribution to the BL band from the deeper donors may be neglected in *n*-type conductive GaN. In contrast, in semi-insulating GaN shallow donors may contribute much less due to their lower concentration and their smaller occupancy. The transitions from the deeper donors are slower and, hence, with increasing excitation density saturation of transitions involving the deeper donors would

take place at lower excitation levels, causing the shift of the broad band with excitation intensity. Another manifestation of this effect is the shift of the PL band with time delay. We indeed observed a red shift of the blue band in Zn-doped GaN by about 50 meV at  $10^{-5}$  s after the excitation pulse provided by N-laser. Note that the origin of the shift of the BL band with excitation intensity is different in Zn- and Mg-doped GaN. While in Zn-doped samples different distribution profiles of relatively shallow donors (with ionization energy of about 100 meV and less) are responsible for different positions and different character of the peak shift with excitation intensity (Fig. 3), the BL band in GaN:Mg, attributed to transitions from a deep ( $\sim 0.6$  eV) donor to the shallow Mg acceptor, always shifts in a similar way (no shift in the low excitation limit and fast shift at high excitation levels) typical for a deep DAP [20]. In contrast to the Zn-related BL band observed in Zn-doped and undoped GaN samples with concentration of Zn acceptor starting from about  $10^{15}$  cm $^{-3}$  [11], the BL band in GaN:Mg appears only at high concentrations of Mg ( $10^{19}$  –  $20^{20}$  cm $^{-3}$ ) [21] because of small probability of transitions between really deep donors and shallow acceptors.

In our previous work [18] we reported on observation of nearly identical decays of PL in insulating and *n*-type degenerate layers of a GaN:Zn sample. In this work transient behavior of the BL band was studied in a few Zn-doped, as well as undoped and Si-doped samples (Fig. 4).

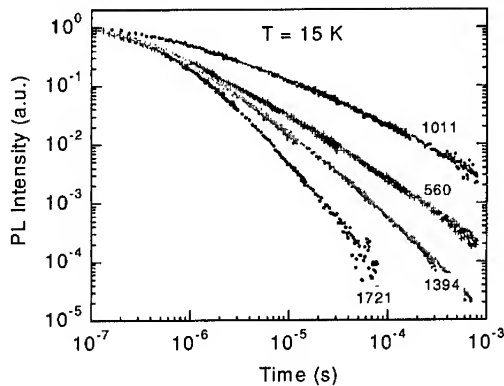


**Figure 4.** PL intensity decay of the BL band (at 2.9 eV) in undoped (#1011), Si-doped (#1721) and Zn-doped (#560 and #1394) GaN samples.

The decay is nonexponential at low temperatures in all the samples. The difference in PL decays for different samples can be explained by difference in concentration of shallow and relatively shallow donors. In particular fast PL decay in the Si-doped GaN and slow decay in undoped GaN correlate well with concentrations of the shallow donors in these samples (respectively  $2.8 \times 10^{18}$  and  $6 \times 10^{17}$  cm $^{-3}$ , as it was estimated from the Hall-effect measurements). In contrast to our earlier report [18], the decay of the BL is not identical in various GaN:Zn samples (Fig. 4) which is in conflict with our tentative assumption that the BL band in GaN:Zn involves transitions from some excited state of the Zn-related defect [18]. To resolve contradiction with the results of the earlier work [18], we propose that when the GaN layer is illuminated from the backside through sapphire substrate, very strong near-band-edge emission from the interfacial degenerate layer resonantly excites defects responsible for the BL band in the entire GaN layer. Therefore unexpectedly slow and identical decays of the BL band excited in front-scattering and back-scattering geometry can be attributed to emission from DAP in whole GaN layer, not in the surface and interface layers as was proposed earlier [18].

Following the method proposed in Ref. [22], we have estimated the effective lifetime of the BL in wide range of temperatures for a few undoped and doped GaN samples (Fig. 5) [22].

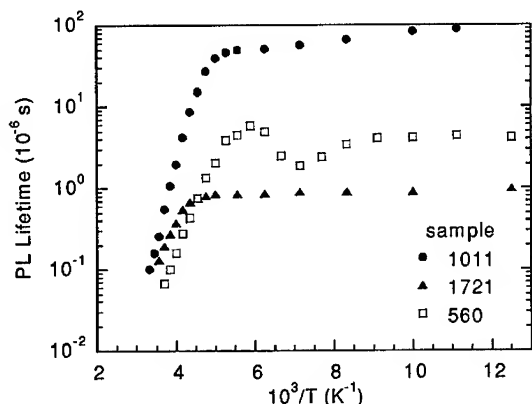


**Figure 5.** Temperature dependence of the effective lifetime of the BL in undoped (#1011), Si-doped (#1721) and Zn-doped (560) GaN samples.

We explain a decrease of the effective lifetime of PL at temperatures above 200 K by thermalization of holes from Zn acceptor to the valence band. The dependence can be fitted with the following equation [22]

$$\tau_{PL}^{-1} = C_n n_0 + Q \exp\left(-\frac{E_A}{kT}\right), \quad (1)$$

where  $C_n$  is the electron-capture coefficient,  $Q$  is a factor depending on the hole-capture characteristics and  $E_A$  is the ionization energy of the acceptor. The ionization energy (300 – 400 meV) is similar in undoped, Si- and Zn-doped samples. This value is consistent with position of the zero-phonon line of the BL (about 3.10 eV), which can be obtained from analysis of the PL spectrum (see Fig. 1 and also Ref. [10]). Furthermore, assuming that transitions from the conduction band to Zn acceptor dominate over DAP-type transitions at temperatures before quenching (at about 200 K) in  $n$ -type GaN samples and accounting for the free electron concentration at 200 K obtained from the temperature-dependent Hall measurements ( $5 \times 10^{17}$  and  $8 \times 10^{17} \text{ cm}^{-3}$  for the samples 1011 and 1721, respectively), we can estimate the electron-capture cross-section,  $\sigma_n$ , for Zn-acceptor:  $\sigma_n = C_n v_n^{-1}$ , where  $v_n$  is the velocity of free electrons in GaN (approximately  $1.9 \times 10^7 \text{ cm/s}$ ). We obtain  $\sigma_n = 2.1 \times 10^{-20} \text{ cm}^2$  (sample 1011) and  $8 \times 10^{-20} \text{ cm}^2$  (sample 1721), within reasonable accuracy close to the values obtained for undoped GaN layers grown by MOCVD ( $1.6 - 3.0 \times 10^{-20} \text{ cm}^2$ ) [22].

## CONCLUSIONS

We demonstrated that the blue luminescence band peaking at about 2.9 eV in undoped (or Si-doped)  $n$ -type conductive GaN has the same origin with the blue luminescence in Zn-doped semi-insulating GaN. The blue band is attributed to DAP-type transitions from relatively shallow donors (from the conduction band at elevated temperatures) to Zn acceptor. The profile distributions of the donor states in semi-insulating GaN:Zn layers are responsible for slightly different positions of the blue band and its shift with excitation intensity.

## ACKNOWLEDGMENTS

This work was funded by AFOSR (Dr. G. L. Witt), NSF (Dr. L. Hess and Dr. U. Varshney), and ONR (Dr. C. E. C. Wood and Dr. Y. S. Park). The authors thank Dr. D. C. Look for

providing the Hall effect data. The Lincoln Laboratory portion of this work was sponsored by the Office of Naval Research under Air Force contract #F19628-00-C-0002. Opinions, interpretations, conclusions and recommendations are those of the authors and not necessarily endorsed by the US Air Force. Work at TDI was supported by MDA and monitored by the ONR (Dr. Colin Wood).

## REFERENCES

1. A. Cremades, J. Piqueras, C. Xavier, T. Monteiro, E. Pereira, B. K. Meyer, D. M. Hofmann, and S. Fischer, *Mat. Sci. and Eng.* **B42**, 230 (1996).
2. C. Trager-Cowan, K. P. O'Donnell, S. E. Hooper, and C. T. Foxon, *Appl. Phys. Lett.* **68**, 355 (1996).
3. E. F. Schubert, I. D. Goepfert, and J. M. Redwing, *Appl. Phys. Lett.* **71**, 3224 (1997).
4. J. C. Carrano, P. A. Grudowski, C. J. Eiting, R. D. Dupuis, and J. C. Campbell, *Appl. Phys. Lett.* **70**, 1992 (1997).
5. M. Herrera Zaldivar, P. Fernandez, J. Piqueras, and J. Solis, *J. Appl. Phys.*, **85**, 1120 (1999).
6. K. Fleisher, M. Toth, M. R. Phillips, J. Zou, G. Li, and S. J. Chua, *Appl. Phys. Lett.* **74**, 1114 (1999).
7. U. Kaufmann, M. Kunzer, H. Obloh, M. Maier, Ch. Manz, A. Ramakrishnan, and B. Santic, *Phys. Rev. B* **59**, 5561 (1999).
8. C.-C. Tsai, C.-S. Chang, and T.-Y. Chen, *Appl. Phys. Lett.* **80**, 3718 (2002).
9. H. C. Yang, T. Y. Lin, and Y. F. Chen, *Phys. Rev. B* **62**, 12593 (2000).
10. M. A. Reshchikov, F. Shahedipour, R. Y. Korotkov, B. W. Wessels, and M. P. Ulmer, *J. Appl. Phys.* **87**, 3351 (2000).
11. M. A. Reshchikov and R. Y. Korotkov, *Phys. Rev. B* **64**, 115205 (2001).
12. M. Toth, K. Fleisher, and M. R. Phillips, *Phys. Rev. B* **59**, 1575 (1999).
13. S. J. Xu, G. Li, S. J. Chula, X. C. Wang, and W. Wang, *Appl. Phys. Lett.* **72**, 2451 (1998).
14. S. A. Brown, R. J. Reeves, C. S. Haase, R. Cheung, C. Kirchner, and M. Kamp, *Appl. Phys. Lett.* **75**, 3285 (1999).
15. S. Dhar and S. Ghosh, *Appl. Phys. Lett.* **80**, 4519 (2002).
16. M. A. Reshchikov, P. Visconti, and H. Morkoç, *Appl. Phys. Lett.* **78**, 177 (2001).
17. B. J. Skromme and G. L. Martinez, *MRS Internet J. Nitride Semicond. Res.* **5S1**, W9.8 (2000).
18. M. A. Reshchikov, D. Huang, H. Morkoç, and R. J. Molnar, *Mat. Res. Soc. Symp. Proc.* **693**, 12.10 (2002).
19. T. Suski and P. Perlin, private communication
20. M. A. Reshchikov, G.-C. Yi, and B. W. Wessels, *MRS Internet J. Nitride Semicond. Res.* **4S1**, G11.8 (1999).
21. U. Kaufmann, M. Kunzer, M. Maier, H. Obloh, A. Ramakrishnan, B. Santic, and P. Schlotter, *Appl. Phys. Lett.* **72**, 1326 (1998).
22. R. Y. Korotkov, M. A. Reshchikov, and B. W. Wessels, *Physica B*, in press.

### Surface-Related Photoluminescence Effects in GaN

M. A. Reshchikov, M. Zafar Iqbal,<sup>a</sup> D. Huang, L. He, and H. Morkoç  
Virginia Commonwealth University, Richmond, VA 23284, U.S.A.

<sup>a</sup> On leave in VCU from the Quaid-i-Azam University, Islamabad, Pakistan

#### ABSTRACT

Photoluminescence (PL) from GaN epilayers is found to be sensitive to the ambient atmosphere and length of UV exposure. We studied the effect of UV illumination in different ambients including air, oxygen, nitrogen and hydrogen gases on room-temperature PL of GaN grown on sapphire by molecular beam epitaxy. In some samples the PL intensity increased markedly in vacuum as compared to excitation in air, whereas in others it decreased appreciably. While air and oxygen showed strong reversible variation of the PL intensity as compared to vacuum, nitrogen and hydrogen atmospheres led to a very small change. In some samples we observed a shift of the yellow luminescence band with change of ambient, in others no shift was detected. PL intensity also changed during UV irradiation when the sample was in air ambient. Possible reasons for our observations are discussed.

#### INTRODUCTION

Surface quality and surface-related effects are of obvious interest for semiconductor device applications. Photoluminescence (PL) from GaN has been reported to show strong dependence on the ambient atmosphere around the samples during excitation. Air evacuation, for instance, is known to cause a strong enhancement of the luminescence and a large decrease in photorefectance as compared to excitation in air [1,2]. On the other hand, exposure to air at room temperature for several days led to reduction of leakage currents, enhancement of barrier heights, and improving ideality factors in AlGaIn Schottky diodes [3]. These effects are believed to be related to the surface states. It is known that due to spontaneous polarization a strong upward band bending is expected at the Ga-face, whereas at N-face surface positive ionized donors largely compensate the downward band bending in *n*-type GaN [4,5]. The band bending is also affected by surface structural defects, broken bonds, oxidation, formation of overlayers of Ga atoms at the surface [6], and presence of adsorbates. Nienhaus *et al.* [7] have demonstrated that adsorption of oxygen increases the ionization energy and electron affinity of GaN and Al<sub>x</sub>Ga<sub>1-x</sub>N surfaces. Furthermore, Bermudez [8] has found that oxygen removes surface states, resulting in reducing the band bending compared to clean GaN surface. As a result, band bending at the surface is reduced from 0.9 to 0.5 eV. In case of the practical surface, the band bending was found to be about 0.4 eV [8]. Oxidation, adsorption of foreign atoms, existence of broken bonds, etc. depend on the growth conditions and surface treatment. Thus we may expect different band bending near the surface, as well as existence of different surface states in GaN prepared in different conditions. In this letter, we report detailed PL study of GaN under different ambient conditions, including air, vacuum, oxygen, nitrogen and hydrogen atmospheres. The effect of UV-laser exposure on PL is also considered.

#### EXPERIMENTAL DETAILS

GaN layers (thickness from 1 to 3 μm) were grown on *c*-plane sapphire by molecular-beam epitaxy (MBE). Samples with both Ga and N polarity, grown by employing AlN and GaN buffer

layers, respectively [9], including samples grown in N- and Ga-rich conditions, were studied. Steady-state PL was excited with a He-Cd laser. The PL was dispersed with a SPEX grating monochromator and detected with Hamamatsu photomultiplier tube R955-P. The PL spectra were corrected for the response of the optical system. The samples were placed in an optical cryostat with the vacuum pressure of about  $3 \times 10^{-4}$  Tor.

## RESULTS AND DISCUSSION

In majority of our samples, regardless of the growth conditions, a strong enhancement in the PL intensity under ultra-violet (UV) illumination was observed as the sample chamber was evacuated [2]. The effect was reversible insofar as allowing air into the chamber restored the emission signal to its original level. However, switching off the excitation light for several minutes did not change the emission intensity on re-excitation. The value of rise of the PL signal upon evacuation was found to be proportional to the UV illumination intensity [2].

In order to ascertain whether oxygen or, for instance, water vapor in air plays a dominant role in the evolution of PL, we carried out experiments with the surface of GaN exposed to various gases. The results for the near-band-edge PL are presented in Fig. 1.

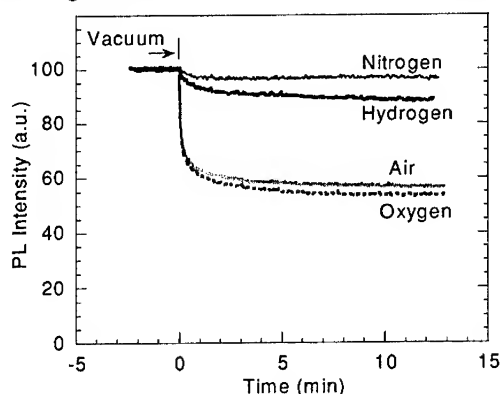


**Figure 1.** Evolution of the near-band-edge emission intensity in the GaN sample 689 under different ambient conditions.

It can be seen that oxygen ambient produces the same kind of effect as air, i.e. a prolonged decay of the PL signal as compared to its value in vacuum, whereas exposure to nitrogen or hydrogen leads to a much smaller decrease in the signal. Exposure to different gases followed by evacuation was repeated several times for one sample, and the effect was found to be reproducible. The clear distinction between the transient changes in PL emission in vacuum and oxygen as compared to other ambients (nitrogen and hydrogen) and similarity of the changes in air and oxygen ambients suggest that oxygen adsorption is responsible for the degradation of the optical quality of the GaN surface. Fig. 2 presents typical PL spectra in vacuum and in different ambients for the same sample.

The spectra include near-band-edge emission and a yellow luminescence (YL) band related to a deep-level acceptor [10]. A noticeable red shift of the YL band has been observed with the various gas ambients, as compared to the peak position in vacuum – about 30 meV for oxygen and air and somewhat lower for other ambients. The red shift of the YL band up to 200 meV was observed in some, but not all, of the samples studied, although no shift or a red shift of only 1 – 2 meV in spectral position of the near-band-edge emission was detected in all the samples studied. Typically, the near-band-edge emission increased noticeably (up to 5 times in some samples) with

air evacuation after UV illumination of the sample, whereas the YL intensity showed no increase in some samples (Fig. 2), increased up to 3 times in others (Fig. 3), and even decreased several times in a few cases (Fig. 4). A change from vacuum to nitrogen gas ambient typically caused much smaller changes in the PL intensity and spectrum.

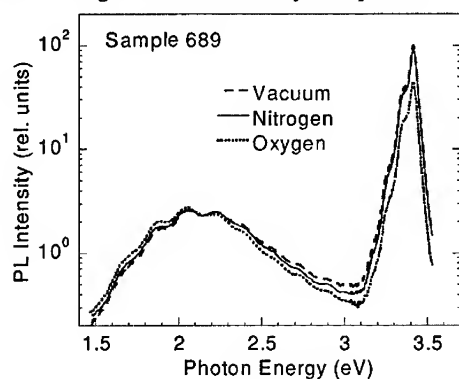


**Figure 2.** Room temperature PL spectra of the GaN sample # 689 (N-polar, Ga-rich) under different ambient conditions. The PL spectrum in air ambient (not shown) nearly coincided with the spectrum in oxygen ambient.

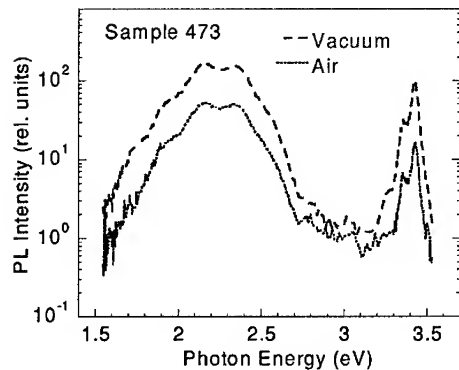


**Figure 3.** Room temperature PL spectra of the GaN sample # 473 (Ga-polar, N-rich) in air and vacuum ambients.

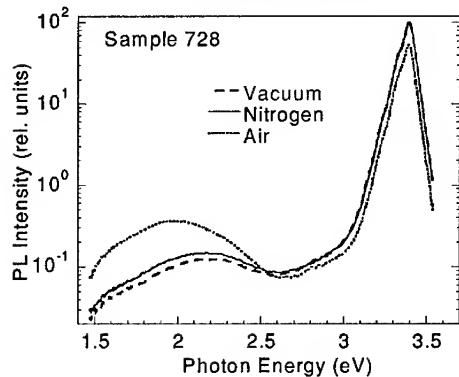


**Figure 4.** Room temperature PL spectra of the GaN sample # 728 (N-polar, N-rich) under different ambient conditions.

Another related phenomenon observed in our experiments is a slow change in the PL intensity during UV irradiation when the sample is in air ambient. Usually this change manifested as a decrease in the PL intensity, which varied from sample to sample, although an increase of the emission intensity has been observed for some time intervals in a few samples (Fig. 5). The change in optical properties with UV illumination was metastable. In most cases only partial restoration of the PL intensity was observed after the sample was kept in dark for a few hours, while the PL intensity being restored to its original value after two weeks.

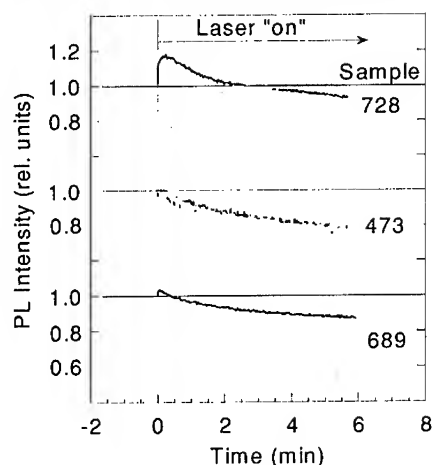


**Figure 5.** Evolution of the PL intensity upon exposure time in air for near-band-edge emission at 3.42 eV (black curves) and YL band at 2.3 eV (gray curves).

## DISCUSSION

We propose that oxygen adsorption creates variety of surface states, the radiative and non-radiative states, which compete with radiative transitions in bulk, resulting in the observed enhancement or suppression of the PL signal in different GaN samples. Our results suggest that nitrogen and hydrogen do not affect the surface states significantly. This could either imply lower adsorption of these gases or more likely that their adsorption does not create surface states in abundant quantities. The observed enhancement (degradation) of PL upon evacuation can be explained by UV-induced removal of the non-radiative (radiative) surface defects introduced by oxygen. Note that evacuation without UV irradiation does not remove oxygen-related states as discerned from the experiments with variation of irradiation intensity [2]. This mechanism is especially plausible for explaining the increase of the YL intensity in air (Fig. 4). The suppression of the near-band-edge emission in air ambient, observed in all studied samples, may suggest another mechanism of PL degradation. Indeed, the surface states, removed by the photo-induced desorption of oxygen, may not participate in recombination, but only change the band bending due to change of electrical charge at the surface. The red shift of the YL band observed in a few samples can also be explained by an increase of the band bending at the surface in air ambient. The surface depletion resulting from this band bending may lead to diagonal (spatially indirect) transitions of free electrons to the deep-level states located closer to the surface. The red shift would be greater for the larger band bending. The variety of PL behaviors upon air or gas evacuation, as displayed in Figs. 2 – 4, suggests that more than one effect is responsible for variations observed in different samples studied.

The decrease of the PL intensity in air ambient (Fig. 5), observed in majority of the studied GaN samples, can be explained as follows. Photogenerated holes can be captured by the surface states and/or accumulate in the surface space region (Fig. 6).

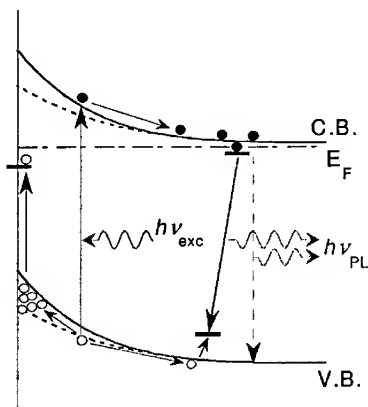


**Figure 6.** Schematic representation of transitions near the surface in unintentionally doped GaN. The band bending leads to accumulation of the holes in the valence band near the surface and at the surface states. Both processes result in accumulation of positive charge near the surface and in increase of the band bending. The increased space separation between the electrons and holes reduces probability of radiative recombination.

The positive charge at or near the surface increases the barrier (band bending) at the surface and, hence, increases the depletion depth. We may expect a decrease of both near-band-edge and defect-related PL intensities in this model. The difference in PL decays for the near-band-edge emission and YL, as well as different rate of the PL degradation in different samples, can be attributed to a variety of depth distributions of the defect states in different samples. In particular, if the defects responsible for the YL band are located at the surface, a fast initial decrease of the YL intensity is expected due to fast saturation of these states by photogenerated holes. In contrast, if in another sample the defects contributing to the YL band are distributed more or less uniformly in bulk and near the surface, the decay may be slow. We suggested previously [11] that different kinds of defects may be responsible for the YL band with nearly the same shape and peak position. Further investigations to understand the variety of PL degradation types, including increases and decreases in the PL intensity (Fig. 5), need to be undertaken. Detailed investigations of the surface-related effects in PL of GaN grown by MBE under different growth conditions are in progress and will be reported elsewhere along with investigations on samples grown by other techniques.

## CONCLUSIONS

We have investigated surface-related effects in the photoluminescence of GaN grown by MBE. In air and oxygen gas ambients, we observed a substantial decrease (but in some samples – an increase) in the PL signal, as compared to vacuum. In contrast, the variations of PL intensity in nitrogen and hydrogen gas environments were negligible. Moreover, we observed a red shift of the YL band in some of the samples for the above-mentioned gas ambients, as compared to vacuum. The observed effects are attributed to the surface states associated with oxygen adsorption. Furthermore, we observed a slow change in the PL intensity during UV irradiation when the sample was in air ambient. This phenomenon is also related to the surface states in GaN. Most of the observed effects could be explained within the framework of the suggested

model, wherein UV illumination leads to accumulation of holes near the surface and at the surface states.

#### ACKNOWLEDGMENTS

This work was funded by AFOSR (Dr. G. L. Witt and T. Steiner), NSF (Dr. L. Hess and Dr. U. Varshney), and ONR (Dr. C. E. C. Wood and Dr. Y. S. Park).

#### REFERENCES

1. U. Behn, A. Thamm, O. Brandt, and H. T. Grahn, *J. Appl. Phys.* **87**, 4315 (2000).
2. M. A. Reshchikov, P. Visconti, K. M. Jones, and H. Morkoç, *Mat. Res. Soc. Symp. Proc.* **680**, E5.4 (2001).
3. E. D. Readinger, B. P. Luther, S. E. Mohny, and E. L. Piner, *J. Appl. Phys.* **89**, 7983 (2001).
4. Hadis Morkoç, Roberto Cingolani, and Bernard Gil, "Polarization Effects in Nitride Semiconductor Device Structures, and Performance of Modulation Doped Field Effect Transistors" *Solid State Electronics*, vol.43, no.10, pp.1909-1927, Oct. 1999
5. U. Karrer, O. Ambacher, and M. Stutzmann, *Appl. Phys. Lett.* **77**, 2012 (2000).
6. J. E. Northrup, J. Neugebauer, R. M. Feenstra, and A. R. Smith, *Phys. Rev. B* **61**, 9932 (2000).
7. H. Nienhaus, M. Schneider, S. P. Grabowski, W. Mönch, R. Dimitrov, O. Ambacher, and M. Stutzmann, *Mat. Res. Soc. Symp. Proc.* **680E**, E4.5 (2001).
8. V. M. Bermudez, *J. Appl. Phys.* **80**, 1190 (1996).
9. D. Huang, P. Visconti, M. A. Reshchikov, F. Yun, T. King, A. A. Baski, C. W. Litton, J. Jasinski, Z. Liliental-Weber, and H. Morkoç, *Phys. Stat. Sol. (a)* **188**, 571 (2001).
10. T. Ogino and M. Aoki, *Jap. J. Appl. Phys.* **19**, 2395 (1980).
11. M. A. Reshchikov, H. Morkoç, S. S. Park, and K. Y. Lee, *Mat. Res. Soc. Symp. Proc.* **693**, 16.19 (2002).

**BEST AVAILABLE COPY**

### Excitons bound to surface defects in GaN

M. A. Reshchikov, D. Huang, and H. Morkoç

Virginia Commonwealth University, Richmond, VA 23284, U.S.A.

#### ABSTRACT

Sharp intense peaks are sometimes detected in the low-temperature photoluminescence (PL) spectrum of undoped GaN samples in the photon energy range of 3.0 – 3.46 eV. Some of these peaks can be attributed to excitons bound to dislocations and inversion domains, whereas some others originate from the GaN surface because they can be affected essentially by surface treatment. In our samples, grown by molecular beam epitaxy on sapphire substrate, the 3.42 eV peak always disappeared after removing the surface layer by etching for a few seconds in hot phosphoric acid. Atomic force microscopy images confirmed that such light etching modifies the surface morphology, although the etched depth is negligibly small. Moreover, intensities of two other peaks (at 3.32 and 3.35 eV) were observed to depend on sample etching, as well as on the length of subsequent exposure to air. The 3.32 and 3.35 eV peaks evolved with time of UV illumination, increasing by several times and demonstrating memory effect at low temperature. We attribute the 3.42 and 3.35 eV peaks to bound excitons, whereas the 3.32 eV peak is tentatively attributed to a surface donor-acceptor pair transition.

#### INTRODUCTION

Structural and surface defects are known to affect markedly electrical and optical properties of semiconductor devices. It is well known that dislocations can bind excitons and be responsible for intense photoluminescence (PL) lines detected well below the bandgap energy [1]. However, excitons can be bound also to other types of structural defects, in particular to surface adatoms [2]. In high-quality undoped GaN, only free excitons and excitons bound to shallow donors and acceptors comprise the low-temperature PL spectrum at photon energies between 3.0 and 3.5 eV [3], along with the characteristic series of peaks due to shallow donor-acceptor pair (DAP) transitions [4]. In less pure samples, sharp unidentified peaks are often detected in the range of 3.0 – 3.46 eV in addition to the well-established transitions in pure samples. The origin of these additional peaks is controversial. For example, the commonly observed 3.42 eV peak [5-8] has been attributed to recombination between electrons bound to oxygen donor and free holes [5], DAP-type transitions involving a very shallow unidentified acceptor [6], and exciton bound to structural defects [7] or to *c*-axis screw dislocations [8]. Sharp lines at 3.31 and 3.36 eV were repeatedly reported [9-14] and attributed to the cubic phase inclusions formed by stacking faults [9,10] or to excitons localized at extended defects in GaN [11-14]. However much less is known about other peaks. In this paper, we discuss in detail the behavior of the 3.32, 3.35 and 3.42 eV peaks in undoped GaN and correlated the appearance of these peaks with surface morphology, crystal structure and sample history.

#### EXPERIMENTAL DETAILS

Undoped GaN layers with thicknesses in the range of 1 to 2  $\mu\text{m}$  were grown on *c*-plane sapphire with AlN buffer layer by MBE with ammonia or radio frequency (RF) plasma as the source of nitrogen. Chemical etching in  $\text{H}_3\text{PO}_4$  at various conditions was used to reveal pits originating from threading dislocations and to analyze transformation of the surface morphology with etching. Polarity of the samples was established from etching characteristics, transmission

electron microscopy (TEM), X-ray diffraction data, and surface morphologies analyzed by atomic force microscopy (AFM) [15].

PL experiments were carried out in the temperature range of 15 – 300 K using a closed cycle optical cryostat. The luminescence was excited with the 325 nm line of a He-Cd laser with excitation densities ( $P_{exc}$ ) ranging from  $10^{-4}$  to 300 W/cm<sup>2</sup>. The luminescence signal was dispersed using a 0.5 m grating monochromator and detected with a Hamamatsu photomultiplier tube. Particular attention was given to any possible artificial peaks from laser lines or oil contamination. The selected samples were etched in boiled aqua regia (HNO<sub>3</sub> : HCl = 1:3) to remove possible organic contaminants.

## EXPERIMENTAL RESULTS

### Oil-related 3.31 and 3.36 eV peaks

There are numerous reports regarding the 3.31 and 3.36 eV lines in GaN [9-14]. Sometimes these lines were reported to appear in PL spectrum of undoped GaN where no emission typical for undoped GaN was observed [9,12,13], other times, they were observed in *p*-type GaN where the near-band-edge emission was absent or very weak [11]. At low temperatures, the 3.36 eV line was reported to be stronger and sharper than the 3.31 eV line. With increasing temperature, the 3.36 eV line quenched faster [9-13] and activation energy of the quenching did not exceed 30 meV [9,13]. A few clearly observed phonon replicas of the 3.31 eV line (separated by about 70 meV) were reported at elevated temperature [11,12,13]. Increasing temperature revealed the doublet nature of the 3.36 eV line [11,12]. No shift in the position of the 3.36 eV line was observed under hydrostatic pressure up to 4.4 GPa, while the band gap of GaN increased by about 190 meV [13]. The 3.31 and 3.36 eV lines were extremely strong and could be excited by light with photon energy below the band gap of GaN [10,11]. The lines were most commonly attributed to the cubic phase inclusions formed by stacking faults [9,10] or to excitons localized at extended defects in GaN [11-14].

The unusual properties of the 3.31 and 3.36 eV lines (zero pressure coefficient, lower than LO phonon energy separations between phonon replicas, appearance of these lines in the samples with very weak or zero background from the usual excitonic emission) lead one to consider the possibility of an artifact of measurements. We observed these lines of questionable origin only when we used oil-based thermal compound for affixing the samples to the sample holder. The detailed study of PL from the thermal compound alone revealed very intense sharp lines with maxima at 3.363 and 3.306 eV at low temperatures, as shown in Fig. 1. The 3.36 eV peak was stronger at low temperatures and quenched faster with increasing temperature. In the temperature range of 40 – 100 K, we observed a doublet nature of the 3.36 eV peak, with a shape very similar to that observed in Refs. [11] and [12]. Three pronounced phonon replicas of the 3.31 eV peak separated by 70-72 meV (Fig. 1) were observed at elevated temperatures. At room temperature, the spectrum from thermal compound evolved into a single broad blue band, in much the same way as that reported in Refs. [10] and [12]. The activation energies obtained from the quenching of the 3.36 and 3.31 eV lines (varying from 15 to 35 meV in the range of 15 – 300 K) were close to the values reported earlier [9,12,13]. We conclude that the 3.31 and 3.36 eV peaks often observed in the low-quality GaN, may be related to oil from thermal compound and/or contamination of the cryostat with oil vapor.

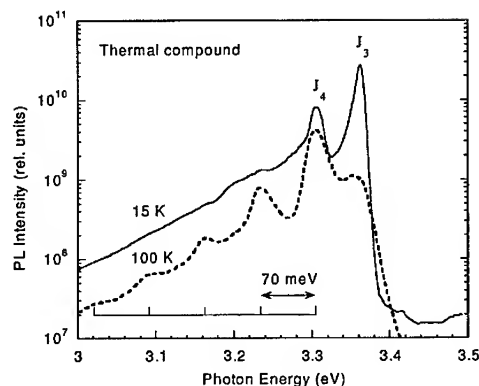


**Figure 1.** PL spectra from oil-based thermal compound (without any GaN sample). Four phonon replicas of the  $J_4$  line with the energy separation of 70 meV are visible at 100 K.

### The 3.32, 3.35 and 3.42 eV lines in GaN

In PL spectrum of many undoped GaN layers we observed the 3.42 eV line and in some samples - also strong lines at 3.35 and 3.30 eV (denoted here respectively as  $Y_2$ ,  $Y_4$ , and  $Y_6$ ), even after careful precautions were taken to provide oil-free environment (cleaning the sample in aqua regia, using of oil-free pump and affixing the sample without any glue or paste). At a first glance the  $Y_4$  and  $Y_6$  lines could be confused with the oil-related 3.36 and 3.31 eV lines (see the previous section), however, their properties were very different from those of the 3.31 and 3.36 eV peaks studied in Refs. [9-14]. With increasing excitation intensity, the 3.35 eV peak did not shift, whereas the 3.42 eV and especially 3.30 eV peak shifted significantly (Fig. 2).

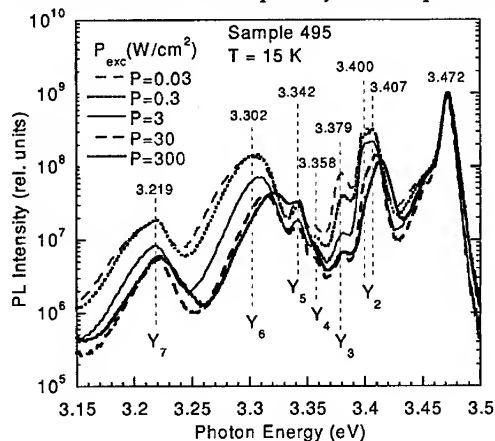


**Figure 2.** Normalized PL spectra of N-polar GaN obtained at different excitation intensities. The peaks denoted as  $Y_3$ ,  $Y_5$ , and  $Y_7$  are related to structural defects in GaN (apparently not at the surface) and they are not discussed in this work.

The shift of the 3.30 eV peak amounted to 18 meV and was reproducible in all the studied samples. The 3.42 eV peak shifted by up to 8 meV in N-polar films and only up to 2 meV in Ga-polar films. The 3.31 and 3.42 eV peaks disappeared or significantly reduced after a brief etching in  $H_3PO_4$  (see Fig. 3).

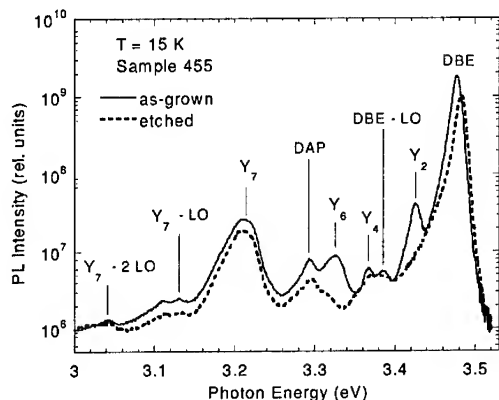


**Figure 3.** Effect of etching of Ga-polar GaN in  $\text{H}_3\text{PO}_4$  at  $160^\circ\text{C}$  for 1 min.  $P_{\text{exc}} = 0.3 \text{ W/cm}^2$ . DAP peak at 3.29 eV disappeared at higher excitation density.

With increasing temperature the studied PL lines quenched and activation energy of this process did not exceed 30 meV at temperatures up to 120 K where the contribution of the LO phonon replicas of the free exciton (FE) peak became substantial. Interestingly, the  $Y_4$  peak appeared to be a doublet with the high-energy component (12 meV above the main peak) emerging at elevated temperatures due to slower quenching (Fig. 4).

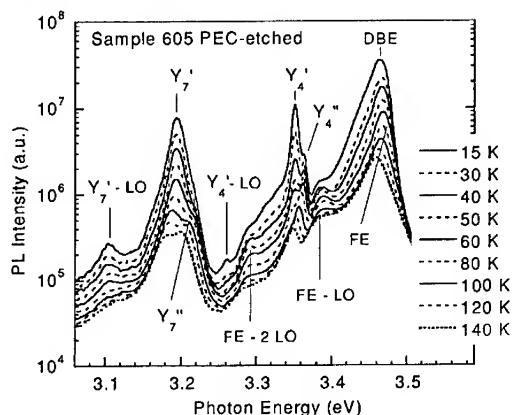


**Figure 4.** Temperature dependence of PL spectrum at  $P_{\text{exc}} = 100 \text{ W/cm}^2$  for the Ga-polar GaN layer. Note LO phonon replica of the 3.35 eV peak at about 3.26 eV.

Note the small peak, 90 meV below the main  $Y_4$  peak, that is attributed to its LO phonon replica (the relative intensity of the phonon replica and the zero-phonon line, called the Huang-Rhys factor, is 0.01), thus confirming that the  $Y_4$  peak originates from GaN.

In some samples, especially after a brief etching in  $\text{H}_3\text{PO}_4$  and extended exposure to air ambient, the 3.30 and 3.35 eV peaks evolved with duration of the UV laser exposure, while the remaining peaks, including the FE and donor-bound exciton (DBE) remained essentially unchanged (Fig. 5). After two hours of UV exposure the intensity of the  $Y_4$  and  $Y_6$  peaks increased several times. This effect, reproduced in many samples, was irreversible at low temperatures. At least after an hour the PL intensity in the illuminated spot remained nearly the same as just after long exposure to UV light, demonstrating an optical memory effect.

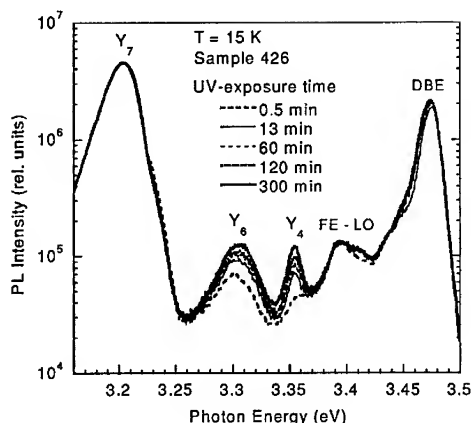


**Figure 5.** Transformation of PL spectrum with time of exposure by HeCd laser at 15 K.  $P_{exc} = 200$  W/cm<sup>2</sup>. The sample was etched in H<sub>3</sub>PO<sub>4</sub> at 160°C for 1 min and subsequently exposed to air during 20 days

## DISCUSSION

The 3.30 and 3.42 eV peaks were detected only in the samples with columnar- or bubble-like surface morphology and they never appeared in the samples with flat surface. In contrast, a few samples with flat surface exhibited the 3.35 eV peak (the PL spectrum for one of these samples is shown in Fig. 4). Moreover, the 3.30 and 3.42 eV peaks were gone or significantly reduced after a brief etching in H<sub>3</sub>PO<sub>4</sub> when the surface bubbles were etched off giving way to relatively smooth surface with etch pits. Based on these observations, we conclude that the 3.30 and 3.42 eV peaks are related to defects in the bubble-like surface layer of GaN. Whether these PL peaks are due to the DAP-type recombination or annihilation of excitons bound to defects is still an open question. Small values of the Huang-Rhys factor (not more than 0.1 for both 3.30 and 3.42 eV emissions) and small activation energy (less than 30 meV in the temperature range of 15 to 120 K) point to the exciton origin of these peaks. However, specific shift of the 3.30 eV peak with excitation intensity (absence of the shift at low excitation limit and gradual shift without saturation in the high excitation limit) is a signature of the DAP-type transitions [16]. The assumption about the surface location of the donors and acceptors in the DAP responsible for the 3.30 eV peak is consistent with prediction of reduced binding energy for the surface donors and acceptors [17]. As for the 3.42 eV peak, a notable shift was observed only in N-polar films and a very small shift in Ga-polar GaN; therefore the origin of the shift may be different from that of the 3.30 eV peak. We attribute the 3.42 eV peak to recombination of excitons bound to some surface defects. Finally, the 3.35 eV peak is evidently related to a bound exciton. Indeed it has a very low Huang-Rhys factor (0.01), linearly increases in intensity and does not shift in energy with the excitation intensity. Evolution of the intensity of the 3.36 eV line (similar to the 3.30 eV line) may point to the surface origin of the corresponding defect, if we adopt the concept that this effect is caused by photo-stimulated desorption of some molecules from the surface which modifies the surface states. However, we cannot exclude the possibility of some charging-discharging process and even a metastable behavior of the defect.

## CONCLUSION

We observed sharp peaks at 3.30, 3.35 and 3.42 eV in the PL spectrum of GaN. The peaks at 3.30 and 3.42 eV disappeared after shallow etching of the surface in hot H<sub>3</sub>PO<sub>4</sub>. The

3.30 and 3.35 eV peaks evolved with length of UV exposure. The 3.30 eV peak shifted by about 18 meV with increasing excitation power, whereas the 3.35 and 3.42 eV peaks in Ga-polar GaN exhibited a negligible shift. Based on the dependence of the PL on temperature, excitation intensity, and etching, we attribute the 3.30 eV peak to the surface DAP and the 3.35 and 3.42 eV peaks to excitons bound to some surface or near-surface defects.

## ACKNOWLEDGMENTS

This work was funded by AFOSR (Dr. G. L. Witt), NSF (Dr. L. Hess and Dr. U. Varshney), and ONR (Dr. C. E. C. Wood and Dr. Y. S. Park) and was motivated in part by the Wood-Witt program.

## REFERENCES

1. Y. T. Rebane and J. W. Steeds, *Phys. Rev. B* **48**, 14963 (1993).
2. N. Ohnishi, Y. Makita, H. Asakura, T. Iida, A. Yamada, H. Shibata, S. Uekusa, and T. Matsumori, *Appl. Phys. Lett.* **62**, 1527 (1993).
3. M. A. Reshchikov, F. Yun, D. Huang, L. He, H. Morkoç, S. S. Park, and K. Y. Lee, *Mat. Res. Soc. Symp. Proc.* **722**, K1.4 (2002).
4. R. Dingle and M. Ilegems, *Sol. St. Commun.* **9**, 175 (1971).
5. B. C. Chung and M. Gershenson, *J. Appl. Phys.* **72**, 651 (1992).
6. B. G. Ren, J. W. Orton, T. S. Cheng, D. J. Dewsnip, D. E. Lacklison, C. T. Foxon, C. H. Malloy, and X. Chen, *MRS Internet J. Nitride Semicond. Res.* **1**, 22 (1996).
7. E. Calleja, M. A. Sánchez-García, F. J. Sánchez, F. Calle, F. B. Naranjo, E. Munoz, U. Jahn, and K. Ploog, *Phys. Rev. B* **62**, 16826 (2000).
8. Y. G. Shreter, Y. T. Rebane, T. J. Davis, J. Barnard, M. Darbyshire, J. W. Steeds, W. G. Perry, M. D. Bremser, and R. F. Davis, *Mat. Res. Soc. Symp. Proc.* **449**, 683 (1997).
9. K. W. Mah, J.-P. Mosnier, E. McGlynn, M. O. Henry, D. O'Mahony, and J. G. Lunney, *Appl. Phys. Lett.* **80**, 3301 (2002).
10. W. Rieger, R. Dimitrov, D. Brunner, E. Rohrer, O. Ambacher, and M. Stutzmann, *Phys. Rev. B* **54**, 17596 (1996).
11. G. Martinez-Criado, A. Cros, A. Cantarero, R. Dimitrov, O. Ambacher, and M. Stutzmann, *J. Appl. Phys.* **88**, 3470 (2000).
12. M. Cazzanelli, D. Cole, J. F. Donegan, J. G. Lunney, P. G. Middleton, K. P. O'Donnell, C. Vinegoni, and L. Pavesi, *Appl. Phys. Lett.* **73**, 3390 (1998).
13. C. Wetzel, S. Fisher, J. Krüger, E. E. Haller, R. J. Molnar, T. D. Moustakas, E. N. Mokhov, and P. G. Baranov, *Appl. Phys. Lett.* **68**, 2556 (1996).
14. B. K. Meyer, D. Volm, C. Wetzel, L. Eckey, J.-Ch. Holst, P. Maxim, R. Heitz, A. Hoffmann, I. Broser, E. N. Mokhov, P. G. Baranov, C. Qiu, and J. I. Pankove, *Mat. Res. Soc. Proc.* **378**, 521 (1995).
15. D. Huang, P. Visconti, K. M. Jones, M. A. Reshchikov, F. Yun, A. A. Baski, T. King, and H. Morkoç, *Appl. Phys. Lett.* **78**, 4145 (2001).
16. M. A. Reshchikov, G.-C. Yi, and B. W. Wessels, *MRS Internet J. Nitride Semicond. Res.* **4S1**, G11.8 (1999).
17. J. D. Levine, *Phys. Rev.* **140**, A586 (1965).

**BEST AVAILABLE COPY**

### Tunnel radiation in the luminescence spectra of GaN-based heterostructures

A.E.Yunovich<sup>1</sup>, V.E.Kudryashov<sup>1</sup>, A.N.Turkin<sup>1</sup>, M.Leroux<sup>2</sup>, S.Dalmaso<sup>2</sup>

<sup>1</sup>M.V.Lomonosov Moscow State University, Dept. of Physics,  
Vorobiovy Gory, 119899, Moscow, Russia

<sup>2</sup>CRHEA -CNRS, Valbonne, France

#### ABSTRACT

Tunnel effects in luminescence spectra and electrical properties of LEDs based on InGaN/GaN-heterostructures made by different technological groups were studied. The tunnel radiation in a spectral region of 1.9 - 2.7 eV predominates at low currents ( $J < 0.2$  mA). The position of the tunnel luminescence maximum  $\hbar\omega_{\max}$  is approximately equal to the voltage  $U$ ,  $\hbar\omega_{\max} = eU$ . The low energy spectral band is described by the theory of tunnel radiative recombination. Tunnel recombination mechanisms in GaN-based heterostructures are caused by high electric fields in the active InGaN/GaN - MQW layers. The energy diagram of the structures is analyzed. The probability of tunnel radiation is higher due to piezoelectric fields in InGaN quantum wells. The tunnel radiation spectral band was not observed in the more effective LEDs with modulated doped MQWs. The spectra of GaN-based LEDs are compared with tunnel radiation spectra of GaAs-, InP- and GaSb- based LEDs. The equation:  $\hbar\omega_{\max} = eU$  describes experimental data in various semiconductors in the range 0.5 - 2.7 eV.

#### INTRODUCTION

It was shown in [1-3] that a tunnel radiation spectral band dominates at low currents in the luminescence spectra of blue light-emitting diodes (LEDs) based on InGaN/AlGaIn/GaN heterostructures with a single InGaIn quantum well. It was pointed out [1, 3] that models of tunnel radiative recombination elaborated for other  $A^{III}B^V$  compounds [4, 5] could be applied to an analysis of the new results. The tunnel spectra and electrical properties of blue LEDs described in [1-3] were studied in details [6, 7]. It was shown that the tunnel effects dominate when the electric field in the active 2D-layer is sufficiently high. Spectra were described using theories of diagonal tunneling.

Then the tunnel radiative recombination was also observed at low currents in green LEDs with multiple QWs [8, 9] and in violet LEDs [10]. The tunnel recombination plays a significant role in the structures with higher electric fields.

In this paper we summarize the experimental results on the GaN-based structures grown by various groups and describe them with the theory of diagonal tunneling. The role of piezoelectric fields is discussed. It is shown that diagonal tunneling in GaN- based (hexagonal) structures and that one in p-n - junctions in cubic  $A^{III}B^V$  semiconductors (GaAs, InP, GaSb) may be analyzed from one general point of view.

#### EXPERIMENTAL RESULTS

We studied LEDs made from heterostructures InGaIn/AlGaIn/GaN grown by MOCVD-methods by different groups: Nichia Chemical [1-3, 6, 7], Hewlett-Packard [8, 9], CRHEA CNRS [10], Uniroyal, LumiLeds [11]. Special attention was paid to spectra at low

currents,  $J < 0.2 \text{ mA}$  ( $j < 0.2 \text{ A/cm}^2$ ). General views of the spectra for various LEDs are shown in Figs. 1-3.

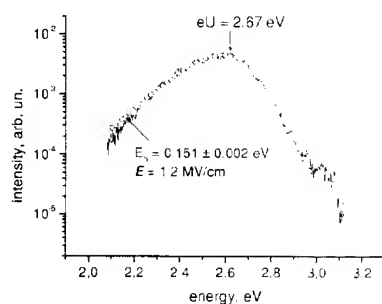


**Figure 1.** Electroluminescence spectrum of violet CRHEA's LED G932 at  $J = 4 \text{ mA}$  and  $U = 2.67 \text{ V}$  and fitting by Eq.1 (circles) with parameters  $E_g = 3.5 \text{ eV}$ ,  $mkT = 32 \text{ meV}$ ,  $E_0 = 0.15 \text{ eV}$ ,  $E = 1.2 \cdot 10^6 \text{ V/cm}$ .

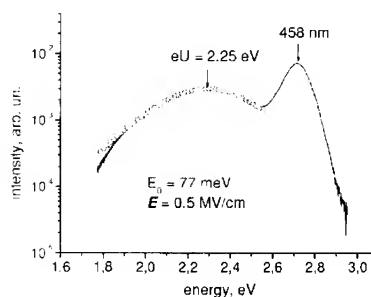


**Figure 2.** Electroluminescence spectrum of blue Nichia's LED at  $J = 0.1 \text{ mA}$  and  $U = 2.25 \text{ V}$  and fitting by Eq.1 (circles) with parameters  $E_g = 2.7 \text{ eV}$ ,  $mkT = 26 \text{ meV}$ ,  $E_0 = 0.077 \text{ eV}$ ,  $E = 0.5 \cdot 10^6 \text{ V/cm}$ .

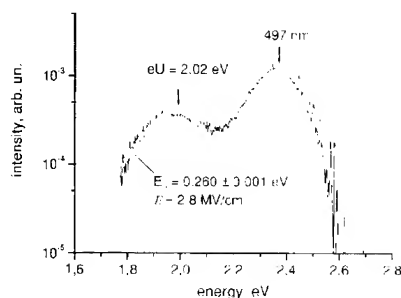


**Figure 3.** Electroluminescence spectrum of a green Hewlett Packard's LED at  $J = 70 \mu\text{A}$  and  $U = 2.02 \text{ V}$  and fitting by Eq.1 (circles) with parameters  $E_g = 2.7 \text{ eV}$ ,  $mkT = 31 \text{ meV}$ ,  $E_0 = 0.26 \text{ eV}$ ,  $E = 2.8 \cdot 10^6 \text{ V/cm}$ .

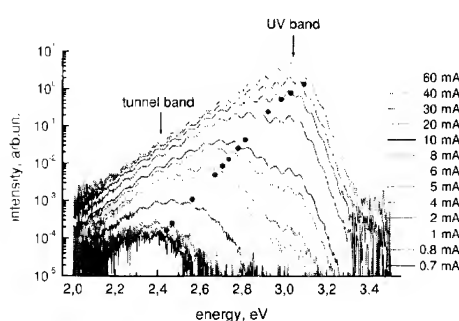


**Figure 4.** An evolution of the electroluminescence spectra with the applied voltage (values of voltage  $V$  multiplied by  $e$  are shown with circles) for a violet CRHEA's LED with a single Si-doped quantum well [10].

The main spectral band at high energy and the low energy side band are distinctly separated at low currents. An evolution of the spectra with the applied voltage is illustrated in Fig. 4 for violet single quantum well LEDs [10]. The main (high energy) band dominates only at high currents,  $J > 10 \text{ mA}$ . Points on the spectral curves show the position of energies  $\hbar\omega = eU$ . The integral intensity  $\Phi$  of the low energy band exponentially depends on the voltage  $U$  as shown in Fig. 5.

**BEST AVAILABLE COPY**

The maxima of the low energy side band versus the voltage  $U$  are shown for various LEDs in Fig. 6. The positions of the maxima  $\hbar\omega_{\max}$  are approximately equal to the applied potential:  $\hbar\omega_{\max} = eU$ . These low energy bands are attributed to tunnel radiative recombination. The relative role of the tunnel band in different diodes is growing as the main blue peak shifts to higher energies.

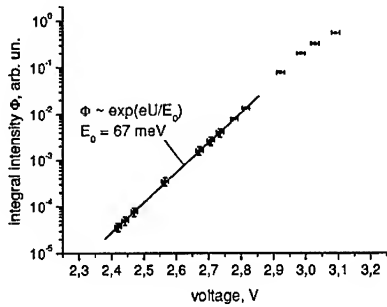


**Figure 5.** Dependence of the integral intensity of the tunnel band on the voltage for violet CRHEA's LED (equation 2a).

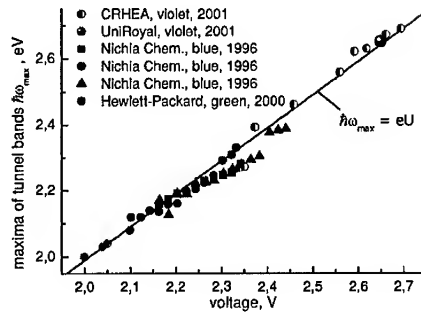


**Figure 6.** Position of the tunnel band spectral maxima  $\hbar\omega_{\max}$  versus applied voltage  $U$  for various LEDs based on InGaN/AlGaIn/GaN quantum well heterostructures.

## DISCUSSION

1. The theory of tunnel radiative recombination [4, 5] was elaborated for homogeneous degenerated p-n-junctions. The spectrum of tunnel radiation can be described by:

$$I(\hbar\omega) \sim [\hbar\omega/(E_g - \hbar\omega)] \cdot [(\hbar\omega - eU)/(\exp((\hbar\omega - eU)/mkT) - 1)] \cdot [\exp(-(4/3)((E_g - \hbar\omega)/E_0)^{3/2})]; \quad (1)$$

$E_g$  is an effective energy gap,  $m$  is a parameter depending on the effective masses ratio. The denominator in the exponent  $E_0$  is given by the theory of the Franz-Keldysh effect:

$$E_0 = [(\hbar/(2m^*_{cv}))^{1/2} \cdot eE]^{2/3}, \quad (2)$$

$m^*_{cv}$  is a reduced effective mass and  $E$  is the effective electric field assumed constant in the region of intersection of electron and hole wave functions. We have used equation (1) in the case of heterojunctions in wurtzite crystals. The integral intensity of the radiation  $\Phi$  exponentially depends on the applied voltage:

$$\Phi \sim \exp(eU/E_0). \quad (2a)$$

2. Let us discuss the modifications of the theory needed for heterostructures with multiple quantum wells of the type InGaN/AlGaIn/GaN shown in Fig. 7. The electric field  $E$  in the structure depends on p- and n-side doping ( $N_A$  and  $N_D$ ), on the width of AlGaIn and GaN barriers, on the width of wells. If we take a built-in contact potential of the structure  $\phi_c$  of the order  $\approx 3$  eV and the width of the whole space charge region of  $w \approx 80 \div 100$  nm [7-9] then an evaluation of the electric field in the structures is in the range:

$$E_{\phi_c} \approx \phi_c/w \approx (0.4 - 0.3) \cdot 10^6 \text{ V/cm}. \quad (3)$$

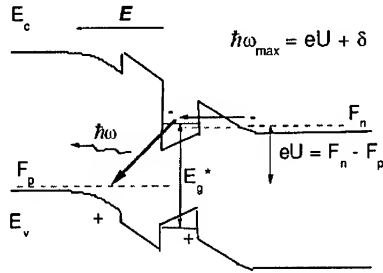


**Figure 7.** An energy diagram of the InGaN/AlGaIn/GaN heterostructure including polarization fields in the wells and barriers. A thick arrow corresponds to the radiative tunnelling of electrons from the well to the holes in the barrier.

The width  $w$  in (3) depend on the distribution of the charged impurities (abrupt or gradual) in our complicated heterostructures. The value  $E_{fc}$  is sufficiently higher than the electric fields in Si or GaAs p-n-junctions. It is to be noted that  $E$  stands in the exponent of the Eq. (1) and that the probability of tunnel radiation crucially depends on this value.

The effective field  $E$  depends also on piezoelectric and spontaneous polarization fields  $E_P$  in barriers and wells. The polarization fields in the wells are directed opposite to the p-n-junction field if the structures are grown on Ga- polarity c-planes. The fields in the barriers are directed in the opposite direction, in the same direction as the p-n-junction field (due to the charges on heterointerfaces). Tunnel effects depend on the intersection of electron and hole wave functions under the barriers. This is why tunnel radiation would be more probable in the structures with higher electric fields  $E_P$  in the barriers due to polarization.

Values of polarization fields were evaluated for InGaN/AlGaIn/GaN structures in [12-14] as  $E_P \approx 0.5 \cdot 10^6$  V/cm, *i.e.* of the same order of magnitude as in equation (3). The experimental data shown in Fig. 4, 5 were measured for a sample highly Si-doped in the wells on the n-side of the junction. This fact confirms a model of radiation caused by electrons tunneling to the p-side barrier. This idea is illustrated in Fig. 7 by a thick arrow from the n- side InGaIn well into the p-side AlGaIn barrier.

The values of reduced masses in Equation (1) depend on crystallographic directions in hexagonal semiconductors:

$$m_{cv}^* = (1/m_c^* + 1/m_v^*)^{-1}. \quad (4)$$

We have taken in our analysis  $m_c^*$  as the  $m_c^*$  value for the c-axis in  $\text{In}_x\text{Ga}_{1-x}\text{N}$  corresponding to a position of the main spectral band in each sample using data from [15] ( $m_{c<0001>}^* = (0.20 - 0.15)m_0$  for  $x = 0 - 0.2$ ). We have taken  $m_v^*$  as for the higher valence band in  $\text{Al}_y\text{Ga}_{1-y}\text{N}$  at the  $\Gamma$  point neglecting tunneling from the lower valence bands ( $m_{v1<0001>}^* = 0.27m_0$ ).

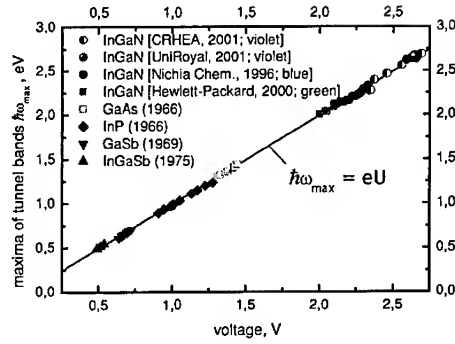


**Figure 8.** Position of the tunnel band spectral maxima  $\hbar\omega_{\max}$  versus applied voltage  $U$  for GaN-based LEDs in comparison with analogous data on the cubic  $\text{A}^{\text{III}}\text{B}^{\text{V}}$  semiconductors GaAs [4], InP [4], GaSb [4, 16] and (Ga,In)Sb [17].

3. A fit of the experimental tunnel radiation spectra using equation (1) taking into account the above evaluations is shown on Figures 1 - 3. The high energy blue line was subtracted from the spectra in [6, 7]. The voltage  $eU$  in (1) was taken equal to the measured voltage  $eV$  on the structure. The effective gap  $E_g$  needed for a good fit was changed in the limits of effective energy gap in the well up to the  $E_g$  value in GaN.

The parameter  $E_0$  in equation (1) needed for a good fit of the spectra was changing in the limits  $E_0 = 0.15 - 0.4$  eV. It was essentially higher than  $E_0 \approx 0.07$  eV determined from the integral intensity versus voltage curve (equation (2a), [6-8], see also Fig. 5). This discrepancy may be understood: the long wavelength spectral slope depends on tunnel radiation through the band tails, not included in the theory [4, 5]. The integral intensity is determined by the density of states at the band gap boundaries, and corresponds better to the theory assuming parabolic bands in the plane of the junction. The integral intensity is less dependent on the band tails.

An evaluation of electric field  $E$  needed for the tunnel radiation effects gives values  $E = (1.2-5) \cdot 10^6$  V/cm if we use  $E_0 = 0.15 - 0.4$  eV from the spectral fit and  $E = (0.3-0.5) \cdot 10^6$  V/cm if we use  $E_0 = 0.07 - 0.08$  eV from the dependence of the integral intensity. The latter value is more realistic and is in a consistence with an evaluation deduced from the analysis of capacitance measurements and charge distributions.

4. The theory [4, 5] gives a dependence of the position of the tunnel band spectral maximum versus temperature  $T$ . The  $(\hbar\omega_{\max} - eU)$  value depend on the statistical part  $[\exp((\hbar\omega - eU)/mkT) - 1]$  in the equation (1). If the temperature is low,  $kT \ll E_0$ , the difference  $(\hbar\omega_{\max} - eU)$  is positive and if it is high,  $kT \gg E_0$ , the  $(\hbar\omega_{\max} - eU)$  value is negative. The maximum  $\hbar\omega_{\max}$  is equal to  $eU$  at  $kT = (1/3) \cdot E_0$  [5]. If we use  $E_0$  equal to  $0.07 \div 0.08$  eV,  $\hbar\omega_{\max} = eU$  at room temperature,  $kT = 0.026$  meV, in good agreement with the results in Fig. 5.

5. The theoretical evaluations of the electric field in the structures do not take into account inhomogeneities in heterojunctions and potential fluctuations caused by InGaN composition fluctuations. Tunnelling is more probable in "hot points" with maximal electric fields. The tunnel band in [8, 9] was seen in the samples with the lower quantum efficiency. We have interpreted this fact as caused by nonradiative tunnel currents due to inhomogeneities in the samples with lower quantum efficiency.

We have studied the luminescent spectra of the high efficiency LEDs grown in LumiLeds laboratories and could not find a tunnel radiation band at low currents [11]. These samples had multiple quantum wells modulated doped by Si donors in the barriers, not in the wells. Electrons from the donors screen polarization fields in these structures. These data confirm the model shown in Fig. 7 in which diagonal tunneling is more probable due to higher electric fields in barriers caused by polarization.

6. It is interesting to compare the results on GaN- based structures with older results of tunnel radiation studies in other (cubic)  $A^{III}B^V$  semiconductors: GaAs [5], InP [5], GaSb [5, 16] and (Ga,In)Sb [17]. A plot of  $\hbar\omega_{\max}$  versus  $U$  (Fig. 8) gives an excellent result: the experimental points in a wide range from the infrared to violet region are situated with a good accuracy on the theoretical line  $\hbar\omega_{\max} = eU$ . This is a proof that tunnel radiative recombination (diagonal tunneling) is a fundamental phenomenon for homo- and hetero- p-n junctions in direct gap  $A^{III}B^V$  semiconductors.

## CONCLUSIONS

Tunnel radiative recombination (diagonal tunnelling), an effect inverse to the Franz – Keldysh effect, is essential in GaN-based p-n- heterojunctions with quantum wells at low currents in high electric fields ( $E = (0.2+1) \cdot 10^6$  V/cm). The probability of this effect is higher if piezoelectric and spontaneous polarization fields play a sufficient role in the AlGaIn/InGaIn heterojunctions.

The experimental electroluminescence spectra of GaN based LEDs at low currents are described by the theory of tunnel radiation. The parameter  $E_0$  of the theory determined from the spectral fitting is higher than the one determined from the dependence of the integral intensity versus voltage. This is described by the band tails influence.

The spectral maxima of the tunnel band  $\hbar\omega_{\max}$  are almost equal to the applied voltage  $eU$  for InGaIn/AlGaIn/GaN heterostructures at room temperature. The diagonal tunneling is a fundamental phenomenon for homo- and hetero- p-n junctions in direct gap A<sup>III</sup>B<sup>V</sup> semiconductors in a wide energy/voltage range:  $eU = 0.5$  to  $2.7$  eV.

## REFERENCES

1. K.G.Zolina, V.E.Kudryashov, A.N.Turkin, A.E.Yunovich, S.Nakamura. MRS Intern. Journ. of Nitride Semic. Res., 1/11.
2. A.N.Kovalev, V.E.Kudryashov, F.I.Manyachin, A.N.Turkin, K.G.Zolina, A.E.Yunovich. Abstr. of ISCS-23, S.-Peterburg, September 1996, Abstr. 03.P3.04.
3. K.G.Zolina, V.E.Kudryashov et al. Semiconductors, 1997, **31** (9), pp.901-907.
4. A.E.Yunovich, A.B.Ormont. ZhETP, 1966, v. 51, N 11, pp.1292-1305.
5. T.N.Morgan. Phys. Rev., 1966, Vol.148, N 2, pp.890-903.
6. V.E.Kudryashov, K.G.Zolina, A.N.Kovalev, F.I.Manyachin, A.N.Turkin, A.E.Yunovich. Semiconductors, 1997, **31** (11), pp.1123-1127.
7. A.N.Kovalev, F.I.Manyakhin, V.E.Kudryashov, A.N.Turkin, A.E.Yunovich. MRS Intern. Journ. of Nitride Semic. Res., 2/11.
8. A.E.Yunovich, A.N.Kovalev, V.E.Kudryashov, F.I.Manyachin, A.N.Turkin, K.G.Zolina. Mat. Res. Soc. Symp. Proc. Vol.449, 1997, p.1167-1172.
9. A.N.Kovalev, F.I.Maniakhin, V.E.Kudryashov, A.N.Turkin, A.E.Yunovich. Fiz. i Techn. Polupr., 2001, v.35, N 7, pp. 861-868.
10. P.Vennégues, B.Beaumont, S.Haffouz, M.Vaille, P.Gibart, J.Cryst.Growth, **187**, 167 (1998).
11. A.E.Yunovich, S.S.Mamakin, F.I.Manyakhin, N.Gardner, W.Goetz, M.Misra, S.Stockman. Mat. Res. Soc. Symp. Proc. 2002, Vol. 711, K2.4.
12. P.Lefebvre, J.Allegre, B.Gil, H.Mathieu, N.Grandjean, M.Leroux, J.Massies, P.Bigenwald. Phys. Rev. B, **59**, 15363 (1999).
13. S.F.Chichibu, S.P.DenBaars, K.Wada, M.Aritta, T.Sota, S. Nakamura et al. Materials Science and Engineering, v. B59, 298 (1999).
14. A.Hangleiter, J.S.Im, H.Kollmer, O.Gfrorer, J.Off, F.Scholz. MRS Internet J. Nitride Semicond. Res., **4S11**, G6.20 (1999).
15. B.Gil. Group III Nitride Semiconductor Compounds: Physics and Applications. Clarendon Press, Oxford, 1998, 459 p.
16. V.M.Stuchebnikov, A.E.Yunovich. FTP, 1969, v.3, N9, p. 1293 (in Russian).
17. A.I.Lebedev, I.A.Strelnikova, A.E.Yunovich. FTP, 1976, v.10, N7, p. 1304 (in Russian).

### Self-Induced Photon Absorption by Screening of the Electric Fields in Nitride-based Quantum Wells

S. Kalliakos, P. Lefebvre, T. Taliercio and B. Gil  
GES – CNRS – Université Montpellier II. CC 074,  
34095 Montpellier Cedex 5, France.

#### ABSTRACT

We have calculated the change of interband absorption spectra of a quantum well based on hexagonal group-III nitride semiconductors under photo-injection of high densities of electron-hole pairs. The screening of internal electric fields by such optical excitation is known to blue-shift and reinforce the ground-state optical transition. Due to the large values of densities of states and of internal fields, we predict novel properties that rather concern optical absorption via transitions between excited states. The absorption coefficient can be strongly enhanced by the optical excitation itself, in this particular spectral region, yielding the possibility for self-induced absorption properties. In other words, if sufficiently intense, an excitation laser can increase the absorption coefficient of the system at its own wavelength, thus providing a strong nonlinear optical response. Finally, we briefly discuss the potential application of these optical phenomena.

#### INTRODUCTION

After the first demonstration of a light emitting device based on hexagonal (wurtzite) group-III nitride semiconductors [1], the interest of the scientific community has risen up considerably. Low-dimensional structures, like quantum wells (QWs) or quantum boxes (QBs) have received the main part of the attention since it was clear that the understanding of the physical processes that are responsible for the light emission mechanisms in these structures would lead to an improvement of the device performance. The main peculiarity of these quantum systems is the presence of huge internal electric fields, in the order of 1 MV/cm, along the growth axis, due to the difference of both spontaneous and piezoelectric polarization between the barrier and well materials [2-4]. Because of this electric field, the optical transitions exhibit a large red-shift, even below the material band-gap, due to the quantum confined Stark effect (QCSE) [5-10]. Also, the electrons and holes are separated at the opposite sides of the well (box) [5,8,11,12] leading to a considerable increase of the radiative recombination time. Lifetime changes by several orders of magnitude can be obtained simply by increasing the well (box) width (height) by few nanometers [8].

In this work, we investigate the behavior of a GaN-based quantum well under high photo-excitation conditions. In particular, we calculate the entire absorption spectrum of such a system, including the excited states, and we follow its evolution when a high density of electron-hole pairs is injected. Until now, a number of interesting phenomena have already been predicted and/or experimentally verified like, for example, the bleaching of the excitonic interaction [13]. We are mainly interested in the screening of the electric field [14-16] which can lead, among others, to (1) a blue-shift of the transition energies due to the partial cancellation of the QCSE [17-20], (2) a reduction of the electron-hole spatial separation and, hence, a decrease in the radiative lifetime [19,23] and (3) a change in the absorption coefficient due to its dependence on the oscillator strength [24-25]. The oscillator strength is proportional to the square overlap integral of the electron and hole wavefunctions (hereafter referred to as the "overlap integral") which can be very small in nitride-based quantum

structures for the e1-h1 transition and depends largely on the well (box) width (height). We should also note that the injection of a high density of carriers in the well can lead to a band-gap renormalization (BGR) due to many-body effects [25-27]. This phenomenon will only affect the spectral position of the optical transitions (by introducing an overall red-shift of the spectrum) but will not cause any change in the electron and hole wavefunctions and to the respective overlap integral.

In the rest of this work, we will show some original phenomena that should be observed in nitride-based quantum systems, linked to the screening of the effective electric field under high photo-excitation. Given the present uncertainty of several physical parameters, our aim is not to give exact prescriptions for the use of these phenomena in optoelectronic devices. Instead, we will present a qualitative description of the physical processes and emphasize on the advantages of the group III-nitride materials.

## THEORETICAL MODEL

In order to calculate the effect of high densities of e-h pairs, we solve self-consistently the Schrödinger and Poisson equations, within the envelope function approximation. We only consider the first three confined subbands for electrons and the first two subbands for "heavy" and "light" holes. In fact, the valence band of wurtzite nitrides is threefold, with the maxima of the so-called A ("heavy-holes": H), B ("light-holes": L) and C bands lying within a few tens of meV. As we assume normal incidence of light, the dipolar matrix element is nonvanishing for H and L hole states and, due to the lattice mismatch biaxial compression [28,29], these matrix elements are nearly equal. Thus, we assume equal oscillator strengths for both A- and B-related valence subbands. Moreover, excitonic effects are not included since it has been shown [13] that, in GaN-based quantum wells, the exciton binding energy drops to zero for carrier densities of  $\sim 10^{11} \text{ cm}^{-2}$ , an order of magnitude lower than those considered in this work.

Assuming continuous-wave excitation, we model a quasi-equilibrium situation leading to a steady-state density of carriers. The population of each subband, together with the corresponding quasi-Fermi level, are calculated by using a two-dimensional density of states proportional to the in-plane effective mass of the carrier. Then, we calculate the resulting potential modification by using the Poisson's equation:

$$\frac{d^2 V_{Pois}}{dz^2} = -\frac{\rho(z)}{\epsilon \epsilon_0} \quad (1),$$

where  $\rho(z)$  is the charge density profile given by:

$$\rho(z) = e \cdot \sum_{i=1}^3 \left[ n_{hi} |f_{hi}(z)|^2 - n_{ei} |f_{ei}(z)|^2 \right] \quad (2),$$

where  $f_{e,h,1,2,3}(z)$  are the envelope functions for the electrons and holes in the well,  $n_{e,h,1,2,3}$  are the carrier populations for each subband,  $i$ . Moreover,

$$n = \sum_{i=1}^4 n_{hi} = \sum_{i=1}^3 n_{ei} \quad (3),$$

where  $n$  is the total density of e-h pairs. By using Eqs. (2) and (3), we account for the fact that the charge distribution in the QW is affected by the population of excited states, and not only of the ground state.

The interband absorption coefficient is calculated by multiplying the overlap integral of the electron and hole wavefunctions by the step-like joint density of states for each transition. The exclusion principle is considered by multiplying the resulting spectrum with another step-

like factor, *i.e.* zero for occupied states and 1 for the unoccupied ones, which corresponds to  $T = 0\text{K}$ . Inhomogeneous broadening is introduced by the convolution of the calculated spectrum with a sigmoidal function :

$$S(E) = \left[ 1 + e^{E_{ij} - E / \Delta E} \right]^{-1} \quad (4),$$

where  $E_{ij}$  is the energy for each transition, with a broadening factor of  $\Delta E = 50\text{ meV}$ . We believe that that it is a reasonable choice considering the state-of-the-art optical features and the high degree of excitation. This broadening is quite larger than the light- to-heavy-hole splitting that we calculate, and we believe that a more tedious treatment of the valence band will not affect, in general terms, the validity of our results.

We use a normalization procedure in order to estimate the optical density of a GaN/AlGaIn QW under normal incidence. Taking the absorption coefficient of GaN ( $10^5\text{ cm}^{-1}$ ) as a reference [30], we calculate the optical density for the fundamental transition of an ideal and wide (8 nm) GaN QW without an electric field, thus with an overlap integral close to unity. Using this value, we calculate the optical densities for all "realistic" situations, accounting for electric fields and narrower wells, being simply proportional to the appropriate overlap integral. Also, we follow a step-by-step procedure when we increase the density of e-h pairs in order to describe correctly the change in energy levels and in the corresponding densities of states.

In order to account for the BGR resulting from the carrier-carrier scattering effects, we referred to previous works [25-27] where the effect is calculated for nitride-based quantum wells including or not the electric field and/or valence band mixing effects. The main effect resulting from the BGR that was described in these works was an overall red-shift of the optical transitions. In fact, the authors of Refs. 26 and 27 have established that this red-shift follows some "universal" behavior for nitride QWs, although electric fields were not included in Ref. 26. We have checked that the calculation in Ref. 27, which includes the electric field, follows the same general behavior. Then, the BGR can be deduced from the following law, which fits the results of Ref. 26:

$$\frac{\Delta E_G}{R_{2D}} = -1.67 (r_{2D})^{-0.71} \quad (5),$$

where  $R_{2D}$  is the binding energy of two-dimensional excitons, *i.e.* four times the three-dimensional value for GaN ( $R_{2D} = 0.1\text{ eV}$ ) and  $r_{2D}$  the so-called "dimensionless interparticle distance", which is deduced from the exciton two-dimensional Bohr radius,  $a_B^{2D} = 0.5 a_B^{3D}$ , by  $r_{2D} = 1 / [\pi n (a_B^{2D})^2]^{1/2}$ , where  $a_B^{2D} = 1.5\text{ nm}$ , for GaN. Using this procedure, we estimate a red-shift of  $0.083\text{ eV}$  for  $n = 2 \cdot 10^{12}\text{ cm}^{-2}$ , and of  $0.136\text{ eV}$  for  $n = 8 \cdot 10^{12}\text{ cm}^{-2}$ .

## RESULTS AND DISCUSSION

We present results obtained for a GaN/Al<sub>0.4</sub>Ga<sub>0.6</sub>N QW with a width of  $L_w = 16$  atomic monolayers (MLs), *i.e.*  $4.1\text{ nm}$  and barriers of  $L_B = 30\text{ ML}$ . By using a scaling procedure based on previous experimental studies [31,32], we estimate an internal electric field of  $1.4\text{ MV/cm}$ . For the carrier masses, we used  $m_e^* = 0.2m_0$  [33],  $m_e^* = 0.2m_0$  [34],  $m_{hh}^* = 1.65m_0$  [35] and  $m_{lh}^* = 0.15m_0$  [35].

In Figure 1 we present the different effects contributing to the absorption onset involving the E1 and H1 subbands: the blue shifts induced by the screening of the electric field and by the filling of the subbands, the red-shift induced by the BGR. In figure 2 we present the optical density spectrum for four different densities of injected e-h pairs. Clearly, the optical density is always very small in the vicinity of the E1H1 transition, precisely due to the QCSE

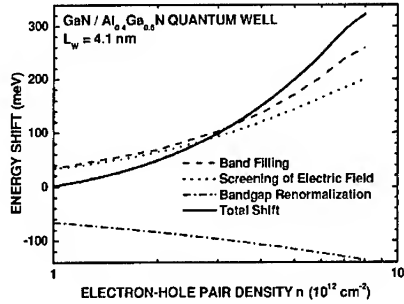


**Figure 1.** The various contributions to the shift of the absorption onset for the E1H1 transition, for a 16 ML-wide GaN/Al<sub>0.4</sub>Ga<sub>0.6</sub>N quantum well.

and the subsequent reduction of the overlap integral. This is not the case for the transitions involving the excited states, where the overlap integral can be larger by two orders of magnitude.

The dynamical aspect of the absorption spectrum is governed by several competitive mechanisms. First, the classical bleaching of lower-energy transitions, by population of the lower subbands, tends to induce a negative differential absorption (NDA) in this region. Second, the screening of the electric field induces a blue-shift of the E1H1 transition together with an enhancement of the optical density for transitions involving some excited states. Finally, the BGR causes an overall red-shift of the spectrum. As a result, a positive differential absorption (PDA) is present for energies above ~3.3 eV. Because of the red-shift induced by the BGR, the PDA is enhanced and occurs in a larger spectral region, compared to the case where the BGR is not included in the calculation. An interesting effect occurs in the region between 3.4 eV and 3.6 eV. When the carrier density is increased, the system exhibits a PDA but above a critical carrier density, due to band-filling effects, the absorption coefficient largely decreases.

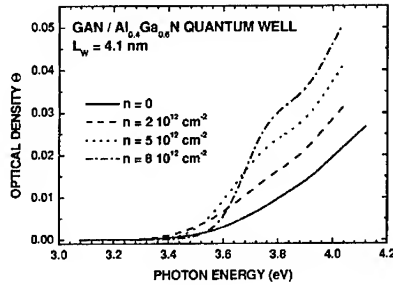


**Figure 2.** Optical density spectra for a 16 ML-wide GaN-Al<sub>0.4</sub>Ga<sub>0.6</sub>N single QW, for densities of electron-hole pairs  $n = 0$  (solid line),  $2 \times 10^{12} \text{ cm}^{-2}$  (dashed line),  $5 \times 10^{12} \text{ cm}^{-2}$  (dotted line) and  $8 \times 10^{12} \text{ cm}^{-2}$  (dash-dotted line).

Nitride-based quantum systems present several great advantages in view of the observation of these phenomena. First of all, their very large density of states will limit the population effects to a small spectral region allowing for the presence of a PDA in a large spectral region where the excited states are present. Also, band-gap differences in the order of 1 eV or more can be easily produced, which leads to an efficient confinement, thus there is a possibility to observe these effects at room temperature.

The absorption coefficient change with an externally applied voltage is the phenomenon upon which electro-optical modulators and bistable switches rely. Moreover, as it was pointed out by Miller *et al.* [36], the enhancement of the absorption coefficient with the increase of the excitation degree of the system can lead to optical bistability even without an external feedback mechanism. We believe that the original phenomena that were described in this work show the potentiality of nitride-based quantum systems as excellent candidates for the realization of sophisticated optoelectronic devices based on "quantum engineering".

## CONCLUSION

We have examined, by using envelope-function calculations, the original nonlinear optical properties induced by high populations of e-h pairs in low-dimensional systems based on wurtzite group-III nitride semiconductors. In addition to the straightforward blue-shift of the ground-state emission, we have found clear possibilities of self-induced photo-absorption. We have explained why these materials can exhibit such effects which could not be obtained with more familiar semiconductor systems.

We believe that this theoretical work opens the way for a new type of "band-gap engineering", accounting for the huge electric fields in these low-dimensional systems. We believe, too, that this work will lead to an interesting experimental research on properties which have not been investigated yet.

## ACKNOWLEDGMENTS

S. Kalliakos acknowledges the financial support provided through the European Community's Human Potential Programme under contract HPRN-CT-1999-00132, CLERMONT. We also acknowledge support of the French Ministry of Education, Research and Technology within the "BOQUANT", "NANILUB" and "INTRANT" Programs.

## REFERENCES

1. S. Nakamura, M. Senoh, A. Nagahama, N. Iwasa, T. Yamada, T. Matsushita and H. Kiyoku, *Appl. Phys. Lett.* **70**, 2753 (1997).
2. F. Bernardini, V. Fiorentini and D. Vanderbilt, *Phys. Rev. B* **56**, R10024 (1997).
3. F. Bernardini, V. Fiorentini and D. Vanderbilt, *Phys. Rev. Lett.* **79**, 3958 (1997).
4. F. Bernardini and V. Fiorentini, *Phys. Rev. B* **57**, R9472 (1998).
5. Jin Seo Im, H. Kollmer, J. Off, A. Sohmer, F. Scholz, and A. Hangleiter, *Phys. Rev. B* **57**, R9435 (1998).
6. M. Leroux, N. Grandjean, M. Lutg, J. Massies, B. Gil, P. Lefebvre and P. Bigenwald, *Phys. Rev. B* **58**, R13371 (1998).
7. P. Lefebvre, J. Allegre, B. Gil, H. Mathieu, N. Grandjean, M. Leroux, J. Massies and P. Bigenwald, *Phys. Rev. B* **59**, 15363 (1999).

8. P. Lefebvre, A. Morel, M. Gallart, T. Taliercio, J. Allègre, B. Gil, H. Mathieu, B. Damilano, N. Grandjean and J. Massies, *Appl. Phys. Lett.* **78**, 1252 (2001).
9. B. Damilano, N. Grandjean, F. Semond, J. Massies, and M. Leroux, *Appl. Phys. Lett.* **75**, 962 (1999).
10. F. Widmann, J. Simon, B. Daudin, G. Feuillet, J.L. Rouvière, N.T. Pelekanos, and G. Fishman, *Phys. Rev. B* **58**, (1998) R15989.
11. M. B. Nardelli, K. Rapcewicz and J. Bernholc, *Appl. Phys. Lett.* **71**, 3135 (1997).
12. T. Honda, T. Miyamoto, T. Sakaguchi, H. Kawanishi, F. Koyanaka and K. Iga, *J. Cryst. Growth* **189/190**, 644 (1998).
13. P. Bigenwald, A. Kavokin, B. Gil and P. Lefebvre, *Phys. Rev. B* **61**, 15621 (2000).
14. P. Boring, B. Gil and K. J. Moore, *Phys. Rev. Lett.* **71**, 1875 (1993).
15. D.L. Smith and C. Mailhot, *Phys. Rev. Lett.* **58**, 1264 (1987).
16. X.R. Huang, D.R. Harken, A.N. Cartwright, A.L. Smirl, J.L. Sanchez-Rojas, A. Sacedon, E. Calleja and E. Muñoz, *Appl. Phys. Lett.* **67**, 950 (1995).
17. G. H. Gainer, Y. H. Kwon, J. B. Lam, S. Bidnyk, A. Kalashyan, J. J. Song, S. C. Choi and G. M. Yang, *Appl. Phys. Lett.* **78**, 3890 (2001).
18. S.P. Łepkowski, T. Suski, P. Perlin, V. Yu. Ivanov, M. Godlewski, N. Grandjean and J. Massies, *J. Appl. Phys.* **91**, 9622 (2002).
19. F. Della Sala, A. Di Carlo, P. Lugli, F. Bernardini, V. Fiorentini, R. Scholz and J. Jancu, *Appl. Phys. Lett.* **74**, 2002 (1999).
20. E. Kuokstis, J.W. Yang, G. Simin, M. Asif Khan, R. Gaska and M.S. Shur, *App. Phys. Lett.* **80**, 977 (2002).
21. A. Reale, A. Di Carlo, P. Lugli and A. Kavokin, *Phys. Stat. Sol. (a)* **183**, 121 (2001).
22. A. Vinattieri, D. Alderighi, J. Kudma, M. Colocci, A. Reale, A. Di Carlo, P. Lugli, F. Semond, N. Grandjean and J. Massies, *Phys. Stat. Sol. (a)* **190**, 87 (2002).
23. A. Reale, G. Massari, A. DiCarlo and P. Lugli, *Phys. Stat. Sol. (a)* **190**, 81 (2002).
24. A. Shikanai, T. Deguchi, T. Sota, T. Kuroda, A. Takeuchi, S. Chichibu and S. Nakamura, *Appl. Phys. Lett.* **76**, 454 (2000).
25. W. Chow, M. Kira and S. W. Koch, *Phys Rev B* **60**, 1947 (1999). [38] S.H. Park and S.-L. Chuang, *Appl. Phys. Lett.* **72**, 287 (1998).
26. S.H. Park and S.-L. Chuang, *Appl. Phys. Lett.* **72**, 287 (1998).
27. S.H. Park and S.-L. Chuang, *Appl. Phys. Lett.* **76**, 287 (2000).
28. B. Gil and A. Alemu, *Phys. Rev. B* **56**, 12446 (1997).
29. B. Gil, F. Hamdani and H. Morkoç, *Phys. Rev. B* **54**, 7678 (1996).
30. A. J. Fischer, W. Shan, J. J. Song, Y. C. Chang, R. Horning and B. Goldenberg, *Appl. Phys. Lett.* **71**, 1981 (1997).
31. M. Leroux, N. Grandjean, M. Laügt, J. Massies, B. Gil, P. Lefebvre and P. Bigenwald, *Phys. Rev. B* **58**, R13371 (1998).
32. P. Lefebvre, M. Gallart, T. Taliercio, B. Gil, J. Allègre, H. Mathieu, N. Grandjean, M. Leroux, J. Massies and P. Bigenwald, *Phys. Stat. Sol. (b)* **216**, 361 (1999).
33. S. L. Chuang and C. S. Chang, *Phys. Rev. B* **54**, 2491 (1996).
34. A.S. Baker and S. Illegems, *Phys. Rev. B* **7**, 53 (1973).
35. M. Suzuki, T. Uenoyama and A. Yanase, *Phys. Rev. B* **52**, 8132 (1995).
36. D. A. B. Miller, A. C. Gossard and W. Wiegmann, *Optics Lett.* **9**, 162-164 (1984).

### Time Resolved Optical Studies of InGaN Layers Grown on LGO

Maurice Cheung, Gon Namkoong<sup>1</sup>, Madalina Furis, Fei Chen, Alexander. N. Cartwright, W. Alan Doolittle<sup>1</sup> and April Brown<sup>2</sup>,  
University at Buffalo, State University of New York,  
Buffalo, NY 14260, U.S.A.

<sup>1</sup>Georgia Institute of Technology, Atlanta, GA

<sup>2</sup>Duke University, Durham, NC

#### ABSTRACT

Radiative recombination processes in bulk InGaN grown by molecular beam epitaxy (MBE) on lithium gallate (LGO or LiGaO<sub>2</sub>) substrates were investigated using microscopic PL and time-resolved photoluminescence (TRPL). The improved structural quality resulting from a better lattice match of the LGO substrate to III-V nitride materials simplifies these investigations because well-defined composition phases can be analyzed for both homogeneous and phased separated InGaN samples. Epilayers of InGaN intentionally grown with and without indium segregation were studied. X-ray diffraction measurements showed that the homogeneous epilayer was high quality In<sub>0.208</sub>Ga<sub>0.792</sub>N and the segregated epilayer exhibited peaks corresponding to both In<sub>0.289</sub>Ga<sub>0.711</sub>N and In<sub>0.443</sub>Ga<sub>0.557</sub>N indicating the presence of higher In concentration regions in this sample. Spatially resolved photoluminescence spectra confirm the existence of these regions. The photoluminescence intensity decay is non-exponential for both samples and a stretched exponential fit to the decay data confirms the existence of local potential fluctuations in which carriers are localized before recombination.

#### INTRODUCTION

InGaN-based emitters are widely used for commercial high-brightness light emitting diodes (LED) from UV to amber [1,2]. There have been numerous reports on the improvement of efficiency in these LED devices due to In-segregation [3-7]. The current theory suggests that the In-rich regions existing inside InGaN act as localization centers, which trap the carriers injected into the system. The probability of non-radiative recombination for a carrier localized in a potential fluctuation is significantly reduced [4,6] and the excitons formed in the vicinity of the localization centers have greater oscillator strength [6]. As a result, the optical efficiency of the LED is greatly improved.

Most of the commercially available InGaN emitters consist of a multiple quantum well (MQW) heterostructures, which are characterized by emission efficiency that depends not only on the In-segregation but also on the built-in electric fields present as a result of the piezoelectric polarization [8-10]. Here, we have studied the changes induced by In-segregation in an InGaN epilayer grown by Molecular Beam Epitaxy (MBE) on a lithium gallate (LGO or LiGaO<sub>2</sub>) substrate. The crystal quality of GaN and InGaN grown on this substrate is significantly improved as a result of a better lattice match between the substrate and the nitride materials [11,12].

In this paper we present the results of confocal photoluminescence (CPL) and time-resolved photoluminescence (TRPL) measurements on two InGaN epilayers. X-ray and CPL confirm the existence of In-segregation in one of the samples. The results of a stretched

exponential fit to the TRPL intensity decay show the carrier lifetimes is nearly 3 times longer in the segregated sample in comparison to the non-segregated one, in agreement with the predicted decrease in the non-radiative recombination rate associated with increased carrier localization.

## EXPERIMENTAL DETAILS

The two samples used in this study are 500nm thick InGaN epilayers grown by MBE on a LGO substrate on the top of an equally thick (500nm) GaN buffer layer. One of the samples was intentionally grown to exhibit In-segregation, whereas the other was grown without In-segregation, thus serving as a reference.

CPL spectra were measured using the 400nm frequency doubled output beam of a Ti:sapphire laser as a pump. The beam was focused on the sample by a confocal microscope system with a lateral resolution of 200nm. The PL signal was collected and spectrally analyzed through a fiber attached to a computer-controlled spectrometer equipped with a CCD camera. During the experiment, several PL spectra were collected at different locations on each of the samples.

TRPL measurements were performed using the 200 fs laser pulses produced by a regenerative amplifier (Coherent: RegA) seeded by a Ti:Sapphire laser at 800nm. An optical parametric amplifier (Coherent: OPA) and a frequency doubling BBO crystal provided the up-conversion of the RegA pulses to 330nm. The excitation wavelength was chosen such that all the incident photons are absorbed in the nitride layers. The incident beam is focused on the sample by conventional optics with a spot size of  $\sim 60 \mu\text{m}$ . The back-scattered light from the sample was collected through conventional optics, and spectrally and temporally resolved by a Chromex 250IS monochromator and a Hamamatsu C4334 streakcamera with a typical jitter of 50ps.

## RESULTS

The X-ray diffraction spectra from the two samples under study are presented in figure 1. The reference sample exhibits three peaks associated with the LGO substrate, the GaN buffer and the InGaN layer. From the difference between the GaN and InGaN peaks we estimate the In concentration to be approximately 20.8%, in very good agreement with the expected nominal value. The peak associated with the  $\text{In}_{0.208}\text{Ga}_{0.792}\text{N}$  has a full width half maximum (FWHM) of 289 arc-s, and is broader than the peak corresponding to the GaN layer having a FWHM of 148 arc-s. The broadening indicates there is likely some partial phase separation in the sample and additional dislocations in the InGaN layer not found in the GaN. The spectrum corresponding to the In-segregated sample exhibits two peaks associated with InGaN: one corresponding to a 28.9% In concentration, and the other to a 44% In concentration. This is an indication that two completely separate phases are present inside the InGaN layer. We can visualize the sample as 44% InGaN “islands” embedded in a 28.9% InGaN “matrix”. The integrated intensity of the x-ray spectra indicates that the 44% In phase makes up  $\sim 15\%$  of the overall InGaN material with the rest of the InGaN attributed to the 28.9% In phase making the average In composition for the entire film  $\sim 31\%$ . The x-ray peak corresponding to the 28.9% InGaN has a FWHM of 278 arc-s compared to the GaN width of 155 arc-s indicating that, besides the existence of In-rich regions, random alloy fluctuations are also present in the “matrix”. The peak corresponding to the  $\text{In}_{0.44}\text{Ga}_{0.56}\text{N}$  is 205 arc-s wide and thus, is likely to have

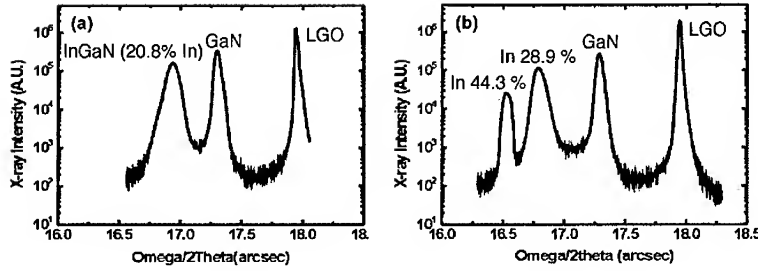


**Figure 1.** X-ray diffraction spectra for the (a) reference and (b) In-segregated samples. The latter exhibits two peaks indicating the existence of two separate phases.

fewer random alloy fluctuations.

CPL studies confirm the presence of a higher concentration phase inside the segregated sample. Figure 2 presents the PL spectra from several randomly chosen locations across the samples. The dotted lines represent the PL taken using conventional optics. Both samples exhibit very broad (FWHM = 400meV) PL features as expected for alloys with high concentrations where the presence of random In fluctuations determines the broadening of the PL. The time-integrated spectrum of the segregated samples shows an overall redshift in comparison to the reference sample suggesting the existence of a higher average In concentration in this sample. The confocal microscope allows us to probe small areas (200nm in diameter) inside the sample and investigate the nature of the redshift observed in conventional PL measurements. Several PL spectra from the reference sample taken at different locations (figure 2(a)) exhibit no significant changes when the beam position is changed on the sample surface. In contrast, the segregated sample PL spectra (figure 2(b)) taken with the same confocal system show significant changes in the PL shape for different beam positions on the sample surface. In fact, there are several peaks, which can be resolved in these spectra. The relative intensity of the peak centered at about 2.5eV to the one centered at 2.1eV varies as a function of beam position. These energies match very well to the bandgaps of  $\text{In}_{0.289}\text{Ga}_{0.711}\text{N}$  (2.5eV) and  $\text{In}_{0.44}\text{Ga}_{0.56}\text{N}$  (2.1eV) [13]. The changes in the relative intensity of the two spectral components prove the existence of well-

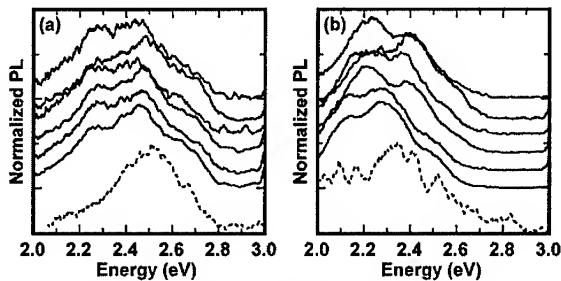


**Figure 2.** Confocal PL (solid lines) and time integrated PL (dotted lines) spectra of the reference sample (a) and segregated sample (b), taken at room temperature.

defined areas where the high In concentration component is dominant. This variation shows that the size of the In-rich areas is large (comparable to the beam size - 200nm), and much bigger than any alloy fluctuations existing in the reference sample.

At low temperature, we observed a much stronger signal for TRPL, allowing us to analyze the lifetimes more readily. Figure 3 shows the TRPL spectra from both samples at 15K. Unlike the spatially resolved measurement, in this experiment, the spot size of the incident beam is much greater than the size of the In-rich regions. Therefore what we observed is the convolution of the PL contribution from several In-rich regions as well as the 28.9% In "matrix". A red shift is observed in the segregated sample similar to room temperature measurements. The tail emission at 2.1eV and the dominant feature at 2.5eV in the segregated sample illustrate the relative abundance of the two phases, mentioned earlier. The PL spectrum is dominated by inhomogeneous broadening due not only to the overlap of PL features associated with the two In phases, but also to the partial phase separation which exists within the 28.9% In phase. The partial phase separation is also present in the reference sample and as a result, its PL spectrum is characterized by a FWHM comparable to that of the segregated sample. The PL intensity decay appears to be slower in the segregated sample. In an attempt to quantify the difference in PL decay, we plotted the decay of the integrated PL intensity for each sample as shown in figure 4(a). The log (PL intensity) vs. time plot clearly shows that the PL decays for both samples are non-exponential in nature. This is most likely caused by the alloy fluctuation in these samples. Previous studies [14] of PL lifetime have shown that the stretched exponential decay model [15,16] can offer insight into the recombination mechanisms in InGaN-related structures. According to this model the PL intensity decay is described by the following expression:

$$I(t) = I(0) \exp \left[ - \left( \frac{t}{\tau} \right)^\beta \right] \quad (1)$$

based on the assumption that potential fluctuations due to alloy disorder exist inside the sample. The carriers are trapped in the potential minima of these fluctuations. The parameter  $\beta$  (the stretched exponential coefficient) represents a measure of the alloy disorder [14].

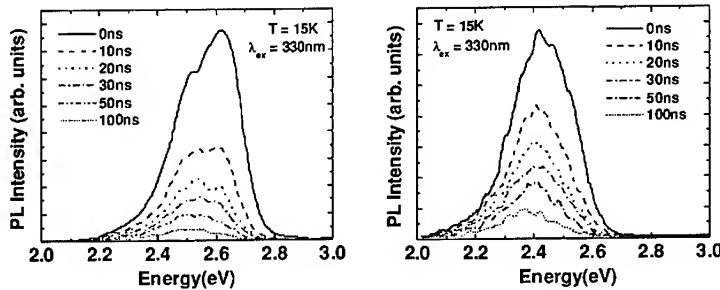


**Figure 3.** TRPL spectra at different delay times measured at 15K for (a) the reference and (b) the segregated sample. The PL spectrum of the segregated sample is redshifted in comparison with the reference sample confirming the presence of a higher indium concentration in this sample

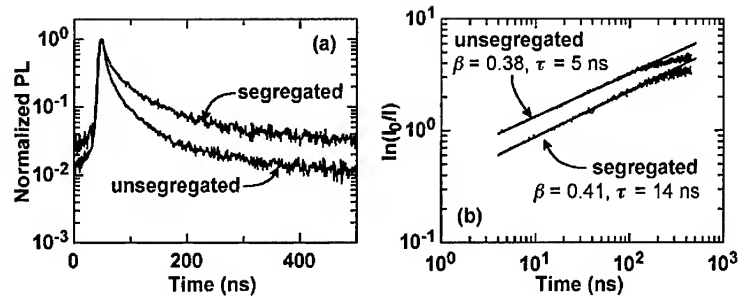


**Figure 4.** (a) Integrated PL decay taken at 15K for the segregated and unsegregated samples and (b) the corresponding  $\ln(I_0/I)$  vs.  $t$  plots with log-log scales, the solid lines show the fitting for  $\beta$  and  $\tau$ .

In our samples, we fitted the decays with the stretched exponential and obtained the results of  $\tau = 5$  ns and  $\beta = 0.38$  for the reference sample, while for the segregated sample,  $\tau = 14$  ns and  $\beta = 0.41$ . Since the In-rich phase only makes up 15% of the overall InGa<sub>N</sub> material in the segregated sample, most carriers are generated in the 28.9% In region. Subsequent to generation carriers with sufficient energy can relax to the potential minima induced by the phase separation. Therefore,  $\beta$  should not be affected by the presence of the In rich regions as long as the 28.9% phase remains dominant. This accounts for the similarity of the  $\beta$  values measured for the two samples. The lifetime that characterizes the segregated sample is nearly 3 times longer than the one measured for the reference sample. Yamaguchi *et al.* and Narukawa *et al.* have shown how segregation and carrier localization can have an effect on the PL lifetime [3,6]. In TRPL, the measured emission decay rate is a combination of the rates of radiative and non-radiative recombination, and the PL decay time is related to the radiative and non-radiative lifetimes ( $\tau_{PL}$ ,  $\tau_R$  and  $\tau_{NR}$ ) through the following equation:

$$\frac{1}{\tau_{PL}} = \frac{1}{\tau_R} + \frac{1}{\tau_{NR}}. \quad (2)$$

With In-segregation, the rate of non-radiative recombination is expected to decrease since carriers are now trapped by the In-rich region and confined away from the non-radiative recombination centers. Assuming  $\tau_R$  is the similar in both samples then the only explanation for a longer  $\tau_{PL}$  is that  $\tau_{NR}$  has been elongated for the segregated sample. Therefore, the longer lifetime observed in the segregated sample is most likely the result of a reduction in non-radiative recombination rate by carrier localization.

## CONCLUSIONS

LGO serves as a very good substrate for growing strain-free GaN and InGa<sub>N</sub> epilayers in which the effects of dislocations induced by lattice mismatch on the emission efficiency are greatly reduced and the influence of In-segregation on radiative recombination can be studied efficiently. We have presented spatially and time-resolved PL studies of InGa<sub>N</sub> epilayers grown

on LGO by MBE. The changes in the spatially resolved CPL spectra as a function of beam position observed in the segregated sample confirmed the existence of In-rich regions indicated by the x-ray measurements on the same sample. The overall redshift of the PL peak energy with respect to that corresponding to a non-segregated samples observed using conventional PL techniques is in agreement with the existence of a high In concentration phase inside the sample. Most importantly, the PL decay times obtained as a result of a stretched exponential fit to the decay data increased by nearly a factor of 3 as a result of In segregation. This observation implies the carriers are no longer trapped by the non-radiative centers but they become localized on radiative states existing in the potential minima created inside the In-rich regions.

#### ACKNOWLEDGEMENTS

The authors would like to thank Dr. Haridas E. Pudavar for his assistance in conducting the confocal microscopy on the samples. This research was in part supported by ANC's NSF CAREER Grant #9733720, ONR YIP Grant # N00014-00-1-0508, and Doolittle's ONR Grant #N00014-99-1-0419

#### REFERENCES

1. S. Nakamura, and G. Fasol, *The Blue Laser Diode*, (1997)
2. T. Mukai, D. Morita and S. Nakamura, *J. Cryst. Growth* **189/190**, 778 (1998)
3. A. Yamaguchi, Y. Mochizuki, and M. Mizuta, *Jpn. J. Appl. Phys.* **39**, 2402 (2000)
4. K. P. O'Donnell, R. W. Martin, and P. G. Middleton, *Phys. Rev. Lett.* **82**, 237 (1999)
5. C. A. Tran, R.F. Karlick Jr., M. Schurman, A. Osinsky, V. Merai, Y. Li, I. Eliashevich, M. G. Brown, I. Ferguson, and R. Stall, *J. Cryst. Growth* **195**, 397 (1998)
6. Y. Narukawa, K. Sawada, Y. Kawakami, S. Fujita, S. Fujita, and S. Nakamura, *J. Cryst. Growth* **189/190**, 606 (1998)
7. Y. Narukawa, Y. Kawakami, S. Fujita, S. Fujita, and S. Nakamura, *Phys. Rev. B* **55**, R1938 (1997)
8. O. Ambacher, J. Majewski, C. Miskys, A. Link, M. Hermann, M. Kickoff, M. Stutzmann, F. Bernardini, V. Fiorentini, V. Tilak, B. Schaff, and L. F. Eastman, *J. Phys.: Condens. Matter* **14**, 3399 (2002)
9. S. F. Chichibu, A. C. Abare, M. P. Mack, M. S. Minsky, T. Deguchi, D. Cohen, P. Kozodoy, S. B. Fleisher, S. Keller, J. S. Speck, J. E. Bowers, E. Hu, U. K. Mishra, L. A. Coldren, S. P. DenBaars, K. Wada, T. Sota, and S. Nakamura, *Material Science and Engineering* **B59**, 298 (2000)
10. L. Peng, C. Chuang, and L. Lou, *Appl. Phys. Lett.* **74**, (1999)
11. A. S. Brown, and W. A. Doolittle, *Applied Surface Science* **166**, 392 (2000)
12. W. A. Doolittle, S. Kang, and A. Brown, *Solid-State Electron* **44**, 229 (2000)
13. W. Shan, W. Walukiewicz, and E. E. Haller, *J. Appl. Phys.* **84**, 4452 (1998)
14. M. Prophristic, F. H. Long, C. Tran, and I. T. Ferguson, *MRS Internet J. Nitride Semicond. Res.* **5S1**, W11.58 (2000)
15. T. Y. Lin, J. C. Fan, and Y. F. Chen, *Semicond. Sci. Technol.* **14**, 406 (1999)
16. L. Pavesi, *J. Appl. Phys.* **80**, 216 (1996)

### Femtosecond pump and probe spectroscopy of optical nonlinearities in an InGaN/GaN heterostructure

Fei Chen and A. N. Cartwright

Department of Electrical Engineering, State University of New York at Buffalo, Buffalo, NY 14260, USA

#### ABSTRACT

The magnitudes and evolutions of two photoinduced absorption nonlinearities, absorption bleaching and field screening, were compared and investigated by employing electroabsorption and femtosecond pump-probe spectroscopy in a biased InGaN/GaN p-i-n double heterostructure. Steady state electroabsorption measurements indicate the field induced absorption coefficient changes in this structure are caused by the Franz-Keldysh effect. The temporal resolution of the absorption bleaching spectra suggests that the photoinduced carriers rapidly relaxed to the InGaN band edge within several picoseconds. As the applied reverse bias field was increased, the transition of the differential absorption spectral signature from the signature for absorption bleaching to the signature for field screening was observed. The magnitude of the change in absorption due to photoinduced carrier screening of the applied field is quantified and compared to absorption bleaching.

#### INTRODUCTION

The development of III-V nitride based laser devices has continued to advance since the first demonstration of an InGaN multiple quantum well (MQW) laser diode in 1996.<sup>1,2,3</sup> Recently the design and performance of a two section InGaN MQW laser diode consisting of an electroabsorption (EA) modulator and amplifier section has been reported.<sup>4</sup> Compared with the traditional direct current modulation, integrated EA modulator reduces the transient heating effects, which makes it attractive for printing applications. The improvements of the device performance of nitride based EA modulators and future applications in all-optical switching and computing, such as self-electro-optic-effect devices (SEEDs), require the detailed study on the absorption nonlinearities in these devices.

Two fundamentally different types of absorption nonlinearities have been clarified in the studies on GaAs-based SEEDs and [111] oriented piezoelectric InGaAs devices: excitonic bleaching and field screening.<sup>5,6,7</sup> Excitonic bleaching is due to various many-body mechanisms.<sup>8</sup> It induces a decrease and broadening of the excitonic absorption and the corresponding change in absorption is dominated by a large negative peak centered at the excitonic peak energy. In field screening, the blue shift of the excitonic absorption due to reduction of the quantum-confined Stark effect and Franz-Keldysh effects (FKEs) produces a change in absorption coefficient which will consist of positive and negative peaks, with a zero crossing that blue shifts as the injected carrier density is increased. However, similar time-resolved studies of absorption nonlinearities on III-V nitride based devices are lacking.

In this article, we present both steady state EA measurements and femtosecond pump-probe spectroscopy to identify different photoinduced changes in absorption in a biased InGaN/GaN double heterostructure at room temperature. The EA measurements show the field induced absorption coefficient changes in the InGaN thin film are caused by the FKE. The contribution of

field screening to the changes in the absorption coefficient is separated from, and compared to the absorption bleaching through time-resolved differential transmission technique.

## SAMPLE AND EXPERIMENTS

The sample used in this study is an InGaN/GaN double heterostructure light emitting diode device grown by metalorganic chemical vapor deposition. This p-i-n diode consists of a n-type GaN:Si layer grown on a sapphire substrate, an undoped 0.1  $\mu\text{m}$   $\text{In}_{0.6}\text{Ga}_{0.94}\text{N}$  active layer, and a 0.25  $\mu\text{m}$  p-type GaN:Mg cap layer.

For the steady state EA measurements, the white light from a 150 W Xenon lamp was spectrally filtered using a 0.25 m spectrometer and then focused to a 1 mm diameter spot on the sample to serve as the probe beam. A modulated reverse bias voltage was applied to the sample and the corresponding modulated transmission signal ( $\Delta T$ ) with and without applied field as a function of probe wavelength was detected by a silicon detector using standard lock-in technique. Using this technique, the absorption changes are given by  $\Delta\alpha = -1/d[\ln(1 + \Delta T/T)]$ ,<sup>7</sup> where  $d$  is thickness of the (optically active) InGaN layer.

In addition to steady state measurements, femtosecond single color pump-white light continuum probe spectroscopy was used to time resolve the differential transmission signatures. For these measurements, a portion of the 760 nm, 150 fs laser pulses from a 250 kHz regenerative amplifier (REGA) was frequency doubled to 380 nm to serve as the pump source for carrier excitation above the InGaN band gap, but below the GaN band gap. The remaining output from the REGA was used to create a broadband white light continuum, with spectral components from 370 nm to 1000nm,<sup>9</sup> which served as the probe beam. The time resolution of this system is limited to  $\sim 300$  fs due to the broadened pulse width of the frequency-doubled pulse and the white-light continuum. The probe beam was focused to an 80  $\mu\text{m}$  diameter spot on the sample and the transmitted light was spectrally resolved using a spectrometer. The pump spot size was chosen to be 160  $\mu\text{m}$  to ensure that the probe beam was monitoring a relatively constant injected carrier density. Similar to EA measurements, standard lock-in techniques were used to measure the difference in the probe transmission ( $\Delta T$ ) with and without the pump present as a function of probe wavelength, and delay time between pump and probe pulse.<sup>7</sup>

## RESULTS AND DISCUSSION

Initially, we performed steady state EA measurements to investigate the field induced absorption coefficient change. The typical EA spectra under various reverse biases are shown in Fig. 1. It is well known that the application of an external electric field in a bulk semiconductor results in the band tilting that alters the envelope electron and hole-wave functions so that they have oscillating behavior in the bands and show exponential decay in the band gap. This phenomena is known as the FKEs. Fig. 1 shows that the electric field leads to an increased absorption below and oscillating absorption above the band gap on this structure. In addition, the EA spectra curves for all applied fields intersect at the band gap energy (3.20 eV, consistent with  $\sim 6\%$  In). This does resemble the typical FKE spectra for bulk semiconductor.<sup>10</sup> Thus, modulating the external electrical field can induce absorption changes as large as  $800\text{ cm}^{-1}$  at the photon energies of 3.15 eV and 3.24 eV as shown in Fig. 1. Such large absorption changes can be utilized to modulate the absorption for the application of EA modulator. In addition to the peak absorption changes, photoinduced absorption bleaching and field screening which affect the

change of absorption coefficient need to be investigated for the optimization of device design. These optical nonlinearities can be employed for all-optical switching applications.

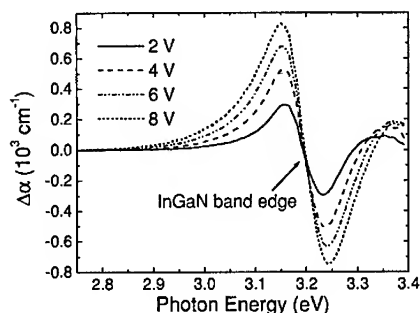


Fig. 1. Reverse bias voltage dependent EA spectra at room temperature.

Subsequent to these EA measurements, femtosecond pump and probe spectroscopy was used to compare and temporally resolve the absorption bleaching and field screening. Fig. 2 shows the variation of differential absorption spectra under a pump fluence of  $400 \mu\text{J}/\text{cm}^2$  and open circuit condition as a function of delay time. At the initial stage of excitation in Fig. 2(a) (0 ps to 2 ps), the bleaching of the photo-absorption was observed in the vicinity of pumping energy immediately after the pump pulse. In contrast, at the photoluminescence (PL) peak energy (3.20 eV, the InGaN band edge) the bleaching signal begins to increase from 0.4 ps and reaches the maximum at 2 ps. This suggests that the photoinduced hot carriers rapidly transferred or relaxed to the InGaN band edge within the time-scale of a few ps. Furthermore, it should be noted that with increasing delay time the peak energy exhibits an evident red shift but the spectra is still dominated by a single negative peak as shown in Fig. 2(b). This observed red shift is consistent with the reduction of band filling effects due to carrier recombination or escape from the InGaN active layer.

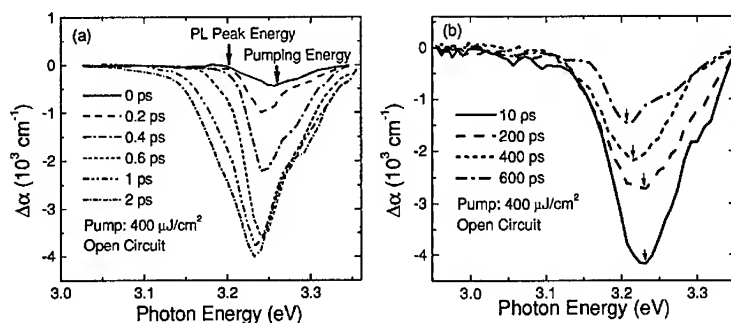


Fig. 2. Differential absorption spectra under a pump fluence of  $400 \mu\text{J}/\text{cm}^2$  as a function of delay time (a) 0 ps to 2 ps, and (b) 10 ps to 600 ps.

By contrast, Fig. 3 shows the detailed differential absorption spectra as function of reverse bias (0 V to 9 V) under a pump fluence of  $60 \mu\text{J}/\text{cm}^2$  at a delay time of 50 ps. This delay time ensures that sufficient relaxation and drift of photo-generated carriers in the InGaN active region have occurred with negligible recombination. At low reverse voltages, a single negative peak due to absorption bleaching dominates the spectra. With increasing reverse bias, the observed spectral signature is consistent with the presence of absorption bleaching and field screening. The spectra at 9 V in Fig. 3 is similar to that observed by EA measurements with a negative-positive swing due to the reduction of the FKE. Specifically, the net change in absorption due to bleaching decreases with increasing reverse bias because of the spatial separation between electrons and holes under the influence of the applied field, while the change in absorption due to screening of the applied field begins to dominate. More importantly, the peak change in the absorption coefficients caused by field screening (9 V) is comparable to the change caused by bleaching (0 V) without applied bias.

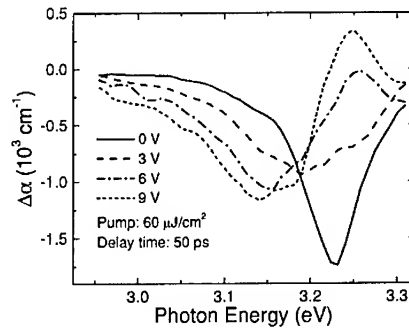


Fig. 3. Differential absorption spectra with a pump fluence of  $60 \mu\text{J}/\text{cm}^2$  at a delay time of 60 ps as a function of reverse bias.

The studies on [100] and [111] oriented InGaAs devices have shown that the magnitude of the continuous-wave absorption change due to field screening comparable to bleaching.<sup>7</sup> The large  $\Delta\alpha$  has been attributed to the accumulation of carriers during the longer lifetime caused by spatial separation between electrons and holes.

## CONCLUSION

In summary, in this article a detailed study including steady state EA and femtosecond pump-probe techniques is used to provide insight into the absorption nonlinearities in an InGaN/GaN double heterostructure. EA measurements indicate the field induced absorption coefficient changes in this structure are caused by FKE. The transition of the differential absorption spectral signature from absorption bleaching to field screening as the applied reverse field increases was found. The observed changes in the absorption coefficients caused by field screening under reverse bias are on the same order of the changes caused by bleaching without an applied bias.

## ACKNOWLEDGEMENTS

The authors gratefully acknowledge Dr. Jeffrey Flynn from ATMI for generously providing the materials used in this study. This work was supported by the National Science Foundation CAREER Award, NSF #9733720, under the direction of Dr. Filbert Bartoli, and the Office of Naval Research Young Investigator Program Award # N00014-00-1-0508 under the direction of Dr. Colin Wood.

## REFERENCES

1. S. Nakamura, M. Senoh, S. Nagahama, N. Iwasa, T. Yamada, T. Matsushita, H. Kiyoku, and Y. Sugimoto, *Jpn. J. Appl. Phys. Part 2* **35**, L74 (1996).
2. S. Nagahama, N. Iwasa, M. Senoh, T. Matsushita, Y. Sugimoto, H. Kiyoku, T. Kozaki, M. Sano, H. Matsumura, H. Umemoto, K. Chocho, and T. Mukai, *Jpn. J. Appl. Phys. Part 2* **39**, L647 (2000).
3. T. Tojyo, T. Asano, M. Takeya, T. Hino, S. Kijima, S. Goto, S. Uchida, and M. Ikeda, *Jpn. J. Appl. Phys. Part 1* **40**, 3206 (2001).
4. M. Kneissl, T. Paoli, P. Kiesel, D. W. Treat, M. Teepe, N. Miyashita, and N. M. Johnson, *Appl. Phys. Lett.* **80**, 3283 (2002).
5. X. R. Huang, A. N. Cartwright, D. R. Harken, D. S. McCallum, A. L. Smirl, J. L. Sánchez-Rojas, A. Sacedón, E. Calleja, and E. Muñoz, *J. Appl. Phys.* **79**, 417 (1995).
6. X. R. Huang, D. R. Harken, A. N. Cartwright, A. L. Smirl, J. L. Sánchez-Rojas, A. Sacedón, E. Calleja, and E. Muñoz, *Appl. Phys. Lett.* **67**, 950 (1995).
7. A. N. Cartwright, D. S. McCallum, T. F. Boggles, A. L. Smirl, T. S. Moise, L. J. Guido, R. C. Barker, and B. S. Wherrett, *J. Appl. Phys.* **73**, 7767 (1993).
8. S. Schmitt-Rink, D. S. Chemla, and D. A. B. Miller, *Phys. Rev. B* **32**, 6601 (1985).
9. C. Nagura, A. Suda, H. Kawano, M. Obara, and K. Midorikawa, *Appl. Opt.* **41**, 3735 (2002).
10. F. Renner, P. Kiesel, G. H. Döhler, M. Kneissl, C. G. Van de Walle, and N. M. Johnson, *Appl. Phys. Lett.* **81**, 490 (2002).

### Excitons of the Structure in Zinc-Blende $\text{In}_x\text{Ga}_{1-x}\text{N}$ and their Properties

Dimiter Alexandrov

Department of Electrical Engineering, Lakehead University  
955 Oliver Road, Thunder Bay, Ontario P7B 5E1, Canada

#### ABSTRACT

The existence of excitons of the structure in zinc-blende  $\text{In}_x\text{Ga}_{1-x}\text{N}$  is reported in this paper. The LCAO electron band structure of zinc-blende  $\text{In}_x\text{Ga}_{1-x}\text{N}$  is calculated as function of both the electron wave vector and the electron radius-vector. The observed optical absorption edge in In-rich regions in  $\text{In}_x\text{Ga}_{1-x}\text{N}$  is explained on the basis of this electron band structure. The excitons of the structure are found on the basis of the electron band structure of zinc-blende  $\text{In}_x\text{Ga}_{1-x}\text{N}$ . The binding energy and the hydrogen like energy levels of these excitons are determined. It is found that these excitons are localized. The observed photoluminescence spectrum in In-rich regions of  $\text{In}_x\text{Ga}_{1-x}\text{N}$  is explained by the excitons of the structure. It is found that destroying of these excitons occurs in their interactions with hetero-junction and that the electrons and the holes of exciton origin penetrate in the semiconductor of wider energy band gap. This phenomenon is used for explanation of the observed spectral blue shift of the electroluminescence in the quantum well structures on  $\text{In}_x\text{Ga}_{1-x}\text{N}$ .

#### INTRODUCTION

The quantum well structures on the basis of  $\text{In}_x\text{Ga}_{1-x}\text{N}$  show interesting optical characteristics. The results obtained by Y. Narukawa *et al.* [1] are connected with photoluminescence spectra of quantum well structures on  $\text{In}_x\text{Ga}_{1-x}\text{N}$ , and the authors explain the spectra by excitons localized in deep traps. S. Chichibu *et al.* [2] and P. Eliseev *et al.* [3] have observed blue shift of the electroluminescence in quantum well structures on  $\text{In}_x\text{Ga}_{1-x}\text{N}$ . Davydov *et al.* [4] have observed interesting optical absorption and photoluminescence spectrum in In-rich regions of  $\text{In}_x\text{Ga}_{1-x}\text{N}$ . Existence of excitons of the structure in zinc-blende  $\text{In}_x\text{Ga}_{1-x}\text{N}$  is reported in this paper. The LCAO (Linear Combination of Atomic Orbitals) electron band structure of zinc-blende  $\text{In}_x\text{Ga}_{1-x}\text{N}$  is calculated as function of both the electron wave-vector and the radius-vector of the quasi-elementary cell where the electron is localized. The energy band intervals corresponding to the different energy sub-bands are determined. The observed optical absorption edge [4] is explained on the basis of these energy intervals. Existence of excitons of the structure in zinc-blende  $\text{In}_x\text{Ga}_{1-x}\text{N}$  is found. Part of the properties of these excitons is determined. The observed blue shift in [2] and [3] is explained on the basis of these excitons. Also the observed photoluminescence spectrum [4] is explained on the same basis as well.

#### ELECTRON BAND STRUCTURE OF ZINC-BLENDE $\text{In}_x\text{Ga}_{1-x}\text{N}$

The electron band structure of zinc-blende  $\text{In}_x\text{Ga}_{1-x}\text{N}$  is calculated by the method developed in [5]. The multinary crystal of zinc-blende  $\text{In}_x\text{Ga}_{1-x}\text{N}$  is considered to be periodical crystal having large primitive super-cell, containing finite number of elementary cells. By definition elementary cell of the primitive super-cell is cell having the same symmetry like the symmetry of the primitive cells of the crystals-constituents (here they are zinc-blende InN and zinc-blende GaN) if the symmetry is defined only on the basis of the positions of both the cations and the anions without consideration the nature of the atoms. It is found [5] that the electron energy in the crystal can be presented in the following way.

$$E(\mathbf{k}) = \sum_{\mathbf{q}} \exp(i\mathbf{k} \cdot \mathbf{R}_{\mathbf{q}}) E(\mathbf{q}) \quad (1)$$

Where  $\mathbf{k}$  is electron wave-vector,  $E(\mathbf{q})$  is electron energy in the elementary cell  $\mathbf{q}$  having radius-vector  $\mathbf{R}_{\mathbf{q}} = q_1\mathbf{a}_1 + q_2\mathbf{a}_2 + q_3\mathbf{a}_3$  ( $\mathbf{a}_1$ ,  $\mathbf{a}_2$  and  $\mathbf{a}_3$  are three basis vectors of the primitive super-cell defined by the elementary cell). The dependence of the electron energy on the coordinates can be found by taking the Fourier transform from both sides of (1)

$$E(\mathbf{r}) = \sum_{\mathbf{q}} \delta(\mathbf{r} - \mathbf{R}_{\mathbf{q}}) E(\mathbf{q}) \quad (2)$$

Where  $\mathbf{r}$  is the radius-vector of the electron, and  $\delta(\mathbf{r} - \mathbf{R}_{\mathbf{q}})$  is delta-function. The expression (2) shows that the electron energy depends on the electron radius-vector - i.e. it depends on the elementary cell where the electron is localized. (The elementary cells are equivalent.)

The electron band structure of zinc-blende  $\text{In}_x\text{Ga}_{1-x}\text{N}$  can be determined on the basis of the interactions within the primitive super-cell, which determine the corresponding sub-bands. Quasi-elementary cell must be introduced according to [5]. It has the same structure as the elementary cell, but the natures of the building atoms are considered (here they are In, Ga and N). According to [5] (and it can be seen in (2)) the electron band structure can be presented by sum of the electron band sub-structures belonging to the elementary cells. (It is very important that this sum contains delta-function.) This one will be applied for the quasi-elementary cells. As a matter of fact the electron band structure of zinc-blende  $\text{In}_x\text{Ga}_{1-x}\text{N}$  determined in this way contains the same sub-bands like these determined for the primitive super-cell of zinc-blende  $\text{In}_x\text{Ga}_{1-x}\text{N}$  without consideration of the localizations of the interactions. However here the corresponding sub-bands are localized in the corresponding quasi-elementary cells and the electron band structure depends on both  $\mathbf{k}$  and  $\mathbf{R}_{\mathbf{q}}$ . The electron band structure  $E(\mathbf{k}, \mathbf{R}_{\mathbf{q}})$  of zinc-blende  $\text{In}_x\text{Ga}_{1-x}\text{N}$  determined in this way is continuous sequence of electron band sub-structures and each of them is calculated for the corresponding quasi-elementary cell.

It is necessary to be used localized wave functions for calculations of the electron band sub-structure of a quasi-elementary cell. In this paper linear combinations of atomic orbitals (LCAO) are used as functional basis and the electron band sub-structures are calculated using LCAO method [6]. Tetrahedral cell of zinc-blende  $\text{In}_x\text{Ga}_{1-x}\text{N}$  will be introduced to represent interactions between the nearest neighbor orbitals. The tetrahedral cell of zinc-blende  $\text{In}_x\text{Ga}_{1-x}\text{N}$  contains two atoms - cation and anion. In the quasi-elementary cells the cations are atoms In and Ga, and anions are atoms N. The tetrahedral cell contains these atoms as well. The orbitals corresponding to both *s*- and *p*-states of the valence electrons of the atoms In, Ga and N are used in the calculations. Also it is considered that non-zero matrix elements are only these, which represent interactions between the nearest neighbor orbitals and between the second neighbor orbitals. Due to the fact that the valence electron states engaged in the interactions are one *s*- and three *p*-states (*p<sub>x</sub>*, *p<sub>y</sub>* and *p<sub>z</sub>*) per atom the corresponding LCAO Hamiltonian matrix of the tetrahedral cell contains 16 rows and 16 columns. The matrix element  $H_{\alpha\alpha}$  for  $\alpha = 1, 2, 3, \dots, 8$  represents orbital energy term when the corresponding atom is in the crystal.

$$H_{\alpha\alpha} = C_{\alpha} \epsilon_{\alpha} \quad (3)$$

The energy terms  $\epsilon_l$  ( $l = s, p$ ) represent the energies of the *s*- and *p*-states of the isolated atoms In, Ga and N. Their values are taken from [7]. The real coefficients  $C_l$  are obtained by the author by using the fitting method for zinc-blende InN and zinc-blende GaN. They describe well the corresponding energy bandwidths and they are in good agreement with the experimental results. It is found that  $C_s=0.65$  and  $C_p=0.26$  for In,  $C_s=0.63$  and  $C_p=0.25$  for Ga,  $C_s=0.65$  and  $C_p=0.26$  for N if this atom is in zinc-blende InN, and  $C_s=0.63$  and  $C_p=0.25$  for N if this atom is in GaN.

**BEST AVAILABLE COPY**

The matrix element  $H_{\alpha\beta}$  ( $\alpha \neq \beta$ ) represents the interaction between atomic orbitals  $l$  and  $l'$  belonging to different atoms

$$H_{\alpha\beta} = E_{ll'} \sum_j e^{i \mathbf{k} \cdot \mathbf{d}_j} \quad (4)$$

Where  $\mathbf{d}_j$  is vector-distance between the orbitals  $l$  and  $l'$  engaged in the interaction and  $E_{ll'}$  is the module of the matrix element. The sum in (4) is over all parts of the interacting orbitals  $l$  ( $l = s, p$ ) and  $l'$  ( $l' = s, p$ ). The modules  $E_{ll'}$  can be expressed in corresponding way [8] by terms  $V_{ss\sigma}$ ,  $V_{sp\sigma}$ ,  $V_{pp\sigma}$  and  $V_{pp\pi}$  representing different types of the interactions. These terms are designated by  $V_{ll'\eta}$  where  $l, l' = s, p$  respectively and  $\eta = \sigma, \pi$  represents the type of the  $p$  orbital. The module  $E_{ll'}$  is equal to zero if there is no interaction between two orbitals.

The matrix elements  $H_{\alpha\beta}$  for ( $\alpha = 1, 2, \dots, 8$  &  $\beta = 1, 2, \dots, 8$  &  $\alpha \neq \beta$ ) represent the interaction between the orbitals of the atoms, which are nearest-neighbors. In this case [8] the terms  $V_{ll'\eta}$  are  $V_{ll'\eta} = \hbar^2 \omega_{ll'\eta} / (m_0 d_j^2)$ , where  $\omega_{ll'\eta}$  is structural factor, and  $m_0$  is the mass of the electron. The inter-orbitals distances  $d_j$  are equal to the corresponding distances between atoms engaged in In-N or Ga-N bonds. The term  $V_{ll'\eta}$  has different values for In-N and Ga-N bonds.

The matrix elements  $H_{\alpha\beta}$  for both ( $\alpha = 9, 10, \dots, 16$  &  $\beta = 1, 2, \dots, 8$ ) and ( $\alpha = 1, 2, \dots, 8$  &  $\beta = 8, 9, \dots, 16$ ) represent interaction between the atomic orbitals belonging to the tetrahedral cell and the atomic orbitals, which are their second neighbors. The muffin-tin orbital method [8, 9] is used by the author for the determination of the terms  $V_{ll'\eta}$  (in the case of the interactions between second neighbors) in zinc-blende  $\text{In}_x\text{Ga}_{1-x}\text{N}$ . The distances between atoms (second neighbors) engaged in the interactions, their tetrahedral covalent radii and the distribution of the valence electrons in the tetrahedral cell are used as the basis of the calculations. It is found: i) in the case of In-In interaction:  $-V_{ss\sigma} = 0.3045$  eV,  $V_{pp\sigma} = 0.0428$  eV,  $-V_{pp\pi} = 0.0214$  eV; ii) in the case of Ga-Ga interaction:  $-V_{ss\sigma} = 0.2928$  eV,  $V_{pp\sigma} = 0.0371$  eV,  $-V_{pp\pi} = 0.0170$  eV; iii) in the case of In-Ga interaction:  $-V_{ss\sigma} = 0.5200$  eV,  $V_{pp\sigma} = 0.2000$  eV,  $-V_{pp\pi} = 0.1000$  eV; iv) in the case of In-N interaction:  $-V_{ss\sigma} = 0.0503$  eV,  $V_{sp\sigma} = 0.0190$  eV,  $V_{pp\sigma} = 0.0071$  eV,  $-V_{pp\pi} = 0.0035$  eV; v) in the case of Ga-N interaction:  $-V_{ss\sigma} = 0.0469$  eV,  $V_{sp\sigma} = 0.0195$  eV,  $V_{pp\sigma} = 0.0079$  eV,  $-V_{pp\pi} = 0.0040$  eV; vi) in the case of N-N interaction:  $-V_{ss\sigma} = 0.0400$  eV if both N atoms are engaged in In-N bonds and  $-V_{ss\sigma} = 0.0372$  eV if both N atoms are engaged in Ga-N bonds,  $V_{pp\sigma} = 0.0010$  eV,  $-V_{pp\pi} = 0.0005$  eV ( $V_{sp\sigma} = 0$  for both anion-anion and cation-cation orbital interactions).

The matrix elements  $H_{\alpha\beta}$  for ( $\alpha = 9, 10, \dots, 16$  &  $\beta = 9, 10, \dots, 16$ ) are taken to be equal to zero because only the interactions between the nearest-neighboring orbitals and the second-neighboring orbitals are considered. The LCAO Hamiltonian matrix of the tetrahedral cell is determined by all cases of matrix elements  $H_{\alpha\beta}$  discussed above. The electron band sub-structure of a quasi-elementary cell can be calculated by Hamiltonian matrix  $|H|$  ( $\alpha = 1, 2, 3, \dots, 16$ ;  $\beta = 1, 2, 3, \dots, 16$ ) of the corresponding tetrahedral cell.

After detail investigation the author has found that in regard to the excitons of the structure (its ground state) it can be taken a part of the LCAO electron band structure of zinc-blende  $\text{In}_x\text{Ga}_{1-x}\text{N}$  corresponding to configuration of quasi-elementary cells giving deepest energy pocket for the electrons in the conduction band, deepest energy pocket for the holes in the valence band, and both energy pockets are on shortest distance. (For other purposes the complete LCAO electron band structure must be considered.) In order these three conditions to be satisfied a configuration of five different types of zinc-blende quasi-elementary cells taken in the following order must be used: – 1) GaN quasi-elementary cell surrounded by second neighboring Ga cations; 2) GaN quasi-elementary cell having half of second neighboring cations Ga and other half In; 3) mixed In-GaN quasi-elementary cell containing one half atoms In, one half atoms Ga and one atom N,

having half of second neighboring cations Ga and other half In. The corresponding tetrahedral cell contains one half atoms In, one half atoms Ga and one atom N; 4) InN quasi-elementary cell having half of second neighboring cations In and other half Ga; 5) InN quasi-elementary cell surrounded by second neighboring In cations. The electron band sub-structures have to be calculated for all quasi-elementary cells and the corresponding configurations of the surrounding cations. Each electron band sub-structure will be localized in conformity with (2) and it forms corresponding sector of the electron band structure. The LCAO energy sub-bands CB1 (the minimum of the conduction band) and VB1 (the maximum of the valence band) are given in Fig.1 under consideration that the electron energy of the vacuum level is equal to zero.

The electron energy state  $\Gamma_{cl}^v$  belongs to the sub-band CB1 of the sector  $v$ , and the electron state  $\Gamma_{v15}^v$  belongs to the sub-band VB1 of the sector  $v$  ( $v = 1, 2, 3, 4, 5$ ). The energy interval ( $\Gamma_{cl}^v - \Gamma_{v15}^v$ ) is direct energy band gap ( $k = 0$ ) corresponding to the quasi-elementary cell of the sector  $v$ . It depends on the number of the surrounding second neighboring cations Ga and In, and it varies: in the range 1.51 – 2.93 eV for sector 2, in the range 1.08 – 1.60 eV for sector 3, and in the range 1.58 – 2.94 eV for sector 4. These energy intervals determine the effective energy band gap of zinc-blende  $\text{In}_x\text{Ga}_{1-x}\text{N}$ , which is equal to the narrowest interval. (The author's calculations for wurtzite  $\text{In}_x\text{Ga}_{1-x}\text{N}$  [5] show variations of these intervals as follows: in the range 3.12 – 3.46 eV for sector 2, in the range 1.90 – 2.87 eV for sector 3, and in the range 1.64 – 2.06 eV for sector 4.) The results obtained by the author are close to these reported in [4] where the optical absorption edge of In-rich regions of  $\text{In}_x\text{Ga}_{1-x}\text{N}$  ( $0.36 < x < 1$ ) is found to be in the range 0.9 – 1.1 eV, and close to these reported in [10] where the energy band gap of  $\text{In}_{0.4}\text{Ga}_{0.6}\text{N}$  is determined to be 1.7 eV. The effective energy band gap is determined by the dominating energy interval in the technological circumstances. The shifts of the sub-bands of Fig.1 and the corresponding energy intervals are due to the defects in the crystal lattice of zinc-blende  $\text{In}_x\text{Ga}_{1-x}\text{N}$  – i.e. the existence of two sorts of cations – In and Ga. The nature of these shifts is different from the nature of the shifts of the boundaries of the energy band gap described in [11, 12].

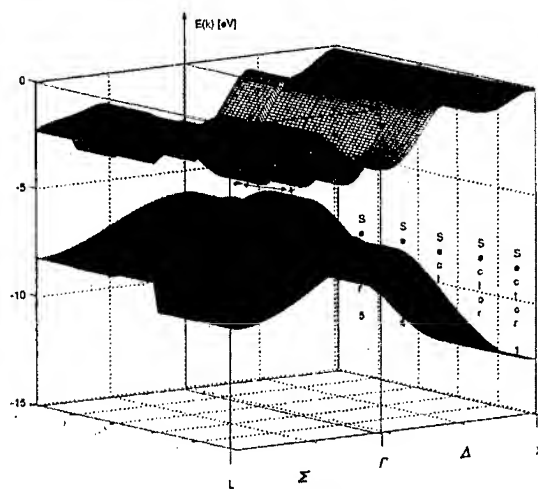


Figure 1. Electron band structure of zinc-blende  $\text{In}_x\text{Ga}_{1-x}\text{N}$

## EXCITONS OF THE STRUCTURE AND THEIR PROPERTIES

Exciton of the structure in zinc-blende  $\text{In}_x\text{Ga}_{1-x}\text{N}$  is the exciton formed by both electron occupying state  $\Gamma_{cl}^4$  (of CB1) and hole occupying state  $\Gamma_{vl5}^3$  (of VB1). According to the conditions for the choice of the configuration of the quasi-elementary cells and the surrounding cations given above both states ( $\Gamma_{cl}^4$  and  $\Gamma_{vl5}^3$ ) are deepest and they are on shortest distance. This state will be defined as ground state of the exciton of the structure in zinc-blende  $\text{In}_x\text{Ga}_{1-x}\text{N}$ . The author has developed method for determination of the properties of the excitons of the structure given in [5]. The following parameters of the excitons of the structure in zinc-blende  $\text{In}_x\text{Ga}_{1-x}\text{N}$  defined according to Fig.1 are determined by the theory given in [5]:

a) The binding energy of the excitons of the structure is

$$E_x = \hbar^2 / (2\mu_x \kappa^2 R_n^2) \quad (5)$$

Where  $R_n = (R/n)$  is defined to be the radius of the  $n^{\text{th}}$ -exciton state ( $R$  is the shortest distance between  $\Gamma_{cl}^4$  and  $\Gamma_{vl5}^3$ ,  $n \geq 1$  is integer and  $n = 1$  for the ground state of the exciton),  $\kappa$  is dielectric constant (it is considered  $\kappa = 1$  for  $n = 1$  because the electron and the hole of the exciton belong to neighboring quasi-elementary cells). Also we have  $\mu_x^{-1} = m_{cl}^4{}^{-1} + m_{vl5}^3{}^{-1}$ , where  $m_{cl}^4$  is the effective mass of the electron in  $\Gamma_{cl}^4$  and  $m_{vl5}^3$  is the effective mass of the hole in  $\Gamma_{vl5}^3$ . The effective masses  $m_{cl}^4$  and  $m_{vl5}^3$  in zinc-blende  $\text{In}_x\text{Ga}_{1-x}\text{N}$  are calculated by the author on the basis of the corresponding sub-bands of Fig.1 and by method for LCAO effective mass calculations given in [6]. It is found that the electron effective mass  $m_{cl}^4$  varies in the range  $0.13m_0 - 0.17m_0$  depending on the number of In and Ga cations surrounding the quasi-elementary cell of sector 4. The effective mass  $m_{vl5}^3$  is  $m_{vl5}^3 = 1.19m_0$ . The binding energy  $E_x$  of the ground state ( $n = 1$ ) depends on the number of Ga and In cations surrounding the quasi-elementary cells of sectors 2, 3 and 4. It is found that  $E_x$  varies in the interval  $1.08 - 1.36$  eV for zinc-blende  $\text{In}_x\text{Ga}_{1-x}\text{N}$ . The author [5] is obtained for wurtzite  $\text{In}_x\text{Ga}_{1-x}\text{N}$  that the binding energy of the ground state varies in the range  $1.06 - 1.17$  eV.

b) The hydrogen like energy level  $E_n$  ( $n \geq 1$ ) is determined [5] as

$$E_n = \Gamma_{cl}^4 - \Gamma_{vl5}^3 - \hbar^2 / (2\mu_x \kappa^2 R_n^2) \quad (6)$$

The energy  $E_n$  of the ground state of the exciton of the structure in zinc-blende  $\text{In}_x\text{Ga}_{1-x}\text{N}$  ( $n = 1$  and  $\kappa = 1$ ) depends on the number of the surrounding cations In and Ga. It varies in the interval  $0.03 - 0.21$  eV. It is necessary to be noted that the energy level  $E_n$  represents energy level occupied by the electron of the exciton of the structure taking into account that the energy level occupied by the hole of the exciton of the structure has energy equal to zero. The corresponding author's result [5] for  $E_n$  of the ground state ( $n = 1$ ) of the excitons of the structure in wurtzite  $\text{In}_x\text{Ga}_{1-x}\text{N}$  shows that  $E_n$  varies in the interval  $0.50 - 0.82$  eV. It means that it should be expected the photoluminescence due to annihilations between the electrons and the holes belonging to the ground state of the excitons of the structure within the energy intervals given above or around them – i.e. the interval  $0.03 - 0.21$  eV for zinc-blende  $\text{In}_x\text{Ga}_{1-x}\text{N}$  and the interval  $0.50 - 0.82$  eV for wurtzite  $\text{In}_x\text{Ga}_{1-x}\text{N}$ . Indeed the authors [4] report about photoluminescence spectra in In-rich regions of hexagonal  $\text{In}_x\text{Ga}_{1-x}\text{N}$  ( $0.36 < x < 1$ ) close to  $\sim 0.7$  eV, and these spectra are below the fundamental absorption edge found to vary in the range  $0.9 - 1.1$  eV.

c) The moving of the exciton of the structure in zinc-blende  $\text{In}_x\text{Ga}_{1-x}\text{N}$  is investigated in the same way like the moving of these excitons in wurtzite  $\text{In}_x\text{Ga}_{1-x}\text{N}$  [5]. It is found that the transmission coefficient  $D_{t,ex}$  of the tunneling of these excitons through the potential barrier of width  $R$  (the shortest one) depends on the numbers of In and Ga cations surrounding the quasi-elementary cells of sectors 2, 3 and 4, and it varies in range  $0.02 - 0.04$ . Conclusion that the excitons of the structure in zinc-blende  $\text{In}_x\text{Ga}_{1-x}\text{N}$  are localized quasi-particles can be made.

d) Energy discontinuously  $\Delta E_c = \Gamma_{c,l}^1 - \Gamma_{c,l}^4$  and  $\Delta E_v = \Gamma_{v,lS}^3 - \Gamma_{v,lS}^1$  are defined for hetero-junction  $\text{In}_x\text{Ga}_{1-x}\text{N} - \text{GaN}$  in terms of the excitons of the structure. This definition is the basis for interaction of the exciton of the structure in ground state and region (cluster) having greater energy band gap. When electrical field having strength  $\mathcal{E}$  is applied on the hetero-junction defined above the exciton of the structure in zinc-blende  $\text{In}_x\text{Ga}_{1-x}\text{N}$  can be destroyed and as result the electron and the hole will penetrate in region (cluster) having wider energy band gap (here it is GaN). The transmission coefficient  $D_{jun,n}$  of the electron belonging to the exciton of the structure in zinc-blende  $\text{In}_x\text{Ga}_{1-x}\text{N}$  through the hetero-junction is found by the author on the basis of the approach described in [5]. It depends on both the electrical field strength  $\mathcal{E}$  and the numbers of Ga and In cations surrounding the quasi-elementary cells of sectors 3 and 4. It is found that  $D_{jun,n}$  varies in the interval  $0 - 0.65$  if the electrical field strength  $\mathcal{E}$  varies in the range  $5.6 \cdot 10^5 - 60 \cdot 10^5$  V/cm. The transmission coefficient  $D_{jun,p}$  of the hole belonging to the exciton of the structure varies in the same range like  $D_{jun,n}$ .

The spectral blue shift in multi- or single quantum well structures observed by S. Chichibu *et al.* [2] and by P. G. Eliseev *et al.* [3] can be explained by scheme [5] which is sequence of the following processes: 1) Destroying of the exciton of the structure in its interaction with hetero-junction. 2) The electron and the hole penetrate in the semiconductor of wider energy band gap. 3) Recombination between penetrated electron and penetrated hole in the semiconductor of wider energy band gap. The difference between wurtzite  $\text{In}_x\text{Ga}_{1-x}\text{N}$  and zinc-blende  $\text{In}_x\text{Ga}_{1-x}\text{N}$  is that the recombination of both the electrons and the holes of exciton origin in zinc-blende  $\text{In}_x\text{Ga}_{1-x}\text{N}$  occurs mostly in the mixed In-GaN quasi-elementary cells having energy band gaps of sector 2 or close to them, because the reported spectral shift is in interval  $2.32 - 2.43$  eV.

## CONCLUSIONS

The results obtained in this paper are the basis for further investigations of other properties of the excitons of the structure – lifetime, distribution of their states according to the structure of zinc-blende  $\text{In}_x\text{Ga}_{1-x}\text{N}$ , interaction of these excitons with radiation, exciton-hole and exciton-electron interactions, influence of these excitons over the transport phenomena in zinc-blende  $\text{In}_x\text{Ga}_{1-x}\text{N}$  etc. These results can be used for design of electron devices using the excitons of the structure.

## REFERENCES

- [1] Y. Narukawa, Y. Kawakami, M. Funato, S. Fujita, Sh. Fujita, S. Nakamura, Appl. Phys. Lett., **70**, 981 (1997)
- [2] S. Chichibu, T. Azuhata, T. Sota, S. Nakamura, Appl. Phys. Lett., **69**, 4188 (1996)
- [3] P. G. Eliseev, P. Perlin, J. Lee, M. Osinski, Appl. Phys. Lett., **71**, 569 (1997)
- [4] V.Yu. Davydov, A.A. Klochikhin, V.V. Emtsev, S.V. Ivanov, *et al.*, International Workshop on Nitride Semiconductors, 22 – 25 July 2002, Aachen, Germany, p.133 (2002)
- [5] D. Alexandrov, Journal of Crystal Growth, **246**, 325 (2002)
- [6] W. A. Harrison, "Electronic Structure and the Properties of Solids", Dover Publ. Inc, (1989)
- [7] F. Herman, B. Skillman, "Atomic Structure Calculations", Prentice Hall (1963)
- [8] O. K. Andersen, Sol. State Commun., **13**, 133 (1973)
- [9] O. K. Andersen, W. Klose, H. Nohl, Phys. Rev., **B 17**, 1209 (1978)
- [10] K. P. O'Donnell, Phys. Stat. Sol., **A 183**, 117 (2001)
- [11] H. Fritzsche, Journal of Non-Crystalline Solids, **6**, 49 (1971)
- [12] A. Efros, B. Shklovskii, "Electronic Properties of Doped Semiconductors", Springer-Verlag, Berlin – Heidelberg (1984)

**BEST AVAILABLE COPY**

### Simultaneous TEM and Cathodoluminescence Imaging of Non Uniformity in $\text{In}_{0.1}\text{Ga}_{0.9}\text{N}$ Quantum Wells

Nicholas M. Boyall<sup>1</sup>, Ken Durose<sup>1</sup>, and Ian M. Watson<sup>2</sup>

<sup>1</sup>Department of Physics, University of Durham, South Road, Durham, DH1 3LE, UK.

<sup>2</sup>Institute of Photonics, University of Strathclyde, Wolfson Centre, 106 Rottenrow, Glasgow, G4 0NW, UK.

#### ABSTRACT

Monochromatic cathodoluminescence (CL) imaging of metal-organic vapour phase epitaxy (MOVPE) grown  $\text{In}_{0.1}\text{Ga}_{0.9}\text{N}$  single quantum wells (QW) has been performed in a scanning transmission electron microscope (STEM). Spatially resolved fluctuations in the CL emission wavelength and intensity of the QW luminescence were recorded. The presence of regions with luminescent features asymmetrically distributed either side of the QW peak emission was inferred. These fluctuations may be attributed to, by for example, variations of  $\pm 0.01$  in the In fraction of the  $\text{In}_{0.1}\text{Ga}_{0.9}\text{N}$  alloy, to changes of up to 0.6nm in the QW thickness. However these factors do not explain the gross fluctuations in QW emission intensity observed in TEM-CL on the scale of  $\sim 1\mu\text{m}$ .

#### INTRODUCTION

Light emitting and laser diodes based on  $\text{In}_x\text{Ga}_{(1-x)}\text{N}$  quantum well (QW) structures have been available commercially for a number of years [1]. However the exact relationship between compositional distributions within the QWs and the efficiency and wavelength of light emission is not fully described. A number of authors describe an emission process based around the localisation of excitation to QW composition fluctuations [2-4]. As means of investigating non uniformity, emission from  $\text{In}_x\text{Ga}_{(1-x)}\text{N}$  QW structures has been investigated by CL microscopy in the scanning electron microscope (SEM) by a number of authors [5-7]. More recently this work has been extended by measurement of CL in transmission electron microscopes with scanning attachments (STEM) [8, 9]. Measurement of CL in a STEM was first reported by Petroff et al [10] and has been reviewed elsewhere [11]. This method allows spectroscopic and micro-structural information to be collected simultaneously. High spatial resolution can be achieved with this technique as the beam broadening in electron transparent TEM foils is small [12], and the effective carrier diffusion length is small due to the proximity of the foil surface. These advantages are traded off against the smaller signal available from a thin foil as a result of losses due to surface recombination and the limits of a small generation volume.

In this work panchromatic and monochromatic STEM-CL imaging and spectroscopy were used to investigate the uniformity of emission from an  $\text{In}_x\text{Ga}_{(1-x)}\text{N}$  /GaN single QW.

#### EXPERIMENTAL DETAILS

##### Specimens

The single QW specimens were grown by metal-organic vapour phase epitaxy (MOVPE) on sapphire (0001) substrates. A GaN buffer layer approximately one micron thick was deposited

on the substrate following deposition of a low temperature nucleation layer. The  $\text{In}_x\text{Ga}_{(1-x)}\text{N}$  QWs were grown at  $832^\circ\text{C}$ , with nominally 2.5nm thickness and were capped with 15nm of GaN. Further details of the growth process can be found elsewhere [13, 14]. High resolution X-ray diffraction studies and grazing incidence Rutherford back-scattering (RBS) analysis indicated the indium content of the wells to be  $x = 0.1 \pm 0.015$  [15]. The RBS technique used averages over an area of approximately  $1\text{mm}^2$ . Cross section electron transparent foils were prepared by mechanical polishing and thinning in a liquid nitrogen cooled Ion Tech argon ion thinner operating at 4kV.

### Apparatus

STEM-CL measurements were carried out in a JEOL 200CX TEM equipped with an Oxford Instruments MonoCL system and JEOL scanning unit. CL was collected using a retractable paraboloidal mirror inserted between the sample holder and upper objective pole piece. A small hole at the top of the mirror allowed the electron beam passage to the sample. The collected CL was measured in either panchromatic or monochromatic imaging modes using a monochromator fitted with a 150 lines/mm grating blazed for peak reflectance at 300nm. A Peltier cooled Burle C31034 photomultiplier was operated in photon counting mode. Spectra could be recorded in both STEM and conventional TEM modes. When acquiring spectra in the STEM operating mode care was taken that the integration time for each wavelength recorded was longer than the time taken for the electron beam to raster over the image area several times. All micrographs and spectra presented in this work were recorded at a nominal temperature of 100K in an Oxford instruments tilt-rotate liquid nitrogen holder.

A factor limiting the spectral resolution of this system is the small CL signal emitted from a TEM foil under electron beam illumination. In order to achieve count rates allowing monochromatic imaging it was necessary to use the spectrometer with the exit slit set at 1mm, corresponding to 21.6nm dispersion.

### RESULTS AND DISCUSSION

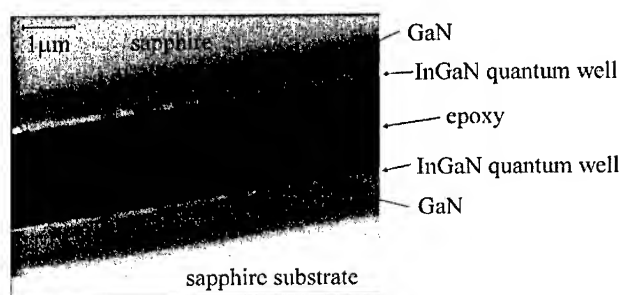


**Figure 1.** Panchromatic cross-section TEM-CL image of a single  $\text{In}_{0.1}\text{Ga}_{0.9}\text{N}/\text{GaN}$  quantum well. The luminescence from the sapphire and GaN appears to be largely uniform whereas the luminescence from the QWs varies in intensity.

Figure 1 shows a panchromatic CL image of a single  $\text{In}_{0.1}\text{Ga}_{0.9}\text{N}/\text{GaN}$  QW. Bright contrast is visible from the outermost surface of the specimens (ie. from where the QW is located) and the CL is inhomogeneous on a sub micron scale. In an earlier paper [9] the present authors report that variations in CL intensity can result directly from variations in the TEM foil thickness. Reference [9] reports a method of normalising the CL intensity for thickness variation using the STEM image intensity as a reference signal. However for the image in figure 1 the variations in thickness over the region of interest are small and such normalisation was unnecessary. The contrast variation along the QW is therefore likely to be a property of the material itself rather than a thickness artefact. Since in panchromatic CL imaging all possible wavelengths are recorded, the contrast seen is considered unlikely to arise from small variations in QW composition or thickness. The influence of dislocations has not been probed in this work. Further studies of these wells were made by CL spectroscopy and monochromatic imaging.

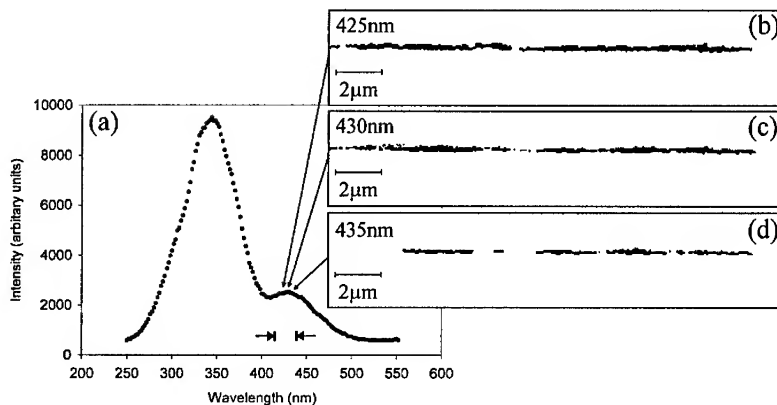


**Figure 2.** CL Spectrum taken in the TEM from an area centred on the  $\text{In}_{0.1}\text{Ga}_{0.9}\text{N}$  QWs. Monochromatic images of the same area are shown in b, c, and d. The image contrast has been inverted from the conventional sense for ease of viewing (black = CL intensity) and the images have been thresholded for clarity.

Figure 2(a) shows a CL spectrum taken in the TEM from a  $24 \times 20 \mu\text{m}$  area centred on the  $\text{In}_{0.1}\text{Ga}_{0.9}\text{N}$  QW. The dominant peak at 350 nm is from the GaN layer whilst the smaller peak at 430 nm is from the QW. Before describing the monochromatic imaging, some differences between these CL and PL spectra reported elsewhere [13] are commented upon. i) In PL the QW luminescence is brighter than that of the barrier. Reversal of this in CL is likely to be due to the sizes of the relative sampling volumes. ii) The shift in the CL peak position relative to PL may be influenced by the difference between the nominal TEM stage temperature and that of the sample itself while electron beam irradiated. It might also be influenced by the high injection density in CL. iii) Finally the much greater breadth of the CL peaks from the QWs compared to PL is due to the low resolution of the CL spectrometer ( $\sim 15 \text{ nm}$ ) chosen to allow high transmission for imaging.

Monochromatic images were recorded with the spectrometer centred on the peak QW emission wavelength of 430 nm as shown in figure 2(c). Images taken with centre wavelengths

of 425 and 435nm are also shown. Attempts to record images with the spectrometer centred at  $\pm 10\text{nm}$  from the peak QW emission were unsuccessful due to the lack of signal. The images shown in figure 2 have been processed to remove noise, and the gain and contrast have been adjusted equally for each image. Intensity line scans from the QWs are shown in figure 3. Inspection of the micrographs in figure 2 and the line scans in figure 3 highlights some regions where there is strong CL emission at all three wavelengths. The line scans taken at 430nm and 435nm have similar intensity, and while they have the same general shape there are slight differences between them. That taken at 425nm shows reduced intensity and further shape differences.

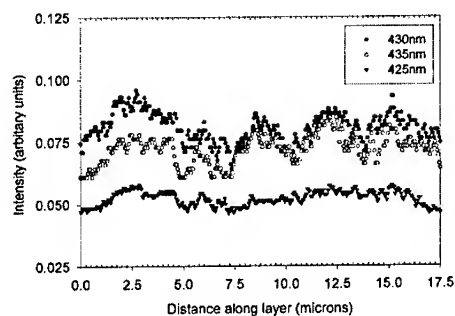


**Figure 3.** Intensity profiles along the monochromatic CL images of the QW shown in figure 2 recorded at 425nm, 430nm and 435nm.

To interpret the micrographs shown in figure 2 it is necessary to briefly discuss the effects that the resolution of the spectrometer had on the observations.

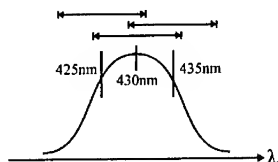


**Figure 4.** Diagram showing the transmission range of the spectrometer ( $\sim 15\text{nm}$ ) with the different centre wavelengths selected for the images in figure 2.

As can be seen in figure 4 all three monochromatic images in figure 2 have a contribution from the peak of QW emission. Hence only features common to all three monochromatic micrographs are unambiguously due to 430nm emission. The differences in fine detail in the intensity line scans may be attributed to localised QW luminescence at non peak wavelengths. Furthermore, since figures 2(b) and (d) differ, these features are distributed asymmetrically about the peak of the QW emission.

Factors which could account for the differences between localised luminescence in the monochromatic images will now be discussed.

To investigate the effect that fluctuations in the In content of the QW would have on emission wavelength, the data recorded by Martin et al [16] for CL peak energy  $E$  vs In composition in  $\text{In}_x\text{Ga}_{(1-x)}\text{N}/\text{GaN}$  epilayers ( $0 < x < 0.23$ ) was used:

$$E = [(3.398 \pm 0.006) - (3.91 \pm 0.05)x] \text{ eV} \quad (1)$$

Hence a decrease in QW emission wavelength from 430nm to 425nm would require a decrease in the In fraction  $x$  of from 0.1 to 0.09. The variations seen between figures 2(b), (c), and (d) could therefore in principle be due to fluctuations in the In composition of the QW of the order of  $\pm 0.01$ . This variation is within the experimental error limits of the composition determination of  $0.1 \pm 0.015$  performed on these samples by RBS [15]. Strain has not been considered in this work.

Considering well thickness, data presented for  $\text{In}_{0.1}\text{Ga}_{0.9}\text{N}$  single QWs by Chichibu et al [4] shows a linear change of effective QW bandgap with QW width over the range 2.9-3.1eV. The gradient of this is  $0.05\text{eV/nm}^{-1}$ . This demonstrates that a change in QW thickness of 0.6nm would be required to account for a 5nm shift in the peak QW emission from 430nm. It is not clear at this stage whether QW thickness fluctuations of this size exist, however the uniformity of PL peak wavelength from wafers is high indicating good QW integrity, but this could be explained by compensatory changes to both the well thickness and indium mole fraction. Quantum confinement in the direction of the electron beam is judged to be unlikely as the area of foil investigated has a thickness greater than several extinction distances, i.e. several hundred nanometers. Hence the data available at this time does not allow us to determine whether the small differences in shape of the line scans in figure 4 are associated with composition fluctuations, QW thickness variations, or a combination of factors.

## CONCLUSIONS

Panchromatic TEM-CL images of single  $\text{In}_{0.1}\text{Ga}_{0.9}\text{N}$  QWs reveal discontinuous luminescence on the scale of  $\sim 1\mu\text{m}$ . Monochromatic CL imaging of single  $\text{In}_{0.1}\text{Ga}_{0.9}\text{N}$  QWs has been performed and micrographs were taken with nominal spectrometer settings at the peak emission wavelength, 430nm, as well as at  $430\pm 5\text{nm}$ . Luminescent areas common to all three images were shown to be associated with the main QW emission peak at 430nm. Small differences between the images were attributed to luminescent features distributed asymmetrically about the QW peak. These differences may arise from fluctuations in the In content of the wells contained within the limits of errors in composition determination ( $x = 0.1 \pm 0.015$ ) by RBS, from variations in QW thickness of up to 0.6nm, or some combination of these or other factors. However, this investigation does not reveal the cause of the gross fluctuations in the QW luminescence on the scale of  $\sim 1\mu\text{m}$ . This shall be the subject of further study by CL and diffraction contrast imaging.

## ACKNOWLEDGMENTS

The author wishes to thank the EPSRC, Royal Microscopical Society, and the British Association for Crystal Growth for financial support.

## REFERENCES

1. S. Nakamura, in *Group III Nitride Semiconductor Compounds*, edited by B. Gil, (Oxford University Press, Oxford, 1998), 391-416
2. K.P. O'Donnell, J.F.W. Mosselmans, R.W. Martin, S. Pereira, and M.E. White, *J. Phys. - Condens. Mat.* **13**, 6977-6991 (2001).
3. K.P. O'Donnell, *Phys. Status Solidi A* **183**(117), 117-120 (2001).
4. S.F. Chichibu, A.C. Abare, M.P. Mack, M.S. Minsky, T. Deguchi, D. Cohen, P. Kozodoy, S.B. Fleischer, S. Keller, J.S. Speck, J.E. Bowers, E. Hu, U.K. Mishra, L.A. Coldren, S.P. DenBaars, K. Wada, T. Sota, and S. Nakamura, *Mat. Sci. Eng. B* **B59**, 298-306 (1999).
5. S. Chichibu, K. Wada, and S. Nakamura, *Appl. Phys. Lett.* **71**(16), 2346-2348 (1997).
6. S.J. Henley, A. Bewick, D. Cherns, and F.A. Ponce, *J. Cryst. Growth* **230**, 481-486 (2001).
7. H. Selke, M. Amirsawadkouhi, P.L. Ryder, T. Bottcher, S. Einfeldt, D. Hommel, F. Bertram, and J. Christen, *Mat. Sci. Eng. B* **59**, 279-282 (1999).
8. M. Albrecht, V. Grillo, J. Borysiuk, T. Remmele, H.P. Strunk, T. Walther, W. Mader, P. Prystawko, M. Leszczynski, I. Grzegory, and S. Porowski, *Inst. Phys. Conf. Ser.* **169**, 267-272 (2001).
9. N.M. Boyall, K. Durose, and I.M. Watson, *J. Microsc.*, (in press)
10. P.M. Petroff, R.A. Logan, and A. Savage, *Phys. Rev. Lett.* **44**(4), 287-291 (1980).
11. J.W. Steeds, *Rev. Phys. Appl.* **24**(6), 65-72 (1989).
12. J. Yuan, S.D. Berger, and L.M. Brown, *J. Phys. - Condens. Mat.* **1**, 3253-3265 (1989).
13. R. Pecharroman-Gallego, P.R. Edwards, R.W. Martin, and I.M. Watson, *Mater. Sci. Eng. B* **93**, 94-97 (2002).
14. P. Hurst, P. Dawson, S.A. Levetas, M.J. Godfrey, I.M. Watson, and G. Duggan, *Phys. Status Solidi B* **228**(1), 137-140 (2001).
15. S. Pereira, E. Pereira, E. Alves, N.P. Barradas, K.P. O'Donnell, C. Liu, C.J. Deatcher, and I.M. Watson, *Appl. Phys. Lett.* **81**(15), 2950-2952 (2002).
16. R.W. Martin, P.R. Edwards, K.P. O'Donnell, E.G. Mackay, and I.M. Watson, *Phys. Status Solidi A* **192**(1), 117-123 (2002).

## An In-Situ TEM-Cathodoluminescence Study of Electron Beam Degradation of Luminescence from GaN and $\text{In}_{0.1}\text{Ga}_{0.9}\text{N}$ Quantum Wells

Nicholas M. Boyall<sup>1</sup>, Ken Durose<sup>1</sup>, and Ian M. Watson<sup>2</sup>

<sup>1</sup>Department of Physics, University of Durham, South Road, Durham, DH1 3LE, UK.

<sup>2</sup>Institute of Photonics, University of Strathclyde, Wolfson Centre, 106 Rottenrow, Glasgow, G4 0NW, UK.

### ABSTRACT

The effect of electron beam irradiation on the cathodoluminescence (CL) emission from  $\text{In}_{0.1}\text{Ga}_{0.9}\text{N}/\text{GaN}$  single quantum wells (QW) has been investigated by in-situ measurement of CL in a transmission electron microscope. Analysis of CL quenching over 600s showed that the QW luminescence decayed more quickly than the barrier emission. Both the  $\text{In}_{0.1}\text{Ga}_{0.9}\text{N}$  and GaN CL decay curves could be fitted to a simple recombination based model suggesting the decay was due to the introduction of non-radiative centres.

### INTRODUCTION

Development of GaN electronic devices for high-power, high-frequency transistors (HFETs) and for use in high radiation environments has led to an interest in the degradation behaviour of GaN under electron irradiation [1, 2]. The transmission electron microscope (TEM) provides an ideal vehicle for such studies. Measurement of cathodoluminescence (CL) [3] is routinely done in scanning electron microscopes, and CL in a TEM has been reported by a number of authors [4-7]. More recently TEM-CL has been used in the investigation of  $\text{In}_x\text{Ga}_{(1-x)}\text{N}$  quantum well (QW) structures [8-11]. With this in mind it is of interest to investigate any effects that high energy electron irradiation in a TEM has on the CL emission from these structures. In this work in-situ monitoring of the CL emission from  $\text{In}_x\text{Ga}_{(1-x)}\text{N}/\text{GaN}$  QWs has been performed in a TEM.

### EXPERIMENTAL

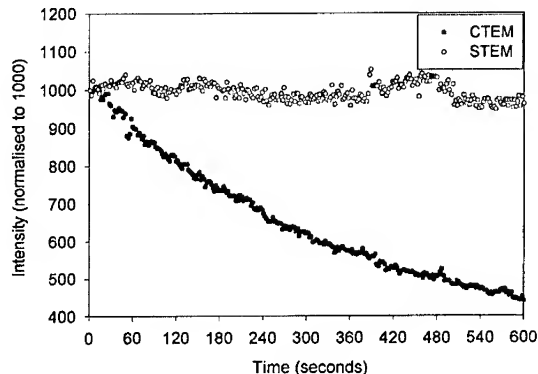
$\text{In}_x\text{Ga}_{(1-x)}\text{N}/\text{GaN}$  single and double quantum wells were grown by MOVPE on sapphire (0001) substrates. Growth was initiated using a thin low-temperature nucleation layer, which was followed by a one micron thick undoped GaN buffer layer grown at 1140°C. The quantum well structures were grown at 832°C. The  $\text{InGaN}$  quantum wells were nominally 2.5nm thick with a 15nm thick GaN cap. High resolution X-ray diffraction studies and grazing incidence Rutherford back-scattering analysis indicated the indium content of the wells to be  $x = 0.1 \pm 0.015$  [12]. Cross section electron transparent specimens (<500nm) were prepared by mechanical polishing and liquid nitrogen cooled Argon ion thinning.

A JEOL 200CX TEM has been adapted to allow the simultaneous collection of CL and transmitted electrons using an Oxford Instruments MonoCL system. CL was collected using a retractable paraboloidal mirror inserted between the sample holder and upper objective pole piece. Collected CL was either measured in panchromatic or monochromatic modes through a monochromator fitted with a 150 lines/mm grating blazed for peak reflectance at 300nm. A Peltier cooled Burle C31034 photomultiplier was operated in photon counting mode. Spectra

were collected whilst operating in both STEM (probe size  $\sim 10\text{nm}$ ) and conventional TEM (CTEM) modes ( $\sim 1\mu\text{m}$  diameter beam spot). All samples examined in this work were held at a nominal 100K in an Oxford instruments tilt-rotate liquid nitrogen holder. All the experiments were performed on electron transparent TEM foils.

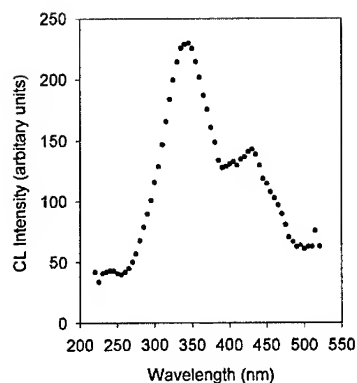
## RESULTS

Figure 1 shows the development of panchromatic CL intensity from an  $\text{In}_{0.1}\text{Ga}_{0.9}\text{N}$  QW structure with time under constant excitation from 120kV electrons in both CTEM and STEM modes. For CTEM illumination the QW structure was positioned at the centre of the  $1\mu\text{m}$  diameter beam spot and the magnification adjusted so that only the QW and GaN buffer layer were illuminated - an equivalent arrangement was used for STEM operation. The sampling time was limited to ten minutes to minimise the effects of specimen drift. The CTEM data shows a smooth decrease in CL intensity with no sign of levelling off after 600 seconds irradiation time. The STEM data shows no such decline over the same period but the data is noisier as a result of the smaller count rates in STEM mode.



**Figure 1.** Decay of total integrated CL versus time under CTEM and STEM illumination, 120keV beam.

A Faraday cup was used to measure the electron beam currents for CTEM and STEM which were 9.5 nanoamps and 0.2 nanoamps respectively. This difference in probe current is suggested as an explanation for the difference in CL degradation rates, the electron fluxes being  $7.5 \times 10^{18} \text{ s}^{-1} \text{ cm}^{-2}$  in CTEM mode and  $5 \times 10^{16} \text{ s}^{-1} \text{ cm}^{-2}$  in STEM mode.



**Figure 2.** CL of  $\text{In}_{0.1}\text{Ga}_{0.9}\text{N}/\text{GaN}$  single QW taken at a nominal temperature of 100K with STEM illumination at 120kV.

To further investigate the components of panchromatic CL degradation seen in figure 1, the decay of monochromatic CL emission has been investigated. Figure 2 shows a spectrum from an area of material similar to that sampled in figure 1. The dominant peak at 350nm is band edge emission from the GaN buffer layer, whilst the peak at 430nm is from the QW. The intensity of the QW peak is less than is typical for photoluminescence (PL) of a similar structure for geometric reasons [11]. Monochromatic decay curves for CL emission at 345 and 430nm are shown in figure 3.

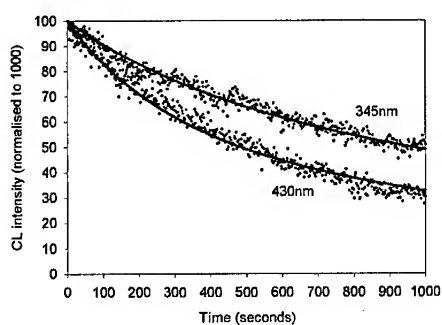


**Figure 3.** Decay of CL intensity at 345nm and 430nm versus time, CTEM mode, 120keV beam.

Analysis of figure 3 shows that the decay curves do not fit a simple one term exponential model. The decay of CL intensity,  $I_{CL}$ , with time  $t$  was described well by an expression for a model in which the luminescent output is decreased by the presence of an increasing population

of non-radiative recombination centres. The form of the equation previously used by Ohno et al [13] for electron beam irradiation of III-V's is:-

$$I_{CL} = \frac{100}{(1 + at)} \quad (1)$$

The fitting parameter,  $a$ , is  $0.0021\text{s}^{-1}$  for the QW emission and  $0.0010\text{s}^{-1}$  for the GaN band edge emission, these values being of a similar magnitude to those reported elsewhere [13] for degradation of CL in a TEM for other III-V materials.

## DISCUSSION

Rapid degradation of CL emission is recorded during CTEM operation, whereas minimal changes are seen in STEM mode. This difference is attributed to differences in electron dose, the flux in CTEM mode being  $7.5 \times 10^{18} \text{ s}^{-1} \text{ cm}^{-2}$  while that for illumination of a similar area in STEM mode is  $5 \times 10^{16} \text{ s}^{-1} \text{ cm}^{-2}$ .

When considering the origin of the decay of the luminescence we first discuss the possible minor contribution of the light blocking action of contamination building up on the specimen under the influence of the electron beam. For a blocking layer with absorption coefficient  $\alpha \text{ cm}^{-1}$ , deposited at a rate of  $k \text{ cm.s}^{-1}$ , the attenuation of CL with time is expected to be of simple exponential form i.e.

$$I = I_0 e^{-akt} \quad (2)$$

However since the data in figure 3 could not be fitted to a simple exponential there is presently no evidence for this contamination/light-blocking mechanism. It is not anticipated that this mechanism is a dominant one. Should experimental evidence be sought for it in the future, then it may be borne in mind that contamination/light-blocking may be independent of sample type for a given wavelength of luminescence.

A more likely mechanism is luminescence quenching by the introduction of beam induced non-radiative recombination centres: equation 1 describes such a model [3, 13], and its fit to the present data is good. Assuming that the capture cross sections for carriers, the carrier velocity, and the carrier lifetimes for radiative and non-radiative recombination are constant during the experiment, then equation 1 describes the introduction of non-radiative centre concentration that increases linearly with electron dose, ie.  $at = a'D$  (where  $D$  is the electron dose and  $a'$  is a constant representing the introduction rate for non-radiative centres). Hence the differences in the parameter,  $a$ , for the QW and GaN band edge emission ( $0.0021 \text{ s}^{-1}$  and  $0.0010 \text{ s}^{-1}$  respectively) are related to the formation rate of a non-radiative centre, or centres. Moreover the larger value for the QW indicates that these centres are being created at a greater rate in InGaN than in GaN. Alternatively the difference in the parameter may be due to the non-radiative centres being deeper in InGaN than in GaN. Further work to investigate the electron energy dependence of the parameter  $a'$  is anticipated.

Higher energy electron irradiation experiments on GaN (2.5 MeV electrons), and characterisation through PL are reported by Buyanova et al [2]. It was shown that an increase in the 0.7-1.1eV band is induced by irradiation, there being a sharp no-phonon line at 0.88eV which

was attributed to a transition between a deep donor and radiation-induced deep acceptor. Transitions in the deep donor range in GaN at 0.8-1.1 eV below the conduction band edge have been previously attributed to  $N_{Ga}$  [14]. Possible deep acceptor levels in GaN are due to  $(N_{Ga}-V_N)$  and  $Ga_N$  [15].

With these native defects in mind an atomistic mechanism for the electron beam induced degradation of GaN and  $In_xGa_{(1-x)}N$  is postulated by analogy with the accepted model of electron beam induced degradation for halides and chalcogenides due to Forty [16, 17]. The process is presented here in terms of the *nominal* charges on the participating species and is as follows: an electron is ejected from the  $N^{3-}$  species by the electron beam, the resulting  $N^{x-}$  ( $0 < x < 3$ ) is a positive hole relative to the lattice; the  $N^{x-}$  is weakly bound in the lattice and is displaced to an interstitial site by recoil or thermal energy; the electron ionised from the nitrogen ion can either enter the conduction band or is captured by a neighbouring  $Ga^{3+}$  ion, this weakens the Ga bonding structure such that the repulsive force from a neighbouring  $V_N$  can eject the  $Ga^{2+}$  ion from the lattice to an interstitial site. The net result is the  $(V_N+V_{Ga})$  strongly bonded vacancy pair and interstitial N and Ga which are free to move in the lattice and may form antisite defects or clusters. The atomistic process has been described above for GaN, however it may be suggested that the same process is also occurring with In atoms in the same manner as for Ga atoms in the  $In_xGa_{(1-x)}N$  alloy. It should be made clear at this point that the proposed model is drawn by analogy and makes no use of for example, calculations of the specific energetics of individual atomistic processes.

The model described would account for the degradation of GaN band edge and  $In_{0.1}Ga_{0.9}N$  QW emission through the formation of alternative recombination routes, and may account for the more rapid decay of the QW emission compared to that of the barrier as the bond energies in InN are weaker than GaN. In addition the model is consistent with PL observations of electron irradiated GaN [2]. However, this is by no means a validation for the model which is only drawn by analogy with Forty's mechanism.

## CONCLUSIONS

The effects of electron irradiation on the CL emission of  $In_{0.1}Ga_{0.9}N$  QW and GaN barriers in a TEM have been investigated. It has been shown that the lower electron dose received during STEM imaging results in minimal CL degradation whereas the larger dose received during CTEM operation causes severe CL degradation. It is therefore recommended that during combined TEM-CL investigations STEM in preference to CTEM mode is used until all CL data required has been recorded.

Fitting the CL decay curves to a simple recombination based model suggests the decay is due to the introduction of competing non-radiative centres through the action of the electron beam. Decay of the luminescence is faster in InGaN than in GaN for a given electron flux. Atomic mechanisms have been discussed with reference to PL studies and by analogy with the electron beam degradation model for halides and chalcogenides. However the experimental evidence of this work is not sufficient to identify the particular mechanisms responsible.

## ACKNOWLEDGMENTS

NMB wishes to thank the EPSRC, Royal Microscopical Society, and the British Association for Crystal Growth for financial support. The authors thank the referee for the constructive comments offered.

## REFERENCES

1. J.-Y. Duboz and M.A. Khan, in *Group III Nitride Semiconductor Compounds*, edited by B. Gil, (Oxford University Press, Oxford, 1998), 343-390.
2. I.A. Buyanova, M. Wagner, W.M. Chen, B. Monemar, J.L. Lindstrom, H. Amano, and I. Aksaki, *Phys. Scripta*, **T79**, 72-75 (1999).
3. B.G. Yacobi and D.B. Holt, *Cathodoluminescence Microscopy of Inorganic Solids*, (Plenum Press, New York, 1990).
4. S.J. Pennycook, A.J. Craven, and L.M. Brown, *Inst. Phys. Conf. Ser.*, **36**, 69-72 (1977).
5. P.M. Petroff, R.A. Logan, and A. Savage, *Phys. Rev. Lett.*, **44**(4), 287-291 (1980).
6. J.W. Steeds, *Rev. Phys. Appl.*, **24**(6), 65-72 (1989).
7. N. Yamamoto, J.C.H. Spence, and D. Fathy, *Philos. Mag. B*, **49**(6), 609-629 (1984).
8. M. Albrecht, V. Grillo, J. Borysiuk, T. Remmele, H.P. Strunk, T. Walther, W. Mader, P. Prystawko, M. Leszczynski, I. Grzegory, and S. Porowski, *Inst. Phys. Conf. Ser.*, **169**, 267-272 (2001).
9. M. Albrecht, H.P. Strunk, J.L. Weyher, I. Grzegory, S. Porowski, and T. Wosinski, *J. Appl. Phys.*, **92**(4), 2000-2005 (2002).
10. N.M. Boyall, K. Durose, and I.M. Watson, *J. Microsc.*, (in press)
11. N.M. Boyall, K. Durose, and I.M. Watson, (this conference)
12. S. Pereira, E. Pereira, E. Alves, N.P. Barradas, K.P. O'Donnell, C. Liu, C.J. Deatcher, and I.M. Watson, *Appl. Phys. Lett.*, **81**(15), 2950-2952 (2002).
13. Y. Ohno, Y. Kawai, and S. Takeda, *Physical Review B*, **59**(4), 2694-2699 (1999).
14. G. Salvati, N. Armani, C. Zanotti-Fregonara, E. Gombia, M. Albrecht, H.P. Strunk, M. Mayer, M. Kamp, and A. Gasparotto, *MRS Internet J. Nitride Semicond. Res.*, **5S1**, W11.50 (2000).
15. D.W. Jenkins and J.D. Dow, *Physical Review B*, **39**(5), 3317-3329 (1989).
16. A.J. Forty, *Brit. J. Appl. Phys.*, **14**, 3-9 (1963).
17. Y.Y. Loginov, P.D. Brown, N. Thompson, and K. Durose, *J. Cryst. Growth*, **117**, 682-688 (1992).

### Room-Temperature Time-Resolved Photoluminescence Studies of UV Emission from GaN/AlN Quantum Wells

Madalina Furis, Fei Chen, Alexander N. Cartwright

Department of Electrical Engineering, University at Buffalo, State University of New York,  
Buffalo NY, 14260

Hong Wu, William J. Schaff

Department of Electrical Engineering, Cornell University, Ithaca NY, 14853

#### ABSTRACT

Room temperature time-resolved photoluminescence (TRPL) studies of multiple quantum well (MQW) structures of the binaries GaN and AlN grown by molecular beam epitaxy are reported. The eventual application of these structures is for GaN intersubband IR light emitters. However, as an initial study, the structures are evaluated at UV to investigate materials parameters relevant to IR light emission. The nominally 0.9, 1.3 and 1.5 nm GaN quantum wells are clad by 6nm of AlN on top of a thick AlN buffer grown on sapphire. All samples consisted of 20 quantum wells. The observed peak energy of the emission spectrum is in excellent agreement with a model that includes the strong confinement present in these structures and the existence of the large built-in piezoelectric field and spontaneous polarization present inside the wells. Furthermore, consistent with screening of the in-well field as carriers are injected in the well, a clear blue shift of the emission is observed at short times after carrier injection. Subsequently, as the carriers recombine, the peak emission red-shifts and the screening of the field is reduced. Moreover, the observed lifetimes were energy dependent as should be expected from field dependent elongation of lifetimes due to spatial separation of the injected carriers. Specifically, the decay time at high energies can be fitted by a stretched exponential with a beta value of 0.8 which is consistent with carrier spatial separation. The lifetimes obtained from the fitting are of the order of 1ns, longer than the reported recombination lifetimes in similar GaN/AlGaIn MQW's. On the low energy side of the PL feature the intensity time decay becomes exponential with lifetimes ranging from 3 to 10ns. The strong UV emission at room temperature makes these structures promising for UV emitters.

#### INTRODUCTION

UV emitters characterized by wavelengths shorter than 350nm are essential for the development of optical storage and biological agent detection devices such as hand-held biosensors. The need for such emitters for biosensors is generated by the nature of the absorption and fluorescence spectra of organic molecules. For example, the fluorescing components in proteins are amino-acids such as phenylalanine, tryptophan and tyrosine. It is proposed that each biological agent is characterized by a distinct ratio between these components of emission determined by analyzing the fluorescence spectrum from proteins. The difficulty resides in exciting this fluorescence since all the amino acids exhibit an absorption edge below 350nm. At the same time, the development of UV lasers will increase the storage capacity of optical storage devices (such as CD's or DVD's) due to the much shorter wavelength and corresponding minimum achievable spot size.

Nitride semiconductors are one of the materials of choice in developing UV LED's and laser structures due to their large bandgaps (as high as 6.2eV in the case of AlN). Structures such as GaN/AlGaIn quantum wells with high aluminum content [1] exhibit emission at short wavelengths. However, the large lattice mismatch between the well and barrier materials results in the presence of growth defects and dislocations which, in turn, causes a decrease in the emission intensity, especially at room temperature where most devices operate. The photoluminescence intensity in this quantum wells decreases by a factor of 100 when the temperature is increased from 10 to 300K. Incorporating Al into the well material has the dual effect of reducing the lattice mismatch, which yields fewer growth defects, while pushing the emission deeper into the UV. Most recently, Chitnis et al. [2] have shown that such  $\text{Al}_x\text{Ga}_{1-x}\text{N}/\text{Al}_y\text{Ga}_{1-y}\text{N}$  heterostructures exhibit improved optical properties. Growth defects can also be avoided by using quaternary alloy AlGaInN heterostructures. Such layers, with different Al and In concentrations in the wells and barriers, can be lattice matched to the buffer. Recent time-resolved photoluminescence (TRPL) measurements on such structures [3] have shown that the emission efficiency at room temperature is greatly improved in comparison with GaN/AlGaIn structures. Despite this improvement, the PL decay is still dominated by non-radiative recombination at room temperature. In fact, both the ternary and quaternary well materials described above are plagued by point defects which are related to alloy fluctuation and compositional disorder. In addition to reduced efficiency, these defects result in broadening of the emission spectrum. Overall, while the reduced lattice mismatch in these structures provides some benefits, the use of ternary and quaternary well materials introduces other problems.

Unlike all other potential UV emitters materials mentioned in the previous paragraph, GaN/AlN heterostructures avoid the issues associated with point defects by utilizing only pure binary materials, which in addition exhibit the largest possible bandgap offset among the nitrides. Despite this attractive characteristic, the large lattice mismatch between GaN and AlN (2.6%) and the lack of thorough optical investigations on the barrier (AlN) material are clear impediments in the development of efficient UV emitters based on such heterostructures. In this work, we present the results of room-temperature time-resolved photoluminescence measurements on GaN/AlN multiple quantum well (MQW) heterostructures showing that, despite the large lattice mismatch, such structures exhibit good luminescent properties and, most importantly, the emission seems to be dominated by radiative recombination at room temperature.

## EXPERIMENTAL DETAILS

The three GaN/AlN MQW samples were grown on a sapphire substrate by plasma-enhanced molecular beam epitaxy (MBE). They contain 20 GaN 0.9, 1.3, or 1.5nm wells separated by 6nm AlN barriers grown on the top of a thick AlN buffer layer. High-resolution x-ray characterization measurements have shown satellite peaks indicating a very good superlattice structure with fully relaxed barriers and strained wells [4].

The TRPL measurements were performed in the backscattering geometry using conventional optics. The excitation was provided by the frequency tripled 800nm output of a Coherent REGA9000 regenerative amplifier. The pump beam is characterized by a 200fs pulse width, a 250kHz repetition rate and an average power of 5mW at 266nm. The photoluminescence was spectrally resolved by a Chromex 250IS monochromator and detected by a Hamamatsu C4334 streak camera with a typical jitter of 50ps.

## DISCUSSION

Normalized time-integrated photoluminescence spectra taken at room temperature from the samples under study are shown in figure 1(a). The energies corresponding to the photoluminescence peak vary as a function of well width and are in good agreement with a calculation of the  $e_1h_1$  transition energy performed using the Numerov method [5,6]. This calculation takes into account the built-in electric field present in the wells and the barriers along the growth direction as a result of the piezoelectric and spontaneous polarization existing in both materials. The magnitude of the piezoelectric component depends on the strain induced by the lattice mismatch and the barrier and well widths. A detailed discussion of the built-in electric fields in nitride heterostructures along with the most recent update on the numerical values of the several physical constants used in our calculations can be found in reference [7]. For the case of the samples under study the electric field is equal to approximately -8MV/cm in the GaN wells and 1MV/cm in the AlN barriers. In the presence of such an electric field along the growth direction, the energy corresponding to the  $e_1h_1$  transition in the quantum well is red-shifted with respect to the zero-field situation (due to the quantum confined Stark effect [8] and the band filling effects). The presence of the built-in electric field is thus confirmed by the blue-shift observed in the PL energy in figure 1(b). At such short times, the space charge field induced by the presence of spatially separated injected carriers in the quantum wells is partially screening the built-in electric field and the PL energy approaches the zero-field value. For the sample in figure 1(b) we estimated the blue shift due to screening effects to be approximately 44 meV (considering we inject approximately  $6 \times 10^{12} \text{ cm}^{-2}$  carriers in each well). The difference between this number and the actual measured blue shift (140meV) is due to band filling effects. The Fermi energy is equal to 72meV for electrons and 14meV for holes. The total estimated blue shift is equal to the sum of the screening and band filling contributions ( $\sim 130\text{meV}$ ) in good agreement with the experimental value. In addition to screening and band filling, another contribution in the blue shift may be due to the large changes in the recombination lifetimes due to well width fluctuations.

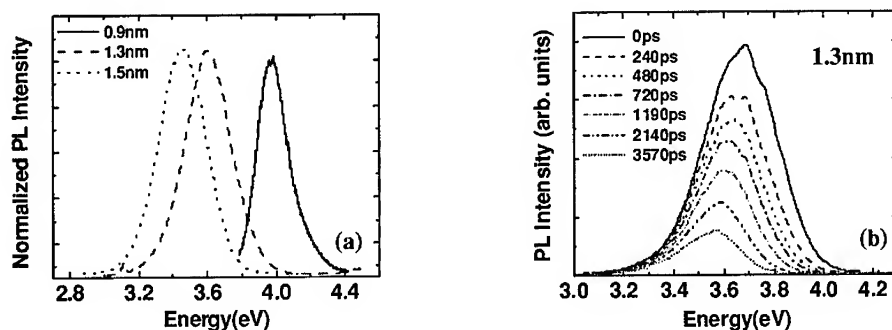


Figure 1. Time-integrated (a) and time-resolved (b) photoluminescence spectra from the samples under study at different delay times. The blue shift at short delay times is due to the partial field screening by the injected carriers and band filling effects.

As the time passes the carriers recombine and the screening effect disappears. The Fermi level is also moving toward the bottom of the first energy band and the emission energy decreases.

The presence of electric fields in quantum well heterostructures results in the spatial separation of the electrons and holes confined in the wells. The carriers accumulate at opposite sides of the quantum well and the electrons and holes wavefunction overlap decreases considerably, as well as the emission efficiency. Our calculations show that, despite the high built-in electric fields, for a thin GaN/AlN well the carriers wavefunctions remain confined in the well due to the large bandgap offset (1.9eV) between the GaN wells and AlN barriers.

The photoluminescence decay times at several energies across the photoluminescence feature are plotted in figure 2(a). On the high energy side of the PL spectrum the decay is non-exponential and characterized by short decay times (shorter than 1ns). On the low energy side the decay becomes exponential and characterized by longer lifetimes (7ns). This behavior is characteristic for nitride heterostructures and has been observed in GaN/AlGaN [9,10] as well as InGaN/GaN [11,12,13] quantum well heterostructures. A calculation [14] of the PL decay times which takes into account the dynamic screening of the built-in electric fields by the injected carriers shows that the lifetime increase on the low energy side of the PL feature and the non-exponential character of the decay can be the result of the presence of built-in electric fields. The field-dependent elongation of carrier lifetimes is a result of the reduction of the wavefunction overlap in the presence of the built-in electric field.

The long lifetime values measured on the low energy side of the PL feature at room temperature indicate the recombination is dominated by radiative processes (non-radiative recombination happens on a much faster scale-hundreds of picoseconds). This demonstrates that the GaN/AlN structures are promising not only for the development of LED's, but possibly for achieving population inversion and lasing.

In order to further investigate the possible origins of the non-exponential PL intensity decay, we fitted the decay data with a stretched exponential:

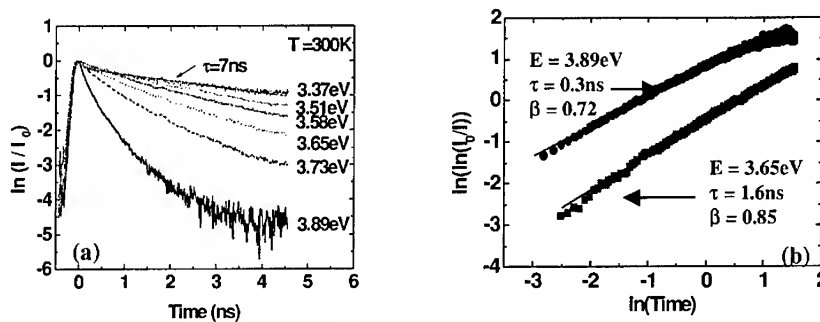


Figure 2. (a) Photoluminescence intensity decay at different energies across the PL feature and (b) Stretched exponential fitting to the decay data on the high energy side of the photoluminescence spectrum.

$$I = I_0 \exp \left[ - \left( \frac{t}{\tau} \right)^\beta \right] \quad (1)$$

The parameter  $\beta$  varies between 0 and 1 and provides information on the recombination mechanism. This type of PL decay has been explored in InGaN/GaN heterostructures [15] and a direct connection has been established between the values of the  $\beta$  parameter and the nature of carrier localization. According to this interpretation, the non-exponential character of the decay is due to the presence of potential fluctuations ( e.g. In -rich regions in the case of InGaN/GaN MQWs) where the carriers are localized before recombining. Since the characteristics of such potential fluctuations are not the same across the sample, we expect considerable differences between the wavefunction overlap of carriers trapped in different potential fluctuations. The nature of localization centers in GaN/AlN structures is not known at the present, however, we can always assume the existence of potential fluctuations associated with interface roughness or growth defects. The non-exponential behavior and the carrier lifetimes dependence on energy can also be due to the presence of such regions where carriers are localized before recombination. The stretched exponential decay model is based on the assumption that there is a possibility for the carriers to move from one potential fluctuation to another through a hopping mechanism. As a result the carrier lifetimes must depend on the hopping distance and the number of potential fluctuations the carrier encounters before recombination. This type of mechanism is described quantitatively by the magnitude of the  $\beta$  parameter, namely  $\beta$  values smaller than 0.5 correspond to the hopping mechanism described, whereas for  $\beta$  values between 0.6-0.9, the carrier lifetimes are elongated by the built-in electric field and the subsequent spatial separation of carriers [16].

Figure 2(b) summarizes the results of a stretched exponential fitting to the decay data on the high-energy side of the photoluminescence feature. The  $\beta$  parameter equals 0.8, indicating no hopping mechanism takes place and the non-exponential character is determined only by the built-in electric fields and possible carrier localization. The effective lifetimes are very short because the high-energy side of the PL reflects the recombination of hot carriers which relax very quickly to the bottom of the conduction band.

## CONCLUSIONS

In conclusion we have shown that, despite the large lattice mismatch, MBE grown GaN/AlN quantum wells exhibit room temperature photoluminescence associated with the radiative recombination of electrons and holes in the GaN wells. The PL peak position is in good agreement with a calculation that takes into account the piezoelectric and spontaneous polarizations existing inside the wells and barriers. A blue shift of the emission is observed at short times, due to the in-well field screening by the carriers injected in the well. The photoluminescence intensity decay varies across the PL feature and can be fitted with a stretched exponential. The values of the  $\beta$  exponent are greater than 0.5 indicating the non-exponential character of the PL decay can be attributed to the built-in electric field and carrier localization. The carrier lifetimes vary as a function of energy. Most importantly, the radiative recombination is the dominant carrier relaxation mechanism at room-temperature making such structures very promising for lasing applications.

## ACKNOWLEDGEMENTS

This work was supported in part by ANC's NSF CAREER Grant #9733720, ONR YIP Grant #N00014-00-1-0508, a Defense University Research Initiative on Nanotechnology Grant #F496200110358 through the Air Force Office of Scientific Research, and WJS's NSF Grant #ECS-0123453 and by DARPA through WJS's Army Research Office Grant #DAAD19-02-0199.

## REFERENCES

1. J. C. Harris, T. Someya, K. Hoshino, S. Kako, and Y. Arakawa, *phys. stat. sol. (a)* **180**, 339 (2000).
2. A. Chitnis, R. Pachipulusu, V. Mandavilli, M. Shatalov, E. Kuokstis, J. P. Zhang, V. Adivarahan, S. Wu, G. Simin, and M. Asif Khan, *Appl. Phys. Lett.* **81**, 2938 (2002).
3. Mee-Yi Ryu, C. Q. Chen, E. Kuokstis, J. W. Yang, G. Simin, and M. Asif Khan, *Appl. Phys. Lett.* **80**, 3943 (2002).
4. H. Wu, W. J. Schaff, M. Furis, A. N. Cartwright, K. A. Mkhoyan, J. Silcox, W. Henderson, W. A. Doolittle, and A. V. Osinsky (submitted to MRS Conference Proceedings)
5. J. M. Blatt, *J. Comp. Phys.* **1**, 382 (1967).
6. B. R. Johnson, *J. Chem. Phys.* **67**, 4086 (1977).
7. O. Ambacher, J. Majewski, C. Miskys, A. Link, M. Hermann, M. Eickhoff, M. Stutzmann, F. Bernardini, V. Fiorentini, V. Tilak, B. Schaff, and L. F. Eastman, *J. Phys.: Condens Matter* **14**, 3399 (2002).
8. G. Bastard, "Effect of Static External Electric and Magnetic Fields on the Energy Levels of Quasi Bi-dimensional Electron Gases", *Wave Mechanics Applied to Semiconductor Heterostructures*, Halsted Press (John Wiley & Sons, 1988) pp. 303-308.
9. P. Lefebvre, B. Gil, H. Mathieu, N. Grandjean, M. Leroux, J. Massies, and P. Bigenwald, *MRS Internet J. Nitride Semicond. Res.* **4S1**, G3.69 (1999).
10. N. Grandjean, B. Damilano, J. Massies, G. Neu, M. Teissere, I. Grzegory, S. Porowski, M. Gallart, P. Lefebvre, B. Gil, and M. Albrecht, *J. Appl. Phys.* **88**, 183 (2000).
11. T. Kuroda, A. Tackeuchi, and T. Sota, *Appl. Phys. Lett.* **76**, 3753 (2000).
12. T. Kuroda and A. Tackeuchi, *J. Appl. Phys.* **92**, 3071 (2002).
13. A. N. Cartwright, P. M. Sweeney, T. Prunty, D. P. Bour, and M. Kneissl, *MRS Internet J. Nitride Semicond. Res.* **4**, 12 (1999).
14. D. Alderighi, A. Vinattieri, J. Kudrna, M. Colocci, A. Reale, G. Kokolakis, A. Di Carlo, P. Lugli, F. Semond, N. Grandjean, and J. Massies, *phys. stat. sol. (a)* **188**, 851 (2001).
15. M. Pophristic, F. H. Long, C. Tran, I. T. Ferguson, and R. F. Karliceck, Jr., *J. Appl. Phys.* **86**, 1114 (1999).
16. L. Pavesi, *J. Appl. Phys.* **80**, 216 (1996).

**Measurements of the Refractive Indices of MOCVD and HVPE Grown AlGa<sub>x</sub>N Films Using Prism-Coupling Techniques Correlated with Spectroscopic Reflection/Transmission Analysis<sup>a</sup>**

Norman A. Sanford

National Institute of Standards and Technology, Boulder, CO 80305, U.S.A.

Lawrence H. Robins, Albert V. Davydov, Alexander J. Shapiro

National Institute of Standards and Technology, Gaithersburg, MD 20899, U.S.A

Denis V. Tsvetkov, Vladimir A. Dmitriev, Technologies and Devices International Inc.

Silver Spring, MD 20904, U.S.A.

Stacia Keller, Umesh K. Mishra, Steven P. DenBaars

University of California, Santa Barbara, CA 93106, U.S.A.

**ABSTRACT**

Waveguide prism-coupling methods were used to measure the ordinary and extraordinary refractive indices of Al<sub>x</sub>Ga<sub>1-x</sub>N films grown on sapphire substrates by HVPE and MOCVD. Several discrete wavelengths ranging from 442 nm to 1064 nm were used and the results were fit to one-term Sellmeier equations. The maximum standard uncertainty in the refractive index measurements was  $\pm 0.005$  and the maximum standard uncertainty in the self-consistent calculation for film thickness was  $\pm 15$  nm. Analysis of normal-incidence spectroscopic transmittance and reflectance measurements, correlated with the prism-coupling results, was used to determine the ordinary refractive index as a continuous function of wavelength from the band gap wavelength of each sample (between 252 nm and 364 nm) to 2500 nm. The Al compositions of the samples were determined using energy-dispersive X-ray spectroscopy analysis (EDS). HVPE grown samples had compositions  $x = 0.279, 0.363, 0.593$ , and  $0.657$ . MOCVD samples had  $x = 0.00, 0.419, 0.507, 0.618, 0.660$ , and  $0.666$ . The maximum standard uncertainty in the absolute EDS-determined value for  $x$  was  $\pm 0.02$ .

**INTRODUCTION**

Al<sub>x</sub>Ga<sub>1-x</sub>N alloys are important for the development of laser diodes and LEDs operating in the blue and ultraviolet. These applications require refractive index data correlated with Al mole fraction and estimates of the uncertainties of these quantities. Various methods have been used to measure refractive indices in Al<sub>x</sub>Ga<sub>1-x</sub>N alloys. Spectroscopic reflectance and transmittance (R/T) has been used to measure the ordinary refractive index.<sup>1,2</sup> Spectroscopic ellipsometry (SE) has been used to measure refractive index, birefringence, and extinction coefficients.<sup>3,4</sup> Both SE and R/T permit quasi-continuous measurement of optical constants over a wide spectral range. Reference 5 describes transmission-electron microscopy (TEM) combined with reflectance studies and SE. Inclusion of TEM analysis enabled modeling the film/substrate interlayers and improved the SE model fitting. In order to obtain the most accurate results, both SE and R/T require measurements of film thickness that are independent of refractive index.

Waveguide prism coupling (WPC) allows measurements of refractive indices and thickness of Al<sub>x</sub>Ga<sub>1-x</sub>N films. If at least two TE (polarization in the plane of the film) or two TM modes (polarization perpendicular to the film) are supported at a given wavelength, then an unambiguous measurement of the refractive index and thickness may be performed.<sup>6</sup> WPC methods have been used for refractive index measurements of MOCVD and MBE-grown GaN and Al<sub>x</sub>Ga<sub>1-x</sub>N films grown on c-plane sapphire substrates.<sup>7,8</sup> These earlier analyses treated the

films as uniform slabs of either extraordinary ( $n_e$ ) or ordinary ( $n_o$ ) refractive index, thus ignoring birefringence in the solution procedure for  $n_e$ . In our approach, we show that a solution for  $n_e$ , obtained from analysis of the effective indices of TM modes, first requires knowledge of  $n_o$ , obtained from a separate analysis of the effective indices of TE modes.<sup>9</sup> Additional problems have been encountered with the calibration of the Al mole fraction for determination of the composition-dependent refractive index of  $\text{Al}_x\text{Ga}_{1-x}\text{N}$  films. It is convenient to use optical absorption and assume a particular form for the bowing of the band gap as a function of Al content where the latter has been separately established. However, as pointed out by Özgür, bowing parameters may depend upon growth methods.<sup>8</sup> It is therefore important to explore alternative direct methods to calibrate the Al content of the samples.

## EXPERIMENTAL PROCEDURE AND RESULTS

Samples were grown with standard MOCVD and HVPE methods using c-plane sapphire substrates. Crystal growth details are given elsewhere.<sup>9</sup> The Al composition of the samples was analyzed with a scanning electron microscope equipped with energy-dispersive X-ray spectroscopy (SEM/EDS) capability. The EDS spectra were normalized using data from GaN and AlN reference samples. Absorption and fluorescence corrections in the EDS spectra were made using the NORAN MICROZ microanalysis software.<sup>b</sup> At least three spectra were recorded from locations near the center and corners on a sample and the results averaged. The samples measured roughly 5 mm square. Each spectrum was recorded with a counting time of 100 s. The typical maximum variation in  $x$  across a sample was  $\pm 0.003$ . However, the estimated largest standard uncertainty in the EDS-determined value of  $x$  was  $\pm 0.02$  for the  $\text{Al}_x\text{Ga}_{1-x}\text{N}$  samples. The nomenclature used herein for the description of uncertainties is summarized in NIST guidelines on error analysis.<sup>10</sup>

Figure 1 illustrates the WPC apparatus used for launching modes into the  $\text{Al}_x\text{Ga}_{1-x}\text{N}$  films. The positions ( $d_i$ ) of the output modes on an observation screen are shown. A rutile prism (optic axis perpendicular to the page) is clamped to the film surface. All samples displayed a significant amount of intermodal optical scatter. Thus, the launch angle, set to preferentially excite one mode, always excited additional modes. With  $d_i$  and the screen-prism separation

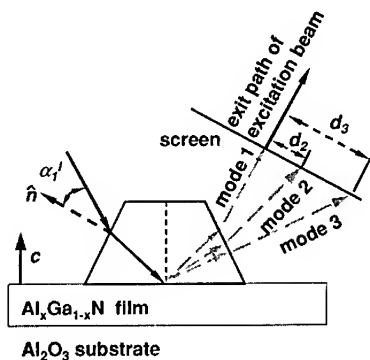


**Figure 1.** Schematic of WPC apparatus. A rutile prism is clamped to the surface of the sample. The launch angle for mode #1 is  $\alpha_1^i$ .

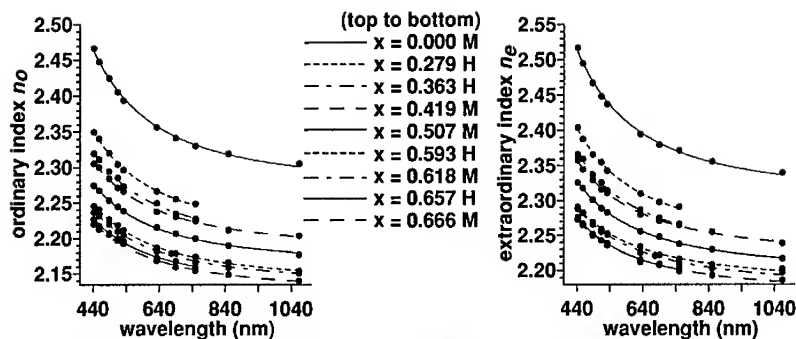


Figure 2. Refractive indices of HVPE (H) and MOCVD (M)  $\text{Al}_x\text{Ga}_{1-x}\text{N}$  samples.

measured, the effective indices of the guided modes were calculated. A numerical routine was then used to compute  $n_o$ ,  $n_e$ , and thickness  $L$  of the  $\text{Al}_x\text{Ga}_{1-x}\text{N}$  films.<sup>9</sup>

Refractive index data resulting from WPC analysis of HVPE (H) and MOCVD (M)  $\text{Al}_x\text{Ga}_{1-x}\text{N}$  samples are shown in Fig. 2. The laser wavelengths used were 442, 457.9, 488, 514.5, 532, 632.8, 690, 750, 850 and 1064 nm. These data were fit to the one-term Sellmeier equations

$$n_o^2 = 1 + A_o \lambda^2 / (\lambda^2 - B_o^2) \quad (1)$$

$$n_e^2 = 1 + A_e \lambda^2 / (\lambda^2 - B_e^2). \quad (2)$$

The wavelength  $\lambda$  is in nanometer units and the coefficients  $A_{o,e}$  and  $B_{o,e}$  are given in Table 1. The table includes a sample with  $x = 0.660$  which, for clarity, is omitted from Fig. 2.

Representative data for  $L$  (also in Table 1) were computed for TE modes at 632.8 nm. The maximum standard uncertainty for  $L$  was estimated to be  $\pm 15$  nm. The maximum standard uncertainty of refractive index was estimated to be  $\pm 0.005$ .

Spectroscopic R/T measurements fit to model functions were used to derive a two-term Sellmeier equation for  $n_o(\lambda)$ . The model functions included effects of optical scattering, loss/absorption, and variation in  $L$ . The R/T data were collected using a spectrophotometer operating over the range of 190 - 2500 nm, and representative R/T data are illustrated in Fig. 3.

$L$ ( $\mu\text{m}$ )	$x$		$A_o$	$B_o$	$A_e$	$B_e$
2.120	0.000	(M)	4.166	186.4	4.316	190.9
0.453	0.279	(H)	3.834	172.7	4.000	177.3
0.455	0.363	(H)	3.773	165.8	3.917	171.1
1.311	0.419	(M)	3.765	159.5	3.925	164.3
1.170	0.507	(M)	3.672	154.5	3.827	161.0
0.552	0.593	(H)	3.568	153.2	3.761	149.3
0.955	0.618	(M)	3.554	149.7	3.732	152.4
0.620	0.657	(H)	3.530	145.6	3.690	150.5
1.025	0.660	(M)	3.520	146.4	3.696	149.0
1.025	0.666	(M)	3.511	145.7	3.695	148.0

Table 1. Sellmeier coefficients derived from WPC methods for  $n_o$  and  $n_e$  as a function of Al mole fraction  $x$ . The wavelength  $\lambda$  is in nanometer units. Sample thickness  $L$  is also given.

A least-squares fitting procedure was used to fit the model functions to the R/T data and a comparison was made both with and without correlation to the WPC results.<sup>9</sup> To perform the correlation, a “pinning” wavelength  $\lambda_p = 632.8$  nm was selected and the fitted refractive index at the pinning wavelength was denoted by  $n_p = n_o(\lambda_p)$ . The sum-of-squares deviation between the model function (uncorrelated with WPC data) and the R/T data is defined as  $\chi_{R/T}^2(n_p)$ . The sum-of-squares deviation between the model function correlated with the WPC results is defined as  $\chi_n^2(n_p)$ . For  $\lambda$  below the band gap,  $n_p$  was found that minimized the sum-of-squares deviation between the  $n_o(\lambda)$  values given by two-term Sellmeier equation

$$n_o^2(\lambda) = 1 + A_1^* \lambda^2 / (\lambda^2 - B_1^{*2}) + A_2^* \lambda^2 / (\lambda^2 - B_2^{*2}), \quad (3)$$

and the corresponding  $n_o$  values measured by prism-coupling methods. The width of the minimum of  $\chi_n^2(n_p)$  is narrower than the width of the minimum in  $\chi_{R/T}^2(n_p)$  by a factor of 80. This illustrates that  $n_p$ , and  $n_o$  at other wavelengths, is determined more accurately by the R/T analysis correlated with WPC data than by R/T alone. The coefficients describing Eq. 3 are given in Table 2 and corresponding graphs of  $n_o(\lambda)$  appear in Fig. 4.

## DISCUSSION

The results obtained here for the MOCVD grown GaN ( $x=0$ ) sample were compared to earlier work that used SE<sup>3,5</sup> and prism coupling<sup>7,8</sup>. With the discrepancies in the literature concerning calibration of Al mole fraction, we confine the discussion to GaN films only. The comparative results of the prism coupling analyses for  $n_o$  between the earlier cited work and the present study are all consistent to within approximately 0.008. The prism coupling results for  $n_e$  are consistent to within approximately 0.003. The deviation of the SE data of Yu et al. (Ref. 3) with all of the prism coupling results is generally larger. However, comparison of our results with the SE work of Goldhaun et al. (Ref. 5), shows that the values of  $n_o$  agree to within 0.005 for  $488 \text{ nm} < \lambda < 856 \text{ nm}$ , and the values of  $n_e$  are found to agree to within 0.005 for  $442 \text{ nm} < \lambda < 1064 \text{ nm}$ . Also, our two-term Sellmeier equation for  $n_o(\lambda)$ , which was derived from correlated R/T and WPC work, generally agrees within 0.005 (over the range  $442 - 1064 \text{ nm}$ ) with our one-term Sellmeier equation for  $n_o$  derived from WPC methods alone. However, for the  $x = 0.279$  HVPE sample, the deviation is greater. Values of  $L$  computed with TM modes generally exceed by 10-30 nm  $L$  values computed with TE modes. However, for the MOCVD sample with  $x = 0.419$ , the disagreement was less than 10 nm. These effects appear unassociated with substrate/film buffer layers present in MOCVD samples since they are still observed in the HVPE samples that lacked buffer layers.

$x$		$A_1^*$	$B_1^{*2}$	$A_2^*$	$B_2^{*2}$
0.000	(M)	0.083	354.7	4.068	180.1
0.279	(H)	0.150	297.8	3.635	172.6
0.363	(H)	0.234	278.5	3.573	143.7
0.419	(M)	0.145	277.2	3.612	153.1
0.507	(M)	0.159	262.5	3.502	149.3
0.593	(H)	0.208	249.5	3.376	138.2
0.618	(M)	0.293	237.5	3.259	137.9
0.660	(M)	0.240	235.7	3.270	139.1
0.666	(M)	0.253	232.2	3.247	139.1

**Table 2.** Sellmeier coefficients for Eq. 3 as a function of  $x$  for  $\lambda$  in nanometer units.

In the SE work of Goldhahn et al. (Ref. 5), effects of non-abrupt interlayers on both sides of the growth interface are included in their models. Such effects may arise from disorder, void formation, strain, and/or scratch filling in the substrate during film growth. Taken together, these observations suggest that discrepancies in  $L$  may result from anisotropy in the defective interface that is manifest by a slightly different optical thickness computed from TE and TM mode data. We have incorporated similar assumptions about the film/substrate interface in the model functions used to fit to the spectroscopic R/T data. Specifically, the quantity  $(n_o-1)$  near the interface was assumed reduced from its bulk value by as much as 7 %. The magnitude of the reduction factor for each film was determined as part of the curve-fitting procedure for the R/T model functions.

#### SUMMARY

The refractive indices of MOCVD and HVPE  $\text{Al}_x\text{Ga}_{1-x}\text{N}$  samples were measured using WPC alone, and R/T analysis correlated with the WPC results. The Al mole fraction  $x$  of the samples was measured with EDS. The estimated maximum standard uncertainty in  $n_o$  and  $n_e$  is  $\pm 0.005$ , and the estimated maximum standard uncertainty in  $x$  is  $\pm 0.02$ . Our results compare favorably with earlier WPC work (for  $x=0$ ) considering the stated uncertainties in the earlier and present studies. Our results compare more favorably with the SE work of Ref. 5, that incorporated film/substrate interlayers to fit their results, than with the SE work of Ref. 3, that apparently did not.

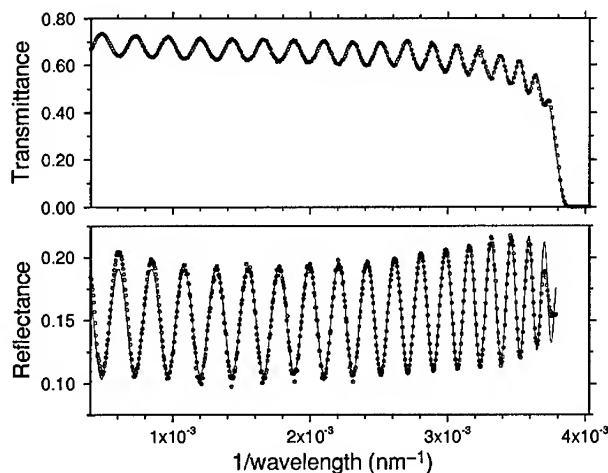


**Figure 3.** R/T spectra of the  $x=0.618$  MOCVD sample plotted as functions of  $1/\lambda$ . Measured R/T data are open circles and the model functions are solid lines.

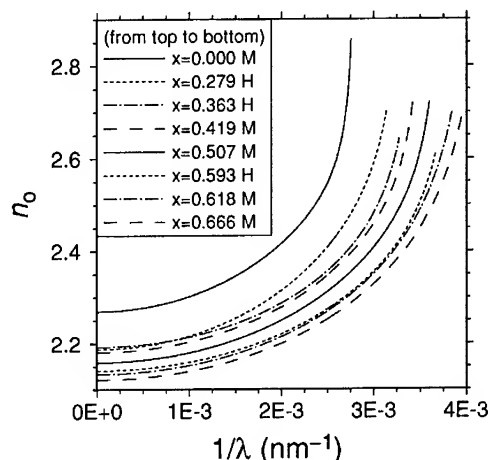


**Figure 4.** Graphs of Eq. 3 using coefficients in Table 2. Results for  $x=0.660$  are omitted for clarity. Fitted functions are extrapolated to  $1/\lambda=0$ , although the lower limit of the measured domain was  $1/\lambda=4\times 10^{-4} \text{ nm}^{-1}$ .

- a. Contribution of an agency of the U. S. Government, not subject to copyright.
- b. Reference to a specific product or service is made only for complete technical description and does not constitute endorsement by the National Institute of Standards and Technology.

#### REFERENCES

1. M. E. Lin, B. N. Sverdov, S. Strite, H. Morkoç, and A. E. Drakin, *Elect. Lett.* 29, 1759 (1993).
2. D. Brunner, H. Angerer, E. Bustarret, F. Freudenberg, R. Höpler, R. Dimitrov, O. Ambacher, and M. Stutzmann, *J. Appl. Phys.* 82, 5090 (1997).
3. G. Yu, H. Ishikawa, T. Egawa, T. Soga, J. Watanabe, T. Jimbo, and M. Umeno, *Jpn. J. Appl. Phys.* 36, L 1029 (1997).
4. G. Yu, G. Wang, H. Ishikawa, M. Umeno, T. Soga, T. Egawa, J. Watanabe, and T. Jimbo, *Appl. Phys. Lett.* 70, 3209 (1997).
5. R. Goldhahn, S. Shokhovets, J. Scheiner, G. Gobsch, T. S. Cheng, C. T. Foxon, U. Kaiser, G. D. Kipidze, and W. Richter, *Phys. Stat. Sol. (a)* 177, 107 (2000).
6. R. Ulrich and R. Torge, *Appl. Opt.* 12, 2901 (1973).
7. M. J. Bergman, Ü. Özgür, H. C. Casey, Jr., H. O. Everitt, and J. F. Muth, *Appl. Phys. Lett.* 75, 67 (1999).
8. Ü. Özgür, G. Webb-Wood, H. O. Everitt, F. Yun, and H. Morkoç, *Appl. Phys. Lett.* 79, 4103 (2001).
9. N. A. Sanford, L. H. Robins, A. V. Davydov, A. Shapiro, D. V. Tsvetkov, A. V. Dmitriev, S. Keller, U. K. Mishra, and S. P. DenBaars, submitted for publication.
10. B. N. Taylor and C. E. Kuyatt, NIST Technical Note 1297, 1994 Edition.

### Optical Band Gap Measurements of InN Films in the Strong Degeneracy Limit

D.B. Haddad,<sup>1</sup> J.S. Thakur,<sup>2</sup> V.M. Naik,<sup>3</sup> G.W. Auner,<sup>2</sup> R. Naik<sup>1</sup> and L.E. Wenger<sup>1</sup>

<sup>1</sup>Department of Physics and Astronomy, Wayne State University, Detroit, Michigan 48201

<sup>2</sup>Department of Electrical and Computer Engineering, Wayne State University, Detroit, Michigan 48202

<sup>3</sup>Department of Natural Sciences, University of Michigan-Dearborn, Dearborn, Michigan 48128

#### ABSTRACT

The optical properties of InN thin films (0.5  $\mu\text{m}$  thick) grown on sapphire substrates by plasma source molecular beam epitaxy deposition have been measured in order to study the effect of electron degeneracy on the band gap measurement. X-ray diffraction measurements show that the films are wurtzite polycrystalline at a growth temperature of 325 °C, whereas a completely c-axis textured growth at a temperature of 475 °C. The Raman bands  $A_1$  (LO) and  $E_2$  are rather broad indicating the presence of a large number of structural defects. Hall effect measurements show that both the films are *n*-type with carrier concentrations of  $(8.0 \pm 1.6) \times 10^{20} \text{ cm}^{-3}$  and  $(3 \pm 0.6) \times 10^{20} \text{ cm}^{-3}$ , respectively. The optical absorption data on these samples show *n* dependent band gap edge and a peak corresponding to plasmon due to strong electron degeneracy. The band gap absorption data were analyzed assuming a direct band gap and incorporating the Moss-Burstein shift effect. By taking into account the non-parabolic dispersion and the band-renormalization effects for the conduction band of InN, the calculated true band gap (0.7 eV) agrees with other recent measurements on high quality InN films.

#### INTRODUCTION

Recently, the value of the optical band gap energy of InN has come under intense reinvestigation due to a disagreement between the generally accepted value of 1.9 eV<sup>1-3</sup> and recently reported values in the range of 0.7-1.0 eV.<sup>4-8</sup> The smaller reported band gap values (< 1 eV) are thought to be associated with improvements in the thin film fabrication techniques leading to higher quality InN films with relatively less disorder, and are more consistent with values predicted by theoretical calculations.<sup>9</sup>

One possible hypothesis for the larger band gap energies measured in earlier InN films is that higher levels of donor impurities existed, which led to an increased concentration of electrons in the conduction band causing a strong electron degeneracy. In addition, a small effective electron mass in this system would promote a larger electron degeneracy.<sup>10</sup> Since the optical absorption, which is traditionally used to determine the band gap value, is sensitive to both electron degeneracy and the existence of impurities, these effects on the band gap determinations must be considered in order to determine the true band gap energy. In this paper, we show that band gap determination using optical absorption data even on polycrystalline InN films yields 0.7 eV in agreement with the most recent values, after accounting for electron degeneracy and band-renormalization effects.<sup>11</sup>

## EXPERIMENT

Thin InN films (thickness  $\sim 0.5 \mu\text{m}$ ) were deposited on (0001) sapphire by a plasma source molecular beam epitaxy (PSMBE) technique<sup>12</sup> utilizing a hollow cathode source lined with MBE grade indium. Base pressures of approximately  $10^{-8}$  torr and substrate temperatures in the range of 325–475 °C were maintained during the growth of the films.  $\theta$ -2 $\theta$  X-ray diffraction scans indicated that films grown at 475 °C were completely *c*-axis textured, whereas film growth at 325 °C resulted in polycrystalline films. Hall effect measurements, using Van-der-Pauw method, show that both the films are *n*-type with carrier concentrations of  $3 \times 10^{20} \text{ cm}^{-3}$  and  $8 \times 10^{20} \text{ cm}^{-3}$ , respectively. These high levels of carrier concentration could result from the presence of defects in the films stemming from oxygen impurities that are typically found in InN films.

Raman scattering was also used to characterize the crystalline quality of these films. Figure 1 shows the Raman spectra of these films measured using the 488-nm excitation line in the backscattering geometry.<sup>13</sup> The observed Raman bands  $A_1(\text{LO})$  and  $E_2$  are rather broad indicating the presence of a large number of structural defects. However, the sharper peak structures observed for the 475 °C grown film indicate improved crystalline quality of this film<sup>14</sup> as compared to the 325 °C grown film. The phonon structure at  $\sim 451 \text{ cm}^{-1}$  and at  $\sim 449 \text{ cm}^{-1}$  in the 325 °C and 475 °C grown film spectra, respectively, matches the experimental and calculated values<sup>15–17</sup> of the  $A_1(\text{TO})$  mode. Although the  $A_1(\text{TO})$  mode is forbidden in the backscattering geometry for a *c*-axis oriented films, a small leakage of the polarization could lead to the observation of the  $A_1(\text{TO})$  peak. This effect could be further reinforced by the presence of any inherent disorder or defects in the films. The observation of the  $A_1(\text{TO})$  mode in the Raman spectra raises the possibility of the  $A_1(\text{LO})$  mode interacting via its macroscopic electric field with a degenerate plasmon (due to high level of carrier concentration), if it is not damped. This coupling would produce two coupled modes whose energy can be analytically calculated<sup>18</sup> from the plasmon and phonon energies, assuming the damping is small. Because of the relatively large plasmon energy (see below) and small damping found in both films, the low-energy coupled-mode (PLP-) would merge with the  $A_1(\text{TO})$  mode, while the high-energy coupled-mode (PLP+) would lie very close to the right hand-side of the corresponding plasmon mode.

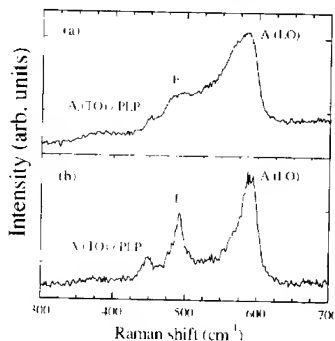


Fig. 1. The Raman spectra of InN films grown at 325 °C (a), and 475 °C (b).

BEST AVAILABLE COPY

Optical transmittance and reflectance spectra were measured from 175 to 3300 nm for both films to calculate the absorbance and hence the absorption coefficient ( $\alpha$ ) plotted as a function of photon energy,  $\hbar\omega$  in Fig. 2. The low-energy absorption peak, which corresponds to plasmon excitations in the conduction band, is followed by a transparent region and a rise near the absorption edge.

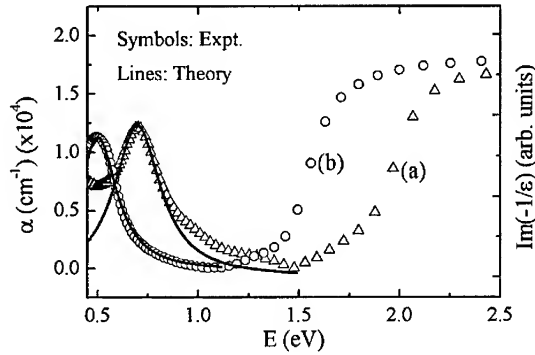


Fig. 2. Absorption spectra measured for InN films grown at 325 °C (a) and 475 °C (b). Theoretical fits to the plasmon absorption peak given by  $\text{Im}(-1/\epsilon)$  are shown by the solid lines.

Due to the large electron carrier concentration, the measured absorption data was fitted using the Drude model for conduction electrons,<sup>19</sup> in terms of the plasmon response of the electron gas and its damping. The corresponding damped dielectric function is given by

$$\epsilon(\omega) = \epsilon_{\infty} \left( 1 - \frac{\omega_p^2}{\omega^2 + i\omega\gamma} \right) \quad (1)$$

where  $\gamma$  is the electron damping due to scattering from randomly distributed stationary impurities,  $\omega_p$  is the plasmon frequency, and  $\epsilon_{\infty}$  is the dielectric response in the high-energy limit for the film. The peak position and width of this low-energy absorption peak can be reproduced by the energy loss function  $\text{Im}\left(-\frac{1}{\epsilon(\omega)}\right)$ . The experimental absorption data for the 325 °C (475 °C) grown film can be reproduced as shown by the solid lines in Fig. 2 for physically reasonable values of  $\epsilon_{\infty} = 6.7$ ,<sup>20</sup>  $\gamma = 0.28$  eV (0.23 eV), and  $\omega_p = 0.71$  eV (0.51 eV). Using this  $\epsilon_{\infty}$  value, and the measured carrier concentrations from Hall effect measurements, the values of effective electron mass  $m_e^*$  have been determined to be  $0.30 \pm 0.06 m_e$  ( $0.24 \pm 0.04 m_e$ ) for the 325 °C (475 °C) grown film. A pronounced increase in the electron effective mass indicate a nonparabolic conduction band in InN.<sup>11</sup>

## CALCULATION OF THE BAND GAP ENERGY

Figure 3 shows the experimental optical absorption coefficient squared ( $\alpha^2$ ) as a function of photon energy. At higher energies, the direct band gap transition dominates the absorption process. The optical transition across the band gap to an empty parabolic conduction band is described by:<sup>21</sup>

$$\alpha \hbar \omega = \alpha_c (\hbar \omega - E_g)^{1/2} \quad (2)$$

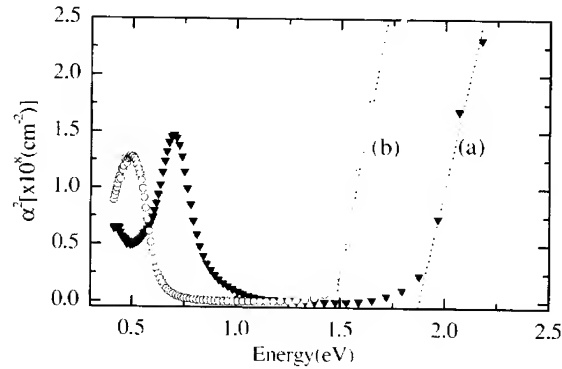


**Fig. 3.**  $\alpha^2$  as a function of photon energy for InN films grown at 325 °C (a) and 475 °C (b). The dotted lines are linear interpolations to determine the band gap energies from the intercepts.

where  $E_g$  is the direct band gap energy and  $\alpha_c$  is a constant. Eq. (2) predicts a linear behavior of  $\alpha^2$  as a function of photon energy and the value of band gap ( $E_g$ ) is determined by extrapolating the linear region to  $\alpha^2 = 0$ . This procedure results in band gaps of  $1.90 \pm 0.05$  eV ( $1.45 \pm 0.05$  eV) for the 325 °C (475 °C) grown InN film. This extrapolation procedure for  $E_g$  is valid for an empty or nearly empty conduction band. However, when the electron carrier density becomes large, the conduction band is not empty at finite temperatures, and the chemical potential may no longer be negligible compared to  $E_g$ . Furthermore, as InN becomes more strongly degenerate at larger carrier concentrations, the Fermi energy can move deep into the conduction band and shift the absorption edge towards higher energies, resulting in overestimations of the band gap energies from the simple linear extrapolation procedure. This shift in absorption edge, the well-known Moss-Burstein effect,<sup>22</sup> becomes more pronounced when carrier densities exceed  $10^{20}$  cm<sup>-3</sup>. Thus in order for the optical transition to take place the incident photon energy must overcome the combined effective energy barrier due to the band gap energy and the chemical potential.

Recently, Wu *et al*<sup>11</sup> have measured the free-electron effective mass ( $m^*$ ) using infrared plasma reflection edge in various InN films. They have shown that the Moss-Burstein shift of the absorption edge observed in InN samples with  $3.5 \times 10^{17} \leq n \leq 5.5 \times 10^{18}$  is well explained by the non-parabolic conduction band model and the true energy bandgap is  $\sim 0.7$  eV. By taking into account the conduction-band renormalization effects due to electron-electron ( $\Delta E_{e-e}$ ) and electron-ionized impurity ( $\Delta E_{e-i}$ ) interactions, the optical absorption edge ( $E$ ) is given by,<sup>11</sup>

$$E = E_G + \frac{\hbar^2 k_F^2}{2m_e} + \frac{1}{2} \left\{ \sqrt{E_G^2 + 4E_P \frac{\hbar^2 k_F^2}{2m_e}} - E_G \right\} + \Delta E_{e-e} + \Delta E_{e-i} \quad (3)$$

where

$$\Delta E_{e-e} = -\frac{2e^2 k_F^2}{\pi \epsilon_s} - \frac{e^2 k_{TF}}{2\epsilon_s} \left\{ 1 - \frac{4}{\pi} \arctan \left( \frac{k_F}{k_{TF}} \right) \right\} \quad (4)$$

$$\Delta E_{e-i} = -\frac{4\pi e^2 n}{a_B \epsilon_s k_{TF}^3} \quad (5)$$

and  $k_{TF} = \left( \frac{2}{\sqrt{\pi}} \right) \left( \frac{k_F}{a_B} \right)^{1/2}$  is the Fermi-Thomas screening wave vector,  $\epsilon_s$  is the static dielectric constant,  $E_G$  is the real energy bandgap, and  $a_B = 0.53 \epsilon_s m_0 / m^*$  is the Bohr radius in Å. Using Eq. 3,  $\epsilon_s = 11.4$  (using Lyddane-Sachs-Teller relation  $\epsilon_s / \epsilon_\infty = \omega_{LO}^2 / \omega_{TO}^2$ ) and  $E_P = 10$  eV,<sup>11</sup> we have evaluated the values of the  $E$  for the samples studied in this work. Using  $E_G = 0.7$  eV, the calculated values of  $E$  are  $2.0 \pm 0.1$  eV ( $1.5 \pm 0.1$  eV) for the sample grown at 325 °C (475 °C). These values are in excellent agreement with the values determined from optical measurements (Fig. 3), suggesting a value of  $\sim 0.7$  eV for the true bandgap of InN. This value is also in agreement with other recently measured values.<sup>11</sup>

## CONCLUSIONS

InN films with large carrier concentrations ( $n = 3-8 \times 10^{20} \text{ cm}^{-3}$ ) have been prepared and the corresponding optical bandgap absorption edge ( $E = 1.5 - 1.9$  eV) and plasmon absorption peaks have been measured. The fitting of plasmon absorption peak using the Drude model for conduction electrons yields free-electron effective masses  $0.24 - 0.30 m_e$ , which are consistent with the values reported in the literature. The band gap absorption data were analyzed assuming a direct band gap and incorporating the Moss-Burstein shift effect. By taking into account the nonparabolic dispersion and the band-renormalization effects for the conduction band of InN, the observed  $n$  dependent absorption edges have been explained using a single bandgap energy value of 0.7 eV. This value is in agreement with recent measurements by other researchers.

## ACKNOWLEDGMENTS

We thank Dr. W.H. Weber for his help with the Raman measurements and Y.V. Danylyuk for his assistance during sample preparation. This work was supported by NSF-IGERT-DGE grant No. 9870720 and by the Center for Smart Sensors and Integrated Microsystems at Wayne State University.

## REFERENCES

1. K. Osamura, S. Naka, and Y. Murakami, *J. Appl. Phys.* **46**, 3432 (1975).
2. T.L. Tansley and C.P. Foley, *J. Appl. Phys.* **59**, 3241 (1986).
3. K. Ikuta, Y. Inoue, O. Takai, *Thin Solid Films* **334**, 49 (1998).
4. T. Inushima, V.V. Mamutin, V.A. Vekshin, S.V. Ivanov, T. Sakon, M. Motokawa, and S. Ohoya, *J. Crystal Growth* **227-228**, 481 (2001).
5. V. Yu Davydov, A.A. Klochikhin, R.P. Seisyan, V.V. Emtsev, S.V. Ivanov, F. Bechstedt, J. Furthmüller, H. Harima, A.V. Mudryi, J. Aderhold, O. Semchinova, and J. Graul, *Phys. Stat. Sol. (b)* **229**, R1 (2002).
6. V. Yu Davydov, A.A. Klochikhin, V.V. Emtsev, S.V. Ivanov, V.V. Vekshin, F. Bechstedt, J. Furthmüller, H. Harima, A.V. Mudryi, A. Hashimoto, A. Yamamoto, J. Aderhold, J. Graul, and E.E. Haller, *Phys. Stat. Sol. (b)* **230**, R4 (2002).
7. J. Wu, W. Walukiewicz, K.M. Yu, J.W. Ager III, E.E. Haller, H. Lu, W.J. Schaff, Y. Saito, and Y. Nanishi, *Appl. Phys. Lett.* **80**, 3967 (2002).
8. T. Matsuoka, H. Okamoto, M. Nakao, H. Harima, and E. Kurimoto, *Appl. Phys. Lett.* **81**, 1246 (2002).
9. C. Persson, R. Ahuja, A. F. da Silva, and B. Johansson, *J. Phys. Cond. Matter* **13**, 8945 (2001).
10. V.A. Tyagai, A.M. Evstigneev, A.N. Krasiko, A.F. Andreeva, and V. Ya Malakhov, *Sov. Phys. Semicond.* **11**, 1257 (1977).
11. J. Wu, W. Walukiewicz, W. Shan, K.M. Yu, J.W. Ager III, E.E. Haller, H. Lu, and W.J. Schaff, *Phys. Rev. B* **66**, 201403 (2002).
12. G.W. Auner, T.D. Lenane, F. Ahmad, R. Naik, P.K. Kuo, and Z.L. Wu, in *Wide Band Gap Electronic Materials*, (Academic, New York, 1995), p. 329.
13. V.M. Naik, W.H. Weber, D. Uy, D. Haddad, R. Naik, Y.V. Danylyuk, M.J. Lukitsch, G.W. Auner, and L. Rimai, *Appl. Phys. Lett.* **79**, 2019 (2001).
14. V. Yu Davydov, V.V. Emtsev, I.N. Goncharuk, A.N. Smimov, V.D. Petrikov, V.V. Mamutin, V.A. Vekshin, V.S. Ivanov, M.B. Smimov, and T. Inushima, *Appl. Phys. Lett.* **75**, 3297 (1999).
15. H. Grille, Ch. Schnittler, and F. Bechstedt, *Phys. Rev. B* **61**, 6091 (2000).
16. C. Bungaro, K. Rapcewicz, and J. Bernholc, *Phys. Rev. B* **61**, 6720 (2000).
17. J.S. Dyck, K.Kim, S. Limpijumnong, W.R.L. Lambrecht, K. Kash, and J.C. Angus, *Solid State Commun.* **114**, 355 (2000).
18. B.B. Varga, *Phys. Rev.* **137**, A1896 (1965).
19. I. Hamberg and C.G. Granqvist, *J. Appl. Phys.* **60**, R123 (1986).
20. A. Kasic, M. Schubert, Y. Saito, Y. Nanishi, and G. Wagner, *Phys. Rev. B* **65**, 115206 (2002).
21. L.H. Hall, J. Bardeen, and F.J. Blatt, *Phys. Rev.* **95**, 559 (1954).
22. T.S. Moss, *Proc. Phys. Soc. B* **67**, 775 (1954); E. Burstein, *Phys. Rev.* **93**, 632 (1954).

BEST AVAILABLE COPY

### A Study of Indium Nitride Films Grown Under Conditions Resulting in Apparent Band-gaps from 0.7 eV to 2.3 eV

K. S. A. Butcher<sup>1</sup>, M. Wintrebert-Fouquet<sup>1</sup>, Motlan<sup>2</sup>, S. K. Shrestha<sup>3</sup>, H. Timmers<sup>3,4</sup>, K. E. Prince<sup>5</sup> and T. L. Tansley<sup>1</sup>

<sup>1</sup>Physics Department, Macquarie University, Sydney, NSW 2109, Australia.

<sup>2</sup>Department of Physics, Faculty of Mathematics and Science, State University of Medan, Indonesia.

<sup>3</sup>School of Physics, University of New South Wales at the Australian Defence Force Academy, Canberra, ACT 2600, Australia.

<sup>4</sup>Department of Nuclear Physics, Research School of Physical Sciences and Engineering, Australian National University, Canberra, ACT 0200, Australia.

<sup>5</sup>Australian Nuclear Science and Technology Organisation, Private Mail Bag 1, Menai NSW 2234, Australia.

#### ABSTRACT

The band-gap of indium nitride has long been believed to be about 1.9 eV with slight variations due to band-tailing in polycrystalline samples and degenerate doping. Recently, other values as low as 0.7 eV have apparently been observed. We have compared samples spanning this apparent range of band-gap using secondary ion mass spectroscopy (SIMS), X-ray Photoelectron Spectroscopy (XPS) and heavy ion elastic recoil detection analysis (ERDA), in conjunction with spectral optical density measurements. Once structural inhomogeneities are taken into account, we show that much of the conflicting data are compatible with direct photoionisation with a threshold energy of about 1.0 eV. This feature was first reported in polycrystalline indium nitride over 15 years ago and attributed to a  $|p\rangle$  like defect state. We ask whether the feature may instead be a direct band-gap.

#### INTRODUCTION

Indium nitride is potentially a very high mobility material, but preparation of satisfactory samples has proven difficult and many of its basic properties are still being assessed. A group of low carrier concentration polycrystalline thin films were grown by RF sputtering in the early 1980s, with one having a mobility of  $2700 \text{ cm}^2/\text{V}\cdot\text{s}$  for a carrier concentration of  $5 \times 10^{16} \text{ cm}^{-3}$  [1]. Those samples, along with a series reported by other workers, established an optical transmission band-gap of 1.89 eV in the low-concentration limit [2] with a systematic carrier concentration dependence ascribed to a Moss-Burstein shift.

Recent MBE InN has been reported to have other band-gaps, apparently as low as 0.7 eV [3-5]. Oxygen has been suggested as being responsible for the 2 eV band-gap. A counter view is that the lower band-gap material may be metal rich as a result of growth near the InN decomposition temperature. Figure 1 illustrates the point by showing the well known reduction in the band-gap of GaN grown under metal rich conditions (inset).

We have carried out a series of measurements in an effort to gain a better understanding of the spread of observed band-gap values. Films from three different laboratories were analysed. MBE grown InN from Cornell University and from the Ioffe Physico-Technical Institute, and RF sputtered

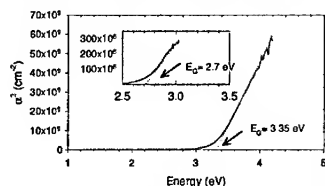


Figure 1. The band-gap of GaN grown under gallium rich conditions (inset).

material from Macquarie University. The InN from these three groups span the range of results observed. We use a combination of ERDA, optical transmission spectroscopy, SIMS and XPS to examine the material differences. We also examine published absorption data.

## THE MATERIALS

The Cornell MBE samples were grown on sapphire substrates with a 200 nm AlN buffer layer. The InN layers supplied to us were between 500 nm and 800 nm thick and were grown at about 500 °C. Room temperature electron mobilities for these samples were between 780 and 1165 cm<sup>2</sup>/V·s, though we note that the Cornell group have recently reported material with mobility as high as 2000 cm<sup>2</sup>/V·s [6]. XRD results indicate single crystal or at least material with a relatively low dislocation concentration. Other characteristics are reported elsewhere [7].

Two Ioffe MBE samples, 330nm and 700 nm thick, were grown directly onto sapphire substrates without a buffer layer at a temperature of 470 °C. Raman measurements indicate material that is probably single crystal, or again has low dislocation density [5]. The material supplied to us has mobilities of up to 660 cm<sup>2</sup>/V·s for a carrier concentration of 2.5×10<sup>19</sup> cm<sup>-3</sup>. Material from this group spans a large range of apparent band-gap values [5], which they have recently attributed to a Moss-Burstein shift from a limit of 0.70 eV for carrier concentrations in the mid 10<sup>18</sup> cm<sup>-3</sup> to 2×10<sup>19</sup> cm<sup>-3</sup> range [4]. Most recently the Ioffe group have asserted that the 2.0 eV band-gap seen in polycrystalline material grown by RF sputtering with carrier concentration of 5×10<sup>20</sup> cm<sup>-3</sup> [4,8] is also a Moss-Burstein shifted value from a base of 0.7 eV. This appears incompatible with the Moss-Burstein shift from 1.89 eV to 2.1 eV demonstrated over a range of carrier concentrations between 5×10<sup>16</sup> cm<sup>-3</sup> to 5×10<sup>20</sup> cm<sup>-3</sup> [2] and would also appear to require a conduction band with unusual properties. The group also reported oxygen as the donor. The role of oxygen in indium nitride has not been clarified. In low temperature grown GaN, however, oxygen forms neutral complex structures, in contrast to its role as a donor impurity in high-temperature grown films [9]. The results obtained for GaN suggest several possible roles for oxygen in InN, including different behaviours in different growth regimes.

The RF sputtered material was grown in the same apparatus originally used to grow the high mobility samples reported by Tansley and Foley [1]. The films produced by this system were grown on glass at approximately 80 °C. The system has been recently upgraded with a significant reduction in carbon incorporation (three orders of magnitude reduction in SIMS signal). The films produced are polycrystalline with a narrow spread of band-gap values as previously reported [2], carrier concentrations are typically above 10<sup>19</sup> cm<sup>-3</sup> though a small number of low carrier concentration samples (~10<sup>17</sup> cm<sup>-3</sup>) have been grown. XRD shows that the material is hexagonal with a strong c-axis orientation [10]. We have recently shown that the high carrier concentrations correlate with high levels of excess nitrogen incorporation [11].

## SIMS, XPS AND ERDA ANALYSIS

The SIMS measurements were carried out using a Cameca 5F dynamic SIMS system with a Cs<sup>+</sup> ion beam. The methodology of Gao [12] was applied, whereby CsM<sup>+</sup> (where M is the element being analysed) molecules are collected instead of M<sup>+</sup>. The influence of Cs<sup>+</sup> ion beam fluctuation was eliminated by normalising the collected signals to the average of the Cs<sup>+</sup> ion beam signal. For all the samples, charging effects at the substrate prevented measurements beyond that point, while for the Cornell samples charging at the AlN buffer layer prevented measurements in that region. The SIMS results are therefore only for

the conductive InN layers. Because there is percentage variation in the elemental compositions for all the samples these SIMS results should only be regarded as qualitative.

Figure 2 show typical SIMS results for the Macquarie, Ioffe and Cornell samples respectively. Only O, N, C, In and Al signals are shown. The apparent high level of the Al signal for the first 100 nm of the samples is actually an artefact due to the collection of COH ions in the presence of the high C, O and H (not shown) species present near the surface. Similarly the apparent increase in the Al at the substrate interface for the Macquarie sample is COH, related to the increase of the component species at the interface. The polycrystalline RF sputtered sample shows a high oxygen signal due to its percolation through intercrystallite boundaries [13]. ERDA indicates the O contents are 9 - 11 atomic percent. Interestingly it has recently proved possible to obtain electron concentrations as low as  $1 \times 10^{17} \text{ cm}^{-3}$  with an order of magnitude reduction in oxygen content.

Cornell and Ioffe sample SIMS results show high levels of Al apparently diffusing from the back interface. This Al diffusion is real, since carbon was low in this region and there is no COH ion interference evident. The Ioffe group have previously reported on the formation of an  $\text{In}_{0.68}\text{Al}_{0.32}\text{N}$  interface transition layer for InN with a 2.1 eV band-gap, MBE grown on sapphire [14]. However, the accompanying oxygen diffusion was not reported and here the SIMS profile shows a graded interface. For the Cornell sample the Al diffusion from the AlN buffer layer appears to be greater.

XPS measurements were performed using a VG ESCALAB 220i-XL spectrometer with  $\text{AlK}\alpha$  X-ray source in order to quantify the Al content of the MBE samples. The Cornell sample GS-1322 was examined using 3 keV argon ion depth profiling. Nitrogen loss during the measurements was significant, especially in the InN layer, however the analysis was carried out through both the InN top layer and AlN buffer layer to determine the metal ratios. Figure 3 shows the metal ratios obtained as a function of depth. The etch rates of the InN and AlN components were known independently and were extrapolated in the interface region. The InN depth given by a Tencor profilometer measurement of the SIMS etch crater was found to be 540 nm, in agreement with the 550 nm provided by Cornell. This value also coincides with the diffusion cross-over point. The XPS results clearly show strong cross diffusion between the AlN buffer layer and the InN layer for the Cornell sample (SIMS indicated the same for all four films analysed). Based on the quantification provided by the

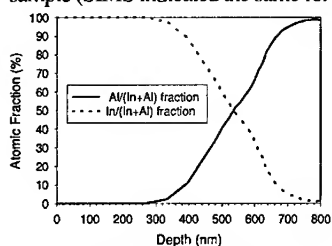


Figure 3. XPS depth profile of In and Al for Cornell sample.

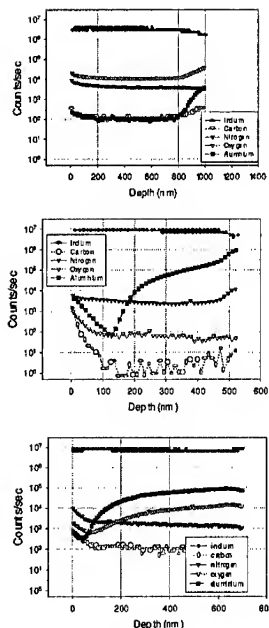


Figure 2. SIMS of a) RF, b) Cornell, c) Ioffe samples.

XPS we would estimate that the Al diffusion into the InN from the sapphire for the Ioffe sample (using the nitrogen signal as a guide for comparison) becomes significant (in percentage terms) at approximately 200-300 nm of sample depth, and that the oxygen appears to become significant at this point as well.

The ERD technique [15], previously applied by us to determine the stoichiometry of GaN films [9], was used here to measure the N/In ratio of all the samples. In addition, it provided information on film thickness and the

compositional changes in the interface region between the InN film and the back contact. For all films analyzed with ERD the spectra confirm that the In and N content is uniform between the sample surface and the onset of the interface region.

For the Ioffe films in the interface region some of the detected N may be bound to Al rather than to In. The N/In ratio measured with ERD is therefore only an upper limit of the actual N/In ratio in the InN film. The SIMNRA simulation for a typical Ioffe sample suggests a film thickness of  $250 \pm 25$  nm and an interface thickness of about 60 nm. Simulations assuming a sharp interface do not agree with the experimental data.

For the Cornell samples the mid-point of the interface region between the film and the buffer layer can be identified in the measured energy spectra for the N recoil ions. By fitting these energy spectra, the total N content measured for these samples has been divided into that below and that above the interface mid-point, respectively. Analysis of the energy spectra for sample GS-1322 using SIMNRA simulation software shows that the mid-point of the interface region, corresponds to  $590 \pm 50$  nm. This is consistent with the results from XPS and SIMS quoted earlier. The simulated energy spectra are well adapted to the experimental data, when the In and Al depth-profiles are assumed to be similar to those shown in Figure 3. The SIMNRA calculation then suggests that the interface region has a thickness of  $420 \pm 40$  nm.

The high nitrogen content of this batch of RF plasma grown samples is noteworthy. It has been confirmed independently by Raman spectroscopy and is discussed in detail elsewhere [11]. The high nitrogen content affects band-gap, extrapolating to 1.89 eV for N/In=1.

**Table I.** N/In ratios for samples.

Sample ID	Band-gap	N/In
RF InN (5-11-01)	2.30 eV	$1.31 \pm 0.03$
RF InN (8-11-01)	2.27 eV	$1.32 \pm 0.04$
		$1.30 \pm 0.03$
RF InN (27-03-02)	2.14 eV	$1.14 \pm 0.03$
Ioffe InN W275	-	$1.04 \pm 0.05$
Ioffe InN W431	-	$1.06 \pm 0.09$
Cornell InN GS-1353	-	$1.19 \pm 0.07$
Cornell InN GS-1322	-	$1.03 \pm 0.05$

## ABSORPTION MEASUREMENTS

Typical room temperature absorption measurement results for the three sets of samples are shown in figure 4. Figure 4 (a) is for the RF sputtered material. The transmission data for these samples fit the relationship

$$\alpha = \alpha_0(hf-E_g)^{1/2} \quad (1)$$

appropriate to a direct band-gap semiconductor with parabolic band structure [16]. The absorption coefficient is found from

$$I = I_0 \exp(-\alpha x) \quad (2)$$

where, properly correcting for reflection effects [16],  $I$  is the transmitted light intensity,  $I_0$  is the incident light intensity and  $x$  is the thickness of the film. These equations assume a uniform film. Hence a plot of absorption coefficient squared (or alternatively  $\ln(I_0/I)$ , the optical density, squared) will have an  $x$  axis intercept equal to the materials band-gap. Close to the band-edge band tailing, bound state and exciton effects become apparent. The region evident at energies below the linear plots of both figures 1 and 4 (a) has an  $\alpha \propto (hf-E_T)^2$  dependency, where  $E_T$  is the ionisation threshold energy for gap states whose symmetry forbids direct ionisation into the conduction band minimum [17]. The region is replotted as  $hf$  against  $\alpha^{1/2}$  in the inset of figure 4 (a) and has strong linearity with  $E_T=1.47$  eV.

The strong interdiffusion at the InN/AlN interface in the Cornell samples means the absorption measurements cannot provide reliable band-gap determination. Figure 4 (b) is typical of the measurements taken for these samples. The inset shows that there is a large region with a strong  $(hf-E_g)^1$  dependence, indicative of neither direct nor indirect band-gap but instead resulting from the combined effects of

absorption throughout the graded heterostructure. The Ioffe sample, shown in figure 4c, appears to be strongly influenced by indirect transitions, though again this may be due to the graded heterostructure at the InN/sapphire interface. Inference of a non-parabolic band structure cannot be drawn from such absorption data. Photoluminescence data derived from graded structures may also indicate properties at a specific location within the heterostructure.

We note that the Cornell group have recently published absorption data that fits a  $(E_g - hf)^{1/2}$  direct band-gap dependence tolerably well, presumably because of the presence of an InN layer much thicker than the interface. In that work by Wu et al. [3], the absorption coefficient versus energy is plotted for a sample that also shows 0.77 eV room temperature photoluminescence (PL) and 0.8 eV 77 K photomodulated reflectance (PR) features. In figure 5 we have appropriately replotted their absorption coefficient data and a 0.98 eV threshold is indicated by extrapolation to the x axis. This implies that the 0.77 eV PL and the 0.8 eV PR features fall well inside the optical band gap. This possibility is strongly supported by the literature, principally by the same group where the same PL peak is observed for various In fractions of InGa<sub>1-x</sub>N [18]. Appropriate replotting of absorption coefficient yields thresholds about 0.5-0.1 eV higher than indicated. Wu et al. [18] show that the photoluminescence peak energy for the InGa<sub>1-x</sub>N alloy system increasingly diverges from the optical band-gap of the InGa<sub>1-x</sub>N as Ga content increases. This further establishes the 0.77 eV PL and 0.8 eV PR features as sub band-gap for InN and increasingly so for the alloy.

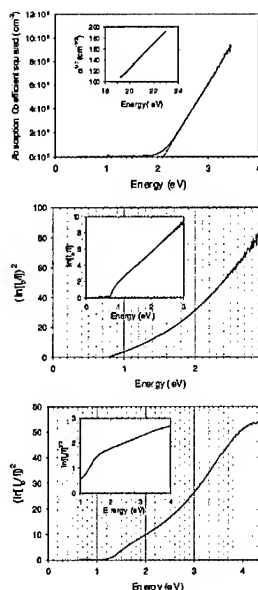


Figure 4. Absorption data for a) RF, b) Cornell and c) Ioffe InN.

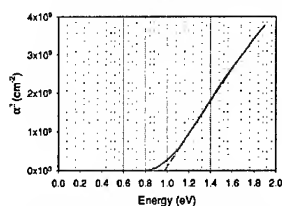


Figure 5. Replotted absorption coefficient data of Wu [3].

Finally it is noteworthy that some of the polycrystalline material reported by Tansley and Foley over 15 years ago, with carrier concentrations between 1 and  $3 \times 10^{17} \text{ cm}^{-3}$ , also included strong sub band-gap absorption. Absorption coefficient squared versus energy plots showed threshold energies between 0.9 and 1.2 eV (see figure 2 of reference [19]) although the strong 1.9 eV band edge was omnipresent. The similarity of this absorption feature to the data shown in figure 5 is remarkable. The earlier report [19] attributed the feature to transitions between bound electrons in  $|p\rangle$  orbitals associated with point defects, and the CB. Further work on the optical properties of InN in conjunction with microcompositional studies is clearly in order.

## CONCLUSIONS

In this work we have used ERDA measurements to confirm that InN grown by RF sputtering can be nitrogen rich. The excess nitrogen content of the films correlates with the 1.89 eV band-gap.

We have shown through a combination of SIMS, XPS and ERDA measurements that MBE InN grown on AlN buffer layers shows strong interdiffusion between the Al of the buffer layer and the In of the InN. Given the relatively low growth temperatures, the strong diffusivity is surprising. Al diffusion was also noted for InN MBE layers grown on sapphire. The graded heterostructures present at the substrate/buffer interface strongly affects the absorption data and there is no need to invoke a nonparabolic conduction band.

Sharper interfaces are required with wide band-gap substrate material for proper evaluation of the absorption data.

It was further shown that the 0.77 eV PL and 0.8 eV PR observed for some MBE grown films are sub band-gap features. A nearby direct absorption feature with threshold energy of approximately 1.0 eV, was observed. We note that the same 1.0 eV absorption has previously been reported for InN polycrystalline material, but was thought at that time to be defect related. The question of the nature of the 1.0 eV transition remains open.

#### ACKNOWLEDGEMENTS

We would like to acknowledge the support of a Macquarie University Research Development Grant and the Australian Institute of Nuclear Science and Engineering. K. S. A. Butcher would also like to acknowledge the support of an Australian Postdoctoral Fellowship. We would also like to thank W. J. Schaff and H. Lu of Cornell University and S. V. Ivanov of the Ioffe Physico-Technical Institute for supplying MBE InN.

#### REFERENCES

1. T. L. Tansley and C. P. Foley, *Electron Lett.* **20**, 1066 (1984).
2. T. L. Tansley and C. P. Foley, *J. Appl. Phys.* **59**, 3241 (1986).
3. J. Wu, W. Walukiewicz, K. M. Yu, J. W. Ager III, E. E. Haller, H. Lu, W. J. Schaff, Y. Saito and Y. Nanishi, *Appl. Phys. Lett.* **80**, 3967 (2002).
4. V. Yu Davydov, A. A. Klochikhin, V. V. Emtsev, S. V. Ivanov, V. V. Vekshin, F. Bechstedt, J. Furthmuller, H. Harima, A. V. Mudryi, A. Hashimoto, A. Yamamoto, J. Aderhold, J. Graul and E. E. Haller, *Phys. Stat. Sol. B*, **230**, R4 (2002).
5. T. Inushima, V. V. Mamutin, V. A. Vekshin, S. V. Ivanov, T. Sakon, M. Motokawa and S. Ohoya, *J. Crystal Growth*, **227-228**, 481 (2001).
6. Private communication with W. J. Schaff of Cornell University.
7. H. Lu, W. J. Schaff, J. Hwang, H. Wu, Wesley Yeo, A. Pharkya and L. F. Eastman, *Appl. Phys. Lett.*, **77**, 2548 (2000).
8. V. Yu Davydov work presented, *International Workshop on Nitride Semiconductors*, Aachen Germany July 2002.
9. K. S. A. Butcher, H. Timmers, Afifuddin, P. P.-T. Chen, T. D. M. Weijers, E. M. Goldys, T. L. Tansley, R. G. Elliman and J. A. Freitas Jr., *J. Appl. Phys.* **92**, 3397 (2002).
10. K. S. A. Butcher, H. Dou, E. M. Goldys, T. L. Tansley and S. Srikeaw, *Accepted for publication Phys. Stat. Sol. B*.
11. K. S. A. Butcher, M. Wintrebert-Fouquet, P. P.-T. Chen, T. L. Tansley, S. Srikeaw, S. K. Shrestha, R.G. Elliman, and Heiko Timmers, *Accepted for publication in the Australian Institute of Physics 2002 Biennial Congress Proceedings*. Also detailed in a recent submission to *Appl. Phys. Lett.*
12. Y. Gao, *Surf. Interface Anal.*, **14**, 552 (1989).
13. S. Kumar, L. Mo, Motlan and T. L. Tansley, *Jpn J. Appl. Phys.*, **35**, 2261 (1996).
14. V. V. Mamutin, T. V. Shubina, V. A. Vekshin, V. V. Ratnikov, A. A. Toropov, S. V. Ivanov, M. Karlsteen, U. Sodervall and M. Willander, *Appl. Surf. Sci.*, **166**, 87 (2000).
15. H. Timmers, T. D. M. Weijers, R. G. Elliman, *Nucl. Instr. Meth. B*, **190**, 393 (2002).
16. S. M. Sze, *Physics of Semiconductor Devices*, second edition, (John Wiley, New York, 1981) pp. 39-41.
17. T. L. Tansley, R. J. Egan and E. C. Horrigan, *Thin Solid Films*, **164**, 441 (1988).
18. J. Wu, W. Walukiewicz, K. M. Yu, J. W. Ager III, E. E. Haller, H. Lu and W. J. Schaff, *Appl. Phys. Lett.*, **80**, 4741 (2002).
19. T. L. Tansley and C. P. Foley, *J. Appl. Phys.*, **60**, 2092 (1986).

### Effect of Pressure on the energy band gaps of $\text{In}_x\text{Ga}_{1-x}\text{N}$ and $\text{In}_x\text{Al}_{1-x}\text{N}$

Z. Dridi<sup>1,2</sup>, B. Bouhafs<sup>1,2</sup>, and P. Ruterana<sup>1</sup>

<sup>1</sup>LERMAT, FRE 2149-CNRS, ISMRA,

6 Boulevard Marechal Juin, 14050 Caen Cedex, France.

<sup>2</sup>Modelling and Simulation in Materials Science Laboratory, Physics Department, University of Sidi Bel-Abbes, 22000 Sidi Bel-Abbes, Algeria.

#### ABSTRACT

Using a first-principles method, we study the effect of pressure on the band gap energies of wurtzite  $\text{In}_x\text{Ga}_{1-x}\text{N}$ , and  $\text{In}_x\text{Al}_{1-x}\text{N}$ . The fundamental band gap energies are direct and increase rapidly with pressure. The pressure coefficients vary in the range of 19.8-24.8 meV/GPa for  $\text{In}_x\text{Ga}_{1-x}\text{N}$ , and 16.7-20.7 meV/GPa for  $\text{In}_x\text{Al}_{1-x}\text{N}$ ; they depend on alloy composition with a strong deviation from linearity. The band gap bowing of the InGaN increases continuously with pressure while those of InAlN strongly decreases at  $p=14$  GPa.

#### INTRODUCTION

The development of light-emitting diodes and laser diodes operating in green and blue spectral regions has stimulated the study of the III-nitrides GaN, InN, AlN and their ternary alloys  $\text{In}_x\text{Ga}_{1-x}\text{N}$ , and  $\text{In}_x\text{Al}_{1-x}\text{N}$ . The first motivation comes from their large and direct band gaps 3.5 eV [1] for GaN, 1.89 eV [2] or 0.8 eV by recent PL measurement [3, 4] for InN, and 6.28 eV [5] for AlN, which would allow to cover an exceptionally large spectrum.

Notwithstanding an important research activity for the last decade on these compounds, a number of their properties are not yet well understood or agreed on such as the band gap bowing parameter of the ternary alloys [6, 7]. Moreover, the band-gap pressure coefficients are not well known. For the InGaN alloys, the available experimental studies reported pressure coefficients for a limited composition range: from 0.04 to 0.14 [8, 9, 10]. These values are almost independent of the composition. Theoretically, to our knowledge only the recent work of Perlin *et al.* [11] reported the pressure coefficients of  $\text{In}_x\text{Ga}_{1-x}\text{N}$ , by means of the full-potential LMTO method. An important dependence of the pressure coefficient on the alloy composition was shown. For  $\text{In}_x\text{Al}_{1-x}\text{N}$ , no results are available.

The InGaN alloys are and will be more and more necessary in LEDs, LDs, as well as in transistors based strained heterostructures. Therefore it is important to know the pressure dependence of their band gap with a given mole fraction in order to calculate the band alignment for designing and optimizing such devices. The  $\text{In}_x\text{Al}_{1-x}\text{N}$  alloy, exhibits the largest variation in the band gap and it is a candidate for less lattice mismatched confinement layers in optical devices.

In the following, we use the full-potential linear augmented plane-wave (FP-LAPW) method, to study the behavior of the band gap under pressure for wurtzite  $\text{In}_x\text{Ga}_{1-x}\text{N}$ , and  $\text{In}_x\text{Al}_{1-x}\text{N}$ , and to investigate the band gap bowing dependence on pressure.

## DETAILS OF CALCULATION

The calculations are performed using the density-functional theory within the local density approximation (LDA) [12], as implemented by the non-scalar relativistic full potential linearized augmented plane waves (FP-LAPW) method (WIEN97 [13]). The LDA functional of Perdew and Wang [14] is used. We have included the 3d of Ga, and 4d of InN as valence state. In the muffin-tin (MT) spheres, the  $l$ -expansion of the non-spherical potential and charge density was carried out up to  $l_{\max}=10$ . In order to achieve energy eigenvalues convergence, the wave functions in the interstitial region were expanded in plane waves with a cutoff  $k_{\max}=8/R_{\text{mt}}$  (where  $R_{\text{mt}}$  is the average radius of the MT spheres). For the ternary alloys, we have chosen the MT radii values of 1.75 bohr for gallium, aluminum, indium, and 1.65 bohr for nitrogen.

To model the  $\text{In}_x\text{Ga}_{1-x}\text{N}$  and  $\text{In}_x\text{Al}_{1-x}\text{N}$  random wurtzite alloys, we have used 32-atom  $X_nY_{16-n}N_{16}$  supercell ( $X=\text{Al}$  or  $\text{In}$  and  $Y=\text{Ga}$  or  $\text{Al}$ ) supercell, which correspond to  $2\times 2\times 2$  supercell which has twice the size of the primitive wurtzite unit cell in both directions of the basal plane and along the  $c$ -axis. For a given number  $n=0,\dots,16$  of  $X$  atoms, different atomic configurations have been optimized structurally. However, it is impossible to treat all different atomic configurations. Therefore, for a given number  $n$  of  $X$  atoms we usually study only a small number of different configurations in which the  $X$  atoms are not really randomly distributed. For each configuration and each atomic number  $n$ , the fundamental physical properties (total energy, and band gap) are determined. The configurationally averaged quantity is computed using the Connolly-Williams approach [15] for each given  $x$ . The composition-dependent weights are determined for an ideal solid solution. We have used only the  $X_{4m}Y_{4(4-m)}N_{16}$  clusters ( $m=0,\dots,4$ ) to calculate the quantities for the entire composition region. A mesh of 7 special  $k$ -points was taken in the irreducible wedge of the Brillouin zone using the Monkhorst and Pack mesh [16]. The two dimensional minimization of the total energy vs ( $u, c/a$ ) for a fixed volume requires that each of the self consistent calculations is converged, so the iteration process was repeated until the calculated total energy of the crystal converged to less than 1 mRyd.

## RESULTS AND DISCUSSION

In a previous work, we studied the effect of the pressure on the binaries, GaN, InN, and AlN [17]. It was shown that for GaN and InN, the fundamental band gap increases and stay direct with pressure, while for AlN, the fundamental band gap becomes indirect ( $K_c-\Gamma_v$ ) at  $P=13.88$  GPa, indicating that AlN probably becomes an indirect band gap material before reaching the phase transition, at least with reference to known experimental data. For the first derivatives  $\alpha$  of the  $\Gamma_c-\Gamma_v$  band gap, our calculations give 31.8 meV/GPa for GaN, 18.8 meV/GPa for InN, and 40.5 meV/GPa for AlN.

In the ternary  $\text{In}_x\text{Ga}_{1-x}\text{N}$  and  $\text{In}_x\text{Al}_{1-x}\text{N}$  alloys, while the lattice parameters  $c$  show an almost linear variation versus concentration, the lattice parameters  $a$  deviate from VCA with a slope of  $-0.09 \text{ \AA}$  and  $-0.16 \text{ \AA}$  [18], respectively. This deviation is due to the relaxation of the In-N and Ga-N bond lengths in  $\text{In}_x\text{Ga}_{1-x}\text{N}$ , and the In-N and Al-N in  $\text{In}_x\text{Al}_{1-x}\text{N}$ . It is important for  $\text{In}_x\text{Al}_{1-x}\text{N}$ , since the lattice mismatch is larger than that of  $\text{In}_x\text{Ga}_{1-x}\text{N}$ . The band gap bowing parameter is 1.7 eV for  $\text{In}_x\text{Ga}_{1-x}\text{N}$ , and 4.09 eV for  $\text{In}_x\text{Al}_{1-x}\text{N}$  [18].

The variation of the energy gap versus volume was calculated using the equilibrium  $u$  and  $\eta$  parameters (at  $p=0$ ). Near equilibrium and at each composition, we calculated the electronic band

**BEST AVAILABLE COPY**

structures at different values of the hydrostatic pressure. The pressure behavior of the fundamental band energy is shown in figure 1 for  $\text{In}_x\text{Ga}_{1-x}\text{N}$ , and  $\text{In}_x\text{Al}_{1-x}\text{N}$ .

For  $\text{In}_x\text{Ga}_{1-x}\text{N}$  (figure 1a) and  $\text{In}_x\text{Al}_{1-x}\text{N}$  (figure 1b), the fundamental band gap decreases when In composition increases. For all In composition (25, 50, and 75 % In), the fundamental band gap ( $\Gamma_c-\Gamma_v$ ) increases and remains also direct versus pressure (from 0 to ~28 GPa). For InGaN, it increases from 1.29 to 1.78 eV for  $\text{In}_{0.25}\text{Ga}_{0.75}\text{N}$ , 0.77 to 1.55 eV for  $\text{In}_{0.5}\text{Ga}_{0.5}\text{N}$ , 0.46 to 0.79 eV for  $\text{In}_{0.75}\text{Ga}_{0.25}\text{N}$ , and for InAlN from 2.22 to 2.63 eV for  $\text{In}_{0.25}\text{Al}_{0.75}\text{N}$ , 1.31 to 1.64 eV for  $\text{In}_{0.5}\text{Al}_{0.5}\text{N}$ , and from 0.72 to 1.03 eV for  $\text{In}_{0.75}\text{Al}_{0.25}\text{N}$ . This variation is consistent with the experimental one for the InGaN [8, 9, 10].

The energy band gaps,  $E_g$ , first  $\alpha$  and second-order  $\beta$  pressure derivatives coefficients of the fundamental band gaps, bulk moduli,  $B$ , and their pressure derivatives,  $B'$ , of  $\text{In}_x\text{Ga}_{1-x}\text{N}$ , and  $\text{In}_x\text{Al}_{1-x}\text{N}$  alloys are given in table I. For  $\text{In}_x\text{Ga}_{1-x}\text{N}$  (table I), there is a decrease of the pressure coefficients with In composition from 24.8 meV/GPa for  $\text{In}_{0.25}\text{Ga}_{0.75}\text{N}$ , to 21.7 meV/GPa for  $\text{In}_{0.5}\text{Ga}_{0.5}\text{N}$ , to 19.8 meV/GPa for  $\text{In}_{0.75}\text{Ga}_{0.25}\text{N}$ . From their photoluminescence results, Shan *et al.* deduced pressure-coefficients of 39 meV/GPa for  $\text{In}_{0.08}\text{Ga}_{0.92}\text{N}$ , 40 meV/GPa for  $\text{In}_{0.11}\text{Ga}_{0.89}\text{N}$  [10], and 35 meV/GPa for  $\text{In}_{0.14}\text{Ga}_{0.86}\text{N}$  [9]. In their photoluminescence measurements and photomodulation spectroscopy [8] on  $\text{In}_x\text{Ga}_{1-x}\text{N}$  alloys ( $0 < x < 0.2$ ), they reported values of pressure coefficients of 39 meV/GPa for GaN, 39 meV/GPa for  $\text{In}_{0.04}\text{Ga}_{0.96}\text{N}$ , 35 meV/GPa for  $\text{In}_{0.08}\text{Ga}_{0.92}\text{N}$ , and 40 meV/GPa for  $\text{In}_{0.11}\text{Ga}_{0.89}\text{N}$ . From these data, no clear dependence of the pressure coefficient on alloy compositions could be drawn.

In our case, the introduction of In reduces the pressure coefficient significantly and does not lead to linear variation with alloy composition. We have a bowing parameter of 15.1 meV/GPa. The recent work of Perlin *et al.* [11] reported pressure coefficients of the  $\text{In}_x\text{Ga}_{1-x}\text{N}$  alloys using FP-LMTO and PL. They showed a dependence of the pressure coefficient of the fundamental band gap ( $\Gamma_c-\Gamma_v$ ) on alloy composition with a significant deviation from those of linear interpolation, in agreement with our calculations.

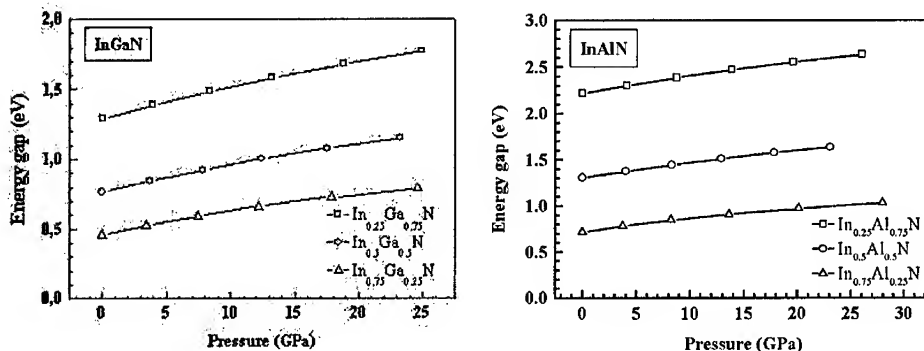


Figure 1. Variation of the fundamental energy band gap versus pressure of (a)  $\text{In}_x\text{Ga}_{1-x}\text{N}$  and (b)  $\text{In}_x\text{Al}_{1-x}\text{N}$ .

**Table I.** Energy band gaps,  $E_g$ , first  $\alpha$  and second-order  $\beta$  pressure derivatives of the fundamental band gap, bulk moduli,  $B$ , and their pressure derivatives,  $B'$ , of  $\text{In}_x\text{Ga}_{1-x}\text{N}$  and  $\text{In}_x\text{Al}_{1-x}\text{N}$ . For  $\text{In}_x\text{Ga}_{1-x}\text{N}$ , The experimental data are given from PL measurements from: <sup>a</sup>Ref. [8], <sup>b</sup>Ref. [9], and <sup>c</sup>Ref. [10], and the theoretical one from <sup>d</sup>Ref. [11].

		$E_g(0)$ (eV)	$\alpha$ (meV/GPa)	$\beta$ (meV/GPa <sup>2</sup> )	$B$ (GPa)	$B'$
<b>InGaN</b>						
This work	GaN	2.22	31.8	-0.23	207	4.37
	$\text{In}_{0.25}\text{Ga}_{0.75}\text{N}$	1.29	24.8	-0.22	186	4.35
	$\text{In}_{0.5}\text{Ga}_{0.5}\text{N}$	0.77	21.7	-0.21	177	4.05
	$\text{In}_{0.75}\text{Ga}_{0.25}\text{N}$	0.46	19.8	-0.25	157	7.04
	InN	0.17	18.8	-0.23	152	4.45
Exp.	$\text{In}_{0.04}\text{Ga}_{0.96}\text{N}$ (10 K)	3.25 <sup>a</sup>	39 <sup>a</sup>			
	$\text{In}_{0.08}\text{Ga}_{0.92}\text{N}$ (10 K)	3.08 <sup>a</sup> , 3.249 <sup>b</sup>	35 <sup>a</sup> , 39 <sup>b</sup>			
	$\text{In}_{0.08}\text{Ga}_{0.92}\text{N}$ (295 K)	3.04 <sup>a</sup>	36 <sup>a</sup>			
	$\text{In}_{0.11}\text{Ga}_{0.89}\text{N}$ (295 K)	2.86 <sup>a</sup>	40 <sup>a,c</sup>			
	$\text{In}_{0.14}\text{Ga}_{0.86}\text{N}$ (10 K)	3.08 <sup>a</sup>	35 <sup>b</sup>			
Other calc.	$\text{In}_{0.0625}\text{Ga}_{0.9375}\text{N}$		33.75 <sup>d</sup>			
	$\text{In}_{0.2}\text{Ga}_{0.8}\text{N}$		28.8 <sup>d</sup>			
	$\text{In}_{0.25}\text{Ga}_{0.75}\text{N}$		28 <sup>d</sup>			
	$\text{In}_{0.5}\text{Ga}_{0.5}\text{N}$		25 <sup>d</sup>			
<b>InAlN</b>						
This work	AlN	4.4	40.5	-0.19	214	3.88
	$\text{In}_{0.25}\text{Al}_{0.75}\text{N}$	2.22	20.7	-0.18	196	4.24
	$\text{In}_{0.5}\text{Al}_{0.5}\text{N}$	1.31	17.6	-0.14	195	2.14
	$\text{In}_{0.75}\text{Al}_{0.25}\text{N}$	0.72	16.7	-0.2	171	7.79
	InN	0.17	18.8	-0.23	152	4.45

For  $\text{In}_x\text{Al}_{1-x}\text{N}$  (table I), there is a strong dependence of the pressure coefficients on alloy composition. It varies from 20.7 meV/GPa for  $\text{In}_{0.25}\text{Al}_{0.75}\text{N}$ , to 17.6 meV/GPa for  $\text{In}_{0.5}\text{Al}_{0.5}\text{N}$ , and to 16.7 meV/GPa for  $\text{In}_{0.75}\text{Al}_{0.25}\text{N}$ , with a strong deviation from linearity. It appears that introducing In decreases the pressure coefficient significantly, for 50 and 75 % of In, the values are lower than that of InN.

From the variation of the fundamental band gap energy with alloy composition for different pressures (between 0 and 20 GPa), we calculated the band gap bowing parameter at each pressure. This is shown in figure 2 for  $\text{In}_x\text{Al}_{1-x}\text{N}$ , and  $\text{In}_x\text{Ga}_{1-x}\text{N}$ . For  $\text{In}_x\text{Al}_{1-x}\text{N}$ , the bowing parameter increases with pressure until a pressure ~14 GPa, after that it decreases rapidly. The reason is the change of the fundamental band gap in AlN from  $\Gamma$  ( $\Gamma_c-\Gamma_v$ ) to  $K$  ( $K_c-\Gamma_v$ ); the  $\Gamma_c-\Gamma_v$  band gap increases quickly in contrast to that of  $K_c-\Gamma_v$  which remains almost constant and

**BEST AVAILABLE COPY**

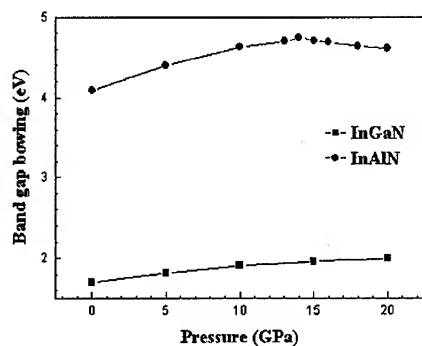


**Figure 2.** Variation of the band gap bowing parameter versus pressure of  $\text{In}_x\text{Ga}_{1-x}\text{N}$  and  $\text{In}_x\text{Al}_{1-x}\text{N}$ .

smaller than that of  $\Gamma_c-\Gamma_v$ , after the crossing of the two bands at  $p = 13.88$  GPa [17]. For  $\text{In}_x\text{Ga}_{1-x}\text{N}$ , the band gap bowing parameter increases continuously with pressure.

## CONCLUSION

In this work, we calculated the pressure coefficient of the InGaN and InAlN alloys over a wide range of composition. We see that the introduction of In in  $\text{In}_x\text{Ga}_{1-x}\text{N}$  and  $\text{In}_x\text{Al}_{1-x}\text{N}$  decreases the pressure coefficient, however this variation is not linear. We report also the variation of the fundamental band gap bowing with pressure. There is a continuous increase with pressure for  $\text{In}_x\text{Ga}_{1-x}\text{N}$ , and the same variation for  $\text{In}_x\text{Al}_{1-x}\text{N}$  until a pressure of  $\sim 14$  GPa, beyond, it decreases significantly. This is in the pressure range where we see that the fundamental band gap of AlN becomes indirect.

## ACKNOWLEDGMENTS

This work is carried out with the support of the Algerian-French Ministries of Foreign Affairs under project CMEP 01 MDU 516. (PR) acknowledges the EU support under contract No HPRN-CT-1999-00040. (BB) acknowledges the Islamic Development Bank (Jeddah, Kingdom of Saudi Arabia).

## REFERENCES

1. B. Monemar, Phys. Rev. B **10**, 676 (1974).
2. T. L. Tansley and C. P. Foley, J. Appl. Phys. **59**, 3241 (1986).
3. J. Wu, E. E. Haller, H. Lu, W. J. Schaff, Y. Saito, and Y. Nanishi, Appl. Phys. Lett. **80**, 3967 (2002).

4. V. Yu. Davydov, A. A. Klochikhin, R. P. Seisyan, V. V. Emtsev, S. V. Ivanov, F. Bechstedt, J. Furthmüller, H. Harima, A. V. Mudryi, J. Aderhold, O. Semchinova, and J. Graul, *phys. stat. sol. (b)* **229**, R1 (2002).
5. P. B. Perry and R. F. Rutz, *Appl. Phys. Lett.* **33**, 319 (1978).
6. S. Yoshida, S. Misawa, and S. Gonda, *J. Appl. Phys.* **53**, 6844 (1982).
7. O. Katz, B. Meyler, U. Tisch, and J. Salzman, *phys. stat. sol. (a)* **188**, 789 (2001).
8. W. Shan, W. Walukiewicz, E. E. Haller, B. D. Little, J. J. Song, M. D. McCluskey, N. M. Johnson, Z. C. Feng, M. Schurman, and R. A. Stall, *J. Appl. Phys.* **84**, 4452 (1998).
9. W. Shan, J. J. Song, Z. C. Feng, M. Schurman, and R. A. Stall, *Appl. Phys. Lett.* **71**, 2433 (1997).
10. W. Shan, P. Perlin, J. W. Ager III, W. Walukiewicz, E. E. Haller, M. D. McCluskey, N. M. Johnson, P. Bour, *Appl. Phys. Lett.* **73**, 1613 (1998).
11. P. Perlin, I. Gorczyca, T. Suski, P. Wisniewski, S. Lepkowski, N. E. Christensen, A. Svane, M. Hansen, S. P. DenBaars, B. Damilano, N. Grandjean, and J. Massies, *Phys. Rev. B* **64**, 115319 (2001).
12. P. Hohenberg and W. Kohn, *Phys. Rev.* **136**, B864 (1964).
13. P. Blaha, K. Schwarz, and J. Luitz, *WIEN97*, Vienna University of Technology, 1997.
14. J. P. Perdew and Y. Wang, *Phys. Rev. B* **45**, 13244 (1992).
15. J. W. D. Connolly and W. R. Williams, *Phys. Rev. B* **27**, 5169 (1983).
16. H. J. Monkhorst and J. D. Pack, *Phys. Rev. B* **13**, 5188 (1976).
17. Z. Dridi, B. Bouhafs, and P. Ruterana, *New Journal of Physics* **4**, 94.1 (2002).
18. Z. Dridi, B. Bouhafs, and P. Ruterana, *phys. stat. sol. (b)* (2002), in press.

**ELECTRICAL AND OPTICAL PROPERTIES OF InN/Si HETEROSTRUCTURE****K. Mizuo, T. Yamaguchi, Y. Saito, T. Araki and Y. Nanishi**Dept. of Photonics, Ritsumeikan Univ., 1-1-1 Noji-Higashi, Kusatsu, Shiga, 525-8577  
Japan**ABSTRACT**

Single crystalline InN films were grown on Si substrates by radio-frequency plasma-excited molecular beam epitaxy. Electrical property of InN/Si heterojunction was investigated. We obtained rectifying characteristics in n-InN/p-Si heterostructure for the first time. Forward I-V characteristics were affected by both the buffer layer deposition and the nitridation process. Strong photoluminescence peaks for both single crystalline and polycrystalline InN films grown on the Si substrates were observed at around 0.8 eV, which were smaller than the previous reported PL emission peak of around 1.9 eV.

**INTRODUCTION**

Nitride semiconductors are promising materials for photonics and electronics. However, growth and characterization as well as device application of InN have not been widely studied compared with other nitrides. This is because of the difficulty to obtain high quality InN due to its low dissociation temperature and high equilibrium vapor pressure. Thus, among nitride semiconductors, physical properties of InN have not been well known up to now enough to be applied to photonic and electronic devices. For example, InN has been understood to have a direct bandgap of 1.9 eV. However, it is reported very recently that the bandgap energy of InN is less than 1 eV [1-3]. Furthermore, high quality InN films with high electron mobility have been obtained on a sapphire substrate [4-7]. These results are getting us to explore new application fields of nitrides semiconductor.

Growth of nitride semiconductors on a Si substrate is also an important issue since using Si as a substrate can overcome several restrictions. For example, a Si substrate is easily obtained at high quality and low cost, and has a variety specification we asked for. In the case of InN growth, the lattice mismatch for a Si (111) substrate (7.6 %) is much smaller than that for a sapphire (0001) substrate (25.4 %). Furthermore, device application using hetero junction of nitride semiconductors on Si has a prospect in semiconductor technology. Some possible devices applying this combination are monolithic integration devices, tandem-type solar cells [8], light emitting diode and so on. In the case of nitride semiconductors, since N atoms are not electrically active in Si, the Si side of the interface is expected to show p-type due to possibly diffused group-III atoms from the nitride semiconductor. Therefore, hetero junction composed of InN and Si is expected to be applicable to pn junction. Recently, Yoshimoto et al. reported fabrication and characterization of InN/Si heterostructure [9,10]. They found that no rectifying characteristic was observed in the heterojunction of n<sup>+</sup>-InN/p-Si due to a large number of interface states. These results suggest that quality of the InN films grown on Si should be improved for achieving the applicable InN/Si heterojunction.

In this paper, we report on successful growth of high quality InN films with single crystalline on Si(111) substrates by radio-frequency plasma-excited molecular beam epitaxy [11,12]. Electrical properties of the InN/Si(111) heterojunction was studied. Rectifying characteristic in the n-InN/p-Si heterostructure was obtained for the first time. Effects of

initial growth processes of InN on the electrical properties were also investigated. Optical properties of InN films grown on Si (111) were also studied. We observed photoluminescence emission at about 0.8 eV for both single crystalline and polycrystalline InN films grown on the Si substrates.

## EXPERIMENTAL

Epitaxial n-InN films were grown on a Si (111) substrate by RF-MBE. The elemental indium (In) was evaporated from a standard Knudsen effusion cell, and RF-plasma source (SVT associates model 4.5) with mass-flow controlled  $N_2$  gas was used to obtain excited nitrogen. The substrates used in this study were p-type conductivity with a resistivity of 0.02  $\Omega\text{cm}$ . Prior to growth, Si substrates were cleaned by organic solutions, etched in HF solution and thermally cleaned over 800°C for 20 min under a pressure of  $1 \times 10^{-9}$  Torr in the growth chamber such that they showed a clear (7×7) reflection high-energy electron diffraction (RHEED) pattern of a clean Si (111) surface. InN films were then grown at 390°C for 1 hour after substrate nitridation and low temperature buffer layer deposition. For comparison, InN films were also directly grown without these initial growth processes. In situ RHEED observations were carried out during growth. The film thickness determined by a mechanical profilometer (DECTAK<sup>3</sup>) was ~250 nm. Aluminum used as contact material was deposited by vacuum thermal evaporation for investigating the electrical properties. The carrier densities were measured by Hall effect measurement at room temperature using van der Pauw method. Forward ( $I_F$ - $V_F$ ) and reverse ( $I_R$ - $V_R$ ) current-voltage curves were measured at room temperature. Optical properties of the InN films were also investigated by photoluminescence (PL). PL measurements were carried out using Ar<sup>+</sup> laser at 77K in the spectral range from 600 to 1700 nm.

## RESULTS AND DISCUSSION

Figure 1 shows RHEED patterns of InN films grown on Si substrates. As shown in Fig. 1(b), when InN film was directly grown on Si substrates, a ring pattern was observed, indicating that polycrystalline InN with poor c-axis orientation was obtained. Using a low temperature InN buffer layer, the RHEED pattern shown in Fig. 1(c) changes a spotty pattern. It is found that c-axis orientation of InN films grown on Si (111) is improved by the low temperature InN buffer layer. However, a double domain structure was still observed as shown in Fig. 1(c) by an arrow, indicating a-axis orientation of InN was random. Figure 1(d) shows a RHEED pattern of the InN film grown after substrate nitridation and the buffer layer deposition. A clear streak pattern of a single domain structure was observed. From these results, we confirmed that single crystalline InN film was successfully grown on Si (111) substrate using the nitridation and the buffer layer deposition.

The InN films used in this study showed n<sup>+</sup>-type conductivity without an intentional doping. The carrier density of InN films was about  $1 \times 10^{21} \text{ cm}^{-3}$ . The current-voltage (I-V) characteristics of InN/Si grown with the low temperature buffer layer are shown in Fig. 2. All heterostructure measured showed rectification at room temperature. The n-InN/p-Si heterostructure exhibited a breakdown voltage of about 4.3 V. A high current could be derived at forward voltage drops of 0.6 ~ 1 V. The I-V characteristics showed an exponential dependence of the current on voltage:  $I = I_0 \exp(qv/nkT)$ . The minimum value of the ideality factor n was about 2.5.

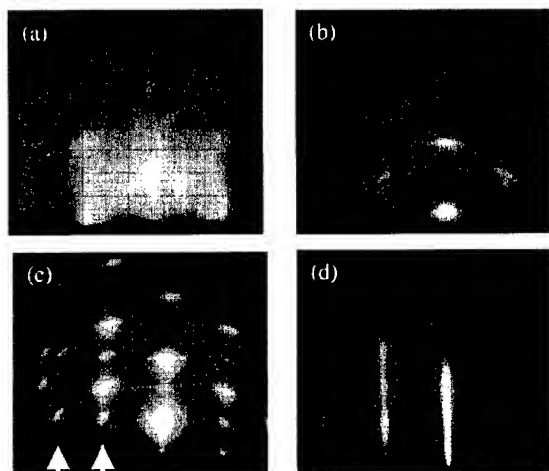


**Figure 1** RHEED patterns of the InN films grown on Si (111); (a) Si(111) substrate, (b) directly growth, (c) with the low temperature buffer layer deposition and (d) with both substrate nitridation and the buffer layer deposition.

Effects of growth processes on the electrical properties of InN/Si heterojunction were investigated. Figure 3 shows I-V characteristics of four types of n-InN/p-Si heterojunctions at room temperature. As shown in Fig. 3(a) and (b), using the buffer layer growth, I-V characteristic of the InN/Si heterojunction was improved compared to the heterojunction in which InN was directly grown on Si. On the other hands, the I-V characteristic was remarkably changed by introducing the nitridation process of Si, and showed similar profile with the InN/Si heterojunction formed without chemical cleaning of Si before InN growth as shown in Fig. 3(c) and (d). As we discussed before in this paper, the nitridation process improved crystallinity of the InN film. However, the InN/Si heterojunction in which InN was grown with the nitridation process exhibited a poor electrical property. These results suggest that the nitridation process has harmful effects on the heterojunction of InN/Si due to possibly formed defects at the interface. We can notice that a new initial growth process without the nitridation process of Si should be considered to realize improvements of both crystal quality and electrical property of InN/Si heterojunction simultaneously.

Figure 4 shows the PL spectrum at 77K from the single crystalline and polycrystalline InN films grown on Si substrates, corresponding to RHEED patterns of Fig. 1(d) and Fig. 1(b), respectively. A strong peak was observed at about 0.8 eV ( $\lambda \approx 1550\text{nm}$ ) for both InN films with single crystalline and polycrystalline. The luminescence peak energy is consistent with recent reports for InN films grown on sapphire substrates. PL peak couldn't be observed at near 1.9 eV (650 nm), which was the previously reported value of bandgap energy of InN. These results confirmed that origin of the difference in InN bandgap between 0.8 eV and 1.9 eV is not depend on neither substrates for InN growth (Si or sapphire) and crystallinity of InN (single or poly). On the other hand, Yodo et al. recently confirmed a PL peak at about 1.8 eV for InN films grown on Si by ECR-MBE [13]. At this moment, reasonable explanation to understand these different results on PL emission of InN is not established. Further study should be necessary for carrier concentration and oxygen incorporation of these InN films, which seem to affect the bandgap of InN [1,14].

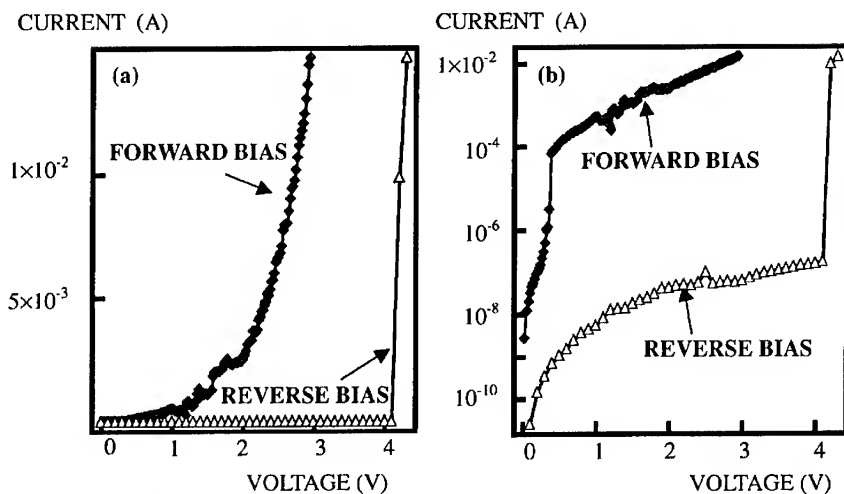


**Figure 2.** I-V characteristics for n-InN/p-Si heterostructure at room temperature. (a) Linear I-V characteristics. (b) Logarithmic I-V characteristics.

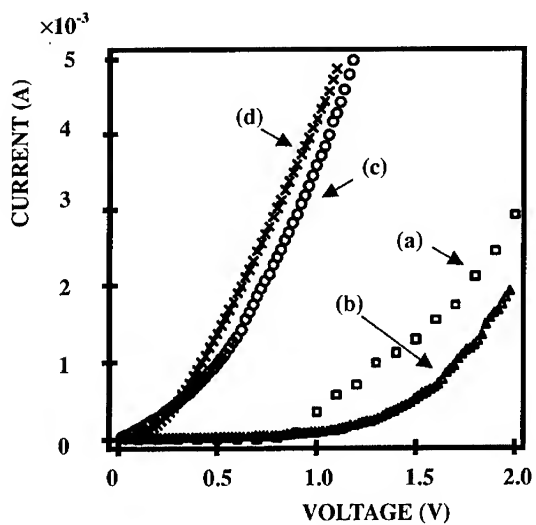


**Figure 3.** I-V characteristics of n-InN/p-Si heterojunction at room temperature. (a) InN film directly grown on Si substrate. (b) InN film grown with low temperature buffer layer deposition on Si substrate. (c) InN film grown with low temperature buffer layer deposition and substrate nitridation on Si substrate. (d) InN film directly grown on Si substrate without chemical cleaning by HF solution.

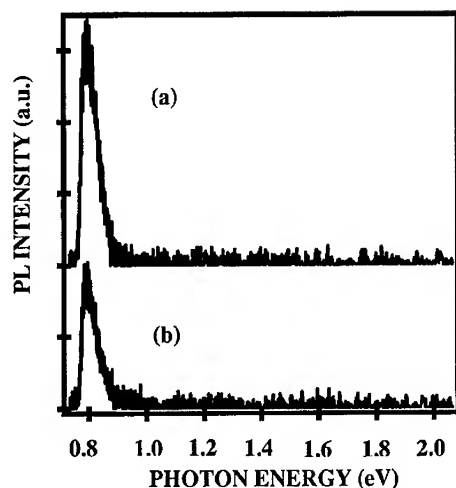


**Figure 4.** PL spectrum at 77K for InN films on Si substrate. (a) polycrystalline InN film. (b) single crystalline InN film.

## Conclusion

Purely hexagonal single crystalline InN films grown on Si substrates could be obtained by using appropriate initial growth processes. Clear rectifying characteristics in n-InN/p-Si heterostructure were obtained. However, it was found the nitridation process has harmful effects on the heterojunction of InN/Si due to possibly formed defects at the interface. We can notice that a new initial growth process without the nitridation process of Si should be considered to realize improvements of both crystal quality and electrical property of InN/Si heterojunction simultaneously.

Strong PL peaks of both single crystalline and polycrystalline InN on Si substrates were observed at around 0.8 eV, which were smaller than reported PL emission peak of about 2 eV. These results confirmed that origin of the difference in InN bandgap between 0.8 eV and 1.9 eV is not depend on neither substrates for InN growth (Si or sapphire) and crystallinity of InN (single or poly).

## Acknowledgements

The author would like to thank Prof. Nishino at Kyoto Institute of Technology for helpful discussion. This work was partially supported by the Ministry of Education, Culture, Sports, Science and Technology, Grant-in-Aid for Scientific Research (B) #13450131, 2002 and Academic Frontier Promotion Project.

## References

1. V. Y. Davydov, A. A. Klochikhin, R. P. Seisyan, V. V. Emtsev, S. V. Ivanov, F. Bechstedt, J. Furthmuller, H. Harima, A. V. Mudryi, J. Aderhold, O. Semchinova and J. Graul; *phys. stat. sol. (b)* **229** (2002) R1.
2. J. Wu, W. Walukiewicz, K. M. Yu, J. W. Ager III, E. E. Haller, H. Lu, J. Schaff, Y. Saito and Y. Nanishi; *Appl. Phys. Lett.* **80** (2002) 3967.
3. T. Matsuoka, H. Okamoto, M. Nakao, H. Harima and E. Kurimoto; *Appl. Phys. Lett.* **81** (2002) 1246.
4. Y. Saito, N. Teraguchi, A. Suzuki, T. Araki and Y. Nanishi; *Jpn. J. Appl. Phys.* **40** (2001) L91.
5. Y. Saito, T. Yamaguchi, H. Kanazawa, K. Kano, T. Araki, Y. Nanishi, N. Teraguchi and A. Suzuki; *J. Cryst. Growth* **237** (2002) 1017.
6. H. Lu, W. J. Schaff, J. Hwang, H. Wu, G. Koley and L. F. Eastman; *Appl. Phys. Lett.* **79** (2001) 1489.
7. M. Higashiwaki and T. Matsui; *Jpn. J. Appl. Phys.* **41** (2002) L540.
8. A. Yamamoto, M. Tsujino, M. Ohkubo and A. Hashimoto; *Solar Energy Mater. Solar Cells* **35** (1994) 53.
9. M. Yoshimoto, T. Nakano, T. Yamashita, K. Suzuki and J. Saraie; *IPAP conf. Series* **1** (2000) 186.
10. M. Yoshimoto, Y. Yoshiaki and J. Saraie; *Extended Abst. of 21st Electronic Materials Symposium* (2002) B2.
11. T. Yamaguchi, K. Mizuo, Y. Saito, T. Araki, N. Teraguchi, A. Suzuki and Y. Nanishi; *Extended Abst. of 21<sup>st</sup> Electronic Materials Symposium* (2002) C3.
12. T. Yamaguchi, K. Mizuo, Y. Saito, T. Araki and Y. Nanishi; *Int. Symp. Comp. Semicond. in Lausanne*. (2002) Mo-P-7.
13. T. Yodo, H. Yona, H. Ando, D. Nosei and Y. Harada; *Appl. Phys. Lett.* **80** (2002) 968.
14. V. Yu. Davydov, A. A. Klochikhin, V. V. Emtsev, S. V. Ivanov, V. V. Vekshin, F. Bechstedt, J. Furthmuller, H. Harima, A. V. Mudryi, A. Hashimoto, A. Yamamoto, J. Aderhold, J. Graul and E. E. Haller; *phys. stat. sol. (b)* **230** (2002) R4.

### Optical Properties of Controllable Self-Assembled Lateral Nanostructures on InN, InAlN, and AlN Thin Films

Yuri Danylyuk,\* Dmitri Romanov,\*\*\* Eric McCullen,\* Daad Haddad,\*\* Ratna Naik,\*\* and Gregory Auner\*

\*Department of ECE, Wayne State University, Detroit, MI 48202, U.S.A.

\*\*Department of Physics, Wayne State University, Detroit, MI 48202, U.S.A.

\*\*\*Department of Physics, Temple University, Philadelphia, PA 19122, U.S.A.

#### ABSTRACT

Utilizing plasma source molecular beam epitaxy (PSMBE), we have grown epitaxial  $\text{In}_x\text{Al}_{1-x}\text{N}$  films on (0001) sapphire substrates; the indium concentration,  $x$ , varied from 0 to 1. The atomic force microscopy of the films reveals characteristic surface patterns of nanometer scale. The feature size distribution is determined by the film composition and thickness. Both absorption and reflection spectra of the films have additional peaks below the fundamental absorption threshold. These peaks cannot be associated with N vacancies or any other known crystal defects and impurities. We attribute the peaks to electron confinement in the hillocks of the lateral structure by the strong electric field of piezoelectric and spontaneous polarization that is characteristic to nitride semiconductor compounds. The calculated values of the electron energy levels are in good agreement with the spectroscopic data; moreover, the electron confinement model explains the observed temperature dependence of the additional peaks. The hillock size control will allow one to control the optical and transport properties of the films.

#### INTRODUCTION

Ternary alloys of AlN and InN have been studied extensively in the regard of their potential application in light-emitting and laser diodes [1], primarily because of their wide direct band gap, tunable by composition and ranging from 0.7 eV for InN[2], to 6.2 eV for AlN. The devices, based on quantum wells or on self-assembled arrays of quantum dots, are expected to cover wavelength region from ultraviolet to near infrared light. Given excellent radiation and thermal stability of the materials, such devices will be especially useful in space and medical applications. However, the progress toward these goals is impeded by technological difficulties of the  $\text{Al}_{1-x}\text{In}_x\text{N}$  film growth [3-6]. These difficulties are associated with spinodal phase separation that frustrates solubility between AlN and InN [7]. Various substrates and various growth techniques have been tried to achieve reliable growth of  $\text{Al}_{1-x}\text{In}_x\text{N}$  thin films: metal-organic vapor phase epitaxy [1], magnetron reactive sputtering [3,6], metal-organic chemical-vapor deposition [4], and microwave-excited metalorganic vapor phase epitaxy [5]. The films obtained varied from spontaneously segregated polycrystalline to highly oriented epitaxial. In the present work, we have studied a series of  $\text{Al}_{1-x}\text{In}_x\text{N}$  alloy films with thickness ranging from 100 nm to 8000 nm and In concentration ranging from 0 to 1. We have identified the presence of a large number of bulges as the specific feature of the film morphology. We focused our attention on how the bulge structure depend on the film composition and growth conditions, and studied theoretically and experimentally the electron localization in the bulges.

## EXPERIMENT

The films of InN, InAlN, and AlN/c-Al<sub>2</sub>O<sub>3</sub> were grown by plasma source molecular beam epitaxy (PSMBE) with unique two Al (99.999%) and In (99.9999%) magnetron-like hollow cathode cells. RF power usually was in range 300 - 40 (Wt). Hollow cathode bias was -500 to -150 V, the ratio of Ar/N<sub>2</sub> flow was 40/10 (SCCM). The system operates at base vacuum  $P_b < 5 \times 10^{-9}$  Torr and dynamic pressure  $P_d = 1 \times 10^{-4} - 1 \times 10^{-3}$  Torr. The growth of AlN buffer layer includes a temperature ramp from 350-400°C. The growth temperature was 400 - 650°C for AlN films and 375°C for InN and InAlN films. The negative substrate bias ranged from -12 to -5 V. Distance from the center of hollow cathode cells to substrate was 80 - 175 mm. The values of In mole fraction have been extracted from (0002) XRD peak position ( $\Theta/2\Theta$ -scans RIGAKU CuK $\alpha$  x-ray spectrometer) and corrected by taking into account for the deviation from Vegard's law. The reflection, transmission, and absorption measurements have been performed using a Perkin-Elmer  $\lambda$ -900 spectrometer with resolution of 1 nm for the wavelength range of 175-3300 nm at 700 K - 71 K temperatures. The atomic force microscopy (AFM) was performed using Molecular Image PICOSPM. The properties of the films are summarized in Table 1.

**Table 1.** The growth conditions and the properties of thin AlInN films.

Sample on c-pl Al <sub>2</sub> O <sub>3</sub>	x (In) (%)	Buffer layer (Å)	Temp. of gr. (°C)	Thickn. of film (nm)	Temp. of gr. (°C)	Structure XRD $\Theta/2\Theta$ -sc.	E <sub>g</sub> optical (eV)	E <sub>h</sub> optical (eV)
#702,AlN	0	200	400	8000	650	Epitaxial	6.2	-
#307,AlN	0	200	400	1000	650	Epitaxial	6.2	-
#702a,AlN	0	-	-	40	400	Epitaxial	5.6	-
#219c,AlInN	20			136		Epitaxial		
#221c,AlInN	40			143	400	Epitaxial		2.21
#814a,AlInN	55	50	400	184	400	Epitaxial	3.6	2.8,1.9
#220c,AlInN	70			143		Epitaxial		
#801,AlInN	82	50	400	100	475	Polycr.	2.6	
#215c,AlInN	90					Epitaxial		
#1114,InN	100	30	325	250	325	Polycr.	1.8-1.9	
#2202,InN	100	-	-	530	475	Epitaxial	1.5	1.3

The AFM studies indicate that the surface of the films contains a large number of bulges, whose typical size depends on the growth temperature and composition. Fig. 1 shows the film surface for an Al<sub>0.45</sub>In<sub>0.55</sub>N film with an AlN buffer layer grown at 400°C (left panel) and for an InN film grown at 475°C without the buffer layer (right panel). For Al<sub>0.45</sub>In<sub>0.55</sub>N film, the average in-plane size of a bulge is 600 Å, the average height of a bulge is 100 Å, while the underlying film thickness is about 800 Å; the density of bulges is  $5 \times 10^8$  cm<sup>-2</sup>. For InN film, the bulge in-plane size is 1100 Å, the bulge height is 150 Å, and the underlying film thickness is about 5000 Å.

The parts of typical absorption curves near the absorption threshold are shown in Fig. 2 for Al<sub>0.45</sub>In<sub>0.55</sub>N (right) and for InN (left). On the right curve, two deep energy levels are clearly seen that are separated by about 1 eV from the conduction band and from each other. On the left curve, there is one deep energy level, about 0.2 eV below the conduction band edge.

**BEST AVAILABLE COPY**

these vacancies are known to act as shallow donors with activation energy in the range of 5 - 70 meV [8]. Such donors would only lead to a smearing of the absorption edge [3].

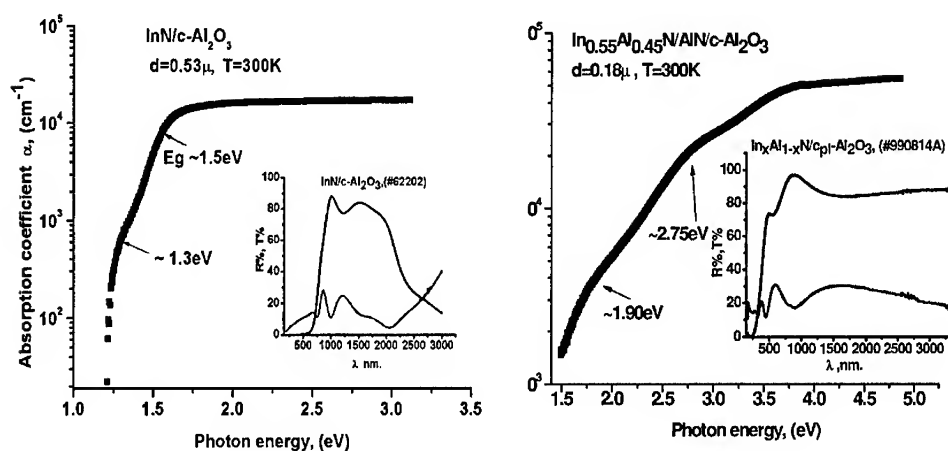
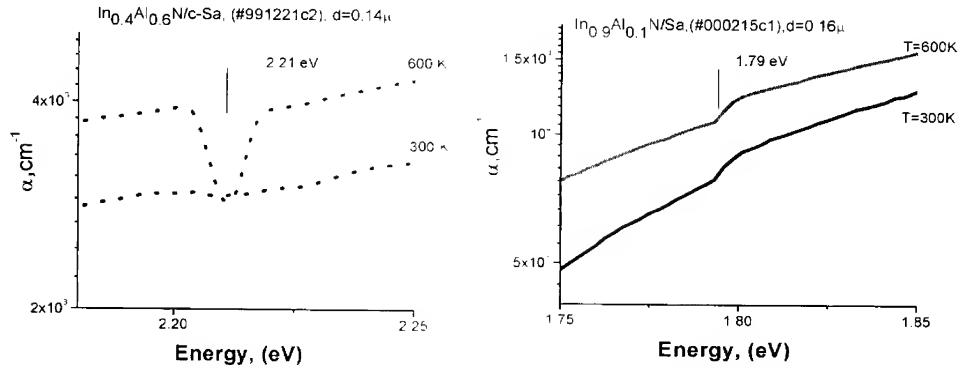


Fig. 2. The absorption coefficient of thin films of InAlN on 100 Å buffer layer (right panel) and InN without buffer layer (left panel) near the absorption threshold. The inserts represent the transmission and reflection coefficients.

Further insight into the nature of the unusual features of the absorption curves is brought about by their temperature dependence. We found out that the additional absorption peaks become more pronounced with growing temperature, as shown in Fig. 3. This behavior is quite unlike the usual temperature smearing of absorption peaks.



**Fig. 3** Temperature evolution of additional absorption peaks for  $\text{In}_{0.4}\text{Al}_{0.6}\text{N}$  film (left panel) and  $\text{In}_{0.9}\text{Al}_{0.1}\text{N}$  film (right panel).

In the following section, we offer a possible explanation of these unusual additional features of the absorption curve as being caused by electron states localized in the bulges. We estimate the characteristic localization energies and show that they lie in the range of the observed levels.

## DISCUSSION

The bulges by themselves could not provide the electron quantization except for extremely low temperatures, because the typical bulge size is  $100\div150$  Å on the background of  $>1000$  Å-thick film. The additional confining mechanism is the strong built-in electric field existing in nitride-compound films. The wurtzite symmetry allows spontaneous polarization, with typical values of  $-0.08$  C/m<sup>2</sup> for AlN and  $-0.03$  C/m<sup>2</sup> for InN [9]. In addition, the piezoelectric coefficients of the nitride compounds are an order of magnitude larger than in traditional III-V, leading to strong piezoelectric polarization of a biaxially strained layer,

$$P_z = 2d_{31} \left( c_{11} + c_{12} - 2 \frac{c_{13}^2}{c_{33}} \right) u_{xx}, \quad (1)$$

where  $d_{31}$  is the relevant component of the piezoelectric tensor,  $c_{ij}$  are the elastic constants, and  $u_{xx}=u_{yy}$  are the in-plane components of the strain tensor. For a pseudomorphic layer of AlN on sapphire,  $u_{xx} \approx 0.12$ ; for InN on sapphire,  $u_{xx} \approx 0.23$  [10]. The coefficient of  $u_{xx}$  in Eq. (1) is almost the same for AlN and InN and is about  $-0.90$  C/m<sup>2</sup>. The total polarization induces electrostatic field  $\mathcal{E} \approx 1.5$  V/nm in InN/AlN/Sapphire structure and  $\mathcal{E} \approx 0.6$  V/nm in InN/Sapphire structure. These fields are strong enough to cause effective electron quantization near the top of a bulge.

To estimate energies of the resulting quantum states, we model a bulge as a parabolic tip,

$$z = z_0 - \rho^2 / R \quad (2)$$

**BEST AVAILABLE COPY**

Here, the film lies in the  $xy$  plane, the  $z$  axis is directed outward the substrate;  $z_0$  and  $R$  are the height and the curvature radius of the bulge. In this case, the parabolic coordinate system,  $\xi, \eta$ , is the natural choice, so that the bulge surface of Eq. (2) coincides with the coordinate surface  $\xi = \xi_0 = R(m^* eE / 2\hbar^2)^{1/3}$ . In these coordinates, the electron wavefunction is factorized,  $\psi(\xi, \eta) = \chi_1(\xi)\chi_2(\eta)$ , the functions  $\chi_1(\xi)$  and  $\chi_2(\eta)$  being determined by the system of two ordinary differential equations,

$$\frac{d^2 \chi_1}{d\xi^2} + \frac{1}{\xi} \frac{d\chi_1}{d\xi} + \left( \frac{\varepsilon}{4} - \frac{C}{\xi} + \frac{\xi}{8} \right) \chi_1 = 0; \quad \frac{d^2 \chi_2}{d\eta^2} + \frac{1}{\eta} \frac{d\chi_2}{d\eta} + \left( \frac{\varepsilon}{4} - \frac{C}{\eta} + \frac{\eta}{8} \right) \chi_2 = 0, \quad (3)$$

coupled through the variable separation constant,  $C$ , and the dimensionless electron energy,  $\varepsilon$ . The total energy of the localized electron state is then determined as

$$E(N, M, z_0, R) = \left( \frac{(e\hbar)^2}{2m} \right)^{1/3} \varepsilon(N, M, \xi_0) - eEz_0, \quad (4)$$

where the quantum numbers  $N$  and  $M$  correspond to the  $\xi$ -coordinate and the  $\eta$ -coordinate, respectively, and  $m$  is the electron effective mass. Typical curves of  $\varepsilon$  as a function of  $\xi_0$  are shown in Fig. 4. When  $\xi_0$  increases, the positive contribution to the localized state energy rapidly decreases, resulting in overall increase of the binding energy in Eq. (4).

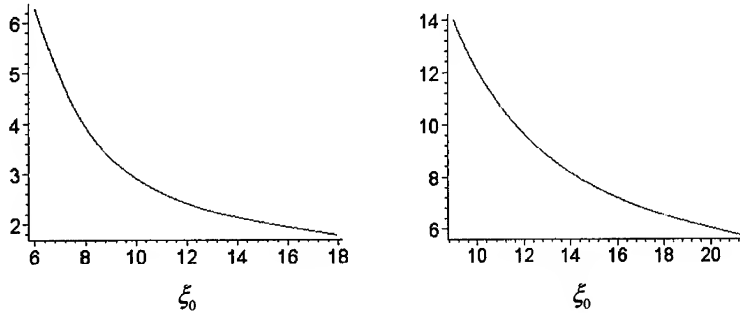


**Fig. 4.** The energy levels of electron states in a bulge as a function of the bulge curvature radius, for the quantum numbers  $N = 0, M = 0$  (left panel) and  $N = 1, M = 2$  (right panel).

For numerical estimates, we considered two cases, in accordance with morphology of the films: (i) the film  $\text{Al}_{0.5}\text{In}_{0.5}\text{N}$  on a buffer layer of  $\text{AlN}$  on sapphire, with  $z_0 = 100 \text{ \AA}$  and  $R = 360 \text{ nm}$ ; (ii) the film  $\text{InN}$  on sapphire, with  $z_0 = 150 \text{ \AA}$  and  $R = 820 \text{ nm}$ . In case (i), we obtain the energies of the first two localized states, those of  $N = 0, M = 0$  and  $N = 0, M = 1$  as  $-1.8 \text{ eV}$  and  $-1 \text{ eV}$ ; in case (ii), the energy of these states are  $-0.17 \text{ eV}$  and  $-0.05 \text{ eV}$ . Thus, the model predicts the energy level values that are in good agreement with the obtained absorption data. These results correlate with recent numerical simulations of small GaN quantum dots [11] and with experimental results on exciton localization in GaN quantum wells [12]. Additional evidence of the electron localization in the bulges is the unusual temperature dependence of the absorption peaks (see Fig. 3). This dependence concurs with our model, because the very electric field that localizes electrons should shove the holes off the tips. This spatial separation of the electrons and

the holes impedes their radiative recombination, unless at higher temperatures. More convincing support of our interpretation can be obtained from the future photoluminescence measurements.

## CONCLUSIONS

We have investigated  $\text{Al}_{1-x}\text{In}_x\text{N}$  films grown by plasma source molecular beam epitaxy on c-plane sapphire (0001) substrates with thin buffer layers of AlN and without such layers. In both cases, we succeeded to obtain films of good epitaxial quality. The common feature of all the obtained thin films is a bas-relief structure of their surface, containing a large number of self-assembled bulges. Absorption spectra of these nanostructures have additional peaks that can be only associated with additional energy levels. We ascribe these levels to electrons, which are confined and quantized in the bulges by strong built-in electric field caused by piezoelectric polarization due to biaxial strain and by spontaneous polarization. This field is capable of capturing and quantizing the electrons near the tops of the bulges. The electron binding energy grows with the bulge height and decreases with the bulge curvature radius. Calculated values of the electron confinement energy are in good agreement with the absorption data. The temperature dependence of the additional peaks also confirms the picture of electron localization and electron-hole separation by the built-in electric field. The electron energy levels may be modified and modulated by external electric field. Photoluminescence experiments are proposed for further investigation of the quantum dots of a new kind.

## ACKNOWLEDGMENTS

This work was supported by the Center for Smart Sensors and Integrated Microsystems at Wayne State University and by NSF-IGERT Grant No. 9870720.

## REFERENCES

1. Y. Arakawa, T. Someya, and K. Tachibana, *Phys. Stat. Sol. (b)* **224**, 1 (2001).
2. J. Wu, W. Walukiewicz, K.M. Yu, J.W. Ager III, E.E. Haller, Hai Lu, and William J. Schaff, *Phys. Rev. B* **66**, 201403 (2002).
3. S. Yamaguchi, M. Kariya, S. Nitta, T. Takeuchi, C. Wetzel, H. Amano, I. Akasaki, *Appl. Phys. Lett.* **76**, 876 (2000) and references therein.
4. T. Peng, J. Piprek, G. Qui, J.O. Olowofaje, K.M. Unruh, C.P. Swann, E. F. Shubert, *Appl. Phys. Lett.* **71**, 2439 (1997).
5. K.S. Kim, A. Saxler, P. Kung, M. Razaghi, K.Y. Lim, *Appl. Phys. Lett.* **71** (1997) 800.
6. K. Kubota, Y. Kobayashi, K. Fujimoto, *J. Appl. Phys.* **66** 2984 (1989).
7. O. Guo, H. Ogawa and A. Yoshida, *J. Cryst. Growth* **146**, 462 (1995).
8. S.C. Jain, M. Willander, J. Narayan, and R. Van Overstraeten, *J. Appl. Phys.* **87**, 965 (2000).
9. V. Fiorentini, F. Bernardini, and D. Vanderbilt, *Phys. Rev. Lett.* **79**, 3958 (1997).
10. Y.-X. Li, L. Salamanca-Riba, K. Wongchotingul, P. Zhou, M.G. Spence, and V.K. Jones, *Mat. Res. Soc. Symp. Proc.* Vol.482, p. 137 (1998).
11. A.D. Andreev, J.R. Downes, and E.P. O'Reilly, *Mat. Res. Soc. Symp. Proc.* 639 G11.25.1-G11.256 (2001).
12. P. Lefebvre, J. Allegre, B. Gil, H. Mathieu, N. Grandjean, M. Leroux, J. Massies, and P. Bigenwald, *Phys. Rev. B* **59**, 15363-15367 (1999).

**BEST AVAILABLE COPY**

### A Study of the Decomposition of GaN during Annealing over a Wide Range of Temperatures

M.A. Rana<sup>1</sup>, H.W. Choi<sup>2</sup>, M.B.H. Breese<sup>1</sup>, T. Osipowicz<sup>1</sup>, S.J. Chua<sup>2</sup> and F. Watt<sup>1</sup>

<sup>1</sup>Research Center for Nuclear Microscopy, Department of Physics, National University of Singapore, Singapore 117542

<sup>2</sup>Department of Electrical Engineering, Center for Optoelectronics, National University of Singapore, Singapore 119260

#### ABSTRACT

Annealing experiments were carried out on gallium nitride layers, which were grown on sapphire through Metal Organic Chemical Vapor Deposition (MOCVD). Rutherford Backscattering Spectrometry (RBS) was performed on as-grown and annealed GaN samples using a 2 MeV proton beam to study the stoichiometric changes in the near-surface region (750 nm) with depth resolution better than 50 nm. No decomposition was measured for temperatures up to 800 °C. Decomposition in the near-surface region increased rapidly with a further increase of temperature, resulting in a near-amorphous surface-region for annealing at 1100 °C. The depth profiles of nitrogen and incorporated oxygen in the decomposed GaN are extracted from the nanoscale RBS data for different annealing temperatures. The surface roughness of the GaN layers observed by atomic force microscopy (AFM) is consistent with RBS decomposition measurements. We describe the range of annealing conditions under which negligible decomposition of GaN is observed, which is important in assessing optimal thermal processing conditions of GaN for both conventional and nanoscale optoelectronic devices.

#### INTRODUCTION

Ultraviolet (UV) and blue wavelengths have numerous applications in optical communication systems, full-color displays and data storage etc. [1]. Therefore, wide bandgap semiconductors, specifically gallium nitride and related materials have great potential for highly efficient blue and UV light emitting diodes (LEDs) and laser diodes (LDs). These materials are also suitable for high temperature devices. Gallium nitride and its alloys are now also of interest due to their use in electronic and optoelectronic nanoscale devices as nanowires and nanorods [2-3]. All these applications are possible due to the wide direct band gap of GaN, the possibility of band gap engineering and its high bond strength and high melting temperature (>1700 °C) [4-7].

High temperature annealing of GaN is an important step in producing blue and UV light emitters and high temperature devices. However, annealing above a certain temperature can cause decomposition of gallium nitride, especially near the surface, where evaporated nitrogen and gallium leave vacancies, which may result in the incorporation of oxygen. This incorporation of oxygen can cause n-type conductivity in initially p-type gallium nitride as discussed in theoretical studies from Mattila and Nieminen [8] and Park and Chadi [9]. A number of authors [10-14] have reported annealing results of gallium nitride but there have not been any studies of the elemental depth distributions in annealed GaN.

We have determined the elemental depth distribution of annealed GaN samples with resolution better than 50 nm in the near-surface region (up to 750 nm) using 2 MeV

backscattered protons. Our results give information on the thermal stability of gallium nitride over a wide range of temperatures and describe quantitatively the evaporation of nitrogen and gallium after decomposition during annealing. Incorporation of oxygen during annealing is also quantified. We describe the range of annealing conditions under which negligible decomposition of gallium nitride is observed. This is important in assessing optimal thermal processing conditions of GaN during device fabrication and operational temperature of GaN based high-temperature devices. Our results of thermal behavior of the near-surface region of GaN with nanoscale depth resolution are also useful for fabrication and operation of GaN based nanoscale devices.

## EXPERIMENTAL DETAILS

Annealing experiments were carried out on GaN layers, which were grown on sapphire through Metal Organic Chemical Vapor Deposition (MOCVD), on top of a 25 nm thick low temperature GaN buffer layer. The samples were annealed at temperatures between 500 and 1100 °C for a time interval of 60 seconds, with ramp up and down times of 20 seconds. Annealing was carried out in nitrogen ambient and samples were kept uncapped during annealing to study the process of decomposition. The sample temperature was maintained within  $\pm 5$  °C from the set temperature during annealing of all the samples.

RBS measurements were carried out using the 3.5 MeV Singletron accelerator at Research Center for Nuclear Microscopy, National University of Singapore. The backscattered protons were detected using a semiconductor surface barrier detector of resolution 13 keV and an area of 50 mm<sup>2</sup>. The detector was located at a scattering angle of 160°. The total beam fluence used for each measurement was 5-10  $\mu$ C. AFM measurements were also carried out on the same as-grown and annealed GaN samples using the tapping mode.

## RESULTS AND DISCUSSION

RBS measurements were carried out on as-grown and all the annealed GaN samples. Figure 1 shows proton backscattering spectra from GaN samples annealed at different temperatures. Stoichiometric changes are observed in the near-surface region during annealing. The different depth scales for gallium, nitrogen and oxygen are indicated, only selected spectra are shown in figure 1 to avoid overlapping. These spectra allow the quantitative depth resolved determination of stoichiometric changes in GaN samples under different annealing conditions. The presence of oxygen in the near-surface region after annealing of GaN samples can be seen clearly. Oxygen was present as an impurity in the ambient nitrogen, which was used during annealing experiments. With increasing temperature, nitrogen and gallium can diffuse from deeper regions to the surface. This decomposition of GaN initiates two processes. One is the displacement of atoms to new equilibrium lattice positions and the other is the diffusion of oxygen from the ambient into the GaN to fill the vacancies produced by evaporation of nitrogen and gallium.

The near-surface region becomes depleted of gallium and nitrogen during annealing due to evaporation. Figure 2 shows the percentage nitrogen (a) and oxygen (b) atoms in annealed

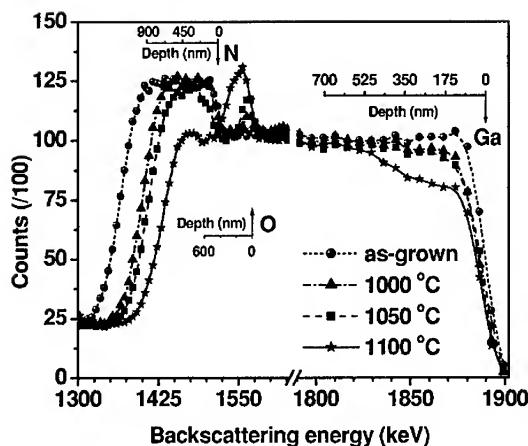


Fig. 1. Proton backscattering spectra from GaN samples annealed at different temperatures for 60 seconds. The spectrum region between 1600-1800 keV has been omitted to highlight the variation of the signal for gallium, oxygen and nitrogen. Vertical arrows show the positions at which signals from gallium, oxygen and nitrogen atoms at the surface are expected to appear. Lines are drawn to guide the eye.

gallium nitride samples as a function of depth. These percentage fractions of above-mentioned species are determined by fitting the random spectra of as-grown and annealed GaN samples using the simulation code SIMNRA [15]. At temperatures above 1000 °C, the width of the depleted region extends at least 100 nm beyond the oxygen-incorporated region.

It is well known that hydrogen enhances incorporation of Mg-dopant in GaN due to the formation of Mg-H complexes, but it must be removed by post-growth annealing [16-17]. The presence of hydrogen is responsible for low p-type conductivity of GaN [18]. Oxygen presence in the ambient during low temperature annealing (up to 600 °C) is useful for activation of Mg-doped GaN [18-19]. Our results show that decomposition of GaN and changes in its stoichiometry is negligible during annealing at temperatures lower than 800 °C, at least for time intervals of 60 seconds. So, ambient nitrogen including oxygen as a fraction can be used during annealing (up to 800 °C) for removal of incorporated hydrogen during Mg-GaN growth.

Figure 3 shows AFM images showing the surface morphologies of as-grown and selected annealed GaN samples. Corresponding annealing temperatures are shown in the figure. Different scales are used along the z-axis because the large changes in texture make it difficult to see the morphology of all the samples at one scale. Surface morphology improves up to 800 °C but degrades with further increase of annealing temperature. This is further indicated in figure 4, which gives the rms roughness of as-grown and annealed GaN samples. During annealing up to 800 °C, incomplete layers on the surface of as-grown samples are smoothened, which decreases surface roughness. Annealing of gallium nitride above 800 °C causes measurable decomposition and at the highest temperature (1100 °C), almost completely disordered near-surface region is observed.

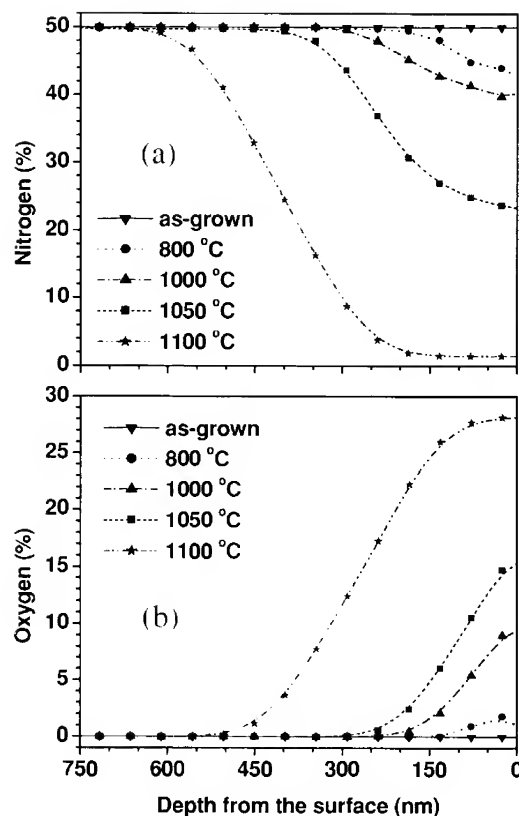


Fig. 2. Percentage nitrogen (a) and oxygen (b) in the near-surface region of GaN as determined using 2 MeV proton beam random backscattering measurements. Lines are drawn to guide the eye.

## CONCLUSIONS

This study shows for the first time the elemental depth distribution of annealed GaN samples with depth resolution better than 50 nm in the near-surface region (750 nm) over a wide range of annealing temperatures between 500 and 1100 °C. Decomposition of GaN is found to be negligible during annealing up to 800 °C and this range of temperature is safe for GaN based materials processing and device operation for high temperature devices. Thermal annealing of GaN beyond 1000 °C causes a considerable decomposition and disruption in the near-surface region, which is important for electronic and optical properties of devices.

**BEST AVAILABLE COPY**

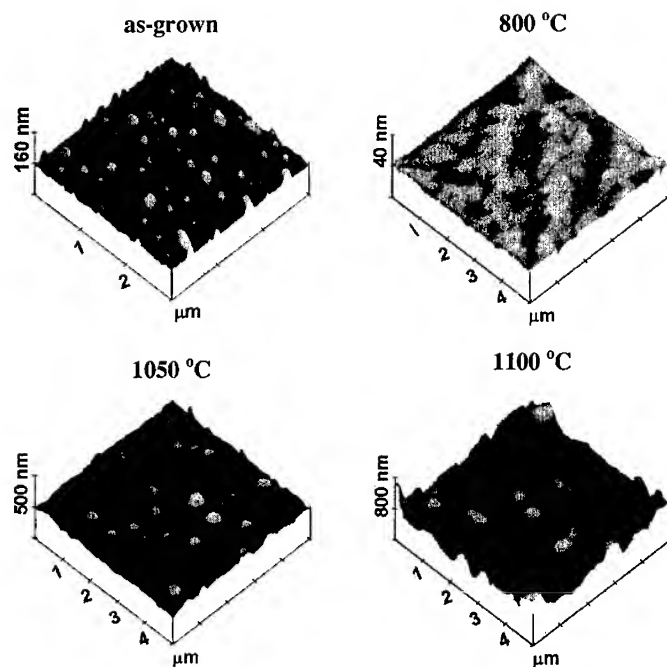


Fig. 3. AFM images showing surface morphologies of as-grown and annealed GaN samples at different temperatures.

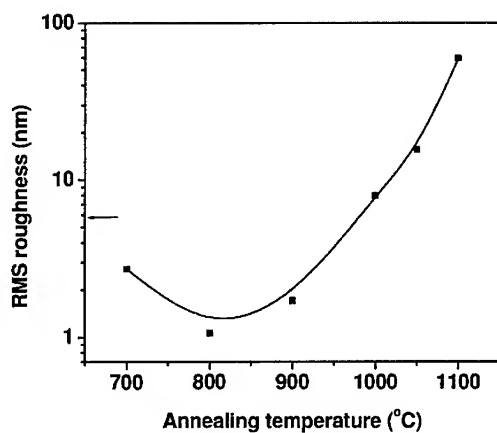


Fig. 4. RMS roughness of annealed GaN samples based on AFM results. Arrow shows the rms roughness of as-grown GaN samples.

## REFERENCES

1. S. Nakamura, *Science* **281**, 956 (1998).
2. Y. Huang, X. Duan and C.M. Lieber, *Nano Lett.* **2**, 101 (2002).
3. W. Han, S. Fan, Q. Li and Y. Hu, *Science* **277**, 1287 (1997).
4. O. Manasreh, *III-Nitride Semiconductors: Electrical, Structural and Defect Properties* (Elsevier Science, Amsterdam, 2000).
5. X. Duan and C.M. Lieber, *J. Am. Chem. Soc.* **122**, 188 (2000).
6. F.A. Ponce and D.P. Bour, *Nature* **386**, 35 (1997).
7. S. Nakamura and G. Fasol, *The Blue Laser Diod: GaN Based Light Emitters and Lasers* (Springer-Verlag Berlin Heidelberg, New York, 1997).
8. T. Mattila and R.M. Nieminen, *Phys. Rev. B* **54**, 166676 (1996).
9. C.H. Park and D.J. Chadi, *Phys. Rev. B* **55**, 12995 (1997).
10. C.F. Lin, H.C. Cheng, C.C. Chang and G.C. Chi, *J. Appl. Phys.* **88**, 6515 (2000).
11. J.C. Zolper, R.G. Wilson, S.J. Pearton and R.A. Stall, *Appl. Phys. Lett.* **68**, 1945 (1996).
12. H.W. Choi, S.J. Chua, A. Raman, J.S. Pan and A.T.S. Wee, *Appl. Phys. Lett.* **77**, 795 (2000).
13. J.M. Hayes, K. Kuball, A. Bell, I. Harrison, D. Korakakis and C.T. Foxon, *Appl. Phys. Lett.* **75**, 2097 (1999).
14. S.J. Pearton, H. Cho, J.R. LaRoche, F. Ren, R.G. Wilson and J.W. Lee, *J. Appl. Phys.* **75**, 2939 (1999).
15. M. Mayer, SIMNRA Users Guide, Report IPP 9/113 (Max-Plank-Institut fur Plasmaphysik, Garching, Germany, 1997-2001).
16. F.A. Reboredo and S.T. Pantelides, *Phys. Rev. Lett.* **82**, 1887 (1999).
17. J. Neugebauer and C. Van de Walle, *Phys. Rev. Lett.* **75**, 4452 (1995).
18. C.H. Kuo, S.J. Chang, Y.K. Su, J.F. Chen, L.W. Wu, J.K. Sheu, C.H. Chen and G.C. Chi, *IEEE Elect. Dev. Lett.* **23**, 240 (2002).
19. C.H. Kuo, S.J. Chang, Y.K. Su, J.F. Chen, L.W. Wu, J.K. Sheu, C.H. Chen and G.C. Chi, *Jpn. J. Appl. Phys.* **41**, L112 (2002).

### Electron Stimulated Desorption of Deuterium from GaN (0001) Surface

Y. Yang,<sup>1</sup> J. Lee, B. D. Thoms, *Georgia State University, Atlanta, GA*

<sup>1</sup>*Present Address: University of California, Santa Barbara, CA*

#### Abstract

Temperature programmed desorption (TPD) was performed on deuterated GaN(0001) surfaces which had been exposed to various doses of 90-eV electrons. TPD of the deuterated surface without electron exposure shows a broad D<sub>2</sub> desorption feature with a peak desorption temperature at ~400 °C. Electron exposure results in a decrease in intensity of the desorption peak which is attributed to removal of surface deuterium by electron stimulated desorption (ESD). This removal of deuterium by ESD produces no change in the peak desorption temperature indicating that recombinative desorption is first order in deuterium coverage.

#### I. Introduction

Gallium Nitride (GaN) and its alloys with InN and AlN have been studied because of their applications in red to UV light emitting diodes, lasers, and detectors, as well as high-temperature, high-power, and high-frequency electronic devices [1-3].

Hydrogen is usually present, intentionally or unintentionally, during GaN growth by techniques including MBE, MOCVD and HVPE and during processing such as etching [4 - 14]. The effects of hydrogen on growth and etching are numerous. First, hydrogen introduced in MOCVD is shown to form Mg-H complexes and passivate the dopant. Although this effect can be reactivated by sample annealing, the entire migration path of hydrogen from Mg dopant sites in p-type GaN has not yet been understood. Both experimental and theoretical studies [15 - 21] of hydrogen bonding sites inside GaN conclude that it first migrates from the dopant to the closest defect site then to the second closest defect site and so on. To find if hydrogen can finally migrate to the surface and desorb requires characterizing the reaction of hydrogen on the GaN surface. Earlier desorption studies are very limited [22-24]. Experiments performed in the author's lab characterized the interaction of hydrogen/deuterium on the GaN (0001) surface by high resolution electron energy loss spectrum (HREELS) [25, 26], ELS [26, 27, 28] and TPD [29]. The surface was determined to be Ga terminated [25]. TPD shows deuterium recombination over a broad temperature range [29]. The broadening of the peaks can be attributed to either a distribution of surface bonding energies or to diffusion during recombinative desorption. This diffusion may involve subsurface hydrogen. Since electron stimulated desorption is a surface sensitive process, studying ESD is useful in discriminating between surface and subsurface species and revealing links between the hydrogen reaction on the GaN surface and bulk migration.

Studying ESD efficiency for hydrogen on GaN (0001) may help develop electron stimulated etching techniques on GaN such as low energy electron enhanced etching (LE4) [30] which does not require reactive chemicals or high temperature in contrast to other dry etching techniques [3, 31-33]. It may also help in developing mask-free patterning techniques on GaN as have been demonstrated on other surfaces [34-38]. Bermudez *et al.* [39] and earlier work in the author's laboratory [27, 28], both using ELS, reported that ESD is an efficient process on hydrogenated or deuterated GaN (0001). However, it is also found that ESD does not completely

return the ELS spectrum of the hydrogenated surface to that of the clean surface. This implies that there is more than one site for hydrogen adsorbates.

## II. Experimental Details

The GaN samples used in this work were grown by MOCVD at the Naval Research Laboratory [40]. Sample preparation and experimental setup for AES, ELS, LEED, D dosing and TPD have been described previously [25, 29]. All desorption data reported here are for exposures of 200 L of  $D_2$ , as determined by an uncorrected ion gauge, where  $1 \text{ L} = 10^{-6} \text{ Torr s}$ . As our earlier experiments showed, 200 L exposures are sufficient to saturate the surface [25,28]. All TPD curves discussed below if not specially mentioned are obtained after preheating to  $190^\circ\text{C}$  for 2 minutes to eliminate the effects deuterium desorption from the sample mount [29].

The ELS apparatus used for our earlier ESD work has a small electron beam spot size. To study the effects of electron exposure by TPD requires exposing the entire sample surface to a uniform electron beam. For this work, electron exposures were performed by placing sample in front of a wide spot electron gun [41]. Electrons emitted from the grounded filament of electron gun hit the sample surface floated to 90 V. A filament current of 4.2 A, produced an electron current measured at the sample mount of up to  $500 \mu\text{A}$  and beam spot size of at least 10 times the area of the sample and mount. Since secondary electrons are generated at the sample surface, the incident beam current should be larger than the measured sample current. Tests from our ELS apparatus show that striking the sample and mount is  $\sim 2$  times the current transmitted through the sample mount. This arrangement is then able to expose the sample to a 90-eV electron beam with uniform current density up to  $\sim 100 \mu\text{A}/\text{cm}^2$ .

Since earlier work from the author's lab shows that Ga-D but not N-D bonds are present on the GaN(0001) surface after atomic deuterium dosing, the TPD curves may be interpreted as desorption from Ga sites on GaN surface.

## III. Results and Discussion

TPD is performed on GaN(0001) which has been exposed to 200 L of atomic deuterium followed by various amounts of electron exposure. TPD of the deuterated surface without electron exposure shows deuterium recombination composed of two overlapping broad peaks with one centered at  $\sim 320^\circ\text{C}$  and the second, which is the majority, at  $\sim 400^\circ\text{C}$  (Fig. 1a). Comparing that with TPD of the deuterated surface followed by 21, 42, and  $170 \mu\text{A h}/\text{cm}^2$  of 90-eV electron bombardment (Figs. 1b, 1c, and 1d, respectively) indicates that both peaks are reduced by electron exposure. Increasing electron exposures produces decreasing TPD intensity with the largest exposure resulting in a much smaller but still present desorption peak at  $400^\circ\text{C}$ . To better understand the effects of the electron bombardment, the TPD curves for various electron exposures (Figs. 1b, 1c, and 1d) are subtracted from the data acquired with no electron exposure (Fig. 1a) to reveal effective TPD of the removed species (Figs. 2a, 2b, and 2c, respectively).

**BEST AVAILABLE COPY**

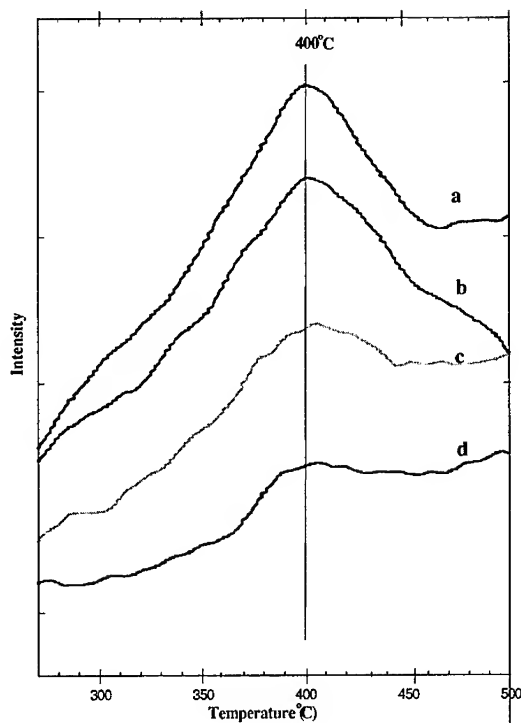
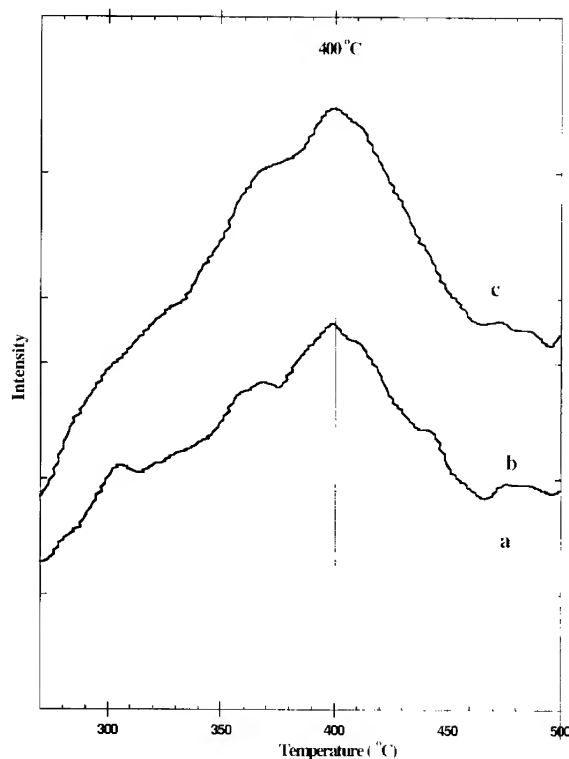


Fig. 1 TPD curves of  $D_2$  recombination from 200 L D exposed GaN(0001) following a) no electron exposure, b) electron exposure of  $21 \mu A \text{ hr/cm}^2$ , c)  $42 \mu A \text{ hr/cm}^2$ , and d)  $170 \mu A \text{ hr/cm}^2$ .

features at 3.4, 6.6 and 11.7 eV are changed by H or D exposure and restored by exposure to 90-eV electrons [23]. From that data, the cross-section for removal of hydrogen by ESD was determined to be  $2 \times 10^{-17} \text{ cm}^2$  and that of deuterium to be  $7 \times 10^{-18} \text{ cm}^2$ . The reduction in the total amount of deuterium desorbed as a function of electron exposure can be used to estimate an ESD cross-section for deuterium of  $\sim 9 \times 10^{-19} \text{ cm}^2$ , however, a more complete data set is needed before conclusions can be reached.

Each of the data curves in Fig. 1 are from a surface with the same initial exposure of atomic deuterium but with different amounts of electron exposure. As is seen by the reduction in area under the curve as the electron exposure is increased, deuterium is being removed by the incident electrons. However, each TPD curve has the same peak desorption temperature despite different deuterium coverages, all peaking at  $400^\circ \text{C}$ . Independence of the peak desorption temperature with varying coverage is a signature of a first order desorption process [42]. Recombinative desorption of  $D_2$  from surface Ga-D species would be expected to be of 2<sup>nd</sup> order. The first order desorption process observed suggests deuterium desorbed in this temperature range do not recombine directly. There probably is a diffusion barrier between their original sites to those surface sites on which the deuterium atoms ultimately recombine. At  $400^\circ \text{C}$  this diffusion mechanism is dominant and shows as a 1<sup>st</sup> order desorption process.

Earlier investigation of the ESD of H and D from GaN(0001) in the author's group shows that ELS



**Fig. 2** Subtraction of  $D_2$  TPD curves acquired after electron exposures of a)  $21 \mu A \text{ hr/cm}^2$  (Fig. 1b), b)  $42 \mu A \text{ hr/cm}^2$  (Fig. 1c), and c)  $170 \mu A \text{ hr/cm}^2$  (Fig. 1d) from curve with no electron exposure (Fig. 1a).

electrons. Comparison of these curves shows a decrease of desorption intensity in the region from 270 to 500 °C and particularly a reduction in the size of the main desorption peak at ~400 °C. The reduction in the desorption intensity is attributed to electron stimulated desorption (ESD) of surface or near-surface deuterium. The peak desorption temperature does not shift as hydrogen is removed by ESD indicating first order desorption and a diffusion mechanism is suggested. From the area under the TPD curves, an ESD cross-section of  $\sim 9 \times 10^{-19} \text{ cm}^2$  is estimated. In earlier work, the author's have reported ESD of hydrogen by two mechanisms, one very efficient process with a cross-section for removal of deuterium of  $7 \times 10^{-18} \text{ cm}^2$  which caused rapid changes in electron energy loss spectroscopy (ELS) and another slower process associated with an ELS feature at 18 eV.

The earlier ESD work also showed that an 18-eV ELS feature was changed by exposure to H or D atoms and only slightly restored by exposure to  $17 \mu A \text{ h/cm}^2$  of 90-eV electrons, which is less than the exposure corresponding to Figs. 1b and 2a. We suggest that the recombinative desorption of deuterium at ~400 °C may be related to this 18-eV feature. Earlier explanations attribute the 18-eV feature to either volume plasmon [43, 44] or surface plasmon [43 - 46] shifted by exposed hydrogen. Since the diffusion mechanism between sites related with this feature and surface Ga sites is suggested, we infer that 18-eV feature and deuterium bonding sites related to ~400 °C desorption are related to the volume plasmon, that is, these sites may involve subsurface layers.

#### IV. Conclusion

Temperature programmed desorption (TPD) curves have been acquired following various amounts of exposure of the entire surface of a deuterium-exposed GaN(0001) sample to 90-eV

**BEST AVAILABLE COPY**

## References

- [1] R. F. Davis, Proc. IEEE **79**, 702 (1991).
- [2] S. Strite and H. Morkoc, J. Vac. Sci. Technol. B **10**, 1237 (1992).
- [3] S. N. Mohammad, A. Salvador, and H. Morkoc, Proc. IEEE **83**, 1306 (1995).
- [4] Z. Yu, S. L. Buczowski, N. C. Gilies, T. H. Myers and M. R. Richards-Babb, Appl. Phys. Lett. **69**, 2371 (1996).
- [5] Y. Okamoto, S. Hashiguchi, Y. Okada and M. Kawabe, Jpn. J. Appl. Phys., **38**, L230 (1990).
- [6] D. D. Koleske, A. E. Wickenden, R. L. Henry, M. E. Twigg, J. C. Culbertson and R. J. Gorman, Appl. Phys. Lett. **73**, 2018 (1996).
- [7] J. Han, T.-B. Ng, R. M. Biefeld, M. H. Crawford and D. M. Follstaedt, Appl. Phys. Lett. **71**, 3114 (1997).
- [8] E. L. Piner, M. K. Behbehani, N. A. El-Masry, J. C. Roberts, F. G. McIntosh and S. M. Bedair, Appl. Phys. Lett. **71**, 2023 (1997).
- [9] Randy J. Shul in *Processing of Wide Band Gap Semiconductors*, 263, edited by S. J. Pearton and J. W. Lee (Noyes Publications, New York, 2000), p.263.
- [10] S. J. Pearton, C. R. Abernathy, F. Ren, J. R. Lothian, P. Wisk, A. Katz and C. Constantine, Semicond. Sci. Technol. **8**, 310 (1993).
- [11] S. J. Pearton and J. W. Lee, in *Semiconductors and Semimetals, Vol. 61*, edited by N. H. Nickel, (Academic Press, San Diego, 1999), p. 471.
- [12] S. Nakamura, N. Twasa, M. Senoh and T. Mukai, Jpn. J. Appl. Phys. **31**, 1258 (1992).
- [13] T. D. Moustaks and R. Molnar, Mater. Res. Soc. Symp. Proc. **281**, 753 (1993).
- [14] S. Nakamura, T. Mukai, M. Senoh and N. Iwasa, Jpn. J. Appl. Phys. **31**, L139 (1992).
- [15] W. Götz, N. M. Johnson, D. P. Bour, M. D. McCluskey and E. E. Haller, Appl. Phys. Lett. **69**, 3725 (1996).
- [16] B. Clerjaud, D. Côte, A. Lebki, C. Naud, J. M. Baranowski, K. Pakula, D. Wasik and T. Suski, Phys. Rev. B **61**, 8238-8241 (2000).
- [17] Y. Okamoto, M. Saito and A. Oshiyama, Jpn. J. Appl. Phys., **35**, L807 (1996).
- [18] J. Neugebauer and C. G. Van de Walle, Phys. Rev. Lett. **75**, 4452 (1995).
- [19] S. Limpijumnong, J. E. Northrup and C. G. Van de Walle, Phys. Rev. Lett., **87**, 205505 (2001).
- [20] A. F. Wright, J. Appl. Phys., **90**, 1164 (2001).
- [21] A. F. Wright, J. Appl. Phys., **90**, 6526 (2001).
- [22] C.-M. Chiang, S. M. Gates, A. Bensaoula and J. A. Schultz, Chem. Phys. Lett. **246**, 275 (1995).
- [23] R. Shekhar and K. Jensen, Surf. Sci. Lett. **381**, L581 (1997).
- [24] M. E. Bartram and J. R. Creighton, MRS Internet J. Nitride Semicond. Res. **4S1**, G3.68 (1999).
- [25] V. J. Bellitto, B. D. Thoms, D. D. Koleske, A. E. Wickenden and R. L. Henry, Surf. Sci. **430**, 80 (1999).
- [26] V. J. Bellitto, B. D. Thoms, D. D. Koleske, A. E. Wickenden and R. L. Henry, Phys. Rev. B **60**, 4816 (1999).
- [27] V. J. Bellitto, Y. Yang, B. D. Thoms, D. D. Koleske, A. E. Wickenden, R. L. Henry, Surf. Sci. Lett. **442**, L1019 (1999).
- [28] V. J. Bellitto, B. D. Thoms, D. D. Koleske, A. E. Wickenden, R. L. Henry, Phys. Rev. B **60**, 4821 (1999).

- 
- [29] Y. Yang, J. Lec, B. D. Thoms, D. D. Koleske and R. Henry, Mater. Res. Soc. Symp. Proc., Vol. 693, 16.48.1.
- [30] H. P. Gillis, D. A. Choutov, K. P. Martin, S. J. Pearton, and C. R. Abernathy, J. Electrochem. Soc. **143** (1996) L251.
- [31] R. Shul *et al.*, Appl. Phys. Lett. **66** (1995) 1761.
- [32] A. T. Ping and I. Adesida, Appl. Phys. Lett. **67** (1995) 1250.
- [33] S. J. Pearton, Mat. Sci. and Engineering. B **44**(1997) 1, and references therein.
- [34] R. S. Becker, G. S. Higashi, Y. J. Chabal, and A. J. Becker, Phys. Rev. Lett. **65** (1990) 1917.
- [35] J. J. Boland, Surf. Sci. **261** (1992) 17.
- [36] J. W. Lyding, T. -C. Shen, J. S. Hubacek, J. R. Tucker, and G. C. Abeln, Appl. Phys. Lett. **64** (1994) 15.
- [37] N. Kramer, H. Birk, J. Jorritsma, and C. Schönenberger, Appl. Phys. Lett. **66** (1995) 1325.
- [38] T. Mitsui, E. Hill, and E. Ganz, J. Appl. Phys. **85** (1999) 522.
- [39] V. M. Bermudez, D. D. Koleske, and A. E. Wickenden, Appl. Surf. Sci. **126**, 69 (1998).
- [40] A. E. Wickenden, D. K. Gaskill, D. D. Koleske, K. Doverspike, S. D. Simons, and P. H. Chi, Res. Mat. Soc. Symp. Proc. **395**, 679 (1996).
- [41] J.-L. Lin and J. T. Yates, Jr., J. Vac. Sci. Technol. A, **12**(5), 2795 (1994).
- [42] P. A. Redhead, Can. J. Phys. **42**, 886 (1964).
- [43] V. M. Bermudez, J. Appl. Phys. **80**, 1190 (1996).
- [44] C. G. Olson, D. W. Lynch, and A. Zehe, Phys. Rev. B **24**, 4629 (1981).
- [45] A. Berger, D. Troost, and W. Mönch, Vacuum **41**, 671 (1990).
- [46] D. Troost, H.-U. Baier, A. Berger, and W. Mönch, Surf. Sci. **242**, 324 (1991).

### Dislocation-related deep states induced by irradiation in HVPE n-GaN

A. Castaldini, A. Cavallini and L. Polenta  
INFN and Dipartimento di Fisica  
Viale Berti Pichat 6/2, I-40127 Bologna, Italy

#### ABSTRACT

This paper deals with defects induced by proton irradiation in n-GaN. The samples were HVPE grown, irradiated with 24 GeV protons. DLTS was performed on both as-grown and irradiated samples with planar and normal collector configurations to evidence the dislocation effect. Two electron traps were identified in the as-grown material by both diode structures: trap EC1 ( $E_C - 0.19\text{eV}$ ) and trap EC2 ( $E_C - 0.25\text{eV}$ ), EC2 being the dominant one. Irradiation consistently affects the pre-existing levels in such a way so as their appearance strongly depends on the diode structure, hence on the region probed by DLTS.

This contribution focuses on the actual existence of two deep traps EC1 and EC2 emitting in GaN at low temperature and on the different nature of the deep levels associated to EC1 and EC2. Their filling kinetics was studied since we supposed that EC2 would be associated to extended defects, as already reported in literature. Indeed, the site density of EC2 logarithmically depends on the filling pulse width, demonstrating that this trap is definitely associated to extended defects. The trap EC1, on the contrary, exhibits the filling kinetics peculiar of point defects.

#### INTRODUCTION

Recently, a strong effort has been devoted to the study of defects induced by irradiation in gallium nitride (GaN) and a wide debate [1,2] is currently running on the nature of the electron traps emitting at low temperature. Indeed, III-nitride semiconductors are in use for space-based applications and it is therefore of major importance to know how irradiation, mainly by electrons and protons, affects the GaN-based device properties. Furthermore, as proved from ages for what concerns silicon, irradiation is a powerful tool to investigate the defect properties since it introduces in a controlled way elemental defects.

Concerning deep level transient spectroscopy (DLTS) investigations, for long time it was suggested that low temperature spectra were due to the convolution of three traps, the levels of which would range from 60 to about 200 meV. However, DLTS conclusions are hard to be drawn because of the closeness of the trap energy values involved, hence of the overlapping of their DLTS peaks. Thus, not a definitive confirmation of how many traps contribute to the low temperature emission nor their association to specific defects has been up to now reached.

This contribution deals with such low temperature emitting traps, comparing their features before and after irradiation with high energy protons. In addition, measurements were carried out in both planar and cross-sectional diode configuration, which produces a depth-dependent variation in the DLTS spectra. As a matter of fact, the two geometries probe regions with different distribution and densities of dislocations so as to evidence possible dislocation-related effects.

## EXPERIMENTAL DETAILS

Unintentionally doped n-type GaN layer grown by hydride vapor phase epitaxy (HVPE) on sapphire, epilayer thickness equal to 72 micrometers,  $N_d = 9.38 \times 10^{16} \text{ cm}^{-3}$ , was irradiated with 24 GeV protons (fluence  $7.5 \times 10^{13} \text{ cm}^{-2}$ ). Schottky barrier diodes were fabricated by evaporation and lithographic processes according to two different geometries (figure 1). The former geometry is the conventional planar structure with the diode fabricated on the epilayer (figure 1a), while the latter geometry provides a cross-sectional configuration with the diode fabricated on the cleaved surface of the epilayer including the epilayer-sapphire interface (figure 1b). From now on the two structures will be called “geometry A” and “geometry B”, respectively. By this way the characteristics of the regions investigated by DLTS significantly differ in terms of dislocation contribution: geometry A essentially probes the slab just under the epilayer surface, where the threading dislocations emerge, and geometry B tests the epilayer across its thickness from the interface-substrate towards the epilayer surface.

DLTS analyses were performed with both diode configurations on as-grown and irradiated samples in the temperature range 80-400 K, but we will focus here only on the results relevant to the temperature range 80-250 K. The reverse quiescent bias  $V_R$  was  $-5 \text{ V}$ , and the forward filling bias  $V_F$  was varied between  $+3$  and  $+5 \text{ V}$ , without significantly different results. The filling kinetics of the deep levels was investigated by changing their filling time with pulse widths  $t_p$  spanning from  $5 \times 10^{-7} \text{ s}$  to  $10 \text{ ms}$ .

Electron beam induced current (EBIC) analyses of scanning electron microscopy were also performed with both geometries to map the recombination activity distribution, particularly that relevant to the cleaved surface of the diode.

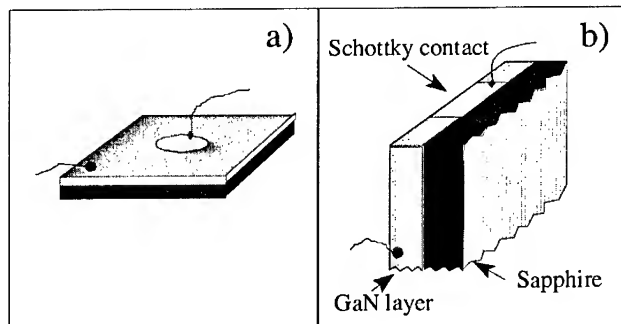


**Figure 1** Schottky barrier diodes fabricated according to the following geometries: a) planar structure with the diode fabricated on the epilayer surface, b) cross-sectional configuration with the diode fabricated on the cleaved surface of the epilayer including the epilayer-sapphire interface.

## RESULTS AND DISCUSSION

Irradiation consistently affects the DLTS spectra, but the changes of the spectra strongly depend on the diode geometry adopted, hence on the region actually probed.

With geometry A it results (figure 2) that before irradiation a trap (from now on labeled EC2) exists, peaked at about 160 K using an emission rate  $e_n = 465 \text{ s}^{-1}$  and a pulse width of 1 ms, at 220-250 meV below the conduction band  $E_C$  and with capture cross section  $\sigma = 1.7 \times 10^{-15} \text{ cm}^2$ , as well known from literature [1, 2, 3, and references therein]. The irradiation does not affect this preexisting level, the concentration of which is  $2.3 \times 10^{13} \text{ cm}^{-3}$  before irradiation and only slightly increases after irradiation, but generates a new trap EC1 located at about 190 meV below  $E_C$ , the density of which is  $3.7 \times 10^{13} \text{ cm}^{-3}$  and the capture cross section is  $\sigma = 5.5 \times 10^{-15} \text{ cm}^2$ . It is worth noting that, due to our experimental conditions where the proton energy dose is very high, the density of the trap EC1 is not only higher than that of the trap EC2 but also the resulting DLTS spectrum is broadened and peaked in correspondence of the emission by EC1. Indeed, the shape of this DLTS spectrum could also be interpreted, as done in the past, as the overlapping of three closely spaced levels in a large energy range.

The DLTS investigations carried out with geometry B add to the above picture some pieces of information which shed light on the nature of the preexisting defects involved in the interaction with protons and on the localization of defects induced irradiation. From careful measurements it emerges that the trap EC1 is already present before irradiation (figure 3,  $\Delta$ )

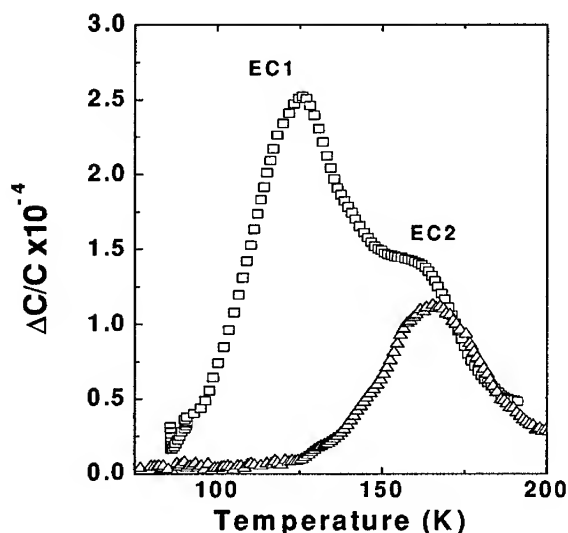
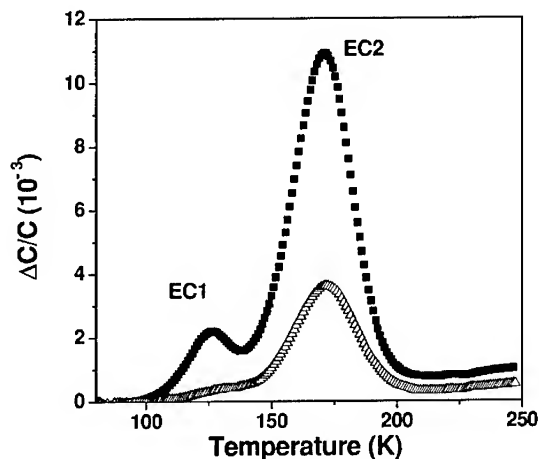


Figure 2. DLTS spectra achieved with geometry A before ( $\Delta$ ) and after ( $\square$ ) proton irradiation. Emission rate  $e_n = 465 \text{ s}^{-1}$ , pulse width 1 ms.



**Figure 3.** DLTS spectra obtained with geometry B before ( $\Delta$ ) and after ( $\blacksquare$ ) proton irradiation. Emission rate  $e_n = 1162 \text{ s}^{-1}$ , pulse width 1 ms.

even if in a very low concentration in comparison to that of the defect EC2, that is equal to  $7.1 \times 10^{14} \text{ cm}^{-3}$ . After irradiation, on the contrary to what happens with geometry A, the DLTS spectrum clearly shows two, well-separated peaks, which correspond to the emissions from EC1 and EC2. Another feature that differentiates the spectrum obtained by investigating the epilayer cross-section is that the dominant peak is now EC2, no more EC1. Indeed, even though the density of the trap EC1 notably increases after irradiation, EC2 keeps dominating: the density of EC1 is now  $3.1 \times 10^{14} \text{ cm}^{-3}$  and that of EC2 is  $1.6 \times 10^{15} \text{ cm}^{-3}$ .

The Arrhenius plots of the two traps detected in geometry A and B, respectively, coincide (figure 4), hence demonstrating that the different shapes of the DLTS spectra originate from the differences in the distribution and/or density of the electrical activity of the regions explored. These findings can be straightforwardly correlated to the EBIC results, which expectedly evidenced that the strength of the electrical recombination activity of the threading dislocations increases moving from the epilayer surface towards the interface epilayer-sapphire. Last, but not least, is the difference in the DLTS signal intensity measured in the two geometries: the scales of figures 2 and 3 significantly differ showing that the DLTS signal relevant to the investigations in cross section configuration is much larger than that in planar configuration.

The above results can be interpreted as follows. In the as-grown epilayer the density of both traps EC1 and EC2 increases moving towards the interface. It is, in other words, associated to the defective region in close proximity of the interface. Thus, probing the layer across a cleaved surface evidences the presence of both traps differently from what happens probing the surface opposite to the interface. This explains both the scaling of the DLTS signal in the two used geometries as well as the detection of the trap EC1 only in geometry B, since in the as-grown layer the density of this trap is much smaller than the one of trap EC2. Proton irradiation generates new defects and, as observed, increases the amount of both traps, but their localization

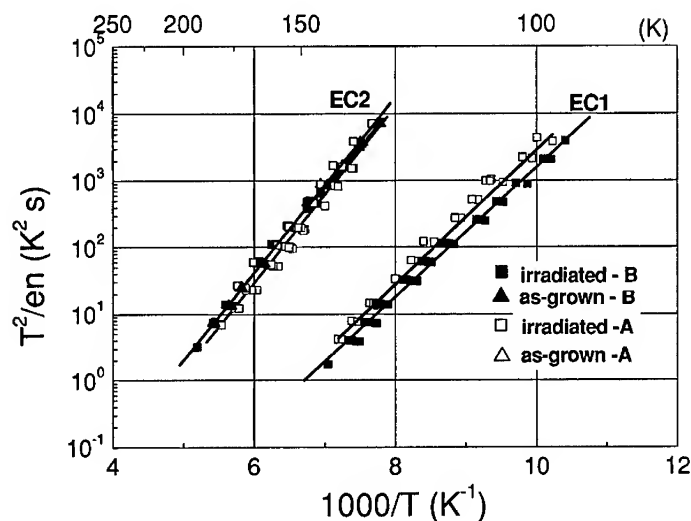


**Figure 4.** Arrhenius plot of the diodes investigated in geometry A and geometry B before and after proton irradiation.

differs as the shape of the DLTS spectra suggests. Traps EC1 is likely generated more homogeneously in the layer, while EC2 is generated mostly in close proximity of the dislocations. Then, EC2 keeps being the densest one in geometry B that probes the region richest in dislocations, while in geometry A after irradiation the trap EC1 prevails.

First results of the filling kinetics analysis performed in geometry B confirm this hypothesis since the peak height of trap EC1 keeps constant changing the filling pulse width  $t_p$  from 2  $\mu$ s to 10 ms while the height of the EC2 peak exhibits a logarithmic filling dependence on  $t_p$ . This indicates [4] that the former trap is associated to point defects and the latter trap is associated to a potential barrier. This result suggests that trap EC2 is likely to be associated to the potential barrier of dislocations. Furthermore, its logarithmic dependence on  $t_p$  is different in as-grown and irradiated epilayers, suggesting that these centers are point-like defects associated to dislocations and multiplied by the irradiation in such a way to affect the dislocation potential barrier. Additionally, the dependence of the peak height on  $t_p$  shows that it can be attributed to localized states [5]. Accounting for a dislocation density of about  $N_{\text{dist}} = 10^{10} \text{ cm}^{-2}$  and the density of the trap EC2 equal to  $1.6 \times 10^{15} \text{ cm}^{-3}$ , the distance among traps roughly results about 500 Å.

It has also to be mentioned the possible effect that the degenerate region close to the interface [6] has on the present results. Indeed, due to the large thickness of this sample, 72  $\mu$ m, this region only slightly should affect the DLTS signal in cross section configuration, as inferred by the very low value of the leakage current (lower than  $10^{-9} \text{ A}$ ) at the bias used ( $V_{\text{Reverse}} = -5 \text{ V}$ ).

## CONCLUSIONS

The results presented in this contribution provide evidence of two defects, EC1 and EC2, multiplied by irradiation, but both existing also in as-grown GaN epilayers. EC1 exhibits features peculiar of point defects randomly distributed, while a local Coulomb potential is associated to EC2, which then could be attributed to point-like defects associated to a potential barrier. From this finding we can infer that EC2 is associated to the pre-existing threading dislocations, even if their nature is not yet clear at this time.

## ACKNOWLEDGMENTS

The authors wish to thank D.C.Look and R. J. Molnar for providing the samples.

## REFERENCES

1. L. Polenta, Z-Q Fang and D.C. Look, *Appl. Phys. Lett.* **76**, 2086 (2000).
2. F.D. Aurret, S.A. Goodman, F.K. Koschnick, J-M. Spaeth, B. Beaumont and P. Gibart, *Appl. Phys. Lett.* **74**, 407 (1999).
3. A.Y. Polyakov, A.S. Usikov, B. Theis, N.B. Smirnov, A.V. Govorkov, F. Jomard, N.M. Schmidt and W.V. Lundin, *Solid-State Electron.* **44**, 1971 (2000)
4. P. Omling, E. R. Weber, L. Montelius, H. Alexander, and J. Michel, *Phys. Rev. B* **32**, 571 (1985).
5. W. Schroeter, J. Kronewitz, U. Gnauert, F. Riedel and M. Seibt, *Phys. Rev. B* **52**, 13726 (1995)
6. D.C.Look et al, MRS Internet J. Nitride Semicond. Res. **6**, 10 (2001)

### High-Temperature Illumination-Induced Metastability in Undoped Semi-Insulating GaN Grown by Metalorganic Vapor Phase Epitaxy

Z.-Q. Fang<sup>1</sup>, B.B. Claflin<sup>1</sup>, D.C. Look<sup>1</sup>, T.H. Myers<sup>2</sup>, D.D. Koleske<sup>3a</sup>, A.E. Wickenden<sup>3b</sup>, and R.L. Henry<sup>3</sup>

<sup>1</sup>Semiconductor Research Center, Wright State University, Dayton, OH 45435

<sup>2</sup>Physics Department, West Virginia University, Morgantown, WV 26506

<sup>3</sup>Electronics Science and Technology Division, Naval Research Laboratory, Washington, DC 20375

<sup>a</sup>Sandia National Laboratories, Albuquerque, NM 87185

<sup>b</sup>Army Research Laboratory, AMSRL-SE-RL, Adelphi, MD 20783

#### ABSTRACT

High-temperature (high-T) illumination-induced metastability in undoped semi-insulating (SI) GaN grown on a-plane sapphire by metalorganic vapor phase epitaxy has been studied using thermally stimulated current (TSC) spectroscopy, photocurrent (PC) and persistent photocurrent (PPC) measurements. The metastability can be induced by illumination at  $390 > T > 300$  K (using either white or 360-nm light), followed by cooling the sample to 83 K in the dark. Without high-T illumination, the SI-GaN sample stays in its normal state ("off" state), and shows at least six TSC traps, B (0.63 eV), B<sub>x</sub> (0.51 eV), C<sub>1</sub> (0.44 eV), C (0.32 eV), D (0.23 eV), and E (0.16 eV). However, after high-T illumination the sample goes into a metastable state ("on" state), and shows a strong increase in both the PC at 83 K and the TSC of traps D, C, and E, accompanied by significant change in their relative densities. PPC at 83 K in the "on" state lasts much longer than that in the "off" state. Association of possible point defects and dislocations with the metastability behavior will be discussed.

#### INTRODUCTION

Undoped semi-insulating (SI) GaN films are preferred for device structures such as AlGaIn/GaN HEMTs. Recently, yellow-luminescence (YL) related optical metastability or memory effects in undoped GaN layers have been studied using photoluminescence (PL) or cathodoluminescence (CL), in conjunction with exposures of samples to either high-intensity ultraviolet light or electron-beam irradiation at room temperature [1,2]. Instead of PL or CL, we have successfully used thermally stimulated current (TSC) spectroscopy, both illumination-temperature and time dependent, and photocurrent (PC), to study photo-induced metastability in undoped SI-GaN samples grown by metalorganic vapor phase epitaxy. The metastability is induced by high-temperature (high-T) illumination at  $390 > T > 300$  K (using white or 360-nm light), followed by cooling the sample to 83 K in the dark. Without high-T illumination, the SI-GaN sample stays in its normal state (or "off" state) and shows at least six TSC traps, B (0.63 eV), B<sub>x</sub> (0.51 eV), C<sub>1</sub> (0.44 eV), C (0.32 eV), D (0.23 eV), and E (0.16 eV). These traps are very similar to the electron traps observed in n-type GaN films by deep level transient spectroscopy (DLTS). High-T illumination puts the sample into a metastable state (or "on" state), which shows a strong increase in both the PC at 83 K and the TSC of traps D, C, and E. The TSC traps also show a significant change in their relative densities in the "on" state. Persistent PC at 83 K in the "on" state lasts much longer than that in the "off" state. Based on the temperature and

illumination-time dependences of the PC, and the relative magnitude of the TSC traps in the "on" and "off" states, we discuss how point defects and dislocations may influence the metastability.

## SAMPLE AND EXPERIMENTS

Unintentionally doped SI-GaN samples (with thicknesses of  $\sim 1.5 \mu\text{m}$ , total dislocation densities of  $\sim 5 \times 10^9 \text{ cm}^{-2}$ , and resistivities as high as  $10^{10} \Omega \text{ cm}$ ) were grown on a-plane sapphire by metalorganic vapor phase epitaxy (MOVPE), using large-grained AlN nucleation layers [3]. One  $\sim 4 \times 4 \text{ mm}^2$  piece cut from such a sample was used in this study. A pair of non-annealed indium contacts was soldered onto the top surface. A Bio-Rad DL4600 system and a Keithley 617 electrometer were used to measure dark current (DC), photocurrent (PC), and TSC under a bias  $V_b=50 \text{ V}$ , with temperatures controlled from 83 to 390 K. PC measurements were conducted using a bare halogen lamp (white light) or with a band-pass filter (light centered at 360 nm). The light intensity could be adjusted by varying the lamp-voltage. For regular TSC measurements, the sample was always cooled from the highest temperature (390 K) to a lower (illumination) temperature ( $T_{\text{illum}}$ ) in the dark. After illuminating the sample for a few minutes ( $t_{\text{illum}}$ ) at a selected  $T_{\text{illum}}$ , the light was switched off for a period of time (called the waiting time  $t_{\text{wait}}$  or decay time) at  $T_{\text{illum}}$ . Finally the sample was cooled to 83 K, and the TSC spectrum was measured upon warming, with a heating rate  $\beta=0.3 \text{ K/s}$ . Persistent photocurrent (PPC) was measured during the waiting or decay period. The sample shows very low DC's (for example,  $\sim 4 \text{ pA}$  at 390 K), which allows us to detect TSC traps peaked at temperatures as high as 300 K.

## RESULTS AND DISCUSSION

Fig. 1 shows TSC spectra, measured at different values of  $T_{\text{illum}}$  (from 83 to 250 K), with  $t_{\text{illum}}$  of 4.5 min and  $t_{\text{wait}}$  of 2 min. At least, six traps can be observed in the spectra. They are B at 300

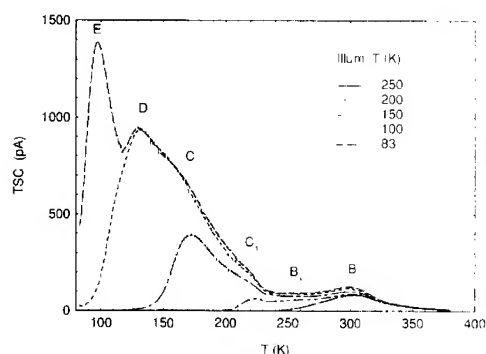


Fig.1 TSC spectra measured by illuminating the sample (using white light) at different values of  $T_{\text{illum}}$  and cooling it to 83 K in the dark. The conditions are:  $V_b=50 \text{ V}$ ;  $\beta=0.3 \text{ K/s}$ ; lamp voltage=10 V; illum. time @ 83 K= 4.5 min; and waiting time= 2 min.

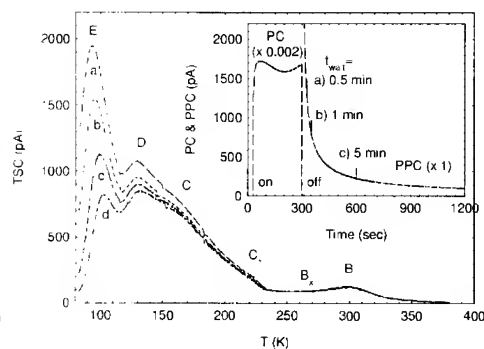


Fig.2 TSC spectra measured by illuminating the sample (using white light) at 83 K and with different values of  $t_{\text{wait}}$ : a) 0.5 min, b) 1 min, c) 5 min, and d) 17 min (inset is PC and PPC measured at 83 K). The other conditions are the same as those in Fig.1.

BEST AVAILABLE COPY

K, B<sub>x</sub> at 255 K, C<sub>1</sub> at 220 K, C at 170 K, D at 130 K, and E at 97 K. The higher T<sub>illum</sub>, the fewer peaks were observed, because of the difficulty of filling shallower traps by illumination at higher T<sub>illum</sub>. Using the approximate equation  $E_T = kT \ln T_m^4/\beta$  for a given TSC peak at T<sub>m</sub> [4], the activation energy E<sub>T</sub> was estimated to be 0.62 eV for B, 0.51 eV for B<sub>x</sub>, 0.44 eV for C<sub>1</sub>, 0.32 eV for C, 0.23 eV for D, and 0.16 eV for E, respectively. Interestingly, these TSC traps are all similar to DLTS electron traps observed in various types of n-GaN layers grown on c-plane sapphire [5], and most of them are believed to be related to point defects. Fig. 2 shows TSC spectra, measured at T<sub>illum</sub>=83 K and with t<sub>wait</sub> ranging from 0.5 to 17 min. PC and PPC data, measured at 83 K with a decay time of 15 min (using white light), is shown in the inset of the figure. Low-T peaks E, D, and C reasonably decrease due to thermal emission during the waiting time; however, the high-T peaks are not affected due to negligible emission at 83 K. For each of the four spectra, it is noted that the value of the TSC at the initial time (immediately after t<sub>wait</sub>) is equal to the value of the PPC at a decay time equal to t<sub>wait</sub>. This observation shows that the PPC is merely the result of electron emission from traps such as E, D, and C. This same correspondence holds for other values of T<sub>illum</sub> (not shown here), which further proves that the PPC observed in our GaN sample is due to contributions of electron emission from relevant traps filled at a particular T<sub>illum</sub>. In order to observe high-T illumination-induced metastability of the PC and TSC, the sample was first illuminated at 380 K (using white light) for 5 min, then cooled to 83 K in the dark, then illuminated at 83 K for 5 min before commencing the regular TSC measurement. Fig. 3 presents an observation of the metastability, i.e., sharp differences in the 83-K PC and in the TSC, caused by the 380-K illumination. Note that both the PC and the PPC at 83 K, as well as the low-temperature portion of the TSC, increase significantly due to the illumination. Without the 380-K illumination, the SI-GaN sample stays in its normal state (or "off" state), while with the 380-K illumination, the sample goes into a metastable state (or "on" state). To better understand this metastability, we use filtered light, centered at 360 nm. TSC spectra for the sample in the "off" and "on" states, measured using different light intensities for

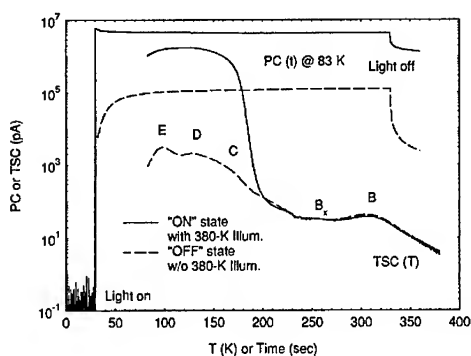


Fig.3 PC at 83 K and TSC measured with and without 380-K, white light illumination. The conditions are: V<sub>b</sub>=50 V; β=0.3 K/s; lamp voltage=7 V; illum. time @380 K=5 min; illum. time @83 K=5 min; and waiting time=2 min.

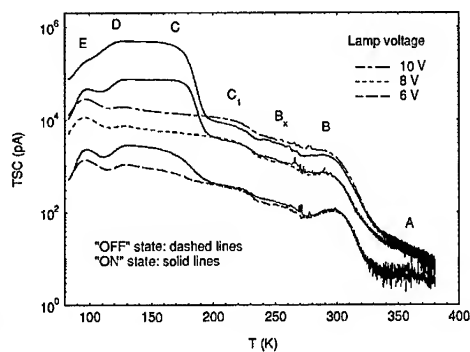


Fig.4 TSC spectra versus light intensity (or lamp voltage), measured with and without 380-K illumination, corresponding "on" and "off" states (using 360-nm light). The other conditions are the same as those in Fig.3.

both 380-K illumination (for the sample going to “on” states) and 83-K illumination (for regular TSC measurements) are pictured in Fig. 4. From the figure, we see that as light intensity increases: i) TSC signals in both the “off” and “on” states rise without saturation; and ii) the spectral difference (at  $T < 200$  K) between the two states becomes larger. Once going into the “on” state, a complete recovery from the “on” state to the “off” state (in the dark) takes many hours or days, depending on the initial light intensity. To understand the mechanism causing the metastability, we measured TSC spectra in the “on” state as a function of illumination- temperature and time, at high- $T_{\text{illum}}$ 's. The TSC spectra, measured at different values of  $T_{\text{illum}}$ , are shown in Fig. 5. An Arrhenius plot of PC vs.  $1/T_{\text{illum}}$  is shown in the inset. From the figure, we see that: i) the TSC signal in the “on” state is greatly increased by raising  $T_{\text{illum}}$  from 320 K to 390 K; ii) the TSC spectral feature at  $T < 200$  K is significantly changed from trap E dominance to traps D/C dominance; and iii) the PC drops, as  $T_{\text{illum}}$  rises, and seems to be controlled by a deep center with  $E_T \sim 2.1$  eV, which is close to the energy of the YL center. “On” state TSC spectra, measured using different values of  $t_{\text{illum}}$  (380-K illumination), are presented in Fig. 6. An inset shows the relationship between the 83-K PC and the logarithmic time. From the figure, we find that: i) the TSC signal in the “on” state increases greatly with increased  $t_{\text{illum}}$ ; ii) the TSC spectral features at  $T < 200$  K are also changed from E dominance to D/C dominance; and iii) the 83-K PC varies logarithmically with  $t_{\text{illum}}$ . Since the PC at 83 K and the TSC at  $T < 200$  K in the “on” state are highly correlated to each other, and since both depend on carrier lifetime ( $\tau$ ) and mobility ( $\mu$ ) [4], it is useful to normalize the TSC by the 83-K PC, i.e.,  $\text{TSC}_{\text{norm}} = \text{TSC}/\text{PC}(83 \text{ K})$ . Normalized TSC spectra as a function of  $T_{\text{illum}}$  and  $t_{\text{illum}}$  are shown in Figs. 7 and 8, respectively. From these figures, we see that the high-T-illumination-induced metastability can be well demonstrated in

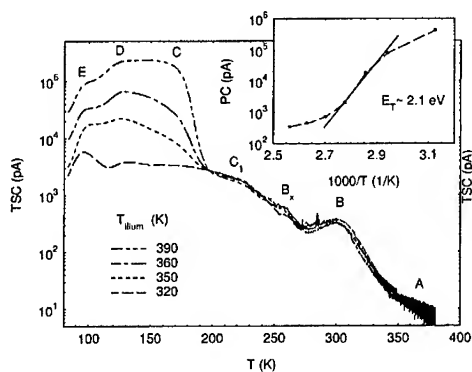


Fig.5 “On” state TSC spectra measured after illuminating the sample at different high- $T_{\text{illum}}$ 's (using 360-nm light). The inset is an Arrhenius plot of PC vs.  $1/T_{\text{illum}}$ . The conditions are:  $V_b = 50$  V;  $\beta = 0.3$  K/s; lamp voltage = 8 V; illum. time @  $T_{\text{illum}}$ 's = 5 min; illum. time @ 83 K = 5 min; and waiting time = 2 min.

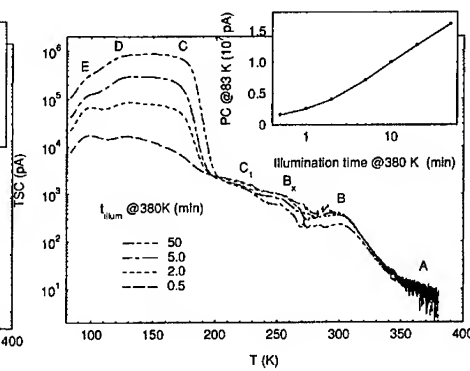


Fig.6 TSC spectra measured using 360-nm light and different values of  $t_{\text{illum}}$  from 0.5 to 50 min for 380-K illumination (inset is plot of PC at 83 K versus logarithmic  $t_{\text{illum}}$  of 380-K illumination). The other conditions are the same as those shown in Fig.5.

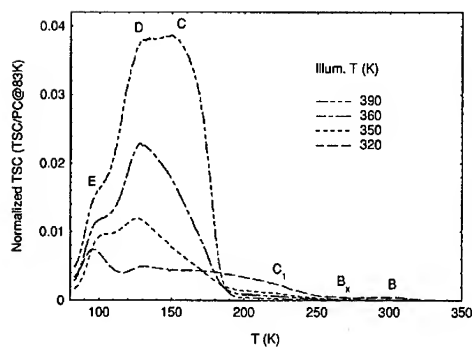


Fig.7 Normalized TSC spectra, demonstrating effect of illumination temperature on TSC traps in the low-temperature range (see Fig. 5 for the measurement conditions).

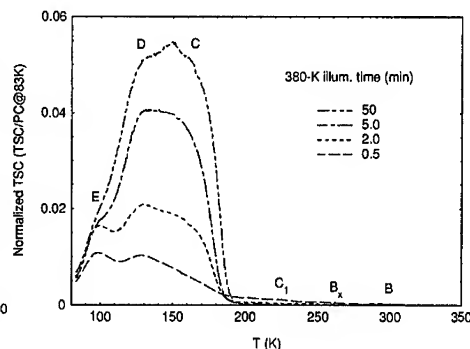


Fig.8 Normalized TSC spectra, demonstrating effect of illumination time at 380 K on TSC traps in the low-temperature range (see Fig. 6 for the measurement conditions).

terms of the absolute and relative strengths of the low-T TSC traps. Furthermore, optically-induced YL-related memory effects, similar to those of Chang et al. [1], were also observed with PL measurements [6].

Based on the observations mentioned above, the deep centers responsible for the high-T-illumination-induced metastability, could be certain TSC traps (C at 0.32 eV, D at 0.23 eV, and E at 0.16 eV) and the YL center at 2.2 eV. By comparing these TSC traps with common DLTS traps, induced by electron irradiation or enhanced by plasma etching in n-GaN layers [7,8], we believe that they are all due to nitrogen-vacancy ( $V_N$ ) related point defects. Moreover, there is some evidence from DLTS and transmission electron microscopy studies on samples with different thicknesses that trap D may be a complex involving both  $V_N$  and the gallium-vacancy ( $V_{Ga}$ ). This evidence, which is indirect, is based on the observation that D is readily observed in thin n-GaN layers with high dislocation densities [9], and that high dislocation densities are correlated with high concentrations of  $V_{Ga}$ , as revealed by positron annihilation studies [10]. Furthermore, the YL center is also strong in such layers, and is indeed thought to be a complex containing  $V_{Ga}$  (for example, see [11]).

It is known that light-induced metastability often involves configurational changes of a given defect or defect complex. For example, in GaAs, the As antisite can move from a tetrahedral to an off-center position, and also, reactions such as  $V_{Ga} \rightarrow V_{As}As_{Ga}$  can occur. In GaN, similar reactions would be  $V_{Ga} \rightarrow V_NN_{Ga}$ , or  $V_N \rightarrow V_{Ga}Ga_N$ . Thus, we believe that traps C, D, and E, as well as the YL center, may be associated with complexes of  $V_N$ ,  $V_{Ga}$ ,  $N_{Ga}$ , and  $Ga_N$ , and that strong light might be able to produce such complexes, or at least to transform one to the other. Also important is the carrier lifetime, which will affect the overall intensity of the TSC and PC. Some of the potential complexes may be more important than others in acting as recombination centers, and reducing carrier lifetime. The PC versus  $1/T$  data shown in the inset of Fig. 5 demonstrates that carrier lifetime probably depends upon the existence of a capture barrier, such as the one associated with  $As_{Ga}$  in GaAs. The electron capture processes due to presence of dislocation-related line-defects have been well studied on thin and thick n-GaN layers grown by

various techniques, using DLTS [12], and on MOVPE-grown undoped n-GaN using long-term photocapacitance decay measurements [13]. In these studies, either DLTS signals for most of traps or photocapacitance after suspension of white light illumination were found to depend on logarithmic filling-pulse width or logarithmic decay time, which were interpreted as anomalous electron capture kinetics due to time-dependent capture barrier associated with dislocation-related line-defects. Here, we find two facts: i) there exists a logarithmic relationship between 83-K PC and 380-K illumination time and ii) there is no saturation of low-T TSC peaks as light intensity increases, both indicating the possible presence of time-dependent capture barrier and dislocation-related line-defects. To determine the detailed structures of the point defects involved in the high-temperature-illumination-induced metastability, further studies are needed.

The work of Z-Q.F and DCL was supported by AFOSR Grant No. F49620-00-1-0347.

## References

1. Y.C. Chang, A.E. Oberhofer, J.F. Muth, R.M. Kolbas, and R.F. Davis, *Appl. Phys. Lett.* **79**, 281 (2001).
2. Y.C. Chang, A.L. Cai, M.A.L. Johnson, J.F. Muth, R.M. Kolbas, Z.J. Reitmeier, S. Einfeldt, and R.F. Davis, *Appl. Phys. Lett.* **80**, 2675 (2002).
3. M.E. Twigg, D.D. Koleske, A.E. Wickenden, R.L. Henry, and S.C. Binari, *Appl. Phys. Lett.* **79**, 4322 (2001).
4. D.C. Look, *Semiconductors and Semimetals* **19**, 75 (1983).
5. Z-Q. Fang, L. Polenta, J.W. Hemsky, and D.C. Look, *2000 International Semiconducting and Insulating Materials Conference (SIMC-XI)*, Canberra, edited by C. Jagadish and N.J. Welham (IEEE, Piscataway, NJ, 2000), p. 35.
6. D.C. Reynolds et al., private communication.
7. Z-Q. Fang, J.W. Hemsky, D.C. Look, and M.P. Pack, *Appl. Phys. Lett.* **72**, 448 (1998).
8. Z-Q. Fang, D.C. Look, X-L. Wang, Jung Han, F.A. Khan, and I. Adesida, submitted to *Appl. Phys. Lett.*
9. Z-Q. Fang, D.C. Look, J. Jasinski, M. Benamara, Z. Liliental-Weber, and R.J. Molnar, *Appl. Phys. Lett.* **78**, 332, (2001).
10. J. Oila, J. Kivioja, V. Ranki, K. Saarinen, D.C. Look, R.J. Molnar, and S.S. Park, submitted to *Appl. Phys. Lett.*
11. S.O. Kucheyev, M. Toth, M. R. Phillips, J.S. William, C. Jagadish, and G. Li, *J. Appl. Phys.* **91**, 5867 (2002).
12. Z-Q. Fang, D.C. Look, and L. Polenta, to be published in *J. Phys.: Condens. Matter*.
13. H-M. Chung, Y-C. Pan, W-C. Chuang, N-C. Chen, C-C. Tsai, M-C. Lee, W-H. Chen, and W-K. Chen, *Jpn. J. Appl. Phys.* **40**, 5871 (2001).

### Spectroscopic Characterization of Ion-Implanted GaN

L. Chen and B.J. Skromme

Department of Electrical Engineering and Center for Solid State Electronics Research, Arizona State University, Tempe, AZ, 85287-5706, U.S.A.

#### ABSTRACT

We investigate implantation of high purity HVPE GaN with Mg, Be, C, Zn, Cd, Ca, N, O, P, As, Ne, and Ar. After annealing at 1300 °C, the material is characterized using low temperature photoluminescence (PL). The Mg acceptors exhibit much better optical activation than Be, C, Zn, Cd, or Ca acceptors implanted and annealed under the same conditions. Acceptor-bound exciton peaks and well-resolved donor-acceptor pair bands are observed for both Mg and Zn. A broad peak centered near 2.78 eV is obtained for Cd, confirming that it is deeper than Zn. Isoelectronic As or P exhibit sharp no-phonon bound exciton lines at 2.952 and 3.200 eV, respectively. Defect-related bands centered at 2.2 and 2.35 eV are studied. Both Be and C strongly enhance the yellow (2.2 eV) PL band, but no other impurities do so, including O.

#### INTRODUCTION

GaN is a developing wide gap semiconductor material with important applications to both optical and electronic devices. Diffusion of most impurities in GaN is impracticably slow, so that ion implantation is the preferred method for selective doping of GaN. Ion implantation also permits the easy, controlled introduction of dopant species without complications due to unintentional passivating agents such as H. The behavior of implanted impurities and defects in GaN is not yet well understood. Therefore, it is useful to survey the properties of various dopant species and defects. In previous work, we studied Mg, C, and Be implants, sometimes together with Ne, Al, P, or Ar co-implantations, using low temperature photoluminescence (PL) [1, 2]. Good optical activation of Mg acceptors was obtained, yielding a spectroscopic binding energy of 224 meV from the conduction band-to-acceptor (e-A<sup>o</sup>) PL peak position. A green band at 2.35 eV and a weaker red band at 1.73 eV were also observed. Co-implantation of Mg, Be, and C acceptors with various other species showed that Mg acceptors incorporate well, whereas Be and C only enhance the yellow PL band. We found that P forms an isoelectronic hole trap on the N site in *n*-type GaN, but a helium-like double donor on the Ga site in *p*-type (Mg-doped) GaN.

Here, we extend this work to additional impurities and defect states. Low dose implantations into high purity starting material are combined with high temperature annealing to obtain highly resolved optical spectra. We study Zn, Cd, and Ca as *p*-type dopants at various doses and compare the optical activation of Mg, Be, C, Zn, Cd, and Ca acceptors. More detailed studies of the yellow PL band at 2.2 eV and the green band at 2.35 eV are performed. Implantation of As and P into *n*-type GaN is studied to compare the behavior of these isoelectronic hole traps. Control samples implanted with inert species and annealed or just annealed are used to confirm the association of PL peaks with specific impurities and defects.

#### EXPERIMENTAL PROCEDURE

The starting material consisted of hydride vapor phase epitaxial (HVPE) layers on sapphire (0001) substrates, about 15.9, 16.5, 20 or 22 μm thick, with residual *n*-type doping in the mid

$10^{16}$  to  $1 \times 10^{17} \text{ cm}^{-3}$  range. Some of these layers contain residual Zn acceptors, as determined by PL prior to implantation. Three implantation energies and doses were used for each species, to produce an approximately flat concentration profile to a depth of  $\sim 300 \text{ nm}$  for O, N, and C; and to  $\sim 120 \text{ nm}$  for P, As, Ca, and Zn. For  $^{114}\text{Cd}$ , the depth was shallower ( $\sim 80 \text{ nm}$ ), using four energies and doses to produce a flat profile (all profiles were designed using range and straggle values from TRIM tables, assuming Gaussian profiles). Energies and doses were adjusted for each impurity, so that heavier species were implanted at higher energies than lighter species. Thus, heavier species cause even greater damage than would be expected from their increased mass alone. The implanted species were  $^{40}\text{Ca}$ ,  $^{64}\text{Zn}$ ,  $^{114}\text{Cd}$ ,  $^{31}\text{P}$ ,  $^{75}\text{As}$ ,  $^{16}\text{O}$ ,  $^{14}\text{N}$ , and  $^{12}\text{C}$ . The implanted samples were encapsulated with sputtered AlON and annealed at  $1300^\circ\text{C}$  for 8 seconds under flowing  $\text{N}_2$ . Low temperature photoluminescence (PL) measurements were performed under  $305.5 \text{ nm}$  excitation at an irradiance of about  $260 \text{ mW/cm}^2$ , unless otherwise noted. All spectra are corrected for the spectral response of the measurement system.

## RESULTS

Low temperature PL spectra are shown in Figure 1 for HVPE GaN samples implanted with  $10^{17} \text{ cm}^{-3}$  Cd, Zn, or Mg and then annealed (the data for Mg implantation were presented previously [1], but are repeated here for reference). The implanted Mg acceptors show much stronger optical activation than do Zn or Cd. The Mg-implanted sample produces a strong donor-acceptor pair ( $\text{D}^0\text{-A}^0$ ) peak at  $3.275 \text{ eV}$ , a neutral acceptor-bound exciton ( $\text{A}^0, \text{X}$ ) peak at  $3.4712 \text{ eV}$ , and a broad deep level peak at  $2.35 \text{ eV}$ . There is also a damage-related deep level peak centered at  $1.78 \text{ eV}$ , which was observed in many of the implanted samples. In the Zn-implanted sample, there is a strongly phonon coupled ( $\text{D}^0\text{-A}^0$ ) peak centered at  $2.92 \text{ eV}$  (note the 3x scale expansion), and an ( $\text{A}^0, \text{X}$ ) peak at  $3.4624 \text{ eV}$ . In the Cd-implanted sample, the originally present neutral donor-bound exciton ( $\text{D}^0, \text{X}$ ) peak is observed at  $3.4798 \text{ eV}$ , and a new, strongly phonon-coupled ( $\text{D}^0\text{-A}^0$ ) peak is centered at  $2.78 \text{ eV}$ . A similar Cd ( $\text{D}^0\text{-A}^0$ ) peak was also reported by Pankove and Hutchby at  $2.7 \text{ eV}$  [3] and by Lagerstedt and Monemar at  $2.72 \text{ eV}$  [4]. Since the Cd-implanted sample (only) contained residual Zn prior to implantation, the Cd ( $\text{D}^0\text{-A}^0$ ) peak overlaps a weaker Zn ( $\text{D}^0\text{-A}^0$ ) peak, which may affect the apparent position of the Cd peak somewhat. Note the 150x scale expansion for the Cd ( $\text{D}^0\text{-A}^0$ ) peak; the optical activation of implanted Cd is much lower than that of Mg or Zn. This may be partially due to the greater implantation damage created by heavy ions such as  $^{114}\text{Cd}$ , which hampers optical activation. The shallower depth of the Cd implant is also a factor, but should only cause a  $\sim 67\%$  reduction. In the Ca-implanted sample (discussed in Figure 6

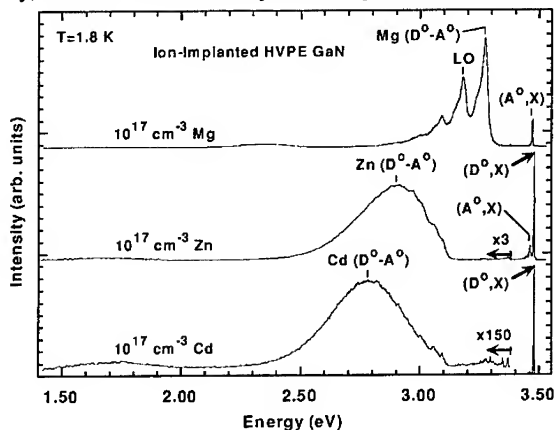


**Figure 1.** Low temperature PL spectra of Cd-, Zn-, and Mg-implanted pieces of HVPE GaN, after annealing.

below), no acceptor-related peaks are observed. This problem is not yet understood.

An expanded view of the excitonic regions of the spectra in Figure 1 is shown in Figure 2. The spectrum of the Cd-implanted sample is virtually unchanged from that before annealing or annealed without implantation (not shown). It shows a sharp (4 meV FWHM) neutral donor-bound exciton ( $D^0, X$ ) peak at 3.4796 eV, together with a LO phonon replica at 3.389 eV. An  $A$  free exciton ( $X_A$ ) peak is observed at 3.4852 eV, 6 meV above the ( $D^0, X$ ) peak. In the Zn-implanted sample, an ( $A^0, X$ ) peak is observed at 3.4624 eV, which was absent in the starting material.

This peak is even more clearly evidenced in the LO phonon replica of the ( $A^0, X$ ) peak at 3.37 eV, which is stronger than the LO phonon replica of the ( $D^0, X$ ) peak. This effect is due to the characteristically much stronger LO phonon coupling strength of ( $A^0, X$ ) peaks compared to ( $D^0, X$ ) peaks [5]. In the Mg-implanted sample, an ( $A^0, X$ ) peak is observed at 3.4712 eV, together with a LO phonon replica at 3.3792 eV, as reported earlier (repeated here for reference) [1]. The localization energies of the Mg and Zn ( $A^0, X$ ) complexes are 12.2 and 24.5 meV, respectively. Some groups have suggested that the 3.4712 eV peak is actually due to ionized donor-bound

( $D^+, X$ ) excitons, and that the  $p$ -type doping merely causes the donors to become ionized in equilibrium, enhancing the ( $D^+, X$ ) intensity [6, 7]. The Zn implants (or Zn doping during HVPE growth, which we have also studied) should also cause this effect, but produce only the 3.4624 eV peak. These observations support an acceptor-specific identification of the 3.4712 eV peak.

A low temperature PL spectrum of a P-implanted sample is shown in Figure 3. The no-phonon (NP) line of the isoelectronic  $P_N$  bound exciton

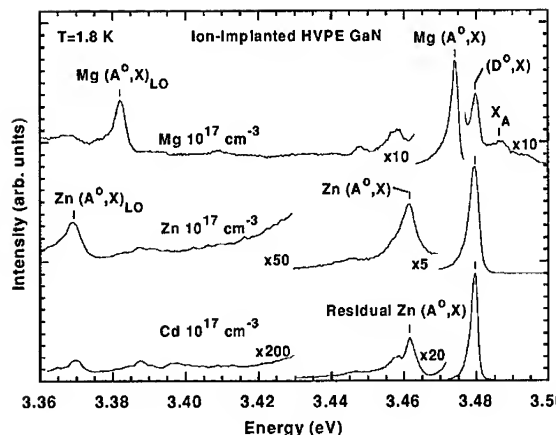


**Figure 2.** As Figure 1, but on an expanded horizontal scale to study the excitonic features. The Mg spectrum was rigidly shifted 3 meV higher in energy to align the ( $D^0, X$ ) peaks and compensate for strain differences.

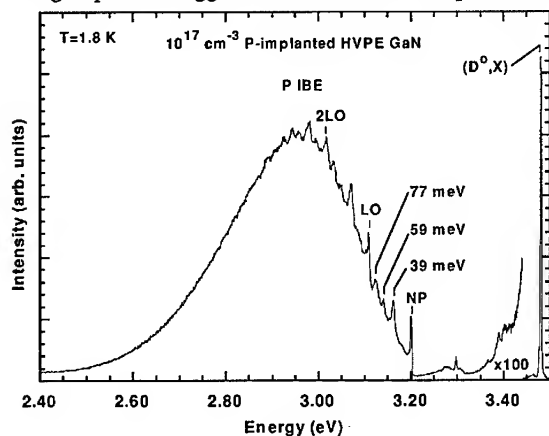


**Figure 3.** Low temperature PL spectrum of the P-implanted sample, showing the no-phonon (NP) line of the isoelectronic P-bound exciton and its phonon replicas.

(IBE) is observed at 3.200 eV, together with various acoustic and optical phonon replicas (with mode energies of 39, 59, 77 and 91 meV). The sharp (2.8 meV FWHM) ( $D^0, X$ ) peak at 3.481 eV was present in the starting material, together with its LO phonon replicas. This spectrum is even better resolved than we reported previously in a P+C co-implanted sample [2]. A similar broad structure was previously observed at slightly lower energy in P-implanted [8] and P-doped [9] GaN. The sharp no-phonon line gives an accurate exciton localization energy of 287 meV by comparison with the  $X_A$  peak position. A theoretical calculation by Mattila and Zunger predicted a value of 220 meV [10], in reasonable agreement with this result.

A low temperature PL spectrum of an As-implanted sample is shown in Figure 4. The no-phonon (NP) line of the isoelectronic As<sub>N</sub> bound exciton (IBE) is observed at 2.952 eV, with phonon replicas involving the same phonon modes as in the P-implanted case. The ( $D^0, X$ ) peak at 3.481 eV was present in the starting material, together with its phonon replicas. This result agrees with a previous study of As-related PL in GaN using implantation of radioactive isotopes [12], but the phonon replicas are better resolved in the present case. The sharp no-phonon line gives an accurate exciton localization energy of 535 meV compared with the  $X_A$  peak position. This result again agrees reasonably well with theoretical predictions of 410 or 310 meV [10,11]. Another important result is that same acoustic and optical phonon modes are observed in the replicas of the Zn ( $D^0-A^0$ ), Mg ( $D^0-A^0$ ), P IBE and As IBE peaks. This result implies that they are lattice and not local modes. The intensity of the As IBE peak is expanded 3000x relative to the ( $D^0, X$ ) peak in the figure, which is much larger than the 100x expansion factor used in the P case. The better optical activation of P compared to As may be due to its lower mass and reduced implantation damage. The As IBE shows stronger phonon coupling than the P IBE, consistent with its more strongly localized hole wave function.

We have also investigated the behavior of defect-related deep level PL bands. To help establish the origin of the yellow PL band at 2.2 eV, we implanted C, O, and N into pieces of the same sample with a dose of  $10^{17} \text{ cm}^{-3}$  in each case. The C implant is performed to confirm our earlier association of enhanced yellow PL after C implantation [1,2], and to compare the effects

of C with other species of similar mass (and therefore similar implantation damage). The O implant is used to test the idea that the yellow PL involves  $V_{Ga}$  complexed with O donors [13], which may stabilize implantation-induced vacancies and prevent their annihilation during the annealing process. Nitrogen is used as a control implant, to create damage similar to that caused by C and O. PL spectra of these three samples are shown in Figure 5, along with a spectrum of a Be-implanted sample from our previous work [1] for comparison. The starting material used for the C, O, and N implants (but not for

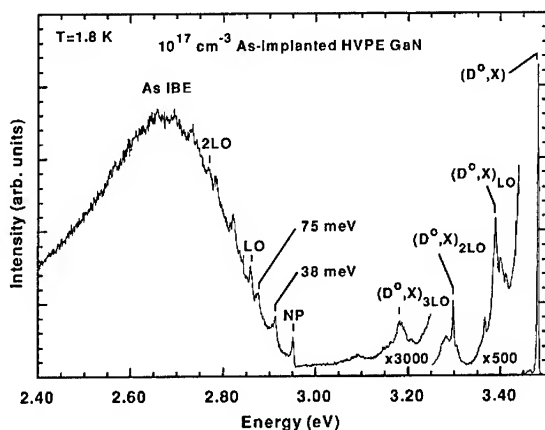


**Figure 4.** Low temperature PL spectrum of the As-implanted sample, showing the no-phonon (NP) line of the isoelectronic As-bound exciton and its phonon replicas.

Be) contained residual Zn acceptors. Both C and Be implants greatly enhance the intensity of the yellow (2.2 eV) PL band. But *none* of the other impurities do so, including O and N, as well as other impurities not shown here (P, As, Al, Mg, Ca, Zn, Ne and Ar). The C, O, and N results are similar to those of Zhang et al. using 300 K PL and  $1 \times 10^{20} \text{ cm}^{-3}$  doped starting HPVE material [14]. These observations provide a useful database to help study the origin or origins of this yellow band. There is general agreement that the 2.2 eV band involves transitions from shallow donors to a deep acceptor level

involving  $V_{\text{Ga}}$ , possibly complexed with donors [13, 15]. This idea is supported by a linear correlation between  $[V_{\text{Ga}}]$  and the yellow band PL intensity in both *n*-type MOCVD GaN [16] and in GaN:Be [17]. Previously, we suggested that the yellow PL is not uniquely related to C, but rather to  $V_{\text{Ga}}$ , which is stabilized by complexing with certain close-approaching donor species [2]. Based on the lack of yellow PL after O implantation, at least at the  $10^{17} \text{ cm}^{-3}$  level, it may be that interstitial impurities such as  $C_i$  or  $Be_i$  are more effective than  $O_N$  to stabilize  $V_{\text{Ga}}$ .

To understand the origin of the 2.35 eV PL band that we observed after Mg implantation [1], samples implanted with other acceptors (Ca and Zn) were investigated. Low temperature PL spectra are shown in Figure 6 for pieces of HVPE GaN that were implanted with  $10^{18} \text{ cm}^{-3}$  Zn,

$10^{18} \text{ cm}^{-3}$  Ca, or  $10^{17} \text{ cm}^{-3}$  Mg. In the Ca and Zn cases (only), the starting material contained residual Zn acceptors. A green band centered at 2.35 eV is observed in all three samples. However, we did not observe this band in samples implanted with  $10^{17} \text{ cm}^{-3}$  or less Zn, or in material implanted with  $10^{17} \text{ cm}^{-3}$  or less C, Be, P, As, Al, Ne or Ar. It is clear that this band is not unique to Mg implantation, but may involve a defect whose formation is favored when the Fermi level is low in the band gap. Since the Ca implants produced no optically evident

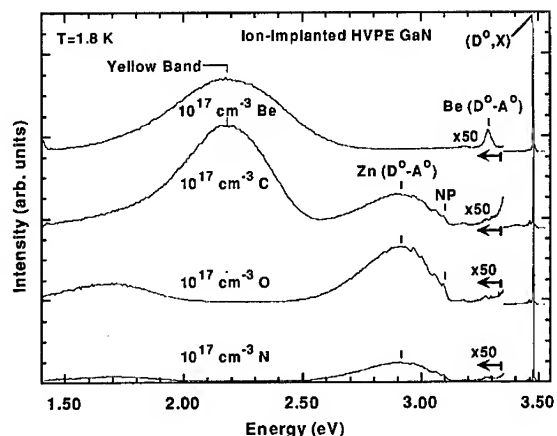


Figure 5. Low temperature PL spectra of Be, C, O, and N-implanted and annealed pieces of HVPE GaN.

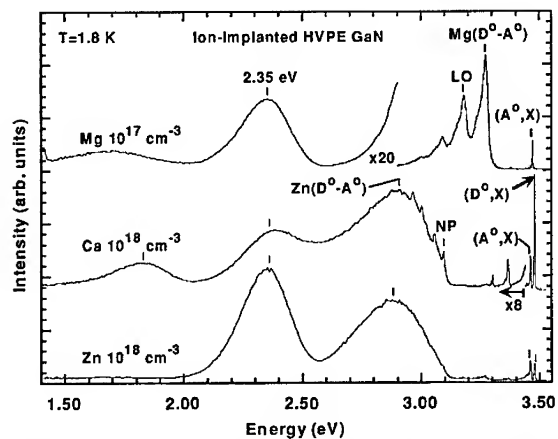


Figure 6. Low temperature PL spectra of Zn, Ca, and Mg-implanted and annealed pieces of HVPE GaN.

acceptor levels to pull down the Fermi level, the residual Zn in the starting material may have stimulated the occurrence of this band. Further experiments are needed to test this hypothesis and to determine the precise nature of this band.

## CONCLUSIONS

Ion-implanted Mg acceptors exhibit much better optical activation than Be, C, Zn, Cd, or Ca acceptors under the same conditions. Different positions of the acceptor-bound exciton peaks for Mg and Zn acceptors suggest that neither peak involves ionized donor bound ( $D^+,X$ ) excitons. Highly resolved spectra of excitons bound to isoelectronic As or P impurities are obtained with sharp no-phonon lines at 2.952 and 3.200 eV, respectively. Defect-related deep level bands centered at 2.2 and 2.35 eV need to be studied further to understand their precise origins.

## ACKNOWLEDGMENTS

We thank R. Molnar for providing the high quality HVPE material used in this work. This work was supported by the Materials Research Science and Engineering Center at ASU, under Grant No. DMR 96-32635 from the National Science Foundation, and by the Office of Naval Research Multidisciplinary University Research Initiative on III-Nitride Crystal Growth and Wafering, Grant No. N00014-01-1-0716, monitored by Dr. C.E.C. Wood.

## REFERENCES

1. B.J. Skromme and G.L. Martinez, MRS Internet J. Nitride Semicond. Res. **5S1**, W9.8 (2000).
2. B.J. Skromme, G.L. Martinez, L. Krasnobaev, and D.B. Poker, Mater. Res. Soc. Sympos. Proc. **639**, G11.39 (2001).
3. J.I. Pankove and J.A. Hutchby, J. Appl. Phys. **47**, 5387 (1976).
4. O. Lagerstedt and B. Monemar, J. Appl. Phys. **45**, 2266 (1974).
5. M.A.L. Johnson, Z. Yu, C. Boney, W.C. Hughes, J.W. Cook, Jr., J.F. Schetzina, H. Zhao, B. J. Skromme, and J.A. Edmond, Mater. Res. Soc. Sympos. Proc. **449**, 215 (1996).
6. B. Santic, C. Merz, U. Kaufmann, R. Niebuhr, H. Obloh, and K. Bachem, Appl. Phys. Lett. **71**, 1837 (1997).
7. D. C. Reynolds, D. C. Look, B. Jogai, V. M. Phanse, and R. P. Vaudo, Solid State Commun. **103**, 533 (1997).
8. W.M. Jadwisieniczak and H.J. Lozykowski, MRS Sympos. Proc. **482**, 1033 (1998).
9. T. Ogino and M. Aoki, Jpn. J. Appl. Phys. **18**, 1049 (1979).
10. T. Mattila and A. Zunger, Phys. Rev. B **58**, 1367 (1998).
11. C.G. Van de Walle and J. Neugebauer, Appl. Phys. Lett. **76**, 1009 (2000).
12. A. Stötzler, R. Weissenborn, and M. Deicher, Mater. Res. Soc. Sympos. Proc. **595**, W12.9 (2000).
13. J. Neugebauer and C.G. Van de Walle, Appl. Phys. Lett. **69**, 503 (1996).
14. R. Zhang, L. Zhang, N. Perkins, and T.F. Kuech, MRS Proc. **512**, 321 (1998).
15. T. Mattila and R.M. Nieminen, Phys. Rev. B **55**, 9571 (1997).
16. K. Saarinen *et al.*, Phys. Rev. Lett. **79**, 3030 (1997).
17. F.B. Naranjo, M.A. Sanchez-Garcia, J.L. Pau, A. Jimenez, E. Calleja, E. Munoz, J. Oila, K. Saarinen, and P. Hautojarvi, Phys. Stat. Sol. (a) **180**, 97 (2000).

### Plane-wave pseudopotential study on mechanical and electronic properties for group III-V binary phases

S. Q. Wang and H. Q. Ye  
Shenyang National Laboratory for Materials Science,  
Institute of Metal Research, Chinese Academy of Sciences,  
72 Wenhua Road, Shenyang 110016, P. R. China

#### ABSTRACT

The result of first-principles density functional calculations of the bulk modulus and related structural and electronic properties of the total 25 group III-V binary phases with zinc-blende and wurtzite structures are presented. The behavior of energy band structure variation under high pressures is also studied. It is found that the bulk modulus is more sensitive to the local atom configuration than the lattice structure. The crystallographic geometry plays an important role in the electronic property of these phases.

#### INTRODUCTION

The combination of III and V elements is characterized by typical covalent bonds. Zinc-blende (ZB) and wurtzite (WZ) are the commonest structures of III-V binary phases. The particular omni-triangulated nature in atomic structure makes these crystals unique mechanical and electronic properties. Most of the III-V solids are semiconductors. Among them GaN, InN and GaAs, due to their excellent electronic and optical properties, have found important application in microelectronic and information industries. However, due to the difficulty in experimental fabrication, only a small portion of these compounds has been fully studied in laboratory.

In this work, we perform a thoroughly computational study within the scheme of density-functional theory (DFT) for the total 25 III-V binary compounds in both of their ZB and WZ polytypes. The lattice parameter, bulk modulus, energy band structures and their electronic behaviors under pressure are calculated and analyzed in detail.

#### COMPUTATIONAL DETAILS

The DFT calculation has become a most important method in theoretical research of solids, nowadays. The generality and efficiency of plane-wave pseudopotential (PW-PP) method makes it as one of the most powerful *ab initio* quantum-mechanical modeling methods presently available [1,2]. Our PW-PP calculations are accomplished using the ABINIT computer code [2]. The LDA pseudopotentials used in present study are the Hartwigsen-Goedecker-Hutter (HGH) relativistic separable dual-space Gaussian pseudopotentials [3]. The details for the general routines of our DFT ground state calculation and energy band structure analyses are described elsewhere [4,5].

## RESULTS

### Lattice parameter and bulk modulus

Bulk modulus is an important parameter for mechanical property of solids. It is directly related to the hardness of materials. One knows from Murnaghan equation [6] that the constant-

**Table I.** Equilibrium lattice constants, bulk modulus  $B_0$  and  $B_0'$  of III-V ZB phases.

Phase	$a_0$ (nm)		$B_0$ (Mbar)		$B_0'$
	Calc.	Exp.	Calc.	Exp.	
AlN	0.4323	0.437	2.032		4.028
AlP	0.5417	0.5467	0.886	0.86	4.037
AlAs	0.5614	0.566	0.747	0.82	4.182
AlSb	0.6090	0.6136	0.561	0.58	4.362
AlBi	0.6266		0.482		5.237
GaN	0.4335	0.450	2.070		4.136
GaP	0.5322	0.5451	0.921	0.88	4.339
GaAs	0.5530	0.5649	0.757	0.77	4.487
GaSb	0.5981	0.6081	0.567	0.56	4.662
GaBi	0.6178		0.461		4.577
InN	0.4801	0.498	1.476		4.060
InP	0.5729	0.5867	0.736	0.72	4.479
InAs	0.5921	0.6054	0.617	0.58	4.545
InSb	0.6346	0.6472	0.476	0.46	4.688
InBi	0.6526		0.398		4.534
BN	0.3582	0.3615	3.923		3.763
BP	0.4478	0.4538	1.734	1.73	3.712
BAs	0.4721	0.4777	1.457		3.984
BSb	0.5177		1.100		4.237
BBi	0.5390		0.877		4.542
TiN	0.4882		1.411		4.349
TiP	0.5747		0.713		4.847
TiAs	0.5946		0.589		4.864
TiSb	0.6356		0.455		4.943
TiBi	0.6544		0.384		4.771

temperature equation of state (EOS) can be uniquely determined by three constants, namely lattice constant, bulk modulus and the pressure derivative of bulk modulus at zero pressure.

The equilibrium lattice and mechanical parameters of III-V ZB and WZ phases from fitting PW-PP ground-state results with Murnaghan EOS are presented in table I and II, respectively. The reliability of our result is evaluated by comparing with available experimental data [7-13] and judging from the value of  $B_0'$ , the pressure derivative of bulk modulus at  $P=0$ . It is seen that the general deviations of the theoretical data from the experimental ones are within 2% and 9% for lattice parameters and bulk modulus, respectively, and  $B_0' \sim 4$  to consistent with the universal theory of EOS [14].

**Table II.** Equilibrium lattice constants, internal parameter  $u$ , bulk modulus  $B_0$  and  $B_0'$  of III-V WZ phases.

Phase	$a_0$ (nm)		$c_0$ (nm)		$u$	$B_0$ (Mbar)		$B_0'$
	Calc.	Exp.	Calc.	Exp.		Calc.	Exp.	
AlN	0.3077	0.3112	0.4923	0.4982	0.382	2.0609	2.10	3.1401
AlP	0.3837		0.6251		0.376	0.8826		4.0448
AlAs	0.4001		0.6405		0.379	0.7414		4.2080
AlSb	0.4312		0.7038		0.375	0.5555		4.3543
AlBi	0.4434		0.7218		0.376	0.4626		4.4678
GaN	0.3066	0.3189	0.5005	0.5185	0.376	2.0759	2.10	4.1965
GaP	0.3763		0.6170		0.374	0.9123		4.3437
GaAs	0.3912		0.6407		0.375	0.7473		4.5048
GaSb	0.4234		0.6923		0.375	0.5580		4.6695
GaBi	0.4408		0.7027		0.380	0.4590		4.5942
InN	0.3406	0.3548	0.5499	0.5760	0.379	1.4845	1.40	4.2538
InP	0.4054		0.6625		0.375	0.7306		4.4913
InAs	0.4192		0.6844		0.375	0.6098		4.5726
InSb	0.4494		0.7337		0.375	0.4690		4.6785
InBi	0.4624		0.7518		0.376	0.3956		4.6095
BN	0.2527		0.4171		0.375	3.9725		3.5639
BP	0.3156		0.5209		0.375	1.7384		3.7182
BAAs	0.3326		0.5486		0.374	1.4602		4.0246
BSb	0.3649		0.6005		0.374	1.1050		4.2538
BBi	0.3799		0.6248		0.375	0.8800		4.4962
TiN	0.3458		0.5603		0.378	1.4234		4.4839
TiP	0.4060		0.6648		0.374	0.7100		4.8992
TiAs	0.4205		0.6866		0.375	0.5857		4.8738
TiSb	0.4497		0.7341		0.375	0.4511		4.9155
TiBi	0.4674		0.7428		0.382	0.3748		4.8486

By comparing table I and table II, it is found that the bulk moduli of ZB phase and its corresponding WZ phase are quite close in value in despite of the significant difference in their lattice configurations. This result indicates that bulk modulus is a measure of bonding strength among local atoms, while there are the same local tetrahedral-bonding configuration in both ZB and WZ phases. Our theoretical data also show a linear relationship between the bulk moduli and the inverse of unit-cell volumes of the total 25 III-V compounds both in ZB and WZ phases as consistent with our previous studies [4, 5]. The following  $B_0$ - $1/V_0$  equation is obtained for these ZB phases by a linear fitting of our theoretical data:

$$B_0 = -0.32202 + \frac{0.19314}{V_0}. \quad (1)$$

Similarly, the equation for WZ phases is

$$B_0 = -0.34199 + \frac{0.09822}{V_0}. \quad (2)$$

### **Energy band and its pressure dependence**

Electronic property is easily explored from the energy band structure of a crystal. In present study, we perform a non-self-consistent calculation to give eigen-energies at a large number of k-points following each self-consistent DFT ground state calculation for band structure analysis. Our result for electronic energy band information of the 25 III-V phases is presented in table III.

It is seen from the table that the electricity-conducting behavior of a solid strongly depends on its crystallographic configuration. Both band-gap and band-type vary with lattice configuration. AlN, AlAs, AlSb and BBi are indirect bandgap semiconductors in ZB structure. However, their WZ counterparts are direct bandgap semiconductors. Cubic GaBi, InBi, TlSb and TlBi are semimetal marked by zero bandgap while their hexagonal correspondents change to semiconductors. It is worth to notice that since LDA result is typically 30-50% less than the experimental measurement for the energy bandgap [15], it is also possible that some of the semimetals predicted in present calculation could be semiconductors with quite small direct bandgap. Even though, our present results give correction estimation of the band types for all the experimental available III-V compounds up to now.

Photoluminescence spectra of semiconductors are sensitive to hydrostatic pressure. Experimental investigation of the pressure dependence of energy band structure provides a direct way to understand the chemical trends and dielectric behaviors of the compound. Our theoretical data for the pressure coefficients  $k = dE_g^T / dP$  are also listed in table III, which may be used to guide experimental band structure analysis. There are two k values for some phases in table III, which is to correspond to the linear fit results of the first and the second part of the curve due to the unique two-part character of their  $E_g^T$ - $P$  curves.

**Table III.** Energy band structure and pressure coefficient  $k=dE_g^f/dP$  of 25 III-V ZB and WZ phases. The band type is classified as semimetal (S), direct (D) or indirect (I) band-gap semiconductors.

Phase	Zincblende			Wurtzite		
	$E_g^f$ (eV)	Bandtype	$k$ (meV/GPa)	$E_g^f$ (eV)	Bandtype	$k$ (meV/GPa)
AlN	4.503	I	45.0	4.620	D	43.3
AlP	3.261	I	94.2	2.261	I	35.3
AlAs	2.048	I	104.5	1.565	D	40.6
AlSb	1.670	I	140.8	0.952	D	41.7
AlBi	0.042	D	118.5	0.022	D	127.6
GaN	3.211	D	41.7	3.355	D	41.8
GaP	2.438	I	98.0	1.439	I	31.1
GaAs	1.008	D	109.4	0.778	D	136.7, 34.3
GaSb	0.547	D	140.3	0.167	D	34.1
GaBi	0.000	S	0.0	0.132	D	2.3
InN	0.753	D	34.0	0.904	D	37.0
InP	1.232	D	88.4	1.270	D	99.4, 30.1
InAs	0.192	D	93.3	0.205	D	90.3
InSb	0.213	D	132.7	0.217	D	144.7, 32.5
InBi	0.000	S	0.0	0.111	D	3.8
BN	8.792	I	11.7	8.307	I	9.9
BP	3.461	I	10.2	2.740	I	3.3
BAs	3.344	I	10.0	2.336	I	35.5
BSb	3.096	I	100.1, 17.6	1.541	I	42.2
BBi	1.134	I	102.2	0.416	D	43.0
TiN	0.000	S	0.0	0.000	S	0.0, 26.1
TiP	0.158	D	86.8	0.233	D	91.12
TiAs	0.000	S	0.0	0.000	S	0.0
TiSb	0.000	S	0.0	0.129	D	4.7
TiBi	0.000	S	0.0	0.118	I	3.8, 2.8

## CONCLUSIONS

We have done PW-PP electronic structure calculation in the local-density approximation by using the Hartwigsen-Goedecker-Hutter relativistic separable dual-space Gaussian pseudopotentials and presented the theoretical results of lattice parameters, bulk moduli and energy band structures of total 25 III-V ZB and WZ phases. We have correctly estimated the band-type for the all known phases by this realization. The calculated data of  $a_0$ ,  $c_0$  and  $B_0$  have been compared with the available results, and a promising consistency is reached. The two full sets of theoretical data show a linear relation between  $B_0$  and the inverse of  $V_0$  both for ZB and WZ phases. To convenient for experimental investigation, the pressure coefficients of bandgap for these materials are also calculated.

## ACKNOWLEDGMENTS

The authors would like to acknowledge the financial support of this work by the National Natural Science Foundation of China (No. 50072035) and the Special Funds for the Major State Basic Research Projects of China (No. G2000067104).

## REFERENCES

1. V. Milman, B. Winkler, J. A. White, C. J. Pickard, M. C. Payne, E. V. Akhmatkaya and R. H. Nobes, *Inter. J. Quan. Chem.* **77**, 895 (2000).
2. X. Gonze, J. M. Beuken, R. Caracas, F. Detraux, M. Fuchs, G. M. Rignanese, L. Sindic, M. Verstraete, G. Zerah, F. Jollet, M. Torrent, A. Roy, M. Mikami, P. Ghosez, J. Y. Raty and D. C. Allan, *Comp. Mater. Sci.* **25**, 478 (2002).
3. C. Hartwigsen, S. Goedecker, J. Hutter, *Phys. Rev. B* **58**, 3641 (1998).
4. S. Q. Wang and H. Q. Ye, *J. Phys.: Condens. Matter* **14**, 9579 (2002).
5. S. Q. Wang and H. Q. Ye, *Phys. Rev. B* (in press).
6. F. D. Murnaghan, *Proc. Natl. Acad. Sci. USA* **30**, 244 (1944).
7. K. H. Hellwege, O. Madelung, *Semiconductor Physics of Group IV elements and III-V compounds*, New series, Group III, Vol. 17, Pt. a (Springer, Berlin, 1982).
8. J. H. Edgar, *Properties of Group III Nitrides*, Electronic Materials Information Service (EMIS) Datareviews Series (Institution of Electrical Engineers, London, 1994).
9. T. Lei, T. D. Moustakas, R. J. Graham, Y. He, S. J. Berkowitz, *J. Appl. Phys.* **71**, 4933 (1992).
10. M. Levinstein, S. Rumyantsev, M. Shur, *Handbook Series on Semiconductor Parameters*, Vol. 1,2 (World Scientific, London, 1999).
11. S. Strite, J. Ruan, D. J. Smith, J. Sariel, N. Manning, H. Chen, *Bull. Am. Phys. Soc.* **37** 346 (1992).
12. S. Strite, H. Morkoc, *J. Vac. Sci. Technol. B* **10** 1237 (1992).
13. M. Levinstein, S. Rumyantsev, M. Shur, *Handbook Series on Semiconductor Parameters*, vol.1 (World Scientific, London, 1996).
14. R. Jeanloz, *Phys. Rev. B* **38**, 805 (1988).
15. M. S. Hybertsen and S. G. Louie, *Phys. Rev.* **34**, 5390 (1986).

**BEST AVAILABLE COPY**

### Surface Passivation of AlGa<sub>N</sub> terminated and Ga<sub>N</sub> Terminated HEMT Structures Studied by XPS

B.P. Gila<sup>1</sup>, E. Lambers<sup>1</sup>, B. Luo<sup>2</sup>, A.H. Onstine<sup>1</sup>, K.K. Allums<sup>1</sup>, C.R. Abernathy<sup>1</sup>,  
F. Ren<sup>2</sup> and S.J. Pearton<sup>1</sup>

<sup>1</sup> Dept. of Materials Science and Engineering, University of Florida, Gainesville, FL 32611

<sup>2</sup> Dept. of Chemical Engineering, University of Florida, Gainesville, FL 32611

#### ABSTRACT

Samples of both AlGa<sub>N</sub> and Ga<sub>N</sub> terminated HEMT structures were studied using x-ray photo spectroscopy (XPS). It was found that the XPS spectra of both AlGa<sub>N</sub> and native oxide surfaces were shifted by a surface charge of 0.5 to 1.0 eV. The samples were then oxidized using an UV-ozone treatment for 25 minutes at room temperature. The ozone oxide XPS spectra of the AlGa<sub>N</sub> terminated surface was found to have the same 0.5 to 1.0 eV shift while the ozone oxide XPS spectra of the Ga<sub>N</sub> terminated surface was found to have a 5.0 eV shift, indicating that the native Ga<sub>N</sub> oxide is more insulating. Processed HEMT devices using both surface terminations were given the same UV-ozone treatment followed by a 10nm MBE grown Sc<sub>2</sub>O<sub>3</sub> film for passivation. The Ga<sub>N</sub> terminated HEMT structures showed on average a 10% increase in channel current (from gate-lag measurements, pulse mode) over the AlGa<sub>N</sub> terminated HEMT structures.

#### INTRODUCTION

Remarkable progress has been made in the field of high performance and high power AlGa<sub>N</sub>/Ga<sub>N</sub> high-electron-mobility transistors (HEMTs); namely, in understanding the device physics and demonstrating excellent microwave power performance.[1] One problem with the implementation of these devices is that the RF power obtained is much lower than that expected from the dc characteristics. This RF power decrease is manifested by a drain current collapse that is believed to be caused by the presence of surface states between the gate and drain, which further depletes the channel.[2-12] This phenomenon can also be observed by a current dispersion between dc and pulsed test conditions or a degraded rf output power.

The carriers in the 2-dimensional electron gas can be lost either to the surface or buffer traps [2,3, 13-16]. The surface traps may be mitigated by the use of appropriate surface passivation, most often SiN<sub>x</sub> deposited by plasma-enhanced chemical vapor deposition (PECVD). The bulk traps are a function of the epitaxial growth conditions and can only be reduced by improving material growth techniques. In the situation in which surface states dominate the current collapse, the use of SiN<sub>x</sub> passivation typically restores 70-80% of the dc current. Other surface passivation has been achieved by employing MgO or Sc<sub>2</sub>O<sub>3</sub> and the recovery of current to is shown to approach 100%.[17-19] After performing identical treatments and passivating oxide growths on AlGa<sub>N</sub> terminated and Ga<sub>N</sub> terminated HEMT structures, tendencies are that Ga<sub>N</sub> terminated HEMTs show a higher degree of current recovery than the

AlGaIn terminated HEMTs, Table 1. In this paper, XPS spectra of as received AlGaIn and GaIn terminated HEMT structures are compared to spectra of ozone treated surfaces.

HEMT	As-received	UV-Ozone Treatment	Sc <sub>2</sub> O <sub>3</sub> Passivation
AlGaIn cap	50% of dc	35% of dc	80% of dc
GaIn cap	40% of dc	40% of dc	95% of dc

Table 1. Comparison of AlGaIn and GaIn capped HEMTs (% of dc refers to the gate pulse measurement compared to the dc measurement at 100%)[19]

## EXPERIMENTAL

Two types of surface terminated HEMT structures were examined. The first structure was undoped AlGaIn(20%Al)/GaIn (30nm/2μm) and second structure was undoped GaIn/AlGaIn(20%Al)/GaIn (5nm/30nm/2μm). Both structures were grown by MOCVD on 2" sapphire substrates. Sections of the HEMT wafers (1cm x 2cm) were loaded into a Perkin-Elmer PHI 5100 X-ray Photoelectron Spectrometer (XPS) with a background pressure of low 10<sup>-10</sup> Torr. The XPS system used a 45-degree nominal takeoff angle between the sample and detector. A Mg anode x-ray (1253.6 eV) source at an energy of 15 kV was employed. The spot size of the XPS system is approximately 5mm x 15mm of the total surface.

The HEMT samples were irradiated by the Mg x-ray source and the photoelectron spectra was collected. The samples were sputtered using an in-situ Ar<sup>+</sup> ion beam (4E-8 Torr, 20mA) to remove the surface adsorbed carbon and native oxides and then the surface spectra of the two HEMTs were collected again. This provided a baseline for a native GaIn and AlGaIn surfaces. The samples were removed from the vacuum system, exposed to ozone from an UV-ozone oven (UV Cleaner model 42-220) for 25 minutes, then returned to the UHV environment of the XPS system. The as-ozone treated samples were rescanned. Subsequent 2 minute Ar<sup>+</sup> sputters followed by surface scans were repeated for a total sputter time of 8 minutes (4 iterations). At this point, the O 1s signal intensity was the same as the as-grown samples after a 2 minute Ar<sup>+</sup> sputter.

## RESULTS AND DISCUSSION

As grown HEMT structures with AlGaIn and GaIn caps were studied with XPS. The native oxide surface showed a surface charge of 0.6 eV for the GaIn capped HEMT and 0.9 eV for the AlGaIn capped HEMT according to the position of the advantageous surface carbon. This surface carbon has a known peak position of 284.5 eV.

From the fitting of the Ga 3d peak and the O 1s peak (Figure 1) of the as-grown GaIn capped HEMT, there is a native surface oxide consisting of Ga<sub>2</sub>O<sub>3</sub>, which agrees with several other GaIn surface studies.[20-25] Post Ar<sup>+</sup> sputtering (2 min.) showed a significant reduction in the O 1s signal, elimination of the carbon signal and reduction of the Ga<sub>2</sub>O<sub>3</sub> portion of the Ga 3d

**BEST AVAILABLE COPY**

signal. The Ga 3d peak shifted 1.2eV to lower energy. A similar shift in the O 1s peak is also seen, however the O 1s peak is greatly reduced in intensity.

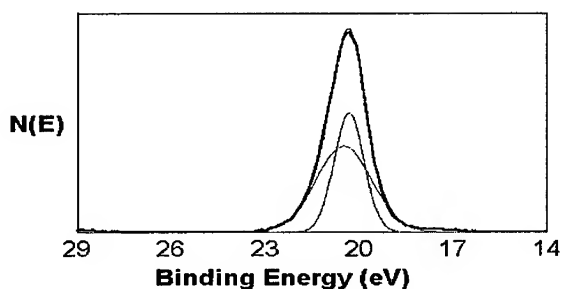


Figure 1. XPS spectra of the as-grown GaN capped HEMT (before Ar+ sputter). The Ga 3d peak is resolved to  $\text{Ga}_2\text{O}_3$  at 20.6eV and GaN at 20.1eV.

From fitting the Ga 3d peak, Al 2p peak and the O 1s peak (Figure 2) of the as-grown AlGaIn capped HEMT, there are native surface oxides of both  $\text{Ga}_2\text{O}_3$  and  $\text{Al}_2\text{O}_3$ . Post Ar+ sputtering (2 min.) of this surface showed a reduction in the O 1s signal and elimination of the carbon signal. The Ga 3d peak and the Al 2p peak showed reduction of both oxide signal portions and a shift of 0.8eV to lower energy, similar to the GaN capped HEMT. A similar shift in the O 1s peak is also seen as well as a reduction in intensity.

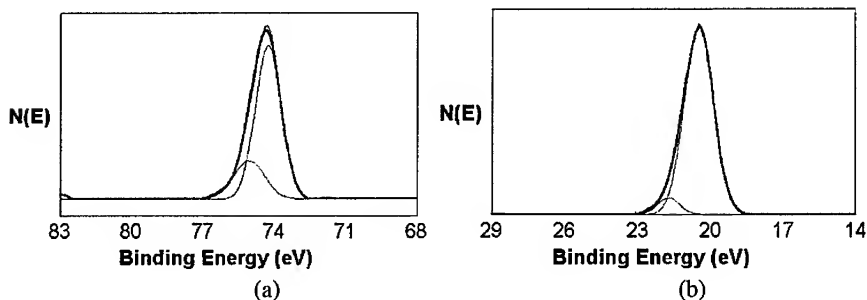


Figure 2. XPS spectra of the as grown AlGaIn capped HEMT (before Ar+ sputter). The Al 2p peak (a) is resolved to  $\text{Al}_2\text{O}_3$  at 75.1eV and AlN at 74.4eV. The Ga 3d peak (b) is resolved to  $\text{Ga}_2\text{O}_3$  at 21.8eV and GaN at 20.5eV.

The HEMT samples were then exposed to UV-ozone. The time for the ozone exposure was determined from earlier studies on preparing GaN and HEMT surface preparation for oxide growth, this was 25 minutes.[26] The samples were then reloaded into the XPS system and the surface spectra were recorded again.

The properties of the AlGaIn surface oxide created by the ozone treatment showed little difference in surface charging (comparing the advantageous carbon peak position to the known

value), however the thickness of the oxide was approximately 4 times thicker. This was determined by comparing the time of Ar<sup>+</sup> sputtering required to reduce the O 1s peak intensity to that of the as received native oxide. The Al 2p peak showed a large increase in its Al<sub>2</sub>O<sub>3</sub> portion (74.7eV) and the Ga 3d peak showed only a slight change in its Ga<sub>2</sub>O<sub>3</sub> portion (Figure 3a,b). After the initial Ar<sup>+</sup> sputter, the Ga, Al, and O peaks all shift to the values corresponding to the as-received sample. As the oxide is sputtered away, the Al<sub>2</sub>O<sub>3</sub> portion is reduced and the AlN portion (73.5eV) is increased.

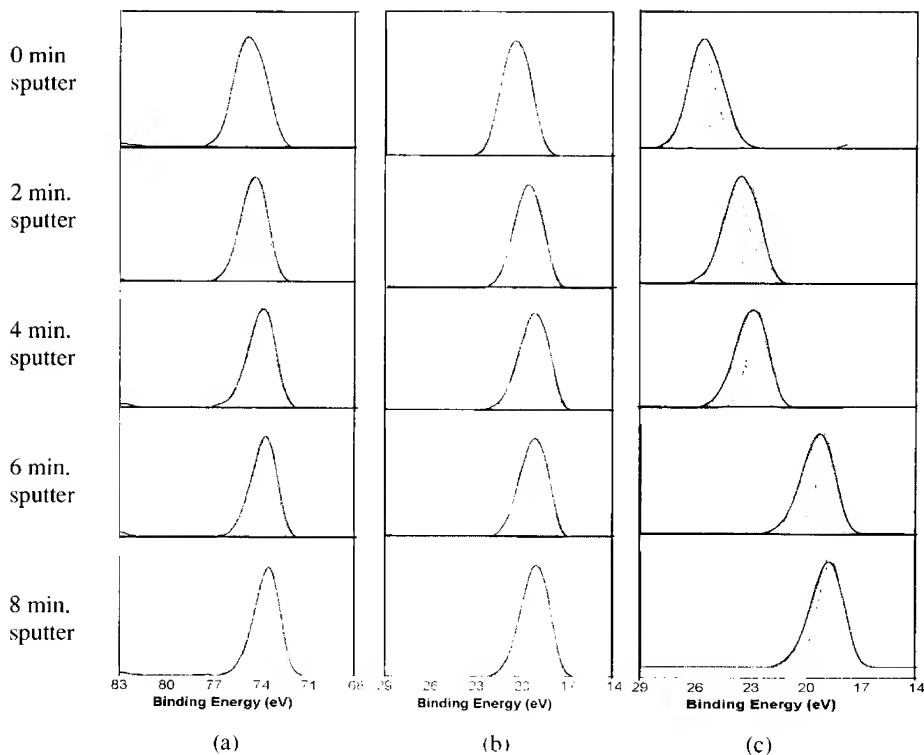


Figure 3. The XPS spectra of the AlGaIn ozone oxide are represented by the Al 2p (a) and the Ga 3d (b) peaks. The GaN ozone oxide is represented by the Ga 3d peak (c). Note the 5eV shift in the spectra (c) and its return to its known position with oxide removal.

The properties of the GaN surface ozone oxide showed a significant increase in surface charge. The advantageous carbon peak is shifted by over 5eV when compared to its known value of 284.5eV, and in fact this 5eV shift is seen in the entire XPS spectra. A lack of mobile charge transport is what allows for the 5eV charge to build up. The spectra does shift back to its known values as the oxide is sputtered. The Ga 3d, N 1s and O 1s peaks return to their correct position at a rate that match the oxide sputter rate. Or in other words, if the oxide is reduced by

**BEST AVAILABLE COPY**

50%, the surface charge is reduced 50% (Figure 3b). This would indicate the charging effect is directly related to the thickness of the oxide produced by the UV-ozone treatment.

## CONCLUSION AND SUMMARY

The addition of Al to GaN has a significant effect on the type of oxide formed on the surface from the UV-ozone treatment. This has implications on the passivation procedure to be employed to reduce the current collapse on the HEMT structure. From this study, employing a GaN cap on the HEMT structure allowed for a better insulating native oxide to be grown before the passivating oxide is deposited. A lack of mobile charge transport allows the 5eV charge to build up. Further research is required to determine the limits the charge transport so more insulating native oxides can be realized.

## ACKNOWLEDGEMENTS

The authors gratefully acknowledge the support of this work by the U. S. Air Force Office of Scientific Research under grant no. U. S. Air Force F49620-02-1-0366(G. Witt) and by the U. S. Office of Naval Research under grant no. US Navy N00014-98-1-0204(H.B. Dietrich) and NSF (DMR010438 and CTS 9901173). The XPS characterization was performed at the Major Analytical Instrumentation Center (MAIC) at the University of Florida.

## REFERENCES

1. S.J. Pearton, J.C. Zolper, R.J. Shul, F. Ren; *Journal of Applied Physics* **86** (1), p.1-78 (1999)
2. B. M. Green, K. K. Chu, E. M. Chumbes, J. A. Smart, J. R. Shealy, and L. F. Eastman, *IEEE Electron. Dev. Lett.*, **21**, 268(2000).
3. S. C. Binari, W. Kruppa, H. B. Dietrich, G. Kelner, A. E. Wickenden and J. A. Freitas Jr, *Solid-State Electron.*, **41**, 1549(1997).
4. L. F. Eastman, V. Tilak, J. Smart, B. M. Green, E. M. Chumbes, R. Dimitrov, H. Kim; O. S. Ambacher, N. Weimann, T. Prunty, M. Murphy, W. J. Schaff, and J. R. Shealy, *IEEE Trans. Electron Dev.*, **48**, 479(2001).
5. E. Kohn, I. Daumiller, P. Schmid, N. X. Nguyen, C. N. Nguyen, *Electron. Lett.* **35**, 1022(1999).
6. J.S. Lee; A. Vescan, A. Wieszt, R. Dietrich, H. Leier, Y.-S. Kwon, *Electron. Lett.* **37**, 130(2001).
7. X. Hu, A. Koudymov, G. Simin, J. Yang, M. Asif Khan, A. Tarakji, M. S. Shur, and R. Gaska, *Appl. Phys. Lett.* **79**, 2832(2001).
8. N. X. Nguyen, C. Nguyen and D. E. Grider, *Electron. Lett.* **35**, 1356(1999).
9. I. Daumiller, C. Kirchner, M. Kamp, K. J. Ebeling, and E. Kohn, *IEEE Electron. Dev. Lett.* **20**, 448(1999).
10. A. Tarakji, G. Simin, N. Ilinskaya, X. Hu, A. Kumar, A. Koudymov, J. Yang, M. Asif Khan, M. S. Shur, and R. Gaska, *Appl. Phys. Lett.* **78**, 2169(2001).
11. E. M. Chumbes, J. A. Smart, T. Prunty and J. M. Shealy, *IEEE Trans. Electron Dev.*, **48**, 416(2001).

12. S. C. Binari, K. Ikossi, J. A. Roussos, W. Kruppa, D. Park; H. B. Dietrich, D. D. Koleske, A. E. Wickenden, and R. L. Henry, *IEEE Trans. Electron Dev.*, **48**, 465(2001).
13. P. B. Klein, S. C. Binari, K. Ikossi, A. E. Wickenden, D. D. Koleske, and R. L. Henry, *Appl. Phys. Lett.* **79**, 3527(2001).
14. P. B. Klein, J. A. Freitas, Jr., S. C. Binari, and A. E. Wickenden, *Appl. Phys. Lett.* **75**, 4016(1999).
15. P. B. Klein, S. C. Binari, J. A. Freitas, Jr., and A. E. Wickenden, *J. Appl. Phys.* **88**, 2843(2000).
16. P. B. Klein, S. C. Binari, K. Ikossi-Anastasiou, A. E. Wickenden, D. D. Koleske, P. L. Henry, D. S. Katzer, *IEEE Electron. Lett.* **37**, 661(2001).
17. B. Luo, J.W. Johnson, B.P. Gila, A. Onstine, C.R. Abernathy, F. Ren, S.J. Pearton, A.G. Baca, A.M. Dabiran, A.M. Wowchack, P.P. Chow, *Solid-State Electronics* v 46 n 4 April 2002 p 467-476
18. Luo B, Johnson JW, Kim J, Mehandru RM, Ren F, Gila BP, Onstine AH, Abernathy CR, Pearton SJ, Baca AG, Briggs RD, Shul RJ, Monier C, Han J; *Applied Physics Letters* 80 (9): 1661-1663 MAR 4 2002
19. B. Luo, R. Mehandru, J. Kim, F. Ren, B.P. Gila, A.H. Onstine, C.R. Abernathy, S.J. Pearton, R. Fitch, J. Gillespie, T. Jenkins, J. Sewell, D. Via, A. Crespo, Y. Irokawa; *Journal of the Electrochemical Society* **149** (11), pp.G613-G619 (2002)
20. K. Prabhakaran, T.G. Andersson, K. Nozawa; *Applied Physics Letters* **69** (21), p.3212 (1996)
21. T.K. Zywiets, J. Neugebauer, M. Scheffier; *Applied Physics Letters* **74** (12), p.1695 (1999)
22. N.J. Watkins, G.W. Wicks, Y. Gao; *Applied Physics Letters* **75** (17), p.2602 (1999)
23. R. Nakasaki, T. Hashizume, H. Hasegawa; *Physica E* **7**, p.953 (2000)
24. S.D. Wolter, J.M. DeLucca, S.E. Mohoney, R.S. Kern, C.P. Kuo; *Thin Solid Films* **371**, p.153 (2000)
25. I. Shalish, Y. Shapira, L. Burstein, J. Salzman; *J. Applied Physics* **89** (1), p.390 (2001)
26. B.P. Gila, J.W. Johnson, R. Mehandru, B. Luo, A.H. Onstine, K.K. Allums, V. Krishnamoorthy, S. Bates, C.R. Abernathy, F. Ren, S.J. Pearton, *phys. stat. solidi (a)* **188**, p.239 (2001)

### Properties of Delta Doped $\text{Al}_{0.25}\text{Ga}_{0.75}\text{N}$ and GaN Epitaxial Layers

Jeffrey S. Flynn, Leah G. Wallace, Joe A. Dion, Edward L. Hutchins, Helder Antunes and George R. Brandes  
Advanced Technology Materials, Inc  
Danbury, CT 06810, U.S.A.

#### ABSTRACT

Delta doping (paused growth doping) was investigated as an alternative to uniformly distributing the dopant in the nitride semiconductor layer. In this work, delta doped layers were produced in MOVPE-grown AlGa<sub>0.75</sub>N and GaN layers at a susceptor temperature of 1220°C by turning off the group III precursors (TMG and TMA) and introducing into the reactor a silicon precursor Si<sub>2</sub>H<sub>6</sub> (disilane) for a fixed period (pause time) before growth was restarted. The compositional and electrical properties as a function of aluminum content and dopant flux were investigated for nitride layers on 2 inch c-plane sapphire substrates. Secondary ion mass spectroscopy (SIMS) measurements revealed a sharp silicon peak with a FWHM of  $5.7 \pm 0.6$  nm for an  $\text{Al}_{0.25}\text{Ga}_{0.75}\text{N}$  sample and  $10.0 \pm 0.6$  nm for a GaN sample with sheet charges of  $7.9 \times 10^{12} \text{ cm}^{-2}$  and  $9.9 \times 10^{12} \text{ cm}^{-2}$ , respectively. Room temperature Hall mobility as high as  $265 \text{ cm}^2 \text{ V}^{-1} \text{ s}^{-1}$  for a sheet charge  $7.9 \times 10^{12} \text{ cm}^{-2}$  was demonstrated for delta doped  $\text{Al}_{0.25}\text{Ga}_{0.75}\text{N}$  layers, but the mobility enhancement saturated and then decreased with increasing sheet charge. Room temperature sheet charge increased with increasing dopant flux for delta-doped AlGa<sub>0.75</sub>N and GaN layers. Sheet charge density as high as  $2.2 \times 10^{13} \text{ cm}^{-2}$  and  $1.3 \times 10^{13} \text{ cm}^{-2}$  was measured at room temperature for  $\text{Al}_{0.25}\text{Ga}_{0.75}\text{N}$  and GaN delta doped layers, respectively. Under identical doping conditions, the Hall sheet charge of the delta doped  $\text{Al}_{0.25}\text{Ga}_{0.75}\text{N}$  layer was approximately half as large as GaN layers. The impurity and electrical characteristics of the delta doped layers are further discussed.

#### INTRODUCTION

High quality delta doped structures have played an important role in conventional III-V semiconductors [1] and are well-known to reduce DX centers and the corresponding deleterious effects in AlGaAs [2], improve p-HEMT mobility, increase breakdown voltage [3,4] and provide improved temperature-stability in laser diodes [5,6]. Given these significant benefits to AlInGaAsP, it is surprising little systematic experimentation of delta doping has been done in III-nitrides. GaN delta doping was demonstrated with relatively narrow C-V profiles, a few nanometers in width, similar to GaAs [7,8]. Delta doped layers in AlGa<sub>0.75</sub>N HEMT heterostructures were recently demonstrated exhibiting high peak transconductance of  $240 \text{ mS mm}^{-1}$  [9] and high mobility of  $12,000 \text{ cm}^2 \text{ V}^{-1} \text{ s}^{-1}$  at 77°K [10]. In this paper we report results of measurements made on samples of delta doped GaN and  $\text{Al}_{0.25}\text{Ga}_{0.75}\text{N}$  grown by low pressure,

MOCVD. The differences between the samples are investigated via SIMS Si impurity profiling, 300°K and 77°K Hall sheet charge and mobility measurements.

## EXPERIMENT

The nitride samples in this study were grown in an AIX 200 / 4 MOCVD reactor on (0001) sapphire substrates with a conventional low temperature nucleation technique described in previous work [11]. Epitaxial growth was performed at a susceptor temperature of 1220°C with TMG and TMA used as the column III-precursors and 2.5slm of NH<sub>3</sub> used as the column V-precursor in an H<sub>2</sub> carrier gas. The growth rate of the Al<sub>0.25</sub>Ga<sub>0.75</sub>N and GaN films was 2.0μm hr<sup>-1</sup> at 100mbar.

To produce the delta doped layers, GaN or AlGa<sub>0.25</sub>N films were first deposited on a sapphire substrate for 54 minutes to yield a thickness of 1.8μm of III-nitride material. Next, the metalorganic precursor(s) were diverted to the vent with only NH<sub>3</sub> and H<sub>2</sub> flowing. After ten seconds, Si in the form of Si<sub>2</sub>H<sub>6</sub> was introduced into the reactor for 75 seconds at a flowrate between 8.6x10<sup>-5</sup> and 3.3x10<sup>-4</sup> sccm. At the end of the 75 second pause time, the Si<sub>2</sub>H<sub>6</sub> was diverted to the vent and the metalorganic(s) were simultaneously reintroduced into the reactor vessel. Finally, 6 minutes of growth was conducted to cap the structures with 0.2μm of AlGa<sub>0.25</sub>N or GaN. Under these conditions, test samples without the Si flux during the pause time resulted in a resistivity of greater than >10<sup>9</sup> Ω cm as determined from high temperature measurements extrapolated to room temperature. After growth, the sheet resistances of the delta-doped layers were measured via Lehighton and then a center 1cm x 1cm piece of material was prepared for Hall measurement with In:Sn contacts. An adjacent piece of material was sent to Charles Evans East for SIMS impurity analysis to determine Si depth profile and Si areal density (sheet density at the interface).

## RESULTS

### SIMS Si Impurity Analysis

For a constant pause time of 75 seconds, Si incorporation in Al<sub>0.25</sub>Ga<sub>0.75</sub>N and GaN was found to be a linear function of Si<sub>2</sub>H<sub>6</sub> flux, as shown in Figure 1. At 2x10<sup>-4</sup> sccm of disilane, Al<sub>0.25</sub>Ga<sub>0.75</sub>N demonstrated about two times lower Si density compared to GaN and a comparable difference in sheet charge. We attribute the difference in Si incorporation under identical doping conditions to differences in either the surface adsorption/desorption process or possibly AlGa<sub>0.25</sub>N SIMS Si analysis error [12,13].

Although the Si incorporation behavior as a function of disilane flux was consistent with results obtained in previous delta doping studies, the FWHM of Si concentration in the GaN and AlGa<sub>0.25</sub>N delta doped layers exhibited an interesting trend. The width of the delta doped layer (as determined by FWHM of the SIMS data) increased in GaN with increasing disilane flux while the width remained constant in the AlGa<sub>0.25</sub>N (Figure 2a). The FWHM of a Si profile of the AlGa<sub>0.25</sub>N layer delta doped with 1.1x10<sup>13</sup>cm<sup>-2</sup> Si was 5.7±0.6 nm while GaN delta doped layer with

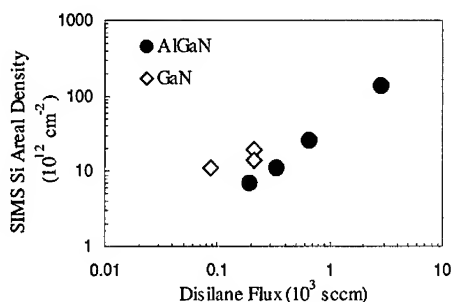


**Figure 1.** SIMS Si areal density at the delta doped GaN and  $\text{Al}_{0.25}\text{Ga}_{0.75}\text{N}$  interface layer as a function of disilane flux at constant pause time of 75 seconds.

$1.4 \times 10^{13} \text{ cm}^{-2}$  Si was  $10 \pm 0.6 \text{ nm}$  as shown in Figure 2 (b). Since these layers were grown under identical cap layer conditions and exhibit comparable SIMS Si areal densities, we suspect the broadening is due to greater impurity diffusion and/or segregation in GaN as a consequence of a higher diffusion constant.

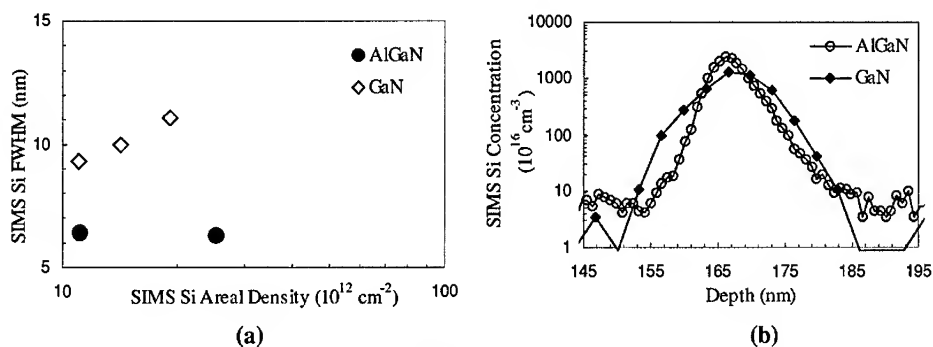


**Figure 2.** SIMS Si impurity profile data (a) SIMS Si profile FWHM as a function of SIMS Si areal density for GaN and  $\text{Al}_{0.25}\text{Ga}_{0.75}\text{N}$  layers and (b) SIMS Si impurity concentration as a function of depth for  $\text{Al}_{0.25}\text{Ga}_{0.75}\text{N}$  (Si density =  $1.1 \times 10^{13} \text{ cm}^{-2}$ ) and GaN (Si density =  $1.4 \times 10^{13} \text{ cm}^{-2}$ )

### Hall and Leighton Electrical Analysis

Delta doped layers exhibit increased room temperature Hall sheet charge as a function of disilane flux, as shown in Figure 3, with GaN layers exhibiting about two times greater sheet charge for a given disilane flux. This is consistent with the SIMS Si impurity incorporation trend as a function of disilane flux discussed in the preceding section.

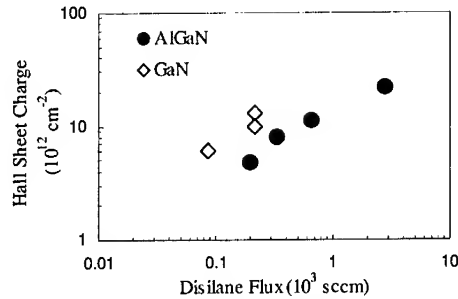


**Figure 3.** Room temperature Hall sheet charge as a function of disilane flux for delta doped  $\text{Al}_{0.25}\text{Ga}_{0.75}\text{N}$  and GaN layers

The Leighton sheet resistance decreased with increasing Hall sheet charge as shown in Figure 4 (a). Interestingly, the delta doped  $\text{Al}_{0.25}\text{Ga}_{0.75}\text{N}$  layer Leighton sheet resistance was lower than GaN delta doped layer for a given Hall sheet charge. We attribute the lower sheet resistance of  $\text{Al}_{0.25}\text{Ga}_{0.75}\text{N}$  delta doped layers to the improved room temperature Hall mobility compared to GaN, as shown in Figure 4 (b). However, as the sheet charge increased above  $2 \times 10^{13} \text{ cm}^{-2}$  for  $\text{Al}_{0.25}\text{Ga}_{0.75}\text{N}$  the mobility was reduced. We suspect the reduced mobility at very high sheet charges is a consequence of the reduced quality and increased carrier interactions. However, mobility as high as  $265 \text{ cm}^2 \text{ V}^{-1} \text{ s}^{-1}$  can be reached in  $\text{Al}_{0.25}\text{Ga}_{0.75}\text{N}$  layers with  $7.9 \times 10^{12} \text{ cm}^{-2}$  room temperature Hall sheet charge while slightly lower mobility can be reached in GaN layers at  $165 \text{ cm}^2 \text{ V}^{-1} \text{ s}^{-1}$  with  $1.1 \times 10^{13} \text{ cm}^{-2}$  Hall sheet charge.

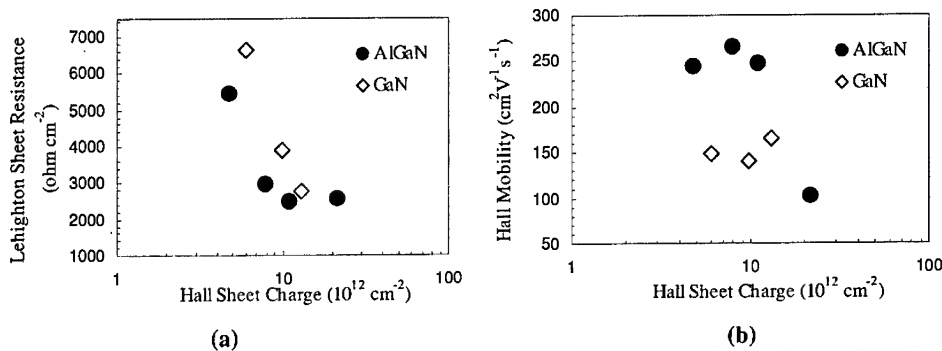


**Figure 4.** Electrical characteristics of delta doped AlGaIn and GaN layers (a) Leighton sheet resistance as a function of Hall sheet charge and (b) room temperature Hall mobility as a function of hall sheet charge.

Although the delta doped layers discussed in this report exhibited good crystallinity and surface morphology as determined by X-ray diffraction peak FWHM and AFM respectively, the fraction of electrically active Si impurities deviated from ideal (one-to-one) behavior. In the case of GaN delta doped layers, there was about one carrier generated for every two Si atoms in the delta doped interface, but the slopes of the two curves (empirical and ideal) were parallel,

indicating that as Si areal density in the delta doped layer was increased, the electrically active Si increased proportionately. The offset between the two curves may indicate there is a defect or other compensation mechanism that varies with silicon concentration.

However, the AlGa<sub>0.25</sub>N delta doping behavior is different. The absolute AlGa<sub>0.25</sub>N SIMS Si level may be as much as a factor of two off due to an inadequate calibration standard, but the relative Si density levels are accurate. The slope of the curve of AlGa<sub>0.25</sub>N sheet charge as a function of Si density changes with increasing Si density, deviating significantly from ideal behavior at high Si areal density. This result indicates that at high Si areal density a lower fraction of Si is activated in the AlGa<sub>0.25</sub>N layers, indicating a different or additional mechanism is reducing the fraction of electrical charge.

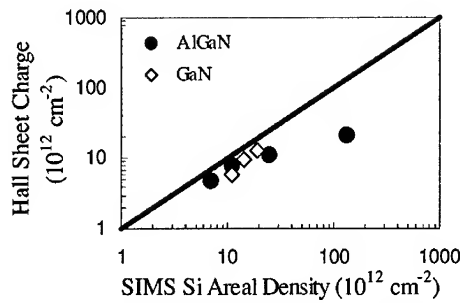


**Figure 5.** Room temperature Hall sheet charge as a function of SIMS Si areal density for AlGa<sub>0.25</sub>N and GaN delta doped layers. Line is ideal one-to-one Si-charge behavior.

Finally, room temperature and low temperature (77°K) Hall characteristics of delta doped Al<sub>0.25</sub>Ga<sub>0.75</sub>N and GaN layers are summarized in Table I. For comparable SIMS Si areal density and room temperature Hall sheet charge, the low temperature Hall characteristics for

**Table I.** Room temperature (300°K) and low temperature (77°K) Hall characteristics of delta doped Al<sub>0.25</sub>Ga<sub>0.75</sub>N and GaN samples.

Sample	SIMS Si areal density (cm <sup>-2</sup> )	300°K Hall sheet charge (cm <sup>-2</sup> )	Hall mobility (cm <sup>2</sup> V <sup>-1</sup> s <sup>-1</sup> )	300°K Hall sheet resistance (Ω cm <sup>-2</sup> )	77°K Hall sheet charge (cm <sup>-2</sup> )	77°K Hall mobility (cm <sup>2</sup> V <sup>-1</sup> s <sup>-1</sup> )	77°K Hall sheet resistance (Ω cm <sup>-2</sup> )
GaN	1.4e13	9.9x10 <sup>12</sup>	140	4459	9.8x10 <sup>12</sup>	139	4574
AlGa <sub>0.25</sub> N	1.1e13	7.9x10 <sup>12</sup>	265	2658	No data	No data	>100000

Al<sub>0.25</sub>Ga<sub>0.75</sub>N and GaN delta doped layers are quite different. Al<sub>0.25</sub>Ga<sub>0.75</sub>N demonstrated a large, two order of magnitude increase in Hall sheet resistance, while the GaN layer remained unchanged in both sheet charge and mobility. An increase in the activation energy for the Si donor in the Al<sub>0.25</sub>Ga<sub>0.75</sub>N layer to approximately 31meV to account for the increased bandgap of AlGa<sub>0.25</sub>N does not account for this magnitude of change. Further investigations are underway to better understand this phenomenon.

## CONCLUSION

Delta doped  $\text{Al}_{0.25}\text{Ga}_{0.75}\text{N}$  and GaN epitaxial layers were grown on sapphire substrates. The Si impurity incorporation increased linearly as a function of disilane flux at constant pause time for both layers. However, more narrow SIMS Si impurity profiles were found in  $\text{Al}_{0.25}\text{Ga}_{0.75}\text{N}$  with FWHM of  $5.7 \pm 0.6$  nm as compared to  $10.0 \pm 0.6$  nm in GaN. Room temperature Hall mobility as high as  $265 \text{ cm}^2 \text{ V}^{-1} \text{ s}^{-1}$  for a sheet charge  $7.9 \times 10^{12} \text{ cm}^{-2}$  was demonstrated for delta-doped  $\text{Al}_{0.25}\text{Ga}_{0.75}\text{N}$  layers, but the mobility enhancement saturated and then decreased with increasing sheet charge. GaN layers demonstrated a lower mobility of  $165 \text{ cm}^2 \text{ V}^{-1} \text{ s}^{-1}$  for  $1.3 \times 10^{13} \text{ cm}^{-2}$  Hall sheet charges. For identical doping conditions,  $\text{Al}_{0.25}\text{Ga}_{0.75}\text{N}$  delta doped layers exhibited 2x lower sheet charge than GaN consistent with the lower Si impurity incorporation. The slope of the  $\text{Al}_{0.25}\text{Ga}_{0.75}\text{N}$  sheet charge versus SIMS Si areal density plot was found to deviate significantly from ideality at higher Si incorporation levels indicating a different defect or compensating mechanism. Finally, low temperature Hall characteristics of  $\text{Al}_{0.25}\text{Ga}_{0.75}\text{N}$  and GaN differed since GaN sheet charge and mobility was preserved at 77°K while the  $\text{Al}_{0.25}\text{Ga}_{0.75}\text{N}$  was not. In fact, the sheet resistance increased to a value  $>100,000 \text{ ohm cm}^{-2}$ . We attribute this difference to more than the difference in carrier concentration arising from lower temperature and the increase in Si activation energy with increased aluminum content.

## REFERENCES

1. E.F. Schubert, J. Vac. Sci. Technol. A **8**, 2980 (1990).
2. E. Munoz, E. Calleja, I. Izpura, F. Garcia, A.L. Romero, J.L. Sanchez-Rojas, A.L. Powell, J. Castagne, J. Appl. Phys. **73**, 4988 (1993).
3. E.F. Schubert, J.E. Cunningham, W.T. Tsang, G.L. Timp, Appl. Phys. Lett. **51**, 1170 (1987).
4. K.L. Tan, IEEE Elec. Dev. Lett. **12**, 213 (1991).
5. O. Buchinsky, M. Blumin, R. Sarfaty, D. Fekete, I. Samid, M. Yust, Appl. Phys. Lett. **68**, 2043 (1991).
6. O. Buchinsky, M. Blumin, D. Fekete, Appl. Phys. Lett. **72**, 1484 (1998).
7. G.Y. Zhao, M. Adachi, H. Ishikawa, T. Egawa, M. Umeno, Appl. Phys. Lett. **77**, 2195 (2000).
8. J. Kim, G. M. Yang, S.C. Choi, J. Y. Choi, H.K. Cho, K.Y. Lim, H.J. Lee, MRS Internet J. Nitride Semicon. Res. **4S1**, G3.49 (1999).
9. R. Dupuis, Elec. Lett. **38**, 428 (2002).
10. S. Keller, S. Heikman, L. Shen, I.P. Smorchkova, S.P. Denbaars, U.K. Mishra, Appl. Phys. Lett. **80**, 4387 (2002).
11. J. Redwing, M.A. Tischler, J.S. Flynn, S. Elhamri, M. Ahoujja, R.S. Newrock, W.C. Mitchel, Appl. Phys. Lett. **69**, 963 (1996).
12. Charles Evans SIMS Si in GaN accuracy  $\pm 20\%$ , Si in AlGaN accuracy  $\pm 50\%$ .
13. F. Yun, J. Appl. Phys. **92**, 4837 (2002).

**AlGaIn/GaN HFETs for Automotive Applications**

**Ronald Birkhahn\***, David Gotthold, Nathan Cauffman, Boris Peres  
EMCORE Corporation, Corporate Research and Development  
145 Belmont Drive, Somerset, NJ 08873 USA  
\*Email: ronald.birkhahn@cmcore.com

Seikoh Yoshida  
The Furukawa Electric Co, Ltd.  
Yokohama R&D Laboratories  
2-4-3, Okano, Nishi-ku, Yokohama  
220-0073, Japan

**ABSTRACT**

AlGaIn/GaN heterojunction field effect transistors (HFET) on sapphire substrates have demonstrated ability as power devices operating with high current densities and high breakdown voltages. Additionally, AlGaIn/GaN HFET devices have a very low on-state resistance. This makes these devices ideal for automotive applications such as switching relays, DC-DC converters, and power inverters. By 2006, switching devices using GaN-based FETs are anticipated to be employed in luxury automobiles and transitioned to the mass market by 2009.

In this presentation, data from AlGaIn/GaN HFET's grown in an Emcore D180 MOCVD system will be presented. Typical production-scale material results (on 2" sapphire substrates) for these wafers were:  $\mu \sim 1000 \text{ cm}^2/\text{Vs}$ ,  $N_s = 1.0 \times 10^{13} \text{ cm}^{-2}$ , and  $R_s \sim 450 \text{ } \Omega/\text{square}$  with <3% variation across the wafer. These wafers were then processed into devices using Pt/Au gate contacts with 2  $\mu\text{m}$  gate length, 200  $\mu\text{m}$  gate width, and a source to drain spacing of 13  $\mu\text{m}$ . A total of 1000 FETs were combined in parallel for an effective gate width of 20 cm for high current operation (10A). These devices have a lower on-state resistance (<0.01  $\Omega\text{-cm}^2$ ) and higher Schottky breakdown voltages (400 V) than the theoretical limit of Si MOSFET devices. These devices demonstrate suitability for insertion in automotive electrical harnesses.

**INTRODUCTION**

The III-Nitride materials system has shown commercial potential for many high power, high temperature applications by virtue of its material properties.<sup>i,ii,iii</sup> Most of the current development in the nitrides, outside optoelectronics, has focused primarily on military applications with the U.S. Defense Department providing much of the funding. This work has focused on AlGaIn on GaN heterostructures creating Heterojunction Field Effect Transistors (HFETs) produced on SiC substrates for high frequency (>3GHz) power device applications. The primary alternative substrate to SiC is sapphire which suffers from greater lattice mismatch and lower thermal conductivity effectively reducing device performance.<sup>iv,v</sup> While not desirable, these material challenges can be designed

around providing for mid-performance low frequency (kHz) devices that are cost-effective.

Automotive applications are one such market for AlGa<sub>N</sub> HFETs on sapphire. These devices require the intrinsic advantages of GaN: stability at high temperatures in corrosive environments, and power handling capability with high breakdown voltages. These applications include switching relays, DC-DC converters, and power inverters to handle large currents (>10 A) and corresponding power (420 W). Targeted initially in luxury automobiles, AlGa<sub>N</sub> HFET devices should see their introduction in 2006 with transition to the broader automotive market by 2009.

#### EXPERIMENT DETAILS

AlGa<sub>N</sub> HFET epilayers were deposited at Emcore using a D180 rotating disk MOCVD reactor. Trimethylgallium and trimethylaluminum were used as sources of Ga and Al respectively with NH<sub>3</sub> as the source of atomic nitrogen. The pressure throughout the entire process was 100 Torr. A low temperature AlN was used to nucleate on sapphire and semi-insulating (SI) GaN and AlGa<sub>N</sub> films were deposited at 1030°C as measured by pyrometer. The SI-GaN thickness was nominally 2 μm and the AlGa<sub>N</sub> was calculated at 25-30 nm at 28% Al composition. Average sheet resistivity of the as-grown samples was 450 ohms/square with ≤3% uniformity. These wafers were then processed at Furukawa into FET devices with Al/Ti/Au metallization for the ohmic source and drain contacts and Pt/Au for the gate. The AlGa<sub>N</sub> surface was passivated using SiO<sub>2</sub> with mesa isolation between devices and the entire structure was sealed with an insulator (Figure 1). Individual FET device dimensions were gate length  $L_g = 2\mu\text{m}$ , gate width  $W_g = 200\mu\text{m}$  with a source-drain distance of  $L_{sd} = 13\mu\text{m}$ . These individual FETs were assembled into a larger assembly (L-FET) that had an effective gate width of 20cm on a 5x5mm<sup>2</sup> chip for large current handling capability.

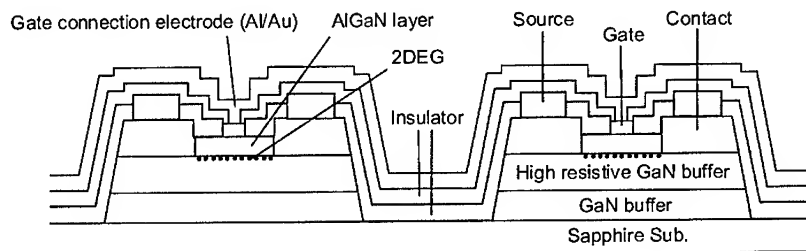


**Figure 1:** Mesa-isolation individual HFETs on sapphire. Device dimensions of  $L_g = 2\mu\text{m}$ ,  $W_g = 200\mu\text{m}$  with a source-drain distance of  $L_{sd} = 13\mu\text{m}$ .

#### RESULTS

The materials properties were uniform from the as-grown AlGa<sub>N</sub> HFET wafers as shown in Figure 2. The sheet charge on the samples averaged around  $1 \times 10^{13}$  carriers/cm<sup>2</sup> with a

mobility of  $1040 \text{ cm}^2/\text{Vs}$ . This uniformity is important for development of large area devices on sapphire since it is difficult to design a circuit around a chip that has regions of different performance. Individual HFETs ( $L_g = 2\mu\text{m}$ ,  $W_g=200\mu\text{m}$ ) processed on these wafers had high reverse breakdown voltages at  $\sim 400\text{V}$  across the wafer. This performance already exceeds that of

traditional Si MOSFETs used in automotive applications and is approaching the performance of SiC MOSFETs. GaN-based FETs already have lower on-state resistance as shown in Figure 3.<sup>vi</sup> The individual HFETs had good linearity with peak current of  $61 \text{ mA/mm}$  (Figure 4) and an average pinch-off voltage of  $-6\text{V}$ .

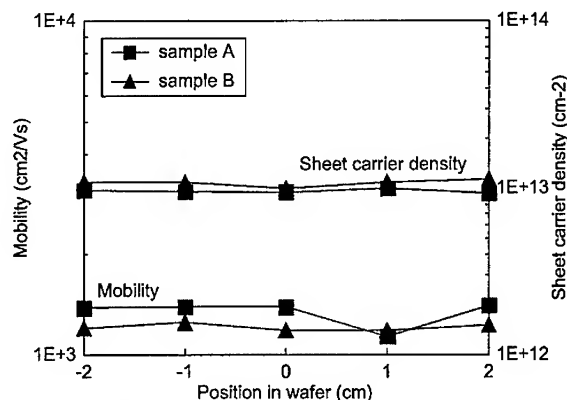


Figure 2: Material uniformity for sheet carriers and mobility of processed AlGaIn HFETs devices.

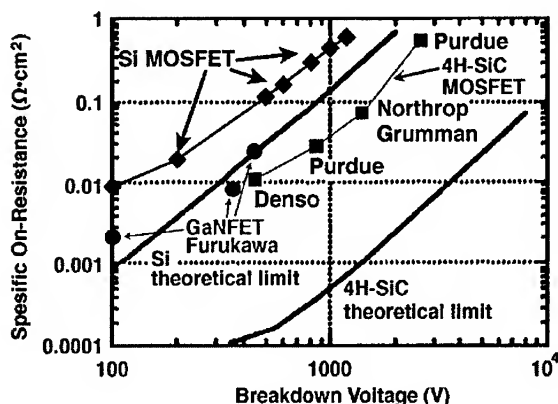


Figure 3: Breakdown voltage vs. On-resistance for the GaN HFETs on sapphire as compared to devices published in literature. Comparison data from C.E. Weitzel et al.

was  $600\text{pF}$  until pinch-off where it drops to  $100\text{pF}$ , an order of magnitude better than a comparable Si MOSFET. The chip could sustain a maximum power of  $100\text{W}$  for 30 seconds before failure. In continuous operation, the L-FET maintained  $30\text{W}$  of power for  $> 1$  hour. It is expected that the performance of these devices can be improved with

These individual FETs were combined in parallel to create a L-FET that could handle currents  $\geq 10\text{A}$  such as those encountered in switches in automotive applications. Initial results are very encouraging for this type of device containing 1000 individual FETs on a  $5\times 5\text{mm}^2$  chip on sapphire. These L-FET devices were air-cooled for all experiments during operation by fan. The L-FET was able to switch  $10\text{A}$  of continuous current at  $50\text{Hz}$ . The gate-source capacitance of this device

advanced packaging techniques such as sapphire substrate thinning and heat-sink bonding or flip-chip with backside vias.

#### SUMMARY

AlGa<sub>N</sub> HFETs epitaxially deposited on sapphire substrates by MOCVD were processed into small FET devices ( $L_g = 2\mu\text{m}$ ) that were arranged into a larger assembly for high current operation. The operation of the individual HFETs already surpass traditional Si MOSFET technology on several key parameters including breakdown voltage, on-state resistance, operation temperature, and gate capacitance. Indeed, a larger assembly consisting of 1000 of these individual HFET devices in parallel can switch 10A of current at 50Hz operation. Further refinement of the materials and device design can lead to improvements in the power handling and reliability of these devices. It is anticipated that AlGa<sub>N</sub>-based HFETs will see their introduction in automotive electrical harnesses in the future.

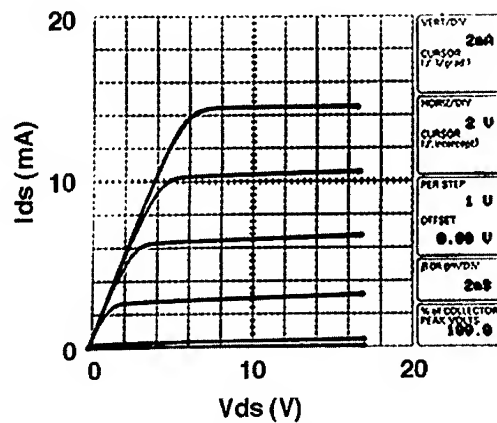


Figure 4: AlGa<sub>N</sub> HFET I-V curves for the devices with  $L_g = 2\mu\text{m}$ ,  $W_g = 200\mu\text{m}$ . Current density at  $V_g = 0$  is 61 mA/mm.

#### REFERENCES

- <sup>i</sup> L.F. Eastman, U.K. Mishra, IEEE Spectrum, May, 28 (2002).
- <sup>ii</sup> L.F. Eastman, Compound Semiconductor, 7 (10), 69 (2001).
- <sup>iii</sup> S.C. Jain, M. Willander, J. Narayan, R. Van Overstraeten, J. Appl. Phys., 87 (3), 965 (2000).
- <sup>iv</sup> J. Newey, Compound Semiconductor, 8 (6), 45 (2002).
- <sup>v</sup> W. Weeks, R. Borges, Compound Semiconductor, 7 (10), 63 (2001).
- <sup>vi</sup> C.E. Weitzel et al., IEDM, 51 (1998).

### Transport Studies on Two-subband-populated AlGa<sub>1-x</sub>N/GaN Heterostructures

D. R. Hang, C. F. Huang, Y. F. Chen, and B. Shen<sup>1</sup>

Department of Physics, National Taiwan University,  
Taipei, Taiwan, 106 Republic of China

<sup>1</sup>National Laboratory of Solid State Microstructures and Department of Physics,  
Nanjing University, Nanjing, 210093, China.

#### ABSTRACT

We report an investigation of electronic properties of two-dimensional electron gas (2DEG) confined at AlGa<sub>1-x</sub>N/GaN heterostructures by magnetotransport measurements. The second-subband population is manifested by the multi-frequency in the Shubnikov-de Haas (SdH) oscillations. The modulated patterns of SdH oscillations which are due to the two-subband occupancy can be drastically enhanced by employing the microwave modulation technique. This unique advantage enables us to provide direct experimental evidence that the 2DEG in the second subband has a higher mobility than that in the first subband in the modulation-doped Al<sub>0.22</sub>Ga<sub>0.78</sub>N/GaN heterostructures by means of microwave-modulated magnetotransport measurements. The carrier concentrations and 2DEG Fermi energy for each subband were determined. It was found that the second-subband population ratio increases with spacer thickness up to 5 nm, while the subband separation decreases.

#### INTRODUCTION

In the past several years, fundamental properties of Al<sub>x</sub>Ga<sub>1-x</sub>N/GaN heterostructures have received a great amount of attention for the application of heterostructure-field-effect transistors (HFETs), which are capable of working at high frequencies in high-power and high-temperature environments [1-4]. They are very promising for applications in microwave and optoelectronic devices. Compared with other III-V material based HFETs, a larger amount of two-dimensional electron gas (2DEG) can be easily accumulated in GaN-based ones. The lattice mismatch of 2.5 % between AlN and GaN and the lack of inversion symmetry in the wurtzite structure result in large induced and spontaneous polarizations [3]. Therefore the better carrier confinement at Al<sub>x</sub>Ga<sub>1-x</sub>N/GaN interface than that at Al<sub>x</sub>Ga<sub>1-x</sub>As/GaAs interface arising from the large conduction-band offset [4] and strong piezoelectric polarization of the Al<sub>x</sub>Ga<sub>1-x</sub>N barrier layer naturally leads to a recent research interest in high-carrier-density Al<sub>x</sub>Ga<sub>1-x</sub>N/GaN heterostructures in which multiple subbands were occupied [5-9]. Because of the different subband wave function distribution profile, the 2DEG mobility is expected to be enhanced once the second subband becomes more populated, and hence eases the design limitations and allows higher frequency performance for microwave and optoelectronic devices. In order to optimize the performance of HFETs with high electron densities, it is important to understand the electronic properties of 2DEG of high densities at Al<sub>x</sub>Ga<sub>1-x</sub>N/GaN heterointerface. In this paper, we report on an investigation of electronic properties of 2DEG confined in spacer-dependent Al<sub>0.22</sub>Ga<sub>0.78</sub>N/GaN heterostructures by magnetotransport measurements.

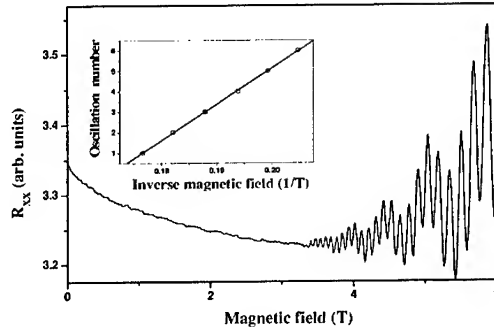


**Figure 1.** Magnetoresistance of 2DEG in  $\text{Al}_{0.22}\text{Ga}_{0.78}\text{N}/\text{GaN}$  heterostructures as a function of magnetic field at 3.6 K in sample A. The inset shows successive oscillation numbers (open circles) as a function of inverse magnetic fields of the SdH minimum.

## EXPERIMENTAL DETAILS

We performed SdH measurements on two modulation-doped  $\text{Al}_{0.22}\text{Ga}_{0.78}\text{N}/\text{GaN}$  heterostructures grown by atmospheric pressure metal-organic chemical vapor deposition on the (0001) surface of sapphire substrates. A nucleation GaN buffer layer was deposited at 488 °C, followed by a unintentionally doped GaN (i-GaN) layer of 2  $\mu\text{m}$  thickness grown at 1071 °C. The barrier layer is a Si-doped  $\text{Al}_{0.22}\text{Ga}_{0.78}\text{N}$  (n-AlGaN) layer of thickness 25 nm for sample A and 30 nm for sample B. The doping concentration is  $1.2 \times 10^{18} \text{ cm}^{-3}$ . The one-side doping results in the triangular confinement of carriers in the heterojunctions. Between the n-AlGaN and i-GaN layer, a 5-nm-thick unintentionally doped  $\text{Al}_{0.22}\text{Ga}_{0.78}\text{N}$  spacer was inserted for sample A to reduced remote impurity scattering. The samples were placed inside a 6 Tesla Oxford superconducting magnet and immersed in liquid helium. The temperature could be cooled down to as low as 3.6 K. The data were taken by conventional lock-in techniques.

In our studies, we additionally employed a novel technique of SdH measurement that can drastically enhance the SdH pattern based on microwave modulation. Here, the measurements were done electrically in phase under microwave modulation. This method has advantages of unchanging carrier concentration and not diminishing modulation pattern compared with other variant techniques like optically modulated SdH and optically-detected microwave modulated SdH measurements. In our previous report [10], we have shown that this technique is suitable for studying novel wide band-gap heterostructures where moderate mobilities and heavier effective mass (rapid damping SdH amplitudes) are frequently encountered.

## RESULT AND DISCUSSION

Figure 1 and 2 show SdH oscillations taken at 3.6 K for sample A and sample B,

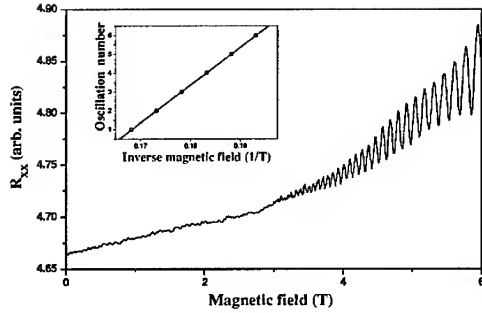


**Figure 2.** Magnetoresistance of 2DEG in  $\text{Al}_{0.22}\text{Ga}_{0.78}\text{N}/\text{GaN}$  heterostructures as a function of magnetic field at 3.6 K in sample B. The carrier concentration can be deduced from the inset.

respectively. The two-dimensional characters have been further confirmed by rotating the sample orientation against the magnetic field. The strong double periodicity of the SdH oscillations is easily recognized for sample A and also exists in sample B, which will be shown below. The modulation doping and the strong polarization field give rise to a large amount of confined 2DEG in the heterointerface. The electrons start to populate the second subband because of the high 2DEG sheet concentrations at the heterointerfaces, resulting in the double periodicity. Besides, it is worth noting that the onset of the SdH oscillations for both samples is almost the same at 3.3 T at this temperature.

It is straightforward to obtain the carrier concentrations corresponding to the first subband from high-frequency oscillations. The successive oscillation numbers as a function of inverse magnetic fields of the SdH oscillation minima for both samples are plotted as open circles in both insets in Fig. 1 and 2. The data can be described by the simple linear equation [11]

$$\frac{1}{B_N} = N \frac{e}{\pi \hbar n} + C, \quad (1)$$

where  $B_N$  represents each magnetic field at successive oscillation minimum,  $N$  is an integer,  $C$  is a constant, and  $n$  is the carrier concentration. The choice of the oscillation number is arbitrary. The solid lines in both insets show the fittings to Eq. (1). The slopes of the lines correspond to carrier densities of  $8.48 \times 10^{12} \text{ cm}^{-2}$  for sample A and  $9.6 \times 10^{12} \text{ cm}^{-2}$  for sample B, respectively.

Figure 3 and 4 display the microwave-modulated SdH patterns at the same temperature under the modulation of a 3.7 GHz microwave radiation for sample A and sample B, respectively. The SdH patterns are considerably enhanced for both samples. It is quite amazing that the visible signal noise is almost washed out and the onset of SdH oscillations is noticeably lowered. For the data taken in sample A, it is significant to note that the short-period oscillations die away at magnetic fields lower than 2.5 T, while the long-period oscillations persist. Therefore we provide direct experimental evidence that the 2DEG in the second subband has a higher mobility than that in the first subband in the modulation-doped  $\text{Al}_{0.22}\text{Ga}_{0.78}\text{N}/\text{GaN}$  heterostructures by means of

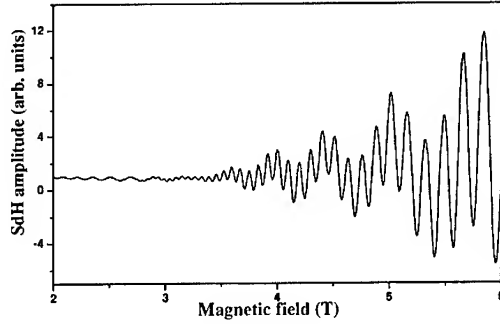


**Figure 3.** The electrically detected microwave-modulated SdH oscillations at temperature 3.6 K for sample A. The long-period oscillations can be clearly observed in the low-field region.

microwave-modulated magnetotransport measurements. On the other hand, the resolution of the conventional SdH measurements under similar condition is not capable of comparing these oscillations due to two-subband occupancy directly. This shows an advantage of the microwave-modulation technique.

From the fit to Eq. (1), the second-subband carrier density in sample A is determined to be  $1.78 \times 10^{12} \text{ cm}^{-2}$ , and the total 2DEG sheet concentration in the triangular well is  $1.02 \times 10^{13} \text{ cm}^{-2}$ . Due to the long-period modulation, the double periodicity in sample B is not straightforwardly recognizable in conventional SdH measurement. But the modulated SdH pattern can be readily identifiable in microwave-modulated SdH oscillations, as shown in Fig. 4. Again, this shows the advantage of the microwave-modulated technique. By the same approach above, the second-subband carrier density is estimated to be  $4.8 \times 10^{11} \text{ cm}^{-2}$ . Thus, the total 2DEG sheet concentration resides in the heterojunction for sample B is  $1.01 \times 10^{13} \text{ cm}^{-2}$ , which is very close to that for sample A.

To optimize the design of  $\text{Al}_x\text{Ga}_{1-x}\text{N}/\text{GaN}$  HFETs, it is of great value to determine the energy separation of the lowest two subbands. Once the oscillations from the upper subband can be separated by means of microwave-modulated SdH measurements, the subband separation can be inferred from the respective carrier concentration, and hence Fermi levels:

$$\begin{aligned} E_{F0} &= E_{F1} + E_{01}, \\ \frac{\pi \hbar^2}{m^*} n_0 &= \frac{\pi \hbar^2}{m^*} n_1 + E_{01}, \end{aligned} \quad (2)$$

where  $m^* / \pi \hbar^2$  is the two-dimensional density of state,  $n_0$  is the carrier concentration of the first subband,  $n_1$  is the carrier concentration of the second subband,  $E_{01}$  is the energy separation between the first and second subbands, and  $E_{F0}$  and  $E_{F1}$  are the energy differences between the Fermi levels and the minima of the first and second subbands, respectively.

The effective mass for the two subbands is assumed to be about the same [2, 9],  $m^* = 0.23 m_0$ , the energy separation between the two subbands can be obtained accordingly. The subband separation is 69.6 and 94.6 meV for sample A and sample B, respectively.

We summarize our results in Table 1. To display the influence of spacer thickness on the

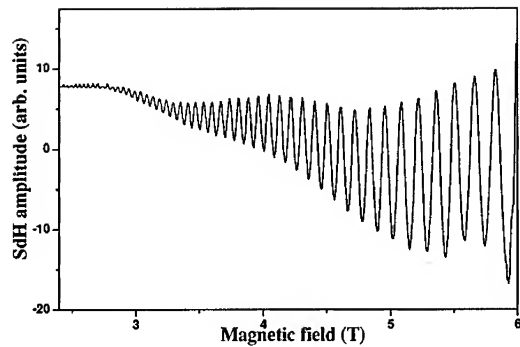


**Figure 4.** The electrically detected microwave-modulated SdH oscillations at temperature 3.6 K for sample B. The modulated SdH pattern can be readily identifiable in this way.

subband properties, we include the results reported by Zheng *et al.* [9] who studied the same  $\text{Al}_{0.22}\text{Ga}_{0.78}\text{N}/\text{GaN}$  heterostructures with different spacer thickness. There are two points that are worthy of mention.

The subband-energy separation decreases as spacer layer thickness increases from 0 to 5 nm. The subband-energy separation depends on the quantum confinement in the potential well; it increases with deeper electron confinement. The band bending in the triangular quantum well, which is determined by the Coulomb interaction, decreases with the increase of spacer layer thickness. As a consequence, the quantum confinement reduces and the energy separation of the two subbands decreases.

Moreover, when the spacer layer thickness increases from 0 to 5 nm, the second-subband population ratio increases. As the spacer layer thickness increases, more confined electrons in the well populate in the second subband possibly due to the lowered second subband, and for this reason the second-subband population increases.

However, the trend found above goes to the reverse side once the spacer thickness increases to 10 nm. The actual mechanism of the anomaly remains unclear and calls for further research.

## CONCLUSIONS

Sample	Spacer thickness(nm)	$B_{\text{onset}}$	$n_t(\times 10^{13} \text{ cm}^{-2})$	$n_1/n_t$ (%)	$E_{01}(\text{meV})$
B	0	3.3	1.01	4.9	94.6
C	3	3.7	1.3	15	93
A	5	3.3	1.02	17	69.6
D	10	4.7	0.93	7.9	81.6

**Table I.** Characteristics of modulation-doped  $\text{Al}_{0.22}\text{Ga}_{0.78}\text{N}/\text{GaN}$  heterostructures with different spacer thickness. Sample C and D are taken from Ref. 9.  $B_{\text{onset}}$  denotes the onset field of SdH oscillations and  $n_t$  is the total two-dimensional carrier density.

In conclusion, we present the investigation of electronic properties of high-density 2DEG confined at  $\text{Al}_{0.22}\text{Ga}_{0.78}\text{N}/\text{GaN}$  heterostructures by magnetotransport measurements. The second-subband population is manifested by the multi-frequency in the SdH oscillations. We demonstrated that the modulated patterns of SdH oscillations due to second-subband occupancy could be drastically enhanced by employing the microwave modulation technique. In addition, the SdH oscillations can be observed at a much lower magnetic field. We provide direct experimental evidence that the 2DEG in the second subband has a higher mobility than that in the first subband in the modulation-doped  $\text{Al}_{0.22}\text{Ga}_{0.78}\text{N}/\text{GaN}$  heterostructures by means of microwave-modulated magnetotransport measurements. The carrier concentrations and 2DEG Fermi energy for each subband were determined. It was found that the second-subband population ratio increases with the increase of spacer thickness up to 5 nm, while the subband separation decreases.

#### ACKNOWLEDGMENTS

This work was partly supported by the National Science Council and the Ministry of Education of the Republic of China.

#### REFERENCES

1. T. Y. Lin, H. M. Chen, M. S. Tsai, Y. F. Chen, F. F. Fang, C. F. Lin, and G. C. Chi, *Phys. Rev. B* **58**, 13793 (1998).
2. D. R. Hang, C. -T. Liang, C. F. Huang, Y. H. Chang, Y. F. Chen, H. X. Jiang, and J. Y. Lin, *Appl. Phys. Lett.* **79**, 66 (2001).
3. J. A. Garrido, J. L. Sánchez-Rojas, A. Jiménez, E. Muñoz, F. Omnes, and P. Gibart, *Appl. Phys. Lett.* **75**, 2407 (1999).
4. D. R. Hang, C. H. Chen, Y. F. Chen, H. X. Jiang, and J. Y. Lin, *J. Appl. Phys.* **90**, 1887 (2001).
5. J. P. Bergman, T. Lundström, B. Monemar, H. Amano, and I. Akasaki, *Appl. Phys. Lett.* **69**, 3456 (1996).
6. S. R. Kurtz, A. A. Allerman, D. D. Koleske, and G. M. Peake, *Appl. Phys. Lett.* **80**, 4549 (2002).
7. C. Y. Fang, C. F. Lin, E. Y. Chang, and M. S. Feng, *Appl. Phys. Lett.* **80**, 4558 (2002).
8. Z. -F. Li, W. Lu, S. C. Shen, S. Holland, C. M. Hu, D. Heitmann, B. Shen, Y. D. Zheng, T. Someya, and Y. Arakawa, *Appl. Phys. Lett.* **80**, 431 (2002).
9. Z. W. Zheng, B. Shen, R. Zhang, Y. S. Gui, C. P. Jiang, Z. X. Ma, G. Z. Zheng, S. L. Guo, Y. Shi, P. Han, Y. D. Zheng, T. Someya, and Y. Arakawa, *Phys. Rev. B* **62**, R7739 (2000).
10. D. R. Hang, C. -T. Liang, J. -R. Juang, T. -Y. Huang, W. K. Hung, Y. F. Chen, G. -H. Kim, Jae-Hoon Lee and Jung-Hee Lee, *J. Appl. Phys.* revised.
11. A. Saxler, P. Debray, R. Perrin, S. Elhamri, W. C. Mitchel, C. R. Elsass, I. P. Smorchkova, B. Heying, E. Haus, P. Fini, J. P. Ibbetson, S. Keller, P. M. Petroff, S. P. DenBaars, U. K. Mishra, and J. S. Speck, *J. Appl. Phys.* **87**, 369 (2000).

### A structural analysis of the Pd/GaN ohmic contact annealing behavior

C.C. Kim<sup>1</sup>, P. Ruterana<sup>a),2</sup>, and J.H. Je<sup>3</sup>

<sup>1</sup> Samsung Electro-Mechanics Co., 314, Maetan-3dong, Suwon, 442-743, Korea

<sup>2</sup> LERMAT, FRE 2149 CNRS, ISMRA, 6, Boulevard Maréchal Juin, 14050 CAEN, FRANCE

<sup>3</sup> Synchrotron X-ray Laboratory, Department of Materials Science and Engineering, Pohang University, Pohang 790-794, South Korea

#### Abstract

For ohmic contact on p GaN, palladium is one of the best candidates showing ohmic characteristics already without annealing. To be realized in devices, it is necessary to know the behavior of the ohmic contacts at accelerated conditions, especially for high temperatures and power. We report on the structural evolution of palladium layers (30 nm) deposited on GaN (0001) by electron beam evaporation without intentional annealing. They were next cut into various pieces which were individually submitted to rapid thermal annealing at 400, 500, 600, 700 and 800°C for 10 sec. We investigate the differences in the microstructure and the location of interfacial phases and their relationships as determined by X-ray diffraction and transmission electron microscopy, we then suggest the formation mechanism based on the relationship. It is shown that the interface is disrupted at annealing above 600°C and by 800°C only very small patches of Pd are still present, however they are completely imbedded in a matrix of intermetallic phases (gallides) formed by the reaction with GaN.

#### Introduction

Gallium based nitrides are direct wide-band-gap semiconductors which have a large potential for high-temperature and high-power applications<sup>1</sup>. However, this wide-band-gap makes the device fabrication difficult for ohmic contacts, especially for p type material. Many extensive studies have been made for developing optimized ohmic contact systems.<sup>2-4</sup> Pd is one of the most competing candidates, showing a promising ohmic characteristics at room temperature<sup>3</sup>. In order for Pd to be used as a reliable metal contact on GaN, it is essential to understand the thermal stability and metallurgy of the contact. In spite of the increasing importance of Pd/GaN system, the detailed microstructure of the Pd layer and the high temperature structure are not yet understood. For device applications at high power and high temperature, it is therefore important to study the structural evolution of metal overlayers and their reactions at elevated temperatures.

In this work, we investigated the structural evolution of Pd/GaN (0001) heteroepitaxy during post annealing process. We reveal the existence of interfacial, epitaxial, Pd grains in the as-deposited Pd film that was evaporated on GaN(0001) at room temperature. During subsequent annealing up to 600°C, the grains of Pd grow and we explain the origin of the Pd epitaxy on GaN(0001) to a six-to-seven matched interface structure, wherein six-Ga atomic distances in GaN match to seven-Pd atomic distances. At high temperature annealings (~700°C), the Pd film transforms, by the Pd-Ga reaction to Ga<sub>2</sub>Pd<sub>3</sub> and Ga<sub>5</sub>Pd gallides which encapsulate the remaining Pd patches and can be in epitaxy to GaN.

<sup>a)</sup> corresponding author: ruterana@ismra.fr

### Experimental procedures

The Mg-doped p-GaN films (1.6  $\mu\text{m}$  thick) were grown on sapphire (0001) substrates using metal-organic chemical vapor deposition (MOCVD). For deposition of Pd films, the GaN samples were first cleaned with organic solvents, then etched in 50 % HF and 50 % HCl, and finally loaded into an e-beam evaporation system, in which the base pressure was  $\sim 1 \times 10^{-7}$  Torr. Pd films were deposited to a nominal thickness of 280  $\text{\AA}$  at a rate of 2  $\text{\AA}/\text{s}$  without heating the samples. The Pd/GaN specimens were then annealed at various temperatures between 400 and 800  $^{\circ}\text{C}$  for 30 s in a rapid thermal annealing (RTA) furnace under  $\text{N}_2$  flowing atmosphere. The surface and the cross section of Pd/GaN films were characterized by atomic force microscopy (AFM) and high resolution electron microscopy (HREM), respectively. HREM observations were carried out along the GaN  $[11\bar{2}0]$  direction on a Topcon 002B electron microscopy operating at 200 kV with a point to point resolution of 0.18 nm ( $C_s=0.4$  mm). To obtain averaged structural information, synchrotron x-ray scattering measurements were carried out at beam line 5C2 of Pohang Light Source (PLS) in Korea. The wavelength of the incident x rays was set at 1.488  $\text{\AA}$  by a double bounce Si (111) monochromator. The structural evolution of the Pd films on GaN was studied by measuring the x-ray powder diffraction profile ( $\theta$ -2 $\theta$  scan) and the x-ray reflectivity curve after post annealing at several temperatures. We employed a four-circle x-ray diffractometer for exploring an arbitrary momentum transfer in 3-dimensional space, which provides information about in-plane crystalline state and structural orientation.

### Results and discussion

The morphological changes of the surface, as well as the metal/GaN interface under the gallide formation, were examined by atomic force microscope (AFM). For the interface, the metal overlayers were etched off using 3:1  $\text{HNO}_3\text{:HCl}$ . The results are shown in Fig. 1. As the annealing temperature was raised from 600  $^{\circ}\text{C}$  to 700  $^{\circ}\text{C}$ , the root-mean-squared (RMS) roughness of the Pd surface (the Pd-interface) increased significantly from 5.2  $\text{\AA}$  (4.5  $\text{\AA}$ ) to 90  $\text{\AA}$  (72  $\text{\AA}$ ), respectively. The deteriorated surfacial and interfacial morphology during the formation of the gallides can be directly related with the optical scattering loss in the light emitting diode (LED) structures. Furthermore, the electrical properties of contact may be greatly changed by the formation of the gallides at the high temperature of 700  $^{\circ}\text{C}$ .

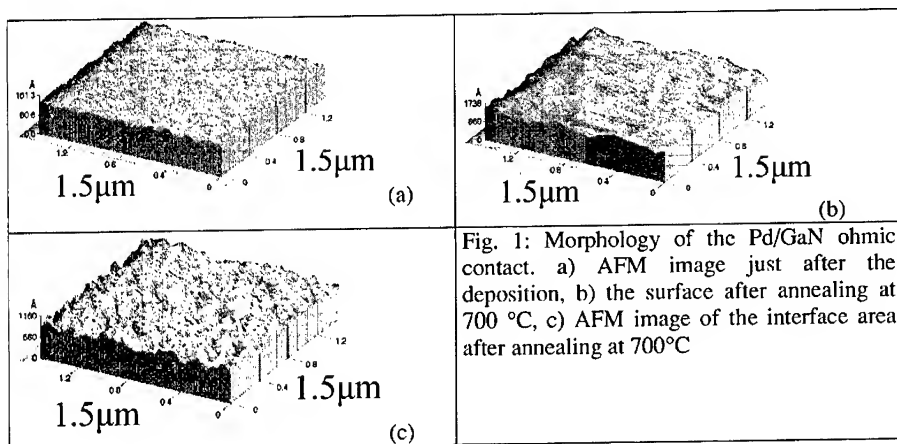


Fig. 1: Morphology of the Pd/GaN ohmic contact. a) AFM image just after the deposition, b) the surface after annealing at 700  $^{\circ}\text{C}$ , c) AFM image of the interface area after annealing at 700  $^{\circ}\text{C}$

We have used the TEM to examine the surface morphology, as can be seen in figure 2 on for the layer annealed at 400°C, the surface is flat, in agreement with the AFM observations. In this image some moiré fringes are visible at the GaN side of the interface. They may be due to interdiffusion between the metal and GaN but also could be artefacts of TEM sample preparation, although the samples were prepared by ion milling at the LN2 temperature. Further work is needed to confirm their occurrence.

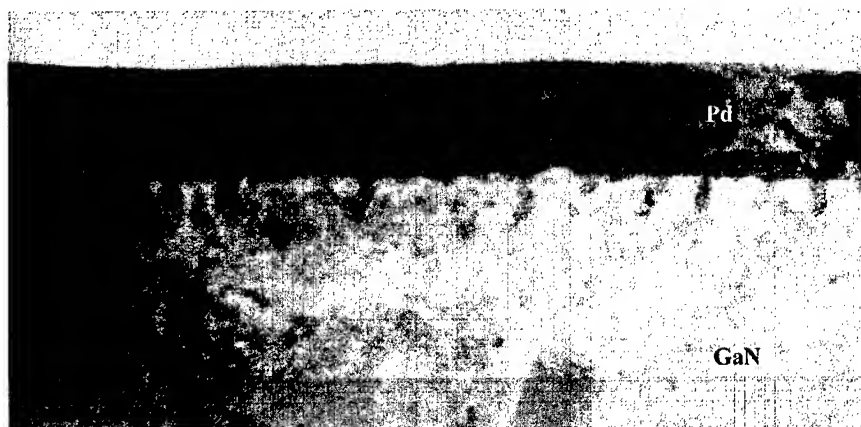


Fig. 2: The morphology of the Pd/GaN ohmic contact after annealing at 400°C

A close examination of the interface structure shows that we have a flat and abrupt interface between GaN and Pd as shown on in figure 3. The (111)Pd/(0001) epitaxial relationship is clearly seen in this figure recorded along the  $[1\bar{1}20]$  zone axis of GaN.



Figure 3: Interface structure and epitaxial relationship of Pd/GaN as observed in the samples after deposition, or rapid thermal annealing up to 600°C.

When the annealing temperature is increased to 700°C, the contact degrades completely. The TEM observations show that all along the surface, the Pd has peered off and also reacted strongly with GaN. Intermediate phases are visible at the interface reaction area and identified as follows by synchrotron X-ray scattering.

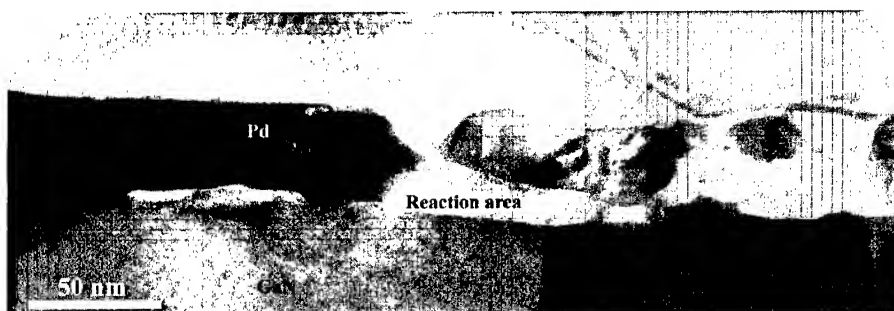


Fig. 4: The Pd/GaN ohmic contact after annealing at 700°C, the reaction area is visible at the interface, and the GaN surface has remarkably degraded.

X-ray scattering observations show that when the Pd film was annealed further to 700 °C, interestingly, the Pd (111) reflection completely disappeared, and two new Bragg reflections at  $q_z = 2.772 \text{ \AA}^{-1}$  and  $q_z = 2.880 \text{ \AA}^{-1}$  were observed. From the in-plane orientation relationships, it turned out that the Bragg reflections at  $q_z = 2.772 \text{ \AA}^{-1}$  and  $q_z = 2.880 \text{ \AA}^{-1}$  corresponded to the  $\text{Ga}_2\text{Pd}_5$  (201) (JCPDS  $2.762 \text{ \AA}^{-1}$ ) and  $\text{Ga}_5\text{Pd}$  (213) (JCPDS  $2.878 \text{ \AA}^{-1}$ ) reflections, respectively. Both  $\text{Ga}_2\text{Pd}_5$  and  $\text{Ga}_5\text{Pd}$  phases were grown epitaxially on  $\text{GaN}(0001)$ , which was revealed by the nonspecular  $\text{Ga}_2\text{Pd}_5$  (221) and the  $\text{Ga}_5\text{Pd}$  (310) reflections that were located  $16.1^\circ$  and  $47.2^\circ$  away from the surface normal direction, respectively. The epitaxial relationship was investigated by observing the orientation of the non-specular reflections of the film with respect to that of the substrate on the azimuthal circles. The scattering profile along the phi scans of these non-specular gallide reflections are shown in Fig. 4.3. The well-defined peaks on the phi scans indicated that the  $\text{Ga}_2\text{Pd}_5$  and  $\text{Ga}_5\text{Pd}$  phases were in fact grown epitaxially on  $\text{GaN}(0001)$ . From the relative directions of the film and the substrate crystalline axes, we summarized the epitaxial relationships of the two gallides as follows. The Pd-rich gallide,  $\text{Ga}_2\text{Pd}_5$  has a crystalline orientation with  $\text{Ga}_2\text{Pd}_5$  (201) //  $\text{GaN}(0001)$  and  $\text{Ga}_2\text{Pd}_5$  [010] //  $\text{GaN}[1\bar{1}20]$ . Meanwhile, the Ga-rich gallide,  $\text{Ga}_5\text{Pd}$  has a crystalline orientation with  $\text{Ga}_5\text{Pd}$  (213) //  $\text{GaN}(0001)$  in the out-of-plane direction, and  $\text{Ga}_5\text{Pd}$  [310] in the same azimuthal angle with  $\text{GaN}[10\bar{1}0]$ .

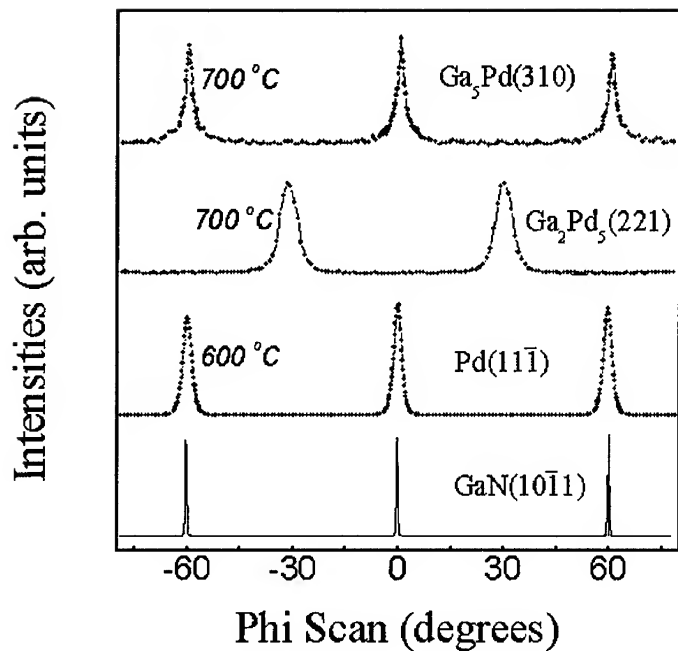


Fig.5: The typical phi scans for the GaN ( $10\bar{1}1$ ), Pd ( $11\bar{1}$ ),  $\text{Ga}_2\text{Pd}_3$  (221), and  $\text{Ga}_5\text{Pd}$  (310) nonspecular reflections along the azimuthal direction. The well defined peaks indicate that Pd and Pd gallides were grown epitaxially on GaN (0001).

At 700°C, there are still Pd/GaN patches which extend from the Pd/GaN interface to the top surface. When the annealing was done at 800°C, the metal layer has reacted much further and is covered by the gallides, at this point, no conduction through Pd would be possible. The surface is completely disrupted and very rough, but small patches of Pd can be still found on the GaN surface, although they are completely imbedded inside the gallide layer (fig. 6).



Fig. 6: The Pd/GaN contact after annealing at 800°C

The intermetallic phases can be epitaxially grown on GaN as determined by the above Xrays experiments, but as seen in figure 6, they are mostly spread all over the metallic layer. The Pd patches still have (111)Pd/(0001)GaN epitaxial relationship, but as can be seen in fig. 7, the interface does not appear to be abrupt, or atomically flat as compared to the non annealed or lower temperature annealed contacts, its extension is 1-1.5 nm.

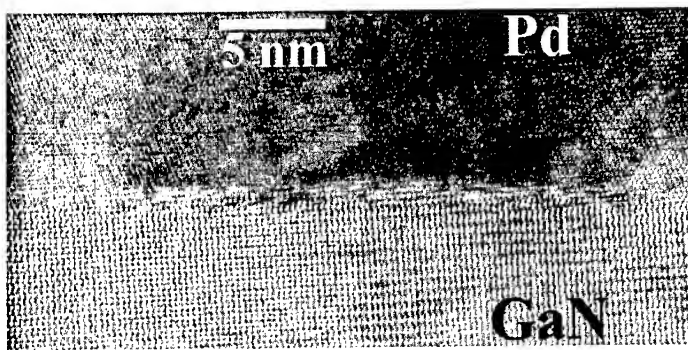


Fig. 7: Atomic scale image of the Pd/GaN interface after annealing at 800°C

#### In Summary

In the Pd/GaN contact, after annealing below 600°C, (Pd-Ga) intermetallic phases are not detected by X-ray diffraction<sup>5</sup> and HREM observations show abrupt and flat Pd/GaN interfaces. Higher temperature annealing leads to a rapid extension of these phases and they finish by embedding the remaining small Pd patches.

#### Acknowledgement

This work is supported by CNRS-KOSEF project 9510.

- [1] M. Asif Khan, M. S. Shur, J. N. Kuznia, Q. Chen, J. Burm, and W. Schaff, Appl. Phys. Lett. 66, 1083 (1995)
- [2] Z. Fan, S. N. Mohammad, W. Kim, O. Aktas, A. E. Botchkarev, and H. Morkoc, Appl. Phys. Lett. 68, 1672 (1996).
- [3] H. Ishikawa, S. Kobayashi, Y. Koide, S. Yamasaki, S. Nagai, J. Umezaki, M. Koike, and M. Murakami, J. Appl. Phys. 81, 1315 (1997).
- [4] J. K. Kim, J. L. Lee, J. W. Lee, H. E. Shin, Y. J. Park, and T. Kim, Appl. Phys. Lett. 73, 2953 (1998).
- [5] CC Kim, PhD dissertation Pohang University of Science and Engineering, 2001

### Ti/Al- GaN Reaction Mechanism Forming Low Contact Resistivity

Yoshimichi Fukasawa, Tomonori Nakamura, Tohru Nakamura  
College of Engineering, Hosei University  
Koganei, Tokyo 184-8584 Japan

#### ABSTRACT

The mechanism of Ti/Al reaction to n-GaN was studied to form ohmic contacts with low contact resistivity. N-GaN layers with a carrier concentration of  $2.17 \times 10^{18} \text{ cm}^{-3}$  were deposited on sapphire substrates. Ti/Al metals were deposited by conventional electron-beam techniques. Contact resistivity decreased as the Ti thickness increased, and increased as the Al thickness increased. The lowest contact resistivity was measured at  $1.20 \times 10^{-6} \Omega \text{ cm}^2$  for 80 nm Ti /100 nm Al. After annealing at 900 °C, Al/AlTi/TiN layers on GaN were formed and AlTi alloy thickness decreased as Ti thickness increased, from 1.5 MeV Rutherford Backscattering Spectroscopy(RBS) measurement. It was found that the contact resistivity was reduced as alloy metal thickness into GaN was increased.

#### INTRODUCTION

GaN has a wide band gap and its applications in high speed, high temperature and high power electronic devices are expected. In these applications, high quality ohmic contact formation is very important to obtain high performance characteristics. Contacts containing Ti/Al layers have observed the lowest contact resistivity to n-GaN[1-3]. Due to a TiN layer formed by Ti reaction to GaN after annealing, a high concentration of N vacancies could be created near the interface, resulting that ohmic contacts with contact resistivity as low as  $8 \times 10^{-6} \Omega \text{ cm}^2$  have been achieved[2]. A contact resistivity about  $10^{-6} \Omega \text{ cm}^2$  on GaN using plasma treatment without annealing at a higher temperature has been reported[4]. However, there is few reports on direct measurements of TiN formation after annealing. This paper reports the reaction between Ti/Al and GaN in order to realize ohmic electrodes with low contact resistivity.

Table 1. The thickness of Ti/Al metal electrodes.

Sample	1	2	3	4	5	6	7
Ti	20 [nm]	50 [nm]	80 [nm]	50 [nm]			100 [nm]
Al	100 [nm]			50 [nm]	100 [nm]	150 [nm]	0

#### EXPERIMENTAL

N-GaN ( $n = 2.17 \times 10^{18} \text{ cm}^{-3}$ ) layers were grown on (0001) sapphire substrates by the MOCVD. Ti/Al metals were deposited on n-GaN epitaxial layers by conventional electron beam techniques. The thickness of Ti/Al bilayer is shown in Table 1. After deposition, thermal annealing was carried out at 900 °C for 3 min in nitrogen atmosphere. 1.5MeV Rutherford Backscattering Spectroscopy (RBS) was used to clarify the composite metal systems.

Measurements of the contact resistivity were made using the TLM patterns which were defined by photolithography. The thickness of Al/Ti and Al/AlTi/TiN layers on GaN was measured using KLA-Tencor alfa-step AS500.

## RESULTS AND DISCUSSIONS

The contact resistivity of the Ti/Al contact to n-GaN as a function of as-deposited Ti thickness is shown in Fig. 1. The contact resistivity becomes low as Ti thickness increases. Minimum contact resistivity of  $1.20 \times 10^{-6} \Omega\text{-cm}^2$  was obtained at Ti(80 nm)/Al(100 nm) system. The contact resistivity as a function of as-deposited Al thickness is shown in Fig. 2. As shown in Fig. 2, the contact resistivity increases as the Al thickness increases.

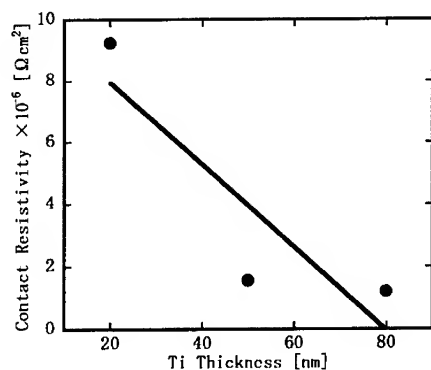


Fig. 1. Contact resistivity of Ti/Al contact to GaN layers as a function of as-deposited Ti thickness.

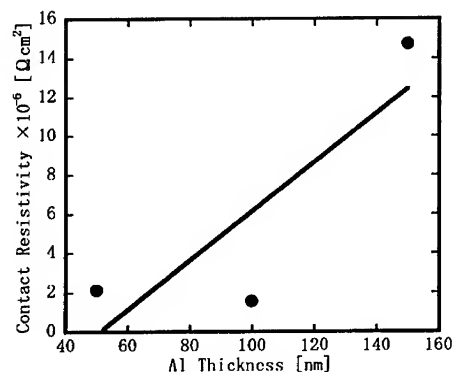


Fig. 2. Contact resistivity of Ti/Al contact to GaN layers as a function of as-deposited Al thickness.

1.5 MeV RBS measurements were used to clarify the mechanism of Ti/Al ohmic contacts to GaN layers. Fig. 3 shows RBS spectra from as-deposited Ti(80nm)/Al(100nm) metals on GaN and after-annealed metals. The channel number 410, 371 and 290 correspond to Ga, Ti, and Al at surface, respectively. After annealing, the Ti thickness increases and maximum yield backscattered from Ti atoms reduces, as shown in Fig. 3. This shows that a TiN and AlTi layers were created, since the interface between Ti and GaN moved into the GaN layer.

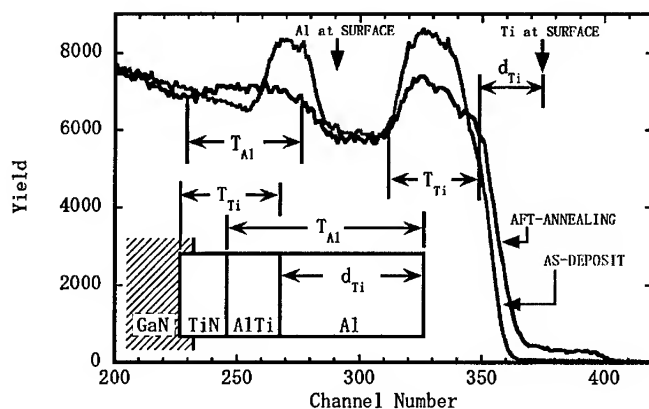


Fig. 3. RBS spectra from as-deposited and after-annealed Ti/Al metals on GaN..

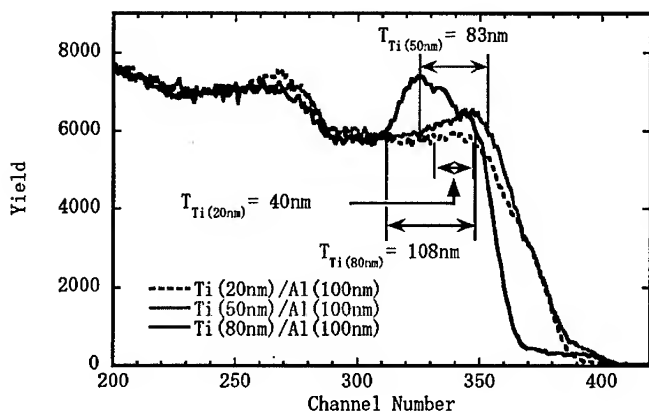


Fig. 4. RBS spectra from Ti (20nm)/Al(100nm), Ti (50nm)/Al(100nm), and Ti(80nm)/Al(100nm) on GaN after an nealing.

RBS spectra from Ti (20nm)/Al(100nm), Ti(50nm)/Al(100nm), and Ti(80nm)/Al(100nm) metals on GaN after annealing, are shown in Fig. 4. When initial Ti thickness is thin, the thickness of Ti and GaN alloy becomes thin. The thickness of a TiN and AlTi layer can be determined at  $T_{Ti}$ , an Al and AlTi layer  $T_{Al}$ , as shown in Fig. 3. An Al thickness can be also determined at  $d_{Ti}$ , which corresponds to  $He^+$  energy loss in Al layer deposited at the surface. Total thickness of Al/AlTi/TiN on GaN layers was measured by alfa-step AS500. The thickness of Al, AlTi and TiN layers created after annealing can be calculated, and are shown in Fig. 5.

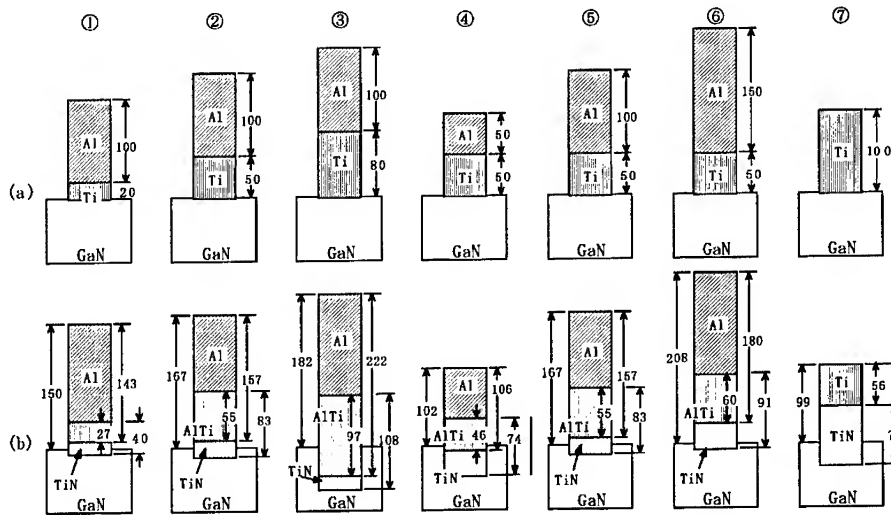


Fig. 5. The thickness of Al, AlTi and TiN metals after annealing.

After annealing at 900 °C, Al/AlTi/TiN layers on GaN were formed and AlTi alloy thickness decreased as Ti thickness increased, but TiN alloy thickness did not depend on both initial Ti and Al thickness. On the other hand, for Ti-only contact to GaN, TiN thickness was 70nm and contact resistivity became low as  $3.02 \times 10^{-7} \Omega \cdot \text{cm}^2$ . This means that contact resistivity of Ti/Al to GaN did not determine only at the thickness of TiN on GaN.

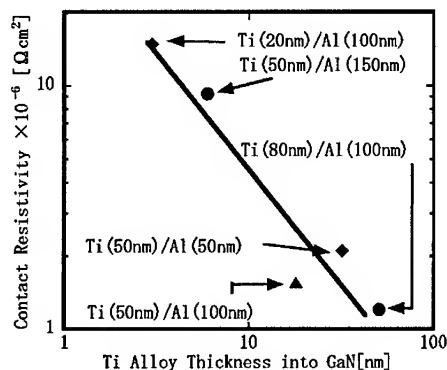


Fig.6. The contact resistivity as a function of Ti-alloy metal thickness into GaN.

The contact resistivity as a function of Ti-alloy metal thickness into GaN is shown in Fig. 6. Contact resistivity is inversely proportional to Ti-alloy metal thickness into GaN. Due to a TiN and an AlTi layers formed by Ti reaction to GaN after annealing, a high concentration of N vacancies could be created near the interface. It is considered that ohmic contacts with low contact resistivity have been achieved, since the concentration of N vacancies depends on Ti-alloy metal thickness into GaN.

## CONCLUSIONS

The mechanism of Ti/Al reaction to n-GaN was studied to form ohmic contacts with low contact resistivity. The contact resistivity becomes low as Ti thickness increases. Minimum contact resistivity of  $1.20 \times 10^{-6} \Omega\text{-cm}^2$  was obtained at Ti(80 nm)/Al(100 nm) system. 1.5 MeV RBS measurements were used to clarify the mechanism of Ti/Al ohmic contacts to GaN layers. After annealing at 900 °C, Al/Ti/TiN layers on GaN were formed and AlTi alloy thickness decreased as Ti thickness increased, but TiN alloy thickness did not depend on both initial Ti and Al thickness. Contact resistivity is inversely proportional to Ti-alloy metal thickness into GaN. Due to a TiN and AlTi layers formed by the reaction of Ti to GaN after annealing, a high concentration of N vacancies can be created near the interface and ohmic contacts with low contact resistivity have been achieved.

## REFERENCES

1. Z.-F. Fan, S. N. Mohammad, W. Kim, O. Aktas, A. E. Botchkarev and H. Morkoc, Appl. Phys. Lett. 68, 1672, (1996).
2. M. E. Lin, Z. Ma, F. Y. Huang, Z. F. Fan, L. H. Allen and H. Morkoc, Appl. Phys. Lett. 64, 1003, (1994).
3. B. P. Luther, S. E. Mohney, T. N. Jackson, M. A. Khan, Q. Chen and J. W. Yang, PII. Phys. Lett. 70, 57, (1997).
4. H. W. Jang, J. K. Kim, C. M. Jeon, J. L. Lee, MRS Internet J. Nitride Semicond. Res. 6, 8, (2001).

### Comparative morphology of AuTiAlTi, AuPdAlTi and AuAlTi ohmic contacts to AlGaIn/GaN

M W Fay, G Moldovan, I Harrison<sup>1</sup>, R.S. Balmer<sup>2</sup>, K P Hilton<sup>2</sup>, B T Hughes<sup>2</sup>, M J Uren<sup>2</sup>, T Martin<sup>2</sup> and P D Brown

School of Mechanical, Materials, Manufacturing Engineering and Management, University of Nottingham, University Park, Nottingham NG7 2RD, UK

<sup>1</sup>School of Electrical and Electronic Engineering, University of Nottingham, University Park, Nottingham NG7 2RD, UK

<sup>2</sup>QinetiQ Ltd, St Andrews Rd, Malvern, Worcs WR14 3PS, UK

#### ABSTRACT

AuTiAlTi, AuPdAlTi and AuAlTi ohmic contacts to AlGaIn/GaN layers rapid thermal annealed at temperatures up to 950°C have been characterised using conventional and chemical transmission electron microscopy techniques. The relationship between the as-deposited metallic structure, annealing temperature, post-anneal interfacial microstructure and contact resistance is examined.

The presence of a TiN interfacial layer is found to correlate with the onset of ohmic behaviour. Ti and Pd barrier layers are found to be ineffective at stopping the diffusion of Au to the interface. Au is implicated in the development of the inclusions, which are associated with threading dislocations. Once activated, the presence of the inclusions has little influence on the ohmic behaviour of the sample.

#### INTRODUCTION

Devices based on AlGaIn/GaN heterostructures are of great interest in the area of high power, high frequency applications. Reproducible, low resistance ohmic contacts are required for such applications.

Ohmic contacts to n-type GaN and AlGaIn are normally based on the reaction of an Al/Ti diffusion couple to form an intermetallic Ti:Al –based layer, with an interfacial Ti-nitride layer and a nitrogen depletion layer at the semiconductor surface to activate the contact. As Al and Ti layers are both susceptible to oxidation, Au capping layers are used as an oxidation resistant material, and to planarise the contact to assist with wire bonding. It was considered undesirable to have Au diffusing to the contact/nitride interface [1], and so diffusion barrier layers of materials such as Ti, Pd, Ni and Pt were introduced within the Au/Al/Ti contact scheme. [2,3,4,5].

However, TEM analysis of such layers indicate that they are ineffective at preventing the diffusion of Au to the semiconductor, and it has more recently been suggested that this may not actually be undesirable [6]

A large number of variables affect the characteristics of a metal diffusion couple contact, including the nature of the GaN wafer, which makes it difficult to compare results published in the literature. It is preferable to compare samples with a single variable altered, processed on the same GaN wafer. In this paper, we consider three contact schemes, typical of multilayer contacts reported in the literature, to AlGaIn/GaN.

## EXPERIMENTAL METHOD

Firstly, a 300nm Au / 60nm Ti / 100nm Al / 20nm Ti contact to AlGaIn/GaN grown by metal organic chemical vapour deposition (MOCVD) on a sapphire substrate with samples annealed at temperatures from 650 to 950°C. Secondly, a 100nm Au / 100nm Pd / 160nm Al / x nm Ti contact annealed at 950°C, where x is 30, 60, 100 or 160nm, to an AlGaIn/GaN sample also grown on a sapphire substrate, and thirdly a 100nm Au / x nm Al (x=60 or 100nm) / 20nm Ti contact to an AlGaIn/GaN layer grown on a SiC substrate, annealed at 950°C. All contacted samples were rapid thermal annealed in flowing nitrogen using a 30 second ramp to the annealing temperature followed by a 30 second hold at temperature, followed by a free cool.

Sequential mechanical polishing and low angle argon ion milling were used to prepare samples for conventional and chemical TEM analysis. Elemental profiles were obtained using a JEOL 2010F for energy dispersive x-ray (EDX) and a JEOL 4000FX for energy filtered TEM (EFTEM). Electrical characterisation was carried out using transmission line method (TLM).

## RESULTS

Bright field images of AuTiAlTi contacts to AlGaIn/GaN, after annealing at (a) 850°C or (b) 950°C are shown in Fig. 1. The structure of the contact/nitride interface is markedly different between the two anneals. At 850°C the AlGaIn layer is still largely intact, with only a few nm of consumption. After annealing at 950°C, a high density of inclusions was observed, penetrating through the AlGaIn layer into the GaN layer beneath.

Varying the thickness of the Ti layer in the AuPdAlTi contacts was found to have a significant difference on the interfacial morphology after annealing at 950°C, as shown in Fig. 2. For a Ti layer of 30nm (Fig 2a), the majority of the AlGaIn layer was still largely intact, with only a low density of inclusions observed. Between these inclusions, the surface of the AlGaIn was only consumed to the depth of a few nm. Increasing the thickness of the Ti layer to 60nm was found to produce a higher density of inclusions, to the extent that the inclusions began to merge together, with little AlGaIn being left intact (Fig. 2b). Increasing the Ti layer thickness further did not increase the number of inclusions formed, but clearly increased the size of the



**Figure 1** – Bright field images of AuTiAlTi contacts to AlGaIn/GaN annealed at a) 850°C and b) 950°C. The AlGaIn layer can still be seen clearly in sample a), while it has been completely consumed by the inclusions in sample b).

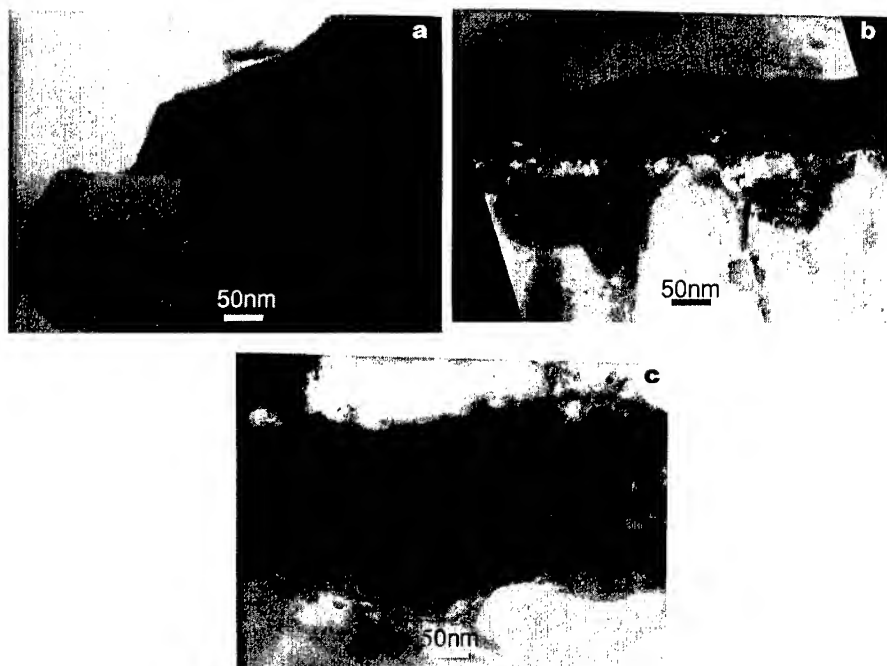


**Figure 2** – A Bright field images of AuPdAlTi contacts annealed at 950°C with a Ti layer thickness of a) 30nm, b) 60nm and c) 100nm. The AlGa<sub>N</sub>/Ga<sub>N</sub> interface is still largely intact in the sample with the thinnest Ti layer, but has been consumed by inclusions in samples with a greater amount of Ti.

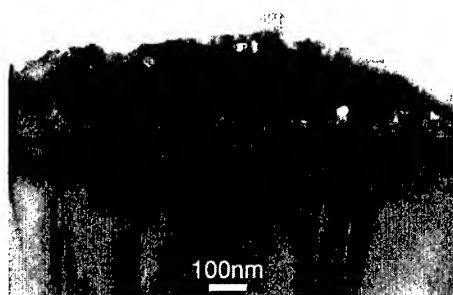


**Figure 3** – Bright field image of an AuAlTi contact to an AlGa<sub>N</sub>/Ga<sub>N</sub> layer grown on a SiC substrate annealed at 950°C. The inclusions observed at the contact/nitride interface are all associated with threading dislocations.

inclusions laterally along the interface, with increased depth of penetration into the GaN to the extent that the inclusions have merged to form a continuous consumption layer parallel to the original contact/nitride interface (Fig. 2c).

Varying the Al thickness in the AuAlTi contact did not lead to any major changes in the contact/nitride interfacial morphology after annealing at 950°C. However, the greatly reduced density of dislocations within GaN layers grown on SiC substrates, as compared with those grown on sapphire substrates, emphasised the association of threading dislocations with inclusion formation. Fig. 3 shows that inclusion formation at the contact/semiconductor interface is directly related to the presence of threading dislocations emerging from the nitride layer surface, with no inclusions being observed in the absence of threading dislocations.

The contact resistances of the samples were obtained by the Transmission Line Method (TLM). For the AuTiAlTi contacts, an anneal of 750°C or higher was required to form an ohmic contact, with anneals at 850°C and 950°C producing similar contact resistances, despite the markedly different interfacial morphologies. In the case of the AuPdAlTi contact, samples with thicker Ti layers were found to have superior contact resistivities after annealing at 850°C as compared with thinner Ti layers, but there was no clear trend in the electrical characteristics after annealing at 950°C. Further, no clear difference in the electrical characteristics was observed for the AuAlTi contacts with varying Al layer thickness after annealing at 950°C.

For samples found to be ohmic, chemical analysis showed a similar structure in all the inclusions and inclusion free regions observed. Line profiles across the entire interface are shown in Figure 4, higher resolution profiles and spot analysis have also been performed to confirm the compositions of features. In all cases, a Ti-nitride layer is identified at the position of the pre-anneal contact/nitride interface. Where no inclusions have formed, a Au layer is found directly adjacent to this Ti-nitride layer (Fig. 4a, c). Where inclusions are observed, the inclusions are also found to be a Ti-nitride, bounded by a thin Al/Au rich layer that may also be present as filaments within the inclusions (Fig. 4b, d). The discrete Ti-nitride layer at the original pre-anneal interface is apparently unaffected by the development of the inclusions. It is also noted that the inclusions in the AuAlTi contacted sample after annealing at 950°C did not appear to be significantly larger than the inclusions observed in the diffusion barrier samples annealed at the same temperature, suggesting that the Pd or Ti barrier layers in the original metallisation contact are inefficient in slowing diffusion of Au to the contact/nitride interface.

These results reaffirm that ohmic behaviour in these contacts is related to the initial formation of a Ti-nitride phase at the pre-anneal contact/semiconductor interface, which has been found by high resolution TEM to be comprised of grains of ~10nm diameter [7,8]. Al, Au and Ti diffuse through this Ti-nitride layer without significantly disrupting it to form the inclusion structures, with displaced Ga diffusing in the opposite direction. The inclusions all originate from the intersection of a dislocation with the contact/semiconductor interface. The implication being that the emergent core of a threading dislocation provides a disrupted surface state that is conducive to enhanced reaction with the metallisation layer during annealing. The development of the inclusions is also dependent on the annealing temperature and the presence of a minimum amount of Ti, while the size of the inclusions is dependent on the thickness of the pre-anneal Ti layer.

~~BEST AVAILABLE COPY~~

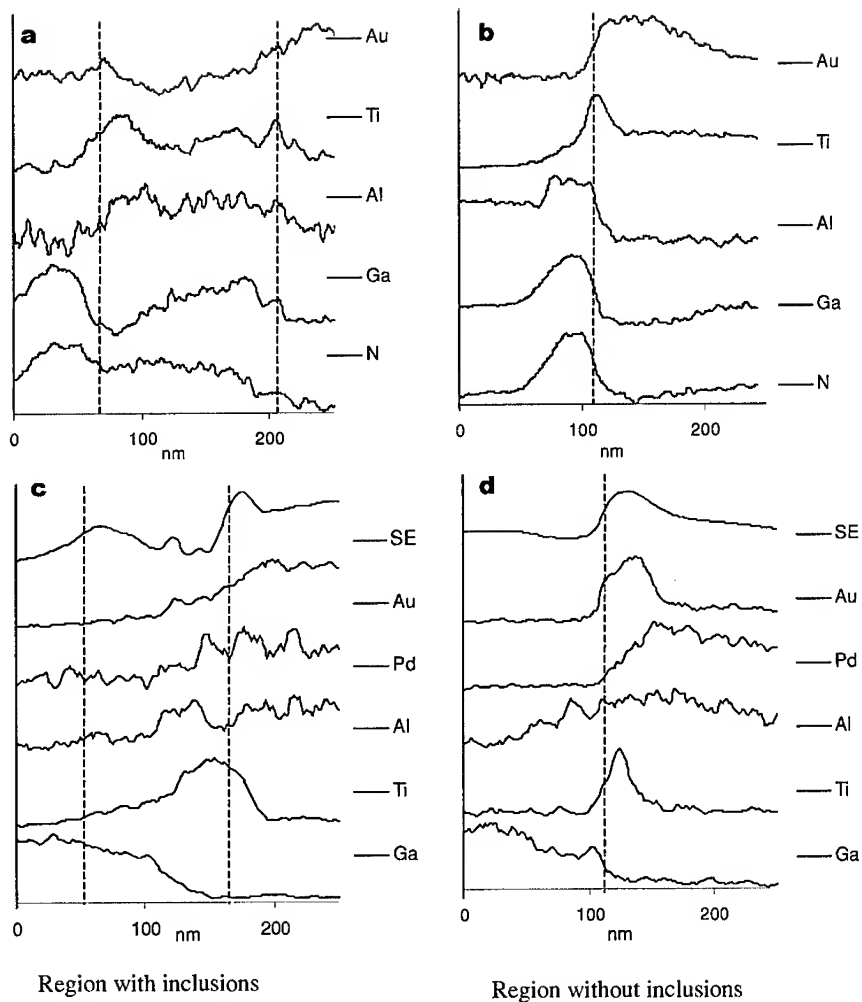


**Figure 4** – a,b) EFTM and c, d) EDX profiles (including Secondary Electron, SE profile) obtained across regions without inclusions and with inclusions respectively, from the GaN (left of profile) to contact layer (right of profile). A Ti-rich interfacial layer is identified at the interface where no inclusions have formed, while the inclusions themselves are also observed to be Ti-rich. The inclusions are bounded by a thin Al/Au rich layer. Another Ti-rich layer is also observed above the inclusion, at a position which corresponds to the pre-anneal contact/nitride interface. Dashed lines mark the diffusion front of the inclusion in a) and c), and the position of the Ti-rich interfacial layer in all profiles.

## CONCLUSIONS

Ti or Pd barrier layers do not prevent the diffusion of Au to the contact/semiconductor interface after high temperature rapid thermal annealing. The presence of threading dislocations and interfacial Au are implicated in the development of Ti-nitride inclusions observed in these contacted samples. The size of these inclusions is related to the amount of Ti present in the contact scheme. However, it is the formation of the thin Ti-nitride interfacial layer rather than the inclusions that are related to the onset of ohmic behaviour, with the subsequent development of the inclusions having no discernable effect on the resultant contact resistivity.

## ACKNOWLEDGEMENTS

MWF wishes to acknowledge EPSRC/QinetiQ for funding under contract number GR/M87078, and would also like to thank Prof Cullis' group at the University of Sheffield. Work at QinetiQ was supported by the Corporate Research Programme of the UKMOD

## REFERENCES

- 1 C.T.Lee And H W Kao, Appl. Phys. Lett. **76**, 2364 (2000)
- 2 S.J. Cai, R. Li, Y.L. Chen, L. Wong, W.G. Wu, S.G. Thomas, K.L. Wang, Electron. Lett. **34**, 2354 (1998)
- 3 S.J.Cai, R. Li, Y.L.Chen, L. Wong, W.G.Wu, S.G. Thomas, K. L. Wang, Electron Lett. **34**, 2354 (1998)
- 4 Z. F. Fan, S. N. Mohammad, W. Kim, O. Aktas, A. E. Botchkarev, and H. Morkoç, Appl. Phys. Lett. **68**, 1672 (1996).
- 5 S.N. Mohammad, Z.F. Fan, A. Salvador, O. Aktas, A.E. Botchkarev, W. Kim, and H Morkoç, Appl. Phys. Lett. **69** 1420 (1996)
- 6 A N. Bright, P. J. Thomas, M. Weyland, D. M. Tricker, C. J. Humphreys and R. Davies, J. Appl. Phys. **89**, 3143 (2001)
- 7 M. W. Fay, G. Moldovan, P. D. Brown, I. Harrison, J. C. Birbeck, B. T. Hughes, M. J. Uren and T. Martin, J. Appl. Phys. **92**, 94 (2002)
- 8 M. W. Fay, G. Moldovan P. D. Brown, I. Harrison, R.S.Balmer, J. C. Birbeck, B. T. Hughes, M. J. Uren and T. Martin, in preparation

### STABLE OHMIC CONTACTS ON GaAs AND GaN DEVICES FOR HIGH TEMPERATURES

A. Piotrowska<sup>1</sup>, E. Kaminska<sup>1</sup>, A. Barcz<sup>1,2</sup>, K. Golaszewska<sup>1</sup>, H. Wrzesinska<sup>1</sup>, T. T. Piotrowski<sup>1</sup>, E. Dynowska<sup>2</sup>, R. Jakiela<sup>2</sup>

<sup>1</sup>Institute of Electron Technology, Warsaw, Poland,

<sup>2</sup>Institute of Physics, PAS, Warsaw, Poland.

#### ABSTRACT

We have studied thermal stability of Nb and NbN contacts to GaAs and GaN by x-ray diffraction and SIMS, and demonstrated their excellent behaviour under high temperature annealing. GaAs/Nb and GaAs/NbN contacts are stable up to 800<sup>o</sup>C and 900<sup>o</sup>C, respectively while GaN/NbN and GaN/Nb/NbN remain stable up to 1000<sup>o</sup>C.

#### INTRODUCTION

Device technology is usually driven by industrial and commercial requirements. This is particularly true in the field of high temperature and high power electronics, where applications range from communication links and electricity networks to high power domestic applications. Consequently, much of the work is concerned with fabrication of power rectifiers, HBTs and HEMTs based on GaAs and GaN, materials offering a high power handling capability. To ensure long-term device reliability in hot environments and power dissipation at a high output power, additional research is required to develop thermally stable metallization systems. Low melting point metallizations, commonly used for low resistivity ohmic contacts, readily react with semiconductor forming multiphase structures. Resultant grain boundaries and voids enhance inter-diffusion at the metal-semiconductor interface and initiate device degradation during operation at high temperatures. Amorphous thin films, free from grain boundaries and nucleation sites, have been shown to have many orders of magnitude lower diffusivities than their polycrystalline counter-partners. Refractory metals and their nitrides, offering an exceptional combination of properties like low resistivity, high melting point and resistance to corrosion [1] are considered as good materials for the development of thermally stable ohmic and gate contacts for high temperature GaAs- and GaN-based electronics. Until now the research effort has concentrated on nitrides and borides of Ti, Zr, Mo, Ta and W [2]. On the other hand, promising results have been obtained with single niobium and niobium nitride metallizations to GaAs and GaN [3-6]. Moreover, niobium being superconductor has attracted recently a big deal of attention for fabricating superconductor/semiconductor hybrid structures involving 2DEG in III-V semiconducting heterostructures [7, 8].

In this work we report on the applicability of thin films of Nb and NbN for thermally stable metallizations to GaAs and GaN. The effect of high temperature annealing on the microstructure of metal/semiconductor contact has been investigated using secondary ion mass spectrometry (SIMS) and x-ray diffraction (XRD) measurements. The electrical characterisation involved measurements of I-V characteristics for rectifying contacts and resistivity for ohmic contacts.

## EXPERIMENTAL DETAILS

Bearing in mind typical device structures with heavily doped semiconductor region adjacent to ohmic contact metallization, the majority of experiments was performed on n-type GaAs epilayers with a doping concentration of  $1 \times 10^{19} \text{ cm}^{-3}$  and n-type GaN films doped to a concentration of  $5 \times 10^{18} \text{ cm}^{-3}$ . 2  $\mu\text{m}$  thick GaAs films were MBE grown on semiinsulating GaAs substrate. 2  $\mu\text{m}$  thick GaN epilayers were grown by MOCVD on sapphire substrates. Highly resistive GaAs and GaN samples have been used for the evaluation of the specific resistance of metallic films.

Surface preparation prior to the deposition of metallization involved cleaning in hot organic solvents, plasma ashing and wet etching. GaAs surface have been processed in 20  $\text{NH}_4\text{OH}$ -7  $\text{H}_2\text{O}_2$ -973  $\text{H}_2\text{O}$  followed by 1  $\text{NH}_4\text{OH}$ -10  $\text{H}_2\text{O}$  dip. GaN surface was etched in 10%  $(\text{NH}_2)_2\text{CS} : \text{HCl} : 15\% \text{H}_2\text{O}_2 = 20 : 1 : 1$ . The surface cleaning was completed in the deposition chamber by *in-situ*  $\text{Ar}^+$  ion sputter etching at 300 V for 30 s.

Thin films of Nb and NbN were deposited by DC magnetron sputtering from Nb target in Ar and Ar/ $\text{N}_2$  discharge, respectively. Nb layers were deposited at a pressure of  $4.3 \times 10^{-3}$  mbar and power density of 2.5  $\text{W}/\text{cm}^2$ , at a rate 0.7 nm/s. As for the fabrication of NbN, the process parameters were first optimised with regard to the stoichiometric composition of deposited films. The following parameters have been chosen as the optimum conditions for the deposition of NbN films: power density 5  $\text{W}/\text{cm}^2$ , the total pressure  $6.8 \times 10^{-3}$  mbar, and the ratio  $\text{Ar}/\text{N}_2$  of 1.7. NbN was deposited at a rate of 0.6 nm/s. 50 nm thick Nb and NbN films were used throughout experiments.

Heat treatments were carried out in a rapid thermal annealer (RTA), in flowing  $\text{N}_2$ , at temperatures in the range 500-1150°C for 30 s.

SIMS was applied to probe composition profiles. The measurements were carried out with a Cameca 6F instrument, using caesium primary beam and detection of  $\text{CsX}^+$  secondary cluster ions. XRD was applied to determine crystalline phases and their orientation. The sheet resistance of thin films was measured with four-point-probe, while their thickness was determined using Alpha-step depth profiler. The electrical characterisation of metal/semiconductor contacts involved measurements of their current-voltage characteristics and the specific contact resistance. These were performed prior to and after heat treatments. Specific resistance of ohmic contacts ( $r_c$ ) was determined by circular transmission line method (cTLM) [9]. To get knowledge on the mechanism of carrier transport through the ohmic contacts, additional measurements of the temperature dependence  $r_c(T)$ ,  $T=300^\circ - 480^\circ\text{K}$  have been carried out.

## RESULTS AND DISCUSSION

The resistivity of 50 nm thick Nb and NbN films is about 130  $\mu\Omega\text{cm}$  and 400  $\mu\Omega\text{cm}$ , respectively.

Both metallizations form ohmic contacts on highly doped ( $n \geq 8 \times 10^{18} \text{ cm}^{-3}$ ) GaAs and GaN, with the specific contact resistance of the order  $10^{-5} \Omega\text{cm}^2$  and  $10^{-4} \Omega\text{cm}^2$ , respectively. The measurements of the temperature dependence of the specific contact resistance have shown that, in the temperature range  $T=300^\circ - 480^\circ\text{K}$ ,  $r_c$  is temperature independent and thus give evidence that tunnelling is the main carrier transport responsible for ohmic behavior.

### Nb and NbN Contacts to GaAs

According to the results of XRD analysis, as-deposited Nb and NbN films on GaAs are amorphous. The influence of the heat treatment on composition profiles of GaAs/Nb contacts is presented in figure 1. It shows that the migration of gallium into metallization film, being a measure of contact stability, after annealing at 800°C is negligible, which indicates outstanding thermal stability of this single metal system. The use of NbN enables to further improve the thermal stability. As the figure 2 shows, sharp interface between GaAs and metallization, with no sign of Ga outdiffusion after 900°C annealing is preserved.

Both Nb and NbN metallizations remain amorphous after high temperature annealing.

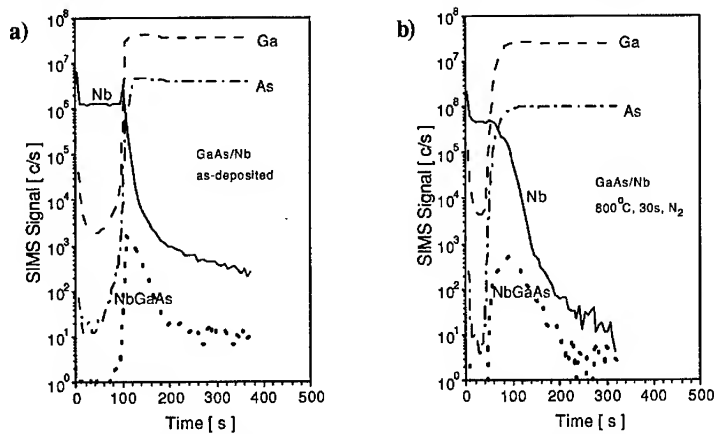


**Figure 1.** SIMS profiles of GaAs/Nb contacts: a) as-deposited contact, b) contact annealed at 800°C.

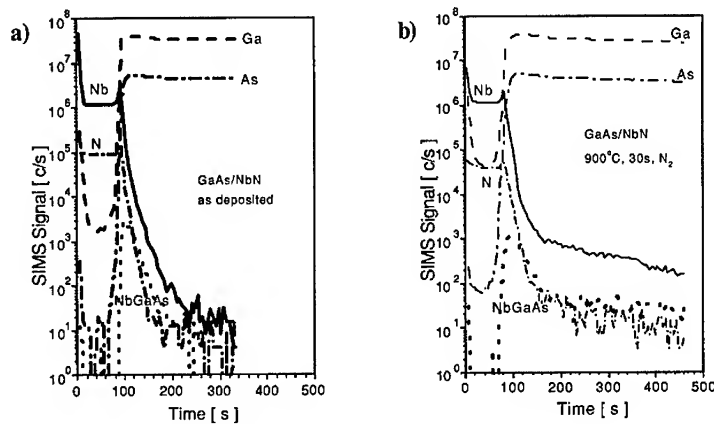


**Figure 2.** SIMS profiles of GaAs/NbN contacts: a) as-deposited contact, b) contact annealed at 900°C.

### NbN and Nb/NbN Contacts to GaN

Nb films on GaN are amorphous, while NbN films deposited either directly on GaN or on Nb film were polycrystalline and highly textured. The results of XRD and SIMS analyses of NbN contacts on GaN are presented in figures 3 and 4. They prove that, in spite of crystalline structure, the integrity of the contact microstructure is saved up to annealing temperatures of 1000°C. Also initial layered structure Nb/NbN deposited on GaN remains unaffected under heat treatment up to 1000°C. The results of XRD and SIMS studies of Nb/NbN contacts on GaN are shown in figures 5 and 6.

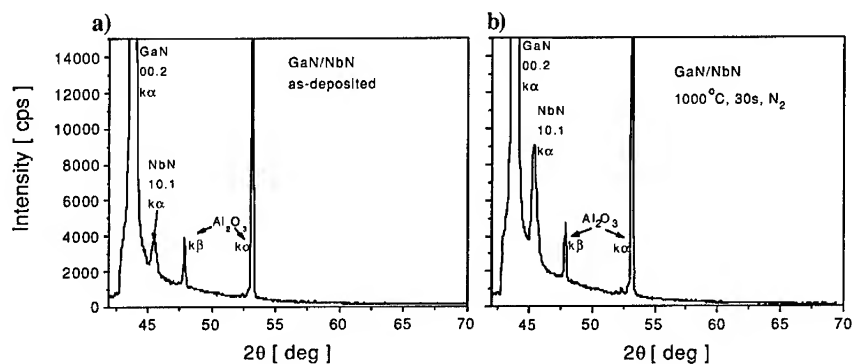


**Figure 3.** XRD spectra of GaN/NbN contacts: a) as-deposited contact, b) contact annealed at 1000°C.

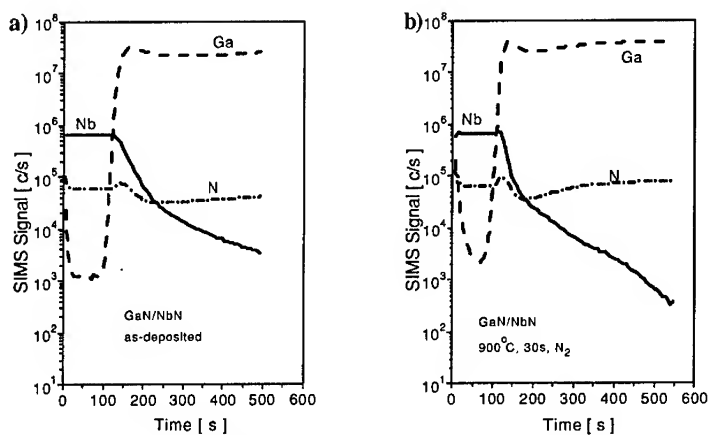


**Figure 4.** SIMS profiles of GaN/NbN contacts: a) as-deposited contact, b) contact annealed at 900°C.

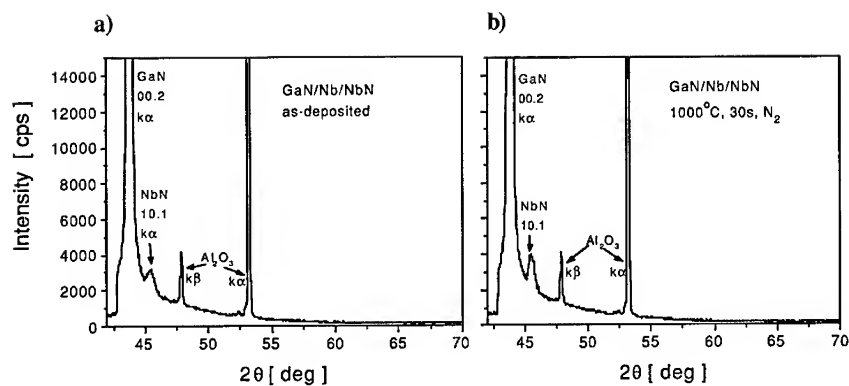


**Figure 5.** XRD spectra of GaN/Nb/NbN contacts: a) as-deposited contact, b) contact annealed at 1000°C.

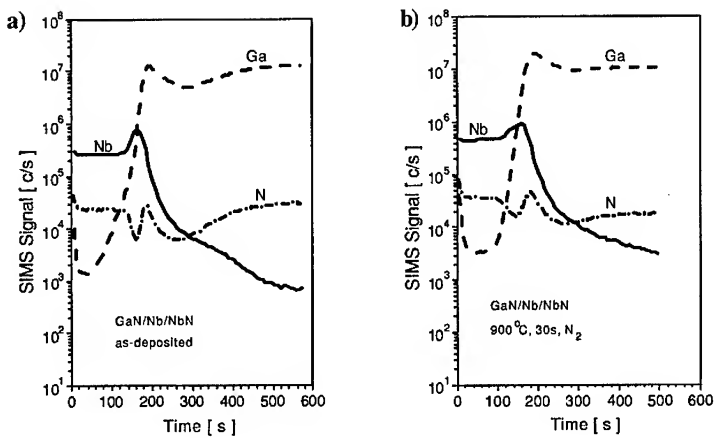


**Figure 6.** SIMS profiles of GaN/Nb/NbN contacts: a) as-deposited contact, b) contact annealed at 900°C.

## CONCLUSIONS

Niobium nitride has been demonstrated as an alternative material for thermally stable metallizations to GaAs and GaN. Pure niobium films, preserving their amorphous structure up to 800°C and 1000°C when deposited on GaAs and GaN, respectively, show higher thermal stability than other commonly used refractory metals.

Another important finding of this work is different thermal behaviour of GaN/Nb/NbN contact comparing to Ti/TiN and Zr/ZrN contacts on GaN [10, 11]. While the former remains stable under annealing at 1000°C, in both Ti-based and Zr-based contacts interfacial reactions were observed at 900°C and 1000°C, respectively.

## ACKNOWLEDGEMENTS

Research is partially supported by grants from European Commission G5RD-CT-2001-00566-DENIS and the Committee for Scientific Research 7T11B 009 20 and PBZ-KBN-044/P03/2001.

## REFERENCES

1. J. R. Shapirio, *Solid State Technol.* **10**, 161 (1985).
2. E. Kaminska, A. Piotrowska, M. Guziejewicz, K. Golaszewska, A. Barcz, A. Turos, E. Mizera, J. Adamczewska, S. Rouvimov, Z. Liliental-Weber, M. D. Bremser, and R. F. Davies, *Electron Technology* **32**, 304 (1999).
3. L. C. Zhang, C. L. Liang, S. K. Cheung, and N. W. Cheung, *J. Vac. Sci. Technol. B* **5**, 1716 (1987).
4. I. Hotovy, J. Huran, D. Buc, and S. Smak, *Vacuum* **50**, 45 (1998).
5. L. Hultman, *Vacuum* **57**, 1 (2000).
6. H. K. Kim, T. Y. Seong, and C. R. Lee, *J. Electron. Mater.* **30**, 266 (2001).
7. J. Knoch, J. Appenzeller, and B. Lengeler, *J. Appl. Phys.* **88**, 3522 (2000).
8. Th. Schapers, R. P. Muller, G. Crecelius, H. Hardtdegen, and H. Luth, *J. Appl. Phys.* **88**, 4440 (2000).
9. G. S. Marlow, M. B. Das, *Solid-State Electronics* **25** (1982) 91.
10. E. Kaminska, A. Piotrowska, M. Guziejewicz, S. Kasjaniuk, A. Barcz, E. Dynowska, M. D. Bremser, O. H. Nam, and R. F. Davis, *Mat. Res. Soc. Symp. Proc.* **449**, 1055 (1997).
11. S. D. Wolter, B. P. Luther, S. E. Mohny, R. F. Karlicek, Jr., and R. S. Kern, *Electrochem. and Solid-St. Lett.* **2**, 151 (1999).

### Ohmic and Rectifying Contacts to n and p-type GaN Films

H. P. Hall, M. A. Awaah, A. Kumah, K. Das and F. Semendy<sup>1</sup>

Tuskegee University, Dept. of Electrical Engineering  
Tuskegee, AL 36088.

<sup>1</sup>Army Research Laboratory  
Adelphi, MD.

#### ABSTRACT

Electrical contacts to both n and p-type GaN films have been investigated using electron-beam evaporated and sputtered films of metals such as Al, Au, Cr, Cu, Ni, Pt, and Ti. Films deposited by electron-beam evaporation for the n-type films with doping levels of  $1 \times 10^{18}/\text{cm}^3$  and lower showed rectifying characteristics with all the metals studied with the exception of Al. Aluminum contact diodes were ohmic in the as-deposited state. The Pt rectifying contact was near-ideal with an ideality factor close to 1.0. Ideality factors for the other metals were much greater than 1. This deviation from thermionic behavior was interpreted as space charge limited current conduction in the presence of deep-level states. Sputtered films showed very similar characteristics to electron-beam deposited films, with the exception of Ti. The Ti contact was ohmic in the as-deposited state. Non-linear Cu contacts to n-type films became ohmic on annealing. However, for p-type films, Ar ion sputter-cleaning prior to metal deposition by sputtering created ohmic contacts with Cu and Pt. Low resistance ohmic contacts were achieved by ion implantation and anneal of Si in n-type and Mg in p-type films, prior to metallization. The implant parameters and anneal temperatures are currently being optimized.

#### INTRODUCTION

Group III nitride based semiconductors have attracted a considerable amount of attention during the last decade [1-2]. Gallium nitride in particular, having a bandgap of 3.39 eV at room temperature, is being used for the fabrication of optoelectronic devices such as light emitting diodes, photodetectors and lasers within the blue and ultraviolet region of the spectrum. Promising operation of GaN MESFETs [3] and AlGaIn/GaN HEMTs [4] and HBTs [5] has been reported. Gallium nitride devices are also expected to operate at high temperatures, frequencies and power levels. Almost all these devices rely on rectifying and ohmic metal-semiconductor contacts for their operation. For the continued development of these devices, electrical properties of the metal-semiconductor contacts need to be thoroughly understood so that sufficient degree of process control can be achieved for obtaining optimal device properties.

In this present paper, we report on the observed electrical properties of metal-GaN contact diodes formed by e-beam evaporated and sputtered metal films on n- and p-type GaN films. Emphasis was placed on developing an understanding of the current transport process for n-type rectifying contacts and establishing low resistance ohmic contacts for both n- and p-type films. The high ideality factors obtained for some of the rectifying contacts on the n-type films indicated that thermionic emission was probably not the dominant current transport mechanism, but instead it was likely to be space charge limited current conduction influenced by the presence

of deep-level states. Annealing of the metallized contacts and pre-metallization Ar sputter-cleaning of some of the contacts resulted in linear current-voltage characteristics. For creating high surface doping concentrations on the GaN films, ion implantation of Si and Mg were used to obtain n and p-type films respectively. Measured contact resistivities are also reported here.

## EXPERIMENTAL PROCEDURE

For this study, heteroepitaxial GaN films on sapphire grown by molecular beam epitaxy (MBE) were obtained from SVT Associates, Eden Prairie, MN. The films were 1  $\mu\text{m}$  thick and grown on a thin nucleation layer of AlN. N-type films were obtained with two different doping concentrations of  $1 \times 10^{17} \text{ cm}^{-3}$  and  $1 \times 10^{18} \text{ cm}^{-3}$ . The p-type film had a doping concentration of  $1 \times 10^{18} \text{ cm}^{-3}$ . The heteroepitaxial wafers were diced into 5 mm x 5mm squares for individual experiments. The samples were cleaned in acetone and methanol followed by rinsing in de-ionized water, then a five minutes buffered oxide etch (BOE) and a final rinse in de-ionized water. Silicon dioxide was then deposited onto the samples as a means of surface passivation.

Samples were photolithographically patterned for lift-off metallization for a diode circular dot pattern, for the study of rectifying properties. To form metal/GaN contact diodes, various metals (Al, Au, Cr, Cu, Ni, Pt and Ti) were deposited onto the GaN surface by electron beam evaporation and sputtering.

For creating a high surface concentrations for achieving low ohmic contact resistivities, n-type samples were implanted with Si and p-type samples with Mg both to a dose of  $1 \times 10^{15} \text{ cm}^{-2}$  with an implant energy of 35 keV. Annealing took place at 1100 °C in a  $\text{N}_2$  ambient. The implanted samples were patterned for lift-off metallization using a transfer length method (TLM) mask for ohmic contact resistivity measurements. Contact metallization employed was a bilayer of Ti (250Å)/Au (1500Å) for the n-type contacts and Ni/Au of the same thickness for p-type contacts. The fabricated contacts were annealed at 550 °C and 900 °C in flowing  $\text{N}_2$  for the p and n-type GaN, respectively. Current-voltage measurements were conducted at room temperature using an HP4155A Semiconductor Parameter Analyzer.

## RESULTS AND DISCUSSIONS

Most of the sputter-deposited and the e-beam evaporated metal contacts to n-type GaN films were rectifying, with the exception of thermally evaporated Al and sputter-deposited Ti. Aluminum and Ti were ohmic in the as-deposited state. The ohmic nature of the Al contact was most likely due to work function difference between Al and GaN. For Ti, probably sputtering-induced formation of TiN and associated N vacancies at the interface resulted in the ohmic behavior. The semi-logarithmic plots of the forward current-voltage (I - V) characteristics for the sputtered contacts are shown in Fig. 1. Ideality factors and barrier heights, shown in Table 1, were calculated on the assumption that thermionic emission prevailed in these contacts. Ideality factors for the sputtered films, calculated from the approximately linear region of the semi-logarithmic plots, ranged from 1.4 to 1.9. The electron beam evaporated contacts also showed high ideality factors, with the exception of Pt (Table 1). The non-ideal behavior of the contacts as displayed by their high ideality factors suggested that thermionic emission was probably not the dominant transport mechanism in these diodes. Features pertaining to space charge limited

current (SCLC) conduction in the presence of deep-level states were observed in the logarithmic plots of the forward characteristics, as shown in Fig. 2, for the sputtered Au contact diode. These features included an ohmic regime at low biases, a sharply rising current regime at intermediate biases followed by a square law regime at high biases. The logarithmic plots for the other sputtered contact diodes are shown in Fig. 3.

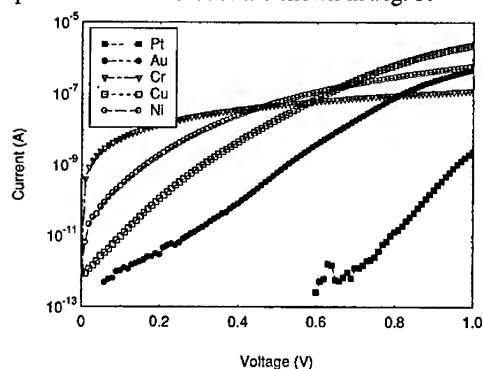


Fig. 1. I-V characteristics of sputtered Pt, Au, Cr, Cu and Ni on n-type GaN.

Table 1. Ideality factor and calculated barrier height for sputtered and evaporated contacts.

Metal	Sputtered Contact		Evaporated contact	
	$n$	$\phi_{bn}$ (eV)	$n$	$\phi_{bn}$ (eV)
Au	1.8	0.88	1.6	1.05
Cr	1.3	0.74	1.5	0.99
Cu	1.4	0.84	-	-
Ni	1.9	1.20	-	-
Pt	1.8	1.31	1.0	0.67
Ti	-	-	1.5	0.84

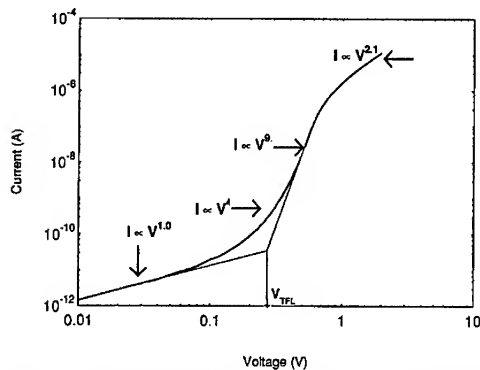


Fig. 2. Logarithmic plot of forward characteristic of Au contact on GaN

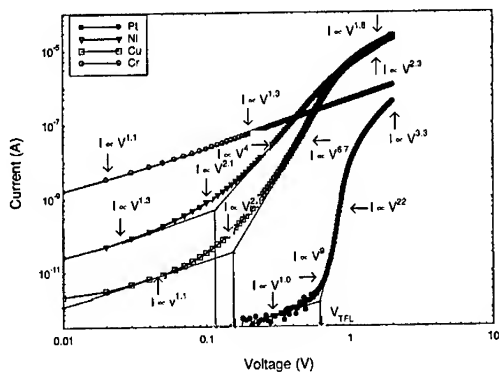


Fig. 3. Logarithmic plots of the forward characteristics for sputtered Pt, Ni, Cu and Cr contacts on GaN. These plots show space charge limited conduction except for the Cr contact which remained in the ohmic regime.

Space charge limited current flow in wide bandgap semiconductors and insulators have been discussed in detail by Mark and Lampert [6]. A sharp rise in current occurs at a voltage designated as  $V_{TFL}$ , where TFL denotes a "trap-filled limit". Using a procedure detailed in Ref. [7], approximate positions of the deep level states in the forbidden gap and concentrations of unoccupied states were determined from the observed  $V_{TFL}$  as given in Table 2.

Table 2. Calculated SCLC conduction parameters.  $p_{to}$  is the hole occupancy of the traps in the active region of the diode and  $n_o$  the effective carrier concentration in the active region of the device.

Metal	Meas. Temp. (°C)	$V_{TFL}$ (V)	$n_o$ (cm <sup>-3</sup> )	$p_{to}$ (cm <sup>-3</sup> )	Deep level below $E_C$ (eV)
Au	RT	0.25	$1.38 \times 10^{13}$	$7.6 \times 10^{15}$	0.35
Cu	RT	0.15	$4.10 \times 10^{13}$	$5.5 \times 10^{15}$	0.32
Ni	RT	0.11	$2.70 \times 10^{14}$	$4.9 \times 10^{15}$	0.27
Pt	RT	0.67	$5.90 \times 10^{11}$	$2.6 \times 10^{16}$	0.43

For the simple analysis used here only one discrete level was considered. A slow rise in current observed in some cases was considered to be due to states distributed in energy and at low biases the slow rise may be an indication that the distributed states were in continuum with the band edge states.

The I-V characteristics of sputtered contacts to p-type GaN were also investigated. Most of these contacts showed highly non-linear behavior. In order to improve the as-deposited I-V characteristics of these contacts, Ar ion sputter-cleaning was used prior to metallization. This sputter-cleaning step resulted in ohmic contacts for Cu and Pt, possibly due to the presence of surface states introduced by sputter-induced damage.

Low resistance contacts of  $1 \times 10^{-7} \Omega \cdot \text{cm}^2$  were obtained for TLM structures fabricated on Si implant-doped GaN, using Ti (250Å)/Au (1500Å) metallization, following a 900 °C anneal. The implantation energy was 35 keV with a dose of  $1 \times 10^{15}/\text{cm}^2$  and annealing of the contacts before metallization was conducted at 1100 °C. These results compare favorably with published data on contact resistivity. Lester et al. [8] reported a contact resistivity of  $1 \times 10^{-5} \Omega \cdot \text{cm}^2$  for non-alloyed Ti (250Å)/Al (1500Å) metallization on Si implanted GaN after a 1120 °C implant activation anneal. Lin et al [9] obtained a contact resistivity of  $8 \times 10^{-6} \Omega \cdot \text{cm}^2$  for MBE grown n-GaN after annealing at 900 °C for 30s. For the p-type Mg implanted samples which were annealed at 1100 °C and metallized with Ni (250Å)/Au (1500Å) TLM structures, contact resistivity of  $1.4 \times 10^{-5} \Omega \cdot \text{cm}^2$  was obtained after a 500 °C anneal. Representative plots of are shown in Fig. 4. However, the 1100 °C implant anneal is known to create N vacancies [10]. These N vacancies act as donors in the GaN film resulting in low contact resistivities for n-type

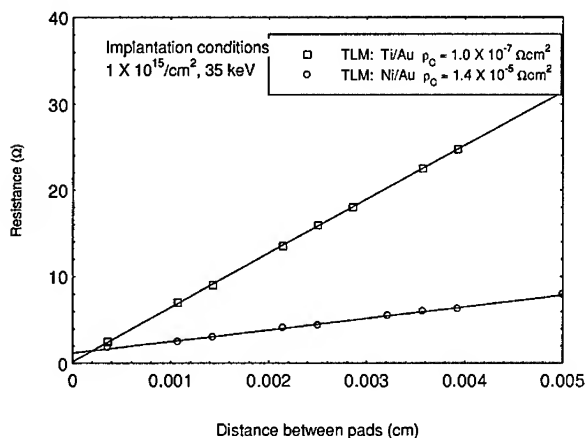


Fig. 4. Resistance as a function of TLM pad spacing (least square linear regression plot)

films. This effect might have possibly resulted in overcompensation of the p-type implanted samples, used in this study, into n-type after the 1100 °C implant. It was reported by Ronning et al [11] that p-type activation in Mg implanted GaN was not achieved by an 1100 °C anneal. However, Kalinina et al [12] reported successful acceptor activation in Mg implanted GaN by an 1100 °C anneal. Thus, it is apparent that more work is warranted in the area of activation of implanted acceptors in GaN.

## CONCLUSIONS

Electrical contacts to both n and p-type GaN films have been investigated using electron beam evaporated and sputtered films of metals such as Al, Cu, Cr, Au, Ni, Pt and Ti. The rectifying contacts, with the exception of e-beam evaporated Pt, were non-ideal and exhibited ideality factors much greater than one. The e-beam evaporated Pt contact diode showed ideal rectifying characteristics. The non-ideal behavior of the other metal contacts was probably due to space charge limited current conduction in the wide bandgap GaN. The space charge limited current was influenced by the presence of deep-level centers/traps in the forbidden energy gap. These states appeared to be located between 0.27 eV and 0.43 eV below the conduction band edge. Platinum contacts showed the deepest states at 0.43 eV. For Cu and Pt contacts deposited on Ar ion sputter-cleaned p-GaN prior to metallization, the I-V characteristics were improved from highly non-linear to ohmic. Low resistance contacts were obtained for n-type GaN using Si ion implantation, anneal and metallization with a bilayer of Ti/Au. For p-type films, Mg ion implantation and a bilayer of Ni/Au were employed. However, it was uncertain if activation of the implanted Mg was obtained. Further study needs to be conducted for the understanding of implant activation of acceptors in GaN.

## REFERENCES

1. N. M. Johnson, A. V. Nurmiko, S. P. DenBaars, *Phys. Today* **53**, 31 (2000).
2. S. Nakamura, *Science* **281**, 956 (1998).
3. M. A. Khan, J. N. Kuzina, A. R. Bhattarai and D. T. Olson, *Appl. Phys. Lett.* **62**, 1786 (1993).
4. G. J. Sullivan, M.Y. Chen, J. A. Higgins, J. W. Yang, Q. Chen, R. L. Pierson and B. T. McDermott, *IEEE Electron Device Lett.* **19**, 198 (1998).
5. L. S. McCarthy, P. Kozodoy, M. Rodwell, S. DenBaars, U. K. Mishra, *Inst. Phys. Conf. Ser.* **162**, 279 (1999).
6. M. A. Lampert and P. Mark, *Current Injection in Solid*, (Academic Press Inc, New York, 1970), p. 3-26.
7. K. Das, H. S. Kong, J. B. Petit, J. W. Bumgarner, R. F. Davis and L. G. Matus, *J. Electrochem. Soc.* **137**, 1598 (1990).
8. L. Lester, J. Brown, J. Ramer, L. Zhang, S. Hersee and J. Zolper, *Appl. Phys. Lett.* **69**, 2737 (1996).
9. M. Lin, Z. Ma, F. Huang, Z. Fan, L. Allen and H. Morkoc, *Appl. Phys. Lett.* **64**, 1003 (1994).
10. J. C. Zolper, *J. of Crystal Growth*, **178**, 157-167 (1997).
11. C. Ronning, E. Carlson and R. F. Davis, *Physics Report* **351**, 349 (2001).
12. E. V. Kalinina, V. A. Solov'ev, A.S. Zubrilov, and V. A. Dmitriev in *GaN and Related Alloys*, edited by C. Kuo, S. Pearton, T. Uenoyama and A. Wright, (Mat. Res. Soc. Proc., Boston, MA, 1998).

**Activation of Mg acceptors in GaN:Mg monitored by  
electron paramagnetic resonance spectroscopy.**

D. Matlock, M.E. Zvanut, Jeffrey R. DiMaio<sup>1</sup>, R.F. Davis<sup>1</sup>, R. L. Henry<sup>2</sup>, Daniel Koleske<sup>3</sup> and Alma Wickenden<sup>4</sup>

Department of Physics, University of Alabama at Birmingham, 310 CH, Birmingham, AL 35294-1170

<sup>1</sup>Department of Materials Science and Engineering, North Carolina State University

<sup>2</sup>Naval Research Laboratory, Code 6861 Washington D.C 20375

<sup>3</sup>Sandia National Laboratories, P.O. Box 5800-0601, Albuquerque, NM 87185-0601

<sup>4</sup>U.S. Army Research Laboratory, Adelphi MD, 20783-1197

**ABSTRACT**

Hydrogen removal from Mg-doped GaN is necessary to activate p-type conductivity, but the exact chemical process is not yet clear. We have investigated this issue by monitoring the intensity of an electron paramagnetic resonance (EPR) signal attributed to Mg through a series of isochronal and isothermal anneals between 600 and 1000 °C. Measurements made on GaN:Mg epitaxial layers deposited on SiC and annealed between 700 and 850 °C indicate that the Mg-related EPR signal increases with temperature as expected for depassivation of a Mg complex by removal of hydrogen. However, data obtained outside this temperature range suggest that additional processes may occur. For example, as-deposited films contain a signal resembling the Mg acceptor that is quenched by a 650 °C N<sub>2</sub> anneal. Also, for all samples, N<sub>2</sub> annealing at T>850 °C irreversibly decreases the signal thought to be due to Mg. Although the presence of the signal in the as-grown films is not fully understood, the effects observed at T>850 °C may be attributed to preferential N-desorption from Mg-N-H complexes.

**INTRODUCTION**

Several experiments have shown that as-deposited CVD GaN doped with Mg is highly resistive. However, the conductivity may be increased to about 1(ohm-cm)<sup>-1</sup> by e-beam irradiation or N<sub>2</sub> annealing [1]. Today, p-type CVD GaN is produced by a post-growth activation anneal at about 800 °C using either a rapid thermal anneal oven or a conventional furnace. The results of many experiments suggest that the observed behavior is related to the passivation of Mg by hydrogen that is moved from the sample during annealing [1-3]. For example, comparisons between conductivity data and secondary ion mass spectroscopy (SIMS) measurements show that hydrogen is released from the film as the conductivity increases during post-deposition annealing [2]. Infrared spectroscopy measurements are consistent with the SIMS results and suggest that the acceptor is a complex of hydrogen, magnesium and nitrogen [4,5]. In addition to these studies, electron paramagnetic magnetic resonance (EPR) spectroscopy reveals a signal in p-type activated GaN:Mg that correlates with the SIMS measured Mg concentration [6]. Studying a variety of activated films grown by molecular beam epitaxy or chemical vapor deposition, Carlos concludes that the EPR signal is related to the acceptor.

EPR spectroscopy detects changes in the magnetic dipole orientation of a dangling bond at a defect site (ie. a 'spin-flip'). For a broad, featureless signal like the Mg-related one in GaN, the defect is simply characterized by its g-value measured at a particular orientation of the magnetic field with respect to the c-axis of the sample. 'g' is obtained from the resonance condition  $B_0 = h\nu/g\mu_B$  where  $B_0$  is the value of applied magnetic field at resonance,  $h$  is Planck's constant,  $\nu$  is the microwave frequency, and  $\mu_B$  is the Bohr magneton. For the Mg signal, two parameters are sufficient to characterize the center,  $g_{\parallel} = 2.1$  and  $g_{\perp} = 2.0$  [6]. Note that a signal is detected only when a defect has an unpaired electron. Since hydrogen is thought to react with the Mg complex in GaN, it likely passivates any unpaired electrons at the acceptor site. Therefore, if the signal measured by Carlos is truly related to the Mg-acceptor, the EPR signature should be absent in as-grown CVD GaN:Mg and gradually increase with annealing temperature and time as hydrogen is driven from the film. Our results are consistent with the latter half of this statement. That is, the amplitude of a EPR line at  $g=2$  increases over the temperatures and time range expected. However, prior to any thermal treatments conducted for the EPR study, as-grown samples reveal a signal with similar g-value and line width as seen for the acceptor signal in p-type activated material. As is shown below, the signal may be distinguished from that in annealed samples by its thermal stability.

## EXPERIMENTAL DETAILS

EPR experiments were performed on 0.7  $\mu\text{m}$ -thick Mg-doped GaN films deposited by organometallic chemical vapor deposition (OMCVD) onto the Si-face of n-type SiC using a 0.1  $\mu\text{m}$  thick AlN buffer layer. Both as-grown films and ones that received a 30 s 800  $^{\circ}\text{C}$  rapid thermal anneal (RTA) in  $\text{N}_2$  were studied. The RTA, which was performed to induce p-type conductivity, will be referred to as the activation anneal to distinguish it from the isothermal and isochronal heat treatments discussed below. CV measurements of the activated samples indicate a carrier concentration of  $2 \times 10^{18} \text{ cm}^{-3}$ , consistent with a heavily doped Mg-film. A separate set of GaN:Mg/SiC samples used for the isothermal anneal experiments were measured using two point-probes on indium contacts. The resistivity values obtained for the unactivated epitaxial layers was greater than  $10^5 \text{ ohm-cm}$ ; while for the activated films, it was about  $10 \text{ ohm-cm}$ . Samples were annealed in 99.999% pure  $\text{N}_2$  at temperatures ranging from 600 to 1000  $^{\circ}\text{C}$ . For the isochronal anneals, the same piece was used for each 60 min anneal; for the isothermal experiments, a separate piece of material was used for each anneal temperature. Unintentional incorporation of  $\text{H}_2$  was minimized by heating the samples in a double-walled quartz furnace tube with a moisture level below 1 ppm, and then cooling them at the exit end of the furnace tube with  $\text{N}_2$  flowing for about three minutes before removal.

Electron paramagnetic resonance spectroscopy was performed at 4K with the c-axis of the sample parallel to the magnetic field. A 48  $\mu\text{m}$  thick GaN film with a prominent donor line was mounted with each sample to provide a standard with which to monitor potential changes in EPR cavity sensitivity between annealing steps. Relative changes in the defect concentration was approximated by monitoring the amplitude of an EPR resonance at  $g=2$  after each anneal.

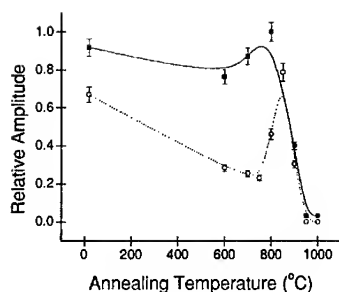


Figure 1. Relative intensity of the  $g=2$  EPR signal during 60 min anneals of unactivated ( $\circ$ ) and activated ( $\blacksquare$ ) GaN:Mg/SiC. The lines are meant as a guide to the eye.

(700-850 °C) is the same as that typically used for the post-deposition activation anneal. In both type of samples, the angular dependence of the resonance line is similar to that reported earlier for the signal attributed to Mg in activated GaN layers grown on sapphire. Therefore, we conclude that the EPR resonance at  $g=2$  in the unactivated material after annealing at  $T > 750$  °C is the same as that seen in activated material and that the signal is due to Mg-related acceptors as suggested by Carlos.

At temperature above 850 °C, the intensity of the EPR line decreases and subsequent annealing at lower temperature did not restore the signal. Although this behavior was not investigated thoroughly, we speculate that the permanent removal of the EPR signal is related to desorption of N, a process well-known to occur in GaN [7,8]. X-ray diffraction measurements of our samples did not indicate any changes in the crystal structure of the film after the 1000 °C anneal. Therefore, it is likely that the high temperature heat treatment preferentially removes nitrogen from N-Mg bonds that are weakened by the presence of the impurity. To avoid permanently quenching the Mg-signal, only temperatures below 800 °C were used for future experiments.

The data shown in Figure 1 indicate the  $g=2$  signal is present prior to heat treatment of unactivated material. The absorption line also appeared in the unactivated GaN:Mg deposited separately from the samples used to obtain spectra for Figure 1, as well as in unactivated GaN:Mg films grown on sapphire by a different supplier. If the signal is due to the same defect as that seen in activated samples, it is difficult to identify it as the Mg-related acceptor because the acceptor EPR signal should be passivated by H in as-deposited CVD GaN layers. To address the identity of the  $g=2$  resonance initially present in as-grown material isothermal anneals were performed at five different temperatures on both unactivated and activated GaN. Spectra obtained at selected times during the 750 °C anneal of the unactivated film are shown in

## RESULTS AND DISCUSSION

The relative amplitude of the  $g=2$  EPR signal is plotted in Figure 1 for the unactivated (unfilled circles) and activated (filled squares) GaN samples heat treated at temperatures between 600 and 1000 °C for 60 min. The unactivated samples exhibit a four-fold increase in signal intensity between 600 and 850 °C. (The temperature dependence below 600 °C will be addressed later.) For the GaN:Mg film that had been subjected to an RTA prior to the isochronal study, the results fluctuate by no more than 10% for temperatures up to 800 °C. The data for  $T > 700$  °C are consistent with the expected behavior of an EPR signal related to the Mg acceptor in GaN. For instance in activated films, the  $g=2$  resonance is observed prior to heat treatment and the amplitude varies only slightly during the  $N_2$  anneals as expected. Additionally, the temperature range over which the signal intensity increases in unactivated material

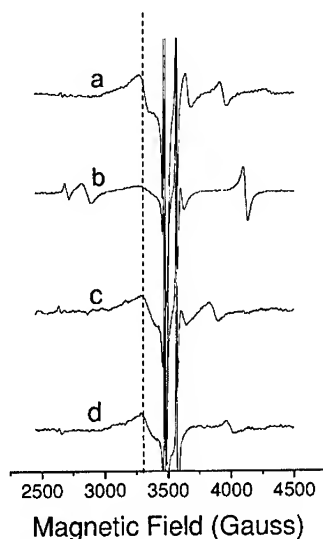


Figure 2. EPR spectra of unactivated GaN:Mg/SiC measured prior to annealing (a) and after 0.5 (b), 6.5 (c), 16.5 min (d)  $N_2$  anneals at 650 °C. Dashed line indicates the position of the  $g=2$  signal.

Figure 2. The dashed line locates the position of the  $g=2$  resonance. All other signals in the scans are due to the n-type GaN standard sample used for calibration, the sapphire substrate of the standard, and the SiC substrate. The data in Figure 3a show the relative amplitude of the signal at  $g=2$  measured during the initial 20 min of the 600 °C and 750 °C heat treatments. The initial decrease seen in Figures 2a-b and 3a distinguishes the  $g=2$  signal observed prior to any heat treatment from that observed in the samples that received a 800 °C RTA. As shown in Figure 3b, the signal intensity in the activated GaN:Mg material does not decrease initially. Apparently, the defect observed in the as-grown material is less stable than the Mg-complex associated with the  $g=2$  resonance in activated samples. It should be noted here, however, that preliminary isothermal annealing data of unactivated Mg-doped GaN grown on sapphire do not exhibit this initial decrease indicating that the thermally induced behavior depends critically on growth conditions and/or substrate material. Clearly, the identity of this defect needs to be determined and, more importantly, its affect on the carrier density should be investigated. Based on the similarity of the  $g$  value and line width with those in activated samples, the moiety is likely similar to the Mg acceptor. The initial heat treatments may quench the EPR signal by inducing a structural reorientation; this may even be necessary in

some films to create favorable kinetics for hydrogen depassivation.

After decreasing, the amplitude of the  $g=2$  EPR signal present in the as-grown unactivated epi-layers increases in a manner consistent with the removal of hydrogen from Mg-acceptor sites saturated with H (Fig. 3a and insert), as deduced from the isochronal experiments discussed earlier. Although a detailed kinetic study is not yet completed, the dependence of the signal intensity on both temperature and time is suggestive of an activated process. For example, at 600 °C the maximum amplitude of the EPR signal is achieved for times greater than 100 min; while at 750 °C, only 10 min is required to reach the maximum intensity. The activated samples also exhibit an increase with time and temperature; however the dependence differs from that seen in unactivated samples and may be related to the removal of hydrogen from complexes remaining after the RTA treatment. That the data seen in Figure 3b represent the completion of a process initiated by a prior treatment is supported by the short time

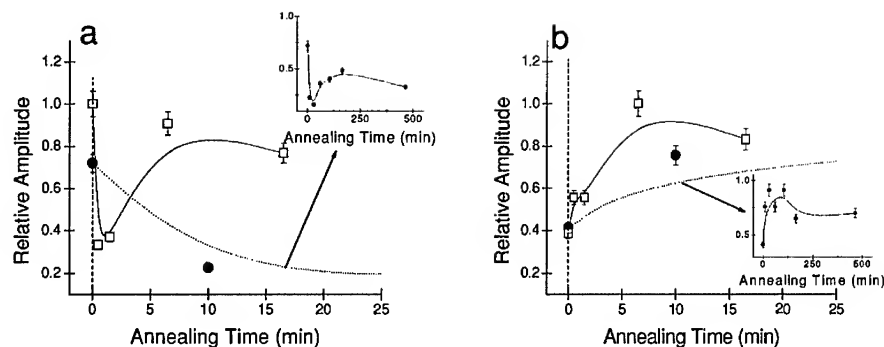


Figure 3. Relative amplitude of  $g=2$  EPR signal measured in unactivated (a) and activated (b) GaN:Mg/SiC during isothermal anneals at 600 °C (●) and 750 °C (□). The lines are meant as a guide to the eye.

(~ 10 min) necessary to reach the maximum value at each temperature. Continued depassivation in the activated GaN films may not be surprising given the differences in temperatures and times between the rapid thermal anneal process and that used for the isothermal heat treatments

In summary, EPR measurements of as-deposited GaN:Mg/SiC reveal the presence of a resonance at  $g \sim 2$  with a linewidth of about 100 G. The intensity dependence on temperature may be divided into three regions: 1) between room temperature and 700 °C, the intensity decreases; 2) For  $700 < T < 850$  °C, the amplitude increases; 3)  $T > 850$  °C, the signal intensity decreases below the detection limit and cannot be revived by subsequent lower temperature anneals. The increase observed during region 2 occurs over a temperature range typically used for removal of hydrogen from the film and activation of p-type conductivity. Therefore, the  $g=2$  resonance that appears after the as-grown signal is minimized is likely due to the Mg-related acceptor complex as has been suggested earlier for activated samples [6]. The time dependence observed during isothermal annealing and the similarity of the EPR parameters with those reported for the signal previously assigned to Mg are consistent with this assignment. The behavior of the  $g=2$  resonance in region three ( $T > 850$  °C) is also consistent with identification as the p-type acceptor. The permanent quenching of the signal is most likely related to preferential removal of nitrogen from the Mg-acceptor complex. Finally, the presence of the  $g=2$  EPR line prior to any thermal treatment in unactivated material appears to contradict the association of this resonance with p-type conductivity. However, we speculate that the defect differs only slightly from that observed in activated material, and that the low temperature anneal reorients the complex such that effective H-depassivation and p-type conduction may occur at higher temperatures.

## ACKNOWLEDGEMENTS

This work is funded by Dr. Colin Wood, Office of Naval Research. The authors thank Mr Tim Cooper and Dr. David Look for their assistance with the resistivity measurements.

## REFERENCES

1. S. Nakamura, N. Iwasa, M. Senoh, and T. Mukai, *Jpn. J. Appl. Phys.* **31**, Pt. 1, 1258 (1992).
2. W. Gotz, N.M. Johnson, J. Walker, and D.P. Bour, *Appl. Phys. Lett.* **67** 2666 (1995).
3. W. Gotz, N.M. Johnson, J. Walker, D.P. Bour, and R.A. Street, "Activation of acceptors in Mg-doped GaN grown by metalorganic chemical vapor deposition", *Appl. Phys. Lett.* **68**, 667 (1996).
4. B. Clerjaud, D. Cote, A. Lebkiri, C. Naud, J. M. Baranowski, K. Pakula, D. Wasik, and T. Suski, *Phys. Rev. B* **61**, 8238 (2000).
5. W. Gotz, N.M. Johnson, D.P. Bour, M.D. McCluskey, and E.E. Haller, *Appl. Phys. Lett.* **69**, 3725 (1996).
6. E.R. Glaser, W. E. Carlos, G.C.B. Braga, J.A. Freitas, Jr. W. J. Moore, B.V. Shanabrook, R.L. Henry, A.E. Wickenden, and D.D. Koleske, *Phys. Rev.* **B65**, 085312 (2002).
7. M.R. Lorenz and B.B. Binkowski, *J. Electrochem. Soc.* **109**, 24 (1962).
8. D.D. Koleske, A.E. Wickenden, R.L. Henry, J.C. Culbertson, and M.E. Twigg, *J. Crystal Growth* **223**, 466-483 (2001).

### Microstructural Defects in Mg-doped AlGa<sub>0.13</sub>N Layers Grown by Metalorganic Chemical Vapor Deposition

Hyung Koun Cho and Gye Mo Yang<sup>1</sup>

Department of Metallurgical Engineering, Dong-A University, Hadan-2-Dong 840, Saha-gu, Busan, 604-714, KOREA;

<sup>1</sup>Department of Semiconductor Science & Technology and Semiconductor Physics Research Center, Chonbuk National University, Duckjin-Dong, Chunju 561-756, Korea

#### ABSTRACT

We have investigated the formation of inversion domain boundaries in Al<sub>0.13</sub>Ga<sub>0.87</sub>N layers grown on sapphire substrates by metalorganic chemical vapor deposition using transmission electron microscopy. By increasing the Mg source flow rate, the reduction of dislocation density occurred up to the Mg source flow rate of 0.103  $\mu\text{mol/min}$ . While the vertical type inversion domain boundaries (IDBs) were observed in the Al<sub>0.13</sub>Ga<sub>0.87</sub>N layers grown with the low Mg source flow rate, the IDBs in the Al<sub>0.13</sub>Ga<sub>0.87</sub>N layers grown with the high Mg source flow rate have horizontally multifaceted shapes. The change of polarity by the IDBs of horizontal type also resulted in the 180° rotation of pyramidal defects within the same AlGa<sub>0.13</sub>N layer. Therefore, We found that the Mg source flow rate affects significantly the dislocation density, the type of IDBs, and the shape of pyramidal defects in AlGa<sub>0.13</sub>N layers.

#### INTRODUCTION

For good photon and current confinement of GaN based devices, a low aluminum (Al) composition AlGa<sub>0.13</sub>N cladding layer is used in the actual InGa<sub>0.13</sub>N/GaN multiple quantum well (MQW) light emitting diode (LED) and laser diode (LD) structures [3]. Also, AlGa<sub>0.13</sub>N layers as the first layer grown on sapphire substrates without underlying GaN layers, which can avoid the generation of cracks, can be applied as wide-bandgap windows and buffer layers in AlGa<sub>0.13</sub>N/GaN optoelectronic devices [1]. Planar defects such as stacking fault, inversion domain boundary (IDB), and stacking mismatch boundary are observed in GaN layers grown on sapphires, in addition to threading dislocations [2]. Two typical types of IDBs have been observed in GaN layers and AlGa<sub>0.13</sub>N/GaN superlattice structures grown on sapphire substrates [3-5]. The polarity of films is inverted at these domains. It has been reported that the control of the polarity greatly affects the optical and structural properties of LED and LD devices [6]. In this work, we observed the shape of IDBs in Mg-doped Al<sub>0.13</sub>Ga<sub>0.87</sub>N layers using TEM.

## EXPERIMENTAL DETAILS

$\text{Al}_{0.13}\text{Ga}_{0.87}\text{N}$  layers were grown on *c*-plane sapphire substrates in a low-pressure MOCVD reactor. Trimethylgallium, trimethylaluminum, ammonia, silane ( $\text{SiH}_4$ ), and biscyclopentadienyl-magnesium ( $\text{Cp}_2\text{Mg}$ ) were used as the source materials for Ga, Al, N, Si, and Mg, respectively. The  $\text{Al}_{0.13}\text{Ga}_{0.87}\text{N}$  layers were grown at 1100 °C after growing the GaN nucleation layers of about 25 nm thickness at 560 °C under the same growth conditions except for the dopant flow rate. The  $\text{Cp}_2\text{Mg}$  flow rate in  $\text{Al}_{0.13}\text{Ga}_{0.87}\text{N}$  layers were changed from 0  $\mu\text{mol/min}$  (undoped) to 3.172  $\mu\text{mol/min}$ , respectively.

In order to characterize the IDB formation in  $\text{Al}_{0.13}\text{Ga}_{0.87}\text{N}$  layers, TEM specimens were prepared in cross section along  $[11\bar{2}0]$  zone axis using Tripod mechanical polishing. Bright-field (BF) images and high-resolution TEM (HRTEM) images were recorded on a JEOL 2000 EX microscope at 200 kV.

## DISCUSSION

Figure 1 shows the cross-sectional bright field TEM micrographs from the undoped, Si, and Mg-doped  $\text{Al}_{0.13}\text{Ga}_{0.87}\text{N}$  layers grown on sapphire substrate. As shown in figures 1(a) and (b), no IDB was observed in undoped and Si-doped  $\text{Al}_{0.13}\text{Ga}_{0.87}\text{N}$  layers. However, IDBs are observed in

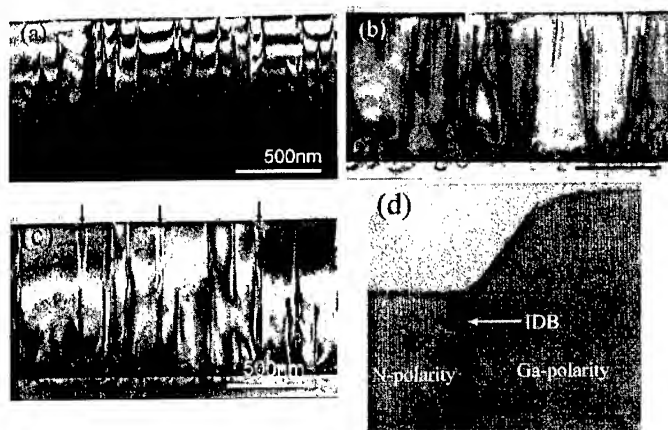


Figure 1. Cross-sectional bright-field TEM images using  $g = 0002$  two beam of the (a) undoped, (b) Si-doped, and (c) Mg-doped ( $\text{Cp}_2\text{Mg}$  flow rate of 0.103  $\mu\text{mol/min}$ )  $\text{Al}_{0.13}\text{Ga}_{0.87}\text{N}$  layers grown on sapphire substrates. (d) High-resolution TEM image of the IDB observed in Mg-doped  $\text{Al}_{0.13}\text{Ga}_{0.87}\text{N}$  layer.

samples with the  $\text{Cp}_2\text{Mg}$  flow rate of  $0.103 \mu\text{mol/min}$ . Black arrows in figure 1(c) indicate vertical shape IDBs which originate in the GaN nucleation layer and pass the whole Mg-doped AlGaIn layer. As shown in figure 1(d), the faceted step on the surface is the top region of inversion domain in the  $\text{Al}_{0.13}\text{Ga}_{0.87}\text{N}$  layers. In the  $\langle 11\bar{2}0 \rangle$  projection, the facet angle is nearly  $52^\circ$  with respect to the basal plane, which corresponds to the  $\{20\bar{2}3\}$  planes. The faceted steps on the inversion domain resulted from the slow growth rate within inversion domains (N-polarity) compared to matrix (Ga-polarity) around them [3]. The exposure of Mg in the (0001) surface can cause an inversion of polarity from Ga-polarity to N-polarity due to the formation of stable phases such as  $\text{Mg}_3\text{N}_2$ , [4,5] as reported by Ramachandra *et al.* [5]. Since all samples were grown under the same growth conditions except doping elements, therefore, the formation of vertical shape IDBs in the  $\text{Cp}_2\text{Mg}$  flow rate of  $0.103 \mu\text{mol/min}$  can probably be explained by the inversion of polarity in very small Mg-rich regions. An IDB may form if, for a Mg concentration above a certain threshold, it is energetically favorable to form a N-polarity surface atom instead of a Ga-polarity surface, which induces the formation of a vertical shape IDB.

For the high  $\text{Cp}_2\text{Mg}$  flow rates (more than  $0.397 \mu\text{mol/min}$ ), in contrast, the different shapes of IDBs are observed in  $\text{Al}_{0.13}\text{Ga}_{0.87}\text{N}$  layers. Bright field TEM images of  $\text{Al}_{0.13}\text{Ga}_{0.87}\text{N}$  layers with the high  $\text{Cp}_2\text{Mg}$  flow rates of  $1.031$  and  $3.172 \mu\text{mol/min}$  are shown in figures 2(a) and (b), respectively. The nearly horizontal shape IDBs are clearly visible, as indicated by the white arrows. High magnification TEM images [figures 2(c) and (d)] of the IDBs of horizontal shape show multifaceted boundaries and no stacking faults around IDB. The facet angle ranges from

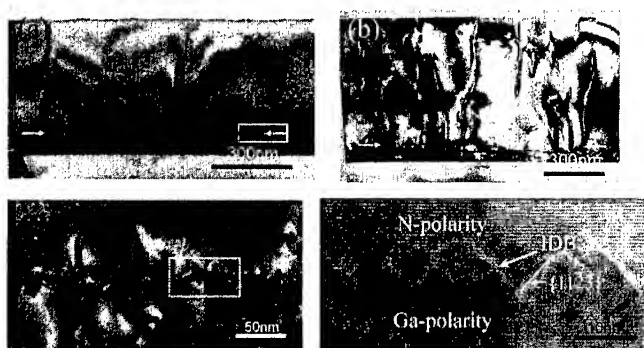


Figure 2. Cross-sectional bright-field TEM images using  $g = 0002$  two beam of samples grown with the  $\text{Cp}_2\text{Mg}$  flow rate of (a)  $1.031 \mu\text{mol/min}$  and (b)  $3.172 \mu\text{mol/min}$ . (c) High magnification image and (d) high resolution TEM image of the horizontal shape IDB of the samples grown with the  $\text{Cp}_2\text{Mg}$  flow rate of  $1.031 \mu\text{mol/min}$ . The magnified areas of figures 4(c) and (d) are indicated as dashed rectangles in figures. 4(a) and (c), respectively.

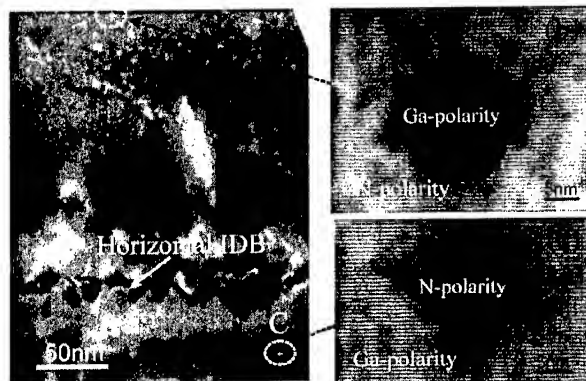


Figure 3. (a) Cross-sectional bright-field TEM image of the horizontal shape IDB of the sample grown with the  $\text{Cp}_2\text{Mg}$  flow rate of  $1.031 \mu\text{mol/min}$ . (b) and (c) high resolution TEM images showing pyramidal shape IDBs with  $180^\circ$  rotation.

$45^\circ$  to  $50^\circ$  with respect to the basal plane, which is consistent with the result of Romano *et al.* for GaN layers grown by MBE on Ga-polarity (0001) templates [4]. Interestingly, the position of the horizontal shape IDB shifts to  $\text{Al}_{0.13}\text{Ga}_{0.87}\text{N/sapphire}$  substrate interface by increasing the  $\text{Cp}_2\text{Mg}$  flow rates.

It has been observed that the shape of pyramidal defects having inclined  $\{11\bar{2}3\}$  facets is very dependent on the polarity of film in Mg-doped GaN layers, that is, the tip of the pyramids always points toward the  $[000\bar{1}]$  direction [7]. For Ga-polarity matrix, therefore, pyramidal defects show the N-polarity and the inverted pyramidal shape. We call them “pyramidal shape IDBs”. It is commonly accepted that Ga-polarity GaN films are usually obtained by MOCVD growth [8], which agrees well with our results. Figure 3 is the magnified TEM image of a sample with the  $\text{Cp}_2\text{Mg}$  flow rate of  $1.031 \mu\text{mol/min}$ . Pyramidal shape IDBs have an inverted shape in the HRTEM images shown above [Figure 3(b)] and below [Figure 3(c)] the horizontal shape IDB, indicating that the change of polarity from Ga-polarity to N-polarity in the high Mg-doped AlGaN layers induces the reverse shape of pyramidal shape IDBs within the same film.

The growth of III-Nitride films under Ga-polarity has resulted in improved structural, electrical, and optical properties with smoother surface morphologies when compared to N-polarity growth [6]. Therefore, the control of polarity during the growth of Mg-doped AlGaN layers is very important in the case of high concentration Mg doping.

## CONCLUSIONS

The vertical, horizontal, pyramidal shape IDBs are observed depending on Mg source flow rate. While the vertical shape IDBs were observed in the  $\text{Al}_{0.13}\text{Ga}_{0.87}\text{N}$  layers grown with the low Mg source flow rate, the IDBs in the  $\text{Al}_{0.13}\text{Ga}_{0.87}\text{N}$  layers grown with the high Mg source flow rate have horizontal shape. The change of polarity by the IDBs of horizontal shape also resulted in the  $180^\circ$  rotation of pyramidal defects within the same AlGaIn layer.

## ACKNOWLEDGMENTS

This work was supported by a grant No. R01-2002-000-00096-0 from Korea Science & Engineering Foundation and University Research Program from Ministry of Information & Communication in the republic of Korea.

## REFERENCES

1. T. Takeuchi, T. Detchprohm, M. Iwaya, N. Hayashi, K. Isomura, K. Kimura, M. Yamaguchi, H. Amano, I. Akasaki, Y. Kaneko, R. Shioda, S. Watanabe, T. Hidaka, Y. Yamaoka, and Y. Kaneko, *Appl. Phys. Lett.* **75**, 2960 (1999).
2. Z. Liliental-Weber, H. Sohn, N. Newman, and J. Washburn, *J. Vac. Sci. Technol.* **B13**, 1578 (1995).
3. B. Pécz, Zs. Makkai, M. A. di Forte-Poisson, F. Huet, and R. E. Dunin-Borkowski, *Appl. Phys. Lett.* **78**, 1529 (2001).
4. L. T. Romano, J. E. Northrup, A. J. Ptak, and T. H. Myers, *Appl. Phys. Lett.* **77**, 2479 (2000).
5. V. Ramachandran, R. M. Feenstra, W. L. Sarney, L. Salamanca-Riba, J. E. Northrup, L. T. Romano, and D. W. Greve, *Appl. Phys. Lett.* **75**, 808 (1999).
6. X. Q. Shen, T. Ide, M. Shimizu, and H. Okumura, *J. Appl. Phys.* **89**, 5731 (2001).
7. P. Vennéguès, M. Benaissa, B. Beaumont, E. Feltin, P. De Mierry, S. Dalmaso, M. Leroux, and P. Gibart, *Appl. Phys. Lett.* **77**, 880 (2000).
8. E. S. Hellman, *MRS Internet J. Nitride Semicond. Res.* **3**, 11 (1998).

---

## **Contacts, Processing and p-Type Nitrides**

### Contacts to High Aluminum Fraction *p*-type Aluminum Gallium Nitride

Brett A. Hull<sup>1</sup>, Suzanne E. Mohny<sup>1</sup>, Uttiya Chowdhury<sup>2</sup>, Russell D. Dupuis<sup>2</sup>, David Gotthold<sup>3</sup>, Ronald Birkhahn<sup>3</sup>, and Milan Pophristic<sup>3</sup>

<sup>1</sup>Department of Materials Science and Engineering, The Pennsylvania State University, University Park, PA 16802

<sup>2</sup>Department of Electrical and Computer Engineering, The University of Texas at Austin, Austin, Texas 78712

<sup>3</sup>Emcore Corporation, Somerset, NJ 08873

#### ABSTRACT

Gold, palladium, platinum or nickel ohmic contacts on Mg doped *p*-type  $\text{Al}_x\text{Ga}_{1-x}\text{N}$  with  $x = 0.4$  and  $x = 0.45$  have been examined. The Au contact provided the lowest contact resistivity with  $\rho_c = 1.8 (\pm 1.1) \times 10^{-3} \Omega\text{cm}^2$ , but only following annealing at 850°C. For the Pd, Au, and Pt contacts annealed at greater than 700°C, a rapid degradation in the current-voltage curves was observed upon testing. The degradation was induced by exposure to sub-bandgap light and was reversed with a mild anneal at 500°C. Possible mechanisms for the degradation are discussed.

#### INTRODUCTION

Efficient optoelectronic devices based on GaN and its related III-nitride alloys (InGaN and AlGaN) that emit from the green to the near ultraviolet (UV) have been successfully developed [1]. Interest is growing to extend the range of light emission of these devices deeper into the UV by incorporating more Al-rich  $\text{Al}_x\text{Ga}_{1-x}\text{N}$  compositions. Historically, one limitation of GaN-based light emitters has been the ohmic contact to the *p*-GaN terminal for hole injection [2]. The most common approach thus far for AlGaN-based UV devices has been to employ a thin capping layer of the lower bandgap *p*-GaN on the *p*-AlGaN active layer to facilitate the formation of an ohmic contact. However, little work has been reported on contacts made directly to *p*-type AlGaN.

There have been no reports of ohmic contacts to *p*- $\text{Al}_x\text{Ga}_{1-x}\text{N}$  near the compositions studied in this investigation ( $x = 0.4$  and  $0.45$ ). There have been reports of ohmic contacts to much lower Al fractions of  $x = 0.06$  [3] and  $x = 0.15$  [4] or contacts to *p*-GaN/ $\text{Al}_x\text{Ga}_{1-x}\text{N}$  superlattices with  $x = 0.1$  or  $0.2$  [5,6]. In this investigation, we examine the electrical properties of Au, Pd, Pt, and Ni single layer contacts to high Al fraction Mg doped *p*-type  $\text{Al}_x\text{Ga}_{1-x}\text{N}$  ( $x = 0.4$  and  $0.45$ ). We have employed single layer contacts rather than the more typical bi- or tri-layer contacts for two reasons: a) there have been no previous investigations of contacts to this  $\text{Al}_x\text{Ga}_{1-x}\text{N}$  composition for comparison, and b) the severe annealing conditions required ( $T > 800^\circ\text{C}$ ) would complicate interfacial reaction analysis due to significant interdiffusion between the metals of multilayer contacts.

#### EXPERIMENTAL PROCEDURE

Two separate epitaxial layers of Mg doped  $\text{Al}_x\text{Ga}_{1-x}\text{N}$  with  $x = 0.4$  and  $x = 0.45$  were grown by metalorganic chemical vapor deposition on sapphire substrates. The layer thicknesses were 170 nm and 125 nm for the *p*- $\text{Al}_{0.4}\text{Ga}_{0.6}\text{N}$  and the *p*- $\text{Al}_{0.45}\text{Ga}_{0.55}\text{N}$ , respectively. The same

growth process employed for growing the  $p\text{-Al}_{0.45}\text{Ga}_{0.55}\text{N}$  epitaxial layer in this investigation was also employed for growing the  $p$ -type layer in a  $p\text{-i-n}$  structure. After activation, capacitance-voltage (C-V) measurements on a series of  $p\text{-i-n}$  mesas of varying area were employed to confirm  $p$ -type conductivity. The capacitance per unit area of each mesa remained constant regardless of the metallization area, indicating that the measured capacitance was that of a  $p\text{-n}$  junction, which confirmed the  $p$ -type conductivity of the Mg-doped  $\text{Al}_{0.45}\text{Ga}_{0.55}\text{N}$ . Further details are provided in ref. 7. No such experiments were performed on the  $p\text{-Al}_{0.4}\text{Ga}_{0.6}\text{N}$  layer, but the behavior of the contacts to this material was identical to that of the contacts to  $p\text{-Al}_{0.45}\text{Ga}_{0.55}\text{N}$ .

Circular transfer length method (CTLM) contact patterns were formed on each sample employing either lift-off (Pt contacts) or etch-back (Au, Ni, and Pd) processing. Etch-back processing was preferred due to metal adhesion problems encountered during lift-off processing. Prior to contact processing, each cleaved sample was activated for 10 min at 850°C in flowing  $\text{N}_2$ . The samples were then treated for 5 min each in ultrasonically agitated acetone and methanol, followed with a deionized (DI) water rinse. The Pt contact samples were then patterned with photolithography prior to final chemical surface treatment for 5 min in 10% HCl solution, with a final rinse in DI water. The Au, Ni, and Pd contact samples were treated in the HCl solution directly following organic solvent treatment. The samples were then loaded into a deposition chamber that was evacuated to a base pressure of approximately  $2 \times 10^{-7}$  Torr for subsequent metal deposition via electron beam evaporation of either 25 nm of Pt or 100 nm of Au, Ni, or Pd. Following deposition, the contact patterns were completed either by lift-off processing in acetone (Pt contacts) or by patterning the metal film (Au, Ni, and Pd contacts) by photolithography followed by a chemical etch in aqua regia solution (3 HCl:1  $\text{HNO}_3$ ). The CTLM pattern consisted of four sets of contacts with a series of six different contact gaps, ranging from 4 to 50  $\mu\text{m}$ .

Following sample preparation, current-voltage (I-V) and CTLM measurements were conducted utilizing a four probe current sweep on all samples in both the as-deposited condition and following each annealing step. Cumulative anneals were conducted in flowing  $\text{N}_2$  for 2 min at each temperature, beginning at 300°C and continuing to 900°C, in a rapid thermal annealing (RTA) furnace. The contact resistivity ( $\rho_c$ ) was extracted from the CTLM measurements, generally based on the voltage at a current of 10  $\mu\text{A}$ . Following annealing at temperatures greater than 700°C for Au, Pd, and Pt contact samples, CTLM measurements were based solely on the 4  $\mu\text{m}$  and 50  $\mu\text{m}$  gap contacts, as explained in the Results section. All I-V measurements were conducted under sub-bandgap white tungsten halogen illumination with a minimum wavelength  $\lambda_{\text{min}} \approx 325$  nm ( $E_{\text{max}} \approx 3.8$  eV).

## RESULTS AND DISCUSSION

Following annealing at temperatures greater than 700°C, the resistance of the Au, Pd, and Pt contacts increased rapidly after I-V probing commenced. Figure 1 shows a sequence of I-V curves for Pd contacts to  $p\text{-Al}_{0.45}\text{Ga}_{0.55}\text{N}$  that were measured following an 800°C anneal over a time frame from zero to 120 min after annealing. The resistance of each I-V curve was calculated from Ohm's law,  $R = V/I$ , employing the voltage measured across a pair of contacts at a current of 10  $\mu\text{A}$ , and is hereafter referred to as total resistance. This total resistance includes the resistance of a pair of contacts as well as the resistance due to the epitaxial layer between them. The inset of Fig. 1 shows the sequence of I-V curves plotted as total resistance vs. time,

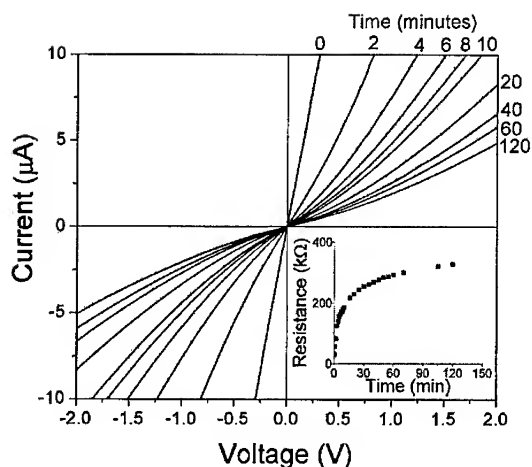


**Figure 1.** Time sequence of I-V curves for Pd contacts to  $p\text{-Al}_{0.45}\text{Ga}_{0.55}\text{N}$  with a  $4\text{ }\mu\text{m}$  gap following an  $800^\circ\text{C}$  anneal. Zero minutes represents first probing after annealing. Inset shows plot of total resistance vs. time.

which can be approximated by a simple exponential growth model with a time constant on the order of a few minutes. The non-degraded I-V curves obtained immediately following the initial high temperature anneal were recovered following a moderate anneal of  $500^\circ\text{C}$  – well below the  $800^\circ\text{C}$  annealing temperature initially employed to achieve the low resistance. Following a reversal anneal, however, the degradation sequence repeated itself with approximately the same magnitude and rate.

CTLM measurements of the Au, Pt, and Pd samples after degradation indicated that both  $\rho_c$  of the contacts as well as the sheet resistance ( $\rho_s$ ) of the  $p\text{-AlGaIn}$  epitaxial layer itself suffered this considerable degradation. In fact, linear four point probe measurements conducted directly on the AlGaIn epitaxial layers showed a  $\rho_s$  increase of nearly two orders of magnitude over 90 minutes following an anneal at  $850^\circ\text{C}$ . Degradation was observed on both of the  $\text{Al}_x\text{Ga}_{1-x}\text{N}$  epitaxial layers utilized in this study ( $x = 0.4$  and  $x = 0.45$ ), which were grown in separate reactors by two separate investigators in this research.

A plot of  $\rho_c$  vs. the annealing temperature for all contacts to  $p\text{-Al}_{0.45}\text{Ga}_{0.55}\text{N}$  is shown in Fig. 2, which also shows  $\rho_c$  of the degraded Au, Pd, and Pt contacts that were annealed at greater than  $700^\circ\text{C}$ . In the as-deposited condition, moderate  $\rho_c$  was obtained and ranged from  $4.8 (\pm 0.5)\text{ }\Omega\text{cm}^2$  for the Pt contacts to  $54 (\pm 6)\text{ }\Omega\text{cm}^2$  for the Ni contacts. No significant changes were observed with annealing up to about  $400^\circ\text{C}$ . With further annealing at temperatures from  $400$  or  $500^\circ\text{C}$  to  $650$  or  $700^\circ\text{C}$ , the Au, Ni, and Pd contacts became highly resistive and rectifying with currents on the order of  $10\text{ nA}$  at voltages from  $1$  to  $20\text{ V}$ . It was impossible to extract  $\rho_c$  from such samples, so a value in excess of  $1000\text{ }\Omega\text{cm}^2$  is plotted in Fig. 2. With further annealing in excess of  $700^\circ\text{C}$ ,  $\rho_c$  recovered for all samples to at least that of the as-deposited contacts. For Au, Pd, and Pt contacts, however, with annealing up to  $850^\circ\text{C}$ ,  $\rho_c$  dropped significantly, reaching a minimum of  $1.8 (\pm 1.1) \times 10^{-3}\text{ }\Omega\text{cm}^2$  for Au contacts annealed at  $850^\circ\text{C}$ .

The open symbols in Fig. 2 show  $\rho_c$  of the Au, Pd, and Pt contacts following degradation. All contacts degraded to within a range of  $8$  to  $30\text{ }\Omega\text{cm}^2$ , regardless of the  $\rho_c$  of each of these contacts prior to degradation. Furthermore, the Ni contacts never exhibited  $\rho_c$  lower than this

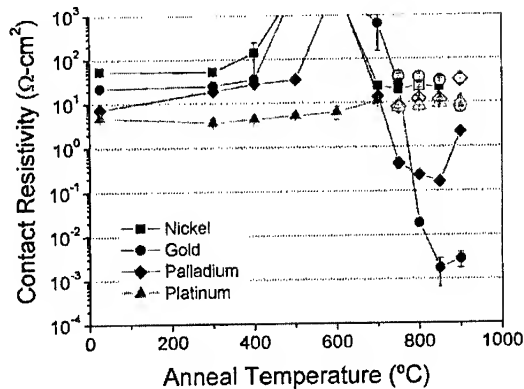
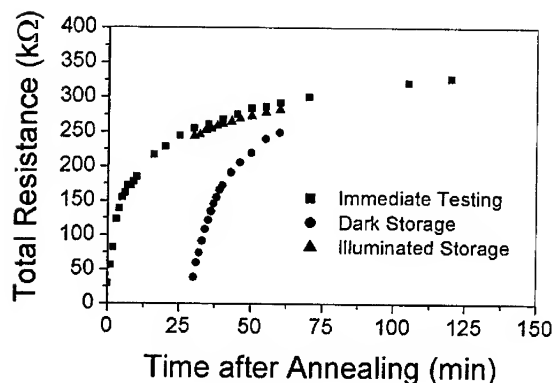


Figure 2. Contact resistivity as a function of cumulative anneal temperature for nickel, gold, palladium, and platinum contacts to  $p\text{-Al}_{0.45}\text{Ga}_{0.55}\text{N}$ , showing the contacts before (closed symbols) and after (open symbols) degradation.

range, even prior to aging, and consequently never showed any measurable degradation. The rapid degradation observed for the Au, Pd, and Pt contacts annealed at greater than 700°C precludes the use of all four sets of six contacts during CTLM measurements. Therefore, the  $p_c$  values shown in Fig. 2 for these contacts prior to degradation were based solely on a single 4  $\mu\text{m}$  and 50  $\mu\text{m}$  contact. At the higher annealing temperatures, the 25 nm thick Pt contacts showed a very large disparity in uniformity across the sample and could not be accurately measured prior to degradation.

A series of experiments were performed to determine the cause of the increase in resistance. A sample consisting of Pd contacts on  $p\text{-Al}_{0.45}\text{Ga}_{0.55}\text{N}$  that had been annealed at 800°C was employed, and the degradation of a pair of contacts with a 4  $\mu\text{m}$  gap was investigated. Following each period of degradation, the sample was annealed at 500°C to revert the sample to its minimum resistance. The I-V curves of the contact were measured (under tungsten halogen illumination) either immediately following the reversal anneal, after storage in the dark for 30 min following annealing, or after being held under tungsten halogen illumination for 30 min following annealing and prior to testing. These three test sequences, plotted as total resistance vs. time after annealing, are shown in Fig. 3, from which we can conclude that the increase in resistance was induced by the exposure to sub-bandgap illumination ( $E_g \approx 4.4$  eV). The illuminated storage sequence indicated that degradation was not caused by biasing the sample. Red filtration of the illumination was also employed, with no measurable changes to the degradation sequence. Thus the degradation appears to be induced by photons of less than approximately 1.9 eV (the maximum energy of transmission of the red filter employed). In order to eliminate environmental effects as the cause of degradation, dark storage was employed in either flowing  $\text{N}_2$  or open to laboratory air. No measurable differences between the dark  $\text{N}_2$  storage and dark air storage were observed, so environmental effects appear to be insignificant.

The optically induced degradation of the  $p\text{-AlGaIn}$  with sub-bandgap illumination, along with the thermal excitation that reverses the degradation, suggests that one or more optically excited metastable deep levels are responsible. Optically excited deep levels located within the bandgap have been attributed to a variety of phenomena in  $\text{Al}_x\text{Ga}_{1-x}\text{N}$  alloys. Persistent photoconductivity (PPC) in both  $n$ - and  $p\text{-GaIn}$  in particular has received a great deal of attention [8,9]. The degradation that we observe resembles an *inverse* PPC, whereby the  $p\text{-AlGaIn}$



**Figure 3.** Total resistance vs. time for Pd contacts to  $p\text{-Al}_{0.45}\text{Ga}_{0.55}\text{N}$  with a 4  $\mu\text{m}$  gap. Contact initially annealed at 800°C, with 500°C reversal anneal between each degradation sequence.

conductivity decreases with optical exposure and is reversed with thermal processing. The degraded state in this experiment seems to persist indefinitely at room temperature, however, even with the removal of illumination.

The DX center, well described for AlGaAs alloys [10], is one type of deep level that may account for the observed degradation. In GaN, oxygen that has been unintentionally incorporated into the lattice acts as a shallow donor [11], but is theorized to undergo a transition to a deep DX-like state in  $\text{Al}_x\text{Ga}_{1-x}\text{N}$  for compositions with  $x$  greater than 0.2 [12] to 0.4 [13]. The DX center is photoexcited to a shallow donor state and reverts to its deep level with the application of thermal energy, and it has been suggested that oxygen DX centers are responsible for PPC in  $n\text{-Al}_{0.39}\text{Ga}_{0.61}\text{N}$  at temperatures below 150K [14]. If present in  $p\text{-type Al}_x\text{Ga}_{1-x}\text{N}$ , an excited DX center would compensate Mg acceptors, thus decreasing the carrier concentration and conductivity. However, we have been unable to distinguish between surface and bulk conduction thus far in this investigation. The charging of surface states has recently been shown to result in drain current collapse within AlGaN/GaN HFETs, which is induced by deep biasing and is reversed with mild thermal anneals and optical excitation [15,16]. A related surface conduction phenomenon might account for the observed degradation in the present investigation. Another possible mechanism for degradation arises from residual H within activated Mg-doped  $\text{Al}_x\text{Ga}_{1-x}\text{N}$ . The role of H in Mg-doped GaN and the thermal dissociation of Mg:H complexes to activate  $p\text{-GaN}$  have been well documented [17,18], and residual H within the lattice might repassivate Mg acceptors during optical excitation, with reactivation following moderate annealing. None of the experiments performed in this investigation, however, can confirm nor refute the proposed mechanisms for the observed degradation. Further experimentation, including an examination of passivated samples, is warranted.

## SUMMARY

Single layer Pd, Au, Ni and Pt ohmic contacts to Mg doped  $p\text{-type Al}_x\text{Ga}_{1-x}\text{N}$  with  $x = 0.4$  or  $0.45$  have been examined. Thermal annealing in excess of 700°C was required to achieve a significant improvement in contact resistivity from the as-deposited condition. The Au contact annealed at 850°C showed the lowest contact resistivity of  $1.8 (\pm 1.1) \times 10^{-3} \Omega\text{cm}^2$ . For the Au, Pt, and Pd contacts that were annealed in excess of 700°C, a rapid increase in the contact

resistivity and the semiconductor sheet resistance was observed during current-voltage measurements. This resistance increase was initiated by exposure to sub-bandgap white light and was reversed with a moderate thermal anneal of 500°C. The exact degradation mechanism was not resolved, but might be attributed either to repassivation by residual hydrogen or to optically excited metastable deep levels either within the bulk or at the surface of the epitaxial layer.

## REFERENCES

1. S. Nakamura, S. Pearton, and G. Fasol, *The Blue Laser Diode: The Complete Story – 2<sup>nd</sup> Edition*, Springer, Berlin (2000).
2. H. Kim, H. Yang, C. Huh, S.-W. Kim, S.-J. Park, and H. Hwang, *Electron. Lett.*, **36**, 908 (2000).
3. T.V. Blank, Y.A. Goldberg, E.V. Kalinina, O.V. Konstantinov, A.E. Nikolaev, A.V. Fomin, and A.E. Cherenkov, *Semiconductors*, **35**, 529 (2001).
4. B.-H. Jun, H. Hirayama, and Y. Aoyagi, *Jpn. J. Appl. Phys.*, **41**, 581 (2002).
5. A.P. Zhang, B. Luo, J.W. Johnson, F. Ren, J. Han, and S.J. Pearton, *Appl. Phys. Lett.*, **79**, 3636 (2001).
6. L. Zhou, A.T. Ping, F. Khan, A. Osinski, I. Adesida, *Electron. Lett.*, **36**, 91 (2000).
7. T. Li, D.J.H. Lambert, M.M. Wong, C.J. Collins, B. Yang, A.L. Beck, U. Chowdhury, R.D. Dupuis and J.C. Campbell, *IEEE J. Quant. Electron.*, **37**, 538 (2001).
8. C. Johnson, J.Y. Lin, H.X. Jiang, M. Asif Khan, and C.J. Sun, *Appl. Phys. Lett.*, **68**, 1808 (1996).
9. M.T. Hirsch, J.A. Wolk, W. Walukiewicz, and E.E. Haller, *Appl. Phys. Lett.*, **71**, 1098 (1997).
10. D.J. Chadi and K.J. Chang, *Phys. Rev. B*, **39**, 10063 (1989).
11. J. Neugebauer and C.G. Van de Walle, *Proc. 22<sup>nd</sup> Intl. Conf. Phys. Semicond.*, ed. D.J. Lockwood, World Scientific, Singapore, 2327 (1997).
12. C.H. Park and D.J. Chadi, *Phys. Rev. B*, **55**, 12995 (1997).
13. C.G. Van de Walle, *Phys. Rev. B*, **57**, R2033 (1998).
14. M.D. McCluskey, N.M. Johnson, C.G. Van de Walle, D.P. Bour, and M. Kneissl, *Phys. Rev. Lett.*, **80**, 4008 (1998).
15. R. Vetury, N.Q. Zhang, S. Keller, and U.K. Mishra, *IEEE Trans. Electron Dev.*, **48**, 560 (2001).
16. S.C. Binari, P.B. Klein, and T.E. Kazior, *Proc. IEEE*, **90**, 1048 (2002).
17. J. Neugebauer and C.G. Van de Walle, *Phys. Rev. Lett.*, **75**, 4452 (1995).
18. S. Nakamura, N. Iwasa, M. Senoh, and T. Mukai, *Jpn. J. Appl. Phys.*, **31**, 1258 (1992).

### Structural Defects in Mg-doped GaN and AlGaIn grown by MOCVD

S. Tomiya<sup>1</sup>, S. Goto<sup>2</sup>, M. Takeya<sup>2</sup> and M. Ikeda<sup>2</sup>

<sup>1</sup> Material Analysis Dept. Technical Solution Center, Sony Corporation

<sup>2</sup> Development Center, Sony Shiroishi Semiconductor, Inc.

#### ABSTRACT

We have investigated the structural defects formed in Mg-doped GaN and AlGaIn epitaxial layers grown by metal organic chemical vapor deposition. These defects have an inverse pyramidal shape and appear when the Mg concentration [Mg] is higher than  $\sim 4 \times 10^{19}/\text{cm}^3$ . The density of the defects increases as [Mg] increases, but the size of the defects becomes smaller as [Mg] increases. The density of the defects also has a strong correlation with the hydrogen concentration in the epitaxial layers. Transmission electron microscope analysis reveals that the defects have an inversion operation to the matrix and that their boundaries are Mg-rich. We also propose a model for defect formation.

#### INTRODUCTION

Minimizing the power consumption of GaN-based laser diodes (LDs) is of critical importance for extending the device lifetime [1]. One of the key issues is the optimization of the Mg doping conditions for GaN and AlGaIn layers in order to lower the resistivity. During the course of our study of LDs, inverse pyramidal-shaped defects (which are hereafter referred to simply as "pyramidal defects") were often found in Mg-doped layers by transmission electron microscope (TEM) observations. The pyramidal defects may increase the resistivity of the *p*-type layers; therefore, these should be eliminated. Such defects have recently been reported by several researchers [2-4], but the formation mechanism of the pyramidal defects is not fully understood. In this paper, we report on the relationship between the pyramidal defects and the atomic concentration of Mg [Mg]. We also briefly discuss the formation of the defects.

#### EXPERIMENTAL DETAILS

The samples investigated here were grown on (0001) c-face sapphire substrates using metalorganic chemical vapor deposition (MOCVD). Trimethylgallium (TMG), trimethylaluminum (TMA), bis-methylcyclopentadienyl-magnesium  $[(\text{MeCp})_2\text{Mg}]$  and ammonia were chosen as the Ga, Al, Mg, and N precursors, respectively. In order to study the effects of Mg doping on the defect structure, Mg step-doped structures were grown, as shown in Fig.1. The growth temperature was  $\sim 1000^\circ\text{C}$ . Growth was carried out under an  $\text{H}_2$ -ambient. TEM was performed on films that were mechanically polished and ion milled to electron transparency. The microstructure was observed using an accelerating voltage of 200kV and was analyzed by conventional diffraction contrast, multiple (0002) dark field imaging and high resolution lattice imaging. The defects were also analyzed by high-angle annular dark field (HAADF) scanning transmission electron microscopy (STEM) operating at 200kV. The Mg and H concentrations were measured by secondary ion mass spectrometry (SIMS).  $\text{O}_2^+$  and  $\text{Cs}^+$ -ion beams were used as the primary ion sources to detect Mg and H ions, respectively. Ion-implanted standard samples were also measured at the same time to obtain a quantitative measure of the impurity concentration. We note that the samples were not annealed prior to TEM and SIMS studies.

Sample 1	Sample 2	Sample 3
undoped GaN	undoped GaN	undoped GaN
GaN:Mg $1 \times 10^{19}/\text{cm}^3$	GaN:Mg $1 \times 10^{21}/\text{cm}^3$	$\text{Al}_{0.05}\text{GaN:Mg}$ $1 \times 10^{19}/\text{cm}^3$
undoped GaN	GaN:Mg $5 \times 10^{20}/\text{cm}^3$	undoped GaN
GaN:Mg $1 \times 10^{20}/\text{cm}^3$	GaN:Mg $1 \times 10^{20}/\text{cm}^3$	$\text{Al}_{0.05}\text{GaN:Mg}$ $1 \times 10^{20}/\text{cm}^3$
GaN:Mg $5 \times 10^{19}/\text{cm}^3$	GaN:Mg $5 \times 10^{19}/\text{cm}^3$	$\text{Al}_{0.05}\text{GaN:Mg}$ $5 \times 10^{19}/\text{cm}^3$
GaN:Mg $1 \times 10^{19}/\text{cm}^3$		$\text{Al}_{0.05}\text{GaN:Mg}$ $1 \times 10^{19}/\text{cm}^3$
GaN:Mg $5 \times 10^{18}/\text{cm}^3$		$\text{Al}_{0.05}\text{GaN:Mg}$ $5 \times 10^{18}/\text{cm}^3$
		$\text{Al}_{0.1}\text{GaN:Mg}$ $5 \times 10^{18}/\text{cm}^3$
undoped GaN	undoped GaN	undoped GaN

**Figure 1.** Schematic illustration of Mg step-doped samples. The figures for Mg concentration [Mg] indicated in each layer are the designed values.

## RESULTS AND DISCUSSION

Figure 2 shows a cross-sectional bright field TEM image together with a SIMS depth profile of Mg for sample 1. Besides threading dislocations, dark bands can be observed in the center of the image. The dark dotted bands consist of many pyramidal defects, although each pyramidal defect is not well resolved in this image because of the low magnification. The dark dotted bands are observed only in layers 4 and 5 of sample 1. This indicates that the pyramidal defects form when [Mg] is higher than  $\sim 4 \times 10^{19}/\text{cm}^3$ .

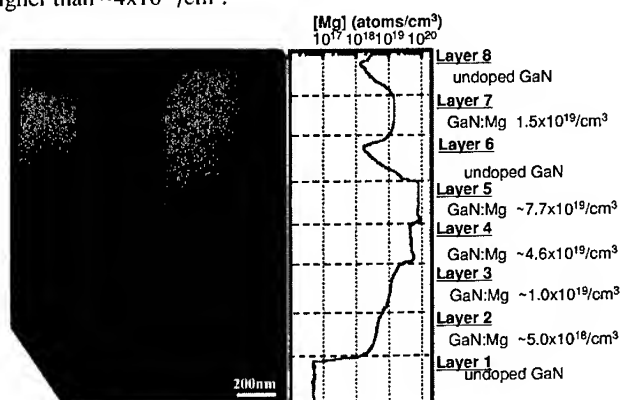


**Figure 2.** Cross sectional TEM image, together with SIMS depth profile of Mg for sample 1.

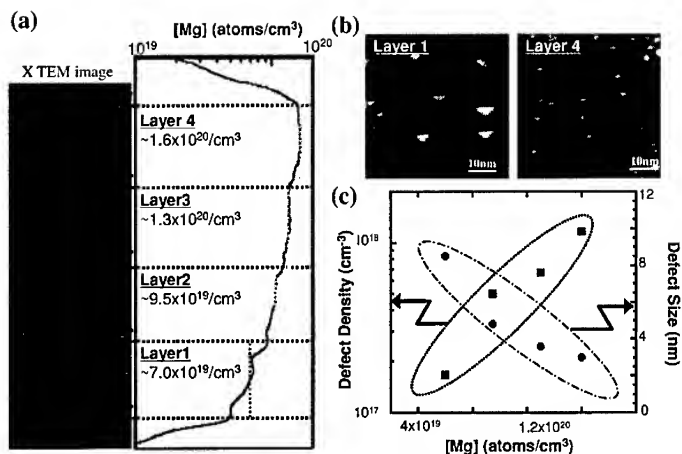


**Figure 3.** (a) Cross sectional TEM image and SIMS depth profile of Mg for sample 2. (b) Magnified weak beam (0002) dark field images of layer 1 and layer 4. (c) The dependence of defect size and defect density on Mg concentration.

Sample 2 was doped with a higher concentration of Mg than sample 1. Figure 3(a) shows a cross-sectional weak beam (0002) dark field TEM image and a SIMS depth profile of Mg for sample 2. Fig.3 (b) shows magnified images of the 1st and 4th Mg doped layers. Projecting triangular shapes are clearly visible, and the tips of the defects are pointing toward the substrate. The size and density dependence on [Mg] is shown in Fig. 3(c). The density of the pyramidal defects increased as [Mg] increased, but their size decreased as [Mg] increased.

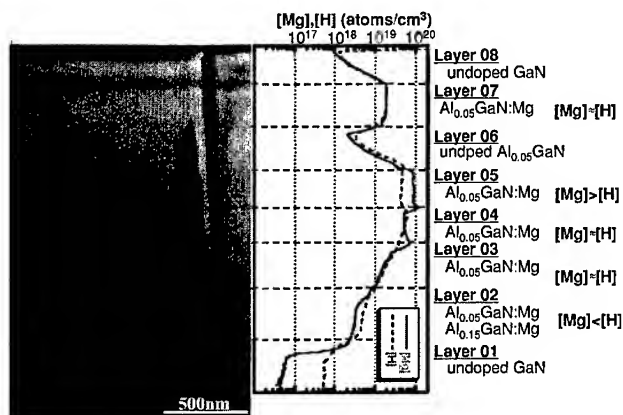


**Figure 4.** Cross sectional TEM image, together with SIMS depth profile of Mg for sample 3.

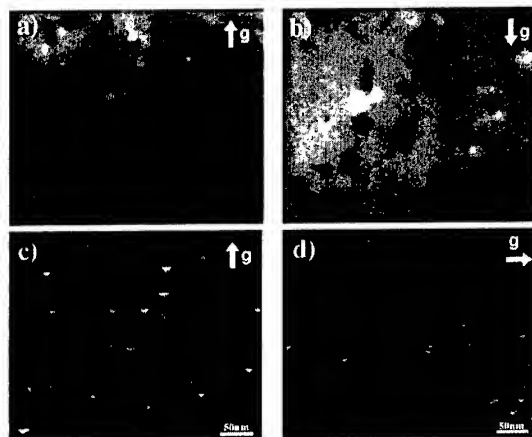


**Figure 5.** Dark field images of the pyramidal defects. (a) and (b) are the multiple (0002) dark field image and the multiple (0002̄) dark field image, respectively. (c) and (d) are the weak beam (0002) dark field image and the weak beam (0002̄) dark field image.

Figure 4 shows a cross-sectional bright field TEM image and a SIMS depth profile of Mg and H for sample 3. The dark bands were also observed only in layers 4 and 5 of sample 3. This situation is similar to that of sample 1. We have also measured the concentration of hydrogen in the layers, [H]. In undoped GaN layers (layer 1), the residual [H] is about  $5 \times 10^{17}/\text{cm}^3$ . [H] increases with increasing [Mg], but becomes saturated at  $\sim 5 \times 10^{19}/\text{cm}^3$  while [Mg] can attain over  $5 \times 10^{19}/\text{cm}^3$ . Comparing the TEM image to the SIMS depth profile, [Mg] tends to be higher than [H] in the defect formation layer. This result suggests that defect formation requires a higher [Mg] compared to [H].

Figure 5 shows various kinds of dark field images of the pyramidal defects. The defects appear brighter than the matrix in the multiple (0002) dark field image and appear darker than the matrix in the multiple (0002̄) dark field image, as shown in Fig. 5(a) and (b), respectively. These contrast changes indicate that there is an inversion operation relationship between the pyramidal defects and the matrix ([3], [5]). In the weak beam (0002) dark field image (Fig. 5(c)), projecting triangular shapes are clearly visible and the pyramidal defects appear bright, which may be due to a small lattice translation between the pyramidal defects and the matrix. This is supported by the results of high resolution TEM observation (not shown here), which show that the lattice planes shift  $\sim c/8$  between the inside of the defects and the outside. Figure 5(d) shows the weak beam (1120) dark field image. Two sides of the projecting triangular shapes are brighter. Since weak beam imaging is sensitive to lattice displacement, the lattice planes at the boundaries are thought to be slightly changed. We therefore speculate that the boundaries of the pyramidal defects are Mg-rich. To confirm this, HAADF-STEM observation of the pyramidal defects in the GaN epitaxial layer were performed as shown in Figure 6, since the intensity of the HAADF-STEM image depends on the atomic number. The defects themselves are darker than the matrix and, moreover, the boundaries are much darker than the inside of the defects. Since Mg is lighter than Ga, the boundaries are thought to be more Mg-rich than the inside of the defects and that part of the boundaries may consist of  $\text{Mg}_3\text{N}_2$ .

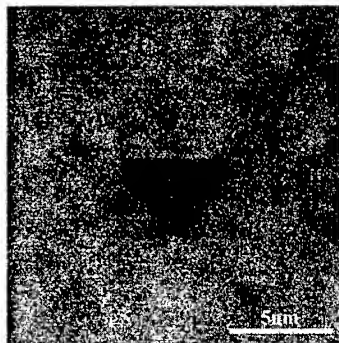


**Figure 6.** HAADF-STEM image of the pyramidal defects.

We now briefly discuss defect formation to explain the size dependence of the pyramidal defects on [Mg]. We adopt the following hypotheses; 1) Surface segregation of Mg occurs during growth, and 2) Hydrogen enhances Mg incorporation in GaN. These two phenomena were reported by Ptak *et al.* for the case of rf-plasma assisted MBE [6] and the latter phenomenon was predicted theoretically [7]. We accept these as being valid for MOCVD growth. As the amount of Mg precursor injected into the reactor increases in order to dope more heavily with Mg, Mg atoms start to segregate at the growth surface. When the concentration of hydrogen at the surface is sufficient, Mg will incorporate uniformly into the layer. However, when the concentration of hydrogen is insufficient, magnesium nitride clusters may be created at the growth surface. High exposure to Mg forms a faceted surface and the subsequent layer is of inverted polarity [8]. Similar phenomena occurred in this case. Growth is suppressed at the point of the magnesium nitride clusters and consequently small pits are formed, just like forming a faceted surface. The polarity is also changed inside the pits. Since the growth rate of an N-polar surface is significantly slower than that of a Ga-polar surface in MOCVD growth, the pits are soon buried by lateral growth from the surrounding Ga-polar matrix. The formation of the pyramidal defects is then terminated. It has been reported that a higher concentration of Mg in the vapor phase enhances the ratio of the lateral growth rate to the vertical growth rate [9]. When [Mg] increases, the defects are consequently buried faster due to an enhancement of the lateral growth rate. This leads that the size of the pyramidal defects becoming smaller.

## SUMMARY

Pyramidal defects formed in Mg-doped GaN and AlGaIn epitaxial layers grown by MOCVD have been studied. TEM and HAADF-STEM studies reveal that the pyramidal defects have an inverse operation to the matrix and that their boundaries are Mg-rich. These defects form when [Mg] is higher than  $\sim 4 \times 10^{19}/\text{cm}^3$ . The density of the pyramidal defects increased as [Mg] increased, but their size decreased as [Mg] increased. The density of the defects is also related to [H], and our results suggest that defect formation requires a higher [Mg] compared to [H]. The inverse proportionality of the defect size to [Mg] can be explained by the enhancement of lateral growth under high Mg concentration in the growth atmosphere.

## ACKNOWLEDGEMENTS

The authors acknowledge Y. Matsusaka and S. Murakami for TEM sample preparation and S. Miwa and R. Imoto for the SIMS measurements used in this work. The authors would also like to acknowledge Dr. Itabashi and Mr. Ooki for their encouragement during the course of this work.

## REFERENCES

1. T. Tojyo, T. Asano, M. Takeya, T. Hino, S. Kijima, S. Goto, S. Uchida and M. Ikeda, *Jpn. J. Appl. Phys.* **40**, 3206 (2001).
2. Z. Liliental-Weber, M. Benamara, J. Washburn, I. Grzegory, S. Porowski, D. J. H. Lambert, C. J. Eiting, and R. D. Dupuis, *Appl. Phys. Lett.*, **75**, 4159 (1999).
3. P. Vennéguès, M. Benaissa, B. Beaumont, E. Feltin, P. De Miery, S. Dalmaso, M. Leroux, and P. Gilbert, *Appl. Phys. Lett.*, **77**, 880 (2000).
4. M. Hansen, L.F. Chen, S.H.Lim, S.P.DenBaars, and J.S.Speck. *Appl. Phys. Lett.*, **80**, 2469 (2002)
5. L. T. Romano, J. E. Northrup, and M. A. O'Keefe, *Appl. Phys. Lett.* **69**, 2394 (1996)
6. A. J. Ptak, T. H. Myers, L.T. Romano, C. G. Van de Walle, and J. E. Northrup, *Appl. Phys. Lett.*, **78**, 285 (2001).
7. J. Neugebauer and C.G.Van der Walle, *Phys. Rev. Lett.*, **75**, 4452 (1995).
8. L.T. Romano, J. E. Northrup, A. J. Ptak, and T. H. Myers, *Appl. Phys. Lett.*, **77**, 2479 (2000).
9. B. Beaumont, S. Haffouz, and P. Gilbert, *Appl. Phys. Lett.*, **72**, 921 (1998).

### The First Wafer-fused AlGaAs-GaAs-GaN Heterojunction Bipolar Transistor

Sarah Estrada,<sup>1</sup> Andreas Stonas, Andrew Huntington, Huili Xing, Larry Coldren, Steven DenBaars, Umesh Mishra, Evelyn Hu  
Departments of Materials and Electrical & Computer Engineering, University of California, Santa Barbara, California 93106-5050

#### ABSTRACT

We describe the use of wafer fusion to form a heterojunction bipolar transistor (HBT), with an AlGaAs-GaAs emitter-base fused to a GaN collector. In this way, we hope to make use of both the high breakdown voltage of the GaN and the high mobility of the technologically more mature GaAs-based materials. This paper reports the first dc device characteristics of a wafer-fused transistor, and demonstrates the potential of wafer fusion for forming electronically active, lattice-mismatched heterojunctions. Devices utilized a thick base (0.15 $\mu\text{m}$ ) and exhibited limited common-emitter current gain (0.2-0.5) at an output current density of  $\sim 100\text{A}/\text{cm}^2$ . Devices were operated to  $V_{\text{CE}}$  greater than 20V, with a low  $V_{\text{CE}}$  offset (1V). Improvements in both device structure and wafer fusion conditions should provide further improvements in HBT performance. The HBT was wafer-fused at 750°C for one hour. Current-voltage characteristics of wafer-fused p-GaAs/n-GaN diodes suggest that the fusion temperature could be reduced to 500°C. Such a reduction in process temperature should mitigate detrimental diffusion effects in future HBTs.

#### INTRODUCTION

The large breakdown field and anticipated saturation velocity of GaN make this novel material particularly promising for high-frequency, high-power devices. With this goal in mind, quite a few researchers are working to develop GaN-based heterojunction bipolar transistors (HBTs).<sup>1,2,3,4,5</sup> Although results have been promising, there are still a number of outstanding materials issues. For example, AlGaN/GaN HBTs appear to be limited by large acceptor ionization energies and low hole mobilities.<sup>6</sup>

An HBT structure utilizing AlGaAs-GaAs for the emitter-base, with GaN as the collector, could potentially combine the high-breakdown voltage of GaN with the high mobility of the technologically mature AlGaAs-GaAs heterostructure. Because the high degree of lattice mismatch between GaAs (lattice constant of 5.65Å) and GaN (3.19Å) precludes an all-epitaxial formation of this device, we have formed the GaAs-GaN heterostructure via the novel technique of wafer fusion, also called direct wafer bonding. The HBT demonstrates a modest current output and a current gain less than unity; however, the common-emitter I-V characteristic and Gummel plot are promising for the first wafer-fused HBT. Optimization of device structure and fusion conditions should improve electrical performance.

<sup>1</sup> [estrada@engineering.ucsb.edu](mailto:estrada@engineering.ucsb.edu), <http://sarah.optimism.us/engineering/>

(a)	(b)
~ 2 $\mu\text{m}$ nGaN ( $10^{18}$ Si)	1 $\mu\text{m}$ pGaAs ( $5 \times 10^{18}$ C)
(001) sapphire substrate	0.5 $\mu\text{m}$ AlAs etch-stop layer
	(100) n <sup>+</sup> GaAs substrate

Figure 1. Starting materials for the diode structures: (a) the n-GaN structure grown by MOCVD, and (b) the p-GaAs structure grown by MBE.

#### DEVICE STRUCTURE AND FABRICATION

Two device structures were studied, a wafer-fused p-GaAs/n-GaN diode and an AlGaAs/GaAs/GaN HBT. Diode starting materials are shown in Figure 1 and HBT starting materials are depicted in Figure 2. The AlGaAs-GaAs emitter-base was grown by molecular beam epitaxy (MBE) at 585°C in a Varian Gen-II system. Carbon, rather than beryllium, was chosen as the p-type dopant in order to minimize dopant diffusion during the high-temperature fusion procedure. The GaN collector (unintentionally doped and nominally n-type) was grown by metal-organic chemical vapor deposition (MOCVD) on c-plane (0001) sapphire at 1160°C.

Prior to fusion "escape channels" were etched into GaAs, to prevent liquid and gas from being trapped at the interface when GaAs and GaN were later brought together. The wafers were cleaved into rectangles (5-10mm) and cleaned with acetone and isopropanol. In order to minimize surface contamination, the wafers underwent two sequential oxidation steps (first by oxygen plasma, then by UV-ozone) and oxide removal steps (in  $\text{NH}_4\text{OH}$ ). GaN and GaAs were rinsed in methanol, joined together in methanol, and annealed ("wafer-fused") for 1 hour under a uniaxial pressure of 2 MPa in a nitrogen ambient. The HBT structure was fused at 750°C. The diode structures were fused over a wide range of systematically varied temperatures (500-750°C). Wafer-fused interfaces can be disordered on the scale of several monolayers (often with amorphous layers, probably oxides). By high resolution transmission electron microscopy

(a)	(b)
> 2 $\mu\text{m}$ und nGaN ( $\sim 5 \times 10^{16}$ Si)	150 nm pGaAs ( $10^{19}$ C)
(001) sapphire substrate	30nm graded nAlGaAs ( $5 \times 10^{17}$ Si)
	120 nm nAl <sub>0.3</sub> Ga <sub>0.7</sub> As ( $5 \times 10^{17}$ Si)
	30nm graded nAlGaAs ( $5 \times 10^{17}$ Si)
	100 nm nGaAs ( $10^{19}$ Si)
	0.5 $\mu\text{m}$ AlAs etch-stop layer
	(100) n <sup>+</sup> GaAs substrate

Figure 2. Starting materials for the HBT: (a) the n-GaN collector structure grown by MOCVD, and (b) the n-AlGaAs/p-GaAs emitter-base structure grown by MBE.

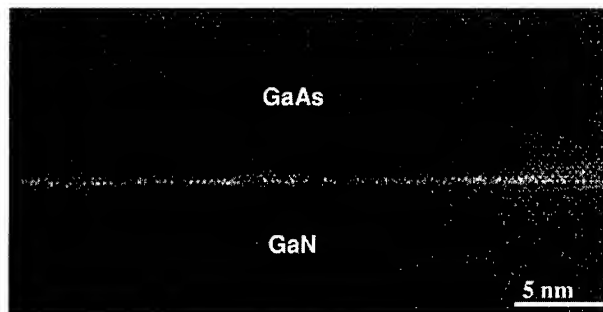


Figure 3. Cross-sectional image of the wafer-fused GaAs-GaN interface, obtained via high resolution transmission electron microscopy, in collaboration with J. Jasinski and Z. Liliental-Weber at Lawrence Berkeley National Laboratory in Berkeley, California.

(Figure 3), it was determined that our GaAs-GaN interface fused at 750°C for 0.25-1 hour exhibits disorder which is limited to 5-10Å.<sup>7</sup>

After fusion the GaAs substrate was removed via wet etching in H<sub>2</sub>O<sub>2</sub>:NH<sub>4</sub>OH. This selective etch terminated at the AlAs layer, which was subsequently removed in HF. For the HBT structure, n-GaAs emitter contacts were AuGeNi annealed at 415°C. Emitter mesas (1x10<sup>-5</sup> cm<sup>2</sup>) and base mesas (5x10<sup>-5</sup> cm<sup>2</sup>) were defined via wet etching in H<sub>3</sub>PO<sub>4</sub>:H<sub>2</sub>O<sub>2</sub>:H<sub>2</sub>O. For the diode structures, larger p-GaAs mesas (100x100μm<sup>2</sup>) were wet-etched. For both the diode and HBT device structures, p-GaAs contacts were ZnAu and n-GaN contacts were AlAu.

## DISCUSSION

Figures 4 and 5 display the common-emitter current-voltage characteristic and Gummel plot. The output current density is a modest but encouraging ~100A/cm<sup>2</sup>. The low V<sub>CE</sub> offset (1V) indicates low parasitic resistance. The offset can be further decreased by annealing the base contacts. Most prominently, the current gain is less than one, and it is important to understand the major limitations of the current gain.

Wafer fusion has proven to be effective in forming a number of heterogeneous devices from lattice-mismatched materials. These devices include GaAs-InP vertical-cavity<sup>8</sup> and microdisk<sup>9</sup> lasers, InGaAs-Si photodetectors,<sup>10</sup> and InGaAsP-AlGaAs photonic crystal lasers<sup>11</sup>. However, the device demonstrated here places stringent demands on the electronic quality of the fused interface, as it serves also as the base-collector junction of an HBT. Uncontrolled bond reconstruction or residual impurities at the fused interface can produce electronic traps, which in turn may produce the less than unity common-emitter current gain observed in these devices. Aside from the issue of bond reconstruction at the fused interface, the elevated temperature of the fusion process (750°C) may itself accelerate dopant and defect diffusion, degrading the entire material structure. We note that the fusion temperature is much higher than the growth temperature of the AlGaAs-GaAs materials (585°C). Fusion at lower temperatures should mitigate the effects of defect and dopant diffusion. Additionally, reduced dopant diffusion

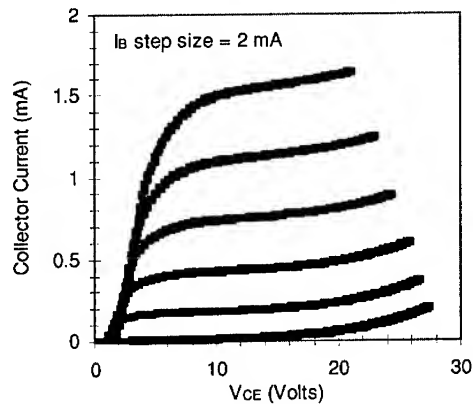


Figure 4. Room-temperature common-emitter current-voltage characteristic for the wafer-fused n-AlGaAs/p-GaAs/n-GaN HBT.

would allow a thinner base, which should reduce base recombination and improve current gain. (In this initial study the p-GaAs base was designed to be thick enough to prevent complete dopant compensation, as dopants cross-diffused across the emitter-base and base-collector interfaces during the high-temperature fusion process.) Our work with wafer-fused GaAs-GaN diodes (Figure 6) suggests that a dramatically reduced temperature (500°C) should still be sufficient in fusing a mechanically stable, electronically active base-collector junction in future HBTs.

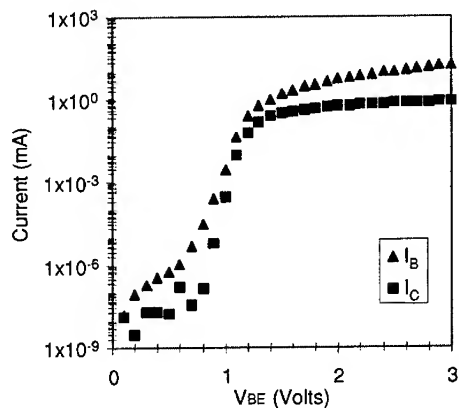


Figure 5. Room-temperature Gummel plot for the wafer-fused n-AlGaAs/p-GaAs/n-GaN HBT.

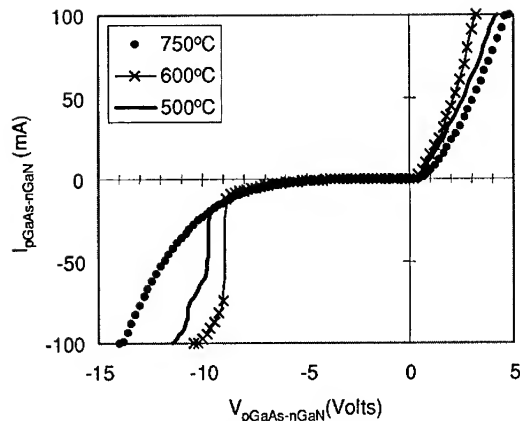


Figure 6. Room-temperature current-voltage characteristic of the p-GaAs/n-GaN diode, wafer-fused over a wide range of systematically varied fusion temperatures (500-750°C).

Moreover, the true GaAs-GaN band gap offset is unknown. It may be that the GaAs-GaN heterojunction (regardless of any fusion-induced conduction band barriers) has a natural barrier or spike in the conduction band, which would also limit collector current and hence current gain. In future work, our HBT will include a setback layer at the base-collector junction. The setback should shift the fused GaAs-GaN interface slightly into the collector, decreasing the barrier prior to the possible spike at the fused GaAs-GaN junction, potentially improving collector current.

## CONCLUSIONS

This study demonstrated the first n-AlGaAs/p-GaAs/n-GaN HBT, in which the lattice-mismatched GaAs-GaN junction was achieved via wafer fusion. The devices displayed low  $V_{CE}$  offset, with a less-than-unity common-emitter current gain. This initial attempt at a wafer-fused HBT provided promising results, with expected improvements in future investigations as we introduce a base-collector setback layer, decrease fusion temperature, and utilize a thinner base. Our work with wafer-fused p-GaAs/n-GaN diodes suggests that the fusion temperature could be reduced to 500°C, which should mitigate detrimental diffusion effects in future HBTs. We believe that these experiments will provide much insight into the applicability of wafer fusion for electronically active, lattice-mismatched heterojunctions, especially involving GaN.

## ACKNOWLEDGMENTS

This work was supported by the DoD Multidisciplinary University Research Initiative (MURI) program administered by the Office of Naval Research under Grant N00014-98-1-0654.

Transmission electron microscopy studies were done in collaboration with Jacek Jasinski and Zuzanna Liliental-Weber at Lawrence Berkeley National Laboratory in Berkeley, California.

## REFERENCES

- <sup>1</sup> H. Xing, S. Keller, Y.-F. Wu, L. McCarthy, I.P. Smorchkova, D. Buttari, R. Coffie, D.S. Green, G. Parish, S. Heikman, L. Shen, N. Zhang, J.J. Xu, B.P. Keller, S.P. DenBaars, and U.K. Mishra, *Journal of Physics: Condensed Matter*, **13** (32), 7139-57 (2001).
- <sup>2</sup> S.-Y. Chiu, A.F.M. Anwar, and S. Wu, *Mater. Res. Soc. GaN and Related Alloys Symposium*, G6.7/6, 1028 (1999).
- <sup>3</sup> J.T. Torvik, M. Leksono, J.I. Pankove, and B. Van Broeck, *Mater. Res. Soc. Internet Journal of Nitride Semiconductor Research*, vol.4S1, (1999).
- <sup>4</sup> S. Yoshida and J. Suzuki, *Japanese Journal of Appl. Phys.* **38** (8A), L851-3 (1999).
- <sup>5</sup> J. Han, A.G. Baca, R.J. Shul, C.G. Willison, L. Zhang, F. Ren, A.P. Zhang, G.T. Dang, S.M. Donovan, X.A. Cao, H. Cho, K.B. Jung, C.R. Abernathy, S.J. Pearton, and R.G. Wilson, *Appl. Phys. Lett.*, **74** (18), 2702-4 (1999).
- <sup>6</sup> Y. Zhang, C. Cai, and P. Ruden, *J. Appl. Phys.* **88**, 1067-72 (2000).
- <sup>7</sup> J. Jasinski, Z. Liliental-Weber, S. Estrada, and E. Hu, *Appl. Phys. Lett.*, **81** (17), 3152-4 (2002).
- <sup>8</sup> J. Piprek, A. Black, P. Abraham, E.L. Hu, and J.E. Bowers, *Conference on Lasers and Electro-Optics Technical Digest (IEEE Cat. No.99CH37013)*, 458-9 (1999).
- <sup>9</sup> D.S. Song, J.K. Hwang, C.K. Kim, I.Y. Han, D.H. Jang, and Y.H. Lee, *IEEE Photonics Technology Lett.*, **12** (8), 954-6 (2000).
- <sup>10</sup> Y.-H. Lo, Y. Kang, P. Mages, P. Yu, J.-H. Baek, Y. Zhou, Z.H. Zhu, *International Conference on Indium Phosphide and Related Materials Proceedings (Cat. No.00CH37107)*, p.497 (2000).
- <sup>11</sup> J.K. Hwang, H.Y. Ryu, D.S. Song, I.Y. Han, H.K. Park, D.H. Jang, and Y.H. Lee, *IEEE Photonics Technology Lett.* **12** (10), 1295-7 (2000).

## AUTHOR INDEX

- Abernathy, C.R., 285, 767  
 Adelman, C., 91, 519  
 Adivarahan, Vinod, 475, 487, 493  
 Akasaki, I., 27, 609  
 Alam, A., 527  
 Alexandrov, Dimitar, 671  
 Ali, G.N., 381  
 Aliberti, K., 349  
 Allerman, A.A., 15, 115, 597  
 Allums, K.K., 285, 767  
 Amano, H., 27, 609  
 Ambacher, O., 279, 361  
 Antunes, Helder, 773  
 Aoki, M., 201  
 Araki, Tsutomu, 163, 169, 719  
 Armitage, R., 603  
 As, D.J., 337  
 Ashby, C.I.H., 15, 115  
 Auner, Gregory W., 701, 725  
 Awaah, M.A., 813  
 Aytur, Orhan, 511  
  
 Baca, A.G., 597  
 Bailey, J.S., 181  
 Baines, Marcus Q., 41  
 Balmer, R.S., 555, 801  
 Ban, Tomoyuki, 469  
 Barcz, A., 807  
 Bardwell, Jennifer A., 549, 567  
 Barjon, J., 369  
 Batchelor, Dale, 615  
 Bates, Simon, 543  
 Beaumont, B., 109  
 Bechstedt, F., 361  
 Bell, A., 27  
 Bellet-Amalric, E., 305, 369  
 Benyoucef, M., 109  
 Bhattacharyya, A., 133, 449  
 Birkhahn, Ronald, 779, 833  
 Biyikli, Necmi, 511  
 Bliss, D.F., 181  
 Boemare, C., 61  
 Bogdanov, M.V., 187  
 Bouhafs, B., 713  
 Bousquet, V., 109  
 Boyall, Nicholas M., 677, 683  
  
 Brandes, George R., 207, 773  
 Brault, J., 91, 369  
 Breese, M.B.H., 731  
 Briggs, R.D., 597  
 Brown, April S., 9, 659  
 Brown, J.D., 3  
 Brown, P.D., 801  
 Bu, Gang, 455  
 Bulashevich, Kirill A., 387  
 Bumgarner, J., 323  
 Bunker, Kristin L., 615  
 Butcher, K. Scott A., 267, 707  
  
 Calleja, E., 157  
 Campbell, Joe C., 499  
 Carlson, E., 323  
 Cartwright, Alexander N., 375, 659, 665, 689  
 Carver, Alexander, 9  
 Castaldini, A., 743  
 Cauffman, Nathan, 779  
 Cavallini, A., 743  
 Chai, B.H., 299, 331  
 Chang, Y.C., 323  
 Chen, C.Q., 193, 299, 331, 439  
 Chen, Fei, 659, 665, 689  
 Chen, Jun, 237  
 Chen, Jyh Chia, 427  
 Chen, L., 201, 755  
 Chen, T.C., 97  
 Chen, Y.F., 783  
 Cherns, David, 27, 41, 609  
 Cheung, Maurice, 659  
 Chierchia, R., 255  
 Chitnis, Ashay, 475, 487, 493  
 Cho, Hyung Koun, 825  
 Choi, H.K., 427  
 Choi, H.W., 433, 731  
 Choi, Jin Ho, 499  
 Chou, M.M.C., 299, 331  
 Chowdhury, Uttiya, 499, 833  
 Chu, George, 97  
 Chua, S.J., 731  
 Cimalla, V., 361  
 Ciplys, Daumantas, 455  
 Claflin, B.B., 749

---

Clarke, Frederick W., 561  
 Coldren, Larry, 845  
 Collazo, Ramón, 591  
 Collins, Charles J., 349, 499  
 Cuomo, J.J., 323  
  
 Dalmasso, S., 411, 647  
 Dalmau, R.F., 187  
 Damilano, Benjamin, 343, 393  
 Danylyuk, Yuri, 725  
 Das, K., 813  
 Daudin, B., 91, 305, 369, 519  
 Davis, Robert F., 121, 255, 381, 591, 819  
 Davydov, Albert V., 695  
 Dawson, M.D., 433  
 Demchuk, Alexander, 79, 543  
 DenBaars, Steven P., 695, 845  
 Deng, Jianyu, 455, 561  
 Denyszyn, Jonathan C., 499  
 Dietrich, M., 417  
 DiMaio, Jeffrey R., 819  
 Dion, Joe A., 773  
 DiSalvo, F.J., 201  
 Dluzewski, P., 393  
 Dmitriev, Vladimir A., 629, 695  
 Doolittle, W. Alan, 9, 375, 659  
 Doppalapudi, Dharanipal, 621  
 Downes, James E., 621  
 Dridi, Z., 713  
 Dupuis, Russell D., 499, 833  
 Durose, Ken, 677, 683  
 Dwikusuma, F., 67  
 Dynowska, E., 807  
  
 Eastman, Lester F., 317  
 Ecke, G., 361  
 Eddy, C.R., 449  
 Edwards, P.R., 433  
 Eickhoff, M., 279  
 Einfeldt, S., 121, 255  
 Enjalbert, F., 305, 369  
 Estrada, Sarah, 845  
 Evstratov, Igor Yu., 387  
  
 Fan, John C.C., 427  
 Fan, Z.Y., 567  
 Fang, Z.-Q., 749  
 Fay, M.W., 801  
 Fedyunin, Y., 349  
 Feenstra, R.M., 293  
 Feick, H., 603  
 Feng, Z.C., 405  
 Fenner, D.B., 97  
 Ferguson, I., 405  
 Flynn, Jeffrey S., 773  
 Follstaedt, D.M., 15, 115  
 Fox, A., 527  
 Fox, Kenneth, 427  
 Fukasawa, Yoshimichi, 795  
 Furis, Madalina, 375, 659, 689  
 Furthmüller, J., 361  
  
 Gaevski, M.E., 299, 331  
 Gainer, G.H., 231  
 Gallagher, J.J., 299, 331  
 Garcia, R., 157  
 Garrett, G.A., 349  
 Gaska, Remis, 193, 439, 455, 561  
 Gaskill, D.K., 249, 273  
 Gehrke, Thomas, 3  
 Gibart, P., 109  
 Gil, Bernard, 343, 653  
 Gila, B.P., 285, 767  
 Glembocki, O.J., 249, 273  
 Gobsch, G., 279  
 Gogneau, N., 305, 369, 519  
 Golaszewska, K., 807  
 Goldhahn, R., 279, 361  
 Gonzalez, Juan Carlos, 615  
 Goto, S., 839  
 Gotthold, David, 779, 833  
 Grandjean, Nicolas, 343, 393  
 Gregie, Joel M., 355  
 Grepstad, Jostein K., 461  
 Guggenheim, Paul J., 219  
 Guo, S.P., 405  
  
 Haddad, Daad B., 701, 725  
 Hall, H.P., 813  
 Han, Bing, 355  
 Han, J.H., 575

Hang, D.R., 783  
 Hangleiter, A., 21  
 Harrison, I., 801  
 Hasegawa, Hideki, 47  
 Hashizume, Tamotsu, 47  
 He, L., 635  
 Henderson, Walter, 9, 375  
 Henry, R.L., 127, 249, 749, 819  
 Hermann, M., 279  
 Heuken, M., 527  
 Hill, D.W., 299, 331  
 Hilton, K.P., 555, 801  
 Hitzel, F., 21  
 Ho, Fat Duen, 561  
 Hoffman, C.B., 201  
 Hofmann, Frank, 543  
 Hofsäss, H., 417  
 Hommel, D., 255  
 Hon, Schang-Jing, 427  
 Honaga, Misako, 311  
 Honda, Tohru, 445  
 Hori, Y., 305  
 Hsu, Julia W.P., 41  
 Hu, Evelyn, 845  
 Hu, G.X., 85  
 Hu, X., 439  
 Huang, C.F., 783  
 Huang, D., 635, 641  
 Hughes, B.T., 801  
 Hull, Brett A., 833  
 Huntington, Andrew, 845  
 Hutchins, Edward L., 207, 773  
  
 Iga, Kenichi, 445  
 Ikeda, M., 839  
 Ilegems, Marc, 225  
 Ingram, David C., 73  
 Iqbal, M. Zafar, 635  
 Ishida, Koichi, 175  
 ISOLDE Collaboration, 417  
 Itoh, Y., 423  
 Iwamura, Y., 399  
 Iyer, Sandeep, 133  
  
 Jakiela, R., 807  
 Jalabert, D., 305, 369, 519  
  
 Jasinski, J., 243, 575  
 Javorka, P., 527  
 Je, J.H., 789  
 Jeon, C.W., 433  
 Jiang, H.X., 567  
 Johnson, M.A.L., 481  
 Jundt, Dieter, 9  
  
 Kalliakos, S., 653  
 Kaminska, E., 807  
 Kang, H., 405  
 Kanie, Hisashi, 261  
 Karmalkar, S., 561  
 Karpov, Sergey Yu., 187, 225, 387  
 Kawanishi, Hideo, 445  
 Keller, Stacia, 695  
 Khan, A., 193, 439  
 Khan, M. Asif, 299, 331, 475, 487, 493, 561  
 Khartchenko, A., 337  
 Khattak, Chandra P., 219  
 Kikawa, J., 423  
 Kim, C.C., 789  
 Kim, J., 285  
 Kimukin, Ibrahim, 511  
 Kimura, Ryuhei, 175  
 Kitamura, K., 169  
 Kobayashi, Naoki, 469, 537  
 Köhler, U., 337  
 Kolbas, R.M., 323  
 Koleske, Daniel D., 15, 115, 127, 249, 597, 749, 819  
 Koley, Goutam, 375  
 Kondratyev, Alexey V., 225  
 Koplit, Brent, 79  
 Kordos, P., 527  
 Kovalenkov, O.V., 231  
 Koyama, Fumio, 445  
 Koynov, S., 61  
 Kret, S., 393  
 Kröger, R., 255  
 Kuball, M., 109, 493, 555  
 Kudo, Yoshihiro, 163  
 Kudryashov, V.E., 647  
 Kuech, T.F., 67  
 Kulik, A.V., 187

- Kumah, A., 813  
 Kuokstis, E., 193, 299, 331, 439  
 Kurtz, S.R., 597  
 Kvit, A., 151  
  
 Lam, Simon K.H., 267  
 Lamarre, P., 449  
 Lambers, E., 767  
 Lapointe, Jean, 549  
 Lee, C.D., 293  
 Lee, J., 737  
 Lefebvre, Pierre, 343, 653  
 Leroux, M., 647  
 Li, Hongwei, 103  
 Li, J., 567  
 Li, J.M., 85  
 Li, Jiang, 145  
 Liliental-Weber, Z., 121, 243, 575  
 Lim, J., 603  
 Lin, J.Y., 567  
 Lin, L.Y., 85  
 Link, A., 279  
 Linthicum, Kevin J., 3  
 Lischka, K., 337  
 Liu, H.X., 85, 201, 381  
 Liu, R., 27, 609  
 Liu, Ying, 549, 567  
 Long, J.P., 481  
 Look, David C., 317, 575, 749  
 Lu, Hai, 317, 361  
 Ludwig Jr., K., 133  
 Luo, B., 767  
 Lymperakis, L., 91, 293  
 Lynch, Michael, 79  
 Lynch, Richard J., 505  
  
 Maciejewski, G., 393  
 Maeda, Narihiko, 537  
 Makarov, Yuri N., 187, 225, 387  
 Malcarne, Joseph A., 207  
 Mamiya, H., 169  
 Mandavilli, Vasavi, 475  
 Manfra, Michael J., 41  
 Marso, M., 527  
 Martin, Denis, 225  
 Martin, R.W., 411, 433  
  
 Martin, T., 555, 801  
 Maruska, H.P., 299, 331  
 Massies, Jean, 343  
 Mastro, M.M., 231  
 Matlock, D., 819  
 Matsunami, Hiroyuki, 139, 311  
 McCullen, Eric, 725  
 McGuinness, Cormac, 621  
 Melo, L., 61  
 Menoni, Carmen, 213  
 Mikhov, M.K., 381  
 Mishra, Umesh K., 279, 695, 845  
 Missert, N.A., 15, 115  
 Mitchell, C.C., 15, 115  
 Miura, Kouhei, 311  
 Miyajima, Takao, 163  
 Mizuo, Kazuhiro, 163, 719  
 Mkhoyan, Karen A., 375  
 Mohnney, Suzanne E., 833  
 Moldovan, G., 801  
 Molina, S.I., 157  
 Molnar, Richard J., 317, 629  
 Monroy, E., 305, 369, 519  
 Monteiro, T., 61  
 Morel, Aurelien, 343  
 Morkoç, H., 243, 629, 635, 641  
 Morris, R.S., 449  
 Motlan, 707  
 Moustakas, Theodore D., 97, 133,  
     349, 449, 621  
 Mula, G., 91  
 Munns, Gordon, 543  
 Murray, Robert T., 505  
 Muth, J.F., 323  
 Myers, T.H., 749  
  
 Naik, Ratna, 701, 725  
 Naik, V.M., 701  
 Nakamura, Tohru, 795  
 Nakamura, Tomonori, 795  
 Nakanishi, Y., 411  
 Namkoong, Gon, 9, 659  
 Nanishi, Yasushi, 163, 169, 719  
 Narayan, J., 151, 427  
 Nemanich, R.J., 323  
 Neugebauer, J., 91, 293

---

Nicol, D., 405  
 Niehus, M., 61  
 Nishi, Yusuke, 311  
 Nishida, Toshio, 469  
 Noguchi, Takuma, 163  
 Northrup, J.E., 293  
 Nouet, Gérard, 237  
 Nussbaum, Peter, 543  
  
 O'Donnell, K.P., 411  
 Okado, Hiroaki, 261  
 O'Keefe, M.A., 243  
 Olson, Dan, 543  
 Olson, Don, 543  
 Onojima, Norio, 139, 311  
 Onstine, A.H., 285, 767  
 Osinsky, A.V., 375  
 Osipowicz, T., 731  
 Ozbay, Ekmel, 511  
  
 Pacheco, F.J., 157  
 Pachipulusu, Radhika, 475  
 Palle, K.C., 201, 381  
 Parbrook, Peter J., 505  
 Park, Minseo, 323  
 Park, S.S., 575  
 Pearton, S.J., 285, 767  
 Pearton, S.W., 273  
 Pechnikov, A.I., 231  
 Peres, Boris, 249, 405, 779  
 Pettersen, Sverre V., 461  
 Piner, Edwin L., 3  
 Piotrowska, A., 807  
 Piotrowski, T.T., 807  
 Polenta, L., 743  
 Ponce, F.A., 27, 609  
 Pophristic, Milan, 405, 833  
 Potthast, S., 337  
 Prince, K.E., 707  
 Prokes, S.M., 273  
 Provencio, P.P., 15, 115  
  
 Rajagopal, Pradeep, 3  
 Rajasingam, S., 555  
 Ramm, M.S., 187  
 Rana, M.A., 731  
  
 Rawdanowicz, T.A., 151  
 Reid, M.F., 417  
 Reitmeier, Z.J., 255, 381  
 Ren, F., 285, 767  
 RENiBEI Network, the, 411  
 Reshchikov, M.A., 629, 635, 641  
 Riedel, N., 21  
 Riedl, T., 21  
 Roberts, John C., 3  
 Robins, Lawrence H., 213, 695  
 Rogers, Henry H., 219  
 Rojo, J.C., 193, 439  
 Rolfe, Stephen J., 549  
 Romanov, Dmitri, 725  
 Rønnekleiv, Arne, 461  
 Ronning, C., 417  
 Rooth, Stig, 461  
 Roskowski, Amy M., 121, 591  
 Rossow, U., 21  
 Russell, Phillip E., 615  
 Ruterana, Pierre, 127, 157, 237, 393,  
     713, 789  
 Ryan, Philip, 621  
 Ryder, P., 255  
 Ryu, M.Y., 299  
  
 Saarinen, K., 575  
 Saito, Yoshiki, 163, 719  
 Saitoh, Tadashi, 537  
 Sakaguchi, Takahiro, 445  
 Salant, Allan D., 207  
 Sampath, A.V., 349, 449  
 Sanchez, A.M., 157, 393  
 Sanchez-Garcia, M.A., 157  
 Sanford, Norman A., 213, 695  
 Sanguino, P., 61  
 Sarua, A., 493, 555  
 Saulys, D., 67  
 Schaff, William J., 317, 361, 375, 689  
 Schetzina, J.F., 481  
 Schlessner, Raoul, 187, 591  
 Schmid, Frederick, 219  
 Schmid, Kurt, 219  
 Schowalter, L.J., 193, 439  
 Schwarz, R., 61  
 Schweigler, Veit, 461

- Segal, Alexander S., 225  
Semendy, F., 349, 813  
Semond, F., 157  
Shao, Y., 97  
Shapiro, Alexander J., 695  
Shapovalova, Y.V., 231  
Shatalov, Maxim, 475, 487, 493  
Shen, B., 783  
Shen, H., 349  
Shigemori, Atsushi, 175  
Shike, Junichi, 175  
Shin, Minseub, 543  
Shokhovets, S., 279, 361  
Shrestha, S.K., 707  
Shur, Michael S., 193, 439, 455, 561  
Si Dang, Le, 305, 369  
Sid'ko, Alexander P., 225  
Silcox, John, 375  
Simin, Grigory, 299, 331, 561  
Simpkins, Blake S., 35  
Simpson, Steven, 79  
Singh, R., 449  
Sitar, Z., 187, 591  
Sizelove, J.R., 575  
Skromme, B.J., 201, 381, 755  
Smirnov, Sergey A., 225  
Smith, David J., 133  
Smith, Kevin E., 621  
Smith, Maynard B., 219  
Smorchkova, I.P., 279  
Soares, M.J., 61  
Song, J.H., 299  
Soukhoveev, V.A., 231  
Speck, James S., 35, 279  
Spencer, N., 405  
Spiess, L., 361  
Stacey, W.F., 449  
Stark, Terrence J., 615  
Steiner, Bruce, 213  
Stodilka, D., 285  
Stonas, Andreas, 845  
Strom, Andy, 543  
Suda, Jun, 139, 311  
Sun, D.Z., 85  
Sun, Jie, 487  
Sun, W.H., 299, 331  
Sunkara, Mahendra K., 103  
Takahashi, Kiyoshi, 175  
Takehara, Hironari, 145  
Takeya, M., 839  
Talalaev, Roman A., 387  
Taliercio, Thierry, 343, 653  
Tamulaitis, G., 193, 439  
Tang, Haipeng, 549, 567  
Tansley, T.L., 707  
Tassev, V.L., 181  
Tawara, Takehiko, 537  
Thakur, J.S., 701  
Thoms, B.D., 737  
Timmers, H., 707  
Tomiya, S., 839  
Trifan, Eugen M., 73  
Tsubaki, Kotaro, 537  
Tsvetkov, Denis V., 231, 629, 695  
Turkin, A.N., 647  
Tut, Turgut, 511  
Twigg, M.E., 127  
Tybell, Thomas, 461  
Tzeng, S.Y., 603  
Ulmer, Melville P., 355  
Uren, M.J., 493, 555, 801  
Usikov, A., 231  
Vaudo, Robert P., 207  
Vennegues, P., 157  
Vetter, U., 417  
Wada, Takahiro, 145  
Wagner, Volker, 225  
Wakahara, A., 411  
Wallace, Leah G., 773  
Waltereit, Patrick, 35  
Walukiewicz, Wladek, 317  
Wang, H., 151, 427  
Wang, J.X., 85  
Wang, S.Q., 761  
Wang, S.-Q., 181  
Wang, X.L., 85  
Wang, Y.Q., 609  
Washburn, J., 243

---

Watson, Ian M., 677, 683  
Watt, F., 731  
Webb, James B., 549, 567  
Weber, E.R., 603  
Weeks, T. Warren, 3  
Wenger, L.E., 701  
Wessels, Bruce W., 355  
Weyburne, D., 181  
Whitehead, Malcolm A., 505  
Wickenden, Alma E., 127, 249, 749,  
819  
Wintrebert-Fouquet, Marie, 267, 707  
Wojtowicz, T., 127  
Wolter, M., 527  
Wong, Michael M., 499  
Wraback, M., 349  
Wrzesinska, H., 807  
Wu, Hong, 375, 689  
Wu, J., 317  
Wu, Shuai, 475, 487  
  
Xing, Huili, 845  
Xu, Xueping, 207  
  
Yamaguchi, S., 399  
  
Yamaguchi, Tomohiro, 163, 719  
Yamamoto, A., 399  
Yamane, H., 201  
Yang, Bo, 499  
Yang, Gye Mo, 825  
Yang, J.W., 193, 299, 331, 439, 561  
Yang, Qing, 603  
Yang, Y., 737  
Ye, H.Q., 761  
Ye, Jinlin, 427  
Yilmaz, I., 193, 439  
Yoshida, A., 411  
Yoshida, Seikoh, 145, 423, 779  
Yoshimura, Takaya, 261  
Yu, Edward T., 35  
Yu, P.W., 299  
Yunovich, A.E., 647  
  
Zakharov, D.N., 121, 243  
Zeng, Y.P., 85  
Zenneck, J., 417  
Zhang, Jian Ping, 475, 487, 493  
Zhu, Ting Gang, 499  
Zimina, Darya V., 225  
Zvanut, M.E., 819

## SUBJECT INDEX

- absorption, 707
- activation, 819
- AlGaInN, 305
- AlGaN, 21, 27, 369, 469, 475, 493, 511, 543, 597, 695, 825, 833
  - HFET, 779
- AlGaN/GaN, 549
  - HFET, 3
  - MOSHFET, 567
- AlN, 139, 689
- aluminum
  - gallium nitride, 255, 481, 773, 801
  - nitride, 187, 417, 439, 455, 591
- amorphous substrates, 103
- atomic force microscopy, 505
- automotive, 779
- bandgap, 701
- breakdown voltage, 567
- buffer layer, 3, 73
- bulk
  - aluminum nitride, 193
  - crystal growth, 187
- cantilever epitaxy, 15, 115
- carbon, 603
- cathodoluminescence, 213, 261, 337, 677, 683
- clusters, 79
- contact(s), 813, 833
  - resistivity, 795
- crystal growth, 219
- cubic, 169
  - gallium nitride, 175
  - GaN/AlGaN MQWs, 337
- deep
  - level transient spectroscopy, 743
  - ultraviolet emitter, 439
- defect(s), 115, 839
- delta doping, 567, 773
- deuterium, 737
- dielectric, 285
  - function, 279, 361
- diffusion length, 261, 337
- dislocation, 35
  - core, 243
  - structure, 41, 609
- DX center, 355
- elastic recoil detection analysis, 707
- electrical properties, 527
- electroabsorption, 665
- electroluminescent device, 445
- electron
  - beam induced current, 615
  - energy distributions, 591
  - localization, 725
  - paramagnetic resonance, 819
- electroreflectance, 279, 597
- ellipsometry, 361
- ELOG, 27
- energy
  - band, 761
  - bandgaps, 713
- epitaxial lateral overgrown GaN, 109
- epitaxy, 73
- ESD, 737
- etching, 267
- europium, 411
- extended defects, 157
- femtosecond pump-probe
  - spectroscopy, 665
- field-effect transistor, 537
- finite element analysis, 109
- flip-chip, 487
- freestanding, 299
- GaAs, 807
- gallium nitride (GaN), 15, 21, 35, 47, 61, 67, 79, 85, 103, 115, 121, 133, 145, 169, 193, 207, 213, 225, 231, 237, 249, 273, 279, 285, 293, 299, 311, 323, 349, 355, 375, 411, 423, 427, 433, 445, 449, 455, 461, 493, 505, 519, 527, 537, 575, 603, 609, 629, 635, 641, 647, 653, 689, 695, 731,

gallium nitride (GaN), (continued)  
 737, 743, 755, 767, 795,  
 807, 813, 819, 839, 845  
 and AlGaN, 405  
 early stages of growth, 73  
 growth, 97  
 nucleation, 127  
 on Si, 3  
 stoichiometry, 41  
 GaN/AlGaN MQWs, 133  
 GaNP, 423  
 gate current modeling, 561

halide vapor phase epitaxy, 181, 225  
 Hall, 773  
   effect, 575  
 HEMT, 249, 527, 767  
 heterojunction, 449  
 HFET, 47, 543, 555, 597  
 high-power, 537  
 high temperature nitridation, 67  
 homoepitaxy, 349  
 6H-SiC (11-20), 139  
 HVPE, 207, 231, 243  
 hydrogen etching, 381

ICP etching, 273  
 illumination-induced metastability,  
   749  
 implantation, 423  
 impurities, 201  
 In composition fluctuations, 393  
 InAlGaN, 493  
 indium  
   gallium nitride, 261, 621, 659,  
     671  
     LED, 615  
   nitride, 163, 361, 701, 707  
 InGa<sub>N</sub>, 343, 387, 665, 677, 683  
 InN, 317, 719  
 insulated gate leakage current, 561  
 inversion domain(s), 157  
   boundary, 825  
 ion implantation, 417, 755  
 iron, 207

irradiation, 743

laser  
   MBE, 151  
   photolysis, 79  
 lateral growth, 21  
 lattice relaxation, 311  
 LED, 427, 469, 493  
   arrays, 433  
 light emitting diode, 475, 481, 487,  
   493  
 lithium  
   gallate, 659  
   niobate, 9  
 luminescence, 411, 647

magnesium oxide, 285  
 magnetotransport, 783  
 MBE, 243, 293, 305, 369  
 MESFET, 145  
 metalorganic  
   chemical vapor deposition, 381  
   vapor phase epitaxy, 505  
 Mg, 839  
   incorporation, 27  
 micro-LEDs, 433  
 mobility, 85  
 MOCVD, 499, 543, 779  
 modeling, 187  
 molecular beam epitaxy, 163, 175,  
   311, 317, 375, 445  
 MOVPE, 387  
 M-plane, 293, 299  
 multiple quantum wells, 375

nanostructures, 725  
 nitridation, 61  
 nitride(s)(-), 181, 267, 399, 783  
   based multiple quantum wells,  
     331  
   semiconductor(s), 127, 157, 393,  
     713, 789  
 nitrogen gas cluster ion beam, 97  
 nonlinear optics, 653  
 [11-20] nonpolar direction, 133

numerical simulation, 225  
 ohmic contact(s), 801, 807  
 optical  
     and electrical properties, 267  
     characterization, 201, 323  
     properties, 695, 725  
     transmittance and reflectance, 701  
 oxynitride, 399  
 P type ohmic contact, 789  
 palladium ohmic contact, 789  
 passivation, 549, 767  
 pendeo epitaxy, 121  
 periodically poled, 9  
 photodetector, 499  
 photoluminescence, 193, 331, 355, 439, 575, 629, 635, 641, 659, 755  
 photoreflectance, 249, 273  
 plane-wave pseudopotential, 761  
 PLD, 61  
 polarity, 85  
 polarization effects, 331  
 polishing damage, 213  
 potential energy calculation, 237  
 pressure coefficients, 713  
 quantitative HRTEM, 393  
 quantum  
     dot, 519  
     well, 343, 653  
 quaternaire, 305  
 Raman, 109, 555  
     spectroscopy, temperature, 493  
 rectifying, 719  
 relaxation, 519  
 Rutherford backscattering  
     spectrometry, 731  
 sapphire  
     etching, 67  
     nitridation, 97  
     plane, 127  
     substrate, 219  
 scanning  
     electron microscopy, 615  
     Kelvin probe, 35  
 Schottky photodiode, 511  
 segregation, 387  
 self assembly, 103  
 semi-insulating, 603  
     GaN, 749  
 Si, 145, 719  
 SiC, 449  
 silicon  
     carbide, 381  
     substrate, 163  
 SIMS, 773  
 single crystal growth, 201  
 slicing, 219  
 soft x-ray  
     absorption, 621  
     emission, 621  
 solar-blind, 499, 511  
 space charge limited current, 813  
 sputtering, 323, 813  
 subband, 783  
 subpicosecond luminescence, 349  
 surface, 635, 641  
     acoustic waves (SAW), 455, 461  
     state, 47  
 surfactant, 369  
 TCF, 461  
 TEM, 41, 677, 683, 825  
 temperature, 555  
 template, 231  
 thermal decomposition, 731  
 thermally  
     stable, 807  
     stimulated current spectroscopy, 749  
 thermopower, 399  
 thickness variation, 427  
 threading dislocations, 15  
 III-nitride, 9, 317  
 III-V semiconductors, 761  
 thulium, 417  
 Ti/Al, 795

---

tilt grain boundary, 237  
time-resolved  
    photoluminescence, 343  
    spectroscopy, 689  
TiO<sub>2</sub>, 169  
transistor, 549  
transmission electron microscopy,  
    121, 255, 609, 801  
tunnel radiation, 647  
  
ultraviolet, 469, 475, 481, 487  
UV, 493  
  
velocity overshoot, 591  
voids, 243  
  
wafer  
    bonding, 845  
    fusion, 845  
wavelength dispersive x-ray, 411  
Williamson-Hall plot, 405  
wurtzite  
    AlN, 151  
    GaN, 151  
  
x-ray diffraction, 139, 175, 255  
XRD, 405  
  
Zn, 629